Advances in Sustainability Science and Technology

Gayadhar Panda
R. T. Naayagi
Sukumar Mishra *Editors*

Sustainable Energy and Technological Advancements

Proceedings of ISSETA 2021

KES International

Springer

Advances in Sustainability Science and Technology

The book series aims at bringing together valuable and novel scientific contributions that address the critical issues of renewable energy, sustainable building, sustainable manufacturing, and other sustainability science and technology topics that have an impact in this diverse and fast-changing research community in academia and industry.

The areas to be covered are

- Climate change and mitigation, atmospheric carbon reduction, global warming
- Sustainability science, sustainability technologies
- Sustainable building technologies
- Intelligent buildings
- Sustainable energy generation
- Combined heat and power and district heating systems
- Control and optimization of renewable energy systems
- Smart grids and micro grids, local energy markets
- Smart cities, smart buildings, smart districts, smart countryside
- Energy and environmental assessment in buildings and cities
- Sustainable design, innovation and services
- Sustainable manufacturing processes and technology
- Sustainable manufacturing systems and enterprises
- Decision support for sustainability
- Micro/nanomachining, microelectromechanical machines (MEMS)
- Sustainable transport, smart vehicles and smart roads
- Information technology and artificial intelligence applied to sustainability
- Big data and data analytics applied to sustainability
- Sustainable food production, sustainable horticulture and agriculture
- Sustainability of air, water and other natural resources
- Sustainability policy, shaping the future, the triple bottom line, the circular economy

High quality content is an essential feature for all book proposals accepted for the series. It is expected that editors of all accepted volumes will ensure that contributions are subjected to an appropriate level of reviewing process and adhere to KES quality principles.

The series will include monographs, edited volumes, and selected proceedings.

More information about this series at https://link.springer.com/bookseries/16477

Gayadhar Panda · R. T. Naayagi · Sukumar Mishra
Editors

Sustainable Energy and Technological Advancements

Proceedings of ISSETA 2021

Springer

Editors
Gayadhar Panda
Department of Electrical Engineering
National Institute of Technology Meghalaya
Shillong, India

R. T. Naayagi
School of Electrical and Electronic Engineering
Newcastle University
Singapore, Singapore

Sukumar Mishra
Department of Electrical Engineering
Indian Institute of Technology Delhi
New Delhi, India

ISSN 2662-6829 ISSN 2662-6837 (electronic)
Advances in Sustainability Science and Technology
ISBN 978-981-16-9032-7 ISBN 978-981-16-9033-4 (eBook)
https://doi.org/10.1007/978-981-16-9033-4

This Springer imprint is published by the registered company Springer Nature Singapore Pte Ltd.
The registered company address is: 152 Beach Road, #21-01/04 Gateway East, Singapore 189721, Singapore

Committee Members

Patron

B. B. Biswal, Director, NIT Meghalaya, India

General Chairs

Sukumar Mishra, IIT Delhi, India
Gayadhar Panda, NIT Meghalaya, India

Technical Program Committee Chairs

Chandan K. Chanda, IIEST Shibpur, India
R. T. Naayagi, Newcastle University, Singapore

Organizing Chairs

Sanjoy Debbarma, NIT Meghalaya, India
Shaik Affijulla, NIT Meghalaya, India

Advisory Board

Akhtar Kalam, Victoria University, Australia
Akshay Kumar Saha, University of KwaZulu-Natal, South Africa
Akshya Kumar Swain, University of Auckland, New Zealand
Alessandro Lo Schiavo, Università degli Studi della Campania, Italy
Antonio J. Marques Cardoso, University of Beira Interior, Portugal
Arindam Ghosh, Curtin University, Australia
Bhim Singh, IIT Delhi, India
Bidyadhar Subudhi, IIT Goa, India
Chem Nayar, Curtin University, Australia
Chiara Boccaletti, Sapienza University of Rome, Italy
Francois Vallée, University of Mons, Belgium
Hassan Haes Alhelou, University College Dublin, Ireland
J. P. Pandey, MMMUT Gorakhpur, India
Jose Luis Rueda Torres, TU Delft, The Netherlands
Jose Rodriguez, Andrés Bello National University, Chile
Pawan Sharma, UiT The Arctic University of Norway, Norway
Pierluigi Siano, University of Salerno, Italy
Ramesh Bansal, University of Sharjah, UAE
Robert J Howlett, KES International Research, UK
Sanjeevikumar Padmanaban, Aarhus University, Denmark
Shunbo Lei, University of Michigan, Ann Arbor
Sivaji Chakravorti, Jadavpur University, India
Suryanarayana Doolla, IIT Bombay, India
Sushil Chauhan, NIT Hamirpur, India
T. Sudhakar Babu, CBIT Hyderabad
Tarlochan S. Sidhu, Ontario Tech University, Canada
Yam Siwakoti, University of Technology, Australia
Venkata Yaramasu, Northern Arizona University, USA
Vijander Singh, NSUT Delhi, India

Technical Program Committee

Ahmet Mete VURAL, Gaziantep University, Turkey
Amalendu Patnaik, IIT Roorkee, India
Anurekha Nayak, DRIEMS Group of Institutions, India
Arun Kumar Verma, MNIT Jaipur, India
Arup Kumar Goswami, NIT Silchar, India
Ashok Kumar Pradhan, IIT Kharagpur, India
Ashok Ranjan Bhoi, IFCAL, India
B. Chitti Babu, IIITDM Kancheepuram, India

B Rajanarayan Prusty, VIT Vellore, India
Bibhu Prasad Panigrahi, IGIT Sarang, India
Ch. V. Rama Rao, NIT Meghalaya, India
Debashisha Jena, NIT Surathkal, India
Gulshan Sharma, Durban University of Technology, South Africa
Jahangir Hossain, University of Technology, Australia
Kailash Chandra Ray, IIT Patna, India
Mohammad Amin, NTNU, Norway
Moushumi Patowary, JEC Assam, India
N. Kumaresan, NIT Tiruchirappalli, India
Nutan Saha, VSSUT Burla, India
P. Rangababu, NIT Meghalaya, India
Parveen Poon Terang, JSSATE Noida, India
Prakash Kumar Ray, CET Bhubaneswar, India
Pratap Sekhar Puhan, SNIST Hyderabad, India
Pravat Kumar Ray, NIT Rourkela, India
Praveen Tripathy, IIT Guwahati, India
Priyabrat Garanayak, IIIT Una, India
Puja Dash, GVPCE Visakhapatnam, India
Ranjan Kumar Behera, IIT Patna, India
Ranjan Kumar Mallick, SOA University, India
Ritula Thakur, NITTTR Chandigarh, India
Sampath Kumar V., JSSATE Noida, India
Sanjiba Kumar Bisoyi, JSSATE Noida, India
Satyabrata Sahoo, NMREC Hyderabad, India
Satyendra Singh Yadav, NIT Meghalaya, India
Shubhrata Gupta, NIT Raipur, India
Smitha Joyce Pinto, MIT Mysore, India
Subrata Banerjee, NIT Durgapur, India
Surmila Thokchom, NIT Meghalaya, India
Sushree Diptimayee Swain, O. P. Jindal University, India
Sze Sing Lee, Newcastle University, Singapore
Trapti Jain, IIT Indore, India
Umashankar Subramaniam, Prince Sultan University, Riyadh, Saudi Arabia
V. Sandeep, NIT Andhra Pradesh, India
Vahid Hosseinnezhad, University College Cork, Ireland

Steering Committee

Anup Dandapat, NIT Meghalaya, India
Ayon Bhattacharjee, NIT Meghalaya, India
Comingstarful Marthong, NIT Meghalaya, India
Deba Kumar Sarma, NIT Meghalaya, India

Diptendu Sinha Roy, NIT Meghalaya, India
Gitish K. Dutta, NIT Meghalaya, India
Harish Chandra Das, NIT Meghalaya, India
Paonam Sudeep Mangang, NIT Meghalaya, India
Paresh Nath Chatterjee, NIT Meghalaya, India
Rabindra Narayan Mahapatra, NIT Meghalaya, India
Saikat Mukherjee, NIT Meghalaya, India

Publication Chairs

Atanu Banerjee, NIT Meghalaya, India
Piyush Pratap Singh, NIT Meghalaya, India

Finance Chairs

Shaik Affijulla, NIT Meghalaya, India
Ksh Milan Singh, NIT Meghalaya, India

Industry Liaison Chairs

Rakesh Roy, NIT Meghalaya, India
Ramyani Chakrabarty, NIT Meghalaya, India
Supriyo Das, NIT Meghalaya, India

Student Committee

Kaibalya Prasad Panda, NIT Meghalaya, India
Narendra Babu P., NIT Meghalaya, India
Pratikanta Mishra, NIT Meghalaya, India
Satyavarta Kumar Prince, NIT Meghalaya, India

Preface

This volume contains the papers presented at the 1st International Symposium on Sustainable Energy and Technological Advancements (ISSETA 2021), which is being organized by the Department of Electrical Engineering, National Institute of Technology Meghalaya, on September 24 and 25, 2021.

This symposium was mainly focused to provide a common forum to the practicing engineers, academicians and researchers to discuss various issues and its future direction in the field of sustainable energy developments. The different tracks in the symposium mainly focus on sustainable energy, power technologies and computing.

This diverse resource on renewable and sustainable energy technologies highlights the challenges and advancements in areas such as photovoltaic system, wind energy integration, hydroelectricity, biomass, geothermal, wave and tidal energy applications. These sources of energy are reusable within a human life without environmental damage. Therefore, all over the world policies and regulations are being set up for sustainable energy consumption, generation and distribution. In addition to this, these energy resources play a key role in the integration and operation of future smart microgrid systems. Smart microgrid systems are a better way of utilizing renewable power and reducing the usage of fossil fuels. Due to the intermittent nature of renewable sources, usage of energy storage becomes mandatory to supply high quality and continuous power to the utility grid/loads. Cyber-attack in grid-tied converters is another major issue that affects system stability, confidentiality and optimal operation and in extreme case the overall system may lead to a shutdown. Therefore, precise detection and mitigation of cyber-attacks become very critical. Machine learning and IoT-based approaches are recent emerging communication techniques that are used to combat cyber-attacks. Many such factors play a major role in monitoring, control and energy management in smart microgrid systems. Considering all these technological advancements this volume is designed to serve as reference material for students, researchers, manufacturers and professionals working in these fields. The topics covered are the cutting-edge research involved in sustainable energy technologies, smart building technology, integration and application of multiple energy sources; advanced power converter topologies and their modulation techniques; and information and communication technologies for smart microgrids.

We all have experienced a very challenging time due to the prevailing COVID pandemic situation. With the safety and well-being of our participants as our top priority, ISSETA 2021 was organized through hybrid mode (both online and offline modes).The response to the initial call for paper was overwhelming with more than 150 papers submitted from across India/globe. After a rigorous review of all the papers by at least three expert reviewers each, only about 50% of papers were accepted for presentation. Apart from this, several keynote talks, panel discussions and technical sessions were also included in ISSETA 2021.

We would like to thank all ISSETA 2021 advisory board members, and steering and student committee members for their constant support. We are grateful to all the authors, invited speakers and distinguished panelists for their participation and contribution in respect of sharing their intellectual/technical experiences. We also acknowledge the support of our technical and financial sponsors.

We are thankful to Springer Publication House for agreeing to publish the accepted papers in the Book Series "Advances in Sustainability Science and Technology."

Shillong, India — Prof. Gayadhar Panda
Singapore — Dr. R. T. Naayagi
New Delhi, India — Prof. Sukumar Mishra

List of Reviewers

Abhilash Sen
Abhisekh Anand
Abhishek Chauhan
Abhishek Kuanar
Abhinav Saxena
Adnan Iqbal
Aishwarya Jogul
Akhila Mohan
Alok Kumar Dubey
Amarnath Yalavarthi
Amit Kumar
Amrit Preetam
Angad Lenka
Ankita Panda
Anwesha Pattnaik
Arabinda Mahakur
Aratipamula Bhanuchandar
Arup Ghosh
Aswani Singh
Avigyan Roy
Avinash Kumar
Avipsa Lall
Ayan Dutta
B Rajanarayan Prusty
Babita Panda
Bhabani Kumari Choudhury
Bibechita Khatoi
Bibhu Prasad Ganthia
Bichitra Sethi
Biresh Dakua
Bishnu Sahu

Bishnu Sethi
Bishnupriya Biswal
Biswanath Dekaraja
Ch. Pooja
Chandan Chanda
Chitti Babu B.
Darshan Borthakur
Debanjan Mukherjee
Debashis Pattnaik
Debasish Behera
Debesh Tripathy
Debidasi Mohanty
Deblina Maity
Deepak Kumar
Dheeraj Dhaked
Dipanjan Bose
Dishashree T. N.
Divya S. Nair
E. Sankararao
Edapha Rhema
Geethanjali N.
Gnana Swathika
Gourab Bhuyan
Gyanchand Sahu
Haricharan Nannam
Harshitha N.
Himadri Bhattacharyya
Ishan Bhand
Jithin S.
Jogi Vijay Kumar
Jyoti Barik
Kaibalya Prasad Panda
Kavyasree Masarapu
Kodari Raj Kumar
Lokesh C.
Madan Kumar Das
Makam Nikitha
Malay Ranjan Khuntia
Manoj Pattnaik
Manoj Deokate
Mayank Singh
Mohammad Karkun
Mohan Pangi
Mondeep Mazumdar
Moushumi Patowary

Mukul Chankaya
Murali Sai
Nageswara Rao
Narendra Babu P.
Nihar Pradhan
Niraj Singh
Nirakar Pradhan
P. ArunMozhi Devan
Parusharamulu Buduma
Parveen Poon Terang
Piklu Das
Piyush Pratap Singh
Prabhat Ranjan Bana
Pradyumna Behera
Pradyumna Sahani
Pragnyashree Ray
Prakash Das
Prakash Gupta
Pranjal Barman
Pratap Sekhar Puhan
Pratikanta Mishra
Pravat K. Ray
Priyabrat Garanayak
Priyanka Sorte
Priyanka Sen
Pushpendra Singh
R. Shivarudraswamy
Raghavendran S.
Rahul S.
Rahul K. A.
Rahul Choudhary
Raja Gandhi
Rajen Pudur
Ramesh Naidu
Ravi Ranjan
Ravi Majji
Ravi Kumar
Ravikanth Mallajoshula
Robin Wilson
Rudrani Pattnaik
Rupam Chaki
Rupashree Sethi
S. Ravichandran
Sadasiva Behera
Saikat Das

Sailakshmi Cherry
Sairam Reddy
Sakshi Tyagi
Samprati Mohanty
Sandeep Kumar Chawrasia
Sangeeta Sahu
Sangita Dash
Santanu Dash
Sasmita Behera
Satabdi Bastia
Satabdy Jena
Satyabrata Sahoo
Satyavarta K. Prince
Savitha Pandurangi
Sayan Kuila
Shajith Ali
Shilpashree S.
Shivam Kumar Yadav
Shobhit Nandkeolyar
Shuyu Cao
Siddhartha Deb Roy
Siddhi Marathe
Smita Sahoo
Sneha S.
Snehashis Ghoshal
Somila Hashunao
Sonali Badpanda
Sonali Acharya
Soudamini Behera
Soumyakanta Samantaray
Sreyasee Rout
Srikant Beura
Subhankar Roy
Subhasish Deb
Sumathi M. S.
Sushanta Gogoi
Sushree Swain
Sushree Pattanaik
Susmita Bhattacharjee
Swarnankur Ghosh
Swathi Krishna
Syeda Samreen
Usharani Raut
VandanaJha
Vartika Pandey

Vulisi Narendra Kumar
Wasmir C.
Yamini Krishna
Yatindra Gopal

Contents

1 Impact of Reverse Power Flow Due to High Solar PV Penetration on Distribution Protection System 1
Divya S. Nair and T. Rajeev

2 Modeling and Performance Evaluation of MPPT-Based PMSG Wind Energy Conversion System with Boost Converter in MATLAB/Simulink Environment 15
Snehashis Ghoshal, Sumit Banerjee, and Chandan Kumar Chanda

3 Optimal Scheduling of Grid Connected PV System with Battery Energy Storage 29
Swathi Krishna and R. M. Shereef

4 Seven-Level Switched-Capacitor-Based Inverter Topology with Reduced Components for Renewable Energy System 43
Priyanka Sen, Vandana Jha, and Ashwin Kumar Sahoo

5 Reference Tracking by Designing State Estimation Observer for Generalized Predictive Control of a Single Inductor Dual Output Buck Converter 53
Kamakshi Manjari and Somanath Majhi

6 Different Oscillator-Controlled Parallel Three-Phase Inverters in Stand-Alone Microgrid 67
Vikash Gurugubelli, Arnab Ghosh, and Anup Kumar Panda

7 Generalized Hybrid Symmetrical and Asymmetrical Multilevel Inverter Topology with Reduced Number of Switches 81
Madan Kumar Das, Parusharamulu Buduma, Perwez Alam, and Sukumar Mishra

8 A New Reduced Device Count of Three-Phase Three-Level Switched Capacitor-Based Grid-Connected Inverter with LCL Filter 95
Aratipamula Bhanuchandar and Bhagwan K. Murthy

9 Reduction in Harmonics for PV-Based Reduced Device Count Multilevel Inverter Wıth Genetic Algorithm 105
Yatindra Gopal, Kaibalya Prasad Panda, Y. N. Vijay Kumar, and G. V. Pradeep

10 Design and Implementation of 165 W Current-Fed Push–Pull Converter for Military and Space Applications 121
T. N. Dishashree, A. Usha, G. Kubendran, Bhoopendra Kumar Singh, and Vinod Chippalkatti

11 A New Single-Phase Five-Level Self-balanced and Boosting Grid-Connected Switched Capacitor Inverter with LCL Filter 135
Aratipamula Bhanuchandar and Bhagwan K. Murthy

12 Comparative Analysis of Different Control Techniques Implementation in UPQC for Power Quality Improvement 147
Pravat Kumar Ray, Pratap Sekhar Puhan, Arun K. Das, D. Pradhan, and L. Meher

13 Design and Implementation of a Control for Solar PV Fed Unified Power Quality Conditioner 163
Akhila Mohan and T. Samina

14 Power Quality Improvement in Distribution Network Using PV Integrated DSTATCOM 181
Pallavi Kumari, P. Narendra Babu, Kaibalya Prasad Panda, Sanjiba Kumar Bisoyi, and Gayadhar Panda

15 Instantaneous Reactive Combined Loss Componenet Power Theory-Based Hybrid Filter for Power Quality Improvement in Distribution System 195
Pratap Sekhar Puhan, Santanu Kumar Dash, Pravat Kumar Ray, Gayadhar Panda, and Manidra Pothauri

16 Space Vector Pulse Width Modulation-Based DSTATCOM for Harmonic Compensation 209
Pushpanjali Shadangi, Sushree Diptimayee Swain, and Gayadhar Panda

17 PV-Fed DC Link Voltage Control Techniques Implementation in Shunt Active Filter 221
Padiyar Dharani Deepika and Pratap Sekhar Puhan

18 Detection and Classification of Transmission Line Faults Using ANN 233
Parveen Poon Terang, Sanjiba Kr Bisoyi, Chitra Ranjan, Aviral Krishna, Aysuh Raman Rai, and Anushka Singh

19 A DWT-RNN-Assisted Intelligent Differential Protection Scheme for Grid-Tied and Islanded DC Microgrid 247
Satyavarta Kumar Prince, Shaik Affijulla, and Gayadhar Panda

20 Application of Differential Evolution to Determine Single-Stage Impulse Circuit Parameters 259
G. Ramarao, B. Hari Krishna, D. Rajesh, A. Ravikumar, and B. Rakesh

21 Frequency Control of GWO-Optimized Two-Area Microgrid with TIDF-II, I-PD and I-TD 267
Sourabh Prakash Roy, Shubham, A. K. Singh, R. K. Mehta, and O. P. Roy

22 A Review on Control Methods Used in Renewable Energy Source-Fed Induction Motors 279
Pranobjyoti Lahon, Aditya Bihar Kandali, Gayadhar Panda, and Moushumi Patowary

23 Solar PV-Powered SRM Drive and Its Speed Control and Torque Ripple Minimization 293
Nutan Saha, Subham Kumar Sahoo, Bidyadhar Rout, Sidhartha Panda, Gayadhar Panda, and Dillip Ku. Sahoo

24 A Linear Quadratic Integral Regulator for a Variable Speed Wind Turbine 307
N. V. A. Ravikumar, Vasupalli Manoj, and N. S. S. Ramakrishna

25 Output Power Tracking and Oscillation Control of a Doubly Fed Induction Generator-Based Wind Energy Conversion System Using Adaptive Neuro-Fuzzy Algorithm 321
Satyabrata Sahoo and Gayadhar Panda

26 Demand Response Management in a Smart Grid with Multiple Users and Utility Companies 339
Pravat Kumar Ray, Shobhit Nandkeolyar, and Nikhil Sai Rama Valiveti

27 Combined Environmental and Economic Dispatch in the Presence of Sustainable Sources Using Particle Swarm Optimization with Adaptive Weighted Delay Velocity 353
Soudamini Behera, Namrata Naik, Sasmita Behera, and Ajit Kumar Barisal

28 Performance Analysis of Controlled Vehicle-To-Grid Charging in 30 Bus Power System for Electric Vehicle 369
Gourab Bhuyan and Bani Kanta Talukdar

29 Automatic Generation Control for Hybrid Power System in Deregulated Environment 381
Parusharamulu Buduma, Madan Kumar Das, Ashwani Kumar Sharma, Gayadhar Panda, and Sukumar Mishra

30 Control of Grid-Connected Photovoltaic System Using Enhanced PLL (EPLL) Technique 395
Pravat Kumar Ray, Pratap Sekhar Puhan, and Ashish Kumar

31 Voltage- and Current-Based Hysteresis Controller-Fed Series Active Filter to Compensate Voltage Sag Problem 411
Ravikanth Mallajoshula and I. E. S. Naidu

32 Comparative Analysis of Fuzzy Logic and Synchronous Reference Frame Controlled LVRT Capability Enhancement in Wind Energy System Using DVR and STATCOM 423
Subash Ranjan Kabat, Chinmoy Kumar Panigrahi, and Bibhu Prasad Ganthia

33 Genetic Algorithm-Based Load Frequency Control of a Grid-Connected Microgrid in Presence of Electric Vehicles 435
Krosuru Anuradhika and Puja Dash

34 Multi-area Load Frequency Control Using a Novel PID-Based Sliding Mode Controller 449
Shobhit Nandkeolyar and Pravat Kumar Ray

35 An EPO Tuned Cascaded 3DOFPIDN-FFOPID Controller for Frequency Regulation in DGR-FACTs Integrated Power System 465
Sunita Pahadasingh, Chitralekha Jena, Chinmoy Kumar Panigrahi, and Subhashree Priyadarshini

36 Modified Particle Swarm Optimized Load Frequency Control of Renewable Energy Sources-Based Integrated Power Systems 483
Ashutosh Jena, Bidyadhar Rout, and Nutan Saha

37 Load Frequency Control of a Four-Area Interconnected Power System Using JAYA Tuned PID Controller and Derivative Filter 497
Smrutisikha Jena, Sthitprajna Mishra, Bibhu Prasad Ganthia, and Sidhartha Kumar Samal

38 Model Predictive Control for Load Frequency Regulation in Power Systems Using a Disturbance Observer 513
Nuvvula S. S. Ramakrishna, Tummala S. L. V. Ayyarao, Vasupalli Manoj, and L. Dinesh

39 Design and Development of a Novel Reverse Polarity Tester for EV Application 525
K. A. Rahul, T. Rajeev, and P. Sreejaya

40 Design of an EV Charging System with Improved Performance 541
Sanjiba Kumar Bisoyi, Parveen P. Terang, Luv Pathak, Abhinav Kumar Singh, Sarthak Singh, and Rishabh Khare

41 Cell Balancing and State of Charge Estimation of Lithium-Ion Cells for Electric Vehicle Applications 559
S. Shilpashree and R. S. Geetha

42 Modelling and Analysis of an Electronic Differential-Based Traction Control System for Distributed Drive Electric Vehicle 575
Pranjal Barman and Sushanta Bordoloi

43 Analysis of Five-Phase Surface PMSM for Application in Electric Vehicles 587
Sangeeta Sahu, Byamakesh Nayak, and Rudra Narayan Dash

44 A Novel Application of BESO-Based Isolated Micro-grid with Electric Vehicle 597
Shubham, Sourabh Prakash Roy, R. K. Mehta, A. K. Singh, and O. P. Roy

45 Frequency Control of SPV/Wind/Biogas/Biodiesel-Based Microgrid Using Fuzzy-Aided PID Controllers 611
Arabinda Mahakur and Debidasi Mohanty

46 Planning of Power Loss and Fuel Cost Minimization by Deployment of DERs Using Evolutionary Algorithm 625
Deblina Maity, Sumit Banerjee, and Chandan Kumar Chanda

47 Investigation on Stability of DC Microgrid for Large-scale Electric Vehicle Charging Station Deployment 637
S. Jithin and T. Rajeev

48 Designing of DC Microgrid with Fast Charging Converter and Control for Solar PV, Fuel Cell and Battery-Integrated Charging Station 647
Dheeraj Kumar Dhaked, Mayank Singh, and Dinesh Birla

49 Location Estimation of Grid Electric Vehicle Aggregator in the Grid System Using Optimization Technique 661
Pravat Kumar Ray, Pratap Sekhar Puhan, and Premananda Sahoo

50 Power Management and Control in Microgrid System 675
Emmanuel Vemuri, Aman Kumar, Ifthakhar Mahmud Tonmoy, Kaibalya Prasad Panda, Satyavarta Kumar Prince, Babu P. Narendra, and Gayadhar Panda

51 A Survey of Cyber Security in Smart Microgrid 687
Zoaya Mohammadi, Smitha Joyce Pinto, Gayadhar Panda, and Surmila Thokchom

52 Data-Driven Event Detection with PMU Data Using a Novel Composite Deep Learning Technique 699
Pushpak Das, Subhash Kumar, Gayadhar Panda, and D. S. Roy

53 Prediction of Solar Power Using Linear Regression 709
Shubham Thombare, V. N. Pande, R. S. Kulkarni, and S. M. Kakade

54 Fuzzy Logic Controller for HVAC System of Passenger Car for Cooling Application 719
Pratik Ramu Bante, Archana G. Thosar, and S. Srikanth

55 Sustainable Farming Using Drone with Seed Dropper 733
Mohammad Suhel Karkun and Sathish Dharmalingam

56 Power System Parameter Estimation Using Signal Processing Techniques 747
Pratap Sekhar Puhan and Pravat Kumar Ray

57 Indoor PV-Based Power Management System for Connected Lighting and Shading Control 759
Anna Merine George, Ciji Pearl Kurian, C. Sravan, and Harsh Garg

58 Doppler Velocity Estimation Employing mHDFT Phase-Locked Loop 773
Abhishek Chauhan and Ksh. Milan Singh

59 Efficiency Optimization of Surface and De-centered PMSM with Silicon Steel and Amorphous Iron Materials for E-rickshaw 785
Anju P. Sivadas and V. P. Mini

60 Time Series Forecasting Model for Chaotic Fractional-Order Rössler System 799
Kishore Bingi, B Rajanarayan Prusty, Kaibalya Prasad Panda, and Gayadhar Panda

61 Application of Fractional-Order Signal Filtering Techniques for Dead-Time Process Plants 811
P. Arun Mozhi Devan, Fawnizu Azmadi Hussin, Rosdiazli Ibrahim, Kishore Bingi, and B Rajanarayan Prusty

62 A Variant of Rossler Type-IV Chaotic System with a Line of Equilibria and Coexisting Attractors 825
Rishabh Jaiswal, Himanshu Raj, Priye Ranjan Kumar, and Piyush Pratap Singh

63 New Performance Evaluation Metrics for Outlier Detection and Correction 837
B Rajanarayan Prusty, Nimish Jain, Kumar Gaurav Ranjan, Kishore Bingi, and Debashisha Jena

64 Time Series Decomposition Techniques for Renewable Generation Applications 847
Satyabrata Das, B Rajanarayan Prusty, Kishore Bingi, Kaibalya Prasad Panda, and Gayadhar Panda

Author Index 857

About the Editors

Prof. Gayadhar Panda received his Ph.D. degree from the Utkal University in 2007 in electrical engineering. He joined NIT Meghalaya as an Associate Professor in 2013. He is currently Professor in the Electrical Engineering Department, National Institute of Technology, Meghalaya, India. Dr. Panda has over 22 years of teaching and research experience. He has published more than 120 technical papers in national and international conferences proceedings/journals and filed 2 patents. He has supervised 7 Ph.D. students and currently supervising 4 Ph.D. Scholars. He is a recipient of the Power Medal, IE (India) for one of the research papers. He has led several research projects on the integration of renewable energy generation and power quality improvement. He is a Senior Member of IEEE, Fellow of IE, and Life Member of ISTE.

Dr. Panda is Associate Editor for IEEE Access, ITES, Wiley and also serves on the editorial board for the IJEEPS, De Gruyter and the technical/steering committees for several conferences. He has organized several technical events like IEEE Conference, Symposium, National Workshops, etc. He has delivered several invited Talks at various national and international events.

His current research interests include automatic generation control, stability improvements using flexible alternating current transmission system devices, power quality, power electronic converters, and distributed power generation. His work involves design, implementation, and operation of AC/DC microgrid with interfacing converters that use digital signal processing, artificial intelligence techniques and other novel control methods.

Dr. R. T. Naayagi received the bachelor's degree (Hons.) in electrical and electronics engineering from Bharathidasan University, Tiruchirappalli, India, in 2000, the master's degree in information technology from Alagappa University, Karaikudi, India, in 2003, the master's degree (Hons.) in power electronics and drives from Anna University, Chennai, India, in 2005, and the Ph.D. degree in electrical and electronic engineering from The University of Manchester, Manchester, UK, in 2010.

She held various roles as a Lecturer/Senior Lecturer/Professor in various institutions in India and UK, from 2000 to 2006 and from 2010 to 2014. She has been with

The Newcastle University in Singapore (NUiS), since 2014, where she is currently an Associate Professor in electrical power engineering, and also the Director of Education. Her research interests include renewable energy integration and applications in smart grid, power electronics for aerospace, electric vehicle applications, low carbon electrical energy systems, and power electronic solutions to sustainability. Dr. Naayagi is a Steering Committee Member of NU Women, UK, a member of the Diversity Working Group, Newcastle University, UK, and Equality and Diversity Champion for NUiS, and an Academic Lead for Athena SWAN Bronze Award application at Newcastle University. She is a Senior Fellow of the Higher Education Academy, UK. She has received several merit certificates for her academic proficiency, including the Best Outgoing Female Graduate Award during her bachelor's and the Outstanding Master's Student Award. She was the first recipient of the Dorothy Hodgkin Postgraduate Award from the School of Electrical and Electronic Engineering, University of Manchester, for her Ph.D., jointly sponsored by Rolls-Royce plc and the Engineering and Physical Sciences Research Council, UK. She received the Woman Engineer Award from the Young Professionals Section Chennai, Institution of Engineering and Technology (IET), UK, in 2012. She received the Newcastle University Teaching Award, in 2016. She is the Chair of NUiS women in science and engineering network and has been organizing many events to promote young professionals, especially young women in engineering and technology. She is an Associate Editor of the *CSEE Journal of Power and Energy Systems* and she has received Excellent Young Subject Editor Award in December 2020 from the journal. She serves as a Reviewer for the *IEEE*, *IET*, and many other international journals and conferences.

Prof. Sukumar Mishra received his M.Tech. and Ph.D. degrees in electrical engineering from the National Institute of Technology, Rourkela, in 1992 and 2000, respectively. After spending nine years as a lecturer at Sambalpur University (Orissa), Prof. Mishra joined BPUT (Orissa) as a Reader at the Electrical Department and served there for two years. Currently he is a Professor with the Indian Institute of Technology (IIT) Delhi and has been its part for the past 17 years, and has been functioning as Associate Dean R&D of IIT Delhi from March 2020.

He has won many accolades throughout his academic tenure of 27 years. He has been a recipient of Young Scientist Award (1999), INSA Medal for Young Scientist (2002), INAE Young Engineer Award (2002), INAE Silver Jubilee Young Engineer Award (2012), The Samanta Chandra Shekhar Award (2016), Bimal Bose Award (2019) and NASI-Reliance Platinum Jubilee Award (2019). He has been selected as the Mission Innovation National Champion (2019) under the Mission innovation initiative to accelerate clean energy in India. He has been granted fellowships from many prestigious technical societies like IET (UK), NASI (India), INAE (India), IETE (India), and IE (India) and is also recognized as the INAE Industry-Academic Distinguish Professor. Apart from all research and academic collaborations, Prof. Mishra is very actively involved in industrial collaborations. He is currently an ABB Chair Professor and has previously delegated as the NTPC, INAE and Power Grid Chair Professor. He has also served as an Independent Director of the Cross

Border Power Transmission Company Ltd., and the River Engineering Pvt. Ltd. Prof. Mishra has also carried out many important industrial consultations with TATA Power, Microtek and others.

He has so far authored more than 80 IEEE Transactions/Journals, 30 IET Journals and 30 other international journal papers. He has supervised 31 Ph.D. students (16 on goings), 40 Master students (2 ongoing). Prof. Mishra has also authored five book chapters so far and has 13 patents to his credit. His research interests include power systems, power quality studies, renewable energy, and smart grid. Prof. Mishra has been working in close association with the IEEE Delhi Section Executive Committee for past few years and is currently serving as an Editor for the *IEEE Transactions on Smart Grid*, *IEEE Transactions on Sustainable Energy* and was an Area Editor for the *IET Generation, Transmission and Distribution.*

Chapter 1
Impact of Reverse Power Flow Due to High Solar PV Penetration on Distribution Protection System

Divya S. Nair and T. Rajeev

Abstract The power generated locally exceeds the demand with the increase in solar PV penetration to the distribution grid, and reverse power flow will occur. As solar PV penetration increases, the reverse power flow and the short-circuit current level increase. Most of the distribution system protective devices are designed to carry unidirectional power flow. The reverse power flow will lead to voltage violation and protective device miscoordination. In this paper, the impact of renewable energy (PV) penetration on the current and power flows is analysed. An IEEE 33 bus system is taken for analysis, and the variation in short-circuit current level and power flows for different PV penetration rates is found out. Test systems are modelled in Python which is an open-source platform with machine learning and data analysis features. The results show that as PV penetration increases, the power flows will get altered and the short-circuit current level changes and hence the operation of protective devices will get affected.

Keywords Renewable energy (RE) · Photovoltaic (PV) · Distributed generation (DG) · Voltage stability index (VSI) · Reverse power flow (RPF)

1 Introduction

Increase in demand for electrical energy, high penetration of renewable energy sources and development of the decentralized systems has produced increase in the penetration of distributed generation (DG) into the power system. Distributed generation will improve the reliability and efficiency of the system along with reduction in transmission cost and CO_2 emission. However, it has some effects on power system like change in operation and control, change in configuration and protection scheme of network, etc. DG can be classified based on the mode of connection to grid. The main types are DGs that can be directly coupled and those connected via inverters. Among the DG that can be connected via inverter, the most significant ones are solar

D. S. Nair (✉) · T. Rajeev
College of Engineering Trivandrum, APJ Abdul Kalam Technological University, Thiruvananthapuram, Kerala, India

G. Panda et al. (eds.), *Sustainable Energy and Technological Advancements*, Advances in Sustainability Science and Technology,
https://doi.org/10.1007/978-981-16-9033-4_1

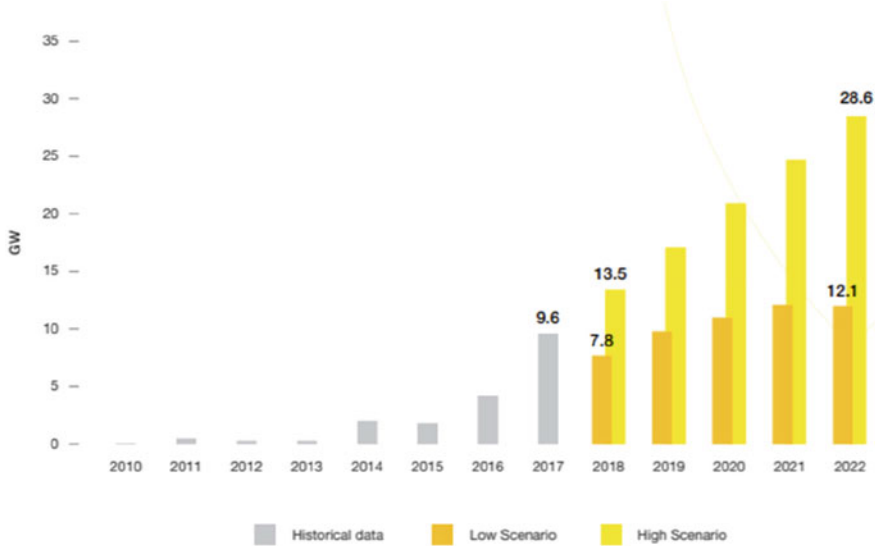

Fig. 1 Solar capacity addition in India

and wind. Solar is the fastest growing power generation source. The utilization of solar energy is dramatically growing due to its environmental-friendly, cost-effective and sustainable nature. As per the Solar Power Europe Report, 2019, Indian government has set out ambitious renewable energy targets in which solar plays a paramount role (Fig. 1). In 2015, Indian government set a RE target of 175 GW by 2022; i.e. it includes a net growth of 150 GW from the installed RE capacity. As per the target, the solar installed capacity was to reach 100 GW by 2022. Rooftop PV is targeted to contribute 40% of solar generation.

But the photovoltaic penetration has certain negative impacts on the system like voltage fluctuation, harmonics, system stability, fault current level, reverse power flow, etc. These impacts depend upon the position of the interconnection of PV units and the percentage of renewable energy penetration. The impact will be significant when the penetration is greater than 20%. The severity of challenges will increase with the increase in the level of penetration. The PV penetration rate can be represented by Eq. (1).

$$\mathrm{PV}_{\mathrm{Penetration}} = \frac{\mathrm{PV}_{\mathrm{pp}}}{S_{\mathrm{p}}} \tag{1}$$

where $\mathrm{PV}_{\mathrm{PP}}$ is the PV output power (peak value) and S_{P} is the load apparent power (peak value).

In a power system network, the main function of the protection system is to isolate the faulty part immediately. Overcurrent protection schemes are mainly employed in distribution system protection [1–3]. The coordination of main and backup overcurrent relays has to be arranged in such a way that if the fault is not cleared by primary or main relay then it should be backed by another relay. But with the introduction of distributed generations, there arise certain challenges to the existing schemes for protection. The intensity of these issues depends upon the type, size and location of the installed distributed energy source. Conventional protection schemes are designed for unidirectional current flows, but with the installation of DG units the current and power will flow in both directions and the existing relay system will fail to operate.

The possible solution for these issues is the usage of directional overcurrent relays that are able to discriminate between upstream and downstream current flows [4]. Another option is to reset the time multiplier settings (TMS) and plug multiplier settings (PMS) of relays after integration of each DG [4]. However, distribution system operators (DSOs) are not in favour of changing the relay settings or network configuration manually. So for proper coordination of relays, many efficient techniques like adaptive, non-adaptive, multi-agent, artificial intelligence (AI), hybrid, etc., are evolved.

In this paper, the impact of renewable energy (PV) penetration on the current and power flows is analysed. An IEEE 33 bus system is taken for analysis, and the variation in short-circuit current level and power flows for different PV penetration rates is found out. This paper indicates the possible research gaps and the necessity for developing a new intelligent and smart solution to cope with future challenges that will arise due to the increase in penetration of renewable energy sources.

2 Impact of High RE Penetration on the Protection System

High renewable energy penetration results in the increase in short-circuit current and reverse power flow which will cause miscoordination of protective equipment. To avoid this, directional elements are incorporated in overcurrent relays but the increased RE penetration will result in different short-circuit levels so that relay may trip when fault occurs but not able to locate the fault, or otherwise, relay will trip even when there is no fault. These conditions are called blinding of protection [5]. The installation of differential relays in the protection scheme would not be able to distinguish an overload from fault current, and also, the price of this implementation is highest. If the DG directly feeds a load and also has connected a line towards the principal grid equivalent, it is necessary to define correct selectivity criteria of the protection system for different scenarios. In a possible scenario of a fault in the line connected to the DG, the relay protection of the generator can view the fault, make the trip for and isolate the generator of the system.

This work analyses the impact of RE on reverse power flow and short-circuit level. First, the system without DG is modelled and the short-circuit level of the system and power flows are evaluated. Then, the contribution of DG to short-circuit current level and RPF is analysed. The impact of DG penetration level on RPF is analysed for different DG penetration levels. This includes the analysis of voltage and short-circuit current-level variations with and without DG. Then, the RPF at the distribution level facing an excess of production in the DG plant and constant demand in the distribution system is examined.

2.1 Optimal Placement of PV Considering Voltage Stability

The system stability and reliability depend upon the position of DG interconnection. Inappropriate selection of location and DG size will lead to a reduction in voltage stability and an increase in network losses. In this paper, the stability of the system is calculated using the voltage stability index (VSI). The VSI for a two bus system is obtained using Eq. (2) (Fig. 2)

$$\mathrm{VSI}_{\mathrm{B2}} = |V_{\mathrm{B1}}|^4 - 4\{P_{\mathrm{B2}} \cdot x_i - Q_{\mathrm{B2}} \cdot r_i\}^2 - 4\{P_{\mathrm{B2}} \cdot x_i + Q_{\mathrm{B2}} \cdot r_i\}|V_i|^2 \tag{2}$$

For a stable system, the voltage stability index of all buses will be greater than zero and less than one. The bus whose VSI is less will be the weak bus (i.e. more sensitive). Hence, the bus with the lowest VSI is more suitable for installing RE to improve system stability [6]. The connection or disconnection of DG will cause an increase or decrease in short-circuit current and reverse power flows, and changes will occur in the characteristic impedance of the system [7]. The reverse power flow occurs when the production of DG exceeds local load demand or when local demand reduces so that power flows in the opposite direction and causes abnormal performance of the protection system.

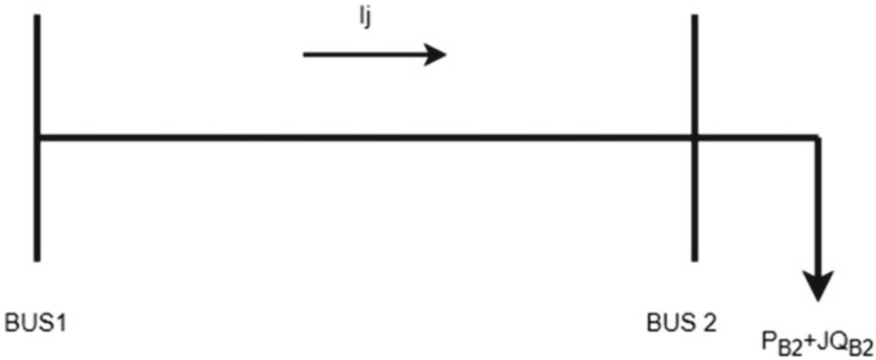

Fig. 2 Two bus system

2.2 Reverse Power Flow Effects in Protection Coordination

In this section, the effect of reverse power flow on the protection coordination scheme is analysed. RPF can be due to surplus production at the DG plant, failures produced in the system and instability in the network. Fault currents in a distribution system are determined and examined, with and without the inclusion of DG.

When the PV penetration increases, the level of fault currents will change. As the solar penetration to distribution system increases, the power generated locally might exceed the local load and it will result in reverse flow of power in line [8]. Most of the distribution system protective devices are designed to carry unidirectional power flow. So, the reverse power flow will lead to voltage violation and protective device miscoordination. The network protective device will prevent the reverse power flow by disconnecting the feeder so as to protect the transformers against upstream faults. When a large number of trips occur, the voltage will collapse even in low PV penetration levels [6]. The DG penetration may lead to false tripping; for example, when fault occurs on the adjacent feeder, it will cause current to flow in the reverse direction in a feeder where DG is installed. When this reverse current magnitude is greater than the relay setting, false tripping occurs.

2.3 Impact of Change in Fault Current Level on Protection Coordination

The setting of a protective device depends upon the fault current level. Hence, change in fault current level affects the coordination of protective devices. The fault current level depends upon the location of PV and distance to the fault location. The magnitude and profile of fault current drastically change with inverter-based distributed energy resource (DER) [9]. The protective devices are designed based on sequence components of synchronous machine equivalent circuit. The relays measure the negative sequence currents. In PV-injected circuit, the inverters will inject balanced currents so the negative sequence currents will be zero and hence protective devices will not work properly. The change in fault current from PV depends upon the voltage of the installed bus, PV location, the load connected to the buses, the impedance between fault and PV location, etc. [10].

Due to the increase in short-circuit level and reverse power flows, the main impact on protection system is relay desensitization, unintentional islanding, blinding of protection, line to ground over-voltage on utility side and miscoordination of protective devices [11].

3 Case Study and Test Scenarios

The simulation is done on an IEEE 33 bus system having 33 buses and 32 branches. The voltage level of the bus is 12.66 kV, and maximum and minimum voltage limits for all buses are considered at ±5%. The network is fed by a synchronous generator, while it is loaded from 3.715 MW and 2.3 MVar connected to thirty-two buses of different power factors [12]. The modelling of the system is done using Python [13]. It is an open-source software having large data analysis and machine learning features and strong support in the area of artificial intelligence. Load flow and short-circuit analysis are done with the help of library Pandapower. PV system is modelled using PVLIB Python. Using Pandapower, we can conduct power flow, optimal power flow, state estimation, topological graph searches and short-circuit calculations according to IEC 60909 [14]. PVLIB Python is a community-supported tool that provides a set of functions and classes for simulating the performance of photovoltaic energy systems [15]. The system line and load data are given in Table 1.

Analysis is conducted considering different positions of solar PV and variation in penetration level also. Position of solar PV is selected based on voltage stability index (VSI) (Table 2). Based on VSI, the buses are classified into weak, strong and neither weak nor strong. PVs are placed at weak buses (bus 18 and 33), strong bus (bus 19) and bus which is neither weak nor strong (bus 6). The study is conducted as different cases where the value of PV penetration will be varying from 12.5 to 40%. The variation in PV penetration and the allocation of PV to each bus are shown in Table 3.

4 Results and Discussion

4.1 Power Flow in 33 Bus System

As renewable energy penetration occurs, the power flow in the line changes. With the increase in penetration rate, the power generated locally exceeds the demand and reverse power flow will occur. This reverse power flow will affect the normal operation of the protection system. Reversed power flow will cause nuisance tripping, blinding of operation, etc. Initially, there was no renewable energy penetration in the system and then as the renewable energy penetration increases the power flow varies. When local generation exceeds, demand power will be fed back to the utility. This is illustrated in Fig. 3 where case 1 is with no RE penetration, case 3 is 12.5% penetration, case 7 is with 25% penetration and case 13 is with 40% penetration at bus 18. Bus 18 is considered as it is weak bus, and integration of renewable energy source at weak bus will improve the voltage stability.

The renewable energy penetration effect is tested for different scenarios where PV systems are integrated at weak bus, strong bus and bus which is neither weak nor strong. The variation in power flow for these cases is shown in Table 4.

Table 1 Line and load data of IEEE 33 bus distribution system

Branch No.	From bus	To bus	*R* (Ω)	*X* (Ω)	*P* (kW)	*Q* (kVAR)
1	1	2	0.0922	0.0477	100	60
2	2	3	0.493	0.2511	90	40
3	3	4	0.366	0.1864	120	80
4	4	5	0.3811	0.1941	60	30
5	5	6	0.819	0.707	60	20
6	6	7	0.1872	0.6188	200	100
7	7	8	1.7114	1.2351	200	100
8	8	9	1.03	0.74	60	20
9	9	10	1.04	0.74	60	20
10	10	11	0.1966	0.065	45	30
11	11	12	0.3744	0.1238	60	35
12	12	13	1.468	1.155	60	35
13	13	14	0.5416	0.7129	120	80
14	14	15	0.591	0.526	60	10
15	15	16	0.7463	0.545	60	20
16	16	17	1.289	1.721	60	20
17	17	18	0.732	0.574	90	40
18	2	19	0.164	0.1565	90	40
19	19	20	1.5042	1.3554	90	40
20	20	21	0.4095	0.4784	90	40
21	21	22	0.7089	0.9373	90	40
22	3	23	0.4512	0.3083	90	50
23	23	24	0.898	0.7091	420	200
24	24	25	0.896	0.7011	420	200
25	6	26	0.203	0.1034	60	25
26	26	27	0.2842	0.1447	60	25
27	27	28	1.059	0.9337	60	20
28	28	29	0.8042	0.7006	120	70
29	29	30	0.5075	0.2585	200	600
30	30	31	0.9744	0.963	150	70
31	31	32	0.3105	0.3619	210	100
32	32	33	0.341	0.5302	60	40

Table 2 Voltage stability index

Bus No.	VSI	Bus No.	VSI
2	1.00	18	0.69
3	0.99	19	0.99
4	0.93	20	0.98
5	0.90	21	0.97
6	0.88	22	0.97
7	0.81	23	0.93
8	0.79	24	0.91
9	0.78	25	0.88
10	0.76	26	0.81
11	0.74	27	0.79
12	0.74	28	0.78
13	0.73	29	0.74
14	0.72	30	0.71
15	0.71	31	0.70
16	0.71	32	0.69
17	0.70	33	0.69

Table 3 PV penetration and value of PV at each location

Case	Penetration rate	Bus at which PV is integrated and power in MW			
		Bus 6	Bus 18	Bus 33	Bus 19
1	No RE	0	0	0	0
2	12.5%	0.37	0	0	0
3		0	0.37	0	0
4		0	0	0.37	0
5		0	0	0	0.37
6	25.0%	0.74	0	0	0
7		0	0.74	0	0
8		0	0	0.74	0
9		0	0	0	0.74
10		0.37	0.37	0	0
11		0	0.37	0.37	0
12	40.0%	1.4	0	0	0
13		0	1.4	0	0
14		0	0	1.4	0
15		0	0	0	1.4

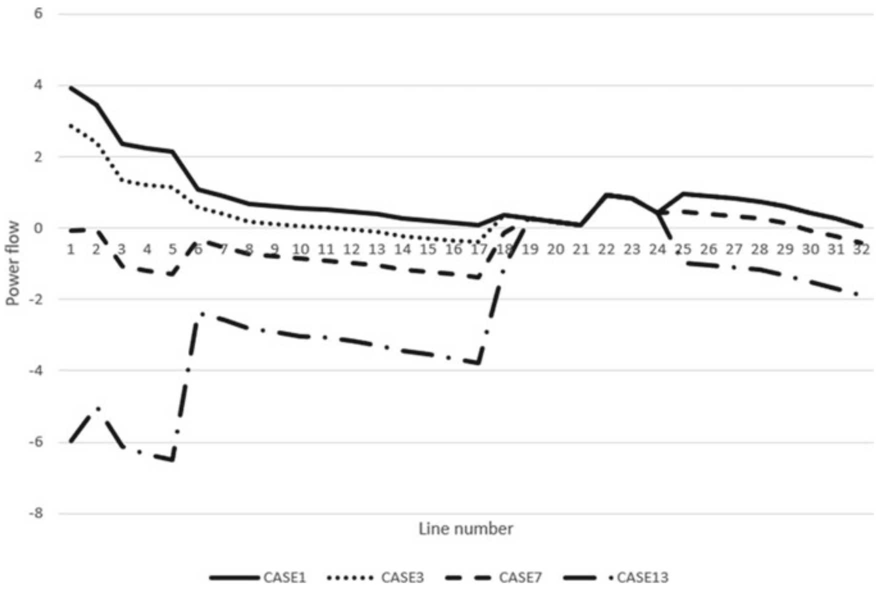

Fig. 3 Power flow in 33 bus system for different PV penetrations

The power flow in line 5 for various solar penetration rates is shown in Fig. 4; it is evident from the result that as PV penetration rate increases the power flow will also get changed. This will affect the initial setting of the protective relays as relays are designed for unidirectional flow of current, and hence, the coordinated operation of relays will get affected.

4.2 Short-Circuit Current on the 33 Bus System

For short-circuit analysis, the three-phase fault is created and short-circuit analysis is done to determine the value of short-circuit current. As RE penetration increases, the short-circuit current level increases. It will affect the entire protection system as the initial setting is dependent on the short-circuit value. Figure 5 shows the variation in short-circuit level for various RE penetrations. The short-circuit current level will increase up to 4 times as PV penetration increases by 40%. The operation of the protective device is primarily dependent upon the short-circuit current value; hence, maloperation of protective devices will be produced as PV penetration increases.

Table 4 Power flow in 33 bus system for different test cases

Line No.	Cases														
	1	2	3	4	5	6	7	8	9	10	11	12	13	14	15
1	3.9	3.4	2.9	2.3	1.9	0.9	−0.1	−1.0	−2.0	−2.8	−3.6	−5.0	−6.0	−7.1	−8.6
2	3.4	2.9	2.4	1.9	1.9	0.9	0.0	−1.0	−1.0	−1.8	−2.6	−4.0	−5.0	−6.1	−6.1
3	2.4	1.9	1.3	0.8	0.8	−0.2	−1.1	−2.0	−2.0	−2.9	−3.7	−5.1	−6.1	−7.3	−7.3
4	2.2	1.7	1.2	0.7	0.7	−0.3	−1.2	−2.1	−2.1	−3.0	−3.9	−5.3	−6.3	−7.6	−7.6
5	2.1	1.6	1.1	0.6	0.6	−0.4	−1.3	−2.2	−2.2	−3.1	−4.0	−5.4	−6.5	−7.8	−7.8
6	1.1	1.1	0.6	0.6	0.6	0.6	−0.3	−0.3	−0.3	−0.8	−1.2	−1.2	−2.4	−2.4	−2.4
7	0.9	0.9	0.4	0.4	0.4	0.4	−0.5	−0.5	−0.5	−1.0	−1.4	−1.4	−2.6	−2.6	−2.6
8	0.7	0.7	0.2	0.2	0.2	0.2	−0.7	−0.7	−0.7	−1.2	−1.6	−1.6	−2.8	−2.8	−2.8
9	0.6	0.6	0.1	0.1	0.1	0.1	−0.8	−0.8	−0.8	−1.2	−1.7	−1.7	−2.9	−2.9	−2.9
10	0.6	0.6	0.1	0.1	0.1	0.1	−0.9	−0.9	−0.9	−1.3	−1.8	−1.8	−3.0	−3.0	−3.0
11	0.5	0.5	0.0	0.0	0.0	0.0	−0.9	−0.9	−0.9	−1.4	−1.8	−1.8	−3.1	−3.1	−3.1
12	0.5	0.5	0.0	0.0	0.0	0.0	−1.0	−1.0	−1.0	−1.4	−1.9	−1.9	−3.2	−3.2	−3.2
13	0.4	0.4	−0.1	−0.1	−0.1	−0.1	−1.0	−1.0	−1.0	−1.5	−2.0	−2.0	−3.3	−3.3	−3.3
14	0.3	0.3	−0.2	−0.2	−0.2	−0.2	−1.2	−1.2	−1.2	−1.6	−2.1	−2.1	−3.4	−3.5	−3.5
15	0.2	0.2	−0.3	−0.3	−0.3	−0.3	−1.2	−1.2	−1.2	−1.7	−2.2	−2.2	−3.5	−3.5	−3.5
16	0.2	0.2	−0.3	−0.3	−0.3	−0.3	−1.3	−1.3	−1.3	−1.8	−2.2	−2.2	−3.6	−3.6	−3.6
17	0.1	0.1	−0.4	−0.4	−0.4	−0.4	−1.4	−1.4	−1.4	−1.9	−2.3	−2.3	−3.8	−3.8	−3.8
18	0.4	0.4	0.4	0.4	−0.1	−0.1	−0.1	−0.1	−1.1	−1.1	−1.1	−1.1	−1.1	−1.1	−2.6
19	0.3	0.3	0.3	0.3	0.3	0.3	0.3	0.3	0.3	0.3	0.3	0.3	0.3	0.3	0.3
20	0.2	0.2	0.2	0.2	0.2	0.2	0.2	0.2	0.2	0.2	0.2	0.2	0.2	0.2	0.2

(continued)

Table 4 (continued)

Line No.	Cases														
	1	2	3	4	5	6	7	8	9	10	11	12	13	14	15
21	0.1	0.1	0.1	0.1	0.1	0.1	0.1	0.1	0.1	0.1	0.1	0.1	0.1	0.1	0.1
22	0.9	0.9	0.9	0.9	0.9	0.9	0.9	0.9	0.9	0.9	0.9	0.9	0.9	0.9	0.9
23	0.8	0.8	0.8	0.8	0.8	0.8	0.8	0.8	0.8	0.8	0.8	0.8	0.8	0.8	0.8
24	0.4	0.4	0.4	0.4	0.4	0.4	0.4	0.4	0.4	0.4	0.4	0.4	0.4	0.4	0.4
25	1.0	1.0	1.0	0.4	0.4	0.4	0.4	−0.5	−0.5	−0.5	−1.0	−1.0	−1.0	−2.3	−2.3
26	0.9	0.9	0.9	0.4	0.4	0.4	0.4	−0.6	−0.6	−0.6	−1.0	−1.0	−1.0	−2.4	−2.4
27	0.8	0.8	0.8	0.3	0.3	0.3	0.3	−0.6	−0.6	−0.6	−1.1	−1.1	−1.1	−2.5	−2.5
28	0.8	0.8	0.8	0.3	0.3	0.3	0.3	−0.7	−0.7	−0.7	−1.2	−1.2	−1.2	−2.6	−2.6
29	0.6	0.6	0.6	0.1	0.1	0.1	0.1	−0.8	−0.8	−0.8	−1.3	−1.3	−1.3	−2.7	−2.7
30	0.4	0.4	0.4	−0.1	−0.1	−0.1	−0.1	−1.0	−1.0	−1.0	−1.5	−1.5	−1.5	−2.9	−2.9
31	0.3	0.3	0.3	−0.2	−0.2	−0.2	−0.2	−1.2	−1.2	−1.2	−1.7	−1.7	−1.7	−3.1	−3.1
32	0.1	0.1	0.1	−0.4	−0.4	−0.4	−0.4	−1.4	−1.4	−1.4	−1.9	−1.9	−1.9	−3.4	−3.4

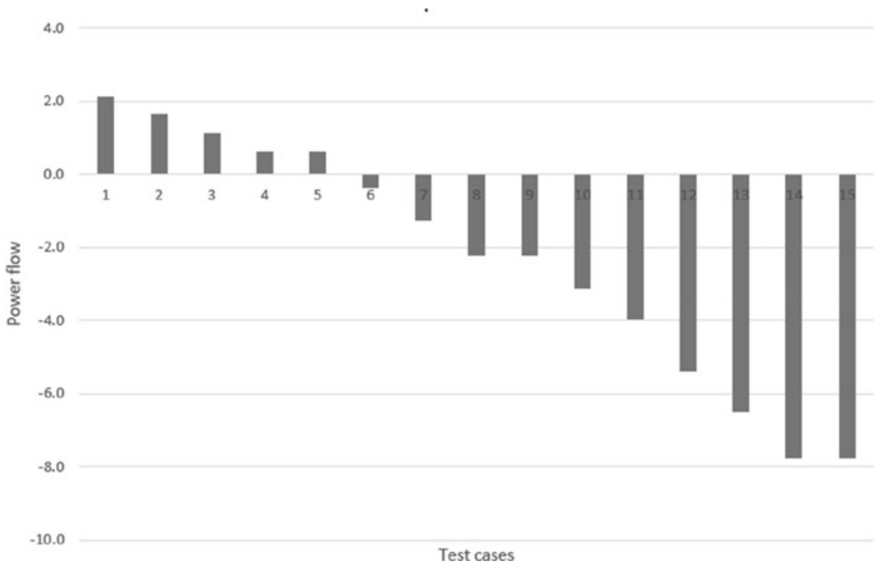

Fig. 4 Power flow in line 5 as PV penetration increases

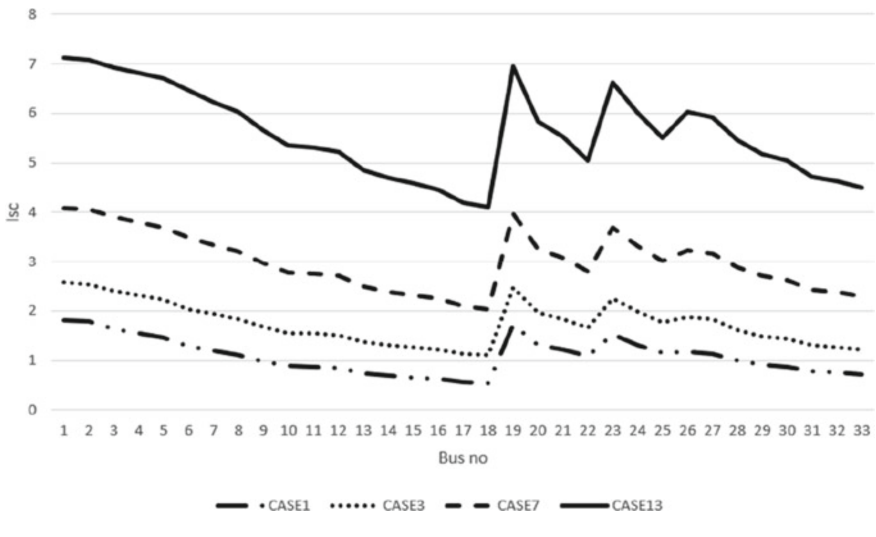

Fig. 5 Variation in short-circuit current with increase in PV penetration

5 Conclusion

The impact of renewable energy penetration on the distribution system is analysed in this paper. With increased renewable energy penetration, the magnitude of reverse power flow increases. The increase in reverse power flow and short-circuit level affects the protective relaying in a distribution network. The result shows that the protection system operates satisfactorily for low penetration levels of solar PV (up to 25%). As the penetration level increases beyond 25%, the impact of reverse power flow and short-circuit level increases and demands a modified relay setting for satisfactory operation. A new intelligent protective relaying scheme needs to be developed to cope up with the increased penetration of solar PV in the distribution system.

References

1. Telukunta V, Pradhan J, Agrawal A, Singh M, Srivani SG (2017) Protection challenges under bulk penetration of renewable energy resources in power systems: a review. CSEE J Power Energy Syst 3(4):365–379
2. El-Khattam W, Sidhu TS (2009) Resolving the impact of distributed renewable generation on directional overcurrent relay coordination: a case study. IET Renew Power Gener 3(4):415–425
3. Mahat P et al (2011) A simple adaptive overcurrent protection of distribution systems with distributed generation. IEEE Trans Smart Grid 2(3):428–437
4. Palmintier B, Broderick R, Mather B, Coddington M, Baker K, Ding F, Reno M, Lave M, Bharatkumar A (2016) On the path to sunshot. Emerging issues and challenges in integrating solar with the distribution system. No. NREL/TP-5D00-65331; SAND2016-2524 R. National Renewable Energy Lab. (NREL), Golden, CO
5. Hooshyar H, Baran ME (2012) Fault analysis on distribution feeders with high penetration of PV systems. IEEE Trans Power Syst 28(3):2890–2896
6. Memarzadeh G, Keynia F (2020) A new index-based method for optimal DG placement in distribution networks. Eng Rep 2(10):e12243
7. Walling RA, Saint R, Dugan RC, Burke J, Kojovic LA (2008) Summary of distributed resources impact on power delivery systems. IEEE Trans Power Delivery 23(3):1636–1644
8. Olowu TO, Sundararajan A, Moghaddami M, Sarwat AI (2018) Future challenges and mitigation methods for high photovoltaic penetration: a survey. Energies 11(7):1782
9. Seguin R, Woyak J, Costyk D, Hambrick J, Mather B (2016) High-penetration PV integration handbook for distribution engineers. No. NREL/TP-5D00-63114. National Renewable Energy Lab. (NREL), Golden, CO
10. Papaspiliotopoulos VA, Korres GN, Kleftakis VA, Hatziargyriou ND (2015) Hardware-in-the-loop design and optimal setting of adaptive protection schemes for distribution systems with distributed generation. IEEE Trans Power Delivery 32(1):393–400
11. Nair DS, Rajeev T (2021) Investigation on impact of solar PV penetration on the operation of protective relays in a distribution system using Python. In: 2021 IEEE conference on technologies for sustainability (SusTech). IEEE, pp 1–8
12. Milano F (2010) Power system modelling and scripting. Springer Science & Business Media
13. Thurner L, Scheidler A, Schäfer F, Menke J-H, Dollichon J, Meier F, Meinecke S, Braun M (2018) Pandapower—an open-source Python tool for convenient modeling, analysis, and optimization of electric power systems. IEEE Trans Power Syst 33(6):6510–6521
14. Stein JS, Holmgren WF, Forbess J, Hansen CW (2016) PVLIB: open source photovoltaic performance modeling functions for Matlab and Python. In: 2016 IEEE 43rd photovoltaic specialists conference (PVSC). IEEE, pp 3425–3430
15. Vita V (2017) Development of a decision-making algorithm for the optimum size and placement of distributed generation units in distribution networks. Energies 10(9):1433

Chapter 2
Modeling and Performance Evaluation of MPPT-Based PMSG Wind Energy Conversion System with Boost Converter in MATLAB/Simulink Environment

Snehashis Ghoshal, Sumit Banerjee, and Chandan Kumar Chanda

Abstract In wind energy conversion system (WECS), the power from the blowing wind is converted to a suitable form. In most of the cases, this power is utilized to generate electricity, and in a few applications, windmill is installed for pumping purpose. In electricity installations, a dedicated wind turbine fitted with necessary accessories such as gear, generator, nacelle, brake system and yaw controller converts the kinetic energy of wind into electrical one. Mostly, AC generators are utilized in WECS applications. In earlier days, asynchronous generators were in use. However, in the present scenario, synchronous machines, particularly permanent magnet synchronous generator (PMSG), are mostly used in wind energy applications. For small-scale applications, output of the WECS is converted to DC through suitable rectifier. However, due to the uncertainty in the wind flow, the power output in such a case scenario is unregulated one and cannot be applied to any load due to huge fluctuation. In this aspect, a power electronic converter is cascaded before the load and the power obtained from WECS is regulated and applied to the load. This application may find its usefulness particularly in coastal areas where abundant wind flow is available and can be efficiently utilized to run charging stations for electric vehicles (EVs). In the present study, a small-scale application of PMSG-based WECS is modeled in MATLAB/Simulink environment along with a DC load system. Output of the WECS is converter to DC through diode bridge rectifier, and then, the unregulated power is regulated by a boost converter. This converter is controlled by a maximum power point tracking (MPPT) controller which works on hill climbing algorithm so that maximum power can be extracted from such a system. The controller controls the duty ratio of the boost converter so that the system nearly extracts maximum power.

S. Ghoshal (✉) · S. Banerjee
Department of Electrical Engineering, Dr. B.C. Roy Engineering College, Durgapur, West Bengal, India

C. K. Chanda
Department of Electrical Engineering, IIEST Shibpur, Howrah, India

G. Panda et al. (eds.), *Sustainable Energy and Technological Advancements*, Advances in Sustainability Science and Technology,
https://doi.org/10.1007/978-981-16-9033-4_2

Keywords Sustainability · Wind energy conversion system · Permanent magnet synchronous generator · MPPT controller · DC–DC converter · Hill climbing algorithm

Symbols

P_{tur}	Mechanical output of turbine, W
ρ	Air density, kg/m^3
A	Turbine swept area, m^2
C_{p}	Power coefficient
λ	Tip–speed ratio
β	Pitch angle, °
v_{w}	Velocity of wind, m/s
ω_{t}	Rotational speed of wind turbine, rad/s
r_{t}	Blade radius, m
c_1	Characteristic constant = 0.5176
c_2	Constant = 116
c_3	Constant = 0.4
c_4	Constant = 5
c_5	Constant = 21
c_6	Constant = 0.0068
V_{d}, V_{q}	$d - q$ stator voltage components, respectively, V
i_{d}, i_{q}	$d - q$ stator current components, respectively, A
R_{s}	Stator resistance
ω_{e}	Angular speed of rotor, rad/s
L_{d}, L_{q}	$d - q$ axis stator inductance, respectively, H
ψ_{d}, ψ_{q}	$d - q$ stator flux linkage, respectively
ψ_{pm}	Permanent magnet flux linkage
P	Number of pole pairs

1 Introduction

Energy plays the key role to thrive civilization. Harnessing of energy from different resources in different forms is a requirement to maintain economic growth, and its amount increases with more and more advancement in science and technology. It is well known that energy cannot be created or destroyed, it can only be converter to suitable form through suitable mechanisms. Among all other forms, electricity is the most compact and flexible form. However, the main constraint in any energy conversion mechanism is the associated heat loss. Energy resources can be classified as either renewables or non-renewables.

Non-renewable resources are fossil fuel-based sources which are polluting by nature and are finite in terms of storage. On the other way, renewable resources are abundant in nature such as solar (PV and solar thermal), wind, biomass, hydropower, tidal, ocean thermal and geothermal. Major advantage of fossil fuel-based resources is its higher energy density along with the fact that several well-established techniques exist to extract them. However, polluting nature of non-renewable resources supersedes its advantages from sustainability point of view, whereas renewable resources are of abundant nature.

It is evident that in coming future fossil fuel resources will not sustain [1] and continuous research is going on in this aspect. Besides, per capita energy consumption must be maintained at a higher level to enhance economic growth [2–5]. In this regard, an optimized mixture between renewable and non-renewable becomes inevitable and can be implemented in any of the following form such as cogeneration, energy efficiency, energy conservation and energy management [6–10].

Presently, wind has a huge potential from electricity generation point of view [11, 12]. It is evident that wind has random nature and hence output from wind turbine fluctuates causing instability [13], voltage flicker and grid frequency fluctuation [14]. In wind firms, mainly variable speed wind turbine (VSWT) is in common use [15]. VSWT systems are generally based on either doubly fed induction generator (DFIG) or permanent magnet synchronous generators (PMSGs). WECS in small-scale possesses a power electronic interface to smooth out the power from the system with improved system reliability. In practice, several controlling techniques for WECS can be categorized in mainly two parts. The first one is controlling the kinetic energy, and the second one is to control scheme adopted in intermediate stage to smooth out power output. Generally, storage-based methods are useful in controlling the kinetic energy from WECS such as flywheel [16], battery [17], magnetic storage [18] and fuel cell [19], although pitch angle control is a promising approach to control the kinetic energy without storage. On the other hand, grid side control [20], DC link control [21], etc., are very useful to control the output from the electricity generation part.

DC line power smoothening is very useful in small-scale DC applications where wind flow profile has a good potential from electricity generation point of view.

In the present study, performance of a DC load-based WECS is analyzed with the help of a power electronic interface in between MATLAB/Simulink environment. The WECS consists of a wind turbine coupled to a PMSG. Output from the generator is converted to DC by a rectifier circuit, and the converted DC is smoothened with a boost converter. The converter regulates the fluctuating DC from the PMSG-based rectifier and supplies to a DC load. Duty ratio of the boost converter is controlled by a MPPT controller which works on hill climbing algorithm. Simulation result of the above system is carried out in MATLAB/Simulink environment, and the results are analyzed.

2 Wind Energy Conversion System

2.1 *Wind Turbine*

Mechanical power output of a wind turbine is obtained from the following expression [22]

$$P_{\mathrm{Tur}} = 0.5\rho A C_{\mathrm{p}}(\lambda, \beta)\upsilon_{\mathrm{w}}^{3} \tag{1}$$

Tip–speed ratio, λ, can be expressed as

$$\lambda = \frac{\omega_{\mathrm{t}} r_{\mathrm{t}}}{\upsilon_{\mathrm{w}}} \tag{2}$$

Turbine power coefficient is based on turbine characteristics and can be obtained by the following expressions as

$$C_{\mathrm{p}}(\lambda, \beta) = c_1\left(\frac{c_2}{\lambda_i} - c_3\beta - c_4\right)\mathrm{e}^{\frac{-c_5}{\lambda_i}} + c_6\lambda \tag{3a}$$

$$\frac{1}{\lambda_i} = \frac{1}{\lambda + 0.08\beta} - \frac{0.035}{\beta^3 + 1} \tag{3b}$$

Figure 1 represents the turbine power characteristics for various wind speeds and 0° pitch angle.

2.2 *Permanent Magnet Synchronous Generator*

In synchronous reference frame, PMSG can be modeled as per the following expressions [23–25]:

$$V_{\mathrm{d}} = R_{\mathrm{s}} i_{\mathrm{d}} + \lambda_{\mathrm{d}} - \omega_{\mathrm{e}}\psi_{\mathrm{q}} \tag{4}$$

$$V_{\mathrm{q}} = R_{\mathrm{s}} i_{\mathrm{q}} + \lambda_{\mathrm{q}} - \omega_{\mathrm{e}}\psi_{\mathrm{d}} \tag{5}$$

Stator flux linkages can be analyzed as per Eqs. (6) and (7) as follows

$$\psi_{\mathrm{d}} = L_{\mathrm{d}} i_{\mathrm{d}} + \psi_{\mathrm{pm}} \tag{6}$$

$$\psi_{\mathrm{q}} = L_{\mathrm{q}} i_{\mathrm{q}} \tag{7}$$

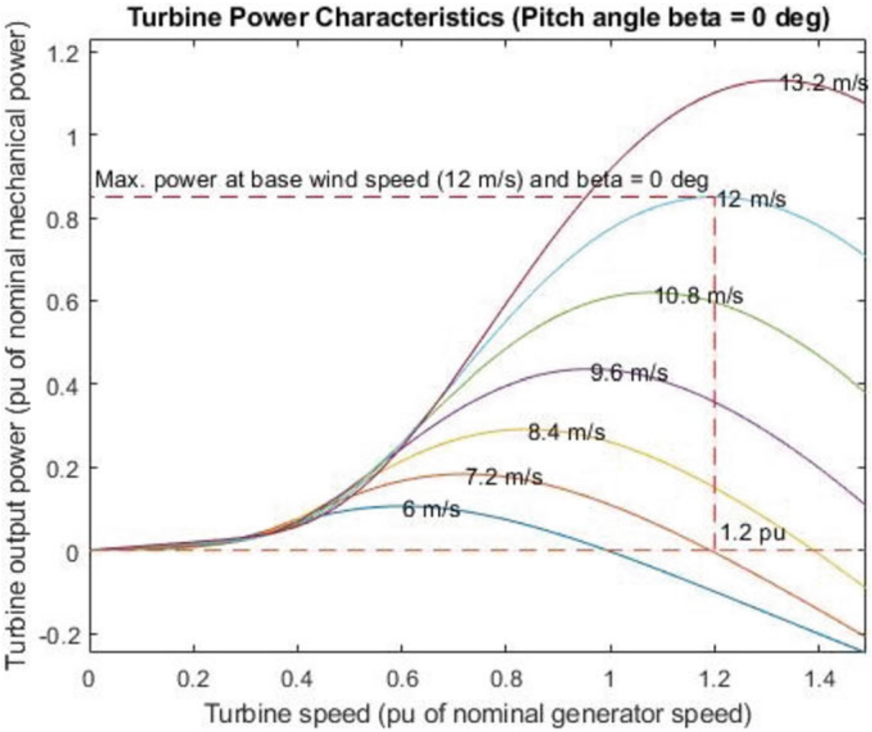

Fig. 1 Turbine power characteristics

Developed electromagnetic torque in the PMSG can be expressed in terms of magnetizing current and flux linkage as per Eq. (8).

$$T_{\mathrm{e}} = 1.5P\left(\lambda_{\mathrm{d}} i_{\mathrm{q}} - \psi_{\mathrm{q}} i_{\mathrm{d}}\right) = 1.5P\left[\psi_{\mathrm{pm}} i_{\mathrm{q}}\right] + \left(L_{\mathrm{d}} - L_{\mathrm{q}}\right) i_{\mathrm{d}} i_{\mathrm{q}} \tag{8}$$

In case of multi-pole PMSG mounted with permanent magnets, direct and quadrature axis self-inductances are equal ($L_{\mathrm{d}} = L_{\mathrm{q}} = L$) and hence the electromagnetic torque in such a scenario becomes

$$T_{\mathrm{e}} = 1.5P\psi_{\mathrm{pm}} i_{\mathrm{q}} \tag{9}$$

It is evident that generator torque can be controlled by the quadrature axis component of stator current. To obtain maximum torque output at highest efficiency, direct axis component of current is set to zero. The system under study is shown in Fig. 2.

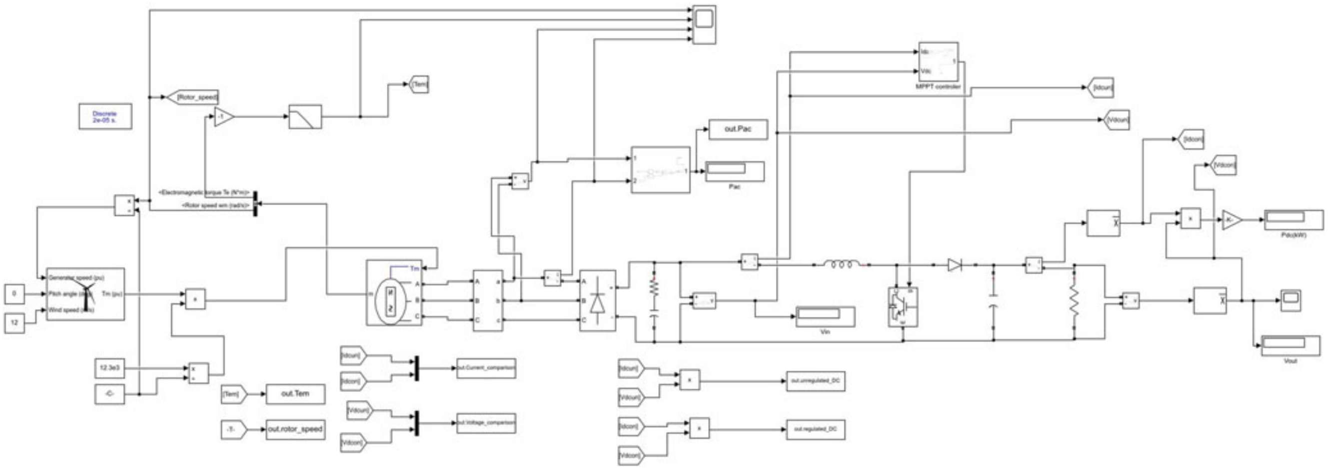

Fig. 2 Representation of the system under consideration

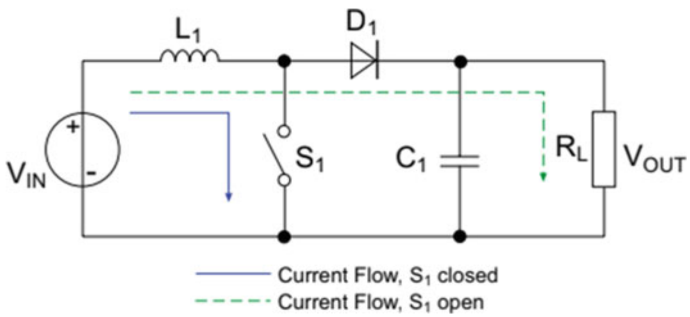

Fig. 3 Representation of a boost converter

3 DC–DC Converter

In the model under study, a boost converter is used as DC–DC power electronic interface connected between the system and load. It is evident that maximum power can be extracted from the system if and only if the supply side and load side possess same impedance value [26]. In this regard, impedance matching becomes essential. In the present study, impedance matching is implemented by controlling the duty cycle of the boost converter according to the scenario. A diode is provided in such a system to provide protection against back flow of current. A brief discussion regarding the boost converter is discussed in brief [27]. The boost converter stabilizes an unregulated DC supply to a stabilized one with relatively high voltage at lower current level. The diagram of the boost converter is shown in Fig. 3.

4 Maximum Power Point Tracking

Maximum power from a WECS depends on various turbine parameters and environmental conditions such as air density and wind velocity. On the other side, extracted power from such a system depends on connected load and attains maximum value when the load possesses an optimal value to satisfy the condition of maximum power transfer. In practice, this condition is never met and to extract as much power as possible MPPT algorithms come into play. This type of algorithm actuates a controller which controls the duty ratio of the power electronic boost converter connected before the load. The output of a WECS is highly depended on environmental conditions. In the system under consideration, the boost converter is actuated by MPPT controller running through hill climbing algorithm.

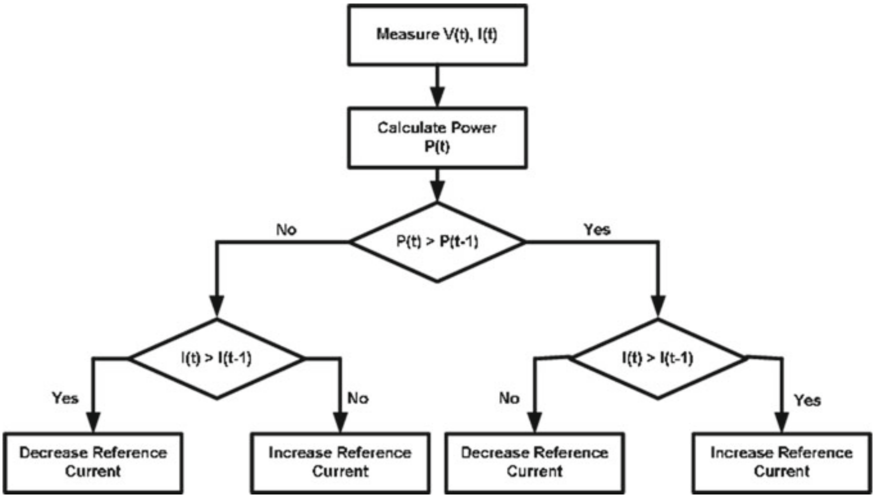

Fig. 4 Flowchart for hill climbing method

4.1 Hill Climbing Method of MPPT

Hill climbing method is a very useful and simple method to implement. It requires a few parameters for analysis. This is a self-optimized method, and by maintaining suitable step size, desirable control action can be obtained. Figure 4 shows the flowchart of the said algorithm. It is evident that, in this method, power at every instant is compared to the previous instant and if power at current instant is larger than the previous one then duty cycle is incremented in the same direction or else decremented in the backward direction. At steady state, the operating point slightly oscillates around the MPP (Fig. 4).

5 Results and Discussion

It has been observed that in coastal area wind potential can be effectively utilized to charge up electrical vehicles, thereby providing a self-sustained and independent way to increase energy efficiency. In order to achieve this, the supply should be as constant as possible. Even, if maximum energy can be extracted from the wind, then system reliability and performance enhance to a much good extent. In the present study, performance of a MPPT controller-based small-scale WECS is analyzed in MATLAB/Simulink environment. The proposed WECS consists of a PMSG machine which converts the kinetic energy of wind to the electrical one. In the present analysis, the pitch angle of the turbine is considered to be at 0°. The PMSG output is rectified by rectifier and is fed to the loading station through a boost converter. The proposed

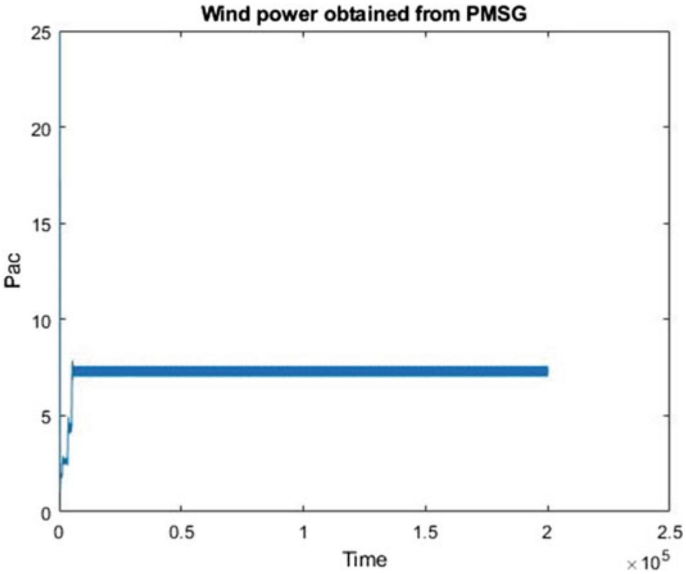

Fig. 5 AC power output from PMSG

boost converter is actuated by a MPPT controller which works on hill climbing method. The turbine was simulated for 0° pitch angle. In the present analysis, the step was maintained at very small value which helps in reducing the oscillatory nature of the system around MPP. However, such an arrangement makes the system slow. Boost converter utilized in this study regulates the output of the proposed system with enhanced system voltage. Different simulation results of this proposed system are analyzed here. Figure 5 shows the profile of unregulated power at the PMSG output.

Torque profile of the system is shown in Fig. 6.

Figure 7 depicts the rotor angle profile of the PMSG under study.

From Figs. 5, 6 and 7, it is clear that an oscillation exists in the system which is due to the uncertain nature of wind flow. Figures 8, 9, 10 and 11 depict the performance analysis on the DC side.

It is evident from Fig. 8 that in the absence of converter the system output is an oscillatory one. Figure 9 shows the regulated power fed to the DC load after the converter. It is clear that how the oscillation as shown in Fig. 8 is reduced due to the presence of the boost converter.

Figure 10 shows the comparative analysis of the voltage before and after the boost converter. It clearly seen that how the oscillation in the voltage is reduced due to the presence of the converter and as it is a boost converter, the yield voltage increases.

Figure 11 shows the comparison of current before and after the converter. It clearly seen that how the oscillation in the current is reduced due to the presence of the converter and as it is a boost converter, the yield current is comparatively low.

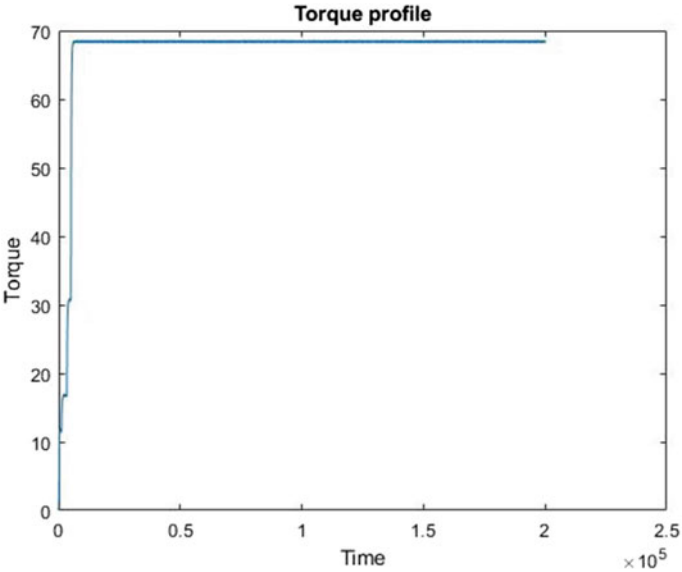

Fig. 6 Torque profile of the PMSG

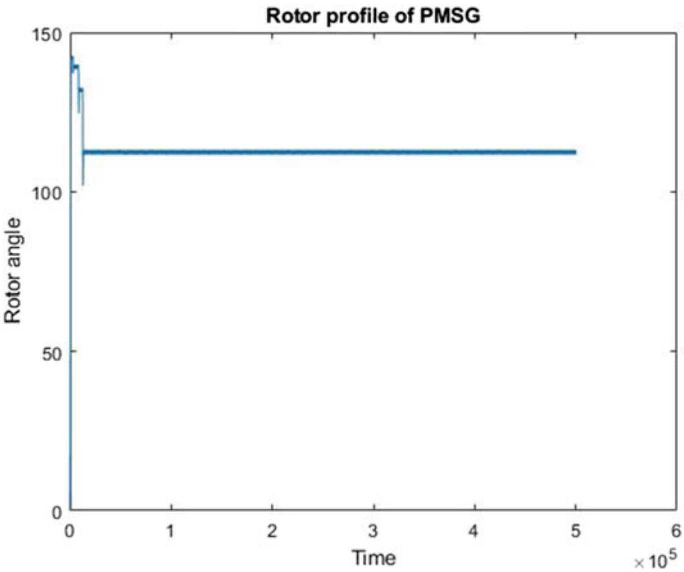

Fig. 7 Rotor profile of PMSG

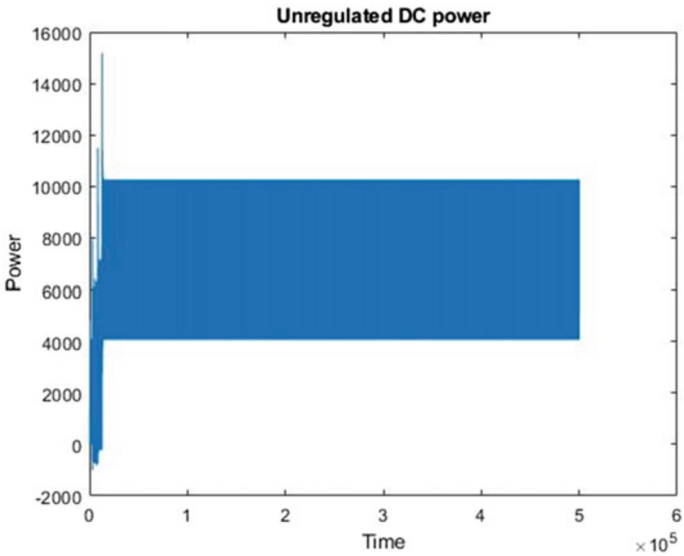

Fig. 8 Unregulated power before the boost converter

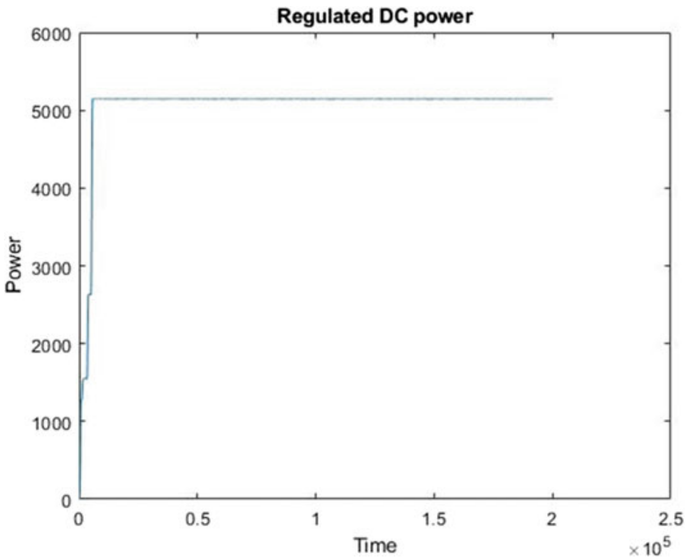

Fig. 9 Regulated DC power from the boost converter

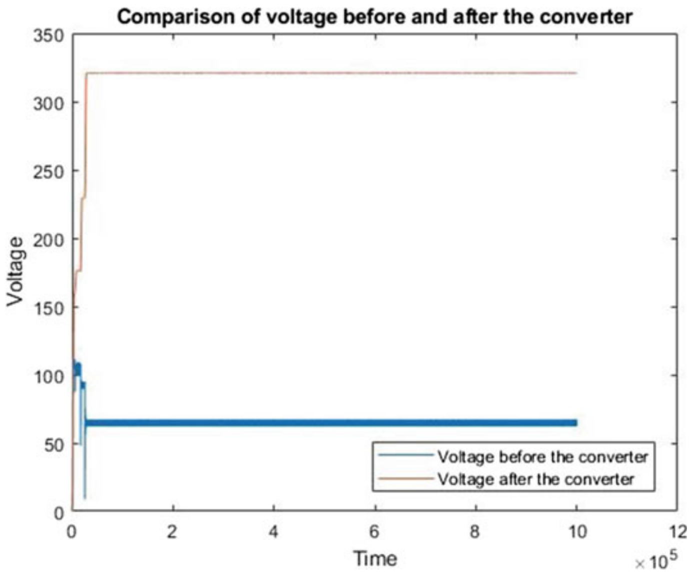

Fig. 10 Comparison of voltage before and after the converter

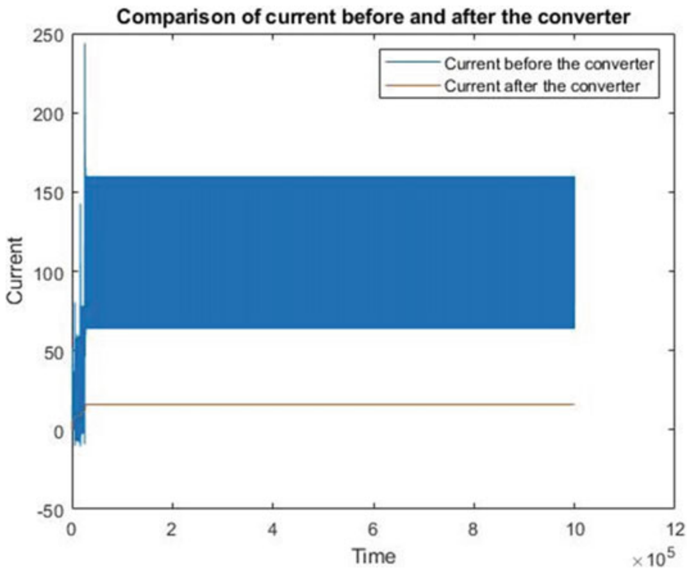

Fig. 11 Comparison of current before and after the converter

From the simulation result, it is evident that boost converter smoothens the unregulated DC output of the WECS to a desirable limit and simultaneously enhances the system voltage. The system reliability also increases.

It can be concluded from the above analysis that the proposed system is very useful in small-scale applications requiring regulated and reliable DC supply. Therefore, the proposed system may be very useful in coastal region for setting up charging station for electric vehicles as wind possesses a good potential for such an implementation. This arrangement makes the system self-sufficient and completely utilizes green energy.

References

1. Jash T (2007) Renewable energy and environment. Geogr Rev India 69:20–24
2. Gollagari R, Rena R (2013) An empirical analysis of energy consumption and economic growth in India: are they casually related? Studia Oecon 58(2):22–40
3. Stern DI, Cleveland CJ (2004) Energy and economic growth
4. Guo WW (2017) An analysis of energy consumption and economic growth of Cobb-Douglas production function based on ECM. In: ICAESEE 2017
5. Koltun P (2010) Materials and sustainable development. Progr Nat Sci Mater Int 20:16–29
6. Gambini M, Vellini M, Stilo T, Manno M, Bellocchi S (2019) High-efficiency cogeneration systems: the case of the paper industry in Italy. Energies
7. https://beeindia.gov.in/sites/default/files/2Ch7.pdf
8. Chaphekar SN, Khatavkar VV, Apte AA (2006) Cogeneration an emerging trend in India for energy crisis. In: 2006 IEEE international conference on industrial technology
9. Thakkar A, Chaudharia K, Shaha M (2020) A comprehensive survey on energy-efficient power management techniques. Procedia Comput Sci 167:1189–1199
10. https://beeindia.gov.in/sites/default/files/BEE%20Final%20Report_1.pdf
11. http://www.aeee.in/wp-content/uploads/2016/03/AEEE-EE-Book-Online-Version-.pdf
12. Simanaviciene Z, Volochovic A, Vilke R, Palekiene O, Simanavicius A (2015) Research review of energy savings changing people's behavior: a case of foreign country. Procedia Soc Behav Sci 191:1996–2001
13. Kamalapur GD, Yaragatti UR (2009) Electrical energy conservation in India—challenges and achievements. In: International conference on control, automation, communication and energy conservation
14. https://www.beeindia.gov.in/sites/default/files/Energy%20conservation%20guidelines%20for%20industries.pdf
15. Shrestha RM, Timilsina GR (1996) Factors affecting CO_2 intensities of power sector in Asia: a Divisia decomposition analysis. Energy Econ 18(4):283–293
16. https://www.oecd.org/greengrowth/greening-energy/49157219.pdf
17. Lekshmanan R (2015) Energy conservation—a case study. Int J Appl Eng Res 10
18. https://beeindia.gov.in/sites/default/files/1Ch3.pdf
19. Chen P, Yan B, Liu C, Wang S, Liu Y (2015) A comparative study on MPPT for photovoltaic generation systems. In: IEEE 2nd international future energy electronics conference (IFEEC), pp 1–6
20. Mohamed N, Shannan AA, Yahaya NZ, Singh B (2013) Single-diode model and two-diode model of PV modules: a comparison. In: Proceedings of ICCSCE, pp 210–214
21. Garg R, Singh A, Gupta S (2014) PV cell models and dynamic simulation of MPPT trackers in MATLAB. In: Proceedings of INDIACOM, pp 6–12
22. Brito MAG, Galotto L Jr, Sampaio LP, Melo GA, Canesin CA (2013) Evaluation of the main MPPT techniques for photovoltaic applications. IEEE Trans Ind Electron 60(3):1156–1167

23. Li Y, Huang W, Huang H, Hewitt C, Chen Y, Fang G et al (2013) Evaluation of methods to extract parameters from current voltage characteristics of solar cells. Sol Energy 90:51–57
24. Maffezzoni P, Codecasa L, D'Amore D (2009) Modeling and simulation of a hybrid photovoltaic module equipped with a heat recovery system. IEEE Trans Ind Electron 56:4311–4318
25. Dondi D, Bertacchini A, Brunelli D, Larcher L (2008) Modeling and optimization of a solar energy harvester system for self-powered wireless sensor networks. IEEE Trans Ind Electron 55:2759–2766
26. Benavides ND, Chapman PL (2008) Modeling the effect of voltage ripple on the power output of photovoltaic modules. IEEE Trans Ind Electron 55:2638–2643
27. Krishan R, Sood YR, Kumar BU (2013) The simulation and design for analysis of photovoltaic system based on MATLAB. In: Proceedings of ICEETS, pp 647–671

Chapter 3
Optimal Scheduling of Grid Connected PV System with Battery Energy Storage

Swathi Krishna and R. M. Shereef

Abstract Management of both load and generation in power system network is considered to be a strategic approach to optimally operate the grid. Grid connected Photo-voltaic (PV) system with Battery energy storage (BES) helps to optimally operate the grid at both off-peak and peak hours. This paper aims for the optimal scheduling of grid connected PV system with BES, by minimizing the total cost of power generation and amount of power imported from upstream grid along with reduction in power loss, improvement of voltage profile, and proper frequency regulation. A modified algorithm for scheduling of grid connected PV system with BES is developed taking unscheduled interchange (UI) cost into account. MATLAB simulation tool MATPOWER is used for optimal power flow (OPF) calculation. The proposed algorithm and its efficiency are demonstrated by simulating various test scenarios of power generation with hourly varying load on an IEEE 14 bus system.

Keywords Optimal scheduling · Grid connected PV system · Battery energy storage

1 Introduction

Fossil fuels are the main source of power generation throughout the world. However, they are the major reason for emission of greenhouse gases, causing global warming and associated natural calamities. Various technical, environmental, and economical effects of fossil fuels lead to the advancement in renewable energy (RE), which are clean, environmental friendly, and sustainable in nature. Since RE sources such as solar and wind are intermittent in nature, storage system along with power electronic converter becomes necessary to connect RE sources to power grid. Management of both loads and generating systems is considered to be a strategic approach for optimal operation of the grid [3]. Proper scheduling of grid connected PV system with BES

S. Krishna (✉) · R. M. Shereef
College of Engineering Trivandrum, Thiruvananthapuram, Kerala, India

G. Panda et al. (eds.), *Sustainable Energy and Technological Advancements*,
Advances in Sustainability Science and Technology,
https://doi.org/10.1007/978-981-16-9033-4_3

can operate the grid optimally. The BES can act as both generator (in discharging mode) and load (in charging mode) [2].

In power system, load demand will not be constant all the time. Fluctuating loads lead to deviations in frequency. Energy storage system helps in maintaining the frequency. Unscheduled generation and withdrawal of electricity put the whole grid and many other electrical equipment to danger by creating large fluctuation in frequency. Unscheduled interchange (UI) is the mechanism developed to improve grid efficiency, grid discipline, accountability, and responsibility by imposing charges on those who defer from their scheduled generation or withdrawal. Unscheduled interchange cost (UI cost) is a frequency-dependent cost of electrical energy. With increase in frequency, UI cost reduces and vice versa [6].

In [10], optimal operating strategy is discussed for cost and emission minimization with generation and storage system. Two simple and straightforward methods to handle multiobjective optimization problems are the weighted sum and the μ-constrained method, both applied in this paper. The weighted sum method provides sufficient conditions for Pareto optimally, but it is not always possible to compute the optimal solution (i.e., non-convex Pareto optimal set) [8]. Sousa et al. proposed a simulated annealing (SA) approach to address energy resources scheduling from the point of view of a virtual power player (VPP) operating in a smart grid [11].

A scheduling algorithm is proposed in [12] for minimizing the expected electric energy cost according to the price variation and the charging demand. It determines the amount of energy to purchase in each time slot, according to the price and the PEV charging demands. The dispatch algorithm determines the time slots where each PEV will be charged. Microgrid intelligent online energy management under cost and emission minimization has been investigated by Chaouachi et al. in [4].

A trading mechanism was introduced in which smart retail consumers submit short-term demand response offers to a retailer. This demand response helps to increase or decrease retailer's energy consumption, through load management with self-production of renewable energy, for every time period, at favorable prices [5]. Demand-side management assistance can enhance microgrid planning and operation. Residential microgrid load management is one way to optimally operate microgrid. Bhamidi and Sivasubramani investigated the impact of demand-side management on distribution system [1].

The problem formulation includes optimal battery scheduling, taking into account the uncertainty of the microgrid exogenous variables and forecasted entities. An artificial neural network ensemble is developed to predict 24 h ahead photovoltaic generation and 1 h ahead wind power generation and load demand.

This paper deals with the optimal scheduling of grid connected PV system with BES, to reduce the cost of total power generation and amount of power imported from upstream grid. Here, a modified algorithm for scheduling of grid connected PV system with BES is developed. MATLAB simulation tool MATPOWER is used for optimal power flow (OPF) calculation.

Rest of the paper is organized as follows. Section 2 discusses the modified algorithm developed for scheduling of grid connected PV system with BES. Section 3 gives a brief description of the system used to test the proposed algorithm. Section 4 deals with results of scheduling of grid connected PV system with BES. Section 5 concludes the paper.

2 Methodology

A modified algorithm is formulated for optimal scheduling of grid connected PV system with BES. The algorithm is tested by generating various scenarios, viz. (i) case 1: grid without PV system and BES, (ii) case 2: grid with BES, and (iii) case 3: grid with PV system and BES. To solve the minimization problem subject to the desired constraints, MATPOWER, a MATLAB simulation tool is used.

2.1 Modified Algorithm for Optimal Scheduling of Grid Connected PV System with BES

A detailed algorithm for scheduling of grid connected PV system with BES is developed (Figs. 1 and 2). Main aim of this algorithm is scheduling of grid connected PV system with BES to minimize the cost of total power generation and amount of power imported from upstream grid. In the algorithm, UI cost is also considered.

In this algorithm, the following assumptions are considered. (i) Energy storage systems such as battery are charged from PV panel during the daytime, (ii) only stored energy in the energy storage system is discharged during peak hours, (iii) RE cost is constant, and (iv) power from solar energy is constant for an hour. 24 h scheduling period is divided into 24 time slots of one hour each. Power from PV panel at time t ($P_{(\mathrm{pv},t)}$), power generated from main grid ($P_{(\mathrm{grid},t)}$), and grid load ($L_{(\mathrm{grid},t)}$) are obtained from day ahead scheduling. (soc_t) is SOC level of battery at instant t. Cost of energy from PV system ($C_{(\mathrm{pv})}$), cost of energy from battery storage system ($C_{(\mathrm{batt},t)}$), and threshold UI cost ($\mathrm{UI}_{\mathrm{Th}}$) are considered constant and are given in \$/MWh. Threshold UI cost ($\mathrm{UI}_{\mathrm{Th}}$) is the UI cost at nominal frequency.

According to the availability of PV power, time slots are categorized into two (i) time slot 1 (1–9 and 18–24 h) and (ii) time slot 2 (10–17 h). For the time slot 1, if UI cost $C_{\mathrm{UI}} < \mathrm{UI}_{\mathrm{Th}}$, battery will be charged from the grid (Fig. 2). If UI cost $C_{\mathrm{UI}} > \mathrm{UI}_{\mathrm{Th}}$, the battery will be discharged. In daytime (10–17 h), energy storage systems are charged from the PV panel, 20% of load is injected into grid by PV panel, and remaining power is used to charge the battery.

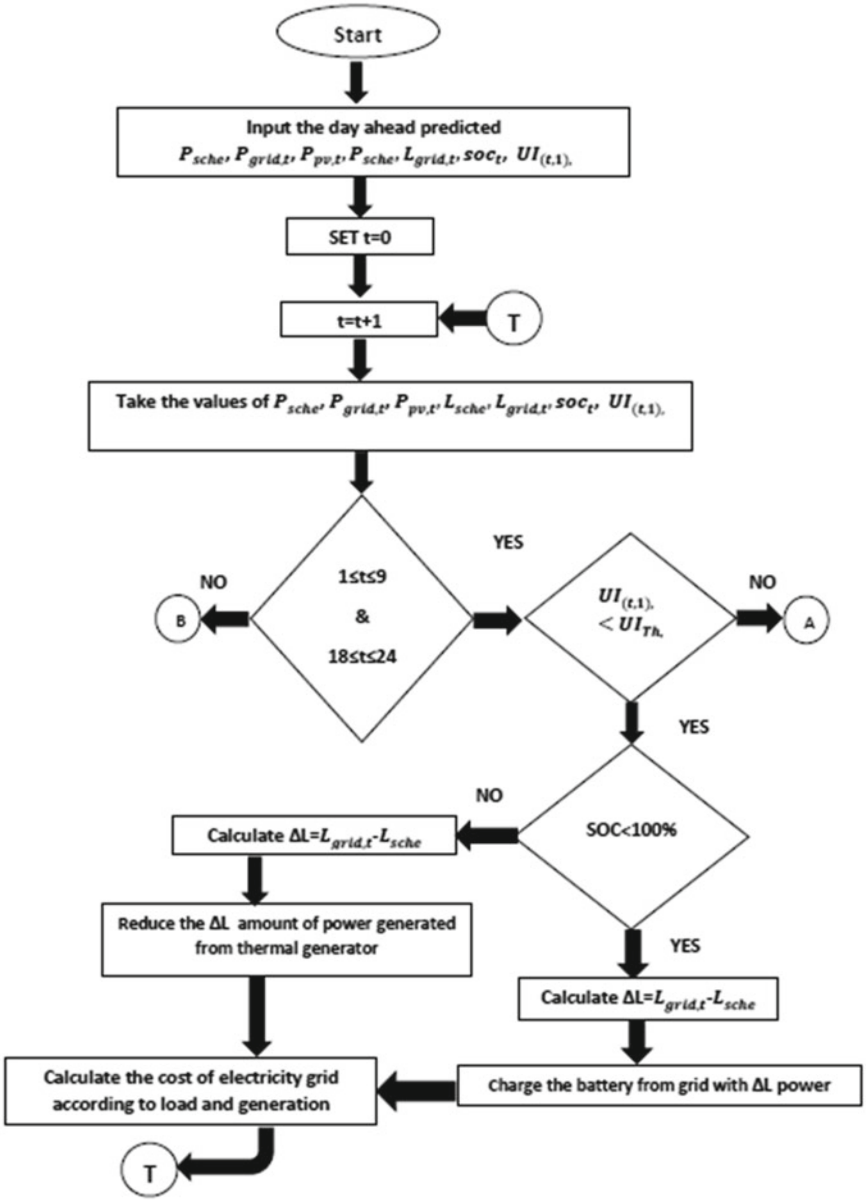

Fig. 1 Algorithm for scheduling of grid connected PV system with BES

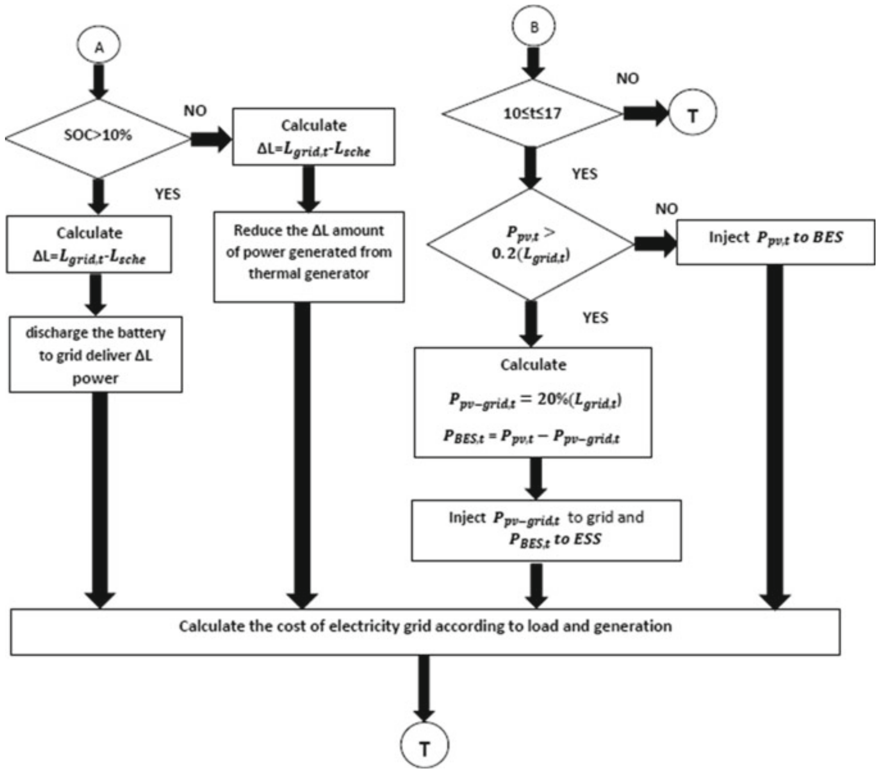

Fig. 2 Algorithm for scheduling of grid connected PV system with BES (continuation of Fig. 1)

2.2 Determination of UI Cost

The perfect balance of scheduled generation and scheduled load results in nominal frequency. Any deviations from schedule will result in deviation from nominal frequency. Unscheduled interchange cost (UI cost) is a frequency-dependent cost. Let f_{nom} be the nominal frequency, f be the current frequency, and $f_{\max}$ be the maximum frequency, where UI_{Th} cost of electricity at nominal frequency.

$$\text{UI cost} = \text{UI}_{\text{Th}} \times \frac{f_{\max} - f}{f_{\max} - f_{\text{nom}}} \tag{1}$$

Equation 1 shows that UI cost is higher for frequencies below nominal value (i.e., when load is greater than generation) and lower for frequencies above nominal value (i.e., when generation is greater than load).

2.3 Optimal Power Flow Using MATPOWER

MATPOWER is a package of MATLAB M files for solving power flow and optimal power flow problems [13]. The standard version of each takes the following form:

$$\min_{x} z(x) \tag{2}$$

subjected to

$$g(x) = 0 \qquad h(x) \leq 0 \qquad x_{\min} \leq x \leq x_{\max} \tag{3}$$

The objective function $z(x)$ consists of the polynomial cost of generator injections, the equality constraints $g(x)$ are the power balance equations, the inequality constraints $h(x)$ are the branch flow limits, and the $x_{\min}$ and $x_{\max}$ bounds include reference bus angles, voltage magnitudes (for AC), and generator real and reactive power injections.

$$z\left(P_{\mathrm{g}}, Q_{\mathrm{g}}\right) = \sum_{i=1}^{n_{\mathrm{q}}} z_{\mathrm{P}}^{i}\left(p_{\mathrm{g}}^{i}\right) + z_{\mathrm{Q}}^{i}\left(q_{\mathrm{g}}^{i}\right) \tag{4}$$

$$g_{\mathrm{P}}\left(\theta, V_{\mathrm{m}}, P_{\mathrm{g}}\right) = P_{\mathrm{ba}}\left(\theta, V_{\mathrm{m}}\right) + P_{\mathrm{d}} - C_{\mathrm{g}} P_{\mathrm{g}} = 0 \tag{5}$$

$$g_{\mathrm{Q}}\left(\theta, V_{\mathrm{m}}, Q_{\mathrm{g}}\right) = Q_{\mathrm{ba}}\left(\theta, V_{\mathrm{m}}\right) + Q_{\mathrm{d}} - C_{\mathrm{g}} Q_{\mathrm{g}} = 0 \tag{6}$$

$$\theta_{i}^{\mathrm{ret}} \leq \theta_{i} \leq \theta_{i}^{\mathrm{ret}}, \quad t \in \mathcal{I}_{\mathrm{ref}} \tag{7}$$

$$V_{\mathrm{m}}^{i,\max} \leq V_{\mathrm{m}} \leq V_{\mathrm{m}}^{i,\max}, \quad i = 1 \ldots n_{\mathrm{b}} \tag{8}$$

$$P_{\mathrm{g}}^{i,\max} \leq P_{\mathrm{g}} \leq P_{\mathrm{g}}^{i,\max}, \quad i = 1 \ldots n_{\mathrm{g}} \tag{9}$$

$$Q_{\mathrm{g}}^{i,\max} \leq Q_{\mathrm{g}} \leq Q_{\mathrm{g}}^{i,\max}, \quad i = 1 \ldots n_{\mathrm{g}} \tag{10}$$

3 System Description

Test system consists of IEEE 14 bus system as upstream grid. Seventh bus is considered as a distribution substation where PV system with BES is connected. PV system with BES can act as generator (in discharging mode) and load (in charging mode).

IEEE 14 bus system comprised of five generators of total capacity 490 MW, total scheduled generation 266 MW, and total scheduled load of 259 MW. Table 1 shows the generator data and load data of test system. For generating the scheduled power of 266 MW, generators at buses 1, 2, and 3 are made *ON*, and the other two generators are made *OFF*.

Table 1 Generator and load data of IEEE 14 bus system

Bus No.	Generator		Load	
	*P*max (MW)	*Q*max (MVAR)	*P* (MW)	*Q* (MVAR)
1	170	10	0	0
2	80	50	21.7	12.7
3	50	40	94.2	19
4	0	0	47.8	−3.9
5	0	0	7.6	1.6
6	90	24	11.2	7.5
7	0	0	0	0
8	100	24	0	0
9	0	0	29.5	16.6
10	0	0	9	5.8
11	0	0	3.5	1.8
12	0	0	6.1	1.6
13	0	0	13.5	5.8
14	0	0	14.9	5
Total	490	148	259	73.5

3.1 PV System with Battery Energy Storage

PV system with BES comprised of PV panel of 98 MW (20% of total generation capacity of upstream grid) capacity and BES system of 300 MWh capacity. Battery size is selected such that it can fulfill the excess load demand during evening hours. PV panel capacity is selected such that it can meet 20% of load demand during daytime along with battery charging. A 35 MVA inverter is used to convert PV panel DC power to AC, and it is also used for reactive power support. Equation 11 shows the maximum energy capacity of BES (E_B) to fulfill the excess load demand at night peak hours (6–11 p.m.). Equation 12 shows the maximum PV panel capacity (P_{PV}) to meet the 20% load demand during daytime along with battery charging, where DoD is the depth of discharge and η_{ch} and η_{disch} are battery efficiency during charging and discharging mode, respectively.

$$E_B = \frac{\text{Extra energy consumption at night peak hours}}{\text{DoD} \times \eta_{ch} \times \eta_{disch}} \times 1.2 \tag{11}$$

$$P_{PV} = 20\% \text{ (Total generation capacity of upstream grid)} \tag{12}$$

Table 2 Specification of battery and inverter

Specification	Values
Battery capacity	300 MWh
Inverter capacity	35 MVA
Charging efficiency of battery	90%
Discharging efficiency of battery	90%
Depth of discharge of battery	80%
Efficiency of inverter	95%

Solar Irradiance The hourly solar irradiance in kWh/m^2/day for the PV system is obtained from [9]. The highest average solar irradiance of 6.04 kWh/m^2/day is in the month of February, whereas the lowest average solar irradiance of 3.44 kWh/m^2/day is in the month of July.

BES System and Inverter PV system with BES consists of 30 MW/300 MWh battery with 98 MW PV plant. It is a 10 h battery storage system which delivers maximum 30 MW at an instant. 35 MVA inverter is used to convert DC power to AC power. Here battery cost is considered as 60 $/MWh. Table 2 shows the specification of battery and inverter.

3.2 Power Generated by PV Panel

Power generated by PV panel ($P_{\mathrm{PV}}(t)$) is calculated by Eq. 13 [7].

$$P_{\mathrm{PV}}(t) = N_{\mathrm{PV}} * V_{\mathrm{oc}}(t) * I_{\mathrm{SC}}(t) * \mathrm{FF} \tag{13}$$

where N_{PV} represents number of PV panel, $V_{\mathrm{oc}}(t)$ is the open circuit voltage of PV panel, and $I_{\mathrm{sc}}(t)$ is the short circuit current of PV panel.

$$V_{\mathrm{oc}}(t) = V_{\mathrm{OCS}} - \tau\,(T_{\mathrm{PV}}(t) - 25^{\circ}) \tag{14}$$

$$I_{\mathrm{sc}}(t) = \left[I_{\mathrm{SCS}} + \varepsilon\,(T_{\mathrm{PV}}(t) - 25^{\circ})\right] * \frac{Q_{\mathrm{PV}}(t)}{1000} \tag{15}$$

$$T_{\mathrm{PV}}(t) = T_{\mathrm{amp}}(t) + \frac{T_{\mathrm{PVmn}}(t) - 20}{800} * Q_{\mathrm{PV}}(t) \tag{16}$$

where V_{OCS} and I_{SCS} stand for open circuit voltage and short circuit current under standard test condition, respectively, τ is the open circuit voltage temperature coefficient, ε is the short circuit current temperature coefficient, $Q_{\mathrm{PV}}(t)$ represents solar irradiance (W/m^2) incident on PV panels, $T_{\mathrm{PV}}(t)$ is solar cell operational temperature, and $T_{\mathrm{PVnm}}(t)$ is the nominal temperature of solar cell in °C, respectively, and

Table 3 Specifications of PV panel

Specification	Values
Open circuit voltage at standard condition	37 V
Short circuit current at standard condition	8.48 A
Open circuit voltage temperature coefficient	638 μV/°C
Short circuit current temperature coefficient	3.305 mA/°C
Fill factor	0.74
Nominal cell temperature	48 °C

$T_{\text{amb}}(t)$ is an ambient temperature (°C). Fill factor (FF) of PV panel is computed using Eq. 17. Specification of PV panel is provided in Table 3

$$\text{FF} = \frac{V_{\text{MPP}} * I_{\text{MPP}}}{V_{\text{OC}} * I_{\text{SC}}} \tag{17}$$

3.3 *Frequency Calculation*

Load variation in a power system leads to frequency variation. Frequency of IEEE 14 bus system is calculated using the following equations.

$$\Delta f = \frac{-\Delta P}{D1 + D2 + D3 + 1/R_1 + 1/R_2 + 1/R_3} \tag{18}$$

$$f_{\text{new}} = f + \Delta f \tag{19}$$

where ΔP change in load in p.u., Δf is the change in frequency due to load change, R is the droop, and D represents the frequency dependency of load. For case 1 (grid without PV system and BES)

$$\Delta P = (L_{\text{gridnew}} + \text{loss}_{\text{new}}) - L_{\text{sche}} + \text{Loss}_{\text{sche}} \tag{20}$$

where L_{gridnew} represents grid load demand at the instant of frequency change and L_{sche} is the scheduled load demand. Losses are also varying with variation of load. $\text{Loss}_{\text{sche}}$ and Loss_{new} are loss for load L_{sche} and L_{gridnew}, respectively.

$$L_{\text{gridnew}} = L_{\text{grid}} \pm P_{\text{BES}} \tag{21}$$

$$L_{\text{gridnew}} = L_{\text{grid}} \pm P_{\text{BES}} - P_{\text{PV}} \tag{22}$$

For case 2 (grid with BES), $L_{gridnew}$ is the sum of grid load demand (L_{grid}) and charging (+) or discharging (−) power of energy storage system (P_{BES}) as shown in Eq. 21. For case 3 (grid with PV system and BES), $L_{gridnew}$ is the grid load demand (L_{grid}), charging (+) or discharging (−) power of energy storage system (P_{BES}), and power from PV panel (P_{PV}) as shown in Eq. 22.

4 Results and Discussion

IEEE 14 bus system is chosen as main grid with PV system and BES integrated at bus number 7. Parameters of system described are shown in Table 4. Optimal scheduling of grid with PV system and battery energy storage is done using MATPOWER. The following three different cases were considered for testing the proposed algorithm. (i) Case 1: Grid without PV system and BES, (ii) case 2: Grid with BES, and (iii) case 3: Grid with PV system and BES OPF results for scheduled generation and scheduled load are shown in Table 5.

As shown in Table 6, grid load demand varies every hour. During charging, BES also acts as load. During daytime (time slot 2), battery is charged from PV system. In both cases 2 and 3, the battery energy storage is used to regulate the frequency at peak and off-peak hours.

Table 4 System parameter

System parameter	Value
Voltage	11 kV
PV panel capacity	98 MW
Battery capacity	300 MWh
Inverter capacity	35 MVA
Renewable energy cost	41.6 $/MWh
Battery cost	60 $/MWh

Table 5 OPF results for scheduled load and generation

OPF result	Value
Generation (MW)	265.76
Load (MW)	259
Cost ($/h)	15,209.06
Power loss (MW)	6.76
Frequency (Hz)	50
UI cost ($/MWh)	63.91
Voltage (p.u.)	1

Table 6 Hourly load demand, power generation, cost of generation, and power loss

Time slot (h)	Hourly load demand (MW)			Power generated by upstream grid (MW)			Cost of active power ($/h)			Power loss (MW)		
	Case 1	Case 2	Case 3	Case 1	Case 2	Case 3	Case 1	Case 2	Case 3	Case 1	Case 2	Case 3
1	236.98	259	259	242.1	265.76	265.76	13,854.67	15,209.06	15,209.06	5.11	6.76	6.76
2	248.99	259	259	254.96	265.76	265.76	14,590.21	15,209.06	15,209.06	5.96	6.76	6.76
3	246.99	259	259	252.81	265.76	265.76	14,467.12	15,209.06	15,209.06	5.81	6.76	6.76
4	242.99	259	259	248.52	265.76	265.76	14,221.59	15,209.06	15,209.06	5.52	6.76	6.76
5	252.99	259	259	259.27	265.76	265.76	14,837.07	15,209.06	15,209.06	6.27	6.76	6.76
6	277	277	277	285.4	265.58	265.58	16,337.69	15,198.81	15,198.81	8.4	6.58	6.58
7	277	277	277	285.4	265.58	265.58	16,337.69	15,198.81	15,198.81	8.4	6.58	6.58
8	279	279	279	287.6	265.58	265.58	16,464.3	15,198.81	15,198.81	8.59	6.58	6.58
9	281.05	281.05	281.05	289.85	265.58	265.58	16,593.92	15,198.81	15,198.81	8.8	6.58	6.58
10	242.99	262.31	262.31	248.52	269.16	197.26	14,221.59	15,404.45	14,132.92	5.52	6.85	2.86
11	238.99	282.76	282.76	244.24	291.45	193.94	13,976.93	16,686	14,930.57	5.24	8.68	2.75
12	214.98	274.79	274.79	218.8	282.72	174.2	12,526.76	16,183.58	14,282.3	3.82	7.93	2.22
13	228.99	285.5	285.5	233.59	294.46	185.69	13,369.04	16,859.21	14,910.81	4.6	8.96	2.5
14	232.99	288.29	288.29	237.84	297.53	188.99	13,611.56	17,036.25	15,080.19	4.85	9.23	2.59
15	244.99	289.86	289.86	250.66	299.26	198.92	14,344.31	17,136.15	15,308	5.67	9.39	2.92
16	275	285.59	285.59	283.2	294.56	224	16,211.32	16,865.02	15,555.18	8.2	8.97	4
17	263	263	263	270.1	269.91	227.89	15,458.2	15,447.06	14,681.78	7.1	6.9	4.2
18	273	273	273	281.01	265.58	265.58	16,085.01	16,038.89	16,038.89	8.01	6.58	6.58
19	277	277	277	285.4	265.58	265.58	16,337.5	16,278.96	16,278.96	8.4	6.58	6.58
20	279	279	279	287.6	265.58	265.58	16,464.22	16,399.1	16,399.1	8.59	6.58	6.58
21	281	281	281	289.8	265.58	265.58	16,591.09	16,519.14	16,519.14	8.8	6.58	6.58
22	279	279	279	287.6	265.58	265.58	16,464.3	16,399.17	16,399.17	8.59	6.58	6.58
23	279	279	279	287.6	265.58	265.58	16,464.34	16,399.21	16,399.21	8.59	6.58	6.58
24	250.99	259	259	257.11	265.76	265.76	14,713.53	15,209.06	15,209.06	6.12	6.76	6.76
Total							364,544.06	381,701.95	368,965.98	165.05	173.36	130.47

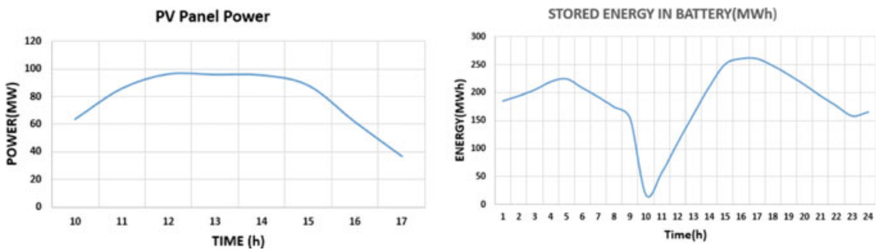

(a) Power output of PV (b) Energy stored in BES

Fig. 3 Power output of PV and energy stored in BES

Amount of power taken from upstream grid is reduced when PV panel is connected into the grid. Upstream grid power generation for each time is given in Table 6. PV panel generates power during time slot 2 (Fig. 3a). PV power is used to supply 20% load demand of upstream grid and charge the battery.

Energy level of BES is shown in Fig. 3b. During daytime, battery is charged to its maximum capacity using PV panel power or from grid. For grid with BES, during evening peak hours, generation is limited to scheduled generation, battery is discharged for extra power needed, and thus frequency is regulated. During evening or night off-peak hours, the BES is charged from the grid. This stored energy is discharged during morning peak hours. For the three test cases, cost of power generated is shown in Table 6.

Frequencies of the system for the three cases are shown in Fig. 4a. For case 1, frequency deviation from its nominal value is high. For case 2, frequency <50 Hz during daytime because battery is charging from the grid. During evening peak hours, battery discharges, and during evening off-peak hours, battery charges to maintain the frequency at 50 Hz. For case 3, daytime frequency is greater than 50 Hz because PV is also generating. Frequency deviation (Δf) for three cases is shown in Fig. 4. Positive value Δf implies frequency greater than 50 Hz, and negative value Δf implies frequency less than 50 Hz. In the case of grid with storage system, during some time slots, frequency deviation is negative because actual load is greater than scheduled load, and frequency is less than 50 Hz. In the case of grid with both PV and storage system, frequency deviation is positive because actual load is less than scheduled load and frequency is greater than 50 Hz (Eqs. 18–20).

Figure 5a shows the UI cost for the three test cases. UI cost at 50 Hz ($\mathrm{UI_{Th}}$) is 63.91 \$/MWh. Battery charges from grid when UI cost $<$ $\mathrm{UI_{Th}}$ and discharges when UI cost is high. As shown in Fig. 5a, during time slot 2, $f > 50$ Hz. In this scenario, grid can sell power to other neighboring power systems to balance the system and gain profit.

Table 6 shows the power loss in each hour for the three cases. For case 2, power loss is increased by 5% than case 1 because of battery charging during off-peak hours. For case 3, power loss is reduced by 20.95% than case 1 because (i) 20% grid

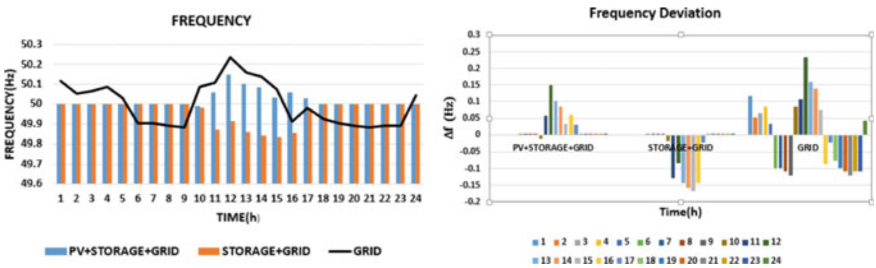

(a) Frequency of the system

(b) Frequency deviation

Fig. 4 System frequency and frequency deviation

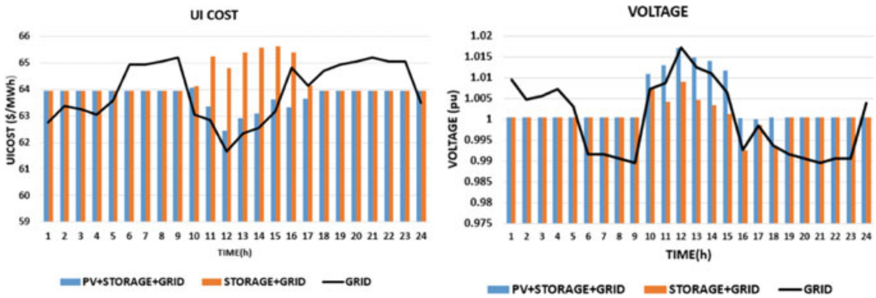

(a) UI cost

(b) Minimum voltages at buses

Fig. 5 UI cost and minimum voltages of IEEE 14 bus system

load is supplied by PV panel during daytime and (ii) discharging of BES at bus 7. Both of these reduce the power loss by reducing the distribution loss.

Figure 5b shows the minimum bus voltage of IEEE 14 bus system for three cases. Voltage of the system drops below 1 p.u. when grid load is greater than the scheduled load and rises above 1 p.u. when grid load is less than scheduled load. For case 2, charging and discharging of BES maintain the voltage magnitude. For case 3, increase in voltage is due to the PV source at bus 7.

5 Conclusions

In this paper, a modified algorithm is formulated for scheduling of grid connected PV system with BES taking UI cost into consideration. Optimal power flow is performed for upstream grid, grid with BES, and for grid connected PV system with BES for various load and generation patterns. BES system was able to regulate the frequency with proper selection of charging and discharging mode based on UI cost. Using the proposed algorithm, it is proved using IEEE 14 bus system that grid connected PV with BES can optimally operate the grid when compared to grid with BES alone. Frequency regulation, reduction in power loss, and improvement of voltage profile are other benefits to grid by the introducing PV system with BES.

References

1. Bhamidi L, Sivasubramani S (2019) Optimal planning and operational strategy of a residential microgrid with demand side management. IEEE Syst J 14(2):2624–2632
2. Carpinelli G, Celli G, Mocci S, Mottola F, Pilo F, Proto D (2013) Optimal integration of distributed energy storage devices in smart grids. IEEE Trans Smart Grid 4(2):985–995
3. Carpinelli G, Mottola F, Proto D, Russo A (2016) A multi-objective approach for microgrid scheduling. IEEE Trans Smart Grid 8(5):2109–2118
4. Chaouachi A, Kamel RM, Andoulsi R, Nagasaka K (2012) Multiobjective intelligent energy management for a microgrid. IEEE Trans Ind Electron 60(4):1688–1699
5. do Prado JC, Qiao W (2018) A stochastic decision-making model for an electricity retailer with intermittent renewable energy and short-term demand response. IEEE Trans Smart Grid 10(3):2581–2592
6. Kharbas B, Fozdar M, Tiwari H (2014) Scheduled incremental and unscheduled interchange cost components of transmission tariff allocation: a novel approach for maintaining the grid discipline. IET Gener Transm Distrib 8(10):1754–1766
7. Koutroulis E, Kolokotsa D (2010) Design optimization of desalination systems power-supplied by PV and W/G energy sources. Desalination 258(1–3):171–181
8. Marler RT, Arora JS (2010) The weighted sum method for multi-objective optimization: new insights. Struct Multidiscipl Optim 41(6):853–862
9. NREL (2020) NSRDB data viewer. https://maps.nrel.gov/nsrdb-viewer/
10. Parisio A, Glielmo L (2012) Multi-objective optimization for environmental/economic microgrid scheduling. In: 2012 IEEE international conference on cyber technology in automation, control, and intelligent systems (CYBER). IEEE, pp 17–22
11. Sousa T, Morais H, Vale Z, Faria P, Soares J (2011) Intelligent energy resource management considering vehicle-to-grid: a simulated annealing approach. IEEE Trans Smart Grid 3(1):535–542
12. Wu D, Aliprantis DC, Ying L (2011) Load scheduling and dispatch for aggregators of plug-in electric vehicles. IEEE Trans Smart Grid 3(1):368–376
13. Zimmerman RD, Murillo-Sánchez CE (2016) Matpower 6.0 user's manual. Power Systems Engineering Research Center, p 9

Chapter 4
Seven-Level Switched-Capacitor-Based Inverter Topology with Reduced Components for Renewable Energy System

Priyanka Sen, Vandana Jha, and Ashwin Kumar Sahoo

Abstract The switched capacitor multilevel inverter (SCMLI) grabbed a special position in power generation from the PV system. The absence of a complex control scheme with the enhancement of output voltage gain is the reason for choosing SCMLI for the PV system. This paper provides a design of seven-level MLI (7L-MLI) with a self-voltage balancing scheme of switched capacitor which can boost the output voltage 1.5 times of source voltage. The focus of attention of the proposed design is the utilization of a fewer number of components as it includes only 7 switches and 2 capacitors with a single source. It also achieved lower total standing voltage (TSV), which makes the design more suitable for high voltage application. The practicality of the system is verified under several testing conditions and also compared with various designs. The simulation results are presented to realize the superiority of the proposed design.

Keywords Switched capacitor multilevel inverter (SCMLI) · Self-balancing scheme · Total standing voltage (TSV) · PV system

1 Introduction

Clean energy generation is an ultimate goal of every nation in current time. Production of electrical energy from PV system is a golden step to fulfill this goal. Power extraction and utilization of PV power becomes more popular owing to the advancement in power electronics technology. For production and distribution of solar energy, power converter technologies are very much required as the output of PV panel is not enough for immediate supply to any load due to low voltage range. The outputs are improved before connecting to the grid. The inverter is required for this purpose. The conventional inverter can be used for this purpose. The issue of high power loss and presence

P. Sen (✉) · V. Jha · A. K. Sahoo
Department of Electrical Engineering, C.V. Raman Global University, Bhubaneswar, Odisha 752054, India

G. Panda et al. (eds.), *Sustainable Energy and Technological Advancements*, Advances in Sustainability Science and Technology,
https://doi.org/10.1007/978-981-16-9033-4_4

of high harmonics generates low power quality output in case of conventional three-level inverter. Bulky low-pass passive filter is utilized for supplying power to the grid in these converter systems, which increases the harmonics. To reduce the high voltage stress and higher switching loss, multilevel inverters (MLIs) are more preferable instead of these conventional inverters. The MLIs are more useful for the reason of its reduced level of switching loss, commendable level of efficiency, capability to operate at high voltage. The electromagnetic interference is also low in case of MLIs [1, 2]. So by the use of MLIs, an improved power quality is observed with the reduction in the level of harmonics.

The various conventional topologies of MLIs such as neutral point clamped (NPC) MLI, flying capacitor (FC) MLI and cascaded H-bridge (CHB) MLIs are more useful than conventional three-level inverter. The NPC and FC MLIs are using a single source, whereas CHB MLI needs multiple sources. Despite this benefit, the CHB MLIs are more suitable due to its modular structure and reliability under fault conditions [1]. The higher number of switches used in these MLIs generates high switching loss, having higher control complexities which became a challenge for the application of these topologies for power generation from PV panels. For these reasons, reduction in the number of switches and reduction of sources become the main objective of researchers. To give a desired boosted level of voltage to MLIs, we need voltage boosting transformer with a proper DC–DC converter which increases the system cost and complexities [3]. The design of various switched-capacitor (SC)-based MLIs can be the solution for these issues [4, 5]. The presence of the capacitor in these MLI topologies can provide higher voltage magnitude and can reduce the number of sources used as compared to the conventional CHB MLIs. The ability to boost the voltage magnitude is more in SCMLIs as compared with the switched diode-based configurations. The desired level of the output voltage is achievable by applying a suitable control scheme [6–8]. In SCMLIs, the capacitors are continuously charged or discharged according to a particular sequence. Some of the MLI topologies are based on the SC technique, but it consists of a large number of semiconductor devices, multiple sources and higher voltage stress levels on switches [9–11]. Therefore, the reduction in a number of circuit devices utilized for SC-based MLI design is the major intention of researchers in the current era. Especially, the employment of the multiple sources in MLI structures is focused to minimize.

The self-balanced SCMLI structures proposed by researchers provide a reduction in the number of switches, with reduced source count [12, 13]. These inverter circuits can provide a triple increase in voltage output with reduced THD but at the cost of the number of switches or diodes. The stress level on switches is lowered to a remarkable level in the SCMLI designed in [14]. Toward higher voltage level synthesis, structure in [15] has a significant advantage. Another crucial issue for use of SCMLI in high voltage applications is higher voltage stress on switches. It should be taken care of during the development of SCMLI-based topologies.

The fact that SCMLI can enhance the output voltage with batter power quality is clearly observable from the above discussion. With reduction in count of semiconductor devices and sources and with optimized voltage stress level, the efficiency of stand-alone-type PV system can be enhanced. Proposed MLI is discussed herein after. After a detailed comparative study, simulations are conducted to verify the operational features.

2 Working Pattern of Proposed System

The proposed SCMLI design utilizes 7 switches (T_1–T_7), two capacitors (C_1–C_2) and 2 diodes (D_1–D_2) as shown in circuit in Fig. 1. This topology provides 7-level output from (0, $\pm 0.5V_{\text{dc}}$, $\pm V_{\text{dc}}$, $\pm 1.5V_{\text{dc}}$). The switching pattern and charging discharging pattern are analyzed as follows:

2.1 Circuit Operation Analysis

The different modes of operation to generate the output levels of SCMLI are as under:

Level-1 ($V_o = 0$)

To achieve this level in output, the switches T_2, T_4, T_7 are conducting. As the capacitors (C_1 and C_2) are in series with the source, they charge up to $0.5\boldsymbol{V}_{\mathbf{dc}}$. The voltage across the load will be 0.

Level-2 ($V_o = 0.5V_{dc}$)

In this stage, the switches T_1, T_4, T_7 are in conduction mode. So, the capacitors C_1 start discharging in series, while no effect on C_2. The voltage across the load will be $0.5\boldsymbol{V}_{\mathbf{dc}}$ as it is in parallel with the capacitor.

Level-3 ($V_o = V_{dc}$)

For producing $\boldsymbol{V}_{\mathbf{dc}}$ across the load, the switches T_2, T_4, T_6 are in conduction mode. So, both the capacitors (C_1 and C_2) are charged as they are in series with source and the load is in parallel with the source.

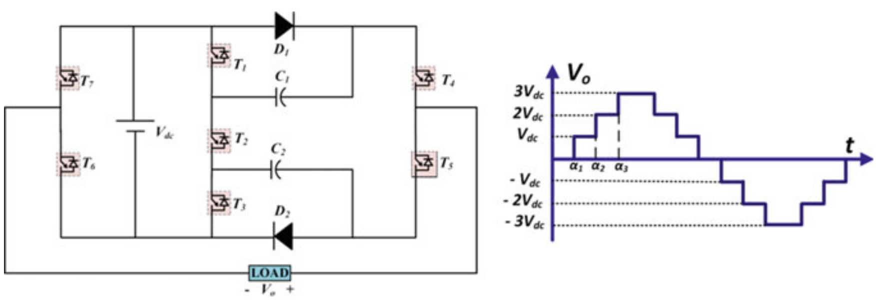

Fig. 1 Proposed MLI with its output voltage pattern

Level-4 ($V_o = 1.5V_{dc}$)

In this stage, the switches T_1, T_4, T_6 are conducting. The capacitor C_1 is discharged, and the voltage of capacitor C_1 and the source voltage are added up and appear across the load. So, the voltage across the load becomes $1.5V_{dc}$.

Level-5 ($V_o = -0.5V_{dc}$)

Similarly, for generating $-0.5V_{dc}$ across the load, the switches T_3, T_5, T_6 are conducting and the capacitor C_2 is discharged. C_1 has no effect. During discharging, the polarity will be opposite; therefore, negative voltage appears across the load.

Level-6 ($V_o = -V_{dc}$)

In this level, the switches T_2, T_5, T_7 are in conduction mode. The capacitors (C_1 and C_2) are in series with source, and charging process continues in this stage. The load voltage becomes $\boldsymbol{-V_{dc}}$. Capacitor C_2 has no effect here as it is not in close path of load.

Level-7 ($V_o = -1.5V_{dc}$)

To generate $-1.5V_{dc}$ across the load, the switches T_3, T_5, T_7 are kept in conduction stage. The capacitor C_2 discharges, and the voltage of source and capacitor C_2 will be added and appears across the load. C_1 has no effect in this stage, as it is in open path.

By using the self-balanced charging and discharging of capacitors, it becomes simpler as compared to conventional design of MLI. The switches in this structure are operated in fundamental frequency. The voltage stress on the switches (T_1, T_2, T_3) is $0.5V_{dc}$. The switches (T_4, T_5) block $1.5V_{dc}$ when not conducting. The switches (T_6, T_7) block $1V_{dc}$ when not conducting. So, the total TSV is $6.5V_{dc}$. Conventional MLI topologies utilize multiple sources for generating multiple level, but the proposed circuit provides the same level with single source. Therefore, the complexity as well as the cost is minimized. With the given switching sequence, the output can be boosted 1.5 times with the presented model, which is much required for application in PV system. Figure 2 shows the working operation of the proposed structure.

3 Comparative Analysis of Presented Design and Other Recent Design

The design potentiality can be judged by comparing the proposed seven-level SCMLI structure with recently designed SCMLIs. In Table 1, a comparative study is given between different recently developed structures. The parameters based on which the structures are compared are the number of switches utilized, the number of diodes and capacitor used, total standing voltage of switches (TSV), gain and ability to handle the inductive load. Model S1 suggests a seven-level SCMLI with the same number of switches as the proposed model, but it contains more capacitors and the output is

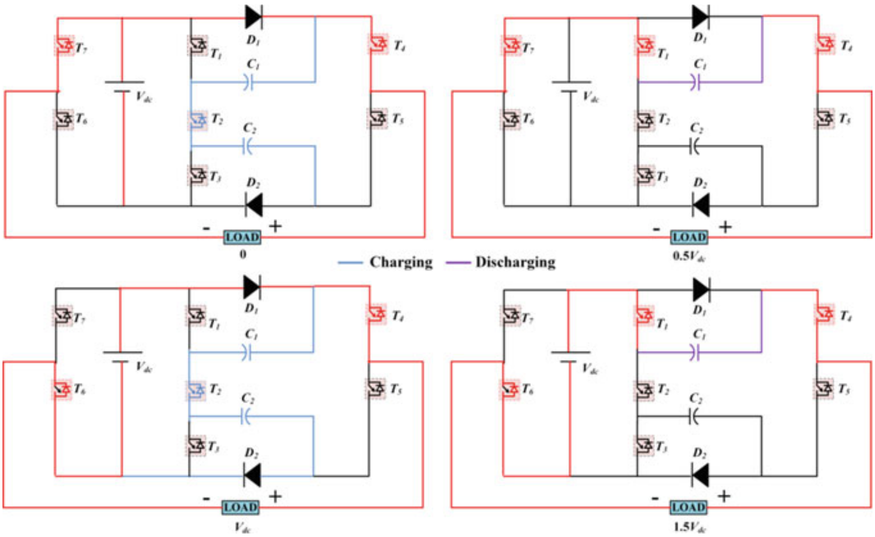

Fig. 2 Working scheme of the proposed 7-level MLI

Table 1 7L-SCMLI topology comparison with single input

Parameters	S1 [16]	S2 [10]	S3 [11]	S4 [17]	S5 [18]	S6 [13]	S7 [9]	S8 [19]	PS
Number of switches	7	10	10	8	16	14	12	9	7
Number of capacitors	3	4	3	2	3	2	2	2	2
Number of diodes	2	0	0	2	0	2	0	1	2
Gain in output	1	1.5	1.5	1.5	3	3	3	3	1.5
TSV (× V_{dc})	5	8	8	7	14	14	16	17	6.5

not boosted. The designed structures S2 and S3 use more switches and capacitors to boost the output voltage 1.5 times as proposed structure. S4 reduces the number of switches significantly. However, the capacitor count and the TSV are more than the proposed SCMLI. More gain in output voltage is obtained by the topologies S5–S8 than the proposed topology, but they use a higher number of switches which makes the system complex and costly. Due to the high level of TSV, these structures will be less suitable for high voltage applications as compared to the proposed topology. S6 and S7 topologies are also boosting the output 3 times, but they utilize larger number of switches which makes the system overpriced. High TSV is observed in S7 and S8 as compared to the presented design, despite the use of a large number of switches. In light of the above analysis, the presented seven-level SCMLI is more appropriate for low-cost–high voltage applications. A reduced number of capacitors also increase the reliability of the proposed MLI running for a long time. Further, the arrangements of the components are such that it operates under any loading condition similar to the other topologies.

The proposed design contains optimal number of switches and capacitors compared to all the discussed recent developed topologies. The TSV which is important for sustainability in high voltage application is very low. The uniqueness of this model can be realized from the features like boosting ability, lower component count and low standing voltage.

4 Simulation Results

The presented SCMLI (7L) includes seven IGBT switches and two capacitors as shown in Fig. 1. The simulation is carried out by MATLAB/Simulink. To validate the feasibility of model, a single DC source of 70 V is chosen. The frequency is 50 Hz, with resistive load of 40 Ω, and the two inductive loads (35 Ω–70 mH and 50–250 mH) are utilized for simulation. The capacitors are of 2200 μF. The rating of capacitor is selected for their longer discharging duration. The modulation techniques generally used to control the switches are carrier-oriented high-frequency technique and some of the low frequency modulation technique such as selective harmonic elimination (SHE) control. It has potential to compute firing angle with different modulation index values. To wipe out 3rd- and 5th-order harmonics, solution of three nonlinear equations is needed. The 3rd- and 5th-order harmonic is aimed to eliminate in this work. The objective function is selected as per [20, 21] to get the desired switching angle. Simulation has been carried out at 0.94 MI. To justify the appropriateness of the design, various testing conditions are utilized and analysis is as follows:

Condition-1 [with low modulation index]

From Fig. 2, it is observable that the proposed model can work successfully with low MI 0.2 and high MI 0.9. In Fig. 3, V_o represents the output voltage, I_o is the load current, and V_{C1} and V_{C2} are the voltages across the two capacitors (C_1 and C_2). In Fig. 3, the simulation is performed with low MI 0.2 and further results are obtained at high MI.

Condition-2 [with variation in load]

Figure 4 shows the design is compatible with inductive load. From 0.1 to 0.14 s, the RL load is of 35 Ω–70 mH; when it changed to 50 Ω–250 mH, it can sustain with the sudden load change efficiently.

Condition-3 [with variation in input voltage]

In Fig. 5, the input voltage is 70 V from 0.1 to 0.14 s, whereas from 0.14 to 0.18 s it

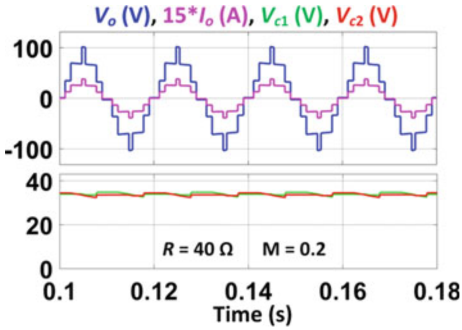

Fig. 3 Simulation under low MI

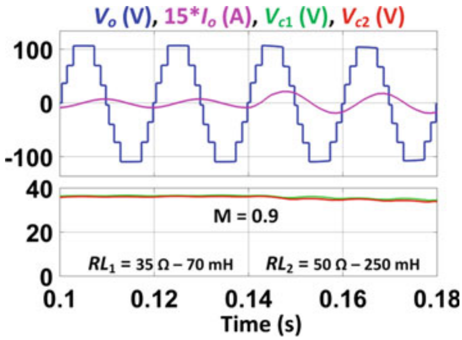

Fig. 4 Simulation under load variation

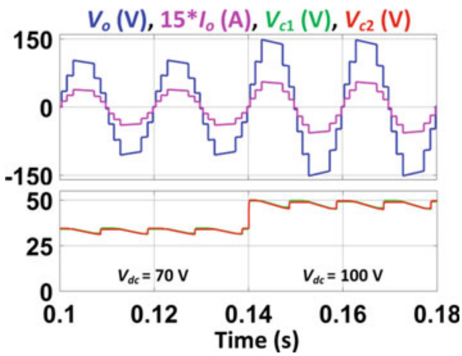

Fig. 5 Simulation under input voltage variation

changed to 100 V. As the SCMLI designed for PV application, it is noteworthy that the system can operate properly with low as well as high input voltage.

The designed topology of MLI can work effectively with distinct MI values. The percentage of THD is lower level, due to removal of 3rd- and 5th-order harmonics with high MI value. The voltage THD is 19.07% with low value of MLI (0.2), and it is 10.15% at high MI (0.94). From the results, it is clear that the topology is suitable for both low- and high-power factor loads.

5 Conclusion

In this work, the SCMLI has been presented for PV application with a lower component count and self-voltage balancing scheme for the capacitor. It is preferable for single-source PV applications and in other low-medium power applications. The low TSV makes the design noteworthy for high voltage applications. The boosting feature and usability with any variation in load as well as variation in MI make it suitable for different applications. Another key point of the model is the size of the capacitors which can be optimized by the use of high-frequency applications. As the switches are operated at the fundamental frequency, the efficiency is more than 97% owing to the reduction in power loss in switches. The simulation study under different testing conditions and comparative analysis with recent models justify the self-voltage balancing capability, boosting capacity and thus the sustainable application of disclosed SCMLI in PV applications.

References

1. Bana PR, Panda KP, Naayagi RT, Siano P, Panda G (2019) Recently developed reduced switch multilevel inverter for renewable energy integration and drives application: topologies, comprehensive analysis and comparative evaluation. IEEE Access 7:54888–54909
2. Bana PR, Panda KP, Panda G (2020) Performance evaluation of a reduced components count single-phase asymmetric multilevel inverter with low standing voltage. Int Trans Electr Energy Syst e12239
3. Bana PR, Panda KP, Panda G (2020) Power quality performance evaluation of multilevel inverter with reduced switching devices and minimum standing voltage. IEEE Trans Ind Inf 16(8):5009–5022
4. Panda KP, Bana PR, Panda G (2020) A switched-capacitor self-balanced high-gain multilevel inverter employing a single DC source. IEEE Trans Circuits Syst II Express Briefs 67(12):3192–3196
5. Panda KP, Bana PR, Panda G (2021) A reduced device count single DC hybrid switched-capacitor self-balanced inverter. IEEE Trans Circuits Syst II Express Briefs 68(3):978–982
6. Babaei E, Gowgani SS (2014) Hybrid multilevel inverter using switched capacitor units. IEEE Trans Ind Electron 61(9):4614–4621
7. Bana PR, Panda KP, Padmanaban S, Panda G (2021) Extendable switched-capacitor multilevel inverter with reduced number of components and self-balancing capacitors. IEEE Trans Ind Appl 57(3):3154–3163
8. Sen P, Bana PR, Panda KP (2019) Firefly assisted genetic algorithm for selective harmonic elimination in PV interfacing reduced switch multilevel inverter. Int J Renew Energy Res (IJRER) 9(1):32–43
9. Siddique MD, Mekhilef S, Shah NM, Ali JSM, Blaabjerg F (2019) A new switched capacitor 7L inverter with triple voltage gain and low voltage stress. IEEE Trans Circuits Syst II Express Briefs 1
10. Lee SS, Bak Y, Kim S-M, Joseph A, Lee K-B (2019) New family of boost switched-capacitor seven-level inverters (BSC7LI). IEEE Trans Power Electron 34(11):10471–10479
11. Liu J, Zhu X, Zeng J (2020) A seven-level inverter with self-balancing and low-voltage stress. IEEE J Emerg Sel Topics Power Electron 8(1):685–696
12. Ye Y, Cheng KWE, Liu J, Ding K (2014) A step-up switched-capacitor multilevel inverter with self-voltage balancing. IEEE Trans Ind Electron 61(12):6672–6680

13. Taghvaie A, Adabi J, Rezanejad M (2018) A self-balanced step-up multilevel inverter based on switched-capacitor structure. IEEE Trans Power Electron 33(1):199–209
14. Panda KP, Bana PR, Panda G (2020) A single source switched-capacitor based multilevel inverter for photovoltaic application. In: 2020 IEEE international conference on power electronics, smart grid and renewable energy (PESGRE2020), Kerala, pp 1–6
15. Panda KP, Bana PR, Kiselychnyk O, Wang J, Panda G (2021) A single-source switched-capacitor-based step-up multilevel inverter with reduced components. IEEE Trans Ind Appl 57(4):3801–3811
16. Choi J, Kang F (2015) Seven-level PWM inverter employing series-connected capacitors paralleled to a single DC voltage source. IEEE Trans Ind Electron 62(6):3448–3459
17. Panda KP, Bana PR, Panda G (2020) Reduced switch count seven-level self-balanced switched-capacitor boost multilevel inverter. In: 2020 IEEE international conference on power electronics, drives and energy systems (PEDES), pp 1–6
18. Sun X, Wang B, Zhou Y, Wang W, Du H, Lu Z (2016) A single DC source cascaded seven-level inverter integrating switched-capacitor techniques. IEEE Trans Ind Electron 63(11):7184–7194
19. Panda KP, Bana PR, Panda G (2020) A self-balanced switched-capacitor boost seven-level inverter for photovoltaic systems. In: 2020 IEEE international conference on computing, power and communication technologies (GUCON), pp 338–343
20. Panda KP, Lee SS, Panda G (2019) Reduced switch cascaded multilevel inverter with new selective harmonic elimination control for standalone renewable energy system. IEEE Trans Ind Appl 55(6):7561–7574
21. Panda KP, Bana PR, Panda G (2020) FPA optimized selective harmonic elimination in symmetric-asymmetric reduced switch cascaded multilevel inverter. IEEE Trans Ind Appl 56(3):2862–2870

Chapter 5
Reference Tracking by Designing State Estimation Observer for Generalized Predictive Control of a Single Inductor Dual Output Buck Converter

Kamakshi Manjari and Somanath Majhi

Abstract A generalized predictive control (GPC) for an unconstrained two output buck converter system is presented in this paper. Stability analysis of predictive control is challenging to prove; hence, a more straightforward idea of stability analysis for a basic GPC optimization is validated for a general GPC cost function. As classical control is less effective in controlling a multi-input multi-output (MIMO) system, in which the outputs are coupled in nature, and predictive control is implemented to show the effectiveness. MATLAB numerical simulation results of the controller are included for validation.

Keywords Single inductor dual output buck converter · Generalized predictive control · Observer design

1 Introduction

Model predictive control (MPC) is a type of optimal control theory in which the plant model is typically utilized to anticipate a plant behavior. MPC has been used in applications including process control [1, 2], electric vehicle [3, 4] and power converters [5–9] to name a few. Application of predictive control also includes control of switching mode power supplies (SMPS) [10, 11] as well. Generalized predictive control (GPC) is a type of predictive control that is widely explored and inherently includes an integrator for an error-free response. However, PI or PID controller is the most commonly used control technique in the process control industry. However, it is a well-known fact that in the presence of plant dead time, the performance of a PID is compromised. For such a closed-loop plant model, an appropriate measure

K. Manjari (✉) · S. Majhi
Department of Electronics and Electrical Engineering, Indian Institute of Technology Guwahati, Guwahati, India
e-mail: kamakshi@iitg.ac.in

S. Majhi
e-mail: smajhi@iitg.ac.in

G. Panda et al. (eds.), *Sustainable Energy and Technological Advancements*,
Advances in Sustainability Science and Technology,
https://doi.org/10.1007/978-981-16-9033-4_5

is to inspect the performance of a good optimal control technique in place of the classical PID controller. The use of GPC is limited because of its complicated tuning guidelines and implementation cost. The high operating frequency range of SMPS is a challenge for GPC implementation. Originally, GPC was designed only for slower dynamic plants, but faster processors have overcome this barrier. Another limitation of GPC is the difficulty of stability analysis compared to a classical controller [12].

GPC has also been successfully implemented to step [13] as well as ramp reference tracking problem [14]. While a traditional GPC [15, 16] is proposed by considering a controlled auto-regressive integrated moving average model (CARIMA) to predict the output prediction, extension of this model to a multivariable plant dynamics is cumbersome. As a result, the augmented state space model [17] is preferred for output prediction obtaining the optimized control sequence. A predictive control consists of a prediction horizon, control horizon and a defined cost function according to the user's need, to obtain an optimized control sequence. The control input obtains a state feedback control by using receding horizon control (RHC). In RHC, only the first input sequence is considered the manipulated variable, and the rest are discarded. If all states are not available to measure, the system states might not be fully controllable. Hence, an observer must be designed for unmeasured states of the plant [18]. Observer design and stability analysis of any controller play an important role in determining the convergence of the error. The usage of low power portable devices is increasing daily, motivating researchers to develop an efficient control algorithm for these devices to achieve the desired output. Recently, multi-output power converters have been researched widely due to their many advantages over single output converters. A single inductor multi-output (SIMO) converter has a small volume compared to a dual inductor system as it works using only a single inductor. Due to a decrease in the number of components, the cost is reduced, and efficiency is improved. SIMO converters are also implemented in electric vehicles (EV) for this reason. However, the effect of output cross-coupling in the chosen plant dynamics is prominent when there is a change in either one of the outputs, which affects the other output because controller tuning is challenging to design for this converter. There have been many successful implementations of classical control techniques to control SIMO power converters, but the advanced controller is preferred for a SIMO power converter device due to complicated system dynamics.

Primary contribution of this presented work is to design a Luenberger-type observer for a GPC to have an error-free reference tracking for a state feedback closed-loop control. Observer gain is determined by using Lyapunov stability criteria for the observer. Numerical simulation results of the closed-loop plant model are presented to validate the design procedure of GPC. Schur complement for the positive definiteness of the chosen Lyapunov function is used to determine the observer gain. The controller designing procedure is validated using a DC–DC single inductor dual output (SIDO) buck converter model.

This paper is organized as follows: The augmented GPC is described in Sect. 2 with a detailed derivation of the state and output prediction model and derivation of the optimized control law. In Sect. 3, the convergence of the chosen control law is presented. A Luenberger-type observer is designed in Sect. 4 with criteria to chose the observer gain matrix. Numerical simulation results are presented in Sect. 5 to validate the estimation by the designed observer. Finally, conclusion of this paper is available in Sect. 6.

2 Generalized Predictive Control

The states space model of a plant can be represented as

$$x_{\mathrm{m}}(k+1) = A_{\mathrm{m}}x_{\mathrm{m}}(k) + B_{\mathrm{m}}u(k), \qquad y_{\mathrm{m}}(k) = C_{\mathrm{m}}x_{\mathrm{m}}(k) \tag{1}$$

where the state $x_{\mathrm{m}} \in \mathbb{R}^{n\times 1}$, output $y_{\mathrm{m}} \in \mathbb{R}^{l\times n}$ and input $u \in \mathbb{R}^{m\times 1}$ are defined accordingly. All the states of the chosen plant model are assumed to be controllable. If the number of states is less than number of outputs, then all outputs cannot be controlled with zero steady-state error independently. From (1), the following equation can be obtained as

$$x_{\mathrm{m}}(k) = A_{\mathrm{m}}x_{\mathrm{m}}(k-1) + B_{\mathrm{m}}u(k-1) \tag{2}$$

To remodel the state space model in $\Delta u(k)$ as input variable, state vector $x_{\mathrm{m}}(k)$ is replaced with $\Delta x_{\mathrm{m}}(k)$ where $\Delta x_{\mathrm{m}}(k) = x_{\mathrm{m}}(k) - x_{\mathrm{m}}(k-1)$. From (1) and (2), $\Delta x_{\mathrm{m}}(k+1)$ can be expressed as

$$\Delta x_{\mathrm{m}}(k+1) = A_{\mathrm{m}}\Delta x_{\mathrm{m}}(k) + B_{\mathrm{m}}\Delta u(k) \tag{3}$$

Similarly, $\Delta y_{\mathrm{m}}(k+1)$ is obtained as

$$\Delta y_{\mathrm{m}}(k+1) = C_{\mathrm{m}}A_{\mathrm{m}}\Delta x_{\mathrm{m}}(k) + C_{\mathrm{m}}B_{\mathrm{m}}\Delta u(k) \tag{4}$$

New state vectors are chosen as $x_{\mathrm{m}} = \left[\Delta x_{\mathrm{m}}(k)\ e(k)\right]$ for the state augmented model, where $e(k) = w(k) - y(k)$. Resulted modified state space model of the plant model is written as

$$\begin{bmatrix} \Delta x_{\mathrm{m}}(k+1) \\ e(k+1) \end{bmatrix} = \begin{bmatrix} A_{\mathrm{m}} & 0_{\mathrm{m}}^{\mathrm{T}} \\ C_{\mathrm{m}}A_{\mathrm{m}} & I \end{bmatrix}\begin{bmatrix} \Delta x_{\mathrm{m}}(k) \\ e(k) \end{bmatrix} + \begin{bmatrix} B_{\mathrm{m}} \\ C_{\mathrm{m}}B_{\mathrm{m}} \end{bmatrix}\Delta u(k) \tag{5}$$

$$e(k) = \begin{bmatrix} 0_{\mathrm{m}} & I_{\mathrm{m}} \end{bmatrix}\begin{bmatrix} \Delta x_{\mathrm{m}}(k) \\ e(k) \end{bmatrix} \tag{6}$$

where I_{m} is identity matrix and 0_{m} is zero matrix. Output prediction equation is obtained by recursion of one step ahead state equation as explained in [17]. $\zeta(k)$ is assumed to be a zero mean Gaussian noise; therefore, the expected value of zero mean Gaussian noise, i.e., $\zeta(k+i|k)$ at future sample i is assumed to be zero. The augmented model in (5) and (6) is

$$x_{\mathrm{n}}(k+1) = A_{\mathrm{n}}x_{\mathrm{n}}(k) + B_{\mathrm{n}}\Delta u(k) \tag{7}$$

$$e(k) = C_{\mathrm{n}}x_{\mathrm{n}}(k) \tag{8}$$

Prediction of the augmented matrix is obtained as

$$x_{\mathrm{n}}(k+1|k) = A_{\mathrm{n}}x_{\mathrm{n}}(k) + B_{\mathrm{n}}\Delta u(k) \tag{9}$$

$$x_{\mathrm{n}}(k+2|k) = A_{\mathrm{n}}^2x_{\mathrm{n}}(k) + A_{\mathrm{n}}B_{\mathrm{n}}\Delta u(k) + B_{\mathrm{n}}\Delta u(k+1|k) \tag{10}$$

$$\vdots$$

$$\begin{aligned} x_{\mathrm{n}}(k+N|k) = A_{\mathrm{n}}^N x_{\mathrm{n}}(k) + A_{\mathrm{n}}^{N-1}B_{\mathrm{n}}\Delta u(k) + \cdots \\ + A_{\mathrm{n}}^{N-M}B_{\mathrm{n}}\Delta u(k+M-1) \end{aligned} \tag{11}$$

Similarly, predicted output is also obtained. New vectors are defined as

$$\Delta U(k) = \left[\Delta u(k)\ \Delta u(k+1)\ \cdots\ \Delta u(k+M-1)\right] \tag{12}$$

$$E_{\mathrm{p}}(k) = \left[e(k+1|k)\ e(k+2|k)\ \cdots\ e(k+N|k)\right]$$

Predicted state space model is expressed as follows:

$$E_{\mathrm{p}}(k+1) = C_{\mathrm{n}}x_{\mathrm{n}}(k) \Rightarrow E_{\mathrm{p}}(k+1) = F_{\mathrm{p}}x_{\mathrm{p}}(k) + Q_{\mathrm{p}}\Delta U(k) \tag{13}$$

where F_{p} and Q_{p} coefficient matrices are represented as

$$F_{\mathrm{p}}^{\mathrm{T}} = \left[\ C_{\mathrm{n}}A_{\mathrm{n}}\ C_{\mathrm{n}}A_{\mathrm{n}}^2 \cdots C_{\mathrm{n}}A_{\mathrm{n}}^N\right]^{\mathrm{T}} \tag{14}$$

$$Q_{\mathrm{p}} = \begin{bmatrix} C_{\mathrm{n}}B_{\mathrm{n}} & 0 & \cdots & 0 \\ C_{\mathrm{n}}A_{\mathrm{n}}B_{\mathrm{n}} & C_{\mathrm{n}}B_{\mathrm{n}} & \cdots & 0 \\ \vdots & \vdots & \vdots & \vdots \\ C_{\mathrm{n}}A_{\mathrm{n}}^{N-1}B_{\mathrm{n}} & C_{\mathrm{n}}A_{\mathrm{n}}^{N-2}B_{\mathrm{n}} & \cdots & C_{\mathrm{n}}A_{\mathrm{n}}^{N-M}B_{\mathrm{n}} \end{bmatrix} \tag{15}$$

The defined quadratic cost function is

$$J(\Delta u) = \mathbf{Q}\sum_{i=1}^{N}\left\|E_{\mathrm{p}}(k)\right\|_2^2 + \mathbf{R}\sum_{i=0}^{M}\|\Delta U(k)\|_2^2 \tag{16}$$

where the weight coefficients are positive definite constant diagonal matrices denoted as $\mathbf{Q}$ and $\mathbf{R}$. Optimized manipulated variable is determined by minimizing the defined cost function (16), i.e., $\frac{\mathrm{d}J}{\mathrm{d}(\Delta U)} = 0$. Solution of this minimization is obtained as $\Delta U = (Q_{\mathrm{p}}^{\mathrm{T}}\mathbf{Q}Q_{\mathrm{p}} + \mathbf{R})^{-1}Q_{\mathrm{p}}^{\mathrm{T}}\mathbf{Q}(w(k) - F_{\mathrm{p}}x_{\mathrm{n}}(k))$. According to RHC, only the first manipulated variable is applied to the plant. The obtained feedback gain matrix is $K_{\mathrm{mpc}} = (Q_{\mathrm{p}}^{\mathrm{T}}\mathbf{Q}Q_{\mathrm{p}} + \mathbf{R})^{-1}Q_{\mathrm{p}}^{\mathrm{T}}\mathbf{Q}$. Optimized control input is expressed as

$$\Delta u(k) = K_{w_1} w(k) - K_{y_1} x_n(k) \tag{17}$$

where K_{w_1} is the first element of K_{mpc} and K_{y_1} is the first element of $K_{mpc}F_p$. The modified state model for closed-loop system is

$$x_n(k+1) = \left(A_n - B_n K_{y_1}\right) x_n(k) + B_n K_{w_1} w(k) \tag{18}$$

Hence, eigenvalues of $\left(A_n - B_n K_{y_1}\right)$ determine the closed-loop system stability.

3 Convergence of Control Law

To analyze convergence of the obtained control law, quadratic cost function ($J \Delta u$) is chosen as the Lyapunov function candidate, $z(f(x_n(k)))$. An equality constraint on the terminal state is considered, which means that the error between reference and output tends to zero. $x_n(k+N) = 0$ is set as the terminal state obtained from optimizing control sequence $\Delta u(k) = K_{mpc} f(x_n(k))$. Lyapunov function candidate $z(f(x_n(k)))$ is positive definite, and it tends to a finite value if $x_n(k)$ is a finite value as the cost function is quadratic in nature. Next Lyapunov criteria to be satisfied are $\Delta z(f(x_n(k+1))) < 0, \forall k \geq 0$. Therefore, $z(f(x_n(k+1))$ is expressed as

$$\Delta z(f(x_n(k+1))) = z(f(x_n(k+1))) - z(f(x_n(k)))$$

Assuming that the optimized solution $\Delta u(k)$ satisfies all constraints at sample instant k, a feasible solution of $f(x_n(k+1))$ for the receding horizon is given by $x_n(k+1)$, which is represented by the prediction model

$$x_n(k+1) = A_n(k) + B\Delta u(k) \tag{19}$$

Obtained optimal solution $\Delta u(k+1)$ is a function of $f(x_n(k+1))$, and it is observed that

$$z(f(x_n(k+1))) \leq \hat{z}(f(x_n(k+1))) \quad \forall k \geq 0 \tag{20}$$

where $\hat{z}(f(x_n(k+1)))$ is the obtained control sequence which is a function of the sequence $x_n(1), x_n(2), \ldots, x_n(k+N-1)$. $\Delta z(f(x_n(k+1)))$ is then bounded by

$$z(f(x_n(k+1))) - z(f(x_n(k))) \leq \hat{z}(x_n(k+1) - z(x_n(k)) \tag{21}$$

For the sample time $k+1, k+2, \ldots, k+N-1$, the difference between these two Lyapunov two functions is obtained as

$$\Delta z(f(x_\mathrm{n}(k+1))) = (x_\mathrm{n}(k+N)|k)^\mathrm{T}\mathbf{Q}(x_\mathrm{n}(k+N)|k) - \\ x_\mathrm{n}(k+1)^\mathrm{T}\mathbf{Q}x_\mathrm{n}(k+1) - \Delta u(k)^\mathrm{T}\mathbf{R}\Delta u(k) \tag{22}$$

From the assumption of final constraint, it can be stated that

$$\Delta z(f(x_\mathrm{n}(k+1))) \leq -x_\mathrm{n}(k+1)^\mathrm{T}\mathbf{Q}x_\mathrm{n}(k+1) - \Delta u(k)^\mathrm{T}\mathbf{R}\Delta u(k) \qquad \forall k \geq 0$$

Hence, the asymptotic stability of the model predictive control system has been proved. To show that $z(f(x(k))) = 0\ \forall\ e(0) = 0$ and $\Delta u(0) = 0$, a new variable $v = [x_n(k)\Delta u(k)]^\mathrm{T}$ is defined. It is assumed, $\exists v \neq 0$ for which $z = v^\mathrm{T}\begin{bmatrix}\mathbf{Q} & 0\\ 0 & \mathbf{R}\end{bmatrix}v = 0$. $\mathbf{Q}$ and $\mathbf{R}$ are already assumed to be diagonal matrices of constant value; hence, z is positive definite as $\begin{bmatrix}\mathbf{Q} & 0\\ 0 & \mathbf{R}\end{bmatrix}$ is positive definite. $z = 0$ when $v = 0$, which contradicts original assumption. Hence, $\Delta z(f(x_\mathrm{n}(k+1))) \leq -(1-\lambda^2)\ \|v(k)\|^2$.

4 Observer Design for State Estimation

In this section, a Luenberger-type [18] observer is designed for the state estimation of the GPC. The observer model is represented as

$$\hat{x}_\mathrm{o}(k+1) = A_\mathrm{n}\hat{x}_\mathrm{o}(k) + B_\mathrm{n}\Delta u(k) + L_\mathrm{o}\left(y(k) - C_\mathrm{n}\hat{x}_\mathrm{o}(k)\right) \quad \forall k \geq 0 \tag{23}$$

where $\hat{x}_\mathrm{o}(k+1)$ is defined as the state estimation obtained by the Luenberger-type observer, and the observer gain is defined as L_o. $\zeta(k)$ is assumed to be zero in the augmented state space model. Defining $e(k) = x_\mathrm{n}(k) - \hat{x}_\mathrm{o}(k)\ \forall\ k \geq 0$, the error in observer estimation is obtained as

$$e(k+1) = (A_\mathrm{n} - L_\mathrm{o}C_\mathrm{n})\,e(k) \quad \forall k \geq 0 \tag{24}$$

$$= \tilde{A}_\mathrm{n}e(k) \tag{25}$$

A Lyapunov function candidate is defined as

$$Z_\mathrm{o}(e(k)) = e^\mathrm{T}(k)Q_\mathrm{o}e(k) \quad \forall k \geq 0 \tag{26}$$

Theorem 1 *Let Q_o be defined as a symmetric positive definite matrix, then there exists a Luenberger gain matrix L_o defined as*

$$L_o = Q_o^{-1}P_o \tag{27}$$

Proof It is defined that $Q_o = Q_o^T > 0$. The Lyapunov function is expressed as in (26). Therefore, $\Delta Z_o(e(k))$ is defined as

$$\Delta Z_o(e(k)) = Z_o(e(k+1)) - Z_o(e(k)) \tag{28}$$

$$= e^T(k+1)Q_o e(k+1) - e^T(k)Q_o e(k) \tag{29}$$

$$= e^T(k)\left(\tilde{A}_n^T Q_o \tilde{A}_n - Q_o\right)e(k) \tag{30}$$

From (30), it can be observed that for $\Delta Z_o(e(k)) < 0$

$$\tilde{A}_n^T Q_o \tilde{A}_n - Q_o < 0 \quad \forall k \geq 0 \tag{31}$$

Therefore, (31) can be expressed as a negative value, and it is assumed that

$$\tilde{A}_n^T Q_o \tilde{A}_n - Q_o < -(1-\epsilon^2)Q_o \quad \forall k \geq 0 \tag{32}$$

Now, (32) is rearranged to

$$\tilde{A}_n^T Q_o \tilde{A}_n - Q_o + (1-\epsilon^2)Q_o < 0 \quad \forall k \geq 0 \tag{33}$$

$$Q_o\epsilon^2 - \tilde{A}_n^T Q_o Q_o^{-1} Q_o \tilde{A}_n > 0 \quad \forall k \geq 0 \tag{34}$$

(34) can be expressed as a Schur compliment in (35)

$$\begin{bmatrix} Q_o & Q_o\tilde{A}_n \\ \tilde{A}_n^T Q_o & Q_o\epsilon^2 \end{bmatrix} > 0 \tag{35}$$

which can be expressed in observer gain matrix form as

$$\begin{bmatrix} Q_o & Q_o\left(A_n - L_o C_n\right) \\ \left(A_n - L_o C_n\right)^T Q_o & Q_o\epsilon^2 \end{bmatrix} > 0 \tag{36}$$

$L_o = Q_o^{-1} P_o$ is defined, hence (36) is represented as

$$\begin{bmatrix} Q_o & Q_o A_n - P_o C_n \\ A_n^T Q_o - C_n P_o^T & Q_o\epsilon^2 \end{bmatrix} > 0 \tag{37}$$

Therefore, it can be concluded that

$$\Delta Z_o(e(k)) < -(1-\epsilon^2)p^T(k)Q_o(e(k)) < 0, \quad \forall k \geq 0, \forall (p(0)) \neq 0$$

Using this observer implementation, states of GPC optimized control $x_n(k)$ are replaced by the observer state vector. Hence, obtained control law can be written as

$$\Delta u(k) = K_{\mathrm{w}_1} w(k) - K_{\mathrm{y}_1} x_{\mathrm{o}}(k) \tag{38}$$

The closed-loop dynamics system equation can be formed as

$$x_{\mathrm{n}}(k+1) = A_{\mathrm{n}} x_{\mathrm{n}}(k) - B_{\mathrm{n}} K_{\mathrm{y}_1} x_{\mathrm{o}}(k) + B_{\mathrm{n}} K_{\mathrm{w}_1} w(k) \tag{39}$$

The observer tracking error is defined as $\bar{x}(k) = x_{\mathrm{n}}(k) - \hat{x}_{\mathrm{o}}(k)$. Model of the observer is expressed as

$$\bar{x}(k+1) = (A_{\mathrm{n}} - L_{\mathrm{o}} C_{\mathrm{n}})\, \bar{x}(k) \tag{40}$$

(39) can be written as

$$x_{\mathrm{n}}(k+1) = \left(A_{\mathrm{n}} - B_{\mathrm{n}} K_{\mathrm{y}_1}\right) x_{\mathrm{n}}(k) + B_{\mathrm{n}} K_{\mathrm{y}_1} \bar{x}(k) + B_{\mathrm{n}} K_{\mathrm{w}_1} w(k) \tag{41}$$

The closed-loop equation combining observer error and the augmented equation can be written as

$$\begin{bmatrix} \bar{x}(k+1) \\ x_{\mathrm{n}}(k+1) \end{bmatrix} = \begin{bmatrix} A_{\mathrm{n}} - L_{\mathrm{o}} C_{\mathrm{n}} & \mathbf{0}_{n \times n} \\ B_{\mathrm{n}} K_{\mathrm{y}_1} & A_{\mathrm{n}} - B_{\mathrm{n}} K_{\mathrm{y}_1} \end{bmatrix} \begin{bmatrix} \bar{x}(k) \\ x_{\mathrm{n}}(k) \end{bmatrix} + \begin{bmatrix} \mathbf{0}_{n \times m} \\ B_{\mathrm{n}} K_{\mathrm{w}_1} \end{bmatrix} w(k)$$

$\mathbf{0}_{n \times n}$ is defined as a $n \times n$ zero matrix and $\mathbf{0}_{n \times m}$ is defined as a $n \times m$ zero matrix. From (42), it can be observed that the observer design and the controller design are independent of each other. The eigenvalues of the closed-loop can be determined as the

$$\det \left[\lambda_i - \begin{bmatrix} A_{\mathrm{n}} - L_{\mathrm{o}} C_{\mathrm{n}} & \mathbf{0}_{n \times n} \\ B_{\mathrm{n}} K_{\mathrm{y}_1} & A_{\mathrm{n}} - B_{\mathrm{n}} K_{\mathrm{y}_1} \end{bmatrix} \right] = 0 \tag{42}$$

5 Numerical Simulation Results

SIDO buck converter shown in Fig. 1 operates in three switching modes. Details of the current slope are shown in Fig. 2. The chosen SIDO converter topology consists of one inductor l at input side, two capacitors c_{a} and c_{b} at output sides. Output voltages are measured across the capacitors which are represented as output voltages e_{oa} and e_{ob}, and one input voltage is represented by e_{in}. Power input to the converter is controlled by input switch S_{in} and freewheeling diode D_{f}. Distribution of input power from the input side to output voltages is controlled by switches S_1 and S_2. During the operation of the converter modes, output voltages are regulated by switch duty cycles d_{in}, d_1 and d_2. In this paper, SIDO buck converter is operated in continuous conduction mode (CCM). CCM can be achieved if operation of switches is followed by $d_1 + d_2 = 1$. In this paper, SIDO buck converter is represented by a TITO plant model with capacitor voltages as outputs and duty ratios as inputs for simulation

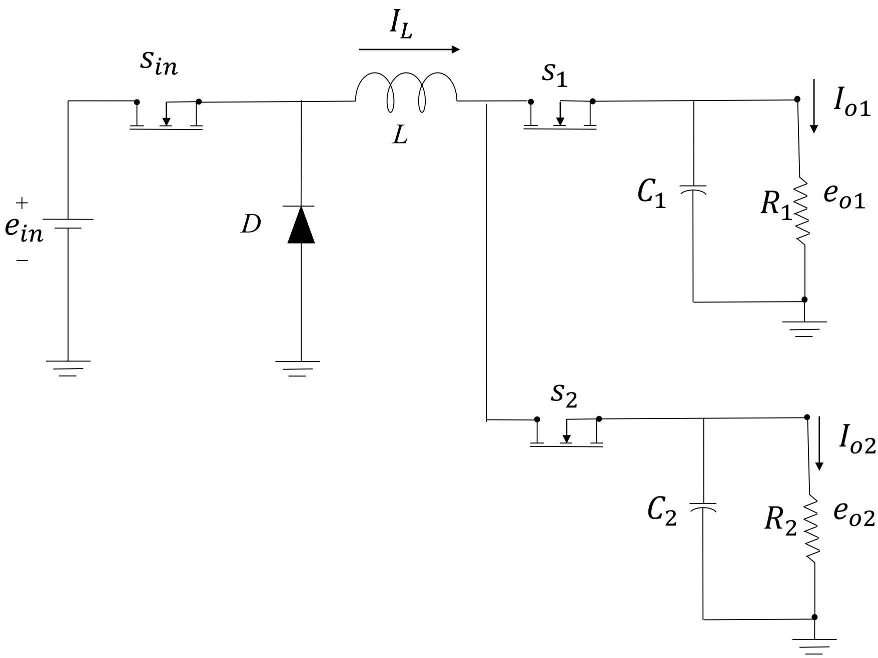

Fig. 1 Circuit diagram of the converter

result. An ideal case is assumed for these analyses, and DC gain of the considered converter system is obtained by using time averaging equivalent circuit approach. The DC voltage gains are expressed as follows:

$$e_{o1} = \frac{d_{in}(1-d_2)R_1 e_{in}}{d_2^2 R_2 + (1-d_2)^2 R_1}, \quad e_{o2} = \frac{d_{in} d_2 R_2 e_{in}}{d_2^2 R_2 + (1-d_2)^2 R_1}, \quad I_l = \frac{e_{o1}}{R_1} + \frac{e_{o2}}{R_2} \tag{43}$$

Steady-state operation of SIDO CCM buck converter under $d_{in} < d_2$ is considered in this paper. There are three modes of operation in a switching cycle. In *Mode 1*, switches S_{in} and S_2 are ON, switch S_1 and freewheeling diode D are OFF, and inductor current increases to a peak value of I_{L1} with a slope of $(e_{in} - e_{o2})/L$. In *Mode 2*, switches S_{in} and S_1 are OFF, S_2 and freewheeling diode D are ON, and inductor current decreases to a value of I_{L2} with a slope of $-e_{o2}/L$. In *Mode 3*, switches S_{in} and S_2 are kept at OFF position, while switch S_1 and freewheeling diode D are ON, inductor current decreases to a value of I_{Lo} with a slope of $-e_{o2}/L$. Duty ratio $\hat{d}_{in}(s)$ and $\hat{d}_2(s)$ are considered to be the inputs for this system, and voltage across resistance R_1 and R_2 are the outputs to be controlled. By choosing these model parameters, the plant is modeled in a two input two output model representation. The reference voltages e_{r1} and e_{r2} are set according to feasible duty ratio, the reference voltages which are desired to track by using GPC. The reference signals are step signals. The plant dynamics are modeled in a two input two output (TITO) form.

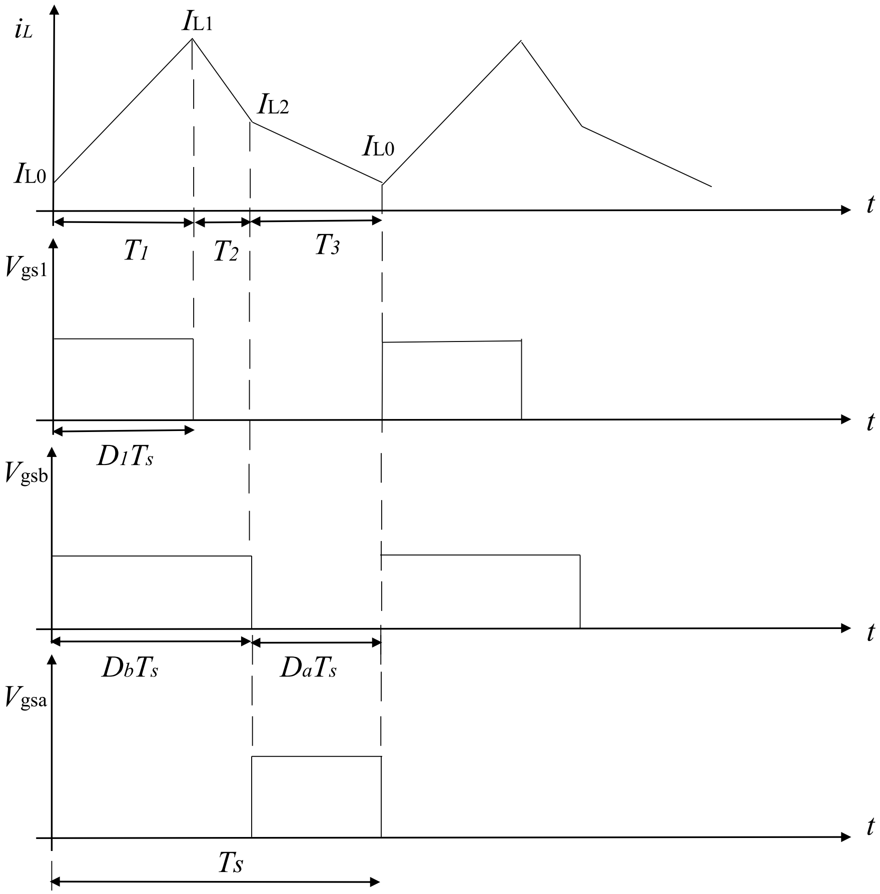

Fig. 2 Switching cycle

From the available transfer functions, transfer function matrix for open-loop SIDO buck converter is obtained as given in Eq. (44)

$$\begin{bmatrix} \hat{e}_{o1}(s) \\ \hat{e}_{o2}(s) \end{bmatrix} = \begin{bmatrix} G_{d11}(s) & G_{d12}(s) \\ G_{d21}(s) & G_{d22}(s) \end{bmatrix} \begin{bmatrix} \hat{d}_{in}(s) \\ \hat{d}_2(s) \end{bmatrix} \tag{44}$$

Numerical simulation results are presented in this section for the designed GPC controller as well as the observer. A dual output buck converter plant model is chosen to implement the GPC in a closed-loop structure described as circuit diagram of SIDO DC-DC buck converter is shown in Fig. 1. The chosen converter model [19] consists of an inductor $L = 200$ µH, two capacitors $C_1 = C_2 = 10$ µF, load resistors $R_1 = 2\ \Omega$ and $R_2 = 3\ \Omega$, output voltages E_{oa} and E_{ob} where $E_{oa} < E_{ob}$ and one input voltage $E_{in} = 5$ V. For steady-state operation, duty ratio of switches

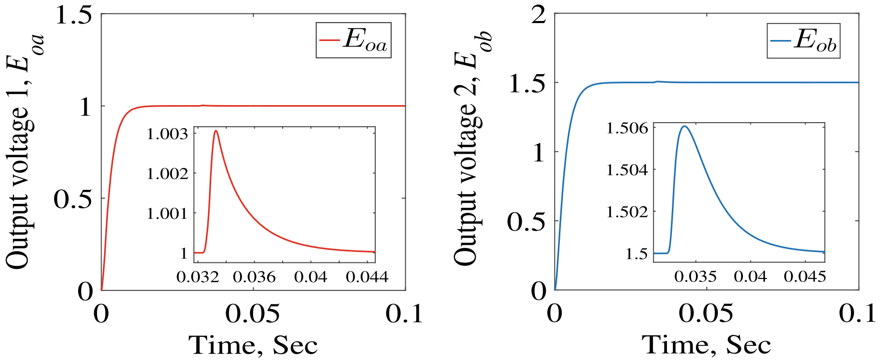

Fig. 3 Output E_{oa} and E_{ob} responses during load variation at load 1

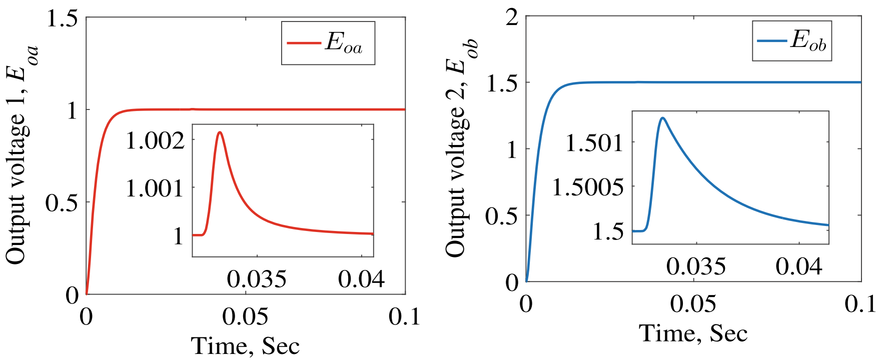

Fig. 4 Output E_{oa} and E_{ob} responses during load variation at load 2

S_1 and S_2 is evaluated as $D_1 = 0.25$ and $D_b = 0.5$, respectively. Output reference voltages are set at $E_{r1} = 1$ V and $E_{r2} = 1.5$ V. Input power through inductor is controlled by switch S_1 and freewheeling diode D. Distribution of power from input to each output is controlled by switches S_a and S_b. Output voltages are regulated by duty ratios D_1, D_a and D_b of switches S_1, S_a and S_b, respectively. The converter can be modeled in a state space form as described in [20]. The robustness of the GPC controller with respect to the 50% load variations is verified. The cross-regulation effect for the designed GPC without observer is shown in Figs. 3 and 4. The effect of load variation has been minimized for the SIDO buck converter. Performance index (P.I.) of the controller can be evaluated by using the formula P.I. = (Overshoot of the observed signal due to load variation)/(Actual voltage) × Load variation (%). The numerical simulation is performed for a 50% load variation by a step disturbance. GPC parameters are obtained as $N = 20$, $M = 2$, $\mathbf{Q} = 10I_N$ and $\mathbf{R} = 0.02I_M$, where I_N and I_M denote identity matrices of dimension as per the horizon. Performance of GPC has been compared with other existing controller design methods for SIDO converters in Table 1, where P.I.

Table 1 Comparison of cross-regulation minimization

Parameter	[21]	This work
Control method	FPGA	GPC
Input voltage	20	5
Settling time (ms)	50–100	5–12
P.I. 1 E_{oa}	0.25	0.15
E_{ob}	0.14	0.2
P.I. 2 E_{oa}	0.06	0.1
E_{ob}	0.02	0.03

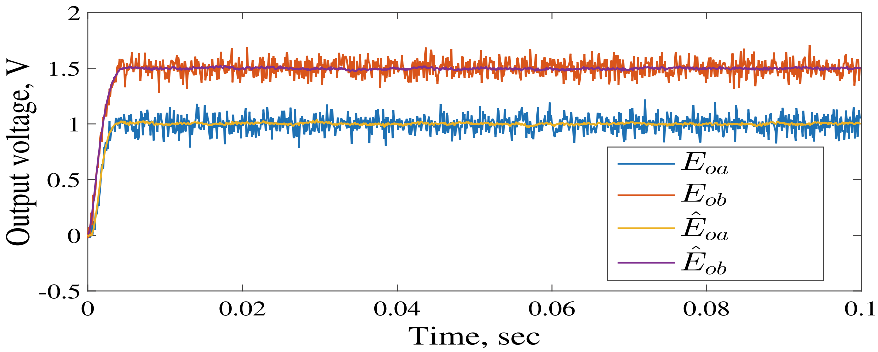

Fig. 5 Comparison of output voltages E_{oa} and E_{ob} with the estimated output of the observer

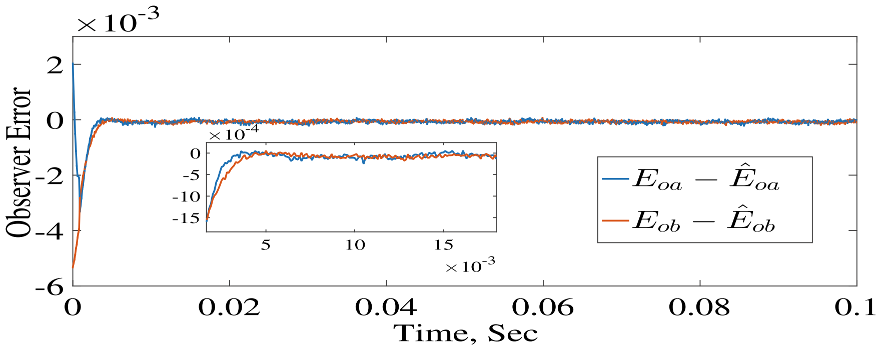

Fig. 6 Observer estimation error for output reference voltage tracking

1 and P.I. 2 in the table refer to performance index due to variation in loads 1 and 2, respectively.

The controller has been designed and validated using numerical simulation using MATLAB®. The plant state space model is converted to an augmented state space model as described. In Figs. 3 and 4, the closed-loop model is simulated for step disturbance signal depicting load variation at R_1 and R_2, respectively, plant model for outputs. The cross-regulation effect for the designed GPC with observer is presented in this paper. The effect has been minimized for the SIDO buck converter. Similarly, other topology of the multiple output converter system can be designed by following GPC design procedure. Reference tracking of the observer-based GPC is presented in Fig. 5. Observer tracking error is presented in Fig. 6. It can be observed that the tracking error is convergent with a satisfactory response. MATLAB software is used to show the performance of the implemented GPC algorithm for a dual output buck converter. Figure 3 illustrates two output voltages for the chosen plant. These figures show that there are two graphs for each output, which are the comparison of GPC for two different tuning algorithms as it can be observed that the output tracks the references in both cases, but there is improvement in transient response for GPC. GPC tuning parameters chosen for tuning are given in Table 1, as shown in the simulated graphs that the outputs e_{o1} and e_{o2} are underdamped for tuning algorithms. But in case of tuning algorithm, the performance is not desirable as it is oscillating in nature.

6 Conclusion

A GPC has been designed for a dual output system to discuss the reference tracking response of the controller. As the system has coupled outputs, the advantages of using a predictive controller are discussed. It is observed that the performance of GPC for reference tracking is satisfactory for the chosen tuning algorithm. The stability of GPC is analyzed by using the Lyapunov stability approach. It was shown that the cost function is a Lyapunov function, and using receding horizon for a finite time cost function results in stable optimizing control input. Although the result is satisfactory, there are many aspects which need to be explored. In this paper, while modeling the plant dynamics, only the cross-coupling transfer function is considered for designing the GPC by ignoring the cross-regulation transfer function. Moreover, in this paper, only the basic implementation strategy is explored to show that although PID controller is preferred over any advanced controller because of easy calibration, nowadays, due to advancement in digital electronics, implementation of any advanced controller is possible, which was considered to be cumbersome earlier.

References

1. Qin SJ, Badgwell TA (2003) A survey of industrial model predictive control technology. Control Eng Pract 11(7):733–764
2. Camacho EF, Bordons C (2013) Model predictive control. Springer Science and Business Media, London

3. Di Cairano S, Yanakiev D, Bemporad A, Kolmanovsky IV, Hrovat D (2008) An MPC design flow for automotive control and applications to idle speed regulation. In: Proceedings of IEEE conference on decision and control, Cancun
4. Falcone P, Borrelli F, Asgari J, Tseng EH, Hrovat D (2007) Predictive active steering control for autonomous vehicle systems. IEEE Trans Control Syst Technol 15(3):566–580
5. Rodriguez J, Cortes P (2012) Predictive control of power converters and electrical drives. Wiley
6. Vazquez S, Leon J, Franquelo L, Rodriguez J, Young H, Marquez A, Zanchetta P (2014) Model predictive control: a review of its applications in power electronics. IEEE Ind Electr Mag 8(1):16–31
7. Scoltock J, Geyer T, Madawala UK (2015) Model predictive direct power control for grid-connected NPC converters. IEEE Trans Ind Electron 62(9):5319–5328
8. Bordons C, Montero C (2015) Basic principles of MPC for power converters: bridging the gap between theory and practice. IEEE Ind Electron Mag 9(3):31–43
9. Kouro S, Perez M, Rodriguez J, Llor A, Young H (2015) Model predictive control: MPC's role in the evolution of power electronics. IEEE Ind Electron Mag 9(4):8–21
10. Wang BF, Kanamarlapudi VRK, Xian L, Peng XY, Tan KT, So PL (2016) Model predictive voltage control for single-inductor multiple output DC-DC converter with reduced cross regulation. IEEE Trans Ind Electron 63(7):4187–4196
11. Kouro S, Cortes P, Vargas R, Ammann U, Rodriguez J (2008) Model predictive control—a simple and powerful method to control power converters. IEEE Trans Ind Electron 56(6):1826–38
12. Mayne DQ, Rawlings JB, Rao CV, Scokaert PO (2000) Constrained model predictive control: stability and optimality. Automatica 36(6):789–814
13. Manjari K, Majhi S, Ramana KV (2019) Pre-computed GPC of a DC-DC Buck converter. IET Circuits Dev Syst 14(1):41–47
14. Cordero R, Estrabis T, Batista EA, Andrea CQ, Gentil G. Ramp-tracking generalized predictive control system based on second-order difference. IEEE Trans Circuits Syst II Express Briefs (Early Access)
15. Generalized predictive control—part I. The basic algorithm. Automatica 23(2):137–148 (1987)
16. Clarke DW, Mohtadi C, Tuffs P (1987) Generalized predictive control—part II. Extensions and interpretations. Automatica 23(2):149–160
17. Wang L (2009) Model predictive control system design and implementation using MATLAB®. Springer Science & Business Media
18. Luenberger DG (1971) An introduction to observers. IEEE Trans Autom Control 16(6):596–602
19. Dasika JD, Bahrani B, Saeedifard M, Karimi A, Rufer A (2014) Multivariable control of single-inductor dual-output Buck converters. IEEE Trans Power Electron 29(4):2061–2070
20. Wang Y, Xu J, Yin G (2019) Cross-regulation suppression and stability analysis of capacitor current ripple controlled SIDO CCM Buck converter. IEEE Trans Ind Electron 66(3):1770–1780
21. Pizzutelli A, Ghioni M (2008) Novel control technique for single inductor multiple output converters operating in CCM with reduced cross regulation. In: Proceedings of 23rd annual IEEE applied power electronics conference and exposition, pp 1502–1507

Chapter 6
Different Oscillator-Controlled Parallel Three-Phase Inverters in Stand-Alone Microgrid

Vikash Gurugubelli, Arnab Ghosh, and Anup Kumar Panda

Abstract This work presents two different types of virtual oscillator controllers (VOCs). Unlike droop and virtual synchronous machine (VSM), VOC is a time-domain control technique. Each voltage source inverter (VSI) in this technique is adjusted to replicate the dynamics of the nonlinearly linked oscillators. Because VSIs are electrically linked, their output voltages synchronise and the load is distributed proportionally to their ratings. The authors discussed nonlinear deadzone-based VOC and nonlinear Vanderpol-based VOC. This paper discusses the design and implementation of the aforesaid control techniques. During a load disturbance, the simulation research is done on a 3-phase parallel VSI system using the above-mentioned control techniques. This research examines both equal and uneven power distributions. The suggested control approaches are validated by the simulation results.

Keywords Voltage source inverter · Deadzone oscillator · Vanderpol oscillator · Microgrid · Parallel operation

1 Introduction

Microgrids (MGs) offer the potential to boost renewable energy (solar, wind and other sources) while also improving dependability and decreasing transmission line losses. The parallel functioning of inverters that form an islanded MG is the subject of this research. The major goals of the islanded system are (i) to minimise or eliminate communication between the inverters that run in parallel, (ii) maintaining system stability and synchronism between inverters despite load fluctuations, (iii) system frequency regulation and (iv) appropriate power-sharing across inverters. To accomplish these goals, we proposed several control techniques based on the synchronisation of linked oscillators.

V. Gurugubelli (✉) · A. Ghosh · A. K. Panda
Department of Electrical Engineering, National Institute of Technology, Rourkela, Odisha, India

A. K. Panda
e-mail: akpanda@nitrkl.ac.in

G. Panda et al. (eds.), *Sustainable Energy and Technological Advancements*,
Advances in Sustainability Science and Technology,
https://doi.org/10.1007/978-981-16-9033-4_6

Droop control is a common decentralised control technique [1, 2], with the drawback of a high rate of change frequency. To alleviate this problem, the VSM idea was proposed in [3–5]. The VOC is a time-domain controller that reacts to current feedback signals immediately without the need for extra filters or power calculations, which is a key benefit in VOC [6–8]. The VOC [9–11] is a novel sophisticated decentralised control approach for mimicking the dynamic characteristics of limit cycle oscillators such as the deadzone and Vanderpol oscillator. VOC was utilised in a 1-phase MG in [12], and it was employed in a 3-phase MG in [13]. Ali et al. [14] elaborated on the requirement for a grid-tied inverter with VOC. In [15, 16], an external loop was introduced, allowing the VOC to measure active and reactive power in grid-connected mode.

This paper makes the following contributions: (a) different VOC strategies are applied to a system of 3-phase inverters that are operated in parallel; (b) the design and implementation of the deadzone and Vanderpol-based VOC are clearly presented; (c) a simulation study is conducted with these two control methods during start-up and load disturbance; (d) the research also covers equal and unequal power-sharing; (e) lastly, conclusions are drawn on the two controllers based on the system's simulation findings.

This work is organised into six sections. The introduction is Sect. 1. Section 2 includes the system description; the design and implementation of deadzone and Vanderpol-based VOC controllers are presented clearly in Sect. 3. Section 4 presents conditions for synchronisation, and results and discussions, respectively. In Sect. 5, concluding remarks are made on the two control methods.

There are five portions to this work. Section 1 is an introduction; Sect. 2 is a system description; Sect. 3 is a clear presentation of the design and implementation of deadzone and Vanderpol-based VOC controllers. The results and discussions are covered in Sect. 4, and the conclusions are provided in Sect. 5.

2 System Description

As shown in Fig. 1, the system in this manuscript is a simple three-phase VSI operating in stand-alone mode. V_{dc} is the input DC supply, which is time-varying and originates from renewable energy sources such as solar panels or fuel cells. The capacitor C is a DC-link capacitor that manages the voltage on the DC bus. The filter resistance, inductance and capacitor are represented as R_{f} (1 Ω), L_{f} (6 mH) and C_{f} (1.2 μF), respectively. V_{t} is the inverter's terminal voltage, which comes before the filter. After the filter, V_{s} (60 V rms) is the inverter output voltage. The capacitor current and load current, respectively, are I_{f} and I_{L}. The inverter is controlled in this study utilising several oscillator-based controllers to provide the appropriate voltage and frequency. The current feedback signals are used by these oscillators. Two VO control methods are described in this paper, in which each inverter is controlled

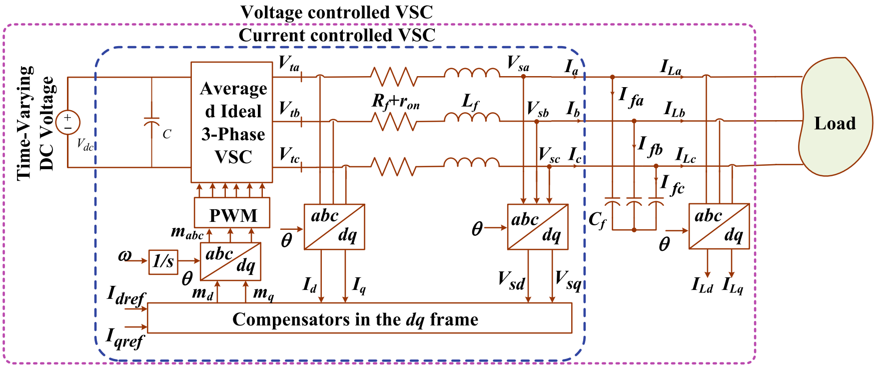

Fig. 1 Schematic diagram of a 3-phase inverter unit in stand-alone mode

to simulate the dynamics of either a deadzone or a Vanderpol oscillator (detailed explanation of these oscillators presented in Sect. 3). As illustrated in Fig. 2, this article shows the aforementioned control techniques in the context of an islanded MG system.

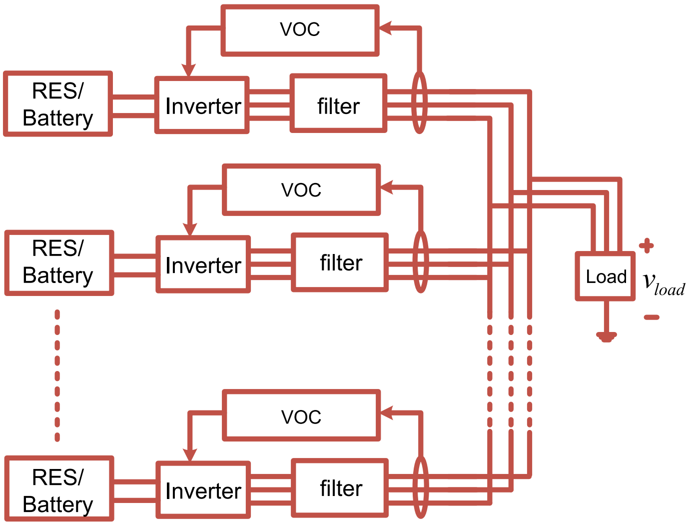

Fig. 2 System of inverters in the context of stand-alone MG using VOCs

3 Control strategies

3.1 Nonlinear Deadzone VOC (NDZVOC)

This controller is motivated by the phenomena of nonlinear oscillator synchronisation in linear time-invariant systems. The NDZVOC schematic is illustrated in Fig. 3a. This has two subsystems, one of which is a parallel RLC circuit and the other is a voltage-dependent current source (VDCS) inspired by the DZ characteristics.

From Fig. 3b(i, ii), one can understand the characteristics of DZ and VDCS, where $f(v_{C_1})$ is the DZ function as shown in (1)

$$f(v_{C_1}) = \begin{cases} 2\sigma(v_{C_1} - \varphi), & v_{C_1} > \varphi \\ 0, & |v_{C_1}| \le \varphi \\ 2\sigma(v_{C_1} + \varphi), & v_{C_1} < -\varphi \end{cases} \tag{1}$$

The dynamics of the oscillator inductor current, i_{L_1}, and the capacitor voltage, v_{C_1}, are given by [11, 12].

$$\begin{aligned} \frac{dv_{C_1}}{dt} &= \frac{1}{C_1}\left[\left(\sigma - \frac{1}{R}\right)v_{C_1} - f(v_{C_1}) - i_{L_1} - i_{o_1}\right] \\ \frac{di_{L_1}}{dt} &= \frac{v_{C_1}}{L} \end{aligned} \tag{2}$$

The implementation of NDZVOC with single-phase inverters is shown in Fig. 4. The parameters of DZ oscillator-based VOC are shown in Table 1. The design and parameter selection have been taken from the [11].

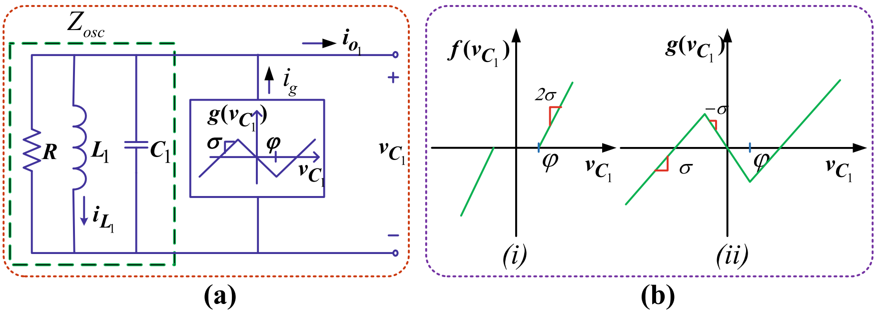

Fig. 3 **a** Electrical schematic of the NDZVOC. **b** (i) DZ characteristics and (ii) VDCS characteristics

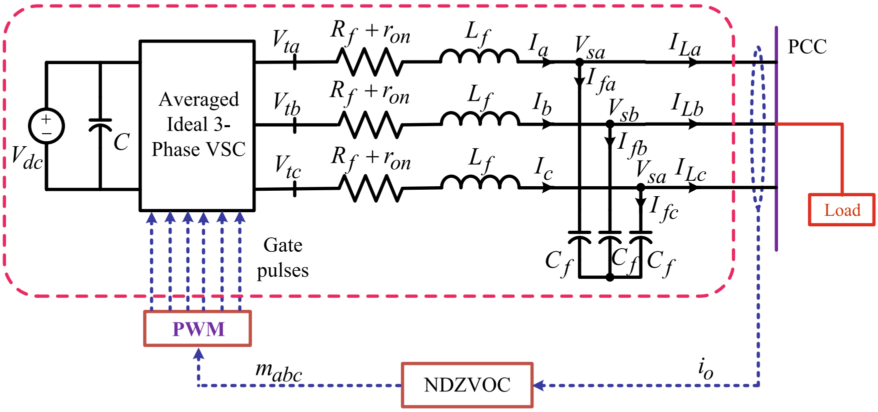

Fig. 4 Schematic of implementation of NDZVOC with 3-phase VSI

Table 1 Parameters of deadzone oscillator-based VOC

Symbol	Description	Value	Units
k_{v_1}	Voltage gain	$60 \times \sqrt{2}$	(V/V)
k_{i_1}	Current gain	0.1125	(A/A)
σ	Slope of DZO	1	(S)
φ	Offset voltage	0.4695	(V)
R	Harmonic oscillator resistance	10	(Ω)
L_1	Harmonic oscillator inductance	500	(μH)
C_1	Harmonic oscillator capacitance	14.1	(mF)

3.2 *Nonlinear Vanderpol VOC (NVPVOC)*

This controller is also motivated by the phenomena of nonlinear oscillator synchronisation in linear time-invariant systems. Figure 5 depicts the NVPVOC schematic. The NVPVOC is composed of two subsystems: a parallel RLC circuit and a cubic nonlinear VDCS [6].

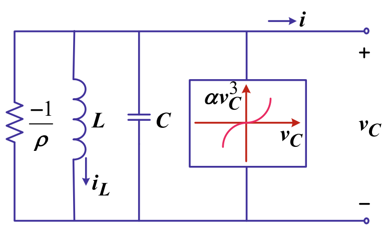

Fig. 5 An electrical schematic of the NVPVOC

The dynamics of the oscillator inductor current, i_{L_2}, and the capacitor voltage, v_{C_2}, are given by

$$L_2 \frac{di_{L_2}}{dt} = \frac{v_2}{k_{v_2}}$$
$$C_2 \frac{dv_2}{dt} = -\alpha \frac{v_2^3}{k_{v_2}^2} + \rho v_2 - k_{v_2} i_{L_2} - k_{v_2} k_{i_2} i_{o_2} \quad (3)$$

The implementation of NVPVOC with three-phase inverter is shown in Fig. 6. The parameters of Vanderpol oscillator-based VOC are shown in Table 2. The design and parameter selection have been taken from the [6].

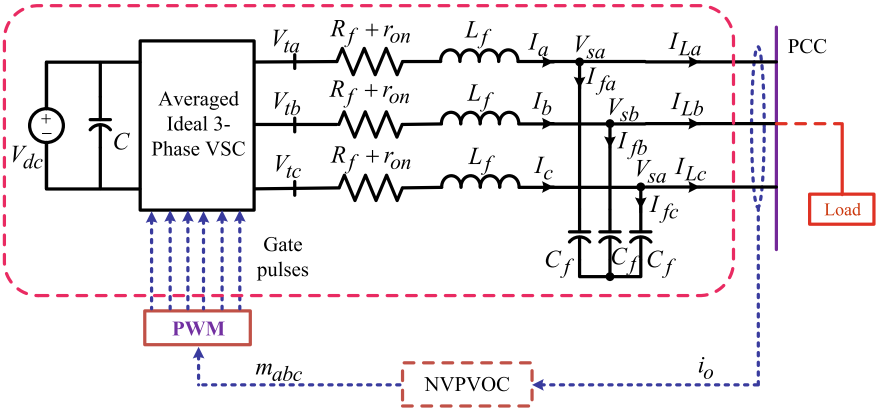

Fig. 6 Schematic of implementation of NVPVOC with 3-phase VSI

Table 2 Parameters of Vanderpol oscillator-based VOC

Symbol	Description	Value	Units
k_{v_2}	Voltage gain	63	(V/V)
k_{i_2}	Current gain	0.57	(A/A)
ρ	Conductance	6.09	(Ω-1)
α	Coefficient of cubic current source	4.06	(A/V3)
L_2	Harmonic oscillator inductance	3.99×10^{-5}	(H)
C_2	Harmonic oscillator capacitance	0.18	(F)

4 Results and Discussion

In the simulation investigation, three 3-phase VSIs are interconnected in parallel. Each inverter is controlled by its own controller in this system (either NDZO or NVPVOC). The parameters of the controllers could be deduced from Tables 1 and 2. Figure 7 illustrates the simulation diagram of the system in islanding mode. The authors investigated two scenarios in their simulation research. Equal power-sharing is the first scenario, whereas unequal power-sharing is the second.

Case I (1:1 power-sharing)

In this scenario, the two inverters have the same power rating. The load is rising when the switch is closed. The starting circumstances of the inverter cannot be predicted in practice. As a result, the inverters' starting circumstances are the same. The voltage synchronisation (line to line rms voltage between *R* and *Y*), current sharing of the inverters (*R*-phase currents) and load current (*R*-phase) of the NDZVOC-driven inverter are illustrated in Fig. 8a–c during start-up and load disturbance, respectively. Initially, the switch is in the open position; after 0.6–0.8 s, the switch is in the closed position (which means, the load step up and step down within 0.2 s, here the load changing from 1000 to 1500 W with 0.89 power factor). Similarly, the NVPVOC-controlled inverter's voltage synchronisation, current sharing and load current are depicted in Fig. 9a–c.

Case II (2:1 power-sharing)

All of the inverters' power ratings are uneven in this scenario. The starting circumstances of the inverters are likewise the same in this scenario. The voltage synchronisation (line to line rms voltage between *R* and *Y*), current sharing of the inverters (*R*-phase currents) and load current (*R*-phase) of the NDZVOC-driven inverter are illustrated in Fig. 10a–c during start-up and load disturbance, respectively. As indi-

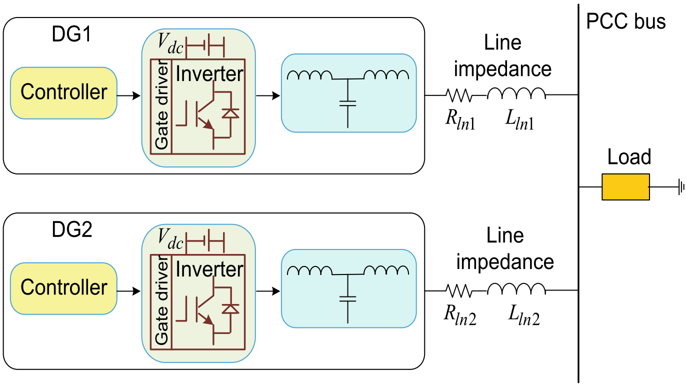

Fig. 7 Model simulation diagram of the system in islanding mode

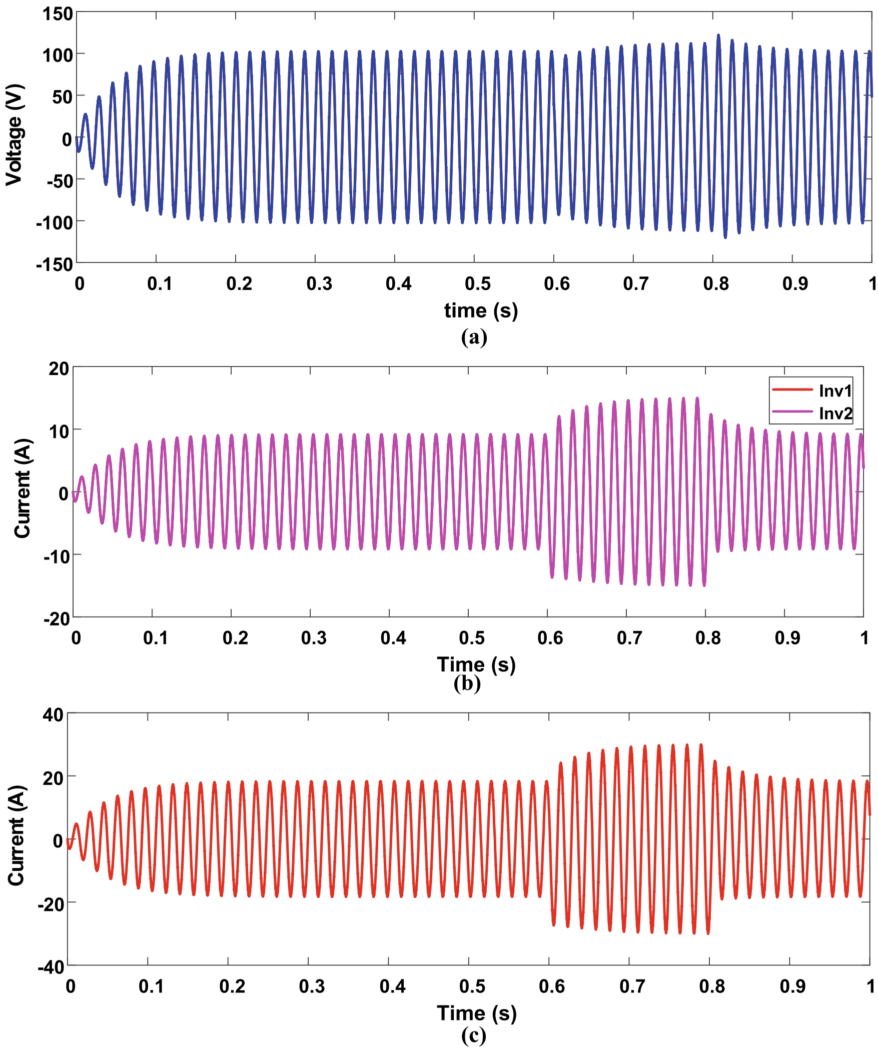

Fig. 8 Waveforms during start-up and load disturbance with 1:1 power-sharing (deadzone oscillator-based VOC), **a** voltage synchronisation, **b** current sharing, **c** load current

cated in the previous section, the load disturbance is taken into account in this situation as well. Similarly, the NVPVOC-controlled inverter's voltage synchronisation, current sharing and load current are depicted in Fig. 11a–c. In NDZVOC, the currents reached a steady state in 0.1 s, but in NVPVOC, it took more than 0.3 s. As a result, NDZVOC outperforms NVPVOC at starting.

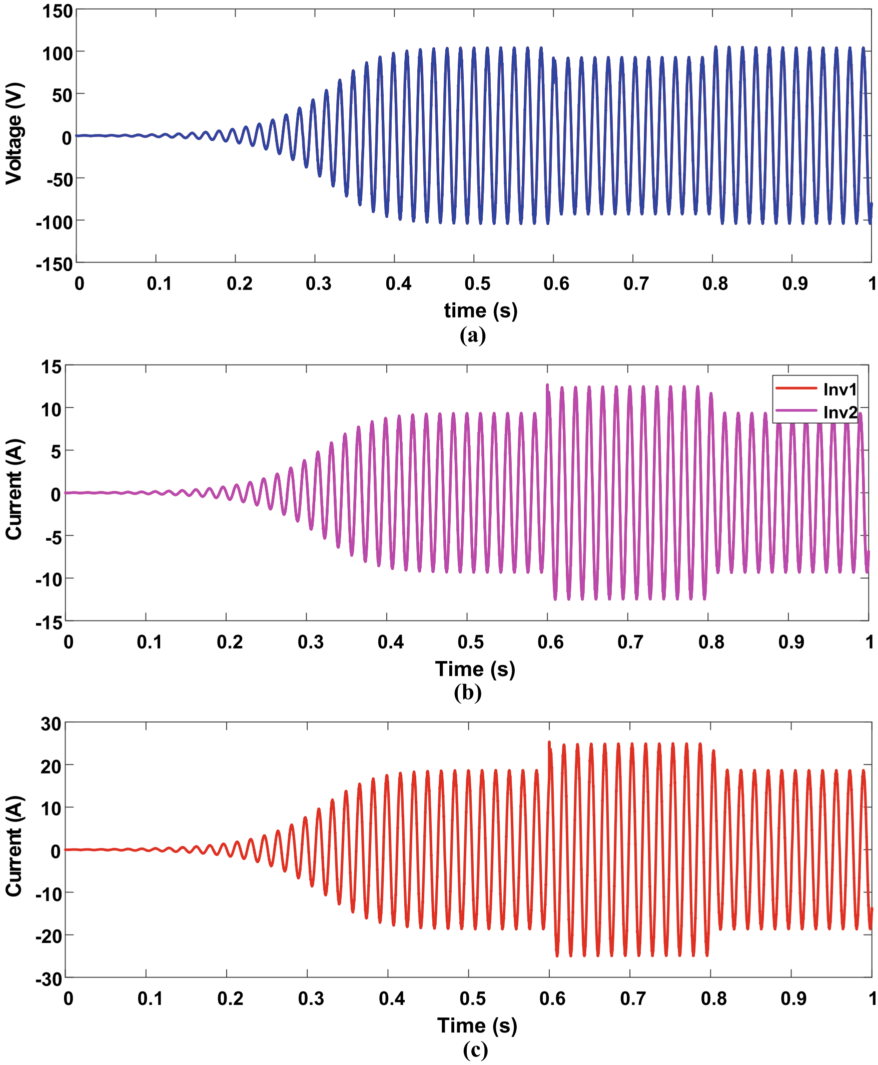

Fig. 9 Waveforms during start-up and load disturbance with 1:1 power-sharing (Vanderpol oscillator-based VOC), **a** voltage synchronisation, **b** current sharing, **c** load current

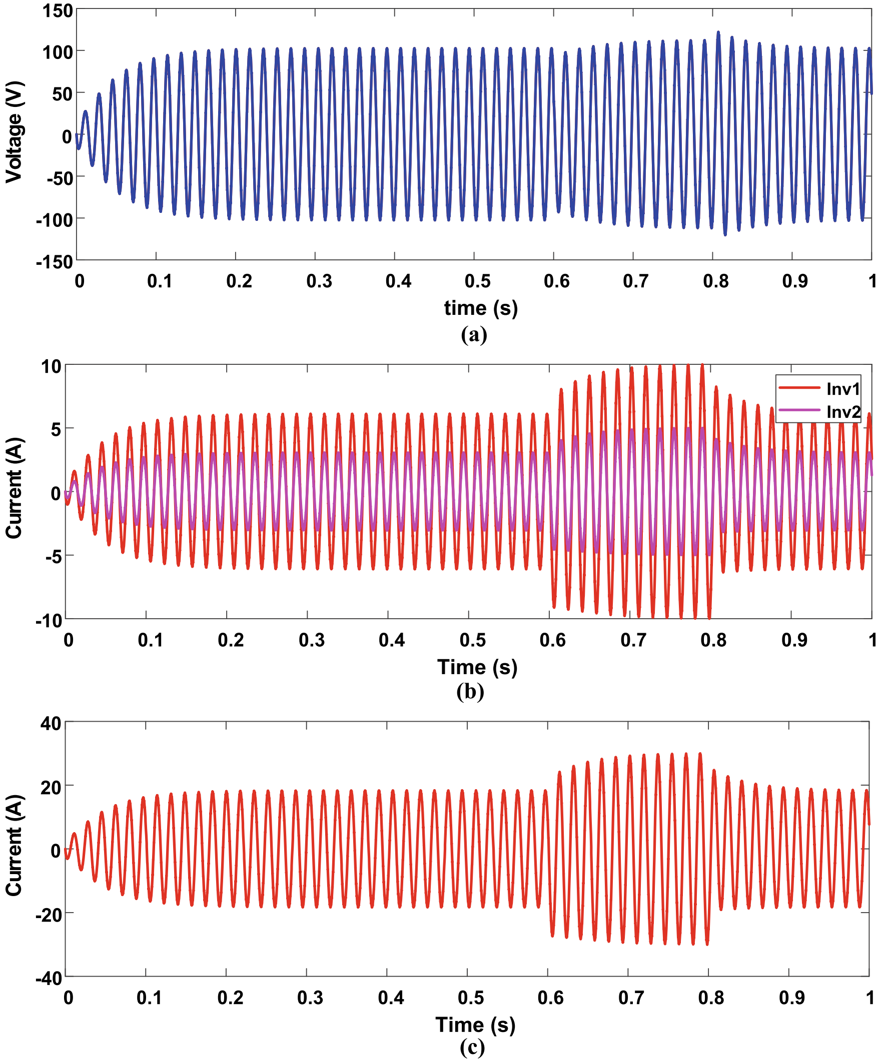

Fig. 10 Waveforms during start-up and load disturbance with 2:1 power-sharing (deadzone oscillator-based VOC), **a** voltage synchronisation, **b** current sharing, **c** load current

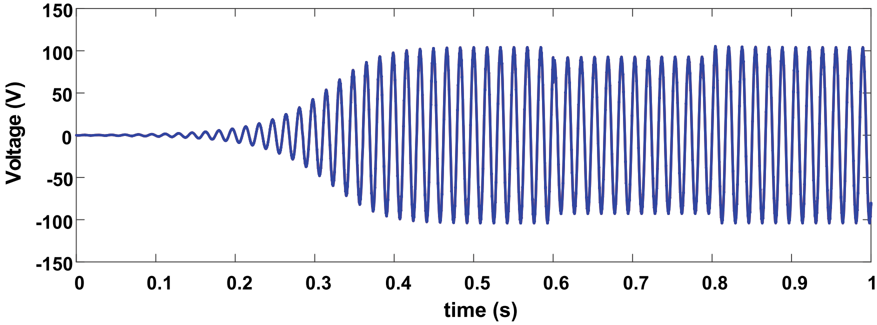

(a)

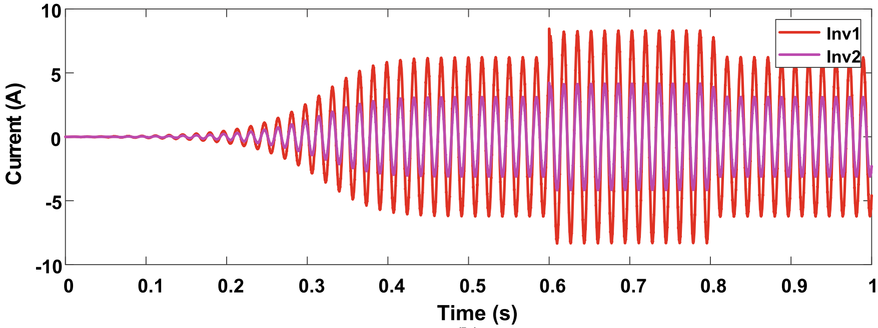

(b)

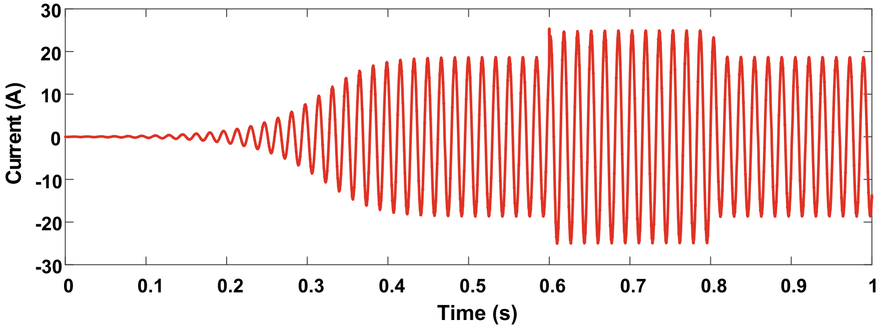

(c)

Fig. 11 Waveforms during start-up and load disturbance with 2:1 power-sharing (Vanderpol oscillator-based VOC), **a** voltage synchronisation, **b** current sharing, **c** load current

5 Conclusion

A parallel three-phase inverter system is treated with two distinct types of VOCs. VOC is a time-domain control technique, unlike droop and VSM. Each VSI imitates the dynamics of nonlinear interconnected oscillators in this way. The design and implementation of the aforesaid control techniques are demonstrated in this study. The simulation research is carried out on a three-phase parallel VSI system utilising the aforesaid control methods during beginning and load disturbance. This research also looks at how power is distributed equally and unequally. NDZVOC has a better current sharing than NVPVOC when it first starts. During start-up, the voltage synchronisation in NDZVOC is quite fast. NVPVOC has slower voltage synchronisation than NDZVOC. During load disruptions, both control methods emphasise current sharing and voltage synchronisation. In both control methods, the third harmonic is dominant. The simulation findings back up the recommended control strategies.

References

1. Rocabert J, Luna A, Blaabjerg F, Rodriguez P (2012) Control of power converters in ac microgrids. IEEE Trans Power Electron 27(11):4734–4749
2. Hou X, Sun Y, Han H, Liu Z, Yuan W, Su M (2018) A fully decentralized control of grid-connected cascaded inverters. IEEE Trans Sustain Energy 10(1):315–317
3. Bevrani H, Ise T, Miura Y (2014) Virtual synchronous generators: a survey and new perspectives. Int J Electr Power Energy Syst 54:244–254
4. Vikash G, Ghosh A, Rudra S (2020) Integration of distributed generation to microgrid with virtual inertia. In: 2020 IEEE 17th India council international conference (INDICON), July 2020. IEEE, pp 1–6
5. Gurugubelli V, Ghosh A (2021) Control of inverters in standalone and grid-connected microgrid using different control strategies. World J Eng
6. Johnson BB, Sinha M, Ainsworth NG, Dorfler F, Dhople SV (2016) Synthesizing virtual oscillators to control islanded inverters. IEEE Trans Power Electron 31(8):6002–6015
7. Gurugubelli V, Ghosh A, Panda AK, Rudra S (2021) Implementation and comparison of droop control, virtual synchronous machine, and virtual oscillator control for parallel inverters in standalone microgrid. Int Trans Electr Energy Syst 31(5):e12859
8. Dhople SV, Johnson BB, Hamadeh AO (2013) Virtual oscillator control for voltage source inverters. In: Proceedings of 51st annual Allerton conference on communication, control, and computing, Oct 2013, pp 1359–1363
9. Vikash G, Ghosh A (2021) Parallel inverters control in standalone microgrid using different droop control methodologies and virtual oscillator control. J Inst Eng (India) Ser B, pp 1–9
10. Johnson BB, Dhople SV, Hamadeh AO, Krein PT (2014) Synchronization of nonlinear oscillators in an LTI electrical power network. IEEE Trans Circuits Syst I Reg Pap 61(3):834–844
11. Johnson BB, Dhople SV, Hamadeh AO, Krein PT (2014) Synchronization of parallel single-phase inverters with virtual oscillator control. IEEE Trans Power Electron 29(11):6124–6138
12. Johnson BB, Dhople SV, Cale JL, Hamadeh AO, Krein PT (2014) Oscillator-based inverter control for islanded three-phase microgrids. IEEE J Photovolt 4(1):387–395
13. Sinha M, Dörfler F, Johnson BB, Dhople SV (2018) Synchronization of Liénard-type oscillators in heterogenous electrical networks. In: Proceedings of Indian control conference, Jan 2018, pp 240–245

14. Ali M, Nurdin HI, Fletcher JE (2020) Synthesizing averaged virtual oscillator dynamics to control inverters with an output LCL filter. In: Proceedings of 46th annual conference of the IEEE industrial electronics society, Oct 2020, pp 3265–3270
15. Awal MA, Yu H, Tu H, Lukic SM, Husain I (2020) Hierarchical control for virtual oscillator based grid-connected and islanded microgrids. IEEE Trans Power Electron 35(1):988–1001
16. Ali M, Nurdin HI, Fletcher J (2021) Dispatchable virtual oscillator control for single-phase islanded inverters: analysis and experiments. IEEE Trans Ind Electron 68(6):4812–4826

Chapter 7
Generalized Hybrid Symmetrical and Asymmetrical Multilevel Inverter Topology with Reduced Number of Switches

Madan Kumar Das, Parusharamulu Buduma, Perwez Alam, and Sukumar Mishra

Abstract Multilevel inverter (MLI) has grown rapidly to achieve higher voltage levels, lesser voltage stress of the power devices, and lesser harmonic distortion of the inverter voltage. This paper presents the analysis of a reduced component hybrid nine-level inverter designed with only three DC sources. The proposed work emphasizes developing a hybrid multilevel inverter using symmetrical and asymmetrical DC sources at the input. The merit of the proposed MLI can efficiently reduce the power of electronic devices to produce the output voltage and generate nine-level using nine IGBTs only. Proposed MLI can be reducing complexity, size, and thus significantly improve inverter cost and performance. Also, a multicarrier-based, level-shifted PWM (LSPWM) method is adopted to generate the desired gate pulses of the IGBT switches using the DSPACE-1103-based controller. A laboratory prototype of the proposed seven-level and nine-level inverters is developed, and the experimental results of the MLIs at RL loading or voltage conditions are present. Further, the inverter losses, efficiency, and the %THD are also analyzed and compared with the other topologies.

Keywords Asymmetrical multilevel inverter (AMLI) · Level-shifted pulse width modulation (LS-PWM) · %THD

1 Introduction

Almost four decades ago, the first multilevel inverter (MLI) was introduced in 1975 [1]. Since then, considerable research is going on in DC-AC power conversion using MLI [2] and their applications like uninterruptible power supply, power factor correction, flexible AC transmission systems, and static VAR compensators high-voltage DC power transmission, and active filters. In addition to these, the integration of

M. K. Das (✉) · P. Buduma · P. Alam · S. Mishra
Department of Electrical Engineering, Indian Institute of Technology, Delhi 110016, India

S. Mishra
e-mail: sukumar@ee.iitd.ac.in

G. Panda et al. (eds.), *Sustainable Energy and Technological Advancements*,
Advances in Sustainability Science and Technology,
https://doi.org/10.1007/978-981-16-9033-4_7

renewable energy sources to the grid, industrial AC motor drives, and drives in hybrid electric vehicles [3–7] becomes effective using MLIs. The MLI gained popularity due to its crucial benefits such as smaller voltage stress of the switches, improved power quality with good electromagnetic compatibility, reduced total harmonic distortion, smaller switching frequency, and switching losses [8]. The classical topologies like cascaded H-bridge-MLI [9] (CHB-MLI), flying capacitor MLI [10] (FC-MLI), and neutral point clamped-MLI [11] (NPC-MLI) are developed industrially. However, the FC-MLIs and NPC-MLIs are limited to low-voltage levels due to the problems of capacitor balancing.

On the other hand, CHB-MLIs have extended to any desired voltage levels without any capacitor voltage balancing issues. Moreover, the CHB-MLI structure has gained wide attention due to its modularity. However, the CHB-MLI required several isolated DC sources [12], which increases the cost of the implementations. Moreover, the traditional MLI topologies require more switches, isolated driver ICs, and conducting switches, resulting in more price and complication [13]. To avoid these limitations, several reduced component MLIs have been proposed in the literature for efficient structure. To prove the superiority of the proposed MLI, several MLIs like [14, 15] are analyzed and are compared in terms of component counts.

A basic MLI structure is proposed in [16], which is further modified in [17]. However, a more number of DC voltage sources and bidirectional power switches are required in the structure discussed in [18]. A concept of connecting a half-bridge at one side of the load point is presented in [19], where the requirement of DC sources and the numbers of the bidirectional power switches are reduced compared to the aforesaid MLIs described in [20]. Thus, it is observed from the literature that most of the reduced switch MLIs either used more bidirectional switches or a more significant number of DC sources and/or capacitors.

A new symmetric/asymmetric design of generalized MLI is presented here with the least number of power electronic devices to overcome the aforesaid problems. In order to obtain a higher voltage level, the MLI proposed here needs a comparatively smaller number of power devices, mainly the bidirectional switches and DC sources. Moreover, the alternating voltage (positive and negative levels) can be generated using H-bridge enables the scope of MLI to use for high-voltage applications. In addition, the value of TSV can be lowered, which may be required to reduce the overall cost of the proposed inverter. The operation of the proposed work is described in the following sections. Section 2 elucidates the working of the proposed MLI configuration. While concerning the control strategies, a level-shifted PWM (LS-PWM) technique is most suitable to obtain the switching pulses using a DS1103 controller. Section 3 describes the switching pulses and modes of operation of the MLI topology develop here. The performance of the MLI proposed is also compared with recently published MLIs [14–20], and exhaustive comparisons are made as explained in Sect. 4.

Nevertheless, the calculation for the total standing voltage (TSV) and voltage levels to the switch ratio (L/S) is also introduced in this work by considering 9 voltage levels are also tested in MATLAB/Simulink platform. The experimental verification is carried out for an RL load as described in Sect. 5. In addition, the power loss of the proposed seven-level inverter is also incorporated in Sect. 3 and followed by a conclusion presented in Sect. 6.

2 Proposed Hybrid Multilevel Inverter Topologies

In this work, a reduced switch hybrid MLI consists of a T-type auxiliary inverter connected with an extra H-bridge circuit is connected for both level and polarity generations required for an AC voltage. The proposed series MLI configuration is depicted in Fig. 1 that can be implemented for both the asymmetrical and symmetrical values of the DC sources. The proposed MLI has the inherent ability to generate both the positive and negative voltage levels without using any additional polarity reversal H-bridge. Usually, the voltage stress of the polarity reversal H-bridge is the highest (equal to the sum of all the sources). However, the proposed inverter consists of only the level generating units having inherent polarity generation capability. The auxiliary circuit only one unidirectional controlled switches (T_{11}, T_{12}, T_{13}, and T_{14} and single bidirectional switches S_{11}) of the leg. Moreover, the cell is supplied from two battery sources of voltage (V_{DC11} and V_{DC12}), which can be equal voltages (1:1) to obtain three voltage levels, both positive and negative magnitude, including zero. The proposed MLI can be better suited for an off-grid/grid-connected PV system, where voltage sources are readily available.

The H-bridge unit consists of four power switches (T_{21}, T_{22}, T_{23}, and T_{24}), supplied with one battery source and a voltage (V_{DC21}) to generate three distinct voltage levels of magnitude $+V_{dc}$, 0, $-V_{dc}$ like the auxiliary circuit. The operations of the proposed inverter configuration with one T-type auxiliary circuit along with a level generating H-bridge are depicted in Fig. 1. The proposed inverter can operate

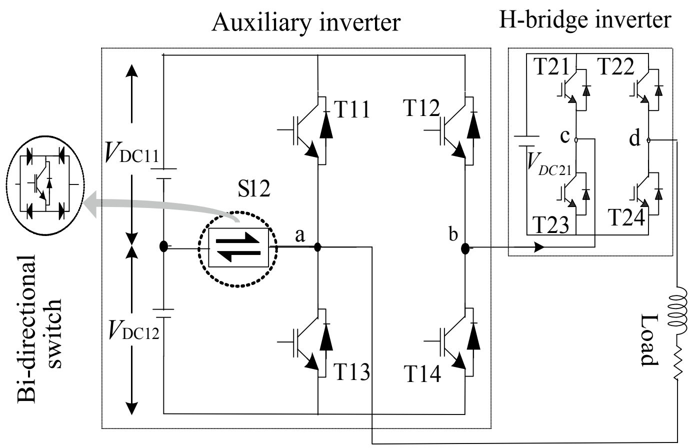

Fig. 1 Proposed hybrid multilevel inverter topology

with asymmetrical (nine-level) as well as symmetrical (seven-level) voltages. Based on the magnitude or ratios of DC voltages (V_{DC11}:V_{DC12} = 1:1) or voltages of H-bridge (i.e., $V_{DC21} = 1$). In this paper, a single-phase multi-winding transformer and the diode-rectifiers and capacitive filters are used to obtain the isolated DC sources for supplying the proposed asymmetrical MLI for experimental verification purposes.

2.1 For Asymmetrical Nine-Level Inverter Configuration

Proposed hybrid asymmetrical nine-level MLI also operates in nine-mode operation to generate nine-level voltage with unequal DC voltage sources of in the auxiliary cell and H-bridge cell and their DC-link voltage ratio are V_{DC11}:V_{DC12}:V_{DC22} = 1:1:2 connected with input of the battery unequal sources. The switches on/off states are depicted in Table 1 for nine-level hybrid inverter. However, the proposed work basically defines a nine-level asymmetrical MLI with equal and unequal voltages sources in the auxiliary cell and H-bridge to produced nine-level output voltage with less power losses or less % THD produced. Here, both of the module auxiliary cell and the H-bridge cell are operated only two switches at a time shown in Fig. 2. Here, a sharp distinction is observed among the switches which conduct/do not conduct for voltage level generation. For the proposed nine-level topology, the bold red lines show the conduction path through the conducting components for different voltage level generations, and the thin (black) lines show that the components are not conducting or contributing at the current state. Table 1, that can be used to generate the same voltage levels, is not depicted in Fig. 2.

Table 1 On/off switching status (S_x) of the nine-mode operation of proposed for nine-level symmetrical inverter (V_{DC11}:V_{DC12}:V_{DC22} = 1:1:2)

Mode	Conducting switches √ = ON; × = OFF									Inv. O/P Voltage (V_o)
	For auxiliary circuit					For H-bridge circuit				
	T_{11}	T_{12}	T_{13}	T_{14}	S_{11}	T_{21}	T_{22}	T_{23}	T_{24}	
1	×	√	√	×	×	×	√	√	×	$4V_{DC}$
2	×	√	√	×	×	×	√	√	×	$3V_{DC}$
3	×	√	×	×	√	×	×	√	√	$2V_{DC}$
4	×	√	×	×	√	×	×	√	√	$1V_{DC}$
5	×	√	√	×	×	√	√	×	×	0
6	×	√	×	×	√	√	√	×	×	$-1V_{DC}$
7	×	√	√	×	×	√	√	×	×	$-2V_{DC}$
8	×	√	×	×	√	√	×	×	√	$-3V_{DC}$
9	×	√	×	×	×	√	×	×	√	$-4V_{DC}$

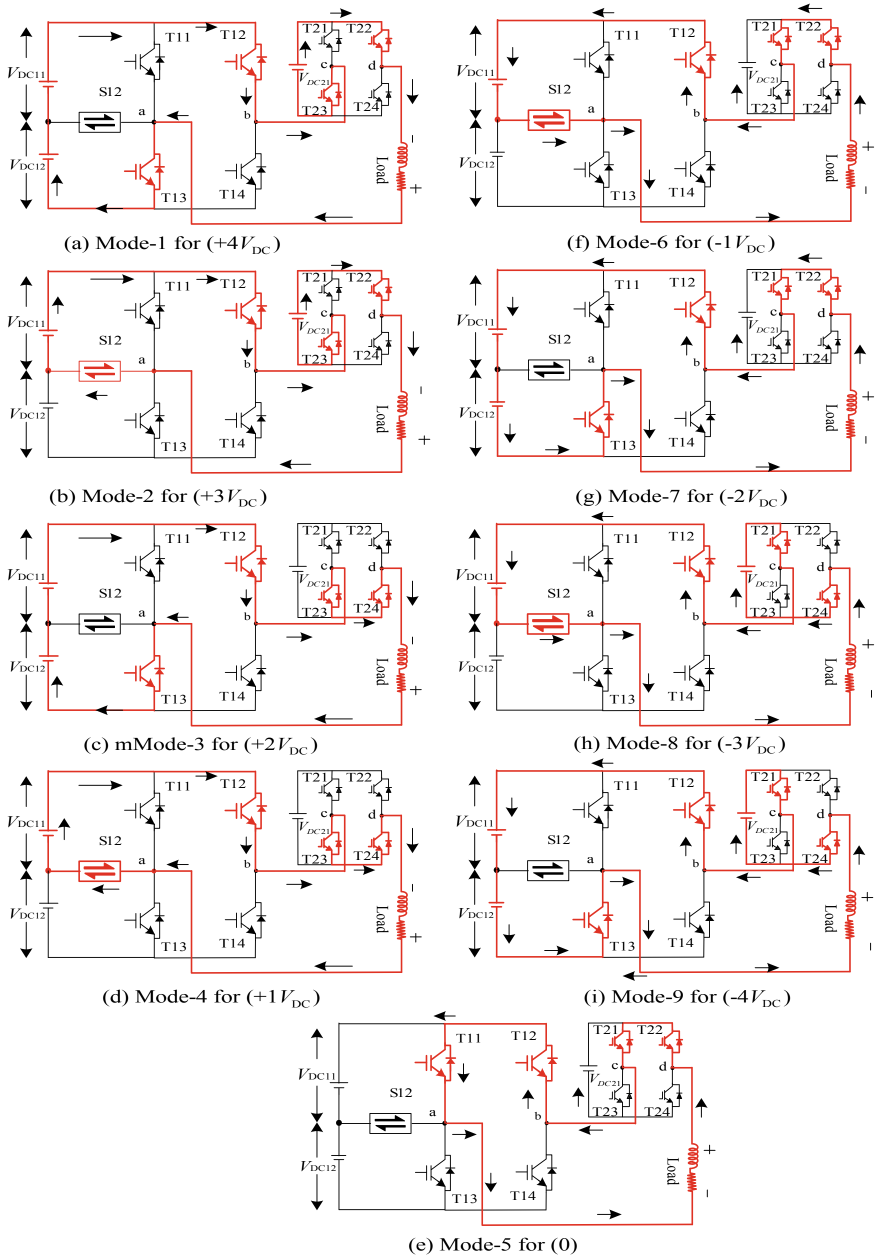

Fig. 2 Voltage generation at different modes with direction of current **a** $+4V_{DC}$, **b** $+3V_{DC}$, **c** $+2V_{DC}$, **d** $+V_{DC}$, **e** 0, **f** $-V_{DC}$, **g** $-2V_{DC}$, **h** $-3V_{DC}$, **i** $-4V_{DC}$

Mode-1: Conduction of the four switches T_{12}, T_{13}, $T_{22,}$ and $T_{23,}$ output voltage magnitude of + $4V_{DC}$ is generated at the inverter output terminals as depicted in Fig. 2a.

Mode-2: Similarly, by the conduction of the four switches, either T_{12}, S_{11}, $T_{22,}$ and T_{23} an output voltage of magnitude + $3V_{DC}$ is generated at the inverter terminals as depicted in Fig. 2b.

Mode-3: In addition, by the conduction of the four switches, either T_{12}, T_{13}, $T_{23,}$ and T_{24} an output voltage of magnitude + $2V_{DC}$ is generated at the output terminals as depicted in Fig. 2c.

Mode-4: Similarly, conduction of the four switches like either T_{12}, S_{11}, $T_{23,}$ and T_{24} output voltage magnitude of + V_{DC} is generated at the inverter output terminals as depicted in Fig. 2d.

Mode 5: Lastly, conduction of the four switches like either T_{12}, T_{13}, $T_{21,}$ and T_{22} or T_{13}, T_{14}, $T_{23,}$ and T_{24} is generated zero (0) at the inverter output terminals as shown in Fig. 2e.

In a similar way, the set of remaining switches is conducting as per Table 1 to obtain the negative voltage levels. The switching frequency for all proposed MLIs in the simulation, as well as the corresponding experimental purpose, is considered as 5 kHz.

2.2 For Symmetrical Seven-Level Inverter Topology

Proposed seven-level inverter modules equal value of all the DC-link voltage sources in both of the configuration (auxiliary cell and the H-bridge cell) symmetrical models and their ratio of DC-link voltages having V_{DC11}:V_{DC12}:V_{DC22} = 1:1:1 in same manner of the symmetrical MLI as depicted in Fig. 1. Here details show the switching status (on/off) of the proposed inverter to generate seven-level output voltages is depicted in Table 2. For the proposed seven-level topology, the bold red lines show the conduction path through the conducting components for different voltage level generations, and the thin (black) lines show that the components are not conducting or contributing at the current state. Many redundant states, as shown in Table 1, that can be used to generate the same voltage levels, are not shown in Fig. 3.

Mode-1: Conduction of the four switches T_{12}, T_{13}, $T_{22,}$ and $T_{23,}$ output voltage magnitude of + $3V_{DC}$ is generated at the inverter output terminals as depicted in Fig. 3a.

Mode-2: Similarly, by the conduction of the four switches, either T_{12}, S_{11}, $T_{22,}$ and T_{23} or T_{12}, T_{13}, T_{23}, and T_{24} an output voltage of magnitude + $2V_{DC}$ is generated at the inverter terminals as depicted in Fig. 3b, c.

Table 2 On/off switching status (S_x) of the seven-mode operation of proposed seven-level symmetrical inverter (V_{DC11}:V_{DC12}:V_{DC22} = 1:1:1)

Mode	Conducting switches √ = ON; × = OFF									Inv. O/P voltage (V_o)
	For auxiliary circuit					For H-bridge circuit				
	T_{11}	T_{12}	T_{13}	T_{14}	S_{11}	T_{21}	T_{22}	T_{23}	T_{24}	
1	×	√	√	×	×	×	√	√	×	$3V_{DC}$
2	×	√	×	×	√	×	√	√	×	$2V_{DC}$
3	×	√	√	×	×	×	×	√	√	
4	×	×	√	×	√	×	×	√	√	$1V_{DC}$
5	√	√	×	×	×	√	√	×	×	0
6	×	√	×	×	√	√	√	×	×	$-1V_{DC}$
7	×	√	√	×	×	√	√	×	×	$-2V_{DC}$
8	×	√	×	×	√	√	×	×	√	
9	×	√	√	×	×	√	×	×	√	$-3V_{DC}$
10	×	√	×	√	×	√	×	×	√	0

Mode-3: In addition, by the conduction of the four switches, either T_{12}, S_{11}, $T_{23,}$ and T_{24} an output voltage of magnitude + $1V_{DC}$ is generated at the output terminals as depicted in Fig. 3d.

Mode-4: Lastly, conduction of the four switches like either T_{12}, T_{13}, $T_{21,}$ and T_{22} or T_{13}, T_{14}, $T_{23,}$ and T_{24} is generated zero (0) at the inverter output terminals as shown in Fig. 3e, h.

In a similar way, set of remaining switches is conducting as per Table 2 to generate the –ve o/p voltage levels. The switching frequency for all proposed MLIs in the simulation and switches conducted at a time only four switches.

3 Control PWM Strategies of the Proposed MLI

To generate the gate pulses for the IGBT switches, several modulation scheme and control paradigms have been discussed so far, such as selective harmonics elimination (SHE- PWM) [18], space vector modulation (SVPWM) [19, 20], sinusoidal pulse width modulation (SPWM) scheme [20], nearest level control [20], etc. Multi-carrier-based level-shifted plus width modulation (M-LSPWM) are chosen among the aforesaid techniques due to its easier implementation in hardware, which can be further fed to the switches like IGBT through appropriate gate driver circuits. Thus, for implementing the LSPWM technique for the proposed seven-level inverter, six triangular carriers (in same phase but are off-set with their +ve and −ve magnitude) for PWM technique for nine-level inverter, eight-triangular carrier signals in the same phase, but their levels are shifted 90° and compared to the reference signal. Here, switching states are decoded in Table 2 for a seven-level and Table 1 for a

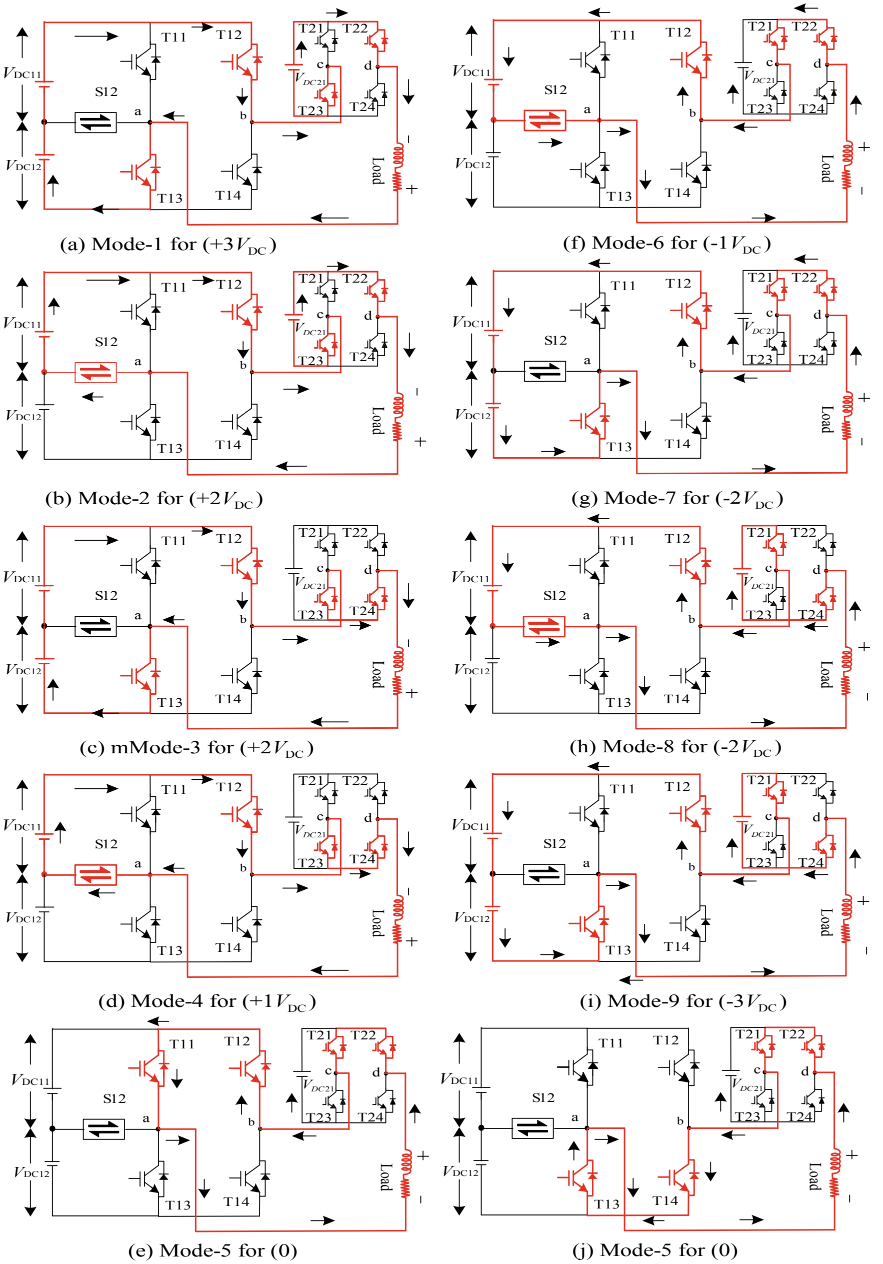

Fig. 3 Voltage generation at different modes with direction of current **a** + 3V_{DC}, **b**, **c** + 2V_{DC}, **d** + V_{DC}, **e** 0, **f** $-V_{DC}$, **g,h** $-2V_{DC}$, **i,j** $-3V_{DC}$

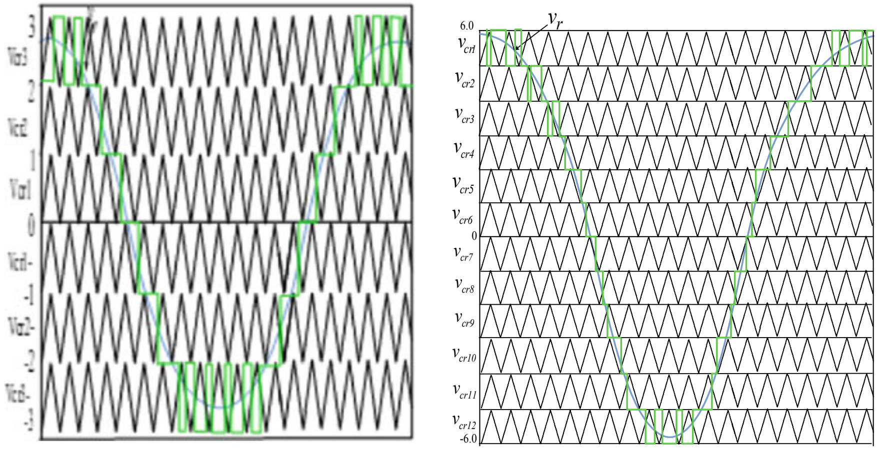

(a) (b)

Fig. 4 LS-PWM technique and the corresponding switching states for **a** seven-level and **b** nine-level inverters

nine-level inverter. The proposed asymmetrical MLIs modulation index (M_i) of a fixed magnitude of the peak carriers (A_c) are presented in Fig. 4,

$$M_i = A_m / A_c \tag{1}$$

4 Comparison Between Proposed MLIs and Traditional MLIs Topologies

In this paper to show the effectiveness of proposed MLI topology, compared to the other reduced switch MLIs proposed (in Tables 3 and 4)indicates the comparison

Table 3 Comparative analysis between classical inverters to the proposed inverter

MLI TOPOLOGIES	Unidirectional switching devices	Bidirectional switching devices	Total no DC sources
NPC, FC, CHB	$2 * [n - 1]$	0	$[n - 1]/2$
Cascaded MLI symmetric–asymmetric [14]	$4n/5$	$n/5$	$2n/5$
Symmetric topology [P]	08	$[n - 6]$	$[n - 1]/2$
Asymmetric topology [P]	08	$[n - 8]$	$[n - 3]/2$

Table 4 Comparison analysis of losses and efficiency of the proposed converter MLIs with the losses of the other classical reviewed MLIs

MLIs	Inverter output power (W)	Inverters output voltage levels	Total standing voltage (TSV)	Employed control strategy	Switching devices and ratings	Efficiency/total power losses (%)
[16]	100	Thirteen-level	$18V_{dc}$	Nearest level control	IGBT: IKW25N120H3 1200 V, 25 A	98.50
[17]	–	Nine-level	$20V_{dc}$	Selective harmonic elimination	IGBT: GT50J325 600 V, 50 A	–
[19]	200	Eleven-level	$21V_{dc}$	Selective harmonic elimination	IGBT: GT50J325 600 V, 50 A	94
Proposed (symmetrical)	288	Seven-level	$14V_{dc}$	SPWM @ 3 kHz	IGBT: CT60AM-18F 900 V, 60 A	96.80
Proposed (asymmetrical)	483	Nine-level	$22V_{dc}$	SPWM @ 3 kHz		96.70

of the proposed inverter between the other usual inverters topology in relations of the no of IGBTs and no of DC-link sources of the proposed inverter configuration required power electronics switches 9 IGBTs to gets output voltage nine-level of 3 DC sources with compared of 16 IGBTs in the following inverter configuration DC, FC, and CHB-MLI are need of 4 DC sources of classical inverters.

5 Results

5.1 For Simulation and Experimental Results

The detailed simulation of the proposed inverter of the nine-level asymmetrical depicted in Fig. 1 is done in MATLAB/Simulink platform. The so-called power circuit consists of the proposed inverter circuit and the isolated DC power sources obtained from an AC supply using rectifier–capacitor arrangements for the laboratory prototype. On the other hand, the control circuit consists of a DS1103-based PWM controller coupled with a PC generating PWM pulses, which is further processed through a TLP250-based IGBT driver circuit as shown in Fig. 8. The simulation and the respective experimental waveforms of the inverter voltage and load current of the proposed at unity modulation index are shown in Fig. 5a, b at a RL load of $R = 50\ \Omega$, $L = 100$ mH. For symmetric (for seven-level) and asymmetric (for nine-level) schemes and inverter topology can be extended to three-phase schemes. Further, the simulation and experimental results of inverter output voltage (V_{inv}) and load current (I_{inv}) for an RL load ($R = 45\ \Omega$, $L = 100$ mH) at the modulation index, $Mi = 0.5$,

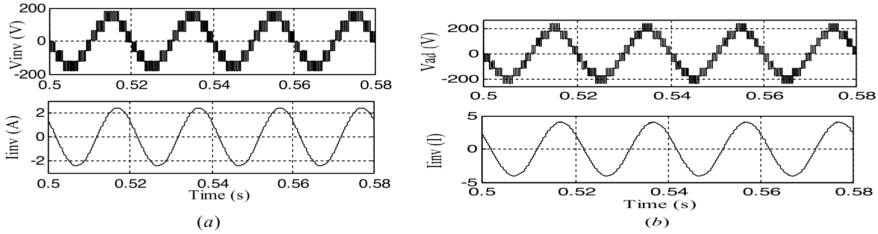

Fig. 5 Simulation result of proposed MLIs **a** for seven-level symmetric inverter, **b** for nine-level asymmetric inverter

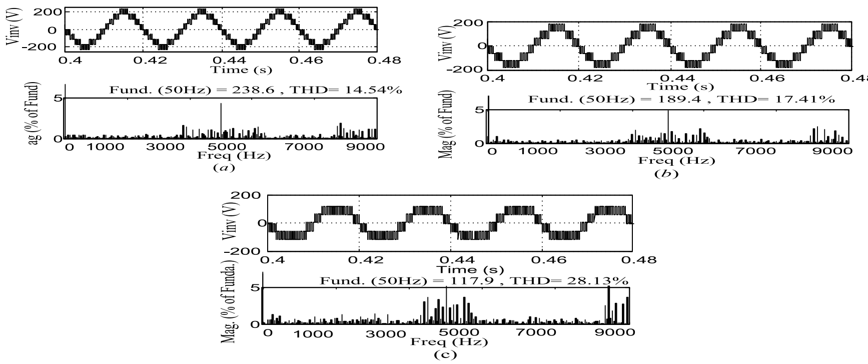

Fig. 6 Simulation and their corresponding %THD at **a** $Mi = 1$, **b** $Mi = 0.8$, **c** $Mi = 0.5$

0.8, and 1 is shown in Fig. 6a–c. From 1 to 0.5 decreases Mi the number of output of voltage also decreases from nine-level to five-level and value of the %THD keeps on increasing. It is also found that the experimental results under steady-state conditions are identical to the respective simulation results given in Fig. 7a (for seven-level symmetric inverter), while Fig. 7b (for nine-level asymmetric inverter), the experimental waveforms of the inverter voltage and the load current under the variable *Mi*, as well as sudden load variations, are also presented in Fig. 7c. However, if the load impedance changes, the magnitude of load current changes without altering the voltage levels, and hence, they are verified using real-time simulators 1103 dSPACE.

6 Conclusion

The goal of this paper was to build a new MLI by cascading each cell with one H-bridge. The proposed inverter can extend to both the symmetric and asymmetric values of DC sources. A lower number of IGBTs, driver circuits are required to

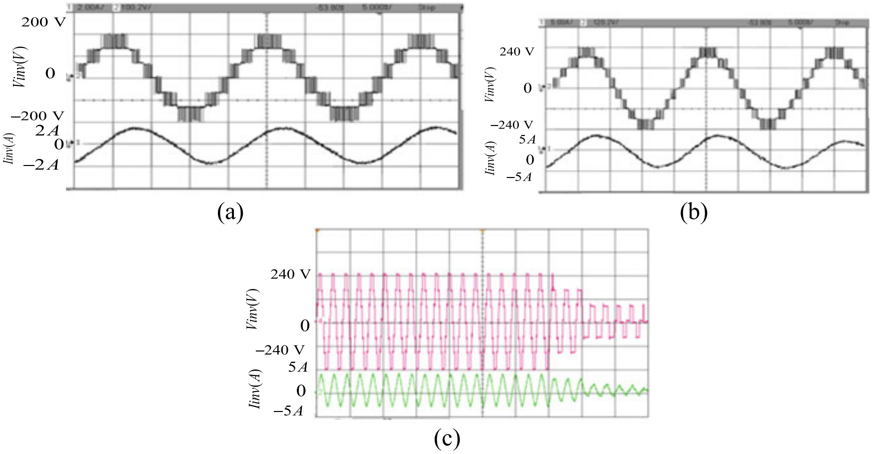

Fig. 7 Experimental results for proposed Inverter output voltage and the load current, **a** symmetrical seven-level and **b** asymmetrical nine-level inverter, **c** modulation index at different modulation indices

Fig. 8 Experimental setup of proposed symmetrical inverter

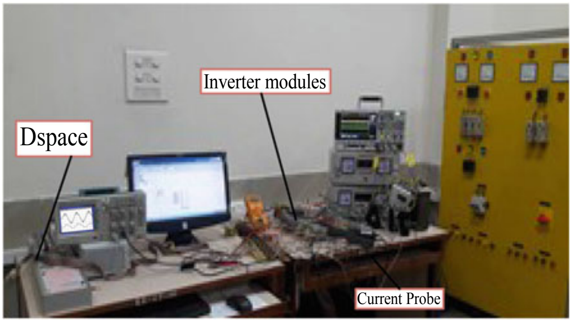

generate the higher voltage levels, resulting in cost reduction, circuit size, control complexity, and area of installation. Depending on the parameters related to the developed experimental prototype, the efficiency of the proposed seven-level is determined less also less switching loss and the conduction loss are found, respectively. Various performance parameters of the proposed MLI are analyzed and have been compared with newly discussed MLI topologies. The analysis is well carried out in some sense—the two categories of switch number/level and DC sources/level are useful for the comparison. For further clarification of performance parameters, i.e., efficiency, LSR, and TSV, are also calculated and compared with the newly discussed MLIs.

References

1. Kiltie O (1940) New type of D-C to A-C vibrator inverter. Trans Am 59(4):245–248
2. Sinha A et al (2018) An inclusive review on different multi-level inverter topologies, their modulation and control strategies for a grid connected photo-voltaic system. J Solar Energy 170:633–657
3. Panda KP et al (2019) Reduced switch cascaded multilevel inverter with new selective harmonic elimination control for standalone. Renew Energy Syst 55(6):7561–7574
4. Das MK et al (2016) A new half-cascaded multilevel inverter topology to improve systems performance parameters. J Mines Metals Fuels 64:267–270
5. Panda KP, Panda G (2018) Application of swarm optimisation-based modified algorithm for selective harmonic elimination in reduced switch count multilevel inverter. IET Power Electron 11(8):1–11
6. Das MK, Chauhan SS, Buduma P, Mishra S, Jana KC (2021) A hybrid novel cascaded asymmetrical 21-level inverter with reduced switches. In: 3rd IEEE international conference on energy, power and environment (ICEPE)
7. Kumar N, Saha TK, Dey J (2019) Multilevel inverter (MLI)-based stand-alone photovoltaic system: modelling, analysis, and control. IEEE Syst 1:1–7
8. Lai JS, Peng FZ (1996) Multilevel converters—a new breed of power converters. IEEE Trans Ind Appl 32(3):509–517
9. Malinowski M, Gopakumar K, Rodriguez J, Pérez M (2010) A survey on cascaded multilevel inverters. IEEE Trans Ind Electron 57(7):2197–2206
10. Jing H, Corzine KA (2006) Extended operation of flying capacitor multilevel inverters. IEEE Trans Power Electron 21(1):140–147
11. Das MK, Sinha A, Jana KC (2019) A novel asymmetrical reduced switch nine-level inverter. J Circuit Syst Comput (World Sci) 29(8)
12. Ahrabi RR, Farakhor A, Ravadanegh SN, Ardi H (2015) Symmetric and asymmetric transformer based cascaded multilevel inverter with minimum number of components. IET Power Electron 8(6):1052–1060
13. Rodríguez J, Lai JS, Peng FZ (2002) Multilevel inverters: a survey of topologies, controls, and applications. IEEE Trans Ind Electron 49(4):724–738
14. Saeedian M, Adabi J, Hosseini SM (2017) Cascaded multilevel inverter based on symmetric–asymmetric DC sources with reduced number of components. IET Power Electron 10(12):1468–1478
15. Das MK, Jana KC, Sinha A (2018) Performance evaluation of an asymmetrical reduced switched multi-level inverter for a grid-connected PV system. IET Renew Power Gener 12(2):252–263
16. Siddique MD et al (2019) Low switching frequency based asymmetrical multilevel inverter topology with reduced switch count. IEEE Access 7:86374–86383
17. Siddique MD, Iqbal A, Memon MA, Mekhilef S (2020) A new configurable topology for multilevel inverter with reduced switching components. IEEE Access 8:188726–188741

18. Das MK, Buduma P, Mishra S (2021) An asymmetrical reduced switch multilevel inverter based grid-connected PV system. In: 3rd IEEE international conference on energy, power and environment (ICEPE)
19. Rawa M et al (2020) Dual input switched-capacitor-based singlephase hybrid boost multilevel inverter topology with reduced number of components. IET Power Electron 13(4):881–891
20. Das MK, Sinha A, Jana KC (2018) A generalized hybrid multilevel inverter with reduced number of switches. In: IEEE 4th international conference on recent advances in information technology (RAIT)

Chapter 8
A New Reduced Device Count of Three-Phase Three-Level Switched Capacitor-Based Grid-Connected Inverter with LCL Filter

Aratipamula Bhanuchandar and Bhagwan K. Murthy

Abstract In this paper, a new reduced device count (RDC) of 3-Ph, 3-L switched capacitor (SC)-based grid-connected inverter (GC1) with LCL filter has been elucidated. In this topology, a common single DC source has been connected to all phases and comprises four unidirectional switches, one discrete diode, and one switched capacitor per phase. It has the capability to produce three levels in pole voltage and five levels in the line voltages. Here, with parallel–series technique, all the switched capacitors are self-balanced without need of any separate balancing circuits/sensors. With respect to single DC source, the respective line voltage provides two times boosting ability in the inverter structure. The topology provides less per unit total standing voltage (TSV) and also provides an equal amount of blocking voltage across all semiconductor devices. At the end, for higher ripple attenuation purpose, an LCL filter has been integrated with grid. The combination of dq-frame current control strategy and unipolar phase disposition (UPD) pulse width modulation (PWM) technique has been applied to the GCI, and with this, the unity power factor (UPF) operation of grid has been elucidated vividly. Finally, the operation of an inverter and control structure has been validated through MATLAB/Simulink platform.

Keywords Grid-connected inverter · Switched capacitor · Total standing voltage · Unipolar phase disposition · Pulse width modulation · Unity power factor

1 Introduction

Power conversion from DC to AC plays an important role and can be effectively used in electric vehicle (EV) and grid-tied applications. Basically, the inverters are classified as two-level and multilevel inverters (MLIs). The main aim of MLI is to synthesize the stepped waveform into following a sinusoidal wave [1]. The traditional three-phase, two-level voltage source inverter (VSI) comprises one DC source and three half-bridge legs. For better power quality, it demands larger filter circuit

A. Bhanuchandar (✉) · B. K. Murthy
National Institute of Technology Warangal, Warangal, Telangana, India

G. Panda et al. (eds.), *Sustainable Energy and Technological Advancements*, Advances in Sustainability Science and Technology,
https://doi.org/10.1007/978-981-16-9033-4_8

arrangement, and at a time, the inverter faces high dv/dt stresses across the switches [2]. The MLI topologies are basically giving better harmonic profile, reduce electromagnetic compatibility problems, less voltage stress, smaller common-mode voltage, reduce dv/dt stresses, drawing input current with lower distortion, small size filter requirements or even eliminated, and high fault-tolerant capabilities [3]. The basic traditional neutral point clamped (NPC), flying capacitor (FC), and cascaded H-Bridge (CHB) inverters are facing the problems like unequal loss distribution among switching devices, pre-charging of capacitors, and requirement of more number of DC sources, respectively, for three-phase operation [4]. The topology [5] needs nearly 20 switches, 8 capacitors, 12 diodes, and one DC source for three-phase operation, and finally, it provides high value of TSV. The TSV decides basically the cost requirement switching devices of an inverter topology. The topology [6] gives TSV as $24V_{\mathrm{dc}}$ with six DC sources. However, in this there is no need of separate discrete diodes. With 24 switches, the topology [7] gives TSV as $36V_{\mathrm{dc}}$ with 2 DC sources. Without discrete diodes and less number of switches, the topology [8] provides the TSV of $40V_{\mathrm{dc}}$. The topologies [9–12] with single DC sources arrangement are providing high value of TSV, and then the cost requirement of switches drastically increases. Most of conventional topologies do not provide self-balancing property of capacitors. To reduce TSV requirement and maintaining self-balancing property of capacitors with single DC source arrangement, a new three-phase, three-level switched capacitor-based grid-connected inverter topology has been reported in this paper with dq-frame current control strategy. For higher ripple attenuation capability, the LCL filter has been integrated with grid. However, careful design should be required while designing the filter with stability considerations [13].

The rest of the paper is summarized as follows. Section 2 describes the operation and control strategy of proposed work. The comparative study has been discussed in Sect. 3. Section 4 represents simulation results for the GCI topology. Finally, the conclusion has been reported in Sect. 5.

2 Operation and Control Strategy of Proposed GCI Topology

2.1 Operation

A reduced switch count (RSC) of three-phase, three-level SC-based grid-connected inverter with LCL filter is depicted in Fig. 1. In this topology, each phase contains four unidirectional switches, one discrete diode, and one SC. A common single DC source arrangement has been provided to all phases. Here, the pole voltage has to be considered between phase point to positive DC bus point, and it can be indicated as V_{AP}. Table 1 shows switching arrangement for three-level output voltage as per phase to be assumed. The zero level is obtained from conduction switches of $S_{2\mathrm{a}}$ and $S_{3\mathrm{a}}$. If $S_{1\mathrm{a}}$ and $S_{3\mathrm{a}}$ are in conduction mode, then the capacitor is discharged and

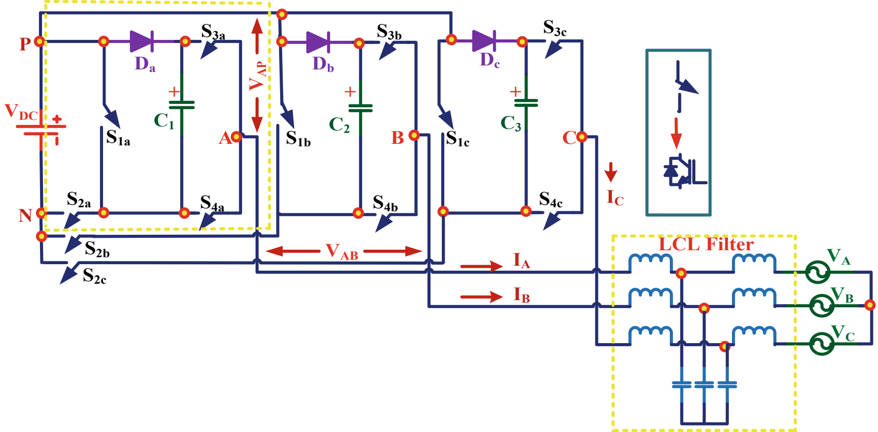

Fig. 1 Proposed three-phase, three-level SC-based GCI with LCL filter

Table 1 Switching table: Phase-A

S. No.	ON state switches	Capacitor (C_1)	Output voltage, V_{AP}
1	S_{2a}–S_{3a}	C	$+\,0V_{dc}$
2	S_{1a}–S_{4a}	–	$-\,0V_{dc}$
3	S_{1a}–S_{3a}	D	$+\,1V_{dc}$
4	S_{2a}–S_{4a}	C	$-\,1V_{dc}$

produces output voltage of $+\,1V_{dc}$. Similarly, if S_{2a} and S_{4a} are in conduction mode, then the capacitor is charged and produces output voltage of $-\,1V_{dc}$. This type of operation is called parallel–series technique. With this technique, the self-balancing of capacitors is possible in all phases that mean there is no need of separate auxiliary circuits or sensors. The SC values are calculated from the longest discharging period (LDP) method. Finally, in pole voltage, a three-level output is present and in the line voltage a five-level output voltage is possible that means it provides boosting factor (BF) as two. In the operation of switching strategy, the voltage stress of each switch does not exceed input DC supply and finally it provides less per unit TSV per phase and is depicted in Table 2.

In [11], with single DC supply, the pole voltage provides boosting ability. However, for generating three-level output it takes more switch count, thereby requirement of heat sink, protection, and gate driver circuits are more. Also, the UPF operation of grid concept has not been explained in this. In proposed topology, an LCL filter has been integrated with grid for higher ripple attenuation capability purpose. By considering stability and resonant peak problems, an LCL filter has been designed according to [13]. The design procedure has been represented in flowchart as shown in Fig. 2. In the next section, the UPF of operation of GCI topology has been explained through proper control strategy action.

Table 2 Calculation of TSV: Phase-A

S. No.	Semiconductor devices	Standing voltage (Phase-A)
1	S_{1a}	V_{dc}
2	S_{2a}	V_{dc}
3	S_{3a}	V_{dc}
4	S_{4a}	V_{dc}
5	Da	V_{dc}
TSV in per unit		**5 p.u.**

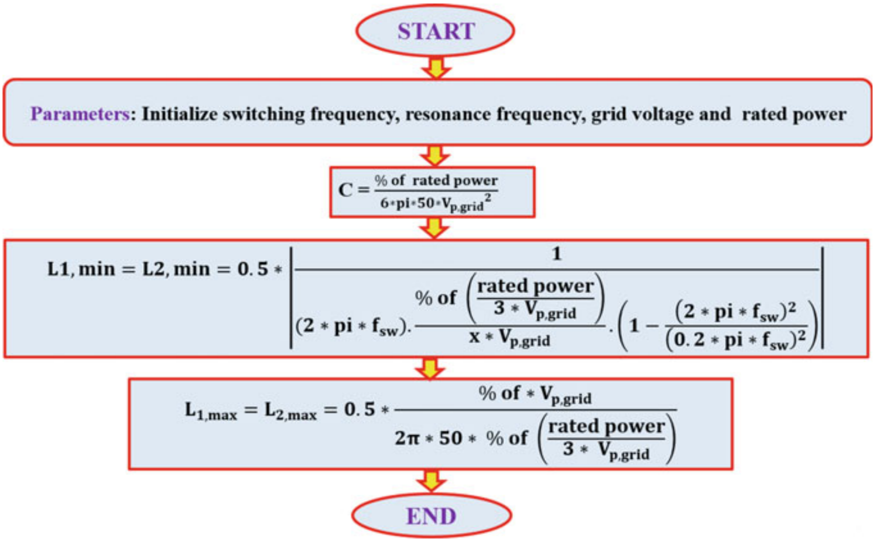

Fig. 2 LCL filter design flowchart

2.2 Control Strategy

Figure 3 shows a dq-frame current control strategy for the proposed grid-connected inverter topology. Firstly, the grid voltages (V_{abc}) have been sensed and generated V_α and V_β components through abc to αβ transformation. From the output, the PLL has been implemented and it provides reference grid variable for the grid synchronization. From $\alpha\beta$ to dq transformation, the respective V_d and V_q components are generated. Secondly, inverter side currents have been sensed and generated I_α and I_β components. From this output, I_d and I_q components are generated using αβ to dq transformation. Here, I_d and I_q are correspond to active and reactive currents, respectively. The I_d and I_q are subtracted from $I_{d(ref)}$ and $I_{q(ref)}$, and then it produces an error. This error is fed to PI controller. From decoupled control strategy, the respective modulating signals are generated. For generating desired modulating signals, a proper gain (P_G) value is used according to line voltage and number of carrier

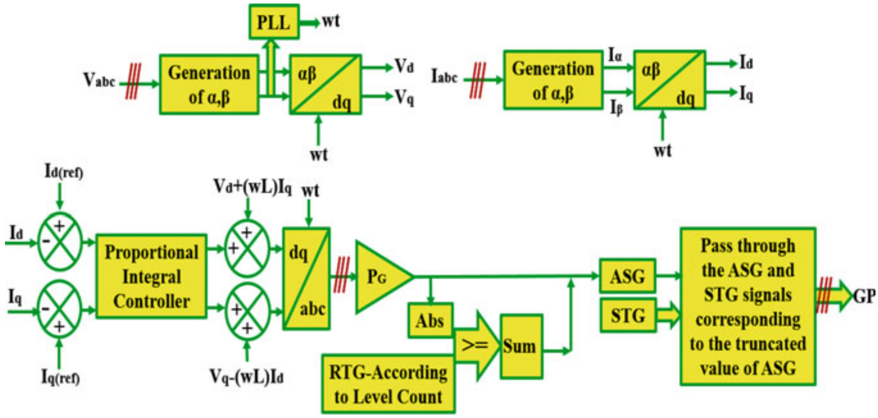

Fig. 3 Control strategy-GCI

count. These desired modulating signals are given to absolute function (Abs), and then it generates unipolar modulating waveforms. The repeating table generation (RTG) has been developed according to level count. After comparison of Abs and RTG signals, the generated output has been added and then finally generated aggregated signal (AS). From the switching table, the switching table generation (STG) has been developed. Both of ASG and STG signals are truncated and finally generate desired gate pulses (GP's) for the grid-connected inverter. Here, the PWM operation is called, "unipolar level shifted in-phase disposition modulation technique."

3 Comparative Study

Table 3 shows comparison of proposed inverter topology with other conventional topologies. As compared, with all conventional topologies, the proposed topology

Table 3 Comparative study with other conventional topologies

S. No.	Topology	Ndc	Nsw	Nc	Nd	TSV
1	[5]	1	20	8	12	43
2	[6]	6	24	6	0	24
3	[7]	2	24	8	0	36
4	[8]	2	16	4	0	40
5	[9]	1	18	6	6	24
6	[10]	1	24	6	0	20
7	[11]	1	21	3	0	21
8	**Proposed**	**1**	**12**	**3**	**3**	**15**

takes less number of switches, diodes, capacitors with single DC supply. The TSV term signifies cost requirement of an inverter topology. The proposed topology gives less amount of TSV as compared with other conventional topologies. In all phases, the respective diodes and switches are faced an equal amount of voltage stress and kept maintaining as V_{dc} only. From switching operation, the proposed topology provides boosting ability in the line voltage with respect to single DC source supply.

4 Simulation Results

Table 4 shows simulation parameters for the proposed grid-connected inverter topology. Figure 4 shows simulation results for proposed GC1 topology with step changes in $I_{d(ref)}$. Figure 5 shows switch and diode voltage stresses of phase-A, and Fig. 6 shows harmonic spectrum of grid current w.r.to Phase-A.

From the proposed control strategy, all switched capacitors are self-balanced at V_{dc} with less voltage ripple even if step changes in $I_{d(ref)}$ operation also. The desired three-level pole voltage and five-level line voltages have been obtained with peak values of 398.7 and 798.7 V, respectively. The peak value of grid voltage is obtained as 585.3 V with pure sinusoidal nature. According to step changes in $I_{d(ref)}$=300 and 500 A, the grid current tracked exactly equal to with peak values of 299.8 and 150.6 A, respectively. Generally, $I_{d(ref)}$ is used to inject active power into the grid and $I_{q(ref)}$ is used to inject reactive power into the grid. By taking $I_{q(ref)}$ as zero, the UPF operation of grid has been achieved. From Fig. 5, it is concluded that all the semiconductor switches are faced an equal amount of voltage stress and these are do not exceed the input DC supply. Finally, from Fig. 6 it is concluded that the grid current THD is obtained as 2.05% and it meets IEEE-519 standards.

Table 4 Simulation parameters—GCI topology

S. No.	Parameters	Value
1	Grid voltage	415 V
2	Switching frequency	10 kHz
3	Grid frequency	50 Hz
4	Resonance frequency	1000 Hz
5	Rated power	100 kVA
6	V_{dc}	400 V
7	Inverter side inductance	490 μH
8	Grid side inductance	490 μH
9	Filter capacitance	100 μF
10	Switched capacitors	6600 μF

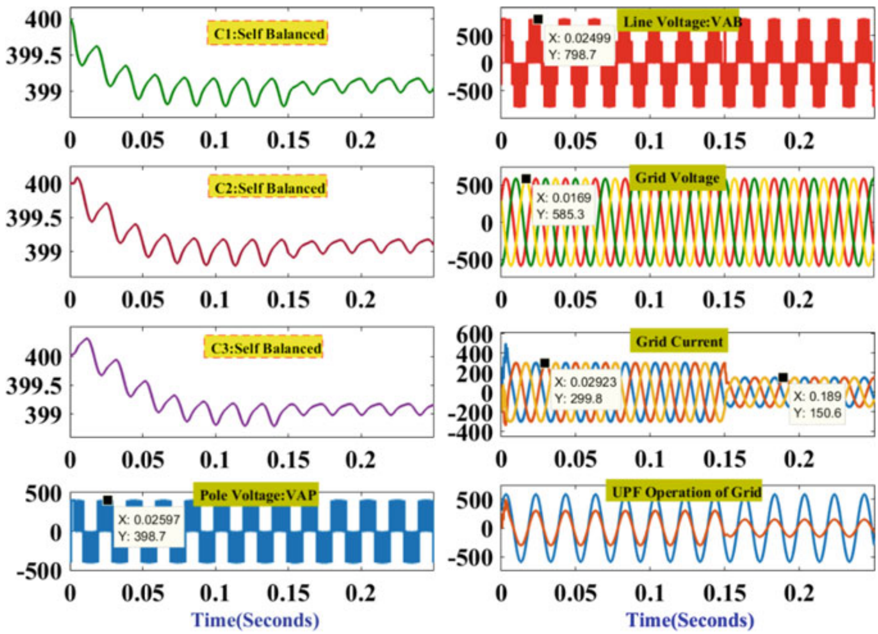

Fig. 4 Simulation results—proposed GCI topology

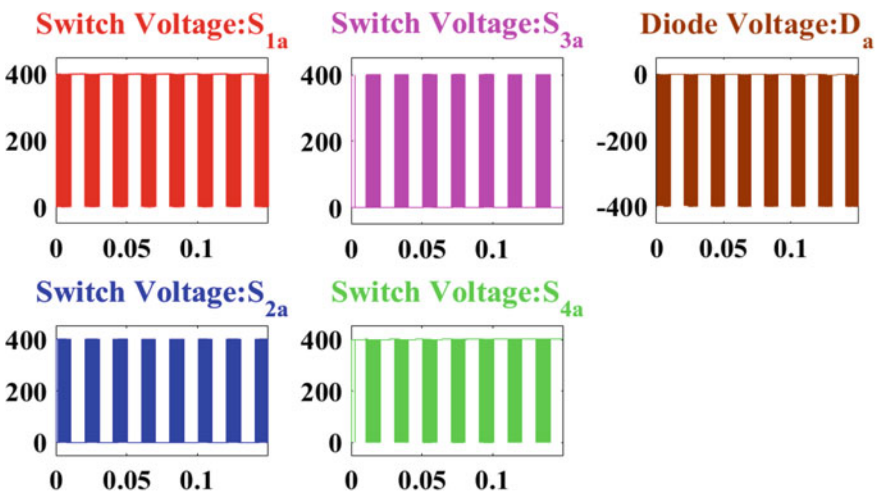

Fig. 5 Voltage stress of semiconductor devices: Phase-A

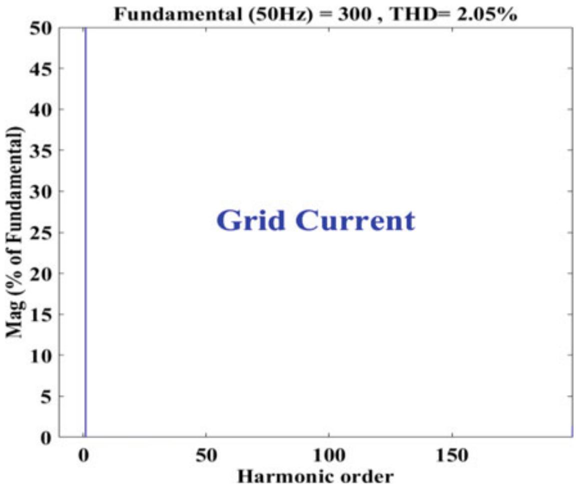

Fig. 6 Harmonic spectrum of grid current with id_ref = 300 A

5 Conclusion

With reduced switch count and self-balancing property of switched capacitors, a new three-phase three-level grid-connected inverter has been elucidated in this paper. Generally, the RSC ensures that respective reduction in gate driver circuit, protection circuit, and heat sink, thereby cost of an inverter can become reduced. The proposed topology provides less per unit TSV per phase and voltage stress of each semiconductor device does not exceed input DC supply. Here, the self-balancing of SC's is eliminating the requirement of sensors and additional balancing circuits. In this topology, the line voltage provides boosting ability with respect to single DC source supply. By dq-frame current control strategy and unipolar level shifted in-phase disposition PWM technique, the UPF operation of grid has been achieved even if step changes in reference direct axis current values. This complete work is suitable for photovoltaic and fuel cell-based grid-connected applications. Suppose if PV panel is considered as input DC supply, then need to concentrate on common-mode voltage (CMV) effect and leakage current analysis is going to be considered as future scope of the work.

References

1. Bana PR, Panda KP, Naayagi RT, Siano P, Panda G (2019) Recently developed reduced switch multilevel inverter for renewable energy integration and drives application: topologies, comprehensive analysis and comparative evaluation. IEEE Access 7:54888–54909. https://doi.org/10.1109/ACCESS.2019.2913447
2. Gupta KK, Ranjan A, Bhatnagar P, Sahu LK, Jain S (2016) Multilevel inverter topologies with reduced device count: a review. IEEE Trans Power Electron 31(1):135–151. https://doi.org/10.1109/TPEL.2015.2405012
3. Bhanuchandar A, Murthy BK (2021) Single phase nine level switched capacitor based grid connected inverter with LCL filter. In: 2020 3rd international conference on energy, power and environment: towards clean energy technologies, pp 1–5. https://doi.org/10.1109/ICEPE50861.2021.9404491
4. Kumari M, Siddique MD, Sarwar A, Tariq M, Mekhilef S, Iqbal A (2021) Recent trends and review on switched-capacitor-based single-stage boost multilevel inverter. Int Trans Electr Energ Syst 31:e12730. https://doi.org/10.1002/2050-7038.12730
5. Dagan KJ, Zuckerberger A, Rabinovici R (2016) Fourth-arm common-mode voltage mitigation. IEEE Trans Power Electron 31(2):1401–1407. https://doi.org/10.1109/TPEL.2015.2417804
6. Nguyen N, Tu Nguyen T, Lee H (2015) A reduced switching loss PWM strategy to eliminate common-mode voltage in multilevel inverters. IEEE Trans Power Electron 30(10):5425–5438. https://doi.org/10.1109/TPEL.2014.2377152
7. Kumar PR, Rajeevan PP, Mathew K, Gopakumar K, Leon JI, Franquelo LG (2014) A three-level common-mode voltage eliminated inverter with single DC supply using flying capacitor inverter and cascaded H-bridge. IEEE Trans Power Electron 29(3):1402–1409. https://doi.org/10.1109/TPEL.2013.2262808
8. Hota A, Jain S, Agarwal V (2017) A modified T-structured three-level inverter configuration optimized with respect to PWM strategy used for common-mode voltage elimination. IEEE Trans Indus Appl 53(5):4779–4787. https://doi.org/10.1109/TIA.2017.2716374
9. Saeedian M, Hosseini SM, Adabi J (2018) Step-up switched-capacitor module for cascaded MLI topologies. IET Power Electron 11:1286–1296. https://doi.org/10.1049/iet-pel.2017.0478
10. Saeedian M, Hosseini SM, Adabi J (2018) A five-level step-up module for multilevel inverters: topology, modulation strategy, and implementation. IEEE J Emerg Select Topics Power Electron 6(4):2215–2226. https://doi.org/10.1109/JESTPE.2018.2819498
11. Sandeep N, Ali JSM, Kumar Verma A, Yaragatti UR (2019)Three-phase magnetic-less boosting multilevel inverter topology with reduced components. In: 2019 IEEE transportation electrification conference (ITEC-India), pp 1–5. https://doi.org/10.1109/ITEC-India48457.2019.ITECINDIA2019-42
12. Panda KP, Bana PR, Panda G (2021) A reduced device count single DC hybrid switched-capacitor self-balanced inverter. IEEE Trans Circuits Syst II Express Briefs 68(3):978–982. https://doi.org/10.1109/TCSII.2020.3018333
13. Sen S, Yenduri K, Sensarma P (2014) Step-by-step design and control of LCL filter based three phase grid-connected inverter. IEEE Int Conf Indus Technol (ICIT) 2014:503–508. https://doi.org/10.1109/ICIT.2014.6894991

Chapter 9
Reduction in Harmonics for PV-Based Reduced Device Count Multilevel Inverter Wıth Genetic Algorithm

Yatindra Gopal, Kaibalya Prasad Panda, Y. N. Vijay Kumar, and G. V. Pradeep

Abstract Production of renewable energy sources (RES) has been exponential in the present years and is essentially driven by factors like the escalation of greenhouse emissions with depleting in fossil fuel reservoirs. Photovoltaic (PV) energy, a prominent RES, produces electricity directly from sunlight. Nowadays, multilevel inverter (MLI) is broadly worn in incorporation with RES and drives application. Among various RESs, PV energy is the most generous and reliable. In this manuscript reduced device count multilevel inverter (RDC MLI) incorporate with PV system with maximum power point tracking technique (MPPT) and compared with cascaded multilevel inverter (CHB MLI). Based on genetic algorithm (GA), selected harmonic elimination (SHE) technique is considered for generate the proper firing angles of PV support MLIs. The obtained firing angles are suitable to reduce the total harmonic distortion (THD) of MLIs. The PV with RDC MLI is produced less THD as compared to PV CHB MLI. Analysis of results is based on MATLAB/Simulink software platform.

Keywords Reduced device count multilevel inverter (RDC MLI) · Selected harmonic elimination pulse width modulation technique (SHEPWM) · Total harmonic distortion (THD) · Genetic algorithm (GA)

Y. Gopal (✉) · Y. N. Vijay Kumar · G. V. Pradeep
Deptament of Electrical and Electronics Engineering, SVCT, Chittoor, AP, India
e-mail: ygopal.phd@rtu.ac.in

K. P. Panda
Department of Electrical Engineering, National Institute of Technology, Meghalaya, Shillong, Meghalaya, India
e-mail: kaibalyapanda@nitm.ac.in

G. Panda et al. (eds.), *Sustainable Energy and Technological Advancements*, Advances in Sustainability Science and Technology,
https://doi.org/10.1007/978-981-16-9033-4_9

1 Introduction

Generation of energy from RES has been exponential in current years and is essentially driven by factors like the escalation of greenhouse emissions with depleting in fossil fuel reservoirs [1–3]. Photovoltaic (PV) energy, a prominent RE source, produces electricity directly from sunlight. Its operation is noiseless and harmless to the environment. The PV system is interfaced with various essential power electronic components to achieve necessary efficiency in energy conversion to harness renewable energy.

Controlling the output voltage of PV cells varies when regulating the irradiation and environmental [4–7]. Hence, the necessity of MPPT technique and boost converter is considered to generate desired output voltage by PV cells. A variety of control techniques has been worn to discover the maximum power point (MPP). Perturbation and observation (P&O) technique is very easy and simplicity with simple implementation. P&O works based on iterative method, and it swings near the point $\mathrm{d}P/\mathrm{d}V = 0$, i.e., MPP. Incremental conductance (IC) technique gives the best dynamic performance and accuracy when fast change in atmospheric environment. In this paperwork, IC MPPT is worn with the adaptive distinction in size of steps. IC method used to solve the difficulty of conventional process when the irradiance changes. IC method evaluates with some further variable step size methods; the worn method is not complex instruction coefficient and estimates to progress the computing speed.

Voltage production by PV is not efficient for network rating and hence considers the DC-DC boost converters to boost the PV panels output. The boost output voltage in form of DC, but requirements in commercial purpose in form of AC seeing as most of the loads are AC loads.

Hence, MLI topologies are used to produce AC voltages to improve the voltage performance with less THD [8–11].

CHB MLI, diode-clamped inverter (DCI), and capacitor-clamped inverter (CCI) are very common topologies and fine expression in the literature [12–15]. CHB MLI has various advantages compared to the conventional MLIs but requirements of devices are more. Hence, RDC MLI configuration topology with GA is used in this paper to minimize the THD.

The number of devices in MLI increases, and then cost, circuit configuration, and reliability also increase. Hence, the configuration of MLIs with less number of devices is the key element [16–29]. To generate the same output voltage levels such as 7-level (7L) CHB MLI, a novel configuration is designed with 7L-RDC MLI devoid of raising the number of bridges.

In this manuscript, SHE technique is taken to solve the nonlinear equations and produced the best results of MLIs. In addition, this manuscript reports the on PV 7-level (7L) RDC MLI topology; this process requires less switches and devices. The voltage produced by 7L-RDC MLI similar voltage output generates via 7L-CHB MLI.

In this work, estimating the values of switching angles is through solving of transcendental nonlinear equations with using GA. Newton–Raphson (NR) and resultant theory (RT) method suffer from some disadvantages to calculate the optimal value of switches [15]. NA and RT methods are not suitable when it applied to higher level MLIs. Hence, in this work bio-inspired optimization method-based GA SHE is used to the development of the system robustness.

GA is useful to solve the constrained and unconstrained troubles through the suitable assortment of unique population and gradually regularly adjust the individual population. By GA, find out the optimal values of angles of PV-based 7-L CHB MLI and 7L-RDC MLI, this work is performed the minimum value of THD.

2 Modeling of PV Cell

The simple way to represent a photovoltaic cell is with one diode model [2]. It consists of parallel with the current to a diode and required parameters such as diode identity factor (a), (V_{oc}) open-circuit voltage, and (I_{sc}) short-circuit current.

The realized characteristics of PV cell by the fundamental equation of a one cell as the source of current are placed in parallel by diode. The current output Eq. 1 is as follows:

$$I = I_{\mathrm{PV}} - I_{\mathrm{o}}\left[e\frac{q(V + \mathrm{IR}_{\mathrm{s}})}{akT} - 1\right] - \left[\frac{V + \mathrm{IR}_{\mathrm{s}}}{R_{\rho}}\right] \quad (1)$$

I_{PV} is the function of irradiance (G) and the mathematical calculation of PV current is given as in Eq. 2

$$I_{\mathrm{PV}} = \left[I_{\mathrm{PV\_STC}} + K_i \Delta T\right]\frac{G}{G_{\mathrm{STC}}} \quad (2)$$

The saturation current (I_{o}) of diode is formulated in Eq. 3 as follows:

$$I_{\mathrm{o}} = I_{\mathrm{o\_STC}}\left(\frac{T}{T_{\mathrm{STC}}}\right)^3 \exp\left[\frac{qEg}{ak}\left(\frac{1}{T_{\mathrm{STC}}} - \frac{1}{T}\right)\right] \quad (3)$$

The flowchart representation of the PV current calculation is given in Fig. 1. The detailed outputs of PV model are shown in Fig. 2.

3 Modeling of Boost Convertors

Boost convector is known as step-up convertor which converts DC to DC power [2]. This is similarly to switched mode power supply (SMPS) among a diode, a transistor

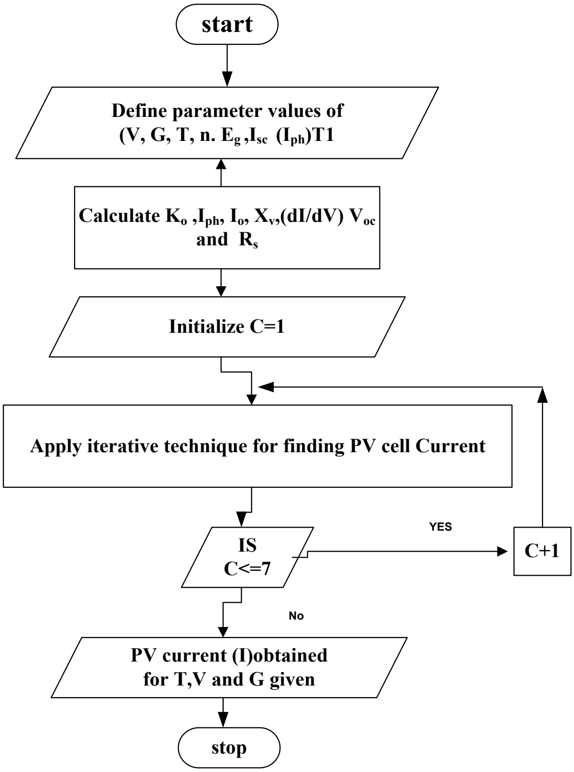

Fig. 1 Flowchart of PV cell current calculation

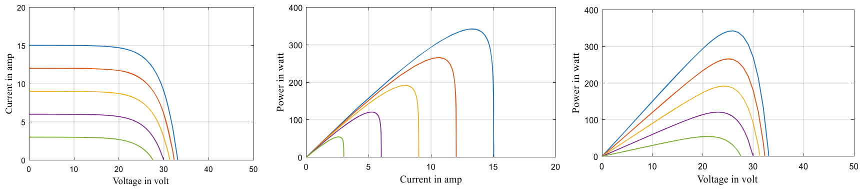

Fig. 2 Output of the PV model

with storage element of energy such as capacitor and inductor. The basic principle of boost convertor is that it can work in two modes. The first one is when the switch is working mode, then energy stores in inductor and energy releases by capacitor. In case when switch is not working, then energy stores in capacitor and released by the inductor. The voltage across the inductor is mathematically given as represented in Eq. 4.

$$v_L = V_s = L\frac{\mathrm{d}i_L}{\mathrm{d}t}$$
$$\frac{V_s}{L} = \frac{\mathrm{d}i_L}{\mathrm{d}t} \tag{4}$$

4 Incremental Conductance Method

IC is the method with the high performance, increased tracking speed better efficiency, and ease in implementation [2].

The basic idea in IC algorithm is that slop of the PV curve becomes zero on MPP. The slope of PV derivative power with respect to the voltage of PV has successive relation with MPP [1, 2].

$\frac{\Delta P}{\Delta V} = 0$ at MPP, $\frac{\Delta P}{\Delta V} > 0$ left side for MPP,

$$\frac{\Delta P}{\Delta V} < 0 \quad \text{Right side for MPP} \tag{5}$$

$$\text{At the MPP}: \frac{\mathrm{d}I}{\mathrm{d}V} = -\frac{I}{V} \tag{6}$$

When working point left side for MPP:

$$\frac{\mathrm{d}I}{\mathrm{d}V} > -\frac{I}{V} \tag{7}$$

When working point right side for MPP:

$$\frac{\mathrm{d}I}{\mathrm{d}V} < -\frac{I}{V} \tag{8}$$

where $\mathrm{d}I/\mathrm{d}V$ is IC and $\frac{I}{V}$ is instantaneous conductance; MPP is found by evaluate instantaneous conductance to the IC. The pictorial form of the IC is shown in Fig. 3, and comparisons of different MPPT techniques are shown in Table 1.

MPPT methods are key enablers of an extra energy sustainable culture, due to their utilization ease, low cost, and malleable operation. The analysis is done on variable irradiance and temperature conditions. It is observed that IC has better performance than P&O techniques.

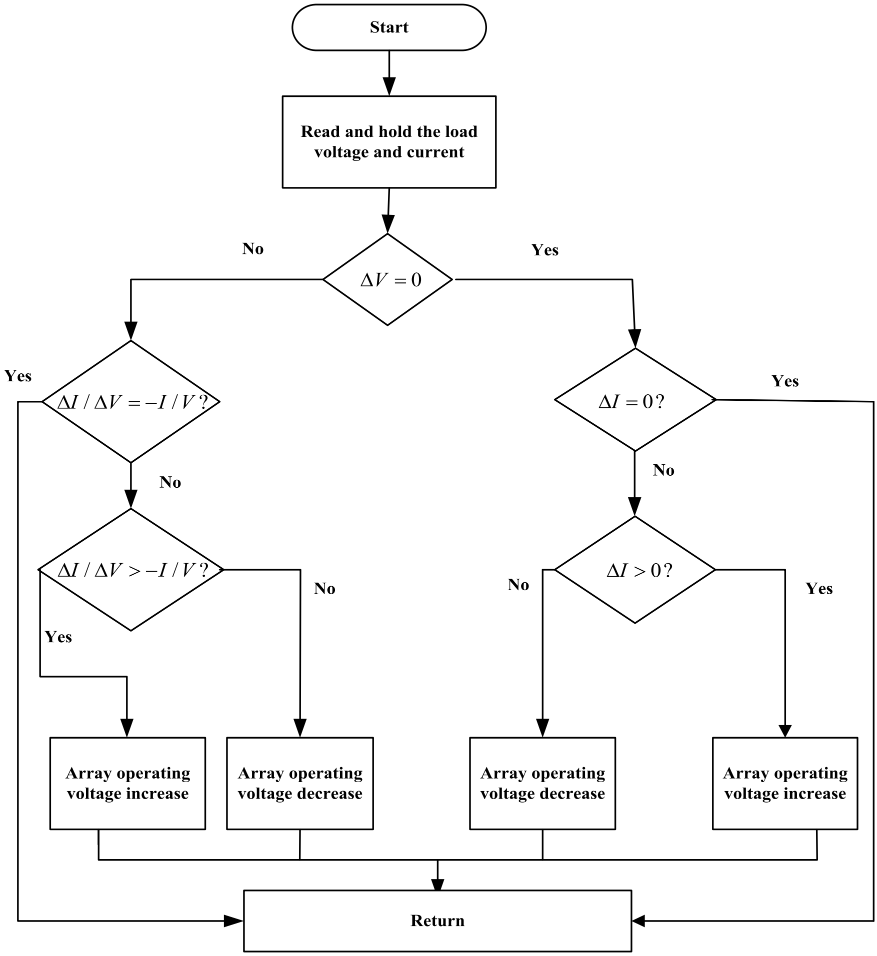

Fig. 3 Flowchart of IC method

5 PV 7L-CHB MLI Topology

CHB MLI modular topology gives the preferred output voltage, power with higher stability. Modular topology feature enables each inverter to be a module with a comparable circuit topology, power arrangement, and modulation [9, 11]. Each inverter level gives three different output voltages, i.e., + V_{dc}, 0 or − V_{dc} [12]. Three-level structure investigated by [12], and total voltage positive half cycle is + $3V_{dc,}$ and in negative, half cycle is $-3V_{dc}$. The number of output phase voltage steps is calculated via $n = (2\,k + 1)$, and here k defines number of DC supply. The PV 7L-CHB MLI configuration scheme is shown in Fig. 4. This configuration produced 7L voltage steps with the use of 12 IGBTs electronics device and 3 DC supply. MLI switching function with 12 switches and 3 DC supply is shown in Table 2.

Table 1 Different of MPPT techniques

S. No.	Methods comparative area	Short circuit current	Short circuit voltage	P&O	IC
1	Tracking speed	Low	Low	Low	High
2	Convergence speed	Average	Average	Average	High
3	Hardware implementation	Easy	Easy	Easy	Easy
4	Level of complexity	High	High	Low	Low
5	Effect on hardware	May damage	May damage	Secure	Secure
6	Power loss	More	More	Medium	Less

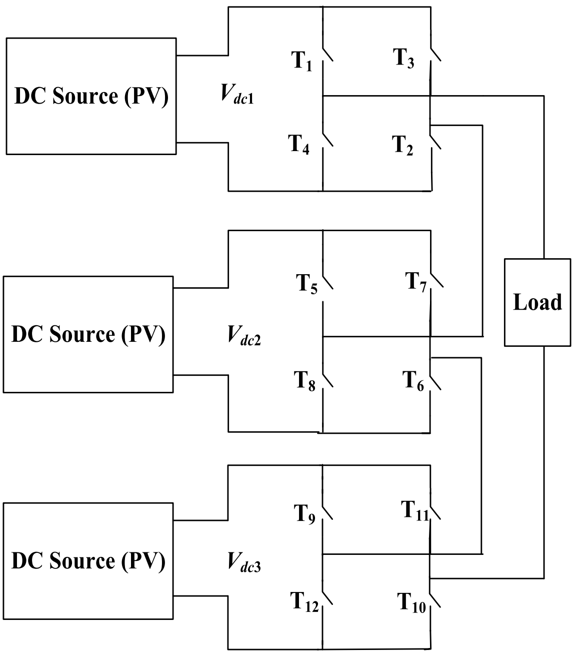

Fig. 4 Configuration of 1-ϕ 7L-CHB MLI with PV scheme

6 PV 7L-RDC MLI Topology

In MLIs, the number of switches represents the price, volume of circuit, reliability, and complexity. So the number of necessary switches to generate the essential voltage level is necessary to designing a MLI. To achieve the same output in 7L-CHB MLI, a novel structure is configured and less count of number of switches exclusive of rising the number of H-bridges. Figure 5a shows the proposed MLI structure, and Fig. 5b

Table 2 Switching function of 7L-CHB MLI

Switching condition	T_1	T_2	T_3	T_4	T_5	T_6	T_7	T_8	T_9	T_{10}	T_{11}	T_{12}
$+\ 3V_{\text{dc}}$	1	1	0	0	1	1	0	0	1	1	0	0
$+\ 2V_{\text{dc}}$	1	1	0	0	1	1	0	0	0	0	0	0
$+\ V_{\text{dc}}$	1	1	0	0	0	0	0	0	0	0	0	0
0	0	0	0	0	0	0	0	0	0	0	0	0
$-V_{\text{dc}}$	0	0	1	1	0	0	0	0	0	0	0	0
$-2V_{\text{dc}}$	0	0	1	1	0	0	1	1	0	0	0	0
$-3V_{\text{dc}}$	0	0	1	1	0	0	1	1	0	0	1	1

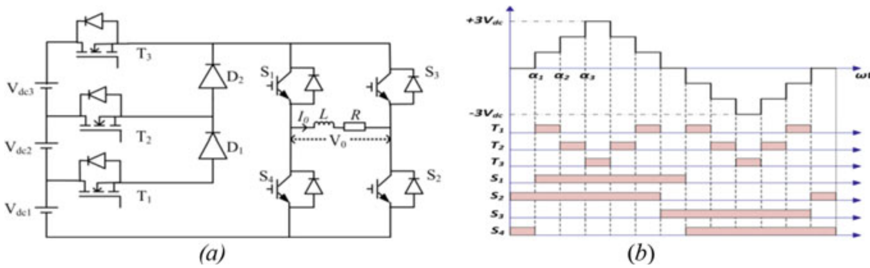

Fig. 5 Seven-level RSMLI and its output voltage **a** Structure of 7L-RDC MLI, **b** Output voltage waveform with corresponding switching condition

shows the novel MLI voltage waveform with consequent switching condition. The switches operation (or polarity generation switches) is working at low switching frequency while the steps formation switches T_1–T_3 working at high switching frequency. Consequently, a price efficient solution is to choose lower switching power equipments of the H-bridge and high switching power equipments for the steps formation.

In comparison with a 7L-CHB MLI, the required number of switches in 7L-RS MLI is very less. In 7L-CHB MLI, 12 switches are used, whereas only 7 switches with 2 discrete diodes are used in design of 7L-RDC MLI. The 7L-RDC MLI working principle is summarized in the following modes.

Mode (a): When T_1 is ON, the current flows through two diodes and H-bridge switches S_1 and S_2. Output voltage at load is $+\ V_{\text{dc}}$. Similarly, S_3 and S_4 are switched ON, and voltage output is $-V_{\text{dc}}$.

Mode (b): In this mode, switch T_2 is make ON and then path of current through diode D_2, switches S_1 and S_2. Output voltage at load is $+\ 2V_{\text{dc}}$. Similarly, S_3 and S_4 are switched ON, and voltage output is $-2V_{\text{dc}}$.

Mode (c): T_3 is ON, and this mode of operation starts. Path of current is switches S_1 and S_2. Output voltage at load is $+\ 3V_{\text{dc}}$. Diodes D_1 and D_2 are not performed operation. Similarly, S_3 and S_4 are switched ON, and voltage output is $-3V_{\text{dc}}$.

Table 3 Switching scheme of 7L-RSC-MLI

Switching state	T_1	T_2	T_3	S_1	S_2	S_3	S_4	D_1	D_2
$+3V_{\text{dc}}$	0	0	1	1	1	0	0	Off	Off
$+2V_{\text{dc}}$	0	1	0	1	1	0	0	Off	On
$+V_{\text{dc}}$	1	0	0	1	1	0	0	On	On
0	0	0	0	1	0	1	0	Off	Off
0	0	0	0	0	1	0	1	Off	Off
$-V_{\text{dc}}$	1	0	0	0	0	1	1	On	On
$-2V_{\text{dc}}$	0	1	0	0	0	1	1	Off	On
$-3V_{\text{dc}}$	0	0	1	0	0	1	1	Off	Off

Mode (d): Any set of S_1 and S_3 or S_2 and S_4 are ON in this mode. Switches T_1, T_2, and T_3 are in OFF condition. Obtained load across voltage is zero.

The RSC-MLI switching scheme is represented in Table 3. The voltage is obtained from a RSC-MLI with corresponding switching states is depicted in Fig. 5a, b.

7 Calculation of THD Using Optimization Algorithm

As described earlier, the SHE technique significantly makes to produce the output voltage of MLIs. MLIs voltage output waveform is positive half is equal to the negative half, i.e., exhibits quarter symmetrical output. The formation of output voltage waveform is shown in Fig. 7b, and it can be defined in Fourier form as,

$$V(\text{t}) = \sum_{n=1}^{\infty} V_n \sin(n\alpha_n) + B_n \cos(n\alpha_n) \tag{9}$$

The even harmonics usual canceled because it is quarter-wave symmetry, i.e., $B_n = 0$ for all n. So the novel equation of output voltage becomes

$$V(\text{t}) = \sum_{n=1}^{\infty} V_n \sin(n\alpha_n) \tag{10}$$

The amplitude V_n can be defined in terms of Fourier form with α varying in the range 0 to π/2,

$$V_n = \frac{4V_{\text{dc}}}{n\pi}(\cos n\alpha_1 + \cos n\alpha_2 + \cos n\alpha_3) \tag{11}$$

Three switching angles α_1,α_2, and α_3, the fundamental component of output voltage is adjust by the modulation index (M). The dominant lower order harmonics is necessary to eliminate from the output voltage. Accordingly, the three nonlinear equations for elucidation of the problem are used in this paperwork as:

$$\begin{aligned} V_1 &= \frac{4V_{\text{dc}}}{\pi}(\cos\alpha_1 + \cos\alpha_2 + \cos\alpha_3) = m \\ V_5 &= \frac{4V_{\text{dc}}}{5\pi}(\cos 5\alpha_1 + \cos 5\alpha_2 + \cos 5\alpha_3) = 0 \\ V_7 &= \frac{4V_{\text{dc}}}{7\pi}(\cos 7\alpha_1 + \cos 7\alpha_2 + \cos 7\alpha_3) = 0 \end{aligned} \tag{12}$$

where$m = \frac{V_f}{(4V_{\text{dc}}/\pi)}$, modulation index = $M = m/N_{\text{DC}}$ and N_{DC} is the number of DC sources, V_f is the required value of fundamental voltage.

Fifth- and seventh-order harmonics are targeted to eliminate by solving the above nonlinear as Eq. 13. The solution of these equations leads to discontinuity for the certain modulation index. Conventional technique such as NR method is able to solve these problems involves much calculation time and difficult mathematical arrangement. In order to reduce this, GA is used here to solve the objective function to find the best value of switching angles. The optimal fitness function (FF) is taken to remove the 5th and 7th component harmonics at optimal values of switching angles. Fundamental component equation goes as under:

$$\text{FF} = \frac{1}{h} * \left[\left|M - \frac{|V_1|}{N_{\text{DC}}V_{\text{DC}}}\right| + \left(\frac{|V_5| + |V_7|}{N_{\text{DC}}V_{\text{DC}}}\right)\right] \tag{13}$$

Subject to condition that,

$$0 < \alpha_1 < \alpha_2 < \alpha_3 < \frac{\pi}{2} \tag{14}$$

To obtain least THD with possible modulation index, the total set is multiplied with a factor $\frac{1}{h}$. The target of this paper, 5th and 7th harmonics are set under the error limit 1% (i.e., $h = 0.01$). To analyze the superiority of voltage THD, it can express and calculated as under:

$$\text{THD}\,(\%) = \left[\frac{1}{V_1^2}\sum_{k=2}^{\infty}(V_k)^2\right]^{\frac{1}{2}} \times 100 \tag{15}$$

where V_k is the voltage of exacting harmonics.

8 Genetic Algorithm (GA)

In this section, GA results obtained for the switching angles of 7L-CHB MLI and 7L-RDC MLI are described. GA [15] is the method of random search process used to find optimal solutions of optimization problems. This is a search technique inspired by biological evolution, such as selection, crossover, and mutation. Usually, evolution starts from a random initial population and repeatedly modifies the solution in each of generation. Multiple switching angles are selected over the successive generation from current population and are used in the next iteration of the algorithm. It is repeated till an optimal solution is reached with defined accuracy.

With continuous number of generations and a large population in each production, the algorithm finally finds for a set of solutions of the problem. It computes the different values of three switching angles to obtain the minimum *FF* keeping the harmonics within the limit. Flowchart collection of the GA shown in Fig. 6 represents the different steps for calculation of FF values.

The GA toolbox results obtained from GA are summarized in Table 4. To use GA toolbox, The following information are entered.

Fitness function: The FF as given entered in the form @FF, where FF.m is a program file that computes the FF.

No of variables: The length of input vector to the FF is entered. Three switching angles are considered as variables.

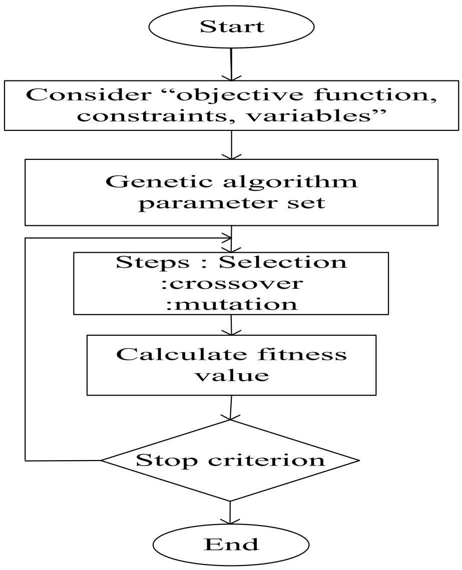

Fig. 6 Flowchart arrangement of the GA

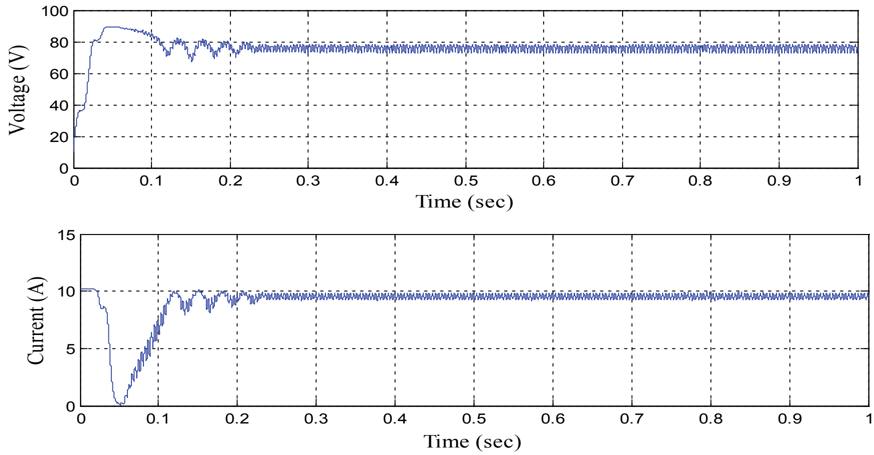

Fig. 7 Output voltage (V) and current (A) of PV system

Table 4 Results obtained from GA FOR 7L-MLIS

Results obtained from GA	Generation count	Obtained switching angles (in degree)			Mean fitness	Best fitness
	100	α_1	α_2	α_3	0.133	0.088
		12.56	49.69	56.89		

Constraint function for the problems is specified in **constraints pane** of toolbox. Boundary variable for the variable is also specified. Population size, initial population, and command are set in the **options pane.**

9 Results and Analysis

The configuration of PV, boost converter (DC-DC), and IC MPPT integrated with MLI is designed at MATLAB platform. The generated voltage and current output by PV without boost voltage are shown in Fig. 7.

The voltage should be increased for each PV panel as shown in Fig. 8. The PV output voltage of 7L-RDC MLI interfaces with boost converter is shown in Fig. 8.

The simulated output voltage is observed from 7L-CHB MLI and 7L-RDC MLI as shown in Fig. 9a, b.

FFT analysis of THD present in 7L- CHB MLI output voltage is 15.50% and 7L-RDC MLI 10.36% at the fundamental frequency of 50 Hz which is as shown in Fig. 10. The comparisons of MLIs performance and different MPPT control schemes are shown in Table 5.

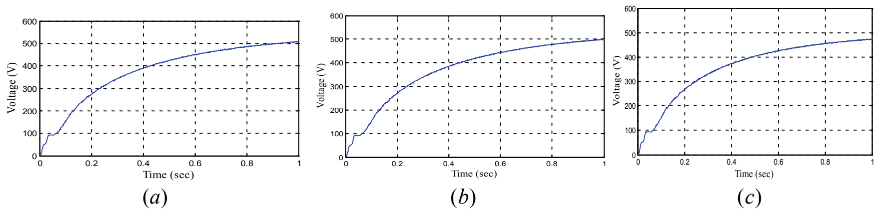

Fig. 8 Output of 7L-CHB MLI between boosted voltage (V) and time (s) of **a** PV panel[1], **b** PV panel[2], and **c** PV panel[3]

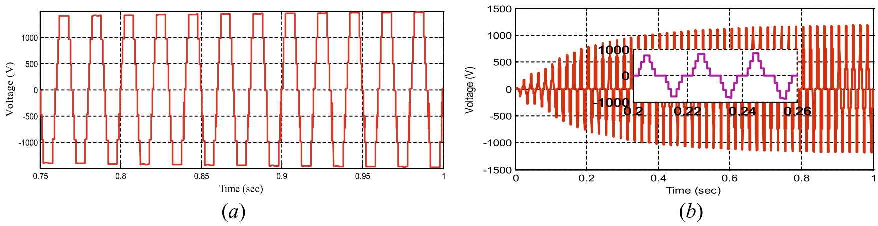

Fig. 9 **a** Overall output voltage of 7L-CHB MLI, **b** 7-L RDC MLI

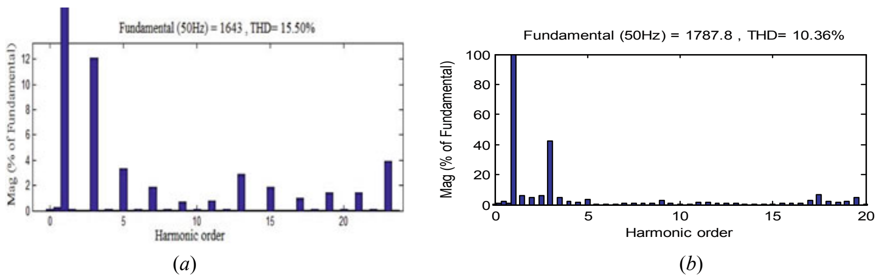

Fig. 10 FFT analysis of THD present in the voltage output for **a** 7L-CHB MLI, **b** 7-L RDC MLI

Using a new 7L-RDC MLI topology reduced switch count was presented and also compared with the conventional 7L-CHB MLI. The total number of switches is almost halved as compared to the CHB MLI topology. So, switching loss is expected to be reduced significantly and cost is also less.

10 Conclusion

This paperwork describes 1-ϕ PV 7L-RDC MLI and 7L-CHB MLI with DC-DC converters, IC control technique and compared it. The feature of PV-based 7L-RDC MLI plays the important role for produce the sufficient power to fulfill the load

Table 5 A comparison of MLIS performance and MPPT

S. No.	Property	Performance
1	Convergence speed (P&O)	More
2	Convergence speed (IC)	Medium
3	Oscillation close to MPP (P&O)	More
4	Oscillation close to MPP (IC)	Medium
5	Implementation complexity	Easy
6	Power loss	Less
7	PV 7L-CHB MLI circuit voltage THD	15.50%
8	PV 7L RSC-MLI circuit voltage THD	10.36%
9	Power semiconductor switches 7L-CHB MLI circuit	12
10	Power semiconductor switches 7L-RDC MLI circuit	7
11	Unbalancing voltage 7L-CHB MLI circuit	Very small
12	Unbalancing voltage 7L-RDC MLI circuit	Very less

demand with fewer number of semiconductor switches. The THD performance of output voltage is improved with less number of components reducing the volume, size, and price of MLIs. The MLIs have less the %THD without any filter circuit requirement. GA optimization technique is used to faster response with less time-consuming. SHE equation of MLIs is solved by GA toolbox, and simulation is done at MATLAB platform. From the calculated results by simulation, it clarifies GA-based SHE technique can be useful to MLI. When the level of MLI is increased, the output voltage waveform just goes to smooth sinusoidal appearance and also decreases the THD.

References

1. Roy T, Kumar PS (2021) A step-up multilevel inverter topology using novel switched capacitor converters with reduced components. Trans Circuits Syst II: Express Briefs 68:236–247
2. Tamrakar V, Gupta S, Sawle Y (2015) Single-diode and two-diode Pv cell modeling using matlab for studying characteristics of solar cell under varying conditions. Electr Comput Eng Int J 4:67–77
3. Upadhyaye H, Gopal Y, Birla D (2019) THD Analysis for PV based cascaded multilevel inverters with MPPT technique. In: Proceedings of international conference on sustainable computing in science, technology and management (SUSCOM), Amity University Rajasthan, Jaipur - India, February 26-28, 2019. Available at SSRN: https://ssrn.com/abstract=3358061 or https://doi.org/10.2139/ssrn.3358061
4. Gopal Y, Kumar K, Birla D, Lalwani M (2017) Banes and boons of perturb & observe, incremental conductance and modified Regula Falsi methods for sustainable PV energy generation. J Power Technol 97:35–43
5. Villalva MG, Gazoli JR, Filho ER (2009) Comprehensive approach to modeling and simulation of photovoltaic arrays. IEEE Trans Power Electron 24:1198–1208

6. Jiang Y, Qahouq JAAA, Orabi M (2011) Matlab/Pspice hybrid simulation modeling of solar PV cell/module. In: 2011 twenty-sixth annual IEEE applied power electronics conference and exposition (APEC), pp 1244–1250
7. Gopal Y, Birla D, Lalwani M (2020) Reduced switches multilevel inverter integration with boost converters in photovoltaic system. SN Appl Sci 2:1–15
8. Salameh Z, Taylor D (1990) Step-up maximum power point tracker for photovoltaic arrays. Sol Energy 44:57–61
9. Shubhada Doifode D, Shend R (2015) Multilevel ınverter modeling—a brief overview. Int J Eng Manage Res 5:401–404
10. Nabae A, Takahashi I, Akagi H (1981) A new neutral-point-clamped PWM ınverter. IEEE Trans Indus Appl IA-17:518–523
11. Swami RK, Samuel P, Gupta R (2016) Power control in grid-connected wind energy system using diode-clamped multilevel inverter. IETE J Res 62:515–524
12. Panda KP, Sahu BP, Samal D, Gopal Y (2013) Switching angle estimation using GA toolbox for simulation of cascaded multilevel inverter. Int J Comput Appl 73
13. Gopal Y, Birla D, Lalwani M (2018) Selected harmonic elimination for cascaded multilevel inverter based on photovoltaic with fuzzy logic control maximum power point tracking technique. Technologies 6:2–17
14. Gopal Y, Panda KP, Birla D, Lalwani M (2016) Swarm optimization-based modified selective harmonic elimination PWM technique application in symmetrical H-bridge type multilevel inverters. Eng Technol Appl Sci Res 9:3836–3845
15. Bektas B, Karaca H (2016) GA based selective Harmonic elimination for five-level inverter using cascaded H-bridge modules. Int J Intel Syst Appl Eng 4:29–32
16. Gopal Y, Lalwani M, Birla D (2017) Genetic algorithm based cascaded H-bridge multilevel inverters for PV system with MPPT technique. In: 2017 ınternational conference on Information, communication, ınstrumentation and control (ICICIC), pp 1–6
17. Taghizadeh TH, Hagh MT (2010) Harmonic elimination of cascade multilevel inverters with non-equal DC sources using particle swarm optimization. IEEE Trans Indus Electron 57:3678–3684
18. Farokhnia PN, Fathi SH, Yousefpoor N, Bakhshizadeh MK (2012) Minimization of total harmonic distortion in a cascaded multilevel inverter by regulating voltages of DC sources. IET Power Electron 5:106–114
19. Bana PB, Panda KP, Naayagi RT, Siano P, Panda G (2019) Recently developed reduced switch multilevel inverter for renewable energy integration and drives application: topologies, comprehensive analysis and comparative evaluation. IEEE Access 7:54888–54909
20. Panda KP, Bana PR, Panda G (2020) A self-balanced switched-capacitor boost seven-level ınverter for photovoltaic systems. In: 2020 IEEE ınternational conference on computing, power and communication technologies (GUCON), pp 338–343
21. Panda KP, Lee SS, Panda G (2019) Reduced switch cascaded multilevel inverter with new selective harmonic elimination control for standalone renewable energy system. IEEE Trans Ind Appl 55(6):7561–7574
22. Panda KP, Bana PR, Panda G (2020) FPA optimized selective harmonic elimination in symmetric-asymmetric reduced switch cascaded multilevel inverter. IEEE Trans Ind Appl 56(3):2862–2870
23. Panda KP, Bana PR, Kiselychnyk O, Wang J, Panda G (2021) A single-source switched-capacitor-based step-up multilevel inverter with reduced components. IEEE Trans Ind Appl 57(4):3801–3811
24. Panda KP, Bana PR, Panda G (2020) Reduced switch count seven-level self-balanced switched-capacitor boost multilevel ınverter. In: 2020 IEEE ınternational conference on power electronics, drives and energy systems (PEDES), pp 1–6
25. Panda KP, Bana PR, Panda G (2020) A single source switched-capacitor based multilevel ınverter for photovoltaic application. In: 2020 IEEE ınternational conference on power electronics, smart grid and renewable energy (PESGRE2020), Kerala, India, pp 1–6

26. Bana PR, Panda KP, Panda G, Performance evaluation of a reduced components count single-phase asymmetric multilevel inverter with low standing voltage. Int Trans Electr Energy Syst e12239
27. Bana PR, Panda KP, Panda G (2020) Power quality performance evaluation of multilevel inverter with reduced switching devices and minimum standing voltage. IEEE Trans Industr Inf 16(8):5009–5022
28. Panda KP, Bana PR, Panda G (2020) A switched-capacitor self-balanced high-gain multilevel inverter employing a single DC source. IEEE Trans Circuits Syst II Express Briefs 67(12):3192–3196
29. Panda KP, Bana PR, Panda G (2021) A reduced device count single DC hybrid switched-capacitor self-balanced inverter. IEEE Trans Circuits Syst II Express Briefs 68(3):978–982

Chapter 10
Design and Implementation of 165 W Current-Fed Push–Pull Converter for Military and Space Applications

T. N. Dishashree, A. Usha, G. Kubendran, Bhoopendra Kumar Singh, and Vinod Chippalkatti

Abstract The aim of this work is to implement the proposed DC-DC isolated converter on a half brick-sized printed circuit broad (PCB), which is achieved in the hardware by using a planar inductor and planar transformer. Current-fed push–pull converter consists of a pre-regulated buck converter stage where the wide range of input is regulated. The inductor of the buck stage acts as current source to the push–pull converter stage. The buck converter output which is pre-regulated is fed as input to the push–pull converter. Here the buck stage switches operate at 300 kHz, and push–pull stage switches operate at half frequency of the buck stage, to reduce filter size of converter. The output obtained is low voltage and high current. Also, in the circuit, synchronous rectification is used to achieve high efficiency. The proposed converter is hardware implemented to validate the design results.

Keywords Half brick-sized PCB · Current-fed push–pull converter · Push–pull converter stage · Pre-regulated buck converter stage

1 Introduction

Current-fed converters are like voltage-fed converters in many ways. In current-fed circuit, the voltage source is replaced by current source and the parallel DC-link

T. N. Dishashree (✉) · G. Kubendran · B. K. Singh · V. Chippalkatti
Centum Electronics, Bengaluru, India

G. Kubendran
e-mail: kubendrang@centumelectronics.com

B. K. Singh
e-mail: bksingh@centumelectronics.com

V. Chippalkatti
e-mail: vinod@centumelectronics.com

A. Usha
EEE Department, BMSCE, Bengaluru, India
e-mail: usha.eee@bmsce.ac.in

G. Panda et al. (eds.), *Sustainable Energy and Technological Advancements*, Advances in Sustainability Science and Technology,
https://doi.org/10.1007/978-981-16-9033-4_10

capacitor is removed and a series inductor is placed, similarly forward blocking devices by symmetric blocking devices. These converters are preferred in medium- to high-power applications (hundreds of kilowatts to megawatts). Some examples for high-power applications are ship propulsion, high voltage and HVDC systems. Current-fed converters are having advantages such as higher reliability and easy recoverability from short-circuit faults these [1].

Buck and push–pull converters which are cascaded are used in several applications such as high-level DC voltage equipments. Current-fed topology can also be implemented, and this eliminates need of inductor at the output stage. For example, medical and industrial X-rays, carbon dioxide laser-based systems and travelling wave tube (TWT) in satellites. Electronic ballast that is used in compact fluorescent lamps and light-emitting diodes also use current-fed push–pull topology that belongs to forward converter topology [2–5].

In a pre-regulated current-fed push–pull converter, the buck converter acts as pre-regulator reducing the voltage stress on push–pull switches. There is an inductor at the input of push–pull stage, and this inductor is large and provides almost a constant current source. The switches of the push–pull stage operate at a duty cycle greater than 0.5. Here, both the switches are closed and current is distributed equally amongst the windings [6–8].

Current-fed converter has some practical advantages which overcome drawbacks of voltage-fed counterpart. Pre-regulated buck stage decreases voltage stress on push–pull stage. In addition, it modulates the pulse width of buck stage and maintains pulse width of the push–pull stage constant. Synchronous rectification used in the converter to supply low-voltage and high-current DC loads [9–11].

A 165 W current-fed push–pull converter which can be powered by DC source is proposed in this work. Closed-loop hardware implementation of the proposed converter is carried out along with design in Mathcad and simulation using Linear Technology spice software. In this work, the converter is used to deliver 165 W power (3.3 V output voltage and 50 A output current) for various power applications in space and defence fields, as the need for low-current and high-voltage applications is increasing, whereas most of the existing topologies are high voltage and low current. The converter is implemented on half brick-sized PCB for wide input voltage that ranges from + 17 V to + 40 V. Further, ambient tests are performed for the developed hardware module, and also, results are tabulated. The proposed converter can be used in military and space applications for radar navigation.

2 Specifications of the Converter

Specifications of the converter are discussed in Table 1, and it depicts the minimum to maximum input voltage range, output voltage, output current, maximum output power, efficiency, line and load regulation and PCB size.

Table 1 Specifications of the converter

Input voltage	17–40 V (DC)
Output voltage	3.3 V
Output current	50 A
Maximum output power	165 W
Efficiency	85% at 50% load
	81% at Full load
Line regulation	± (0.1–0.3) %
Load regulation	± (0.1–0.3) %
PCB size	60 mm × 58 mm × 4.8 mm

3 Circuit Design and Function

The buck converter which has buck regulation stage cascaded with a push–pull isolation stage which also provides voltage reduction in transformer forms a current-fed push–pull converter. The buck circuit is synchronous, both the upper and lower MOSFETs are N-channel devices, and LM5101 driver is employed. Signals to this driver are acquired from LM5041, and in turn, LM5041 drives directly the push–pull converter switches.

Push–pull converter accesses directly from inductor current of the buck stage. The buck inductor needs a current path, so the push–pull duty cycles slightly overlap. Proper flux balance in the transformer is provided by applying one cycle of buck regulator for each of the push and pull switching events.

When transformer operated in case, for both the primary windings are active during the short overlapping time and this will not cause a problem to either transformer or current source. The impedance at V_{CT} node falls towards zero and the magnetomotive force of transformer breaks down when both windings are active. During this period, the inductor source current divides evenly between both the primary windings. As switching losses need both voltage and current to be present, and some of the losses are avoided in the current-fed push–pull topology.

The output stage makes use of synchronous rectification to avoid a large percentage of the 3.3 V output by the forward voltage drop of a Schottky rectifier. A feedback is taken from the output and processed by reference amplifier, and it is coupled back to the LM5041 controller via opto-coupler. Block diagram of the proposed converter is illustrated in Fig. 1.

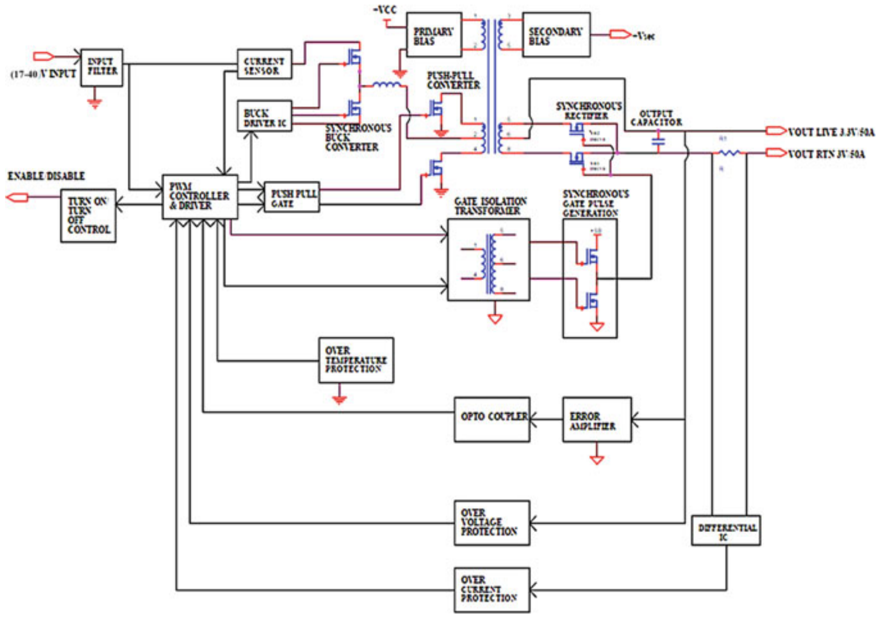

Fig. 1 Proposed converter block diagram

3.1 Pulse Generation Circuits

Feedback is acquired from current source, protection circuits and under-voltage lockout, and this is applied as the input to comparators. The output of comparators is applied to the logic circuit and SR flip flop to generate the pulses which in turn drives the buck stage. The circuit diagram for this is demonstrated in Fig. 2.

Oscillator timing resistor pin and sync (RT/Sync) is accessed from a RC circuit to set the frequency, and this is the input to the oscillator where the clock pulse is generated. The output is divided by two and is applied to the driver of push–pull stage. The circuit diagram for this is illustrated in Fig. 3.

3.2 MOSFET Selection and Design for Buck Stage

The buck stage is synchronous, both the upper and lower MOSFETs are N-channel, and here both the MOSFETs are driven by LM5101 which in turn acquires signals by LM5041.

The MOSFET selected for the upper part is BSZ096N10LS5ATMA1 with $V_{ds} =$ 100 V, $R_{ds} = 9.7$ mΩ, 40 A.

where V_{ds} is drain to source voltage and R_{ds} is drain to source resistance.

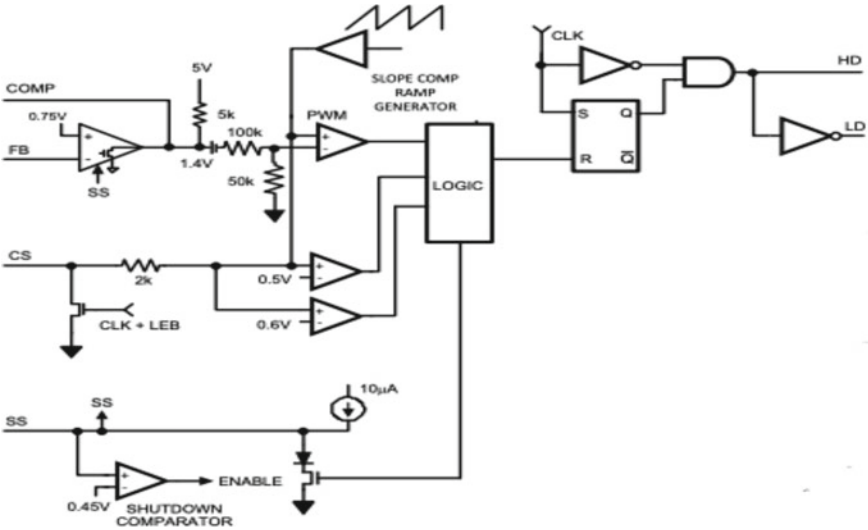

Fig. 2 Buck stage driver circuit

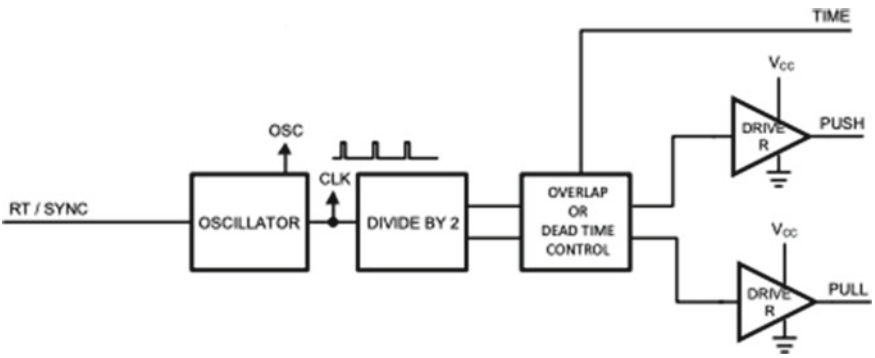

Fig. 3 Circuit to generate push–pull stage pulses

The MOSFET selected for the lower part is BSZ018NE2LSIXT with $V_{ds} = 25$ V, $R_{ds} = 1.5$ mΩ, 40 A.

Some of the key features considered while selecting these MOSFETs are voltage, current and temperature rating, switching frequency and lower R_{ds}.

3.3 *Inductor Design*

Inductor acts as current source to the push–pull stage.

- Synchronous buck minimum inductance is given by

$$L_{\text{min}} = \frac{(V_{\text{in-max}} - BV_{\text{out1}})BD_{\text{min}}}{\Delta bI * BI_{\text{out1}} * \text{Buck}_{\text{FSW}}} \tag{1}$$

where L_{min} is minimum synchronous buck inductance, $V_{\text{in-max}}$ is maximum input voltage, BV_{out1} is nominal buck output voltage, BD_{min} is minimum buck duty cycle.

ΔbI is input buck current ripple (20%), BI_{out1} is buck output current, and $\text{Buck\_F}_{\text{SW}}$ is buck switching frequency.

- Required inductor area Ap (Area product m^4m^4) is given by

$$A_pM = \frac{2\text{PLE}_{\text{max}}}{\text{IB}_{\text{m}} * \text{IK}_{\text{W}} * \text{IK}_{\text{c}} * \text{IJ} * 10^4} \tag{2}$$

where A_pM is required inductor area product, PLE_{max} is maximum energy handled by inductor, IB_{m} is inductor maximum flux density, IK_{w} is inductor window utilization factor, IK_{c} is inductor crest factor, and IJ is inductor current density.

3.4 MOSFET Selection and Design for Push–Pull Stage

The stress across MOSFETs in push–pull stage is represented as,

$$\text{Voltagestress} = (V_{\text{out}} * N * 2) + V_{\text{spike}} \tag{3}$$

where V_{out} is output voltage, N is number of transformer's turns, and V_{spike} is voltage spike caused by leak inductance.

In this converter, push–pull MOSFET stress depends only on V_{out} and not on the V_{in} for the input voltage range from 17 to 40 V.

The MOSFET selected for the push–pull stage is BSZ096N10LS5ATMA1 with $V_{\text{ds}} = 100$ V, $R_{\text{ds}} = 9.7$ mΩ, 40 A.

3.5 Push–Pull Stage Transformer

Push–pull stage of converter work in two quadrants of BH curve swaying as each of primary winding is activated, because of this the maximum power capability of a push–pull converter is double to that of forward converter.

Required transformer area Ap (Area product m^4) is represented by,

$$\mathrm{TA_p}M = \frac{1 - \mathrm{PD_{min}}}{\mathrm{TB_m} * \mathrm{TK_W} * P_{\mathrm{Freq}} * \mathrm{TJ} * 10^4} * \left(V_{\mathrm{ct}} * \mathrm{TI_{prms}} + \mathrm{PV_{out}} * \mathrm{TI_{srms}}\right) \tag{4}$$

where $\mathrm{TA_p}M$ is required transformer area product, $\mathrm{PD_{min}}$ is minimum push–pull duty cycle, $\mathrm{TK_w}$ is transformer window utilization factor, TJ is transformer current density, $\mathrm{TB_m}$ is transformer maximum flux density, P_{Freq} is push–pull frequency, V_{ct} is transformer centre-tap voltage, $\mathrm{TI_{prms}}$ is max rms current of transformer primary, $\mathrm{PV_{out1}}$ is push–pull output voltage, and $\mathrm{TI_{srms}}$ is max secondary rms current.

3.6 MOSFET Selection for Synchronous Rectification Stage

The voltage stress across MOSFETs in synchronous rectification stage is presented as follows:

$$\text{Voltage stress} = (V_{\mathrm{out}} * 2) + V_{\mathrm{spike}} \tag{5}$$

In this converter, push–pull MOSFET stress depends only on V_{out} and not on the V_{in} for the input range 17–40 V.

The current stress through MOSFETs in synchronous rectification stage is represented by,

$$\text{Current stress} = \frac{I_{\mathrm{out}}}{2} \tag{6}$$

where I_{out} is output current.

3.7 Overlap Time

Push–pull circuit receives input from the inductor current of buck stage, and this inductor current needs a path, because of which the push–pull duty cycles overlap slightly; however, this slight overlap does not cause any problem in transformer or current source even if the transformer is operating when both the primary windings are active.

The overlap time is presented as follows:

$$\text{Overlap Time(ns)} = (3.66 * R_{\mathrm{set}}) + 7 \tag{7}$$

where R_{set} is external resistor to set the overlap time.

The overall transfer function for buck and push–pull converters together is represented by.

Buck stage transfer function:

$$V_{ct} = V_{in} * D \tag{8}$$

where V_{in} is input voltage and D is duty cycle.

Push–pull stage transfer function:

$$V_{out} = \frac{V_{ct}}{N} \tag{9}$$

Overall transfer function from (8) and (9):

$$V_{out} = \frac{V_{in} * D}{N} \tag{10}$$

4 Experimental Results and Discussions

The PCB top view for the hardware module and hardware setup is illustrated in Fig. 4a, b, respectively. It consists of the converter, DC voltage source, regulated DC source for DC fan, digital storage oscilloscope (DSO) and electronic load. The input voltage is varied from 17 to 40 V at minimum, nominal and maximum load conditions and efficiency, ripple voltages, line and load regulations are all tabulated as presented in the tables below.

Fig. 4 **a** Printed circuit board top view and **b** Hardware setup module

Table 2 Input power at min, max and nominal load

Input voltage V_{in} (V)	Input current I_{in} (A)	Input power P_{in} (W)
17	11.73	199.41
28	7.27	203.67
40	5.15	206.01

Table 3 Output power and efficiency at min, max and nominal load

Output voltage V_{out} (V)	Output current I_{in} (A)	Output power P_{out} (W)	Efficiency η (%)
3.32	50	166.25	83.37
3.32	50	166.2	81.60
3.32	50	166.3	80.72

Table 4 Ripple voltage at min, max and nominal load

Input voltage V_{in} (V)	Ripple voltage $\Delta V_{pk\text{-}pk}$ (mV)		
	10% Load	50% Load	100% Load
17	21.6	23.2	58.0
28	42.4	41.6	64.0
40	30.4	43.2	64.0

4.1 Efficiency

The efficiency is calculated at minimum, nominal and maximum input voltages varying from 17 to 40 V at full load, and these are tabulated in Tables 2 and 3, respectively. The output voltage and input current are also presented which is later used to calculate input and output power.

4.2 Ripple Voltage

Ripple voltage is measured for minimum, nominal and maximum input voltages that vary from 17 to 40 V at 10, 50% and full load which is presented in Table 4.

4.3 Line and Load Regulations

Line and load regulations are calculated for minimum, nominal and maximum input voltages that vary from 17 to 40 V at 10, 50% and full load, which is tabulated in Table 5.

Table 5 Line and load regulation at min, max and nominal load

Input voltage V_{in} (V)	Load condition			Load regulation (%)
	10% Load	50% Load	100% Load	
17	3.32	3.32	3.32	−0.03
28	3.32	3.32	3.32	−0.03
40	3.32	3.32	3.32	−0.06
Line regulation (%)	0.00	−0.03	−0.03	–

$$\text{Line regulation} = \frac{V_{out}(\text{at}V_{\text{in-min}}) - V_{out}(\text{at}V_{\text{in-max}})}{V_{out}(\text{at}V_{\text{in-nom}})} * 100 \tag{11}$$

$$\text{Load regulation} = \frac{V_{out}(\text{at}10\%\text{load}) - V_{out}(\text{at}100\%\text{load})}{V_{out}(\text{at}50\%\text{load})} * 100 \tag{12}$$

4.4 Experimental Waveforms

The buck converter switching mode for input voltage (V_{in}): 40 V and full load current (I_{out}) 50 A are illustrated in Fig. 5. Also, it is observed from the waveform that the drain to source voltage (V_{ds}) is 61.2 V.

The push switching mode for push–pull converter for the input voltage (V_{in}): 40 V and full load current (Iout) 50 A is illustrated in Fig. 6. Further, it is observed from the waveform that the drain to source voltage (V_{ds}) is 84.0 V.

Pull switching mode for push–pull converter for the input voltage (V_{in}): 40 V and full load current (I_{out}) 50 A is illustrated in Fig. 7. Also, it is observed that the drain to source voltage (V_{ds}) is measured to be 77.0 V.

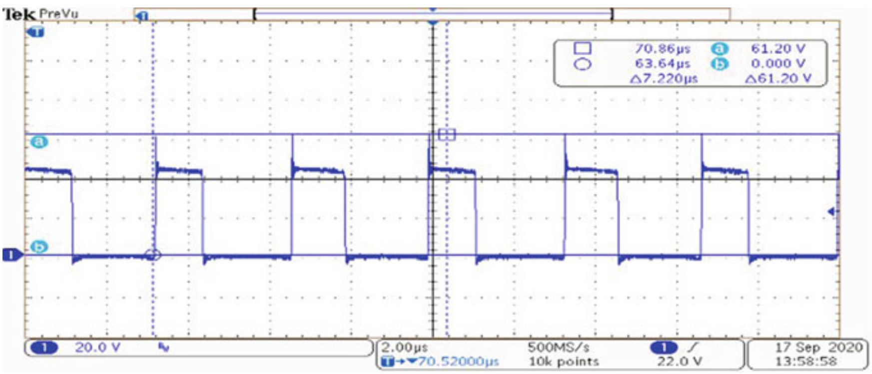

Fig. 5 Buck converter switching mode at $V_{\text{in-max}}$ and $I_{\text{out-max}}$

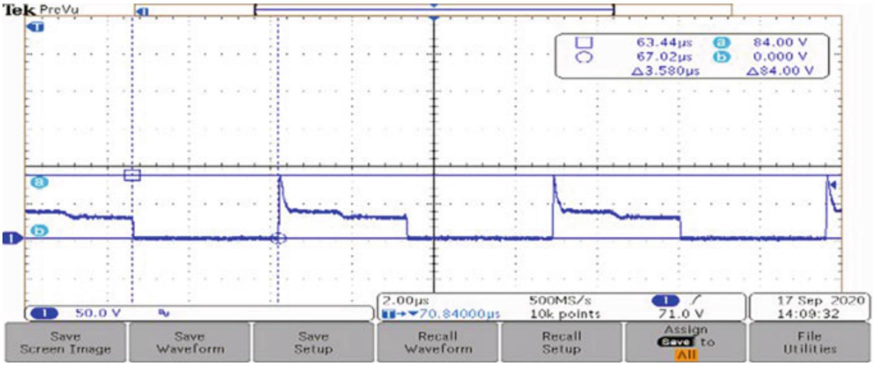

Fig. 6 Push switching mode V_{ds} at $V_{in\text{-}max}$ and $I_{out\text{-}max}$

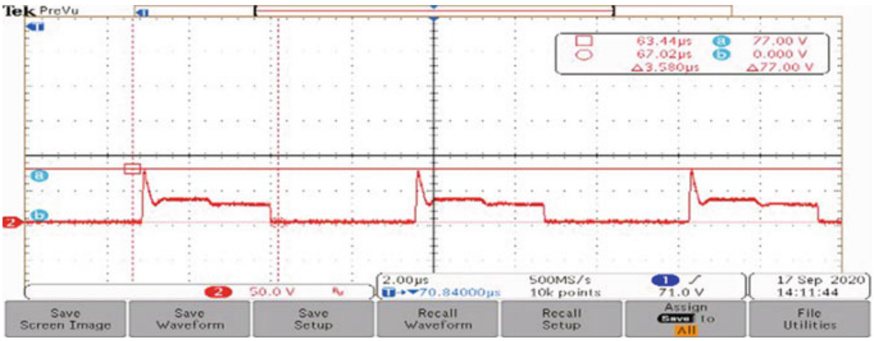

Fig. 7 Pull switching mode V_{ds} at $V_{in\text{-}max}$ and $I_{out\text{-}max}$

Synchronous rectifier, upper leg MOSFET's drain to source voltage (V_{ds}) measured for input voltage (V_{in}): 40 V and full load current (I_{out}) 50 A is illustrated in Fig. 8. Also, from the waveform the drain to source voltage (V_{ds}) is observed to be 19.2 V.

Synchronous rectifier, lower leg MOSFET's drain to source voltage (V_{ds}) measured for input voltage (V_{in}): 40 V and full load current (I_{out}) 50 A is illustrated in Fig. 9. Further, the drain to source voltage (V_{ds}) is observed to be 17.2 V.

The ripple voltage for input voltage (V_{in}): 40 V and full load current (I_{out}) 50 A is illustrated in Fig. 10. It is observed from the waveform that the maximum peak-to-peak ripple voltage ($\Delta V_{pk\text{-}pk}$) is 64 mV which is within the set limits.

The output voltage waveform for input voltage (V_{in}): 40 V and full load current (I_{out}) 50 A is presented in Fig. 11.

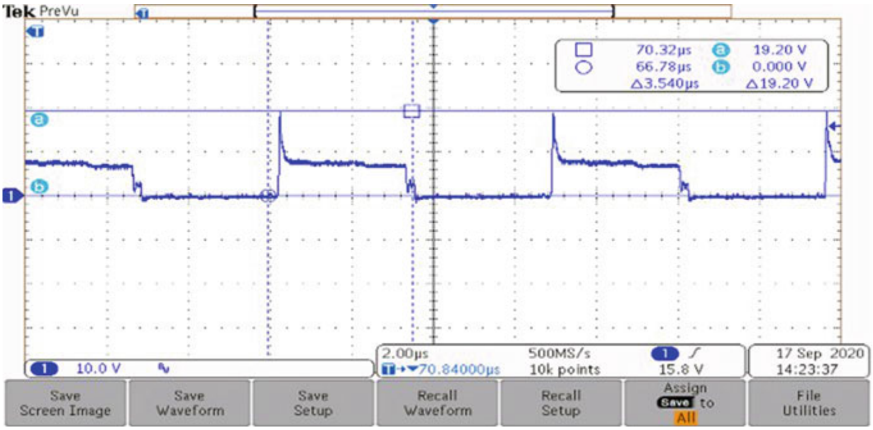

Fig. 8 Synchronous rectifier, upper leg MOSFET's V_{ds} at $V_{\text{in-max}}$ and $I_{\text{out-max}}$

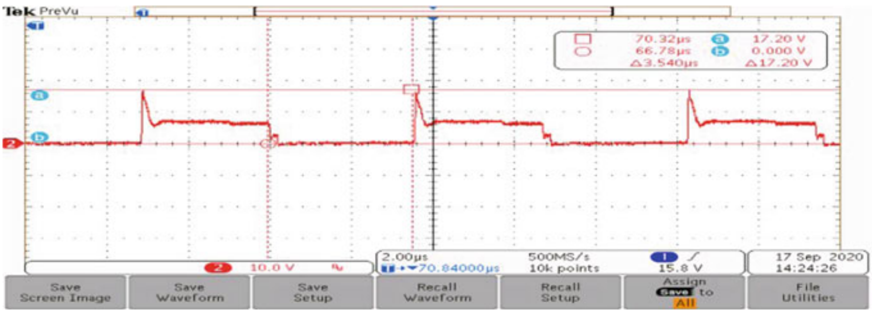

Fig. 9 Synchronous rectifier, lower leg MOSFET's V_{ds} at $V_{\text{in-max}}$ and $I_{\text{out-max}}$

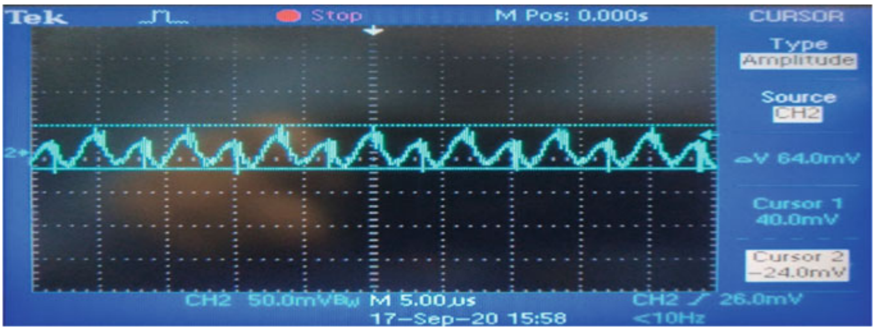

Fig. 10 Ripple voltage at $V_{\text{in-max}}$ and $I_{\text{out-max}}$

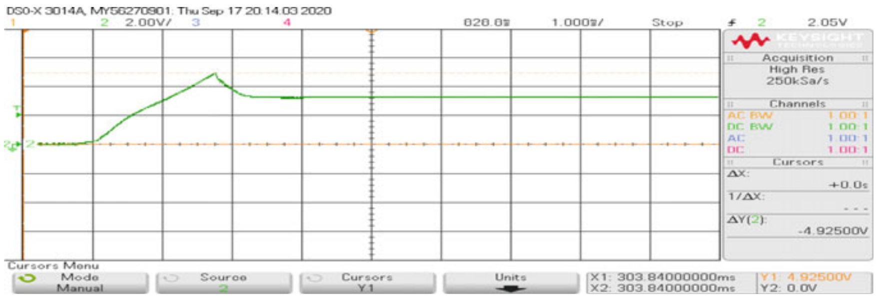

Fig. 11 Output voltage at $V_{\text{in-max}}$ and $I_{\text{out-max}}$

5 Conclusion

The hardware setup for current-fed push–pull converter is successfully implemented on half brick-sized PCB in CENTUM Electronics Laboratory. Here, input voltage is pre-regulated using a suitable buck converter. Further, low output voltage and high output current are achieved with the help of synchronous rectification. Efficiency is obtained for minimum, nominal and maximum input voltages, and it is observed that its value higher than 85% at half load and more than 80% for full load. Ripple voltages, line regulation and load regulation are also realized by experimental results.

References

1. Umanand L (2009) Power electronics: essentials & applications. Wiley
2. Thottuvelil VJ, Wilson TG, Owen HA (1981) Analysis and design of a push-pull current-fed converter. In: IEEE power electronics specialists conference, Boulder, Colorado, USA
3. Richard Redl NOS (1980) Push-pull current-fed multiple-output dc/dc power converter with only one inductor and with 0 to 100% switch duty ratio. In: IEEE power electronics specialists conference, Atlanta, Georgia, USA
4. Redl R, Sokal NO (1981) Push-pull current-fed multiple-output regulated wide-input-range DC/DC power converter with only one inductor and with 0 to 100% switch duty ratio: operation at duty ratio below 50%. In: IEEE power electronics specialists conference, Boulder, Colorado, USA
5. Pressman AI (1991) Switching power supply design. McGrw-Hill
6. Ned Mohan TMUWPR (2003) Power electronics: converters, applications, and design. Wiley
7. Krishna Gopinathan MI (2015) Pre-regulated push pull converter for hybrid. IEEE international conference on technological advancements in power & energy, Bengaluru, India
8. Hart DW (2010) Power electronics. McGraw-Hill
9. Flores L, Soto A, Alou P, Garcia O, Cobos J (2004) Current fed push-pull topology with self driven synchronous rectification applied to low voltage. In: 9th IEEE international power electronics congress, 2004. CIEP 2004, Celaya, Gto, Mexico
10. Ananda BMM (2016) Pre-regulated current fed push pull converter for hybrid energy systems. In: International conference on computation of power, energy information and communication (ICCPEIC), Karnataka, India

11. Maiti NMSBD (2010) Design procedure of a push pull current-fed DC-DC converter. In: Proceedings of national power electronics conference, Roorkee, India
12. Bose BK (2002) Modern power electronics and AC drives. Prentice Hall-PTR
13. Wu Q, Wang M, Zhou W, Huang C, Liu G, Wang X (2020) High frequency active-clamped zero-current switching current-fed push-pull converter for micro-converter applications. In: IEEE energy conversion congress and exposition (ECCE), Detroit, MI, USA
14. Tandon S, Rathor AK (2020) Partial series LC resonance-pulse assisted zero current switching current-fed push-pull converter. IEEE Industry Applications Society Annual Meeting, Detroit, MI, USA
15. Maini AK (2018) Handbook of defence electronics and optronics: fundamental, technologies and systems. Wiley

Chapter 11
A New Single-Phase Five-Level Self-balanced and Boosting Grid-Connected Switched Capacitor Inverter with LCL Filter

Aratipamula Bhanuchandar and Bhagwan K. Murthy

Abstract In this paper, a new single-phase five-level grid-connected switched capacitors (SC) inverter with LCL filter has been presented. It comprises nine unidirectional switches, one discrete diode, one switched capacitor and one DC source. At the end of an inverter output, the LCL filter has been integrated with grid. Basically, the LCL filter provides greater ripple attenuation capability as compared with L and LC filters. Based on parallel-series technique, the topology provides self-balancing property of SC and also gives two times boosting ability with single DC source arrangement. The topology also provides less per unit total standing voltage (TSV) and maintains uniform voltage stress among all semiconductor devices. Before going to grid connection, the level output with RL load case has been checked with proposed universal rounding control scheme (URCS), and it is the modified version of nearest-level control (NLC) technique. In grid-connected case, the dq frame current control strategy and unipolar phase disposition (UPD) pulse width modulation (PWM) techniques have been applied. With step changes in direct axis current reference values, the unity power factor (UPF) operation of grid has been elucidated. Finally, the operation and control strategies with both RL load- and grid-connected cases have been validated through MATLAB/Simulink platform.

Keywords Universal rounding control scheme · Switched capacitor · Total standing voltage · Unity power factor · Pulse width modulation

1 Introduction

The concept of reduced device count (RDC)-multilevel inverters (MLIs) is very popular in renewable energy source applications, and these produce stair case waveform with imitation of sinusoidal wave [1]. Conventionally, there are three types of MLIs that have been reported, viz., neutral point clamped (NPC), flying capacitor (FC), and cascaded H-bridge (CHB). Generally for any MLI, the number of switch

A. Bhanuchandar (✉) · B. K. Murthy
Electrical Engineering Department, NIT Warangal, Warangal, Telangana, India

G. Panda et al. (eds.), *Sustainable Energy and Technological Advancements*,
Advances in Sustainability Science and Technology,
https://doi.org/10.1007/978-981-16-9033-4_11

count, input DC sources, gate drivers, discrete diodes, capacitors, and total blocking voltage (TBV/TSV) are important to decide the size of the inverter and requirement of filter size in grid connection. For generating five-level output, the NPC inverter takes more number of diodes and more number of capacitors, and voltage gain becomes unity. Additionally, to balance the capacitors, separate auxiliary circuits or complex control schemes are required [2]. In FCMLI, the number of capacitor requirement is more as compared with NPC, and for better operation, the capacitors must be precharged [3]. As compared with NPC and FC, CHB MLI has higher modularity but requires more number of isolated DC sources [4]. The TBV is more in [5] for generating five-level output with single DC source. Generally in most of MLIs, less TSV has been preferred for reducing the cost. The topology [6] provides five-level output with single DC source and two capacitors, but TBV/TSV becomes more, and there is no boosting ability. For generating five-level output with single DC source, it takes TSV of $11V_{\mathrm{dc}}$ [7]. The topologies [8, 9] produce TBV of $12V_{\mathrm{dc}}$ with the same number of component count for generating five-level output, and separate backend H-bridge is required in [9] for generating negative voltage levels. The topology [10] requires two DC sources with TSV of $10V_{\mathrm{dc}}$ for generating five-level output, but drawback of this topology is unity voltage gain that means there is no boosting ability. For generating five-level output, the topologies [11, 12] require two capacitors and single DC source. Here, both topologies give TSV of $14V_{\mathrm{dc}}$. The topology [13] gives less TBV but requires two DC sources, and there is no boosting ability. The topologies [14–18] require high amount of TSV. The topology [19] gives TSV as $8V_{\mathrm{dc}}$, but there is no boosting ability. To alleviate aforementioned problems, a new five-level inverter topology has been introduced in this paper, and it provides self-balancing of capacitors and boosting ability with single DC source. Conventionally, there are different types of modulation techniques [20] which are available, and in this paper, a new URCS has been reported in RL load case by taking reference of nearest-level control (NLC) technique. For higher ripple attenuation purpose, the LCL filter has been integrated with grid [21, 22].

The rest of the paper work is organized as follows: The operation and control schemes of proposed grid-connected inverter (GCI) topology have been presented in Sect. 2. In Sect. 3, the comparative study has been described. Section 4 presents simulation results for both RL load and grid-connected cases. Finally, the conclusion has been presented in Sect. 5.

2 Operation of Proposed GCI Topology and Control Schemes

A. *Operation of Proposed GCI Topology*

The schematic of proposed single-phase, five-level SC-based GCI topology with LCL filter is depicted in Fig. 1. The inverter topology consists nine unidirectional

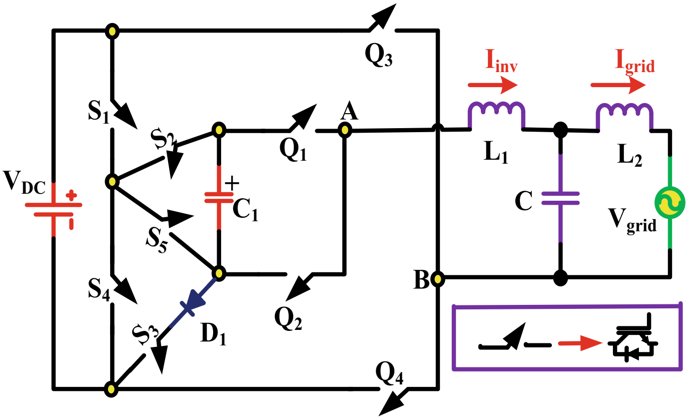

Fig. 1 Proposed GCI topology with LCL filter

switches, one discrete diode, one SC, and one DC source. For higher ripple attenuation capability, an LCL filter has been integrated with grid. However, careful design should be required while considering resonant peak problems and stability. Here, the filter values are designed from [21, 22], and respective flowchart is depicted in Fig. 2. In this topology, the single DC source arrangement can be assumed as either PV with boost converter or fuel cell with boost converter or batteries. If more number of PV

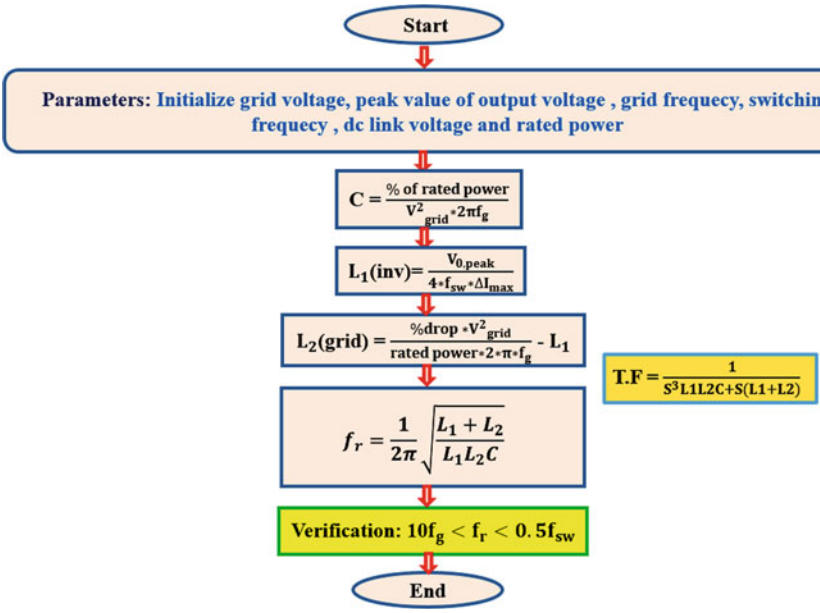

Fig. 2 Flowchart—LCL filter design [21]

Table 1 Switching table

S. no.	Switches in ON state	C_1	Level output
1	$S_1 - S_2 - S_3 - Q_1 - Q_3$	C	0
2	$S_1 - S_2 - S_3 - Q_1 - Q_4$	C	$+V_{DC}$
3	$S_1 - S_5 - Q_1 - Q_4$	D	$+2V_{DC}$
4	$S_1 - S_2 - S_3 - Q_2 - Q_3$	C	$-V_{DC}$
5	$S_2 - S_4 - Q_2 - Q_3$	D	$-2V_{DC}$

panels are considered, then there is no requirement of boost converter for maintaining proper DC link voltage. For making zero leakage current, the grid neutral is directly connected to negative DC source point, and it is known as "common ground system."

Table 1 shows switching arrangement for generating five-level output and also shows respective charging (C) and discharging (D) action of SCs. Basically, the SC value can be calculated from the concept of longest discharging period (LDP) method. From Table 1, the boosting factor is obtained as two with single DC source. By parallel-series technique, the switched capacitor is self-balanced at V_{dc} with very less voltage ripple, then there is no need of sensor arrangement and additional balancing circuits. The sum of maximum blocking voltages of all switches can be indexed with total standing voltage (TSV), and it decides the cost requirement of semiconductor devices. Generally, each switching device should require respective protection circuit, gate driver circuit, and heat sink; thereby, the number of requirement of switch count is more important in RSC-MLI topologies. Table 2 shows the per unit TSV calculation of proposed topology. From this, the topology gives five per unit TSV and maintains uniform voltage stress among all semiconductor devices. Here, the voltage stress of each semiconductor device does not exceed input DC supply. Finally, the proposed topology provides self-balancing property of SC, boosting ability, and less per unit TSV. However, there is a possibility of inrush current issue because of continuous fast charging and discharging operation. To curtail this problem, a small value of indicator should be added in the charging loop. By using PLECS/PSIM software, it is possible to calculate switching and conduction losses easily through thermal modeling approach with respective data sheet values. Suppose if all semiconductor devices are made up with silicon carbide (SiC) material, then the switching losses are further decreased; thereby, efficiency of the system becomes improved.

Table 2 Calculation of per unit TSV

S. no.	Switches	Standing voltage
1	S_1 to S_5	$5{*}V_{DC}$
2	Q_1 to Q_4	$4 * V_{DC}$
3	D_1	V_{DC}
TSV (p.u)= $\frac{10V_{DC}}{2V_{DC}} = 5$ p.u		

Fig. 3 Universal rounding control scheme—URCS

B. ***Proposed Control Schemes***

(i) ***URCS RL load case***

The new URCS has been applied to the five-level inverter topology with RL load, and its strategy has been depicted in Fig. 3. The proposed control scheme is the modified version of NLC technique, and it is also called as universal rounding control scheme (URCS). The URCS provides less computation time as compared with conventional SHE PWM technique. Basically, it is more suitable for higher-level inverter topologies. For lower-level inverter topologies, there is a possibility of lower-order harmonics in the inverter output voltage. However, here, just for checking level count, the URCS has been applied.

In this scheme, modulating signal is given to rounding function, and it generates aggregated signal (AS). The switching table generation (STG) is taken from Table 1. Because of truncation, there is no need of logic gate requirement for generating gate pulses (GP). This control scheme is basically fundamental switching frequency technique; thereby, switching losses greatly reduce, and it also provides self-balancing of capacitors. It is universally applicable for any MLI topology with valid switching table.

(ii) ***dq frame current control strategy—grid-connected case***

The control strategy for five-level SC inverter in grid-connected case has been depicted in Fig. 4. Firstly, sense the grid voltage (let, $V_{\text{grid}} = V_{\beta}$), and through proper PLL, the V_{d} and V_{q} components have been generated. Here, PLL has been used to generate reference variable for grid synchronization. Similarly, the I_{d} and I_{q} components have been generated by sensing inverter current (let, $I_{\text{inv}} = I_{\beta}$). To inject active and reactive power into the grid, $I_{\text{d(ref)}}$ and $I_{\text{q(ref)}}$ have been used. From decoupling control strategy, the modulating β-component signal has been generated. By using proper gain (P_{G}) value, it is possible to generate desired modulating signal. By taking absolute function, it is possible to curtail the number of high-frequency carriers present in repeating table generation (RTG) block. After truncation of ASG and STG, the required switching pulses/gate pulses (GP) have been generated. By taking $I_{\text{q(ref)}}$ equal to zero, then it is possible to get UPF operation at grid side.

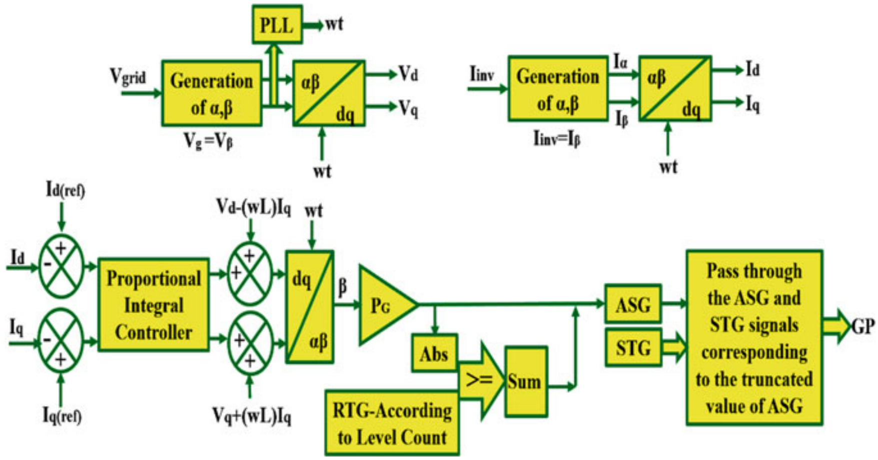

Fig. 4 Proposed dq frame current control strategy

3 Comparative Study

Table 3 shows the comparative study with different conventional five-level inverter topologies. From this table, it is concluded that proposed topology gives less TBV with single DC source supply; thereby, the cost requirement of switches becomes decreased. Generally, switch requirement is reduced means respective protection circuit, gate driver circuit, and heat sink also reduce; thereby, size of inverter becomes decreased. The proposed topology also provides boosting ability and maintains uniform voltage stress among all semiconductor devices.

Table 3 Comparative study with different conventional five-level inverter topologies

S. no.	Description	[5]	[7]	[8]	[10]	[11]	[9]	[13]	[12]	[14]	[15]	[16]	[17]	Proposed
1	Number of levels	5	5	5	5	5	5	5	5	5	5	5	5	5
2	Number of switches	12	6	8	6	8	8	8	10	6	9	8	8	9
3	Number of drivers	12	6	8	5	8	8	8	9	6	9	8	8	9
4	Number of diodes	12	7	8	6	10	8	10	10	7	11	9	8	10
5	Number of sources	1	1	2	2	1	2	2	1	1	1	1	1	1
6	Number of capacitors	2	1	0	0	2	0	0	2	1	2	2	1	1
7	TSV	20	11	12	10	14	12	10	14	11	16	13	15	10

4 Simulation Results

A. *RL Load Case*

Table 4 shows simulation parameters with consideration of RL load. For producing 400 V peak value at the inverter output, the input DC source $V_{dc} = 200$ V is considered. The URCS has been applied to the proposed topology with step change in MI values at $t = 0.02$ s, and respective simulation results are depicted in Fig. 5. In this, the first result shows modulating and aggregated signals (AS) with MI values

Table 4 Simulation parameters—RL load case

S. no.	Parameters	Value
1	V_{dc}	200 V
2	Boosting factor (BF)	2
4	R	100 Ω
5	L	30 mH
6	C1	2200 μF
7	Control scheme	URCS

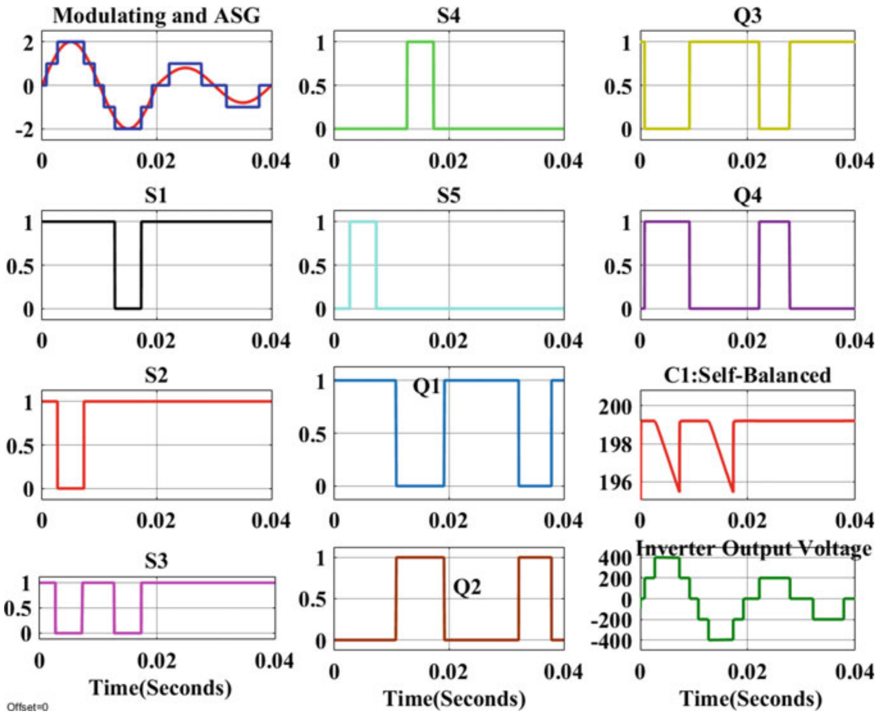

Fig. 5 Simulation results with step change in MI values at $t = 0.02$ s—RL load case

Table 5 Simulation parameters—grid-connected case

S. no.	Parameters	Value
1	Grid voltage	230 V (RMS)
2	Switching frequency	10 kHz
3	Grid frequency	50 Hz
4	Resonance frequency	1405 Hz
5	Rated power(s)	2 kVA
6	V_{dc}	200 V
7	Inverter side inductance	3.9 mH
8	Grid side inductance	4 mH
9	Filter capacitance	5.9 μF
10	Switched capacitors	4700 μF

1 and 0.4. From 2 to 10, results show switching pulses for the proposed topology. The 11th result shows self-balancing property of SC, and it is closely balanced at $V_{dc} = 200$ V. Finally, the five-level output is obtained with $MI = 1.0$, and three-level output is obtained with $MI = 0.4$. In the five-level and three-level outputs, the peak values are obtained as 400 and 200 V, respectively. Finally, it is concluded that the topology provides both self-balancing property and boosting ability.

B. ***Grid-connected Case***

Table 5 shows simulation parameters with consideration of grid. The dq frame current control strategy and UPD-PWM technique have been applied to the proposed grid-connected system, then the following simulation results are obtained with step change $I_{d(ref)}$ values at $t = 0.05$ s, and it is depicted in Fig. 6. By considering $I_{d(ref)} =$ 20 A, the SC-C_1 is self-balanced at 199 V with very less voltage ripple, and inverter produces five-level output with peak value of 399.1 V. Because of filter involvement, a pure sinusoidal grid voltage is obtained with peak value of 325 V. According to $I_{d(ref)} = 20$ A, the grid current is exactly tracked and gives peak value of 19.95 A. Similarly, by considering $I_{d(ref)} = 10$ A, the grid current is exactly tracked and maintains UPF operation. Finally, even step changes in $I_{d(ref)}$ values, the SC-C_1 is self-balanced, with less voltage ripple, and always maintains UPF operation of grid by considering $I_{q(ref)}$ as zero. Fig. 7 shows harmonic spectrum of inverter output voltage with $I_{d(ref)} = 20$ A. At fundamental frequency, the peak value is obtained as 337.2 V and THD is obtained as 36.40%. Figure 8 shows harmonic spectrum of grid current with $I_{d(ref)} = 20$ A. At fundamental frequency, the peak value is obtained as 19.94 A and THD is 0.28%; that is, it finally meets the IEEE-1547 standards.

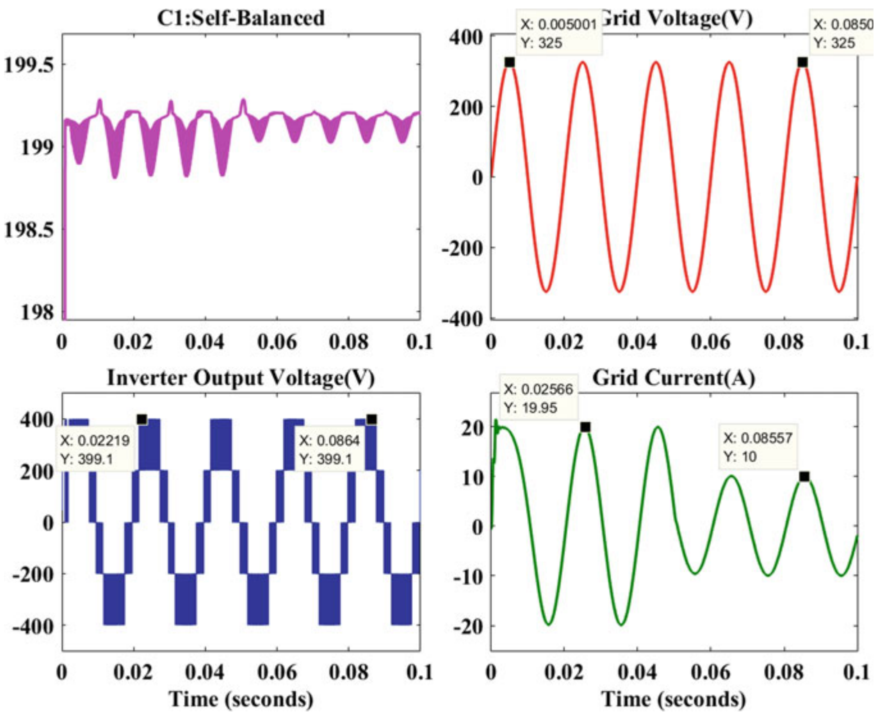

Fig. 6 Simulation results with step change in I_{d_ref} values at $t = 0.05$ s—grid-connected case

Fig. 7 Harmonic spectrum—five-level inverter output voltage

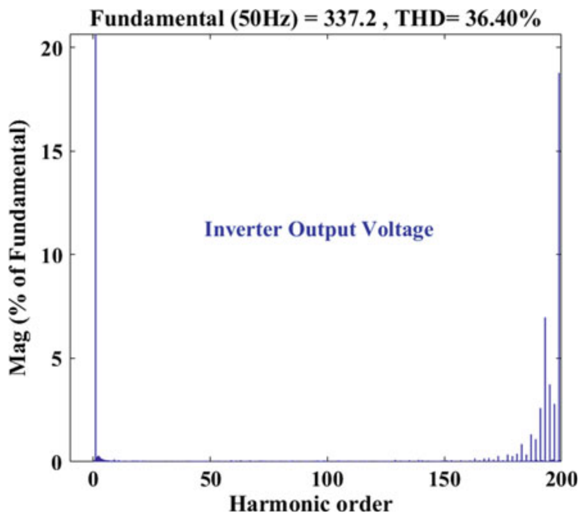

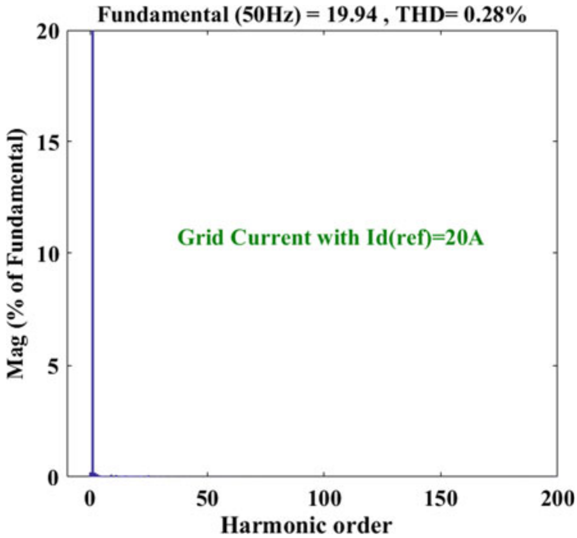

Fig. 8 Harmonic spectrum—grid current with $I_{\mathrm{d(ref)}} = 20$ A

5 Conclusion

With single DC source arrangement, a new single-phase five-level SC-based GCI with LCL filter has been elucidated vividly in this paper. Without involvement of additional circuits or sensors or complex control schemes, the SC is self-balanced with parallel-series technique operation. The topology provides two times boosting ability and also provides less per unit TSV. A comparative study is also done with other conventional five-level inverter topologies. It also gives uniform voltage stress among all semiconductor devices. With step change in modulation index values, the inverter-level output has been verified using URCS. Similarly, with step change in direct axis reference current values, the UPF operation of grid has been achieved using dq frame current control strategy. In real time, a small value of an inductor should be added in the charging loop to mitigate high inrush current present in SC-based topologies. Suppose if PV panel is considered as input DC source, then it needs to concentrate on constant CMV for making zero leakage current, and it can be considered as the future scope of the work.

References

1. Bana PR, Panda KP, Naayagi RT, Siano P, Panda G (2019) Recently developed reduced switch multilevel inverter for renewable energy integration and drives application: topologies, comprehensive analysis and comparative evaluation. IEEE Access 7:54888–54909. https://doi.org/10.1109/ACCESS.2019.2913447
2. Nabae A, Takahashi I, Akagi H (1981) A new neutral-point-clamped PWM inverter. IEEE Trans Indus Appl IA-17(5):518–523. https://doi.org/10.1109/TIA.1981.4503992

3. Shukla A, Ghosh A, Joshi A (2007) Capacitor voltage balancing schemes in flying capacitor multilevel inverters. In: 2007 IEEE power electronics specialists conference, Orlando, FL, USA, pp 2367–2372. https://doi.org/10.1109/PESC.2007.4342381
4. Peng FZ, Lai J-S, McKeever J, Van Coevering J (1995) A multilevel voltage-source inverter with separate DC sources for static VAr generation. In: IAS '95. Conference record of the 1995 IEEE industry applications conference thirtieth IAS annual meeting, Orlando, FL, USA, 1995, pp 2541–2548, vol 3. https://doi.org/10.1109/IAS.1995.530626
5. Cheng C, He L (2016)Flying-capacitor-clamped five-level inverter based on switched-capacitor topology. In: 2016 IEEE energy conversion congress and exposition (ECCE), Milwaukee, WI, USA, 2016, pp 1–5. https://doi.org/10.1109/ECCE.2016.785512
6. Bharath GV, Hota A, Agarwal V (2020) A new family of 1-φ five-level transformerless inverters for solar PV applications. IEEE Trans Indus Appl 56(1):561–569. https://doi.org/10.1109/TIA.2019.2943125
7. Barzegarkhoo R, Kojabadi HM, Zamiry E, Vosoughi N, Chang L (2016) Generalized structure for a single phase switched-capacitor multilevel inverter using a new multiple DC link producer with reduced number of switches. IEEE Trans Power Electron 31(8):5604–5617. https://doi.org/10.1109/TPEL.2015.2492555
8. Ruiz-Caballero DA, Ramos-Astudillo RM, Mussa SA, Heldwein ML (2010) Symmetrical hybrid multilevel DC–AC converters with reduced number of insulated DC supplies. IEEE Trans Industr Electron 57(7):2307–2314. https://doi.org/10.1109/TIE.2009.2036636
9. Su G-J (2005) Multilevel DC-link inverter. IEEE Trans Indus Appl 41(3):848–854. https://doi.org/10.1109/TIA.2005.847306
10. Hari Priya V, Sreenivasarao D, Siva Kumar G (2017) Improved pulse-width modulation scheme for T-type multilevel inverter. IET Power Electron 10(8):968–976. https://doi.org/10.1049/iet-pel.2016.0729
11. Niu D et al (2019) A novel switched-capacitor five-level T-type inverter. In: 2019 2nd international conference on smart grid and renewable energy (SGRE), Doha, Qatar, pp 1–6. https://doi.org/10.1109/SGRE46976.2019.9021066
12. Ranjan A, Gupta KK, Kumar L, Jain S (2012) A switched-capacitors based multilevel boost inverter with single input source. In: 2012 IEEE 5th India international conference on power electronics (IICPE), Delhi, India, pp 1–6. https://doi.org/10.1109/IICPE.2012.6450373
13. Madhukar Rao A, Sivakumar K (2015) A fault-tolerant single-phase five-level inverter for grid-independent PV systems. IEEE Trans Indus Electron 62(12):7569–7577. https://doi.org/10.1109/TIE.2015.2455523
14. Babaei E, Gowgani SS (2014) Hybrid multilevel inverter using switched capacitor units. IEEE Trans Industr Electron 61(9):4614–4621. https://doi.org/10.1109/TIE.2013.2290769
15. Bharath GV, Hota A, Agarwal V (2020) A novel single-phase five-level transformerless H9 inverter with voltage boosting capability. In: 2020 IEEE international conference on power electronics, drives and energy systems (PEDES), pp 1–5. https://doi.org/10.1109/PEDES49360.2020.9379512
16. Bharath GV, Hota A, Agarwal V (2017) A novel 1-ϕ, 5-level transformerless inverter with voltage boosting capability. Natl Power Electron Conf (NPEC) 2017:370–373. https://doi.org/10.1109/NPEC.2017.8310487
17. Hota A, Sonti V, Jain S, Agarwal V (2021) A novel single-phase switched-capacitor based 5-level inverter topology featuring voltage boosting capability and common mode voltage reduction. Int Conf Sustain Energy Future Electric Transp (SEFET) 2021:1–5. https://doi.org/10.1109/SeFet48154.2021.9375761
18. Panda KP, Bana PR, Panda G (2020) A switched-capacitor self-balanced high-gain multilevel inverter employing a single DC source. IEEE Trans Circuits Syst II Express Briefs 67(12):3192–3196. https://doi.org/10.1109/TCSII.2020.2975299
19. Dhara S, Hota A, Jain S, Agarwal V (2021) A transformerless 1-φ, 5-level half-bridge PV inverter configuration based on switched-capacitor technique. IEEE Trans Indus Appl 57(2):1619–1628. https://doi.org/10.1109/TIA.2021.3050975

20. Rodriguez J et al (2009) Multilevel converters: an enabling technology for high-power applications. Proc IEEE 97(11):1786–1817. https://doi.org/10.1109/JPROC.2009.2030235
21. Ali A, Shanmugham P, Somkun S (2017) Single-phase grid-connected voltage source converter for LCL filter with grid-current feedback. In: 2017 international electrical engineering congress (iEECON), Pattaya, Thailand, pp 1–6. https://doi.org/10.1109/IEECON.2017.8075720
22. Bhanuchandar A, Murthy BK (2021) Single phase nine level switched capacitor based grid connected inverter with LCL filter. In: 2020 3rd international conference on energy, power and environment: towards clean energy technologies, pp 1–5. https://doi.org/10.1109/ICEPE50861.2021.9404491

Chapter 12
Comparative Analysis of Different Control Techniques Implementation in UPQC for Power Quality Improvement

Pravat Kumar Ray, Pratap Sekhar Puhan, Arun K. Das, D. Pradhan, and L. Meher

Abstract Selection of proper control techniques and its implementation plays the most important roles for improvement of power quality. In this paper, different control techniques are implemented in the proposed unified power quality conditioner (UPQC) to enhance the power quality in a distribution system. The proposed UPQC is designed with the combination of both shunt and series controller. Shunt controller is used to mitigate the current harmonics, and the series filter is used to mitigate the voltage harmonics in conjunction with hysteresis current and hysteresis voltage controller, respectively. At first, the series part of the UPQC is controlled with UVTG and hysteresis technique based on voltage and after that, unit vector template generation (UVTG), D-Q theory, P-Q theory, and D-STATCOM-based control approach applied for the reference signal generation in the shunt part of the proposed UPQC. Hysteresis control based on current techniques is associated with the four methods for generation of switching signal. The effectiveness of all the controller is verified with simulation using MATLAB/Simulink platform, and a comparative analysis presented and the effectiveness of the D-STATCOM-based control techniques is proved as the best technique for UPQC to improve power quality.

Keywords Harmonics · Power quality · UPQC · UVTG · D-Q theory · P-Q theory · D-STATCOM · Hysteresis technique

P. K. Ray · A. K. Das · D. Pradhan · L. Meher
Department of Electrical Engineering, National Institute of Technology Rourkela, Rourkela 769008, India
e-mail: rayp@nitrkl.ac.in

A. K. Das
e-mail: 115ee0485@nitrkl.ac.in

P. S. Puhan (✉)
Department of Electrical and Electronics Engineering, Sreenidhi Institute of Science and Technology, Hyderabad 501301, India
e-mail: pratapsekhar@sreenidhi.edu.in

G. Panda et al. (eds.), *Sustainable Energy and Technological Advancements*, Advances in Sustainability Science and Technology,
https://doi.org/10.1007/978-981-16-9033-4_12

1 Introduction

In these days, there is first-rate significance of electrical power as it is far the maximum well-known form of energy and all are hugely counting on it. Without supply of electricity, life is very difficult. Initially, people thought about the reliability of the power system which means the continuity of power supply. Instead of reliability now people are thinking about the quality power termed as power quality [1–3]. The modern power system utilizes a vast power semiconductor device starting from transmission to distribution level, and these devices are the main cause of polluting the signals which deteriorate the power quality. It is not only the domestic sector but also industrial sector, commercial sector, transportation sector, communication sector, etc., where power quality is important. A customer needs the quality power, and it is the responsibility of the utility to provide the best solution for the same. The power quality problems are inter-related issues between customer, utility, and manufacture also [4, 5]. There are various power quality issues such as voltage and current variation and events. Voltage magnitude variation, voltage phase variation, voltage distortion, current magnitude, and phase variation are coming under voltage and current variation whereas long interruption due to any kind of fault comes under event [6, 7]. Voltage-related problem such as sag, swell, overvoltage, under voltage is threat to the sensible equipments in the power system, and similarly, voltage- and current-related harmonics are also a great threat to the customer [7]. As per the evolution of the power quality conditioner is concern, initially low-pass filter is preferred [1–3], and it was found; it is not suitable because of the large and bulky size and resonance problem [8]; it affects the performance of other equipment [9]. The development of active power filter with different topology enhances the mitigating capacity of the power quality problems [10, 11]. Unified power quality conditioner is one of the mitigating equipment which incorporates both series and shunt part to solve both current- and voltage-related issues [5]. Conventional and soft computing approach-based control techniques are the recent trend for active filters. Indirect current control, synchronous detection, PQ theory, DQ theory, fuzzy logic, neural network, combination of both NN and fuzzy [12, 13] have played a major in this area. Besides these some of the optimization techniques such as genetic algorithm, bacteria foraging optimization, participle swarm optimization are used to optimize the gain of controller to achieve better performance for the filtering [14, 15]. Researchers suggested the best technique to improve the power quality in power system network, and still research is going on in various fields such as distributed generation, combining renewable-based distribution system with grid [13] to improve the same. A three-phase series active filter is designed to solve the voltage issues [2]. UPQC-P and UPQC-Q reactive power analyses are presented [6]. Synchronous detection techniques [7, 12, 16, 17] are presented, and comparative analysis is presented. D-Statcom-based shunt APF using SPWM technique is presented [14]. Hysteresis controller used in many papers [15, 18] for achieving the proper signal. Combine of fuzzy-NN, fuzzy hysteresis presented [13, 17].

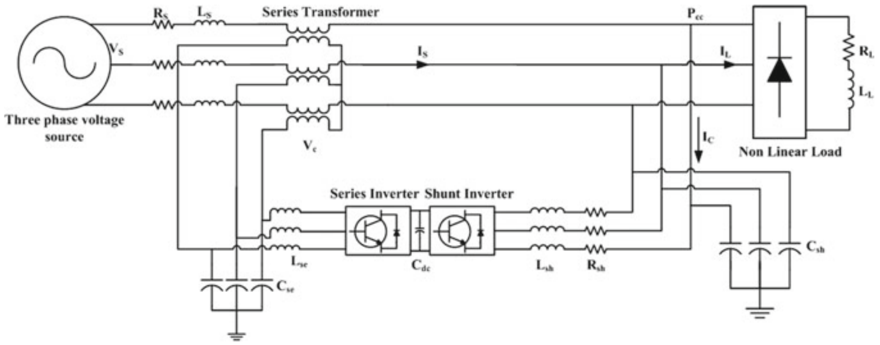

Fig. 1 Proposed system for this work

There are total of five sections followed by introduction in Sect. 1. Sections 2 and 3 present the proposed UPQC and different control approach to the UPQC. Sections 4 and 5 associate with analysis of the obtained results and conclusion, respectively.

2 Design of the Proposed System

The proposed UPQC is designed to maintain constant voltage across the load and regulate it properly as and when required. It also filters the harmonic contents signals which come from the source and maintain distortion-free signal. It is the combination of series-connected voltage source inverter and shunt-connected voltage source inverter. [4] both are connected through a common DC link [3]. Figure 1 shows the proposed UPQC model used in this work. The parallel one is termed as the shunt compensator and series-connected one is treated as series compensator. Shunt compensator tracks the current-related problem, and series compensator is the best appropriate to tackle the voltage-related problem. Three-phase load which is bridge rectifier with resistance, and inductance is connected to the system. This load is intensely connected to the system to develop harmonics. One interfacing inductor L_{sh} and capacitor C_{sh} is connected to the network for coupling purpose and removal of switching frequency component. The LC filter is provided to filter out the higher-order harmonics. The transformer linked the series inverter, and system works as step up and step down as per the voltage-related problem.

3 Different Control Approach

In this work, first the series part of the controller is implemented to obtain the voltage across the load same as the supply with unit vector template generation and hysteresis voltage controller techniques, four control techniques such as synchronous reference frame (SRF) theory or D-Q method, unit vector template generation or UVTG method, instantaneous reactive power (IRP) theory or P-Q method, distribution static compensator or D-STATCOM method along with hysteresis voltage and current controller technique used for reference current and switching signal generation for the UPQC. The process of implementation of the techniques is described below.

3.1 Control Algorithms of Series Part of the UPQC

Reference signal for the series filter estimated using various algorithms both in time and frequency domain [5]. In this work, unit vector template generation (UVTG) is used.

3.1.1 UVTG in UPQC

A simple control algorithm based on UVTG [1] is used to control the series APF of proposed topology. Injection voltages (V_{fa}, V_{fb}, V_{fc}) cancel out the supply voltages (V_{sa}, V_{sb}, V_{sc}) and make (V_{la}, V_{lb}, V_{lc}) perfectly sinusoidal with the desired amplitude at PCC.

3.1.2 Hysteresis Band-Based Controller

PWM signal for the proposed series active filter is achieved using hysteresis band based on voltage controller. The sensed output and UVTG used reference voltage signals are compared, and accordingly, the hysteresis control acts taking the error signals in to consideration for the voltage source inverter. On and off operation of the switching is depending on [6].

3.2 Control Algorithms of Shunt Part of the UPQC

After achieving the load voltage very much close to ideal, different control techniques as discussed are implemented one by one in the shunt part of the UPQC.

3.2.1 Synchronous Reference Frame (SRF) Theory or D-Q Method

This is used to extract the harmonics components with the help of reference frame current generation. Park's transformation simplified the algorithm [4]. One PLL is used for synchronization purpose. The mathematical steps for the reference signals are presented in Eqs. 1 and 2. Park's transformation is carried out as:

$$\begin{bmatrix} i_{\mathrm{Ld}} \\ i_{\mathrm{Lq}} \\ i_{\mathrm{L0}} \end{bmatrix} = \frac{2}{3}\begin{bmatrix} \cos\varphi & -\sin\varphi & \frac{1}{2} \\ \cos\left(\varphi - \frac{2\Pi}{3}\right) & -\sin\left(\varphi - \frac{2\Pi}{3}\right) & \frac{1}{2} \\ \cos\left(\varphi + \frac{2\Pi}{3}\right) & \sin\left(\varphi + \frac{2\Pi}{3}\right) & \frac{1}{2} \end{bmatrix}\begin{bmatrix} i_{\mathrm{La}} \\ i_{\mathrm{Lb}} \\ i_{\mathrm{Lc}} \end{bmatrix} \tag{1}$$

Inverse Park transform is done as:

$$\begin{bmatrix} i^*_{\mathrm{sa}} \\ i^*_{\mathrm{sb}} \\ i^*_{\mathrm{sc}} \end{bmatrix} = \frac{2}{3}\begin{bmatrix} \cos\varphi & \sin\varphi & 1 \\ \cos\left(\varphi - \frac{2\Pi}{3}\right) & \sin\left(\varphi - \frac{2\prod}{3}\right) & 1 \\ \cos\left(\varphi + \frac{2\Pi}{3}\right) & \sin\left(\varphi + \frac{2\prod}{3}\right) & 1 \end{bmatrix}\begin{bmatrix} i_{\mathrm{d}} \\ i_{\mathrm{q}} \\ i_{0} \end{bmatrix} \tag{2}$$

where 'φ' is the output which is synchronized through PLL block [5]. The control strategy for the (d-q) method is shown in Fig. 5

3.2.2 Unit Vector Template Generation or UVTG Method

In this method. PI controller output is treated as the reference current magnitude ($I * m$). Three in-phase reference current signal is obtained by multiplying ($I * m$) and in-phase unit current vectors [1, 6].

3.2.3 PQ Method

This method uses instantaneous reactive power results from power oscillations between source and load, and it is basically applied in both balanced and unbalanced sinusoidal voltage signals [4, 9]. The mathematically steps for the Clarke transformation are described in the below equations.

$$\begin{bmatrix} v_\alpha \\ v_\beta \\ v_0 \end{bmatrix} = \sqrt{\frac{2}{3}}\begin{bmatrix} 1 & -\frac{1}{2} & -\frac{1}{2} \\ 0 & \frac{\sqrt{3}}{2} & -\frac{\sqrt{3}}{2} \\ 1 & \frac{1}{\sqrt{2}} & \frac{1}{\sqrt{2}} \end{bmatrix}\begin{bmatrix} V_{\mathrm{a}} \\ V_{\mathrm{b}} \\ V_{\mathrm{c}} \end{bmatrix} \tag{3}$$

$$\begin{bmatrix} i_\alpha \\ i_\beta \\ i_0 \end{bmatrix} = \sqrt{\frac{2}{3}}\begin{bmatrix} 1 & \frac{-1}{2} & \frac{-1}{2} \\ 0 & \frac{\sqrt{3}}{2} & \frac{-\sqrt{3}}{2} \\ 1 & \frac{1}{\sqrt{2}} & \frac{1}{\sqrt{2}} \end{bmatrix}\begin{bmatrix} i_{\mathrm{a}} \\ i_{\mathrm{b}} \\ i_{\mathrm{c}} \end{bmatrix} \tag{4}$$

The power component P and Q related to α-β voltages and current is represented as follows

$$\begin{bmatrix} p \\ q \end{bmatrix} = \begin{bmatrix} V_\alpha & V_\beta \\ V_\beta & -V_\alpha \end{bmatrix}\begin{bmatrix} i_\alpha \\ i_\beta \end{bmatrix} \tag{5}$$

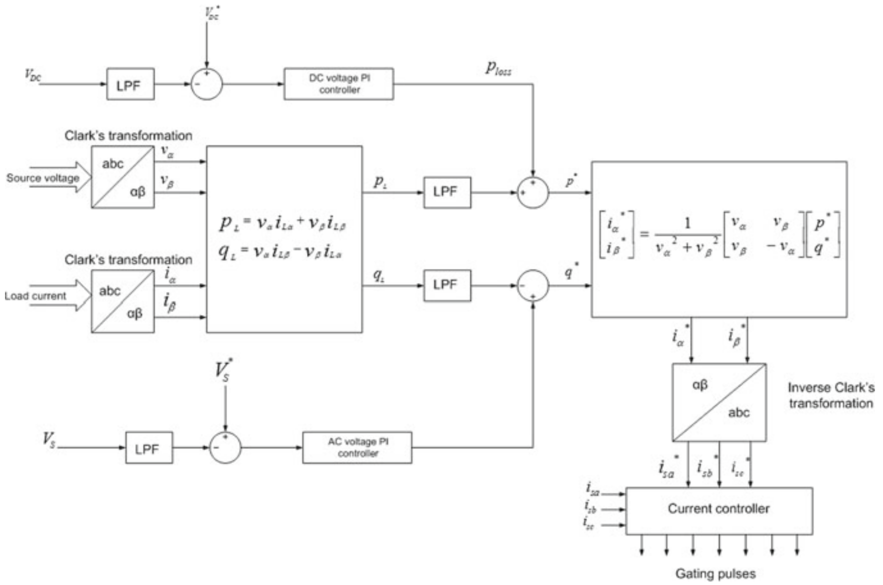

Fig. 2 Control of *P-Q* method

After selecting the powers to be compensated, the α-β currents are calculated as:

$$\begin{bmatrix} i_\alpha^* \\ i_\beta^* \end{bmatrix} = \frac{1}{V_\alpha^2 + V_{\beta 2}^2} \begin{bmatrix} V_\alpha & V_\beta \\ V_\beta & -V_\alpha \end{bmatrix} \begin{bmatrix} -p_c^* \\ q{*}_c \end{bmatrix} \tag{6}$$

Now inverse Clark transformation is done using the following equation as [9]

$$\begin{bmatrix} i_{ca}^* \\ i_{cb}^* \\ i_{ca}^* \end{bmatrix} = \sqrt{\frac{2}{3}} \begin{bmatrix} 1 & 0 \\ \frac{-1}{2} & \frac{\sqrt{3}}{2} \\ \frac{-1}{2} & \frac{\sqrt{3}}{2} \end{bmatrix} \begin{bmatrix} i_\alpha^* \\ i_\beta^* \end{bmatrix} \tag{7}$$

The control strategy for (*P-Q*) method is in Fig. 2

3.2.4 D-STATCOM

It is a reactive power-based controlled method, and the main components are the voltage source converter [3]; the main function of this method is to maintain the voltage constant at point where the sensitive loads are connected to the system in case of system disturbances [7]. The switching pulse generation using D-STATCOM and sinusoidal pulse width modulation (SPWM) is presented [9] followed by Fig. 3

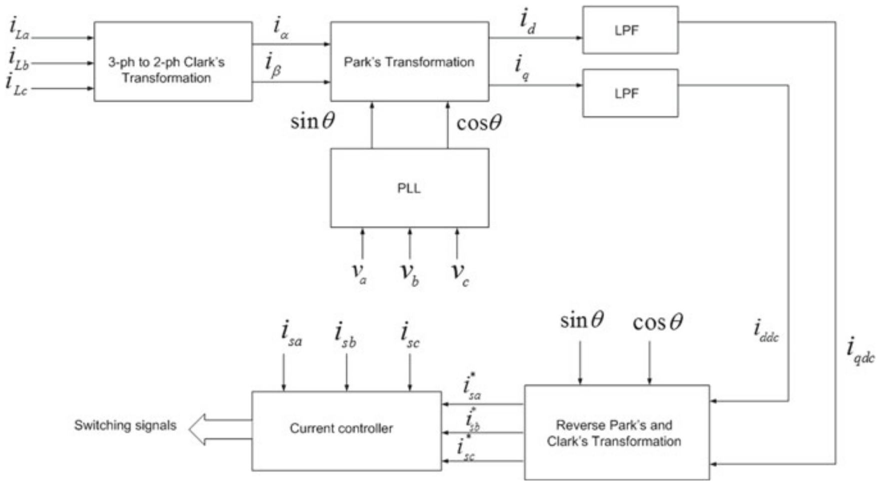

Fig. 3 Control block diagram D-STATCOM

All the four techniques hysteresis techniques based on current are implemented [15].

4 Simulation Results and Comparative Analysis

The simulation test system data for different control techniques is presented in Table 1. The model is designed, and the implementation of the control techniques carried out.

The simulation results obtained are discussed in Table 2.

4.1 Series Part of UPQC Using UVTG Method

At first, a source voltage waveform with sag and swell of each 20% is developed. Then the UVTG techniques are implemented along with hysteresis voltage controller to generate the proper switching signal for injection of the compensated voltage. The source voltage with sag and swell, injected voltage and the load voltage after compensation of both sag and swell is presented in Figs. 4, 5, and 6, respectively. The load voltage after compensation is showing very close to sinusoidal nature.

Table 1 Simulation parameters MATLAB/Simulink

Systems	Parameters	UVTG	D-Q	P-Q	D-Statcom
Source	Voltage	415 V (RMS)	415 V (RMS)	415 V	415 V
Source impedance	Resistance, Inductance	0.01 Ω, 1.5 mH	1 Ω, 1e-3H, 1e-6F	1e-6 Ω, 1e-8H	1e-3 Ω, 1.2e-8H
Load	Diode rectifier, resistor, inductor	Six diode, 42 Ω, 35 mH	1Ω, 1e-3H, 1e-6F	Six diode, 5 Ω, 0.1 mH	Six diode, 1 Ω, 1 1
Line	Resistance, Inductance, frequency	1 Ω, 1e-3H, 50 Hz	1 Ω, 1e-3H, 1e-6F, 50 Hz	1e-6 Ω, 1e-4H, 50 Hz	1 Ω, 1 mH, 1 μF, 50
Dc Link, Shunt Converter	Reference DC voltage, capacitance, Resistance, Inductance	650 V, 4000 μF, (2.1 mH, 0.1 Ω), 10 kHz	650 V, 4000 μF, 1 Ω, 1e-3H	600 V, 400e-6 μF, 1.8e-3 mH	600 V, 400e-6 μF, 1 mH
Series converter	filter inductor, Capacitance, resistance	2.1 mH, 60 μF, 0.1 Ω			
Voltage sag and swell		20%			

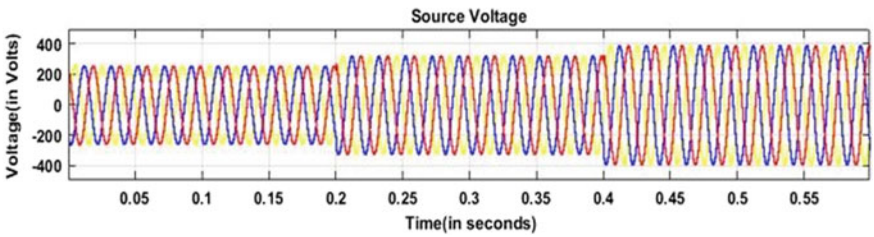

Fig. 4 Source voltage with 20% voltage sags and swells

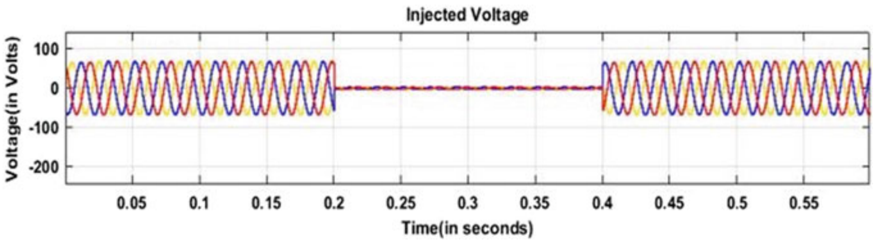

Fig. 5 Injected voltage to compensate voltage sag and swell

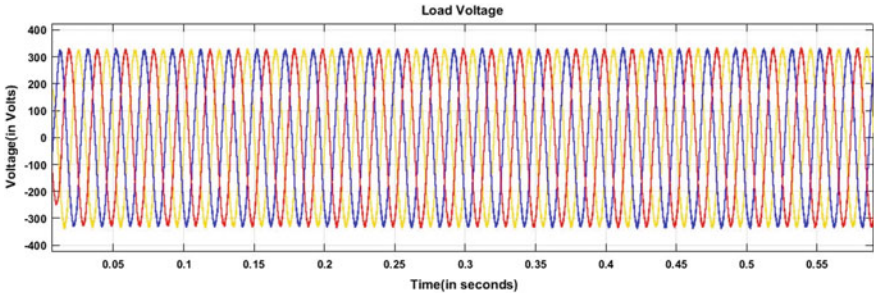

Fig. 6 Load voltage at PCC after compensation

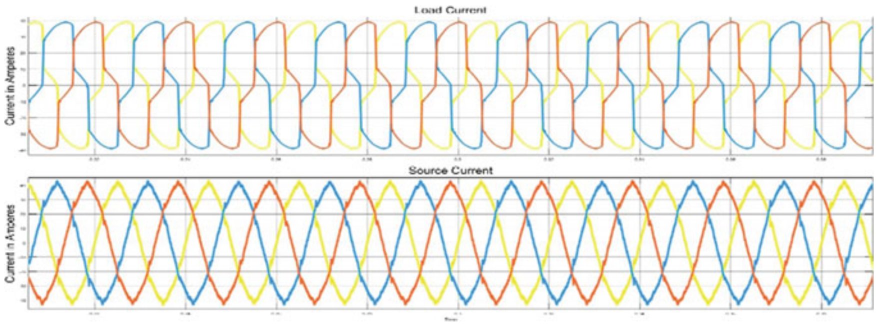

Fig. 7 Load and source current with SRF

4.2 *Shunt Part of UPQC with Different Control Approach*

Once the voltage is obtained, the load is fed and the simulated waveform of the load current and source current is presented.

4.2.1 Synchronous Reference Theory (D-Q Method)

The simulated waveform of the load current before controller implementation and after control implementation is in Fig. 7. The FFT analysis of the same is in Figs. 8, and 9. FFT analysis shows total harmonic distortion (THD) and reduces from 29.08% percentage of fundamental to 4.75%

4.2.2 UVTG Controller Technique

The simulated waveform of both load and source signal is presented along with FFT diagram in Figs. 10, 11, and 12. FFT analysis shows the total harmonic distortion

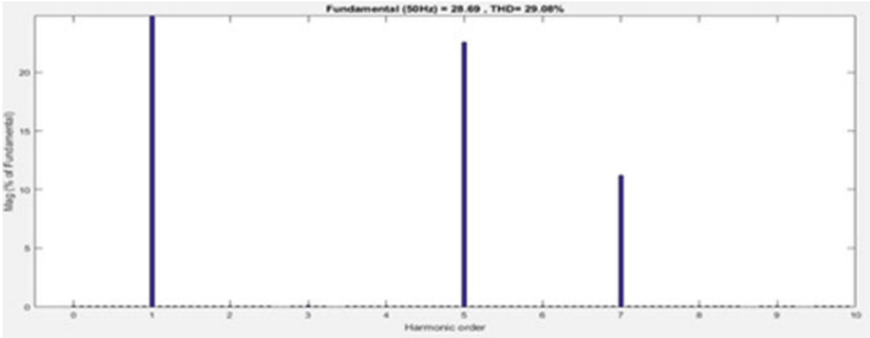

Fig. 8 FFT analysis before compensation SRF

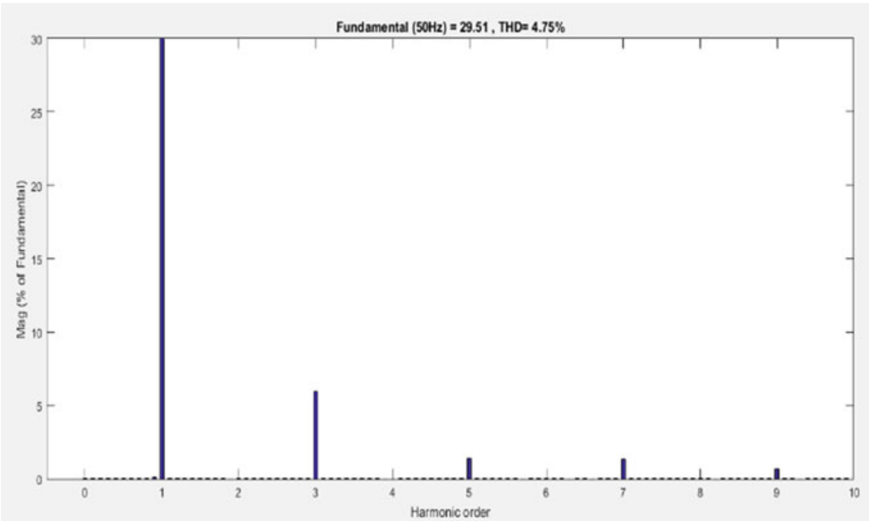

Fig. 9 FFT analysis after compensation SRF

(THD) and reduces from 26.76% percentage of fundamental to 4.56% fundamental which is encouraging and acceptable by IEEE 519.

4.2.3 Instantaneous Real and Reactive Power Theory (P-Q Method)

The simulated waveform of both load and source signal is presented along with FFT diagram in Figs. 13, 14, and 15. FFT analysis shows the total harmonic distortion (THD) and reduces from 43.74% percentage of fundamental to 3.04% fundamental which is encouraging and acceptable by IEEE 519.

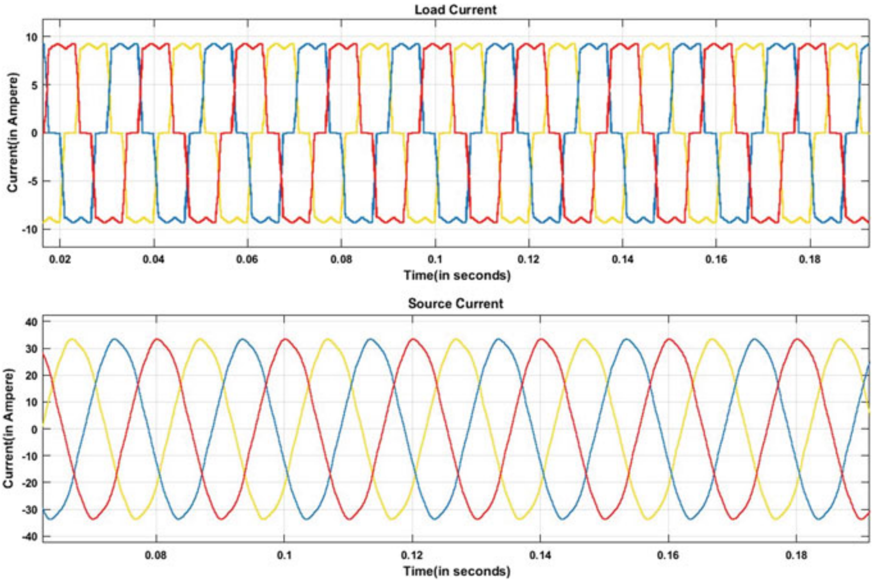

Fig. 10 Load and source current with UVTG

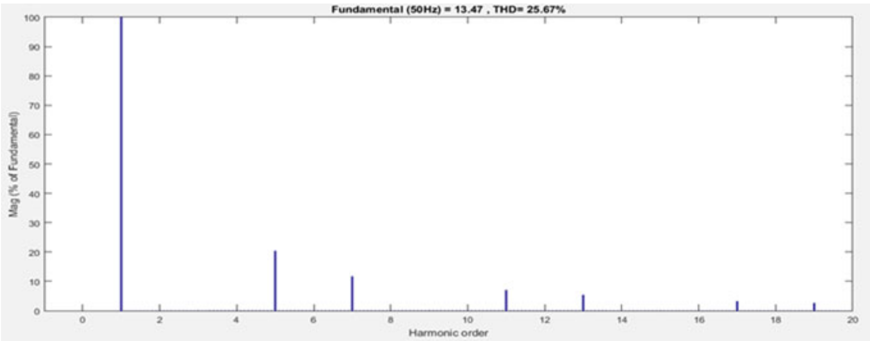

Fig. 11 FFT analysis before compensation UVTG

4.2.4 D-STATCOM Technique

The simulated waveform of both load and source signal is presented along with FFT diagram in Figs. 16, 17, and 18. FFT analysis shows the total harmonic distortion (THD) and reduces from 28.78% percentage of fundamental to 2.81% fundamental which is encouraging and acceptable by IEEE 519.

The comparative analysis of total harmonics distortion (THD) is presented in Table 2. All the obtained THD from different techniques is quite satisfactory but THD of D-STACTCOM technique is very much encouraging, and it is justifying to

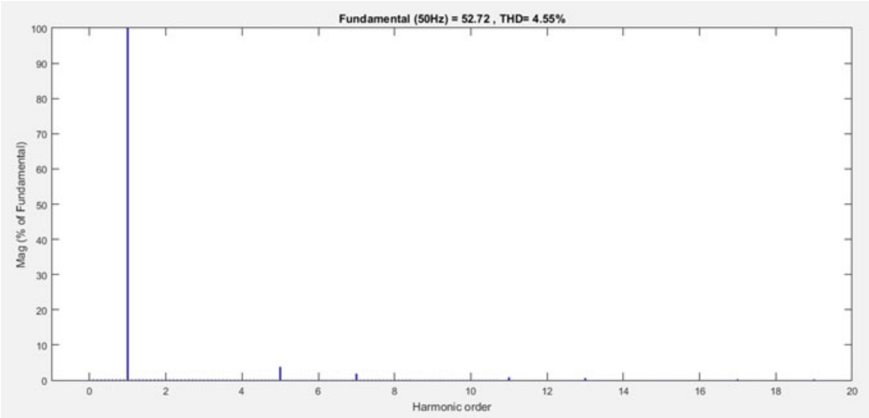

Fig. 12 FFT analysis after compensation UVTG

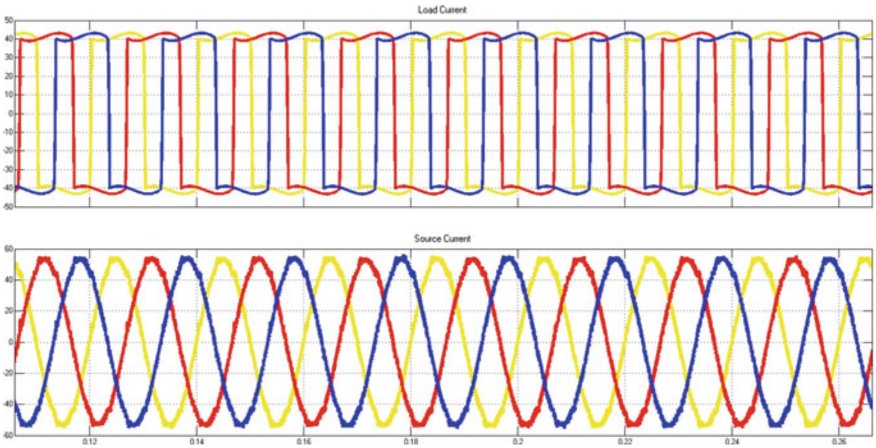

Fig. 13 Load and source current with P-Q

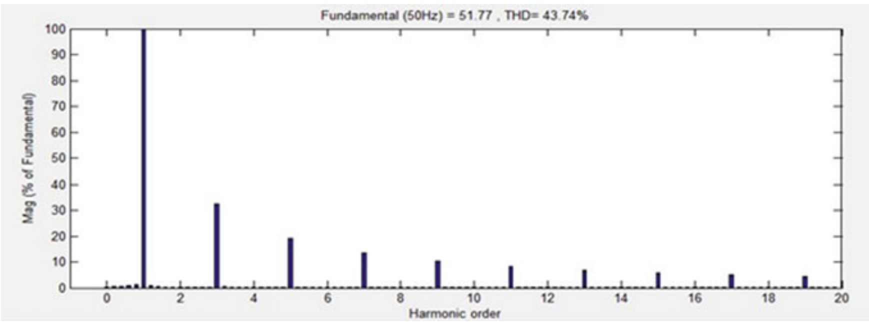

Fig. 14 FFT analysis before compensation P-Q

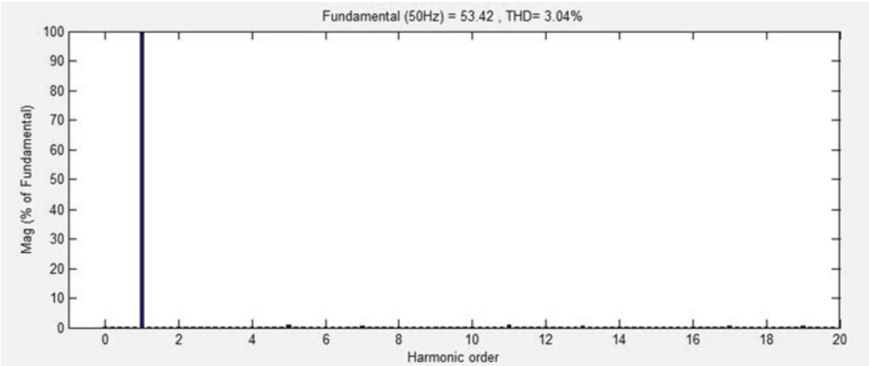

Fig. 15 FFT analysis after compensation P-Q

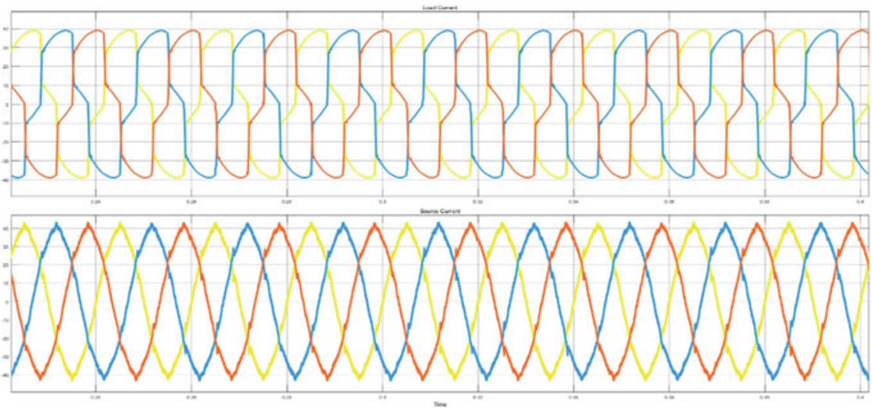

Fig. 16 Load current and source current D-STATCOM

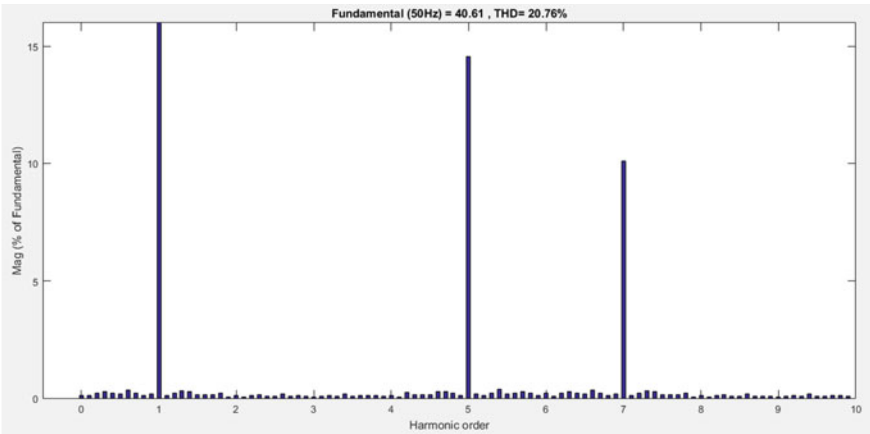

Fig. 17 FFT analysis before compensation D-STATCOM

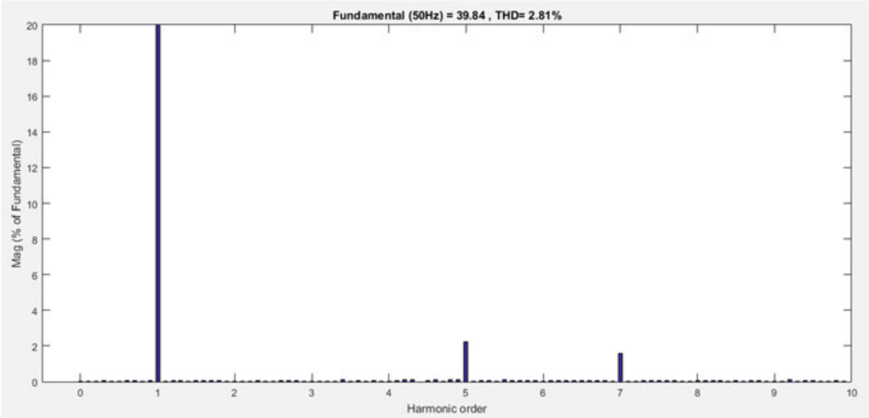

Fig. 18 FFT analysis after compensation D-STATCOM

Table 2 THD analysis of simulation results

Control technique used	THD before compensation	THD after compensation
D-Q method	29.08	4.75
UVTG controller	25.67	4.55
P-Q method	43.74	3.04
D-STATCOM	*20.76*	*2.81*

use this D-STACTCOM-based control technique for power quality improvement in UPQC.

5 Conclusions

The effectiveness of all the controllers has been verified. The voltage profile of the UPQC is maintained through series controller using unit vector template generation (UVTG) along with hysteresis voltage controller. The source voltage after compensation which appears at the point of common coupling is nearly equal to sinusoidal. The current profile of the system is maintained through controlling the shunt part of the UPQC with different techniques such as D-Q method, UVTG method P-Q method, and the combination of D-STACTCOM and SRF, in each and individual cases the THD is calculated and analyzed. It observed from the analysis D-STACTCOM with SRF techniques shows very encouraging results to maintain the current profile and also improve the reactive power capacity.

Acknowledgements The authors would like to thank DST, the Government of India for supporting the research video no. DST/INT/Thai/P-12/2019

References

1. Yash P, Swarup A, Singh B (2012) A new topology of three-phase four-wire UPQC with a simplified control algorithm. Majlesi J Electr Eng 6:24–30
2. Singh B, Hadded K, Chandra A (1999) A review of active filters for power quality improvement. IEEE Trans Ind Electron 46:960–971
3. Khadkikar V, Chandra A, Barry A (2011) Power quality enhancement utilizing single-phase unified power quality conditioner: digital signal processor-based experimental validation. IET Power Electron 4:323–331
4. Afonso JL, Couto C, Martins J (2000) Active filters with control based on the p-theory. IEEE Ind Elect Soc News 47:5–10
5. Kesler M, Ozadmir E (2011) Synchronous reference frame based control method of UPQC under balanced and distorted load conditions. IEEE Trans Ind Elect 58:3967–3975
6. Morán LA (1999) Using active power filters to improve power quality. In: 5th Brazilian Power Electronics Conference, 3
7. Masoud F et al (2014) A study on the performance of custom power devices for power quality improvement. In: IEEE innovative smart grid techno, Malaysia, pp 153–157
8. Tripura P, Kishorebabu YS, Tagore YR (2011) Space vector pulse width modulation schemes for two-level voltage source invert. ACEEE Int J Control Syst Inst 3:96–100
9. Mahajan V, Agarwal P, Gupta O (2012) Simulation of shunt active power filter using instantaneous power theory. Applied power electronic, Orlando, United States
10. Zhang X, Zhang Y et al (2010) Unified power quality conditioner with model predictive control. In: Proceedings of 5th international conference on computer science education (ICCSE), vol 32, pp 1239–1244
11. Basu M, Das S, Dubey GK (2007) Comparative evaluation of two models of UPQC for suitable interface to enhance power quality. Electr Power Syst Res 77:821–830
12. Puhan PS et al (2018) A comparative analysis of artificial neural network and synchronous detection controller to improve power quality in single phase system. Int J Power Electron 9:385–401
13. Puhan PS et al (2016) Development of real time implementation of 5/5 rule based fuzzy logic controller shunt active power filter for power quality improvement. Int J Emerg Electric Power Syst 17(6):607–617
14. Khadkikar V, Chandra A (2009) A novel structure for three-phase four wire distribution system utilizing unified power quality conditioner(UPQC). IEEE Trans Ind Appl 45:1897–1902
15. Srinath M, Selven P, Vinothkumar K (2010) Comparative evaluation of performance of different control strategies on UPQC connected distribution system. In: 5th International conference on industrial and information systems, India, July 29–August 01, 2010
16. Puhan PS et al (2015) A comparative analysis of SAPF and HAPF with different control technique applied for harmonic elimination in a single phase system. Int J Model Ident Control 24:19–28
17. Puhan PS et al (2021) Performance analysis of shunt active filter for harmonics compensation under varios non linear load. Int J Emerg Electron Power Syst 22:21–29
18. Lakshmi V, Puhan S, Sahoo S (2021) Active filter with 2-fuzzy ıntelligent controller: a solution to power quality problem. In: Networks and systems book series (LNNS), vol 185

Chapter 13
Design and Implementation of a Control for Solar PV Fed Unified Power Quality Conditioner

Akhila Mohan and T. Samina

Abstract In this work, a solar photovoltaic (PV) array-integrated unified power quality conditioner (PV-UPQC) system is presented for power quality (PQ) improvement. Major task in the control of UPQC is generation of reference signal. The control algorithms in time domain (TD) and frequency domain (FD) do not consider DC offset present in the input signal and this got affected in the reference signal generation. A control algorithm based on modified second-order generalized integrator (MSOGI) with DC offset elimination capability is presented in this work. This MSOGI is integrated with conventional pq-theory-based control for extracting in phase fundamental and quadrature fundamental component of distorted input signal and for eliminating DC offset present in the input signal. The dynamic performance of the system is evaluated under various dynamic conditions like grid voltage sag and swell and change in solar irradiation in MATLAB Simulink. The proposed system improves power quality and generates clean energy from PV array and also enables operation of the system in the absence of grid. The total harmonic distortion (THD) of system is limited according to the IEEE-519 and IEEE-1159 standards.

Keywords Power quality · PV-UPQC · Series VSC · Shunt VSC · DC offset · MSOGI

1 Introduction

In earlier situation, our researches are mainly concentrated on supply of electrical energy at the consumer side; therefore, the quality of supply was rarely an issue. Later in 1980s, PQ problems arise with the introduction of commercial and industrial power system and presently AC distribution systems are facing severe PQ issues. The primary objective of electric utilities is to supply an uninterrupted sinusoidal voltage to customer, but high reactive power burden, unbalanced loads, harmonic rich load

A. Mohan (✉) · T. Samina
Department of Electrical Engineering, College of Engineering Trivandrum, Trivandrum, Kerala, India
e-mail: akhilamhn030@gmail.com

G. Panda et al. (eds.), *Sustainable Energy and Technological Advancements*,
Advances in Sustainability Science and Technology,
https://doi.org/10.1007/978-981-16-9033-4_13

Table 1 FD-based control algorithms with their behaviour

FD-based algorithms	Behaviour
Discrete Fourier transform [1]	Detects different harmonic components, accuracy is least under frequency variation
Fast Fourier transform [2]	High computational burden and require more memory
Kalman filter [3]	Utilized to calculate voltage and current component of frequency, more complex
Wavelet transformation [4]	Detect the load changing moment, amount of load change and component need to be injected, design of mother wavelet is a challenge

currents, an excessive neutral current etc., destroys the PQ at the consumer end. The electric utilities were unable to avoid the voltage swell, sag, flicker and harmonics in the supply voltages.

Renewable energy sources (RES) like PV systems and wind energy systems are commonly used now because it generates clean energy and ensures operation during unavailability of grid. The intermittent nature of RES makes voltage distortion at point of common coupling (PCC) causes poor PQ. Therefore, to maintain the quality of power at distribution network, custom power devices (CPD) are used. The CPD can be connected in parallel, series or a combination of the two with distribution network. Shunt-connected devices like distribution static compensator (DSTATCOM) compensate PQ issues related to current. Series-connected devices like dynamic voltage restorer (DVR) compensate PQ issues related to voltage. Therefore, a UPQC, which is a combination of series (DVR) and shunt (DSTATCOM) compensator, is proposed as a single solution for mitigating PQ issues. The integration of UPQC with PV array results in improved PQ.

A UPQC's power circuit consists of two voltage source converters (VSCs) or current source converters (CSCs) connected back to back at the DC bus by a common DC link capacitor or inductor, respectively. In order to improve PQ in current and voltage, DSTATCOM and DVR are needed to control separately. In the control, reference signals for DVR (load voltage) and DSTATCOM (grid current) are generated. TD and FD algorithms are used for the control of UPQC and these algorithms generate gating signals for respective converters. Behaviour of control algorithms in FD and TD are given in Tables 1 and 2. Compared to FD algorithms, TD algorithms offer several advantages such as high accuracy, better disturbance rejection capability and low sensitivity to disturbance and grid voltage variation.

DC offset in the input signal is a major problem for the reference signal generation and it is mainly due to measuring problems, rectifiers, analog to digital converters (ADC) and distributed generation (DG) systems. For resolving these issues an additional DC offset, elimination loop is added with second-order generalized integrator (SOGI), i.e., a modified SOGI circuit MSOGI is introduced in this work. The MSOGI is integrated with conventional pq-theory-based control for extracting fundamental component of reference signal and for eliminating DC offset. The proposed algorithm

Table 2 TD-based control algorithms with their behaviour

TD based algorithms	Behaviour
dq-theory [5]	d axis contains double harmonic component of current during unbalanced load condition, require low pass filter with low cut off frequency
pq-theory [6]	Extended to single phase system, poor harmonic filtering capability
Delay signal cancellation [7]	Reference signals calculated from fundamental frequency positive sequence voltage using pq-theory, high computational burden
Instantaneous symmetrical component theory [8]	Poor harmonic filtering capability during load unbalanced condition due to the presence of third order harmonic component in the load current
Artificial neural network [9]	Improved convergence during dynamic operating conditions, poor DC offset filtering capability
Least mean fourth [10]	Operated by minimizing a cost function with order 4, poor steady state performance
Second-order generalized integrator [11]	Less complex, does not eliminate higher order harmonics

eliminates all the drawbacks associated with conventional pq-theory. The dynamic performance of the system is checked under various dynamic conditions like grid voltage sag and swell and various solar irradiance in MATLAB Simulink. A comparison between conventional SOGI and MSOGI is also described in this work by analysing the frequency response plot and DC offset elimination capability.

2 Configuration of Grid Connected PV-UPQC System

The configuration of a grid connected three-phase three-wire VSC-based right shunt PV-UPQC system is shown in Fig. 1. UPQC consists of shunt VSC and series VSC which are connected to a common DC link. A solar PV array is also connected in parallel with the common DC link through a reverse blocking diode. Here, series VSC is connected before the load in series with grid using matching transformer and interfacing inductors. Shunt VSC is connected in parallel with grid at the PCC through interfacing inductors. Thus, forming a right shunt UPQC. Grid-connected three-phase three-wire PV-UPQC system is connected to nonlinear load. Rectifier with RL components are treated as nonlinear load. Interfacing inductors act as a buffer between converter voltage and PCC voltage because converter output voltage varies from PCC voltage. RC ripple filters are connected across the series transformer and PCC for eliminating the switching harmonics. Series, shunt VSCs control algorithms generate switching pulses for respective VSCs. PV array operated at a point of maximum power. For getting maximum power, perturb and observe MPPT algorithm is utilized here.

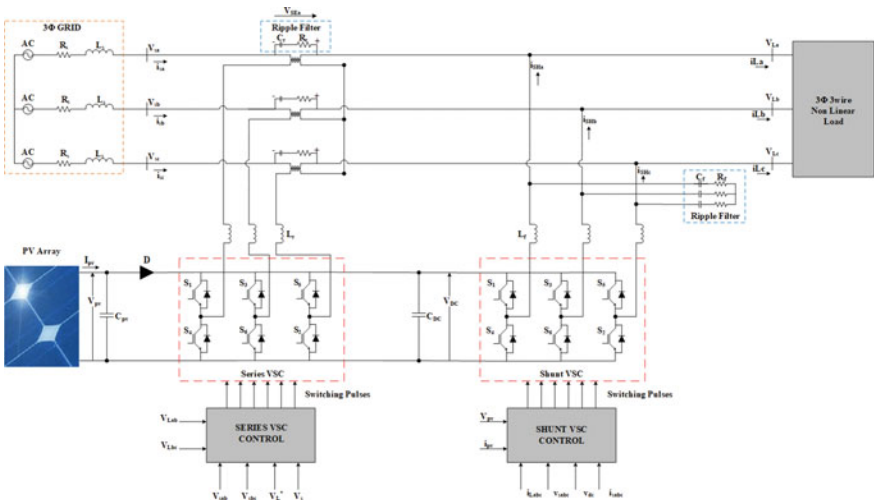

Fig. 1 Schematic diagram of grid connected three-phase three-wire PV-UPQC system

3 Design of Grid-Connected PV-UPQC System

The design of grid connected PV-UPQC system includes the design of PV array, DC link voltage, DC link capacitor, interfacing inductor and series connected transformer. The design of grid-connected PV- UPQC is described below [5].

3.1 PV Array Parameters

The PV array parameters are taken in such a way that it handles load active power and feeds power into the grid. The shunt VSC need to handle the peak power from the PV array; based on this, its ratings are taken. PV array parameters are given as, $P_{pv} = 23.4$ kW, $N_s = 22$, $N_p = 5$, $V_{oc} = 36.6$ V and $I_{sc} = 7.97$ A.

3.2 DC Link Voltage

For a three-phase system, DC link voltage should be greater than twice the peak of per phase voltage. Here, 400 V, 50 Hz system is taken as grid. The DC link voltage is given as,

$$V_{dc} = \frac{2\sqrt{2}V_{LL}}{\sqrt{3}m} = 653 \text{ V} \quad (1)$$

where m is the depth of modulation and its value is arbitrarily chosen as 1. V_{LL} is the line value of grid voltage. The DC link voltage is taken as 700 V (approx.).

3.3 DC Link Capacitor

The DC link capacitor is selected based on DC link voltage and power requirement. The energy balance equation of DC link capacitor is,

$$C_{dc} = \frac{3kaV_{ph}I_{sh}t}{0.5 * \left(V_{dc}^2 - V_{dc1}^2\right)} = 1.569 \text{ mF} \tag{2}$$

where V_{dc} is average DC link voltage = 700 V, V_{dc1} is lowest required value of DC link voltage = 653 V, V_{ph} is phase value of grid voltage = 230.9 V, I_{sh} is per phase value of shunt compensator current = 20 A, k is energy variation factor = 0.1, a is overloading factor = 1.2 and t is minimum time for attaining stability after disturbance = 30 ms.

3.4 Interfacing Inductor for Shunt VSC

The interfacing inductor of the shunt VSC depends upon ripple current, switching frequency and DC link voltage. The expression for the interfacing inductor is,

$$L_f = \frac{\sqrt{3}V_{dc}}{2\pi a f_s I_{rp}} = 8 \text{ mH} \tag{3}$$

where f_s is switching frequency = 10 kHz and I_{rp} is inductor ripple current = 2 A (10% of grid current).

3.5 Series Transformer

The grid connected PV-UPQC is designed to compensate a sag of 0.3 pu, i.e., 69.27 V. The injected voltage is 69.27 V for sag. For injecting a voltage corresponding to sag or swell, a transformer of turns ratio 1:1 is used. V_{SE} is the series VSC voltage and I_{SE} is the series VSC current.

$$S_{SE} = 3V_{SE}I_{SE} = 4 \text{ kVA} \tag{4}$$

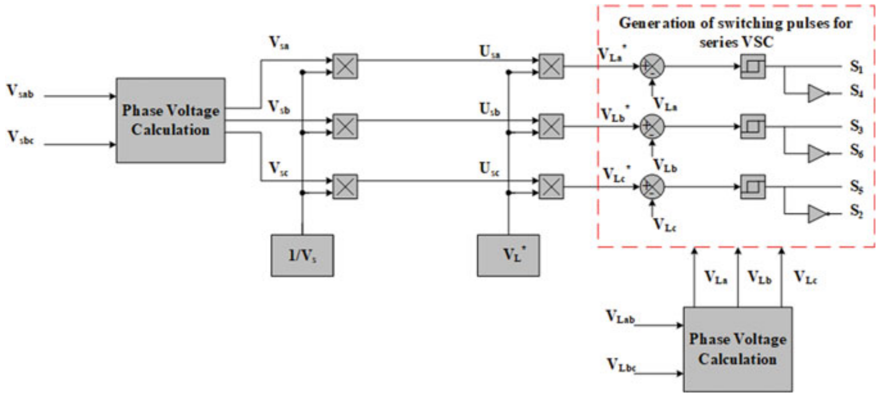

Fig. 2 Control structure of series VSC

4 Control Scheme of Grid-Connected PV-UPQC System

Grid-connected PV-UPQC system needs to control in a proper manner to provide compensations for voltage and current-related PQ issues. Control of series and shunt VSC is described in this section.

4.1 Control of Series VSC

Control of series VSC is given in Fig. 2. The series VSC control is designed in such a way that PCC voltage is free from sag/swell occurs in the source side. For this series, VSC injects appropriate voltage through series connected transformer. Injected voltage is in-phase with grid voltage during sag and out-off phase with grid voltage during swell. Thus, maintains a constant voltage across load.

For calculating the reference load voltage, first need to estimate the unit values of source voltage. This unit values of source voltage for each phase represent angular displacement. The line value of grid voltage is given to phase voltage calculation block where phase voltage is calculated as follows.

$$V_{sa} = \frac{2V_{sab} + V_{sbc}}{3} \tag{5}$$

$$V_{sb} = \frac{-V_{sab} + V_{sbc}}{3} \tag{6}$$

$$V_{sc} = \frac{-V_{sab} - 2V_{sbc}}{3} \tag{7}$$

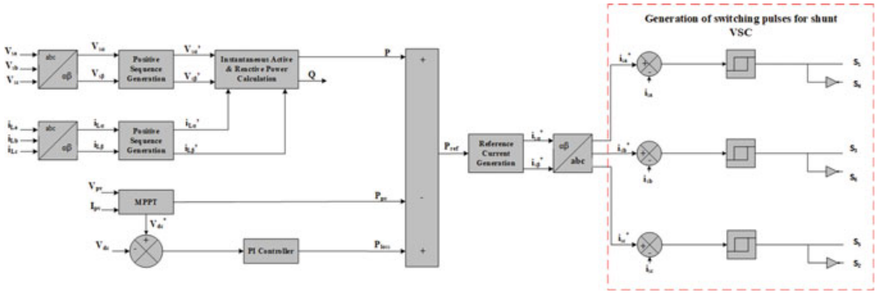

Fig. 3 Control structure of shunt VSC

where V_{sab} and V_{sbc} represent line value of grid voltage, V_{sa}, V_{sb}, and V_{sc} represent phase value of grid voltage.
The grid voltage amplitude, V_S is calculated as follows.

$$V_S = \sqrt{\frac{2\left(V_{sa}^2 + V_{sb}^2 + V_{sc}^2\right)}{3}} \tag{8}$$

The unit values of voltage for each phase, U_{sa}, U_{sb} and U_{sc} are calculated by dividing phase voltage with grid voltage amplitude. Reference load voltages are calculated by multiplying reference PCC voltage V_L^*, with unit values of grid voltage. V_L^* is peak value of per phase grid voltage. The phase value of actual load voltage is calculated in the same way as described in Eqs. (5)–(7). Reference load voltage and actual load voltage of each phase are compared and given to hysteresis controller which generates switching pulses for the series VSC.

4.2 Control of Shunt VSC

Control of shunt VSC is given in Fig. 3. The shunt VSC provides compensation for current-related PQ problems that occurs at load side such as distorted current and unbalanced loading. It also compensates reactive power. Thus, maintains unity power factor at source side. Along with this, shunt VSC supplies real power into the load and grid from PV array.

In practical condition, grid voltage may deviates from ideal voltage because of the presence of DC offset. Even if DC offset is absent in source voltage, it may get introduced in load current because of data conversion and measurement errors. The grid voltage is represented as follows.

$$\begin{bmatrix} V_{sa} \\ V_{sb} \\ V_{sc} \end{bmatrix} = \begin{bmatrix} V_m \sin(\omega t) + V_{a0} \\ V_m \sin(\omega t - \frac{2\pi}{3}) + V_{b0} \\ V_m \sin(\omega t + \frac{2\pi}{3}) + V_{c0} \end{bmatrix} \tag{9}$$

where V_{m} and ω are the grid voltage magnitude and frequency, respectively. V_{a0}, V_{b0} and V_{c0} are the DC offset.

In conventional pq-theory-based control, grid voltage and load current is converted into the $\alpha - \beta$ domain for calculating instantaneous active and reactive power. By applying Clark's transformation, the grid voltage is expressed as,

$$\begin{bmatrix} V_{\mathrm{s}\alpha} \\ V_{\mathrm{s}\beta} \\ V_{\mathrm{s}0} \end{bmatrix} = \sqrt{\frac{2}{3}} \begin{bmatrix} 1 & -\frac{1}{2} & -\frac{1}{2} \\ 0 & \frac{\sqrt{3}}{2} & -\frac{\sqrt{3}}{2} \\ \frac{1}{\sqrt{2}} & \frac{1}{\sqrt{2}} & \frac{1}{\sqrt{2}} \end{bmatrix} \begin{bmatrix} V_{\mathrm{s}a} \\ V_{\mathrm{s}b} \\ V_{\mathrm{s}c} \end{bmatrix} \tag{10}$$

Instantaneous active and reactive power are represented by Eqs. (11) and (12). The α, β component of load current with DC offset is calculated in the same way as grid voltage. The α, β component of grid voltage and load current are utilized for calculating instantaneous active and reactive power with pq-theory.

$$P = V_{\mathrm{s}\alpha} i_{\mathrm{L}\alpha} + V_{\mathrm{s}\beta} i_{\mathrm{L}\beta} \tag{11}$$

$$Q = V_{\mathrm{s}\beta} i_{\mathrm{L}\alpha} - V_{\mathrm{s}\alpha} i_{\mathrm{L}\beta} \tag{12}$$

The instantaneous active and reactive power calculated from Eqs. (11) and (12) contain both fundamental component and oscillating component. The reference current calculated for compensation is given by Eqs. (13) and (14), where $i^*_{\mathrm{s}\alpha}$ and $i^*_{\mathrm{s}\beta}$ represent α and β component of reference source current. Reference power P_{ref} is calculated by Eq. (15).

$$i^*_{\mathrm{s}\alpha} = \frac{V_{\mathrm{s}\alpha} P_{\mathrm{ref}}}{V^2_{\mathrm{s}\alpha} + V^2_{\mathrm{s}\beta}} \tag{13}$$

$$i^*_{\mathrm{s}\beta} = \frac{V_{\mathrm{s}\beta} * P_{\mathrm{ref}}}{V^2_{\mathrm{s}\alpha} + V^2_{\mathrm{s}\beta}} \tag{14}$$

$$P_{\mathrm{ref}} = P + P_{\mathrm{loss}} - P_{\mathrm{pv}} \tag{15}$$

P_{loss} represent active power losses in the VSCs and filters. To get P_{loss}, a PI controller is used which also regulates DC link voltage to the desired value V_{DCref}. The error between V_{DCref} and actual DC link voltage is fed to the PI controller with gain $K_{\mathrm{p}} = 61$ and $K_{\mathrm{i}} = 1$ which provides P_{loss} component. The reference value of DC link voltage V_{DCref} is obtained from perturb and observe MPPT algorithm. P_{pv} represents maximum PV power from the MPPT algorithm. P_{ref} indicates the power required to be drawn from grid. The reference current generation depends upon α and β component of source voltage and load current. Hence, the DC offset present in the source voltage and load current get influenced in the reference current generation.

For improving the filtering performance, α and β component of source voltage and load current pass through a fundamental positive sequence component (PSC) generation structure represented in Fig. 4, which calculates fundamental PSC ($V'_{\mathrm{s}\alpha}$,

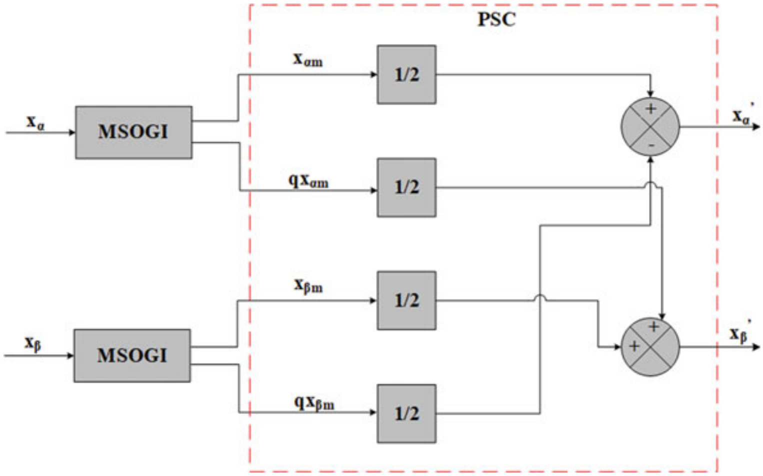

Fig. 4 Extraction of positive sequence components with MSOGI

$V'_{s\beta}$, $i'_{L\alpha}$ and $i'_{L\beta}$) of the input signal and is free from DC offset. This structure consists of two MSOGI. MSOGI represented in Fig. 5 contains an additional DC offset elimination loop with conventional SOGI structure. The value of k is selected as 1.41 for better filtering performance and stability [12]. Thus, MSOGI gives two orthogonal signals x_m and qx_m as output which are free from DC offset. This signal is further utilized for generating fundamental PSC of input signal. The $\alpha - \beta$ component from PSC generation structure are utilized to generate P and Q as described in Eqs. (11) and (12). The $i^*_{s\alpha}$, $i^*_{s\beta}$ and P_{ref} are calculated in the same way as described in Eqs. (13)–(15) with modified $\alpha - \beta$ component of source voltage and load current. Reference source current i^*_{sa}, i^*_{sb} and i^*_{sc} are calculated from $i^*_{s\alpha}$ and $i^*_{s\beta}$ by applying inverse Clark's transformation as described in Eq. (16). The *abc* component of reference current compared with source current and error signal given to hysteresis controller which provides switching signals for shunt VSC.

$$\begin{bmatrix} i^*_{sa} \\ i^*_{sb} \\ i^*_{sc} \end{bmatrix} = \sqrt{\frac{2}{3}} \begin{bmatrix} 1 & 0 \\ -\frac{1}{2} & \frac{\sqrt{3}}{2} \\ -\frac{1}{2} & -\frac{\sqrt{3}}{2} \end{bmatrix} \begin{bmatrix} i^*_{s\alpha} \\ i^*_{s\beta} \end{bmatrix} \tag{16}$$

5 Simulation Results

The grid-connected PV-UPQC system is simulated in MATLAB Simulink. The performance of this system is checked for different dynamic conditions like grid voltage sag, swell and variable irradiance. Following signals are included in the simulation

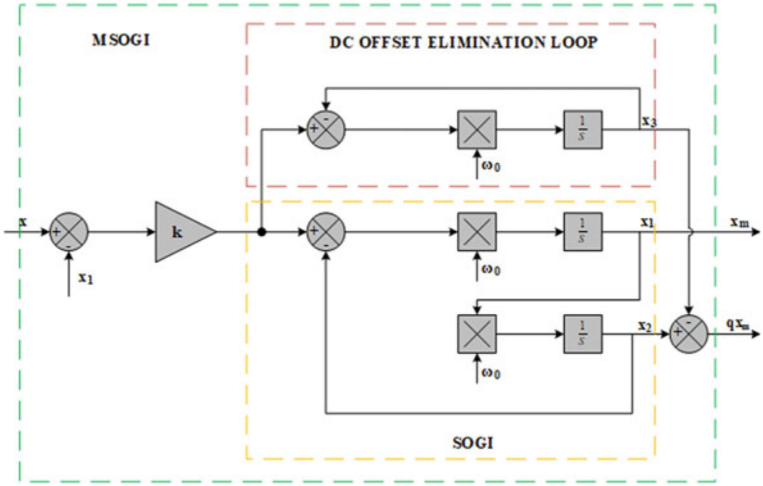

Fig. 5 Internal structure of MSOGI

results, grid voltage V_s, load voltage V_L, injected voltage by series VSC V_{SE}, DC link voltage V_{DC}, grid current i_s, load current i_L, PV array current I_{pv}, solar irradiance G, PV array power P_{pv}, grid active power P_s, grid reactive power Q_s and load active power P_L for different dynamic conditions.

5.1 System Performance During Grid Voltage Sag and Swell

The performance of grid-connected PV-UPQC system during grid voltage sag and swell is given in Figs. 6 and 7. The voltage sag and swell of 0.3 p.u. are applied for duration $t = 1$ to $t = 1.1$ s and $t = 1.5$ s to $t = 1.6$ s, respectively. The sag applied is more than the voltage sag limit, 10% of grid voltage and similarly swell applied is more than the voltage swell limit, 5% of grid voltage that described in IEEE-1159 standard. Series VSC injects 98 V (Peak value) in-phase and out-off phase with grid voltage during sag and swell, respectively. Thus, maintains a constant voltage across load. For maintaining grid power balance, an increase in grid current occurs during sag condition and grid current is decreased during the swell condition. Even if load current contains distortions, source current is free from distortions. Because of the action of shunt VSC, grid reactive power is zero and operates at nearly UPF. The solar irradiance is fixed at 1000 W/m^2 during the operation. The PV array supplies the load power and also feeds power into the grid. DC link voltage is maintained at the constant value of 700 V by the PI controller.

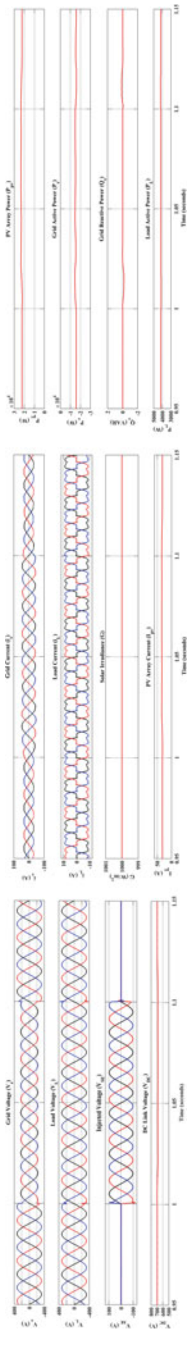

Fig. 6 Performance of grid connected PV-UPQC system for voltage sag (V_{S}, V_{L}, V_{SE}, V_{DC}, i_{S}, i_{L}, G, I_{pv}, P_{pv}, P_{S}, Q_{S}, P_{L})

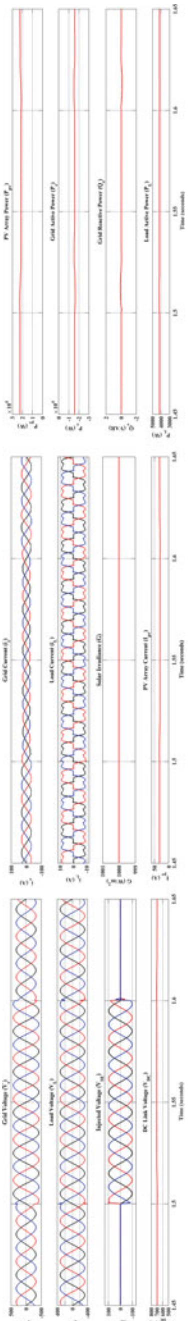

Fig. 7 Performance of grid connected PV-UPQC system for voltage swell (V_S, V_L, V_{SE}, V_{DC}, i_S, i_L, G, I_{pv}, P_{pv}, P_S, Q_S, P_L)

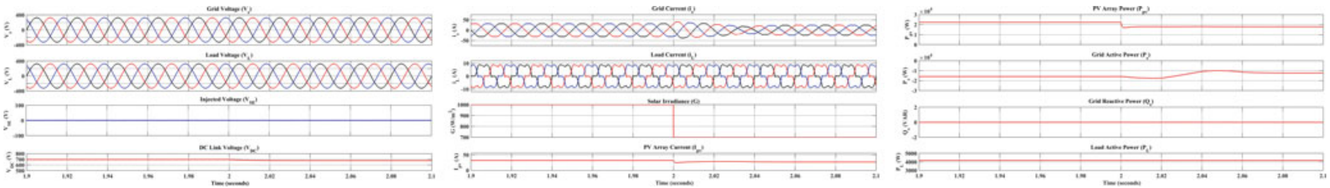

Fig. 8 Performance of grid connected PV-UPQC system for irradiation change (V_s, V_L, V_{SE}, V_{DC}, i_s, i_L, G, I_{pv}, P_{pv}, P_s, Q_s, P_L)

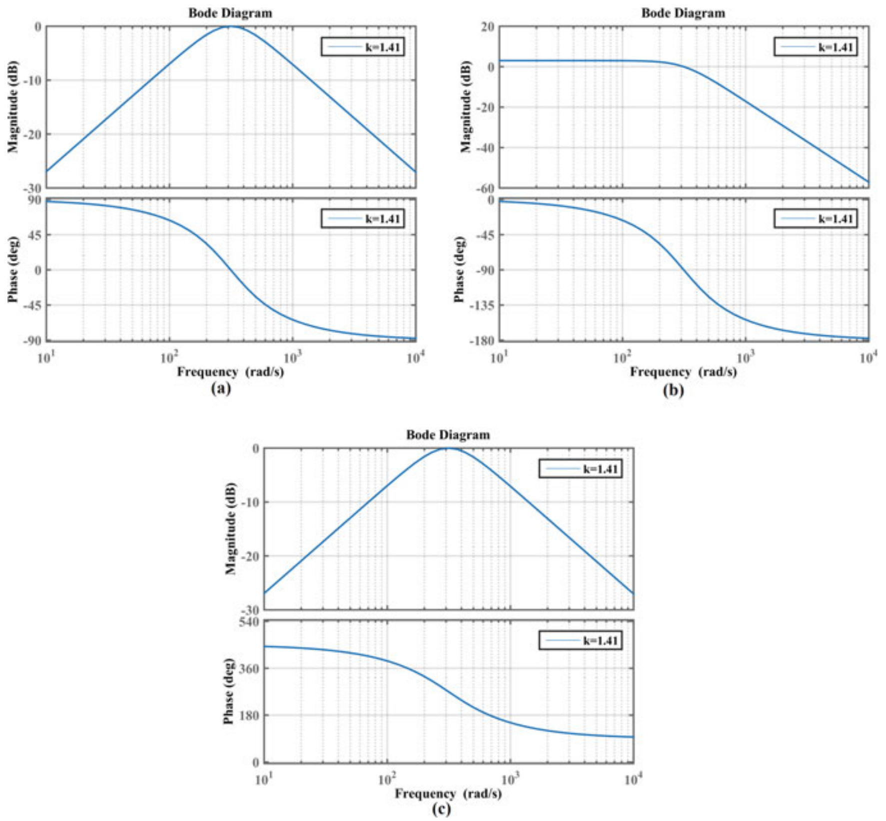

Fig. 9 Bode plot of **a** in-phase component for SOGI and MSOGI, **b** quadrature component for SOGI, **c** quadrature component for MSOGI

5.2 System Performance During Irradiation Change

The performance of grid-connected PV-UPQC system for irradiation change is given in Fig. 8. The solar irradiation changes from 1000 to 700 W/m^2 at time 2 s. During irradiation change, there is no change in load voltage. Because of irradiation change, PV power and current are decreased. Here, PV array feeds power into the grid and load. Thus, power feeding to the grid from PV array and grid current are reduced. If PV array does not generate sufficient power, then excess power required by the load is taken from grid. The DC link voltage maintained at constant reference value of 700 V. Shunt VSC compensates reactive power $Q_{\mathrm{s}} = 0$, and thus maintains nearly UPF operation.

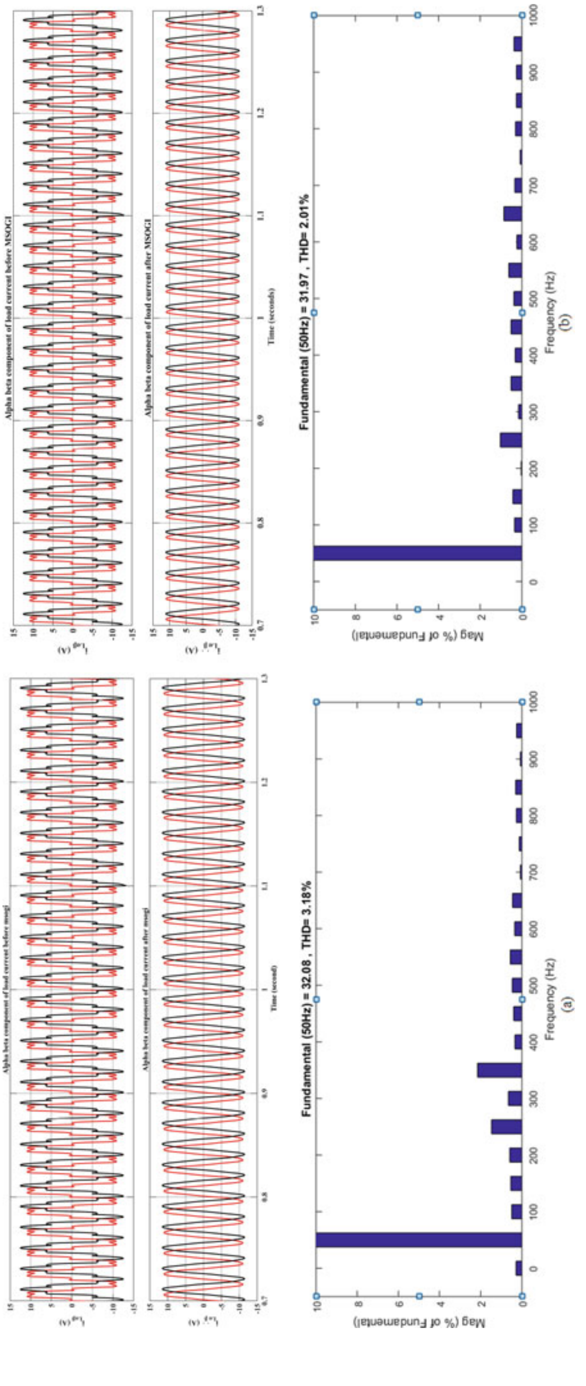

Fig. 10 DC offset elimination capability of **a** SOGI, **b** MSOGI

5.3 Comparative Performance of MSOGI and SOGI

The performance of MSOGI and SOGI are analysed with the frequency response plot given in Fig. 9. The bode plot of in-phase component of MSOGI and SOGI are same, and it is given in Fig. 9a. The in-phase component has band pass filter characteristics with better filtering performance and phase angle is 0°. The bode plot of quadrature component for SOGI and MSOGI are given in Fig. 9b, c, respectively. SOGI shows LPF characteristics and phase shift is 90° with poor DC offset elimination capability. But MSOGI shows BPF characteristics with better DC offset elimination capability and phase shift is 90°. Figure 10a represents alpha–beta component of load current before and after SOGI with THD analysis. The same for MSOGI is given in Fig. 10b. DC offset is present in the alpha–beta component of load current after SOGI. But for MSOGI, DC offset is completely eliminated. The absolute value of DC offset for SOGI is 0.03 and THD is 3.18%. The absolute value of DC offset in the MSOGI is 0.0007063 with THD of 2.01%. Thus, the presented MSOGI circuit shows better DC offset elimination capability.

6 Conclusions

The control of a grid-connected PV-UPQC system is presented in the work. Simulation with MATLAB Simulink demonstrates the effectiveness of the system. Here, a modification of SOGI is presented for extracting fundamental component of reference signal along with DC offset elimination capability. MSOGI is integrated with conventional pq-theory-based control. Thus, it eliminates the drawbacks of conventional pq-theory-based control. This system shows better performance for different dynamic conditions like grid voltage sag and swell and irradiation change. The filtering performance of proposed system is improved by the addition of MSOGI and control has less complexity compared to existing techniques. The system supplies clean energy from PV array and also operates in the absence of grid. Comparative analysis between SOGI and MSOGI is described in this work. The grid currents and voltages are balanced and operates in UPF and THD is within limits according to IEEE-519 and IEEE-1159 standards. The integration of PV-UPQC system with energy storage system is considered as future scope for this work.

References

1. Neves FAS (2010) A space-vector discrete Fourier transform for unbalanced and distorted three-phase signals. IEEE Trans Ind Electron 57(8):2858–2867
2. Kazemi A, Mokhtarpour A (2006) A new control strategy for unified power quality conditioner (UPQC) in distribution systems. In: International conference on power system technology

3. Kwan KH, So PL (2012) An output regulation-based unified power quality conditioner with Kalman filters. IEEE Trans Ind Electron 59(11):4248–4262
4. Forghani M, Afsharnia S (2007) Online wavelet transform-based control strategy for UPQC control system. IEEE Trans Power Delivery 22(1):481–491
5. Devassy S, Singh B (2018) Design and performance analysis of three-phase solar PV integrated UPQC. IEEE Trans Ind Appl 54(1):73–81
6. Khadkikar V (2009) A novel structure for three-phase four-wire distribution system utilizing unified power quality conditioner (UPQC). IEEE Trans Ind Appl 45(5):1897–1902
7. Devassy S, Singh B (2017) Modified pq theory-based control of solar-PV-integrated UPQC-S. IEEE Trans Ind Appl 53(5):5031–5040
8. Suma J (2013) Instantaneous symmetrical component theory based algorithm for characterization of three phase distorted and unbalanced voltage sags. In: 2013 IEEE international conference on industrial technology
9. Bhattacharya A, Chakraborty C (2011) A shunt active power filter with enhanced performance using ANN-based predictive and adaptive controllers. IEEE Trans Ind Electron 58(2):421–428
10. Singh AK (2018) Double-stage three-phase grid-integrated solar PV system with fast zero attracting normalized least mean fourth based adaptive control. IEEE Trans Ind Electron 65(5):3921–3931
11. Hackl CM (2020) Modified second-order generalized integrators with modified frequency locked loop for fast harmonics estimation of distorted single-phase signals. IEEE Trans Power Electron 35(3):3298–3309
12. Zhang C (2018) A grid synchronization PLL method based on mixed second- and third-order generalized integrator for DC offset elimination and frequency adaptability. IEEE J Emerg Sel Top Power Electron 6(3):1517–1526

Chapter 14
Power Quality Improvement in Distribution Network Using PV Integrated DSTATCOM

Pallavi Kumari, P. Narendra Babu, Kaibalya Prasad Panda, Sanjiba Kumar Bisoyi, and Gayadhar Panda

Abstract In the modernization, enlargement and improvement of electricity grids, applicable usage of electrical networks could be very essential. Because of the excessive price of production and improvement of electrical networks, mitigation of voltage profile issues, voltage instabilities, reliability troubles, etc., is inevitable. Distribution static compensator (DSTATCOM) is used as an efficient solution for these issues for improving power, voltage fluctuation and stability of power system. DSTATCOM a shunt-connected FACTs controller device particularly used to compensate reactive power and unbalance due to numerous loads in distribution side. As the clan energy generation demand is increasing, thus this paper presents photovoltaic (PV)-DSTATCOM operation and analysis as a great solution. The PV-DSTATCOM has been modelled and simulated in MATLAB/Simulink for enhancing the power quality of distribution side considering linear loads and nonlinear loads connected to the system.

Keywords DSTATCOM · Photovoltaic system · Voltage regulation

P. Kumari · P. Narendra Babu · K. P. Panda (✉) · G. Panda
Department of Electrical Engineering, National Institute of Technology Meghalaya, Shillong 793003, India
e-mail: kaibalyapanda@nitm.ac.in

P. Kumari
e-mail: b18ee32@nitm.ac.in

P. Narendra Babu
e-mail: narem.perumal@nitm.ac.in

G. Panda
e-mail: gayadhar.panda@nitm.ac.in

S. K. Bisoyi
Department of Electrical Engineering, JSS Academy of Technical Education, Noida, India
e-mail: sanjibabisoyi.eed@jssaten.ac.in

G. Panda et al. (eds.), *Sustainable Energy and Technological Advancements*,
Advances in Sustainability Science and Technology,
https://doi.org/10.1007/978-981-16-9033-4_14

1 Introduction

Nowadays, power system mainly consists of nonlinear load because of growth in electronic devices that consume high power, whereas the three-phase distribution network is going through excessive power quality issues such as bad voltage regulation, excessive reactive power burden, harmonics current and unbalancing due to connected load and also decreases the operating frequency. Integration of non-traditional generation technology like gasoline cells, wind generators and PV system with utility grids which frequently needs power electronic interfaces. The power electronic systems additionally make contribution towards power quality problems (producing harmonics). Expansion of flexible and adaptable solutions for power quality problems, with calls for passive filter, active filter, hybrid filter and custom power devices time to time. Lossless passive filters (LC) have been applied for a long time to minimize oscillations and to address the reactive power compensation issues. Passive filters, on the other hand, have prolonged compensation and resonating mostly with distribution network that is often overcome by active filters. Exploration of active filters in shunt, series, series-series and shunt-series configurations have been applied to compensate current and voltage-based distortions; however, they have got few drawbacks in terms of rating and costly also. Thus, hybrid filters are taken into consideration certainly considered one among alternatives owing to reduce price, simple design, controllable and high reliability in comparison with other alternatives for improving the power quality. Electronic power stability controllers, also known as custom power devices, are used to improve the quality of power on the consumer end. The word "custom power" refers to the future value of electric power or energy providers companies will give to their consumers. The power electronic applications in power distribution system for the benefit of a customer or group of customers are called custom power. The Distribution static compensator (DSTATCOM) is one such custom power device connected in shunt that can effectively compensate for the power quality problems [1–5].

Various power quality problems like overvoltage, voltage unbalance, dip/swells and harmonics propose a unique perception of operating PV inverters as PV-DSTATCOM with new control topologies for enhancement of better power quality. DSTATCOM's voltage control method is used to prevent system voltage infractions caused by excessive power production during maximal solar irradiation periods, allowing solar energy to be efficiently utilized. Various solutions have been examined and suggested within the literature [1, 2], and customized power devices play an important role in the electrical network. For current associated power quality issue, DSTATCOM is one among of the custom power devices used in distribution system. DSTATCOM follows self-supporting topologies that were suggested based on the current research [3, 4], and the AC grid is used to provide active electricity to keep the inverter capacitor voltage constant.

PV systems integrated DSTATCOM schemes [4-10] have now been explored for more than a few years. The authors introduced a PV integrated DSTATCOM design in [4], in which Icos$\varnothing$ control is used to maintain the system's power quality. The authors investigated an adaptable control mechanism in [5], which is a reweighted zero attracting system model that extracts the source grid frequency using this control method. When PV system generates energy, this approach works as a solar array system with DSTATCOM functionalities in power grid. When PV services are not available, it acts as a shunted active filter, and the system switches to DSTATCOM state, all power from the grid and the converter device delivered towards the load. In [6], the PV converter in addition to active filter characteristics is known as PV integrated DSTATCOM (Photovoltaic-Distribution Static Compensator), needed as it changes the DC-AC voltage and tries to solve the power problems by enhancing the quality of power by proscribing harmonic distortions, compensating reactive power so that balanced all the three phases in the distribution system. In [7], investigation on grid-connected PV-DSTATCOM technique collects maximal PV power and delivers it to the load linked while also delivering excess power to the grid, as well as several maximum power point tracking (MPPT) algorithms used.

Furthermore, the DC-link voltage is regulated depending on the peak voltage of the PV array to extract energy from solar energy source, as determined by the maximum power point tracking (MPPT) method, for all previous topologies presented in the literature. Furthermore, as the DC-link voltage rises, the switching losses rise as well [10]. In order to address this, the researcher calculated the lowest DC-link voltage related to the linked reactive load for a hybrid active power filter [10–12]. Even though the DC-link voltage is flexibly regulated as per filter current in [11–13], it has a delayed reaction and a ripple in the DC-link voltage. The DC-link voltage is maintained by the converter in [12, 13], to adjust the DC-link voltage, multiple switching methods are employed.

VSC is controlled by producing a load essential factor and then using the same algorithm to achieve both synchronization and power quality enhancement. The ability of a DSTATCOM controller to extract the performance of current signal. Many control systems have been investigated that use filters to acquire the reference current signals from the load currents, such as synchronous reference frame (SRF), instantaneous reactive power theory (IRPT), hybrid Least Mean Square-Least Mean Fourth (LMSLMF) and leaky LMS current control. The reference current waveforms are also extracted using phase-locked loops. Moreover, the suggested technology solves the power system's impact for nonlinear loads while maintaining total harmonic distortion (THD) within IEEE standard 519-1992 [12–14].

2 DSTATCOM Principle

A power electronics switching device, either GTO or IGBT, a capacitor bank as an energy storage device, a coupling transformer and a controller are illustrated in a single-line schematic of a DSTATCOM. The VSC, which is based on IGBTs, converts the DC voltage across the storage device into three-phase AC output voltages. Through the coupling transformer's reactance, these voltages are in phase with the AC system (Fig. 1).

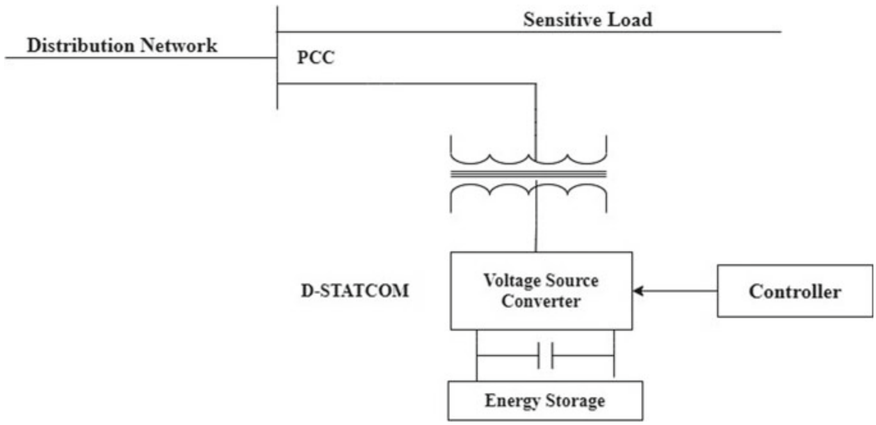

Fig. 1 Single-line schematic diagram of DSTATCOM

The active and reactive power conservations between the DSTATCOM and the AC grid could be effectively controlled by adjusting the phase and magnitude of the DSTATCOM output voltages. The reactive power exchange of the DSTATCOM with the AC system is controlled by regulating the amplitude of the DSTATCOM output voltage. DSTATCOM supplies the reactive power that is-

$$\text{(Reactive power) } Q = \frac{(V_c - V_s) * V_s}{X}$$

where

V_c represents DSTATCOM output voltage
V_s represents voltage source
X represents the equivalent impedance between DSTATCOM and the network

DSTATCOM operating modes:

- If $V_c > V_s$, the DSTATCOM is in capacitive mode and is supplying reactive power to the grid.
- If $V_s > V_c$, the DSTATCOM is inductively working and absorbing reactive power from the grid.
- If the magnitude of $V_c = V_s$, no reactive power is exchanged between the grid and the DSTATCOM, and the DSTATCOM is in a floating condition.

Both the voltage source inverter (VSI) and the current source inverter (CSI) topologies can be used to build a DSTATCOM configuration. Mainly VSI is commonly in use for the DSTATCOM.

2.1 Power Quality Issues

Concern about power quality is very normal because of increasing nonlinear load. The advancement of power electronics-based equipments has a significant effect on electric power supply quality. Harmonics in network voltages are caused by the widespread usage of electronic equipment such as information technology equipment and power electronics devices. Voltage fluctuation, imbalance and flicker are also caused by classical loads such as huge arc furnaces and welding machines. When these loads function at the same time, they become the primary victims of power quality issues. As a result, power quality has significant financial consequences for consumers, utilities and electrical appliances.

2.2 PV Energy Storage System

According to a recent study, the PV inverter can operate as a DSTATCOM—a Flexible AC Transmission System (FACTS) device, which is termed as PV-DSTATCOM. The PV inverter has been shown to improve the connection of neighbouring wind farms and the power transfer capacity over long transmission lines using these STATCOM capabilities. PV-STATCOM uses the whole solar inverter capacity at night and the remnant inverter energy during real power production through the day to interchange reactive power with the grid to achieve various goals such as voltage control, current control and so on (Fig. 2).

PV-DSTATCOM'S MAIN COMPONENTS INCLUDE: The voltage source converter (VSC), SPV array, transformer and ripple filter are the key components of DSTATCOM. Through a tie reactor and capacitor, the VSC converts a DC voltage into

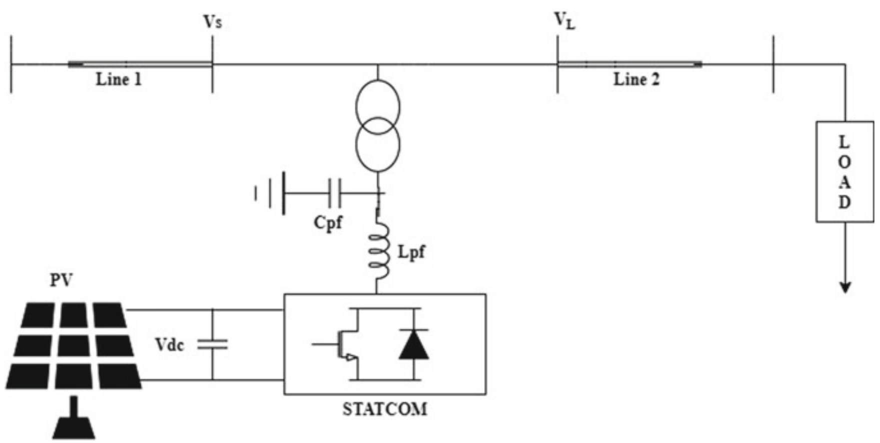

Fig. 2 Single-line diagram of PV-DSTATCOM

a three-phase AC voltage that is synced with the PCC. To match the inverter output to the line voltage, a transformer is employed. PV energy sources are renewable source of energy which are expected to contribute in the development of fulfilling future energy demands. Grid-connected PV systems often use a hysteresis-band current controller to shape grid current to follow a specified sinusoidal reference.

2.3 PV Integration with Distributed Generation

Renewable energy is becoming increasingly popular around the world as a result of its several benefits, including pollution-free, low cost of input power and friendly with nature and user usage. It is possible to construct a DSATCOM that will inject active power from this renewable source while also improving the power quality of the grid bus to which it is linked. Because the electrical energy supplied by this renewable source is normally DC, it must first be converted to a fixed DC using a DC–DC converter in order to maintain a constant DC bus voltage. Electric power generation that is physically distributed within a distribution network or on the customer side of the network is referred to as distributed generation. The power flow in distributed generation is bidirectional, which means it can travel from the grid to the load and back again when the power is generated by distributed generation, such as a PV system. The DC–AC converters can connect the PV system's power to the grid's AC bus directly. An inverter with a PV array and an active filter function designated as PV-Distribution Static Compensator PV-(DSTATCOM) were designed to transform DC voltage into AC and enhance stability by suppressing switching losses, to compensate the reactive power and to maintain balance in all three phases of power distribution network. PV systems will continue to advance in future, with the goal of becoming an important component in the generation of power for houses and industries. Despite the fact that it has a low acceptance rate because of its high price and low efficiency, current research is eliminating these restrictions, and PV electrical sources are becoming more popular.

2.4 Detailed System Description

The structure of the system is depicted in Fig. 3 which includes an AC grid having linear and nonlinear loads, a PV integrated DSTATCOM along with VSI is coupled to the AC grid's point of common coupling (PCC), and VSI control mechanism is also implemented. PV-DSTATCOM is connected to the AC grid's PCC via the interface inductance. RC ripple filters, on the other hand, can be used to remove ripple caused by switching. The SRF control approach is used for the shunt coupled VSI by correlating the control signal of grid current with the produced reference grid current. PV-DSTATCOM extracts the maximum power from PV regardless of irradiance when PV power is available, and the incremental conductance algorithm

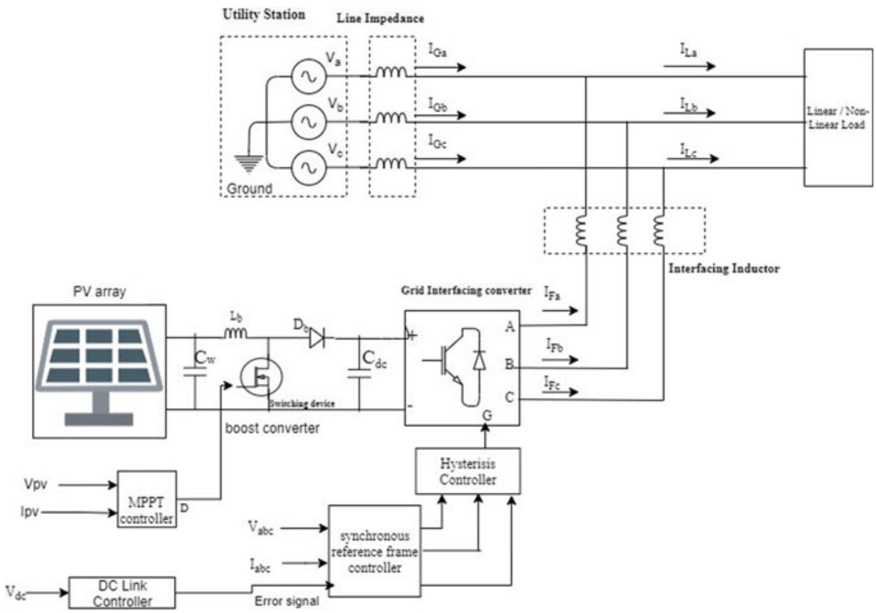

Fig. 3 Schematic diagram of VSI-based PV integrated DSTATCOM

is used to track the maximum power point from the PV system. If PV power is unavailable, the DC-link voltage can be adjusted based on the linked capacity or load to minimize VSI power wastage for improved operation.

2.5 Control Scheme

A. **Maximum power point tracking (MPPT) controller**

The irradiance, temperature and current drawn from a PV system comprising one or more PV cells determine the electricity delivered. It is utilized to get the most power out of these systems. Under certain conditions, MPPT is a rechargeable battery algorithm which collects the most available power from such a PV modules. The peak power voltage of a PV module is the voltage at which it can produce the maximum electricity. Maximum power is affected by sun radiation, temperature change and PV cells temperature. MPPT is much more beneficial in the following situations. Weather that is cold, rainy, or hazy. In cold weather, PV modules frequently perform better, and MPPT is employed to obtain the most electricity feasible. Also, if the battery's state of charge lowers and the battery is deeply exhausted, MPPT could also draw additional current and charge the battery.

There are numerous methods for increasing the power output of a PV system. The power conversion engineer must weigh the various possibilities based on the final use and the irradiance dynamic.

(1) Perturb and observe (P&O)
(2) Incremental conductance (IC)
(3) Fractional open-circuit voltage
(4) Fractional short-circuit voltage
(5) Fuzzy logic control.

The most prevalent approach is perturbed and observed, but the incremental conductance method overcomes the limitation of perturb and observe in tracking peak power under rapidly changing atmospheric circumstances.

$$P = V^{*}I \tag{1}$$

where P denotes the power of a solar module, V denotes the voltage of a solar module, and I denotes the current of a solar module.

Differentiating w.r.t V

$$\frac{\mathrm{d}P}{\mathrm{d}V} = 1 + V * \frac{\mathrm{d}I}{\mathrm{d}V} \tag{2}$$

The above equation serves as the foundation for the entire method. At its most powerful,

$$\frac{\mathrm{d}P}{\mathrm{d}V} = 0 \tag{3}$$

$$\frac{\mathrm{d}I}{\mathrm{d}V} = -I/V \tag{4}$$

If the power curve's operating point is to the right, we obtain

$$\frac{\mathrm{d}P}{\mathrm{d}V} < 0 \tag{5}$$

$$\frac{\mathrm{d}I}{\mathrm{d}V} < I/V \tag{6}$$

If the power curve's operating point is to the left, we obtain

$$\frac{\mathrm{d}P}{\mathrm{d}V} > 0 \tag{7}$$

$$\frac{\mathrm{d}I}{\mathrm{d}V} > I/V \tag{8}$$

Using Eqs. (4), (6) and (8), the maximum peak power can be traced.

This technique outperforms perturb and observe in that it can tell when the MPPT has arrived at the MPP, whereas perturb and observe oscillate about the MPP. In addition, incremental conductance is more accurate than perturb and observe at tracking quickly increasing and declining irradiance conditions. Because it requires two sensors, this approach has a higher level of complexity than perturb and observe. For example, current and voltage require two sensors, whereas the P&O approach just requires one, which is voltage.

B. **Voltage source controller**

Depending on the compensation required, a voltage source converter is utilized to generate an output voltage wave, that is, regulated in magnitude and phase angle to provide either leading or lagging reactive current. It transforms the DC voltage across storage devices into a three-phase AC output voltage set. It could be three-phase, three-wire VSC or a three-phase, four-wire VSC. A VSC converter can be a two-level or three-level converter. The most common PLL approach is the synchronous reference frame phase-locked loop (SRF-PLL), which is mostly employed in three-phase systems in grid-connected power converters. The SRF-PLL is used to synchronize the grid voltage, frequency and phase. The reference current is extracted using the synchronous reference frame method (SRF), and the reference current is compared to the filter current in the hysteresis loop, with appropriate pulses delivered for inverter switching (Figs. 4 and 5).

3 Results and Simulation

Here simulation performed for 100 kW PV array is connected to a 25 kV grid via a DC-DC boost converter and a three-phase three-level voltage source converter in this PV-DSTATCOM (Table 1).

Case 1 [0.05–0.6 s] Throughout this period of time, solar irradiance and temperature are set 1000 W/m^2 and 25 °C, respectively, where V_{ref}; i.e. DC-link voltage is regulated as 500 V as shown in Fig. 6. Steady state is reached at 0.2 s, resulting V_{pv} is 250 V, and the output PV array power is about 96 kW, whereas specified maximum power is 100 kW at 1000 W/m^2 sun irradiance. Grid voltage and current are in same phase in this interval. The voltage corresponding to the solar PV's maximum power point, as desired by the incremental conductance method, is too high, and the power provided to the grid is insufficient. Also, stress is provided across the switch VSC(V), i.e. 500 V which is same as the DC-linked voltage. For connected loads, the switch from PV-DSTATCOM to DSTATCOM mode began.

Case 2 [0.6–1.2 s] In this time interval, as shown in Fig. 8a, sun irradiance level started ramped down and decreased from 1000 W/m^2 to 250 W/m^2 at t = 1.1 it fully ramped down. The conversion from PV-DSTATCOM mode to DSTATCOM

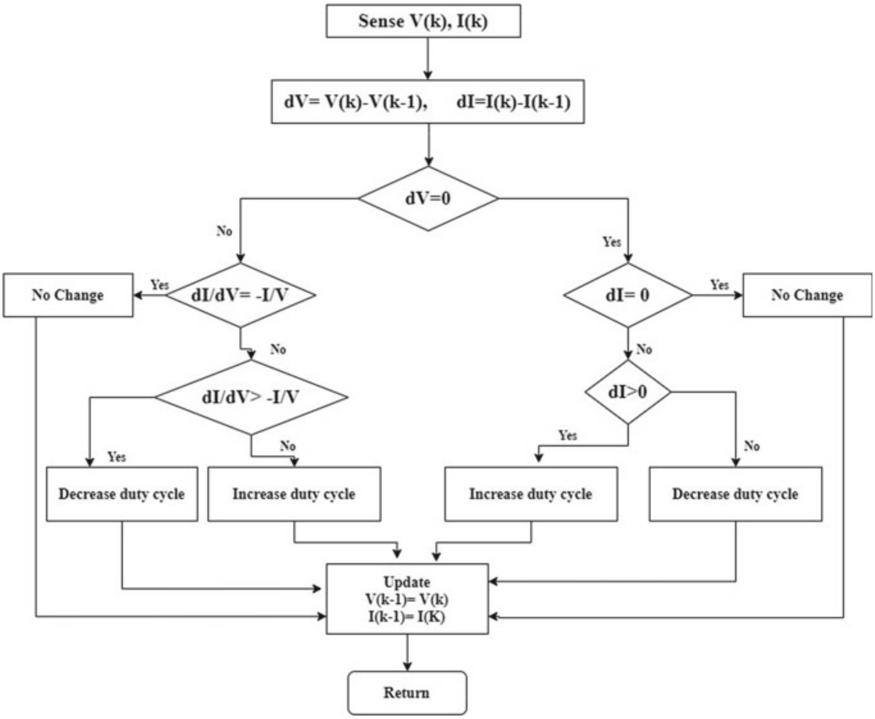

Fig. 4 Flowchart of MPPT using incremental conduction

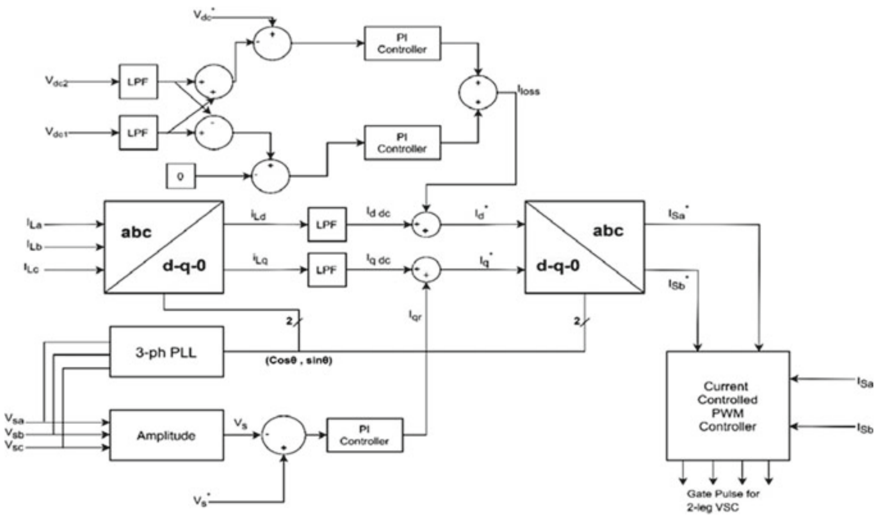

Fig. 5 Synchronous Reference frame theory

Table 1 System parameters

PV panel	Module: SunPower (SPR-305E-WHT-D), maximum at 100 kW at 1000 W/m^2 sun irradiance 66 model string, 2 parallel string 100 kW panel, $V_{oc} = 64.2$ V, Isc = 5.96A Voltage and current at maximum power: Vmp = 54.7 V, Imp = 5.58 A
3-level 3-phase VSC	1.98 kHz-500 V
DC-DC boost converter	5 kHz–500 V
Capacitor bank	10 kvar
Utility	100 kVA, 260 V/25 kV 25 kV distribution feeder 2 MW linear load (R), Nonlinear load (R–L) 30 MW-2 Mvar & 20 MW-2 Mvar at 60 Hz

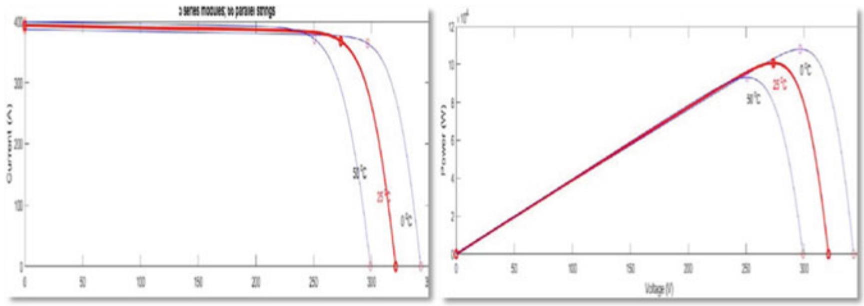

Fig. 6 I_pv & P_pv characteristics of PV module

mode takes place for the same load connected as in the previous scenario. During this rapid irradiance change, the reference DC-link voltage estimation begins as PV power drops to 25 kW and the DC-link voltage is managed to roughly 500 V, and MPPT continues to track maximum power. The compensatory current is injected by VSI, causing the grid current to become sinusoidal and in phase with the grid voltage, keeping THD below 5%. When PV electricity is unavailable, the AC grid steps in to provide full power to the associated load. As indicated in Fig. 7a, the DC-link voltage and controlled stress voltage are both 500 V. Here gird current shows harmonic and its amplitude decreases as grid power comes to 25 kW.

Case 3 [1.2–2.5 s] In this time interval, sun irradiance level is started to restored back to 1000 W/m^2 and then the temperature is increased to 50 °C as shown in Fig. 9. As the temperature increases from 25°C to 50 °C at t = 2.1 s, the PV power output decreases from 100 kW to 93 kW that can be verified from Fig. 8. Here transition occurred from DSTATCOM mode to PV-DSTATCOM mode. Here also grid current shows harmonic and its amplitude increases because VSI injecting compensating current so that grid current and voltage remain in same phase. DC-link voltage and VSI voltage maintain dynamic.

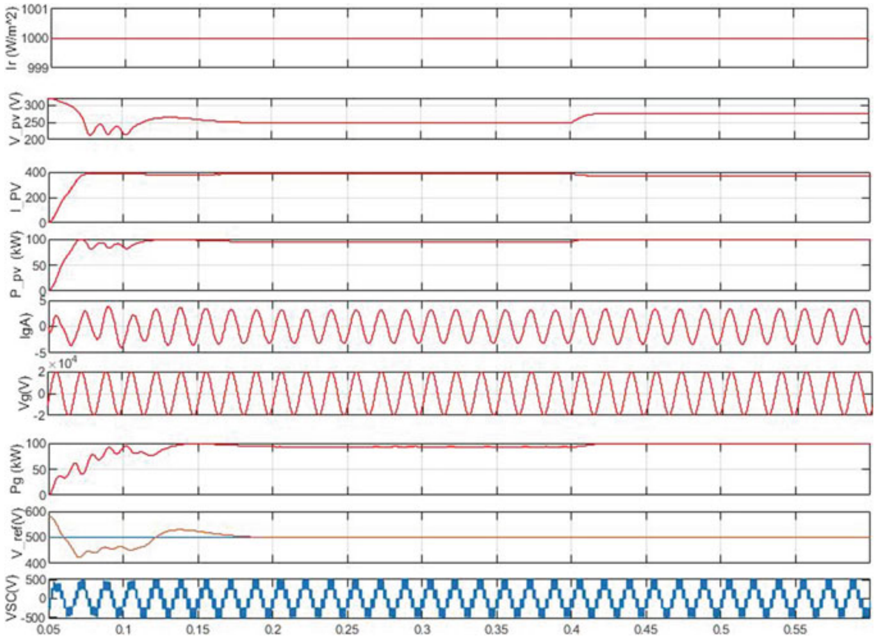

Fig. 7 Simulation result of PV-DSTATCOM, sun irradiance I_r(W/m^2), V_{pv} (V), I_{pv} (A), P_{pv} (kW), grid current I_g (A), gird voltage V_g (V), grid power P_g (kW), $V_{ref,}$ i.e. DC-link voltage(V), voltage across inverter, i.e. switch stress voltage VSC(V)

Case 4 The current THD under different loading is shown in Fig. 10 matched with IEEE standard 519 for the power system.

When PV power is unavailable, the DC-link voltage is maintained depending on the nature of load to improve PV-DSTATCOM performance, and when PV energy is available, the DC-link voltage is matched with the MPPT peak, with the PV system's peak voltage extracting maximum power as determined by incremental conductance technique.

4 Conclusion

A study of PV-DSTATCOM operation is performed, and results are obtained through simulation. The DSTATCOM has been modelled and analysed for the PV systems and being integrated into the low-voltage distribution power grid towards the customer side by employing DSTATCOM to mitigate harmonics from the grid side and other loads. The DSTATCOM's main goal is to circulate excess power throughout the phases in order to improve power quality. At the same time, it is predicted that sources

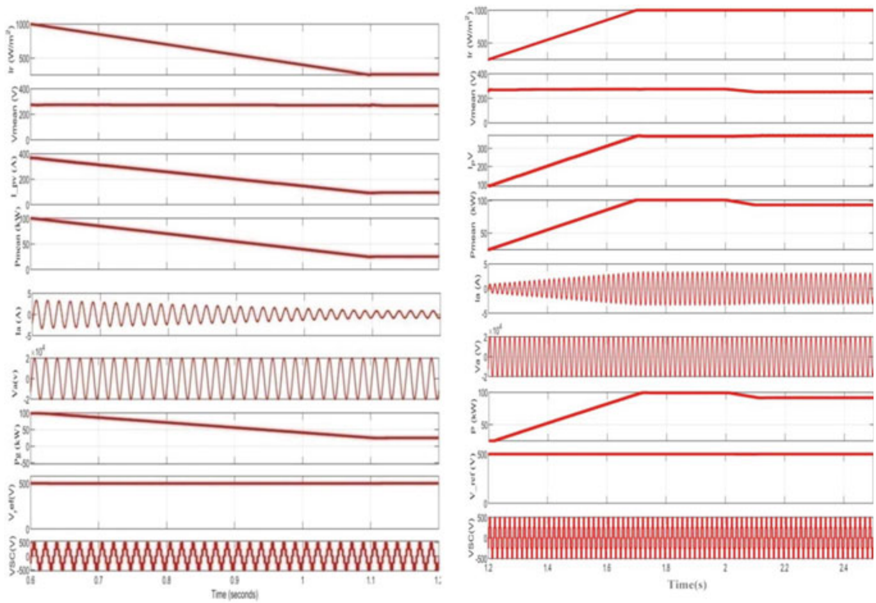

(a) (b)

Fig. 8 Simulation result of PV-DSTATCOM, sun irradiance I_r (W/m^2), V_{pv} (V) or V_{mean}, I_{pv} (A), P_{pv} (kW) or P_{mean}, grid current I_g (A), gird voltage V_g (V), grid power P_g (kW), V_{ref}, i.e. DC-link voltage (V), voltage across inverter, i.e. switch stress voltage VSC(V)

Fig. 9 Temperature curve w.r.t time set to PV array

will be able to operate at unity power factor. Results' analysis under dynamic operating condition shows the power quality that is maintained well within the specified standard.

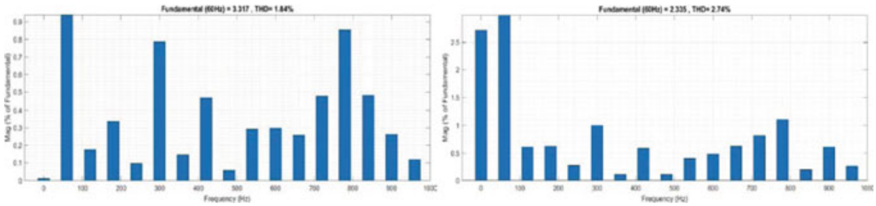

(a) linear load **(b) Non-Linear loads**

Fig. 10 THD analysis at different load

References

1. Arrillaga J, Watson NR (2004) Power system harmonics. Wiley
2. Bollen MH (2000) Understanding power quality problems, vol 1. IEEE, Piscataway, pp 1–35
3. Sorte PK, Panda KP, Peesapati R, Panda G (2020) An improved control strategy for single-phase single-stage grid-tied PV system with current reference MPPT control. In: 2020 IEEE international conference on computing, power and communication technologies (GUCON), pp 461–466
4. Singh B, Jayaprakash P, Kothari DP, Chandra A, Al Haddad K (2014) Comprehensive study of DSTATCOM configurations. IEEE Trans Indus Inf 10(2):854–870
5. Prince SK, Panda KP, Panda G (2020) Kalman filter variant intelligent control for power quality improvement in photovoltaic active power filter system. Int Trans Electr Energy Syst 30(3)
6. Singh B, Kandpal M, Hussain I (2018) Control of grid tied smart PVDSTATCOM system using an adaptive techniques. IEEE Trans on Smart Grid 9(5):3986–3993
7. Prince SK, Panda KP, Kumar VN, Panda G (2018) Power quality enhancement in a distribution network using PSO assisted Kalman filter—based shunt active power filter. In: 2018 IEEMA Engineer Infinite Conference (eTechNxT), pp 1–6
8. Modi G, Kumar S, Singh B (2020) Improved widrow-hoff based adaptive control of multi-objective PV-DSTATCOM system. IEEE Trans Indus Appl 56(2):1930–1939
9. Prince SK, Panda KP, Patowary M, Panda G (2019) FPA tuned extended Kalman Filter for power quality enhancement in PV integrated Shunt active power filter. In: 2019 international conference on computing, power and communication technologies (GUCON), pp 257–262
10. Sorte PK, Panda KP, Panda G (2021) Current reference control based MPPT and investigation of power management algorithm for grid-tied solar PV-battery system. IEEE Syst J 1–11
11. Murali S, Panda KP, Panda G (2018) PV-HESS fed BLDC driven water pumping system with PSO-based MPP tracking employing zeta converter. In: 2018 IEEE innovative smart grid technologies—Asia (ISGT Asia), pp 196–201
12. Lam C-S, Choi WH, Wong MC (2012) Adaptive DC-link voltage controlled hybrid active power filters for reactive power compensation. IEEE Trans Power Electron 27:1758–1772
13. Hareesh M, Siva Kumar G, Sreenivasarao D (2017) Dynamic DC voltage regulation of split-capacitor DSTATCOM for power quality improvement. IET Generation Transmission Distribution 11(17):4373–4383
14. Kiran Prasad K, Myneni H, Ganjikunta SK (2019) Power quality improvement and PV power injection by DSTATCOM with variable DC link voltage control from RSC-MLC. IEEE Trans Sustain Energy 10:876–885

Chapter 15
Instantaneous Reactive Combined Loss Componenet Power Theory-Based Hybrid Filter for Power Quality Improvement in Distribution System

Pratap Sekhar Puhan, Santanu Kumar Dash, Pravat Kumar Ray, Gayadhar Panda, and Manidra Pothauri

Abstract This paper presents an improved instantaneous reactive power theory control technique for successful operation of hybrid filter to improve power quality. Power quality issues due to different types of nonlinear loads are analyzed and accordingly a hybrid filter is designed. The performance of the hybrid filter is enhanced with the proposed control technique, in this technique loss component of the shunt active filter is incorporated with the power to generate the reference signal. Then the actual power is compared with instantaneous power of load. The obtained error passes to the next level for successful switching action of shunt active filter. The effectiveness of the developed controller is verified through simulation and experimentation.

Keywords Hybrid filter · Improved IPR control technique · Harmonics · Power quality

1 Introduction

Harmonics in power system network and its mitigations with different method are one of the recent trends of research in power quality [1]. In the past, impact of

P. S. Puhan (✉) · M. Pothauri
Department of Electrical and Electronics Engineering, Sreenidhi Institute of Science and Technology, Hyderabad 501301, India
e-mail: pratapsekhar@sreenidhi.edu.in

S. K. Dash
TIFAC-CORE, Vellore Institute of Technology (VIT) University, Vellore, Tamilnadu, India

P. K. Ray
Department of Electical Engineering, National Institute of Technology, Rourkela, India
e-mail: rayp@nitrkl.ac.in

G. Panda
Department of Electical Engineering, National Institute of Technology, Shilong, Meghalaya, India
e-mail: gayadhar.panda@nitm.ac.in

G. Panda et al. (eds.), *Sustainable Energy and Technological Advancements*, Advances in Sustainability Science and Technology,
https://doi.org/10.1007/978-981-16-9033-4_15

harmonics in the electrical network was less. The vast use of power semiconductor and microprocessor-based equipment after 1980s raises the concern of harmonics parameters which is becoming one of the major problems for degradation of power quality. [1, 2]. There are many reasons for power quality issues such as variation of loads, switching on and off the motor, external events which includes lighting and weather condition [3, 4], but the use of nonlinear loads are the main source of harmonic currents in the power system network and leads to voltage distortion which affects the system performance. [5] The nonlinear current includes fundamental and harmonics if proper filtration mechanism is not provided then these harmonics leads to inter harmonics and sub harmonics which have also degrades the efficiency of the system so, it is important and crucial to analyze the harmonics and remove it from the system so that an efficient system can be achieved. [6, 7]. Though other power quality issues such as transient, over voltage, under voltage, voltage sag, voltage swell, voltage fluctuation, voltage flicker et are there, but the work concentrate on harmonics. To eliminate the harmonics, different mitigating devices such low pass filter, series active filter, shunt active filter and hybrid filter has already been developed and still research is going on for newer device to come. All these developed devices have associated with some advantage and also disadvantage [5, 6, 8]. Low pass filter has resonant problem [9]; shunt filter has the problem to mitigate voltage related issues, whereas series filter has the problem of suppressing current related issues [7, 9, 10]. Though hybrid filter is used to overcome the issues but the design complexity is not suitable for all applications [11]. So, it is better to recommend different types of configuration for specific problems. The performance of all the discussed harmonics mitigating devices is not only depends on the design but also depends on the implementation of control techniques. The working of the filters needs the generation of a reference signal which is to be compared with the actual signal and accordingly the error originates fed to a controller to generate pulses for the voltage source converter which is the main components of the filters. Several reference signal generation algorithms such as indirect current control technique, synchronous detection techniques, instantaneous reactive power theory, and unit vector template generation techniques have already been developed and implemented in many filters [12, 13]. For generation of pulses current controller techniques-based PWM controller also used in many filters [14].

In this work, further improvement of performance of a hybrid filter [8] is presented in which the reference signal is achieved by incorporating the loss component of the filters in the existing instantaneous reactive power theory. The gate pulses are generated using the conventional hysteresis current controller.

In this paper, total six sections presented including Sect. 1. Section 2 describes proposed hybrid filter. Section 3 presents the implementation of the improved controller Sect. 4 result and analysis, Sect. 5 experimental verification and finally in Sect. 6 conclusions.

2 Description of the Proposed System with Controller

Figure 1 shows the developed hybrid shunt power filter with details of specification and configuration. The filter is connected in the distribution system in parallel between the supply mains and the power electronics-based nonlinear load [9–11] In the proposed system, diode bridge with RL, RC, R connected as nonlinear load.

The proposed system consists of hybrid filter and its control techniques first component is a low pass filter with inductor and capacitor are the main element. Second one is the active components constitutes six IGBT and a capacitor. The passive filter is responsible for higher order harmonics, whereas the shunt active filter is responsible for elimination of third harmonics which is very dangerous to the system. For proper operation of the hybrid filter, an improved and modified instantaneous reactive power theory is implemented for efficient and smoothing switching action of the voltage source converter. The low pass part is tuned to eliminate higher order harmonics. In this work, at first harmonics are generated intentionally by connecting different types of nonlinear load in the source. One. PQ theory is developed followed by the steps.

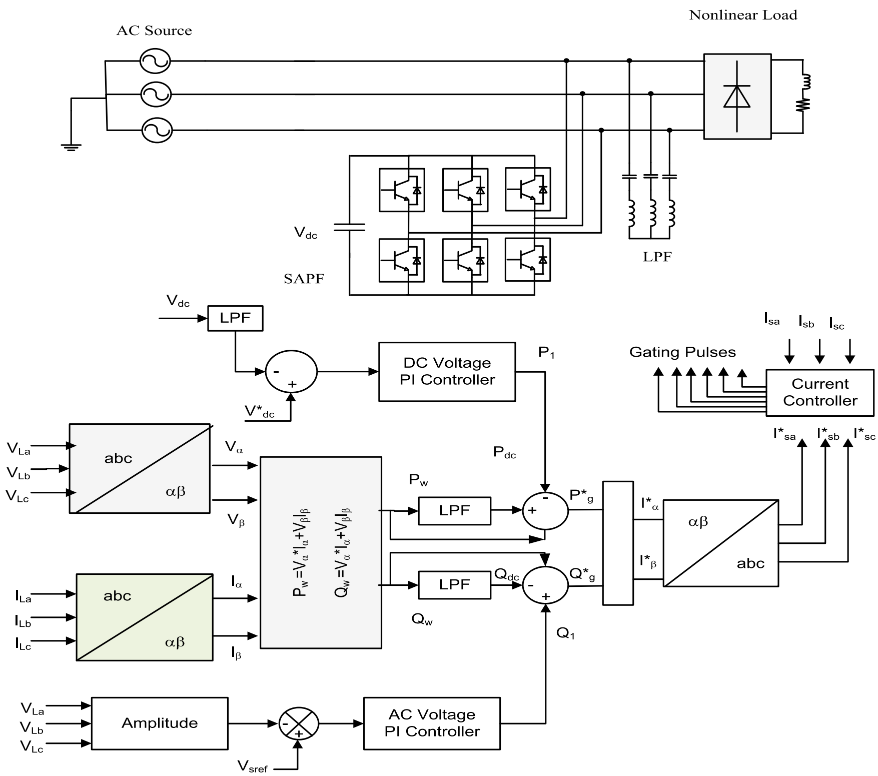

Fig. 1 Proposed system with improved controller

3 Improved Instantanou Reactive Power Theory

In this work, at first harmonics are generated intentionally by connecting different types of nonlinear load in the source. One part of the hybrid filter consists of LC passive filter to eliminate the higher order harmonics, other part of the same hybrid ffilter, i.e., the shunt active filter works to eliminate the lower order harmonics. The main focus is to develop one control technique taking the PQ theory incorporating the loss component for generation of reference signal in the proposed converter. PQ theory is developed followed by the steps [4, 8, 15].

$$\begin{bmatrix} i_\alpha \\ i_\beta \end{bmatrix} = \begin{bmatrix} 1 & -0.5 & -0.5 \\ 0 & 0.866 & -0.866 \\ 0.5 & 0.5 & 0.5 \end{bmatrix} \begin{bmatrix} i_{La} \\ i_{Lb} \\ i_{Lc} \end{bmatrix} \tag{1}$$

In the same manner, α, β components of the system voltage can be expressed as follows

$$\begin{bmatrix} V_\alpha \\ V_\beta \end{bmatrix} = 0.66 \begin{bmatrix} 0 & -0.5 & -0.5 \\ 0 & 0.866 & -0.866 \\ 0.5 & 0.5 & 0.5 \end{bmatrix} \begin{bmatrix} V_{sa} \\ V_{sb} \\ V_{sc} \end{bmatrix} \tag{2}$$

From the above two equation, instantaneous active and instantaneous reactive power drawn by the load can be expressed as refer in [8]

$$p_L = V_\alpha i_\alpha + V_\beta i_\beta = P_{\text{LDC}} + P_{\text{LAC}} \tag{3}$$

$$q_L = V_\alpha i_\beta + V_\beta i_\alpha = Q_{\text{LDC}} + Q_{\text{LAC}} \tag{4}$$

V_α, V_β presents the instant voltage at point of common coupling and i_α, i_β along α, β axis represents the instantaneous value of the load current. The DC values of P_{LDC} and Q_{LDC} stands for active and reactive powers of the load in the fundamental component, whereas P_{LAC}, Q_{LAC} stands for ripples of active and reactive power which are the results of harmonics and negative sequence components of current due to nonlinear load. To extract the DC value of P_{LDC}, in the proposed hybrid filter a second-order low pass filter with cut off frequency of 20 Hz is inserted. The component of the power passes through the low pass filter to remove the oscillating component which is responsible for harmonics. Then a comparison is made between them V_{DC} and another DC voltage of designed 700 V and the error generated is passed through the proportional integral controller and loss in the active part is calculated. The loss in the active part is added to the P_{Lowpass} to find the value of total $P_{\text{Component}}$, then $p_{\text{Component}}$ and the actual power p is compared. The error obtained P_{Error} is passed to the next level. Now the instantaneous current $i_{\alpha x}$ and $i_{\beta x}$ can be calculated as per the following equations

$$i_{\alpha x} = \frac{V_\alpha P_{\text{Error}}}{V_\alpha^2 + V_\beta^2} \tag{5}$$

$$i_{\beta x} = \frac{V_\beta P_{\text{Error}}}{V_\alpha^2 + V_\beta^2} \tag{6}$$

Now reverse Clarke's transformation is implemented and the reference grid currents are obtained followed by the below equation

$$\begin{bmatrix} i_{sa}^* \\ i_{sb}^* \\ i_{sc}^* \end{bmatrix} = \begin{bmatrix} 1 & 0 \\ -0.5 & -0.866 \\ -0.5 & -0.866 \end{bmatrix} \begin{bmatrix} i_{ax} \\ i_{bx} \end{bmatrix} \tag{7}$$

Switching action of converter initiates after the error generates by making a comparison with reference current and actual source current i_s fed to the hysteresis controller. The block diagram of the complete control technique for generation of switching action is given in Fig. 1.

4 Simulation Results and Comparative Analysis

In this section, the performance of the developed hybrid shunt power filter with the proposed improved reactive power theory has been verified by connecting three different types of nonlinear load such as R-L load with diode bridge rectifier, R-L and L with diode bridge rectifier and RC load with the diode bridge rectifier in the system.

4.1 Case 1-Diode Bridge Rrectifier and R-L Load

Details of the simulation work has been carried out by using MATLAB/SIMULINK. At first the model is prepared as per the magnitude of the parameter and improved reactive power theory is implemented for switching action of the converter along with hysteresis controller for three phase system with R-L connected with the diode bridge rectifier. The simulated waveform of source voltage, load ccurrent, filter current and source current after compensation is shown in the Fig. 2a–d the corresponding FFT analysis of the ssource current before compensation and after compensation is shown in the Fig. 3a, b, respectively. From FFT analysis, it is clearly understood that the THD without using active power filter was 21.41% and it is reduces to a value of 1.45%., which is within IEEE-519 standard. Each content of the harmonics amplitude and phase after compensation is presented in Table 1.

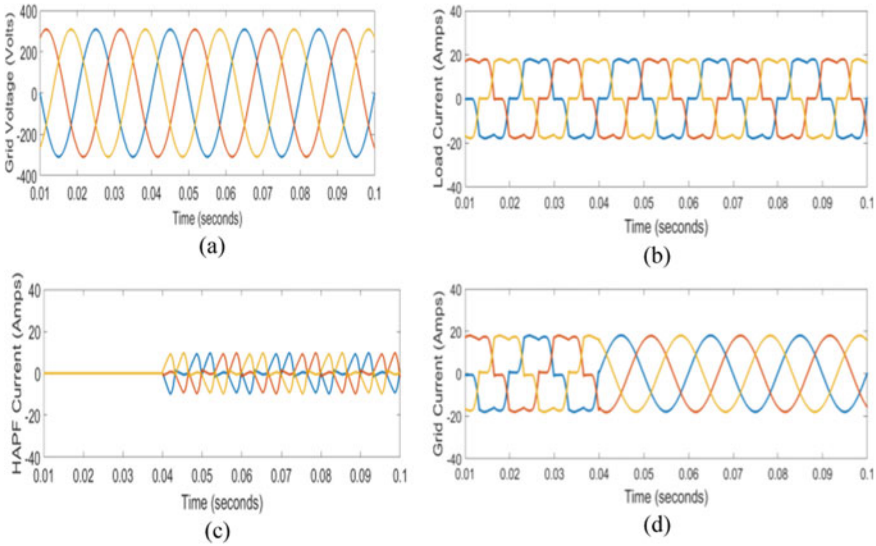

Fig. 2 Diode bridge rectifier with R-L load simulated waveform of **a** grid voltage, **b** load current, **c** filter current, **d** source current

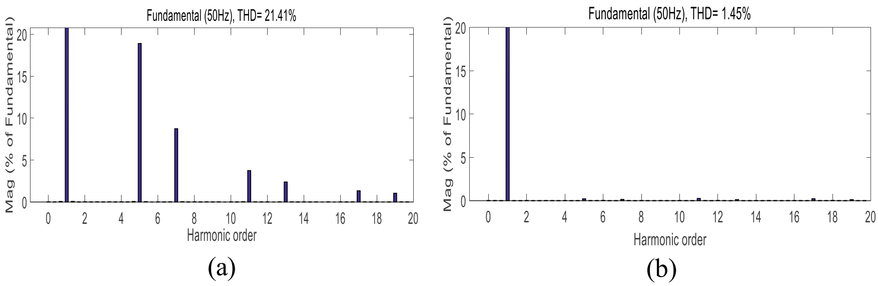

Fig. 3 FFT analysis of diode bridge rectifier with R-L load, **a** load current, **b** source current

Table 1 Magnitude and phase of each harmonic's contents of R-L Load

Harmonic order	Percentage of reduction of magnitude with the Improved controller	Phase angle with the improved controller in degree
0 Hz (DC)	0.02	270.0
50 Hz (Fund)	100	1.5
150 Hz (h3)	0.01	58.2
250 Hz (h5)	0.24	201.4
350 Hz (h7)	0.16	93.7
450 Hz (h9)	*0.03*	*159.0*

4.2 *Case 2-Diode Bridge Rrectifier and R-L and R Load*

Three phase system with R-L and R connected with the diode bridge rectifier. The simulated waveform of source voltage, load current, filter current and source current after compensation is shown in the Fig. 4a–d. The corresponding FFT analysis of the source current before compensation and after compensation is shown in the Fig. 5a, b, respectively. From FFT analysis, it is clearly understood that the THD without using active power filter was 21.41% and it is reduces to a value of 1.52% by connecting the developed hybrid filter with the proposed improved reactive power theory, which

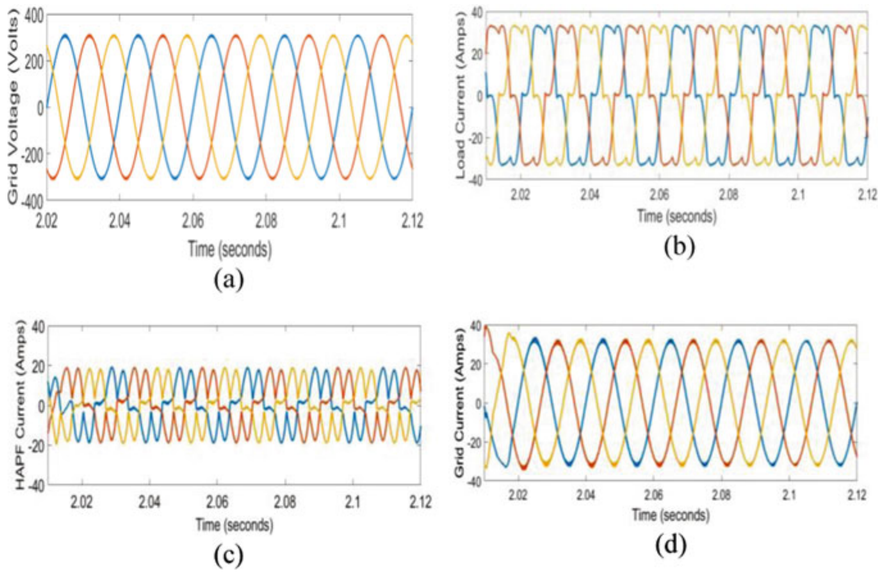

Fig. 4 Diode bridge rectifier with R-L with R load simulated waveform of, **a** grid voltage, **b** load current, **c** filter current, **d** source current

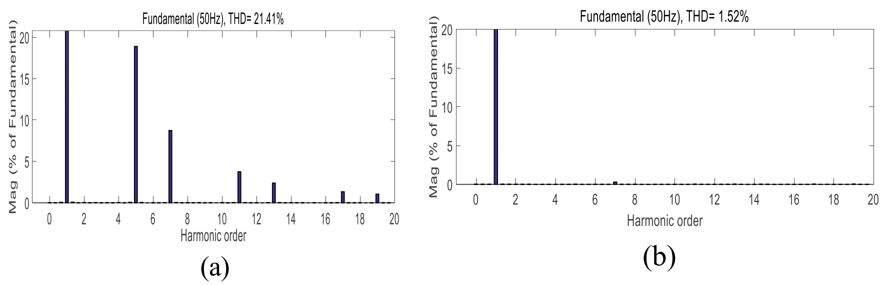

Fig. 5 FFT analysis of diode bridge rectifier with R-L and R load, **a** load current, **b** source current

Table 2 Magnitude and phase of each harmonic's contents of R-L and R Load

Harmonic order	Percentage of reduction of magnitude with the improved controller	Phase angle with the improved controller in degree
0 Hz (DC)	0.80	90.0
50 Hz (Fund)	100.00	0.9
150 Hz (h3)	0.32	268.5
250 Hz (h5)	0.06	267.3
350 Hz (h7)	0.26	129.0
450 Hz (h9)	*0.01*	*105.3*

is within IEEE-519 standard. Each content of the harmonics amplitude and phase after compensation is presented in Table 2.

4.3 *Case 3-Diode Bridge Rrectifier and R and C Load*

Three phase system with Rand C connected with the diode bridge rectifier. The simulated waveform of source voltage, load current, filter current and source current after compensation is shown in the Fig. 6a–d and corresponding FFT analysis of the source current before compensation and after compensation is shown in Fig. 7a–b, respectively. From FFT analysis, it is clearly understood that the THD without using

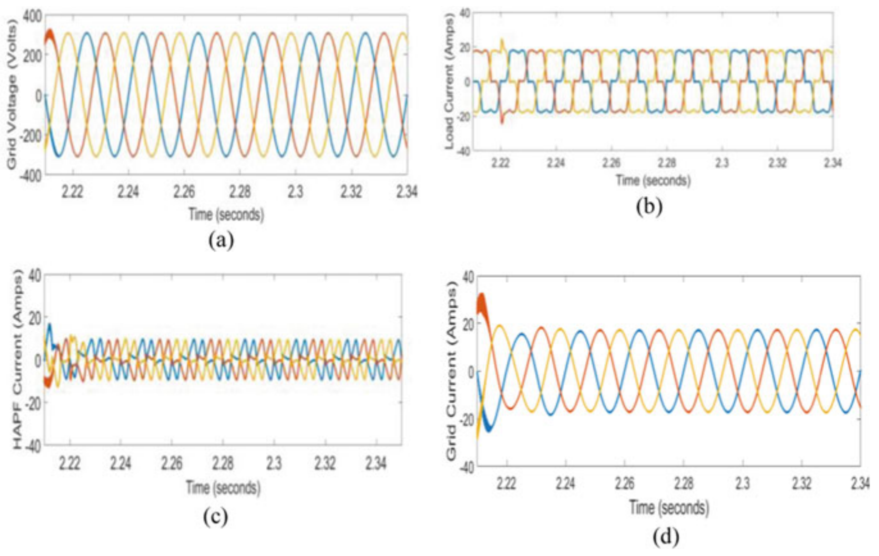

Fig. 6 Diode bridge rectifier with R–C load simulated waveform of, **a** grid voltage, **b** load current, **c** filter current, **d** source current

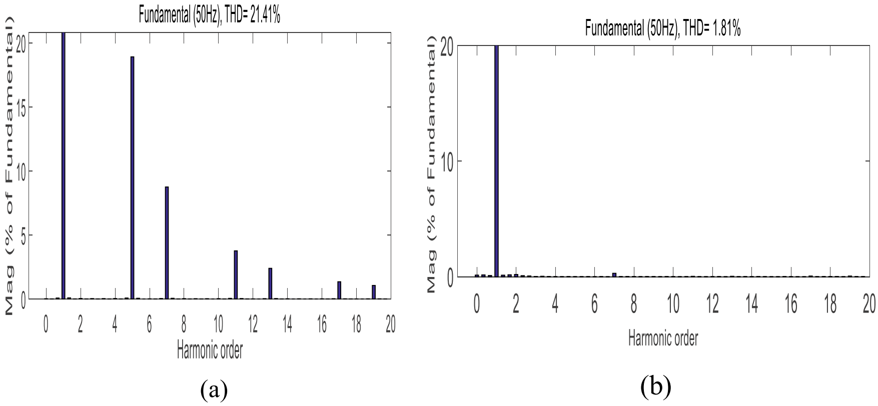

Fig. 7 FFT analysis of diode bridge rectifier with R–C load, **a** load current, **b** source current

active power filter was 21.41% and it is reducing to a value of 1.81% by connecting the developed hybrid filter with the proposed improved reactive power theory.

Each content of the harmonic's amplitude and phase before and after compensation is presented in Table 3. In Table 4, THD before and after compensation of three cases presented.

Table 3 Magnitude and phase of each harmonic's contents of R and C Load

Harmonic order	Percentage of reduction of magnitude with the Improved controller	Phase angle with the improved controller in degree
50 Hz	100.00	1.6
150 Hz	0.16	−78.8
250 Hz	2.53	188.7
350 Hz	2.07	16.6
450 Hz	*0.05*	*−62.0*

Table 4 Analysis of THD for the three different loads

S. No	Diode bridge rectifier	THD before compensation	After compensation
1	R-L	21.41	1.45
2	R-L and R	21.41	1.52
3	*R and C*	*21.41*	*1.81*

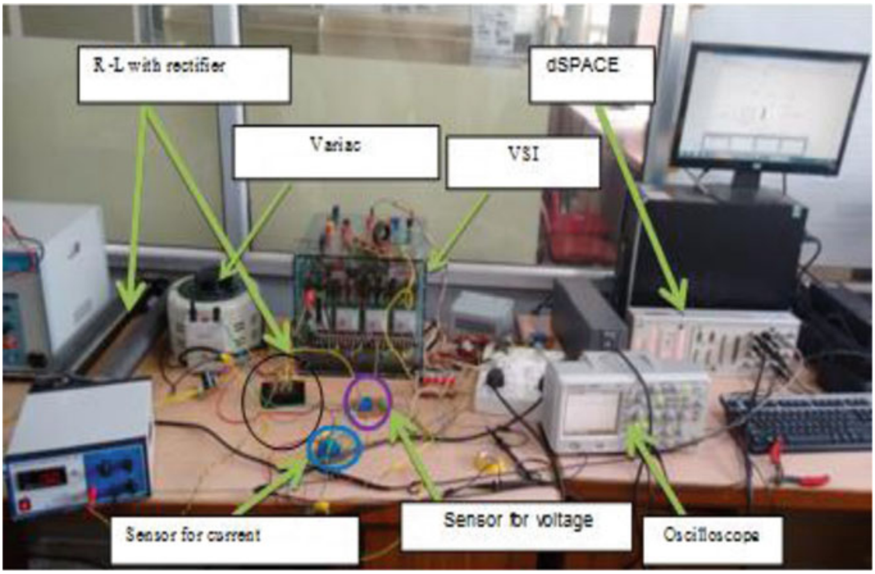

Fig. 8 Experimental setup

5 Experimental Validation

The validation of the efficiency of hybrid power filter with the discussed controller is carried out through experimental work, a laboratory prototype is set up in the power system laboratory in. For the laboratory prototype development, programmable AC source, Semikron inverter with diode bridge rectifier, resistive, inductive and capacitive load banks have been utilized. For the controller implementation dSPACE embedded control board has been employed.

This control board received sensed voltage and current signals by utilizing voltage and current sensors. By the execution of controller switching signals has been generated for the hybrid shunt power filter to provide the compensating signals. The current harmonics present in the load current due to the presence of nonlinear loads have been mitigated by the hybrid shunt filter.

The experimental setup along with the results are shown in the Figs. 8 and 9a–b, respectively. THD analysis of the experimental results shown in Fig. 10a, b.

6 Conclusions

The proposed hybrid active filter with the improved reactive power theory implementation as controller for switching operation is verified through simulation and experimentation. It is observed that improved reactive power theory with combine

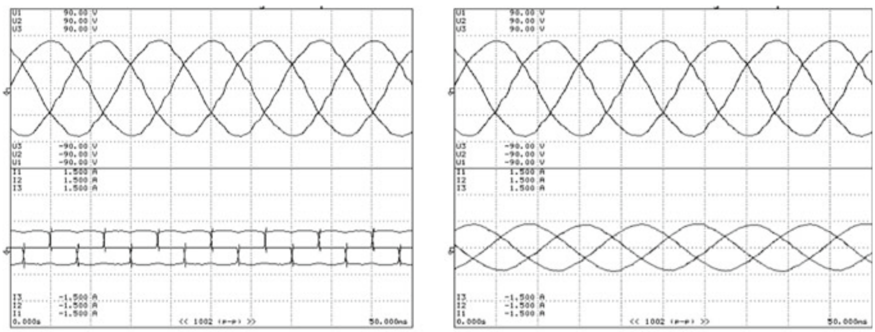

(a) (b)

Fig. 9 **a** Source voltage and load current, **b** source voltage and source current

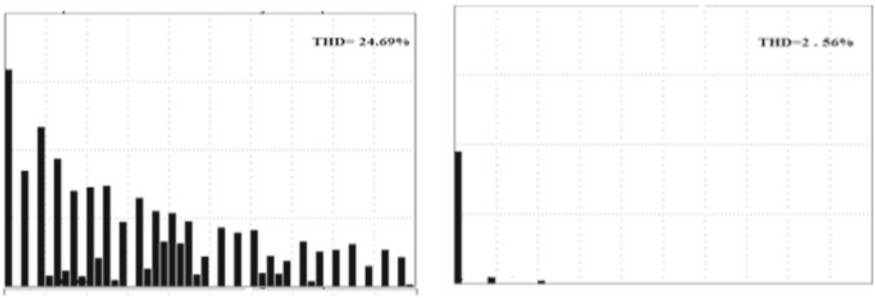

(a) THD load current **(b)** THD source current

Fig. 10 **a** THD load current, **b** THD source current

current controller works efficiently to reduce the level of harmonics in different types of load such as diode bridge rectifier with RL, R-L and R, R and C. In each case the total harmonics distortion is measured before compensation and after compensation. This result is acceptable by the standards of IEEE 519. In conventional reactive power theory the low pass filter error has not been taken into account but in this improved method error has been taken in to consideration which leads to better performance.

7 Appendix

Circuit Parameter	Values
Nominal frequency in Hz	50
Source voltage (Line Voltage) in Volt	120

(continued)

(continued)

Circuit Parameter	Values
Line inductance in H	0.001
Reference dc voltage in Volt	400
Dc bus capacitance in micro farad	1000
PI controller gain chosen	0.3
Load resistance and inductance in Ohm and Henry	3, 0.010
APF inductance value in mH	*1*

References

1. Akagi H (1996) A new trends in active filters for power conditioning. IEEE Trans Indus Appl 32:1312–1322
2. Mohan N (1993) A novel appr. to minimize line current harmonics in the interfacing power electronics equipment with 3-phase utility systems. IEEE Trans Power Deliv 8:1395–1401
3. Akagi H, Knaawaza Y, Nabae A (1984) Insta. reactive power compensators comprising switching devices without energy storage components. IEEE Trans Indus Appl 20:625–630
4. Mohan LA, Dixon JW, Wallace R (1995) A three phase active power filter operating with fixed switching frequency for reactive power and current harmonic compensation. IEEE Trans Indus Electron 42:402–408
5. Singh B, Jain C, Goel G (2016) A sustainable solar photovoltaic energy system interfaced with grid-tied voltage source converter for power quality improvement. Electr Power Compon Syst 45:171–183
6. Ibrahim WR, Morcos M (2002) Artificial intelligence and advanced mathematical tools for power quality applications. A Surv IEEE Trans Power Deliv 7:668–673
7. Puhan PS, Ray P, Panda G (2016) Development of real time implementation of 5/5 rule based fuzzy logic SAF for power quality improvement, 17(6):607–617
8. Singh B, Sahani DT, Verma A (2014) IRPT based control of a 50 kw grid interfaced solar photovoltaic power generating system with power quality improvement. In: 4th IEEE international symposium on power electronics for distributed generation systems (PEDG), pp 1–8
9. Tey LH, So PL, Chu YC (2002) Neural controlled unified power quality conditioner for system harmonics compensation. In: Proceedings of IEEE/PES transmission and distribution conference and exhibition, Asia Pacific, vol 2, pp 1038–1043
10. Puhan PS, Ray P, Panda G (2015) A comp. analysis of shunt active power filter and hybrid active power filter with different control technique applied for harmonic elimination in a single phase system. Int J Model Identif Control 24:19–28
11. Puhan PS, Ray P, Panda G (2018) A comp. analysis of artificial neural network and syn. detection controller to improve power quality in single phase system. Int J Power Electron 9:385–401
12. Dash S, Ray P (2018) Desi. and model. of single-phase PV-UPQC scheme for power quality improvement utilizing a novel notch filter-based control algorithm: an experimental approach. Arab J Sci Eng 43:3083–3102
13. Mishra S, Dash S, Ray P, Puhan S (2021) Analysis and experimental evaluation of novel hybrid fuzzy-based sliding mode control strategy for performance enhancement of PV fed DSTATCOM. Int Trans Electr Energ Syst 1–21
14. Czameckki S (2006) Instant. Reactive power p-q theory and power properties of three-phase systems. IEEE Tran Power Electron 21:362–367

15. Gupta N, Dubey SP, Singh SP (2010) Neural network based active filter for power quality improvement. In: IEEE PES general meeting, Providence, RI,USA, 1–8

Chapter 16
Space Vector Pulse Width Modulation-Based DSTATCOM for Harmonic Compensation

Pushpanjali Shadangi, Sushree Diptimayee Swain, and Gayadhar Panda

Abstract This article deals with the implementation of Distribution Static Compensator (DSTATCOM) with space vector pulse width modulation (SV-PWM) technique for harmonic compensation. To create reference current for compensation, here, we are applying Modified Instantaneous Reactive Power Theory (M-IRPT) control mechanism. Pulses pattern for switching is generated by using SV-PWM technique. Main objective of using this control mechanism is to bring down total harmonic distortion (THD) below 5% to satisfy the IEEE-519-1992 standard recommendation for THD. The proposed model is simulated by using Simulink version of MATLAB2016 for M-IRPT control scheme for SV-PWM followed by experimental verification. The obtained result is then again verified for both techniques by using SV-PWM technique and carrier-based pulse width modulation (CB-PWM).

Keywords Harmonics · DSTATCOM · Modified instantaneous reactive power theory (MIRPT) · Space vector pulse width modulation (SV-PWM) · Carrier based pulse width modulation (CB-PWM)

1 Introduction

When we talk about harmonic compensation, the first element comes in our mind is DSTATCOM [1] (distribution static compensator) is nothing but a member of flexible alternating current transmission systems [2] (FACTS) ancestry, which is fabricated to tackle all power quality-related issues. As everybody knows about the applications

P. Shadangi · S. D. Swain (✉)
O.P. Jindal University, Raigarh, India
e-mail: sushree.swain@opju.ac.in

P. Shadangi
e-mail: pushpanjali.shadangi@opju.ac.in

G. Panda
National Institute of Technology Meghalaya, Meghalaya, India
e-mail: gayadhar.panda@nitm.ac.in

G. Panda et al. (eds.), *Sustainable Energy and Technological Advancements*,
Advances in Sustainability Science and Technology,
https://doi.org/10.1007/978-981-16-9033-4_16

of nonlinear loads [3] in all the load centers, they absorb non-sinusoidal component of power for their operations. These loads like converters, switching devices, furnaces etc. These nonlinear loads generate bulk amount of distortions in the power supply, consequences of which affects the operations of all the connected devices. It disturbs the stability and power quality parameters. These nonlinear loads cause harmonic pollution in the power electronics environment. A power system is said to performs better when it satisfies all the IEEE standards. With the use of ample amount of thyristor-based devices in load centers are generating harmonic distortions [4]. There are many devices such as cyclo-converters, furnaces, thyristor rectifiers and inverter-based appliances. The nonlinear loads creates the power quality [5] problems; they create poor performance, worst power factor and also diminishes the machines working span. These creates insulation breakdown of insulators. Distribution static compensator (DSTATCOM) mitigates all harmonic content of current of higher orders. As the application of nonlinear loads are widely used by the sectors such as in industries and commercial.

Due to vast applications of nonlinear loads, harmonic distortions of power supply take place. Results into load perturbations and produces more power quality issues. Main causes of harmonics generations influences poor quality and leads to many more disturbances. DSTATCOM environment is very helpful and mature technology for reactive power compensation [6], bus voltage regulation, load balance and neutral harmonic current suppression in the mains. DSTATCOM is mainly utilized for the reactive power equilibrium and neutral current compensation [7]. It also overcomes the voltage-related issues. DSTATCOM is very much suitable for current-related power quality issues.

Performance of DSTATCOM depends upon the reference current generation scheme [8]. M-IRPT (modified instantaneous reactive power theory) is proposed by Akagi is utilized here. There are lots of methods to generate reference frames are available like instantaneous-reactive-power-theory (IRPT) [9], synchronous-frame-theory (d–q theory), modified IRPT, dual IRPT etc. Main motive of considering DSTATCOM technology is the advent of fast self-recovery from waveform distortion due to use of insulated gate bipolar transistor (IGBT) [10].

Control algorithm is designed to rectify the power factor, elimination of harmonics distortions. DSTATCOM injects the compensating current at common coupling point. DSTATCOM with some improvements is able to provide fast corrections for the dynamically changing loads such as arc furnace and traction. Pulse width modulation [11] scheme eliminates frequency fluctuation issues.

SV-PWM [12] is a specific switching plan combines six IGBTs. The switching pulses [13] of device can be adjusted easily.

SV-PWM is most versatile due to its robustness both in hardware and software. SV-PWM is very critical if it is very sophisticated while generation of switching pulses. SV-PWM depends on CB-PWM (carrier based PWM) [14] to obtain best output. Motive of writing this paper for dealing with SV-PWM, the difference between M-IRPT-SVPWM and M-IRPT, CB-PWM. To get better control such type of control scheme is required.

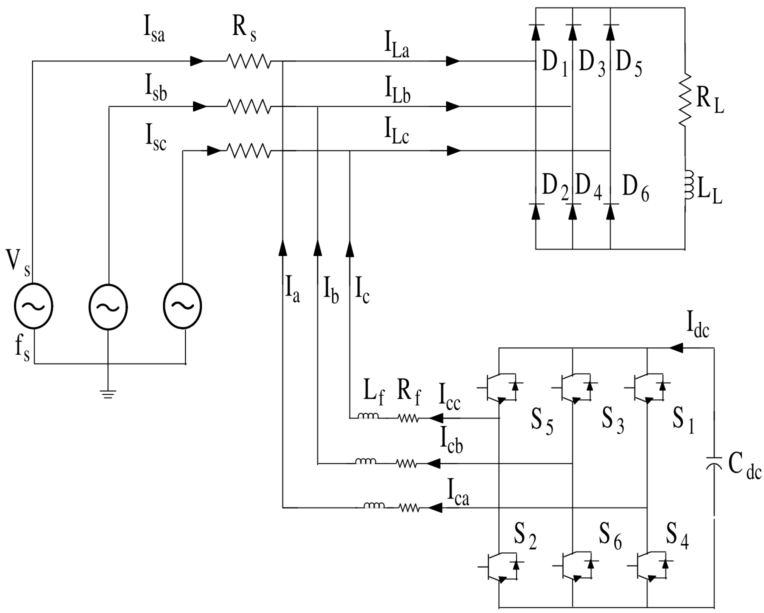

Fig. 1 Circuit diagram of DSTATCOM

In this paper, SV-PWM and CB-PWM control approach is proposed for the DSTATCOM. Proposed scheme is to enhance the compensation capability of DSTATCOM. The execution characteristics of scheme is used to maintain the power balance [15] at three-phase three-wire system.

The paper organized as: Sect. 1 dictates introduction, Sect. 2 elaborates the model configuration along with providing deep information about existing controller. Section 3 shows controller designing and mathematical analysis of M-IRPT algorithm. Section 4 explains about SV-PWM technique. Sections 5 and 6 deal with the simulation and exploratory results part respectively and the last section, i.e., Sect. 7 wind up of article with superior outcomes.

2 Model Configurations

The topology of DSTATCOM is presented by Fig. 1. The diode bridge-rectifier connected series (*R*–*L*) load, chosen as nonlinear load. R_s represents source resistance.

In M-IRPT DSTATCOM system with resistive impedance R_f and inductance, L_f of balanced source is couples with a dynamic load via transmission system.

3 Controller Design

3.1 Mathematical Modeling of Modified Instantaneous Reactive Power Theory (M-IRPT)

The IRPT is based on *a*–*b*–*c* to *d*–*q*–0. This theory considers whole into a single unit. The p-q theory is a set of real matrix which contains three phase quantities into alpha–beta stationary frame. Only $\alpha - \beta$ components will be considered here because no zero component exist in the three-phase three-conductor system analysis. In IRPT-based algorithm of DSTATCOM, load currents and voltages at the point of common coupling is sensed for calculating the instantaneous reactive and active powers as shown in Fig. 2.

$$\left[\frac{v_\alpha}{v_\beta}\right] = \sqrt{\frac{2}{3}}\begin{bmatrix} 1 & -\frac{1}{2} & -\frac{1}{2} \\ 0 & \frac{\sqrt{3}}{2} & -\frac{\sqrt{3}}{2} \end{bmatrix}\begin{bmatrix} v_{\mathrm{s}a} \\ v_{\mathrm{s}b} \\ v_{\mathrm{s}c} \end{bmatrix} \tag{1}$$

$$\left[\frac{i_\alpha}{i_\beta}\right] = \sqrt{\frac{2}{3}}\begin{bmatrix} 1 & -\frac{1}{2} & -\frac{1}{2} \\ 0 & \frac{\sqrt{3}}{2} & -\frac{\sqrt{3}}{2} \end{bmatrix}\begin{bmatrix} i_{\mathrm{L}a} \\ i_{\mathrm{L}b} \\ i_{\mathrm{L}c} \end{bmatrix} \tag{2}$$

The above two Eqs. (1) and (2), real and reactive power can be as evaluated Eq. (3).

$$\left[\frac{p}{q}\right] = \begin{bmatrix} v_\alpha & v_\beta \\ -v_\beta & v_\alpha \end{bmatrix}\begin{bmatrix} i_\alpha \\ i_\beta \end{bmatrix} \tag{3}$$

DC and AC components of active-reactive power can be written as in Eqs. (4) and (5).

$$p = \bar{p} + \tilde{p} \tag{4}$$

$$q = \bar{q} + \tilde{q} \tag{5}$$

In given expressions, DC powers must be evaluated by applying filters. Power factor correction mode is considered for power calculation as given below:

$$p = \tilde{p} + p_{\mathrm{loss}} \tag{6}$$

$$q = 0 \tag{7}$$

Reference current can be written as shown in Eqs. (8) and (9).

$$\left[\frac{i^*{}_{\mathrm{c}\alpha}}{i^*{}_{\mathrm{c}\beta}}\right] = \frac{1}{{v_\alpha}^2 + {v_\beta}^2}\begin{bmatrix} v_\alpha & v_\beta \\ -v_\beta & v_\alpha \end{bmatrix}\begin{bmatrix} \tilde{p} + p_{\mathrm{loss}} \\ -q \end{bmatrix} \tag{8}$$

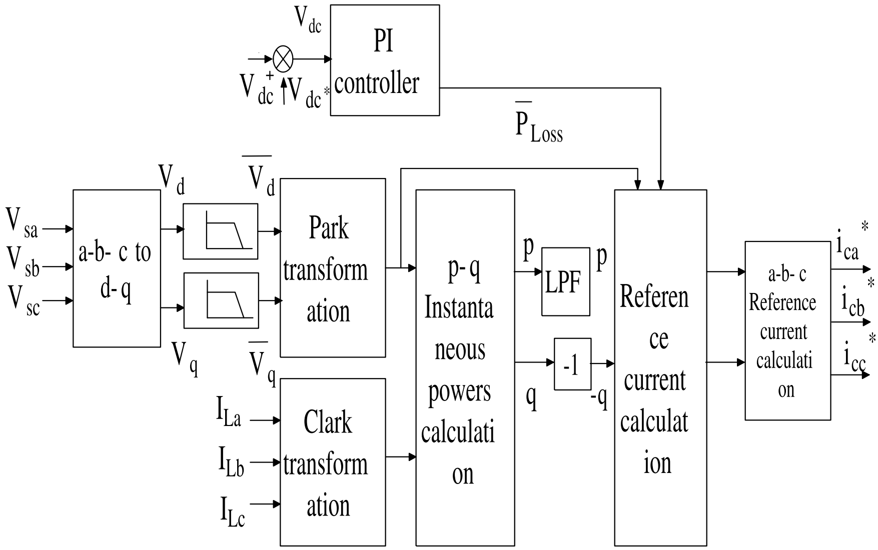

Fig. 2 Block diagram of M-IRPT reference signal generator

$$\begin{bmatrix} i^*{}_{ca} \\ i^*{}_{cb} \\ i^*{}_{cc} \end{bmatrix} = \sqrt{\frac{2}{3}} \begin{bmatrix} 1 & 0 \\ -\frac{1}{2} & \frac{\sqrt{3}}{2} \\ -\frac{1}{2} & -\frac{\sqrt{3}}{2} \end{bmatrix} \begin{bmatrix} i^*{}_{c\alpha} \\ \hline i^*{}_{c\beta} \end{bmatrix} \tag{9}$$

$$\begin{bmatrix} v_{\mathrm{d}} \\ \hline v_{\mathrm{q}} \end{bmatrix} = \sqrt{\frac{2}{3}} \begin{bmatrix} \cos\omega t & \sin\omega t \\ -\sin\omega t & \cos\omega t \end{bmatrix} \begin{bmatrix} 1 & -\frac{1}{2} & -\frac{1}{2} \\ 0 & \frac{\sqrt{3}}{2} & -\frac{\sqrt{3}}{2} \end{bmatrix} \begin{bmatrix} v_{sa} \\ v_{sb} \\ v_{sc} \end{bmatrix} \tag{10}$$

ω is the angular rotation of d–q axes. Voltages v_{d} and v_{q} as in Eq. (10) are then send to filters for harmonic filtration by using filter having cut-off 50 Hz. Harmonic filtration for voltage is given by using M-IRPT control technique for source voltage harmonics filtration to make it perfectly sinusoidal. Zero-sequence voltage components are filtered out. The obtained results after harmonics elimination, v_{d} and v_{q} are converted to $\alpha\beta$ by applying conventional IRPT method as in Eq. (11):

$$\begin{bmatrix} v_{c\alpha} \\ \hline v_{c\beta} \end{bmatrix} = \begin{bmatrix} \cos\omega t & \sin\omega t \\ -\sin\omega t & \cos\omega t \end{bmatrix} \begin{bmatrix} \overline{v_{\mathrm{d}}} \\ \hline \overline{v_{\mathrm{q}}} \end{bmatrix} \tag{11}$$

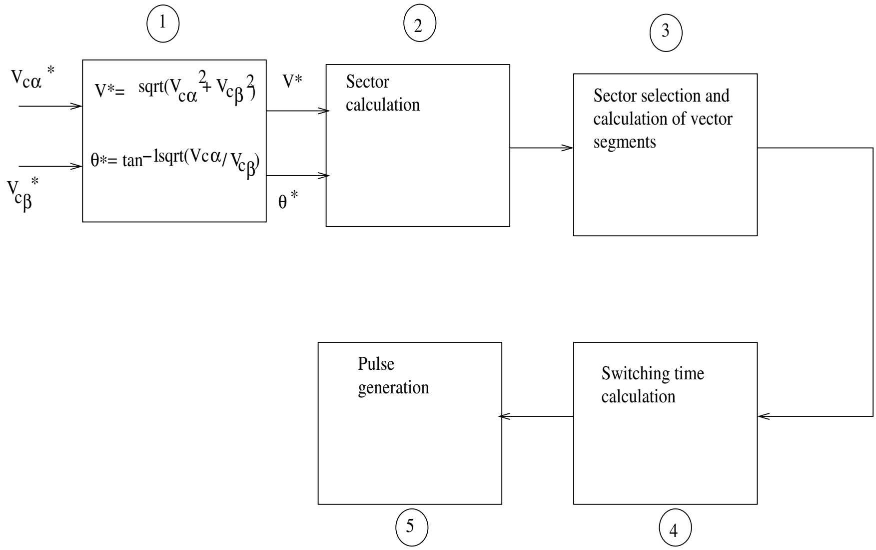

Fig. 3 SV-PWM implementation block

4 Controller Design for DSTATCOM Using SV-PWM Technology

Voltage controllers are applied to control the switching operation of IGBT's in DSTATCOM is space vector pulse width modulation (SV-PWM). It has six number of IGBT switches (from s_1 to s_6). Different switching combination are used, this controller generates many combination of outputs. This SV-PWM is an another kind of pulse width schemes. It generates a vector as a reference signal. SV-PWM method is superior than other pulse width modulation techniques. Reference vector is a testimonial recompense voltage evaluated by M-IRPT method using d–q-plane in $\alpha\beta$. The ON–OFF conditions of IGBT's are depends on the availability of recompense voltage vector on $\alpha - \beta$-plane.

Probable combination of commuting pulses are: 000, 001, 010, 011, 100, 101, 110, 111. Total eight pulses, switching pulses (v_1–v_6) and dual-zero pulse states is (V_0). There are some certain steps are required for SV-PWM control signal generation: Step-1: Calculate the reference signal magnitude and vector. Step-2: Calculation pulse duty cycle T_A, T_B, T_C for individual zone. Step-3: Determination of on-off duty of IGBT switch. Step-4: Comparison of duty triangular wave to produce six-pulses for IGBT's. Control pulse generation procedure for SV-PWM scheme is shown as Fig. 3.

Step-1: Reference voltage vector parameters is written as:

$$\left|V^*\right| = \sqrt{V_{c\alpha}^{*2} + V_{c\beta}^{*2}} \tag{12}$$

$$\theta^* = \tan^{-1}\left(\frac{V^*_{c\beta}}{V^*_{c\alpha}}\right) \tag{13}$$

${V^*}_{c\alpha}$ and ${V^*}_{c\beta}$ are recompense voltage components by M-IRPT method in $\alpha\beta$-plane, V^* is the recompense pulse vector, θ^* is angle of reference signal.

Step-2: Switching duty and switching pattern calculation: Duty period: V^* creates dual active and single zero vector. For sector-1 (0–$\pi/3$): V^* are created with V_0, V_1, V_2. V^* can be estimated in terms of time duration as:

$$V_{\text{ref}} \cdot T_c = V_1 \cdot T_1/T_2 + V_2 \cdot T_2/T_c + V_0 \cdot T_0/T_c \tag{14}$$

$$V^* = V_1 T_1 + V_2 T_2 + V_0 T_0 \tag{15}$$

T_c is the total cycle

$$T_c = T_1 + T_2 + T_0 \tag{16}$$

V^*, V_1, V_2, V_0 is written in the form of magnitude and vector as given below:

$$V^* = V^* r^{j\theta} \tag{17}$$

$$V_1 = \frac{2}{3} V_{dc} \tag{18}$$

$$V_2 = \frac{2}{3} V_{dc} e^{j\frac{\pi}{3}} \tag{19}$$

$$V_0 = 0 \tag{20}$$

$$r^{j\theta} = \cos\theta + j\sin\theta \tag{21}$$

$$e^{j\frac{\pi}{3}} = \cos\frac{\pi}{3} + j\sin\frac{\pi}{3} \tag{22}$$

Place the values of V^*, V_1, V_2 and V_0

$$T_c * V^* * \begin{bmatrix} \cos\theta \\ \sin\theta \end{bmatrix} = T_1 * \frac{2}{3} V_{dc} \begin{bmatrix} 1 \\ 0 \end{bmatrix} + T_2 * \frac{2}{3} V_{dc} \begin{bmatrix} \cos\frac{\pi}{3} \\ \sin\frac{\pi}{3} \end{bmatrix} \tag{23}$$

Separate real and imaginary terms given Eq. (23), T_1 and T_2 can be calculated as

$$T_1 = T_c * \frac{\sqrt{3} V^*}{V_{dc}} \sin\left(\frac{\pi}{3} - \theta\right) = T_c * a * \sin\left(\frac{\pi}{3} - \theta\right) \tag{24}$$

$$T_2 = T_c * a * \sin\theta, \tag{25}$$

$$0 < \theta < \frac{\pi}{3} \tag{26}$$

Modulation index is 'a'. The calculation of duty times for 'n' no. of sectors is,

$$T_1 = T_c * a * \sin\left(\frac{\pi}{3} - \theta + \frac{n-1}{3} * \pi\right) \tag{27}$$

$$T_1 = T_c * a\left[\sin\left(\frac{n\pi}{3}\right) * \cos\theta - \cos\left(\frac{n\pi}{3}\right) * \sin\theta\right] \tag{28}$$

$$T_2 = T_c * a\left[-\cos\theta * \sin\left(\frac{(n-1)\,\pi}{3}\right) + \sin\theta * \cos\left(\frac{(n-1)\,\pi}{3}\right)\right] \tag{29}$$

$$T_0 = T_c - T_1 - T_2 \tag{30}$$

Step-3: Pulse with timing evaluation for every slot contains seven switching pulse states for every cycle. For example, when first sector goes through switching states as follows: 000–100–110–111–110–100–000, one complete cycle then returns to its initial point. That happens at the interval T_c and can be divided into seven switching pulse slots. There are three zero vectors.

$$T_c = \frac{T_0}{4} + \frac{T_1}{2} + \frac{T_0}{2} + \frac{T_2}{2} + \frac{T_1}{2} + \frac{T_0}{4} \tag{31}$$

For first sector, the switch kept "ON" in duration T_0 and $T_c - \frac{T_0}{4}$ in the first cycle of phase, then between $\frac{T_0}{4} + \frac{T_1}{2}$ for second cycle of phase, and like wise. The duty period of every slot can be seen from Table 1.

Step-4: Comparison of T_1, T_2, T_0 with the triangular carrier six pulse generation needed with IGBT's.

5 Simulation Results

The block form representation of M-IRPT with SV-PWM modeled DSTATCOM can be realized by using MATLAB simulation. Effectiveness of the proposed plan is examined with verification is also confirmed. Availability of total harmonics distortions (THD), are they confined with in the IEEE standard tolerance band or not? After the examinations it can understood that the THD remains under IEEE Standard 519-1992. For the validity of M-IRPT with SV-PWM modeled DSTATCOM, two chronologies have been taken which are (i) Case-1: For diode modeled rectifier coupled to R–L type load, (ii) Case-2 For system parameter variations.

Table 1 Switching pattern generation

Sector	Top switches: S-1, S-3, S-5	Bottom switches: S-4, S-6, S-2
1	$S1 = T_A + T_B + \frac{T_0}{2}$ $S3 = T_B + \frac{T_0}{2}$ $S5 = \frac{T_0}{2}$	$S4 = \frac{T_0}{2}$ $S6 = T_A + \frac{T_0}{2}$ $S2 = T_A + T_B + \frac{T_0}{2}$
2	$S1 = T_A + \frac{T_0}{2}$ $S3 = T_A + T_B + \frac{T_0}{2}$ $S5 = \frac{T_0}{2}$	$S4 = T_B + \frac{T_0}{2}$ $S6 = \frac{T_0}{2}$ $S2 = T_A + T_B + \frac{T_0}{2}$
3	$S1 = \frac{T_0}{2}$ $S3 = T_A + T_B + \frac{T_0}{2}$ $S5 = T_B + \frac{T_0}{2}$	$S4 = T_A + T_B + \frac{T_0}{2}$ $S6 = \frac{T_0}{2}$ $S2 = T_A + \frac{T_0}{2}$
4	$S1 = \frac{T_0}{2}$ $S3 = T_A + \frac{T_0}{2}$ $S5 = T_A + T_B + \frac{T_0}{2}$	$S4 = T_A + T_B + \frac{T_0}{2}$ $S6 = T_B + \frac{T_0}{2}$ $S2 = \frac{T_0}{2}$
5	$S1 = T_B + \frac{T_0}{2}$ $S3 = \frac{T_0}{2}$ $S5 = T_A + T_B + \frac{T_0}{2}$	$S4 = T_A + \frac{T_0}{2}$ $S6 = T_A + T_B + \frac{T_0}{2}$ $S2 = \frac{T_0}{2}$
6	$S1 = T_A + T_B + \frac{T_0}{2}$ $S3 = \frac{T_0}{2}$ $S5 = T_A + \frac{T_0}{2}$	$S4 = \frac{T_0}{2}$ $S6 = T_A + T_B + \frac{T_0}{2}$ $S2 = T_B + \frac{T_0}{2}$

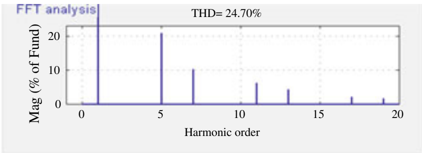

(a)

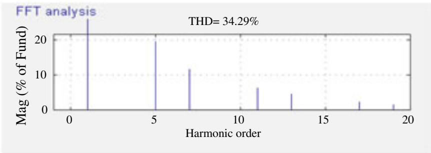

(b)

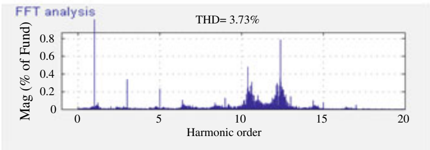

(c)

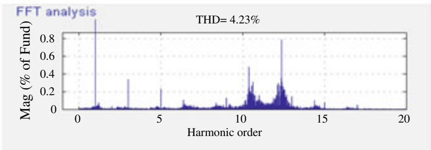

(d)

Fig. 4 Source current THD without compensation **a** Case-1, **b** Case-2; source current THD with compensation **c** Case-1, **d** Case-2

Before compensation, simulation results of source current for *R–L* load condition for Case-1 is 24.7% and for Case-2 is 34.29%. Figure 4a, b shows that THD is now reduced up to 3.73 and 4.23% displayed in Fig. 4c, d, which is very less and under the IEEE standards.

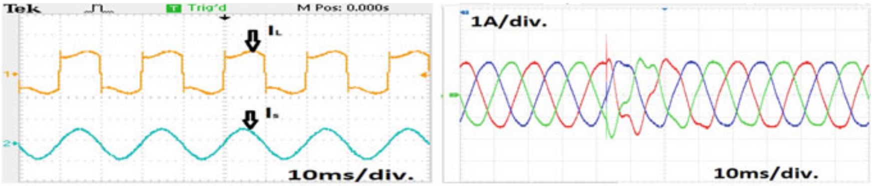

(a) (b)

Fig. 5 Experimental results obtained for **a** before compensation load current waveform, post compensation source current waveform for Case-1, **b** post compensation source current waveform of Case-2

6 Experimental Results

For validating the working characteristics of M-IRPT with SV-PWM modeled DSTATCOM, an experimental set-up has been prepared. For different load fluctuations like (i) Case-1: For diode modeled rectifier with *R*–*L* load, (ii) Case-2 For system parameter variations are taking into account for experiment. Supply voltage of value 100 V was chosen for investigation purposes. SEMIKRON-based inverter interpolates as ON-OFF component.Results obtained from hardware set ups are visualized by CRO. Figure 5a displays load current waveform before compensation and source-current post corrections for Case-1. The experimental source current waveforms with by M-IRPT modeled DSTATCOM for Case-2 displayed by Fig. 5b.

7 Conclusion

DSTATCOM implemented with control algorithm of M-IRPT with SV-PWM as a reference signal generation has been proposed in this paper. This strategy exploits harmonic components by employing proposed control approach. As we all know that conventional control technique-based DSTATCOM has been studied by many researchers are very simple in realization achieved good performance under specific load dynamics. But there is a time delay in the conventional methods found, hence, the DSTATCOM performance became slow. Hence, harmonic suppression is not fast. Therefore, a SV-PWM along with M-IRPT based DSTATCOM is developed. A real-time realization of DSTATCOM model has been executed on experimental hardware set up. Simulation using MATLAB as well as exploratory performances proves the efficaciousness of the model SV-PWM with M-IRPT approach. Source current output obtained from simulation without compensation with *R*–*L* load for Case-1 is 24.7% and for Case-2 is 34.29%. Figure 4 shows that the THD is decreased up to 3.73 and 4.23%. From experimental result, we can see the clarity and smoothness of load current and source current wave forms. This investigation specifies the requirement of compensating network set up with appropriate control mechanism is required while working with any kind of power system functioning.

References

1. Kumar C, Mishra MK, Mekhilef S (2020) A new voltage control strategy to improve performance of DSTATCOM in electric grid. CES Trans Electr Mach Syst 4(4):295–302
2. Parastvand H, Bass O, Masoum MAS, Chapman A, Lachowicz S (2020) Cyber-security constrained placement of FACTS devices in power networks from a novel topological perspective. IEEE Access 8:108201–108215
3. Ahmed NA, Alhuwaishel FM (2021) Solar powered unmanned aerial vehicle with active output filter under non-linear load conditions. IEEE Access 9:77212–77228
4. Hernández-Barrios Y, Cerdeira A, Tinoco J, Iñiguez B (2019) Features of the nonlinear harmonic distortion in AOSTFTs. IEEE Trans Electron Devices 66(12):5177–5182
5. Yu J, Xu Y, Li Y, Liu Q (2020) An inductive hybrid UPQC for power quality management in premium-power-supply-required applications. IEEE Access 8:113342–113354
6. Ismail B, Abdul Wahab NI, Othman ML, Radzi MAM, Naidu Vijyakumar K, Mat Naain MN (2020) A comprehensive review on optimal location and sizing of reactive power compensation using hybrid-based approaches for power loss reduction, voltage stability improvement, voltage profile enhancement and loadability enhancement. IEEE Access 8:222733–222765
7. Zhu H, Yang Z, Sun X, Wang D, Chen X (2020) Rotor vibration control of a bearingless induction motor based on unbalanced force feed-forward compensation and current compensation. IEEE Access 8:12988–12998
8. Lei X, Chan C-H, Zhu Y, Martins RP (2019) A 4-b 7-μ W phase domain ADC with time domain reference generation for low-power FSK/PSK demodulation. IEEE Trans Circuits Syst I Reg Pap 66(9):3365–3372
9. Jiao S, Ramachandran Potti KR, Rajashekara K, Pramanick SK (2020) A novel DROGI-based detection scheme for power quality improvement using four-leg converter under unbalanced loads. IEEE Trans Ind Appl 56(1):815–825
10. Wang B et al (2021) Thermal performances and annual damages comparison of MMC using reverse conducting IGBT and conventional IGBT module. IEEE Trans Power Electron 36(9):9806–9825
11. Qamar MA, Wang K, Zheng Z, Wang S, Li Y (2020) A simplified virtual vector PWM algorithm to balance the capacitor voltages of four-level diode-clamped converter. IEEE Access 8:180896–180908
12. Richardson MT, Patterson V, Parchment A (2021) Microcontroller based space vector pulse width modulation speed control of three-phase induction motor. In: SoutheastCon 2021, pp 1–6
13. Li Q, Chen J, Jiang D (2020) Periodic variation in the effect of switching frequency on the harmonics of power electronic converters. Chin J Electr Eng 6(3):35–45
14. Odeh CI, Lewicki A, Morawiec M (2021) A single-carrier-based pulse-width modulation template for cascaded H-bridge multilevel inverters. IEEE Access 9:42182–42191
15. Chu G, Wen H, Hu Y, Jiang L, Yang Y, Wang Y (2020) Low-complexity power balancing point-based optimization for photovoltaic differential power processing. IEEE Trans Power Electron 35(10):10306–10322

Chapter 17
PV-Fed DC Link Voltage Control Techniques Implementation in Shunt Active Filter

Padiyar Dharani Deepika and Pratap Sekhar Puhan

Abstract Issues of power quality on combined conventional and non-conventional-based sources and its solution are one of the recent researches in the area of power quality. This paper presents power quality improvement using a PV-fed shunt active power filter. The proposed system is designed to keep two things in mind: PV-based renewable source is used to maintain the capacitor voltage of inverter constant and also maintain the supply as and when required and conventional PQ theory and P&O algorithm used in the system for smooth operation of the filter and maximum power point tracking, respectively. The performance of the proposed system is verified through simulations.

Keywords Harmonics · PQ · SAPF · PQ theory · P&O · MPPT

1 Introduction

Harmonics in generating station is very less, and it is negligible, but in distribution system, it is becoming more and more as the use of power semiconductor devices increases in a rapid rate in the recent age [1–3]. Starting from the domestic sector to other important sector such as industrial, communication and transportation, electronics equipment plays the major role as load. These loads are nonlinear in nature and draw nonlinear current from the source; the nonlinear current that multiplies with source impedances results in nonlinear voltage; when this nonlinear voltage is removed from the sinusoidal source voltage, the result is a non-sinusoidal voltage which will appear across the point of common coupling in the distribution system [4–6] and affect the operation and performance of all other equipment connected to the same PCC [3], so it is crucial and necessary to maintain the voltage across all the loads constant so that the power quality can be maintained properly [7, 8].

P. D. Deepika · P. S. Puhan (✉)
Department of Electrical and Electronics Engineering, Sreenidhi Institute of Science and Technology, Hyderabad 501301, India
e-mail: pratapsekhar@sreenidhi.edu.in

G. Panda et al. (eds.), *Sustainable Energy and Technological Advancements*, Advances in Sustainability Science and Technology,
https://doi.org/10.1007/978-981-16-9033-4_17

The effect of these harmonics is suppressed through different types of arrangement in the past. Recent development trends are toward the active filters, hybrid filters, etc. [9]. Though many work in the literature discussed the performance development of different types of filters [10] using various techniques to improve the power quality in a distribution system, still research is going on for further development in this area [11].

The use of conventional source of energy in the recent age is not only creating different types of adverse effect such as stability issues, pollution of the environment [7], but also it gradually depleted, so the alternative is the renewable energy source, and now, distributed generations are coming with a large number. The combination of conventional and non-conventional-based power systems is one of the best alternatives for stability and environmental aspect.

In this work, a system is proposed to eliminate the impact of harmonics contents and maintain the power quality, and a shunt active filter is designed to eliminate the harmonics due to the nonlinear load. The accurate operation of the filter not only depends on the reference signal generation technique but also depends on the magnitude of the DC voltage across the voltage source converter. In order to maintain the voltage constant a PV source is fed to it, the main objective of the PV connection is maintaining voltage of the filter and giving supply to the load as and when required. Though several work is reported in this area [12, 13], the design aspect and proper control implementation in the active power and proper operation of the PV source play the major role for further performance improvement to maintain the power quality.

The paper's introduction is discussed in Sect. 1 which includes some reviews based on power quality analysis through different configuration, Sect. 2 presents the proposed system of the work, Sect. 3 presents the details about maximum point tracking and the PQ theory implementation for generation of reference signals, and Sects. 4 and 5 present the result and analysis and conclusions, respectively.

2 Proposed System

The proposed system is designed to keep two problems in mind: First, the system supply will continue throughout the operation and harmonics contents suppression due to load. The system consists of both conventional and non-conventional PV sources, a shunt active filter, and diode bridge rectifier along with *R*–*L* as load. The used filter is a voltage source filter which constitutes of six IGBT and DC link capacitor. To maintain the voltage in the link constant throughout the operation for successful switching action of the inverter, PV source is fed to the capacitor through a boost converter which consists of several components such as IGBT, inductor, capacitor, and a diode bridge as shown in Fig. 1. The PV source is associated with voltage and current sensors as it is required for MPPT. MPPT controller gives the signal to the boost converter as and when required. The control technique implementation is in the proposed filter, and PV source is described in the next section.

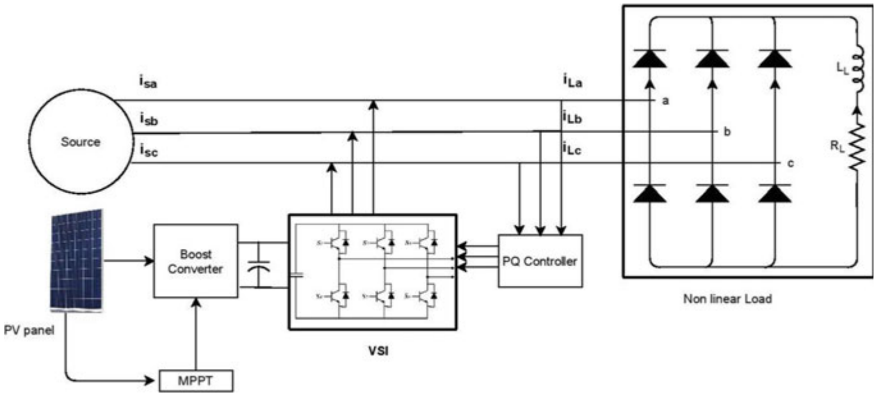

Fig. 1 Basic configuration of the system

3 Control Techniques in the Proposed System

In this work, two important control techniques are implemented to the PV source and proposed filter to extract the maximum power and generation of the reference signals, respectively. The control techniques are described separately for simplicity.

3.1 MPPT Algorithm Implementation in PV Source

PV cell along with DC/AC modules frames the PV system. When the PV system comes under the influence of sunlight, photons are observed and develop hole which is proportional to the radiation. The output current equations for the analysis and maximum power point tracking using P&O algorithm are accessible from Fig. 2 and flowchart in Fig. 3.

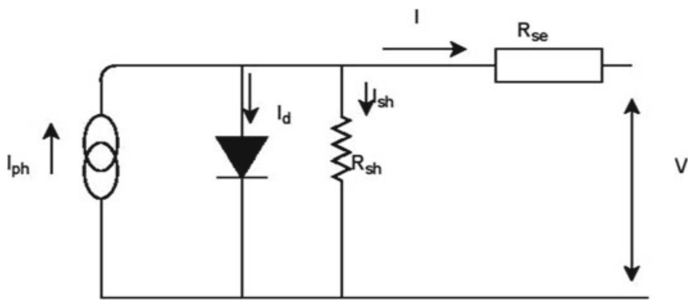

Fig. 2 Proposed circuit of PV system

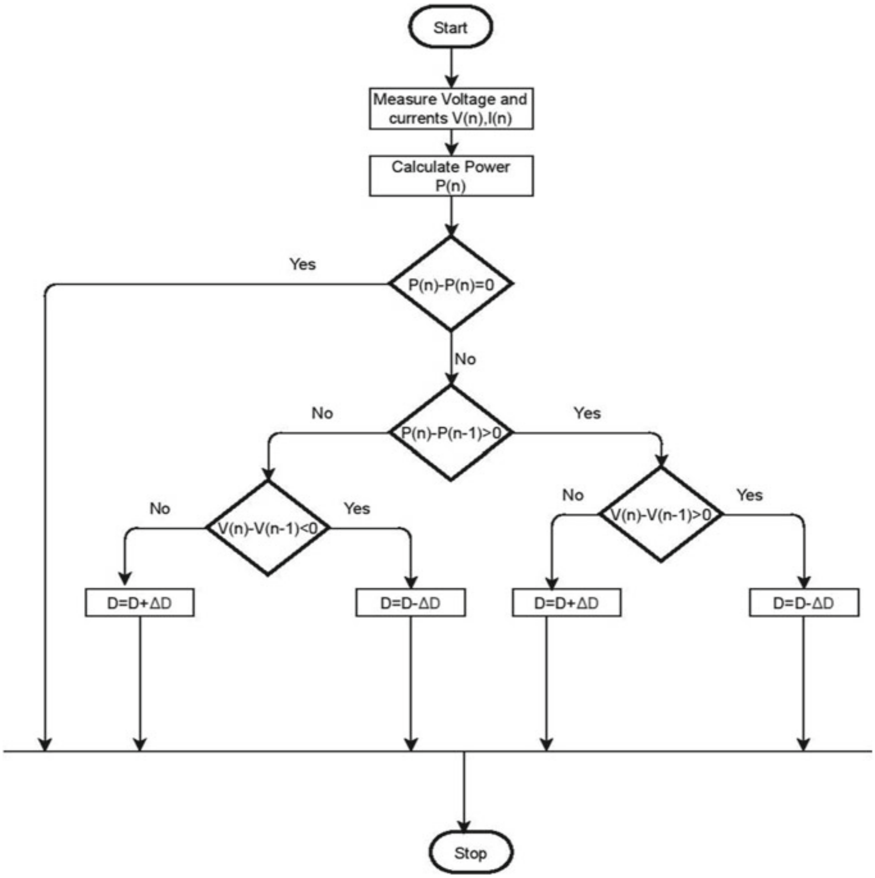

Fig. 3 Flowchart for P&O algorithm

In the given figure, the total current and photon current are related by the equations

$$I = I_{\text{phi}} - I_{\text{di}} - I_{\text{shi}} \tag{1}$$

I_{phi}, I_{di}, I_{shi} stand for light, diode, and resistance current.

Ideal diode current magnitude is expressed as

$$I_{\text{di}} = I_0\left[\exp(v + I R_{\text{sh}}/n v_{\text{t}}) - 1\right] \tag{2}$$

n, I_0, v_{t} stand as diode factor, current saturation, and voltage in the thermal range. $v_{\text{t}} = \frac{K T_{\text{c}}}{Q}$. K is constant.

Combining the equation for diode current and shunt current, the output current equation is given by

$$I = I_{\mathrm{Phi}} - I_0\big[\exp(v + I R_{\mathrm{sh}}/n v_{\mathrm{t}}) - 1\big] - \frac{v + I_{\mathrm{shi}}}{R_{\mathrm{sh}}} \tag{3}$$

The most popular algorithm P&O is used in this work which is dependent on current and voltage incremental conductance values to track maximum power point (MPP) due to its simplicity [7, 12]. The VI Characteristics and PV characteristics are shown in (Figs. 4 and 5). The P&O algorithm can be understood by the flowchart as shown in Fig. 6 and used in this work to track the maximum power.

As per the work, IV and PV characteristics are extracted at a value of 1000 W/m, 2500 W/m^2, and 100 W/m^2 at 25 °C and are presented in Figs. 7 and 8, respectively. The solar power increases as radiation increases, keeping temperature constant, and solar power decreases as temperature varies, keeping radiation constant.

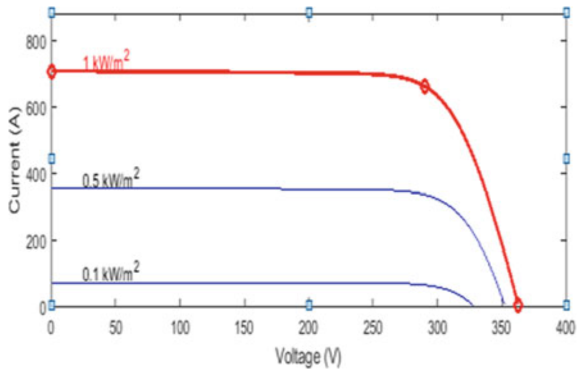

Fig. 4 *V–I* characteristics of solar panel

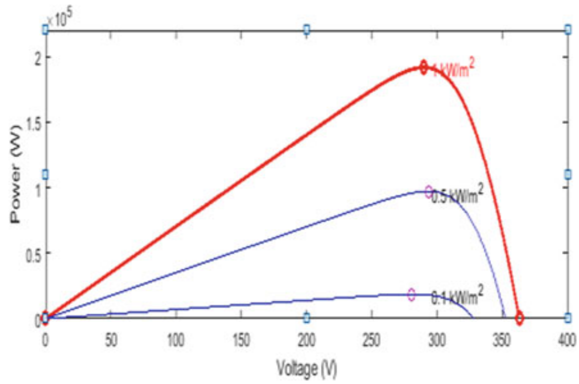

Fig. 5 PV characteristics of solar panel

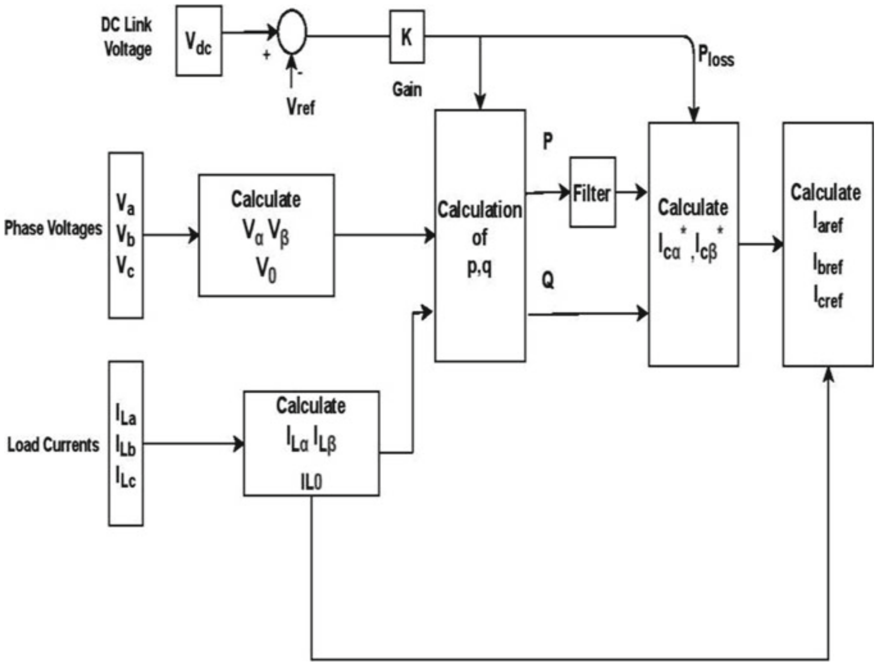

Fig. 6 Block diagram of PQ theory

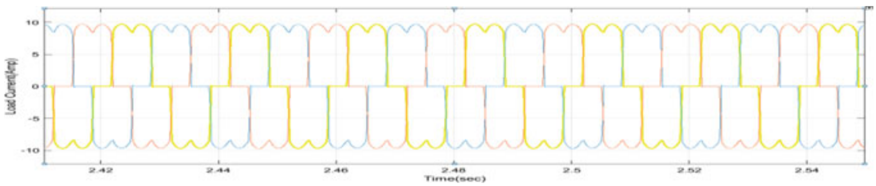

Fig. 7 Load current

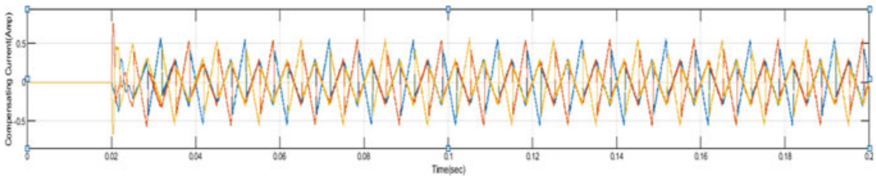

Fig. 8 Compensating current

3.2 PQ Theory Implementation in the Proposed Filter

The accurate switching signal generation of the proposed shunt active filter for injection of compensating current is achieved if the reference signal generation is appropriate. Many works in the literature reported PQ theory for its accurate estimation of reference signal [12], and this work is also PQ theory [13]. The mathematical steps presented are followed by the block diagram shown in Fig. 6, assuming the voltage of the voltage source inverter is constant, and it is maintained by the PV system.

This theory transforms the voltage and current of the load into two components as α, β followed by the below equations

$$\begin{bmatrix} V_\alpha \\ V_\beta \end{bmatrix} = \sqrt{\frac{2}{3}} \begin{bmatrix} 1 & -\frac{1}{2} & \frac{1}{2} \\ 0 & \frac{\sqrt{3}}{2} & -\frac{\sqrt{3}}{2} \end{bmatrix} \begin{bmatrix} V_a \\ V_b \\ V_c \end{bmatrix} \tag{4}$$

$$\begin{bmatrix} i_{\mathrm{L}\alpha} \\ i_{\mathrm{L}\beta} \end{bmatrix} = \sqrt{\frac{2}{3}} \begin{bmatrix} 1 & -\frac{1}{2} & \frac{1}{2} \\ 0 & \frac{\sqrt{3}}{2} & -\frac{\sqrt{3}}{2} \end{bmatrix} \begin{bmatrix} i_{\mathrm{L}a} \\ i_{\mathrm{L}b} \\ i_{\mathrm{L}c} \end{bmatrix} \tag{5}$$

Active and reactive power at a particular instant under consideration

$$\begin{bmatrix} P_\mathrm{L} \\ Q_\mathrm{L} \end{bmatrix} = \begin{bmatrix} V_\alpha & V_\beta \\ V_\beta & -V_\alpha \end{bmatrix} \begin{bmatrix} i_{\mathrm{L}\alpha} \\ i_{\mathrm{L}\beta} \end{bmatrix} \tag{6}$$

P_L and Q_L are expressed as follows

$$\begin{aligned} P_\mathrm{L} &= \tilde{P} + p \\ Q_\mathrm{L} &= \tilde{Q} + q \end{aligned} \tag{7}$$

where $\tilde{P}$, p, $\tilde{Q}$, q stand as desired real, compensating, desired reactive, and compensating power at the particular instant.

Compensating power is expressed as follows in Eq. 7

$$\begin{aligned} p_\mathrm{c} &= -p + p_\mathrm{loss} \\ q_\mathrm{c} &= -q_\mathrm{L} \end{aligned} \tag{8}$$

where loss compensation is done by active power loss as p_loss. Inversion of matrix takes the loss component into consideration for reference

$$\begin{bmatrix} i^*_{\mathrm{c}\alpha} \\ i^*_{\mathrm{c}\beta} \end{bmatrix} = \frac{1}{v_\alpha^2 + v_\beta^2} \begin{bmatrix} V_\alpha & V_\beta \\ V_\beta & -V_\alpha \end{bmatrix} \begin{bmatrix} -p + p_\mathrm{loss} \\ -q_\mathrm{L} \end{bmatrix} \tag{9}$$

$$\begin{bmatrix} i_{a\text{ref}} \\ i_{b\text{ref}} \\ i_{c\text{ref}} \end{bmatrix} = \sqrt{\frac{2}{3}} \begin{bmatrix} 1 & 0 \\ -\frac{1}{2} & \frac{\sqrt{3}}{2} \\ \frac{1}{2} & \frac{-\sqrt{3}}{2} \end{bmatrix} \begin{bmatrix} i_{c\alpha}^{*} \\ i_{c\beta}^{*} \end{bmatrix} \tag{10}$$

For separation of the instantaneous power direct term from alternating one, a low pass filter (LPF) with feedforward effect is used. DC link voltage regulator is responsible for compensation as well as for transient response. Hence, the actual value of DC capacitor voltage has to be compared with the reference one, and the differential error is fed to a PI control.

4 Results and Analysis

The results of simulation of PV-fed filter can be observed in the figures. Proposed filter is perfectly filtered out the harmonics by using PQ theory which reduces the THD of the system and improves power quality of the system and also supplies the PV output power to the load. The simulated waveform of the load current is presented in Fig. 7, the load current signal is distorted, and to make it sinusoidal, filter current is injected from the shunt active filter after $t = 0.02$ s. The simulated waveform of the filter current and source current is shown in Figs. 8 and 9, and the source voltage is shown in Fig. 10.

At $t = 2$ s, PV system is connected. Figures 11 and 12 present the DC voltage with and without PV and source current with and without PV, and source current is decreased as the PV system is connected at $t = 2$ s to $t = 5$ s which means the contribution of power to load is higher from PV. The transfer of real power from source to the load also reduced at $t = 2$ s as shown in Fig. 13 means the higher contribution from solar. Figure 14 shows the active power which is compensated at $t = 0.02$ the shunt active filter.

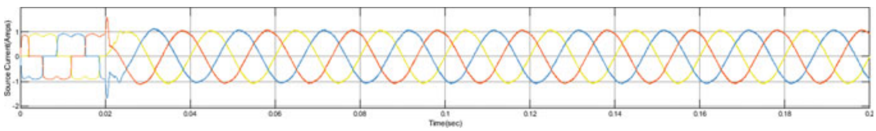

Fig. 9 Source current

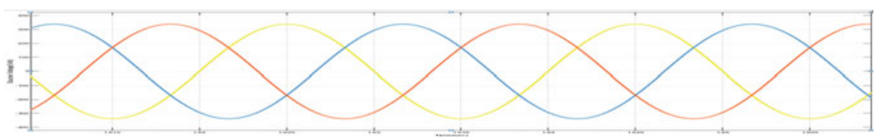

Fig. 10 Source voltage

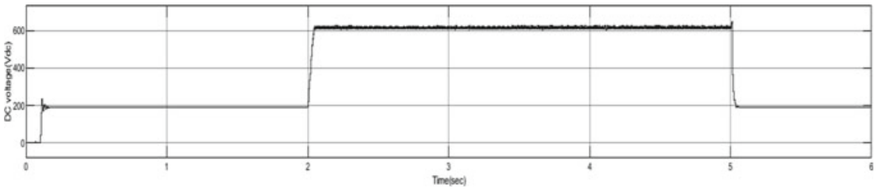

Fig. 11 DC voltage with and without PV

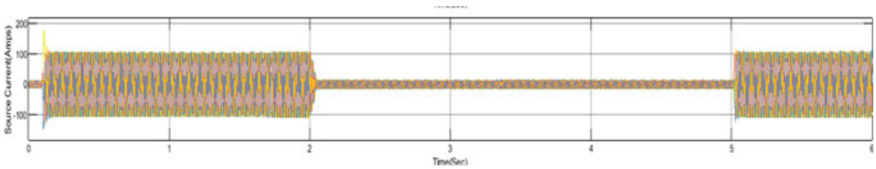

Fig. 12 Source current with and without PV

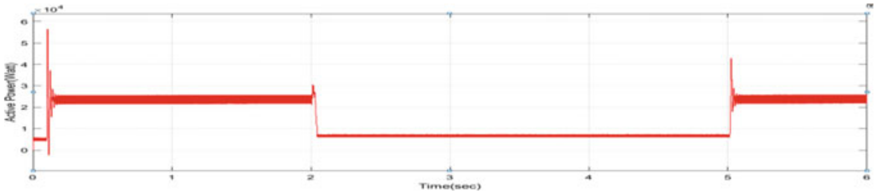

Fig. 13 Active power with and without PV

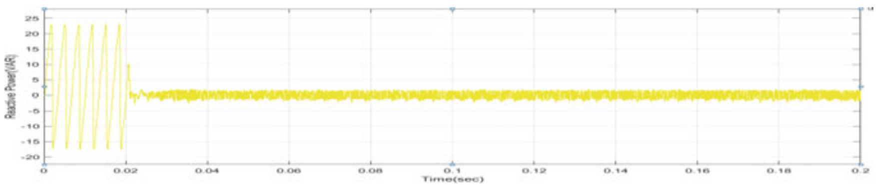

Fig. 14 Reactive power with and without PV

The analysis of power quality with PV and without PV is carried out through total harmonics distortions (THD). In the presence of nonlinear load, the harmonics content is 28.33% of fundamental as shown in Fig. 15. The moment the filter is on it comes down to 4.98% of fundamental, and when PV is fed to shunt, it comes down to 3.33% of fundamental followed in Figs. 16 and 17, respectively.

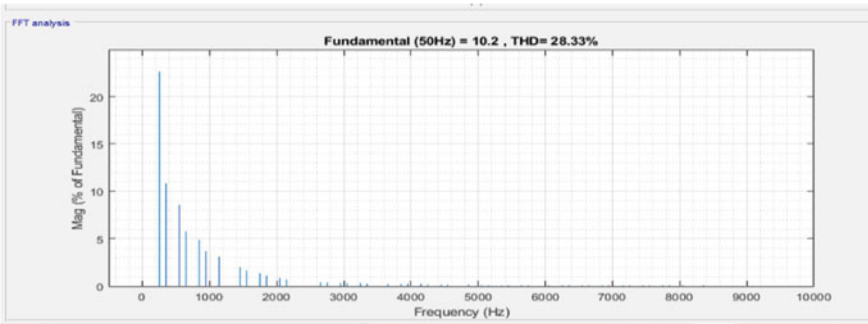

Fig. 15 THD analysis without filter

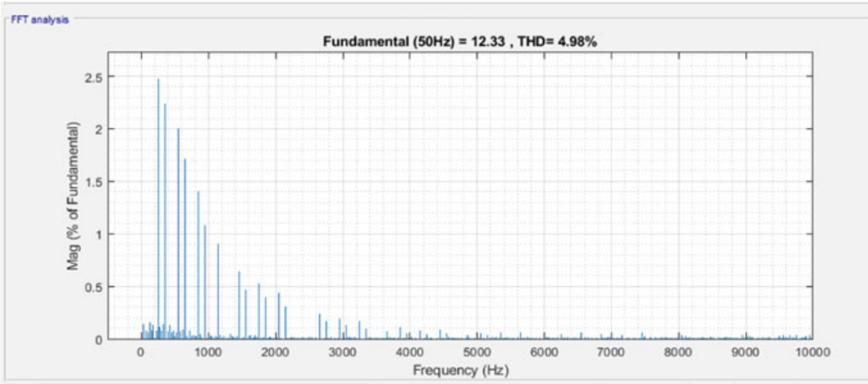

Fig. 16 THD analysis without PV

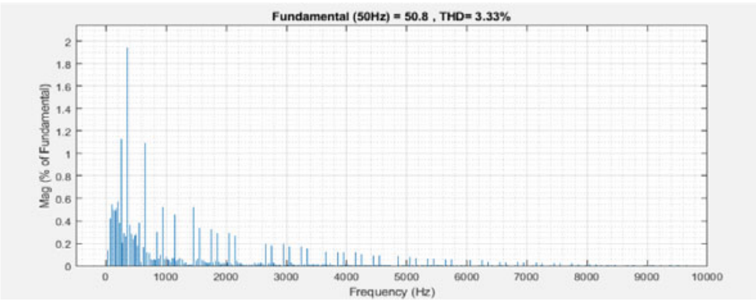

Fig. 17 THD analysis of shunt active filter with PV

5 Conclusions

The efficient operation of the proposed system for the power quality is verified through simulation. PV-fed shunt active power filter not only reduces the harmonics contents in the signals efficiently but also compensates the reactive power in an efficient manner. MPPT algorithm implementation is suitable to export the maximum active power to the load as and when required. It also supplies the PV power to the load the moment when some disturbances occurred in the conventional system. THD analysis of source current without PV gives good results, but with PV, the performance is improved by reducing the harmonics contents which are within the IEEE 519 standard.

References

1. Math B (1999) Understanding power quality problem. Wiley
2. Padmavathi K, Sudha K (2019) Optimal sizing and placement of dynamic voltage restorer in the distribution system using firefly algorithm. Int J Energy Technol Policy 15:148–165
3. Zhou Y, Li H (2014) Analysis and suppression of leakage current in cascaded multilevel inverter based PV systems. IEEE Trans Power Electron 29:5265–5277
4. Singh M, Khadkikar V, Chandra A, Verma K (2011) Grid interconnection of renewable energy sources at the distribution level with power quality improvement features. IEEE Trans Power Delivery 26(1):307–315
5. Puhan PS, Ray P, Panda G (2015) A comparative analysis of shunt active power filter and hybrid active power filter with different control technique applied for harmonic elimination in a single phase system. Int J Model Identif Control 24:19–28
6. Vavilapalli S, Padmanaban S, Subramaniam U, Mihet-Popa L (2017) Power balancing control for grid energy storage system in photovoltaic applications—real time digital simulation implementation. Energies 10:928
7. Baratar D, Buticchi G, Lorenzani E, Concari C (2014) Active common-mode filter for ground leakage current reduction in grid-connected PV converters operating with arbitrary power factor. IEEE Trans Ind Electron 61:3940–3950
8. Babes B, Rahmani L, Bouafassa A, Hamouda N (2005) Real time implementation of shunt active power filter for harmonic suppression and power quality improvement. IEEE Trans Ind Electron 52
9. Dehini R, Ferdi B, Dib SL (2013) Influence des paramètres du réseau électrique sur le filtrage des harmoniques. Mediamira Sci Publ 54
10. Djeghloud H, Bentounsi A, Benalla H (2011) Sub and super-synchronous wind turbine-doubly fed induction generator system implemented as an active power filter. Int J Power Electron 3(2)
11. Puhan PS, Ray P, Panda G (2018) A comparative analysis of artificial neural network and synchronous detection controller to improve power quality in single phase system. Int J Power Electron 9:385–401
12. Romero-Cadaval E, Spagnuolo G, Franquelo LG, Ramos-Paja C-A, Suntio T, Michael Xiao W (2013) Grid-connected photovoltaic generation plants. IEEE Ind Electron 7(3):6–20
13. Akagi H, Kanazawa Y, Nabae A (2008) Instantaneous reactive power compensators comprising switching devices without energy storage components. IEEE Trans Ind Appl 3:625–630

Chapter 18
Detection and Classification of Transmission Line Faults Using ANN

Parveen Poon Terang, Sanjiba Kr Bisoyi, Chitra Ranjan, Aviral Krishna, Aysuh Raman Rai, and Anushka Singh

Abstract Transmission lines of any electrical power system are a crucial means to provide electricity continuously to the end consumers. However, since these transmission lines are vulnerable to their surroundings, there are higher chances of an event leading to a run down. Such a disruption needs to be remedied quickly to protect the power system and continue the flow of electricity as per demand. Therefore, this paper has an objective to present a valid solution to control such a situation for betterment of the power system. The work attempted in this paper is an absolute, reliable and swift technique using the artificial neural network (ANN) to detect and classify the faults that occur in electrical transmission lines. The proposed idea takes into account an IEEE 9 bus system for generating data sets for training the ANN. Implementation of the presented method is done on the IEEE 9 bus system for detection and identification of fault types to provide evidence of its credibility.

Keywords Artificial neural network · Backpropagation · Fault detection · Fault classification · IEEE 9 bus system · Mean square error (MSE)

1 Introduction

Transmission lines are an integral segment of the electrical system that is complex and spreads over an extensive area and performs a pivotal role of connecting both the generation and the distribution subsystems. They transfer power to the load sites making them a crucial segment of the electrical power system. Exposure of transmission lines to the environment makes them susceptible to the surrounding, subsequently making them more prone to faults. There could be various environmental

P. P. Terang · S. K. Bisoyi · C. Ranjan · A. Krishna (✉) · A. R. Rai · A. Singh
Department of Electrical Engineering, JSS Academy of Technical Education, Noida, India

P. P. Terang
e-mail: ppterang.eed@jssaten.ac.in

S. K. Bisoyi
e-mail: sanjibabisoyi.eed@jssaten.ac.in

G. Panda et al. (eds.), *Sustainable Energy and Technological Advancements*, Advances in Sustainability Science and Technology,
https://doi.org/10.1007/978-981-16-9033-4_18

conditions responsible for the occurrence of faults such as strong winds, storms or deposition of snow or ice on the lines. Fault is an anomalous condition of flow of current in the electrical system [1]. The faults that occurred could be open and also could be a short-circuit fault [1]. Open circuit or series fault disturbs the symmetry of the system and causes unbalance. The short-circuit fault can be classified further into two parts. Symmetrical faults, i.e. three-phase fault is an acute fault occurring albeit it occurs rarely. When a conductor comes in contact with the ground, an L–G fault takes place. Seventy per cent of L–G faults occur, whereas L–L or L–L–G faults occur 15% and 10% times, respectively. The unsymmetrical faults have to be corrected as soon as possible to avoid the cascading of faults which could lead to a three-phase fault which damages the entire system. Pressure is applied on the system during a fault that is capable of harming the insulation and the various other elements of the system [2–4]. In order to rectify the fault, it is paramount to determine and classify the faults. Different methods each having their own pros and cons have been invented through the course of time, namely Fourier transform [5, 6], wavelet method [7–9], fuzzy logic [10–12], artificial neural network [13–15]. Researchers these days are inclined towards the use of intelligent methods so as to obtain a better result for fault recognition.

In this paper, an attempt has been made to lay emphasis on the application of artificial neural network (ANN) for obtaining a system that determines and classifies the faults occurring in an IEEE 9 bus system. ANN is a popular technique when it comes to prediction and modelling because of its generalization capacity, robustness, high processing speed and tolerance to faults even in large and complex systems. The system in this work takes into account all the ten faults that occur in the system. MATLAB/Simulink is used for simulation of the 9 bus system, and the neural network toolbox is used for the detection and classification purpose.

2 Proposed System

The standard system taken into consideration is IEEE 9 bus system. This system consists of nine buses, three sources, three transformers, three loads and one fault box. Here, the three sources include two PV generators and one swing generator. In the case of buses, Bus 1 is a slack bus connected with a swing generator, and Buses 2 and 3 are voltage buses connected with a PV generator. All the remaining buses are load buses connected with the three loads. The loads taken are three-phase RLC parallel loads. All the transformers here are step-up transformers, a transformer at Bus 1 steps-up the voltage from 16.5 to 230 kV, a transformer at Bus 2 steps-up the voltage from 18 to 230 kV, and a transformer at Bus 3 steps-up the voltage from 13.8 to 230 kV. A nominal pi model transmission line is taken here, having a length 100 km, and the frequency used for RLC specification is 60 Hz. The fault box, which is placed in between two buses, is there to provide the type of fault which is to be considered in this system (Fig. 1).

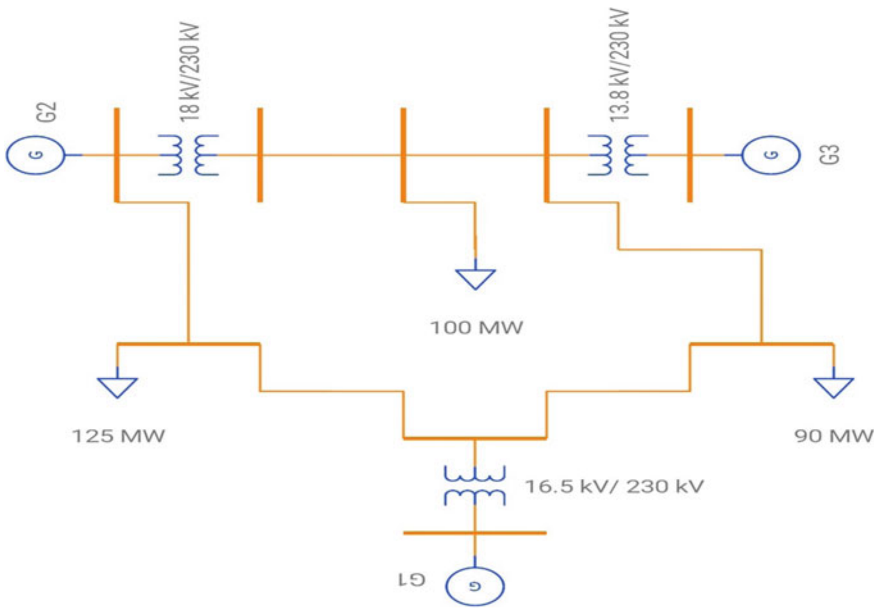

Fig. 1 SLD of the considered system

3 Methodology

Figure 2 shows the flowchart of the methodology. This flowchart shows the step-by-step process followed to use ANN for fault detection in electrical transmission lines. First of all, the different fault conditions are created using the IEEE 9 bus system Simulink model. The fault between Bus 8 and Bus 9 was assumed for simulation of faults. Different fault conditions were created which were single line-to-ground, line-to-line and double line-to-ground and three-phase faults. Then, the faulty voltage and current values were obtained and tabulated in an Excel sheet for different phases that gave a total of ten types of faults. The values obtained were used as the input data set for the ANN toolbox that helps in the fault detection and classification processes [16]. The ANN was trained using the neural network toolbox. The feedforward back-propagation algorithm used as in the output set was used as a feedback to the input. The Levenberg–Marquardt algorithm was used as the training algorithm for both the processes of identification and classification. Training is done for fault classification in ANN after the successful completion of the fault detection. The output obtained is swift, accurate and reliable through training and testing of ANN done until the desired performance is satisfactorily obtained. In the final step, implementation was done after running the ANN by adding it to the simulation model.

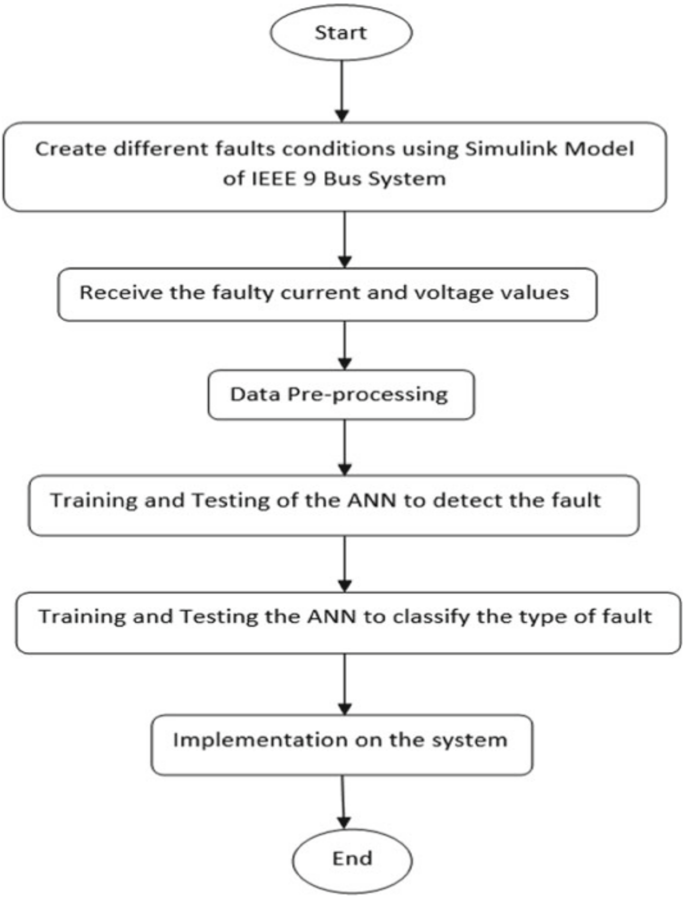

Fig. 2 Methodology

4 Artificial Neural Network

The word neural comes from the name coined for the basic unit of the nervous system called the 'neuron'. The network of such is regarded as the neural network. When the power of a network of neurons in a brain is implemented into an artificial set of things which can somewhat simulate a similar behaviour, thus it is regarded as artificial neural networks. ANN can be described as a set of primary neurons that are interlinked in biologically inspired simulations configured to do certain tasks like clustering, detection, classification, pattern recognition. These neuron-termed units are organized in several layers, and the architecture of ANN can be understood with the layers it comprises as shown in Fig. 3.

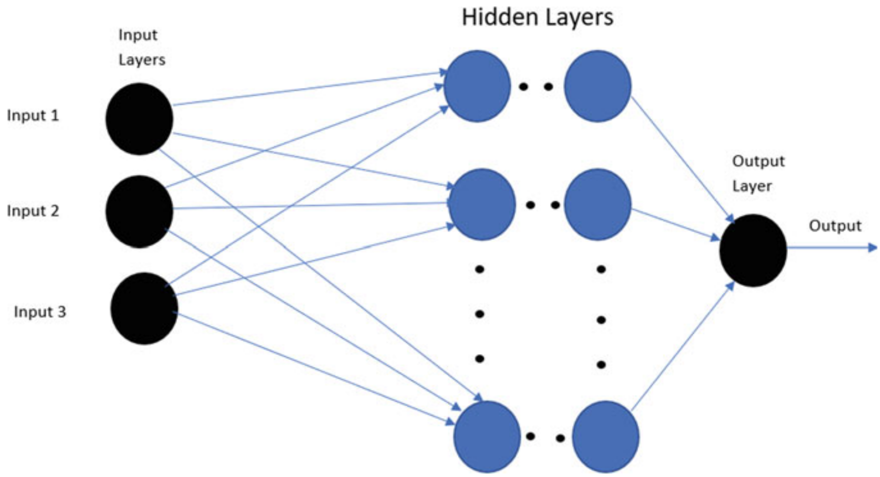

Fig. 3 Model of artificial neural network

1. Input Layer
   The artificial neurons (termed as units) received as input from the experimenter comprise the input layers. The actual learning and recognition on the network happen in this part of the architecture.
2. Hidden Layer
   The hidden layers are the middle layers hidden in between input layers and the output layers. The significant role of a hidden layer is to take the input from the input layers and derive something meaningful to transform this data for the output layer to use it in some useful way.
3. Output Layer
   The last layer, that is the output layer, consists of units that react to the data fed into the system and also understand whether the system learned any/null tasks.

4.1 Characteristics

ANN is a highly accepted and implied method for fault detection and identification due to the following mentioned characteristics of ANN implication:

1. ANN can model nonlinear problems to predict output for a given input from the training values.
2. The functionality of ANN is affected by the training algorithm employed.
3. The quantity of the output data set is somehow directly proportional to the number of variables recognizable.
4. Multiple transmission line configurations are possible for training and testing of ANN.
5. Simulation of the network can be done with various methods.

6. ANN is highly capable to deal with the physical changes in the power system.
7. Its working depends on simple operations, and the result obtained is quick, accurate and reliable.
8. It can easily deal with problems having massive amount of information.
9. It has a great degree of fault tolerance and processing speed which deal with complicated calculations easily.
10. Its ability to learn the relation between the selected input and output allows the users to test and explore the simulation easily and in a short duration of time.

4.2 Backpropagation Algorithm (BPNN)

Backpropagation algorithm is a technique with the help of which the weights are tuned to decrease the error rate. In this algorithm, the output has been used as a feedback to input which helps in calculating the changes in value of weights. The product of input data and weights is used as an input into the hidden layer, and then products of weight and output of the hidden layer are given into the output layer as an input which has then been compared to the output of the output layer and target output by which MSE is calculated. If MSE is within the permissible boundary, then the algorithm will end, but if it is very large or not good, then this goes back to the input layer, and now, weights are changed, and this process is repeated until we get the best result. This whole process is done in each iteration until a zero or very less error is obtained; which means the difference in target output and system output is zero or very less [17].

5 Fault Detection Using ANN

For fault detection, the neural network fitting tool in MATLAB has been used. For this, one input layer with six neurons which are the RMS value of currents and voltages of all the three faults, twelve hidden layers and one output layer with one neuron which will either be 0 or 1 has been considered. In this method, six inputs are the RMS voltage value of all three-phases and the RMS current value of all three phases. The target output has been set as 0 and 1, which means 0 for no fault conditions and 1 for fault conditions. In this work, 850 values of RMS voltages and RMS currents of each of the 10 faults were taken; total of 8500 values for fault and 1000 values of RMS voltage and RMS current of all three phases for no-fault condition. For training purposes, algorithm used is the Levenberg–Marquardt algorithm which is the most robust and fastest algorithm [18]. In Table 1, it can be clearly seen how the input and target output has been taken (Fig. 4).

Table 1 Input data and target output data

Input data						Target output data
Voltage			Current			Target output
Phase a	Phase b	Phase c	Phase a	Phase b	Phase c	
9979.366	9911.603	3392.361	2773.193	2874.185	4231.629	1
19,979.38	9911.609	3392.356	2773.229	2874.16	4231.622	1
9979.395	9911.613	3392.352	2773.265	2874.135	4231.614	1
9979.411	9911.616	3392.347	2773.301	2874.11	4231.607	1
9979.428	9911.619	3392.343	2773.338	2874.086	4231.599	1
9979.447	9911.62	3392.34	2773.375	2874.063	4231.591	1
9979.466	9911.62	3392.337	2773.413	2874.04	4231.582	1
9979.486	9911.618	3392.334	2773.451	2874.018	4231.573	1
9979.507	9911.615	3392.332	2773.489	2873.996	4231.565	1
9979.529	9911.611	3392.33	2773.527	2873.975	4231.555	1
9997.69	9997.493	9997.928	2840.113	2840.094	2840.209	0

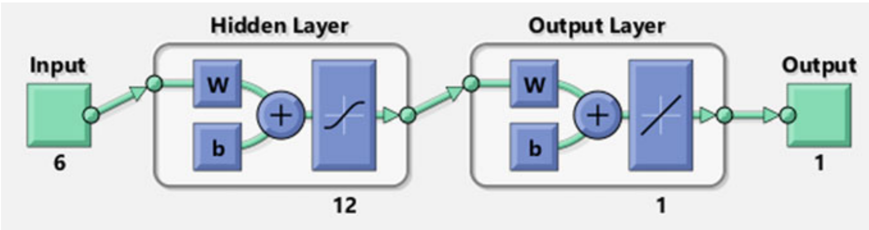

Fig. 4 Neural network configuration 6-12-1

6 Fault Classification Using ANN

Fault classification was also done by using a neural network fitting tool. In classification, one input which has six neurons, the same as in fault detection which are RMS value of currents and voltages of all three phases, was considered. In addition, 16 hidden layers and 1 output layer with 4 neurons which are three phases and ground were considered. For classification, four neurons are output with three phases and ground, so as an example, if there is a fault of type a–g fault, then output will be 1 for Phase a and ground and 0 for Phases b and c. In classification, the training set is the same as fault detection which is 8500 values of fault which means 850 values of each of the 10 faults and 1000 values for no fault. For training purposes, the same algorithm which is the Levenberg–Marquardt algorithm has been used. In Table 2, the input and target output data have been shown in a tabular form (Fig. 5).

Table 2 Input and target output data of fault classification

Input data						Target output data			
Va	Vb	Vc	Ia	Ib	Ic	*a*	*b*	*c*	*g*
9997.69	9997.493	9997.928	2840.113	2840.094	2840.209	0	0	0	0
3410.011	9983	9909.681	5277.715	2773.43	2878.279	1	0	0	1
9941.627	7128.565	10,088.18	2783.374	6254.565	2846.215	0	1	0	1
9980.351	9910.591	3392.672	2772.521	2873.175	4230.954	0	0	1	1
2571.511	3383.13	9902.602	7116.9	6678.951	2809.955	1	1	0	1
7788.08	10,029.3	7762.816	4443.239	2788.458	3674.896	1	0	1	1
10,025.96	7450.482	7565.086	2787.279	6854.456	3983.794	0	1	1	1
4573.124	6193.073	9997.573	7654.959	6050.137	2840.369	1	1	0	0
6475.096	9997.645	4915.066	3663.368	2840.392	5924.391	1	0	1	0
9997.264	5919.223	7284.161	2840.151	5959.867	4211.249	0	1	1	0
2690.251	2620.84	3055.978	6680.631	6867.707	4691.82	1	1	1	0

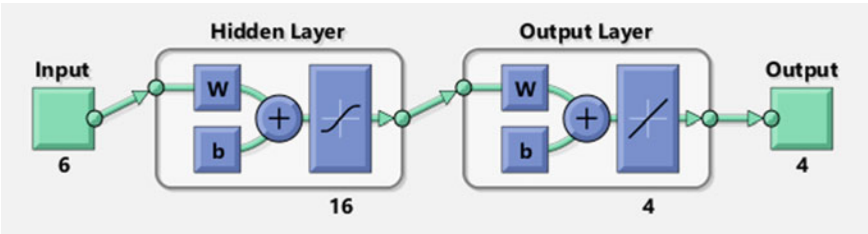

Fig. 5 Neural network configuration 6-16-4

7 Result and Implementation

(a) Result of fault detection: After running the training process several times, the best performance of ANN for fault detection is in configuration 6-12-1. Result is shown in Fig. 6, for this configuration showing a very small MSE of

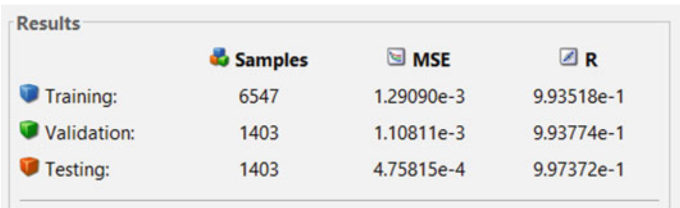

Results

	Samples	MSE	R
Training:	6547	1.29090e-3	9.93518e-1
Validation:	1403	1.10811e-3	9.93774e-1
Testing:	1403	4.75815e-4	9.97372e-1

Fig. 6 Result of fault detection ANN

$1.29090 * 10^{-3}$. This training is very good as seen in the graph between mean square error and iterations in Fig. 7, where it can be concluded that MSE is decreasing with each iteration in both validation and testing. After the MSE graph, the observation of the regression graph is in Fig. 8 in which coefficient correlation is indicated by *R* and its value is 0.99408 which is near to 1 allowing a conclusion that the output obtained is very close to the target output. These

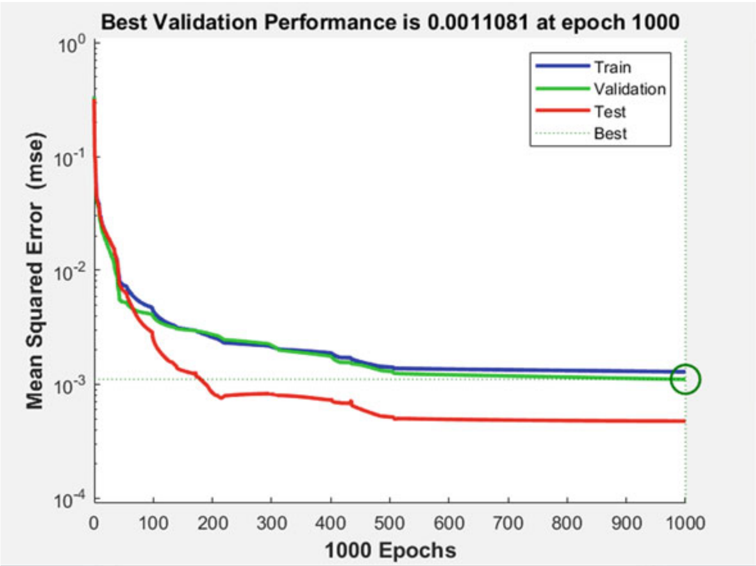

Fig. 7 Performance graph of fault detection

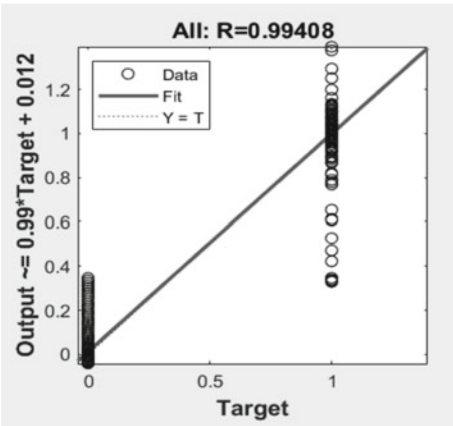

Fig. 8 Regression graph of fault detection

two graphs show that the performance of our artificial neural network for fault detection gives very promising results.

(b) Result of fault classification: In classification, here, the configuration used is 6-16-4 which gives good performance while classifying the fault. From Fig. 9, it can be said that the result of all three training, validation and testing is very good as it can be seen that the mean square error is very less. From the performance graph in Fig. 10, which have four lines—test, train, validation and best, which is a dotted line, it can be clearly seen that all the three lines are overlapping or very near to the best line which means that results are very satisfying and the error is very less. In Fig. 11, there is the regression graph where it can be seen that the coefficient of correlation is 0.98 which means that the overall accuracy of ANN is 98%.

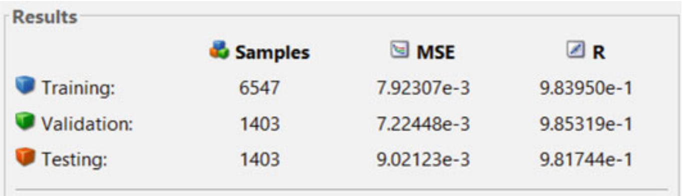
Results

	Samples	MSE	R
Training:	6547	7.92307e-3	9.83950e-1
Validation:	1403	7.22448e-3	9.85319e-1
Testing:	1403	9.02123e-3	9.81744e-1

Fig. 9 Result of fault classification model

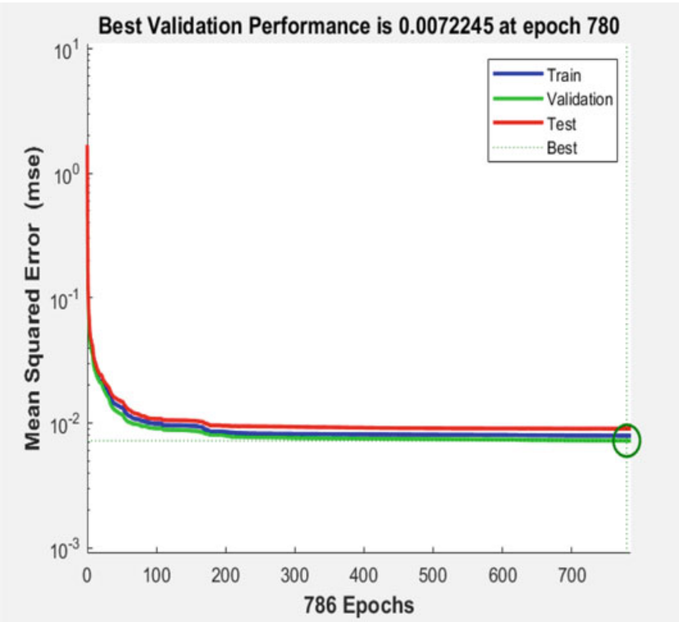

Fig. 10 Performance graph of fault classification

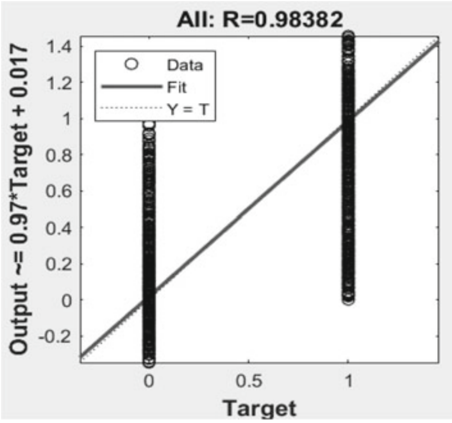

Fig. 11 Regression graph of fault classification

(c) Implementation: After running both the ANN, they have been connected to the simulated model as shown in Fig. 12. RMS currents and voltages values are an input to both the models of ANN. Fault detecting model output is given to the display block as 1 for fault and 0 for no fault, and fault classification model output is sent to the logical box. With the help of logic gates, an input is given to the scope. In scope, all ten faults and one graph of fault detector shown in Fig. 13 are obtained, for example if there is an a-to-g fault, then the value in the graph of the detector will be seen for a time period of the fault, and the

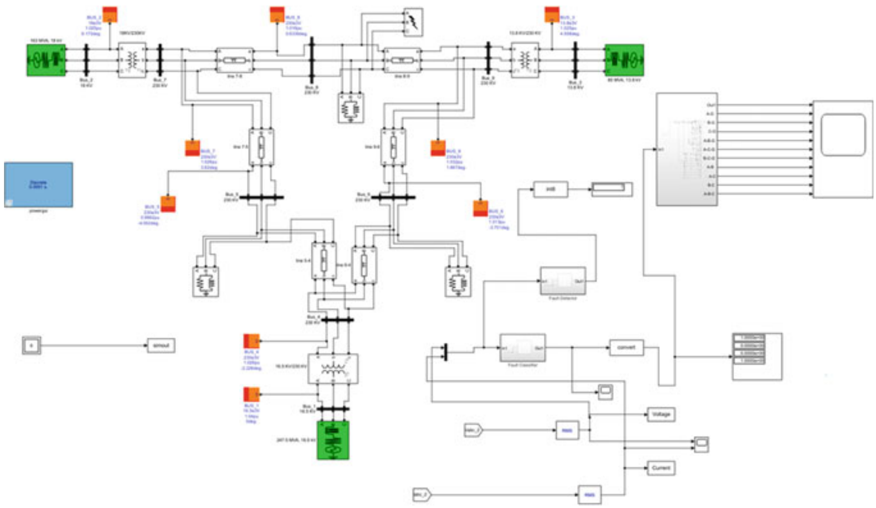

Fig. 12 Simulink model

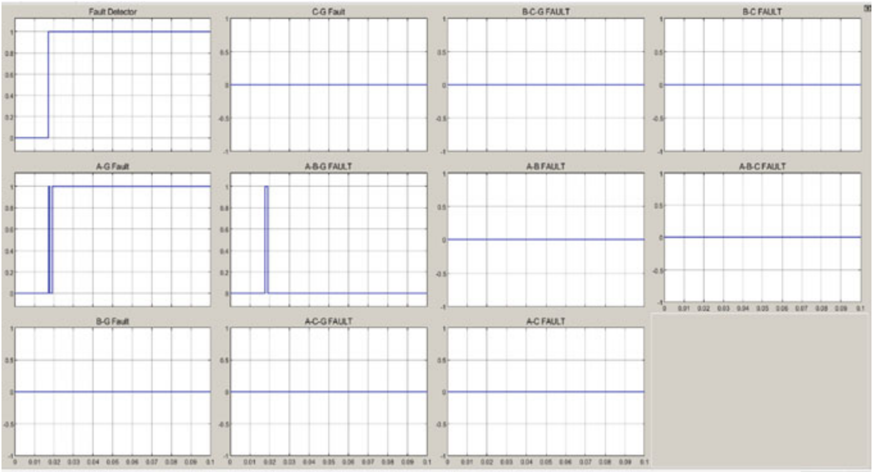

Fig. 13 Result of implementation

graph of a-to-g fault shows 1 for the time period in which fault is occurring, and rest all graph shows zero.

8 Conclusion

It is very crucial to find the fault in a transmission line in the shortest possible time and even more important is to do so accurately. Therefore, the work attempted in this paper is to apply ANN for fault detection and fault classification. It is a suitable method to use to prevent any cascade damage to the power system with good performance. The software tools used for performing the proposed technique are MATLAB software and ANN toolbox. The ANN utilized three-phase voltage and current values obtained from the standard IEEE 9 bus system as an input data set for training. The completion of the identification and classification is calculated using the mean square error (MSE) and linear regression. The detection obtained a tolerable MSE of 4.75815e−04. The correlation of 0.99408 is obtained for detection, giving a suitable performance of the system. The classification obtained a tolerable MSE of 9.02123e−03. The correlation of 0.98382 is obtained for classification. An accuracy of 98% is obtained proving that this method is acceptable and predicts good performance. By altering the size of the training data set, the number of hidden layers and the number of neurons in each layer can help in further enhancing the overall performance of the proposed method [19–21].

References

1. Yadav A, Dash Y (2014) An overview of transmission line protection by artificial neural network: fault detection, fault classification, fault location, and fault direction discrimination. Adv Artif Neural Syst 2014
2. Behera A, Mohanty S (2018) Power quality improvement of a 25 kV distribution system under 3 phase fault using UPQC. In: 2018 technologies for smart-city energy security and power (ICSESP), pp 1–4. https://doi.org/10.1109/ICSESP.2018.8376677
3. Bendre A, Divan D, Kranz W, Brumsickle W (2004) Equipment failures caused by power quality disturbances. In: 39th IAS annual meeting. Conference record of the 2004 IEEE Industry applications conference, 1
4. Bakshi UA, Bakshi MV (2009) Protection and switchgear. Technical Publications
5. Prasad CD, Nayak PK (2019) A DFT-ED based approach for detection and classification of faults in electric power transmission networks. Ain Shams Eng J 10(1):171–178. ISSN 2090-4479
6. Agarwal S, Swetapadma A, Panigrahi C, Dasgupta A (2017) Fault detection in direct current transmission lines using discrete Fourier transform from single terminal current signals. In: 2017 1st international conference on electronics, materials engineering and nano-technology (IEMENTech), pp 1–5
7. Avagaddi P, Edward B (2016) Application of wavelet technique for fault classification in transmission systems. Procedia Comput Sci 92:78–83. https://doi.org/10.1016/j.procs.2016.07.326
8. Patel TK, Panda PC, Swain SC, Mohanty SK (2017) A fault detection technique in transmission line by using discrete wavelet transform. In: 2017 second international conference on electrical, computer and communication technologies (ICECCT), pp 1–6. https://doi.org/10.1109/ICECCT.2017.8118052
9. Gautam N, Ali S, Kapoor G (2018) Detection of fault in series capacitor compensated double circuit transmission line using wavelet transform. In: 2018 international conference on computing, power and communication technologies (GUCON), pp 760–764. https://doi.org/10.1109/GUCON.2018.8675071
10. Adhikari S, Sinha N, Dorendrajit T (2016) Fuzzy logic based on-line fault detection and classification in transmission line. Springerplus 5:1002. https://doi.org/10.1186/s40064-016-2669-4
11. Raju GV, Koley E (2016) Fuzzy logic based fault detector and classifier for three phase transmission lines with STATCOM. In: 2016 international conference on electrical power and energy systems (ICEPES), pp 469–474. https://doi.org/10.1109/ICEPES.2016.7915976
12. Patel A, Prashant MVS, Sahu J, Kujur AP, Verma S (2018) Protection scheme based on fault detection and fault classification using fuzzy inference system in IEEE-9 bus system. In: 2018 international conference on recent innovations in electrical, electronics & communication engineering (ICRIEECE), pp 626–638. https://doi.org/10.1109/ICRIEECE44171.2018.9008548
13. Tarafdar Hagh M, Razi K, Taghizadeh H (2007) Fault classification and location of power transmission lines using artificial neural network. In: 2007 international power engineering conference (IPEC 2007), pp 1109–1114
14. Fayaz F, Isa A, Verma HK, Deb S (2016) Improved ANN-based algorithm for detection and classification of faults on transmission lines. In: 2016 1st India international conference on information processing (IICIP), pp 1–6. https://doi.org/10.1109/IICIP.2016.7975360
15. Sahoo BK, Pradhan S, Panigrahi BK, Biswal B, Patel NC, Das S (2020) Fault detection in electrical power transmission system using artificial neural network. In: 2020 international conference on computational intelligence for smart power system and sustainable energy (CISPSSE), pp 1–4. https://doi.org/10.1109/CISPSSE49931.2020.9212274
16. Abbas A, Hamza A, Habbi HMD (2016) Fault detection and diagnosis based on artificial neural network. Int J Sci Eng Res 7(5):1690–1697

17. Technologiae M (2016) The application of artificial neural networks to transmission line fault detection and diagnosis. University of South Africa
18. Singh R (2017) Fault identification and classification in transmission line by ANN technique using Levenberg-Marquardt algorithms. Int J Adv Eng Res Dev 4(11):951–958
19. Leh NAM, Zain FM, Muhammad Z, Hamid SA, Rosli AD (2020) Fault detection method using ANN for power transmission line. In: 2020 10th IEEE international conference on control system, computing and engineering (ICCSCE)
20. Maqsood A, Oslebo D, Corzine K, Parsa L, Ma Y (2020) STFT cluster analysis for DC pulsed load monitoring and fault detection on naval shipboard power systems. IEEE Trans Transp Electrif
21. Mohanty SK, Karn A, Banerjee S (2020) Decision tree supported distance relay for fault detection and classification in a series compensated line. In: 2020 IEEE international conference on power electronics, smart grid and renewable energy (PESGRE2020)

Chapter 19
A DWT-RNN-Assisted Intelligent Differential Protection Scheme for Grid-Tied and Islanded DC Microgrid

Satyavarta Kumar Prince, Shaik Affijulla, and Gayadhar Panda

Abstract The integration of renewable sources into a DC microgrid offers clear advantages such as high efficiency and effective simple control. Despite this, the high penetration of distributed generators can cause problems such as safety, and islands in the microgrid can affect the reliability of the power system. Because the nature of the fault current in the DC, microgrid is different from that of AC, which brings a great challenge for fault detection and diagnosis. To address this issue, this paper presents an intelligent differential protection scheme for microgrids that employ the machine learning (discrete wavelet transform and ANN) method. The proposed differential protection scheme employs DWT for fault detection and ANN for event classification. The discrete Fourier transform is used in this study to preprocess the voltage and current signals in order to calculate the microgrid fault formation. Subsequently, available ANN-based classifiers are presented to evaluate the proposed scheme's efficiency in terms of defect detection, identification, and classification. This study collects data from various aspects by simulating different fault and no fault cases for the microgrid configuration in grid-tied and island modes of operation. The simulation is performed on a standard medium-voltage microgrid employing MATLAB/Simulink. The results also show that the proposed method can detect the faults in grid-tied and islanded microgrids.

Keywords Distributed energy resources · DC microgrids · Artificial neural networks · Discrete wavelet transform (DWT) · Fault detection · Islanding detection techniques · Microgrid protection

S. K. Prince (✉) · S. Affijulla · G. Panda
Department of EE, NIT Meghalaya, Shillong, Meghalaya, India

S. Affijulla
e-mail: shaik.affijulla@nitm.ac.in

G. Panda
e-mail: gayadhar.panda@nitm.ac.in

G. Panda et al. (eds.), *Sustainable Energy and Technological Advancements*,
Advances in Sustainability Science and Technology,
https://doi.org/10.1007/978-981-16-9033-4_19

1 Introduction

The concept of microgrid has been developed to increase the efficiency of modern power system and avoid the problem of blackout with proper use of renewable energy [1, 2]. High demand and loss of partial production due to cyber attacks or natural disasters can be factors contributing to these blackout incidents. Distributed generators (DGs), energy storage systems (ESSs), microgrids with controllable loads can overcome these problems to some extent by self-healing [3]. Renewable energy sources microgrid systems have gained popularity due to modern loads with PV interfaces in energy storage devices and especially DC in nature. Hence, the DC microgrid provides more efficient and reliable power delivery with fewer energy conversion steps than the AC microgrid [4]. Along with this, problems like frequency regulation, phase synchronization, reactive power flow are not found in DC microgrid system. Microgrids can be performed on grid-connected or island mode to enhance local energy balance and robust transmission efficiencies. The inherent randomness of energy fluctuations in renewable energy sources can also lead to problems such as extreme power inequality, insufficient transmitting capacity, and power quality disturbances [5–7].

When working with microgrids, problems such as safety, grounding, and landing can be the most seriously challenging. In inverter-based PV and battery systems, the fault current characteristic is much lower than in synchronous generators [8]. This can be a major problem when the DC microgrid is operating in island mode, as the overcurrent protection scheme may not be effective. DC microgrids have different fault current characteristics than AC, because in DC systems, short lines/cables of converters and DC link capacitors cause severe current flow during a fault [9, 10]. Faults in DC system cables occur due to cable insulation failure caused by electrical stress, environmental conditions, ageing, and physical damage. Pole-to-ground faults are common in DC cables, whereas pole-to-pole faults are rare due to severe insulation impair to both the positive and negative conductors.

DC fault current can cause damage to the converter and other nearby equipment due to its large amplitude and fast transients. Short-circuit levels are significantly reduced when the DC microgrid is functioned in islanded mode [11]. The current relaying scheme may not be adequate to protect the microgrid from the challenging environment. A fault detection method for AC microgrids in island mode uses variances in current frequency components at both ends of the line to detect faults. The AC microgrid has been protected using a travelling wave protection principle [12]. However, the feasibility of using this scheme for DC or hybrid microgrids has yet to be determined. Negative sequence impedance is used to detect faults in this directional overcurrent relay-based protection scheme [13].

As a result, for DC microgrids, current-differential protection is the best option. When a branch current (such as a fault branch) cannot be measured, the vector sum of the inflow and outflow currents equals the fault branch current. The scheme, however, endures from the large computational complexity of the s-transform in calculating the differential energy, resulting in a delayed response time during the fault [14].

Given the aforementioned safety concerns, there is a robust incentive to develop an intelligent protection relay capable of providing comprehensive protection for the microgrid. A DWT-based intelligent current-differential scheme is proposed for protection of microgrids in grid-connected and islanded modes.

This paper develops a new DWT-ANN-based differential protection schemes for fault detection and classification under pole-ground fault. In this method, when there are a grid fault and island fault detection, the system current changes during different pole-ground fault condition accordingly. The rest of the parts in this paper are arranged as follows: Sect. 2 illustrates the test system and presents a theoretical background of fault detection techniques. Then, in Sect. 3, the developed fault detection algorithm is described. The results of evaluation of the effectiveness of the system by the proposed method are represented in Sect. 4. Finally, the conclusion is obtained in Sect. 5.

2 Fault Detection Method for DC Microgrid

This section discusses the proposed ANN-based differential protection scheme in detail, including the microgrid architecture employed to test the efficacy of fault detection in the MATLAB/Simulink platform.

2.1 Model Description

The performance of the proposed protection scheme in both grid-connected and islanded modes is evaluated using a six-bus microgrid system, as manifested in Fig. 1. In the event of a pole-to-ground fault, the protection in this configuration has been found to be more robust and reliable. This microgrid system is linked to a solar photovoltaic (PV) system via a DC–DC converter [15] and a wind turbine via an AC-to-DC converter via a VSC. The maximum power point tracking principle is used by both of these converters. VSC and an AC-to-DC converter connect the diesel generator source and the grid to the DC bus. DC and AC loads of constant resistance are used. Energy-storage systems are used to keep the load and generation in balance. The grid VSC controls the DC bus voltage in grid-connected mode, whereas a battery converter controls the DC bus voltage in island mode. Table 1 displays the ratings for the DC microgrid modules. The status of the switch determines the operating modes (grid connected or islanded). Furthermore, faults (F1–F6) are incepted at the midpoint of each feeder to determine the fault currents detected by relays (R1–R12). Meanwhile, whether in grid-connected mode or island mode, the protection system must detect the fault for proper operation of the microgrid. In such a case, an ANN-based differential protection scheme is used under the pole-ground fault, as shown in Fig. 2.

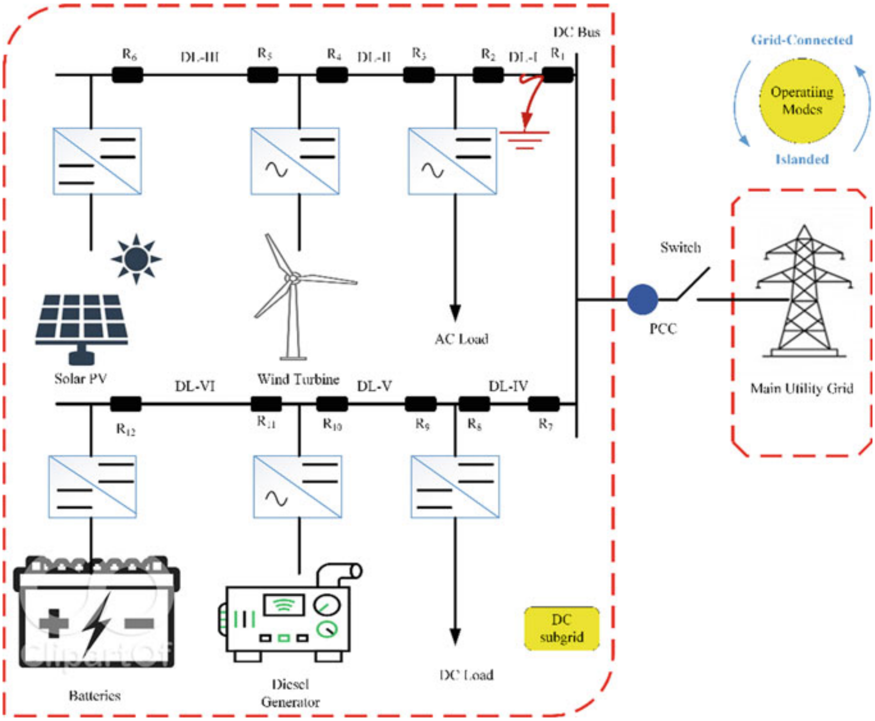

Fig. 1 Typical islanded and grid-connected DC microgrid system with pole-to-ground fault condition

Table 1 DC microgrid parameters

Parameter	Specification
System voltages	$V_{dc} = 500$ V
Short-circuit current	$I_{sc} = 5.69$ A
System voltages	$V_{dc} = 500$ V
Line parameter	$R = 0.1$ Ω/km, $L = 0.4$ Ω/km
Wind energy conversion system	PMSG, $P_m = 20$ kW
Battery	0.5 MW, 1.5 kAh, nickel cadmium
Loads	Load 1 = 10 kW, load 2 = 5 kW

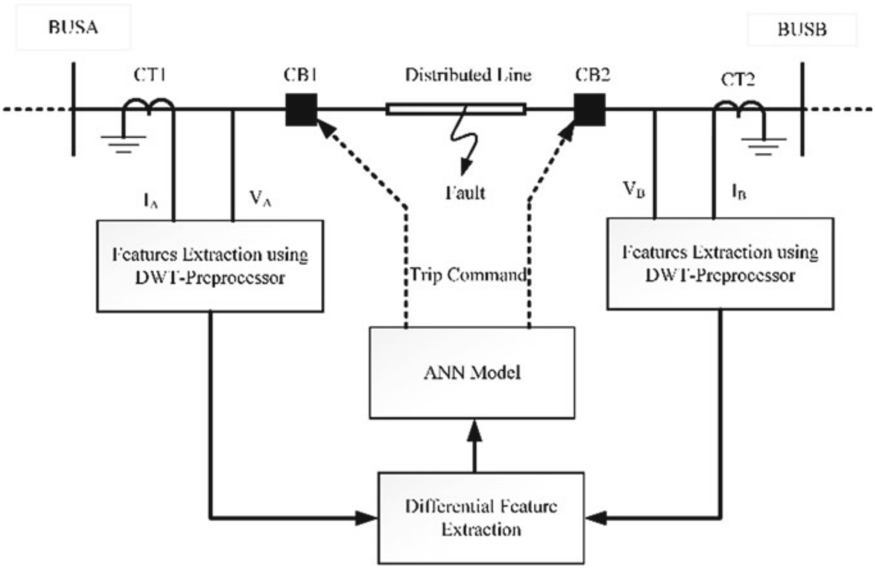

Fig. 2 Proposed DWT-ANN-assisted intelligent differential protection scheme

3 Proposed Fault Detection Method

3.1 *Fault Analysis*

In a DC microgrid system, there are two types of faults: (a) pole-ground faults and (b) pole-pole faults. The aim of this research is to propose a novel DWT-ANN-based protection scheme for a DC microgrid arrangement in grid-connected and islanded modes in order to address the aforementioned issues. The viable protection challenges are stated in Sect. 1 and studying the test system as depicted in Fig. 1 for various fault instances. Regarding the differential (usual) protection scheme, the Relays R1, R3, R5, R7, R9, and R11 are used to protect the microgrids DLI, DLII, DLIII, DLIV, DLV, and DLVI, respectively.

3.2 *Current-Differential Protection Scheme*

The current must contain sufficient information to distinguish between a fault and no fault. As a result, a differential current-based protection scheme is used, which measures the errors caused by distinct CT characteristics in the two row ends. At non-fault, the systems relay to measure false differential currents. The differential relay calculates the current from an initial point along a curve that increases in proportion to the current. This natural rise in trip point enables relay system errors to be proportional to current level. CT measurement errors and analogue circuitry errors are two examples of such effects.

The sum of the local (I_A) and remote current (I_B) is called the operating current:

$$|I_A + I_B| = I_{\text{differential}} \tag{1}$$

The restraint quantity is usually a function of the total current, and the function is frequently a constant k:

$$k(|I_A| + |I_B|)/2 = I_{\text{Restraint}} \tag{2}$$

The following criteria must be met for a differential relay to operate:

$$I_{\text{Differential}} > I_{\text{Restraint}} + I_{\min} \tag{3}$$

where k is the slope.

Neglecting $I_{\min}$ for calculation as it is not of significant value.

The operation of a differential relay is

$$|I_A + I_B| > K(|I_A| + |I_B|)/2 \tag{4}$$

Based on the ANN, the proposed scheme constructs an intelligent differential protection relaying scheme for microgrid protection. The method took into account PG faults at multiple locations along distribution lines that were closely linked to the grid as well as islanded modes of microgrid. The proposed method retests the fault current and voltage at two ends of the relevant feeders and carries forward sensitive characteristics such as rate of change of current at both ends of the feeder through a DWT preprocessor. The features at both ends of the feeder are utilized to calculate the differential features. The differential features are employed in the construction of the ANN-based prototype for accounting the fault situation and issuing the tripping command. Figure 2 depicts a schematic diagram of the proposed intelligent differential microgrid protection scheme based on ANN.

4 Results and Discussions

The test platform and DC microgrid model are shown in Fig. 1, where the differential protection scheme is performed for grid-connected and isolated modes and the rated voltage is 500 V. In this study, the bus voltage and line current behaviour are investigated by switching any protection devices during a pole-to-ground fault. Since simulation is mainly used to identify distribution line faults and verify isolation by the proposed method, here, the distributed power supply is operated in a DC bus. The developed scenarios are based on different operating modes for distribution lines under pole-ground faults. The effectiveness of ANN-based differential protection for different switching condition and for a period of 0.6–1.5 s is shown in the simulation. In each situation, a pole-ground fault is made at $t = 1.0$ s.

4.1 Case 1: Validation of System Performance Under Pole-to-Ground Fault Scenarios During Grid-Tied DC Microgrid

The fault currents observed by relays (R1, R3, R5, R7, R9, and R11) in faulty distribution lines under pole-ground fault (PG) in grid-connected mode are shown in Fig. 3, whereas the peak fault currents observed by the other-end relays (R2, R4, R6, R8, R10, and R12) are given in Table 2. It is observed that in grid-connected mode, the fault current seen by the relay placed at End 1 is higher than End 2 because of the

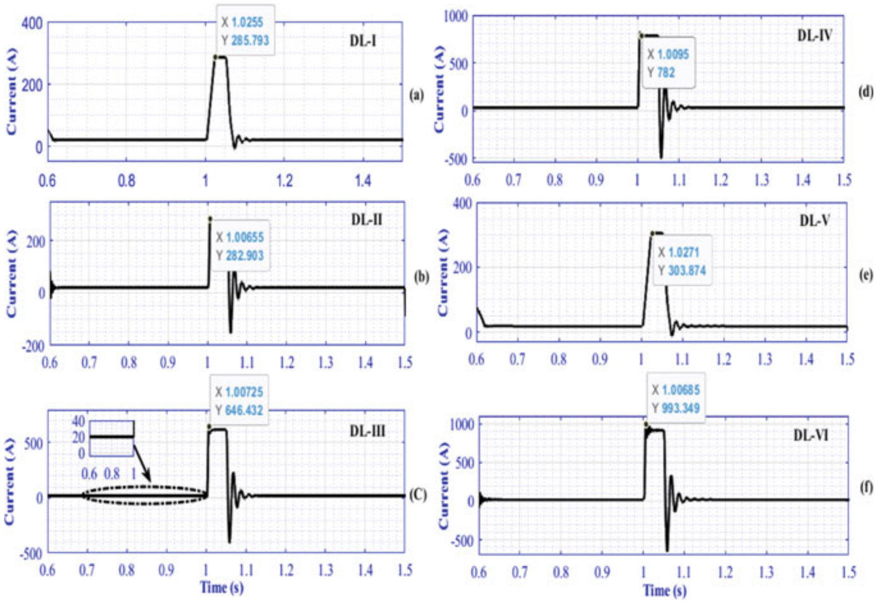

Fig. 3 Waveform of line current of DL1, DL2, DL3, DL4, DL5, and DL6 during pole-to-ground fault at grid-connected mode

Table 2 Fault current measured for grid-connected and islanded modes at 1.005 s

Operating modes	Relays					
	R2	R4	R6	R8	R10	R12
Grid-connected mode of End 2 (A)	250	234	540	580	254	825
Islanded mode of End 2 (A)	310	250	210	195	181	260

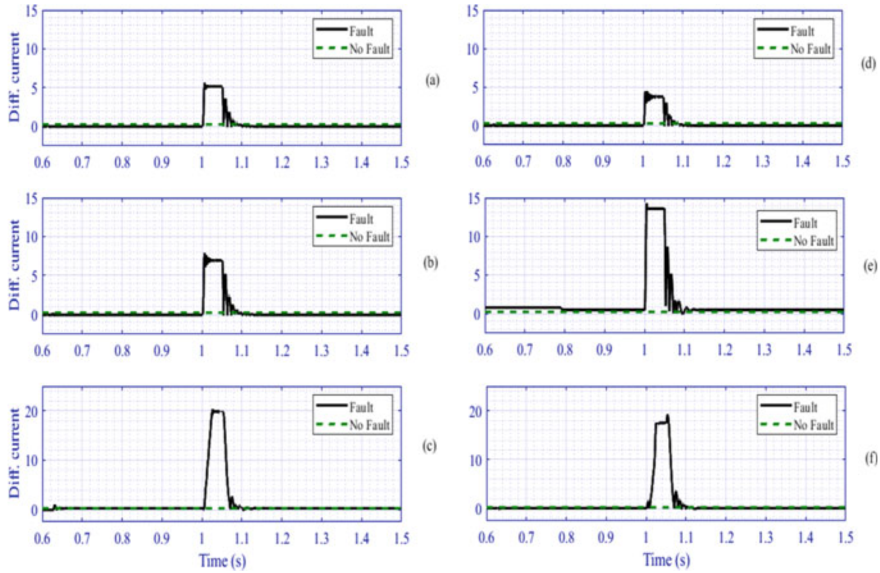

Fig. 4 Differential features extraction during pole-to-ground at grid-connected mode

fault current influence from the utility. Figure 3 shows the fault current observed by the relay for the various distributed lines under the pole-to-ground fault conditions, and Fig. 4 shows the feature extraction using differential protection scheme on grid-connected mode.

4.2 Case 2: Validation of System Performance Under Pole-to-Ground Fault Scenarios During Islanded DC Microgrid

When the grid is lost, the fault current view by the various relays in the different distribution lines is depicted in Figs. 5 and 6. It is noticed that in islanded mode, the value of fault current is less as compared to grid-connected mode due to restricted current offering from the local DGs only, whereas for islanded mode, the fault current observed by the relay placed at End 1 (R1, 3, 5, 7, 9, and 11) is found to be smaller than that at End 2 (R2, 4, 6, 8, 10, and 12), and the fault current observed by relays placed at End 1 (R5 and R7) is larger than End 2 (R6 and R8). This related fault situation occurs because of the entry level of the DG. It is easily observed that the differential protection scheme is successfully discriminated between fault and no fault conditions.

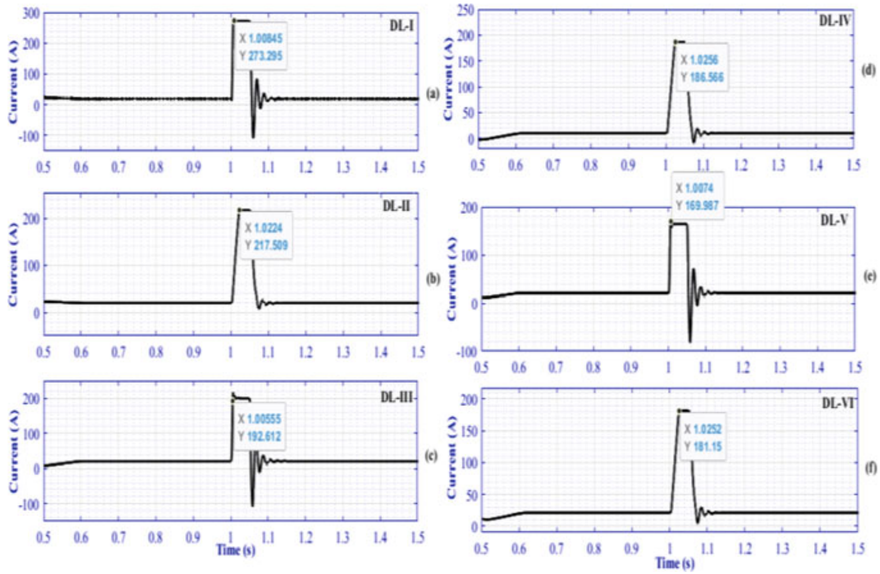

Fig. 5 Waveform of line current of DL1, DL2, DL3, DL4, DL5, and DL6 during pole-to-ground fault at islanded mode

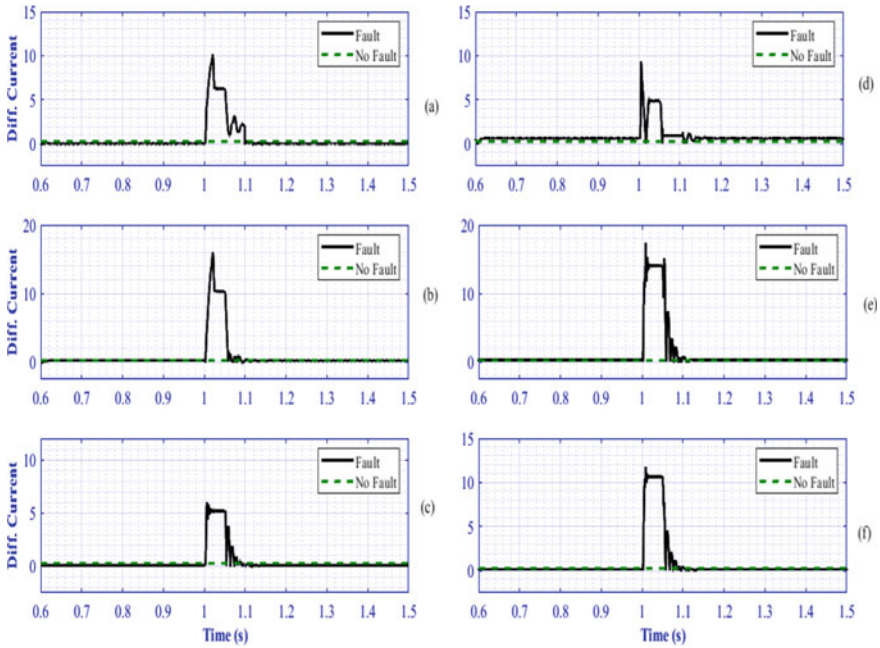

Fig. 6 Differential features extraction during pole-to-ground at islanded mode

5 Conclusion

In this paper, a novel fault detection technique based on discrete wavelet transform and ANN is proposed under pole-ground fault condition. In this technique, the fault line is identified by determining its high peaks. In this protection scheme, each line is provided with two relays at both ends, which process the current measurement. Each relay preprocesses the current module using DWT and ANN and trains the signal for distinguishing between fault and no fault. For detection accuracy assessed by discrete wavelet transform, the proposed method shows more stable and accurate classification performance. Simulation results have shown a more authentically superior performance than other methods. Thus, the proposed fault detection algorithm performs better even in islanded mode.

Acknowledgements This research work is supported by the Department of Science and Technology (DST). This is a project sponsored by the Government of India under grant EMR/2017/001880.

References

1. Schneider KP et al (2017) Evaluating the feasibility to use microgrids as a resiliency resource. IEEE Trans Smart Grid 8(2):687–696
2. Prince SK, Affijulla S, Panda G (2021) Fault detection in IEEE 9-bus DC microgrid system using differential current method. In: 2020 3rd international conference on energy, power and environment: towards clean energy technologies, pp 1–6
3. Chen B, Chen C, Wang J, Butler-Purry KL (2018) Multi-time step service restoration for advanced distribution systems and microgrids. IEEE Trans Smart Grid 9(6):6793–6805
4. Baranwal M, Askarian A, Salapaka S, Salapaka M (2019) A distributed architecture for robust and optimal control of DC microgrids. IEEE Trans Industr Electron 66(4):3082–3092
5. Dhar S, Dash PK (2016) Harmonic profile injection-based hybrid active islanding detection technique for PV-VSC-based microgrid system. IEEE Trans Sustain Energy 7(4):1473–1481
6. Chishti F, Murshid S, Singh B (2020) Robust normalized mixed-norm adaptive control scheme for PQ improvement at PCC of a remotely located wind-solar PV-BES microgrid. IEEE Trans Ind Inf 16(3):1708–1721
7. Devassy S, Singh B (2021) Performance analysis of solar PV array and battery integrated unified power quality conditioner for microgrid systems. IEEE Trans Ind Electron 68(5):4027–4035
8. Zhang Z, Chen Q, Xie R, Sun K (2019) The fault analysis of PV cable fault in DC microgrids. IEEE Trans Energy Convers 34(1):486–496
9. Chen L et al (2019) Application and design of a resistive-type superconducting fault current limiter for efficient protection of a DC microgrid. IEEE Trans Appl Supercond 29(2):1–7
10. Prince SK, Affijulla S, Panda G (2021) Total harmonic distortion based fault detection in islanded DC microgrid. In: 2020 3rd international conference on energy, power and environment: towards clean energy technologies, pp 1–6
11. Ahmadi S, Sadeghkhani I, Shahgholian G, Fani B, Guerrero JM (2021) Protection of LVDC microgrids in grid-connected and islanded modes using bifurcation theory. IEEE J Emerg Sel Top Power Electron 9(3):2597–2604
12. Li X, Dyśko A, Burt GM (2014) Traveling wave-based protection scheme for inverter-dominated microgrid using mathematical morphology. IEEE Trans Smart Grid 5(5):2211–2218

13. Haddadi A, Zhao M, Kocar I, Karaagac U, Chan KW, Farantatos E (2021) Impact of inverter-based resources on negative sequence quantities-based protection elements. IEEE Trans Power Delivery 36(1):289–298
14. Kar S, Samantaray S (2014) Time-frequency transform-based differential scheme for microgrid protection. IET Gener Transm Distrib 8:310–320
15. Prince SK, Panda KP, Patowary M, Panda G (2019) FPA tuned extended Kalman filter for power quality enhancement in PV integrated shunt active power filter. In: 2019 international conference on computing, power and communication technologies (GUCON), Sept 2019, pp 257–262

Chapter 20
Application of Differential Evolution to Determine Single-Stage Impulse Circuit Parameters

G. Ramarao, B. Hari Krishna, D. Rajesh, A. Ravikumar, and B. Rakesh

Abstract Differential evolution optimization algorithm (DEOA) is effectively utilized in this paper to determine the parameters of single-stage impulse generator circuit (SSIGC) (such as R_1, R_2, C_1, and C_2) for generating standard lightning impulse (SLI) waveform in the high voltage (HV) testing laboratory. Further, this SLI waveform is sufficient to evaluate dielectric strength of HV equipment used in power system network. The results that are evaluated and illustrated in this paper are beneficial to generate SLI voltage waveforms as given in standards IEC 62305-1, 2010 and IEEE 4-2013. The attempt made in this paper is the first of its kind to use DEOA as searching tool to determine the parameters of SSIGC. This methodology assists to conquer the conventional methods for determining the parameters SSIGC. These results reported in this paper are validated through the SSIGC prototype developed in MATLAB/Simulink.

Keywords Differential evolution optimization algorithm · High voltage equipment · Lightning impulse

1 Introduction

Distribution of electric power from generating station to receiving-end station is predominant continuous activity in power system in order to ensure the reliable operation. The bulk amount of voltage needs to be transmitted for longer distances due to economic considerations as per standards. For doing so, the high voltage (HV) apparatus plays a vital role to meet desirable objectives. Generally, these HV apparatus used in the power system network are exposed socio-environment. Hence, there is chance of deterioration in insulation due to over voltages induced in them due to the direct or indirect lightning strokes that occur inside or nearby by them. The insulation of HV apparatus portrays a significant role in maintaining reliable

G. Ramarao (✉) · B. Hari Krishna · D. Rajesh · A. Ravikumar · B. Rakesh
Department of EEE, AITAM, Tekkali, AP 532201, India

G. Panda et al. (eds.), *Sustainable Energy and Technological Advancements*,
Advances in Sustainability Science and Technology,
https://doi.org/10.1007/978-981-16-9033-4_20

operation of power system. In order to assess the withstand capacity of insulation of HV apparatus, those need to undergo impulse testing in HV laboratory [1–3].

Basically, the impulse testing carried out in HV laboratory is primarily depending upon on the generation of lightning impulse (LI) voltage waveforms in prescribed shapes as given in IEEE and IEC standards. Generation of these LI voltage waveforms is tough task. There are two ways to generate standard lightning impulse (SLI) waveforms. Theoretical generation through double exponential (DEXP) function (given by Eq. 1) and practical generation by single- or multi-stage impulse generation circuits (Fig. 2) [4, 5].

$$V = V_0[e(-\alpha t) - e(-\beta t)] \tag{1}$$

where in Eq. (1), V_0 is peak voltage and α, β are the DEXP function constants. There are two ways to maintain LI waveform polarities, one is positive, and other one is negative. In order to generate LI waveform with positive polarity, the constant as DEXP function must follow the condition, i.e., $\beta > \alpha > 0$ [6] and vice versa. K is the correcting factor for peak amplitude [7]. The SLI voltage waveform provided in Fig. 1 is basically characterized by the major physical parameters, namely rise time, tail time, and peak amplitude. The time difference between 90% of peak value and 10% of peak value in wavefront portion is defined as rise time, the time difference between 50% peak value in tail portion and 10% of peak value in wavefront portion is defined as tail time, and finally, the peak voltage is defined as the waveform reaches to its peak value [8].

The generation of LI is pretty easy to generate LI voltage waveforms in theoretical way, but it is difficult to generate the SLI voltage waveforms practically (i.e., through SSIGC) which is given in Fig. 2. The values of the practical SSIGC parameters (R_1, R_2, C_1, and C_2) should be properly evaluated for the generation of SLI voltage waveforms as illustrated in the standards (IEEE and IEC). Hence, the researchers

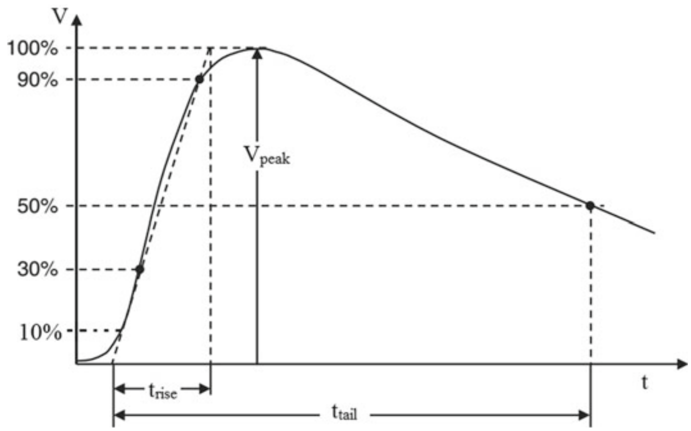

Fig. 1 Standard lightning impulse (1.2/50 μs) [9, 10]

Fig. 2 SSIGC [16]

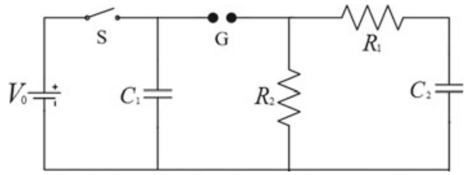

are trying to evaluate the parameters for generating SLI waveforms theoretically as well as practically. The trial-and-error method has previously been used to evaluate DEXP and SSIGC parameters. The design details of very low energy SSIGC for generating the impulse voltage waveforms are illustrated in [11]. The time parameters estimation of standard and non-standard switching impulse voltages is evaluated and presented in [12]. The aforementioned literature has discussed about to generate the standard lightning and switching impulse waveforms by designing of SSIGC but unable to focus on evaluation of SSIGC parameters. For doing so, the parameters of DEXP along with single and multi-stage impulse generation circuit parameters are evaluated and reported in [13, 14]. The SSIGC parameters are evaluated by using PSO algorithm and are reported in [15]. In line this, a new methodology is developed based on differential evolution optimization algorithm (DEOA) that is effectively utilized in this paper to generate the parameters of SSIGC.

2 Application of DEOA to Evaluate SSIGC Parameters

DEOA is a population-based metaheuristic globally search optimization algorithm. The complete details about the DEOA are illustrated in [17]. In this article, the parameters of SSIGC (such as R_1, R_2, C_1, and C_2) are determined by effective utilization of DEOA. The objective function or fitness function is the main heart of whole work. The objective function is formed from the physical parameters SLI voltage waveform such as rise time (t_{rise}) and tail time (t_{tail}). The MATLAB code is effectively written based on aforementioned fitness function and is considered in this paper to generate the unknown parameters of SSIGC. The fitness function is formed and given by Eq. (2) to diminish the error between two physical parameters (such as rise and tail times) of desired and computed SLI waveforms.

$$\text{Fitness function, } f = \left|\frac{t_{\mathrm{riseD}} - t_{\mathrm{rise}}}{t_{\mathrm{riseD}}}\right| + \left|\frac{t_{\mathrm{tailD}} - t_{\mathrm{tail}}}{t_{\mathrm{tailD}}}\right| \tag{2}$$

where f is the fitness function, t_{rised} is the rise time of SLI voltage waveform, t_{risec} is the rise time of the computed LI voltage waveform, t_{taild} is the tail time of SLI voltage waveform, and t_{tailc} is the tail time of the computed LI voltage waveform. Herein DEOA, the size of population is taken as 50, total number of iterations is considered as stopping criteria, and its value is taken as 200 (Fig. 3).

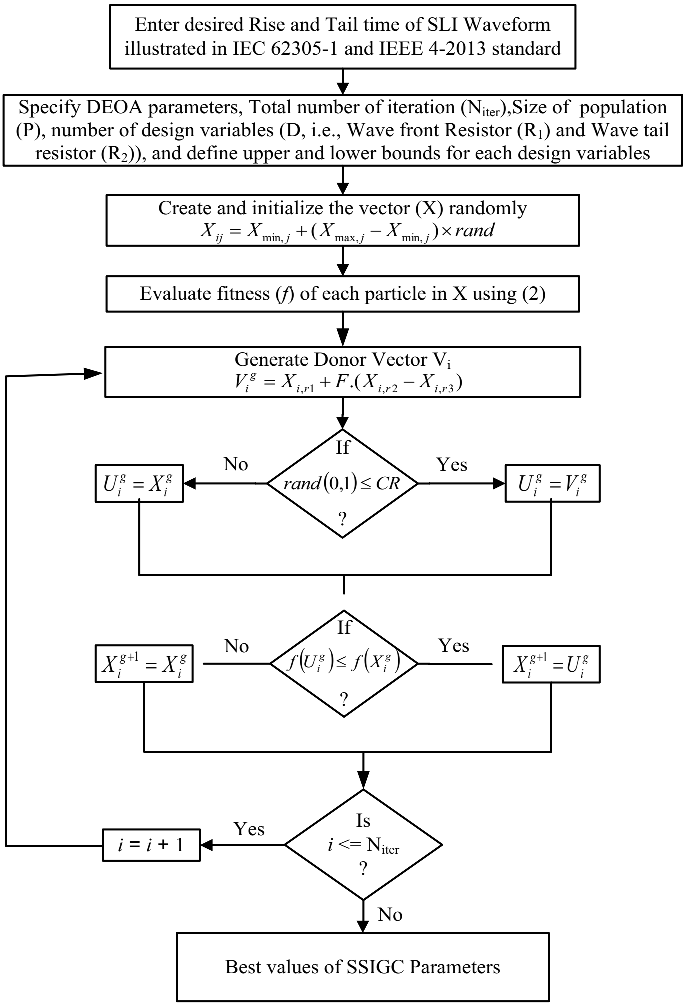

Fig. 3 DEOA flowchart for determining the parameters of SSIGC to generate SLI waveform

3 Results from Proposed Methodology

The parameters of SSIGC, i.e., C_1, C_2, R_1, and R_2 for producing the SLI voltage waveform are evaluated from proposed methodology given in Sect. 2 and are reported in Table 1.

The SSIGC parameters for generation of SLI waveform as shown in Table 1 need to be validated so that they can be used in HV laboratory for testing of insulation of HV apparatus. The results validation and the discussion on percentage error between the waveform obtained from proposed methodology and SLI will be discussed in Sect. 4.

Table 1 Results of SSIGC parameters obtained from DEOA

Standard lightning impulse waveform physical parameters (rise and tail times) (μs)	Results of SSIGC parameters evaluated from DEOA			
	C_1 (μF)	C_2 (μF)	R_1 (Ω)	R_2 (Ω)
1.2/50	0.1	0.001	607.88	679.1

4 Results Analysis and Validation

The SSIGC prototype is developed in MATLAB [18] and illustrated in Fig. 4. Figure 4 is used here to validate the results obtained from the proposed methodology. The parameters of SSIGC (C_1, C_2, R_1, and R_2) reported in Table 1 are substituted in their places in Fig. 4 for the validation purpose. The LI voltage waveform generated by MATLAB prototype circuit (Fig. 4) is illustrated in Fig. 5 and represented with black solid line. The SLI waveform is also merged in same Fig. 5 and is represented with red dashed line. The SLI waveform is precisely compared with the LI waveform obtained from proposed methodology. The percentage error is precisely computed in three basic physical parameters between SLI voltage waveform and computed LI voltage waveform obtained from DEOA and reported in Table 2.

Eventually, it is clearly concluded from Fig. 5 that the LI voltage waveform that is produced by the proposed methodology exactly merges with the SLI voltage waveform. Also, it is observed from Table 2 that the maximum error observed between SLI and computed LI is less than or equal to 0.24%. Moreover, the results obtained and reported in this paper are compared with results reported in [13] and identified that the proposed method exhibits least percentage error. Due to this lower percentage error, it can be concluded that the parameters of SSIGC definitely help to precisely

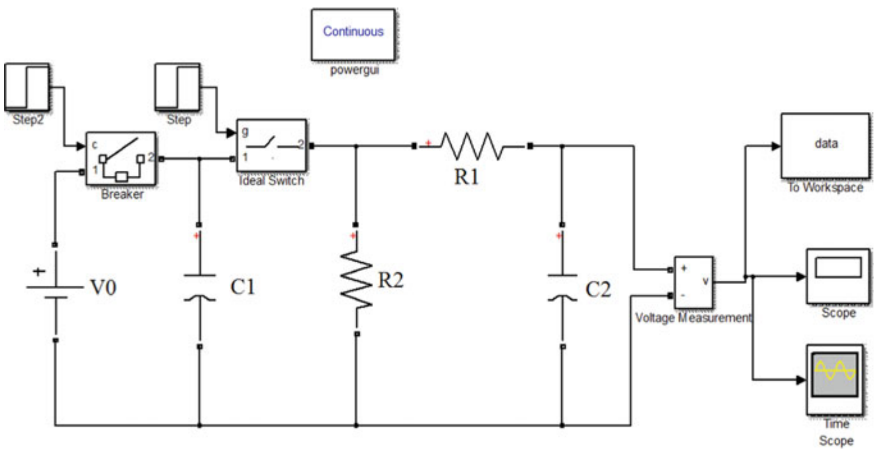

Fig. 4 SSIGC developed in MATLAB

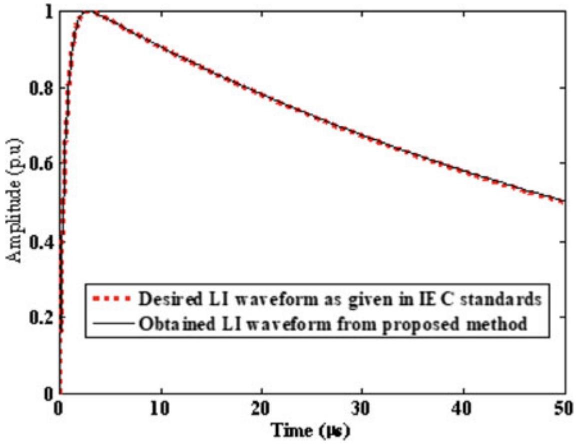

Fig. 5 Comparison between SLI waveform and computed waveform

Table 2 Comparison between SLI waveform and computed LI waveform by DEOA

Rise time (%)	Tail time (%)	Peak voltage (normalized) (%)
0.24	−0.14	0.00

develop the SLI in HV testing laboratory in order to test the insulation of HV power equipment effectively.

5 Conclusion

Differential evolution optimization algorithm (DEOA) is effectively utilized here to evaluate the parameters of SSIGC. The parameters of SSIGC are evaluated and reported in this paper. These results are theoretically validated through SSIGC prototype implemented in MATLAB/Simulink. The percentage error is precisely calculated in all physical parameters between the SLI voltage waveform and computed waveform by proposed methodology. Maximum error observed in the proposed approach based on DEOA is less than 0.24%. Thus, the SSIGC parameters evaluated and reported in this paper are definitely helpful in HV testing laboratory for generating SLI voltage waveforms. Further, these waveforms are needful for testing of the insulation of HV equipment.

References

1. Fitch RA (1971) Marx- and Marx-like—high-voltage generators. IEEE Trans Nucl Sci 18(4):190–198

2. Wu G (2014) Shape properties of pulses described by double exponential function and its modified forms. IEEE Trans Electromagn Compat 56(4):923–931
3. Yutthagowith P, Pattanadech N (2016) Improved least-square prony analysis technique for parameter evaluation of lightning impulse voltage and current. IEEE Trans Power Delivery 31(1):271–277
4. Cooray V (2010) Lightning protection. The Institute of Engineering and Technology, London
5. Kuffel E, Zaengl WS, Kuffel J (2000) Impulse voltages. In: High voltage engineering fundamentals. Butterworth Heinemann, Oxford, pp 48–66
6. Magdowski M, Vick R (2010) Estimation of mathematical parameters of double exponential pulses using the Nelder Mead algorithm. IEEE Trans Electromagn Compat 52(4):1–3
7. Qin F, Mao C, Wu G, Zhou H (2016) Characteristic parameter estimation of EMP energy spectrum. In: 7th Asia Pacific international symposium on electromagnetic compatibility, vol 1113
8. Camp M, Garbe H (2004) Parameter estimation of double exponential pulse (EMP, UWB) with least squares and Nelder Mead algorithm. IEEE Trans Electromagn Compat 46(4):675–678
9. IEEE Standard 4-2013 (2013) IEEE standard technique for high-voltage testing
10. IEC Standard 60060-1 (2010) High-voltage test techniques part 1: general definitions and test requirement
11. Joe YZ, Steven AB (2004) Low energy single stage high voltage impulse generator. IEEE Trans Dielectr Electr Insul 11(4):597–603
12. Filipovic-Gricic B, Filipovic-Gricic D (2018) A new method for estimation of time parameters of standard and non-standard switching impulse voltages. Electr Power Energy Syst 96:126–131
13. Ramarao G, Chandrasekaran K (2017) Calculation of multistage impulse circuit and its analytical function parameters. Int J Pure Appl Math 114(12):583–592
14. Ramarao G, Chandrasekaran K (2017) Evaluation of circuit and its analytical function parameters for lightning and switching impulse. In: International conference on innovations in electrical, electronics, instrumentation and media technology, Coimbatore, pp 302–305
15. Ramarao G, Jayaram N, Ram Mohan Naidu P, Vamsi A, Krishna Prasad M, Jagadeesh D (2021) Implementation of particle swarm optimization to evaluate single-stage impulse generation circuit parameters. In: Lecture notes in electrical engineering, vol 702, pp 537–543
16. Naidu MS, Kamaraju V (1995) High voltage engineering. Tata McGraw-Hill
17. Storn R, Price KV (1997) Differential evolution—a simple and efficient heuristic for global optimization over continuous spaces. J Glob Optim 11:341–359
18. MATLAB—the language of technical computing from MathWorks Inc. http://www.mathworks.com

Chapter 21
Frequency Control of GWO-Optimized Two-Area Microgrid with TIDF-II, I-PD and I-TD

Sourabh Prakash Roy, Shubham, A. K. Singh, R. K. Mehta, and O. P. Roy

Abstract This paper presents modelling of two-area microgrid system. The proposed system includes biogas, solar, wind, tidal and Archimedes wave energy conversion generating units. Furthermore, storage units are also modelled as flywheel energy storage, battery energy storage, super magnetic energy storage and static synchronous series compensator. The performance of the microgrid is studied with three controllers, namely TIDF-II, I-PD and I-TD. The controllers are tuned using grey wolf optimizer. Finally, comparative analysis of all the controllers is done.

Keywords Two-area · Microgrid · Metaheuristic · GWO · TIDF-II · I-PD · I-TD · 2-DOF · Step load · Random load change

1 Introduction

Microgrid is a type of energy system which is self-sufficient when operating autonomously, i.e. islanding. Microgrid provides opportunities to serve the needs of communities in extreme cases like power outage, grid failure etc. [1]. They are more localized, resilient and flexible. They can also increase the reliability of critical infrastructure like military installation, telecommunication system, space centre etc. For a typical microgrid, voltage control, power control and frequency control are required for proper working of the system. In this paper, we have exclusively put our attention to frequency control.

The frequency control is required for microgrid because of the following reasons

1. Frequency deviation affects the operation and reliability.
2. Large frequency error will result in abnormal condition of the microgrid leading to the damage of expensive equipment and instability.

In order to control frequency, different types of controllers are put forwarded in the literature. Some of them are PI, PID, FOPID, TID and other cascaded controllers [2].

S. P. Roy · Shubham (✉) · A. K. Singh · R. K. Mehta · O. P. Roy
Electrical Engineering Department, NERIST, Nirjuli, Arunachal Pradesh, India

G. Panda et al. (eds.), *Sustainable Energy and Technological Advancements*, Advances in Sustainability Science and Technology,
https://doi.org/10.1007/978-981-16-9033-4_21

Manual tuning of these controllers is time-consuming and cumbersome. Therefore, these controllers are tuned with different types of algorithms.

Heuristics means "to find" and meta means "beyond". Heuristics are the rules that are used to find solution to complex optimization problems. Problem with them is that the obtained solution is local optimum not global optimum. Metaheuristic algorithms are used to solve optimization problems in finite amount of time. They escape the local optimum and try to reach towards global optimum by using exploitation and exploration. Many metaheuristic algorithms are being developed to solve the problems, some of them are—GA, BFOA, TS, ABC, DE, ICA, QOHS, ALO and TLBO [3]. In this paper, GWO is used to tune the parameters of TIDF-II.

Guha et al. [4] model two-area non-reheat thermal generating unit. The controller used is proportional cascaded tilt–integral–derivative controller (CC-TID) whose control parameter is tuned using salp swarm algorithm (SSA) technique. The result is compared with I-, PI-, PID-, cascade PI-PD and TID-controllers. Kumari and Shankar [5] model multi-source two-area interconnected system comprising thermal, hydro and nuclear generating unit with non-linearities. The integral–tilt–derivative (I-TD) controller, fine-tuned using water cycle algorithm (WCA), and result is compared with conventional proportional–integral–derivative controllers.

Kumar and Shuhag [6] model multi-source hydro-thermal non-linear power system. The control parameter of the PID controller is tuned using differential evolution (DE) algorithm. The impact of thyristor-controlled phase shifter (TCPS) and superconducting magnetic energy storage (SMES) on the LFC performance is analysed. Yang et al. [7] use model predictive control for LFC with wind turbines generators. Power generated due to wind turbines are unpredictable, due to which frequency control becomes problematic. Authors used MPC for wind power prediction for smoothing the frequency.

Mahto and Mukherjee [8] model two-area hybrid system with thermal and wind diesel unit. The energy storage devices connected for compensation of load demand are capacitive energy storage and static synchronous series compensator. The PID controller is tuned using quasi-opposition harmony search (QOHS) algorithm. The result is compared with binary coded genetic algorithm. Saha and Saikia [9] model three-area dissimilar interconnected system with non-linearities. The cascade combination of integer order integral–derivative with filter (IDN) and fractional order proportional derivative (FOPD) is considered. The control parameter of IDN-FOPD is tuned using whale optimization algorithm. The simulation result of proposed controller is compared with integral, proportional–integral and proportional–integral–derivative with filter (PIDN).

Contributions of this paper

(a) Modelling of biogas, solar, wind, tidal, AWEC generating plants to form proposed isolated microgrid.
(b) Designing of TIDF-II, I-PD and I-TD controllers and tuning them using GWO.
(c) Stability and performance analysis for the two-area microgrid.

The work in the paper is arranged as follows: Sect. 2 describes two-area configuration of the considered system. In Sect. 3, controller design methodology is discussed.

A brief overview of the GWO algorithm is expressed in Sect. 4. Lastly, result and discussion as well as conclusion is illustrated in Sects. 5 and 6, respectively.

2 Two-Area Configuration

The system comprises of many renewable energy sources like biogas, solar, wind, tidal and AWEC. Also, energy storage elements are also added. The values for speed regulator R_1 and R_2 are 2.4, $M = 0.2$ and $D = 0.012$. The proposed system as in Fig. 1 consists of two areas—in area 1, solar and AWEC are the generating units and FESS, SMES, SSSC are the energy storage devices, whereas in area 2, wind and tidal are the generating units and BESS, SMES are the energy storage devices. Biogas-based generating unit is common to both areas. The realistic model of BESS and FESS [10] is included. Power balance equation of the system is given by

$$\Delta P_{\mathrm{gen1}} = \Delta P_{\mathrm{BG}} + \Delta P_{\mathrm{S}} + \Delta P_{\mathrm{AWEC}} \pm \Delta P_{\mathrm{FESS}} \pm \Delta P_{\mathrm{SMES}} - \Delta P_{\mathrm{load}} - \Delta P_{\mathrm{T12}} + \Delta P_{\mathrm{SSSC}} \tag{1}$$

$$\Delta P_{\mathrm{gen2}} = \Delta P_{\mathrm{BG}} + \Delta P_{\mathrm{w}} + \Delta P_{\mathrm{TD}} \pm \Delta P_{\mathrm{BESS}} \pm \Delta P_{\mathrm{SMES}} - \Delta P_{\mathrm{load}} - \Delta P_{\mathrm{T21}} + \Delta P_{\mathrm{SSSC}} \tag{2}$$

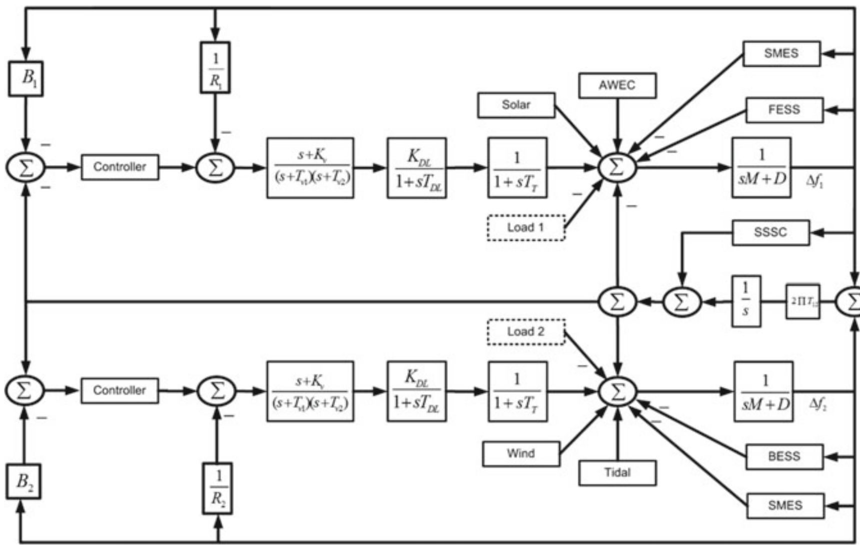

Fig. 1 Two-area microgrid representation

2.1 Biogas Turbine Generator

Biodegradable scraps and wastes are used for production biogas, which is then used for power generation. It consists of inlet valve, combustor and turbine [11]. Model is given by Eq. (3)

$$\Delta P_{\mathrm{BG}} = \left(\frac{s + K_{\mathrm{v}}}{(s + T_{\mathrm{v1}})(s + T_{\mathrm{v2}})}\right)\left(\frac{K_{\mathrm{DL}}}{1 + sT_{\mathrm{DL}}}\right)\left(\frac{1}{1 + sT_{\mathrm{T}}}\right) \tag{3}$$

2.2 Tidal Power Generator

It produces electricity using tides of ocean [12]. It is conceptually similar to wind turbines. Its model is given by Eq. (4)

$$\Delta P_{\mathrm{TD}} = \frac{1}{1 + sT_{\mathrm{TD}}} \tag{4}$$

2.3 Archimedes Wave Energy Conversion Generator

In this generator, mechanical energy is converted into electrical energy when AWS (Archimedes wave swing) is coupled with PMSG [13]. Linearized model is given by Eq. (5)

$$\Delta P_{\mathrm{AWEC}} = \frac{1}{1 + sT_{\mathrm{AW}}} \tag{5}$$

3 Controller Design Methodology

Three controllers are tested in the proposed system, namely TIDF-II, I-PD and I-TD. Wherein, I-PD and I-TD are 2-DOF controllers whereas, TIDF-II is a type of 1-DOF fractional order controller. Figures 2, 3 and 4 depict the structure of the control strategy used to stabilize the two areas. The tuned controller gains are indicated in Tables 1 and 2.

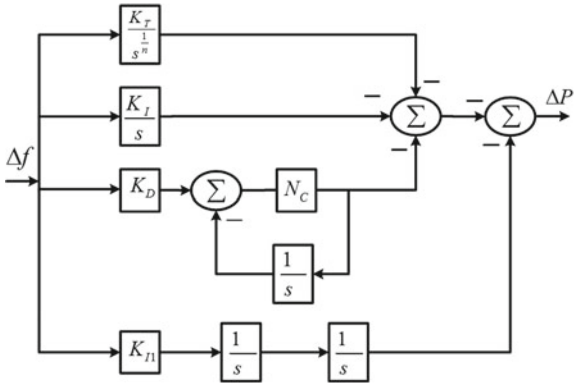

Fig. 2 TIDF-II controller representation

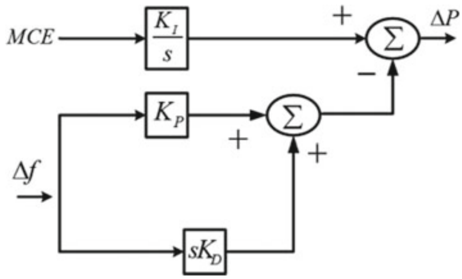

Fig. 3 I-PD controller representation

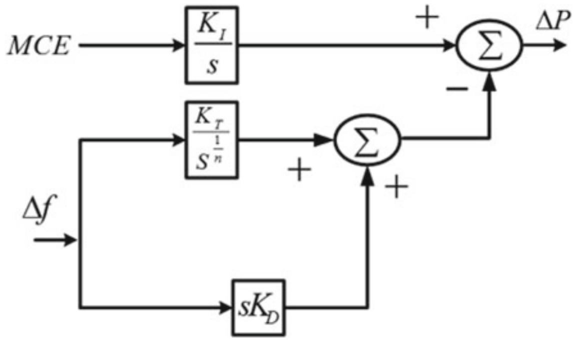

Fig. 4 I-TD controller representation

4 GWO Algorithm

In 2014, Mirjalili and others proposed grey wolf optimizer in the paper [14]. The said optimiser is a type of swarm-based intelligent algorithm. Grey wolves are native to European, Asian and North American continents. Optimizer utilizes the cooperative hunting plan of wolves. Wolves packs are separated into four types based on their roles namely alpha, beta, delta and omega. As the name suggests, alpha are the

Table 1 Two-area system models and its values

S. No.	Generating unit	Transfer function	Values
1.	Biogas	$\left(\frac{s+K_{\mathrm{v}}}{(s+T_{\mathrm{v1}})(s+T_{\mathrm{v2}})}\right)\left(\frac{K_{\mathrm{DL}}}{1+sT_{\mathrm{DL}}}\right)\left(\frac{1}{1+sT_{\mathrm{T}}}\right)$	$K_{\mathrm{v}}=0.6$, $T_{\mathrm{v1}}=1$, $T_{\mathrm{v2}}=0.05$, $K_{\mathrm{DL}}=0.01$, $T_{\mathrm{DL}}=0.23$, $T_{\mathrm{T}}=0.2$
2.	Solar	$\left(\frac{1}{1+sT_{\mathrm{s}}}\right)\left(\frac{1}{1+sT_{\mathrm{IN}}}\right)\left(\frac{1}{1+sT_{\mathrm{IC}}}\right)$	$T_{\mathrm{s}}=1.8$, $T_{\mathrm{IN}}=0.04$, $T_{\mathrm{IC}}=0.004$
3.	Wind	$\frac{1}{1+sT_{\mathrm{w}}}$	$T_{\mathrm{w}}=1.5$
4.	Tidal	$\frac{1}{1+sT_{\mathrm{TD}}}$	$T_{\mathrm{TD}}=0.08$
5	AWEC	$\frac{1}{1+sT_{\mathrm{AW}}}$	$T_{\mathrm{AW}}=0.3$
S. No.	Energy storage	Transfer function	Values
1.	BESS	$\left(\frac{1}{1+sT_{\mathrm{C}}}\right)\left(\frac{1}{1+sT_{\mathrm{CM}}}\right)\left(\frac{1}{1+sT_{\mathrm{DM}}}\right)$	$T_{\mathrm{C}}=0.1$, $T_{\mathrm{CM}}=0.01$, $T_{\mathrm{DM}}=0.1$
2.	FESS	$\left(\frac{1}{1+sT_{\mathrm{C}}}\right)\left(\frac{1}{1+sT_{\mathrm{CM}}}\right)\left(\frac{1}{1+sT_{\mathrm{DM}}}\right)$	$T_{\mathrm{C}}=0.1$, $T_{\mathrm{CM}}=0.01$, $T_{\mathrm{DM}}=0.1$
3.	SMES	$\left(\frac{1+sT_1}{1+sT_2}\right)\left(\frac{1+sT_3}{1+sT_4}\right)\left(\frac{K_{\mathrm{SMES}}}{1+sT_{\mathrm{SMES}}}\right)$	$T_1=0.121$, $T_2=0.8$, $T_3=0.011$, $T_4=0.148$, $K_{\mathrm{SMES}}=0.297$, $T_{\mathrm{SMES}}=0.03$
4.	SSSC	$\left(\frac{1+sT_{\mathrm{s1}}}{1+sT_{\mathrm{s2}}}\right)\left(\frac{1+sT_{\mathrm{s3}}}{1+sT_{\mathrm{s4}}}\right)\left(\frac{K_{\mathrm{SSSC}}}{1+sT_{\mathrm{SSSC}}}\right)$	$T_{\mathrm{s1}}=0.2587$, $T_{\mathrm{s2}}=0.2481$, $T_{\mathrm{s3}}=0.2333$, $T_{\mathrm{s4}}=0.060$, $K_{\mathrm{SSSC}}=0.2035$, $T_{\mathrm{SSSC}}=0.03$

Table 2 Value of controller parameter

S. No.	Controller			Parameters values			
1.	TIDF-II	Area 1	K_{T}, n	K_{I}	K_{D}	K_{I1}	N_{c}
			100, 0.0651	23.077	100	0.0702	78.970
		Area 2	K_{T}, n	K_{I}	K_{D}	K_{I1}	N_{c}
			99.824, 0.189	38.314	99.989	0.297	51.748
2.	I-PD	Area 1	K_{I}	K_{P}	K_{D}		
			6.549	45.195	77.985		
		Area 2	K_{I}	K_{P}	K_{D}		
			16.249	21.120	32.639		
3.	I-TD	Area 1	K_{I}	K_{T}, n	K_{D}		
			17.179	36.763, 0	79.401		
		Area 2	K_{I}	K_{T}, n	K_{D}		
			19.858	3.400, 0.727	87.973		

Fig. 5 Pseudocode of GWO

```
Input: Initialize the population of grey wolves;
       Initialize a, A, and C
Output: Pα
Calculate fitness values of each search agents;
Pα = Alpha wolf and best search agent;
Pβ = Beta wolf and second best search agent;
Pδ = Delta wolf and third best search agent;
while N < Max. no. of iterations do
    for each search agent do
        Update the position of the current search agent;
    end
    Update a, A, C;
    Calculate fitness values of all search agents;
    update Pα, Pβ, Pδ;
    N = N + 1;
end
return Pα
```

leaders, beta are the enforcers, delta are the scouts and omega are the scapegoats of the pack. Hunting plan involves

1. Searching the game
2. Following the game
3. Harassing the game
4. Striking the game.

The pseudocode of GWO is depicted in Fig. 5, which includes following nomenclature: $a = 2 - N * ((2)/\text{Max } N)$, it decreases linearly from 2 and 0; $A = 2 * a * r_1 - a$ and $C = 2 * r_2$ are the coefficient vector which includes r_1 and r_2 as random number.

The idea behind choosing GWO algorithm for tuning of controllers is because it shows very competitive performance as compared to other algorithms [14]. Also, it has faster convergence rate and avoids local optimum values.

5 Result and Discussions

The whole system is modelled in MATLAB R2016a. Proposed system is simulated for 250 s with search agents = 10 and number of iterations = 50. All the three controllers TIDF-II, I-PD and I-TD are tuned with the GWO algorithm for calculation of its parameters. Comparative study of the above-mentioned controllers are also done. TIDF-II shows good dynamic performance as compared to the other controllers. All the energy sources like solar, wind, tidal and AWEC are modelled to be fluctuating in nature. Figure 6 represents the input of solar and AWEC in area 1, whereas Fig. 7 shows the input response of area 2. The response of energy storage devices is exhibited in Fig. 8.

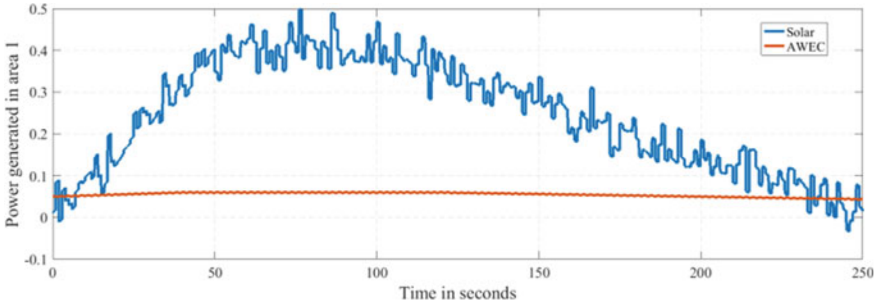

Fig. 6 Power generated in area-1 in pu

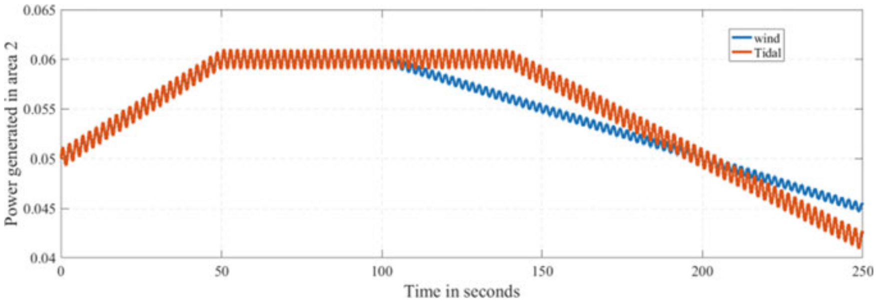

Fig. 7 Power generated in area-2 in pu

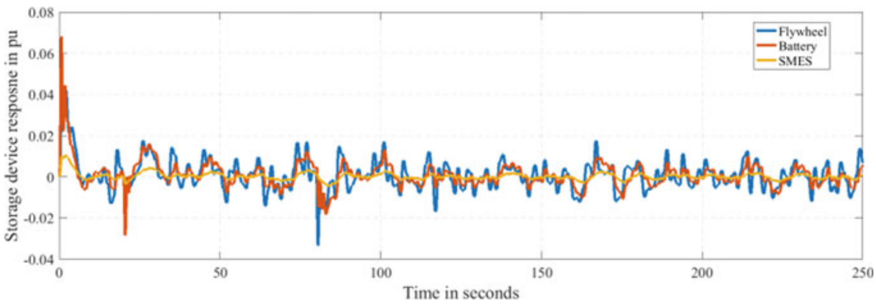

Fig. 8 Storage devices responses in pu

There is 5% step load change in area-1 at 80 s and 3% step load change in area-2 at 20 s are applied in the system for examining the performance of the system as shown in Fig. 9. The frequency variation for the two areas and tie-line power between them is communicated by Figs. 10, 11 and 12, respectively. The frequency deviation in given GWO TIDF controller is smallest among the entire controller. Also, all the three responses—frequency deviation of area 1, 2 and tie-line response—try to reach the condition of minimum steady-state error (Tables 3 and 4).

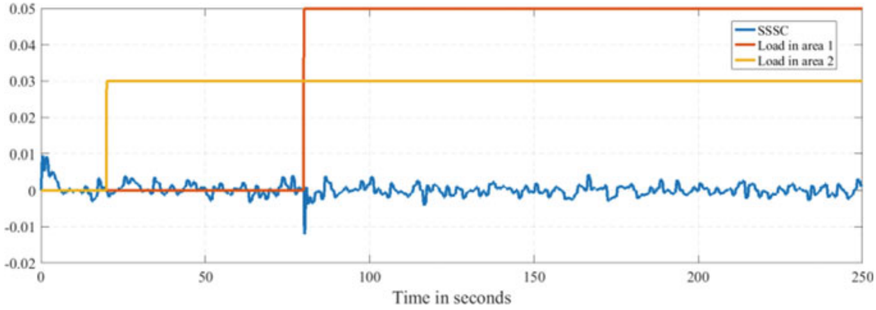

Fig. 9 Load demand of area-1, 2 and SSSC response of the microgrid

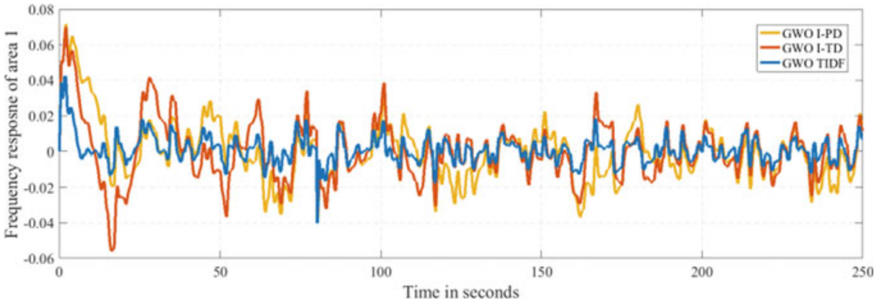

Fig. 10 Frequency response of area-1 in pu for different controllers

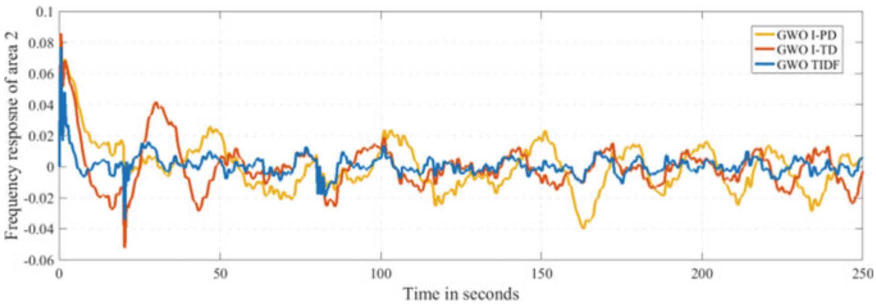

Fig. 11 Frequency response of area-2 in pu for different controllers

6 Conclusions

This paper successfully conducts the modelling of two-area microgrid. The GWO-tuned TIDF-II controller is found to be superior among the other controllers used in the paper. The frequency and tie-line power response of the TIDF-II is found to be satisfactory and gives improved performance.

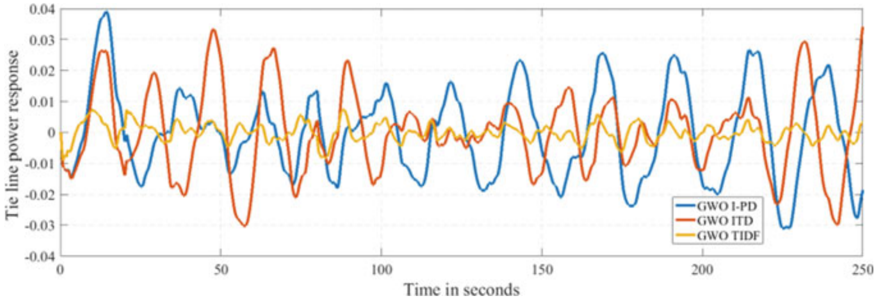

Fig. 12 Tie line power response for different controllers

Table 3 Controllers performance parameters

S. No.	Controller	Elapsed time (s)	Best score (ISE)
1.	TIDF-II	755.541	0.0252
2.	I-PD	279.403	0.155
3.	I-TD	552.321	0.143

Table 4 Controllers upper bounds and lower bounds

S. No.	Controller	Lower bounds	Upper bounds
1.	TIDF-II	[0 0 0 0 0 0 0 0 0 0 0 0]	[100 1 100 100 100 1 100 1 100 100 100 1]
2.	I-PD	[0 0 0 0 0 0]	[100 100 100 100 100 100]
3.	I-TD	[0 0 0 0 0 0 0 0]	[100 100 1 100 100 100 1 100]

Furthermore, the paper work can be extended to include other renewable energy sources. Also, comparative analysis of other newly developed algorithms can be incorporated in the model.

References

1. Roosa SA (ed) (2020) Fundamentals of microgrids: development and implementation. CRC Press
2. Tungadio DH, Sun Y (2019) Load frequency controllers considering renewable energy integration in power system. Energy Rep 5:436–453
3. Radosavljević J (2018) Metaheuristic optimization in power engineering. Institution of Engineering and Technology
4. Guha D, Roy P, Banerjee S (2018) A maiden application of salp swarm algorithm optimized cascade tilt-integral-derivative controller for load frequency control of power systems. IET Gener Transm Distrib 9:25–36
5. Kumari S, Shankar G (2018) Novel application of integral-tilt-derivative controller for performance evaluation of load frequency control of interconnected power system. IET Gener Transm Distrib 12(14):3550–3560

6. Kumar A, Shuhag S (2019) Impact of TCPS, SMES and DFIG on load frequency control of nonlinear power system using differential evolution algorithm. J Inst Eng (India) Ser B 100(2):153–167
7. Yang J, Sun X, Liao K, He Z, Cai L (2019) Model predictive control-based load frequency control for power systems with wind-turbine generators. IET Renew Power Gener
8. Mahto T, Mukherjee V (2016) Load frequency control of a two-area thermal-hybrid power system using a novel quasi-opposition harmony search algorithm. J Inst Eng (India) Ser B 97(3):367–380
9. Saha A, Saikia LC (2019) Renewable energy source-based multiarea AGC system with integration of EV utilizing cascade controller considering time delay. Int Trans Electr Energy Syst 29(1):e2646
10. Babaei M, Abazari A, Muyeen SM (2020) Coordination between demand response programming and learning-based FOPID controller for alleviation of frequency excursion of hybrid microgrid. Energies 13(2):442
11. Barik AK, Das DC (2018) Expeditious frequency control of solar photovoltaic/biogas/biodiesel generator based isolated renewable microgrid using grasshopper optimisation algorithm. IET Renew Power Gener 12(14):1659–1667
12. Latif A, Das DC, Barik AK, Ranjan S (2020) Illustration of demand response supported coordinated system performance evaluation of YSGA optimized dual stage PIFOD-(1+PI) controller employed with wind-tidal-biodiesel based independent two-area interconnected microgrid system. IET Renew Power Gener 14(6):1074–1086
13. Latif A, Das DC, Barik AK, Ranjan S (2019) Maiden coordinated load frequency control strategy for ST-AWEC-GEC-BDDG-based independent three-area interconnected microgrid system with the combined effect of diverse energy storage and DC link using BOA-optimised PFOID controller. IET Renew Power Gener 13(14):2634–2646
14. Mirjalili S, Mirjalili SM, Lewis A (2014) Grey wolf optimizer. Adv Eng Softw 69:46–61

Chapter 22
A Review on Control Methods Used in Renewable Energy Source-Fed Induction Motors

Pranobjyoti Lahon, Aditya Bihar Kandali, Gayadhar Panda, and Moushumi Patowary

Abstract In this paper, a detailed review of conventional controllers and sensorless control techniques used in renewable energy source (RES)-fed induction motor (IM) is presented in order to justify their best uses. From the study, it is observed that the sensorless control techniques outperform the conventional ones in terms of hardware complexity, cost, immunity to noise, reliability and robustness. RES has been extensively integrated into the power network due to the advancement in power converter topologies and has been a potential solution for increasing energy demand issues due to its various advantages such as clean power generation, cost-effective, easy availability and abundances. Appropriate IM control technique can reduce losses and increase the efficiency of a system. Various control techniques are available for IM drive, but sensorless control techniques have been widely used nowadays in RES-fed AC motors for industrial as well as domestic applications. Whereas, conventional techniques like proportional integral (PI) and proportional integral derivative (PID) generally have fixed gain which are sensitive to any changes in parameter and load disturbances. It is found that sensorless controllers are the most accurate and alternate forms in overcoming the disadvantages arising in the conventional ones.

Keywords Sensorless control · Conventional control · Renewable energy source · Induction motor

P. Lahon (✉)
The Assam Kaziranga University, Jorhat, Assam 785006, India

A. B. Kandali · M. Patowary
Jorhat Engineering College, Jorhat, Assam 785007, India
e-mail: moushumi.patowary@nitm.ac.in

G. Panda
National Institute of Technology, Meghalaya, Shillong 793003, India

G. Panda et al. (eds.), *Sustainable Energy and Technological Advancements*, Advances in Sustainability Science and Technology,
https://doi.org/10.1007/978-981-16-9033-4_22

1 Introduction

Induction motor (IM) finds its wide applicability in industrial and domestic applications due to its design simplicity, low cost, compactness, greater reliability, wide range of speed, robust and easier maintenance. As compared to DC and permanent magnet machines, IM requires more complex control methods [1–3]. The conventional speed control techniques of an induction motor are limited to drives with constant speed. Therefore, it is significant to investigate efficient control techniques for wide operating range [4]. Conventional methods for estimation of IM rotor speed/position use electromechanical position sensors which increases the weight, cost, size, hardware complexity and reliability problem. These drawbacks led to the development of sensorless control techniques. For high performance AC drives, electrical and mechanical sensors are commonly opted with high resolution, but the factors such as economic and sensor characteristics weakens the performance. Sensorless control techniques are advantageous due to its high reliability, cost-effectiveness, increase in mechanical robustness, wide operating range, superior stability, less maintenance requirements and elimination of the sensor cable [5–8]. Renewable energy sources such as solar and wind have emerged as a potential and clean energy resource to meet the increasing energy demand, and its use has been encouraged by developed/developing countries to reduce the dependency of fossil fuel and conventional sources. Utilization of the power drawn from the renewable energy sources are done either in standalone applications or can be fed to the utility grid [9–11].

This paper introduces the developments in sensorless control techniques used in RES fed IM for both industrial and household applications. Various conventional control techniques used in RES fed IM are discussed in Sect. 2. Section 3 deals with the sensorless control techniques used in IM drives. The advantages and disadvantages of the control techniques are presented in tabular form in Sects. 2 and 3.

2 Conventional Control Techniques Used in RES-Fed IM

Conventional control techniques discussed in this section are proportional integral (PI), integral proportional (IP), proportional resonant (PR), proportional integral derivative (PID) and predictive control (PC). Table 1 gives the summary of advantages and disadvantages of conventional control techniques. PI controller is the most common for speed control of IM. The authors in [12] discussed a concurrent PI control method for IM using indirect vector control where the stator current dynamics is used. The robustness to variations in rotor resistance and load torque are incorporated in the design problem. However, PI controller has some drawbacks such as undesirable speed overshoot and slow response to abrupt disturbances [13]. The disadvantages of PI controller led to the proposal of an integral proportional

Table 1 Advantages and disadvantages of conventional control techniques

Conventional control technique	Advantages	Disadvantages
Proportional integral	Simple in design	High starting overshoot
[10–13, 20]	No steady-state error	Sluggish response to sudden disturbances
Integral proportional	Reduced speed overshoot	Fixed gain
[11, 13, 14]		
Proportional resonant	Less harmonics	Sensitive to parameter variations
[11, 15–17]	Improved time response	
Proportional integral derivative	Simple in design	Proper tuning is required otherwise the system would be unstable
[10, 12, 18]	Process independent	Hunting
Predictive control	Fast response	Large computational complexity
[16, 19, 21]	Suitable for control constraints and non-linear systems	

(IP) controller. The overshoot problem that occurs in PI is reduced in IP controller due to the absence of zero in IP controller. Literature [14] proposed an integral plus proportional (IP) controller for speed estimation in induction motor. Simulation results showed better performance in speed overshoot, steady-state error and settling time. The proportional resonant (PR) controllers have been used in various power converter applications [15]. PR controller provides an infinite gain at chosen frequencies [16]. Literature [17] proposed a proportional resonant (PR) controller for closed-loop semi-converter three-phase induction motor. PID control is a stable control which uses a control loop feedback mechanism to control process variables. Literature [18] shows the application of PID controllers. It is difficult to achieve the desired control performance in conventional PID controller due to the presence of unknown nonlinearities, time delays, disturbances and variations in system parameters. In literature [19], the authors compared predictive control methods for speed control of IM with respect to their performances and design parameters. Reference and disturbance steps are applied to the system in different operational modes to evaluate the control behaviour.

The conventional methods suffered from various disadvantages such as increase in cost, size, hardware complexity and reliability issues. On the other hand, sensorless control techniques gained much attention for IM applications due to its advantages such as reduced hardware complexity, high reliability, low cost and superior stability which is discussed in Sect. 3. The advantages and disadvantages of the conventional control techniques are presented in Table 1.

3 Sensorless Control Techniques Used in RES-Fed IM

Sensorless control of IM drive has been a significant area for researchers in recent times. The key sensorless techniques are frequency signal injection, model reference adaptive system (MRAS), sliding mode observer (SMO), extended Kalman filter (EKF), adaptive flux observer (AFO), artificial neural network (ANN) and fuzzy logic control (FLC).

3.1 Frequency Signal Injection Method

The stability of IM operation at zero stator current frequency can be obtained in this method. Developments on high-frequency and low-frequency signal injection method is presented in this section. Information regarding rotor position can be acquired from the stator winding by injecting a frequency signal into the rotor winding and utilizing rotor slot harmonic, saturated and leakage inductance. The phase difference of stator and rotor voltages of the IM can be termed as a function of the rotor position [22, 23].

In literature [24], the authors described a sensorless IM control to detect the flux angle of the rotor from stator voltages and currents by injecting high-frequency signal. Experiments provided satisfactory results of 150% output of the rated torque at zero speed and zero frequency. Proper design of IM is required for correct extraction of position of rotor from feedback current information. Hinkkanen et al. [25] presented a low-frequency current signal injection method in the current loop to find the position of rotor from current back emf. In literature [26], the authors proposed a low-frequency signal injection method for sensorless vector control of induction motor at very low speed. The error in angle is found by introducing a low-frequency signal to the stator currents to estimate the rotor position and speed. Leppanen and Luomi in [27] proposed a low-frequency current signal injection method for IM, and experimental results showed that the fundamental IM model is required only and the method is not dependent on the motor parameter variations. This technique is not widely used in industry as it relies on the motor design and requires anisotropy of magnetic field.

3.2 Model Reference Adaptive System (MRAS)

MRAS is a popular adaptive control method used to track and observe the system parameters and states. MRAS is commonly used due to its easiness and reduced computational effort [28–31]. Figure 1 shows the MRAS control diagram. Literature [32] described an MRAS for speed estimation of IM using the terminal voltages and currents. Moderate bandwidth speed control can be achieved by using the speed

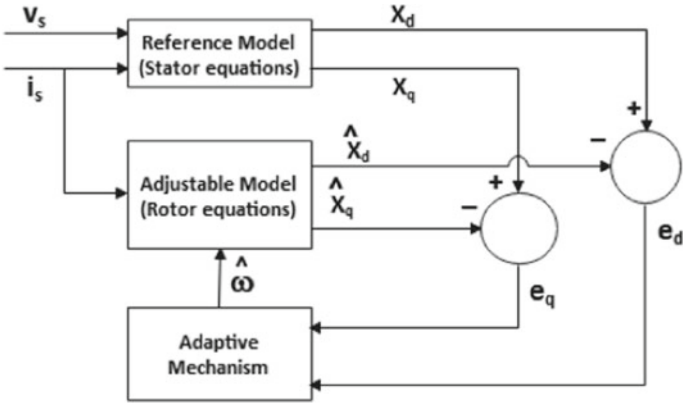

Fig. 1 MRAS control diagram

estimated as the feedback without using shaft-mounted transducers. Literature [33] describes an MRAS with field-oriented control for speed estimation of IM. The terminal voltages and current values are taken for sensorless estimation of speed and rotor fluxes. The current control is done at synchronously rotating reference frame, and the estimated speed information is used for transformation of reference frame of the current controller. The authors in [34] described that MRAS control is less responsive to problems related to integrator, and also, the estimation of speed at or near zero is quite accurate.

3.3 Sliding Mode Observer (SMO)

Sliding mode observer (SMO) has gained much attention in sensorless IM drives due to its robustness to parameter changes, rejection of disturbances, reduction in system order, no extensive computations and simplicity of implementation [35–40]. Figure 2 shows the control diagram of SMO. Literature [41, 42] presented SMOs for rotor flux observation. The observers do not employ variation of rotor speed so remained unaffected by speed error estimation. The observers could sustain speed as low as 3 r/min. In [43], Zhao et al. presented a sensorless speed control of an IM built on sliding mode super-twisting algorithm and MRAS estimation theory where the variation of stator resistance and rotor resistance are studied. The chattering behaviour is reduced in the proposed scheme. SMO based on the current model of IM is investigated in [44–48] to estimate the rotor flux linkage, rotor speed and rotor time constant.

According to dynamic behaviour of IM model, new structures of SMO are designed to provide robustness to the observer against motor parameter variations. The proposed observers work well over wide range of speed. Similarly, a new SMO is designed using two SMOs in [49] with optimized structure. Literature [50] presents an

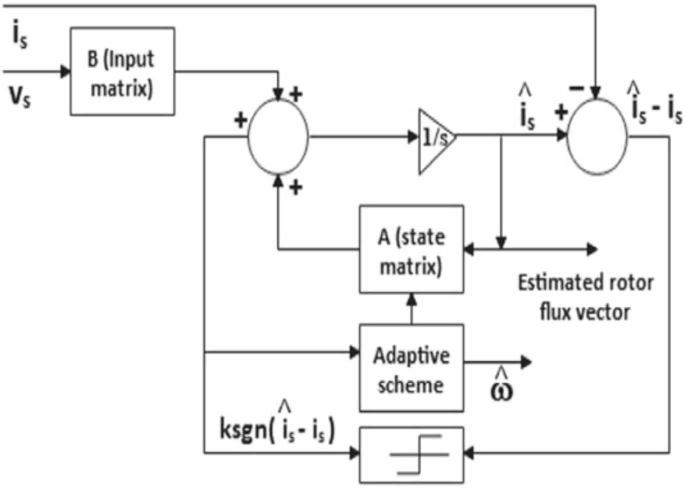

Fig. 2 SMO control diagram

SMO using modified IM model for estimation of flux linkage. The proposed observer showed that even after using inaccurate input estimated speed signal, accurate flux linkage estimation can be done by the observer. In [51], the authors introduced a fuzzy logic algorithm to reduce the chattering effect by replacing the sign function. A robust performance is obtained from the proposed fuzzy-SMO in low and high range of speed.

3.4 Extended Kalman Filter (EKF)

EKF is suitable for sensorless IM drive as it can provide accurate estimation of state variables under noise condition [52]. EKF is widely used to estimate the load torque and rotor speed of IM. Figure 3 shows the control diagram of EKF. Barut et al. in [53] developed estimation algorithms using EKF for sensorless speed and torque control of IM. The method proved its efficiency over a wide range of velocity by limiting the errors in current estimation within a certain band limit. The error in velocity estimation obtained for zero-speed operation lies within 2–4 r/min. The authors in [54] designed a method for direct vector sensorless control of speed of an IM by rotor orientation. The load torque, resistance of rotor and the states required for the control algorithm are estimated by EKF. A speed and rotor flux estimation for IM using extended Kalman filter (EKF) is described in [55]. Literature [56] presented a novel extended Kalman filter (EKF) for direct torque controlled induction motor. In [57], a robust Kalman filter observer has been proposed in which least square principle is used to design an adaptive law for speed estimation of IM.

Fig. 3 EKF control diagram

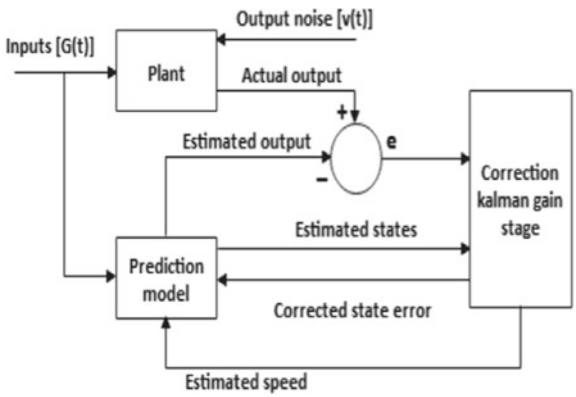

3.5 Adaptive Flux Observer (AFO)

AFO is a sensorless control technique for speed estimation of IM based on machine model. Figure 4 shows the control diagram of AFO. Literature [58] presented an AFO method which is insensitive to variations in stator resistance for sensorless control of IM. The AFO showed robustness to sudden variations in load. Results showed that the AFO could estimate accuracy in speed in region where the speed is very low. Machine model-based estimation for sensorless control operation at low frequencies is quite difficult [59].

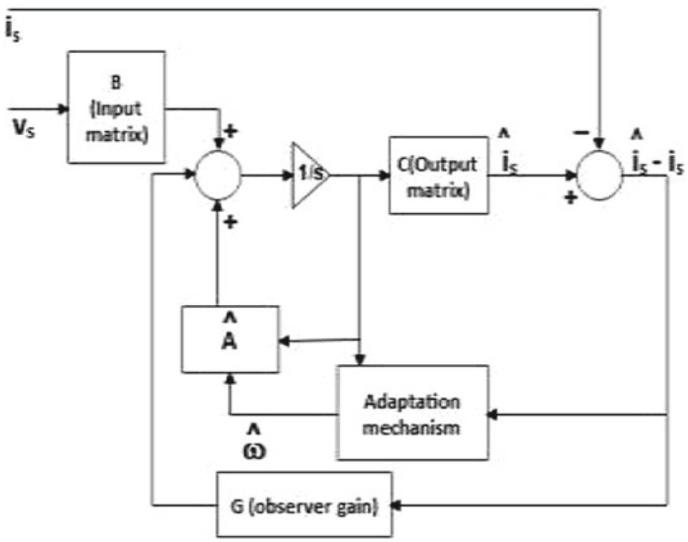

Fig. 4 AFO control diagram

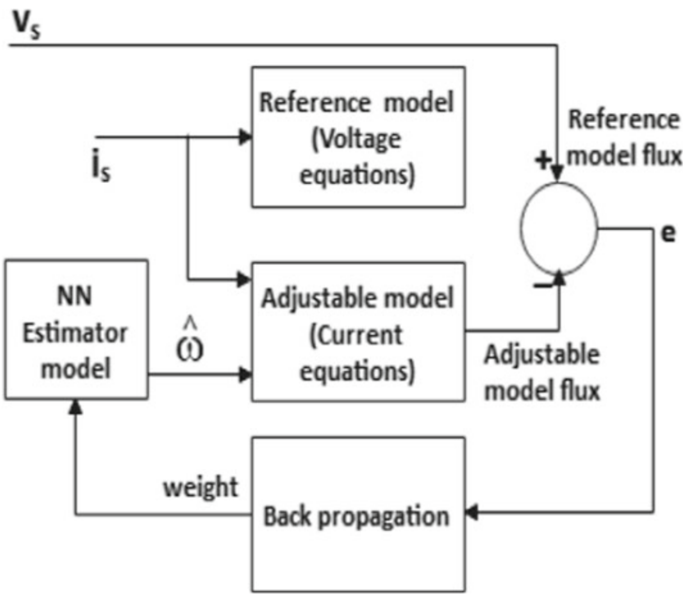

Fig. 5 ANN control diagram

3.6 Artificial Neural Network (ANN)

Figure 5 shows the ANN control diagram. In literature [60], the authors presented an intelligent controller based on neural network for controlling the speed of an IM by indirect vector control without using flux and speed sensors. Experimental results showed that a speed of 120 rad/s was obtained at 2.1 s. Nguyen et al. [61] presented an ANN method to estimate the speed of a three-phase IM. Backpropagation of the rotor flux linkages error in the adaptive and reference model was done so that the neural network model weights were adjusted to approximate the speed of the motor.

3.7 Fuzzy Logic Control (FLC)

Fuzzy logic control is used for various motor control applications [62]. Figure 6 shows the control diagram of FLC. In literature [20], a fuzzy logic control (FLC) is applied in an IM for constant speed application when there is a variation in load. Authors in [63] presented a fuzzy logic speed controller for an IM based on indirect vector control. Experimental results showed that the proposed fuzzy logic controller is insensitive to temperature variations, inertia changes and disturbances in load torque.

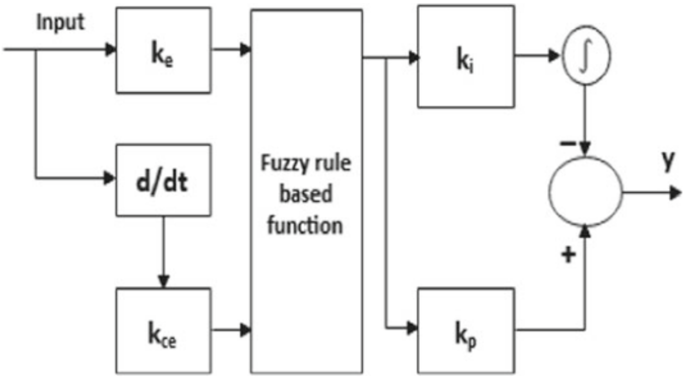

Fig. 6 FLC control diagram

Advantages and disadvantages of various sensorless control techniques after detailed study are presented in Table 2.

4 Conclusion

This paper provides a detailed review on the recent progress in control techniques for RES-fed IM to justify their best uses. Renewable energy systems have been widely used for solving issues related to increasing energy demand. Sensorless control techniques are the replacements for overcoming the disadvantages of conventional controllers. The conventional control methods have various difficulties such as their dependency on the accuracy of the mathematical system model, load variations, motor saturation and thermal variations. Whereas, sensorless control techniques can achieve reduction in hardware complexity, high reliability, low cost and better noise immunity so that the overall performance is improved for an IM drive system. Sensorless control technique is preferred over conventional control for higher efficiency and reliability over a wide operating range for IM applications. From the literatures, it is observed that sensorless control technique could sustain low speed of 3 r/min as well.

Table 2 Advantages and disadvantages of sensorless control techniques

Sensorless technique	Advantages	Disadvantages
Frequency signal injection [22–27, 64, 65]	Machine parameters are not required to implement the algorithm	Usually moderate dynamic response
Sliding mode observer (SMO) [35–39, 47–49, 66–70]	Dynamic response is fast	Accuracy in control is low due to chattering effect
	Robustness	Power circuits possess a high amount of heat loss
	Implementation is easy	Control loop is unstable
Model reference adaptive system (MRAS) [2, 7, 28–31, 66, 71, 72]	Simplicity in design	Sensitive to IM parameter changes
	Robustness to parameter variations	Performance limitation at low and zero-speed operating region
	High speed of adaptation	
Extended Kalman filter (EKF) [8, 22, 52–57, 73, 74]	Good dynamic behaviour	Absence of design and tuning criteria
	Can work even at standstill conditions	Heavy computational burden
		Complex in design
Adaptive flux observer [22, 32, 46, 50, 58, 75]	Better stability	Difficulty in design of adaptation mechanism
	Robust dynamic performance	Unstable at zero stator frequency
Artificial neural network (ANN) [47, 60–62, 76, 77]	Wide speed range	Heavy computational requirements
	Better stability	Relatively complicated
Fuzzy logic control [1, 4, 18, 20, 51, 62, 63, 76, 77]	Unaffected by variations in temperature, disturbances in load torque and changes in inertia	Dependent on human knowledge and expertise
	Exact mathematical model of the system is not required	High computational burden

References

1. Rashidi F (2004) Sensorless speed control of induction motor drives using robust and adaptive neuro-fuzzy based intelligent controller. IEEE Int Conf Ind Technol (ICIT) 2:617–627
2. Pal A, Das S, Chattopadhyay AK (2018) An improved rotor flux space vector based MRAS for field-oriented control of induction motor drives. IEEE Trans Power Electron 33(6)
3. Nandi S, Ahmed S, Toliyat HA, Bharadwaj RM (2003) Selection criteria of induction machines for speed-sensorless drive applications. IEEE Trans Ind Appl 39(3):704–712
4. Chitra V, Prabhakar RS (2006) Induction motor speed control using fuzzy logic controller. World Acad Sci Eng Technol 23
5. Holtz J (2002) Sensorless control of induction machines—with or without signal injection. IEEE Trans Ind Electr 53(1):7–30
6. Holtz J (2002) Sensorless control of induction motor drives. IEEE Proc 90(8):1359–1394

7. Merrassi WE, Abounada A, Ramzi M (2021) Advanced speed sensorless control strategy for induction machine based on neuro-MRAS observer. Mater Today Proc
8. Lesan AYE, Doumbia ML, Sicard P (2012) Comparative study of speed estimation techniques for sensorless vector control of induction machine. In: IECON 2012—38th annual conference on IEEE industrial electronics society
9. Prince SK, Panda KP, Patowary M, Panda G (2019) FPA tuned extended Kalman filter for power quality enhancement in PV integrated shunt active power filter. In: International conference on computing, power and communication technologies (GUCON), pp 27–28
10. Zahedi B, Vaez-Zadeh S (2009) Efficiency optimization control of single phase induction motor drives. IEEE Trans Power Electron 24(4):1062–1071
11. Chang GW, Espinosa-Perez G, Mendes E, Ortega R (2000) Tuning rules for the PI gains of field oriented controllers of induction motors. IEEE Trans Ind Electron 47(3):592–602
12. Jain JK, Ghosh S, Maity S (2018) Concurrent PI controller design for indirect vector controlled induction motor. Asian J Control
13. Sreekumar T, Jiji KS (2012) Comparison of proportional-integral (P-I) and integral-proportional (I-P) controllers for speed control in vector controlled induction motor drive. In: 2nd international conference on power, control and embedded systems
14. Hashim A, Ahmed O (2014) Speed control of vector controlled induction motors using integral-proportional controller. SUST J Eng Comput Sci (JECS) 15(2)
15. Yepes AG, Freijedo FD, López Ó et al (2011) Analysis and design of resonant current controllers for voltage-source converters by means of Nyquist diagrams and sensitivity function. IEEE Trans Ind Electron 58(11):5231–5250
16. Maccari LA, AmaralSantini CLD, Pinheiro H et al (2015) Robust optimal current control for grid-connected three-phase pulse-width modulated converters. IET Power Electron 8(8):1490–1499
17. Geeta M, Aspalli S (2020) Proportional resonant controller for semi converter three phase VSI fed induction motor drive to enhance time response. In: International conference on power electronics & IoT applications in renewable energy and its control (PARC)
18. Dongale TD, Jadhav SR, Kulkarni SV, Kulkarni TG, Mudholkar RR, Uplane MD (2012) Performance comparison of PID and fuzzy control techniques in three phase induction motor control. Int J Recent Trends Eng Technol 7(2)
19. Ahmed AA, Koh BK, Lee Y (2018) A comparison of finite control set and continuous control set model predictive control schemes for speed control of induction motors. IEEE Trans Ind Inform 14(4)
20. Arulmozhiyal R, Baskaran K (2009) Speed control of induction motor using fuzzy PI and optimized using GA. Int J Recent Trends Eng 2(5)
21. Xu D, Wang B, Zhang G, Wang G, Yu Y (2018) A review of sensorless control methods for AC motor drives. CES Trans Electr Mach Syst 2(1)
22. BabaLawan M, Samaila YA, Tijjani I, Mustapha M, Sarki MA (2019) Review of the rotor position and speed estimation method of induction motor drives. ASPL Int J Inf Technol 8(1):74–91. ISSN: 2360-9981
23. Sun W, Gao J, Yu Y, Wang G, Xu D (2016) Robustness improvement of speed estimation in speed-sensorless induction motor drives. IEEE Trans Ind Appl 52(3):2525–2536
24. Ha J, Sul S (1999) Sensorless field-orientation control of an induction machine by high-frequency signal injection. IEEE Trans Ind Appl 35(1):45–51
25. Hinkkanen M, Leppanen VM, Luomi J (2005) Flux observer enhanced with low-frequency signal injection allowing sensorless zero-frequency operation of induction motors. IEEE Trans Ind Appl 41(1):52–59
26. Li Y, Wu S (2009) A new method of speed-sensorless control of induction motor at very low speed. In: 8th international symposium on advanced electromechanical motion systems & electric drives joint symposium
27. Leppanen VM, Luomi J (2003) Observer using low-frequency injection for sensorless induction motor control-parameter sensitivity analysis. In: IEEE international electric machines and drives conference, IEMDC'03

28. Rao P, Nakka J, Shekar R (2013) Sensorless vector control of induction machine using MRAS techniques. In: International conference on circuits, power and computing technologies (ICCPCT)
29. Finch JW, Giaouris D (2008) Controlled AC electrical drives. IEEE Trans Ind Electron 55(2):481–491
30. Kumar R et al (2015) Review on model reference adaptive system for sensorless vector control of induction motor drives. IET Electr Power Appl 9(7):496–511
31. Blaabjerg F, Teodorescu R, Zelechowski M, Lach P, Rozanski P (2005) Rotor flux and speed estimators for induction motor drives. A performance evaluation. In: IEEE ISlE, vol I, pp 19–24
32. Schauder C (1992) Adaptive speed identification for vector control of induction motors without rotational transducers. IEEE Trans Ind Appl 28(5):1054–1061
33. Bekhiti B, Nail B, Abdellah K (2015) Model reference adaptive system MRAS control to three-phase induction motor. Int J Adv Electr Eng 2(1)
34. Maiti S, Chakraborty C, Hori Y, Ta MC (2008) Model reference adaptive controller-based rotor resistance and speed estimation techniques for vector controlled induction motor drive utilizing reactive power. IEEE Trans Ind Electron 55(2):594–601
35. Zhang YC, Zhao ZM, Zhang YCH, Song GS (2008) A full sliding mode sensorless control of three-level inverter-fed induction motors. In: Conference of Rec. IEEE PESC'08, vol 3, pp 2825–2831
36. Tursini M, Petrella R, Parasiliti F (2000) Adaptive sliding-mode observer for speed-sensorless control of induction motors. IEEE Trans Ind Appl 36(5)
37. Utkin VI, Guldner JG, Shi J (1999) Sliding mode control in electromechanical systems. Taylor & Francis, New York
38. Rao S, Buss M, Utkin V (2009) Simultaneous state and parameter estimation in induction motors using first- and second-order sliding modes. IEEE Trans Ind Electron 56(9):3369–3376
39. Trabelsi R, Khedher A, Mimouni MF, M'sahli F (2012) Backstepping control for an induction motor using an adaptive sliding rotor-flux observer. Electr Power Syst Res 93:1–5
40. Chen J, Huang J (2017) Online decoupled stator and rotor resistances adaptation for speed sensorless induction motor drives by a time-division approach. IEEE Trans Power Electron 32(6):4587–4599
41. Lascu C, Andreescu GD (2006) Sliding-mode observer and improved integrator with DC-offset compensation for flux estimation in sensorless-controlled induction motors. IEEE Trans Ind Electron 53(3):785–794
42. Lascu C, Boldea I, Blaabjerg F (2009) A class of speed-sensorless sliding-mode observers for high-performance induction motor drives. IEEE Trans Ind Electron 56(9):3394–3403
43. Zhao L, Huang J, Liu H, Li B, Kong W (2014) Second-order sliding-mode observer with online parameter identification for sensorless induction motor drives. IEEE Trans Ind Electron 61(10):5280–5289
44. Derdiyok A, Güven MK, Rehman H, Inanc N, Xu L (2002) Design and implementation of a new sliding-mode observer for speed-sensorless control of induction machine. IEEE Trans Ind Electron 49(5):1177–1182
45. Derdiyok A (2003) Simple method for speed and rotor resistance estimation of induction machines. IEEE Proc Electr Power Appl 150(3):289–294
46. Rehman H, Derdiyok A, Güven MK, Xu L (2002) A new current model flux observer for wide speed range sensorless control of an induction machine. IEEE Trans Power Electron 17(6):1041–1048
47. Derdiyok A (2005) Speed-sensorless control of induction motor using a continuous control approach of sliding-mode and flux observer. IEEE Trans Ind Electron 52(4):1170–1176
48. Jiménez E, Jaramillo O, Sánchez-Torres J, Boteroy H (2015) A second order sliding mode state and parameter estimator for induction motors. In: Proceedings of the 12th international conference on electrical engineering, computing science and automatic control (CCE), Mexico City, pp 1–6
49. Tursini M, Petrella R, Parasiliti F (2000) Adaptive sliding mode observer for speed sensorless control of induction motors. IEEE Trans Ind Appl 36(5):1380–1387

50. Comanescu M (2016) Design and implementation of a highly robust sensorless sliding mode observer for the flux magnitude of the induction motor. IEEE Trans Energy Convers 31(2):649–657
51. Kandoussi Z, Boulghasoul Z, Elbacha A, Tajer A (2015) Fuzzy sliding mode observer based sensorless indirect FOC for IM drives. In: Proceedings of third world conference on complex systems (WCCS), Marrakech, pp 1–6
52. Zhang Y, Zhao Z, Lu T, Yuan L, Xu W, Zhu J (2009) A comparative study of Luenberger observer, sliding mode observer and extended Kalman filter for sensorless vector control of induction motor drives. In: IEEE energy conversion congress and exposition
53. Barut M, Bogosyan S, Gokasan M (2007) Speed-sensorless estimation for induction motors using extended Kalman filters. IEEE Trans Ind Electron 54(1)
54. Barut M, Gokasan M, Bogosyan OS (2003) An extended Kalman filter based sensorless direct vector control of induction motors. In: IECON'03. 29th annual conference of the IEEE industrial electronics society (IEEE Cat. No. 03CH37468)
55. Alonge F, D'Ippolito F (2010) Extended Kalman filter for sensorless control of induction motors. In: First symposium on sensorless control for electrical drives
56. Demir R, Barut M, Yildiz R, Inan R, Zerdali E (2017) EKF based rotor and stator resistance estimations for direct torque control of induction motors. In: International conference on optimization of electrical and electronic equipment (OPTIM) & international of Aegean conference on electrical machines and power electronics (ACEMP)
57. Alonge F, D'Ippolito F, Sferlazza A (2014) Sensorless control of induction-motor drive based on robust Kalman filter and adaptive speed estimation. IEEE Trans Ind Electron 61(3):1444–1453
58. Zaky MS (2011) A stable adaptive flux observer for very low speed-sensorless induction motor drives insensitive to stator resistance variations. Ain Shams Eng J 2(1):11–20
59. Zaky MS, Maksoud HA, Azazi HZ (2018) Sensorless induction motor drives using adaptive flux observer at low frequencies. Eng Technol Appl Sci Res 8(1):2572–2576
60. Mishra A, Choudhary P (2012) Artificial neural network based controller for speed control of an induction motor (IM) using indirect vector control method. Int J Power Electron Drive Syst (IJPEDS) 2(4):402–408
61. Nguyen T, Pham PH, Pham TV, Ha HX, Nguyen CT (2017) A sensorless three-phase induction motor drive using indirect field oriented control and artificial neural network. In: 12th IEEE conference on industrial electronics and applications (ICIEA)
62. Afonso JL, Fonseca J, Martins JS, Couto C (1997) Fuzzy logic techniques applied to the control of a three-phase induction motor. In: ISIE'97-IEEE international symposium on industrial electronics, Guimaraes, 7–11 July 1997, pp 1179–1184
63. Uddin MN, Radwan TS, Rahman MA (2002) Performances of fuzzy-logic-based indirect vector control for induction motor drive. IEEE Trans Ind Appl 38(5):1219–1225
64. Xu L, Inoa E, Liu Y, Guan B (2012) A new high-frequency injection method for sensorless control of doubly fed induction machines. IEEE Trans Ind Appl 48(5)
65. Holtz J, Quan J (2003) Drift- and parameter-compensated flux estimator for persistent zero-stator-frequency operation of sensorless-controlled induction motors. IEEE Trans Ind Appl 39(4):1052–1060
66. Comanescu M, Xu L (2006) Sliding-mode MRAS speed estimators for sensorless vector control of induction machine. IEEE Trans Ind Electron 53(1):146–153
67. Zhang Y, Yin Z, Zhang Y, Liu J, Tong X (2020) A novel sliding mode observer with optimized constant rate reaching law for sensorless control of induction motor. IEEE Trans Ind Electron
68. Utkin VI (1993) Sliding mode control design principles and applications to electric drives. IEEE Trans Ind Electron 40(1):23–36
69. Yang S, Li X, Ding D, Zhang X, Xie Z (2016) Speed sensorless control of induction motor based on sliding-mode observer and MRAS. In: IEEE 8th international power electronics and motion control conference (IPEMC-ECCE Asia)
70. Rao S, Buss M, Utkin V (2009) Simultaneous state and parameter estimation in induction motors using first and second-order sliding modes. IEEE Trans Ind Electron 56:3369–3376

71. Zaky MS, Khater MM, Yasin H, Shokralla SS, El-Sabbe A (2007) Speed-sensorless control of induction motor drives. Eng Res J Minoufiya Univ 30(4)
72. Korzonek M, Tarchala G, Orlowska-Kowalska T (2019) A review on MRAS-type speed estimators for reliable and efficient induction motor drives. ISA Trans 93:1–13
73. Jingchuan L, Longya X, Zheng Z (2005) An adaptive sliding-mode observer for induction motor sensorless speed control. IEEE Trans Ind Appl 41(4):1039–1046
74. Smidl V, Peroutka Z (2012) Advantages of square-root extended Kalman filter for sensorless control of AC drives. IEEE Trans Ind Electron 59(11):4189–4196
75. Suwankawin S, Sangwongwanich S (2006) Design strategy of an adaptive full-order observer for speed-sensorless induction-motor drives—tracking performance and stabilization. IEEE Trans Ind Electr 53(1):96–119
76. Yoo JY, Park TS, Kim SH, Park GT (2001) Speed-sensorless vector control of an induction motor using neural network speed estimation. IEEE Trans Ind Electron 48(3):609–614
77. Majdi M, Rashidi F (2005) Sensorless speed and position control of induction motor servo drives using MLP neural network and sliding mode controller. In: 4th WSEAS international conference on non-linear analysis, non-linear systems and chaos, Sofia, pp 94–102

Chapter 23
Solar PV-Powered SRM Drive and Its Speed Control and Torque Ripple Minimization

Nutan Saha, Subham Kumar Sahoo, Bidyadhar Rout, Sidhartha Panda, Gayadhar Panda, and Dillip Ku. Sahoo

Abstract Electric vehicle (EV) is the need of present hour. EV operated by battery put limitation on the miles covered by it. In this work, control of photovoltaic (PV) energy-driven switched reluctance motor (SRM) is analyzed. The speed control with torque ripple minimization is designed for PV energy-fed SRM drive based on cosine adapted modified whale optimization algorithm (CamWOA). This CamWOA-dependent control mechanism is compared with whale optimization algorithm (WOA)-based control of PV energy-fed SRM drive. It is found that CamWOA-dependent control of PV-fed SRM provides improved performance than WOA-based controller.

Keywords Photovoltaic (PV) · Switched reluctance motor (SRM) · Cosine adapted modified whale optimization algorithm (CamWOA) · Whale optimization algorithm (WOA)

1 Introduction

Application of electric vehicle (EV) has significantly improved due to improvement in power converters, battery. Due to limitation in covering driving miles operated by battery, it put limitation on its use [1, 2]. Speed control and lessening of torque ripple of switched reluctance motor (SRM) driven by photovoltaic panel are discussed in this work. Cosine adopted modified whale optimisation algorithm is used for control of SRM. SRM is used as electric drive. A self-sustainable energy source is obtained by mounting PV panel on top of EV.

Switched reluctance motor is by inherent simple in construction, rugged and high torque to mass ratio. High torque pulsation and acoustic noise persist in SRM [3–5].

N. Saha (✉) · S. K. Sahoo · B. Rout · S. Panda · D. Ku. Sahoo
Department of EE, VSSUT, Burla, Odisha, India

G. Panda
Department of EE, NIT Meghalaya, Shillong, India
e-mail: gayadhar.panda@nitm.ac.in

G. Panda et al. (eds.), *Sustainable Energy and Technological Advancements*,
Advances in Sustainability Science and Technology,
https://doi.org/10.1007/978-981-16-9033-4_23

This is due to nonlinear T–i–θ characteristics or nonlinear magnetic characteristics [6]. Many approaches have been made to reduce the torque ripple [7, 8] like fuzzy logic network, neural network. All methods are complex for mathematical analysis. Optimization techniques use large information of system's issue by deep-rooted models and have strong potential. This causes modern heuristic optimization technique to be used for formulation for designing of a controller. Metaheuristic algorithm has very high computational efficiency [9].

Mirjalili et al. described a new metaheuristic optimization named as whale optimization algorithm [10] in the year 2016. WOA is based on hunting plan of Humpback whale. WOA often entangles in local optima. This causes that the output has an affinity of low convergence with search space expansion. Thus, a number of variation [11, 12] are possible that can be applied for improvement of WOA. Thus, modern heuristic optimization technique is always a good choice for finding solution of real-world problem. Optimization techniques are also used for formulation and designing of a controller.

PI controller is always the most choicest controller in industries because of its simple, reliable, effective and complementary proportion between the price and performance.

In this work, performance comparison of PI controller implemented for speed control of PV-fed SRM is done. The controller is based on cosine adapted modified whale optimization algorithm (CamWOA) and WOA optimization technique. In CamWOA [13] method, WOA is modified by employing a cosine function for decay of control parameter, and correction factors are employed for upgrading search agents position. In this work, CamWOA performance is analyzed by applying on 30-dimensional unimodal functions and then compared with other metaheuristic algorithms. CamWOA is again applied on PV-fed SRM drive for its control and is compared with WOA-based controller. CamWOA is always proved to give better performance than other optimization algorithms.

2 PV Energy

Photovoltaic energy acts as the driving source to SRM drives. This decreases its dependency on battery. This is achieved by mounting PV panel on top of the EV. Thus, a sustainable energy source is achieved. Figure 1 shows PV-fed SRM drive.

3 Mathematical Modeling of SRM Drive System

SRM run on reluctance torque. Reluctance torque is due to saliency in construction present in rotor and stator. Electricity supply is to stator only as excitation winding present in it. In SRM, electrical power is supplied to stator windings instead of rotor part, which significantly simplifies the mechanical design. Rotor constructed

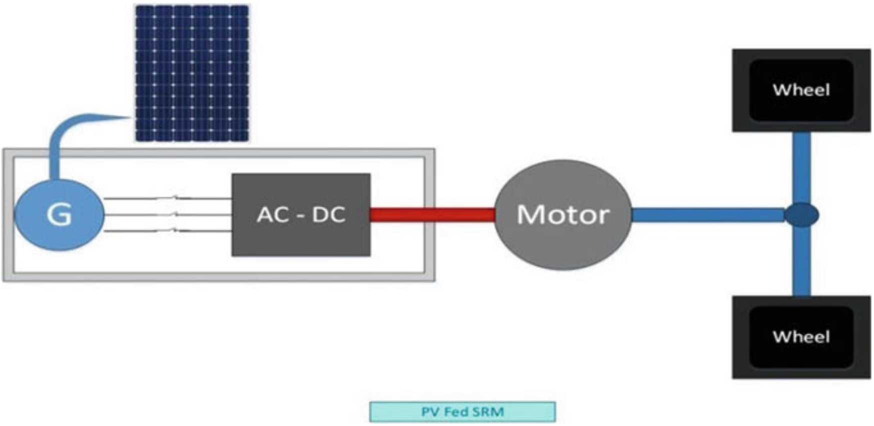

Fig. 1 PV energy-fed SRM drive

of lamination made of steel and with no excitation winding. With electric supply given to stator, due to reluctance torque, rotor tries to align itself to lowest reluctance position. This rotation continues if supply given to stator in proper sequence. This requires a complicated control and switching circuit.

Mathematical modeling (analytical modeling) of a 75 kW, 4-phase 8/6 SRM [14, 15] is a rigorous mathematical process. For simple mathematical analysis, mutual inductance between different phases is ignored. Presence of saliency in both stator and rotor leads to nonlinear magnetic characteristics. This causes the stator flux to exhibit a nonlinear relation to rotor position (θ) as well as stator current (i).

Flux linkage expression is given as

$$\Psi_s(t) = \Psi_s(i, \theta) \tag{1}$$

Stator's phase voltage expression is given below:

$$\Psi_s(t) = \int_0^t (V_S - R_S I_S)\mathrm{d}t \tag{2}$$

Here, stator winding resistance is R_S, $\Psi_s(t)$ is linkage flux, V_S represents stator voltage, and I_S is a stator current. All the above-mentioned terms are vector quantities. θ is rotor position. Flux linkage (Ψ) exhibits nonlinear relationship to I_S and θ. Mathematical expression for stator current $i(\Psi, \theta)$ is obtained from magnetization characteristics $\Psi_s(i, \theta)$.

Equation 3 shows expression of electromagnetic torque $T_e(i, \theta)$ of any single phase of SRM. It is the derivative of machine's co-energy $\left(w'(i, \theta)\right)$.

Table 1 Machine parameters

Machine parameter	Value	Machine parameter	Value
Power (output)	75 kW	Load torque	4 nm
Rotor speed	1000 RPM	Aligned inductance	23.62 mH
Resistance of stator	0.05 Ω	Unaligned inductance	0.67 mH
Friction	0.02 Nm	DC link voltage (input)	220 V
Stator pole arc	32°	Rotor pole arc	45°
Number of stator pole	8	Maximum flux linkage	0.486 mH
Number of rotor pole	6	Saturated inductance	0.15 mH

$$T_{\mathrm{e}}(i,\theta) = \frac{\partial w'(i,\theta)}{\partial \theta} \tag{3}$$

Co-energy $w'(i,\theta)$ is obtained by

$$w'(i,\theta) = \int_0^i \Psi(i,\theta) \tag{4}$$

The total electromagnetic torque of machine is the summation of torque developed by each and every phase. The dynamics of mechanical system is given below.

$$T_{\mathrm{e}} = J\frac{\partial \omega_{\mathrm{m}}}{\partial t} + B\omega_{\mathrm{m}} + T_{\mathrm{l}} \tag{5}$$

where ω_{m} is angular velocity, J is moment of inertia, T_{l} is load torque, and B represents friction coefficient.

Table 1 shows machine parameter of a 75 kW, 4-phase 8/6 SRM.

Figure 2 shows plotting of magnetization characteristics.

4 Control of SRM

Figure 3 explains speed control for SRM using PI controller. The control system consists of two PI controllers as speed controller and current controller. In addition to it, hysteresis controller and commutation angle controller are also present. This control plan provides speed control and minimization of torque ripple as well using optimum choice of mentioned eight parameters. These are parameters of PI speed

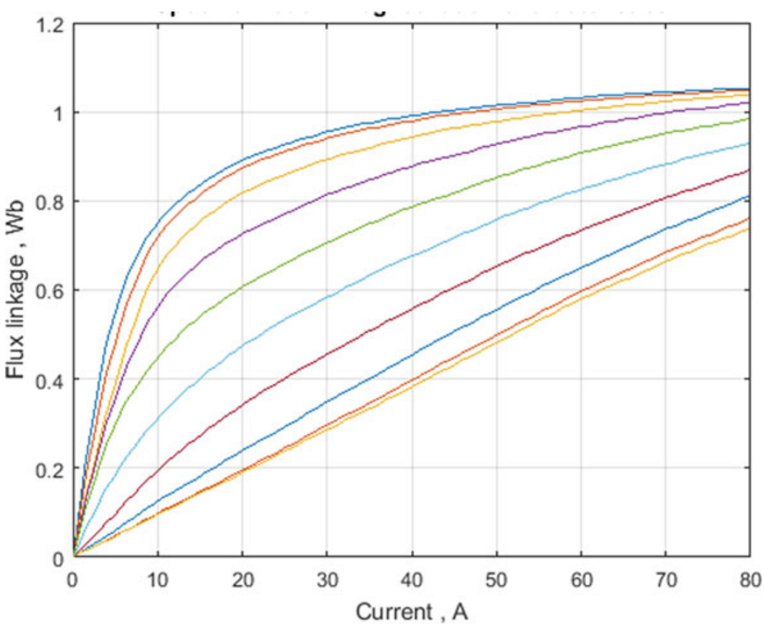

Fig. 2 Plot of magnetization characteristics of 75 kW, 4-phase, 8/6 SRM

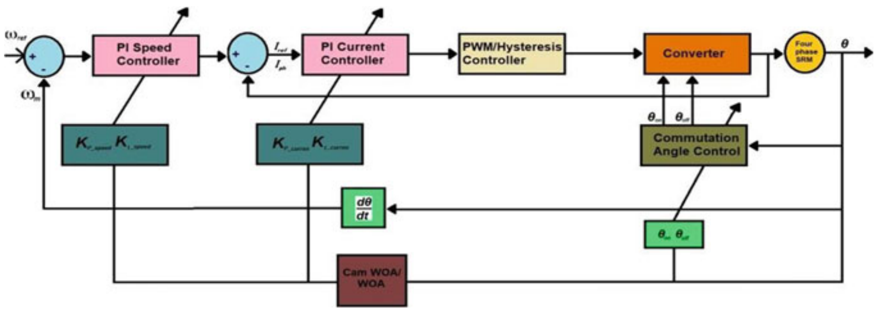

Fig. 3 Speed control of SRM

controller and PI current controller, turn on and turn off angle. All parameters are obtained by using CamWOA and WOA technique. Performance is compared by speed controller/current controller made of conventional PI controller. Rotor position feedback information is required for choosing turn on angle (θ_{ON}) and turn off angle (θ_{OFF}) for electrical switches. Current hysteresis controller is employed for current control.

5 Overview of Cosine Adapted Modified Whale Optimisation Algorithm

In CamWOA, modifications are done in two steps. (i) Correction factors (ζ_1 and ζ_2) are used for decreasing step size in position upgrading of search particle, thus leading fine search, (ii) cosine function is employed for decay of control parameter, i.e., 'd' of WOA during iteration. The advantage of using a cosine function for 'd' in CamWOA is that it provides varying combination of exploration and exploitation. These modifications that are made in WOA give accurate balancing between exploration and exploitation phase which leads to exact estimation of global optima.

The cosine function has cyclic pattern which causes a solution to repositioning around other solutions. This method ensures better exploitation of search region indicated among two solutions. While exploring search region, solutions are capable of searching beyond space as well as between respective destinations.

The current best solution is assumed as target krill and all other search agent update their position according to the target as shown by below equations.

$$\gamma = \frac{\left| C \cdot \overrightarrow{m^*}(t) - \overrightarrow{m(t)} \right|}{\zeta_1} \tag{6}$$

$$\vec{m}(t+1) = \frac{\overrightarrow{m^*(t)} - \vec{\mathcal{A}} \cdot \gamma}{\zeta_2} \tag{7}$$

$\overrightarrow{m^*(t)}$ is the present best solution, t represents present iteration, and $\overrightarrow{m(t)}$ represents position vector. Vector coefficients $\vec{C}$ and $\vec{\mathcal{A}}$ are obtained from Eqs. (8) and (9), respectively.

$$\vec{C} = 2 \cdot \vec{R} \tag{8}$$

$$\vec{\mathcal{A}} = 2 \cdot \vec{d} \cdot \vec{R} - \vec{d} \tag{9}$$

Here, $\vec{R}$ is any random number in between 0 and 1. Adjustment vectors $\vec{\mathcal{A}}$ and $\vec{C}$ are used to achieve different position around best agent.

In WOA, $\vec{d}$ reduces linearly from 2 to 0 to ensure shrinking nature of encircling prey. Whereas CamWOA [13] employs a cosine function responsible for decay of control parameter 'd' during iteration as depicted by Eq. (10).

$$d = 1 + 0.5 * \text{Cosine}\left(\pi \frac{\text{ITER}}{\text{ITER}_{\text{MAX}}}\right) \tag{10}$$

where ITER_{MAX} is maximum number of iterations occurred.

5.1 Bubble Net Strategy of Attacking (Exploitation Phase)

Bubble net method of attacking employs two approaches.

5.1.1 Shrinking Encircling Strategy

In CamWOA, cosine function is used as discussed in Eqs. (9) and (10). This leads to $\vec{\mathcal{A}}$ to be a random value chosen between $[-d, d]$. Setting $\vec{\mathcal{A}}$ in range of $[-1, 1]$, search agent's position is assured between original and current best position of search particle.

5.1.2 Spiral Updating Position

First the separation between whale position (m, n) and prey position (m^*, n^*) is evaluated. Helix-shaped motion of Humpback whales is designed by below equations.

$$\overrightarrow{m(t+1)} = \frac{\left(\overrightarrow{\gamma'} \cdot e^{bl} \cdot \cos(2\pi l) + \overrightarrow{m^*(t)}\right)}{\zeta 2} \tag{11}$$

$$\overrightarrow{\gamma'} = \frac{\left|\overrightarrow{m^*}(t) - \overrightarrow{m(t)}\right|}{\zeta_1} \tag{12}$$

In Eq. (11), γ' symbolizes distance in between ith and best solution come so far. Constant 'b' determines appearance of spiral path. 'l' is any random value chosen between $[-1, 1]$.

Swimming nature of Humpback whales is modeled by assuming 50% probability each for shrinking encircling and spiral-shaped path for updating whales position during optimization, which is explained below:

$$\vec{m}(t+1) = \begin{cases} \frac{\overrightarrow{m^*(t)} - \vec{\mathcal{A}} \cdot \overrightarrow{\gamma'}}{\zeta_1} & \text{if } p < 0.5 \\ \overrightarrow{m(t+1)} = \frac{\left(\overrightarrow{\gamma'} \cdot e^{bl} \cdot \cos(2\pi l) + \overrightarrow{m^*(t)}\right)}{\zeta 2} & \text{if } p \geq 0.5 \end{cases} \tag{13}$$

where p is any random numerical selected between 0 and 1.

5.1.3 Foraging for Prey Locations (Exploration Phase)

During foraging process, agents are picked randomly. $\vec{\mathcal{A}}$ is a random number which may be greater than 1 or less than -1. $\vec{\mathcal{A}}$ forces the search particle to move apart from reference search agent. Search agent's position is upgraded according to a randomly selected search particle in lieu of best search entity got. Vector $\vec{\mathcal{A}}$ operate like global optimizer. Emphasis on exploitation is given when $|\mathcal{A}|<1$, whereas emphasis on exploration is given when $\overrightarrow{|\mathcal{A}|} > 1$. Particle's position is upgraded by a random selection of search particle, as explained by below equations. This causes random motion of whales. In CamWOA, correction factors ζ_1 and ζ_2 are introduced for position updating of whale as explained below.

$$\gamma = \frac{\left|\vec{C} \cdot \overrightarrow{m_{\text{rand}}} - \vec{m}\right|}{\zeta_1} \tag{14}$$

$$\vec{m}(t+1) = \frac{\overrightarrow{m_{\text{rand}}} - \vec{\mathcal{A}} \cdot \vec{\gamma}}{\zeta 2} \tag{15}$$

$\overrightarrow{m_{\text{rand}}}$ is any random search particle taken from current population.

6 Operational Analysis of CamWOA Technique

The convergence of characteristic is guaranteed, as the remaining solution updates itself according to the best solution obtained. Here, $\vec{\mathcal{A}}$ reduces size of change adapted in solution. It also helps to converge in proportion to computed iteration.

The initial population is a random selection, and the algorithm evolves based on this initial population. Thus, it is always advisable to have multiple runs of this metaheuristic algorithm. In this work, the functionality of CamWOA is studied by applying on seven benchmark functions. These functions [16] include fixed dimensional functions. The exploitation ability of any metaheuristic algorithm is analyzed by testing it on unimodal functions, whereas the exploration ability is measured by applying it on multimodal and fixed dimensional multimodal functions. As unimodal functions is characterized with no local optima but have unique global optima. Multimodal and fixed dimensional multimodal functions are characterized with many local optima and unique global optimum. Further, for better performance analysis of CamWOA, it is compared with other metaheuristics like WOA [10], Lightning search algorithm (LSA) [17] and other optimization algorithms like differential search algorithm (DSA) [12], harmonic search algorithm (HSA) [18], particle swarm optimization (PSO) [19], backtracking search algorithm (BSA) [20] and firefly algorithm (FFA) [21], as described in the literature [17]. The control parameter used in all the above algorithm is discussed in Appendix A, Table AIV [17]. Maximum number of generation as well as population size is kept as common parameters for abovementioned optimization techniques. Thus, number of search agents and number of iterations are kept at 50 and 500 for all the optimization techniques. Each technique is allowed to run for 50 times for each benchmark function. The outcomes

Table 2 Unimodal benchmark function

Functions	Dimen	Range	$f_{\min}$
$p_1(y) = \sum_{i=1}^{n} y_i^2$	30	$[-100, 100]^{30}$	0
$p_2(y) = \sum_{i=1}^{n} \|y_i\| + \prod_{i=1}^{n} y_i$	30	$[-10, 10]^{30}$	0
$p_3(y) = \sum_{i=1}^{n} \left(\sum_{j-1}^{i} y_j \right)^2$	30	$[-100, 100]^{30}$	0
$p_4(y) = \max_i\{\|y_i\|, 1 \leq i \leq n\}$	30	$[-100, 100]^{30}$	0
$p_5(y) = \sum_{i=1}^{n-1} \left[100\left(y_{i+1} - y_i^2\right)^2 + (y_i - 1)^2 \right]$	30	$[-30, 30]^{30}$	0
$p_6(y) = \sum_{i=1}^{n} ([y_i + 0.5])^2$	30	$[-100, 100]^{30}$	0
$p_7(y) = \sum_{i=1}^{n} i y_i^4 + \text{random}[0, 1)$	30	$[-1.28, 1.28]^{30}$	0

are presented below. To prove operational efficiency and its application in practical problem, a challenging engineering problem is also solved.

6.1 Analysis of Functions ($p_1(y)$–$p_7(y)$)

In Table 1, 30-dimensional unimodal functions $p_1 - p_7$ are tabulated.

The statistical result of CamWOA and WOA derived after 50 runs on unimodal functions and results of other mentioned six algorithms in literature [17] is detailed in Table 2. It is analyzed from Table 2 that CamWOA algorithm is able to surpass all other optimization technique in four unimodal functions, i.e., $p_3(y)$, $p_4(y)$, $p_5(y)$, $p_7(y)$ among seven unimodal functions. For function $p_1(y)$ and $p_2(y)$, the CamWOA gives competitive result by providing second best results among all the optimization technique mentioned in Table 2. CamWOA provides third best result for $p_6(y)$ (Table 3).

7 Speed Control and Reducing Torque Ripple of SRM

SRM drive is subjected to machine's co-energy variation according to stator flux linkage and rotor current, which leads to high torque ripple. By control of stator current profile, by intelligent choice of turn on (θ_{ON})/turn off angle (θ_{OFF}) [5], the

Table 3 Statistical results of algorithms got for 50 runs on 30 dimensional, unimodal benchmark function

Fun	CamWOA		WOA		LSA		DSA	
	Av	Std. dev.	Av	Std. dev.	Av	Std. dev.	Av	Std. dev.
$p_1(y)$	1.1593e−59	4.877e−59	3.0063e−72	1.6466e−71	4.81067e−8	3.40126e−07	11.58475	6.93844
$p_2(y)$	2.5745e−33	2.874e−33	1.1189e−51	2.8691e−51	0.03680654	0.15623302	1.0060366	0.3579108
$p_3(y)$	1.6209e−56	6.097e−56	42,289.253	14,705.725	43.2408040	29.921944	20,888.933	6907.3089
$p_4(y)$	6.2449e−32	2.817e−31	49.2251	29.2213	1.49327573	1.30282704	27.810328	7.0770831
$p_5(y)$	26.3645	0.353131	28.1028	0.489595	64.2816030	43.7557611	1108.1807	572.42094
$p_6(y)$	0.1047	0.046469	0.44119	0.28478	3.34000000	2.08600780	15.740000	11.295312
$p_7(y)$	0.00011465	0.0001284	0.0037228	0.0048686	0.02407967	0.0057269	0.1230751	0.0653463
Fun	BSA		FFA		PSO		HSA	
	Av	Std. dev.	Av	Std. dev.	Av	Std. dev.	Av	Std. dev.
$p_1(y)$	9.96736178	9.8122469	0.0116107	0.0042959	2.76284e−5	4.3213e−5	24.711181	6.671103
$p_2(y)$	1.19715081	0.5285104	0.3733268	0.1014310	0.00492327	0.00333475	1.4574900	0.2681027
$p_3(y)$	2720.31053	1182.1964	1808.8063	659.65397	27.8639655	9.57949818	6878.6585	1943.0886
$p_4(y)$	9.83475144	2.2732874	0.0766947	0.0146060	0.61023703	0.14601838	9.3854319	1.2265122
$p_5(y)$	471.548541	231.14198	128.28961	278.63448	68.7229259	57.8107697	830.03255	474.19966
$p_6(y)$	13.9400000	17.300949	0.0000000	0.0000000	0.10000000	0.30304580	25.100000	7.5329209
$p_7(y)$	0.05449849	0.0161183	0.0352289	0.0239832	138.834311	22.0774487	0.4632411	0.1127224
$p_1(y)$	9.96736178	9.8122469	0.0116107	0.0042959	2.76284e−5	4.3213e−5	24.711181	6.671103

torque ripple can be decreased. Thus, speed control of SRM is devised using appropriate selection of switching angle and control of stator current profile. Optimal combinations of parameters of PI speed controller, PI current controller and commutation angle controller are used here for performance improvement of SRM. The intelligent combination of all these parameter leads to performance advancement of SRM.

For measuring speed error, current error, the integral square error (ISE) conditioned is implemented as explained below:

$$\mathrm{ISE(speed)} = \int (\omega_{\mathrm{ref}} - \omega_{\mathrm{m}})^2 \mathrm{d}t \tag{16}$$

$$\mathrm{ISE(current)} = \int \left(I_{\mathrm{ref}} - I_{\mathrm{phase}}\right)^2 \mathrm{d}t \tag{17}$$

Here, ISE(speed) is integral squared error of speed, and ISE(current) is integral squared error of current.

Torque ripple coefficient (T_{ripple}) is [5] as explained below.

$$T_{\mathrm{ripple}} = \frac{T_{\max} - T_{\min}}{T_{\mathrm{mean}}} \tag{18}$$

where $T_{\min}$ and $T_{\max}$ represent minimum and maximum value of torque. T_{mean} is the mean value of torque.

8 Objective Function Formulation

A multiobjective optimization problem formulation is done by combining $\mathrm{ISE(speed)},\ \mathrm{ISE(current)}$ and T_{ripple}.

Minimization of ISE of speed is given as

$$y_1 = \min(\mathrm{ISE(speed)}) \tag{19}$$

Minimization of T_{ripple} is given as

$$y_2 = \min\left(T_{\mathrm{ripple}}\right) \tag{20}$$

Minimization of ISE of current is given as

$$y_3 = \min(\mathrm{ISE(current)}) \tag{21}$$

The problem for final objective function Y is formulated below:

$$\min(Y) = \alpha_1 y_1 + \alpha_2 y_2 + \alpha_3 y_3 \tag{22}$$

$\alpha_1, \alpha_2, \alpha_3$ is considered as weighing factor. The weighing factor of Eq. (22) are selected in such a way that all the terms in right hand side of equation are to be in same range. Selection of $\alpha_1, \alpha_2, \alpha_3$ is chosen to make every term competitive in the process of optimization, i.e., normalizing of objectives y_1, y_2 and y_3 in a uniform scale.

9 Simulation in Time Domain

Modeling of control techniques is designed depending on WOA, CamWOA technique in MATLAB/Simulink environment. Here, MATLAB software is used because it is good in programming, in graphics quality and friendly to user. Table 4 shows lower and upper limits of gains for PI controller.

For evaluating performance comparability of PV energy-fed SRM, many statistical outcomes are considered like best, mean, worst and standard deviation of ISE of speed, ISE of current and torque ripple's coefficient and are presented in Table 5. The proportional constant and integral constant of speed controller, proportional constant and integral constant of current controller, turn on and turn off angle of commutation

Table 4 Lower and upper limit of gains for PI controller and commutation angle controller

Gains	Lower limit	Upper limit
K_{P_S}	0	200
K_{I_S}	0	200
K_{P_C}	0	2000
K_{I_C}	0	100
θ_{ON}	32	36
θ_{OFF}	54	58

Table 5 Statistical analysis

Method	Parameters	Best value	Worst value	Mean value	Std deviation
CamWOA (PI controller)	T_{ripple}	18.3606	20.4731	19.4363	0.0164
	ISE(speed)	1.678e + 04	1.7682e + 04	1.7142e + 04	102.152
	ISE(current)	121.1329	143.537	132.53	1.362
	Y	1.6157e + 6	2.734226e + 6	2.7290e + 06	3.5509e + 03
WOA	T_{ripple}	19.4869	23.173	18.15857	0.0628
	ISE(speed)	1.7786e + 04	1.928e + 04	1.8503 + 04	1.472e + 03
	ISE(current)	211.1329	287.3984	263.363	39.264
	Y	1.6179e + 06	2.749e + 6	2.736e + 6	3.382e + 04

angle controller for obtaining minimum objective function of WOA-based controller are 0.9, 0.89, 80.5224, 0.978, 31.99 and 53.89, respectively. The proportional constant and integral constant of speed controller, proportional constant and integral constant of current controller, turn on and turn off angle of commutation angle controller for obtaining minimum objective function of CamWOA-based controller are 0.899, 0.97, 301.4081, 0.986, 31.89 and 53.99, respectively.

10 Conclusion

It was seen that CamWOA provides better operational performance than WOA, LSA, DSA, BSA, FFA, PSO and HSA techniques in 4 out of 7 unimodal test functions. Next CamWOA was also applied for performance improvement of SRM drive using goal of control of speed, minimization of ripple in output torque and current error. It was seen that there is advancement in combined objective function by CamWOA with PI controller compared to WOA with PI controller. The combined objective function obtained by CamWOA controller is 1.6157e + 6, whereas it is 1.6179e + 06 obtained by WOA controller. The torque ripple, ISE of speed and ISE of current obtained by CamWOA-based controller are 18.3606, 1.678e + 04 and 121.1329, respectively, and WOA-based controller are 19.4869, 1.778e + 04 and 211.1329, respectively. This shows the performance improvement obtained by CamWOA-based controller as compared to WOA-based controller. Future work includes inclusion of advanced controller such as fractional order control, fuzzy logic controller and advanced optimization technique.

References

1. Bose LK (2013) Global energy scenario and impact of power electronics in 21st century. IEEE Trans Ind Electron 60(7):2638–2651
2. Santiago JD et al (2012) Electrical motor drivelines in commercial all electric-vehicles: a review. IEEE Trans Veh Technol 61(2):475–484
3. Harris MR (1989) Comparison of design and performance parameters in switched reluctance and induction motors. In: Fourth international conference on electrical machines and drives, pp 303–307
4. Valdivia V, Todd R, Bryan FJ, Barrado A, Lajaro A, Forsyth J (2014) Behavioral modeling of a switched reluctance generator for aircraft power systems. IEEE Trans Ind Electron 61(6):2690–2699
5. Hussain I (2002) Minimization of torque ripple in SRM drives. IEEE Trans Ind Electron 49:28–39
6. Miler TJE (1993) Switched reluctance motor and their control. Magna Physics Publishing, Lebanon, OH
7. Brandsletter P, Hrbac R (2006) Application of fuzzy logic in control of switched reluctance motor. Adv Electr Electron Eng 5:68–71
8. Lin Z, Reay S, Williams W (2006) Torque ripple reduction in switched reluctance motor drives using B-spline neural networks. IEEE Trans Ind Appl 2:1445–1453

9. Nesmachnow S (2014) An overview of metaheuristics: accurate and efficient methods for optimisation. Int J Metaheuristics 320–347
10. Sayedali M, Lewis A (2016) The whale optimization algorithm. Adv Eng Softw 95:51–67
11. Saremi S, Mirjalili S, Lewis A (2017) Grasshopper optimization algorithm: theory and application. Adv Eng Soft 105:30–47
12. Civicioglu P (2012) Transforming geocentric Cartesian coordinates to geodetic coordinates by using differential search algorithm. Comput Geosci 46:229–247
13. Saha N, Panda S (2020) Cosine adapted modified whale optimization algorithm for control of switched reluctance motor. In: Computational intelligence. Wiley
14. Torrey DA, Niu XM, Unkauf EJ (1995) Analytical modeling of variable reluctance machine magnetization characteristics. IEE Proc Electr Power Appl 142:14–22
15. Hoang LH, Brunelle PA (2005) Versatile nonlinear switched reluctance motor in Simulink using realistic and analytical magnetic characteristics. In: Proceedings of 31st annual conference of IEEE industrial electronics society
16. Molga M, Smutnicki C (2005) Test functions for optimization needs. Robert Marks.org
17. Shareef H, Ibrahim AA, Mutlag AH (2015) Lightning search algorithm. Appl Soft Comput 3103:1–19
18. Geem KZW, Kim JH, Loganathan GV (2001) A new heuristic optimization algorithm: harmony search. SIMULATION 76:60–70
19. Kennedy J, Eberhart R (1995) Particle swarm optimization. In: Proceedings of the IEEE international conference on neural networks, pp 1942–1948
20. Civicioglu P (2013) Backtracking search optimization algorithm for numerical optimization problems. Appl Math Comput 219:8121–8144
21. Yang XS (2010) Firefly algorithm in engineering optimisation. Wiley

Chapter 24
A Linear Quadratic Integral Regulator for a Variable Speed Wind Turbine

N. V. A. Ravikumar, Vasupalli Manoj, and N. S. S. Ramakrishna

Abstract The growing demands of wind power globally led to the design and development of numerous control methods. The control of the generator speed via blade pitch angle control has gained momentum and is quite predominantly explored. In this paper, the speed of a wind turbine is controlled by the design of a linear quadratic integral regulator (LQIR) to maintain its rated speed in the presence of unpredictable variations in wind speeds. A multi-input multi-output (MIMO) mathematical model in state-space domain is considered for analysis. The designed LQIR regulates the speed of the wind turbine based on linear quadratic regulator (LQR) approach arranged by adding integral action to obtain the steady-state performance. The developed regulator measures and controls the parameters such as rotor speed, blade pitch angle and generator speed. The results are then compared with the standard PID and LQR controllers. The advantages of the developed control over existing architecture have been shown in transient as well as in steady-state conditions. The simulations are performed in MATLAB R2015a environment.

Keywords LQIR · LQR · MIMO · PID · Wind turbine

1 Introduction

Wind energy is one of the fastest growing energy conversion technologies in the world due to its many advantages over other sources, like pollution free, clean and prominent of those is that wind is available free of cost. Moreover, wind energy

N. V. A. Ravikumar (✉) · V. Manoj
Department of Electrical and Electronics Engineering, GMR Institute of Technology, Rajam, Srikakulam, A.P. 532127, India
e-mail: ravikumar.nva@gmrit.edu.in

V. Manoj
e-mail: manoj.v@gmrit.edu.in

N. S. S. Ramakrishna
Department of Electrical and Electronics Engineering, VIT, Vellore, Tamil Nadu, India

G. Panda et al. (eds.), *Sustainable Energy and Technological Advancements*, Advances in Sustainability Science and Technology,
https://doi.org/10.1007/978-981-16-9033-4_24

generation also addresses the concern to environmental issues and deterioration of fossil fuels. According to Bonn, [1] that was stated in April 2020 by world wind energy association (WWEA), the worldwide overall capacity has reached 650.8 GW by all the installed wind turbines by 2019 end which can satisfy around 6% of the world's electricity demand. The National Institute of Wind Energy (NIWE) followed the directives and guidance of Ministry of New and Renewable Energy (MNRE) has assessed a 302,251 MW of installable wind capacity at above 100 m ground level in India [2]. In other words, the rise in the capacity of wind energy leads to increased use of wind turbines. The two types of wind turbines are the Horizontal Axis Wind Turbine (HAWT) and the Vertical Axis Wind Turbine (VAWT), with the former having advantages over the latter [3]. The performance of HAWT machine is a major concern for control strategists. Many advanced control strategies were designed to improve the performance of HAWTs that are nonlinear in nature and which are dynamically linear time varying HAWT machines [4–11]. They possess multi-region operating characteristics, flexible structures and aeroelastic interactions. In [4], closed-loop controllers' designs were reviewed and analyzed in the context of pitch control and torque control. The pitch control primarily limits power in high winds and significantly addresses the load variation effects on wind turbine, while the torque control focusses on maximizing energy capture by variable speed turbines in below rated wind speed region and limiting the torque in above rated wind speed region. The dynamics and control of wind turbines and wind farms are explicitly discussed [5], wherein the recent developments and open research problems are emphasized.

The basics of wind turbine along with its control (pitch and torque), components and three regions of wind speeds are given extensively in [6]. A horizontal-axis, three-bladed wind with changeable speed and pitch. Turbine is given in [7]. The overall stability of the WECS based on the permanent magnet synchronous generator (PMSG) is studied [8] by modifying its active and reactive powers. The short-term frequency regulation, voltage regulation and oscillation damping are the set of control loops incorporated in the wind farm to achieve these tasks. Furthermore, in [9], the researchers studied the application of fuzzy logic algorithm on a set of proportional-integral-derivative (PID) parameters designed for blade pitch angle control of wind turbine effectively in high wind speed region. The steady-state reference is tracked [10] by augmenting integral action to a linear quadratic regulator designed for a doubly fed induction generator. The various control methods associated with wind turbines is presented in [11–15] for further reading while the socio-economic evaluation of wind turbines is presented in [16].

It is necessary to regulate the wind turbine's rotational speed in order to maximize power production and keep turbine components within their designed speed and torque limits. Centrifugal force on spinning blades grows as the square of rotation speed, making this structure subject to over speeding. It is necessary to build turbines that can withstand far larger wind loads (such as gusts of wind) than those from which they can actually generate electricity. For this reason, wind turbines are built

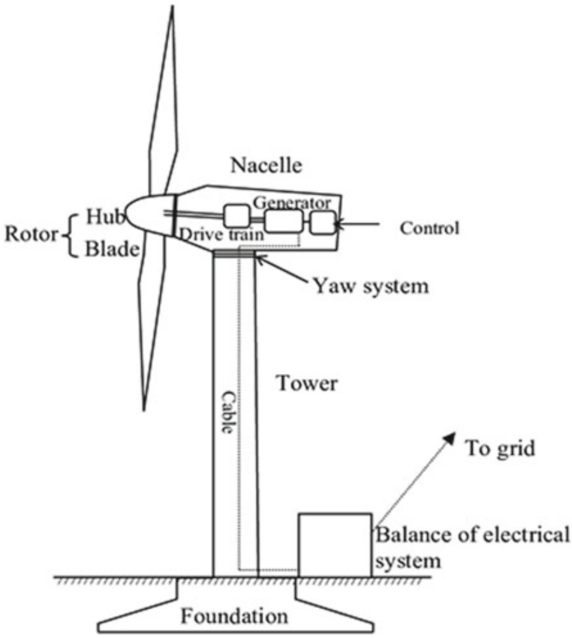

Fig. 1 The components of a Horizontal Axis Wind Turbine (HAWT) [16]

to operate at a variety of wind speeds. Cut-in speed [6] for most turbines is 3–4 m/s, with a cut-out speed of 25 m/s. It is necessary to reduce the power when wind speed is greater than rated. Almost all wind turbines are built to operate at a maximum windspeed termed the survival speed, above which they are damaged.

HAWT [16] is shown in Fig. 1 as a schematic diagram with its basic components. Rotor (hub and blade), nacelle (which houses the generator and powertrain), yaw control mechanism, tower, etc., are some of the main components seen in this image. Before creating a genuine system for converting wind energy into electrical energy, a suitable controller is required for its control. This is necessary because the wind turbine will be subjected to the unpredictable, intermittent, stochastic nature of the wind speeds which regulates the mechanical output power of the wind turbine. System stability and good performance can be achieved by using the linear quadratic regulator (LQR), a well-known technique that delivers ideally managed feedback gains. It is the time integral of a quadratic form in the state vector x and input vector u that determines the cost functional. Full state feedback has the main advantage of obtaining the ideal input signal $u(t)$, i.e., $u = -Kx$ for some K matrix. The feedback matrix K is obtained by solving the Ricotta equation associated with the LQR problem at hand.

2 Basic Structure of Wind Turbine

A wind turbine is one of the ways to convert kinetic energy into electrical energy. Aerodynamic, mechanical, electrical and actuator subsystems make up the majority of the wind turbine. Wind forces are converted into torque and thrust force by the aerodynamic subsystem, which is one of the subsystems. The mechanical system's drivetrain delivers rotor torque to an electrical generator. To ensure that the entire system is stable, the blade pitch and generator torque actuator subsystems, which are part of the control system, are essential. There is a detailed description of the various subsystems in [7]. Figure 2 shows the fundamental model structure of the wind turbine and the interactions between the different dynamic components of the model. The state-space model of the variable speed turbine can be described as follows from [7]; the general mathematical model and the subsequent equations are considered from [7], after which the following equations hold

$$\begin{aligned} \dot{x}_e(t) &= A(v_m)x_e(t) + B_1(v_m)w(t) + B_2u_e(t) \\ z_e(t) &= Cx_e(t) + D_1w(t) + D_2u_e(t) \end{aligned} \tag{1}$$

where

$$x_e = \begin{bmatrix} \Delta\theta_e \\ \Delta\omega_r \\ \Delta\omega_g \\ \Delta\beta \end{bmatrix} \in \mathcal{R}^4;\ w = \Delta v_{wind} \in \mathcal{R}^1;\ u_e = \begin{bmatrix} \Delta\beta_{ref} \\ \Delta T_g \end{bmatrix} \in \mathcal{R}^2;\ z_e = \begin{bmatrix} \Delta\omega_g \\ \Delta T_g \end{bmatrix} \in \mathcal{R}^2;$$

$$A(v_m) = \begin{bmatrix} 0 & 1 & -\frac{1}{\eta_{gear}} & 0 \\ -\frac{K_s}{J_r} & \frac{1}{J_r}\frac{\partial T_r}{\partial \omega_r}|_{op} & 0 & \frac{1}{J_r}\frac{\partial T_r}{\partial \omega_r}|_{op} \\ \frac{\eta_{gear}K_s}{\eta_{gear}J_g} & 0 & 0 & 0 \\ 0 & 0 & 0 & -\frac{1}{\tau\beta} \end{bmatrix};$$

$$B_1 = \begin{bmatrix} 0 \\ \frac{1}{J_r}\frac{\partial T_r}{\partial v}|_{op} \\ 0 \\ 0 \end{bmatrix};\ B_2 = \begin{bmatrix} 0 & 0 \\ 0 & 0 \\ 0 & -\frac{1}{J_g} \\ \frac{K\beta}{\tau\beta} & 0 \end{bmatrix};\ C = \begin{bmatrix} 0\ 0\ 1\ 0 \\ 0\ 0\ 0\ 0 \end{bmatrix};\ D_1 = \begin{bmatrix} 0 \\ 0 \end{bmatrix};\ D_2 = \begin{bmatrix} 0\ 0 \\ 0\ 1 \end{bmatrix}$$

there are different steady-state operating points and the corresponding system matrices of linearized model at these operating points are denoted as

$$\begin{bmatrix} A(v_{m,i}) & B_1(v_{m,i}) & B_2 \\ C & D_1 & D_2 \end{bmatrix} := \begin{bmatrix} A_i & B_{1,i} & B_2 \\ C & D_1 & D_2 \end{bmatrix} \quad \forall i = 1, 2, 3, \ldots, L.$$

In addition, the control inputs in the linearized model are then constructed by

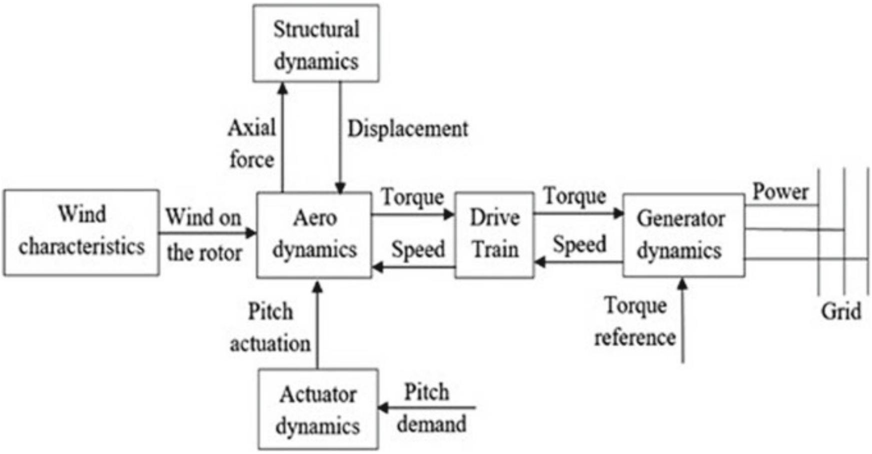

Fig. 2 Block diagram representation of a Horizontal Axis Wind Turbine (HAWT) [3]

$$|u_{\mathrm{e},j}(t)| \leq u_{\mathrm{e},j,\max} \quad \forall t \geq t_{\mathrm{o}},\ j = 1, 2, \ldots \tag{2}$$

with

$$u_{\mathrm{e},1,\max} := \min(|u_{1,\max} - u_{\mathrm{d},1}|, |u_{1,\min} - u_{\mathrm{d},1}|)$$

$$u_{\mathrm{e},2,\max} := \min(|u_{2,\max} - u_{\mathrm{d},2}|, |u_{2,\min} - u_{\mathrm{d},2}|)$$

3 LQIR Design for Wind Turbine

The novel state-space model obtained is a type-0 servo system which does not involve integrator in the dynamics of current and speed. However, the integral action needs to be incorporated in the feed forward path between the error comparator and the plant. This will include additional states to the system. The mathematical formulation of LQR-based state feedback control with integral action is detailed in the following sections.

3.1 Mathematical Formulation of Error Dynamics

The state-space model of a general type-0 MIMO servo system utilizing integral action, using state augmentation can be expressed mathematically as

$$\begin{aligned} \dot{x}(t) &= Ax(t) + Bu(t) \\ y(t) &= Cx(t) \\ \zeta(t) &= r(t) - y(t) = r(t) - Cx(t) \end{aligned} \tag{3}$$

where
$x = \left[x_1\ x_2\ \ldots\ x_n\right]^{\mathrm{T}}$ represents the $(n \times 1)$ state vector,
$u = \left[u_1\ u_2\ \ldots\ u_m\right]^{\mathrm{T}}$ represents the $(m \times 1)$ input vector,
$y = \left[y_1\ y_2\ \ldots\ y_p\right]^{\mathrm{T}}$ represents the $(p \times 1)$ output vector,
$r = \left[r_1\ r_2\ \ldots\ r_p\right]^{\mathrm{T}}$ represents the $(p \times 1)$ reference input vector,
$\zeta = \left[\zeta_1\ \zeta_2\ \ldots\ \zeta_p\right]^{\mathrm{T}}$ is the $(p \times 1)$ error vector representing the integral of the tracking errors (augmented states),
C represents the output matrix,

and the following equation represents the linear state feedback law comprising both the nominal and added states which can be given as:

$$u(t) = -Kx(t) + K_1\zeta(t) \tag{4}$$

where K is the $(m \times n)$ state feedback gain matrix and K_1 is the $(m \times p)$ integral matrix.

The state-space dynamic model for the system obtained after the state augmentation can be written in matrix form as:

$$\begin{bmatrix} \dot{x(t)} \\ \zeta(t) \end{bmatrix} = \begin{bmatrix} A & 0 \\ -C & 0 \end{bmatrix} \begin{bmatrix} x(t) \\ \zeta(t) \end{bmatrix} + \begin{bmatrix} B \\ 0 \end{bmatrix} u(t) + \begin{bmatrix} 0 \\ I \end{bmatrix} r(t) \tag{5}$$

In the steady-state the equation can be further written as:

$$\begin{bmatrix} \dot{x(\infty)} \\ \zeta(\infty) \end{bmatrix} = \begin{bmatrix} A & 0 \\ -C & 0 \end{bmatrix} \begin{bmatrix} x(\infty) \\ \zeta(\infty) \end{bmatrix} + \begin{bmatrix} B \\ 0 \end{bmatrix} u(\infty) + \begin{bmatrix} 0 \\ I \end{bmatrix} r(\infty) \tag{6}$$

Now, it can be defined as

$$\begin{aligned} \dot{x}(t) - \dot{x}(\infty) &= x_{\mathrm{e}}(t) \\ \zeta(t) - \zeta(\infty) &= \zeta_{\mathrm{e}}(t) \\ u(t) - u(\infty) &= u_{\mathrm{e}}(t) \end{aligned} \tag{7}$$

Hence, the following expression can be obtained

$$\begin{bmatrix} \dot{x}_{\mathrm{e}}(t) \\ \dot{\zeta}(t) \end{bmatrix} = \begin{bmatrix} A & 0 \\ -C & 0 \end{bmatrix} \begin{bmatrix} x_{\mathrm{e}}(t) \\ \zeta_{\mathrm{e}}(t) \end{bmatrix} + \begin{bmatrix} B \\ 0 \end{bmatrix} u_{\mathrm{e}}(t) \tag{8}$$

If $((n + m) \times 1)$ is an order of the error vector, it can be represented as

$$e(t) = \begin{bmatrix} x_e(t) \\ \zeta_e(t) \end{bmatrix}$$

Then, Eq. (8) can be written as:

$$\dot{e}(t) = \bar{A}e(t) + \bar{B}u_e(t) \tag{9}$$

where, $\bar{A} = \begin{bmatrix} A & 0 \\ -C & 0 \end{bmatrix}$; $\bar{B} = \begin{bmatrix} B \\ 0 \end{bmatrix}$ and

$$\dot{e}(t) = -Kx_e(t) + K\zeta_e(t) = -\bar{K}e(t) \tag{10}$$

where, $\bar{K} = \begin{bmatrix} K & -K_1 \end{bmatrix}$ now the closed loop error dynamics are given as

$$\dot{e}(t) = (\bar{A} - \bar{B}\bar{K})e(t) \tag{11}$$

Thus, it becomes evident that the problem of designing a state feedback law to track the reference values is transformed to a regulator design problem. The gain matrix $\bar{K}$ is to be designed such that error vector $e(t)$ converges to zero at steady state.

3.2 Control Dynamics

The dynamics necessary for control are based on the following equations. The generalized state-space model [7] of the wind turbine is given in Eq. (12).

$$\begin{aligned} \dot{x_e}(t) &= A(v_m)x_e(t) + B_1(v_m)w(t) + B_2u_e(t) \\ z_e(t) &= Cx_e(t) + D_1w(t) + D_2u_e(t) \end{aligned} \tag{12}$$

where

$$x_e = \begin{bmatrix} \Delta\theta_e \\ \Delta\omega_r \\ \Delta\omega_g \\ \Delta\beta \end{bmatrix} \in \mathcal{R}^4;\ w = \Delta v_{wind} \in \mathcal{R}^1;\ u_e = \begin{bmatrix} \Delta\beta_{ref} \\ \Delta T_g \end{bmatrix} \in \mathcal{R}^2;\ z_e = \begin{bmatrix} \Delta\omega_g \\ \Delta T_g \end{bmatrix} \in \mathcal{R}^2;$$

and Δ represents the variations in the corresponding parameter, while

$$A(v_m) = \begin{bmatrix} 0 & 1 & -\frac{1}{\eta_{gear}} & 0 \\ -\frac{K_s}{J_r} & \frac{1}{J_r}\frac{\partial T_r}{\partial \omega_r}|_{op} & 0 & \frac{1}{J_r}\frac{\partial T_r}{\partial \omega_r}|_{op} \\ \frac{\eta_{gear}K_s}{\eta_{gear}J_g} & 0 & 0 & 0 \\ 0 & 0 & 0 & -\frac{1}{\tau\beta} \end{bmatrix};$$

$$B_1 = \begin{bmatrix} 0 \\ \frac{1}{J_r}\frac{\partial T_r}{\partial v}|_{op} \\ 0 \\ 0 \end{bmatrix}; B_2 = \begin{bmatrix} 0 & 0 \\ 0 & 0 \\ 0 & -\frac{1}{J_g} \\ \frac{K\beta}{\tau\beta} & 0 \end{bmatrix}; C = \begin{bmatrix} 0\,0\,1\,0 \\ 0\,0\,0\,0 \end{bmatrix}; D_1 = \begin{bmatrix} 0 \\ 0 \end{bmatrix}; D_2 = \begin{bmatrix} 0\,0 \\ 0\,1 \end{bmatrix}$$

At each fixed operating point corresponding to $v_{m,i}$, the system matrices $\begin{bmatrix} A_i & B_{1,i} & B_2 \\ C & D_1 & D_2 \end{bmatrix}$ of linearized model are constant, as per Eq. (12) that represents the matrix inequality optimization problem.

4 Results and Discussions

4.1 Simulation of Results with Slowly Varying Wind Speed

The simulation is performed with a sampling time of $T = 10$ s. The tuning parameters are chosen as $r_c = 0.2$. The bounds of the pitch angle are $u_{1,\min} = 0^o$ and $u_{1,\max} = 30^o$ and the bounds of generator torque are $u_{2,\min} = 0$ Nm and $u_{2,\max} = 35.3$ kN m. The mean wind speeds vary from 1 to 16 m/s in 9 s and from 16 to 18 m/s in 20 s, respectively, and determine three operating points.

$$x_{d,1} = \left[0.0138\ 3.6853\ 105.7670\ 23.3645\right]^T \text{ for input } u_{d,1} = \left[23.3645\ 3781.9\right]^T$$

$$x_{d,2} = \left[0.0138\ 3.6853\ 105.7670\ 20.6103\right]^T \text{ for input } u_{d,2} = \left[20.6103\ 3781.9\right]^T$$

$$x_{d,3} = \left[0.0138\ 3.6853\ 105.7670\ 25.6616\right]^T \text{ for input } u_{d,3} = \left[25.6616\ 3781.9\right]^T$$

Take the above three operating points for example, the corresponding system matrices of linearized model are

$$A_1 = \begin{bmatrix} 0 & 1 & -0.0348 & 0 \\ -36.7757 & -0.1627 & 0 & -0.0380 \\ 12407.97 & 0 & 0 & 0 \\ 0 & 0 & 0 & -2.8571 \end{bmatrix}; B_{1,1} = \begin{bmatrix} 0 \\ 0.0949 \\ 0 \\ 0 \end{bmatrix}$$

$$A_2 = \begin{bmatrix} 0 & 1 & -0.0348 & 0 \\ -36.7757 & -0.1145 & 0 & -0.0295 \\ 12407.97 & 0 & 0 & 0 \\ 0 & 0 & 0 & -2.8571 \end{bmatrix}; B_{2,1} = \begin{bmatrix} 0 \\ 0.0898 \\ 0 \\ 0 \end{bmatrix}$$

$$A_3 = \begin{bmatrix} 0 & 1 & -0.0348 & 0 \\ -36.7757 & -0.2093 & 0 & -0.0470 \\ 12407.97 & 0 & 0 & 0 \\ 0 & 0 & 0 & -2.8571 \end{bmatrix}; B_{3,1} = \begin{bmatrix} 0 \\ 0.0992 \\ 0 \\ 0 \end{bmatrix}$$

$$B_2 = \begin{bmatrix} 0 & 0 \\ 0 & 0 \\ 0 & 0.0452 \\ 2.8571 & 0 \end{bmatrix}; C = \begin{bmatrix} 0 & 0 & 1 & 0 \\ 0 & 0 & 0 & 0 \end{bmatrix}; D_1 = \begin{bmatrix} 0 \\ 0 \end{bmatrix}; D_2 = \begin{bmatrix} 0 & 0 \\ 0 & 1 \end{bmatrix}$$

4.2 Simulation Results of Various Parameters Using LQIR Controller

The results that are furnished in this section are simulations done in MATLAB environment. The controlled parameters via LQIR controller are shown in this section. The simulation results of controlled parameters of wind turbine using LQIR controller are presented with inputs as pitch angle, torque and wind speed and outputs are angular displacement, rotor speed, generator speed and pitch angle. The graphs of these outputs with the corresponding inputs are plotted subsequently and are compared with the plots of PID and LQR controllers.

The controller's performance while pitch angle is controlled: The controlled value of angular displacement is depicted in Fig. 3a. The red line indicates the performance of LQIR controller. The achieved rise time is 0.00579 s, settling time is 0.0103 s and the peak overshoot is 0%. The rise time, settling time for PID and LQR controllers are 1.16, 1.89 and 0.00582, 0.0104 s, respectively. The peak overshoot is 11% and 0% for PID and LQR, respectively. The controlled value of rotor speed is depicted in Fig. 3b for the corresponding change in pitch angle with an LQIR controller and is represented in red color. The rise time is 1.9 s, settling time is 3.45 s and peak overshoot is 0%. The rise time, settling time for PID and LQR controllers are 6.52, 11.2 and 22.4, 19.9 s, respectively. The peak overshoot is 11% and 0% for PID and LQR, respectively. The controlled value of generator speed is depicted in Fig. 3c and is represented in red color. The rise time is 0.00582 s, settling time is 0.0104 s and peak overshoot is 0%. The rise time, settling time for PID and LQR controllers are 6.52, 22.4 and 0.00582, 0.0104 s, respectively. The peak overshoot is 11% and 0% for PID and LQR, respectively. The controlled pitch angle β is depicted in Fig. 3d and is represented in red color. The rise time is 0.0015 s, settling time is 0.00184 s and the Peak overshoot is 0%. The rise time, settling time for PID and LQR controllers are 6.52, 22.4 and 0.00582, 0.0104 s, respectively.

The controller's performance while torque is controlled: The peak overshoot is 11% and 0% for PID and LQR, respectively. The graph shown in Fig. 4a represents the plot of angular displacement with the corresponding change in torque of an LQIR controller which is represented in red color. The rise time is 0.00582 s, settling time

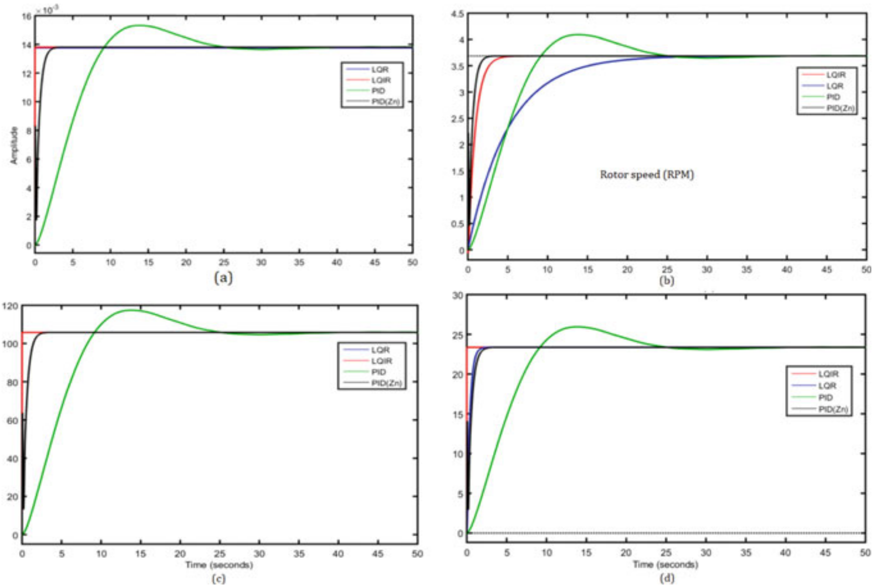

Fig. 3 While controlling the pitch angle, the designed controller controls the parameters **a** angular displacement (cm/s), **b** rotor speed in rpm, **c** generator speed in rpm, **d** controlled pitch angle in degrees

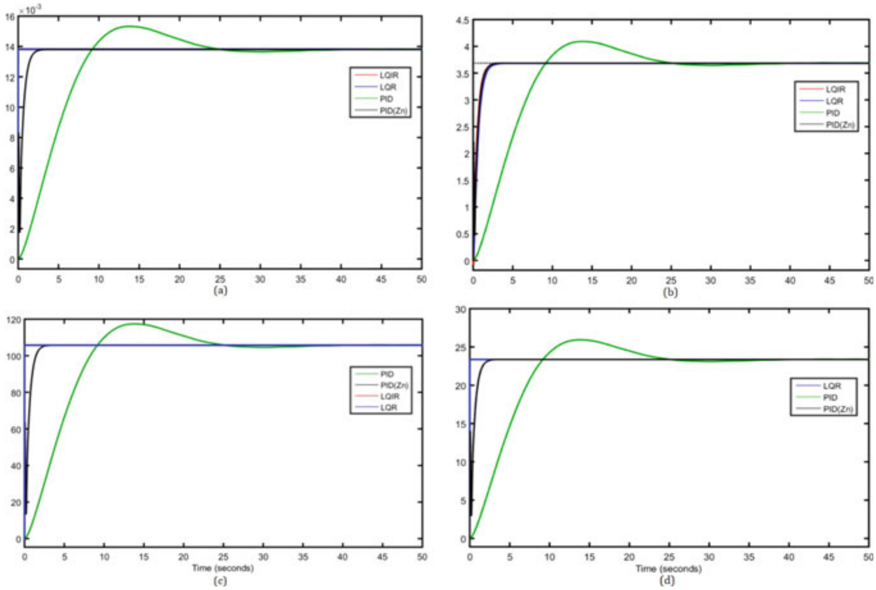

Fig. 4 While controlling the torque, the designed controller controls the parameters **a** angular displacement (cm/s), **b** rotor speed in rpm, **c** generator speed in rpm, **d** the controlled pitch angle in degrees

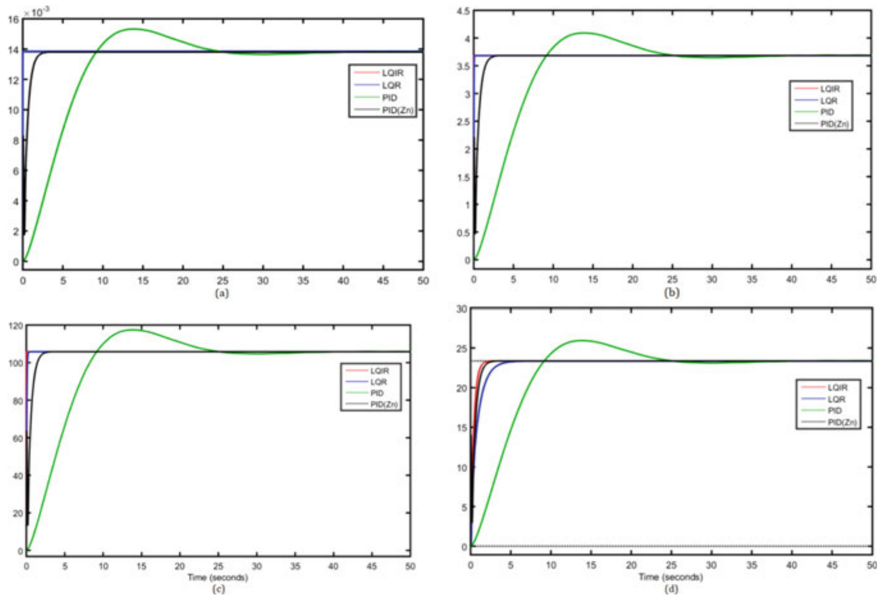

Fig. 5 For change in the wind speed, the designed controller controls the parameters **a** angular displacement (cm/s), **b** rotor speed in rpm, **c** generator speed in rpm, **d** the controlled pitch angle in degrees

is 0.0104 s and Peak overshoot is 0%. Rise time, settling time for PID and LQR controllers are 1.16, 1.89 and 0.00582, 0.0104 s, respectively. The peak overshoot is 11% and 0% for PID and LQR, respectively. The graph shown in Fig. 4b represents the plot of rotor speed when torque is controlled by the LQIR controller (red color). The rise time is 0.974 s, settling time is 1.79 s and the peak overshoot is 0%. The rise time, settling time for PID and LQR controllers are 1.16, 1.89 and 1.17, 2.15 s, respectively. The peak overshoot is 11% and 0% for PID and LQR, respectively. The graph shown in Fig. 4c represents the plot between variation of generator speed with the corresponding change in torque of an LQIR controller which is represented in red color. The rise time is 0.00582 s, settling time is 0.0104 s and the Peak overshoot is 0%. The rise time, settling time for PID and LQR controllers are 1.16, 1.89 and 0.00582, 0.0104 s, respectively. The peak overshoot is 11% and 0% for PID and LQR, respectively. The graph shown in Fig. 4d represents the plot between variation of pitch angle with the corresponding change in torque of an LQIR controller which is represented in red color. The rise time is 0.00568 s, settling time is 0.0101 s and the peak overshoot is 0%. The rise time, settling time for PID and LQR controllers are 1.16, 1.89 and 0.00568, 0.0101 s, respectively. The peak overshoot is 11% and 0% for PID and LQR, respectively.

The controller's performance for changes in wind speed: The graph shown in Fig. 5a represents the plot between variation of angular displacement with the corresponding change in windspeed of an LQIR controller which is represented in red

Table 1 Comparison with four controllers for changes in wind speed

Controller	Rise time (s)	Peak time (s)	% Peak overshoot	Settling time (s)	Steady-state value
PID	6.52	13.8	11	22.4	105.7670
PID-ZN	1.16	2.85	0.0139	1.89	105.7670
LQR	0.113	0.287	0.00	0.202	105.7670
LQIR	0.0101	0.0211	0.00	0.0173	105.7670

color. The rise time is 0.00582 s, settling time is 0.0104 s and the Peak overshoot is 0%. The rise time, settling time for PID and LQR controllers are 1.16, 1.89 and 0.00582, 0.0104 s, respectively. The peak overshoot is 11% and 0% for PID and LQR, respectively. The graph shown in Fig. 5b represents the plot between variation of rotor speed with the corresponding change in windspeed of an LQIR controller which is represented in red color. The rise time is 0.00582 s, settling time is 0.0104 s and the peak overshoot is 0%. The rise time, settling time for PID and LQR controllers are 1.16, 1.89 and 0.0361, 0.0646 s, respectively. The peak overshoot is 11% and 0% for PID and LQR, respectively. The graph shown in Fig. 5c represents the plot between variation of generator speed with the corresponding change in windspeed of an LQIR controller which is represented in red color. The rise time is 0.0101 s, settling time is 0.0173 s and the Peak overshoot is 0%. The rise time, settling time for PID and LQR controllers are 1.16, 1.89 and 0.113, 0.202 s, respectively. The peak overshoot is 11% and 0% for PID and LQR, respectively. The graph shown in Fig. 5d represents the plot between variation of generator speed with the corresponding change in wind speed of an LQIR controller which is represented in red color. The rise time is 0.0101 s, settling time is 0.0173 s and the peak overshoot is 0%. The rise time, settling time for PID and LQR controllers are 1.16, 1.89 and 0.113, 0.202 s, respectively. The peak overshoot is 11% and 0% for PID and LQR, respectively. The comparison is presented in Table 1 which shows the values of the operating parameters using different designed controllers, PID controller, LQR controller and LQIR controller. From the operating parameters, it is observed that the developed LQIR controller is superior to the other standard controllers.

5 Conclusions

The different strategies for controlling the parameters of a HAWT are studied and a new control strategy is developed. The following conclusions are drawn from the results. The wind disturbances play an important role in determining the output generator speed of the turbine. Hence, along with the average wind speed, the wind disturbances are also considered in this paper. Using a standard PID controller, output generator speed is controlled using only the wind speed and the time taken for controlling is relatively high, which is not preferable in day-to-day operations. The developed LQIR controller controls twelve parameters within very short time thereby increasing the efficiency of the overall plant. The rise time is 0.0121 s, peak time is 0.0211 s, peak overshoot is 0.0009% and settling time is 0.0255 s which is much superior to existing controllers. This paper provides an important control architecture which is suitable for HAWT for maintaining constant generator speed which is very vital for constant power generation. The developed controller can also be useful in extreme conditions where the prediction of wind speeds are pretty much difficult. The LQIR controller and the data so obtained can be applied for future large-scale systems.

Acknowledgements Supported by GMR Institute of Technology, Rajam, Srikakulam.

References

1. WWEA homepage. https://wwindea.org/world-wind-capacity-at-650-gw/. Accessed 26 Aug 2021
2. INWEA homepage. http://inwea.org/wind-energy-in-india/wind-power-potential/. Accessed 26 Aug 2021
3. TurbinesInfo homepage. https://www.turbinesinfo.com/types-of-wind-turbines/. Accessed 26 Aug 2021
4. Bossanyi EA (2000) The design of closed loop controllers for wind turbines. Wind Energy 3(3):149–163
5. Pao LY, Johnson KE (2016) A tutorial on the dynamics and control of wind turbines and wind farms. In: Editor F, Editor S (eds) American control conference 2009. LNCS, vol 9999. Springer, Heidelberg, pp 1–13. https://doi.org/10.10007/1234567890
6. Pao LY, Johnson KE (2011) Control of wind turbines. IEEE Control Syst Mag 31(2):44–62
7. Miaomiao M, Hong C, Xiangjie L, Frank A (2014) Moving horizon control of variable speed wind turbines with actuator saturation. IET Renew Power Gener 8(5):498–508
8. Revel G, Leon AE, Alonso DM, Moiola JL (2014) Dynamics and stability analysis of a power system with a PMSG-based wind farm performing ancillary services. IEEE Trans Circuits Syst 1 Reg Pap 61(7):2182–2193
9. Civelek Z, Luy M, Cam E, Barisci N (2016) Control of pitch angle of wind turbine by fuzzy PID controller. Intell Autom Soft Comput 22(3):463–471
10. Gurung N, Bhattarai R, Kamalasadan S (2017) Optimal linear quadratic integral controller design for doubly-fed induction generator. IEEE Power Energy Soc Gen Meet 17(4):386–405
11. Menezes EJN, Araujo AM, Da Silva NSB (2018) A review on wind turbine control and its associated methods. J Clean Prod 171(2):915–953
12. Ravikumar NVA, Saraswathi G (2019) Robust controller design for speed regulation of a flexible wind turbine. EAI Endorsed Trans Energy Web 6(23)
13. Ravikumar NVA, Saraswathi G (2020) Towards robust controller design using μ-synthesis approach for speed regulation of an uncertain wind turbine. Electr Eng 102(2):515–527
14. Ravikumar NVA, Saraswathi G (2019) Robust controller design for speed regulation of a wind turbine using 16-plant theorem approach. EAI Endorsed Trans Energy Web 6(24)
15. Ravikumar NVA, Saraswathi G (2017) Model order reduction and linear quadratic regulator controller design on a large-scale linear time invariant system. Int J Mech Prod Eng Res Dev 7(6):533–542
16. Mohammed A (2010) On techno-economic evaluation of wind based DG. PhD thesis, Sultan Qaboos University

Chapter 25
Output Power Tracking and Oscillation Control of a Doubly Fed Induction Generator-Based Wind Energy Conversion System Using Adaptive Neuro-Fuzzy Algorithm

Satyabrata Sahoo and Gayadhar Panda

Abstract The output power oscillation of a wind turbine heavily depends on the cubic power of wind speed. When this stochastic wind speed changes, the magnitude of oscillation in the output power also varies. This phenomenon leads to the power quality problem. Pitch angle control is employed for smoothing of the oscillation in the output power. In fact, by simultaneously regulating the torque of the generator and pitch angle, speed of the generator and its output power oscillation are reduced. This paper presents on a power oscillation control scheme based on multiple adaptive neuro-fuzzy inference system (multiple ANFIS). By combining the neural network and the Takagi–Sugeno type fuzzy inference system, the suggested adaptive neuro-fuzzy controller is developed. The efficacy of the proposed controller is evaluated by pursuing an extensive simulation study through conventional proportional integral (PI) control and another superior technology control, i.e. model predictive control (MPC). From the acquired results, it is noticed that the suggested multiple ANFIS-based controller shows superior power quality performance in comparison to both MPC and PI controller.

Keyword Wind energy conversion system · Power oscillation · Model predictive control · Adaptive neuro-fuzzy algorithm

S. Sahoo (✉)
Department of Electrical and Electronics Engineering, Nalla Malla Reddy Engineering College, Hyderabad 500088, India

G. Panda
Department of Electrical Engineering, National Institute of Technology Meghalaya, Shilong 793003, India
e-mail: gayadhar.panda@nitm.ac.in

G. Panda et al. (eds.), *Sustainable Energy and Technological Advancements*,
Advances in Sustainability Science and Technology,
https://doi.org/10.1007/978-981-16-9033-4_25

1 Introduction

The demand for generation of electrical power from renewable energy sources, particularly from wind energy system is growing day by day. Its annual growth rate is around 12–15% [1]. With the use of wind energy conversion systems (WECS), the wind energy is generated from it and is cubically proportional to the speed of the wind. So the model of wind energy conversion system is of nonlinear in nature. Therefore, in modern wind energy conversion systems, control system plays a very vital role. A variable speed variable pitch wind turbine has two operating regions [2], which is shown in Fig. 1. The first region is in between cut-in and rated wind speed, known as variable speed region. The second region is in between rated and cut-out wind speed, known as variable pitch region. This paper focuses on the second region. Here, the output power goes beyond the generator rated value; hence, it is to be tracked and controlled through the wind turbine by adjusting its pitch angle and generator torque. By doing this, speed of the generator and its output power oscillation is reduced and tracked with in the desired rating.

Variable speed variable pitch wind turbine system has multiple inputs multiple outputs. Hence, it is cumbersome to design its control model. Conventional control method like proportional-integral-derivative (PID) control method is used by different authors in wind turbine control in papers [3, 4]. Because of its cost and ease of implementation, most of the industrial controllers are used today are PID controllers.

Conventional control methods are not appropriate for handling nonlinear and complex systems. The control aspect issues of these complex systems can be sorted out by using intelligent systems. The intelligent techniques such as fuzzy inference systems provide a feasible alternative to capture the approximate, qualitative aspects of human reasoning and decision-making processes. Hence, the human language is expressed by means of fuzzy logic. By the use of human experience and expertise, fuzzy rules are generated. These rules are used to convert a linguistic control strategy in to an automatic control strategy by the use of fuzzy logic controller. In fact, in wind energy conversion technology problems [5, 6], fuzzy control is an appropriate choice through pitch angle control implementation.

But the design procedure of the fuzzy controller relies upon the knowledge and experience of the operator. To resolve this issue, one more intelligent control

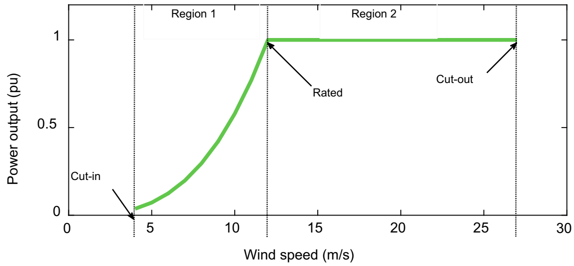

Fig. 1 Power curve characteristics for WECS

paradigm is used, i.e. artificial neural network (ANN). A number of successful applications of ANN has been reported in [7, 8] that include variable speed wind turbine control design. However, the ANN control takes excessive training time.

As DFIG-based WECS is of multivariable in nature, to control this system, we need two decentralized conventional PI/Fuzzy/ANN controller to control the generator speed and the quality of power. These constraints are significantly resolved by the use of an advanced multivariable control technique such as model predictive control [9]. In [10, 11], model predictive control is suggested for control of a WECS. But some difficulty will arise in the MPC of WECS, such as lack of adaptivity in handling intermittent variation of wind speed.

To overcome this difficulty, 'neuro-fuzzy' architecture is used. Adaptive neuro-fuzzy inference system (ANFIS) [12] is the one of such powerful neuro-fuzzy architecture. ANFIS utilizes the learning capability of ANN and modelling superiority of fuzzy logic. For estimation of wind speed, ANFIS is used in wind energy conversion system [13]. In [14], ANFIS is used for WECS power control. In this paper, we have presented a multiple ANFIS controller performance to control the output power oscillation of a DFIG-based WECS and also to track its power within the rating of the generator.

This paper is structured as follows; first, description of system with dynamic modelling is discussed. Then, the proposed control technique, i.e. multiple ANFIS controller is discussed. Before conclusion, simulation results were compared with MPC and PI controller.

2 Description of System with Dynamic Modelling

The schematic diagram of variable speed variable pitch WECS is shown in Fig. 2. This system is mainly divided into aerodynamic system, generator model, actuator dynamics, drive train model and wind model [11]. The SIMULINK model is derived from the dynamic equations of the different parts of the WECS.

The aerodynamic power available at the rotor disc is given by

Fig. 2 Schematic diagram of WECS [11]

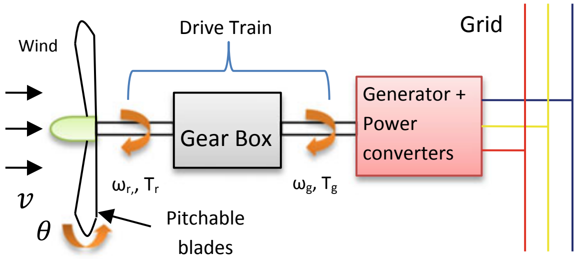

$$P_{\mathrm{z}} = \frac{1}{2}\xi\pi R^2 v^3 \tag{1}$$

where ξ is the air density, R is the radius of swept area or blade length and ν is the effective wind speed. Only a fraction of the available power P_z, can be converted to the rotor power P_{t}. The rotor power P_{t} is given by

$$P_{\mathrm{t}} = P_{\mathrm{z}} C_{\mathrm{p}}(\lambda, \theta) \tag{2}$$

where $Cp(\lambda, \theta)$ is known as power coefficient. It has a theoretical upper limit of 0.593 known as Betz limit. It is a function of tip speed ratio λ and blade pitch angle θ.

$$C_{\mathrm{p}}(\lambda, \theta) = 0.5176\left(\frac{116}{\varsigma_{\mathrm{i}}} - 0.4\theta - 5\right)e^{-21/\varsigma_{\mathrm{i}}} + 0.0068\lambda \tag{3}$$

$$\frac{1}{\varsigma_{\mathrm{i}}} = \frac{1}{\lambda + 0.08\theta} - \frac{0.035}{\theta^3 + 1} \tag{4}$$

where the tip speed ratio λ is the ratio between effective wind velocity and the blade tip speed. It is written as

$$\lambda = \frac{R\omega_{\mathrm{r}}}{v} \tag{5}$$

where ω_r is the rotor speed. Three-dimensional and two-dimensional plots of efficiency coefficient C_{p} (λ, β) are depicted on Figs. 3 and 4, respectively. From (2) and (3), we find by changing the blade pitch angle θ (blade rotation about its longitudinal axis); the value of power coefficient C_{p} (λ,θ) will change to change the output power P_{e}. This is the basic principle of wind turbine power control through pitch angle θ.

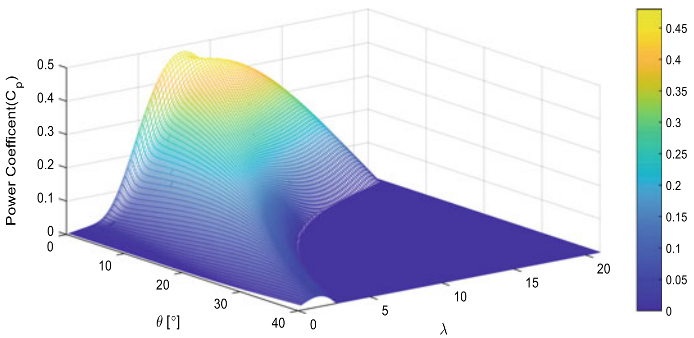

Fig. 3 Turbine efficiency coefficient

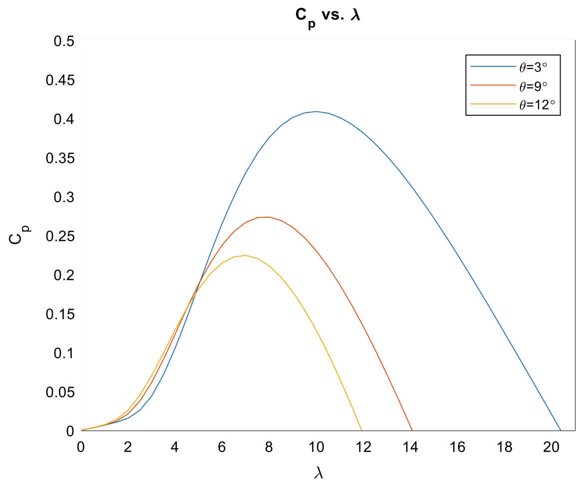

Fig. 4 Maximum power characteristics with varying pitch angle

It is given by

$$P_{\mathrm{e}} = T_{\mathrm{g}}\omega_{\mathrm{g}} \tag{6}$$

$$T_{\mathrm{g}} = \frac{P_{\mathrm{e}}}{\omega_{\mathrm{g}}} \tag{7}$$

where ω_{g} is the generator speed and T_{g} is the generator torque.

The dynamic modelling of a DFIG is based on dq equivalent model [15] shown in Fig. 5 is derived from space vector model of induction generator. It is given by

$$v_{\mathrm{ds}} = r_{\mathrm{s}} i_{\mathrm{ds}} + \frac{\mathrm{d}\psi_{\mathrm{ds}}}{\mathrm{d}t} - \omega_{\mathrm{s}}\psi_{\mathrm{qs}} \tag{8}$$

$$v_{\mathrm{qs}} = r_{\mathrm{s}} i_{\mathrm{qs}} + \frac{\mathrm{d}\psi_{\mathrm{qs}}}{\mathrm{d}t} + \omega_{\mathrm{s}}\psi_{\mathrm{ds}} \tag{9}$$

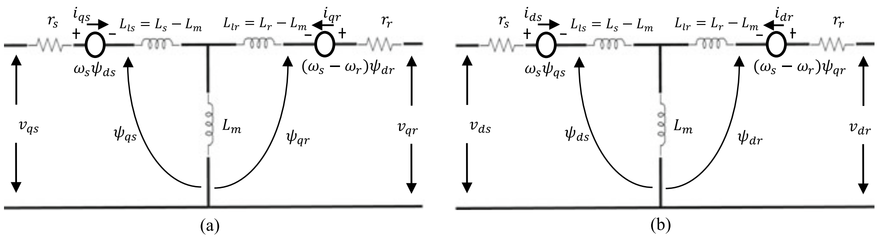

Fig. 5 Dynamic dq equivalent circuits of DFIG, **a** q-axis circuit, **b** d-axis circuit

$$v_{\mathrm{dr}} = r_{\mathrm{r}} i_{\mathrm{dr}} + \frac{\mathrm{d}\psi_{\mathrm{dr}}}{\mathrm{d}t} - s\omega_{\mathrm{s}}\psi_{\mathrm{qr}} \tag{10}$$

$$v_{\mathrm{qr}} = r_{\mathrm{r}} i_{\mathrm{qr}} + \frac{\mathrm{d}\psi_{\mathrm{qr}}}{\mathrm{d}t} + s\omega_{\mathrm{s}}\psi_{\mathrm{dr}} \tag{11}$$

where v the voltage, r the resistance, i the current, ω_s the stator electrical frequency, ψ the flux linkages and s is the rotor slip. In (8)–(11), the indices d and q indicate the direct and quadrature axis components and the subscript s and r represents the stator and rotor quantities. The value of rotor slip s is given by

$$s = \frac{\omega_s - p\omega_g}{\omega_s} \tag{12}$$

Here, p is number of pole pairs, ω_{g} is the generator speed, and it is proportional to mechanical rotor speed. The flux linkages in (8)–(11) can be calculated by using the following equations

$$\psi_{\mathrm{ds}} = (L_{\mathrm{ls}} + L_{\mathrm{m}}) i_{\mathrm{ds}} + L_{\mathrm{m}} i_{\mathrm{dr}} = L_{\mathrm{s}} i_{\mathrm{ds}} + L_{\mathrm{m}} i_{\mathrm{dr}} \tag{13}$$

$$\psi_{\mathrm{qs}} = (L_{\mathrm{ls}} + L_{\mathrm{m}}) i_{\mathrm{qs}} + L_{\mathrm{m}} i_{\mathrm{qr}} = L_{\mathrm{s}} i_{\mathrm{qs}} + L_{\mathrm{m}} i_{\mathrm{qr}} \tag{14}$$

$$\psi_{\mathrm{dr}} = (L_{\mathrm{lr}} + L_{\mathrm{m}}) i_{\mathrm{dr}} + L_{\mathrm{m}} i_{\mathrm{ds}} = L_{\mathrm{r}} i_{\mathrm{dr}} + L_{\mathrm{m}} i_{\mathrm{ds}} \tag{15}$$

$$\psi_{\mathrm{qr}} = (L_{\mathrm{lr}} + L_{\mathrm{m}}) i_{\mathrm{qr}} + L_{\mathrm{m}} i_{\mathrm{qs}} = L_{\mathrm{r}} i_{\mathrm{qr}} + L_{\mathrm{m}} i_{\mathrm{qs}} \tag{16}$$

where L_{ls}, L_{lr}—stator and rotor leakage inductances; L_{s}, L_{r}—stator and rotor self inductances and L_{m} is mutual inductance between stator and rotor.

The flux linkage in (13)–(16) given above can be represented in matrix form

$$\begin{bmatrix} \psi_{\mathrm{ds}} \\ \psi_{\mathrm{qs}} \\ \psi_{\mathrm{dr}} \\ \psi_{\mathrm{qr}} \end{bmatrix} = \begin{bmatrix} L_{\mathrm{s}} & 0 & L_{\mathrm{m}} & 0 \\ 0 & L_{\mathrm{s}} & 0 & L_{\mathrm{m}} \\ L_{\mathrm{m}} & 0 & L_{\mathrm{r}} & 0 \\ 0 & L_{\mathrm{m}} & 0 & L_{\mathrm{r}} \end{bmatrix} \begin{bmatrix} i_{\mathrm{ds}} \\ i_{\mathrm{qs}} \\ i_{\mathrm{dr}} \\ i_{\mathrm{qr}} \end{bmatrix} \tag{17}$$

The stator rotor currents in the above equation can be expressed in terms of stator and rotor flux linkages. This can be obtained by applying the inverse inductance matrix on both sides of (17), using the following matrix manipulation

$$\begin{cases} [\psi] = [L][i] \\ [L]^{-1}[\psi] = [L]^{-1}[L][i] \\ [i] = [L]^{-1}[\psi] \end{cases} \tag{18}$$

$$\begin{bmatrix} i_{\mathrm{ds}} \\ i_{\mathrm{qs}} \\ i_{\mathrm{dr}} \\ i_{\mathrm{qr}} \end{bmatrix} = \frac{1}{\Upsilon} \begin{bmatrix} L_{\mathrm{r}} & 0 & -L_{\mathrm{m}} & 0 \\ 0 & L_{\mathrm{r}} & 0 & -L_{\mathrm{m}} \\ -L_{\mathrm{m}} & 0 & L_{\mathrm{s}} & 0 \\ 0 & -L_{\mathrm{m}} & 0 & L_{\mathrm{s}} \end{bmatrix} \begin{bmatrix} \psi_{\mathrm{ds}} \\ \psi_{\mathrm{qs}} \\ \psi_{\mathrm{dr}} \\ \psi_{\mathrm{qr}} \end{bmatrix} \tag{19}$$

where $Y = L_{\mathrm{s}}L_{\mathrm{r}} - L_{\mathrm{m}}^2$ and by using (8)–(16) the active power P_e and reactive power Q_e generated by the DFIG [16] is given by

$$\begin{cases} P_{\mathrm{e}} = 1.5\left(v_{\mathrm{ds}}i_{\mathrm{ds}} + v_{\mathrm{qs}}i_{\mathrm{qs}}\right) \\ Q_{\mathrm{e}} = 1.5\left(v_{\mathrm{qs}}i_{\mathrm{ds}} + v_{\mathrm{ds}}i_{\mathrm{qs}}\right) \end{cases} \tag{20}$$

The dynamic equation of induction generator and electromagnetic torque of generator is also given [17] by

$$\omega_{\mathrm{t}} = \frac{p}{J_{\mathrm{r}}S}\left(T_{\mathrm{g}} - T_{\mathrm{t}}\right) \tag{21}$$

$$T_{\mathrm{g}} = pL_{\mathrm{m}}\left(i_{\mathrm{dr}}i_{\mathrm{qs}} - i_{\mathrm{qr}}i_{\mathrm{ds}}\right) \tag{22}$$

Time constants play a crucial role in dynamic modelling of a system because it is different for electrical and mechanical system. So to keep a balance between them, generator system [18] is modelled as follows.

$$\dot{T}_{\mathrm{g}} = -\frac{1}{\tau_{\mathrm{t}}}T_{\mathrm{g}} + \frac{1}{\tau_{\mathrm{t}}}T_{\mathrm{gr}} \tag{23}$$

where T_{gr} is the reference value for generator torque and it is the output of actuator.

Pitch actuator systems are used to control the position of the blade along the wind flow direction. Generally, these pitch actuators are operated with an electric or hydraulic technique. In this technique, blades are turned in to its longitudinal axis. The simulation modelling for actuator is [19] given as

$$\begin{cases} \frac{\mathrm{d}\theta}{\mathrm{d}t} = -\frac{1}{\tau_\theta}\theta + \frac{1}{\tau_\theta}\theta_d \\ \theta_{\min} \le \theta \le \theta_{\max} \end{cases} \tag{24}$$

where θ_{d} is the reference value of blade pitch angle, $\theta_{\min}$ and $\theta_{\max}$ are minimum and maximum pitch angle of the blade. The dynamic equations of a flexible drive train [20] is given by

$$J_{\mathrm{t}}\frac{\mathrm{d}\omega_{\mathrm{t}}}{\mathrm{d}t} = -NT_{\mathrm{tw}} + T_{\mathrm{t}} \tag{25}$$

$$\dot{\omega}_{\mathrm{t}} = -\frac{N}{J_{\mathrm{t}}}T_{\mathrm{tw}} + \frac{1}{J_{\mathrm{t}}}T_{\mathrm{t}} \tag{26}$$

$$J_{\mathrm{g}}\frac{\mathrm{d}\omega_{\mathrm{g}}}{\mathrm{d}t} = T_{\mathrm{tw}} - T_{\mathrm{g}} \tag{27}$$

$$\dot{\omega}_{\mathrm{g}} = \frac{1}{J_{\mathrm{g}}}T_{\mathrm{tw}} - \frac{1}{J_{\mathrm{g}}}T_{\mathrm{g}} \tag{28}$$

$$T_{\mathrm{tw}} = k_{\mathrm{d}}\beta_{\mathrm{tw}} + B_{\mathrm{d}}\left(N\omega_{\mathrm{t}} - \omega_{\mathrm{g}}\right) \tag{29}$$

$$\dot{T}_{\mathrm{tw}} = k_{\mathrm{d}}\,\dot{\beta}_{\mathrm{tw}} + B_{\mathrm{d}}\left(N\,\dot{\omega}_{\mathrm{t}} - \dot{\omega}_{\mathrm{g}}\right) \tag{30}$$

$$\dot{T}_{\mathrm{tw}} = k_{\mathrm{d}}N\omega_{\mathrm{t}} - k_{\mathrm{d}}\omega_{\mathrm{g}} - \left(\frac{N^2B_{\mathrm{d}}}{J_{\mathrm{t}}} + \frac{B_{\mathrm{d}}}{J_{\mathrm{g}}}\right)T_{\mathrm{tw}} + \frac{NB_{\mathrm{d}}}{J_{\mathrm{t}}}T_{\mathrm{t}} + \frac{B_{\mathrm{d}}}{J_{\mathrm{g}}}T_{\mathrm{g}} \tag{31}$$

The generator and the turbine inertia constants are J_{g} and J_{t}, respectively; β_{tw} is twist angle of the shaft; N is the gear ratio; B_{d}, k_{d} are the damping coefficient and shaft stiffness, respectively.

Because of stochastic in nature, an exact modelling of this wind speed $v(t)$ is a cumbersome process. For ease of modelling, wind speed is composed of two altered frequency components [21], i.e. a turbulence component $v_{\mathrm{t}}(t)$ and a low-frequency component $v_{\mathrm{l}}(t)$. To make the model simpler wind shear, tower shadow and rotational sampling effects are included.

$$v(t) = v_{\mathrm{l}}(t) + v_{\mathrm{t}}(t) \tag{32}$$

The simulation model of the DFIG-based wind energy conversion system shown in Fig. 1 is now obtained by comprising (1)–(32).

3 Multiple ANFIS Controller

The control block diagram of PI controller used in this work is shown in Fig. 6. The generator speed and power are the outputs of the WECS, which are feedback to the input side. After comparison with reference value, the error is send to the proportional and integral (PI) controller. In fact, these PI controllers are replaced with adaptive neuro-fuzzy inference system (ANFIS) in multiple ANFIS controller is shown in Fig. 7.

The base of the ANFIS network is the fuzzy inference system, i.e. FIS. In FIS, crisp data is converted to fuzzy variable, and then to be used in the system, it is again converted back to crisp data. FIS is classified into three types, i.e. Sugeno type, Tsukamato type and Mamdani type. All the three types are similar to one another

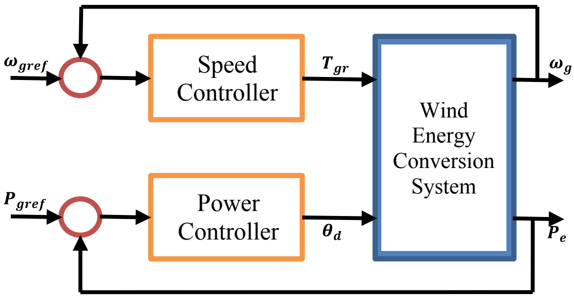

Fig. 6 Bock diagram of PI controlled WECS

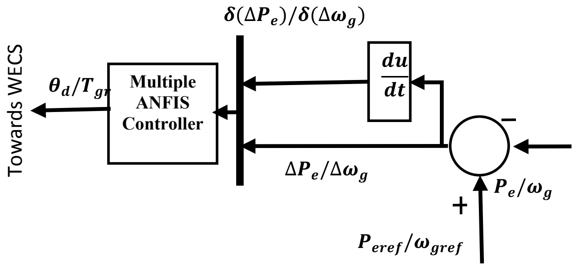

Fig. 7 Multiple ANFIS is used as controller

except with their consequents. In Sugeno type, input variable function is used as the rule consequent. The function which is utilized here is of linear or constant, and these values are updated by using differ rent adaptive techniques. Thus it is designated as adaptive neuro-fuzzy inference system (ANFIS).

In Fig. 8, an ANFIS of Sugeno type FIS [22] with five layered structure is shown. Its inputs are x_1 and x_2 and outputs are functions of x_1 and x_2. For this ANFIS, the rule base is

$$\text{If } x_1 \text{ is } C_i \text{ and } x_2 \text{ is } D_i\text{, then } y_i = p_i x_1 + q_i x_2 + r_i;\ i = 1, 2 \tag{33}$$

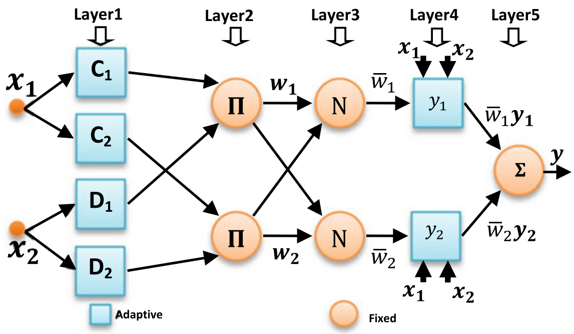

Fig. 8 ANFIS structure layout

where C_i and D_i is antecedent part and p_i, q_i and r_i is consequent part of the aforesaid rule. In this ANFIS structure, the output of every specific layer is designated by y_i^l.

Layer 1: All the nodes in this layer are represented by square boxes and are adaptive in nature. It is known as input linguistic layer. In this layer crisp inputs x_1 and x_2 are fuzzified. Output of this layer is

$$y_i^1 = \begin{cases} \mu_{C_i}(x_1) \\ \mu_{D_i}(x_2) \end{cases} i = 1, 2 \tag{34}$$

where μ is the input membership functions. This membership function may be triangular, trapezoidal, Gbell, Gaussian or sigmoidal type. Gbell type membership function is used here. It is represented by

$$\mu_c(x_1) = \frac{1}{1 + \left[\left(\frac{x_1 - c_i}{a_i}\right)^2\right]^{b_i}} \tag{35}$$

where a_i, b_i and c_i are the set of parameters. These parameters are to be changed and upgraded during learning. Then membership functions are adjusted through varying the bell-shaped functions.

Layer2: Here, nodes are represented by round boxes and all are fixed nodes. The output is

$$y_i^2 = w_i = \mu_{C_i}(x_1) * \mu_{D_i}(x_1) \quad i = 1, 2 \tag{36}$$

Layer 3: This layer is recognized as rule layer and all of its nodes are fixed. This layer computes the normalized firing strengths in its output and is given by

$$y_i^3 = \overline{w}_i = \frac{w_i}{w_1 + w_2} \tag{37}$$

Layer 4: In this layer, all the nodes are adaptive in nature, and it is recognized as consequent layer. The layer output is

$$y_i^4 = \overline{w}_i y_i = w_i(p_i x_1 + q_i x_2 + r_i) \tag{38}$$

where p_i, q_i and r_i are defined as the consequent parameter.

Layer 5: In this layer, all the node signals are summed up. This layer is recognized as linguistic layer. Here, the fuzzified input is converted to defuzzification. The layer output is

$$y_i^5 = \text{overall output} = \sum_i \overline{w}_i y_i = \sum_i y_i^4 \tag{39}$$

It is observed from the ANFIS structure that its rule base consists of two parts, i.e. consequent part and antecedent part. The parameters in the antecedent part are nonlinear parameter, and parameters in the consequent part are linear parameter. By exploiting several optimization methods, these two parts can be optimized so that the parameters present in it will optimize. Hybrid learning method is utilized here. In this learning, backward pass and forward pass mode are used. Actually, ANFIS adapts the parameters in the adaptive network by using gradient descent and least square estimator algorithms. Finally, the overall output of the ANFIS from Fig. 8 can be represented as

$$
\begin{aligned}
y &= \frac{w_1}{w_1 + w_2} y_1 + \frac{w_2}{w_1 + w_2} y_2 = \bar{w}_1 y_1 + \bar{w}_2 y_2 \\
y &= (\bar{w}_1 x_1) p_1 + (\bar{w}_1 x_2) q_1 + (\bar{w}_1) r_1 + (\bar{w}_2 x_1) p_2 + (\bar{w}_2 x_2) q_2 + (\bar{w}_2) r_2
\end{aligned} \tag{40}
$$

The consequent parameters p_1, q_1, r_1, p_2, q_2 and r_2 are to be identified by least square method in forward pass mode. In backward pass, the error rate signal is propagated back and the premise parameters are updated by the gradient descent.

In this paper, we are using two inputs and two outputs for a DFIG-based WECS, which is shown in Fig. 6. To cope with this, multiple ANFIS is used here, and they are sharing their inputs by placing parallel to one another. The multiple ANFIS controller control design is shown in Fig. 7. But for the design of an ANFIS controller, input and output data are required. Here, the data for generator power and its speed is collected from a Simulink model. In Fig. 9, ANFIS created data for training of both power of the generator and its speed is displayed. By utilizing either subtractive clustering or grid partition method, this structure of ANFIS model is generated. The grid partitioned method is used here. It divides the input subspace by utilizing the minimum and maximum amplitudes of data generated. Thereafter, through learning algorithm, these data were trained. The training of the ANFIS is performed with 'gbell' membership function with 500 epochs. In Fig. 10, the MFs for initial and final conditions of speed of generator and its power is presented. Finally, the expected outcome for generator power and its speed is shown in Figs. 11 and 12 through the use of proposed multiple ANFIS controller.

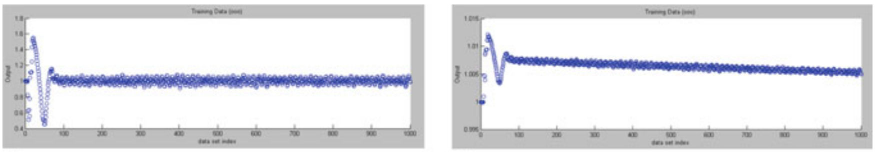

(a) (b)

Fig. 9 ANFIS training data for, **a** generator power, **b** generator speed

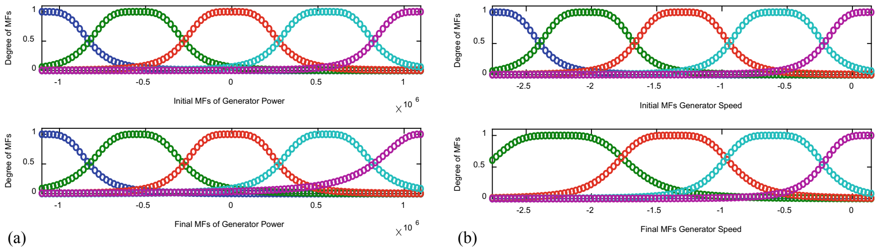

Fig. 10 Initial and final MF for, **a** generator power, **b** generator speed

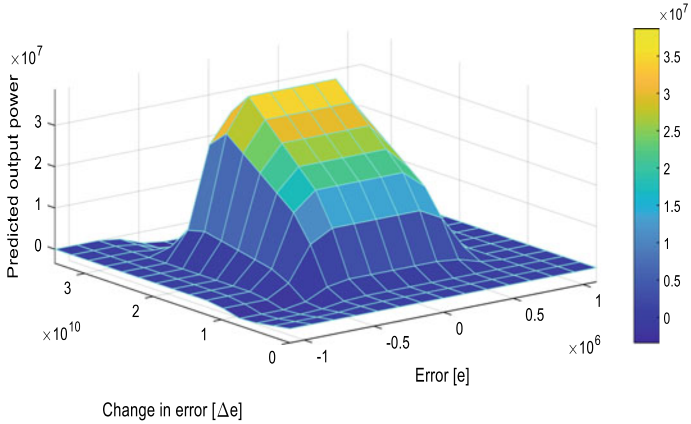

Fig. 11 Predicted output of ANFIS for generator power

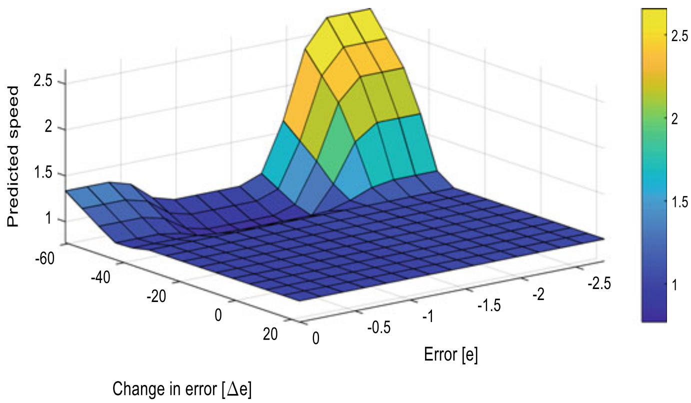

Fig. 12 Predicted output of ANFIS for generator speed

4 Simulation Results and Discussion

The proposed multiple ANFIS controller and other known controllers, e.g. proportional-integral (PI) and model predictive control (MPC) were implemented in a DFIG-based WEC Simulink model through (1)–(31) and the parameters [11] are given in Table 1. The wind speed with magnitude 26 and 12 m/s is chosen here as cut-out and rated wind speed. To test the performance of proposed controller, it is compared PI and MPC controller by using simulated continuous wind speed.

Magnitude and direction representation of a stochastic wind speed is difficult in nature. To represent it in MATLAB with a simpler manner, statistical evaluation has been practiced by creating the data for wind speed using Gaussian noise generator. A continuous variable simulated wind speed is shown in Fig. 13a. This wind speed comprised of a slow and fast variation speed of wind as presented in (32). The variable wind speed which is used here varies between 18 and 22 m/s, with an average of 20 m/s. In Fig. 13 b–e, responses of the torsional torque, speed of generator, pitch angle and power output is displayed, respectively.

The functioning of above controllers, namely multiple ANFIS, MPC and PI were assessed and analysed in Fig. 13. In Fig. 13b, drive train torsional torque (T_{tw}) fluctuations are very high for conventional controller. Fluctuations are reduced in MPC case but starting time overshoots and undershoots are very high. In proposed controller case, torsional torque perfectly tracks 1 pu, and there are no overshoots and undershoots at the time of starting. Because of reduction in both torsional torque fluctuation and generator speed, its consequence is reflected on the power of the generator and drive train system components. This results in increased life time of the drive train component and improved generator power quality. In Fig. 13c,

Table 1 Parameters of DFIG-based WECS

S. No	Parameter	Unit	Value
01	Rated turbine power, $P_{t,\,rat}$	(MW)	2
02	Rated rotor speed, $w_{r,\,rat}$	(rad/s)	3.0408
03	Damping coefficient, B_d	(N m s/rad))	212.2
05	Blade radius, R	(m)	33.29
06	Pitch actuator constant, τ_θ	(s)	0.1
07	Max. blade pitch, θ_{max}	(deg)	45^o
08	Min. blade pitch, θ_{min}	(deg)	0^o
09	Max, blade pitch rate, $\dot{\theta}_{max}$	(deg/s)	10^0
10	Min, blade pitch rate, $\dot{\theta}_{min}$	(deg/s)	-10^0
11	Gear ratio, N	(–)	74.38
12	Generator inertia, J_g	(kg m^2)	56.29
13	Rotor inertia, J_t	(kg m^2)	1.86×10^6
14	Generator time constant, τ_t	(s)	20×10^{-3}

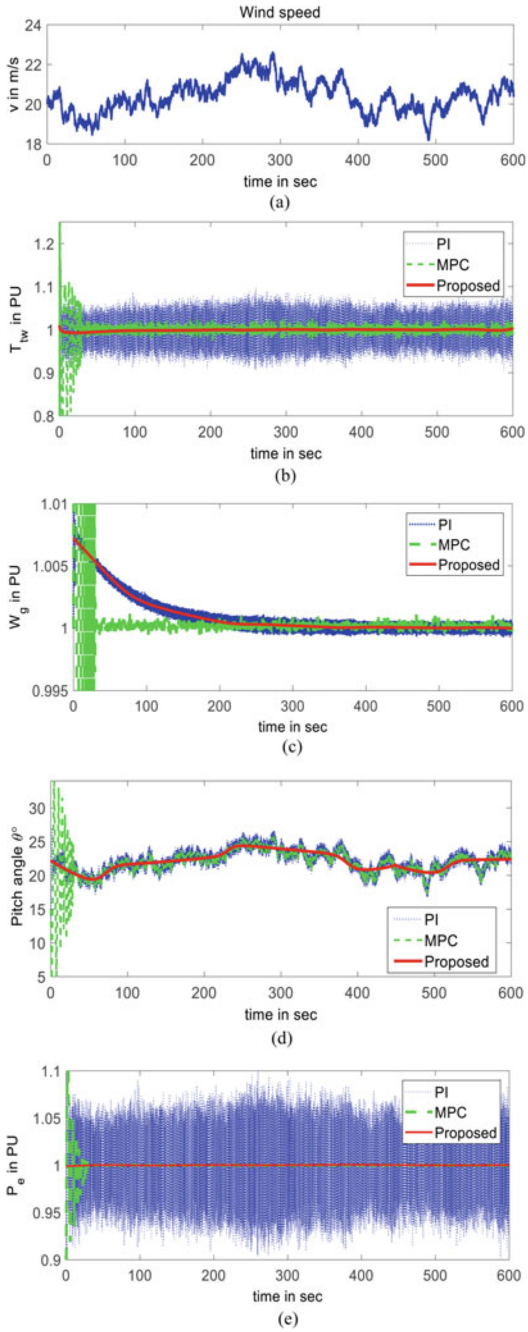

Fig. 13 **a** Wind speed, **b** drive train torsional torque, **c** generator speed, **d** pitch angle and, **e** generator power with PI, MPC and multiple ANFIS controller comparison for DFIG-based WECS

Table 2 Deviation of wind power with different controller for a DFIG based WECS

Controller	Min (P_e)	Max (P_e)	% of Deviation
PI	0.9043	1.1045	18.1258
MPC	0.9917	1.0469	5.2727
Multiple ANFIS	0.9956	1.0058	1.0141

fluctuation in speed of the generator (ω_g) is much more and more in case of PI and MPC controllers, respectively. Further, in MPC instance, there is an undershoot and an overshoot at the time of starting for a time of 30 s, but thereafter, it fluctuates about 1 per unit (pu). In case of proposed controller, overshoots, undershoots and oscillations are decreased and followed the path at 1 pu perfectly. From Fig. 13d, it is observed that oscillations are existing in pitch angle (θ) case for both PI and MPC controllers. In the case of MPC, though fluctuations are of lesser magnitude, it yields more overshoots and undershoots at the time of starting. Because of this, the rating of pitch actuator servo is increased which in turn increases the tariff of the generated wind energy. In case of the proposed controller, both the pitch angle oscillations and pitch rate are decreased.

It is observed from Fig. 13e that the oscillations in the output power of generator (P_e) is much more for the occasion of conventional controller in contrast to MPC and proposed controller. But for the MPC, overshoot and undershoot are found in generator power at the beginning of the responses, and thereafter, it is reduced and tracks around 1 pu with lower magnitude of oscillation. Oscillations, undershoots and overshoots are reduced completely in case of the proposed controller. Despite the variations in wind speed, the proposed controller tracks the preferred generator power output at 1 pu. Therefore, the generator operates with in its rated value and delivers the maximum quality output power to the load.

Statistics given in Table 2 for generator power output with continuous wind speed (initial 10 s not considered) confirms the aforementioned observations. It can be seen in Table 2 that power deviation for multiple ANFIS controller reduces to 1.01% in comparison to PI and MPC controller, which is 18.13% and 5.27%, respectively. It is observed from the result analysis and statistics that the generation of quality power is increased by the use of multiple ANFIS controller in comparison to MPC and PI controller.

5 Conclusion

This paper suggests a multiple ANFIS controller to track and control the generator power oscillation through simultaneously regulating the torque of the generator and pitch angle. By doing so, the output power fluctuation is reduced and subsequently quality of power is improved. Here, the multiple ANFIS controller is utilized because of its modelling superiority, learning ability and adaptive capability. The reduction of output power oscillation and its tracking performance operation of the proposed controller is equated with MPC and PI controllers. It is observed from the performance analysis and statistics that the proposed multiple ANFIS controller excels in each aspect in comparison to MPC and conventional PI controller.

References

1. Gielen D, Boshell F, Saygin D, Bazilian MD, Wagner N, Gorini R (2019) The role of renewable energy in the global energy transformation. Energ Strat Rev 24:38–50
2. Karimirad M (2012) 2.09—mechanical-dynamic loads, comprehensive renewable energy. Elsevier, pp 243–268
3. Pan LH, Wang X (2020) Variable pitch control on direct-driven PMSG for offshore wind turbine using repetitive-TS fuzzy PID control. Renew Energy 159:221–237
4. Asgharnia A, Shahnazi R, Jamali A (2018) Performance and robustness of optimal fractional fuzzy PID controllers for pitch control of a wind turbine using chaotic optimization algorithms. ISA Trans 79:27–44
5. Kesraoui M, Lagraf SA, Chaib A (2015) Aerodynamic power control of wind turbine using fuzzy logic. In: 2015 3rd international renewable and sustainable energy conference (IRSEC), pp 1–6
6. Sahoo S, Subudhi B, Panda G (2016) Pitch angle control for variable speed wind turbine using fuzzy logic. In: IEEE international conference on information technology (ICIT), IIIT, Bhubaneswar, India, pp 28–32
7. Aguilar O, Tapia R, Valderrabano A, Minor H (2015) Design and performance comparison of PI and adaptive current controllers for a WECS. IEEE Lat Am Trans 13(5):1361–1368
8. Sandeep V, Bala Murali Krishna V, Namala KK, Rao DN (2016) Grid connected wind power system driven by PMSG with MPPT technique using neural network compensator. In: 2016 international conference on energy efficient technologies for sustainability (ICEETS), pp 917–921
9. Maciejowski. J.: Predictive control with constraints, 1st Edition. Printice-Hall, (2000).
10. Jassmann U, Berroth J, Matzke D, Schelenz R, Reiter M, Jacobs G, Abel D (2014) Model predictive control of a wind turbine modelled in Simpack. J Phys Conf Ser IOP Publishing 524(012047):1–11
11. Soliman M, Mallick OP, Westwick D (2011) Multiple model multiple-input multiple-output predictive control for variable speed variable pitch wind energy conversion systems. IET Renew Power Gener 5(2):124–136
12. Chang F, Chang Y (2006) Adaptive neuro-fuzzy inference system for prediction of water level in reservoir. Adv Water Resour 29:1–10
13. Mohandes MRS (2011) Estimation of wind speed profile using adaptive neuro-fuzzy inference system (ANFIS). Appl Energy 88:4024–4032
14. Oguz Y, Guney I (2010) Adaptive neuro-fuzzy inference system to improve the power quality of variable-speed wind power generation system. Turk J Elec Eng Comp Sci 18(4):625–645
15. Fadaeinedjad R, Moallem M, Moschopoulos G (2008) Simulation of a wind turbine with doubly fed induction generator by FAST and Simulink. IEEE Trans Energy Convers 23(2):690–700
16. Jauch C, Islam SM, Sorensen P, Jensen BB (2007) Design of a wind turbine pitch angle controller for power system stabilization. Renew Energy 32(14):2334–2345
17. Soliman M, Mallick OP, Westwick D (2011) Multiple model predictive control for wind turbines with doubly fed induction generators. IEEE Tran Sustain Energy 2(3):215–225
18. Huang C, Li F, Ding T, Jin Z, Ma X (2015) Second-order cone programming-based optimal control strategy for wind energy conversion systems over complete operating regions. IEEE Trans Sustain Energy 6(1):263–271
19. Subudhi B, Ogeti PS (2016) Non-linear autoregressive moving average with exogenous input model-based adaptive control of a wind energy conversion system. J Eng IET 7:01–09

20. Munteanu I, Bratcu AI, Cutululis NA, Ceanga E (2008) Optimal control of wind energy systems, 1st edn. Springer
21. Munteanu I, Bratcu AI, Cutululis NA, Ceanga E (2005) Ootimization of variable speed wind power systems based on a LQG approach. Control Eng Pract 13(7):903–912
22. Muralikumar K, Ponnambalam P (2021) Comparison of fuzzy and ANFIS controllers for asymmetrical 31-level cascaded inverter with super imposed carrier PWM technique. IEEE Access 9:82630–82646

Chapter 26
Demand Response Management in a Smart Grid with Multiple Users and Utility Companies

Pravat Kumar Ray, Shobhit Nandkeolyar, and Nikhil Sai Rama Valiveti

Abstract In a smart grid, demand response is an important aspect to efficiently manage the demand generation balance, decrease the cost of power generation as well as the cost to the consumers. The implementation of DR in a power grid consisting of multiple utility companies and consumers is still a challenging task. A Stackelberg game has been proposed in this paper between the users and the utilities in order to maximize the monetary returns. It has been shown that an equilibrium exists in the Stackelberg game. Algorithms have been designed which reach the equilibrium even though localized knowledge regarding the utilities and consumers is available.

Keywords Demand response (DR) · Nash equilibrium · Non-cooperative game theory · Smart grid · Stackelberg game · Stackelberg equilibrium

1 Introduction

The ever-increasing electrical consumption is a result of the rising requirement for smart electrical appliances, automation, hybrid/fully electric vehicles. Population expansion is also a major contributing factor. The conventional power grid lacks information exchange between the supply and demand sides. It also lacks flexibility in design. Blackouts are caused by the lack of reliable operation. Hence, we need to move toward smart grid which deals with all the above issues in an efficient and cost-effective manner by utilizing smart meter-based infrastructure integrated with wireless communication. An important aspect of smart grid is demand response

---

P. K. Ray · S. Nandkeolyar (✉) · N. S. R. Valiveti
Department of Electrical Engineering, National Institute of Technology, Rourkela 769008, India

P. K. Ray
e-mail: rayp@nitrkl.ac.in

N. S. R. Valiveti
e-mail: 714ee4116@nitrkl.ac.in

G. Panda et al. (eds.), *Sustainable Energy and Technological Advancements*,
Advances in Sustainability Science and Technology,
https://doi.org/10.1007/978-981-16-9033-4_26

management (DRM). It is instrumental in maintaining a proper balance between demand and supply. In this way, it can be utilized for load shedding and shaving operations from the grid and consumer's perspective. The consumers are inclined to participate as they get monetary benefits in their tariff and the utility companies (UC) can implement a real-time pricing approach.

The work done in DRM can be classified into either consumer side or UC side. Here, we have considered communication among multiple consumers and UCs unlike the single consumer–UC interaction in most of the recent research works. The consumers and UCs play a non-cooperative game, and the game strategy of each player has influence on others. The players communicate via bidirectional communication channels. In this paper, we have mathematically modeled the complex interactions among the various consumers and UCs using the Stackelberg game while recognizing its distinctive Stackelberg equilibrium. A distributed algorithm has been developed to find the optimal power demand by the consumers and the unit energy prices for each UCs when only a limited knowledge regarding the consumer's power consumption, and own available power is available with the individual UCs.

A lot of research work has been done in the past on DRM [1–4]. An energy demand schedule has been introduced in [1] where the UCs fix their tariff based on the time and energy generation level. A DRM arrangement in which consumers alter their loads on per hour basis, and the UCs fix their hourly energy price in response to that has been proposed in [2]. A variable price tariff scheme has been introduced in [3] where the consumers get monetary incentives on the basis of their daily load profile. A distributed algorithm has been designed to configure a cooperative game approach among the various consumers and UCs in the energy market. The authors in [4] focused on the end consumer satisfaction part of DRM. They studied the consumer's preferences in order to improve energy efficiency. The concept of Stackelberg game has been utilized in the area of Cooperative Cognitive Radio Networks and for reducing network congestions in situations where consumers are charged on their bandwidth usage [5, 6]. In [7], the authors have introduced an objective problem to maximize the profits in DRM. The method also focused on the learning of the consumer's behavior. In [8], the authors have proposed a concept of two-level game for DRM for various UCs.

The major contribution of this paper is in the development of a convex optimization problem along with constraints on the consumer's side which provides optimal value of consumer's power demand upon solving. Similar objective problem has been presented in the supply side as well along with the utility side constraints. The solution of this problem provides the unit energy price of the UCs. Stackelberg equilibrium has also been shown to exist. Here, it has been considered that the UCs do not have any knowledge about how much power is available with other UCs unlike the previous cases present in the literature. The aim here is to develop a distributed algorithm in order to find the optimum values of unit energy price as well as the power consumption such that the payoffs are maximized. Two cases were discussed, and the results were presented. In the first case, fewer number of consumers and UCs were considered and the budgets of consumers are variable. In the second case, large number of consumers were considered with fixed number of UCs in the energy market.

The remaining sections of the paper are organized as: Section 2 presents the system modeling; Sect. 3 illustrates the interaction between the consumers and the utilities via the Stackelberg game theory; Sect. 4 develops the distributed algorithm in order to find the most optimal solution; Sect. 5 presents the results and discussion; and Sect. 6 presents the final conclusion.

2 Modeling of the System

It has been assumed that the total number of users is N while the total number of utility companies (UC) are M. The UCs could be generated from either renewable, or non-renewable sources of energy, or both. Figure 1 illustrates the overall diagram of the smart grid. Addition of renewable generation at the utility side brings certain complexities in the system. The consumers can be divided into different categories based on their power consumption level such as residential and industrial consumers. A utility function can be defined for the end consumer wherein the value of the function increases with an increase in the power consumption of that consumer. A constraint for every consumer has also been defined. The energy price and consumption data can be communicated between the consumers and UC via smart meters as shown in Fig. 2. Wireless technologies like WiMAX or LTE can be used to carry out the communication.

The power system operator (PSO) fixes the energy prices. All the UCs play a non-cooperative game where there is no cooperation among the utilities participating in the energy market. There is an imperfect competition among the UCs. In a perfect market where there is healthy competition, there is no monopoly. Hence, the UCs can raise the unit price up to a point where their marginal cost of energy production equals the market energy price. This holds true for a scenario where there are a large amount of UC and none of the UCs control larger energy production. Here we have

Fig. 1 Smart grid with multiple energy sources and users

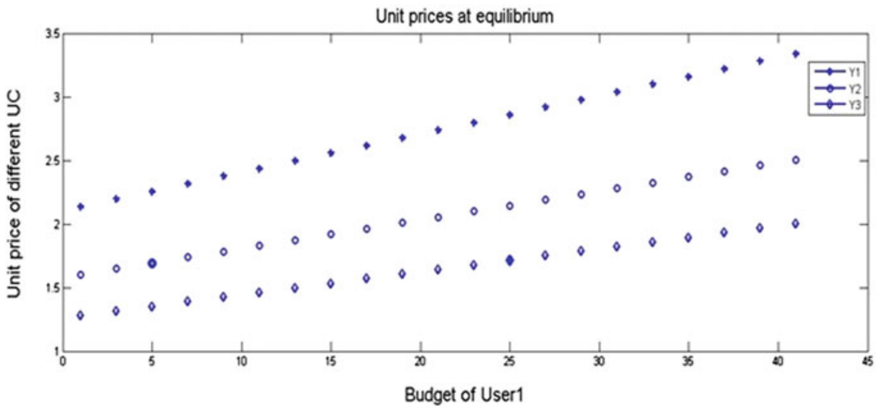

Fig. 2 Unit prices of power at equilibrium for different UC

considered a finite amount of UC, and they influence the market energy price. This leads to imperfect competition and UCs fix the unit energy price according to the available power.

3 Utility User Interaction Stackelberg Game

Here, we are trying to model more than one UC and they have different price points. Hence, the cost to the consumers will be different if they take the services from a different UC. In the energy market, each UC has a significant effect in fixing the unit energy price to maximize their profit. Game theory is a tool, from economics, to model the complex relationship among the UCs and the consumers where the UCs fix the energy price and the consumers communicate their energy demands via smart meter. This is a sequential process and can be effectively modeled using the Stackelberg game. In this game, the UCs are the leaders as they set their prices first, whereas the consumers are the followers as they make their demands according to the set prices [8]. The game is among multiple leaders and followers. The energy demand of each consumer is limited by their budget constraint. Each UC has to find the optimal price in accordance with the consumer's response.

3.1 *User Side Analysis*

The power consumption of nth consumer from mth UC is denoted by $x_{n,m}$. The utility serving the nth consumer $U_{\text{user},n}$ can be denoted as:

$$U_{\text{user},n} = \omega_n \sum_{m \in M} \ln(\theta_n + x_{n,m}) \tag{1}$$

In (1), ω_n and θ_n are constant quantities. ln has been used due to the fact that it is widely utilized to model the consumer satisfaction in economics. For larger values, the function is not affected significantly much like the characteristics of consumer satisfaction function. y_m denotes the energy price per unit of mth UC while C_n denotes the nth consumer's budget. Consumer $n \in N$ for a set of price values $\left(y_1, y_2, y_{3,} \ldots y_m\right)$. On solving the aforementioned problem, we get optimal consumer demand.

$$x_n := \max_{\{x_{n,m}, \forall m \in M\}} U_{\text{user},n} \tag{2}$$

where

$$\sum_{m \in M} y_m x_{n,m} \leq C_n \tag{3}$$

$$x_{n,m} \geq 0; \forall m \in M \tag{4}$$

After the optimization problem has been solved, $x_{n,m}$ is:

$$x_{n,m} = \frac{C_n + \theta_n \sum\limits_{m \in M} y_m}{M y_m} - \theta_n \tag{5}$$

3.2 Utility Side Analysis

Let us assume that $P_m > 0$ be the available power with UC m for selling. Every UC has to make sure that they have a minimum amount of available power left with them at the commencement of a deal. Here, multiple UCs are considered because with only one UC the analysis would be constrained, as all the users will have to depend on that particular UC. As a result, that one and only available UC will charge high unit price on the users to fetch maximum revenue due to zero competition. Therefore, to avoid this issue, there are two constraints imposed on UCs, which prevent them from charging a higher unit energy price. They are the competition among various UCs in the energy market and the budget constraint of the consumer. Here, there is a lack of cooperation among the UCs while fixing the optimal unit energy price for the consumers. It is assumed that P_m is the power available for all $m \in M$. The power generation cost is known for the chosen P_m. So, the revenue of UC can be obtained by using (6).

$$U_{\text{gen},m}(y_m, y_{-m}) = y_m \sum_{n \in N} x_{n,m} \tag{6}$$

where the y_m is the price of the UCs except m. Constraints imposed on utility side are as follows:

$$y := \max_{\{y_m, \forall m \in M\}} U_{\text{gen},m}(y_m, y_{-m}) \tag{7}$$

$$\sum_{n \in N} x_{n,m} \leq P_m \tag{8}$$

$$y_m > 0, m \in M \tag{9}$$

$$y_m = \left[C + B\left(\sum_{g \in m, g \neq m} y_g \right) \Big/ \text{MP}_m + B(m-1) \right] \tag{10}$$

3.3 Stackelberg Equilibrium

In this non-cooperative game, the Stackelberg equilibrium is same as the Nash equilibrium point. Then, the list of finalized unit prices by each UCs is provided to the consumers. The principle of the equilibrium game strategy for any of the followers must be such that the decided approach by the leader(s) must receive optimal response.

Let $\Psi_{\text{gen},m}$, and $\lambda_m = 10$ be the strategy sets for the nth user and the mth UC, respectively. The strategy sets of all the UCs are represented by $\Psi_{\text{gen}} = \Psi_{\text{gen},1} \times \Psi_{\text{gen},2} \times \cdots \Psi_{\text{gen},M}$ and for different consumers are $\Psi_{\text{user}} = \Psi_{\text{user},1} \times \Psi_{\text{user},2} \times \cdots \Psi_{\text{user},N}$. The $y_m^* \in \Psi_{\text{gen},m}$ is an equilibrium strategy for the mth UC if $\forall m \in M$

$$U_{\text{gen},m}(y^*, x(y^*)) \geq U_{\text{gen},m}(y_m, y_{-m}^*, x(y_m; y_{-m}^*)) \tag{11}$$

The income of the mth UC is more than the unit energy price of any of the UCs or any user's strategy according to the above inequality relation with the strategy y_m^* and at $x := \{x_1, x_2, ...x_N\}$.

3.4 Existence and Uniqueness of Stackelberg Equilibrium

The maximum power demand of the users and the highest revenue by the UCs both are achieved at a unique unit price y. Therefore, it can be noted that game has a distinct equilibrium point, if the game between the UCs results in a distinct Nash equilibrium.

4 Distributed Algorithm

In the above-discussed sections, certain formulations have been carried out to determine the optimal demand by considering the information about the UCs regarding unit prices and power availability associated with UCs. But the UCs go according to other UCs' strategies. But, the above study will not be applicable if UCs have no information about the available power of the others companies. Therefore, a distributed algorithm is developed which makes it possible to achieve Stackelberg equilibrium without even knowing the available power with other UCs.

In this case, each UC begins by assuming a unit price $Y_{m,\,1} > 0$ and provides the information about the updated unit price to the users through the communication channel of smart grids. Then, the users keep the record of the unit price through the installed smart meters and they decide their share of optimal load demand from each UC $\left\{x_{n,m,1}, \forall m \in M\right\}$ using equation X. After receiving the demand matrix from the users, each UC then evaluates the difference between the available power with them and the total power demanded by the users. Accordingly, the UC then decides the unit price, which is updated using (12):

$$y_{m,i+1} = y_{m,i} + \frac{\sum_{n \in N} x_{n,m,i} - P_m}{\lambda_m} \tag{12}$$

where λ_m is the adjustment parameter for speed of convergence of UC, m is chosen to be a large number, and i is the number of iteration. Whenever there is any modification in unit price made by UCs, this must be informed to the users so that can make changes in their load demand and update that to the utility companies. These steps are repeated iteratively until the unit price converges.

Let us consider this algorithm as algorithm1. Here, $n = 1$ indicates user 1.

1) Randomly assume $y_{m,i+1}$, for i=1
2) Run loop when i=1, 2, ...
3) Consumer Variable n=1,2,3,…N
4) Do
5) Find $x_{n,m,i}$ using (2, 3, and 4) for provided y_i with the help of (5)
6) Communicate $x_{n,m,i}$ to every m
7) End of Do
8) Solve for $y_{m,i+1}$ for the m[th] UC whose unit price isn't updated for i+1 iteration, with the help of (12)
9) **If** $y_{m,i+1}$ - $y_{m,i}$ = 0
10) Convey an unaltered signal to the consumers.
11) Go to 8
12) **Else**
13) Communicate the updated unit energy price to consumers
14) Go to 3
15) **End** of If when condition (10) is met
16) **If** $y_{m,i+1} == y_{m,i}$ $\forall m \in M$ then End
17) **Else** go to 2
18) **End** of if when condition (12) is met

5 Results

From the results obtained, it is observed that depending on the optimal unit price charged by the UCs, the optimal load demand is decided by the consumers. Moreover, based on the user budget constraints and the available power with UCs, UCs optimize the unit price. The convergence rate of distributed algorithm is evaluated using MATLAB. For study, 3 UCs and 5 users are considered with parameters $\omega_n = 1, \theta_n = 1 \; \forall n \in N$. The budget of users is given as $C_1 = 5$, $C_2 = 10$, $C_3 = 15$, $C_4 = 20$, $C_5 = 25$. and the available power of the UCs is $P_1 = 10$, $P_2 = 15$, $P_3 = 20$.

5.1 *Stackelberg Game*

The plot in Fig. 2 presents the demands of users at equilibrium. In Figs. 2, 3, 4, and 5, it has been depicted that rise in budget of the user1 from 2 to 40 has affected the user demands, unit prices, revenues of UCs. With increase in the budget of user 1, the demand of that user increases. However, the overall load demand remains almost unaltered because the demand of other users reduces as user 1 demands more. With

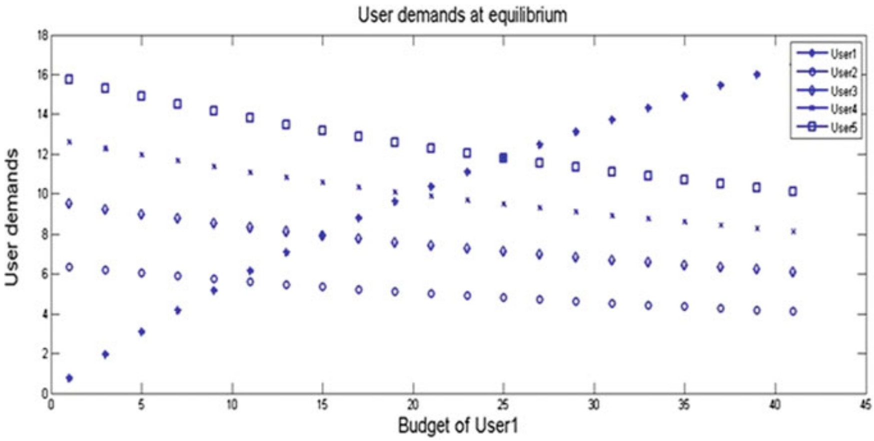

Fig. 3 User demands at equilibrium

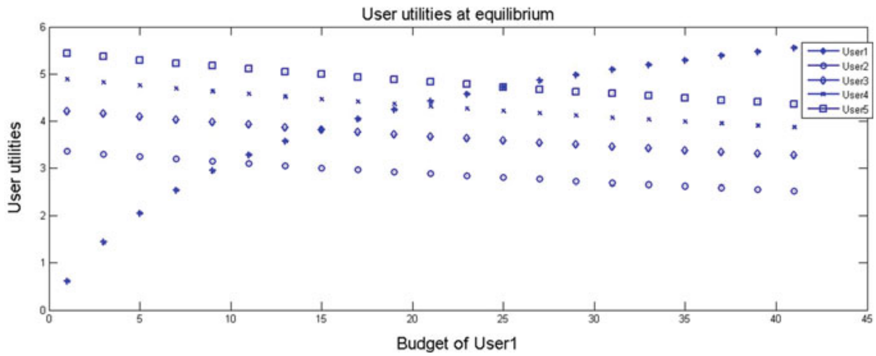

Fig. 4 User utilities at equilibrium

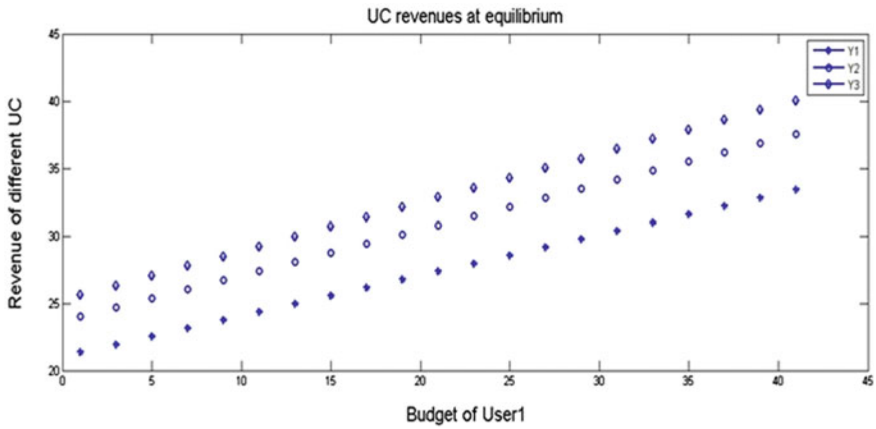

Fig. 5 UC revenues at equilibrium

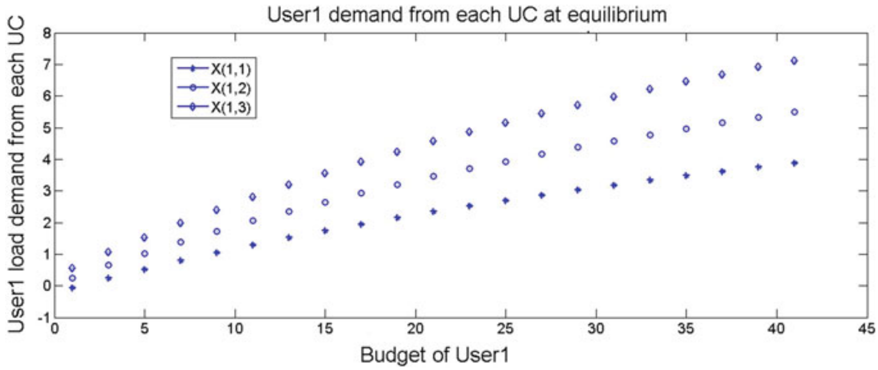

Fig. 6 User 1 demand from each UC at equilibrium

no alteration in the changes applied previously, the user utilities at equilibrium which is depicted in Fig. 3. The effect of increase in budget of user 1 on the unit prices of UC is given in Fig. 4. It can be observed that there is a linear increment in unit prices for all the UCs due to more budget and demand of user 1. The UC with least available power charges the highest unit price on users to receive maximum revenue. It can be seen in Fig. 5 that despite charging the highest unit prices, UC1 has achieved the lowest revenue due to the lowest available power. However, the UC3 received highest revenue for the lowest unit price charged due to the highest available power. With varying budget, the change in load demand of user 1 from each UC at equilibrium is shown in Fig. 6.

After analyzing the Stackelberg equilibrium for small number of users, the same analysis is carried out for large number of users. The study is performed for 100 users and 5 UCs. The constraint on cost for user 1 is varied from 2 to 400. And that for users 2–25, users 26–50, users 51–75, and users 76–100 are 10, 15, 20, 25, respectively. The available power with all the 5 UCs is $P_1 = P_2 = 150$ units, $P_3 = P_4 = 200$ units, $P_5 = 250$ units. Characteristics of plots in case of large number of users remain unchanged as compared with that of a smaller number of users.

The rise in budget of only user 1 increases the load demand by user 1. Despite increase in load demand by user 1, there is no significant change in the load demand of other users because the number of users is high, and hence, the plot obtained is a straight line as shown in Fig. 7b. The user utility plot in Fig. 7a behaves same as the user demand plot. It can be noted from Fig. 7c that the UC with the highest available power gets the highest load demand and the UC with the lowest available power gets the lowest load demand. Unit prices and revenues of the UCs increase linearly with increase in the budget of the user 1 as given in Fig. 7d, e, respectively.

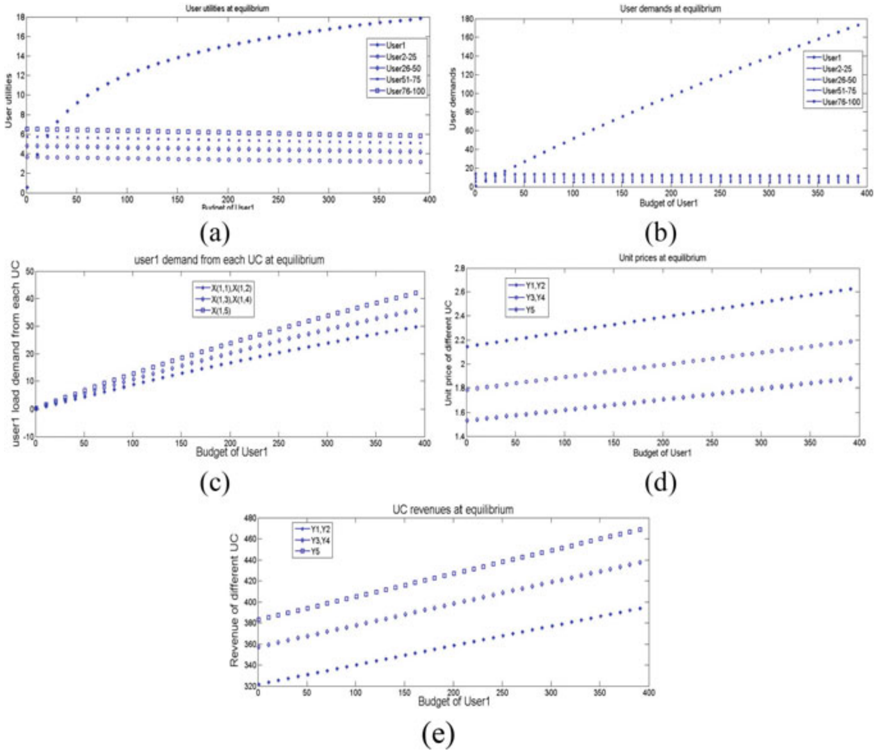

Fig. 7 Large number of users, **a** user utilities at equilibrium, **b** user demands at equilibrium, **c** user 1 demand from each UC at equilibrium, **d** unit prices at equilibrium, **e** UC revenues at equilibrium

5.2 Distributed Algorithm

The plots obtained using distributed algorithm for $\lambda_m = 40 \forall m \in M$ are presented in Figs. 8, 9, 10, 11, and 12. Without knowing, the any local information regarding the power availability of the other UCs, the equilibrium point is reached. At first, a unit energy price is chosen then corresponding power demand is evaluated; and depending on that another unit energy price is fixed for the UC. This process continues. Following few runs, Stackelberg equilibrium point is reached; i.e., optimal value of unit price and load demand is obtained. Hence, this proves that power demand and unit price both are quickly converging to the equilibrium point. By comparing Figs. 8, 9, 10, 11, and 12 with Figs. 2, 3, 4, 5, and 6, it can be clearly seen that the distributed algorithm converges to the same expected optimum values under same set of given data. With different values of mth UC's initial unit energy price $y_{m,1}$, and the speed varying parameter λ_m, the algorithm's performance is studied. For $\lambda_m = 10 (m = 1, 2, 3, \ldots)$, the algorithm is converging faster to the same expected values as compared to the smaller value of λ_m as shown in Fig. 13a. In Fig. 13b, it is depicted that algorithm converging to the same value for different assumed initial

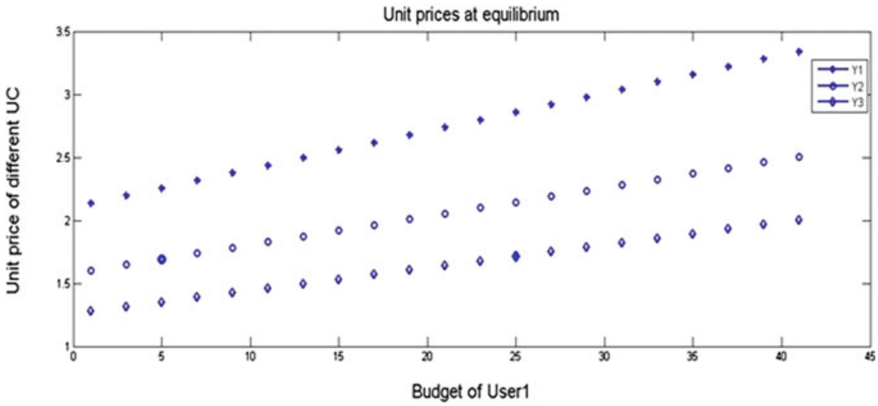

Fig. 8 UC revenues at equilibrium

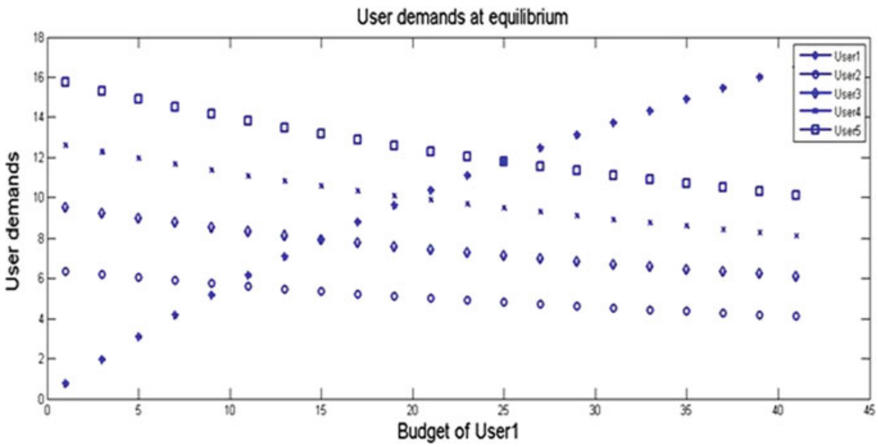

Fig. 9 Unit prices at equilibrium

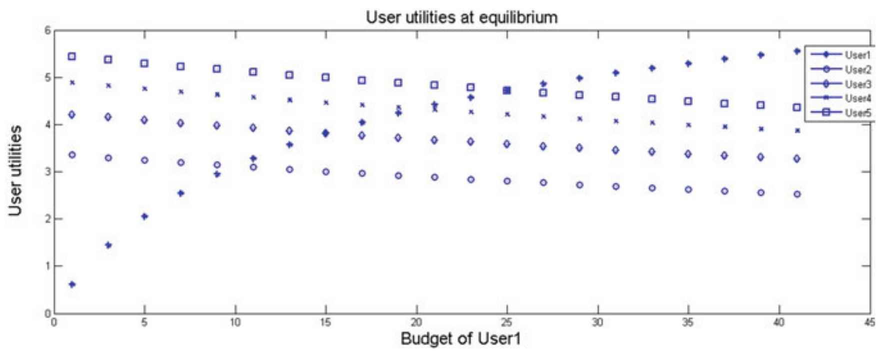

Fig. 10 User demands at equilibrium

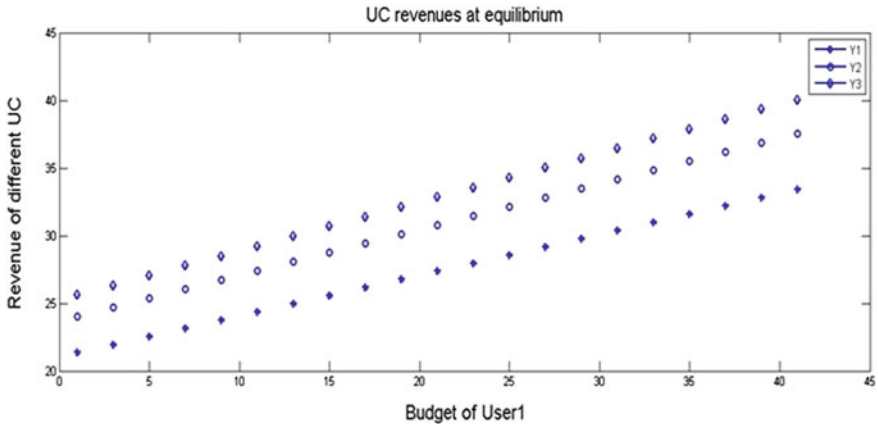

Fig. 11 User 3 demand from each UC at equilibrium

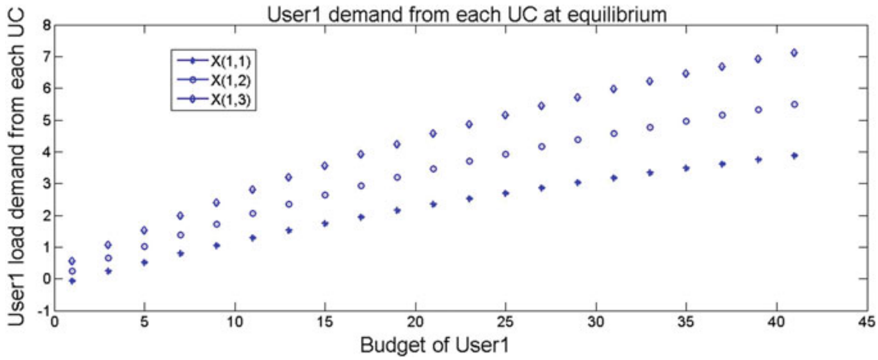

Fig. 12 User utilities at equilibrium

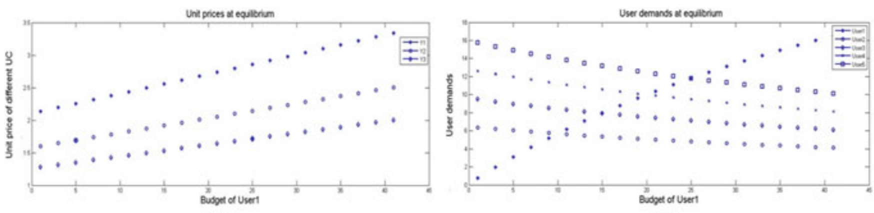

(a) (b)

Fig. 13 Distributed algorithm plots at different speed convergence factors and different initial values of unit price of UCs, **a** for $y_{m,1} = 5$, $\lambda_m = 50$. **b** for $y_{m,1} = 10$, $\lambda_m = 10$

unit price $y_{m,1.}$ Hence, it shows that the speed of convergence is only linked with the value of λ_m, $\forall m \in M$; and irrespective of the initial value assumed, the algorithm converges to same value.

6 Conclusion

In this particular paper, the Stackelberg game has been reviewed between various users simultaneously with multiple number of UCs to estimate the equilibrium point of the game which includes optimum unit price and users optimum demand for large and small selection of users. Further, the results were examined by MATLAB plots. For the condition, when UCs do not have any knowledge about the available power of other UCs, the convergence point is successfully obtained by the development of distributed algorithm.

Acknowledgements The authors would like to thank DST, Government of India for supporting the research video no. DST/INT/Thai/P-12/2019.

References

1. Mohsenian-Rad H, Wong VWS, Jatskevich J, Schober R, Leon-Garcia A (2010) Autonomous demand side management based on game theoretic energy consumption scheduling for the future smart grid. IEEE Trans Smart Grid 1(3):320–331
2. Conejo J, Morales JM, Baringo L (2010) Real-time demand response model. IEEE Trans Smart Grid 1(3):236–242
3. Dai Y, Gao Y, Gao H, Zhu H (2018) A demand response approach considering retailer incentive mechanism based on Stackelberg game in smart grid with multi retailers. Int Trans Electr Energy Syst 28(9):e2590
4. Başar T, Srikant R (2002) Revenue-maximizing pricing and capacity expansion in a many-users regime. Proc IEEE Infocom 1:294–301
5. Zhang J, Zhang Q (2009) Stackelberg game for utility-based cooperative cognitive radio networks. In: Proceedings of MobiHoc'09: 23–32
6. Meng F, Zeng X (2016) A profit maximization approach to demand response management with customers behavior learning in smart grid. In: IEEE transactions on smart grid: 7(3):1516–1529
7. Chai B, Chen J, Yang Z, Zhang Y (2014) Demand response management with multiple utility companies: A two-level game approach. In: IEEE transactions on smart grid: 5(2):722–731
8. Başar T, Olsder GJ (1999) Dynamic non cooperative game theory, ser. SIAM series in classics in applied mathematics. SIAM, Philadelphia: 265–363

Chapter 27
Combined Environmental and Economic Dispatch in the Presence of Sustainable Sources Using Particle Swarm Optimization with Adaptive Weighted Delay Velocity

Soudamini Behera, Namrata Naik, Sasmita Behera, and Ajit Kumar Barisal

Abstract Recently, the excessive utilization of fossil fuels in power plants requires the concern of environmental safety. In general, the economic power dispatch (ED) does not convene environmental safety as its major intention is a reduction of the overall generation cost of the system. The accurate solution of economic dispatch is acquired only by concerning the environmental issues. So ED becomes combined environmental and economic dispatch (CEED) with cost and emission as two objective functions. In this study, particle swarm optimization (PSO) with adaptive weighted delay velocity (PSO-AWDV) algorithm is used for solving the CEED dilemma for a coordinated ten thermal unit and sustainable energy sources like wind and solar system with weighting method and fuzzy decision-making (FDM) method. The obtained outcomes indicate the inclusion of sustainable sources with the thermal units is more economical as compared to the thermal system, and the outcomes are correlated with PSO, sparrow search algorithm (SSA), sequential quadratic programming (SQP), evolutionary programming (EP), and hybrid of SQP and EP.

Keywords CEED · PSO-AWDV · Renewable energy sources (RES) · FDM · ED · Emission dispatch

S. Behera (✉) · N. Naik
Government College of Engineering, Kalahandi, Odisha, India

S. Behera
Veer Surendra Sai University of Technology, Sambalpur, Odisha, India

A. K. Barisal
Odisha University of Technology and Research, Bhubaneswar (OUTR), Bhubaneswar, Odisha, India
e-mail: akbarisal@cet.edu.in

G. Panda et al. (eds.), *Sustainable Energy and Technological Advancements*, Advances in Sustainability Science and Technology,
https://doi.org/10.1007/978-981-16-9033-4_27

1 Introduction

Combined environmental and economic dispatch (CEED) is the online practice of allocation of the load among the accessible generators to accomplish the load demand with the reduction of net generation cost and emission with fulfilling the system bounds. The prime goal is the economical operation of the power system so that all the load demand is fulfilled at the minimum cost of generation and emission of harmful gases like CO_2, SO_2, and NO_X. In this work, the PSO-AWDV method is used to solve this CEED dilemma.

Kennedy and R. Eberhart have introduced PSO. PSO was projected to decipher the multi-objective dilemma in [1]. Hybrid particle swarm optimization (HPSO) algorithm is employed to decipher the CEED dilemma in [2]. Advanced PSO (APSO) is applied to explain the CEED problem in [3]. Solar generating systems (SGS) are considered on CEED of the power system in [4]. The consequence of wind on CEED has been discussed in [5]. The non-dominated sorting genetic algorithm-II is applied for explaining the DEED dilemma of a hydro–wind–thermal power system in [6]. Phasor particle swarm optimization (PPSO) is proposed to explain economic load dispatch (ELD) dilemmas with several system bounds [7]. The dynamic economic dispatch (DED) dilemma with valve point effects (VPE) has been discussed in [8]. The constriction factor-based particle swarm optimization (CFBPSO) algorithm is employed to solve the CEED dilemma of a thermal–wind–solar power system with dynamical load demand [9]. A ten thermal units system with RESs is thoroughly analyzed for dynamic CEED [10]. The major handouts of this work are: (1) A novel PSO with adaptive weighted delay velocity (PSO-AWDV) is flourished by adaptively revising the velocity inertia weight of the PSO-WDV algorithm which offers some supremacy to the particles to overcome from the local trap. [11]. (2) The supremacy of the projected algorithm is investigated with some earlier developed optimization algorithms like SSA [12], PSO [1], SQP, EP, EP-SQP method [13] and are applied to decipher the CEED dilemma of a ten thermal unit with sequential quadratic programming sustainable energy sources like wind and solar energy source. (3) The multi-objective CEED dilemma can be changed to a solo objective with the weighting function method [14]. The section-wise organization of the paper is given below:

Sect. 2 describes the formulation of load dispatch problem, Sect. 3 describes CEED using PSO-AWDV, Sect. 4 explains the case studies and results obtained, and Sect. 5 finally concludes the research work and shows the future scope for further research.

2 Optimal Load Dispatch Problem Formulation

2.1 Problem Formulation for Economic Dispatch (ED)

The ED dilemma in power systems is to share the load among the devoted generator unit in such a fashion that the cost of generation is reduced by appeasing the load demand and system bounds.

The minimum fuel cost of i th unit is formulated as:

$$F_c(P_i) = a_i * P_i^2 + b_i P_i + c_i \$/h \tag{1}$$

Subject to:

(a) Equality constraints

$$\left(\left(\sum_{i=1}^{n} P_i\right) - P_{\mathrm{L}} - P_{\mathrm{D}}\right) = 0 \tag{2}$$

where

a_i, b_i, c_i	are coefficients of cost of ith thermal unit (TU)
P_i	is power generation of ith unit
n	is the total figure of TUs.

P_{L} indicates the power loss which is neglected here, P_{D} is load demand, and n is the maximum number of thermal units.

2.2 Problem Formulation for Emission Dispatch

The emission released from a power plant should be within a permitted limit and the emission constraint can likewise be taken as in (3).

$$E_m(P_i) = \alpha_i * P_i^2 + \beta_i P_i + \gamma_i P_i^2 + \varepsilon_i \times \exp^{(\delta i \times Pi)} \text{ kg/h} \tag{3}$$

where α_i, β_i, γ_i, ε_i, and δ_i are coefficients of GHGs emission of ith unit, exp is an exponential function.

2.3 Problem Formulation for CEED

The weighting function method is applied to convert the multi-objective dilemma into a single objective as in (4)

$$\text{Min } F_T = \sum_{i=1}^{n} (w_1 F_c(P_i) + w_2 E_m(P_i)) \tag{4}$$

where F_{T} is a combined objective function to be limited. When all the sources are considered, then the combined objective function is as in (5)

$$\text{Min } F_T = F_i(P_i) + E_i(P_i) \tag{5}$$

where $F_i(P_i)$ and $E_i(P_i)$ are the total generation cost and total emission cost of thermal, wind, and solar plant, respectively.

Subject to:

$$\begin{aligned} &P_D + P_L - \sum_{i=1}^{n} P_i - \sum_{j=1}^{m} P_{gsj} - \sum_{z=1}^{q} P_{gwz} = 0 \\ &P_{i\ \min} \le P_i \le P_{i\ \max} \end{aligned} \tag{6}$$

$P_{i\ \min}$ is the lowest and $P_{i\ \max}$ is the highest generation limit of ith unit in MW.

where P_{gsj} is power accessible from jth solar plant and P_{gwz} is power available from zth wind plant. The solar and wind power plant sharing the load with m and q generating units, respectively.

The effect of valve point loading (VPE) can be modeled by adding a sinusoidal term to the main cost function as in (7)

$$F_c(P_i) = \sum_{i=0}^{Ng} \left(a_i * P_i^2 + b_i P_i + c_i\right) + |d_i \sin(e_i * (P_{i\ \min} - P_i))| \quad [\$/h] \tag{7}$$

d_i, e_i are the coefficients of VPE of the i th unit. $P_{i\ \min}$ is the minimum generation limit of i th unit in MW.

3 CEED Using PSO-AWDV Technique

3.1 Formulation of PSO with Adaptive Weighted Delay Velocity

In the search space, the velocity and position influence the search behavior of PSO. The particles are updated as per the following equations.

$$v_i^{(r+1)} = w * v_i^{(t)} + c_1 * r_1 * (x_{ip\,\text{best}}^{(t)} - x_i^{(t)}) + c_2 * r_2 * (x_{ig\text{best}}^{(t)} - x_i^{(t)}) \tag{8}$$

$$x_i^{(t+1)} = x_i^{(t)} + v_i^{(t+1)} \tag{9}$$

where t is maximum iterations (generations), w is inertia weight factor.

c_1, c_2 are learning factors, r_1, r_2 are random values in the range [0–1].

$v_i^{(t)}$ is velocity of particle i at iteration t and $x_i^{(t)}$ is current position of particle at iteration t. $v_i^{(t+1)}$ and $x_i^{(t+1)}$ are new velocity and position of particle i, respectively.

Inertia weight is revised after each iteration and is expressed as in (10)

$$w = w_{\max} - \frac{w_{\max} - w_{\min}}{t_{\max}} * t \tag{10}$$

where $w_{\max}$ and $w_{\min}$ are the highest and lowest value of inertia weight. $t_{\max}$ is maximum number of iterations. The flowchart of PSO-AWDV algorithm for dispatch problem is Fig. 1.

The updating functions of PSO-AWDV are

$$\begin{aligned} v_i^{(t+1)} = {} & w * v_i^{(t)} + (1 - w) * v_i^{(t-1)} + c_1 * r_1 * (x_{ip\text{best}}^{(t)} - x_i^{(t)}) \\ & + c_2 * r_2 * (x_{ig\text{best}}^{(t)} - x_i^{(t)}) \end{aligned} \tag{11}$$

$$x_i^{(t+1)} = x_i^{(t)} + v_i^{(t+1)} \tag{12}$$

$x_{ip\text{best}}^{(t)}$ and $x_{ig\text{best}}^{(t)}$ are the best positions experienced by the ith particle and the particle swarm up to the current iteration.

where c_1, c_2 are cognitive and social acceleration factors, *rand*, *Rand* are random numbers arbitrarily chosen between 0 and 1.

w is the inertia weight of the velocity $v_{ipbest}^{(t)}$ and $w < 1$; $(1 - w)$ is the inertia weight of the delayed velocity $v_i^{(t-1)}$.

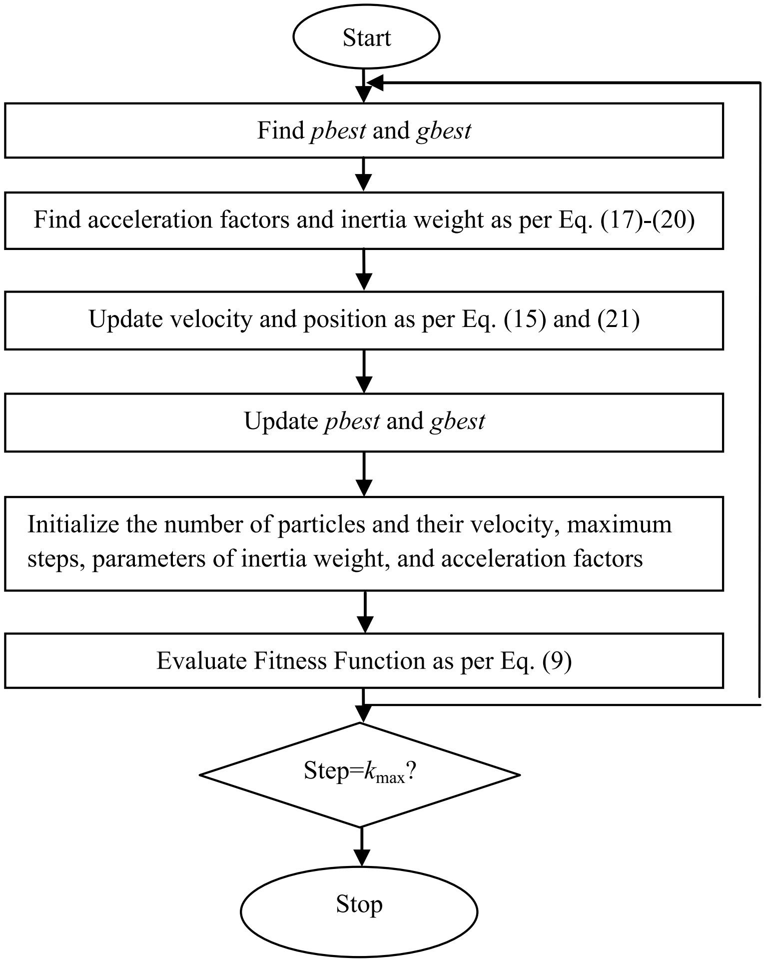

Fig. 1 Flowchart of PSO-AWDV

4 Case Studies and Simulation Results

4.1 Ten Thermal Units Without VPE: Case 1

In this scenario, PSO-AWDV is implemented to decipher the CEED dilemma for minimizing the fuel and emission cost for ten number of thermal generating units (TUs) without considering VPE. The hourly system load demand and the generator cost coefficients of ten units thermal system as in [8] and emission coefficients of ten units thermal system as in [15] (Table 1).

Table 1 Result for Case 1 with FDM method

Weighting functions		CEED cost	Fuel cost	Emission cost	Membership function		Accomplishment function
w_1	w_2	C	F	E	μ_1	μ_2	μ_d^k
1	0	1,007,408.41	1,007,408.45	31,280.31	0.9664	0.0736	0.0425
0.95	0.05	958,933.66	1,007,731.9	31,767.54	0.9509	0	0.0388
0.9	0.1	909,551.37	1,007,085.24	31,746.62	0.9819	0.0032	0.0402
0.85	0.15	860,389.99	1,006,708.49	31,251.84	1	0.078	0.044
0.8	0.2	812,169.65	1,007,440.35	31,086.86	0.9649	0.1029	0.0436
0.75	0.25	761,567.1	1,006,886.54	31,610.46	0.9915	0.0237	0.0415
0.7	0.3	713,573.08	1,008,942.93	30,941.39	0.8927	0.1249	0.0415
0.65	0.35	664,848.59	1,007,633.06	30,851.31	0.9556	0.1385	0.0447
0.6	0.4	614,627.39	1,007,184.11	31,011.39	0.9772	0.1143	0.0446
0.55	0.45	567,974.85	1,007,939.11	30,240.74	0.9409	0.2308	0.0478
0.5	0.5	518,835.09	1,007,743.12	29,927.07	0.9503	0.2782	0.0502
0.45	0.55	468,220.44	1,007,704.49	29,623.29	0.9522	0.3241	0.0521
0.4	0.6	421,075.7	1,008,680.17	29,339.39	0.9053	0.367	0.052
0.35	0.65	371,962.65	1,009,387.6	28,733.85	0.8714	0.4586	0.0543
0.3	0.7	322,821.15	1,010,457.76	28,119.78	0.82	0.5514	0.056
0.25	0.75	273,598.08	1,011,902.57	27,496.59	0.7506	0.6456	0.057
0.2	0.8	224,217.7	1,013,612.4	26,994.95	0.6686	0.7214	0.0568
0.15	0.85	174,397.15	1,016,733.97	26,253.75	0.5187	0.8334	0.0552
0.1	*0.9*	*125,790.56*	*1,020,160.48*	*25,661.7*	*0.3542*	*0.9229*	*0.0581*
0.05	0.95	75,320.03	1,025,208.9	25,325.88	0.1118	0.9737	0.0443
0	1	25,151.84	1,027,538.2	25,151.84	0	1	0.0408

In this scenario, PSO-AWDV is implemented to decipher the CEED dilemma for minimizing the fuel and emission cost for ten number of thermal generating units without considering VPE. The hourly system load demand and the generator cost coefficients of ten thermal units system as in [8] and emission coefficients of ten thermal units system as in [15].

4.2 *Ten Thermal Units with VPE: Case 2*

In this case, PSO-AWDV is implemented to solve the CEED problem for minimizing the fuel and emission cost for ten number of thermal generating units considering VPE. The best-compromised result obtained by applying the FDM method in Case 2 is displayed in Table 2. It is observed that the obtained outcomes are slightly increased than the earlier case1 when the VPE of the thermal system is taken into

Table 2 Results of the power ratings for CEED for the ten thermal system in Case 2

Time (h)	P_1 (MW)	P_2 (MW)	P_3 (MW)	P_4 (MW)	P_5 (MW)	P_6 (MW)	P_7 (MW)	P_8 (MW)	P_9 (MW)	P_{10} (MW)	Cost ($)	Emission (ton)
1	150	135	97.88	96.25	120.61	131.93	95.08	74.7	79.52	55	30,022	360.71
2	163.91	152.41	101.94	96.32	150.54	131.22	95.21	105.3	58.11	55	32,444.19	410.44
3	247.96	155.04	111.03	116.58	167.24	153.83	82	94.11	75.16	55	36,000.72	532.18
4	221.73	198.48	134.09	134.86	184.92	158.48	119.9	118.48	80	55	39,006.37	630.66
5	216.68	212.86	146.18	146.47	212.78	160	130	120	80	55	40,123.86	701.61
6	329.92	248.16	157.05	158.05	214.06	135.73	130	120	80	55	41,294.6	921.74
7	241.1	312.4	183.24	177.24	243	160	130	120	80	55	41,326.88	990.41
8	296.45	296.21	197.65	197.67	243	160	130	120	80	55	41,474.01	1011.67
9	335.39	311	270.2	222.17	243	157.22	130	120	80	55	48,211.3	1270.99
10	388.13	388.13	253.86	253.86	243	160	130	120	80	55	50,179.41	1651.47
11	410.96	411.03	268.04	267.96	243	160	130	120	80	55	50,132.81	1813.9
12	183.01	460	340	300	243	160	130	120	80	55	50,133.74	2044.28
13	388.13	388.12	253.86	253.87	243	160	130	120	80	55	50,172.75	1647.47
14	342.27	342.11	225.73	225.86	243	160	130	120	80	55	50,602.27	1352.39
15	337.91	266.93	179.63	205.35	242.82	160	128.3	119.99	80	55	45,281.43	1102.09
16	269.33	228.52	158.5	166.99	195.09	155.87	126.5	119.67	78.48	55	42,107.01	802.25
17	209.6	239.01	145.92	144.54	199	159.74	130	119.44	77.71	55	40,551.59	702.42
18	312.87	261.25	177.56	167.33	206.89	160	94.27	112.83	79.95	55	42,092.47	925.00
19	268.22	332.19	188.16	199.41	243	160	130	120	80	55	41,981.05	1102.62
20	325.72	426.25	309.24	222.77	243	160	130	119.99	80	55	50,451.93	1691.69
21	330.26	335.65	251.46	218.62	243	160	130	119.99	80	55	50,520.08	1360.6

(continued)

Table 2 (continued)

Time (h)	P_1 (MW)	P_2 (MW)	P_3 (MW)	P_4 (MW)	P_5 (MW)	P_6 (MW)	P_7 (MW)	P_8 (MW)	P_9 (MW)	P_{10} (MW)	Cost ($)	Emission (ton)
22	299.12	241.31	169.78	170.53	222.83	160	125	104.39	80	55	41,404.15	901.93
23	158.88	215.54	131.7	140.87	198.29	158.09	79.44	114.16	80	55	37,641.46	581.51
24	150	203.39	140.58	97.01	146.87	132.5	96.23	100.75	61.63	55	33,961.64	471.54
Using PSO-AWDV Total =											1,027,117.72	24,981.57
Using PSO =											1,027,316.72	25,068.57
Using SSA											1,027,472.23	25,188.28
Using hybrid EP and SQP [13]											1,035,748.00	
Using EP [13]											1,048,638,481	
Using SQP [13]											1,051,163.00	

consideration. The fuel cost obtained by the projected method is less as compared to sparrow search algorithm (SSA), PSO, SQP, EP, and hybrid of EP and SQP method. It is realized from the outcomes that the projected method is quite effective in solving the CEED problem.

4.3 Ten Thermal Units with VPE + Wind Plant: Case 3

In this case, PSO-AWDV is implemented to solve the CEED problem for minimizing the fuel and emission cost for ten number of TUs with VPEs and a wind plant. The capacity of wind and solar plants is considered as 30 and 40 MW, respectively [15, 16]. The result obtained in Case 3 at $w_1 = 0.05$, $w_2 = 0.95$ is CEED total cost, fuel cost, and emission 125,750.7 \$, 1,021,313.55 \$, and 25,609.59 ton, respectively. The outcomes give evidence that the projected approach is quite effective in solving the CEED problem.

4.4 Ten Thermal Units with VPE + Solar Plant: Case 4

In this case, PSO-AWDV is implemented to solve the CEED problem for minimizing the fuel and emission cost for ten number of TUs considering VPEs with solar and emission impact. The best-compromised result obtained at $w_1 = 0.15$, $w_2 = 0.85$ is the CEED total cost, fuel cost, and emission 127,045.7 \$,1,022,885.5 \$, and 27,029.4 ton, respectively.

4.5 Ten Thermal Units with VPE + Wind + Solar Plant: Case 5

In this case, PSO-AWDV is implemented to solve the CEED problem for minimizing the fuel and emission cost for ten number of thermal generating units considering VPE with both renewable energy sources (solar and wind). Table 3 demonstrates the real power ratings for the 10 generators in this scenario at $w_1 = 0.1$, $w_2 = 0.9$. The convergence plot of this case is displayed in Fig. 2, and it is realized from the figure that the projected method is quite effective in solving the CEED problem.

In case 2, when VPE of thermal units is considered, then cost increases but more practical results are obtained. In case 3, when wind source is included with the thermal system, both cost and emission are reduced. Similarly, in case 4 when a solar source is included with the thermal system, both cost and emission are reduced. In case 4, cost and emission are slight increases as compared to case 3. The comparison of all cases is exhibited in Table 4 and in Figs. 3 and 4, respectively. It is observed that in

Table 3 Results of the power ratings for CEED for the ten thermal system in Case 5

Time	P_1 (MW)	P_2 (MW)	P_3 (MW)	P_4 (MW)	P_5 (MW)	P_6 (MW)	P_7 (MW)	P_8 (MW)	P_9 (MW)	P_{10} (MW)	Cost	Emission	CEED
(hr)	MW	MW	MW	MW	MW	MW	MW	MW	MW	MW	($)	(ton)	($)
1	150.00	135.00	73.03	120.42	172.73	145.15	93.06	47.00	20.00	55.00	28,232.71	403.32	3180.95
2	287.96	135.02	73.01	66.25	172.58	122.48	94.03	47.00	20.00	55.00	29,642.35	428.98	3424.05
3	150.00	222.20	157.52	113.26	172.72	123.13	130.00	47.14	52.07	55.00	32,864.61	470.98	3774.71
4	226.24	309.58	185.14	126.28	122.73	122.67	93.25	85.32	52.06	55.00	36,223.96	627.13	4286.01
5	155.54	309.53	259.22	176.30	122.90	131.07	129.97	85.31	52.06	55.00	38,702.88	670.52	4673.47
6	303.18	222.63	185.25	179.53	209.50	159.93	129.61	119.99	52.06	55.00	41,894.62	884.35	5013.02
7	379.87	309.30	185.32	120.49	181.37	149.63	130.00	120.00	52.10	55.00	43,138.19	1022.92	5288.11
8	303.16	309.58	200.38	226.41	222.59	126.39	129.62	120.00	52.06	55.00	44,727.43	1120.76	5493.08
9	303.25	396.80	184.87	236.64	222.60	160.00	129.59	120.00	80.00	55.00	48,179.25	1261.36	6012.22
10	303.23	396.93	292.37	241.09	231.28	160.00	129.61	120.00	80.00	55.00	50,869.11	1529.63	6494.42
11	379.89	396.80	278.60	241.18	225.14	160.00	129.70	120.00	79.99	55.00	52,137.17	1601.71	6713.84
12	379.88	460.00	297.40	241.26	241.88	160.00	129.59	85.32	80.00	55.00	53,836.54	1652.68	7065.54
13	303.25	396.80	186.38	300.00	243.00	160.00	130.00	120.00	80.00	55.00	50,452.17	1502.30	6396.79
14	379.87	309.53	193.24	180.94	222.73	160.00	129.73	120.00	80.00	55.00	46,828.53	1208.63	5778.90
15	379.93	222.28	203.54	180.84	222.74	160.00	101.67	85.31	80.00	55.00	44,045.77	1132.64	5369.53
16	226.64	309.55	190.21	126.19	172.88	160.00	99.84	85.33	80.00	55.00	39,766.00	902.64	4704.43
17	276.75	222.22	182.88	120.41	222.45	122.46	93.06	85.29	52.05	55.00	37,769.83	791.74	4454.29
18	371.88	387.06	174.29	120.55	172.12	122.65	93.25	54.84	51.72	55.00	41,628.95	910.12	5176.22
19	226.59	309.25	295.87	179.35	222.31	159.90	130.00	119.54	52.01	55.00	44,504.67	1171.04	5502.97
20	456.49	396.80	188.83	300.00	223.34	132.59	129.65	85.40	80.00	55.00	51,596.52	1601.84	6752.81

(continued)

Table 3 (continued)

Time	P_1 (MW)	P_2 (MW)	P_3 (MW)	P_4 (MW)	P_5 (MW)	P_6 (MW)	P_7 (MW)	P_8 (MW)	P_9 (MW)	P_{10} (MW)	Cost	Emission	CEED
21	303.25	309.52	285.19	240.55	240.96	159.93	129.59	120.00	80.00	55.00	49,215.32	1400.52	6168.32
22	301.26	309.50	182.63	177.57	172.71	124.31	129.46	118.34	51.93	55.00	41,759.55	1011.69	5050.18
23	150.00	288.67	181.53	179.12	122.83	122.19	93.16	84.78	50.40	55.00	35,676.01	630.41	4186.22
24	226.62	135.00	185.22	62.67	122.89	129.33	129.86	85.34	52.07	55.00	31,774.22	550.79	3654.55
										Total =	1,015,466.35	24,488.80	124,614.63

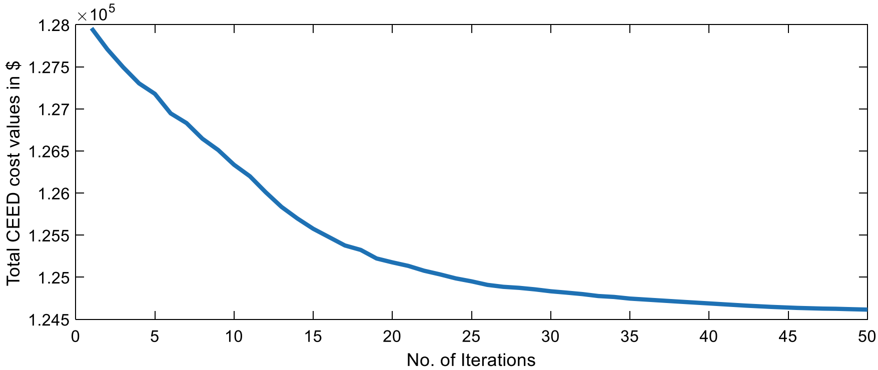

Fig. 2 Convergence characteristic for Case 5

Table 4 Analogy of all cases concerning cost, emission, and CEED total cost

Case	Cost in $	Emission in ton	CEED Total cost in $
Case 1(only Thermal without VPE)	1,020,160.48	25,661.7	125,790.56
Case 2(only Thermal with VPE)	1,027,117.72	24,981.57	127,011.2
Case 3 (Thermal with VPE + Wind)	1,021,313.55	25,609.45	125,750.7
Case 4(Thermal with VPE + Solar)	1,022,885.5	27,029.27	126,407.7
Case 5(Thermal with VPE + Wind + Solar)	1,015,466.35	24,488.80	124,614.63

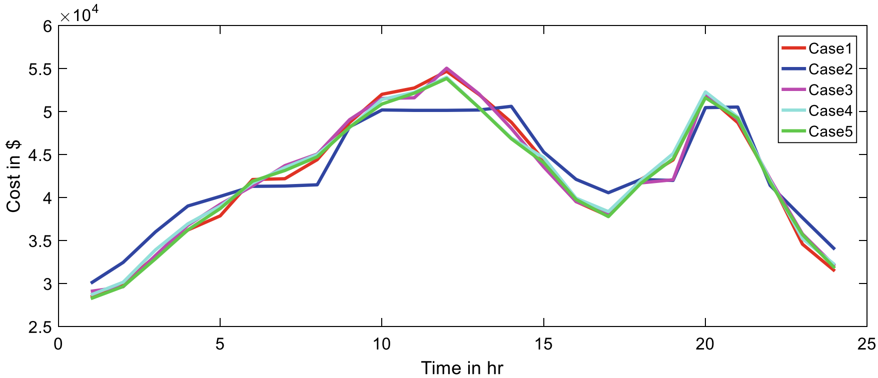

Fig. 3 Analogy of all cases concerning to cost

case 5 when both conventional and renewable energy sources are considered cost, emission, and CEED cost reduces as compared to all the four cases, and the proposed algorithm PSO-AWDV gives better outcomes as compared to other algorithms like SSA, PSO, SQP, EP, and EP-SQP and is presented in Fig. 5.

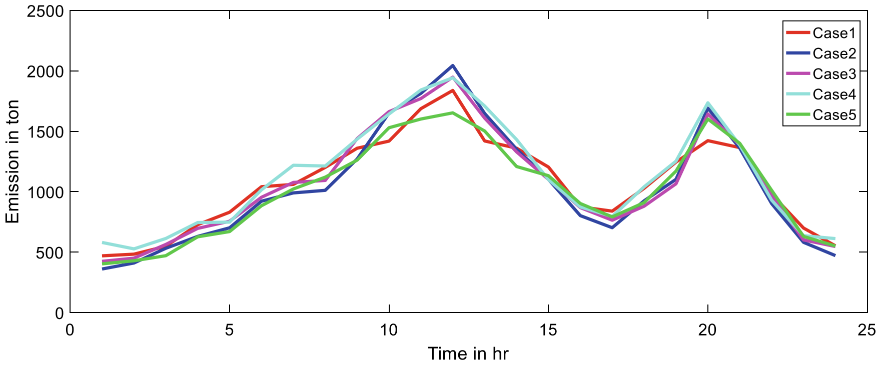

Fig. 4 Analogy of all cases concerning to emission

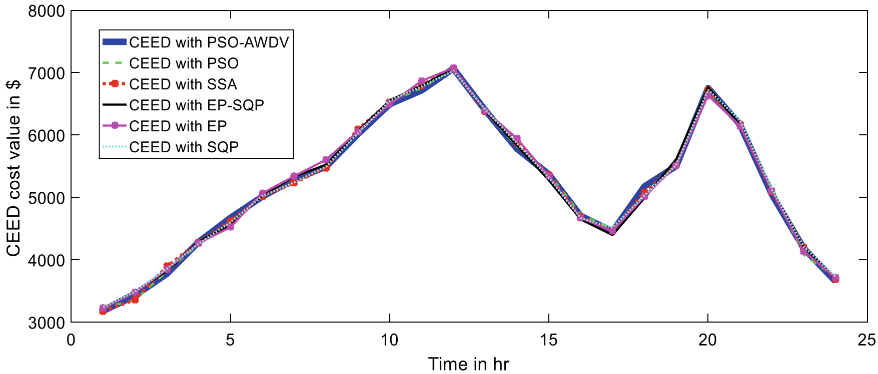

Fig. 5 Discrimination of all algorithms for Case 5 concerning to CEED cost value

5 Conclusion

This work offers the PSO algorithm with adaptive weighted delay velocity to solve the CEED dilemma. The CEED problem has been successfully solved by PSO-AWDV which minimizes generation cost and emission. The efficacy of the PSO-AWDV algorithm is tested in a complicated scenario, where sustainable sources and valve point effect are considered. It is noticed that net generation cost and emission both reduce in the scenario when we considered thermal and both sustainable sources. Also, the dynamic variation of load at the demand side is considered, and the generators' power dispatch within 24 h is described. The outcomes prove the efficacy of the projected method for the solution of the CEED dilemma. The areas that can be are researched further are: application to larger test systems, like 60 - generator, 100 - generator test to examine how the algorithm reacts in those scenarios and application to real systems such as actual power systems and power pools to realize its full benefit to society.

References

1. Manojkumar T, Singh NA (2018) Solution of environmental /economic (EED) power dispatch problem using particle swarm optimization technique. In: International conference on control, power, communication and computing technologies (ICCPCCT), Kannur, pp 347–351. https://doi.org/10.1109/ICCPCCT.2018.8574256
2. Soni S (2020) Using hybrid PSO for solving EELD problem. In 2020 ınternational conference on power electronics and IoT applications in renewable energy and its control (PARC), Mathura, Uttar Pradesh, India, pp 153–158. https://doi.org/10.1109/PARC49193.2020.236578.
3. Rezaie H, Abedi M, Rastegar S, Rastegar H (2019) Economic emission dispatch using an advanced particle swarm optimization technique.World J Eng https://doi.org/10.1108/WJE-04-2018-0126
4. Khan NA, Awan AB, Mahmood A, Razzaq S, Zafar A, Sidhu GA (2015) Combined emission economic dispatch of power system including solar photovoltaic generation. Energy Convers Manageme 92:82–91
5. Ghasemi A, Gheydi M, Javad M, Eslami M (2016) Modeling of wind/environment/ economic dispatch in power system and solving via an online learning meta-heuristic method. Appl Soft Comput J 43:454–468
6. Basu M (2019) Multi-area dynamic economic emission dispatch of hydro-wind-thermal power system. Reinf Plast 28:11–35
7. Gholamghasemi M, Akbari E, Asadpoor MB, Ghasemi M (2019) A new solution to the non-convex economic load dispatch problems using phasor particle swarm optimization. Appl Soft Comput 79:111–124
8. He D, Yang L, Wang Z (2018) Adaptive differential evolution based on simulated annealing for large-scale dynamic economic dispatch with valve-point effects. Math Prob Eng
9. Behera S, Behera S, Barisal AK, Sahu P (2020) Dynamic economic emission dispatch of thermal-wind-solar system with constriction factor-based particle swarm optimization algorithm. World J Eng
10. Behera S, Behera S, Barisal AK (2021) Dynamic combined economic emission dispatch integrating plug-in electric vehicles and renewable energy sources. Int J Ambient Energy 1–18
11. Xu L, Song B, Cao M (2021) An improved particle swarm optimization algorithm with adaptive weighted delay velocity. Syst Sci Control Eng 9(1):188–197
12. Xue J, Shen B (2020) A novel swarm intelligence optimization approach: sparrow search algorithm. Syst Sci Control Eng 8(1):22–34
13. Attaviriyanupap P, Kita H, Tanaka E, Hasegawa J (2002) A hybrid EP and SQP for dynamic economic dispatch with a nonsmooth fuel cost function. IEEE Trans Power Syst 17(2):411–416
14. Kour Dutta V, Kaur Dhami J, Singh L (2016) Weighting sum method to solve combined economic emission dispatch problem. Int J Eng Res Technol (IJERT) ACMEE 4(15):1–4
15. Gholami A, Ansari J, Jamei M, Kazemi A (2014) Environmental/economic dispatch ıncorporating renewable energy sources and plug-in vehicles. IET Gener Transm Distrib 8(12):2183–2198. https://doi.org/10.1049/iet-gtd.2014.0235
16. Saber AY, Venayagamoorthy GK (2010) Efficient utilization of renewable energy sources by grid able vehicles in cyber-physical energy systems. IEEE Syst J 4(3):285–294

Chapter 28
Performance Analysis of Controlled Vehicle-To-Grid Charging in 30 Bus Power System for Electric Vehicle

Gourab Bhuyan and Bani Kanta Talukdar

Abstract Electric vehicles (EVs) are making an impact on vehicle markets sooner than we expected. Due to its widespread popularity of being environment friendly, it brings some solutions to the highly debated environmental problem of carbon emission. As the EVs promote green energy, it can be completely run without burning any fossil fuels. However, the actual challenge lies in charging the same. Charging an electric vehicle has highlighted some of the potential impacts on grids. To make EVs popular, companies are trying to reduce its battery charging time by introducing fast chargers. With decreasing the charging time, charging power is increasing for a fast charger. Using high power load can cause immediate impact on power system stability and voltage regulation. The problem of high power requirements can be controlled with a charging strategy. This paper focuses on the study of impacts on grid by a high power EV charging load and providing a controlled charging method supporting vehicle-to-grid (V2G) technology. In this paper, study on different cases taken during a day with respect to available charging power in a power system is presented in this report to improve overall performance of the charging strategy.

Keywords Electric vehicle · Vehicle-to-grid (V2G)

1 Introduction

The modern-day world is rapidly increasing population and developing technologies, and the usage of individual vehicles and public vehicles is increased to provide the mobility. IC engine vehicles dominate the field of transportation by fair and square, but due to increasing environmental concerns, rising petroleum prices, the uncertainty of fossil fuel is enhancing the popularity of electric vehicles (EV) [1]. The EVs are fueled by the rechargeable battery pack, which powers the electric motor during the

G. Bhuyan (✉)
Assam Engineering College, Guwahati, India

B. K. Talukdar
Department of Electrical Engineering, Assam Engineering College, Guwahati, India

G. Panda et al. (eds.), *Sustainable Energy and Technological Advancements*, Advances in Sustainability Science and Technology,
https://doi.org/10.1007/978-981-16-9033-4_28

drive. To get the attention of customers, advancement in the fields of battery technologies such as fast-charging infrastructure and battery capacity must be developed [2]. In the Indian scenario, large EV penetration will solve problems like air pollutions, energy savings, noise-level reduction, energy efficiency, and emissions of greenhouse gases [3]. The mass adoption of fast-charging may degrade power systems though the EV brings one of the most welcomed greener options for transportation. To ease the mode of driving fast-chargeable batteries with high-density charge would increase the battery capacity and driving range [2]. Literature also suggested bidirectional communication-enabled smart grid infrastructure for less impact on a power system. The bidirectional energy flow is proved efficient to provide power back to the grid. A discussion on EV charging infrastructure is carried out by NTPC [3] and highlighted potential marketplace for EVs. It was shown that it would increase as high as 50% of all vehicles on Indian roads by 2030. In [4], a study emphasizes on charging time to be less to cope up with the popularities of conventional vehicles.

A study on stability was carried in [5], where the EV load model was suggested to stabilize the system was also shown. A reliability study was carried by [6] showed that considerable losses occur during charging EV. A high voltage (HV) system study carried out in the city of Perth, Western Australia, is presented in [7]. The study assumes all vehicles in Perth metropolitan area to be plug-in electric vehicles (PEV) and carried out an analysis to find the impact of charging them in the grid. The uncontrolled charging of PEV fleet has caused a peak demand which exceeded the forecasted generation. EV charging load is modeled in [8] and showed that it has constant power behavior or a combination of constant power and exponential load behavior. In a park and charge model with scheduling to minimize EV battery degradation cost [9]. Another study [10] showed limited V2G application where discharging mode is only applied when high demand arises. The system load study with respect to the very dynamic load curve has not been operated in details in any of the studies. This work is to improve the voltage profiles of a system with a V2G-enabled control strategy, which will monitor charging limit and V2G support during different cases. This work is to highlight the improvement made by V2G charging during different periods of the day which reflects upon practical scenario.

1.1 Objective of This Study

The objective of this study is to provide round the clock analysis of charging of EVs in a power system. The system study was performed taking three different cases of charging in different periods of the day. The end result shows how effective V2G control charging method would be than an uncontrolled one. Advantages of pre-define charging limit and V2G support would effectively improve the voltage profiles. The rest of this paper is organized as follows: A review of existing approaches is presented in introduction section. Section 2 describes the modeling of V2G charging with detailed modeling of loads along with 30 bus power system. Load flow calculations are defined in this part. Section 3 consists of daily load and different test cases and parameters for the study. Results of the simulations are discussed in Sect. 4 followed by detailed conclusions.

2 Modellıng V2G Envıronment

2.1 Modeling of V2G Load

EV charging loads are the most crucial component to this analysis. Building an V2G-enabled charging load is crucial to this work. A universal input EV charger consists of an active rectifier front end, and a buck converter at the battery end is modeled here. It is capable of providing unity power factor and regulated voltage, despite grid voltage variations and supply point voltage. It enables vehicle-to-grid

(V2G) mode of operation by allowing bidirectional power flows. Further, it has become an attractive solution for medium power applications above several kW [8].

The number of EVs in area is taken as n, which are set of all the charging and V2G support operations. A parking data probability curve is used to predict number of vehicles will available at parking. These vehicles will be the source which will draw powers during the charging mode and provide power during V2G mode. The charging and V2G power levels are been taken as constant for all the n vehicles. The total power at the system at any time t would be

$$\sum \mathrm{P} = \sum \mathrm{PGEN} + \sum \mathrm{P\ V2G} - \left(\sum \mathrm{P\,DEM} + \sum \mathrm{P\,EV}\right) - \sum \mathrm{P\,LOSS}$$

2.2 Newton Raphson Load Flow with 30 Bus System

The case study on IEEE 30 bus system is carried out for calculating the effects on power system. Output parameters like voltage magnitude and system losses are observed. For the calculation of real and reactive power drawn by bus in power system, it is necessary to define bus voltages and bus admittances of buses present in the system. For the *i*th bus, equation of the bus voltage is denoted in Eq. (1).

$$V_i = |V_i|\angle\delta_i = |V_i|(\cos\partial_i + j\ \sin\partial_i) \tag{1}$$

Admittance of the *i*th bus represented by Eq. (2)

$$Y_{ij} = \left|Y_{ij}\right|\angle\theta_{ij} = \left|Y_{ij}\right|(\cos\theta_{ij} + j\sin\theta_{ij}) = G_{ij} + jB_{ij} \tag{2}$$

For a system consisting of *n* buses, the current at bus i can be expressed in the form of Eq. (3)

$$I = Y_{11}V_1 + Y_{12}V_2 + \cdots + Y_{in}V_n = \sum_{k=1}^{n} Y_{ik}V_k \tag{3}$$

Complex power Eq. (4) can be simplified further to find real and reactive powers of individual buses.

$$\begin{aligned} P_i - jQ_i &= V_i^* I_i = V_i^* \sum_{k=1}^{n} Y_{ik}V_k \\ &= \sum_{k=1}^{n} |Y_{ik}V_iV_k|[\cos(\theta_{ik} + \delta_k - \delta_i) + j\ \sin(\theta_{ik} + \delta_k - \delta_i)] \end{aligned} \tag{4}$$

Comparing the real and imaginary parts, two equations are formed for the calculations of real and reactive power for each buses of the system.

$$P_i = \sum_{k=1}^{n} |Y_{ik}V_iV_k| \cos(\theta_{ik} + \delta_k - \delta_i) \tag{5}$$

$$Q_i = -\sum_{k=1}^{n} |Y_{ik}V_iV_k| \sin(\theta_{ik} + \delta_k - \delta_i) \tag{6}$$

2.3 Load Flow Analysis by Newton–Raphson Method

If the n-bus power system will contain a total np number of P–Q (load bus) buses while the number of P–V (generator bus) buses be ng such that $n = np + ng + 1$. Addition of 1 is assumed to be the slack or reference bus. The technique of Newton–Raphson load flow is similar to that of solving a system of nonlinear equations using the Newton–Raphson method. Each iteration is to form a Jacobian matrix and to solve for the corrections.

$$\begin{bmatrix} \Delta\delta_2 \\ \vdots \\ \Delta\delta_n \\ \frac{\Delta V}{V} \\ \vdots \\ \frac{\Delta|V_{1+n_0}|}{|V_{1+n_0}|} \end{bmatrix} [J] = \begin{bmatrix} \Delta P_2 \\ \vdots \\ \Delta P_n \\ \Delta Q \\ \vdots \\ \Delta Q_{1+n_0} \end{bmatrix} \tag{7}$$

$$J = \begin{bmatrix} J_{11} & J_{12} \\ J_{21} & J_{22} \end{bmatrix} \tag{8}$$

With the voltage and angle at slack bus fixed at $V_1\angle\delta_1$**,** all PQ buses are at $|V|$, $\angle\delta$ and all PV buses assumed to have δ at all the buses. For the rth iteration, power mismatch equations are checked

$$\Delta P_i^r = P_{iInj}^r - P_{iCalc}^r$$
$$\Delta Q_i^r = Q_{iInj}^r - Q_{iCalc}^r$$

Power mismatch values are checked for minimum, the iteration stops if found less than the prescribed tolerance. If the convergence criteria are not fulfilled, the voltage magnitudes and angles are updated.

$$|V|^{(r+1)} = |V|^r + |\Delta V|^r$$

This process is continued until the convergence is less than the prescribed value of tolerance, once found entire solution is printed. This solution technique is used to calculate output parameters (Fig. 1).

3 Daily Load Curve Situation, Parameters, and Charging Limits

For case study on 30 bus system, different types of EV charging loads are modeled. Different constraints of time like early morning, mid-day, afternoon, and night are taken into consideration. Load demand patterns are identified for different time of the day. While working on these data, practical situation-based data were preferred. Data were collected from IEEE and other official websites [11].

3.1 Case Study

This case study of EV charging load has taken consideration of four period of time in a day. The daily load curve has four significant changes of load during a day. These periods are named *night lean*, *morning peak*, *day lean,* and *evening peak;* four different load patterns can be seen from Indian daily load curves. The changes of loads during intermediate periods and load characteristics are almost similar for each period [12]. With the addition of EV charging loads into the account, the load curve will show characteristics as that of the old one. The dynamic behavior of EV charging load will bring unpredictability to the load requirement. This behavior or unpredictability is studied with simulations, named as *uncontrolled EV charging*. The uncontrolled charging will affect on the voltage level and stability of the system. To overcome this problem, a control charging method is adapted which comes with vehicle-to-grid support. The analysis emphasizes on three states of EV charging on

Fig. 1 Newton–Raphson load flow algorithm

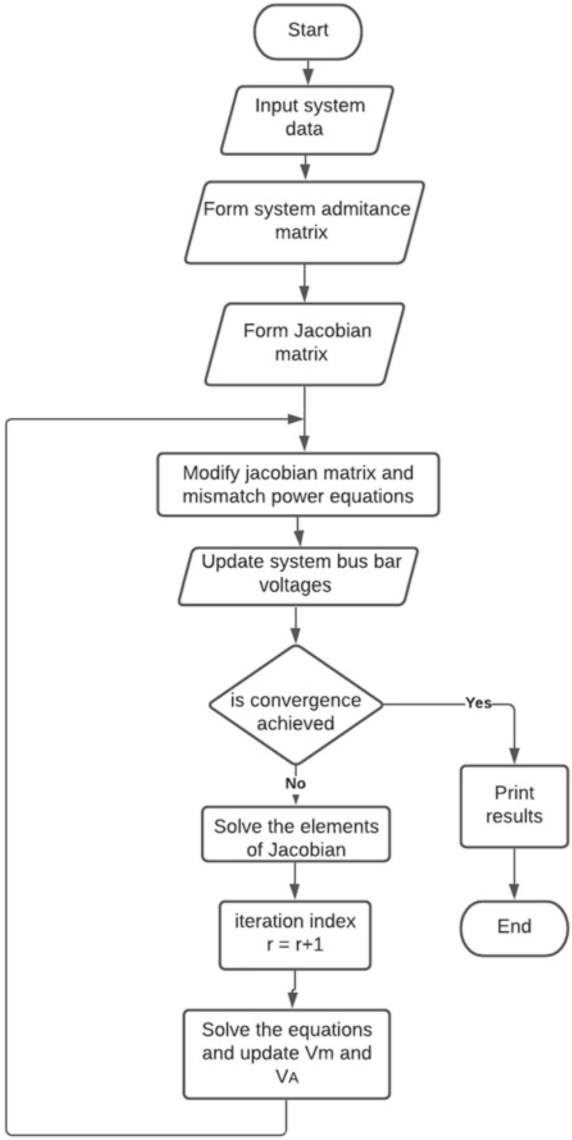

four different periods of the day. The states are named as 'no EV load,' 'uncontrolled EV charging,' and V2G controlled charging. Voltage magnitude and voltage angles are calculated from all the cases.

Fig. 2 Arrival of EVs in home and workplace

3.2 Parking Pattern Throughout the day

The amount of time that EV charging station takes is quite higher than a conventional fuel station. The convenient method for charging an EV would be in parking spaces of offices, housing complexes, commercial hubs, etc., to be equipped with charging facilities [10]. Figure 2 explains parking behavior or the electric vehicles arrival at home and office.

3.3 Allowed Charging Levels and V2G Support During Controlled Charging

During control charging method, charging powers were made available for EV charging according to the load demand in the system. During the night lean period, charging power was made available up to. The V2G support of highest was supported for the duration of peak demand. This V2G support was crucial to improve stability during the periods of high load demands (Fig. 3).

The total available charging power is taken as 50 MW for this project work. The penetration of EV is considered as very low to have minimum effect on the case system.

4 Results and Discussions

In uncontrolled charging state, the charging loads are increasing in uncontrolled manner. However, one key highlights of the state are that it increases the system peak

Fig. 3 Control charging strategy

voltage, which provides an important analysis on voltage variation. On controlled V2G support state, the charging loads are modeled with V2G support and also restricted with limited charging power during the time of peak demand of the region (Table 1; Fig. 4).

As the loading on EV loads has increased, bus voltage in the respective buses shows decrease in magnitudes. When the controlled V2G charging method is used,

Table 1 Total loads in different cases and different periods of the day

Load case	Time period	No EV load		Uncontrolled charging		Controlled V2G support	
		MW	MVAR	MW	MVAR	MW	MVAR
Night lean	1:00–5:00	185.2	64.8	197.2	66.1	224	72.1
Morning peak	8:00–11:00	220.2	72.3	248.3	74.6	232	70.7
Day lean	13:00–16:00	202	66.6	230.2	68.5	229	69.8
Evening peak	18:00–21:00	232.3	75.4	276.2	78.5	241	69.4

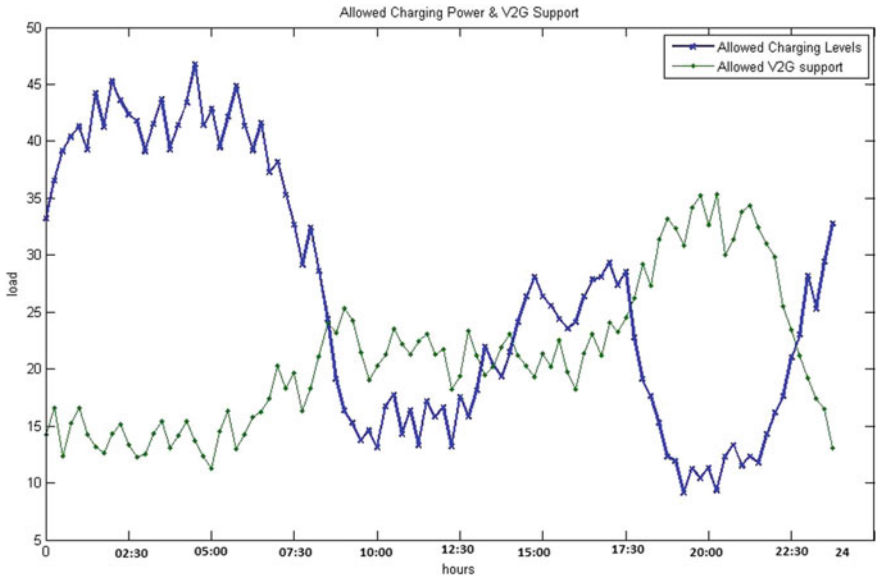

Fig. 4 Allowed charging and V2G power (MW)

the system showed improvement in voltage magnitudes. Index for voltage magnitude variations from no EV load (VM_{NL}) to uncontrolled charging is ($VM_{UC} - VM_{NL}$) = ΔVM_{UCNL} and index for variations in voltage magnitude from uncontrolled charging (VM_{UC}) to V2G charging ($VM_{V2G} - VM_{UC}$) = Δ VM_{V2GUC}.. These indices are used in Table 2.

From Table 1, test cases are taken and results were plotted in Fig. 5.

Figure 5 represents all the voltage buses in different periods of the day. From the above periods, morning peak and evening peak were most affected among all.

During night period all the buses were under 0.95 pu limits, as more EVs are putting into charging during this period. During the night lean period, simulation was done as the maximum number of EV users is putting their vehicles to charge. At bus 30, lowest 0.965 pu was recorded. At morning peak duration, bus 26 and bus 30 are recorded 0.926 pu and 0.952 pu. During day lean period, worst-affected buses were bus 26 (0.945 pu) and bus 30 (0.953 pu). During evening peak, bus 26 (0.899 pu), bus 29(0.948pu), and bus 30 (0.932 pu) were affected the most. The ΔVM_{UCNL} value is significantly high in bus no 26 for all the noted cases comparing to other cases. The V2G support was provided the most in the evening peak duration, as all the affected buses are showing great improvement during this period. The control strategy for coordinated charging is as per in Fig. 3.

Table 2 Voltage magnitudes during different periods

EV load bus	Night lean			Morning peak			Day lean			Evening peak		
	VM_{NEVL}	VM_{UC}	VM_{V2G}	VM_{NEVL}	VM_{UC}	VM_{V2G}	VM_{NEVL}	VM_{UC}	VM_{V2G}	VM_{NEVL}	VM_{UC}	VM_{V2G}
4	0.987	0.986	0.982	0.982	0.977	0.983	0.984	0.980	0.983	0.980	0.973	0.983
8	0.976	0.974	0.970	0.971	0.966	0.972	0.973	0.969	0.971	0.969	0.960	0.972
9	0.987	0.986	0.984	0.984	0.982	0.984	0.985	0.983	0.984	0.983	0.973	0.985
18	0.977	0.975	0.970	0.968	0.964	0.971	0.974	0.970	0.974	0.967	0.960	0.975
19	0.976	0.974	0.969	0.967	0.963	0.969	0.974	0.970	0.972	0.966	0.959	0.972
25	0.993	0.989	0.983	0.990	0.981	0.993	0.991	0.983	0.992	0.989	0.973	0.995
26	0.972	0.967	0.957	0.957	**0.926**	***0.988***	0.963	**0.945**	***0.991***	0.951	**0.899**	***0.994***
28	0.985	0.983	0.977	0.979	0.972	0.980	0.982	0.976	0.980	0.977	0.966	0.981
29	0.980	0.977	0.968	0.973	0.964	0.975	0.974	0.968	0.974	0.970	**0.948**	***0.975***
30	0.968	0.965	0.960	0.962	0.952	0.971	0.962	0.953	0.966	0.959	**0.932**	***0.971***

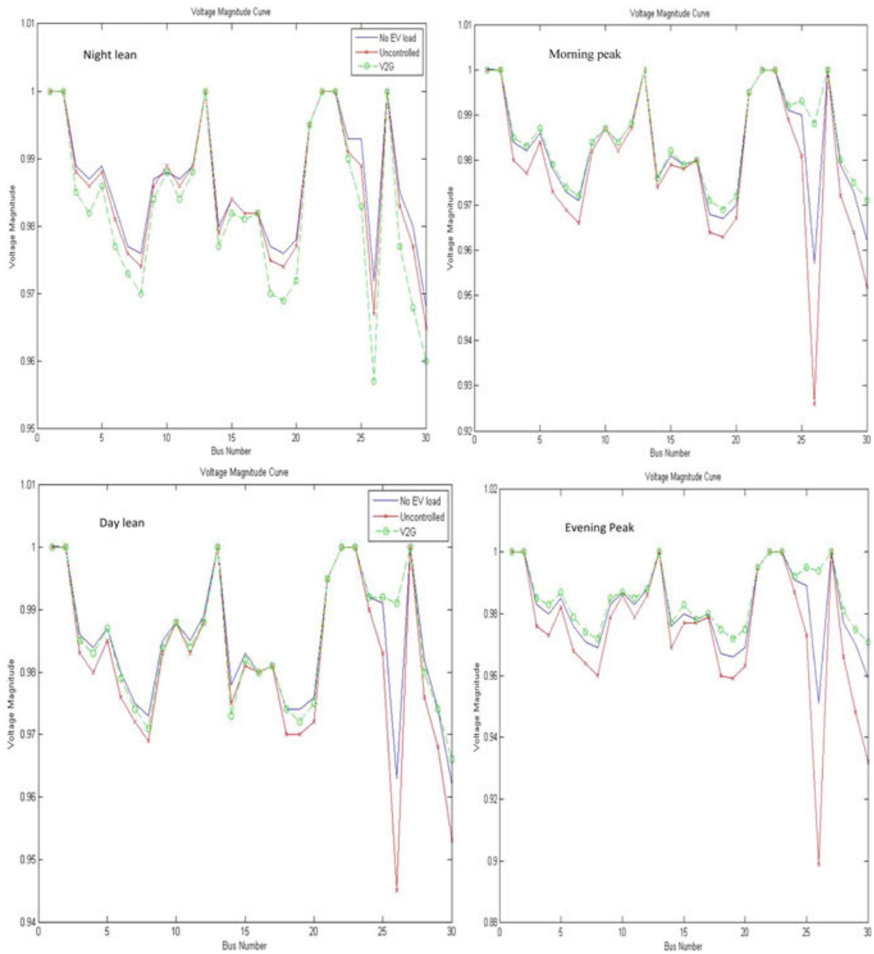

Fig. 5 Voltage magnitude during different periods, i.e., night, morning, day, and evening

5 Conclusion

This paper is focused on the analysis of the control charging method to improve power system performance during a day. Simulation was carried on IEEE 30 bus system, and results were discussed. It was seen that increasing the EV loads on specific bus resulted in a decrease in voltage profiles. Implementation of V2G controlled charging throughout the day drastically improves the scenario. The penetration of EV was taken as very low considering the present scenario of low popularity of EV. It is confirmed from the study that an increase in EV charging would have an impact on the power system if it is not controlled and grid operators should focus on improving the same. Improvement in power quality devices will minimize the system losses and well-equipped V2G support with battery packs, and renewable sources will help grid operators to balance the power demands during the daily operations. Further, improvisation of the controlled charging method can be done with better-trained algorithms.

References

1. Dharmakeerthi CH, Mithulananthan N, Saha TK (2011) Overview of the impacts of plug-in electric vehicles on the power grid. In: 2011 IEEE PES innovative smart grid technologies, Perth, WA, pp 1–8. https://doi.org/10.1109/ISGT-Asia.2011.6167115
2. Bora Y, Önen UB, Umurkan N (2017) A review of electric vehicles and their ımpacts on grid. Int J Sci Technol Res 6(10). ISSN 2277-8616
3. Busıness of chargıng ınfrastructure for electrıc vehıcles & energy storage and ıts ımpact on power market ııt, NTPC, Kanpur 27.07.2019
4. Collin R, Miao Y, Yokochi A, Enjeti P, von Jouanne A (2019) Advanced electric vehicle fast-charging technologies. Energies 12:1839
5. Dharmakeerthi CH, Mithulananthan N, Saha TK (2014) Impact of electric vehicle fast charging on power system voltage stability. Electr Power Energy Syst 57:241–249
6. Deb S, Tammi K, Kalita K, Mahanta P (2018) Impact of electric vehicle charging station load on distribution network. Energies 11:178
7. McCarthy D, Wolfs P (2010) The HV system impacts of large scale electric vehicle deployments in a metropolitan area. In: Universities power engineering conference (AUPEC), 2010 20th Australasian, pp 1–6
8. Dharmakeerthi CH, Mithulananthan N, Saha TK (2012) "Modeling and planning of EV fast charging station in power grid. In: 2012 IEEE power and energy society general meeting, San Diego, CA, pp 1–8. https://doi.org/10.1109/PESGM.2012.6345008
9. Tae-Hoon K, Seung-Jun L, Woojin C (2011) Design and control of the phase shift full bridge converter for the on-board battery charger of the electric forklift. In: IEEE 8th international conference on power electronics and ECCE Asia (ICPE & ECCE), pp 2709–16
10. Chtioui H, Boukettaya G (2020) Vehicle-to-grid management strategy for smart grid power regulation. In: 2020 6th IEEE ınternational energy conference (ENERGYCon), pp 988–993. https://doi.org/10.1109/ENERGYCon48941.2020.9236530
11. Song N, Kwak B (2019) International standard trend of vehicle to grid (V2G) communication ınterface for wireless communication and RPT. In: 2019 IEEE transportation electrification conference and Expo, Asia-Pacific (ITEC Asia-Pacific), pp 1–5. https://doi.org/10.1109/ITEC-AP.2019.8903797
12. Hassan Mohamed T, Ahmed Hassan H (2018) Terminal voltage and power regulation using vehicle-to-grid (V2G) schemes connected to a two-area power system. In: 2018 20th ınternational middle east power systems conference (MEPCON), 2018, pp 203–208. https://doi.org/10.1109/MEPCON.2018.8635159

Chapter 29
Automatic Generation Control for Hybrid Power System in Deregulated Environment

Parusharamulu Buduma, Madan Kumar Das, Ashwani Kumar Sharma, Gayadhar Panda, and Sukumar Mishra

Abstract With the restructuring of power sector operations worldwide, many new entities have come into the market with fair and open access to the transmission facilities managed by an independent system operator (ISO). Automatic Generation Control (AGC) in this environment has been identified as an key ancillary service with a challenge. In this paper, an integral controller has been used to control the AGC in a three-area hybrid power system in deregulated market. For dynamics control, the AGC system has been modified to take into consideration bilateral contracts. The use of a three-Area deregulated electricity system with two Gencos and Discos in each area, as well as hybrid turbines, has been studied. The Disco Participation Matrix (DPM) is being used to characterize the bilateral contracts for three-area AGC. For a three-area system with hybrid combinations of turbines, the system's performance is investigated for various bilateral contract instances.

Keywords Automatic Generation Control · Disco Participation Matrix · Hybrid Power System · Bilateral Contracts

1 Introduction

In open access environment, issue of Automatic Generation Control (AGC) has gained more importance as the real-time load balance has become a critical issue due

P. Buduma (✉) · M. K. Das · S. Mishra
Indian Institute of Technology Delhi, Delhi, India

S. Mishra
e-mail: Sukumar.Mishra@ee.iitd.ac.in

A. K. Sharma
National Institute of Technology Kurukshetra, Kurukshetra, India

G. Panda
National Institute of Technology Meghalaya, Meghalaya, India
e-mail: gayadhar.panda@nitm.ac.in

G. Panda et al. (eds.), *Sustainable Energy and Technological Advancements*,
Advances in Sustainability Science and Technology,
https://doi.org/10.1007/978-981-16-9033-4_29

to the entry of direct negotiation of power purchase agreements without the involvement of a third party. In this competitive climate, Load Frequency Control (LFC) has been regarded as an effective supplementary service. Previously, subsidiary services were delivered by a single utility called Area of Control (CA). Every CA owns producing resources, distribution, and transmission capacities inside its limits. Deregulation aimed to make a competitive environ in generation and transmission services could be bought and sold based on market demand and supply. This new framework allows for the separation of auxiliary services and the emergence of new entities, such as Distribution-Companies (Discos), Generation-Companies (Gencos), Transmission-Companies (Transcos), and Independent Contract Administrators (ICAs). [1] explains the notion of LFC after and before the before deregulation in great detail. There has been a detailed comparison of AGC after and deregulation [2]. The supply of frequency regulation auxiliary services in other deregulated markets throughout the world has been discussed in this article.

A critical literature review of contemporary philosophies of AGC control strategies has been presented in [3]. Overview of AGC schemes have been presented in [4] & [5]. PI, PID, and optimal controllers were proposed by several researchers. An optimal control [6–9] and structure variable control [9–12] were employed to operate the system in normal conditions. Electrical utilities worldwide are transforming their electrical supply systems to open access environments, also known as competitive electricity markets, restructured power systems, or deregulated power systems due to many technical, economic, and environmental issues. In this competitive market, operating the power system poses additional challenges in terms of LFC. In [13–16], the AGC is well presented for a deregulated system. The concept of Disco Participation Matrix (DPM) is proposed, which helps the visualization and implementation of the Independent Contract Administrative (ICA). GA application to optimize bias factors and integral gains for AGC are presented for a deregulated system in [17]. In [18], the authors presented an LQG approach for LFC in the deregulated environment. In this work, the gains of an integral controller with DPM for hybrid three area systems for load frequency management have been obtained using a traditional technique. For the AGC study in the de-regulated environment, the different scenarios of the DPM have been investigated for these hybrid unit combinations. For each situation, their results have been compared. MATLAB/SIMULINK has been used to model the system.

2 AGC for Hybrid Power System with Three Areas

In an open environment, with the unbundling of a conventional power system, new entities called Gencos, Discos, Transcos, and an Independent System Operator (ISO) have emerged for the competitive operation of the system. The ISO with significant responsibilities of providing fair and open access to transmission, the security of the system, and has the responsibility to provide ancillary service to the system. One of the essential ancillary services is the LFC in the new environment with crucial

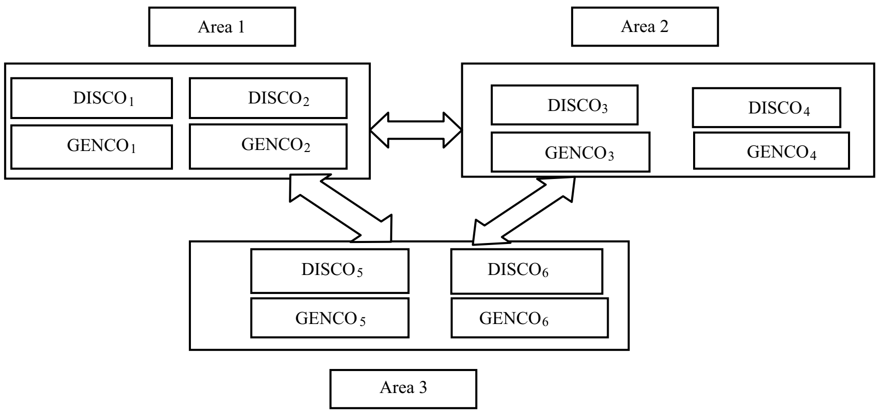

Fig. 1 The deregulated power system's configuration

differences between operations of a system in the deregulated regime. In this instance, a Disco can have a power contract with other Gencos, and these transactions are settled using the DPM concept [15] under the supervision of the ISO. In this work, the effects of bilateral contracts on the dynamics of the system for AGC consisting of three areas with two Gencos and two Discos are described. In a three-area power system, hybrid turbine units are considered to be present. The proposed three area systems along with Gencos and Discos in each area are shown in Fig. 1.

Any Genco in a particular location has the ability to supply both Discos from its own pool as well as Discos from other areas via tie-lines. A Disco's involvement in a contract with a Genco is granted by the DPM. The rows in DPM correspond to the number of Gencos in the power system, while the columns correspond to the number of Discos. Any DPM entry is a proportion of the total load power that a Disco has contracted to a Genco. As a result, the total entries in the column belong to the DPM's Disco $\sum_i cp_{ij} = 1$.

The DPM for a three-area system with two Discos as well as two Gencos in each area is described as

$$DPM = \begin{bmatrix} cp_{11} & cp_{12} & cp_{13} & cp_{14} & cp_{15} & cp_{16} \\ cp_{21} & cp_{22} & cp_{23} & cp_{24} & cp_{25} & cp_{26} \\ cp_{31} & cp_{32} & cp_{33} & cp_{34} & cp_{35} & cp_{36} \\ cp_{41} & cp_{42} & cp_{43} & cp_{44} & cp_{45} & cp_{46} \\ cp_{51} & cp_{52} & cp_{53} & cp_{54} & cp_{55} & cp_{56} \\ cp_{61} & cp_{62} & cp_{63} & cp_{64} & cp_{65} & cp_{66} \end{bmatrix} \tag{1}$$

where, *cp* stands is factor of contract participation. The portion of the load contracted by Disco1 from Genco 2 is reflected in the DPM by the (2,1) entry. The Discos in one location are linked to the Gencos in another via off diagonal pieces. Each area has a large number of Gencos, and the Area Control Error (ACE) signal must be shared by all of them in terms of their contributions. ACE participation factors (aps) is coefficient that measure ACE sharing $\sum_{j=1}^{m} ap_j = 1$ where $m =$ Total Gencos in one area. The scheduled tie line power flow is given as:

$$\Delta P_{1\text{scheduled}}(k) = \Delta P_{1-2\text{scheudule}}(k) + a_{31}\Delta P_{3-1\text{scheduled}}(k) \tag{2}$$

$$\Delta P_{2\text{scheduled}}(k) = \Delta P_{3-2\text{scheudule}}(k) + a_{12}\Delta P_{1-2\text{scheduled}}(k) \tag{3}$$

$$\Delta P_{3\text{scheduled}}(k) = \Delta P_{3-1\text{scheudule}}(k) + a_{23}\Delta P_{2-3\text{scheduled}}(k) \tag{4}$$

where $a_{12} = a_{23} = a_{31} = -1$, $P_{\text{r1}} = P_{\text{r2}} = P_{\text{r3}}$ is power rating in area and k represent the sampling index. The following is the power error defined in the previous equations:

$$\Delta P_{\text{ierror}} = \Delta P_{\text{iactual}} - \Delta P_{\text{ischeduled}} \tag{5}$$

In the steady state, this error signal is used to generate its ACE signal as follows:

$$\text{ACE}_{\text{i}} = B\Delta F_{\text{ierror}} + \Delta P_{\text{ierror}}; \quad i = 1, 2, 3 \tag{6}$$

In this work, the following are three different power contract instances that have been considered:

Case-1: Equal power share in area 1 only: Because all of the ACE participation variables are 0.5 in this scenario, each area's contribution is equal. In a steady-state operation, any Genco generation in a given area must match the demand of the Discos in that area according to the terms of the contract. The following is how the Genco generation is stated in terms of DPM and Disco demand: $\Delta P_{\text{Mi}} = \sum cp_{ij}\Delta P_{Lj.}$

$$\text{DPM} = \begin{bmatrix} 0.5 & 0.5 & 0 & 0 & 0 & 0 \\ 0.5 & 0.5 & 0 & 0 & 0 & 0 \\ 0 & 0 & 0 & 0 & 0 & 0 \\ 0 & 0 & 0 & 0 & 0 & 0 \\ 0 & 0 & 0 & 0 & 0 & 0 \\ 0 & 0 & 0 & 0 & 0 & 0 \end{bmatrix} \tag{7}$$

*Case-2: Un-equal power share in all areas:*The following DPM applies to the deal between Discos and Gencos:

$$\mathrm{DPM} = \begin{bmatrix} 0.3 & 0.25 & 0 & 0.4 & 0.1 & 0.6 \\ 0.2 & 0.15 & 0 & 0.2 & 0.1 & 0 \\ 0 & 0.15 & 0 & 0.2 & 0.2 & 0 \\ 0.2 & 0.15 & 1 & 0 & 0.2 & 0.4 \\ 0.2 & 0.15 & 0 & 0.2 & 0.2 & 0 \\ 0.1 & 0.15 & 0 & 0 & 0.2 & 0 \end{bmatrix} \tag{8}$$

It is assumed that each Disco in the area demands 0.1 p.u.The tie-lines power scheduled can be obtained as:

$$\Delta P_{12\text{schduled}} = \sum_{i=1}^{2}\sum_{j=3}^{4} cp_{ij}\Delta P_{Lj} - \sum_{i=3}^{4}\sum_{j=1}^{2} cp_{ij}\Delta P_{Lj} \tag{9}$$

$$\Delta P_{23\text{schduled}} = \sum_{i=3}^{4}\sum_{j=5}^{6} cp_{ij}\Delta P_{Lj} - \sum_{i=5}^{6}\sum_{j=3}^{4} cp_{ij}\Delta P_{Lj} \tag{10}$$

$$\Delta P_{31\text{schduled}} = \sum_{i=5}^{6}\sum_{j=1}^{2} cp_{ij}\Delta P_{Lj} - \sum_{i=1}^{2}\sum_{j=5}^{6} cp_{ij}\Delta P_{Lj} \tag{11}$$

Case-3: violation in Contract: When a Disco seeks more power than the contract specifies, it is said to be in violation of the contract. Uncontracted electricity is thought to have to be distributed by Gencos in the same region as the Disco in this case [13]. Instead of being the correct demand, the contract's surplus power demand should be viewed as a local load for the area. The uncontracted load of Disco of Area 1 is reflected in Gencos of Area 1.

3 Control Design for AGC System

In this AGC system, the error in the system frequency (Δf) is fed through an integrator for the speed change as shown in Fig. 2. The proportional plus integral controller gives zero error in steady state ($.\Delta f|_{\text{steady state}} = 0$).

$$\Delta F(s) = -\frac{K_\mathrm{p}}{(1+T_p) + (\frac{1}{R_1} + \frac{1}{R_2} + \frac{apf_1 K_\mathrm{i}}{s} + \frac{apf_2 K_i}{s}) \times \frac{K_\mathrm{p}}{(1+T_\mathrm{G}s)(1+T_\mathrm{t}s)}} \times \frac{\Delta P_\mathrm{D}}{s} \tag{12}$$

$$= -\frac{RK_\mathrm{p}s(1+T_\mathrm{G}s)(1+T_\mathrm{t}s)}{s(1+T_\mathrm{G}s)(1+T_\mathrm{t}s)(1+T_\mathrm{ps}s)R + K_\mathrm{p}(2apf\,K_\mathrm{i}R + 2s)} \times \frac{\Delta P_\mathrm{D}}{s} \tag{13}$$

Let us take $R_1 = R_2 = R$, $apf_1 = apf_2 = apf$. We reach the following results by applying the final value theorem:

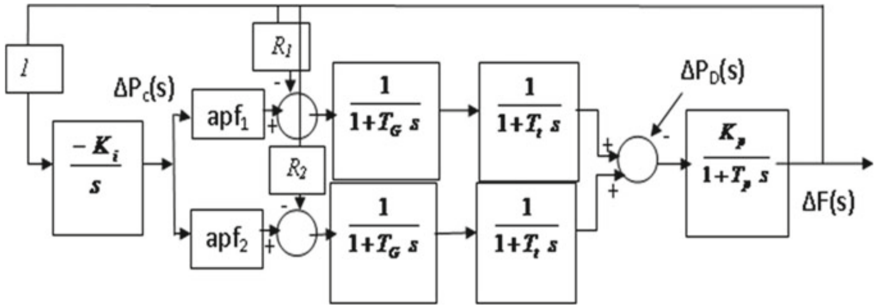

Fig. 2 Block diagram of integral control for area 1 of three area thermal systems

$$\Delta F|_{\text{steadystate}} = \underset{s \to 0}{s \Delta F(s)} = 0 \tag{14}$$

ACE is the signal that is fed to the integrated controller. We need to design individual controller each area for three area system. Assume there is no contraction and interconnection for designing individual conventional controller.

For the designing of control, we modified Eq. (12) taking, $T_G = T_t = 0$

$$\Delta F(s) = -\frac{R \times K_p s}{s(1 + T_p s)R + K_p(2apf K_i + 2s)} \times \frac{\Delta P_D}{s} \tag{15}$$

$$= -\frac{R \times K_p s}{sR + s^2 T_P R + K_p(2apf K_i + 2s)} \times \frac{\Delta P_D}{s} \tag{16}$$

$$sR + s^2 T_p R + 2apf K_p K_i R + 2K_p s \tag{17}$$

$$T_p \times R(s^2 + \frac{s}{T_p} + \frac{2apf K_p K_i}{T_p} + \frac{2K_p s}{RT_p}) \tag{18}$$

By simplification, we get:

$$\Delta F(s) = -\frac{K_p}{T_p} \times \frac{\Delta P_D}{s^2 + s\left[(1 + \frac{2K_p}{R})/T_p\right] + \frac{2apf K_i K_p}{T_p}} \tag{19}$$

The denominator can also be written as:

$$\left[s + \frac{1 + \frac{2K_p}{R}}{2T_p}\right]^2 + \frac{2apf K_i K_p}{T_p} - \left[\frac{1 + \frac{2K_p}{R}}{2T_p}\right]^2 \tag{20}$$

The integral gain K_i determines the nature of the pole.

If

$$\frac{2apf K_\text{i} K_\text{p}}{T_\text{p}} > \left[\frac{1 + \frac{2K_\text{p}}{R}}{2T_\text{p}} \right]^2 \tag{21}$$

Or if

$$K_\text{i} > \frac{1}{8apf T_\text{p} K_\text{p}} \left(1 + \frac{2K_\text{p}}{R} \right)^2 = K_{i,\text{critical}} \tag{22}$$

By using the values of K_p, T_p and R, we obtain the control gain as $K_\text{i} = 1.06$.

4 Results and Discussion

In this paper, a study of AGC of three area power system with Reheat Thermal-Reheat Thermal-Diesel(TTD), Reheat Thermal-Reheat Thermal-Hydro (TTH), and Reheat Thermal-Diesel-Hydro (TDH), have been proposed. The results have been determined with a conventional integral controller for all the hybrid turbine cases with three different scenarios of bilateral contracts, as explained in section II. For all three areas, the findings were obtained for frequency variations, tie-line deviations, and Gen-cos share towards contractual electricity. Figure 3 shows the SIMULINK block for Case 1 of a three-area system with a TTD unit and an integral controller. Similarly, findings for additional TTH and TDH units were obtained by altering the model for Case 1 with different turbine models. Other sorts of contracts can easily be incorporated into the scheme. For various contract scenarios, the findings for deviations in frequency and tie-line power, and power share of Gencos are displayed in Figs. 3, 4 and 5 for areas 1, 2, and 3. According to the observation, the frequency deviations settle at zero steady states in 20 s for TTD (Case 1) for area 1, while it takes longer for other regions to settle to steady-state. Case 2 and Case 3 take longer to reach zero in terms of tie-line power deviations, and Case 2 and Case 3 take longer in terms of other areas. In case 1, Gencos' generating power settles at a steady state in 20 s; in other circumstances, it takes longer to settle due to the exchange of more power than in case 1. Figures 6, 7 and 8 show the TTH results for all of the cases. The frequency deviation settles to zero steady-state error in about 20 secs for all cases of bilateral contracts. The tie-line power deviations settle to steady-state in 20 s for case 1, and for other cases, it takes some more time. The deviation in frequency and tie-line power flow devia-tions, and aslo power share of Gencos are all observed in the same way for TDH system. Comparing the AGC in the deregulated system with the conventional integral controller, it is observed that the TTH system behaves better compared to the other combinations of turbines. Based on the results obtained for all cases, we observe the following important points: There are no static errors in tie-line power and frequency deviations. When the steady-state is reached, the frequency errors of three areas are equal. The Gencos generation is governed by agreement between Gencos and Discos. The TTH outperforms all other systems in

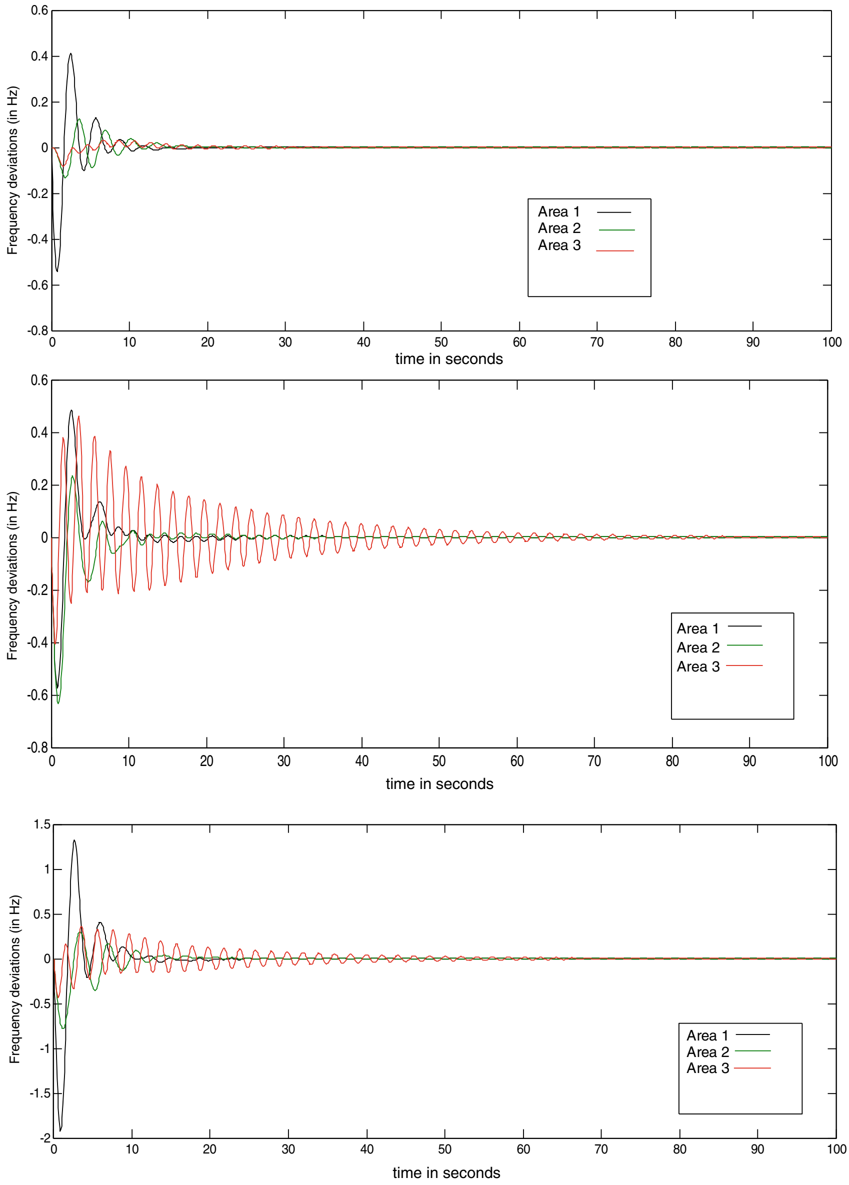

Fig. 3 Frequency deviations in TTD system (For three cases respectively)

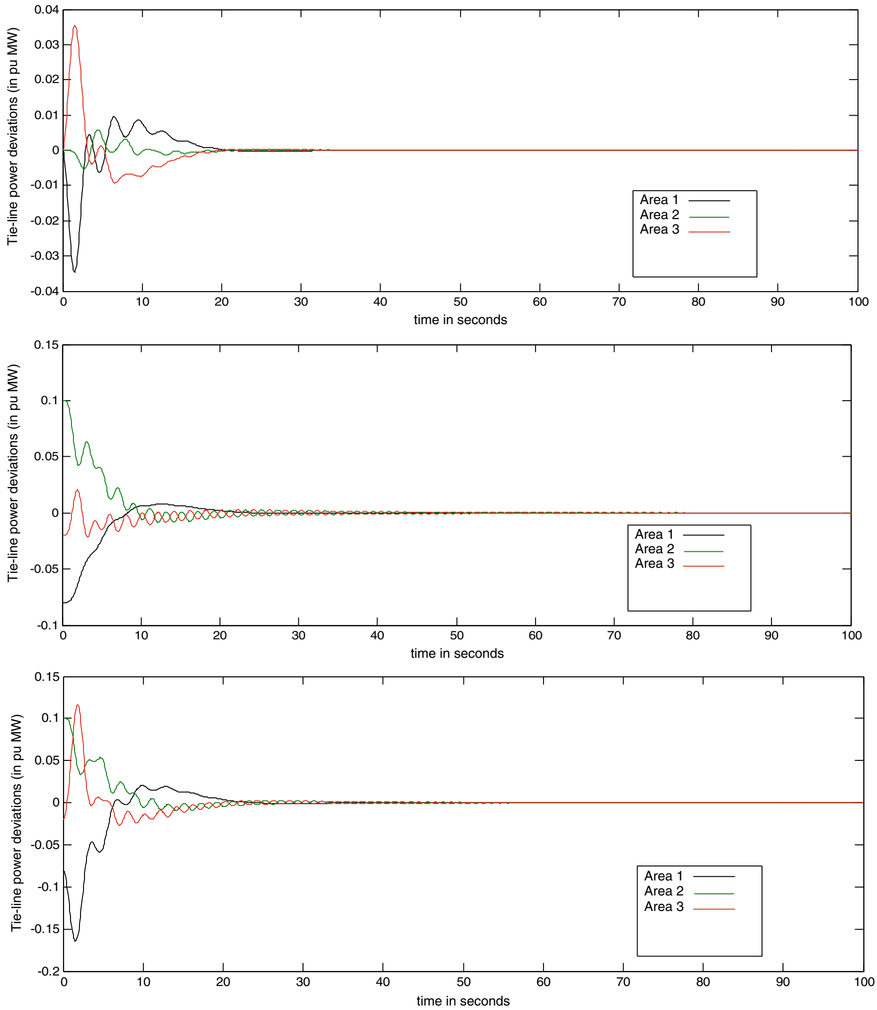

Fig. 4 Tie-line power deviations in TTD system (For three cases respectively)

terms of tie line, frequency variations, and generated power of Gencos. In hybrid systems, TTH system has low settling time, and for TTD system, peak overshoot is minimum. Genco share is observed as per DPM in each case; other Gencos also share remaining uncontracted power.

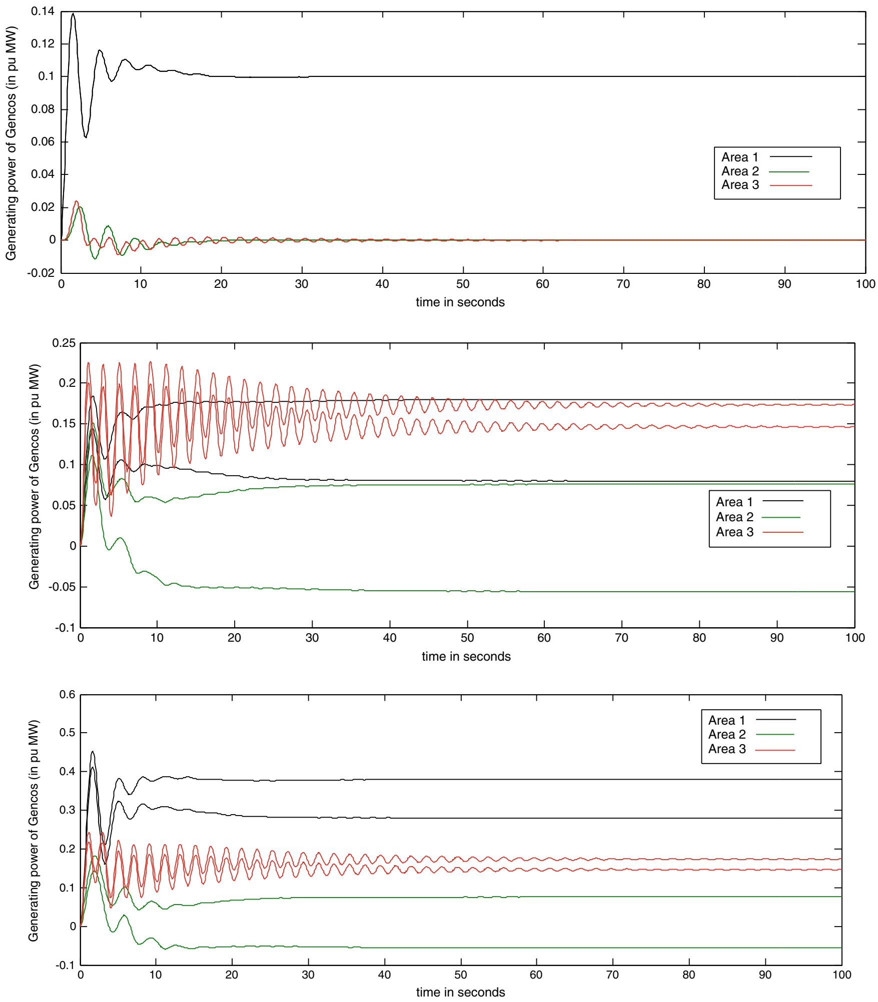

Fig. 5 Generating power of Gencos for TTD system (For three cases respectively)

5 Conclusion

AGC in a deregulated power system with hybrid turbines is discussed in this research. The conventional and deregulated regimes of the hybrid system's power system models have been explained. The analysis took into account a variety of contracts that exist between Gencos and Discos. In each case of the deregulated power system, frequency deviations and tie-line power variances are zero, according to the results. For all scenarios of bilateral contracts, the integral controller reduces the rising time, settling time, and the steady-state error to zero.

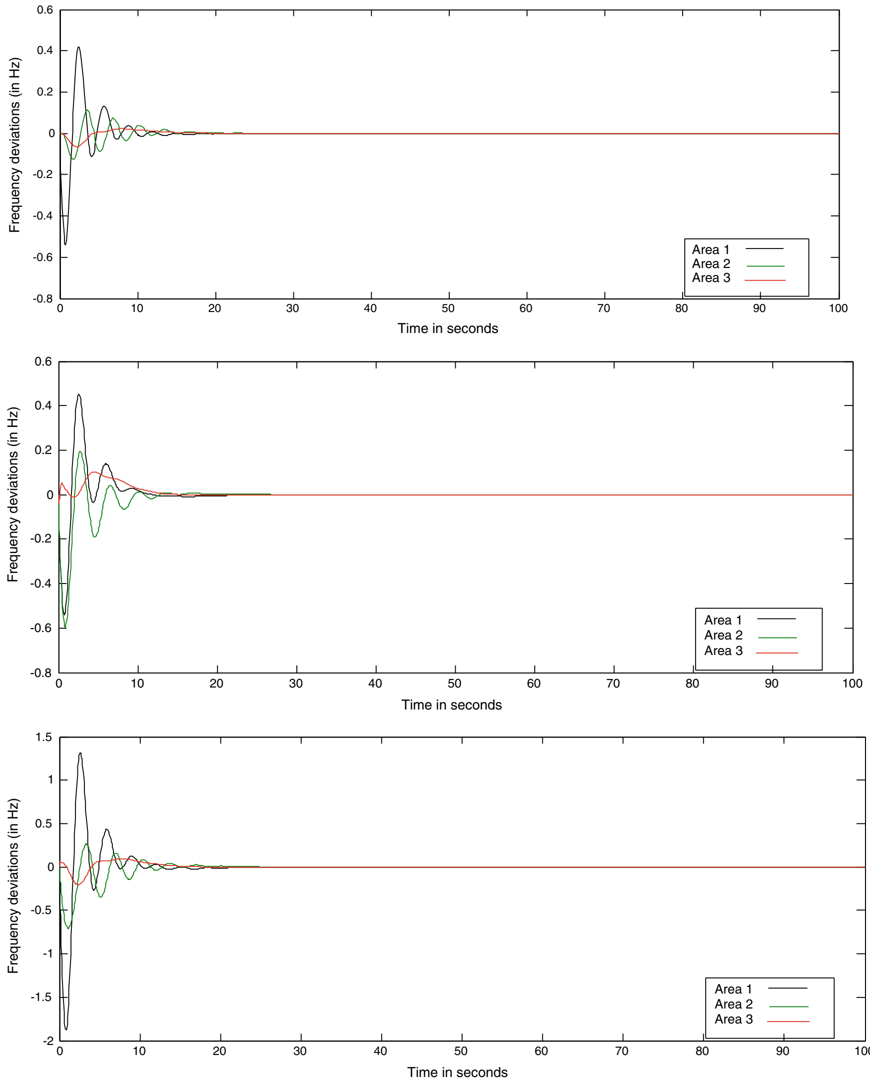

Fig. 6 Frequency deviations in TTH system (For three cases respectively)

Thus, the integral controller proposed here is suitable for three areas system in the deregulated power system:

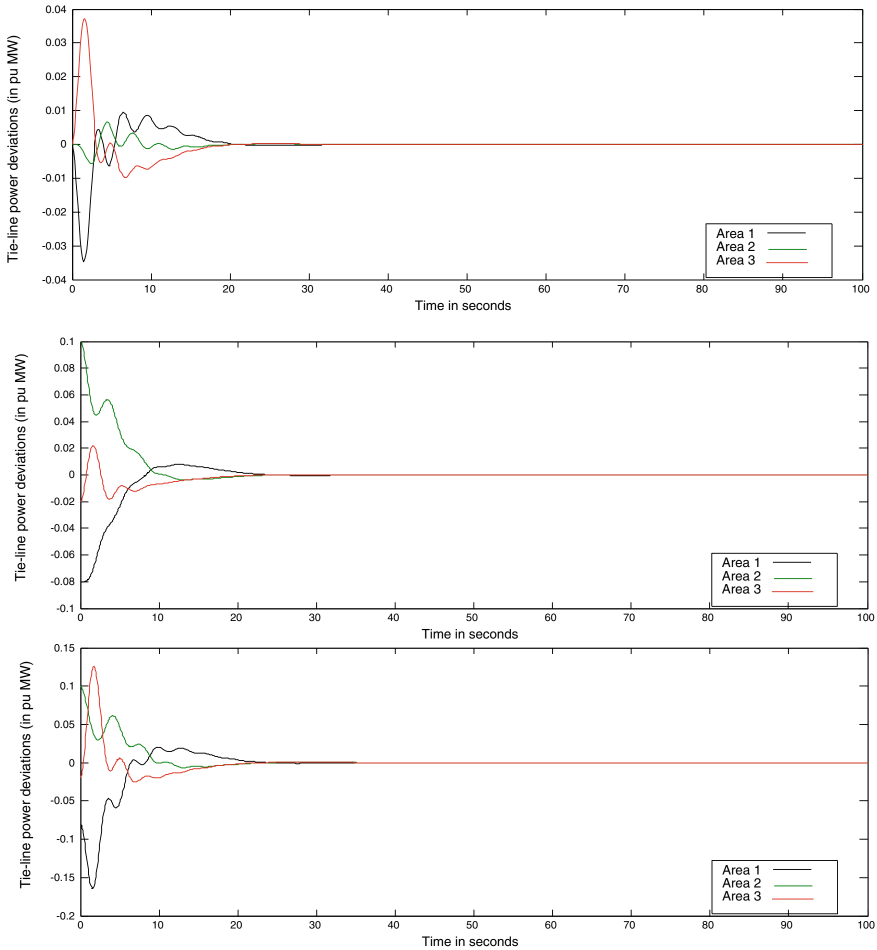

Fig. 7 Tie-line power deviations in TTH system (For three cases respectively)

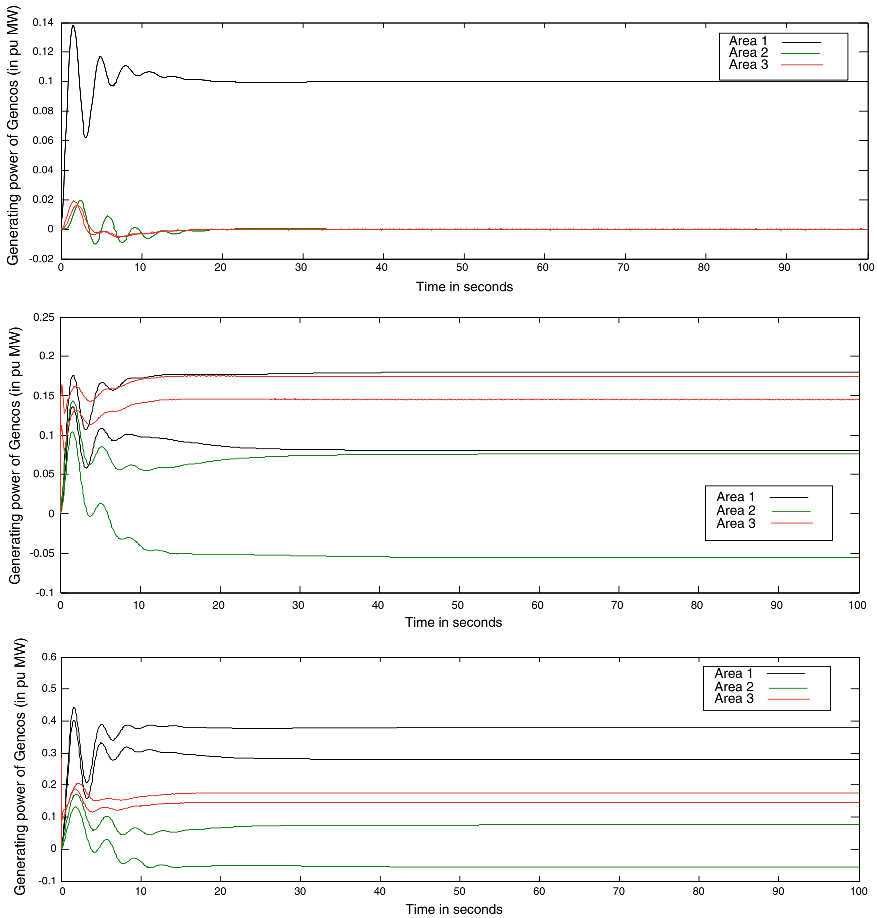

Fig. 8 Generating power of Gencos in TTH system (For Three cases respectively)

References

1. Ejegi EE, Rossiter JA, Trodden P (2016) Generalized model for load frequency control studies in a deregulated environment. In: Control conference, pp 1800–1805, European
2. Banaja M, Prakash KH (2015) Comparative performance analysis of fruit fly optimisation algorithm for multi-area multi-source automatic generation control under deregulated environment. IET-Gen Trans Dist 9(14):1845–1855
3. Ibrahim PK, Kothari DP (2005) Recent philosophies of automatic generation control strategies in power systems. IEEE Trans Power Syst 20(1):346–357
4. Jaleeli N, VanSlyck SN, Ewart DN, Fink LH, Hoffmann AG (1992) Understanding automatic generation control. IEEE Trans Power Syst 7(3):1106–1112
5. Fosa CE, Elgerd OI (1972) The megawatt-frequency problem: a new approach via optimal control theory. IEEE Trans Power Apparatus Syst PAS-89:563–577
6. Miniesy SM, Bohn EV (1972) Optimal load frequency continuous control with unknown deterministic power demand. IEEE Trans Power Apparatus Syst PAS-91:1910–15

7. Calovic M (1972) Linear regulator design for load frequency control. IEEE Trans Power Apparatus Syst PAS-91:2271–85
8. Glover JD, Schweppe FC (1972) Advanced load frequency. IEEE Trans Power Apparatus Syst PAS-91:2095–2103
9. Hsu YY, Chan WC (1984) Optimal variable structure controller for load frequency control of interconnected hydro-thermal system. Electr Power Energy Syst 6:221–229
10. Das D, Kothari ML, Kothari DP, Nanda J (1991) Variable structure control strategy to AGC of an interconnected reheat thermal system. Proc IEE Pt. D 138:579–585
11. Ali Hamouz ZL, Abdel Magid YL (1993) Variable structure load frequency controller for multi area power systems. Int J Electr Power Enetrgy Syst 15(5):90–101
12. Elgerd OI, Fosa CE (1970) Optimum megawatt frequency control of multi area electric energy systems. IEEE Trans Power Apparatus Syst PAS-89:556–563
13. Christie RD, Bose A (1996) Load frequency control issues in power system operations after deregulation. IEEE Trans Power Syst 11(3):1191–1200
14. Nobile E, Bose A, Tomsovic K (2000) Bilateral market for load following ancillary services. Proc PES Summer Power Meeting, July 15–21, Seattle, WA
15. Donde V, Pai MA, Hiskens IA (2001) Simulation and optimization in an AGC system after deregulation. IEEE Trans Power Syst 16(3):481–489
16. Liao K, Xu Y (2018) A robust load frequency control scheme for power systems based on second-order sliding mode and extended disturbance observer. IEEE Trans Indus Inf 14(7):3076–3086
17. Demerorenion A, Zeynelgil HL (2007) GA application to optimization of AGC in three area power system after deregulation. Electr Power Energy Syst 29:230–240
18. Berjeev T, Srivastava SC (2005) A LQG based load frequency controller in competitive environment. Int J Emerg Elect Power Sys 2(2)

Chapter 30
Control of Grid-Connected Photovoltaic System Using Enhanced PLL (EPLL) Technique

Pravat Kumar Ray, Pratap Sekhar Puhan, and Ashish Kumar

Abstract Recent trends on synchronization of grid to distributed generation play an important role as the fossil fuel is depleting day by day. Renewable sources are the future fuel of electricity and that needs to be properly utilized and controlled. In this paper, solar energy-based distributed generation is synchronized with a three-phase grid; in the process of synchronization, power quality issues rises as power electronics-based converter is the intermediate device between the distributed generation and the grid. To maintain the source current and source voltage pure sinusoidal, an enhanced phase-locked loop control technique along with hysteresis controller is implemented for the proper generation of switching signal of the converters. Maximum power tracking of the solar PV array is obtained with MPPT algorithm. The work is analyzed through simulation with balanced *R* and *R*-*L* load.

Keywords DG · PQ · MPPT · PLL · EPLL

1 Introduction

Fossil fuel is depleting in a fast rate and its adverse impact to the environment showing the path to use renewable energy source to the power sector. The recent development in this area is the renewable energy-based power system in the power sector of India and abroad. The integration of renewable energy source with the power distribution is coming up with more advantages in terms of operation, control and efficiency. Distribute generation (DG) is the alternate name of this combination [1, 2]. The consumption of renewable energy is increasing with an average of 2.9% per annum reported [3, 4], and it is believed that the total power generating capacity

P. K. Ray · A. Kumar
Department of Electrical Engineering, National Institute of Technology, Rourkela 769008, India
e-mail: rayp@nitrkl.ac.in

P. S. Puhan (✉)
Department of Electrical and Electronics Engineering, Sreenidhi Institute of Science and Technology, Hyderabad 501301, India
e-mail: pratapsekhar@sreenidhi.edu.in

G. Panda et al. (eds.), *Sustainable Energy and Technological Advancements*,
Advances in Sustainability Science and Technology,
https://doi.org/10.1007/978-981-16-9033-4_30

from the non-conventional source will have the same capacity of thermal power generating station by 2040. The report estimated half of the total power generation from the conventional sources will be from wind and solar by 2040 [4]. Recently, solar generation capacity is increasing in a tremendous manner with an average increase of 8.3% percentage in every annum [5–8]. Apart from solar, wind and geothermal-based renewable energy source, power plant has also major role in the distributed generation. The combination of both conventional and non-conventional power plants increases the use of power electronics-based converter which needs a better control action for the power quality issues [9–11]

The various areas where solar energy systems are used are solar photovoltaic plants, residential sector photovoltaic source, photovoltaic lightning systems etc., both standalone mode or grid integration mode of operation is suitable for residential photovoltaic system. The place where grid issues are their like remote location, it is better to use standalone system or grid integration. In case of standalone system, converters are directly connected with the load, but in case of grid integration, the converter output is injected directly to the grid. In residential area, solar-based distributed generation is interfaced with the grid through single-phase voltage source inverter. Exchange of power in distributed generation and the grid is done by controlling the current injected to the grid separately. The injected current control generation by the injected current. For proper component generation, a current controller is designed based on different techniques. The designed controller must perform in such way that it can possess unit power factor during the steady-state operation, capacity to fed quality current to the interfaced grid, fast dynamic response and regulate the parameters to manage the power demand. The problem of the renewable energy-based sources is to maintain the synchronization effectively between the energy source and the distributed generation. Modified synchronous frame reference phase-locked loop, EPLL has already been developed [6, 7].

EPLL has been implemented in single-phase system to improve the value of power factor [10] with wind-based distributed generation for PQ improvement. It is observed that in this method, it is very difficult to filter out the DC component when the input of EPLL is comes under a fault. This DC component results in oscillations which is difficult to mitigate [9–11].

In this work, an EPLL-based controller has been designed to control the load current of the system along with controller with hysteresis band to maintain the power quality. The designed controller was tested with balanced loads.

In the paper, Sect. 2 explain the system, Sect. 3 discusses all the control approach. Section 4 results and Sect. 5 conclusion.

2 Proposed System Structure

The design of solar PV array, design of DC–DC boost converter, selection of DC capacitor voltage, selection of the AC inductor and design of link capacitor. The proposed work is explained in Fig. 1. At first the solar PV module is designed and

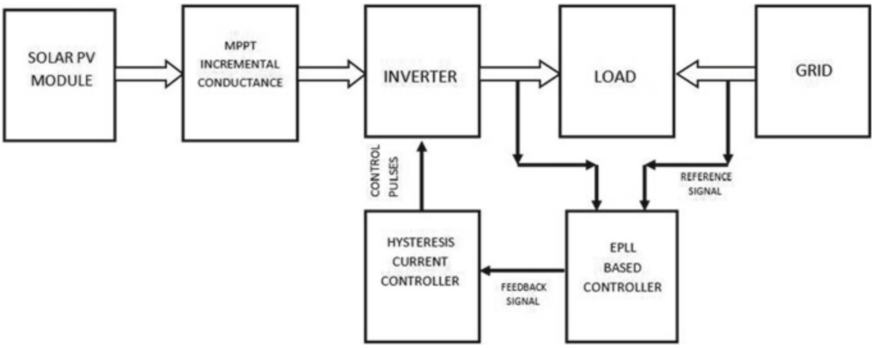

Fig. 1 Proposed system for this work

MPPT algorithm is applied to extract maximum power under various environmental conditions. The voltage source inverter takes the power and its output is connected to the load. The conventional grid is also fed to the load. The reference signal and the actual signal is fed to the EPLL-based control, and the error signal is fed to the hysteresis current control for the proper switching action of the inverter. The design of different parts of the system is described below.

2.1 PV Array Design

Its maximum capacity is 7.84 kW, 415 V AC grids, the rating of the short-circuit current I_{SC} an open-circuit module voltage is 3.8 amp and V_{OC} 21 V, respectively [9]

Solar PV array maximum power is

$$P_{\mathrm{mppva}} = \left(n_{\mathrm{s}} * V_{\mathrm{mp}}\right) * \left(n_{\mathrm{p}} * I_{\mathrm{mp}}\right) = 7.84\,\mathrm{kW} \tag{1}$$

n_{s} and n_{p} stands as series and parallel strings of the PV Module.

V_{mp}, I_{mp} & P_{mpva} represent the voltage, current and power at module of the MPPT.

P_{mppva} is achieved by the below Eq. (2)

$$P_{\mathrm{mp}} = (n_{\mathrm{s}} * 85\%\text{ of }V_{\mathrm{ocn}}) * \left(n_{\mathrm{p}} * 85\%\text{ of }I_{\mathrm{SC}}\right) = 7.84\,\mathrm{kW} \tag{2}$$

For each module, I_{mp} is 3.23 Amp and $V_{\mathrm{mp}} = 17.85$ V.

Modules connected in series

$$n_{\mathrm{s}} = \frac{600}{11} = 29$$

parallel.

$n_{\mathrm{p}} = 5$, as the maximum current of the PV array is calculated as

$$I_{mp} = 15.37\,\text{Amp}$$

So the proposed PV array with a capacity of 7.84 kw is required for 29 modules series and 5 parallel string.

2.2 Boost Converter—DC/DC

It is treated as step up converter. The when sudden changes of in input current is there, inductor resist it. During OFF and ON condition of the switching action, inductor stores and discharges the magnetic form of energy, respectively. It is assumed that the output circuit is large which results high-time constant RC, and it ensures a constant output voltage by comparing it with switching period.

The design is based on [3], value of the parameter is as follow.

Ripple current ΔI_1

$$\Delta I_1 = \frac{P_{mppv}}{V_{mpp}} = 15.37\,\text{Amp},\ L_b = 2.488\,\text{mH}$$

2.3 DC Capacitor Voltage

The DC link voltage

$$V_{DC} = \frac{2\sqrt{2} * 415}{\sqrt{3} * 0.95} = 713.27 \approx 700\,\text{V}$$

2.4 A.C Inductor

The value of the inductor associated with current ripple, switching frequency and over loading factor represents as ΔI, f_s, h, respectively

$$L_f = \frac{\left(\sqrt{3} m V_{dc}\right)}{12 h f_s \Delta I} \approx 3.8\,\text{mH}$$

2.5 DC Link Capacitor

It depends on the following parameters [4]

$\omega =$ angular frequency, $V_{\mathrm{dcr}} = 1\%$ of V_{DC}, $C_{\mathrm{DC}} = 2,547.71\,\mu F$,But selected as 2300 μF.

2.6 PV Generation with Proposed MPPT

The MPPT is the algorithm used for getting the highest or the maximum power available from the PV cells. The incremental conductance (IC) is used in this work to extract power from the PV system. MPPT algorithm with IC is a recursive method and its work based on [3]

$G + \mathrm{d}G = 0$ At MPPT, $G + \mathrm{d}G > 0$ Left of MPPT, $G + \mathrm{d}G < 0$ Right of MPPT, direct duty ratio control incremental conductance MPPT used in this work.

3 Controller Design

In this work, control aspects of the proposed system depends on the voltage source inverter control with EPLL and hysteresis current control. The details of the individual techniques is described.

3.1 Control of Voltage Source Inverter

Fundamental component extraction depends on load, current depends on components to measure reference grid currents. V_{sa}, V_{sb}, V_{sc} are the voltages at the PCC, I_{la}, I_{lb}, I_{lc} are the load currents and V_{dc},

$$V_{\mathrm{t}} = \sqrt{\left(\frac{2}{3}\right)}\left(V_{\mathrm{sa}}^2 + V_{\mathrm{sb}}^2 + V_{\mathrm{sc}}^2\right) \tag{3}$$

The unit vector in-phase voltages are derived as

$$U_{\mathrm{ap}} = \frac{V_{\mathrm{sa}}}{V_{\mathrm{t}}}, U_{\mathrm{bp}} = \frac{V_{\mathrm{sb}}}{V_{\mathrm{t}}}, U_{\mathrm{cp}} = \frac{V_{\mathrm{sb}}}{V_{\mathrm{t}}} \tag{4}$$

The unit vectors in quadrature [2]

$$U_{\mathrm{ap}}, U_{\mathrm{bp}}, U_{\mathrm{cp}}$$

3.2 Enhanced Phase-Locked Loop (EPLL) System

The demerits double-frequency error associated with the PLL is overcome by EPLL [2]. It is used in various applications such as linear modelling, building blocks of numerous developments and operation. [2]. EPLL produces $i_{\mathrm{Lfa}} = I_1 \sin\theta$ from i_{la}. Thus, fundamental component measure the maximum value and phase angle. The stable synchronization is achieved when the estimations are carried out in a systematic approach.

The mathematical analysis is described by the below two equations.

$$i_{\mathrm{Lfa}} = \left[\left\{\int (e)\sin\theta k_1 d\theta\right\}\sin\theta + eK_0\right] \tag{5}$$

where

$$\theta = \int\left[\int ek_2\cos\theta\,\mathrm{d}\theta + \omega\,\sin\theta\,\mathrm{d}\theta + \int ek_3\cos\theta\right] \tag{6}$$

3.3 Components Measurement Both Active and Reactive

Load fundamental active and reactive power currents ($i_{\mathrm{Lpb}}, i_{\mathrm{Lqb}}$) and ($i_{\mathrm{Lpc}}, i_{\mathrm{Lqc}}$) are also estimated in Phases B and C. The load currents average active power component I_{LPA} is estimated as

$$I_{\mathrm{LPA}} = \frac{i_{\mathrm{Lpa}} + i_{\mathrm{Lpb}} + i_{\mathrm{Lpc}}}{3},\ I_{\mathrm{LQA}}\text{ is} \tag{7}$$

$$I_{\mathrm{LQA}} = \frac{i_{\mathrm{Lqa}} + i_{\mathrm{Lqb}} + i_{\mathrm{Lqc}}}{3} \tag{8}$$

3.4 Active Power Components of the Grid Current

The error voltage

$$V_{\mathrm{dcerr}(n)} = V^{*}_{\mathrm{dc}(n)} - V_{\mathrm{dc}(n)} \tag{9}$$

$$I_{\mathrm{wp}(n)} = I_{\mathrm{wp}(n-1)} + K_{\mathrm{pdc}}\left\{V_{\mathrm{dcerr}(n)} - V_{\mathrm{dcerr}(n-1)}\right\} + K_{\mathrm{idc}}V_{\mathrm{dcer}(n)} \tag{10}$$

where $I_{\mathrm{mp}(n)}$ grid current.

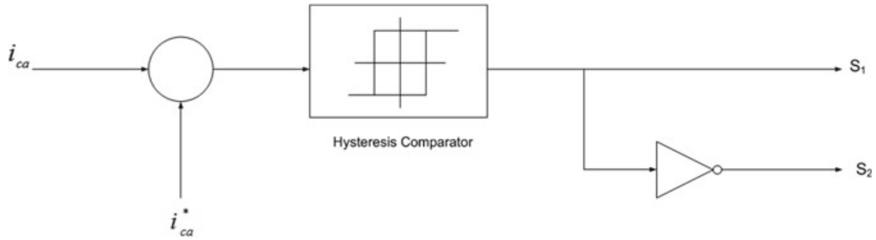

Fig. 2 Hysteresis controller

K_{Pdc} and K_{idc} gains,

$$I^*_{\mathrm{rp}} = I_{\mathrm{LPA}} + I_{\mathrm{WP}} \tag{11}$$

$$i^*_{\mathrm{saqu}} = I^*_{\mathrm{rq}} * u_{\mathrm{aq}}, i^*_{\mathrm{sbqu}} = I^*_{\mathrm{rq}} * u_{\mathrm{bq}}, i^*_{\mathrm{scqu}} = I^*_{\mathrm{rq}} * u_{\mathrm{cq}} \tag{12}$$

3.5 Hysteresis Current Control

Hysteresis controller is used to generate the proper switching signal due to its fast response in transient condition, stability and very much approaching toward accuracy level. The production of switching signal is produced by estimating the error present in the tolerance band. The error calculation is done between the actual and reference.

When $i_{\mathrm{ca}} < i^*_{\mathrm{ca}} - \frac{\mathrm{HB}}{2}$ ON upper and OFF lower.

When $i_{\mathrm{ca}} > i^*_{\mathrm{ca}} + \frac{\mathrm{HB}}{2}$ vice-versa. The hysteresis controller along with the developed band is shown in the Figs. 2 and 3, respectively.

4 Simulation Results and Comparative Analysis

The simulation test system parameters and their values of each part of the system is presented.

4.1 Results of Solar PV Module

At first, the solar PV system is developed. The P–V and I-V characteristics of the panel were plotted for different values of irradiance, respectively, as shown in Figs. 4 and 5. Different parameters used in simulation studies are given in Table 1. The

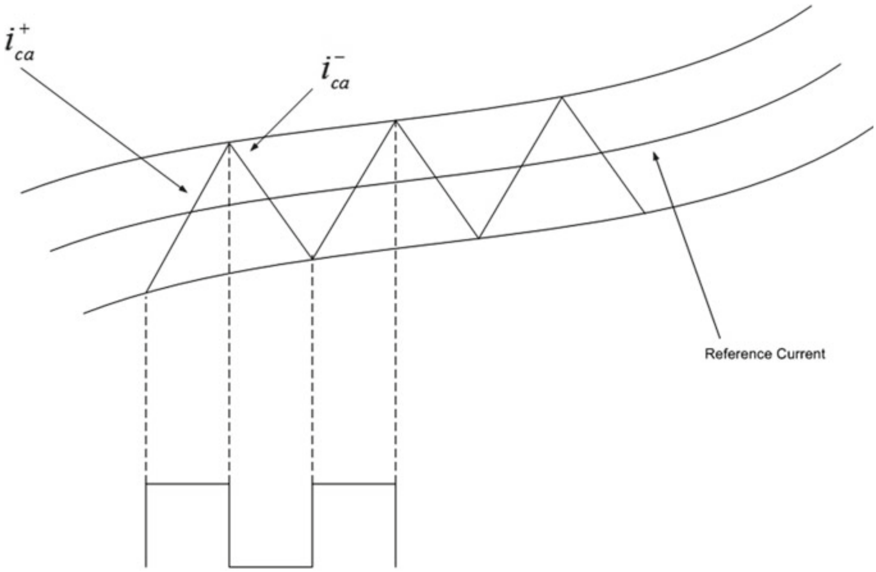

Fig. 3 Corresponding band

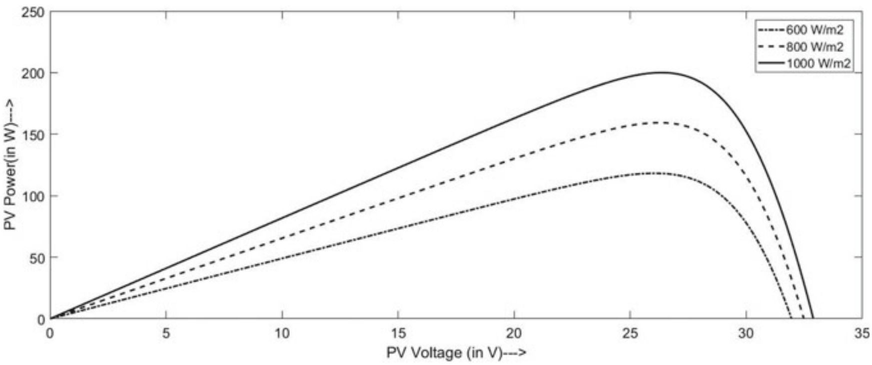

Fig. 4 Power and voltage curve with different solar radiation

tracking of the power and voltage and current characteristics are presented in Figs. 4 and 5, respectively. The maximum power extract using the MPPT with incremental conductance algorithm at 1000 $\frac{W}{m^2}$ at 25 °C is presented in Fig. 6

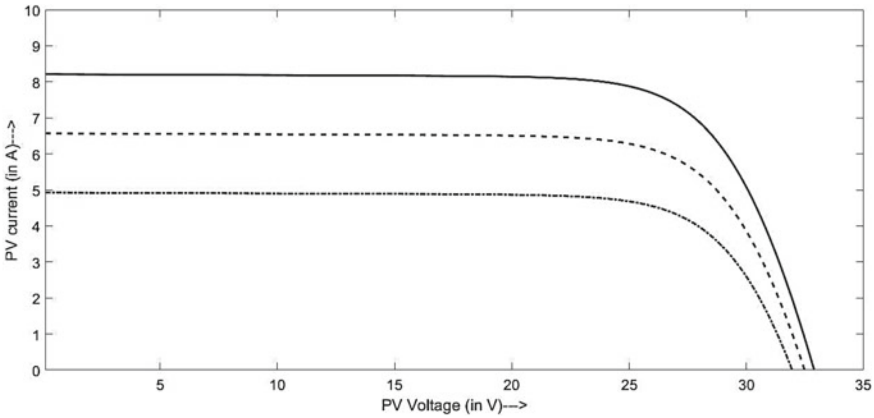

Fig. 5 Current and voltage characteristics for different values of radiation

Table 1 Simulation parameters

Symbol	Parameter name	Value
Parameters of solar PV module		
$I_{sc} V_{ocn}$	Short circuit current, open circuit voltage	3.8 A, 21 V
I_{mp}, V_{mp}	Current at Max. Power point, voltage at Max. power point	4.23 A, 17.85 V
$n_s n_p$	No. of Series and parallel connected modules	29,5
$K_V K_i$	Voltage and current temperature coefficient	− 80e − 3 V/K0. 0029A/K
N_S	*No of series cells*	*36*
DC-DC boost converter parameter		
$L_b D$, f	Inductor, duty ratio, switching frequency	2.5 mH, 0.2–0.5, 20 kHz
Parameter of VSC		
$V_s f_s$	Voltage, frequency	415 V, 2 kHz
$C_{DC} L_S$	DC capacitor, line inductance)	2300 μF, 0.5 mH
K_{pd}	DC voltage controller, linear loads, nonlinear loads	0.023, 50 Ω, 1 mH, 50 Ω
$f V_{DC}$	Frequency, DC voltage	50 Hz, 700 V
$L_f R_s$	Inductor, line resistance	3.8 mH, 0.01 Ω
K_{id}	*Dc voltage controller*	*1.2*
Ripple filter:		
$C_f R_f$	Filter capacitor, filter resistance	10 mF, 5 Ω
PI controller (V_{DC})		
$K_p K_i$	Proportionality constant, integrator constant	0.08, 1.1
Voltage PI controller		
$K_p K_i$	Proportionality constant, ıntegrator constant	0.5, 1.1
EPLL gain parameters		
K_1, K_2, K_3		10,1,0.9

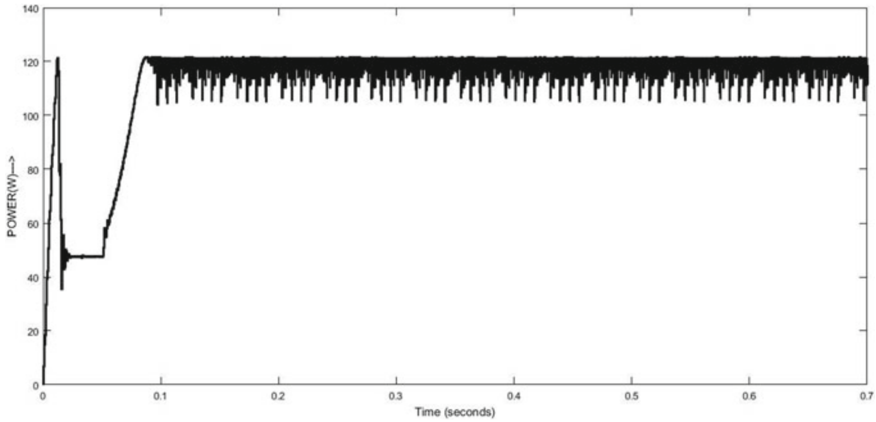

Fig. 6 Power tracking using MPPT algorithm

4.2 *Performance with Balanced Resistive (R) Load*

Under balanced linear load, the output currents of the enhanced phase-locked loop were not as exactly as sinusoidal, and these were shown in Fig. 7. The inverter

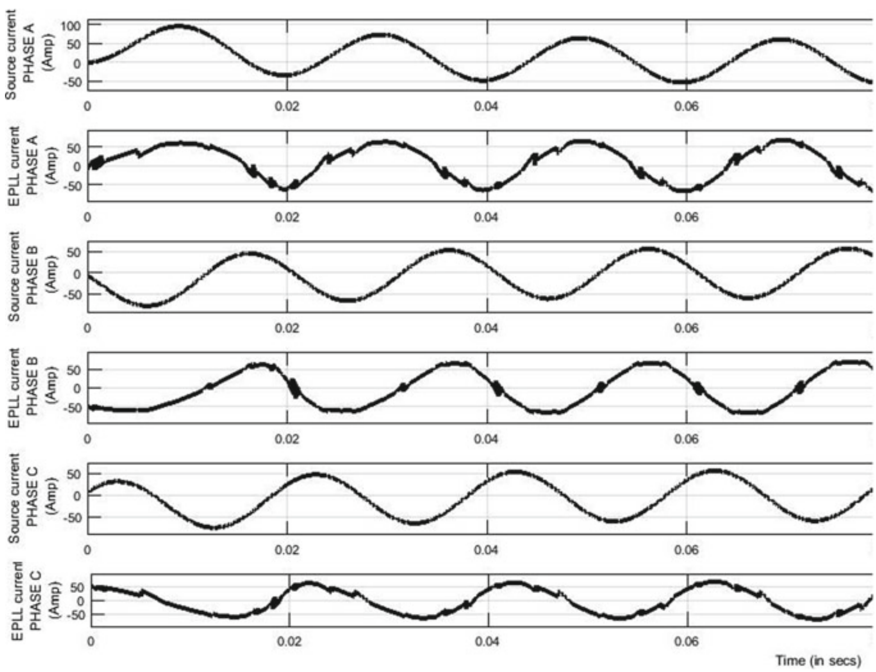

Fig. 7 Load current and source current

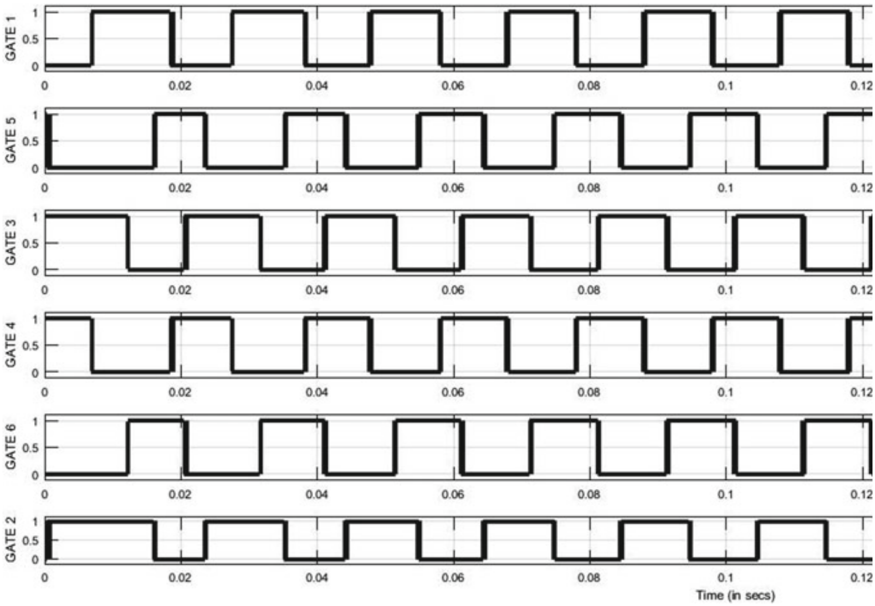

Fig. 8 Pulse generation

firing pulses were controlled by using hysteresis current controller, and by suitably selecting the threshold value of current controller, the gate pulses for the thyristor switches were controlled. These pulses in Fig. 8. The load currents and load voltages in Figs. 9 and 10

4.3 Performance with Balanced Resistive-Inductive (R-L) Load

The output currents of the enhanced phase-locked loop were not as exactly as sinusoidal and shown in Fig. 11. The inverter firing pulses were controlled by using hysteresis current controller, and by suitably selecting the threshold value of current controller, the gate pulses for the thyristor is generated as shown in Fig. 12. The load current and load voltage simulated waveform shown in Fig. 13 after switching action of the inverter.

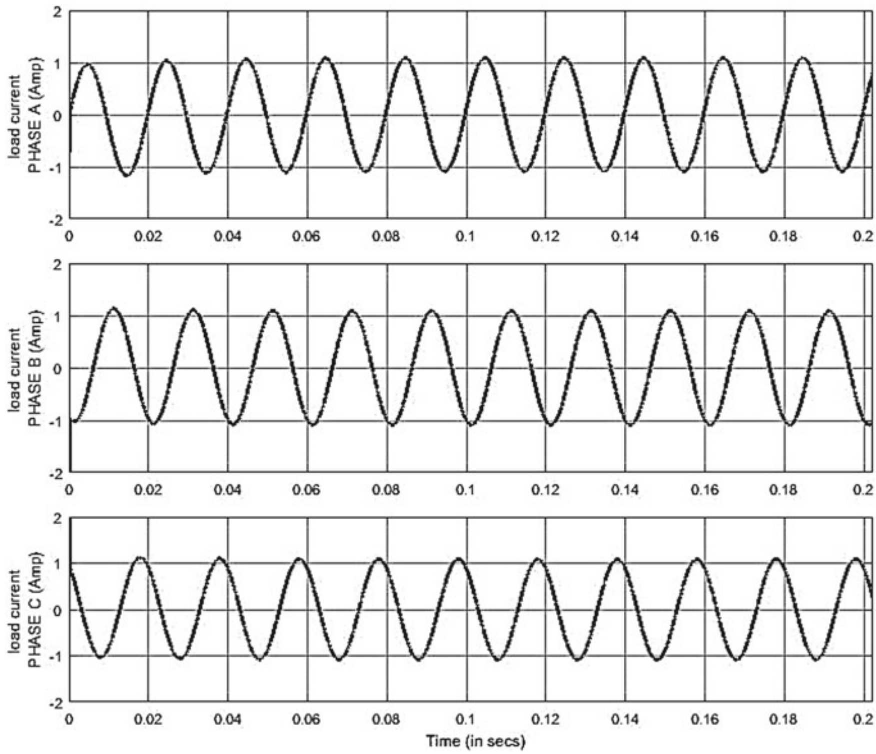

Fig. 9 Load current after switching signal

5 Conclusions

In this work, PV Grid with EPLL techniques is analyzed for proper synchronization and power quality solution with balanced *R* and *R-L* load. It is verified from the simulated wave form that the enhanced PLL is one of the best techniques to improve the performance of mitigation of harmonics and improve the power quality. The main advantage of this work is first and speed response even though there is an instantaneous change of load.

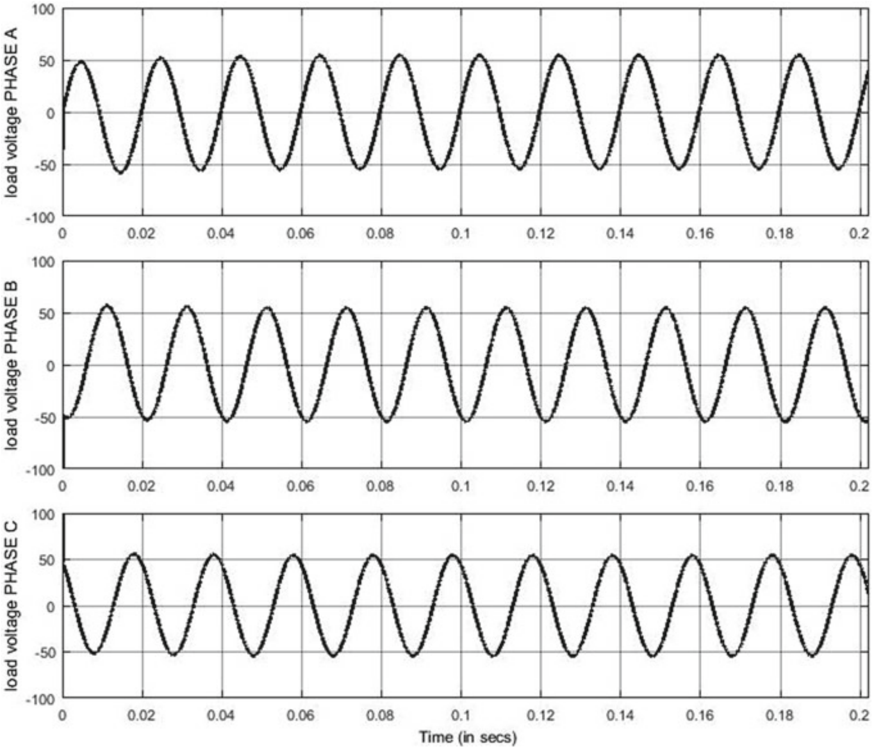

Fig. 10 Load voltage after switching signal

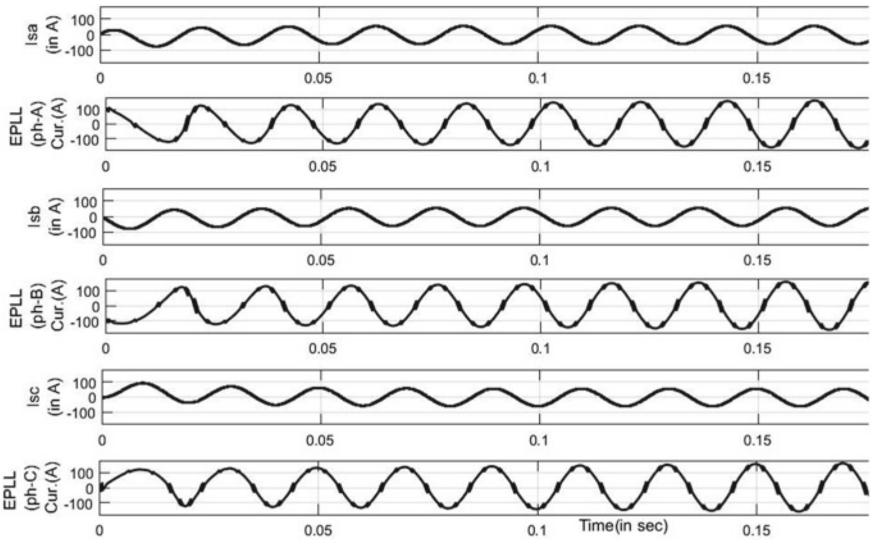

Fig. 11 Comparison of source and EPLL current waveforms for the R-L load

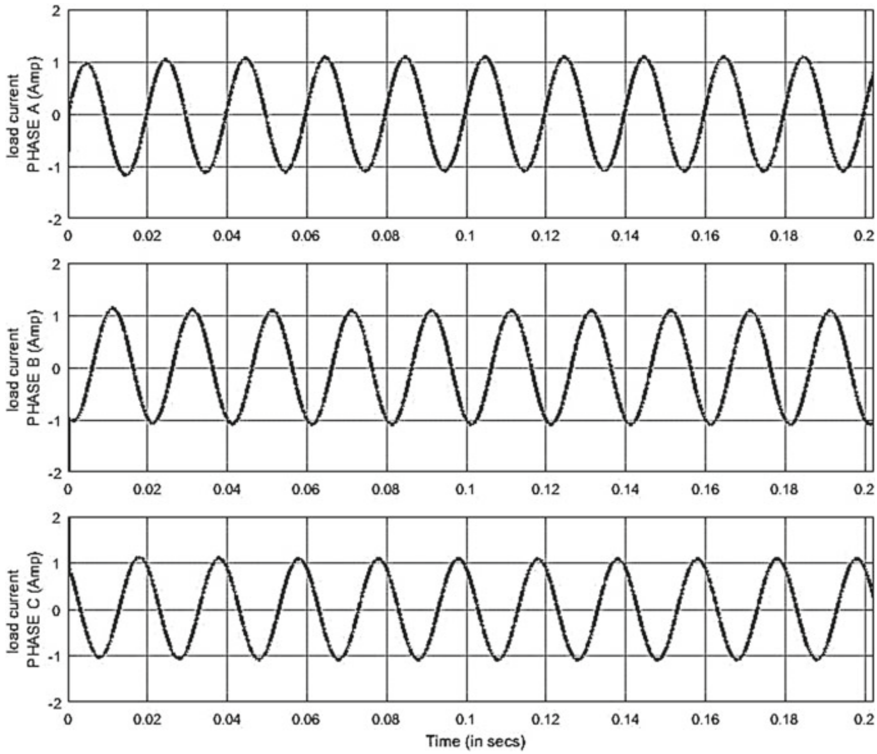

Fig. 12 Load current after switching signal

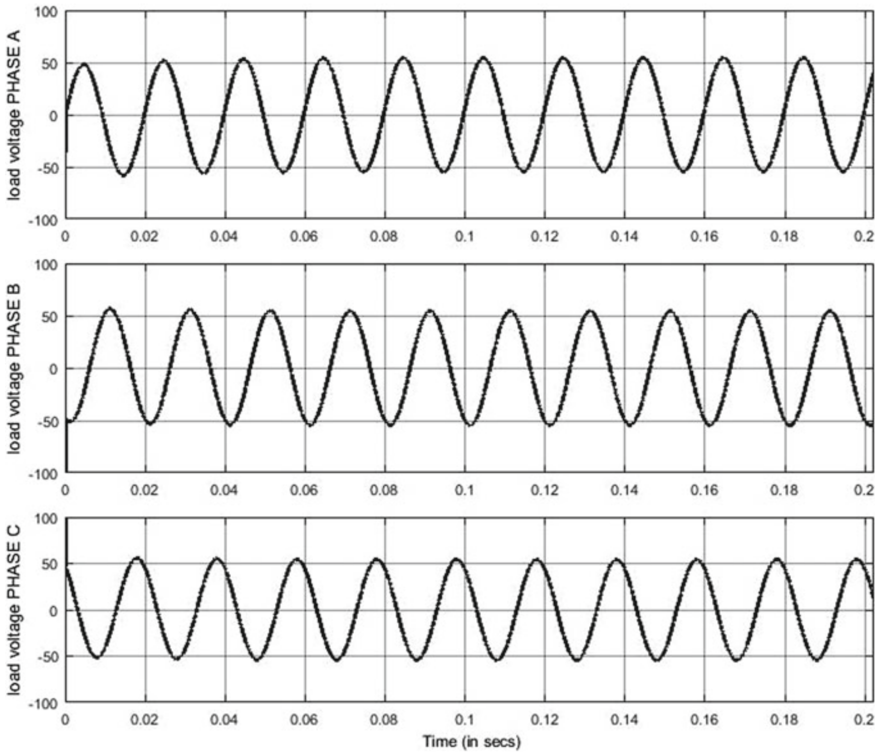

Fig. 13 Load current after switching signal

References

1. Verhoeven B, Kema BV (1998) Utility aspects of grid connected photovoltaic power systems. International energy agency, photovoltaic power system. Prog, Switzerland
2. Verma, a.k., Singh, B., and Shahani, D.T.: Grid interfaced solar photovoltaic power generating system with power quality improvement at ac mains. in *Proc. IEEE 3rd Int. Conf. Sustainable Energy Technologies (ICSET)*,177–182 (2012)
3. Shahani SB, Verma AK (2012) Power balanced based control of grid interface solar photo voltaic power generating system with improved power quality. In: IEEE, international conference power electronics drives and energy system (PEDES), pp 1–7
4. Balathan S, Edringtion CS, Henry SD, Cao J (2012) Analysis and control of a photo voltaic system-application to a high penetration case study. IEEE Syste Jou 6:213–219
5. Subudhi B, Pradhan R (2013) A comparative study on maximum power point tracking techniques for photo voltaic power systems. IEEE Trans Sustain Energy 4:89–98
6. Mei M, Shah L, Guerrero JM (2011) A novel improved variable step size incremental resistance MPPT method for PV System. IEEE Trans Ind Electronic 8:2427–2434
7. Madhurima E, Puhan PS (2020) Performance analysis of photovoltaic fed series active power filter for power quality ımprovement. IEEE. Int confer. In: 3rd ınternational conference on energy, power and environment: towards clean energy technologies, NIT, Meghalya
8. Chyun G, Hsieh C, Hung C (1996) Phase locked loop technique. IEEE Trans Ind Electron 43:609–615

9. Liccardo F, Marino P, Raimondo G (2011) Robust and fast three-phase PLL tracking system. IEEE Trans Ind Electron 58:221–231
10. Ghartemani MK, Ziarani AK (2004) Performance characterization of a non-linear system as both an adaptive notch filter and a phase-locked loop. Int J Adapt Control Signal Process 18:23–53
11. Villalva MV, Gazoli JR, Filho ER (2009) Comprehensive approach to modeling and simulation of photovoltaic arrays. IEEE Trans Power Electron 24:1198–1208

Chapter 31
Voltage- and Current-Based Hysteresis Controller-Fed Series Active Filter to Compensate Voltage Sag Problem

Ravikanth Mallajoshula and I. E. S. Naidu

Abstract Different types of mitigation techniques have been developed to solve the power quality issues in distribution systems. In this paper, a series active power filter is developed to mitigate the sag problem in a distribution system. The performance of the series active filter is enhanced using unit vector template generation (UVTG) along with both hysteresis voltage and current controller technique implementation separately. The reference signal for the voltage source converter is derived using UVTG, and the error between the reference signal and actual signal is fed to the hysteresis controller for switching pulse of the converters. The effectiveness of this controller is verified through simulation, and finally, a comparison is made between hysteresis current and voltage controller.

Keywords Power quality · Voltage sag · SAPF · UVTG · Hysteresis voltage controller · Hysteresis current controller

1 Introduction

The objective of the electric power station is to transfer electrical energy from generating station to the terminals of all electrical equipment safely and smoothly. The terminal equipments receive the ideal voltage without any disturbances through the system network leads to good reliability of the system [1, 2]. Previously, the research was on reliability of the system but it gradually changes to the term power quality as power electronics-based loads came to picture after 1980s. In 1978 the term power quality was introduced by one of the researchers [3]. Though the term power quality was there in the past, its impact was less as of now; recently, the term is becoming more popular than reliability. Different agencies define the term power quality in different approaches, and some of the researchers found the main cause of power quality which is the voltage disturbances in the system due to the various reasons [4–6]. Use of electronics and power semi-conductor-based equipment has very much

R. Mallajoshula (✉) · I. E. S. Naidu
Department of EECE, GITAM Institute of Technology, Visakhapatnam Campus, GITAM (Deemed to be University), Visakhapatnam 530045, India

G. Panda et al. (eds.), *Sustainable Energy and Technological Advancements*, Advances in Sustainability Science and Technology,
https://doi.org/10.1007/978-981-16-9033-4_31

sensitive to voltage disturbances, and it not only harms the domestic sector but also hampers the industrial sector reducing loss of production leads to huge loss [5–7]. Equipment tripping due to disturbances in the supply voltage is referred as bad power quality by the customers but utility take it on other way by blaming the end-user equipment [8]. The main cause of voltage disturbances is the huge use of converter-driven equipment such as adjustable speed drives, consumer electronics, computers, and laptops [9–11]. In the converter-based loads, the main problem is drawing of non-sinusoidal current that leads to harmonics in the supply which later results in voltage harmonics [9]. The main concerns of the power quality are the deviation of voltage and current from its ideal, deviation fails to maintain the system frequency and power factor value approaches to unity. Voltage magnitude variation is the result of variation of loads; operation of tap changer of the transformer, switching on and off the capacitor and reactor, etc., in the network [8], voltage frequency variation is due to the mismatch between the power generation and load demand. Under voltage variation based on the existence of duration is represented by different names. Short duration under voltage is termed as voltage sag or voltage dip by IEC. Similarly, if the under voltage persists for long duration it is treated as interruption [12]. If the magnitude of the supply voltage is reduced 90% to 1%, and it recovers the value between 10 ms and 1 minute; it is treated as voltage sag by IEC, and IEEE defines drop in voltage as sag. Short circuit in the system by any means or staring of motor is the main cause of voltage SAG. Voltage magnitude event prescribed by IEEE Std.1159 is shown in the form of one schematic diagram in Fig. 1 [3]

The main interest to do the work on voltage sag is its adverse impact on consumer electronics, computers, and processes control equipment, and these equipments are modeled as a single-phase rectifier and under voltage at the DC voltage leads to tripping, and the second one is adjustable speed AC drives whose main components are a three-phase rectifier trips when it comes under the influence of under voltage and

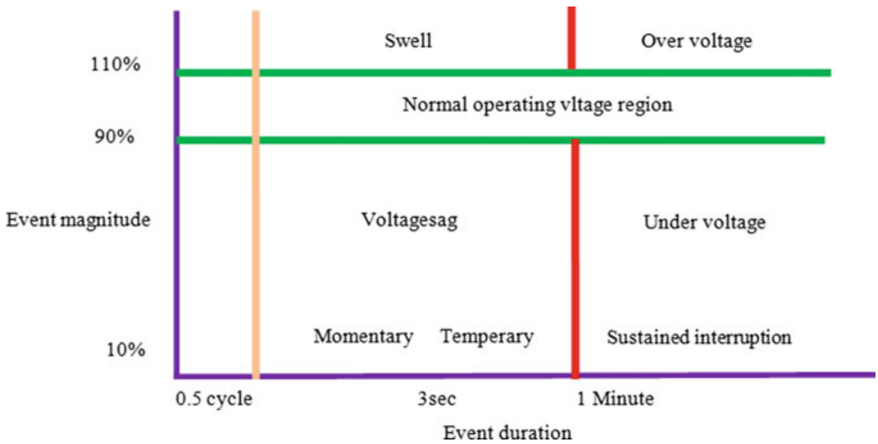

Fig. 1 Schematic diagram of voltage magnitude event as per IEEE1159 Std

third one is adjustable DC drives which associate with firing angle control leads to trip if there is a problem on the control side [6]. Different mitigation techniques have been suggested by many researchers for voltage sag. As short circuit is one of the causes of voltage sag, it can be minimized by reducing the faults and reduction of faults can be achieved by many ways such as replacement of overhead line by underground cables, using shied cables in the over headline, making police for tree trimming, increase the rate of maintenance work, etc. Instead of reducing the faults, if the fault clearing time is reduced, then it can be more advantageous. Current limiting fuses are used to reduce the fault clearing time [5]. Uninterruptible power supply (UPSs) are popular in computers, process control equipment, etc., whereas motor-generator set is used in industrial equipment. Voltage source converters are recently used to solve the voltage sag problems [9, 10]. Series controller use voltage source converter as its main component to compensate voltage sag in a system. There are various control mechanisms to control the voltage source converter successful operation starting from conventional to soft computing approach. DQ theory, synchronous detection technique, indirect current control technique, UVTG, etc., and various soft computing such as neural network and fuzzy logic are used [5–9, 13]. Though a number of control algorithms have been developed, still there is a scope to further improving the performance using different techniques. In this work, a series active power filter is designed to compensate for the voltage sag problem in the system. Unit vector template generation with both voltage- and current-based controller implemented separately.

The paper has five sections. Section 1 describes the introduction, Sect. 2 presents the proposed system and design of the series filter, Sect. 3 presents the control techniques briefly. Sections 4 and 5 present results and conclusions.

2 Design of the Proposed Filter

The block diagram of the system under the analysis of voltage sag is shown in Fig. 2. Three-phase supply is fed to a nonlinear load, and sag is developed. A series active power filter is designed with some control mechanism to compensate for the sag problem. The proposed series active filter is a system–equipment interface device called a voltage source converter. İt is a power semi-conductor device able to generate a voltage at desired magnitude, phase, and frequency. In the occurrence of sag, it replaces the supply or generates the missing voltage which is a part of the supply. It consists of six IGBTs, coupling inductor, resistor, DC link capacitor, and a coupling transformer [14]. The DC-link capacitor should have constant voltage throughout the operation with the help of energy storage devices [15, 16]. The coupling transformer input is connected to the output of voltage source inverter.

The desired output voltage is achieved using PWM switching pattern. The magnitude of the filter inductance, capacitance, and resistance is taken from [15]. The series controller operates on the principle, the sum of controller voltage and sag voltage is equal to the load voltage after compensation, and it is represented in Eq. 1.

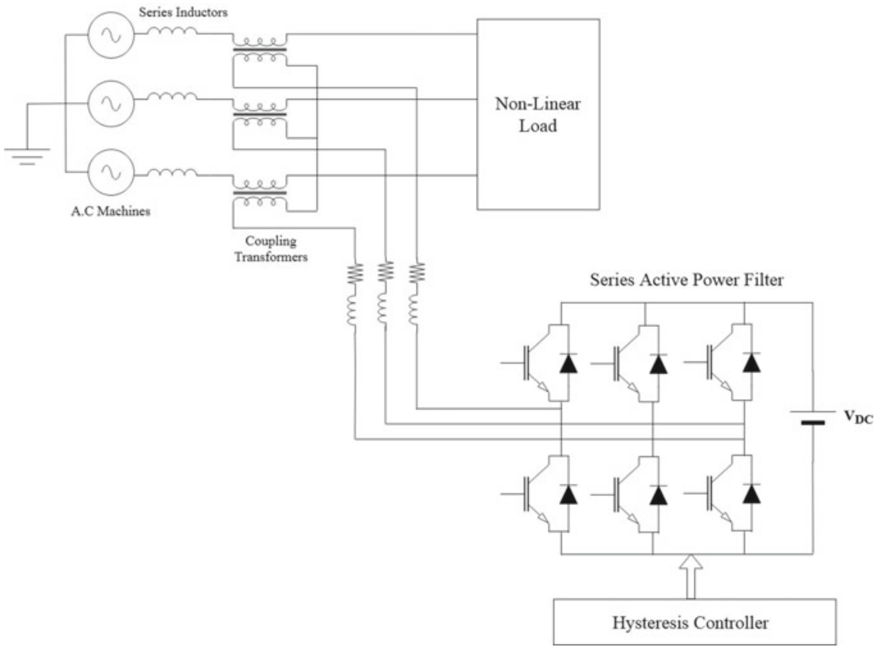

Fig. 2 Proposed system for this work

$$V_{\text{Load}} = V_{\text{Cont}} + V_{\text{Sag}} \tag{1}$$

3 Control Techniques

The performance of the proposed series filter depends on the implementation of the control techniques for generation of best switching pulses. In this work, unit vector template generation techniques along with hysteresis-based voltage and current controller techniques are used to generate the reference signal and pulses, respectively. First unit vector template generation is used for reference signals, and after that, voltage-based and current-based hysteresis controller acted separately.

3.1 Case 1—UVTG and Hysteresis Voltage Controller

UVTG is a simple algorithm, and it is implemented in [15]. The filter is controlled in such a manner it will inject $V_{fa,} V_{fb,} V_{fc}$ to compensate for the sag problem and maintain constant voltage at the point of common coupling. The schematic diagram of UVTG along with hysteresis voltage controller technique is shown in Fig. 3.

First the distorted voltage from the supply is sensed and fed to the PLL. The PLL will generate two unit vectors, in-phase sine and cosine. Once the output is generated, PLL is used to calculate the supply in phase and 120° phase difference of three unit vectors U_a, U_b, U_c as present in Eq. 2.

$$\begin{bmatrix} U_a \\ U_b \\ U_c \end{bmatrix} = \begin{bmatrix} 1 & 0 \\ -\frac{1}{2} & -\frac{\sqrt{3}}{2} \\ -\frac{1}{2} & \frac{\sqrt{3}}{2} \end{bmatrix} \begin{bmatrix} \sin\theta \\ \cos\theta \end{bmatrix} \tag{2}$$

The above input vectors multiplied with the desired value V_{lm}^*. The reference voltage is present in Eq. 3

$$\begin{bmatrix} V_{la}^* \\ V_{lb}^* \\ V_{lc}^* \end{bmatrix} = V_{lm}^* \begin{bmatrix} U_a \\ U_b \\ U_c \end{bmatrix} \tag{3}$$

The error of this voltage and sensed voltage V_{la}, V_{lb}, V_{lc} is fed to the hysteresis voltage controller. Hysteresis voltage controller is used to generate the PWM signal for the proposed voltage source converter. The instant output voltage crosses hysteresis band, and switching action occurs. The hysteresis controller and corresponding band are presented in Fig. 4a, b.

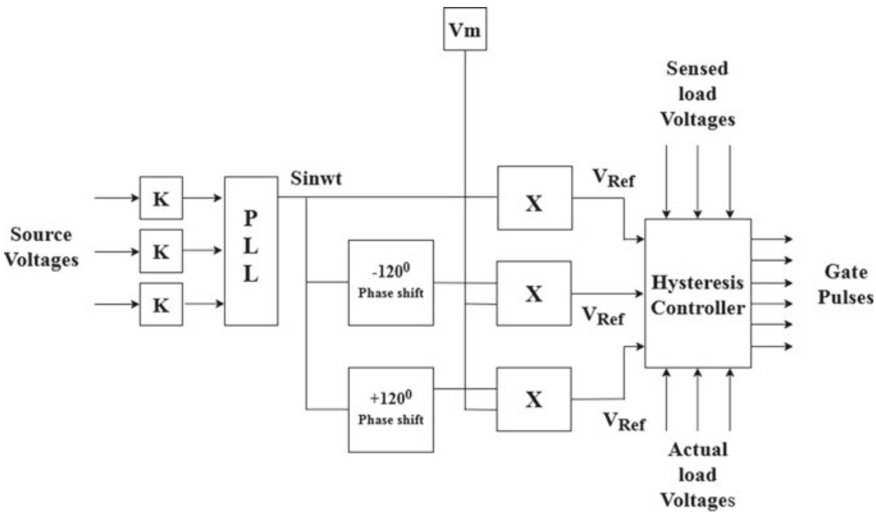

Fig. 3 Proposed hysteresis voltage-based controller

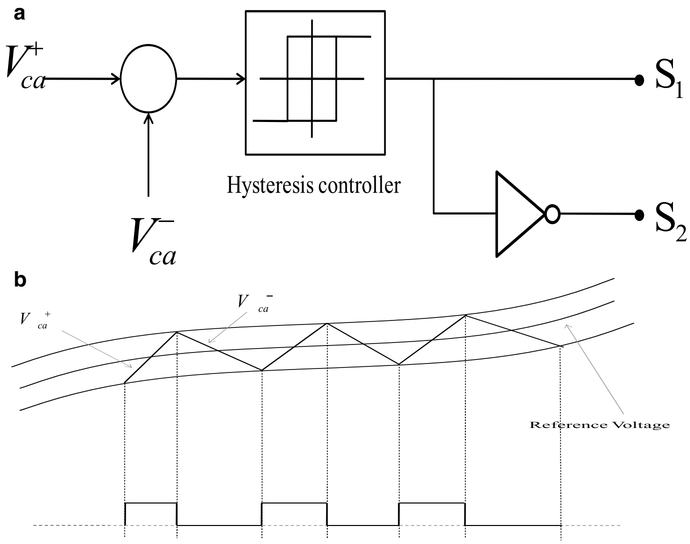

Fig. 4 **a**, **b** Voltage-based hysteresis controller and corresponding band

When

$$V_{ca} > V_{ca}^{*} + \frac{\mathrm{HyB}}{2} \text{ Upper switch is OFF and lower is on}$$

$$V_{ca} < V_{ca}^{*} - \frac{\mathrm{HyB}}{2} \text{ Upper switch is ON and lower is off}$$

3.2 Case 2—UVTG and Hysteresis Current Controller

UVTG and hysteresis current controller-based technique are explained through block diagram presented in Fig. 5. This algorithm has three unit vectors such as in phase and 120 displacements. The magnitude of the reference current is calculated from the DC voltage error which is fed to the PI controller. The voltage error is the difference of average and reference value. Multiplying each phase unit vectors with their magnitude $I_m{}^*$ results in three reference supply current [14]. Then a comparison is made between the calculated and sensed supply current, the error obtained is fed to the proposed controller for switching pulse of the voltage source inverter. The switching on and off operation is carried out by following the equations

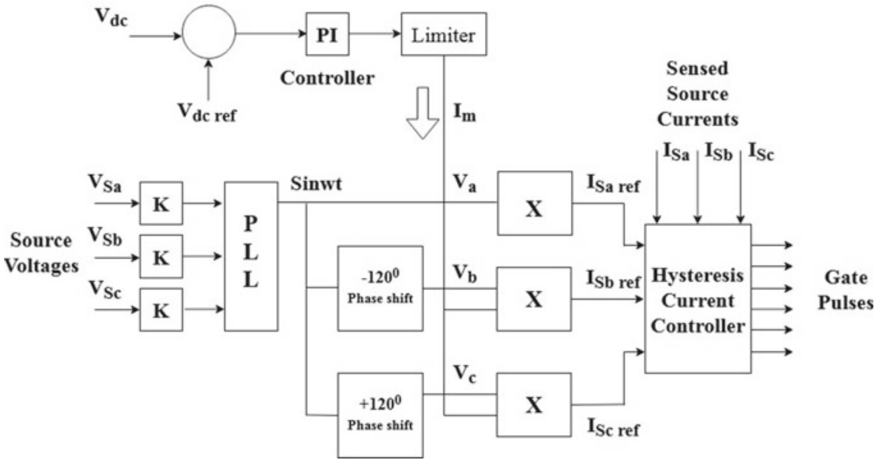

Fig. 5 Proposed hysteresis current-based controller

When

$$i_{\mathrm{ca}} > i_{\mathrm{ca}}^{*} + \frac{\mathrm{HyB}}{2} \quad \text{Upper switch is off and lower switch is on.}$$

$$i_{\mathrm{ca}} < i_{\mathrm{ca}}^{*} - \frac{\mathrm{HyB}}{2} \quad \text{Lower switch is off and upper switch is on}$$

The hysteresis controller with its band is shown in Fig. 6a, b, respectively.

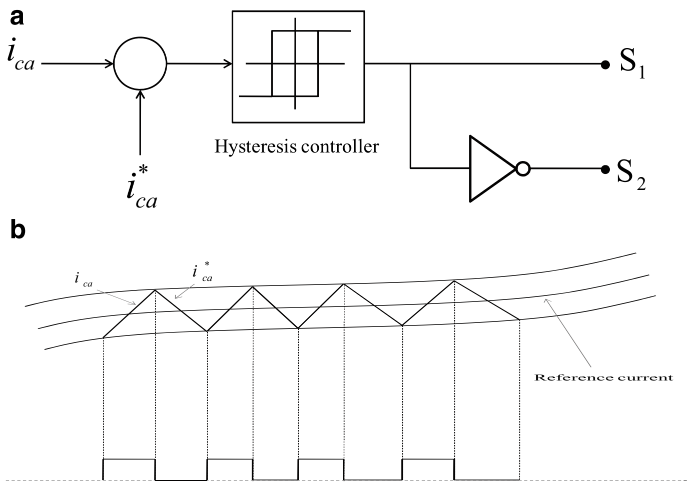

Fig. 6 **a**, **b** Current-based hysteresis controller and corresponding band

4 Result and Analysis

The proposed series filter is designed, and the implementation of the controller is carried out. At first, a nonlinear load is connected to the three-phase supply, and the series filter is placed in between the source and load with all other arrangements. The voltage sag is created, and accordingly, the series filter injects the voltage with the help of controller to compensate it. The proper timing of injection depends on the proper and smooth operation of the entire controller. The filter is simulated with the help of MATLAB/Simulink platform, two separate cases such as hysteresis voltage and hysteresis current controller implementation carried out successfully, and the obtained results are presented.

4.1 UVTG and Hysteresis Voltage Controller

The UVTG and voltage-based hysteresis controller implementation are carried out successfully in the proposed model, and voltage sag is developed during 0.1–0.3 s. The simulated waveform of supply voltage and current before and after compensation is presented in Figs. 7 and 8, respectively. The FFT analysis of source current in terms of THD is shown in Fig. 9. The THD of source current obtained is 4.70% of

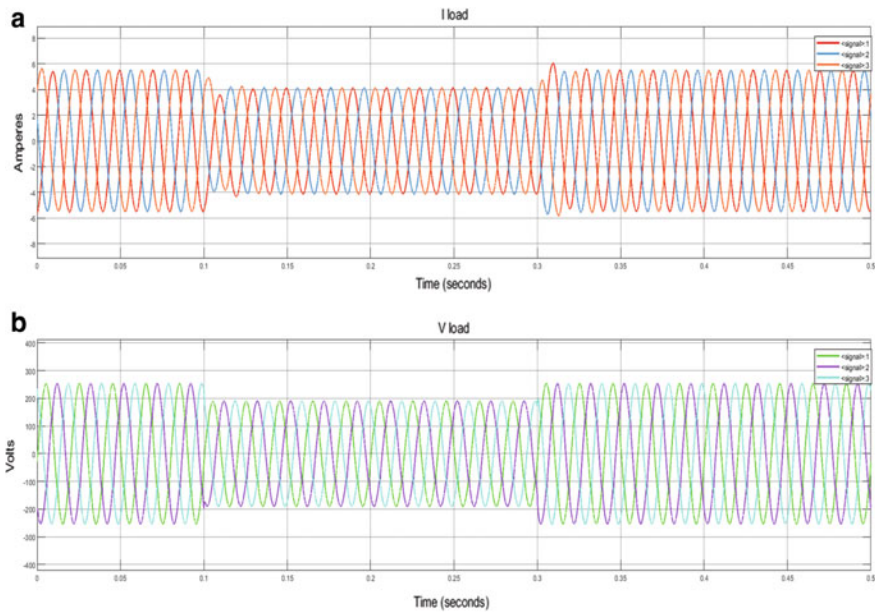

Fig. 7 Voltage-based hysteresis controller simulated waveform before compensation, **a** source current, **b** source voltage, a-upper one, b-lower one

fundamental, and it comes under IEEE-519 standard. The voltage waveform after compensation is close to sinusoidal.

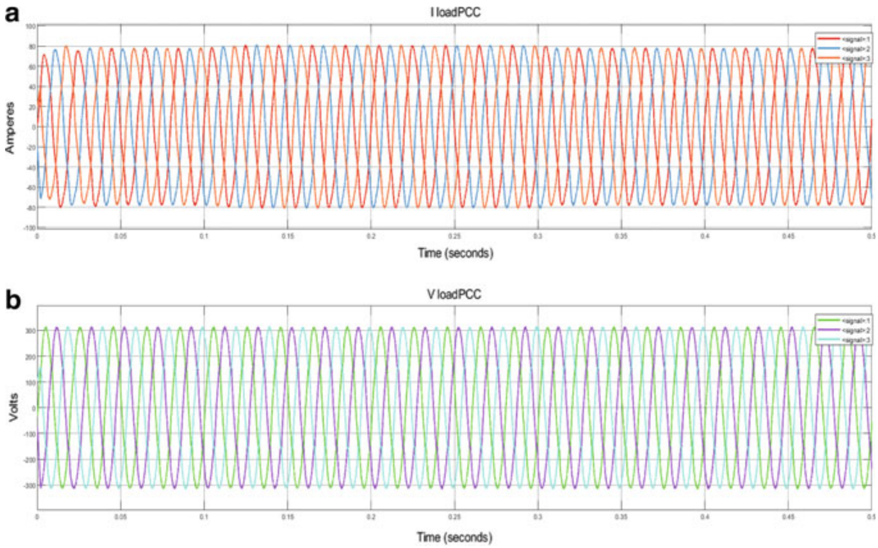

Fig. 8 F Voltage-based hysteresis controller simulated waveform after compensation, **a** source current, **b** source voltage, a-upper one, b-lower one

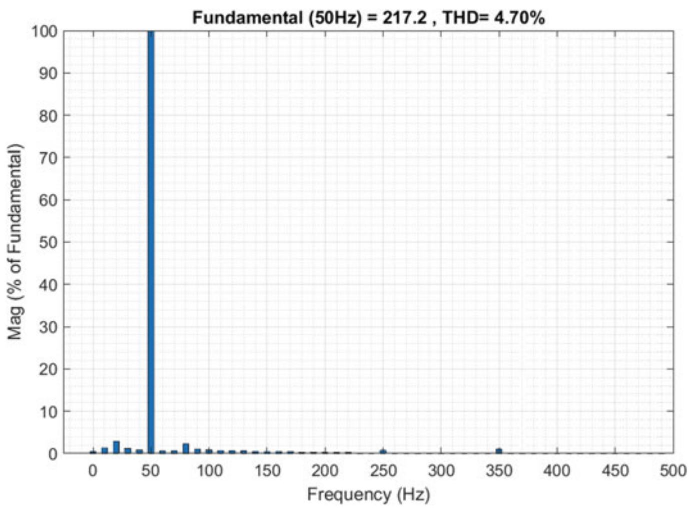

Fig. 9 FFT analysis of source current after voltage sag compensation with hysteresis voltage controller

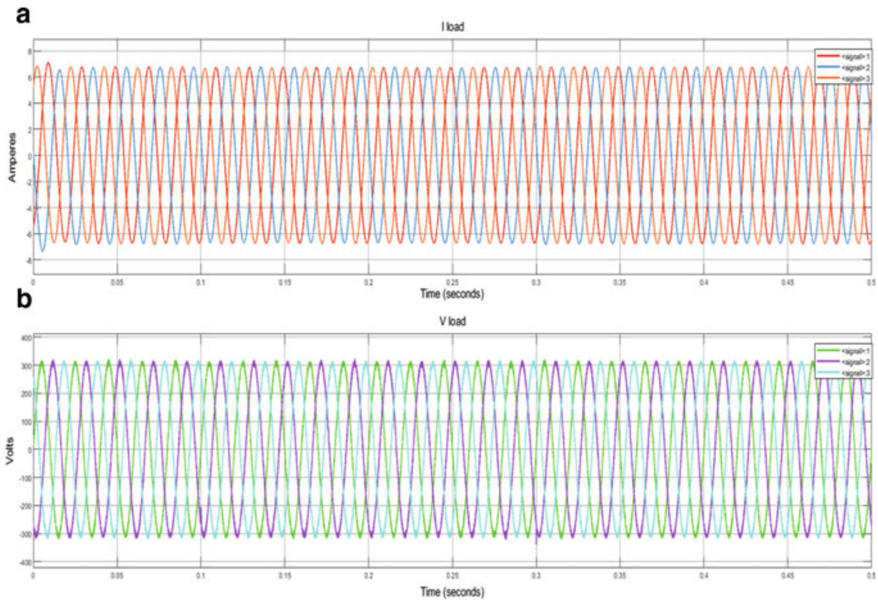

Fig. 10 Current-based hysteresis controller simulated waveform after compensation, **a** source current, **b** source voltage, a-upper one, b-lower one

4.2 Case 2—UVTG and Hysteresis Current Controller

In this technique, the same sag is developed in the duration of 0.1–0.3 s as shown in Fig. 7a, b. The UVTG and current-based hysteresis controller implementation are carried out successfully in the proposed model, and the simulated waveform of supply voltage and current after compensation is extracted and presented in Fig. 10a, b. The FFT analysis of source current in terms of THD is shown in Fig. 11. The THD of source current obtained is 3.18% of fundamental, and it comes under IEEE-519 standard. This result is very encouraging, and the voltage waveform after the compensation is very close to sinusoidal. From the THD, it is observed that current control-based hysteresis gives more accurate results in comparison to voltage-based hysteresis controller. Table 1 shows the results of THD after compensation of the two cases.

5 Conclusions

The proposed series active filter with unit vector template generation techniques along with voltage-based hysteresis controller and current-based hysteresis controller is implemented in the system successfully, and the effectiveness of the controllers is

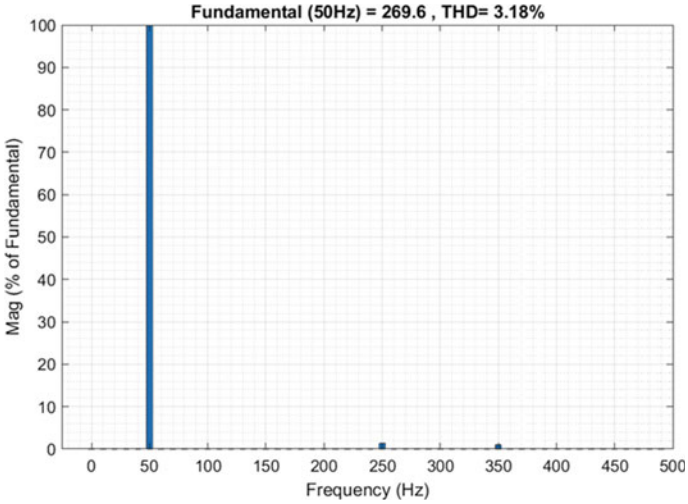

Fig. 11 FFT analysis of source current after voltage sag compensation with hysteresis current based controller

Table 1 THD comparison of voltage and current based hysteresis controller

Case	Techniques used	THD of source current after compensation
1	UVTG and voltage-based hysteresis controller	4.70
2	UVTG and current-based hysteresis controller	3.18

verified. It is observed and analyzed from the work, though voltage-based hysteresis current controller gives good results for voltage sag compensation, current-based hysteresis controller gives more accurate and encouraging results for the same problem because the presence of PI controller keeps DC voltage of the filter as close as its reference value, and also, it justifies from the results.

References

1. Wang P, Jenkins N, Bollen MJH (1998) Experimental investigation of voltage sag magnitude by an advanced static Var compensator. IEEE Trans Power Delivery 13
2. Sannino A, Miller M, Bollen M (2000) Overview of voltage sag nitigation. Power engineering society winter meeting, vol 4. IEEE
3. Bollen MHK, Understanding power quality problems. IEEE Press Series on Power Engineering
4. Zhang Y, Jovica V, Millanavic (2010) Global voltage sag mitigation with-facts based deviceses. IEEE Trans Power Delivery 35:4
5. Daund M, Gautam P, Jain A (2016) Exploration of voltagesag and its mitigation technique. In: International conference on electrical, electronics and optomization techniques. IEEE

6. Bhumkittipich K, Mithulananthan (2011) Performance enncement of DVR for mitigating voltage sag/swell using vector control strategy. Energy Procedia 9:366–379
7. Rojas H, Cruz A, Rojas H (2017) Technical comparision of alternatives for voltage sag mitigation in distribution systems. Tecciencia 12:13
8. Dash S, Ray P (2018) Design and modeling of single-phase PV-UPQC scheme for power quality improvement utilizing a novel notch filter-based control algorithm: an experimental approach. Arab J Sci Eng 43:3083–3102
9. Goswami A, Gupta C, Singh G (2015) Voltage sag mitigation strategy for an Indian power system: a Case study. J Inst Eng 96:165–174
10. Delghavi M, Choboghloo S (2020) Voltage sag mitigation in DER-connected distribution network by D-STATCMO. Electr Power Comp Syst 48
11. Swain SD, Ray P, Mohanty K (2017) Improvement of power quality using a robust hybrid series active power filter. IET Trans Power Electron 32:3490–3498
12. Omar R, Rahim M (2012) New configuration of a three phase dynamic voltage restorer for voltage disturbances mitigation in electrical distribution system. Arb J Sci Eng 37:2205–2220
13. Puhan PS, Ray P, Panda G (2015) A comparative analysis of shunt active power filter and hybrid active power filter with different control technique applied for harmonic elimination in a single phase system. Int J Model Identif Control 24:19–28
14. Mekri F, Ahmed N, Mochmoum M, Mazari B (2008) A Novel hysteresis voltage control of series active filter. In: European conference on power electronics and its application. IEEE
15. Madhurima M, Puhan PS, Sumantha K (2021) Performance analysis of photo voltaic fed series active power filter for power quality improvement. In: International conference on energy, power and environmement towords clean energy technology. IEEE
16. Mansoor M, Rahim M (2012) Phase angle analysis for three-phase PWM-sswitched auto transformer voltage sag compensator. Arb J Sci Eng 37:1987–2001

Chapter 32
Comparative Analysis of Fuzzy Logic and Synchronous Reference Frame Controlled LVRT Capability Enhancement in Wind Energy System Using DVR and STATCOM

Subash Ranjan Kabat, Chinmoy Kumar Panigrahi, and Bibhu Prasad Ganthia

Abstract This study examines the different techniques utilized to enhance the low-voltage ride through (LVRT) capabilities of double-fed induction generators (DFIG)-based wind turbine systems (WT). As the globe uses around 20–25% of renewable energy from wind, the Type-III WT machine, which is largely based on DFIG, is immediately linked to the grid without the digital interface of power, causing the terminal voltage or reactive electricity output to be unmanageable. As a result, this study presented new LVRT methods based on the implementation of additional active interface technologies. Many techniques are presently being investigated to address the low voltage fault problem. By analyzing LVRT techniques for DFIG-based WECS, this report aims to determine such working methods by bridging the gap in terms of total adaptive performance, operative complexity of controllers, and cost-effectiveness. This study highlights the techniques to increase LVRT's ability to depend on the relationship setup in three main areas based on their grid integrations. In this paper, DVR and STATCOM are connected to the wind turbine system for active and reactive power control under fault detection process. With synchronous reference frame and without synchronous reference frame operations are highlighted in this work, and using STATCOM with SRF theory gives better response during faults to improve active and reactive power. The mathematical models of the entire system are simulated and examined using MATLAB Simulink.

Keywords DVR · STATCOM · LVRT · DFIG · WT · FACT · WECS

S. R. Kabat (✉) · C. K. Panigrahi
School of Electrical Engineering, KIIT Deemed to be University, Bhubaneswar, Odisha 751024, India

B. P. Ganthia
Electrical Engineering, IGIT, Sarang, Dhenkanal, Odisha 759146, India
e-mail: bibhuganthia@igitsarang.ac.in

G. Panda et al. (eds.), *Sustainable Energy and Technological Advancements*, Advances in Sustainability Science and Technology,
https://doi.org/10.1007/978-981-16-9033-4_32

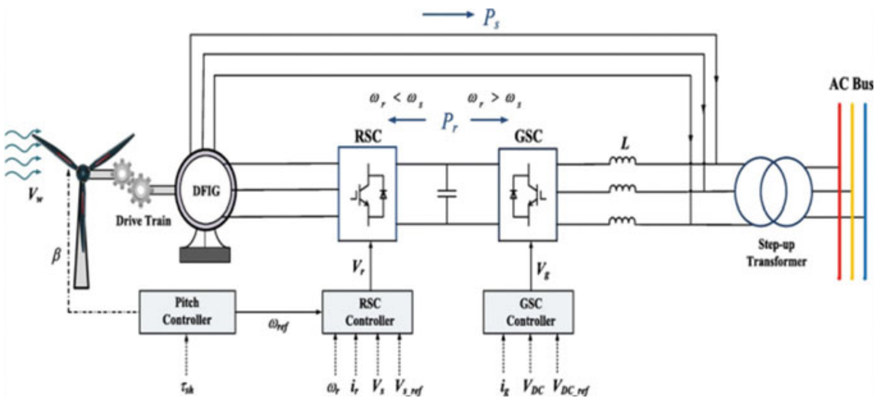

Fig. 1 Model of wind energy conversion system

1 Introduction

Wind generates sporadic sunshine, which heats the atmosphere.The formation of hot and cold air regions results in pressure levels. The air movement from a high-pressures area in a low-pressure area is responsible for the wind flow. Water's kinetic energy is referred to as "energy in motion."The diagram of the network wind power conversion block with both parts is seen in Fig. 1. This cinematic energy affects the wind turbine's aerodynamically engineered blades, which cause it to rotate. Wind speed is always insufficient to drive the blades at a pace that is electricity-neutral. In certain WECS topologies, the gearbox aids in increasing the rotor shaft's rpm. The generators convert the shaft's mechanical energy into electricity. This energy is transmitted to the grid [1]. A wind turbine variable speed system with a double-fed induction generator is the second kind (DFIG) [2–4]. The winding rotor electric converter has a power rate of around 30%, and the DFIG winding stator is directly connected to the grid. A variable wind turbo with a fully rated synchronous generator or SCIG electronic conversion system is the third kind. A multi-stage transmission is typically used by two generators. Synchronous generators, such as permanent synchronous magnet generators, can be powered directly by low-ratio gearbox systems (PMSG). A single- or two-phase gearbox is an intriguing option [5, 6].

2 Doubly Fed Induction Generators

The mathematical model of the DFIG is shown in Fig. 2. All the equations in the model, like flux, voltage, and torque equations, are included. The outflow stator current and the input rotor current in this article are considered positive. This describes the positive direction of the current. In the following diagram [7], the architecture of DFIG is displayed in a d–q rotating synchronous co-ordination system.

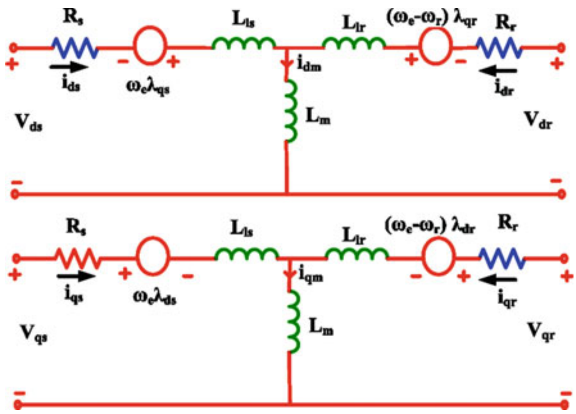

Fig. 2 Equivalent circuit diagram of DFIG for both direct axis and quadrature axis

$$V_{\mathrm{ds}} = R_s i_{\mathrm{ds}} + d\Psi_{\mathrm{ds}}/dt - \omega_{\mathrm{dqs}}\Psi_{\mathrm{ds}} \tag{1}$$

$$V_{\mathrm{qs}} = R_s i_{\mathrm{qs}} + \mathrm{d}\Psi_{\mathrm{qs}}/\mathrm{d}t + \omega_{\mathrm{dqs}}\Psi_{\mathrm{qs}} \tag{2}$$

$$V_{\mathrm{dr}} = R_r i_{\mathrm{dr}} + \mathrm{d}\Psi_{\mathrm{dr}}/\mathrm{d}t - \omega_{\mathrm{dqr}}\Psi_{\mathrm{qr}} \tag{3}$$

$$V_{\mathrm{qr}} = R_r i_{\mathrm{qr}} + d\Psi_{\mathrm{qr}}/dt + \omega_{\mathrm{dqr}}\Psi_{\mathrm{dr}} \tag{4}$$

$$\Psi_{\mathrm{ds}} = L_{\mathrm{ss}} i_{\mathrm{ds}} + L_m i_{\mathrm{dr}} \tag{5}$$

$$\Psi_{\mathrm{qs}} = L_{\mathrm{ss}} i_{\mathrm{qs}} + L_m i_{\mathrm{qr}} \tag{6}$$

$$\Psi_{\mathrm{dr}} = L_m i_{\mathrm{ds}} + L_{\mathrm{rr}} i_{\mathrm{dr}} \tag{7}$$

$$\Psi_{\mathrm{qr}} = L_m i_{\mathrm{qs}} + L_{\mathrm{rr}} i_{\mathrm{qr}} \tag{8}$$

$$(\mathrm{Torque})T_m = 1.5pL_m\left(i_{\mathrm{qs}} i_{\mathrm{dr}} - i_{\mathrm{ds}} i_{\mathrm{qr}}\right) = 1.5p(\Psi_{\mathrm{ds}} i_{\mathrm{qs}} - \Psi_{\mathrm{qs}} i_{\mathrm{ds}}) \tag{9}$$

In the equations given below, *u*, *i*, ψ refer to the voltage, instant current, and flow of winding in each stator and rotor winding, respectively, in *d*-*q* sync. *R*-*s* and *R*-*r* are the stator and rotor resistance of the windings. The leakage inductances for the stator and rotor DFIG model are referred to in Lls and Llr. *L*-*m* and *L*-ss symbolize the self-inducting stator side, satisfying, *L*-ss = *L*-*m* + Llr, *L*-*s*, *L*-rr symbolizes the self-inducting rotor side, which is based on the following model equation: *L*-*m*. The rotary magnetic field of rotating angular velocity is symbolized as ω_r, respectively, by the stator-side magnetic fields *L*-rr = *L*-m + Llr, *l*-dqs, and *l*-dqr' [8, 9]. The

Fig. 3 LVRT curve

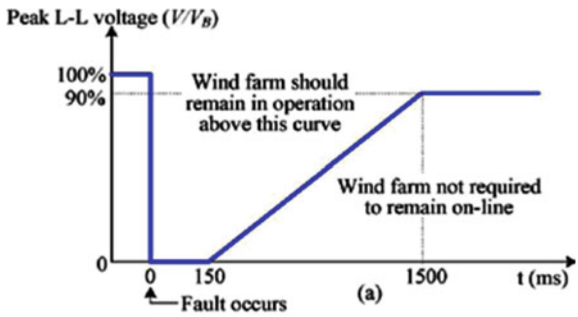

equation of the motion of the rotor is defined as follows:

$$T_m - T_e = \frac{J}{P}\frac{\mathrm{d}w_r}{\mathrm{d}t} \tag{10}$$

where the mechanical torque is represented by T-m. The torque acting for the DFIG is the input torque. T_e is the electromagnetic torque of the DFIG. J represents the rotational inertia of the DFIG [10–12].

3 Low-Voltage Ride Through Technique

In comparison with the internal control loop PI control, the actual portion of the rotor current irq with Irqref is limited to zero. Rotor-side vrq voltage converter is the current controls output. The required three-phase voltages for rotor winding are used by a similarly operated portion of the ground and the vrd driving the ground and raq to reference values. In other words, depending on the wind speed, the rotor side converter produces different frequencies of excitement [13–17]. In order to run an induction generator according to stator-flux vector position, a synchronous dq-axis framework is used to the axis. This is called vector power from SFO. SFO is the name. The controls are also available individually for active and reactive purposes. In the typical inductor generator control, orientation frames such as rotor flux orientation and magnetizing flux orientation can often be used. The statistically powered direction is also commonly used in DFIG vector controllers (SVO) [18–21] The Fig 3 illustrates the LVRT curve for the operating regions of wind energy system.

4 Dynamic Voltage Restorer Control and Operation

Power quality is nothing more than the ideal power supply in tolerances with voltage and frequency. The breakdown of consumer equipment might be the cause

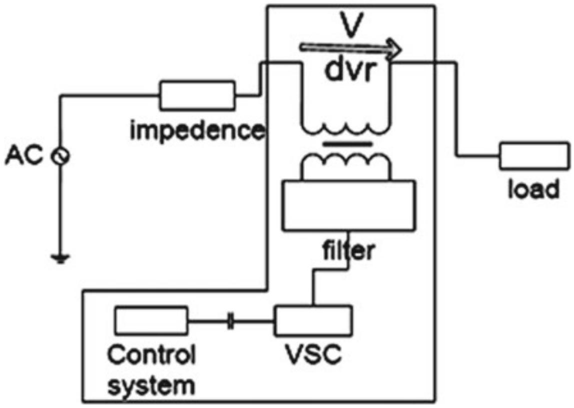

Fig. 4 Configuration of DVR

behind the quality electricity. These concerns are connected to concerns connected to voltage, such as voltage slope, swell, harmonics, inadequate power factor, and voltage imbalance that affect electrical equipment efficiency.

It is also utilized as an electrical high-power controller. For harmonic reduction, fault current restrictions and transient reductions, DVR is employed. A DVR includes an ICT, VSC, energy storing unit, and filter as illustrated in Fig. 4 [22–27].

5 STATCOM Control and Operation (Static Synchronous Compensator)

A STATCOM is a reactive power-controlled device that can be regulated. It offers voltage support without the use of huge external or capacitor banks by producing or absorbing reactive power at the point of common connection. Figure 5 depicts the

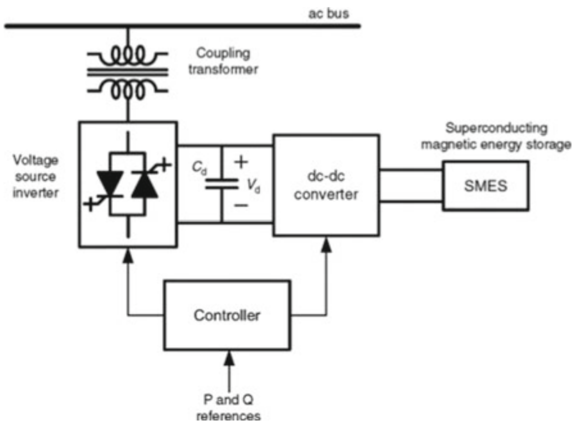

Fig. 5 Configuration of STATCOM

basic voltage source conversion system.

STATCOM's features clearly show that it can handle extremely low system voltages, as low as 0.15 per unit, which is the value associated with the coupling transformer reactance. When contrasted to an SVC, which, at maximum capacitive output, becomes an uncontrolled capacitor bank; this is a stark difference. As long as the DC capacitor can retain enough energy to supply losses, a STATCOM can sustain system voltage at extremely low voltages.

6 Fuzzy Logic Controller

The flow diagram of the plan presented is shown in Fig. 6. Two fuzzy inference systems have been developed. First of all, the incorrect stage(s) are detected, and then the earth is detected [28–32].

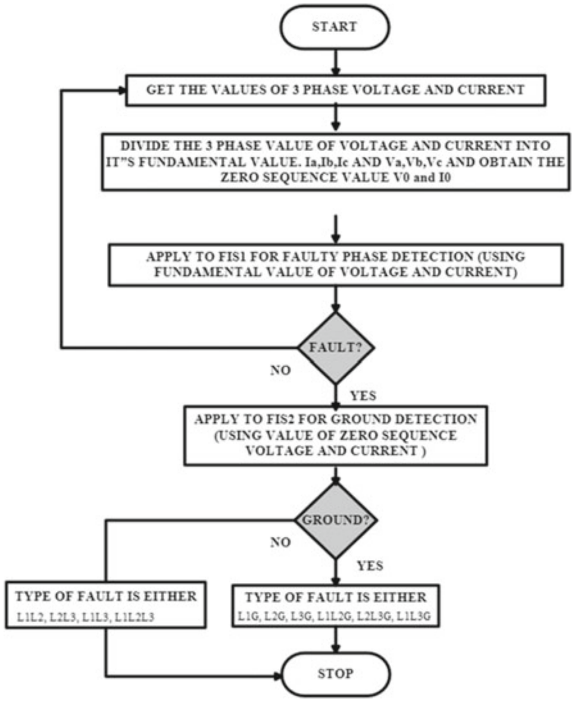

Fig. 6 Flow chart for controller fuzzy logic fault current detection

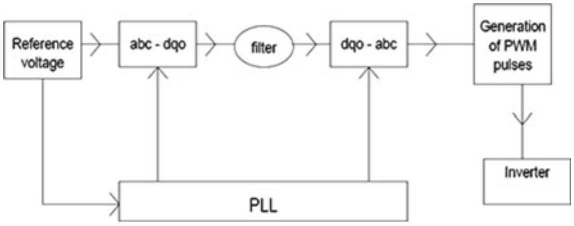

Fig. 7 Basic proposed diagram of SRF theory

7 Synchronous Reference Frame Theory

SRF theory is the most predictable and suitable for DVR and STATCOM among STATCOM's multiple control schemes. The primary conception of the phrase is to have a frame rotating at synchronous velocity. Compared with other approaches, SRF-based controls have admirable characteristics, but need PLL technology [33, 34]. The principal benefit of SRF theory is that there is no time-dependent translation of spatial co-ordinates. The SRF theory uses the park equation. This process transforms the three-phase current or voltages into a *d*-*q* reference frame synchronously revolving [35–38]. The work presented includes transformations from *a*-*b*-*c* to *d*-*q*-*o*, filters, inverters, and PLL as shown in Fig. 7. DVR and STATCOM control the voltage injected by the injection transformer in this technology. The utilities are sent into *d*-*q*-*o*, and filter circuits are utilized for the components necessary and reverse transformations are carried out to gain *a*-*b*-*c*. PLL is also utilized for the calculation of reference voltage [39–41].

8 Simulink Results (Comparison Using DVR and Statcom)

The voltage source converter is a dynamic voltage restorer illustrated in Fig. 8. The static synchronous compensator, as shown in Fig. 9, is a reactive power regulated device. The comparative results using two FACTS devices (DVR and STATCOM) are shown. Figure 10 illustrates the terminal voltage settling after transient without SRF Theory, and Fig. 11 illustrates the terminal voltage settling after transient with SRF Theory (Table 1).

9 Conclusion

An important characteristic that allows STATCOM to generate/consume active and reactive power is voltage modulus and angle independent regulation. Consumed and generated capacities were calculated and simulated, and the circular power chart was depicted. Through the circular power chart, it could be inferred that as the converter

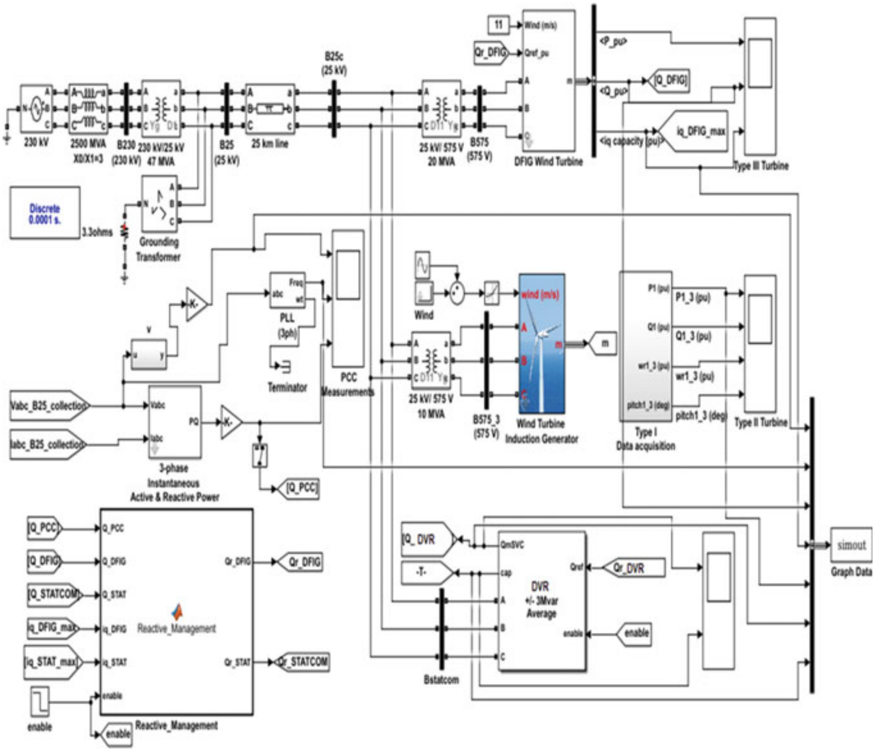

Fig. 8 Simulink model for fault detection using DVR

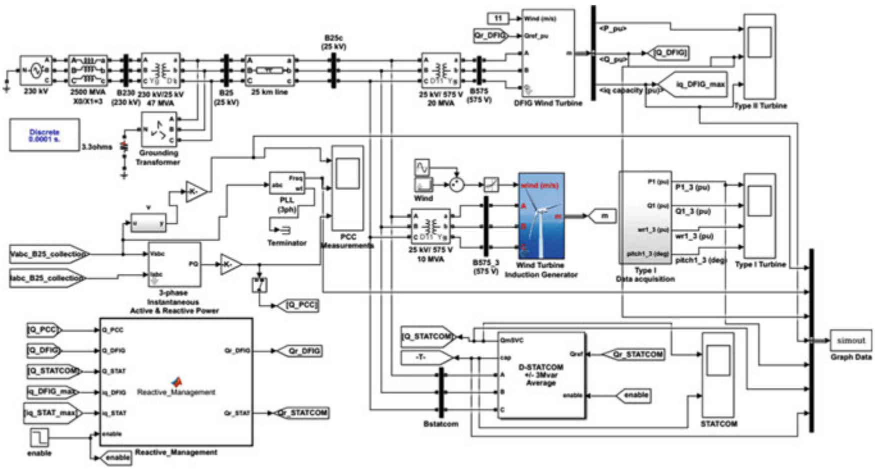

Fig. 9 Simulink model for fault detection using STATCOM

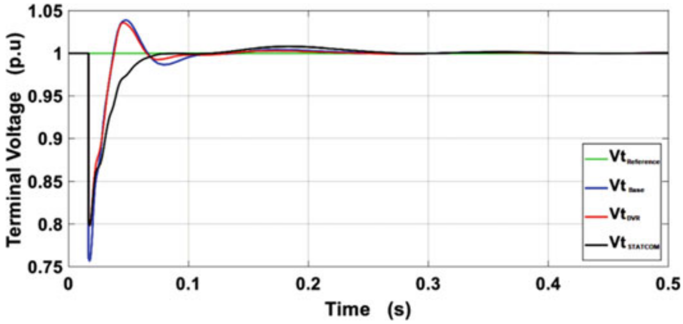

Fig. 10 Terminal voltage settling after transient without SRF theory

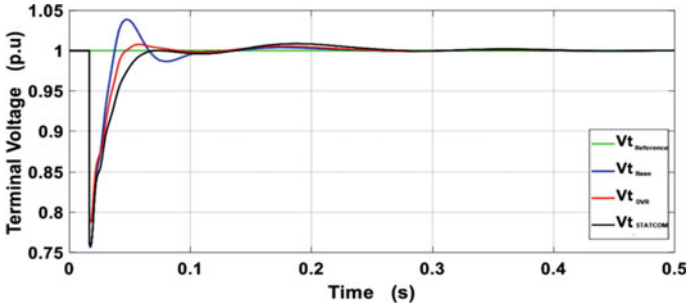

Fig. 11 Terminal voltage settling after transient with SRF theory

Table 1 LVRT capability settling times (in msec)

Controller	References	Base	DVR	STATCOM
Wind variation 4 m/s	[8]	12	11.3	11.04
Wind variation 8 m/s	[9]	12.5	12.8	11.2
Wind variation 12 m/s	[10]	13.5	13.7	12.7
Wind variation 16 m/s	[11]	14.5	13.9	13.3
Remark			Fast	Faster

voltage increases, the STATCOM consumed/generated power also does. Therefore, as converter voltage amplitude increases, so does power consumed or generated. This means power can be adjusted by modifying converter voltage values. Furthermore, regulation is done by changing the transistor control system's sinusoidal source phase.

References

1. Blaabjerg F, Chen Z (2006) Power electronics for modern wind turbines, 1st edn. Morgan and Claypool Publishers
2. Marques J, Pinheiro H, Grundling H, Pinheiro J, Hey H (2003) A servey on variable-speed wind turbine system. In: Proceedings of Brazilian conference of electronics of power, vol 1, pp 117–125
3. Chinchilla M, Arnaltes S, Burgos JC (2003) Control of permanent magnet generators applied to variable speed wind energy systems connected to the grid. In: IEEE power electronics specialist conference, MESC'03, June 2003, pp 748–753
4. Mayosky MA, Cancelo GIE (1999) Direct adaptive control fo wind energy conversion systems using Gaussian networks. IEEE Trans Neural Netw 10(4):898–906
5. Iyasere E, Salah MH, Dawson DM, Wagner JR, Tatlicioglu E (2012) Robust nonlinear control strategy to maximize energy capture in a variable speed wind turbine with an ınternal ınduction generator. J Control Theory Appl 10(2):184–194
6. Benchagra M, Maaroufi M, Ouassaid M (2012) Nonlinear MPPT control of squirrel cage ınduction generator-wind turbine. J Theoret Appl Inf Technol 35(1):26–33
7. Nguyen HM, Naidu DS (2012) Direct fuzzy adaptive control for standalone wind energy conversion systems. In: Proceedings of the world congress on engineering and computer science, San Fransisco, USA, Vol II, pp 994–999
8. Mayosky MA, Cancelo GIE (1999) Direct adaptive control of wind energy conversion systems using Gaussian networks. IEEE Trans Neural Netw 10(4)
9. Tao G (2003) Adaptive control design and analysis. Wiley, New York
10. Slotine JE, Li W (1991) Applied nonlinear control. Prentice Hall, Englewood Cliffs; Wang LX (1996) A course on fuzzy systems, 1st edn. Prentice Hall; Polycarpou MM (1996) Stable adaptive neural control scheme for nonlinear systems. IEEE Trans Autom Control 41(3):447–451
11. Ganthia BP, Barik SK (2020) Steady-state and dynamic comparative analysis of PI and fuzzy logic controller in stator voltage oriented controlled DFIG fed wind energy conversion system. J Inst Eng India Ser B 101:273–286
12. Ganthia BP, Barik SK, Nayak B (2020) Shunt connected FACTS devices for LVRT capability enhancement in WECS. Eng Technol Appl Sci Res 10(3):5819–5823
13. Honrubia-Escribano A, Jiménez-Buendía F, Gómez-Lázaro E, Fortmann J (2018) Field validation of a standard type 3 wind turbine model for power system stability, according to the requirements ımposed by IEC 61400-27-1. IEEE Trans Energy Convers 33(1):137–145
14. Sun L, Peng C, Hu J, Hou Y (2018) Application of type 3 wind turbines for system restoration. IEEE Trans Power Syst 33(3):3040–3051
15. Guest E, Jensen KH, Rasmussen TW (2018) Sequence domain harmonic modeling of type-IV wind turbines. IEEE Trans Power Electron 33(6):4934–4943
16. Hu J, Sun L, Yuan X, Wang S, Chi Y (2017) Modeling of type 3 wind turbines with df/dt ınertia control for system frequency response study. IEEE Trans Power Syst 32(4):2799–2809
17. Ganthia BP, Barik SK, Nayak B, Wind turbines in energy conversion system. Types Tech
18. Ko H-S, Yoon G-G, Kyung N-H, Hong W-P (2008) Modeling and control of DFIG-based variable-speed wind-turbine. Electr Power Syst Res 78(11):1841–1849
19. Ganthia BP, Agarwal V, Rout K, Pardhe MK (2017) Optimal control study in DFIG based wind energy conversion system using PI & GA. In: International conference on power and embedded drive control (ICPEDC), pp 343–347
20. Ganthia BP, Rana PK, Patra T, Pradhan R, Sahu R (2018) Design and analysis of gravitational search algorithm based TCSC controller in power system. Mater Today: Proc 5(1):841–847
21. Moghadasi A, Sarwat A, Guerrero JM, A comprehensive review of low-voltage ride through a methods for a fixed speed wind power generators. Renew Sustain Energy Rev
22. Siraj K, Siraj H, Nasir M (2014) Modeling and control of a doubly fed induction generator for grid integrated wind turbine. In: Power electronics and motion control conference and exposition (PEMC)

23. Kim H-W, Kim S-S, Ko H-S (2010) Modeling and control of PMSG-based variable-speed wind turbine. Electr Power Syst Res 80(1):46–52
24. Qiao W, Zhou W, Aller JM, Harley RG (2008) Wind speed estimation based sensorless output maximization control for a wind turbine driving a DFIG. IEEE Trans Power Electron 23(3):1156–1169
25. Ganthia BP, Mohanty M, Maherchandani JK (2022) Power analysis using various types of wind turbines. In: Fekik A, Benamrouche N (eds) Modeling and control of static converters for hybrid storage systems. IGI Global, Hershey, pp 271–286
26. Ganthia BP, Barik SK, Nayak B (2022) Comparative analysis of various types of control techniques for wind energy conversion system. In: Fekik A, Benamrouche N (eds) Modeling and control of static converters for hybrid storage systems. IGI Global, Hershey, pp 143–174
27. Ghennam T, Berkouk EM, Francois B (2009) Modeling and control of a doubly fed ınduction generator (DFIG) based wind conversion system
28. Ganthia B, Sahu S, Biswal S, Abhisekh A, Kumar Barik S (2019) Genetic algorithm based direct torque control of VSI fed ınduction motor drive using MATLAB simulation. Int J Adv Trends Comput Sci Eng 8(5):2359–2369
29. Ganthia BP (2020) Application of hybrid facts devices in DFIG based wind energy system for LVRT capability enhancements. J Mech Cont Math Sci 15(6):245–256
30. Ganthia BP (2020) Application of hybrid facts devices in DFIG based wind energy system for LVRT capability enhancements. J Mech Cont Math Sci 15(6):139–157
31. Prasad GB, Krishna R (2016) Deregulated power system based study of AGC using PID and fuzzy logic controller. Int J Adv Res 4:847–855
32. Ganthia BP, Aabhisikta A, Pradhan D, Pradhan A (2018) A variable structured TCSC controller for power system stability enhancement. Mater Today: Proc 5(1, Part 1):665–672. ISSN 2214-7853
33. Ganthia BP, Pritam A, Rout K, Singhsamant S, Nayak J (2018) Study of AGC in two-area hydro-thermal power system. In: Garg A, Bhoi A, Sanjeevikumar P, Kamani K (eds) Advances in power systems and energy management. Lecture Notes in Electrical Engineering, vol 436. Springer, Singapore
34. Ganthia BP, Pradhan R, Sahu R, Pati AK (2021) Artificial ant colony optimized direct torque control of mathematically modeled ınduction motor drive using PI and sliding mode controller. In: Kumar J, Jena P (eds) Recent advances in power electronics and drives. Lecture Notes in Electrical Engineering, vol 707. Springer, Singapore
35. Ganthia BP, Mohanty S, Rana PK, Sahu PK (2016) Compensation of voltage sag using DVR with PI controller. In: International conference on electrical, electronics, and optimization techniques (ICEEOT), pp 2138–2142
36. Ganthia BP, Barik SK, Nayak B, Low voltage ride through capability enhancement using series connected fact devices in wind energy conversion system. J Eng Sci Technol (JESTEC)
37. Jin K-M, Thinh QN, Kim E-H (2012) DVR control of DFIG for compensating fault ride-through based on stationary and synchronous reference frame. In: Proceedings of The 7th ınternational power electronics and motion control conference, Harbin, pp 3004–3009
38. Pires VF, Marques GD, Sousa D (2011) Phase-locked loop topology based on a synchronous reference frame and sliding mode approach for DVR applications. In: IEEE EUROCON—international conference on computer as a tool, Lisbon, 2011, pp 1–4
39. Satpathy SR, Pradhan S, Pradhan R, Sahu R, Biswal AP, Ganthia BP (2021) Direct torque control of mathematically modeled ınduction motor drive using PI-type-I fuzzy logic controller and sliding mode controller. In: Udgata SK, Sethi S, Srirama SN (eds) Intelligent systems. Lecture Notes in Networks and Systems, vol 185
40. Pragati A, Ganthia BP, Panigrahi BP (2021) Genetic algorithm optimized direct torque control of mathematically modeled induction motor drive using PI and sliding mode controller. In: Kumar J, Jena P (eds) Recent advances in power electronics and drives. Lecture Notes in Electrical Engineering, vol 707. Springer, Singapore
41. Ganthia BP, Pritam A, Rout K, Singhsamant S, Nayak J (2018) Study of AGC in two-area hydro-thermal power system. In: Garg A, Bhoi A, Sanjeevikumar P, Kamani K (eds) Advances in power systems and energy management. Lecture Notes in Electrical Engineering, vol 436

Chapter 33
Genetic Algorithm-Based Load Frequency Control of a Grid-Connected Microgrid in Presence of Electric Vehicles

Krosuru Anuradhika and Puja Dash

Abstract The frequency stability of the power system is becoming more serious with the increase in renewable energy penetration. Due to fast response and vehicle to grid capability, electric vehicles (EVs) are involved in improving the frequency stability of the power system. In this paper, hybrid generation consists of thermal power generation involving solar photovoltaic (PV), wind turbine generators (WTGs), geothermal power plant (GTPP) renewable generations and electric vehicle aggregators. An improvement in stability is achieved with different number of electric vehicles. Genetic algorithm (GA) with integral time absolute error (ITAE) performance indices as objective function is used to obtain the optimality of the controllers. The effects on transient behaviour of the microgrid is probed with PI, PID and GAPID controllers. Susceptibility analysis is executed on GAPID controller to prove the robustness under uncertainty conditions with both SLP and RLP.

Keywords Electric vehicle aggregator · Genetic algorithm · Load frequency control · Renewable energy systems

1 Introduction

In recent years, the demand for renewable energy power generation is increased in the aspect of conservation of environment and economic growth. Renewable energy generation is penetrated into the utility gird, but there is a disadvantage in the aspect of power system stability [1]. As the speed of the wind is variable in a day and also depends on the place, the power output and the frequency of the wind power plant is varying; the solar photovoltaic (PV) generation depends on the sun irradiance, which is not constant throughout the day causes output power and frequency of the PV generation to fluctuate.

K. Anuradhika (✉) · P. Dash
Department of EEE, Gayatri Vidya Parishad College of Engineering and Technology, Autonomous, Vishakhapatnam, India

G. Panda et al. (eds.), *Sustainable Energy and Technological Advancements*, Advances in Sustainability Science and Technology,
https://doi.org/10.1007/978-981-16-9033-4_33

Increase in the renewable energy generation in the grid leads the power system imbalance. So, the management of frequency in the microgrid is difficult with the frequent change in power generations. Also, the load is varying all the time in the power system which causes the power imbalance in the system [2]. Therefore, the frequency regulation is the major challenge for the development of microgrid. The reasonable solution for the difficulties with renewable energy usage is to integrate the microgrid with electric vehicles (EV). EVs served as the energy storage and their fast response due to the battery acts as a tool for demand response.

However, the highly robust controller with fast controlling ability plays a major role in the smooth performance of microgrids. Therefore, an adaptive frequency controller is urgently pursued to reduce the influence of various power imbalances. In [3], integration of conventional plants with plants. Integrating EV in the smart grid and different optimization techniques for the controlling of EV in hierarchy maintaining the LFC. In [4], a review of renewable energy sources interconnecting power plant and classical approach and innumerable optimization techniques. In [5], load frequency control problem is instantiated as the disturbance rejection along with system control. In [6], the interconnection of the output feedback derivation with decentralized PI controllers has been addressed for ensuring the systems stability. The geothermal system can also be considered as non-renewable energy sources and can also be included in AGC studies. For example [7, 8] the effect of integrating the geothermal plant with conventional plants in tie line power with sine–cosine algorithm for optimizing the controller parameters.

Integrating renewable energy sources reduces the power effect on the main grid [9] LFC of a hybrid generation solar, wind, thermal optimization of PID controller by bacterial foraging technique under various instabilities and uncertainties. In [10], the impact of solar photovoltaic system in grid-connected and its performance in transformer less mode under Indian ambient conditions. The wind power generation [11] is based on the grid demand. The pitch control is activated to maintain the rated value, when the extracted power exceeds the limits. The effects on wind and its controlling [12, 13]. The transient stability of the storage-based renewable energy generation power system is achieved with the application of overlapping decentralized decomposition controller. The effective control of real power generation of microgrid, proportional-integral (PI) controllers are implemented for wind turbine generators and distribution generation system so that the frequency deviation is minimized.

In order to maintain the stability in the power system due to the power deviations occurred by RESs. The robust performance of the controllers is necessary, so the electric vehicles are introduced for the load frequency control [14–16] which support the grid. So, Jia et al. in [17] the rapid development of vehicle to grid process and manageable loads of electric vehicles are considered as storage devices and supply systems. The effect of increasing the EVs on the frequency stability. The control plants considered are thermal and EV as aggregators. Generally, performance indices [18, 19] ITAE, ISE, IAE are used for the better performance in AGC studies. ITAE [17] is reducing the transient response of the system. For the better controller gains and ITAE value, Inthiyaz et al. [19] gains of PID are tuned with genetic algorithm.

From the brief literature studies, the robust and rapid performance in the frequency regulation is must; this paper develops an EV integrated microgrid with renewable energies wind, solar and geothermal plants along with the thermal power plant are taken. For the load frequency control, thermal plant, geothermal plant and EV aggregators with different number of elective vehicles are participated. The PI, PID control strategies are applied to the microgrid and the performance is improved with the soft computing technique, i.e. genetic algorithm (GA). GA with ITAE performance index as objective function is used to optimize the control parameters.

The remaining sections of the paper are organized as follows: Sect. 2 explains the detailed system configuration; Sect. 3 explains the optimization technique along with objective function. Section 4 presents the Result and analysis. The paper is concluded with Sect. 5.

1.1 Contribution

From the brief literature survey, the following contributions have been proposed in this paper:

1. Grid-connected microgrid with hybrid generation system consists of thermal power generation involving solar photovoltaic (PV), wind turbine generators (WTGs) and geothermal power plant (GTPP) has been studied with different combinations of EVs with the EV aggregator.
2. Area participation factor-based EV aggregator has been modelled with the presence of different numbers of EVs.
3. Genetic algorithm has been opted for optimizing the controller gains.
4. Dynamic analysis of the microgrid has been carried out with both SLP and RLP.

2 System Modellıng

The 12 MW capacity microgrid considered in this work is in grid-connected mode, having the thermal system [1], geothermal system [8], solar photovoltaic plant [2, 10], wind power plant [11] and electric vehicle aggregators [4, 17]. Base case has been considered here with 50% base loading with 1% SLP at 4 s. The system model is shown in Fig. 1.

3 Genetic Algorithm

Genetic algorithm is an evolutionary process which is based on the natural biological process. GA iteratively modifies the population called as chromosomes. It selects

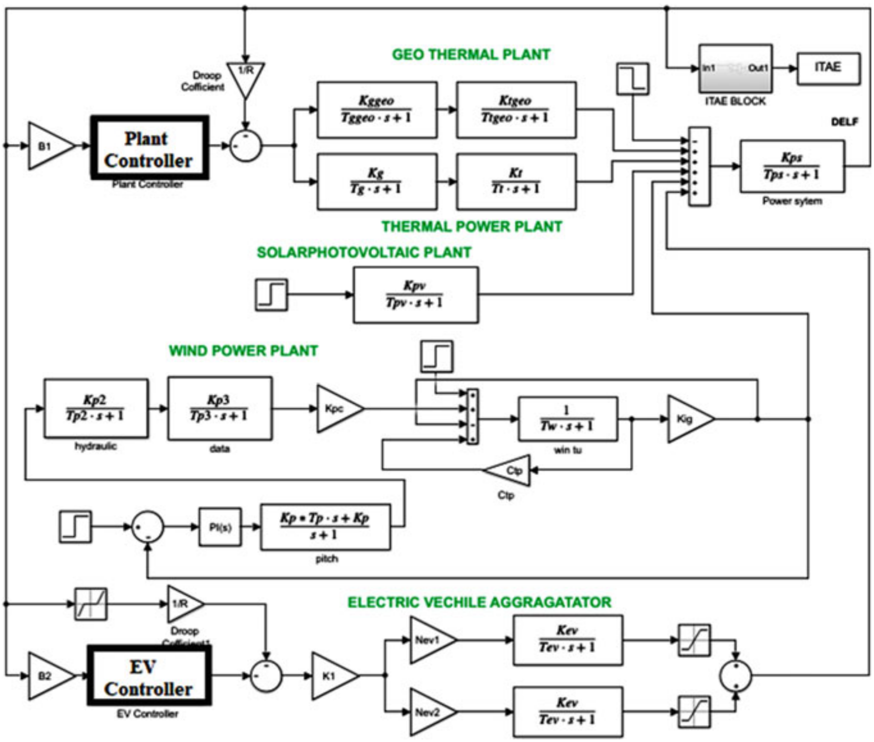

Fig. 1 System model

the individuals to be parents at random from the current population to produce children for the next generation. Process is continued until the minimum fitness value is obtained, through the selection, crossover and mutation. This is done for every iteration which is termed as generation. The fitness function is evolved through an objective function for each individual. Over successive iterations, the optimal solution has been obtained. Three main steps of GA are *Selection*, *Crossover and Mutation.*

***Objective Function*—**A fitness function qualifies the optimality of as solution (chromosome) so that the particular solution is ranked against all other solutions. A fitness function is derived from the objective function and is used in successive operations. The ITAE performance indices are taken as fitness function. The performance indices are given by the equations below,

$$\text{ITAE} = \int_{0}^{t} t|\Delta f|dt \tag{1}$$

$$\eta_{\varepsilon} = \frac{1}{\text{ITAE}} \tag{2}$$

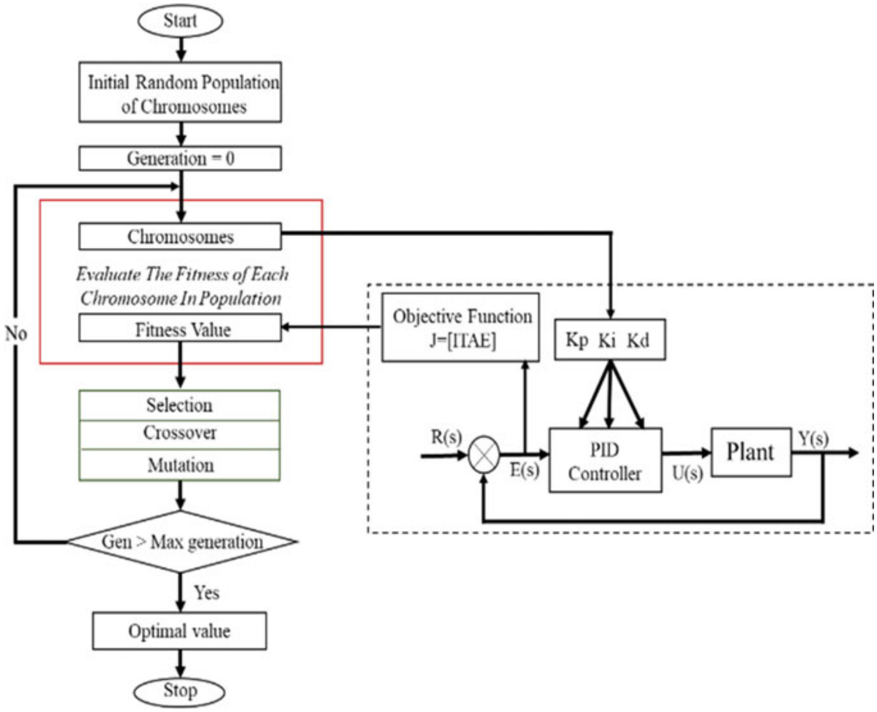

Fig. 2 Flow chart of genetic algorithm optimized PID controller

Table 1 GA parameter considered

.	.

The PID control parameters are optimized with the genetic algorithm, and the step-by-step process is represented with the flow chat in Fig. 2. Each chromosome consists of individual strings P, I, D terms. The chromosome is passed into the evaluation function. These PID values are inserted into the PID block and the simulation is executed. After running the simulation, the ITAE objective function is calculated and fitness values are evaluated (Table 1).

4 Simulation Results and Analysis

In this section, the performance of EVs in the grid connected microgrid. The plant is investigated separately without EVs and the effect of EVs integrating in the plant.

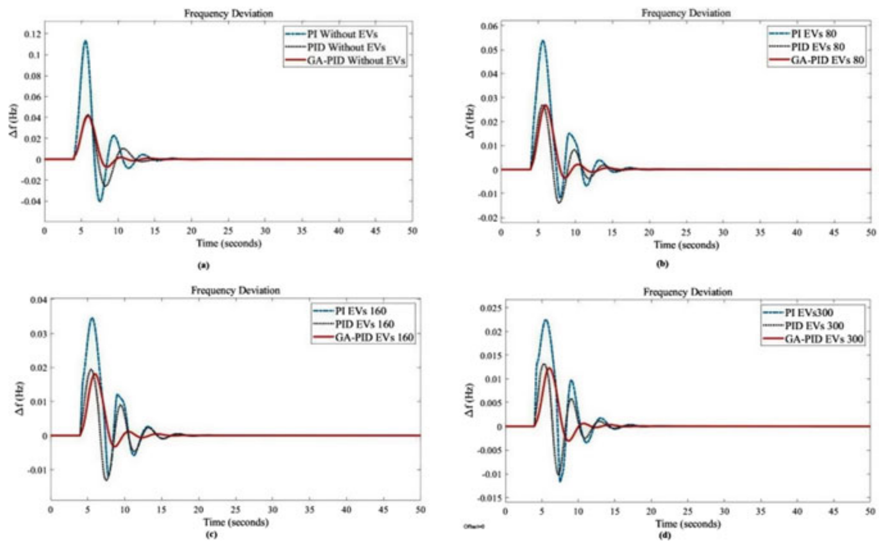

Fig. 3 Dynamic performance comparison with 1% SLP: **a** frequency deviation without EVs; **b** frequency deviation with 80 nos. of EVs; **c** frequency deviation with 160 nos. of EVs; **d** frequency deviation with 300 nos. of EVs

4.1 Performance Analysis of PI, PID and GA-PID Controllers Without and with EV Aggregators

The plant is investigated separately without EVs and the effect of EVs integrating in the plant. At 4 s, SLP 1% is applied and the frequency response is observed without presence and with the 80 ($N_1 = 30$, $N_2 = 50$) EVs, with 160 ($N_1 = 100$, $N_2 = 60$) EVs and with 300 ($N_1 = 100$, $N_2 = 200$) EVs. The dynamic responses corresponding to PI, PID (manually tuned) and optimized GA-PID controllers are attained and weighted up (Fig. 3). The settling time and the peak deviations are noted from Fig. 3 and shown in Table 2.

The comparison from the responses corresponding to GA-PID with 300 EVs has been improved the stability in comparison with other combinations with less settling time and the peak deviations.

4.2 Comparison of the System Performance at Random Load Pattern

Further, the system study has been carried out with random loading pattern (RLP) (shown in Fig. 4) for 150 s runtime. The corresponding dynamic responses has been shown on Fig. 5. The dynamic responses clearly evinced that the GA-PID controller in each case showing the better performance when compared to the others maintaining the long-term system stability.

Table 2 Values of setting time and peak deviations of Fig. 5

Controllers	PI			PID			GA-PID		
	T_{ST} (s)	M_{PO}	M_{PU} (−ve)	T_{ST} (s)	M_{PO}	M_{PU} (−ve)	T_{ST} (s)	M_{PO}	M_{PU} (−ve)
Figure 3a	20.91	0.1132	0.0397	20.79	0.0422	0.0252	17.32	0.0414	0.0072
Figure 3b	22.04	0.0537	0.0112	21.47	0.0269	0.0136	16.31	0.0268	0.0033
Figure 3c	20.3	0.0224	0.0113	20.4	0.0194	0.0126	16.1	0.0179	0.0029
Figure 3d	19.47	0.0224	0.0117	19.13	0.0131	0.0101	16.12	0.0122	0.0029

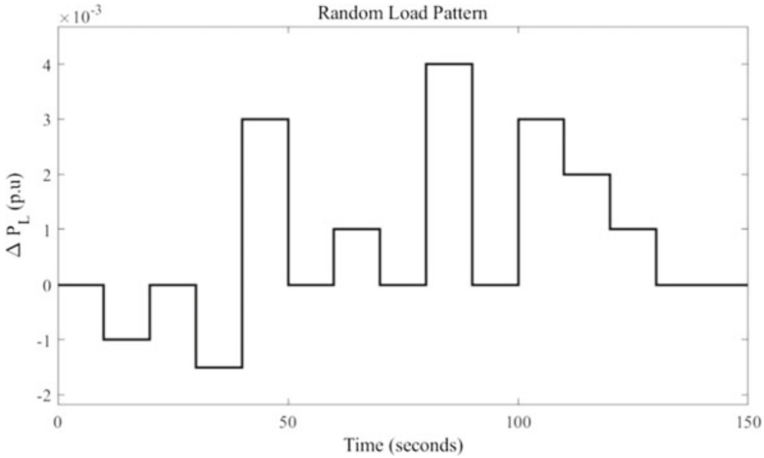

Fig. 4 Random load pattern (RLP) considered

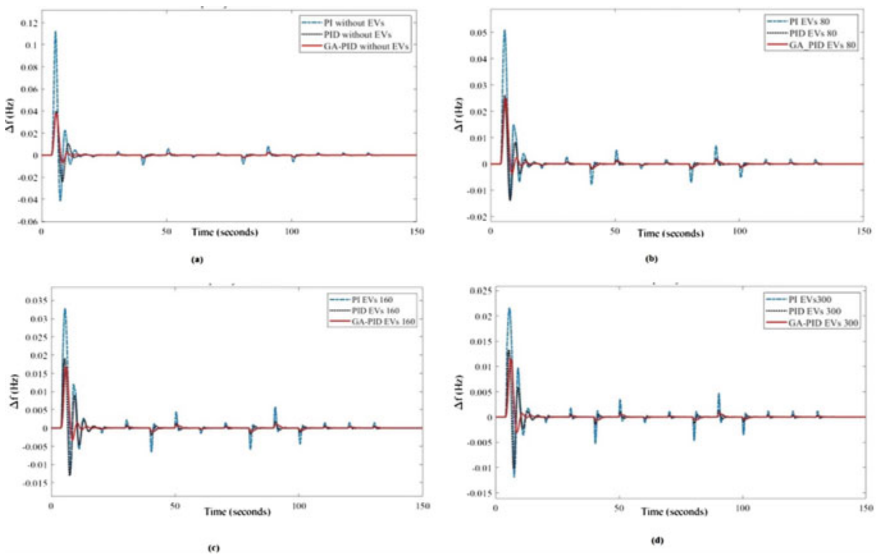

Fig. 5 Dynamic performance comparison with RLP: **a** frequency deviation without EVs; **b** frequency deviation with 80 nos. of EVs; **c** frequency deviation with 160 nos. of EVs; **d** frequency deviation with 300 nos. of EVs

4.3 Susceptibility Analysis of the Proposed Controller

Susceptibility analysis has been performed to observe the robustness of the optimum gains of GA-PID with 300 EVS at nominal loading conditions to an allowable changes in the magnitude of SLP (shown in Fig. 6) and corresponding peak deviations are

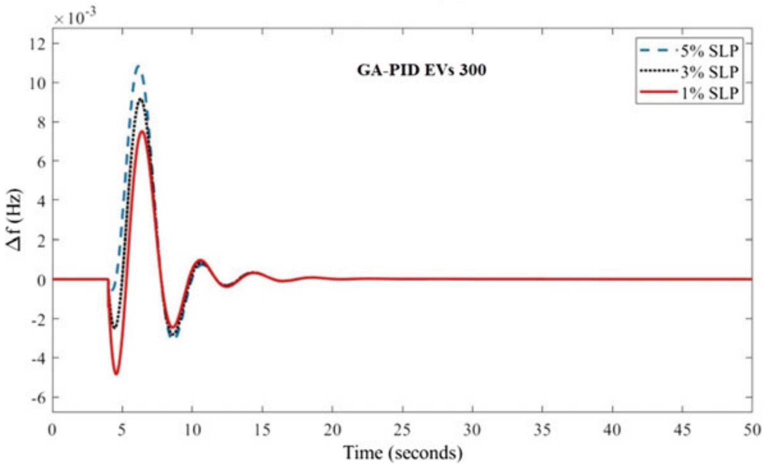

Fig. 6 $\Delta f(t)$ at 50% loading at 1%, 3%, 5% SLP with GA-PID with 300 EVs

noted in Table 3. Also, further study has been done with a wide changes in the system loading conditions (30 and 80% loadings) with RLP (shown in Fig. 7 and Table 4).

By observing the responses, it has been seen that the responses are presenting similarity in regaining the steady state after the observing the disturbance. This clearly indicated that the GA-PID controller can withstand with the wide system changes and maintain the system stability.

5 Conclusıons

In this paper, an effort is made to revamp the stability of a grid connected microgrid in presence of genetic algorithm. The individual PID controller is optimally designed for thermal power generation and electric vehicle aggregator using the genetic algorithm employing the ITAE-based fitness function. The GAPID controller has given better responses in terms of fast settling time, less overshoot and less undershoot and a smaller number of oscillations in comparison to PI and PID controllers. Increasing the number of EVs results in better load frequency control with the combination of GA-PID. From the sensitivity analysis, it has been observed that GA-PID controller in presence of SLP and RLP is robust.

Table 3 Values of setting time, peak overshoot and peak undershoot of Fig. 5

Controllers	1% SLP			3% SLP			5% SLP		
	T_{ST} (s)	M_{PO}	M_{PU} (−ve)	T_{ST} (s)	M_{PO}	M_{PU} (−ve)	T_{ST} (s)	M_{PO}	M_{PU} (−ve)
Figure 6	16.12	0.0122	0.0029	20.75	0.0090	0.0028	21.08	0.0075	0.00308

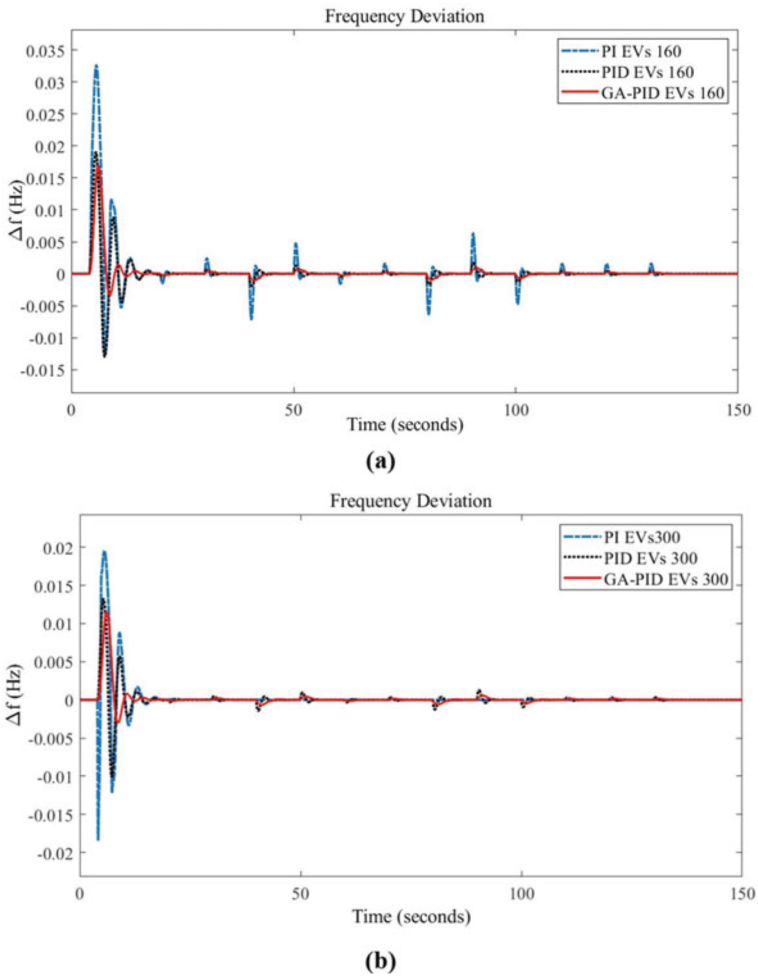

Fig. 7 Comparison of frequency deviation versus time at 50% loading with K^*_{Pi}, K^*_{Ii}, K^*_{Di}, **a** 30%; **b** 80% loading with RLP

Table 4 Gain parameters of the controllers

	Plant	Wind system	EV aggregator
EV^0	$G_{Kp} = -0.5090$	$G_{Kp} = -0.1942$	$G_{Kp} = 0.2646$
	$G_{Ki} = -0.7489$	$G_{Ki} = 0.1526$	$G_{Ki} = -0.1920$
	$G_{Kd} = 0.1038$	$G_{Kd} = 0.3199$	$G_{Kd} = 0.0033$
EV^{80}	$G_{Kp} = -0.5127$	$G_{Kp} = -0.1939$	$G_{Kp} = 0.2614$
	$G_{Ki} = -0.7456$	$G_{Ki} = 0.1518$	$G_{Ki} = -0.1938$
	$G_{Kd} = 0.1048$	$G_{Kd} = 0.3164$	$G_{Kd} = 0.0049$
EV^{160}	$G_{Kp} = -0.4546$	$G_{Kp} = -0.5966$	$G_{Kp} = 0.3522$
	$G_{Ki} = -0.8048$	$G_{Ki} = 0.2112$	$G_{Ki} = -0.5286$
	$G_{Kd} = 0.2561$	$G_{Kd} = 0.3522$	$G_{Kd} = -0.1187$
EV^{300}	$G_{Kp} = -0.4066$	$G_{Kp} = -0.5992$	$G_{Kp} = -0.4049$
	$G_{Ki} = -0.7101$	$G_{Ki} = 0.1968$	$G_{Ki} = -0.5454$
	$G_{Kd} = 0.2091$	$G_{Kd} = 0.3195$	$G_{Kd} = -0.0885$

Appendix

$K_{\text{ggeo}} = 0.05$, $T_{\text{tgeo}} = 0.1$, $K_{\text{g}} = 0.1$, $T_{\text{t}} = 0.3$, $K_{\text{pv}} = 1$, $T_{\text{pv}} = 1.8$, $K_{\text{pw}} = 1.3$, $T_{\text{pw}} = 1$, $K_{\text{i}} = 1.47$, $C_{\text{tp}} = 0.59$, $T_{\text{ev}} = 0.35$, $B_1 = 0.6$, $B_2 = 0.4$.

References

1. Elgerd OI (1982) Electric energy systems theory, an introduction, 2nd edn. McGraw Hill Book Company, New York
2. Kundur P, Balu NJ, Lauby MG (1994) Power system stability and control. McGraw-Hill, New York
3. Mu C, Liu W, Xu W (2018) Hierarchically adaptive frequency control for an EV-integrated smart grid with renewable energy. IEEE Trans Ind Inform 14(9):4254–4263
4. Pandey SK, Mohanty SR, Kishor N (2013) A literature survey on load-frequency control for conventional and distribution generation power systems. Renew Sustain Energy Rev 25:318–334
5. Aldeen M, Trinh H (1994) Load-frequency control of ınterconnected power systems via constrained feedback control schemes. Comput Electr Eng 20(I):71–88
6. Saxena S, Hote YV (2013) Load frequency control in power systems via internal model control scheme and model-order reduction. IEEE Trans Power Syst 28(3):2749–2757
7. Tasnin W, Saikia LC (2018) Comparative performance of different energy storage devices in AGC of multi-source system including geothermal power plant. J Renew Sustain Energy 10(2):1–11
8. Tasnin W, Saikia LC, Raju M (2017) Deregulated AGC of multi-area system incorporating dish-Stirling solar thermal and geothermal power plants using fractional order cascade controller. Int J Electr Power Energy Syst 101:1–11
9. Koley I, Bhowmik PS, Datta A (2017) Load frequency control in a hybrid thermal-wind-photovoltaic power generation system. In: 2017 4th international conference on power, control embedded systems, ICPCES 2017, pp 1–5

10. Datta A, Bhattacharya G, Mukherjee D, Saha H (2016) Modelling and simulation-based performance study of a transformer less single-stage grid-connected photovoltaic system in Indian ambient conditions. Int J Ambient Energy 37(2):172–183
11. Wu S, Wang Y, Cheng S (2013) Extreme learning machine-based wind speed estimation and sensor less control for wind turbine power generation system. Neurocomputing 102:163–175
12. Khayyer P, Özgüner Ü (2014) Decentralized control of large-scale storage-based renewable energy systems. IEEE Trans Smart Grid 5(3):1300–1307
13. Veronica AJ, Kumar NS, Gonzalez Longatt F (2020) Design of load frequency control for a microgrid using D-partition method. Int J Emerg Electr Power Syst 21(1):1–11
14. Pham TN, Trinh H, Van Hien L, Wong KP (2016) Integration of electric vehicles for load frequency output feedback H_∞ control of smart grids. IET Gener Transm Distrib 10(13):3341–3352
15. Vachirasricirikul S, Ngamroo I (2014) Robust LFC in a smart grid with wind power penetration by coordinated V2G control and frequency controller. IEEE Trans Smart Grid 5(1):371–380
16. Nguyen, Zhang HC, Mahmud MA (2014) Smart charging and discharging of electric vehicles to support grid with high penetration of renewable energy. IFAC Proc 47(3):8604–8609
17. Jia H et al (2018) Coordinated control for EV aggregators and power plants in frequency regulation considering time-varying delays. Appl Energy 210(2017):1363–1376
18. Ramakrishna KSS, Bhatti TS (2007) Sampled-data automatic load frequency control of a single area power system with multi-source power generation. Electr Power Comp Syst 35(8):955–980
19. Inthiyaz S, Nalli R, Rakesh, Subbarao TK, Ahammad SH, Rajesh V (2021) GA based PID controller: design and optimization. In: 2021 6th ınternational conference on ınventive computation technologies (ICICT), pp 285–289

Chapter 34
Multi-area Load Frequency Control Using a Novel PID-Based Sliding Mode Controller

Shobhit Nandkeolyar and Pravat Kumar Ray

Abstract In any power system, area load frequency control has become an important aspect. A robust and efficient controller is very much essential in today's complex power system. In this research work, output feedback sliding mode controller (OFSMC) is developed, and a novel sliding mode controller which is based on proportional integral derivative (PID) sliding surface (PID-SMC) has been designed to deal with the load-frequency control problem. A simple two-area interconnected non-reheat turbine model is considered. OFSMC is designed for the two-area system. For OFSMC, output feedback is considered as sliding surface. Teaching–learning-based optimization (TLBO) algorithm is utilized to optimize the parameters of the switching vector and the feedback gain. Dynamic response of OFSMC is compared with PI and PID controllers tuned with recent competitive algorithms. Performance improvement is observed with OFSMC controller. In order to achieve a significant improvement in the system performances, the above-mentioned hybrid PID sliding surface-based SMC is designed.

Keywords Multi-area control · Load frequency control · PID controller · Sliding mode controller · TLBO

1 Introduction

Power generation is used to transform natural energy into electrical energy. Three-phase AC power is one of the most economic means for transmission of power to far off places. A proper balance between the AC load demands and active as well as reactive power must be maintained while transmission. There is a shift in the stable operating point whenever either the system voltage or frequency varies. A properly operating system efficiently ensures the setting up the voltages and frequency at

S. Nandkeolyar (✉) · P. K. Ray
Department of Electrical Engineering, National Institute of Technology, Rourkela 769008, India

P. K. Ray
e-mail: rayp@nitrkl.ac.in

G. Panda et al. (eds.), *Sustainable Energy and Technological Advancements*,
Advances in Sustainability Science and Technology,
https://doi.org/10.1007/978-981-16-9033-4_34

required values even if there are random load changes [1]. Indeed, both active and reactive power cannot be sustained without regulation which may result in a shift in frequency and voltage. For restricting the voltages and frequency of the power system within a specified range, a control system needs to be in place for negating the consequence of any variation in overall load demand of the system. Since the active and reactive power has a cumulative effect on the system's voltages and frequency, the issue of regulating the voltages and frequency within specified limits can be eliminated. Frequency is primarily linked with the consumption and demand of active power, whereas the system's voltage is primarily linked to the reactive power [2–5]. Consequently, the power systems control problem may be classified into two separate problems. Load frequency control (LFC) is the control of frequency through active power. Even for varying active power consumption, the LFC's main role is to maintain a constant value of frequency under unknown outer disturbances [6–9].

A significant role of LFC is the power exchange error. A power system usually consists of multiple generating units. The generating units are attached by tie-lines to increase the fault tolerance of the overall power system. An additional error is created due to tie-line power in the control problem, and it is called the power exchange error in a tie-line [10]. When the active power load switches instantly in an area, it gains energy from other areas by means of tie-lines. The area subjected to the load shift should gradually balance it with no outer assistance; otherwise, economic disputes would arise among the areas. This is why every area needs a LFC separately to monitor the tie-line power exchange error for allowing the setpoints to be different for all the areas in a connected system [11–14]. In short, the LFC is responsible for two main functions: maintaining the optimal frequency value and also maintaining the power exchange under schedule in case of a change of load. Besides, unknown outer interruptions and system models and parameter variations must not influence the LFC [15].

OFSMC (Output Feedback Sliding Mode Controller) and PID (Proportional-Integral-Derivative) surface Sliding Mode Controller (SMC) control system regulates the turbines used to tune the generators; and the steady systems' frequency errors are also minimized by tuning the feedback gains, switching vector for OFSMC, and PID constants for PID sliding surface SMC. To optimize the above values of OFSMC and PID sliding surface SMC for the LFC of an interconnected multi-area power system, teaching–learning-Based optimization (TLBO) algorithms have been used. In this study, TLBO is used for its simplicity, and the algorithm is quite indifferent toward the size of the problem. With its implementation, large nonlinear optimization problems can be solved effectively.

It is evident form the above literature review that several studies have been carried out on SMC. Some research was carried out on PID sliding surface SMC and was successfully applied to electromechanical plants [16] and electro-hydraulic actuator [17]. But it has not been applied on load frequency control. This motivated us to delve into the designing of a robust PID sliding surface SMC for LFC. So, the contribution of this research work is the designing of a PID sliding surface-based SMC for a two-area power unit, developing an OFSMC for the same two-area system, optimization of the parameters of the above-mentioned controllers using TLBO algorithm, comparing the results of these controllers to TLBO optimized PID controller.

The rest portion of the paper is arranged as mentioned: Sect. 2 presents detailed information about OFSMC and PID sliding surface SMC for a two-area power system network in combination with TLBO for tuning the relevant parameters of the above controllers. Section 3 describes the OFSMC and PID sliding surface SMC performance assessment in a two-area power system. Section 5 concludes the entire research work of the paper. In addition, the scope for future work and potential extension is discussed.

2 Proposed Sliding Mode Controller

In the early 1960s, the SMC controller was developed, and the fundamental principle of which is derived from variable control of the structure. The nonlinear SMC control has been proven to be able to sustain control stability in different models which are exposed to device parameter changes and disturbances, because of its ability; SMC has been applied widely in several engineering applications, including load frequency systems [18], permanent magnet synchronous motor's velocity control, electromechanical system, etc.

The most significant step in the evolution of SMC control is the sliding surface structure that is required to attain the expected control criteria. The control signal to the sliding surface should remain on the surface and slide to the point of origin, i.e., the desired location. It has been shown in Fig. 1.

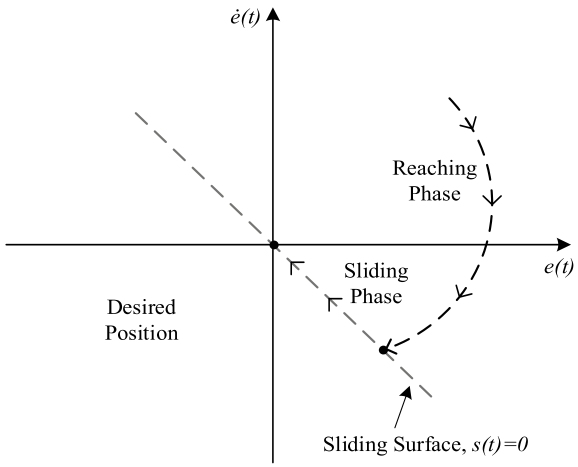

Fig. 1 Design of sliding mode control (SMC) structure

The difference between the actuator's actual location and the required direction trajectory results in the tracking error which is represented as

$$e(t) = X_r(t) - X_P(t) \tag{1}$$

where

$X_r(t) =$ Actual actuator value.

$X_d(t) =$ Desired value.

The SMC control law is represented by Eq. 2 as

$$\hat{u} = u_{eqv} + u_{sw} \tag{2}$$

where

$u_{eqv} =$ equivalent control law.

$u_{sw} =$ switch control law.

A sign function is used for switch control law and is given as

$$u_{sw} = \omega * s(t) + k * \text{sign}(s(t)) \tag{3}$$

where

$\omega =$ positive constant.

$k =$ positive controller gain for switch controller.

$s(t) =$ sliding surface.

$$sign(s(t)) = \begin{cases} 1 & \text{if } s(t) > 0 \\ 0 & \text{if } s(t) = 0 \\ -1 & \text{if } s(t) < 0 \end{cases}$$

In this work, a hybrid approach has been introduced where PID sliding surface is utilized in tandem with SMC for performing load frequency control. The proposed sliding surface($s(t)$) is given as

$$s(t) = K_P \Delta x_i(t) + \frac{K_I}{s} \int \Delta x_i(t) + K_D s \frac{\mathrm{d}}{\mathrm{d}t} \Delta x_i(t) \tag{4}$$

where the subscript of gain *K,* namely *P*, *I* and *D,* stands for proportional, integral and derivative.

For area LFC, $\Delta x_i = \Delta f_i$.

Two-area LFC system is first mathematically expressed.

For area 1, Eq. 4 may be modified as

$$s_1(t) = K_{p1}\Delta x_1(t) + \frac{K_{I1}}{s}\int \Delta x_1(t) + K_{D1}s\frac{\mathrm{d}}{\mathrm{d}t}\Delta x_1(t) \tag{5}$$

As the system considered is a third-order system, sliding surface for area 1 is given as

$$\ddot{s}_1(t) = K_{P1}\Delta\ddot{x}_1(t) + \frac{K_{I1}}{s}\Delta\dot{x}_i(t) + K_{D1}\Delta\dddot{x}_1(t) = 0 \tag{6}$$

Using these equations, SMC control law was derived in simulation and was applied to a two-area control system.

2.1 Output Feedback Sliding Mode Controller

The system which has been considered for this research work can be expressed mathematically as follows:

$$\dot{X} = AX + BU \tag{7}$$

$$y = CX \tag{8}$$

Here, X represents the state vector having dimension n, and y represents the output vector having dimension k. A is the system matrix, while B is the input matrix of order $[n \times n]$ and $[n \times m]$, respectively; C is a matrix of order $[k \times n]$; U represents the control vector of dimension m.

In this work, frequencies Δf_1, Δf_2 and area control errors which are represented by ACE_1, ACE_2 have been taken as the output feedback states. The simplified diagram of output feedback sliding mode controller (OFSMC) has been illustrated in Fig. 2.

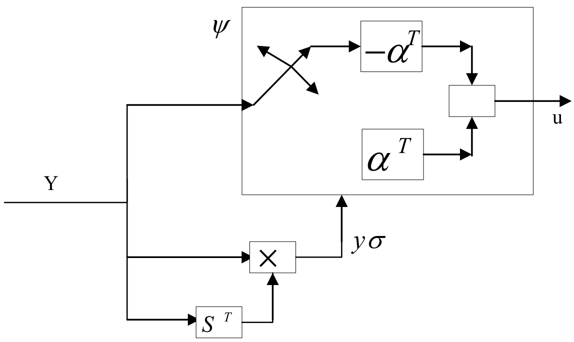

Fig. 2 Block diagram of OFSMC

The SMC control law (u_i) for the power system under consideration is expressed as

$$u_i = -\psi_i y = -\Sigma \psi_{ij} y_j \tag{9}$$

where

$$\psi_{ij} = \begin{Bmatrix} \alpha_{ij} & \text{if } y_j \sigma_i > 0 \\ -\alpha_{ij} & \text{if } y_j \sigma_i < 0 \end{Bmatrix} \tag{10}$$

and

$$\sigma_i = S_i y \tag{11}$$

where

S is the switching vector.

The parameters of OFSMC, i.e., the switching vectors and the feedback gains (α_{ij}) are optimized by the TLBO algorithm.

2.2 Teaching–Learning-Based Optimization (TLBO) Algorithm

TLBO is a recently introduced meta-heuristic algorithm. A similar technique for nonlinear optimization problems has been introduced here in this research work to achieve the solution with greater efficiency and reduced computational burden. The basic principle of operation of TLBO algorithm is the teaching and learning theory. Teachers will surely have an influence on the outcome of learners in a classroom. TLBO approach is focussed on this aspect. In this sense, the grades or outcomes are taken into account. The teacher is normally a highly educated person who imparts her/his experience with their learners. The teacher's level influences the learners' output. Learners get better grades or marks when a good teacher teaches them. Not only that, they also benefit by interacting with their peers. This is very beneficial for improving their performance.

An entire learner's category or class is considered as a population as this is an algorithm based on population, while the grade points of various subjects being taught to the learners constitute the solution vector for the optimization problem. In other population-based approaches, a student's outcome is equivalent to the fitness function, which represents the supremacy of the solutions. TLBO is an effective method of optimizing the nonlinear objective problems. Since fewer computations are needed for updating the solutions, this algorithm is faster. The algorithm's entire process is analyzed by splitting it into two stages, i.e., learner phase and teacher phase.

In the teacher phase, students are inspired by the influence of the highly qualified teacher, and their knowledge is enhanced.

By this process, teacher enhances the academic performance of their students. During the learner process, students enhance their academic performance not only by learning from their teacher but also gain knowledge by mutual interacting with their batchmates. The student's final assessment is made based on their academic performance. Figure 3 displays the flowchart of TLBO.

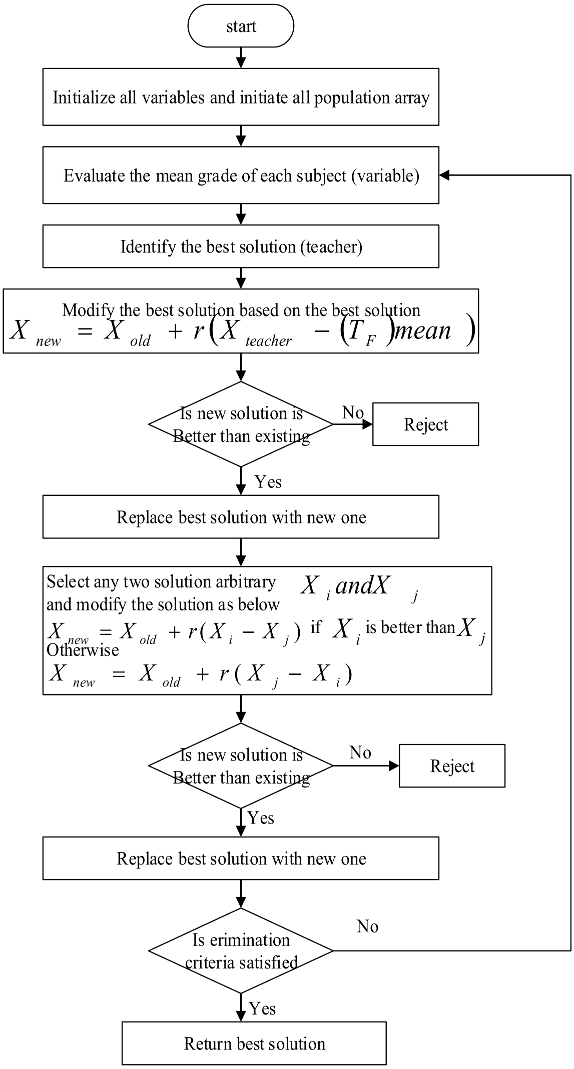

Fig. 3 Flowchart diagram for TLBO

2.3 Objective Function

The optimization is aimed at adjusting the parameters. The objective function is nothing but the integral time absolute error (ITAE) criteria. It is a function of time and error. Here, the emphasis is on the ITAE criterion's minimization. Here, the objective function has been represented by *j*. For the LFC of a two-area system, the ITAE comprises change in frequency and the tie-line power. Here, the objective function can hence be defined as

$$j = \int_{0}^{\infty} t((|\Delta f_1|)+(|\Delta f_2|) + \Delta P_{\text{tie}}) \tag{12}$$

3 Simulation Results

The system configuration which has been considered here in the current work is a two-area system. It was tested in the MATLAB/Simulink environment. Appendix gives the data regarding the relevant parameters. The objective function was formulated and utilized in the proposed algorithm, for optimization. The entire operation was iterated for every individual present within the population. All the parameters must be defined for implementing TLBO. Initially, the size of the population and the maximum iteration count was set at $NP = 150$ and $Z = 120$, respectively, for this study.

The above parameters were varied, and it was observed that superior solutions were achieved when $NP = 100$ and when the total iteration count was set at 100. Any increase in the population size *NP* and total iteration count required for convergence over 100 will marginally increase solution precision, to the downside of considerably increasing the computation time. By utilizing the objective function *j*, the optimum values of the feedback gains and the switching vector were found out.

3.1 Performance Analysis

A two-area, non-reheat thermal system has been considered for this study. The nominal parametric values of the system under consideration are presented in the appendix. Optimal OFSMC and PID-SMC controllers are designed for the system, and the TLBO technique is used to tune the parameters of the controllers. The results are compared with the hBFOA-PSO, PSO and BFOA techniques [12–14] in order to establish the effectiveness of the controller.

The system's performance is analyzed by employing a 10% step change in the load demand of area 1. The values of the switching vector and feedback gain parameters are taken from Eqs. 13 and 14, respectively. As seen from Table 1, the improvement in

Table 1 Comparative system performances of proposed method (OFSMC) for the system after 10% SLP in area-1

Optimization techniques	Δf_1			Δf_2			ΔP_{tie}			ITAE
	OS × 10^{-3}	US	ST	OS × 10^{-3}	US	ST	OS × 10^{-3}	US	ST	
hBFOA-PSO	250	–	5.05	210	–	4.39	80	–	4.8	3.34
BFOA	240	–	5.32	190	–	6.22	70	–	5.72	1.53
PSO	240	–	5.46	190	–	6.31	70	–	4.95	1.55
TLBO	22.9	−0.25	7.08	15.4	−0.19	7.13	0.994	−0.06	5.63	0.8597
OFSMC	41.5	−0.11	4	40.5	−0.09	4.21	4.3	−0.03	3.1	0.2927

the objective function is 91.23%, 80.86%, 81.11% and 65.95% compared to hBFOA-PSO, BFOA, PSO and TLBO optimized PI controller, respectively. The performance of the system in terms of settling time (ST), overshoot (OS) and undershoot (US) of area frequency error at area 1, area 2 and tie-line power is mentioned in Table 1. As seen from Table 1, the settling time of TLBO optimized OFSMC controller is minimum when compared to other techniques considered in this research work. The percentage improvement of settling time at area 1 with TLBO optimized OFSMC is 20.79%, 24.81%, 26.73% and 43.50% compared to hBFOA-PSO, BFOA, PSO and TLBO optimized PI controller, respectively, which indicates the good performance of the proposed OFSMC. Similarly, the settling time improvement at area 2 with TLBO optimized OFSMC is 4.1%, 32.31%, 33.28% and 40.95%, and for tie-line power, the settling time improvement is 35.41%, 45.80%, 37.37% and 44.93% as compared to hBFOA-PSO, BFOA, PSO and TLBO optimized PI controller, respectively.

Dynamic system performances with 10% step load change are shown in Fig. 4a–c. Minimum oscillation and less settling time are attained with TLBO optimized OFSMC controller as observed from Fig. 4a–c, compared to other techniques considered.

$$\begin{aligned} &S_{11} = 0.47;\ S_{12} = 0.35;\ S_{13} = 0.37;\ S_{14} = 0.38; \\ &S_{21} = 0.25;\ S_{22} = 0.97;\ S_{23} = 0.66;\ S_{24} = 0.50 \end{aligned} \tag{13}$$

$$\begin{aligned} &\alpha_{11} = 0.19;\ \alpha_{12} = 0.10;\ \alpha_{13} = 0.88;\ \alpha_{14} = 0.36; \\ &\alpha_{21} = 0.45;\ \alpha_{22} = 0.064;\ \alpha_{23} = 0.85;\ \alpha_{24} = 0.27 \end{aligned} \tag{14}$$

In the previous analysis, it is observed that even though the settling time and oscillations are reduced, overshoots and undershoots are more when compared to tuned PI controller. So, to further improve the system performance, PID sliding surface SMC is designed. TLBO algorithm is employed in order to find the optimal values for the parameters of PID-SMC controller. The optimally tuned PID-SMC gains are mentioned in Eq. 15. The improvement in the ITAE objective function of 43.25% and 49.57% is obtained with TLBO optimized PID-SMC as compared to TLBO optimized OFSMC and PID controller. The information about the system performance with PID-SMC in terms of settling time (ST), overshoot (OS) and undershoot (US) of area frequency and tie-line power are mentioned in Table 2. It is observed from Table 2 that minimum values of settling time (ST), overshoot (OS) and undershoot (US) are obtained compared to TLBO optimized OFSMC and PID controller. The settling time improvement is 45%, 54.16% for Δf_1; 19.23%, 33.33% for Δf_2; and 3.87%, 3.76% for tie-line power as compared to TLBO optimized OFSMC and PID controller. The overshoot improvement is 99.18%, 94.63% for Δf_1; 95.11%, 17.5% for Δf_2; and 51.16%, 76.13% for tie-line power as compared to TLBO optimized OFSMC and PID controller. Similarly, the undershoot improvement is 76.64%, 62.19% for Δf_1; 80.18%, 42.05% for Δf_2; and 84.26%, 54.61% for tie-line power as compared to TLBO optimized OFSMC and PID controller.

The dynamic system performances are depicted in Fig. 5a–c. It can be observed

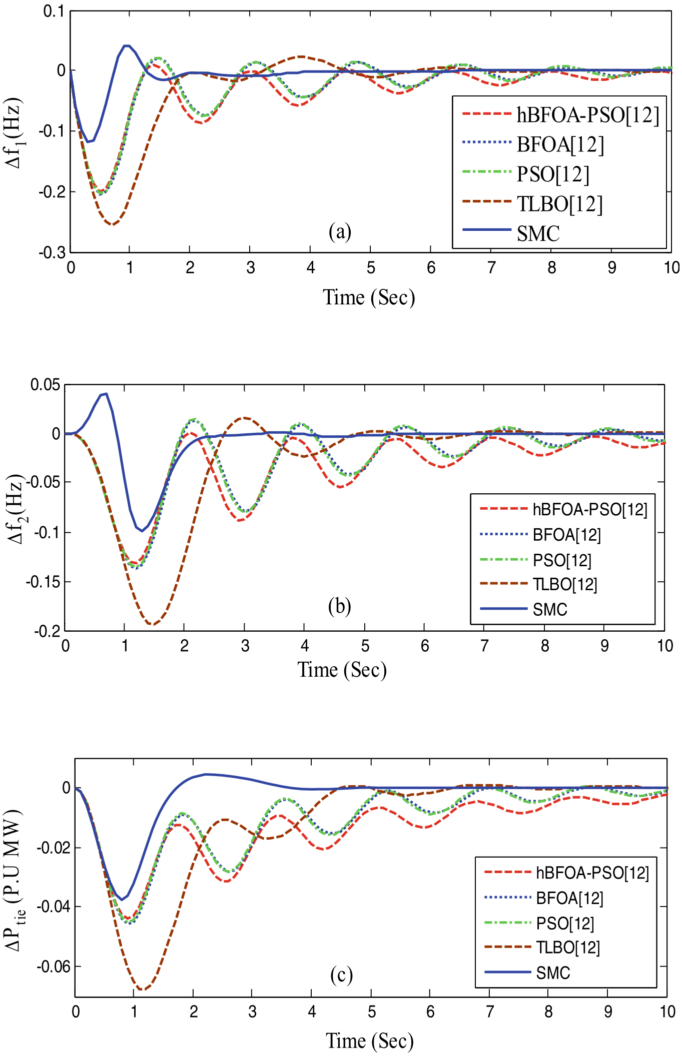

Fig. 4 Dynamic performance of the system with 10% SLP at area-1 using OFSMC, **a** Δf_1 versus time, **b** Δf_2 versus time and **c** ΔP_{tie} versus time

Table 2 Comparative system performances of PID-SMC for the system after 10% SLP in area-1

Optimization techniques	Δf_1	Δf_2	ΔP_{tie}	ITAE
	ST	ST	ST	
TLBO-PID	4.84	5.13	3.03	0.2452
OFSMC	4	5	3.1	0.2927
PID-SMC	2.2	3.4	2.98	0.1661

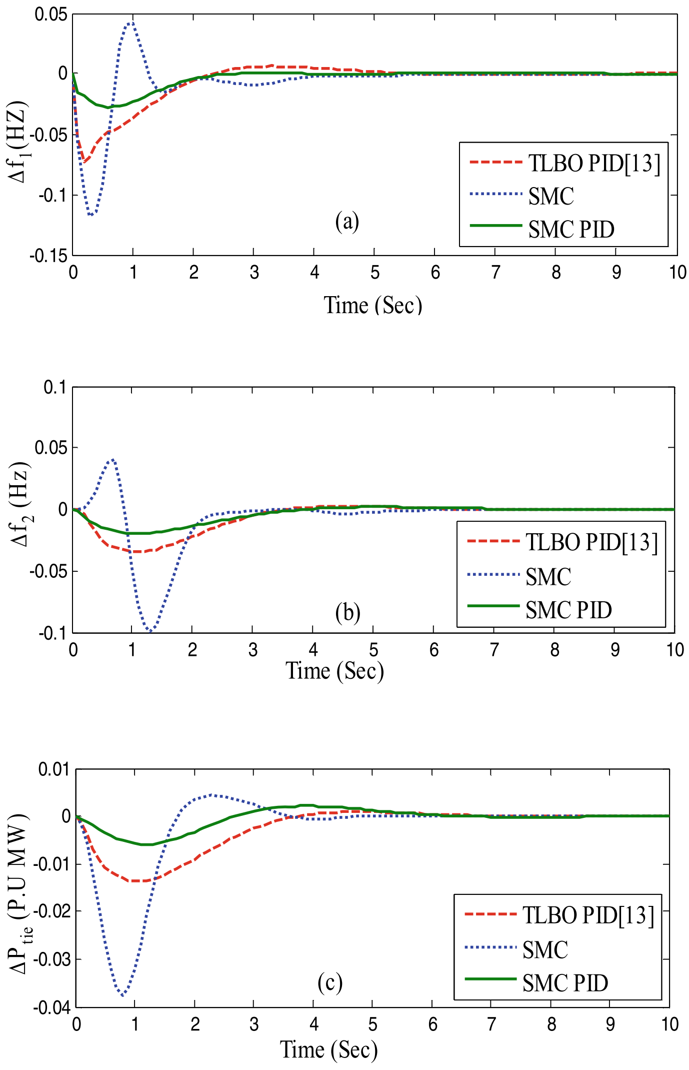

Fig. 5 Dynamic performance of the system with 10% SLP at area-1 using SMCPID, **a** Δf_1 versus time, **b** Δf_2 versus time and **c** ΔP_{tie} versus time

from Fig. 5a–c that minimum number of oscillations and less overshoots are achieved with TLBO optimized PID-SMC than compared to SMC and PID controller.

$$K_{P1} = 1.99;\ K_{P2} = 1.53;\ K_{I1} = 2.59;\ K_{I2} = 1.53;\ K_{D1} = 0.99;$$
$$K_{D2} = 1.32;\ K_1 = 0.024;\ K_2 = 0.029;\ \omega_1 = 1.60; \tag{15}$$

The frequency deviation responses Δf_1, Δf_2 and tie-line power deviation (ΔP_{tie}) for 10% step load change in area-1 with variation in governor time constant (T_g) are shown in Fig. 6a–c, respectively. The frequency deviation responses Δf_1, Δf_2 and tie-line power deviation (ΔP_{tie}) for 10% step load change in area-1 with variation in turbine time constant (T_t) at area-2 are shown in Fig. 7a–c, respectively.

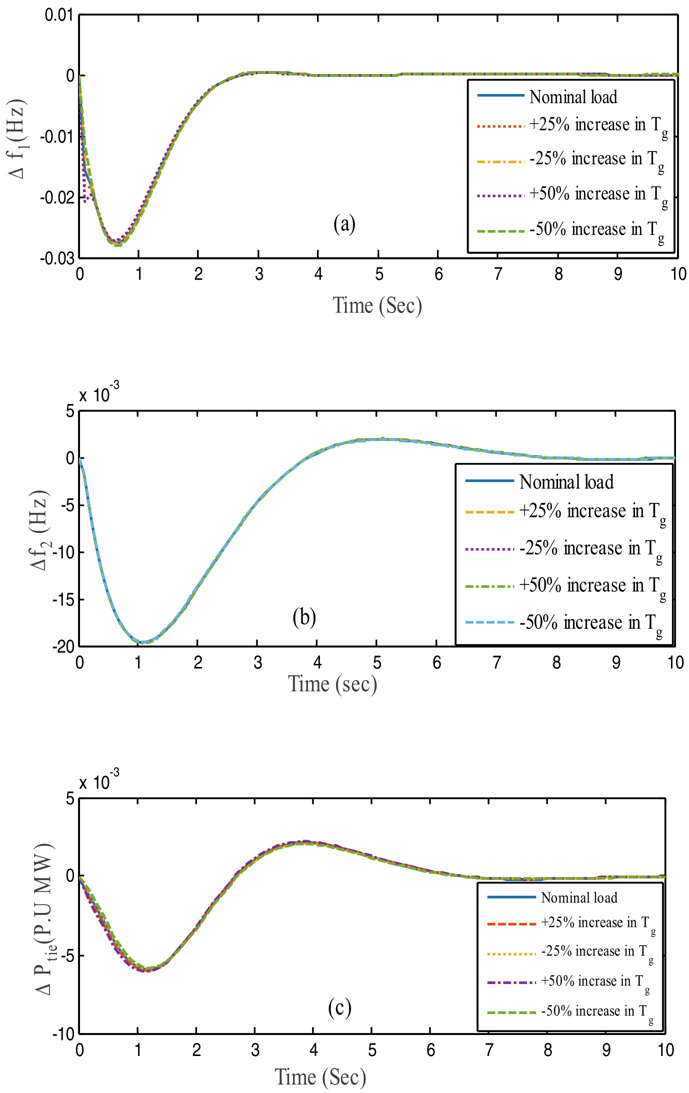

Fig. 6 Performance of the system with 10% SLP by varying governor time constant (T_g), **a** Δf_1 versus time, **b** Δf_2 versus time and **c** ΔP_{tie} versus time

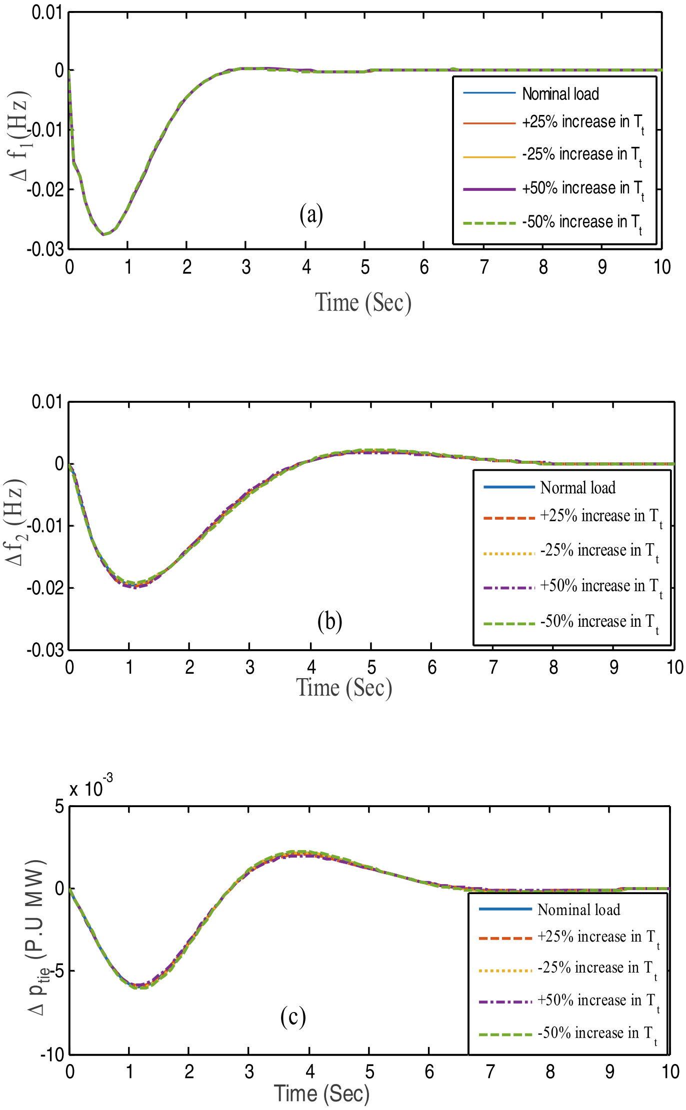

Fig. 7 Performance of the system with 10% SLP by varying turbine time constant (T_t), **a** Δf_1 versus time, **b** Δf_2 versus time and **c** ΔP_{tie} versus time

4 Conclusion

In this paper, a SMC with PID sliding surface was designed for load frequency control in a two-area system. The mathematical model of the system consisting of non-reheat type turbine considered in this research work has been provided. Mathematical modeling of governor, turbine, power system, tie-line power and ACE has been presented. Thereafter, OFSMC is designed. Variation of frequency and ACE of both the areas are taken as inputs to the controller. The switching vector and feedback gain values are tuned with TLBO. After developing OFSMC, hybrid PID-SMC is designed. The equivalent control input for the controller is derived mathematically and implemented through simulation. Result analysis is done by comparing the performance of PID sliding surface SMC with TLBO tuned PID controller and OFSMC. In future work, PID sliding surface SMC with generation rate constant given to turbine can be designed. The controller can then be modified by considering multi-generating non-renewable and renewable sources in each area.

Appendix

$T_{g1}, T_{g2} = 0.08s$; $T_{t1}, T_{t2} = 0.03s$; $T_{p1}, T_{p2} = 20s$; $K_{p1}, K_{p2} = 120$; $B_1, B_2 = 0.454$

$R_1, R_2 = 2.4\,\mathrm{MW/Hz}$, $T_{12} = 0.545$.

References

1. Ibraheem, Kumar P, Kothari DP (2005) Recent philosophies of automatic generation control strategies in power systems. IEEE Trans Power Syst 20(1):346–357
2. Bevrani H (2009) Robust power system frequency control, vol 85. Springer, New York
3. Bevrani H, Hiyama T (2011) Intelligent automatic generation control. CRC Press, New York
4. Juang C, Lu C (2006) Load-frequency control by hybrid evolutionary fuzzy PI controller. IEE Proc Gener Transm Distrib 153(2):196–204
5. Tang L, McCalley J (2016) Two-stage load control for severe under-frequency conditions. IEEE Trans Power Syst 31(3):1943–1953
6. Dhamanda A, Bhardwaj AK, Automatic generation control in three area interconnected power system of thermal generating unit using evolutionary controller
7. Guha D, Roy P, Banerjee S (2017) Quasi-oppositional symbiotic organism search algorithm applied to load frequency control. Swarm Evol Compu 33:46–67
8. Kumar N, Gupta V, Kakkar S, Tanwar A, Goyal S (2012) Integral and optimal AGC of 3 area interconnected power systems and modifications in UI mechanism. In: Power India conference. IEEE, pp 1–6
9. Sanjiv JK, Bhargava A, Pal RK (2015) Three area power system load frequency control using fuzzy logic controller. In: International conference on computer, communication and control (IC4). IEEE, pp 1–6
10. Das D, Kothari ML, Kothari DP, Nanda PJ, Variable structure control strategy to automatic generation control of interconnected reheat thermal system. In: IEE Proceedings D-control theory and applications, vol 6, pp 579–585
11. Lekshmi RR, Balamurugan S, Sasi KK (2016) Decentralized automatic generation control strategy for a three area bilateral power market. In: IEEE biennial international conference on power and energy systems: towards sustainable energy (PESTSE), pp 1–6
12. Shiva CK, Shankar G, Mukherjee V (2015) Automatic generation control of power system using a novel quasi-oppositional harmony search algorithm. Int J Electr Power Energy Syst 73:787–804

13. Sahu RK, Panda S, Rout UK, Sahoo DK (2016) Teaching learning based optimization algorithm for automatic generation control of power system using 2-DOF PID controller. Int J Electr Power Energy Syst 77:287–301
14. Jianping G, Dong L (2015) Sliding mode based load frequency control for a two-area interconnected power system. Int J Intell Control Syst 20(1):16–25
15. Hosseinnia S, Hassan IT, Vinagre BM, Sierociuk D (2012) Boolean-based fractional order SMC for switching systems: application to a DC-DC buck converter. Sig Image Video Process 1–7
16. Al-Hamouz Z, Al-Duwaish H, Al-Musabi N (2011) Optimal design of a sliding mode AGC controller: application to a nonlinear interconnected model. Electr Power Syst Res 81(7):1403–1409
17. Zhang B, Pi Y, Luo Y (2012) Fractional order sliding-mode control based on parameters auto-tuning for velocity control of permanent magnet synchronous motor. ISA Trans 51(5):649–656
18. Delavari H, Ghaderi R, Ranjbar A, Momani S (2010) Fuzzy fractional order sliding mode controller for nonlinear systems. Commun Nonlinear Sci Num Simul 15(4):963–978

Chapter 35
An EPO Tuned Cascaded 3DOFPIDN-FFOPID Controller for Frequency Regulation in DGR-FACTs Integrated Power System

Sunita Pahadasingh, Chitralekha Jena, Chinmoy Kumar Panigrahi, and Subhashree Priyadarshini

Abstract This study reveals the maiden application of emperor penguin optimization (EPO)-based load frequency control of multi area system integrated with distributed generation resources. Intermittent power output nature of wind turbine under regular and frugal load adjustment in distributed generation resources (DGR) bears the vagueness in the system frequency and tie line power instability. Henceforth, it is imperative to revision the system performance of current power system along with integrated DG resources. A novel cascade of three degrees of freedom proportional integral derivative with fuzzy fractional order proportional integral derivative (3DOFPIDN-FFOPID) controller is premeditated by commending a maiden application of EPO algorithm to spread out an amended dynamic performance. Further EPO algorithm is executed by integral time absolute error (ITAE) as a cost function to improve the performance of controller. Studies unveil the greater performance of 3DOFPIDN-FFOPID over other controllers in providing the reduced peak, least settling time and lesser value of cost function. The superiority of EPO algorithm is compared with local unimodal sampling teaching learning-based optimization (Lus-TLBO) and ant lion optimization (ALO) algorithm. Finally outcome of high-voltage DC link in adding with FACTs devices has conferred to enrich the power system stability.

Keywords Distributed generation resources · Secondary controllers · Cost functions · Cascade controllers · Flexible ac transmission devices · And step load perturbation

S. Pahadasingh (✉) · C. Jena · C. K. Panigrahi
School of Electrical Engineering, KIIT University, Bhubaneswar, Odisha, India

C. Jena
e-mail: chitralekha.jenafel@kiit.ac.in

S. Priyadarshini
IGIT Sarang, Dhenkanal, Odisha, India

G. Panda et al. (eds.), *Sustainable Energy and Technological Advancements*, Advances in Sustainability Science and Technology,
https://doi.org/10.1007/978-981-16-9033-4_35

1 Introduction

Modern power system is an interconnection of more than one control areas to which common generation control is applied through tie lines. If there is a sudden change in a control area, this causes some undesirable effects such as oscillation of frequency and power interchange and that leads to mismatch between active power generation and demand. This unbalance is overcome by load frequency control (LFC). Consequently, the key impartial of LFC is to sustain constant system frequency and tie line power by maintaining a proper balance between generation and demand. In the former works, ample of studies have been conceded on LFC [1, 2]. Many disputes of conventional generations such as losses of transmission and distribution network, flexibility and viability at desired locations, extraction arrangement difficulties of generated power leads to DG conceptions. Distributed energy resources (DERs) are mostly renewable in nature in which power generated near load centres through small grid connected units. Now a day's hybrid interconnected power system comprising of conventional units like thermal, hydro, gas, etc., and renewable energy sources is the extensive research area in LFC [3–5].

Control strategy is needed not only for constant frequency but also achieve zero steady state error and unintended interchange. Many researchers have already discussed the conventional controllers [6] such as proportional, proportional integral (PI), proportional integral derivative (PID) controller. Mostly PID controller is castoff in LFC for simplification and less parameter is to be optimized. Then degree of freedom [7] concept is introduced in PID such as 2DOF and 3DOF to increase the stability of gain parameters and performances. All these above controllers are integer-based controllers which are simple to design but not giving satisfactory performance when considering the non-linearity and parameter variations. Fuzzy PID controller [8] is suitable for non-linearity conditions but time consumption is more due to membership functions and fuzzy rules. Recently, non-integer controllers gain more popularity due to flexibility and more robust towards the non-linearity and variation of parameters. The non-integer controllers such as integral tilted derivative (ITD) tilted integral derivative (TID) [9] and fractional order controllers are discussed in recent papers. FOPID controller [4] find its wide applications in process control industry and is received remarkable attention in recent literature. Conventional feed-forward single loop controller intellect the disruption formerly initiation of control action. However, direct measurement of disturbance and knowing of power system model beforehand calculated output of suitable controller is the major drawback of feed-forward controller. Hence, cascade controller [10–12] can be castoff as a substitute to lighten the closed-loop system performance by retaining secondary measurement and feedback arrangement. The flexible AC transmission system (FACTS) devices [13–15] encompass the augmentation of power system firmness and governing the power flow among several control areas. On the other hand, the high-voltage direct current (HVDC) transmission lines are used to transmit the bulk power to longer distances and draw the attention of researchers [16]. Controller parameters are generally optimized by optimization techniques such as local unimodal sampling teaching learning-based optimization (Lus-TLBO) [17], symbiotic organism search (SOS) [18], adaptive symbiotic organism search (ASOS) [19], salp swarm algorithm (SSA) [20], sine cosine algorithm (SCA) [21]. For optimization of controller parameters objective function is necessary which are basically in time domain. Different performance indexes such as integral absolute error (IAE), integral square error (ISE), integral absolute square error (ITSE) and integral time absolute error (ITAE). Mostly, ITAE is considered as objective function. Previously in the paper [14] three area hybrid power systems with DG sources are described by using FOPID controller optimized by ALO technique. First time EPO [22, 23] algorithm is implemented with this system for cascade controller. The main contribution of this paper is:

1. Forming of three area thermal hydro LFC system with DGR considering SLP of 1% in area1.
2. The sovereignty and feasibility of cascaded 3DOFPIDN-FFOPID controller have been acknowledged over FFOPID and 3DOFPIDN controllers.
3. Solicitation of EPO has been elucidated for dynamic assessment of 3DOFPID-FFOPID-TID controller gains likened with Lus-TLBO and ALO algorithms.
4. To endorse the worth of proposed cascaded controller, different variation of step load perturbation (VSLP) for control areas are projected.

2 Proposed Model

2.1 *Three Area System*

In this paper, a three area LFC system model is used which consists of thermal units and hydro units as multi sources in area 1, area2 and area 3, respectively. Here in each control area, system non-linearities are taken such as GDB, GRC and reheat turbine connected by means of AC tie lines. DG resources is applied to area 1 which consists of wind turbine generator (WTG), fuel cell (FC), aqua electrolyser (AE), diesel engine generator (DEG) and battery energy storage system (BESS). ACE is taken as input to each controller. Modelling of proposed power system, DGR system and controller structure are shown in Figs. 1, 2 and 3.

2.2 *Controller Design*

Customarily PID controller [6] has three parameters for optimization (K_P, K_I, K_D). However it has unambiguous fluctuations. So, control action can be realised by multiple control loops called as degrees of freedom. The dynamic responses upgrading can be reached by using 3DOFPID controller [7] which encloses added three control loops to enrich the stability of the system and suppression of instabilities

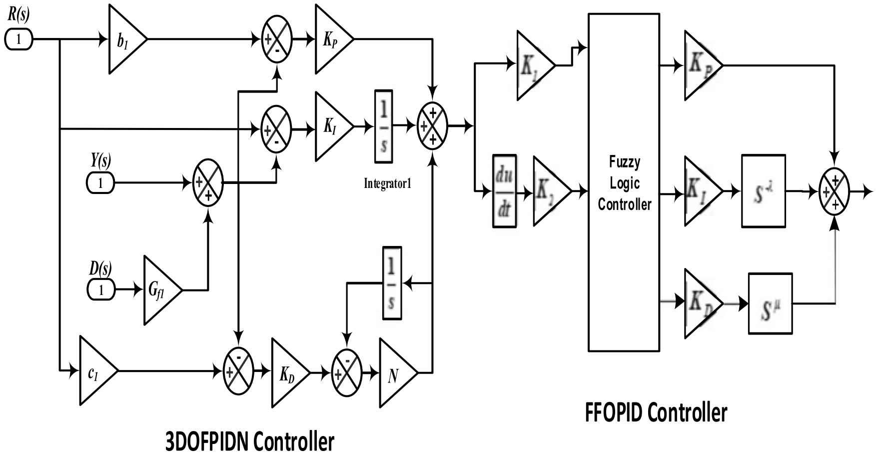

Fig. 1 Controller structure citation [4]

Fig. 2 DGR systemcitation [5]

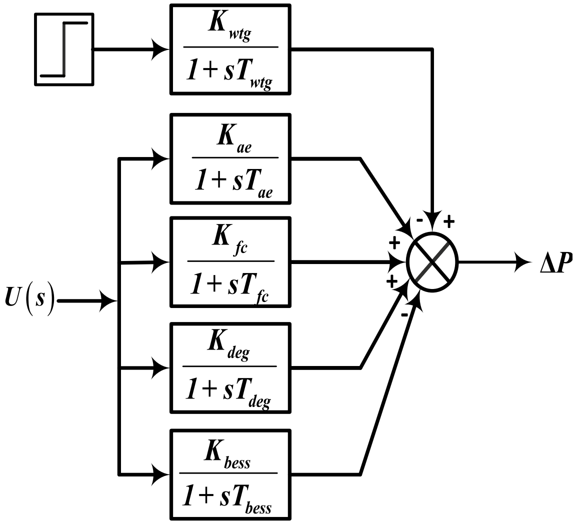

happening in the power system. Again, the rule base fuzzy controller [8] compromises more tractability in scheming and conveying the clarifications of linguistic depiction. Auxiliary, the execution of controller parameters tuning in closed-loop control system with nonlinearity by fuzzy rule is enhanced comparatively. However, fuzzy logic controller (FLC) consumes more computational time because of membership functions and fuzzy rules. Therefore, fractional order concept [4] is introduced for better adjustment of system dynamics. In the proposed combined fuzzy logic with fractional order control strategy, scaling factor of the proportional, integral, and derivative terms are obtained using FLC. Using these scaling factors, the controller

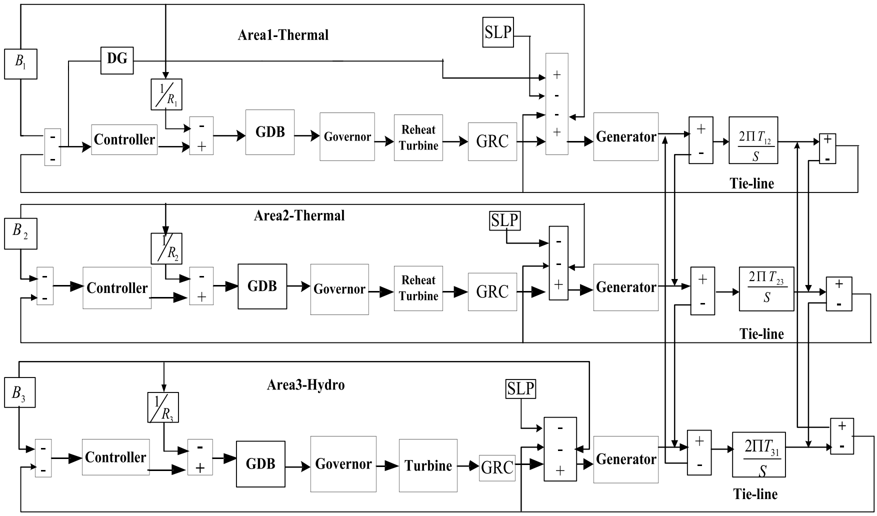

Fig. 3 Modelling power system citation [14]

gain magnitude will be updated at each sampling period. Finally, 3DOFPIDN and FFOPID controllers are combined for better tuning and disturbance denunciation.

The epitomized model in Fig. 1 entails individual sources like hydro, thermal and DERs whose momentary response is dissected impressive 3DOFPIDN, FFOPID and 3DOFPIDN-FFOPID controllers. The recommended controllers are intended by relating a bio-inspired algorithm named EPO supported by an ITAE cost function to diminish the ACE. The suitability function 'J' is given in Eq. (1) [11]

$$J_{\text{ITAE}} = \int_{0}^{T} [|\Delta f_1| + |\Delta f_2| + |\Delta P_{\text{tie}}|] t \, \mathrm{d}t \tag{1}$$

To reduce the error of the cost function '*J*' effectively, dissimilar constraints related are accredited in altered intervals. All the gain parameters are varied in between 0.01 to 2, filter coefficient (*N*) between 100 and 300.

2.3 Optimization Technique

In LFC, tuning by traditional technique is a tiresome trade because of some assumptions related to this methods mistaken the system response. Therefore, optimal tuning of controller parameters for higher order complex system can be reduced by implementation of soft computing optimisation techniques. Different optimization algorithms have studied for the LFC system in last decade but in this paper a maiden emperor penguin optimization [23] algorithm is used for this proposed system which basically mimics the huddle behaviour of emperor penguin. Emperor penguins are the only classes that cluster to subsist all through the Antarctic winter. An imperative piece of this bunching behaviour is that each penguin has an identical prospect to the warmth of huddle. Pseudo code of the EPO is portrayed underneath:

Initialize the emperor penguins population
Elect the initial parameters and estimate fitness value of each search agent
For i = 1: itermax
    Determine he hurdle margin of emperor penguins
    Calculate the temperature profile around hurdle
    Compute the distance between the emperor penguins
    Update the positions of search agents
    Check the boundary of search agents within search space
    Re-examine the rationalized search agent fitness and positions
    Lastly, select the superlative performing agent
End

3 Simulation Results

Case1: Comparison of performances for different optimization algorithms
In this paper, the controller parameters of cascaded 3DOFPIDN-FFOPID are first optimized ALO algorithms. For control area 1, 14 parameters of proposed controller are tuned by ALO algorithm with 50 numbers of iterations and populations. Then Lus-TLBO algorithm with same number of populations and dimensions is considered for optimization. Finally, the controller parameters are optimized by EPO algorithm with same number of dimensions and populations. The dynamic performances of different algorithms are depicted from Figs. 4 and 5. Performance values are mentioned in

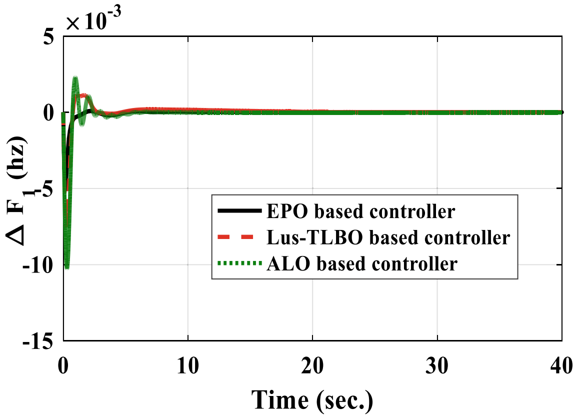

Fig. 4 Frequency distinction for area 1

Fig. 5 Power interchange between area 1 and area 2

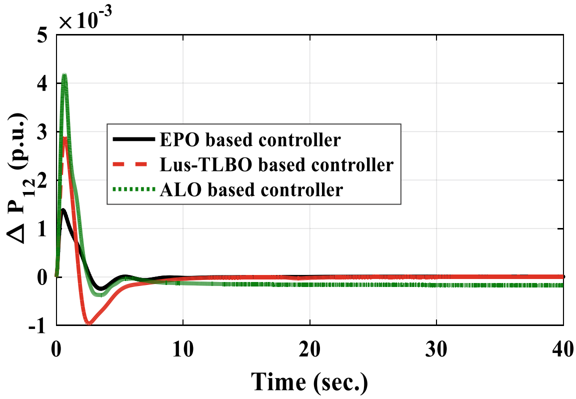

Table 1.

Figure 4 represents comparison result of frequency deviation for cascaded controller optimized by EPO with other techniques. Similarly, Fig. 5 shows the comparative simulation results for tie line power deviations. Form this results, it is clearly visible that EPO algorithm has superior vibrant performances as compared to Lus-TLBO-based and ALO-based controller in terms of reduced settling time, undershoot and overshoot. The computational time of EPO algorithm (298.3774 s) is faster as compared to Lus-TLBO (343.1973s) and ALO (418.6339 s).

Table 1 notified the controller performance values optimized three different algorithms. EPO-based 3DOFPIDN-FFOPID controller has less settling time, peak and undershoot as compared to the other controllers optimized by Lus-TLBO and ALO-based controllers.

Case 2. Comparison of dynamic performances of controller

In this paper, three types of secondary controllers are used to satisfy the main objective of LFC. At first, a 3DOFPID with filter (N) is used where ACE taken as input for this system. Through numerous simulations using EPO algorithm the controller gain parameters are optimized for each area. In this paper, distributed generation sources area applied to only area 1 with SLP of 1%. Since 3DOFPIDN controller has 7 gain parameters (K_p, K_i, K_d) for each area, 21 parameters are to be tuned by this optimization algorithm. Then fuzzy fractional order PID controller is taken with 25 rules and triangular membership function of 21control parameters (K_1, K_2, K_p, K_i, K_d, λ and μ) for each area are to be optimized. After that a cascade connection of 3DOFPIDN and FFOPID controller is used here for each area also with DGR system. The corresponding dynamic assessments (Δf_i, ΔP_{i-j}) are compared and plotted in Figs. 6, 7, 8, 9, 10 and 11. The obtained optimum values are mentioned in Table 3. Figures 6, 7 and 8 shows the frequency variations of control area 1, area2 and area 3, respectively. From those results, it is clearly observable that the proposed 3DOFPIDN-FFOPID controller has minimum overshoot and undershoots with diminished oscillations. Similarly, tie power eccentricities of control areas are

Table 1 Performance analysis of controllers optimized by three different algorithms

Algorithms		EPO			Lus-TLBO			ALO		
		3DOFPIDN-FFOPID	FFOPID	3DOFPIDN	3DOFPIDN-FFOPID	FFOPID	3DOFPIDN	3DOFPIDN-FFOPID	FFOPID	3DOFPIDN
$\Delta f_1 in\, hz$	$T_s(s)$	4.394	5.425	9.127	5.450	6.902	11.27	6.591	7.052	12.082
	U_{sh}	−2.9298	−8.1026	−9.4538	−3.3848	−8.9157	−10.0092	−4.0998	−9.4652	−10.9496
	O_{sh}	1.7581	3.9083	4.5749	2.1080	4.0630	6.6839	2.6544	4.1812	6.7286
$\Delta f_2 in\, hz$	$T_s(s)$	6.91	10.64	12.42	6.983	11.212	12.788	7.247	12.121	13.861
	U_{sh}	−1.5423	−2.109	−3.1545	−2.0169	−2.8782	−3.2912	−2.7813	−3.0119	−4.2029
	O_{sh}	0.5120	0.9796	1.4049	0.6852	1.1150	1.4560	0.4178	1.2785	2.1800
$\Delta f_3 in\, hz$	$T_s(s)$	4.713	9.698	11.44	5.783	10.544	12.385	6.386	11.669	13.543
	U_{sh}	−1.9213	−3.9397	−4.1097	−2.4536	−3.9694	−4.3940	−3.1498	−4.4144	−4.4584
	O_{sh}	0.8998	1.4536	1.7739	1.3831	1.4575	2.2374	1.5844	2.1954	2.5399
$\Delta P_{12} in\, pu$	$T_s(s)$	6.712	11.43	13.52	7.581	11.906	14.379	12.87	15.189	15.899
	U_{sh}	−1.5135	−2.3740	−3.35111	−2.1654	−3.2427	−3.5558	−3.1126	−3.4815	−3.7421
	O_{sh}	0.8559	1.1008	1.9128	1.3386	1.1676	1.9343	1.4229	1.6526	2.4514
$\Delta P_{23} in\, pu$	$T_s(s)$	9.586	13.76	15.14	10.132	14.604	15.893	11.483	15.407	16.629
	U_{sh}	−0.3494	−0.5469	−0.8400	−0.6569	−0.7793	−1.2475	−0.7528	−0.9229	−1.1730
	O_{sh}	0.8697	1.3258	1.9134	1.1099	1.5082	2.5653	1.3542	1.8535	2.8022
$\Delta P_{13} in\, pu$	$T_s(s)$	10.26	13.56	14.88	10.92	15.071	15.987	12.270	16.82	17.512
	U_{sh}	−0.4023	−0.4491	−1.8372	−1.3315	−1.4872	−2.1216	−1.9277	−2.3616	−2.8504
	O_{sh}	1.4039	2.2883	3.6124	1.9350	3.2426	4.0198	2.1754	3.5031	4.1229

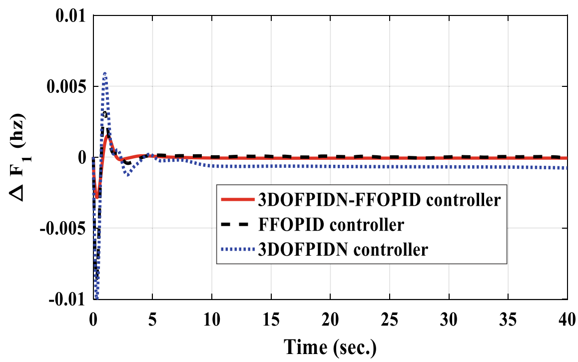

Fig. 6 Frequency aberration for area 1

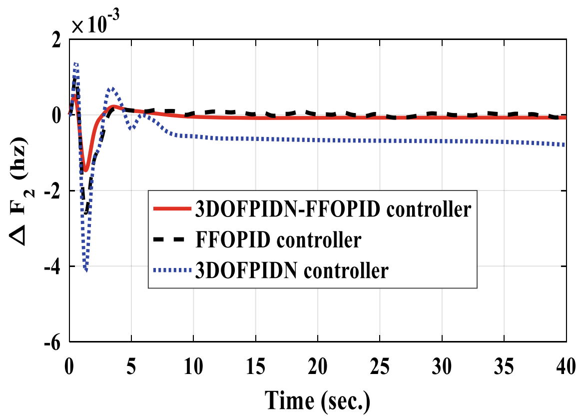

Fig. 7 Frequency aberration for area 2

represented in Figs. 9, 10 and 11. Transient performances of cascade proposed controller is superior as compared to others.

Case3: Effect of HVDC link to the proposed system

In this case, HVDC link is connected along with prevailing AC link. The accomplished optimal values of the cascaded controller are mentioned in Table 3. The system dynamics with and without HVDC link are compared in Figs. 12 and 13. From Fig. 12, it is prominently grasped that with HVDC link the dynamics of the system are upgraded significantly for frequency deviations. Moreover, the degrees of fluctuations for tie line deviations are reduced in Fig. 13.

Case4: Effect of FACTs devices

In this case firstly FACTs devices, GCSC and RFB are engaged in the tie lines of all control areas. Each time the gain and controller parameters are optimized by EPO algorithm. After that coordination of both FACTs devices are explored**.** With the acquired finest values, system dynamics are compared in Figs. 14 and 15 with FACTS (coordinated GCSC and RFB, GCSC, RFB) and without FACTS (optimum

Fig. 8 Frequency aberration for area 3

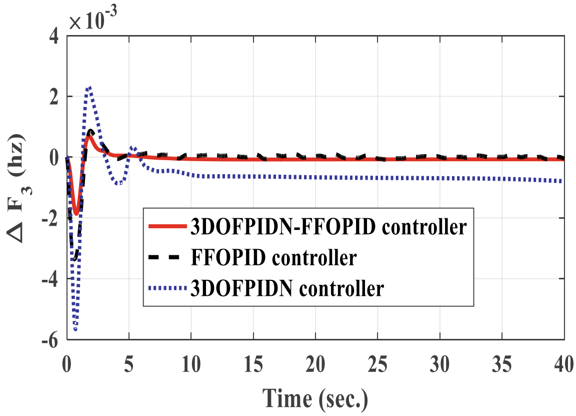

Fig. 9 Tie line power aberration T_{12}

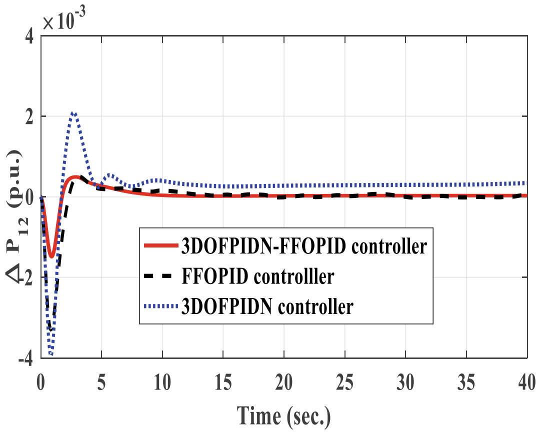

Fig. 10 Tie line power aberration T_{23}

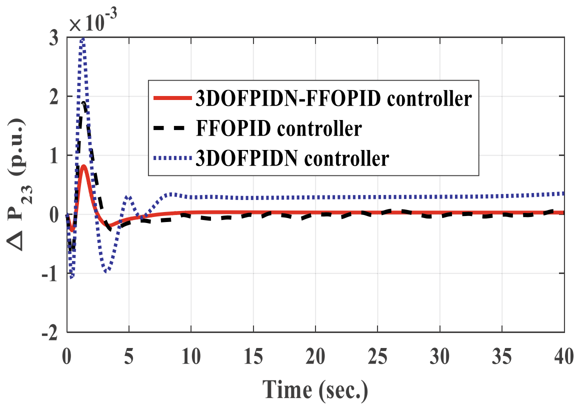

Fig. 11 Tie line power aberration T_{31}

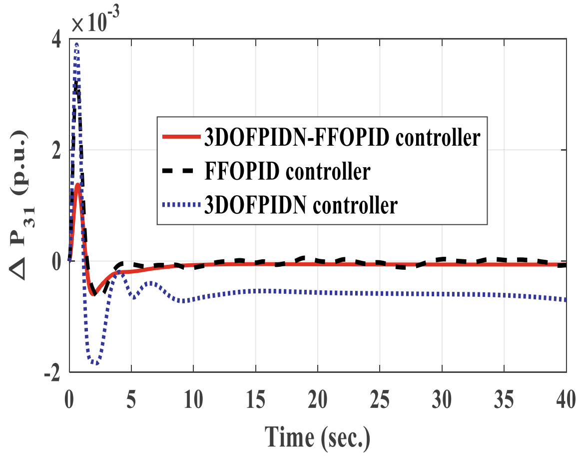

Fig. 12 Frequency eccentricities with HVDC link

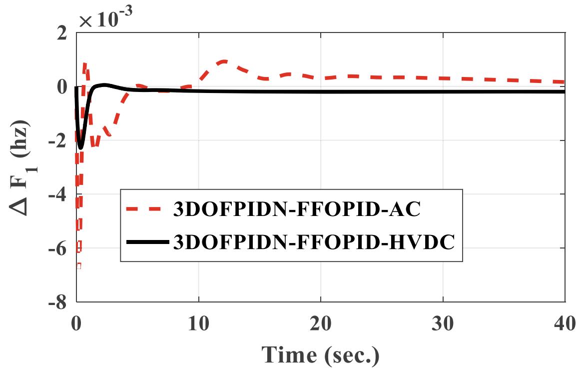

Fig. 13 Tie power eccentricities with HVDC link

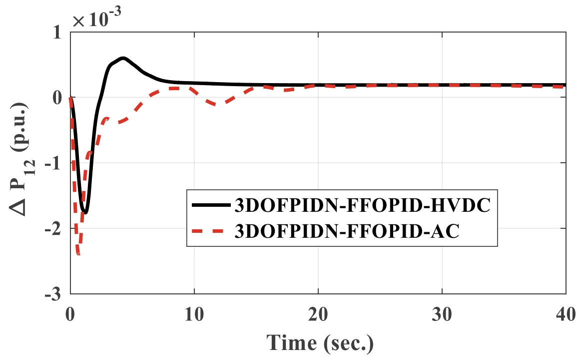

values of Table 2) devices for cascade controller. It is realized from Figs. 14 and 15 that with the unification of FACTS devices, the system dynamics are amended significantly. Additionally, it is also observed that coordinated GCSC and RFB devices is carrying out healthier than individual GCSC and RFB related to slighter settling time, minimum peak deviations and abated oscillations (Table 3).

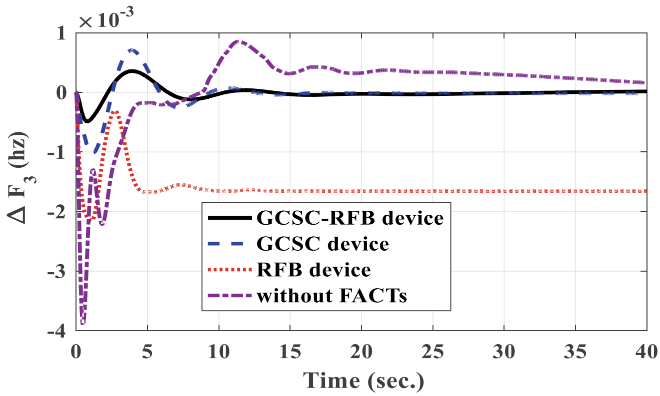

Fig. 14 Change in frequency deviations with FACTs

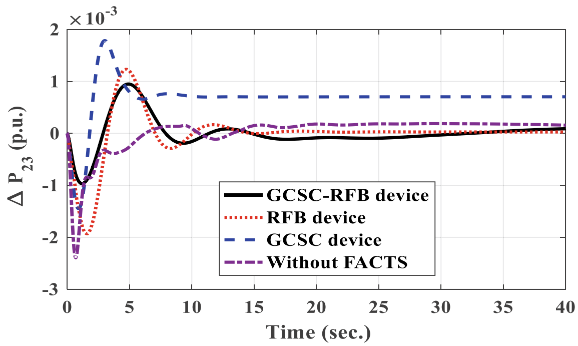

Fig. 15 Change in tie power deviations with FACTs

Table 2 Dynamic performance values of cascade controller with FACTS and without FACTs devices

Performance characteristics	FACTs devices	$\Delta f_1\ in\ Hz$	$\Delta f_2\ in\ Hz$	$\Delta f_3\ in\ Hz$	$\Delta P_{12}\ in\ pu$	$\Delta P_{23}\ in\ pu$	$\Delta P_{31}\ in\ pu$
Undershoot (U_{sh}) in put	RFB-GCSC	−2.2820	−0.3403	−0.4877	−0.9671	−0.4915	−0.9987
	RFB	−3.4116	−0.5163	−0.8773	−1.2099	−0.5039	−1.0974
	GCSC	−3.8353	−0.7286	−1.0067	−1.9322	−0.6601	−1.4627
	Without FACT	−6.7765	−3.6793	−3.9081	−2.3976	−0.8759	−2.2330
Overshoot (O_{sh}) in put	RFB-GCSC	0.8757	0.2732	0.3571	0.6497	0.6255	1.1891
	RFB	0.5626	0.3526	0.4001	0.8866	0.9483	1.2551
	GCSC	1.4134	0.3786	0.7049	0.9872	1.1729	1.9030
	Without FACT	1.9535	0.9965	0.8516	1.2324	1.2921	1.9343

Table 3 Optimum values of controller parameters optimized by EPO algorithm

Gain data	Controller	Area1 (thermal)	Area1 (DGR)	Area2 (Thermal)	Area3 (Hydro)
b_1	3DOFPIDN-FFOPID	1.0324	0.3245	1.3821	0.3101
c_1		1.0987	1.1354	0.5786	0.5546
Gf_1		0.8441	1.2121	0.4398	1.0225
K_{p1}		1.7937	0.7547	1.9918	1.8012
K_{i1}		1.4002	0.4468	1.3291	1.3955
K_{d1}		0.4665	1.9192	0.2289	0.4601
N		198.723	193.533	176.093	231.421
K_1		1.0227	1.4552	1.4963	1.6909
K_2		1.6804	1.3700	1.1423	1.0749
K_{p2}		0.3313	0.5534	0.7441	0.3286
K_{i2}		1.2802	0.0820	0.7245	1.6809
K_{d2}		1.9872	0.0190	0.4381	1.9900
λ		0.0100	0.7915	1.9647	0.4572
μ		1.0032	0.6053	0.2360	1.0034
b_1	3DOFPIDN	1.5573	0.0100	1.9147	0.9642
c_1		0.2967	0.5244	1.2634	1.1894
Gf_1		1.3387	1.8046	0.6114	1.6752
K_{p1}		0.1117	0.4769	0.0417	0.3565
K_{i1}		2.0000	0.2590	0.2977	0.4456
K_{d1}		0.1565	0.0100	1.1449	1.7206
N		0.2767	0.4655	0.0417	0.8492
K_1	FFOPID	1.8293	0.7722	0.9051	1.7918
K_2		0.9623	0.2381	0.8461	1.3973
K_{p1}		0.0100	0.8897	0.7697	0.4972
K_{i1}		1.6839	0.3167	1.4120	1.8334
K_{d1}		0.0100	0.3893	0.2998	0.5411
λ		1.0025	0.0001	1.2311	0.0001
μ		1.5048	0.7129	1.8936	0.8493

4 Conclusion

In this study, cascaded 3DOFPIDN-fuzzy FOPID controller is anticipated as a secondary controller for hybrid power system. The suggested cascade controller establishes remarkable performance over other 3DOFPIDN and FFOPID controllers because of better ability to reduce disturbance and good set point tracking. In this study, a maiden EPO technique is proposed as optimization technique for tuning of gain as well as controller parameters. The improved dynamic performances of EPO-based controller has compared with other two algorithms such as TLBO and ALO algorithms. The anticipated cascade controller optimized by EPO algorithm has remarkable performance in terms of diminished settling time and lowest oscillations. Finally, the incorporation of coordinated GCSC and RFB devices with HVDC link delivered the enhanced handling of fluctuations in this suggested hybrid system.

Appendix

System parameters		Time constant (s)	Gain coefficient
Frequency (f) in Hz	50		
Steam turbine (T_{CH})	–	0.3	–
Speed Governor for thermal unit (T_G)	–	0.1	–
Speed Governor for hydro unit (T_G)	–	0.2	–
Inertia constant (M) for thermal unit	–	10	–
Inertia constant (M) for hydro unit	–	6	–
Wind turbine generator (WTG)	–	1.5	0.000833
Fuel cell (FC)	–	0.5	0.02
Aqua electrolyser (AE)	–	4	0.01
Diesel engine generator (DEG)	–	2	0.0003
Battery energy storage system (BESS)	–	0.1	−0.0003
Frequency bias coefficient (B)	0.425	–	–
System damping (D)	1	–	–
Speed regulation (R)	0.08	–	–
Transient droop regulation (R_t)	0.38	–	–
Reset time (T_r)		5	–
Start time of water (T_w)		1	
Synchronizing power coefficient (T_i)	15	–	–
Tie line power deviation (ΔP_{tie})	0.06	–	–

References

1. Gupta DK et al (2021) Load frequency control using hybrid intelligent optimization technique for multi-source power systems. Energies 14:1581
2. Rahman A, Saikia LC, Sinha N (2016) AGC of an unequal four-area thermal system using biogeography based optimised 3DOF-PID controller, IET Renew Power Gener
3. Hussain I, Ranjan S, Das DC et al (2017) Performance analysis of flower pollination algorithm optimized PID controller for wind-PV-SMES-BESS diesel autonomous hybrid power system. Energy Resour 7:643–651
4. Jena NK, Sahoo S, Sahu BK (2020) Fractional order cascaded controller for AGC study in power system with PV and diesel generating units. J Interdiscip Math 23(2):425–434 (Taylor& Francis Group)
5. Pahadasingh S, Jena C, Panigrahi CK (2020) Incorporation of distributed generation resources for three area load frequency control using fractional order PID controller. ICREISG, pp 186–191, 9174200
6. Guha D, Roy PK, Banerjee S (2016) Load frequency control of interconnected power system using grey wolf optimization. Swarm Evol Comput 27:97–115
7. Patel NC, Debnath MK, Bagarty DP, Das P (2018) GWO tuned multi degree of freedom PID controller for LFC. Int J Eng Technol 7:548–552
8. Nayak RJ, Sahu KB (2017) Load frequency control of hydro thermal system using fuzzy PID controller optimized by hybrid DECPSO algorithm. Int J Pure Appl Math 114:147–155
9. Pahadasingh S, Jena C, Panigrahi CK (2021) Incorporation of distributed generation resources for three-area load frequency control optimized tilted integral derivative controller. Lect Notes Electr Eng 691:57–68
10. Raju M, Saikia LC, Sinha N (2018) Maiden application of two degree of freedom cascade controller for multi-area automatic generation control. Int Trans Electr Energy Syst 1–20
11. Guha D, Roy PK, Banerjee S (2019) Maiden application of SSA optimized CC-TID controller for LFC of power systems. IET Gener Transm Distrib 13:1110–112
12. Pahadasingh S, Jena C, Panigrahi CK (2021) TLBO based CC-PID-TID controller for load frequency control of multi area power system. ODICON, 9429022
13. Dash P, Saikia LC, Sinha N (2015) Comparison of performances of several FACTS devices using Cuckoo search algorithm optimized 2DOF controllers in multi-area AGC. Electr Power Energy Syst 1:316–324
14. Raju M, Saikia LC, Sinha N (2019) Load frequency control of a multi-area system incorporating distributed generation resources, gate controlled series capacitor along with high-voltage direct current link using hybrid ALO-pattern search optimised fractional order controller. IET Renew Power Gener 13(2):330–341
15. Arya Y, Kumar N (2016) AGC of a multi-area multi-source hydrothermal power system interconnected via AC/DC parallel links under deregulated environment. Electr Power Energy Syst 75:127–138
16. Pahadasingh S, Jena C, Panigrahi CK (2020) Load frequency control incorporating electric vehicles using FOPID controller with HVDC link, vol 630. Springer Book Series IEPCCT, pp 181–203
17. Sahu BK et al (2016) A novel hybrid LUS–TLBO optimized fuzzy-PID controller for load frequency control of multi-source power system. Int J Electr Power Energy Syst 74:58–69
18. Guha D, Roy PK, Banerjee S (2018) Symbiotic organism search based load frequency control with TCSC. In: Proceedings of fourth international conference on recent advances in information technology, IIT (ISM) Dhanbad, pp 1–6
19. Nayak JR, Shaw B, Sahu BK (2018) Application of adaptive-SOS (ASOS) algorithm based interval type-2 fuzzy-PID controller with derivative filter for automatic generation control of an interconnected power system. Eng Sci Technol Int J 21:465–485
20. Nayak JR, Shaw B, Sahu BK (2020) Implementation of hybrid SSA–SA based three-degree-of-freedom fractional-order PID controller for AGC of a two-area power system integrated with small hydro plants. IET Gener Transm Distrib 14:2430–2440

21. Pahadasingh S, Jena C, Panigrahi CK (2021) SCA based load frequency control incorporating electric vehicle using cascaded controller. In: International conference on power electronics and energy, ICPEE, 9358648
22. Balasubbareddy M, Dwivedi D (2019) Hybrid emperor penguin optimization algorithm for solving optimal power flow problem. Pramana Res J 9(4)
23. Dhiman G, Chahar V (2018) Emperor penguin optimizer: a bio inspiredalgorithm for enginnering problem. Knowl Based Syst 159:20–50

Chapter 36
Modified Particle Swarm Optimized Load Frequency Control of Renewable Energy Sources-Based Integrated Power Systems

Ashutosh Jena, Bidyadhar Rout, and Nutan Saha

Abstract This paper presents the study of a modified particle swarm optimization algorithm in load frequency control for an integrated power system. The system to be studied is a two-area system whose generation is covered by a wind turbine unit in addition to a thermal unit in the first area and a photovoltaic (PV) unit along with a thermal unit in the second area. Proportional integral derivative (PID) controller has been taken into consideration to minimize the performance index of integral squared error (ISE) of the system, which in turn reduces the deviation in frequency of corresponding areas and the tie-line power between those areas using the modified particle swarm optimization (mPSO) algorithm. This algorithm is compared with some new optimization techniques as well as some robust optimization techniques like particle swarm optimization (PSO), genetic algorithm (GA) and ant lion optimization (ALO) and then efficiency is evaluated for the mPSO algorithm.

Keywords Load frequency control · Interconnected system · Modified particle swarm optimization · PV · Wind

1 Introduction

The modern electrical system is shifting towards microgrid, interconnected systems and smart-grid. And with this shift, new generation technologies are coming into picture. Some of the new methods of generation include renewable energy sources (RESs) that include PV, wind, biomass, fuel cell, plug-in hybrid vehicles (PHEVs), etc. Load frequency of multi-hybrid interconnected area is demonstrated by Raju et al. [1]. Since most of these resources are capable of producing only a few kW outputs , they are used locally and then interconnected to other resources within

A. Jena (✉) · B. Rout · N. Saha
Department of Electrical Engineering, VSSUT, Burla, Odisha, India

G. Panda et al. (eds.), *Sustainable Energy and Technological Advancements*, Advances in Sustainability Science and Technology,
https://doi.org/10.1007/978-981-16-9033-4_36

different areas. However, most of the RESs are non-linear in nature, and generally, they are linearized using various approximation techniques. Frequency control of non-linear transfer functions is demonstrated in [2, 3] and that of an approximated linear transfer function is demonstrated in [4]. Also, the output of most of these resources is independent of load variation. Because of this reason, generally, they are connected along with a hydro or a thermal power plant which is capable of readjusting their mechanical input to counteract the changes in frequency due to mismatch in power generation and demand. During load variation in the demand side, excess load demand is met by increasing the mechanical power input which is regulated by governor action. Therefore, every area consists of an output-controllable power plant if there exists an output-uncontrollable power plant (i.e. RESs like PV-based power plant) in the same area.

This paper deals with controlling load frequency deviation to load variation as well as power generation variation by using a PID controller [5]. Every system has the inherent ability to come back to a steady state after a disturbance has occurred on the system; however, with the help of controllers, the transient and steady-state characteristics can be improved to a great extent. To decide the optimal gain values of the controllers, the controllers are trained by various algorithms. In this paper, a modified particle swarm optimization algorithm (mPSO) is discussed. And then, the output of mPSO approach is compared with some of the new optimization techniques like ant lion optimization (ALO), arithmetic optimization algorithm (AOA) [6], atomic search optimization (ASO) [7], Harris hawk optimization (HHO) [8] and two robust tools for optimization such as particle swarm optimization (PSO) [9] and genetic algorithm (GA) [10]. PSO is modified and studied in various mathematical studies in many different fields, and the efficiency of strategies behind all those modifications is demonstrated by Bansal et al. [11]. In this paper, range of inertia weight is varied rather than varying the function itself. And the inertia weight function is taken as "chaotic random". Table 1 represents the nomenclature of various notations used in this paper.

This paper is divided into five sections. First section briefly introduces the concept behind the model. Second section deals with the mathematical model of the systems under study. Third section briefly introduces the optimization algorithm under study. Fourth section consists of results and observations. Finally, conclusions are made in fifth section. Values and various control parameters used throughout this paper are included in the appendix section.

2 Mathematical Modelling

2.1 Thermal Generator Model

First system in this paper is a standalone conventional thermal generation system which is modelled as follows [12]:

Table 1 Nomenclature for various notations used in this paper

Notations	Nomenclature
T_{ij}	Coefficient of synchronization with area j
P_{gi}	Change in output of governor of area i
P_{mi}	Change in mechanical input in area i
P_{Li}	Load change
P_{ci}	Controlled power of area i
H_i	Inertia constant for area i
D_i	Damping coefficient for area i
R_i	Speed droop characteristic for area i
x_i^k	Position of ith particle after kth generation
v_i^k	Velocity of ith particle after kth generation
$p\text{best}_i^k$	*pbest* of ith particle for kth generation
$g\text{best}_i^k$	*gbest* of ith particle for kth generation
v_i^{k+1}	Present velocity of ith particle
W	Inertial weight for the ith particle
c_1 and c_2	Constriction factors
rand()	Random number between upper and lower bound
$\text{pres}_{\text{iter}}$	Present iteration
max_{iter}	Maximum number of iteration

$$G_{\text{gov}} = \frac{k_g}{T_g s + 1} \tag{1}$$

$$G_{\text{turb}} = \frac{k_t}{T_t s + 1} \tag{2}$$

$$G_{\text{rh}} = \frac{k_r T_r s + 1}{T_r s + 1} \tag{3}$$

where G_{gov}, G_{rh}, and G_{turb} are the first-order transfer functions of the governor, re-heater and the steam-based turbine and k_g, k_r and k_t are, respectively, the gains of governor, re-heater and steam-based turbine. The generator transfer function can be written as follows:

$$G_{\text{gen}} = \frac{k_p}{T_p s + 1} \tag{4}$$

where k_p is the gain of generator. T_g, T_r, T_p and T_t are, respectively, the time constants in case of governor, re-heater, generator and steam-based turbine.

2.2 Wind Turbine Model

Very commonly in wind turbines, doubly-fed induction generators (DFIG) are used, which operates familiar to synchronous generators but also provides the advantage of variable speed. The mechanical power output from the wind turbine is dependent upon the speed of the wind [13]. And it is given as,

$$P_w = \frac{1}{2}\rho A_r C_p v_w^3 \tag{5}$$

where ρ, A_r, C_p and v_w are density of air, area swept by the blade of the wind turbine, power coefficient representing the available power after wind turbine extracts energy from the wind and velocity of the wind, respectively. The values for the above-mentioned physical parameters are given in the appendix section. And the equation to calculate the exact value of C_p is given in [13]. In this paper, the wind speed is varied to achieve varying mechanical power output. Wind turbine plays a major role of introducing non-linearity in the system. However, after linearization, the transfer function of the turbine can be approximately given by,

$$G_{\mathrm{WTG}} = \frac{K_{\mathrm{WTG}}}{T_{\mathrm{WTG}}s + 1} \tag{6}$$

where K_{WTG} and T_{WTG} are the gains of wind generator and the time constant of the same, respectively.

2.3 Photovoltaic Array Model

Generally, a PV array takes temperature and solar irradiance as input to the system. Both parameters are non-linear and depend upon the natural factors, so the input to the solar panel can be considered as a time-varying non-linear input signal. However, the average output power from the PV array is given by, Eq. (7)

$$P = A_s \eta_s G[1 - 0.005(T_a + 25)] \tag{7}$$

where A_s, η_s and T_a are areas of the PV array (in m^2), energy conversion efficiency of one module and ambient temperature (in degree Celsius), respectively, of a PV plant. And the values of the above-mentioned physical parameters of PV array is taken from [13] and it is given in the appendix section. G is the irradiance (in kW/m^2) which is considered to be varying in this paper.

After removal of all the non-linearities from the system, the transfer function of the PV system is roughly approximated as,

$$G_s = \frac{\Delta P_s}{\Delta G} = \frac{k_s}{T_s s + 1} \tag{8}$$

where ΔP_s is the power output from the PV array and ΔG is the change in irradiance. K_s and T_s represent the gain and time constant of the solar plant, respectively.

2.4 Load Frequency Control of Two Area

When there is a sudden change in active power in an area, the region starts feeding on the power supplies of other regions [4, 10, 12]. Therefore, the main task of the load frequency control (LFC) of an interconnected system is to make sure the compensation of the local area frequency and the corresponding tie-line power. The deviations in frequency, as well as tie-line power, is due to the difference between generation and load side demand, so for a connected system, tie-line power of every area has to be taken into consideration. For an area *i*, the power system is modelled as:

$$\Delta \dot{f}_i = \left(\frac{1}{2H_i}\right)\Delta P_{mi} - \left(\frac{1}{2H_i}\right)\Delta P_{Li} - \left(\frac{D_i}{2H_i}\right)\Delta f_i - \left(\frac{1}{2H_i}\right)\Delta P_{\text{tie},i} \tag{9}$$

$$\Delta \dot{P}_{mi} = \left(\frac{1}{T_{ti}}\right)\Delta P_{gi} - \left(\frac{1}{T_{ti}}\right)\Delta P_{mi} \tag{10}$$

$$\Delta \dot{P}_{gi} = \left(\frac{1}{T_{gi}}\right)\Delta P_{ci} - \left(\frac{1}{R_i.T_{gi}}\right)\Delta f_i - \left(\frac{1}{T_{gi}}\right)\Delta P_{gi} \tag{11}$$

The change in tie-line power is expressed as follows:

$$\Delta \dot{P}_{\text{tie},i} = 2\pi\left[\sum_{\substack{j=1\\ j\neq i}}^{N} T_{ij}\Delta f_i - \sum_{\substack{j=1\\ j\neq i}}^{N} T_{ij}\Delta f_j\right] \tag{12}$$

Frequency control in power system is categorized into flat tie-line control (FTC), fixed frequency control (FFC), and tie-line power frequency deviation control (TBC). TBC based LFC is used in this paper, regional area control error (ACE) is given by the following equations:

$$\text{ACE}_i = \Delta P_{\text{tie},i} + B_i \Delta f_i \tag{13}$$

$$\Delta f_i = \frac{1}{2H_i s + D_i} \sum \Delta P_i \tag{14}$$

$$\Delta P_{\text{tie},i} = \frac{2\pi}{s} \sum_{\substack{j=1 \\ j \neq i}}^{n} T_{i,j}\left(\Delta f_i - \Delta f_j\right) \tag{15}$$

where $\Delta P_{\text{tie},i}$ is the total tie-line power deviation between area i and the rest of the areas and Δf_i is the frequency deviation in area-i. B_i is the frequency deviation factor, expressed in Eq. (13), and it is given by Eq. (16),

$$B_i = \frac{1}{R_i} + D_i \tag{16}$$

2.5 Control Strategy

To obtain the controller output, the input to the controller is taken as ACE_i. In this paper, PID controller has been put into use. u_i is the output of the controller and it is obtained as,

$$u_i = K_{pi}(\text{ACE}_i) + K_{ii} \int ACE_i \text{d}t + K_{di} \frac{\text{dACE}_i}{\text{d}t} \tag{17}$$

Equation (17) represents the controller equation for a PID controller.

The objective of the optimization is to reduce the ISE of frequency and tie-line power deviation obtained from both areas. The objective function, ISE is given by Eq. (18).

$$\text{ISE} = \int (\Delta P_{\text{tie},i}^2 + \sum \Delta f_i^2) \tag{18}$$

3 Overview of Modification in Particle Swarm Optimization

Particle swarm optimization algorithm (PSO) is originally developed by Kennedy and colleague Eberhart in the year 1995. The idea behind this optimization technique is based on the nature of hunting shown by a school of fish. This technique indulges in randomly locating a population of search agents in a given search space. The search agent closest to the optimum value is called the best agent of that particular iteration. In the next iteration, all the other search agents are directed towards the direction of the best search agent obtained in the first iteration by updating the velocity and position accordingly. However, in the original PSO algorithm, Kennedy and Eberhart failed to put forward how to direct the search path in the direction of global or a local optimum. Therefore, PSO was later modified by introducing the parameter "inertia weight" by Shi and Eberhart [14]. The equation of inertia weight has been modified over the years in various papers related to different optimization problems. In this paper, a new approach to calculate inertia weight during successive iteration has been introduced. The underlying principle of PSO is expressed in the form of the following equations.

$$v_i^{k+1} = w \times v_i^k + c_1 \text{rand}()\left(p\text{best}_i^k - x_i^k\right) + c_2 \text{ rand}()\left(g\text{best}_i^k - x_i^k\right) \tag{19}$$

$$x_i^{k+1} = x_i^k + v_i^{k+1} \tag{20}$$

$$w = w_{\max} - \frac{(w_{\max} - w_{\min}) \times \text{present\_iter}}{\text{max \_iter}} \tag{21}$$

The modification in w is done by changing the range of $w_{\max}$ and $w_{\min}$ in every iteration to quickly converge to the optimal solution. And the logic applied is if the local_best > global_best in the second half of optimization then the range of w is widened to obtain a better global optimum. But if global_best > local_best, then the range of w is reduced in steps, for better exploitation. The second half of optimization starts after the tenth iteration here. And the above logic is mathematically expressed by the following sets of equations.

$$w_{\max} = w_{\max_0} - \left\{0.3 \times \frac{\left(\text{pres}_{\text{iter}} - 10\right)}{\left(\text{max}_{\text{iter}} - 10\right)}\right\} \tag{22}$$

$$w_{\min} = w_{\min_0} + \left\{0.2 \times \frac{\left(\text{pres}_{\text{iter}} - 10\right)}{\left(\text{max}_{\text{iter}} - 10\right)}\right\} \tag{23}$$

At the end of the iteration, the optimal gain value is obtained.

4 Results and Observation

Two-area system consisting of a thermal unit and a wind unit in the first area and a thermal unit and a PV unit in the second area is modelled in MATLAB/Simulink. The thermal unit is modelled using transfer functions defined in Sect. 2.1 and the controlled power output from PID controller-1 is fed to the thermal unit of area 1.

The power output from the wind turbine is connected as a constant power source, and it is modelled as defined in Sect. 2.3 of the paper. The power output of wind turbine is varied along with the wind speed. A white band noise input is used to simulate the time to time-varying wind speed. Since, practically, the wind speed varies in long intervals, the simulation time for the noise input signal is kept to around 20 s. On the other hand, the thermal unit of the second area is designed similar to that of the first area and PID controller-2 regulates the controlled output and feeds it to the thermal unit. PV unit is modelled using transfer functions given in Sect. 2.2 of the paper. Again, PV is connected as constant power output and a white band noise signal is used to describe the varying nature of irradiance. In this case, the sample time for noise signal is kept to around 5 s, considering the practical scenario on a cloudy day. And both areas are interconnected using a tie-line which is already described by equations given in Sect. 2.4. The inputs of both controllers are the ACE of respective areas, which is defined in Sect. 2.5. A load disturbance of 4% is introduced at the 20th second of simulation time at the load end of area 1 and the algorithms were run. While running the algorithms, the initialization parameter population and maximum iteration are taken ranging from 50–200 and 16–24, respectively. While the definition parameters of various algorithms are varied to their best potential in obtaining optimal gain. The proposed mPSO algorithm takes in 50 search agents and 16 iterations to converge into the final optimal value. PSO and ASO worked better with 200 search agents and 16–24 iterations. Whereas for the rest of the algorithms, total search agents were selected 150–250 and 16–24 iterations. The algorithm's purpose was to minimize the ISE value over the limited number of iterations. Each algorithm is run multiple times, and ISE and time are recorded and compared with the proposed algorithm. The variation in time ranges from 10^4 s to 2×10^5 s for various algorithms, while the mPSO consumes time in the range of 5500–7500 s. In the aspect of convergence, every other algorithm converges to their respective final solution within the tenth iteration, while proposed mPSO converges within 8th–12th iteration and still searches for a global solution till last iteration. ISE is reduced to around 9.8×10^{-5} by mPSO whereas the least ISE obtained by the combined algorithms is 2.1×10^{-4}. The model under study is represented by Fig. 1. The controller parameters along with other observational data are listed in Table 2. The input to the constant output sources (i.e. wind and PV) and the proposed load disturbance is shown in Fig. 2. And the output due to various algorithms is depicted in Figs. 3, 4 and 5.

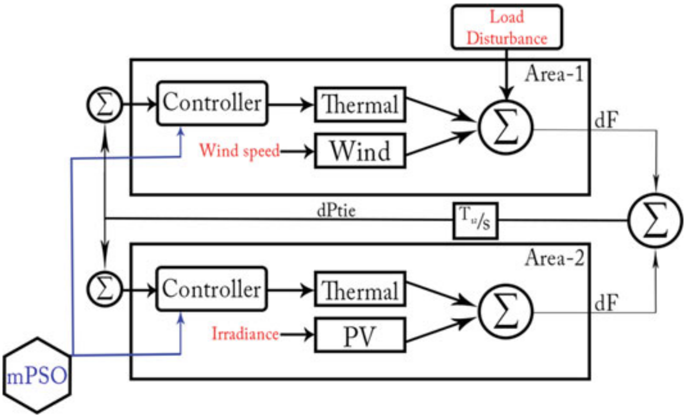

Fig. 1 The proposed model of two-area LFC consisting of RESs like wind and solar power. Load disturbance is injected at area-1. Irradiance and wind speed are considered to be fluctuating

Table 2 Comparison table among various algorithms studied

Algorithms	mPSO	PSO	ASO	AOA	ALO	GA	HHO
K_{p1}	−213.9	−173.6	−90.27	−211.8	−198	−245.5	−51.60
K_{i1}	−1623	−998.7	−537.7	−557.5	−693.2	−666.7	−491.1
K_{d1}	−74.16	−56.01	−77.99	−85.72	−49.81	−80.24	−53.14
K_{p2}	−228.9	−127.1	−130.1	−369.5	−235.5	−733.3	−53.23
K_{i2}	−2000	−798.2	−1443	−397.5	−351.2	−1163	−975
K_{d2}	−78.02	−90.32	−28.89	−461.9	−185.5	−570.9	−110.1
ISE	9.8e−5	2.4e−4	2.1e−4	0.015	7.7e−4	7.3e−4	4e−4
Average time per iteration (in s)	346	618	792	1138	740	921	1394
Total time (in s)	5546.6	9902.7	12,677	18,210	11,854	14,738	22,318

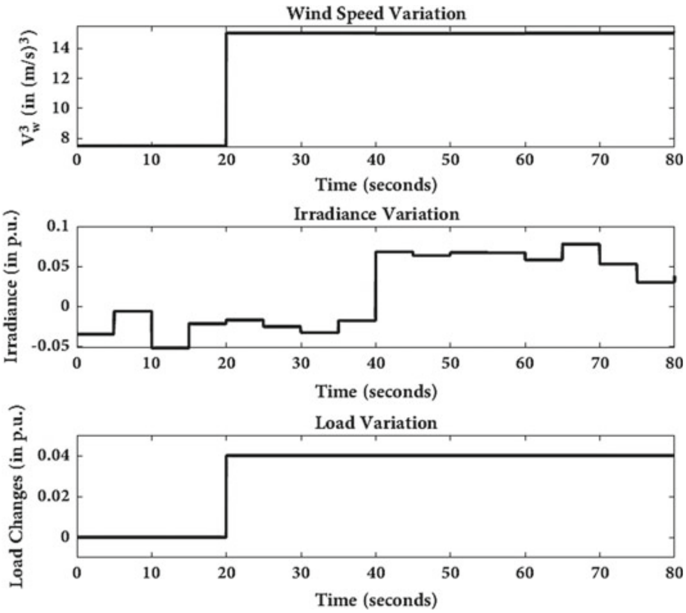

Fig. 2 Disturbances in the system. Due to natural factors at the source side and due to load variation at the load end

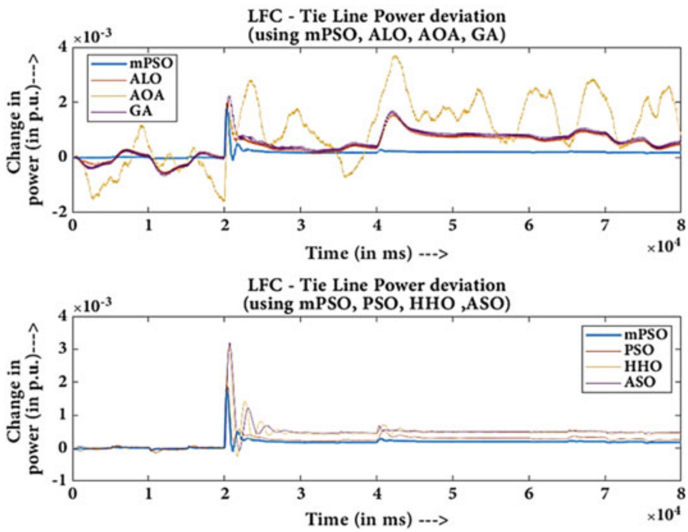

Fig. 3 Control of change in tie-line power by using various optimizers. Major deviation in the power is observed at 20 s is caused due to the variation in wind speed and load demand. The rest of the minor deviations are caused due to irradiance variation

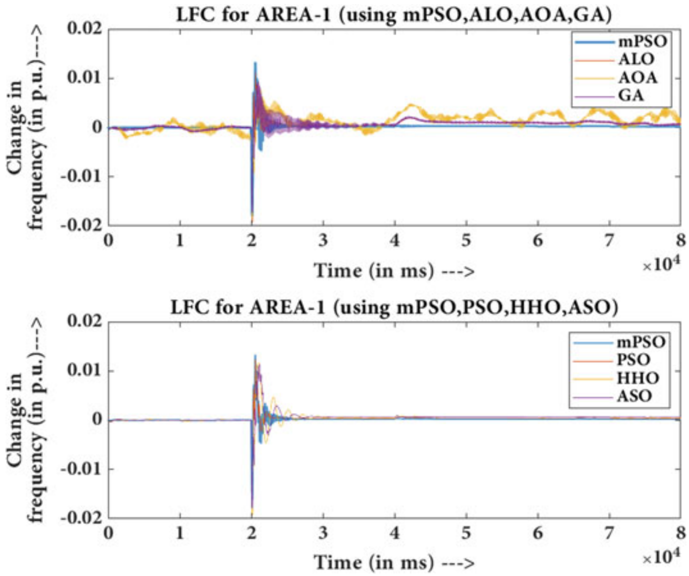

Fig. 4 Area 1: Control of frequency deviation by various algorithms. Major deviation in the frequency is observed at 20 s is caused due to the variation in wind speed and load demand. The rest of the minor deviations are caused due to irradiance variation

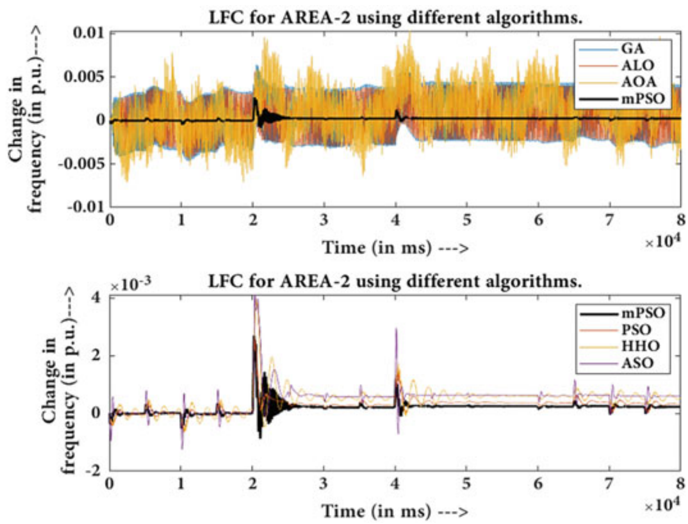

Fig. 5 Area 2: Control of frequency deviation by various algorithms. Major deviation in the frequency of the second area is observed at 20 s, however, at various intervals, irradiance deviation is more effective whenever large fluctuation is there, and can be seen at 10 s, 40 s, 65 s, 70 s and 75 s

5 Conclusion

This paper presents the viability of a new modified swarm optimizer mPSO when incorporated in load frequency control of integrated power system of RESs and conventional sources. The proposed mPSO strategy is compared with some of the new optimizers (AOA, HHO and ASO) in the market and some of the robust optimizers for LFC (PSO, GA and ALO). The algorithm is tested on a basic PID controller. The aspects of comparison taken into consideration in this paper mainly include the accuracy of finding optimal gain value by exploration and exploitation, time taken to converge to final result following minimizing error. After a series of simulations and iteration, it is found that in every aspect the proposed mPSO technique, while working on the LFC of two area system, gives better results than the other algorithms it is compared with. The least value of ISE is obtained with mPSO, which is 0.000098, whereas the second-least value obtained using ASO is 0.00021. The total iteration time taken by mPSO algorithm to obtain optimal gain value is 5546.6 s, which is the fastest among other algorithms, whereas the next fastest algorithm is PSO and it consumes 9902.7 s to obtain the optimal gain value. Also, while most of the algorithms rely on more search agents (50–100) for better exploration, the proposed mPSO technique requires comparatively lesser search agents (30–50). It is because in the first half of iteration the algorithm has the widest range of inertia weight (i.e. $w_{\max} = 0.9$ and $w_{\min} = 0.2$) which helps to search for global optimum and in the second half of the iteration, the algorithm exploits the best global optima for nearby local optima by reducing the inertia weight in steps as described in Eqs. (22 and 23) in Sect. 3. By doing this, a considerable amount of accuracy is achieved along with a significant reduction in search agents required to exploit and time spent per iteration.

Appendix

See Tables 3 and 4.

Table 3 Block parameters for two area control

Parameters	Values	Parameters	Values
K_g	1	T_t	0.3
T_g	0.08	K_p	100
K_t	1	T_p	20
K_{TWG}	1	T_{TWG}	1.5
R_{blade} (in m)	23.5	ω (in rad/s)	3.14
β (in rad)	0	ρ (kg/m^2)	1.25

(continued)

Table 3 (continued)

Parameters	Values	Parameters	Values
A_r (in m^2)	1735	P_{rated} (in kW)	3600
η_s	0.09–0.12	T_a (°C)	25
K_{pv}	1	T_{pv}	1.8
A_s (in m^2)	4048	K_r	0.33
T_r	10	T_{12}	0.545
R	2.5	B	0.8

Table 4 mPSO parameters for LFC of 2 area

Parameters	Values	Parameters	Values
No. of particles	100	w_{maxo}	0.9
No. of generations	16	w_{mino}	0.2
Fitness function	ISE	c_1 and c_2	2
ub	0	lb	−2000

References

1. Raju M, Saikia L, Sinha N (2017) Load frequency control of multi-area hybrid power system using symbiotic organisms search optimized two degree of freedom controller. Int J Renew Energy Res 7(4):1664–1674
2. Mohanty B, Panda S, Hota PK (2014) Differential evolution algorithm based automatic generation control for interconnected power systems with non-linearity. Alex Eng J 53(3):537–552
3. Sahu RK, Panda S, Padhan S (2015) A novel hybrid gravitational search and pattern search algorithm for load frequency control of nonlinear power system. Elsevier Science Publishers B. V. 29(C):310–327
4. Datta A, Bhattacharjee K, Debbarma S, Kar B (2015) Load frequency control of a renewable energy sources based hybrid system. In: 2015 IEEE conference on systems, process and control (ICSPC), pp 34–38
5. Bansal HO, Sharma R, Shreeraman PR (2012) PID controller tuning techniques: a review. J Control Eng Technol 2(4):168–176
6. Abualigah L, Ali D, Mirjalili S, Mohamed AE, Amir HG (2021) The arithmetic optimization algorithm. In: Computer methods in applied mechanics and engineering, vol 376
7. Weiguo Z, Liying W, Zhenxing Z (2019) Atom search optimization and its application to solve a hydrogeologic parameter estimation problem. Knowl-Based Syst 163:283–304
8. Heidari AA, Faris H, Aljarah I, Mirjalili S, Mafarja M, Chen H (2019) Harris hawks optimization: algorithm and applications. Futur Gener Comput Syst 97:849–872
9. Kennedy J, Eberhart R (1995) Particle swarm optimization. In: Proceedings of ICNN'95—international conference on neural networks, vol 4, pp 1942–1948
10. Nour El Yakine K, Menaa M, Hasni M, Boudour M (2017) A new optimal load frequency control based on hybrid genetic algorithm and particle swarm optimization. Int J Electr Eng Inform 9:418–440
11. Bansal JC, Singh PK, Saraswat M, Verma A, Jadon SS, Abraham A (2011) Inertia weight strategies in particle swarm optimization. In: Third world congress on nature and biologically inspired computing, pp 633–640
12. Parmar K, Majhi S, Kothari D (2012) Load frequency control of a realistic power system with multi-source power generation. Electr Power Energy Syst 42:426–433

13. Lee D, Wang L (2008) Small-signal stability analysis of an autonomous hybrid renewable energy power generation/energy storage system Part I: time-domain simulations. IEEE Trans Energy Convers 23(1):311–320
14. Shi Y, Eberhart R (1998) A modified particle swarm optimizer. In: IEEE international conference on evolutionary computation proceedings. IEEE world congress on computational intelligence (Cat. No.98TH8360), pp 69–73

Chapter 37
Load Frequency Control of a Four-Area Interconnected Power System Using JAYA Tuned PID Controller and Derivative Filter

Smrutisikha Jena, Sthitprajna Mishra, Bibhu Prasad Ganthia, and Sidhartha Kumar Samal

Abstract This study presents a MATLAB/Simulink model to design load frequency control (LFC) for a four-area interconnected power system. Load frequency control maintains the frequency of a power system within a prescribed limit. Various controllers for LFC of a power system have been proposed by many researchers. PID controller is a classical approach of LFC. PID controller using a filter in the derivative part amplifies the high-frequency noise and smoothes it out. Selection of appropriate optimization technique to tune controller gains plays a vital role for LFC. In this work, the PID controller and the PID controller using a derivative filter (PIDN) are optimized using particle swarm optimization (PSO) and JAYA optimization. After studying and comparing the results, with genetic algorithm (GA) from it has been observed that PID controller using a derivative filter (PIDN) optimized using JAYA algorithm provides better LFC in terms of settling time, overshoot, undershoot, and performance index of the system compared to the PID controller. The results obtained by JAYA tuned PIDN show better performance compared to the PID controller.

Keywords Load frequency control · AGC · Tie line · PIDN · PSO · JAYA

1 Introduction

In AGC at the centre, there is a generator which is generating active power generation P_g and reactive power generation Q_g. The generator is getting an input power from turbine, and the turbine is getting an input power from boiler. While the steam is coming from the boiler, there is a governor valve placed at the boiler to control the steam [1–4]. When the active power is delivering to the bus, there is a comparator over the bus which receives the frequency that means the frequency which comes from the generator f_g is sensed by the comparator. In comparator, we have to give

S. Jena (✉)
Electrical Engineering, VSSUT Burla, Burla, Odisha, India

S. Mishra · B. P. Ganthia · S. K. Samal
Electrical Engineering, IGIT Sarang, Dhenkanal, Odisha 759146, India

G. Panda et al. (eds.), *Sustainable Energy and Technological Advancements*,
Advances in Sustainability Science and Technology,
https://doi.org/10.1007/978-981-16-9033-4_37

a reference frequency f_{ref} that means the frequency which has to be maintained. If there is any difference between f_g and f_{ref}, then there will be an error f_e which will be operated by the generator valve and the whole closed loop is called as LFC [5–7].

2 Interconnected System

The operation of more than one interconnected area is known as interconnected system or power pool or pool operation. Under normal operating conditions, each control area carries its own load and each control area adopts beneficial regulating and control strategies. These are two basic operating principles of multi-control area system [8]. Unlike small system where sudden change in load causes large frequency drop which results in complete blackout of system, interconnected systems do not have these problems. In interconnected power system, sudden change in load causes large frequency drop. As the peak, demands occur at various hours of the day in various areas in an interconnected system, so the ratio of peak and average load is smaller than that of individual load. In an interconnected system, a control area is characterized by the same frequency throughout, and the frequency deviations in different areas are represented as $\Delta F1$, $\Delta F2$, $\Delta F3, \ldots$ like this. In an interconnected system, each area has generator, speed governing system and turbine. Each area has three inputs which are the controller input (ΔP_{ref}), load distribution (ΔP_D) and tie line power error (ΔP_{tie}) [6]. Each area has two outputs which are the generator frequency (ΔF) and area control area (ACE) which is the signal fed into the integrator.

$$\text{ACE} = B\Delta F + \Delta P_{\text{tie}}$$

where B is the frequency bias parameter (Figs. 1 and 2).

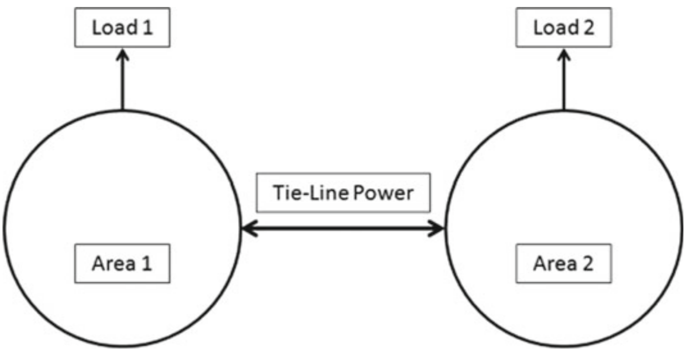

Fig. 1 Linear representation of tie line

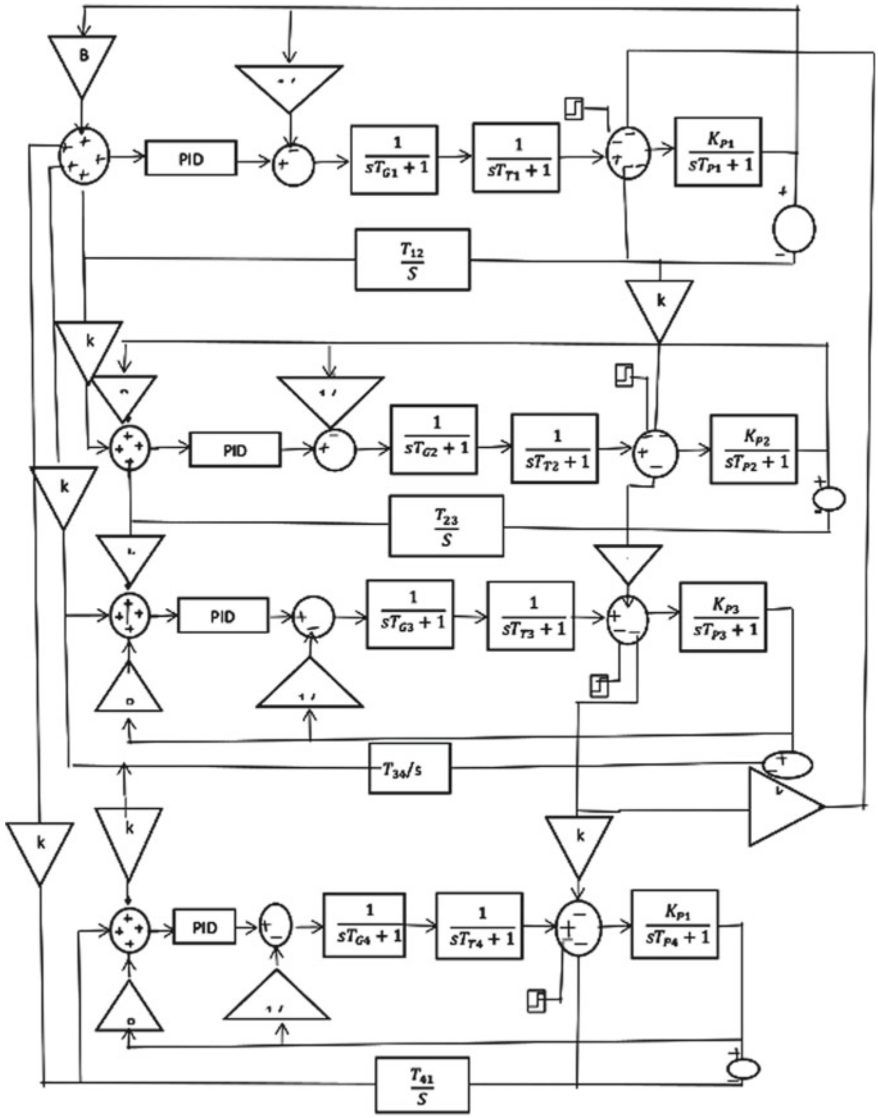

Fig. 2 Simulation model of four area power system

3 PID Controller

As the name indicates of this proportional–integral–derivative (PID) controller, the output is the combination of all proportional controller, integral controller, derivative controller. In case of derivative controller, we are having steady-state error problem, in case of integral controller we are having stability problem. So these problems are

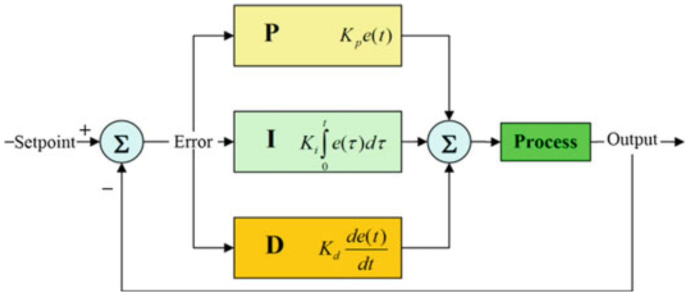

Fig. 3 Block diagram of PID controller

overcome in this PID controller [9]. The output of PID controller is directly proportional to the combination of error signal, integral of error signal, and differentiation of error signal. The integral action eliminates the offset or steady-state action. The derivative action provides necessary damping for hunting. So the PID controller is basically characterized by short-time rise, giving very rapid response, non-oscillatory stable, offset free output. We have to adjust or tune the values of the constraints K_p, K_i, K_d to get the better performance, and this method is known as tuning of PID controller [10]. Mathematically we can write,

$$u(t) \propto e(t) + \int e(t) + \frac{\mathrm{d}}{\mathrm{d}t} e(t)$$
$$u(t) = k_p e(t) + k_i \int e(t) + k_d \frac{\mathrm{d}}{\mathrm{d}t} e(t)$$

Taking Laplace of both sides (Fig. 3),

$$U(s) = E(s)\left[k_p + \frac{k_i}{s} + k_d s\right]$$
$$\frac{U(s)}{E(s)} = k_p + \frac{k_i}{s} + k_d s$$
$$\Rightarrow \frac{U(s)}{E(s)} = k_p\left[1 + \frac{k_i}{k_p s} + \frac{k_d}{k_p} s\right]$$
$$\Rightarrow \frac{U(s)}{E(s)} = k_p\left[1 + \frac{1}{T_i s} + T_d s\right]$$

where $T_i = \frac{k_p}{k_i}$, $T_d = \frac{k_d}{k_p}$.

4 PID Controller with Derıvatıve Filter (PIDN)

When a system like interconnected power system or microgrid is subjected to change, then it is very crucial and important to tune the gain parameters of the PID controller. As the PID controller often ignores the noise and nonlinear effect, so most of the time it does not work properly for practical problems. So here we put a first-order filter on the derivative term to tune it. As it reduces the high-frequency noise and smoothes it out so the chattering due to noise does not occur and the derivative will not reduce the high-frequency noise [11]. The transfer function of the PID controller with derivative filter (PIDN) is given here (Fig. 4)

$$TF_{\mathrm{PIDN}} = K_p + K_i\left(\frac{1}{s}\right) + K_d\left(\frac{1}{\frac{1}{N}+\frac{1}{s}}\right)$$

The objective of the study is to find the optimal values of the decision variables of the controller. These optimal values minimize the deviation of frequency. The most used objective functions are integral of time multiplied absolute error (ITAE), integral of square error (ISE), integral of time multiplied square error (ITSE). ITAE settles down the response of oscillation to steady value with minimum settling time and minimum overshoot which cannot be obtained from ISE, ITSE. So ITAE is assumed to be better objective function in LFC and that is why ITAE is chosen in this project for assessing the worth of a solution in the optimization algorithm [12]. The expressions of these objective functions are described below;

$$\mathrm{ISE} = \int_0^T (\Delta f)^2 \mathrm{d}t$$

$$\mathrm{ITSE} = \int_0^T t(\Delta f)^2 \mathrm{d}t$$

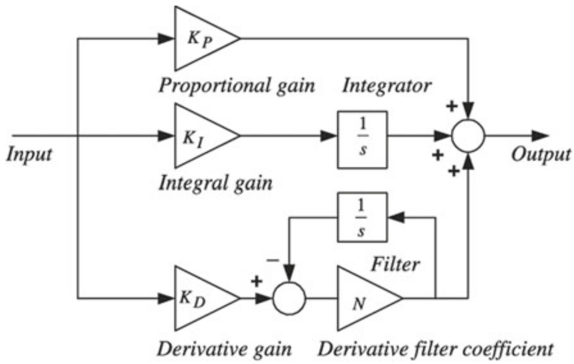

Fig. 4 Simulink model of PIDN controller

$$\mathrm{ITAE} = \int_0^T t|\Delta f|\mathrm{d}t$$

5 Particle Swarm Optimization

PSO is a robust stochastic optimization technique based on the movement and intelligence of swarm. Here we search for the optimum value by updating the generation or iteration. Instead of birds we use the word particle. To evaluate the fitness values for each particle, we use a fitness function. Fitness function is used in metaheuristic algorithm for optimization. Optimization means the optimum point where the conditions are best and most favourable [13]. We do this optimization to find out the best or better among different possible solution, and we are using objective function to maximize or minimize values that we are trying to optimize. Right now we are doing the optimization to find the minimum value which is the optimum point. In each iteration, every particle is updated by following the two best values. In every step, we have to check the fitness value $f(x_i^t)$ and then again we have to find the global best (gBest). We have to repeat this process until the condition is not the best condition.

In step 5, we have to update the $t = t + 1$.

In the last step, step 6 the output comes as gBest and x_i^t.

6 JAYA Algorithm

JAYA algorithm is a specific parameter less algorithm which is proposed by Rao RV in 2016. The word JAYA has been taken from the Sanskrit word JAYA which meaning is victory means the good is going to be win on the bad.

This algorithm has been formulated for solving various kinds of constrained as well as unconstrained optimization problems [14]. This is the concept in such a way that the solution we gained for a given particular problem should move towards its best solution as well as the major objective is the victory means this should avoid the worst solution [15]. Like other algorithms JAYA algorithm also have some control parameters. These are population size, number of generation. But unlike other algorithms, JAYA algorithm does not have any specific parameters. For example in PSO algorithm, we have to update inertia coefficient (w) and c_1, c_2, r_1, r_2. But in case of JAYA algorithm, such kind of specific parameters are not required to make the optimal solution. It tries to concentrate solution generation only [16–19].

7 Result and Discussion

The Simulink model shown in Figs. 5 and 6 is simulated using MATLAB/Simulink

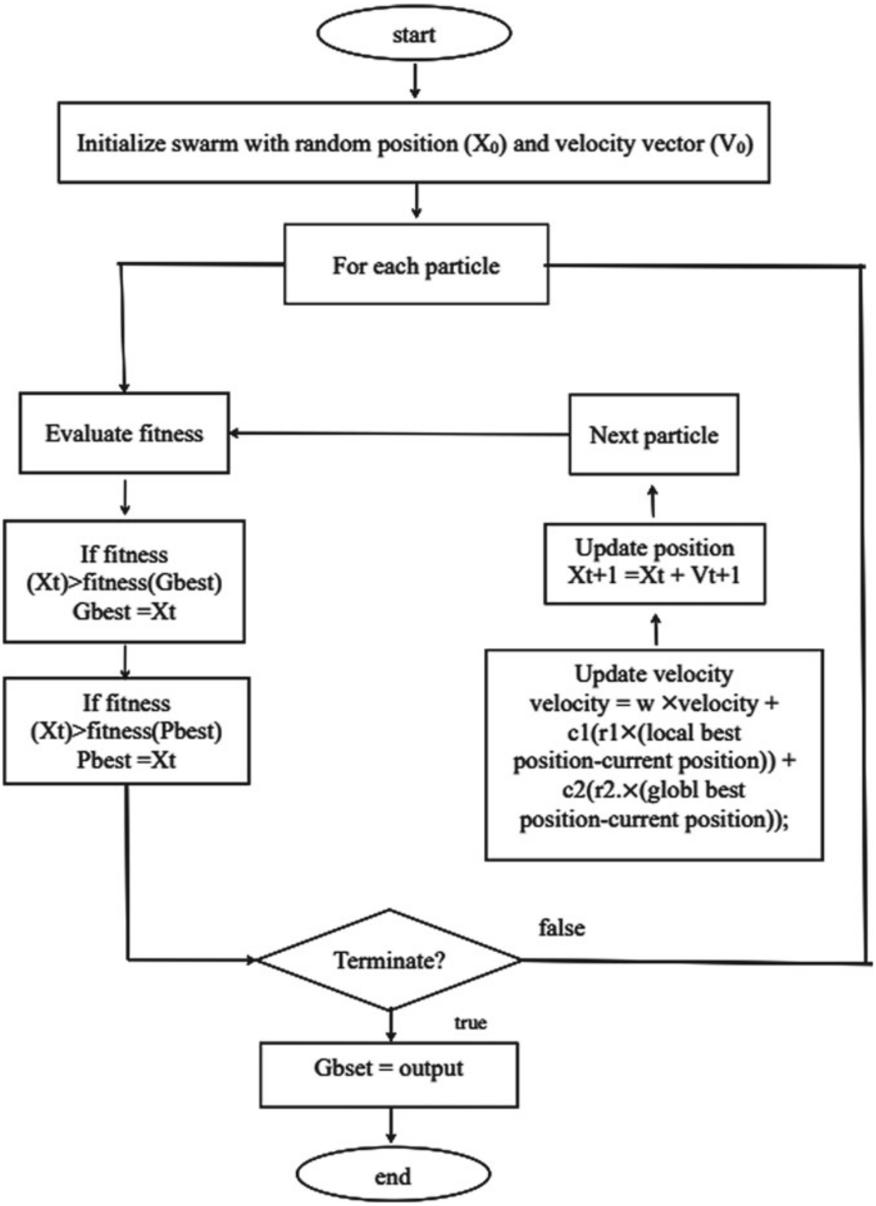

Fig. 5 Flowchart of PSO algorithm

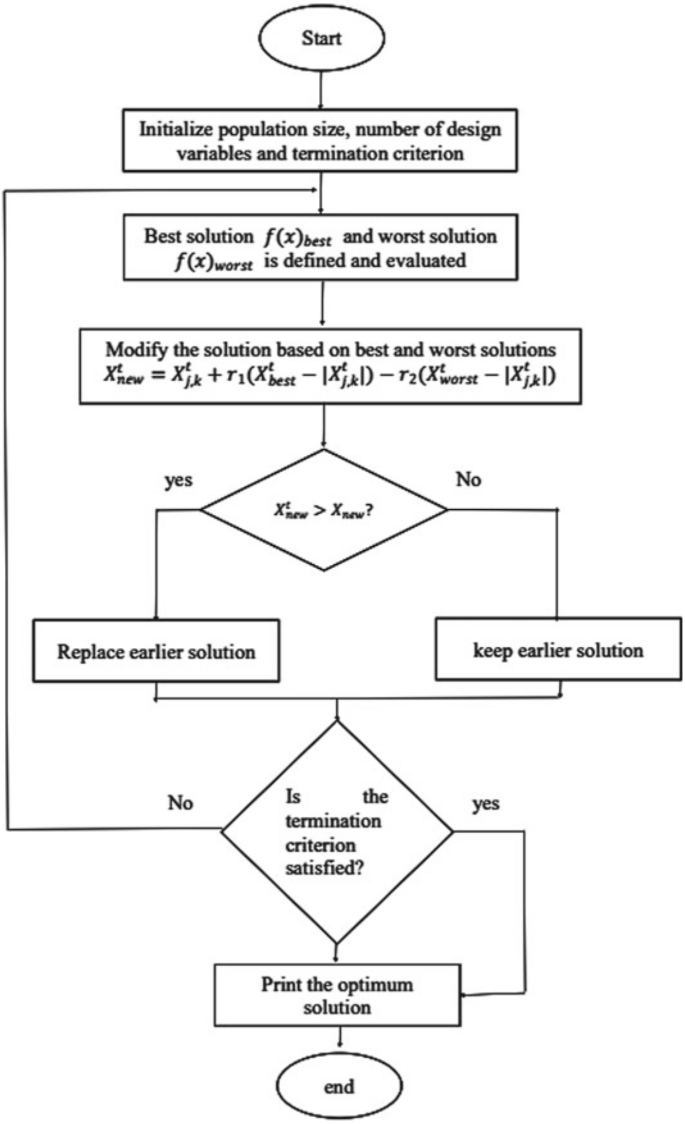

Fig. 6 Flowchart of JAYA algorithm

under PSO, JAYA algorithm. Both these solutions are compared with GA algorithm referring [11]. Here the population are taken as 30, number of iteration as 50, the range of parameters are taken as [−1, 1]. The program is run 30 times to obtain the best final solution. The best solution which is obtained is shown below.

System Performance Using PID Controller

Changes in the system frequency of the four-area system using a PID controller against a step load disturbance of 0.1 per unit is applied in all four areas are shown in Figs. 7, 8, 9, and 10. The deviation in frequency and corresponding tie line power are investigated. The value of proportional constant, integral constant, derivative constant, and different objective functions are obtained after optimizing with PSO and then JAYA optimization. The effectiveness of JAYA algorithm-based PID controller is shown by comparing it with the simulation result of PSO and GA [20–25]. The change in frequency and corresponding tie line deviation under the load disturbance of 0.1 p.u in four areas are shown in Figs. 7, 8, 9, and 10 (Table 1).

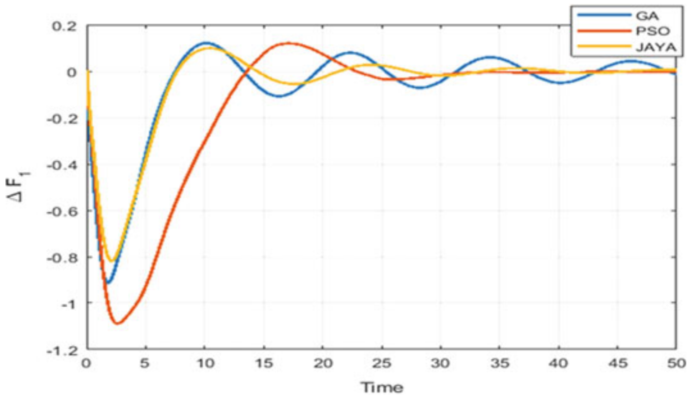

Fig. 7 Frequency response of area 1 using PID controller

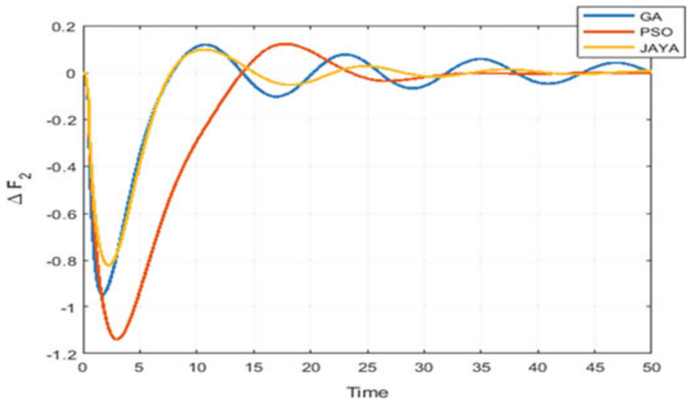

Fig. 8 Frequency response of area 2 using PID controller

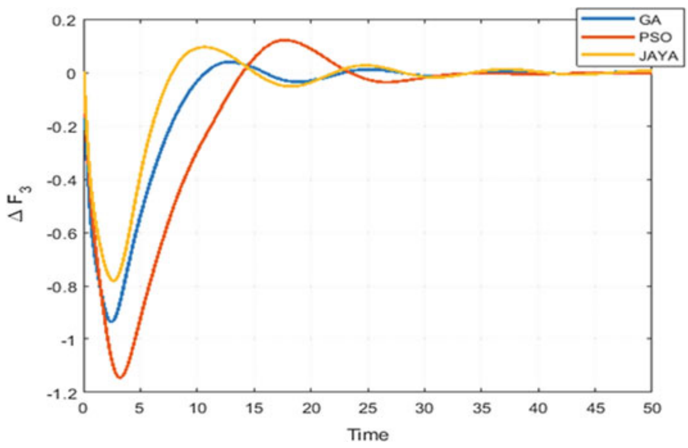

Fig. 9 Frequency response of area 3 using PID controller

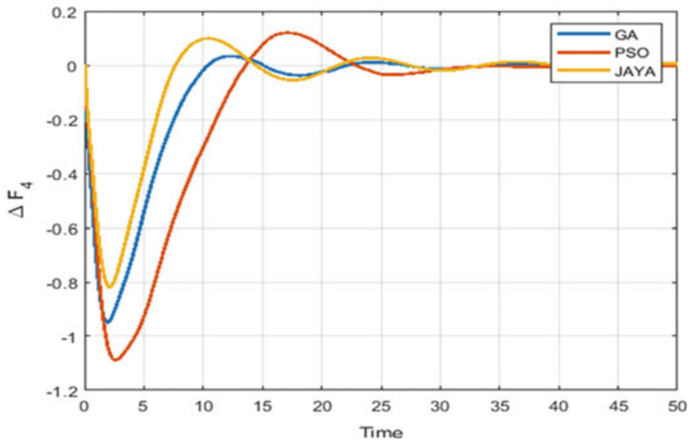

Fig. 10 Frequency response of area 4 using PID controller

System Performance Using PID Controller Using Derivative Filter (PIDN)
Changes in the system frequency of the four-area system using a PID controller using a derivative filter (PIDN) against a step load disturbance of 0.1 per unit is applied in all four areas are shown in Figs. 11, 12, 13, and 14. The deviation in frequency and corresponding tie line power are investigated. The value of proportional constant, integral constant, derivative constant, derivative filter, and an objective function is obtained after optimizing with PSO and then JAYA optimization. The efficacy of JAYA algorithm-based PID controller with derivative filter is shown by comparing with the simulation result of PSO. The change in frequency and corresponding tie line deviation under the load disturbance of 0.1 p.u in four areas are shown in Figs. 11, 12, 13, and 14 (Table 2).

Table 1 Tuned PID controller gains

Controller gains	PSO	JAYA
Kp1	0.0112	0.0218
Ki1	6.5402	2.7319
Kd1	3.7943	4.7272
ITAE1	4.7943	4.7272
Kp2	0.2176	0.2762
Ki2	3.2531	2.4062
Kd2	5.7291	5.4251
ITAE2	5.7291	5.4251
Kp3	0.0221	0.2373
Ki3	4.6011	2.1165
Kd3	4.1982	3.4231
ITAE3	4.1982	3.4231
Kp4	0.0262	0.0254
Ki4	4.7198	2.3068
Kd4	3.6846	3.3076
ITAE4	3.6846	3.3076

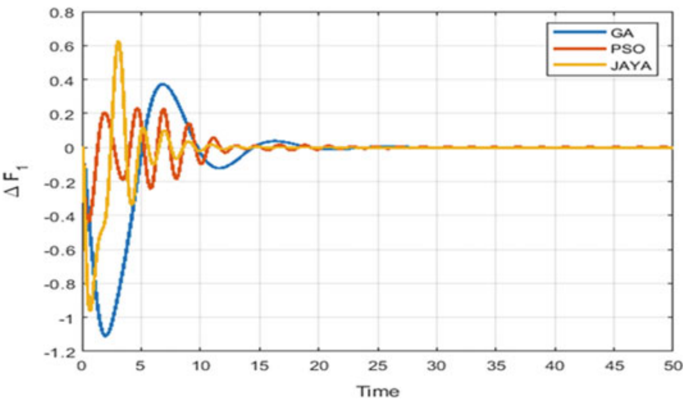

Fig. 11 Frequency response of area 1 using PIDN controller

8 Conclusion

The research is based on PSO, JAYA optimized PID, PIDN controller in a four-area power system. This proposed approach has been compared with conventional GA algorithm referring [11]. The results are analysed with PID and PIDN controller. The simulations are performed using MATLAB/Simulink. It is observed that the JAYA

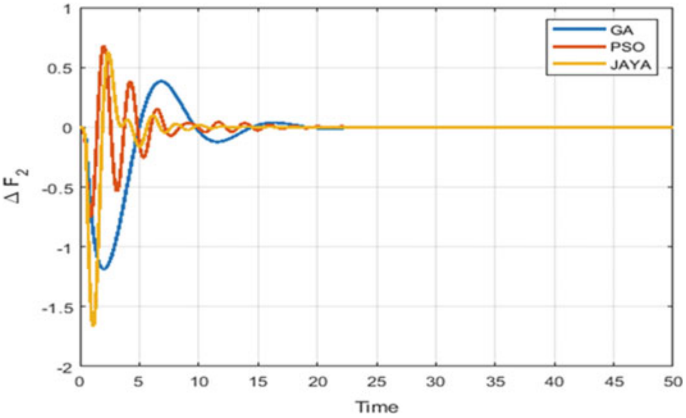

Fig. 12 Frequency response of area 2 using PIDN controller

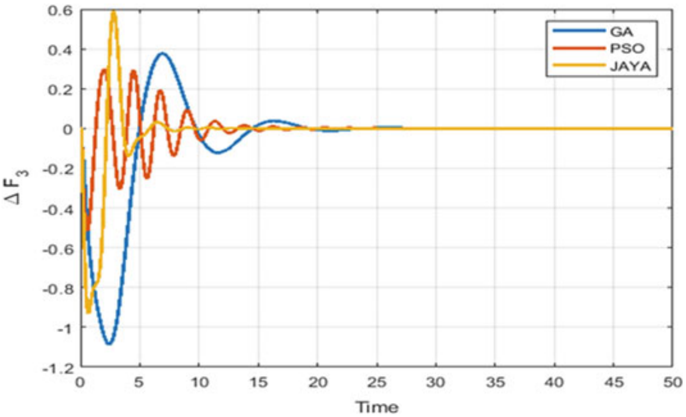

Fig. 13 Frequency response of area 3 using PIDN controller

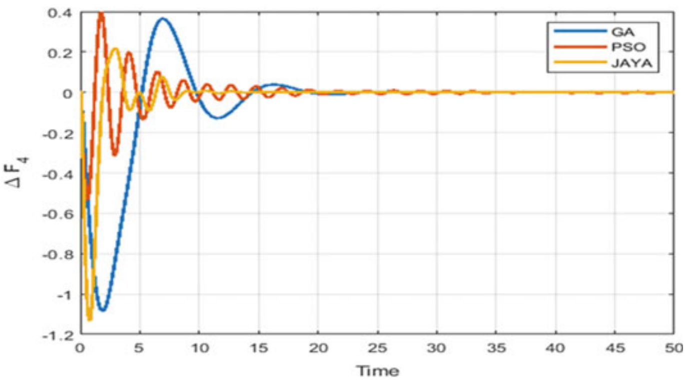

Fig. 14 Frequency response of area 4 using PIDN controller

Table 2 Tuned PIDN controller gains

Controller gains	PSO	JAYA
Kp1	0.0729	0.0157
Ki1	6.6028	8.6430
Kd1	1.8753	1.7332
N1	0.0112	0.2718
ITAE1	1.8659	1.7442
Kp2	0.0921	0.0177
Ki2	5.4005	6.3127
Kd2	1.9834	1.7387
N2	0.2176	0.7762
ITAE2	1.9745	1.8837
Kp3	0.0972	0.0120
Ki3	7.9814	9.0570
Kd3	1.9924	1.6551
N3	0.0221	0.2373
ITAE3	1.9833	1.6231
Kp4	0.3093	0.0293
Ki4	8.9082	10.3215
Kd4	2.5103	2.4500
N4	0.0262	0.4254
ITAE4	2.5003	2.4500

tuned PIDN controller gives the best performance in terms of settling time, peak overshoot, undershoot. Thus, the JAYA-based PID controller with derivative filter (PIDN) outperforms the PID controller without derivative filter. Further, analysis on this topic can be carried out using different new optimization techniques. Different controllers, like fractional-order proportional derivative controller (FOPID), FOPID(1 + PI) can be tested for improved ALFC in a power system.

References

1. Ganthia BP, Pritam A, Rout K, Singhsamant S, Nayak J (2018) Study of AGC in two-area hydro-thermal power system. In: Garg A, Bhoi A, Sanjeevikumar P, Kamani K (eds) Advances in power systems and energy management. Lecture Notes in Electrical Engineering, vol 436. Springer, Singapore. https://doi.org/10.1007/978-981-10-4394-9_39
2. Sankar R, Pradhan SR, Chatterjee K, Mandal R (2017) A comprehensive state of the art literature survey on LFC mechanism for power system. Renew Sustain Energy Rev 76:1185–1207
3. Shah NN, Chafekar AD, Mehta DN, Suthar AR (2012) Automatic load frequency control of two area power system with conventional and fuzzy logic control. Int J Eng Res Technol (IJERT) 1(3):343–347

4. Passino KM, Quijano N (2002) Proportional-integral-derivative control with derivative filtering and integral anti-windup for a DC servo. Department Electrical Engineering, The Ohio State University Neil Avenue, Columbus, OH 43210-1272, 22 March
5. Dhamanda A, Dutt A, Bhardwaj AK (2015) Automatic generation control in four area interconnected power system of thermal generating unit through evolutionary technique. Int J Electr Eng Inform 7(4)
6. Panda S, Mohanty B, Hota PK (2014) Controller parameters tuning of differential evolution algorithm and its application to load frequency control of multisource power system. Int J Electr Power Energy Syst 54:77–85
7. Valle YD, Venayagamoorthy GK, Mohagheghi S, Hernandez JC, Harley RG (2008) Particle swarm optimization: basic concepts, variants, and applications in power system. IEEE Trans Evol Comput 12(2):171–195
8. Abd-El-Wahed WF, Mousa AA, El-Shorbagy MA (2011) Integrating particle swarm optimization with genetic algorithms for solving nonlinear optimization problems. J Comput Appl Math 235(5):1446–1453. https://doi.org/10.1016/j.cam.08.030,(2010)
9. Rao RV (2016) Jaya: a simple and new optimization algorithm for solving constrained and unconstrained optimization problems. Int J Ind Eng Comput 7(1):19e34
10. Singh SP, Prakash T, Singh VP, Ganesh Babu M (2017) Analytic hierarchy process based automatic generation control of multi-area interconnected power system using Jaya algorithm. Eng Appl Artif Intell 60:35–44
11. Golpira H, Barvani H (2017) Application of GA optimization for automatic generation control design in an interconnected power system. Energy Convers Manage 52:2247–2255
12. Bhongade S, Parmar VP (2018) Automatic generation control of two-area ST-thermal power system using Jaya algorithm. Int J Smart Grid 2(2)
13. Alrifai MT, Zribi M (2005) Decentralized controllers for power system load frequency control. ASCE J 5(II)
14. Sahu SRK, Panda S, Rout UK (2013) DE optimized parallel 2-DOF PID controller for load frequency control of power system with governor dead-band non linearity. Int J Electr Power Energy Syst 49
15. Ganthia B, Rout K (2016) Deregulated power system based study of AGC using PID and fuzzy logic controller. Int J Adv Res 4(06)
16. Pritam A et al (2017) Automatic generation control study in two area reheat thermal power system. IOP Conf Ser Mater Sci Eng 225:012223
17. Ganthia BP, Mohanty S, Rana PK, Sahu PK (2016) Compensation of voltage sag using DVR with PI controller. In: International conference on electrical, electronics, and optimization techniques (ICEEOT), Chennai, pp 2138–2142. https://doi.org/10.1109/ICEEOT.2016.7755068
18. Ganthia BP, Agarwal V, Rout K, Pardhe MK (2017) Optimal control study in DFIG based wind energy conversion system using PI & GA. In: International conference on power and embedded drive control (ICPEDC), Chennai, pp 343–347
19. Ganthia BP, Mohanty M, Maherchandani JK (2022) Power analysis using various types of wind turbines. In: Fekik A, Benamrouche N (eds) Modeling and control of static converters for hybrid storage systems. IGI Global, Hershey, pp 271–286. https://doi.org/10.4018/978-1-7998-7447-8.ch010
20. Ganthia BP, Barik SK, Nayak B (2022) Comparative analysis of various types of control techniques for wind energy conversion system. In: Fekik A, Benamrouche N (eds) Modeling and control of static converters for hybrid storage systems. IGI Global, Hershey, pp 143–174. https://doi.org/10.4018/978-1-7998-7447-8.ch006
21. Ganthia BP, Rana PK, Patra T, Pradhan R, Sahu R (2018) Design and analysis of gravitational search algorithm based TCSC controller in power system. Mater Today: Proc 5(1):841–847
22. Ganthia BP, Barik SK, Nayak B (2020) Shunt connected FACTS devices for LVRT capability enhancement in WECS. Eng Technol Appl Sci Res 10(3):5819–5823

23. Ganthia BP, Pradhan R, Sahu R, Pati AK (2021) Artificial ant colony optimized direct torque control of mathematically modeled induction motor drive using PI and sliding mode controller. In: Kumar J, Jena P (eds) Recent advances in power electronics and drives. Lecture Notes in Electrical Engineering, vol 707. Springer, Singapore. https://doi.org/10.1007/978-981-15-8586-9_35
24. Pragati A, Ganthia BP, Panigrahi BP (2021) Genetic algorithm optimized direct torque control of mathematically modeled induction motor drive using PI and sliding mode controller. In: Kumar J, Jena P (eds) Recent advances in power electronics and drives. Lecture Notes in Electrical Engineering, vol 707. Springer, Singapore. https://doi.org/10.1007/978-981-15-8586-9_32
25. Ganthia BP, Barik SK (2020) Steady-state and dynamic comparative analysis of PI and fuzzy logic controller in stator voltage oriented controlled DFIG fed wind energy conversion system. J Inst Eng India Ser B 101:273–286. https://doi.org/10.1007/s40031-020-00455-8

Chapter 38
Model Predictive Control for Load Frequency Regulation in Power Systems Using a Disturbance Observer

Nuvvula S. S. Ramakrishna, Tummala S. L. V. Ayyarao, Vasupalli Manoj, and L. Dinesh

Abstract Power systems experience high load frequency changes as a result of increasing renewable energy additions and fluctuating demand levels. Model predictive control (MPC) for automatic generation control (AGC) in power systems is proposed using an observer for nonlinear disturbances (NDO). Load disturbances and un-modeled nonlinearities which adversely affect the output prediction in MPC are considered as a net disturbance, and it is estimated using a NDO. An offset-free MPC control law is obtained by optimizing the receding-horizon stage with the predicted disturbance. Power systems with single-area and three-area distribution are subjected to this proposed approach of frequency regulation, which has been shown to be effective in simulations.

Keywords AGC · Load frequency regulator · Model predictive control · Disturbance observer

1 Introduction

With increased industrial production, demand for uninterrupted power supply, increased revenue in renewable energy generation, and change in government policies lead to increased energy additions. With the abundant source available in nature, the installations of medium and high rating wind turbines are rapidly increased, and this trend will remain the same in the near future also. Increased share of renewable energy in power systems leads to load frequency fluctuations as the renewable energy is intermittent in nature. The concept of load frequency has attracted many control engineers around the globe, and several control solutions are proposed in the literature. Load frequency regulation by linear controllers like PI, PID, and LQR are

N. S. S. Ramakrishna (✉) · T. S. L. V. Ayyarao · V. Manoj
School of Electrical Engineering, Vellore Institute of Technology (VIT), Vellore, India

Electrical and Electronics Engineering, GMR Institute of Technology, Rajam, India

L. Dinesh
Electrical & Electronics Engineering, ANITS, Visakhapatnam, India

G. Panda et al. (eds.), *Sustainable Energy and Technological Advancements*, Advances in Sustainability Science and Technology,
https://doi.org/10.1007/978-981-16-9033-4_38

conventional methods proposed and vast research is invested on the tuning methods of these controllers [1–5]. But there are many limitations with these linear controllers, and one of these limitations is that the performance of linear controllers is not robust to load disturbances and parametric variations. This issue can be tackled by applying the robust control theory. Sliding mode control, control, synthesis, and fractional order control are some of the useful robust controllers [6–10].

Model predictive control (MPC) is another powerful method that can be useful for controlling a process/plant. The concept of MPC was developed in 1960s and became popular from 1990s. The applications of MPC are accelerated from 2000 onwards. It is based upon controlling a process/plant for a given cost function with future prediction. MPC-based load frequency control of power system was discussed in [11–14]. Disturbances and parametric variations on plant may degrade the MPC output prediction. The performance of MPC can be enriched by estimating the disturbance and including it the prediction stage. For the frequency regulation of a power system network, a sliding mode controller design method is described in this article. LFC system model uses a sliding surface with four parameters. GWO and PSO approaches are used to optimize the controller parameters in order to get the best results. When optimizing frequency and tie-line power transfer, the goal function has been defined as the integral of the square of inaccuracy of deviation.

Its key contribution is the invention of a decentralized load frequency controller based on MPC for interconnected power systems using disturbance observer and some of the highlights of the proposed method are A NDO estimates the net disturbance that affects the load frequency. In order to minimize the effect of parametric variations, un-modeled nonlinear dynamics, and load disturbances, the estimated disturbance is included in the output prediction stage. A nonlinear control law is derived based on receding-horizon optimization that minimizes the cost function. This avoids online optimization of control parameters and thus saves computational effort.

In this paper, the load frequency is regulated by automatically adjusting the thermal power generation. Both single-area and three-area systems are used to test the proposed approach for calculating load frequency. The rest of the paper is organized as follows: Section 2 summarizes the small signal model of power systems. The theory of NDO-based offset-free MPC is outlined in Sect. 3. Application of MPC for load frequency regulation is discussed in Sect. 4. Finally, in Sect. 5, the effectiveness of the suggested strategy is evaluated using simulation results for single-area and three-area systems, and conclusions are drawn (Fig. 1).

2 The Multi-area Power System Mathematical Model

This is a distributed system that is very nonlinear and linearized around an operating point. The dynamical model of ith area interconnected power systems is given in this section.

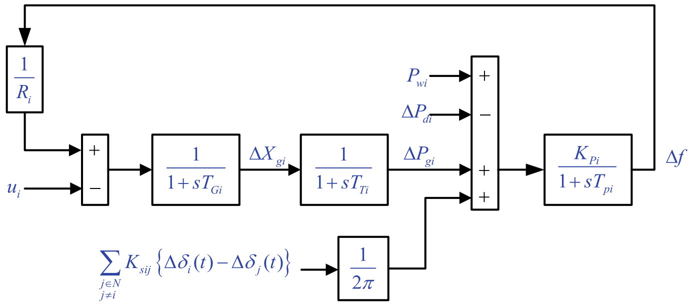

Fig. 1 Small signal of *i*th area power systems

2.1 Dynamics of *i*th Area Power System Model

$$\Delta \dot{f}_i(t) = -\frac{1}{T_{Pi}}\Delta f_i(t) + \frac{K_{Pi}}{T_{Pi}}\Delta P_{gi}(t) - \frac{K_{Pi}}{T_{Pi}}\Delta P_{di}(t) - \frac{K_{Pi}}{2\pi T_{Pi}}\sum_{\substack{j\in N\\ j\neq i}} K_{sij}\{\Delta\delta_i(t) - \Delta\delta_j(t)\} + \frac{K_{Pi}}{T_{Pi}}\Delta P_{wi}(t) \tag{1}$$

$$\Delta \dot{P}_{gi}(t) = -\frac{1}{T_{Ti}}\Delta P_{gi}(t) + \frac{1}{T_{Ti}}\Delta X_{gi}(t) \tag{2}$$

$$\Delta \dot{X}_{gi}(t) = -\frac{1}{R_i T_{Gi}}\Delta f_i(t) - \frac{1}{T_{Gi}}\Delta X_{gi}(t) - \frac{1}{T_{Gi}}u_i(t) \tag{3}$$

$$\Delta\dot{\delta}(t) = 2\pi\Delta f_i \tag{4}$$

where Δf_i is the alteration in frequency; ΔP_{gi} is the alteration in generator power output; ΔP_{di} is the alteration in load demand; ΔP_{wi} is the alteration in wind power input; K_{Pi} is power system addition; T_{Pi} is the power system period constant; T_{Ti} is the turbine period constant; ΔX_{gi} is the change in governor valve position; T_{Gi} is the governor time constant; R_i is the speed regulation coefficient; u_i is the control input; $\Delta\delta_i$ is the change in rotor angle.

Let us consider lumped disturbance on the system is ϖ_i

$$\varpi_i = -\frac{K_{Pi}}{T_{Pi}}\Delta P_{di}(t) - \frac{K_{Pi}}{2\pi T_{Pi}}\sum_{\substack{j\in N\\ j\neq i}} K_{sij}\{\Delta\delta_i(t) - \Delta\delta_j(t)\} + \frac{K_{Pi}}{T_{Pi}}\Delta P_{wi}(t) \tag{5}$$

Accordingly, (1) is modified as

$$\Delta \dot{f}_i(t) = -\frac{1}{T_{Pi}}\Delta f_i(t) + \frac{K_{Pi}}{T_{Pi}}\Delta P_{gi}(t) + \varpi_i \tag{6}$$

1. ***Wind Energy system***

Wind energy system is a stochastic system, and hence, it is modeled as a random process. As the wind speed v_w continuously changes with time, it is mathematically modeled as [15]

$$v(t) = V_{\text{avg}} + \sum_{l=1}^{z} V_l \cos(w_l t + \Phi_l) \tag{7}$$

where V_{avg} is the mean wind speed, l is the number of samples, w_l is the discretized frequency, V_i is the magnitude of the wind speed, and Φ_l is the random phase angle.

$$\text{The wind turbine output is } P_{wi} = 0.5\rho\pi R_{wT}^2 C_p v^3 \tag{8}$$

3 NDO-Based Offset-Free MPC

An example linear system will be examined using the representation of state space as

$$\dot{x} = Ax + Bu + D\varpi \quad \text{and} \quad y = Cx \tag{9}$$

where $x \in \Re^n$ is the state vector, $u \in \Re^m$ is the control vector, $\varpi \in \Re$ is the net disturbance on the system, $y \in \Re^m$ is the output vector, and matrices A, B, C, D have their own meaning.

The following assumptions are useful for the design of NDO-based MPC.

Assumption 1: The system pair (A, B) is controllable.

Assumption 2: All states of the system are measurable.

Assumption 3: The system's net disruption is constrained by its boundaries, i.e., $\|\varpi\| \leq \varpi_\infty$ where ϖ_∞ is a positive value.

Assumption 4: The overall system disturbance slows varies with time, i.e., $\lim_{t\to\infty} \dot{\varpi} = 0$.

Assumption 5: The control order of the system is r (Fig. 2).

3.1 Nonlinear Disturbance Observer Design

Many approaches exist to estimate the net disturbance on the system, including the NDO, extended state disturbance observer, perturbation observer, sliding mode observer, etc. [16]. As part of the design process, a virtual state with given dynamics

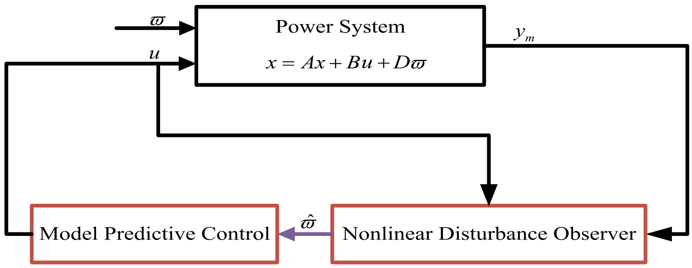

Fig. 2 NDO-based MPC

is evaluated in order to estimate the net disturbance on the system (10 and 11).

$$\dot{\xi} = -GD\hat{\varpi} - G(Ax + Bu) \tag{10}$$

$$\hat{\varpi} = \xi + Gx \tag{11}$$

4 Offset-Free Model Predictive control

There are three major essentials in the design of MPC [17], namely

1. Prediction model
2. Formulation of objective function
3. Generating the control law.

The main objective of the MPC is to minimize the cost function given in (12)

$$\Im = \frac{1}{2}\int_0^{T_p}\left(\left\|\hat{y}(t+\tau) - \hat{y}_r(t+\tau)\right\|^2 + \left\|\hat{u}(t+\tau)\right\|^2\right)\mathrm{d}\tau \tag{12}$$

where $\hat{y}(t+\tau)$ is the future projected output, $\hat{y}_r(t+\tau)$ is the forthcoming orientation trajectory, T_p is the predictive period, and $\hat{u}(t+\tau)$ is the future control law.

The output prediction in MPC can be enhanced by including the estimated disturbance in the design process without upsetting the performance of the controller under nominal conditions. The design is based on receding-horizon optimization. Following the procedure given in [18, 19], the future output is predicted using Taylors series and is given by (13)

$$y(t+\tau) = y(t) + \tau y^{[1]}(t) + \cdots + \frac{\tau^{n+r}}{(n+r)!}y^{[n+r]}(t) \tag{13}$$

where

$$y^{[n]} = CA^n x + \sum_{i=0}^{n-1} CA^{n-1-i} D\varpi^{[i]} + CA^{n-1} Bu \tag{14}$$

$$y^{[n+r]} = CA^{n+r} x + \sum_{i=0}^{r} CA^{n+r-1-i} Bu^{[i]} + \sum_{i=0}^{n+r-1} CA^{n+r-1-i} D\varpi^{[i]} \tag{15}$$

Representing (13)–(15) in a matrix form as

$$\hat{y}(t+\tau) = \begin{bmatrix} \overline{\mathrm{T}} & \tilde{\mathrm{T}} \end{bmatrix} \begin{bmatrix} \hat{\overline{Y}} \\ \hat{\tilde{Y}} \end{bmatrix} \tag{16}$$

where

$$\overline{\mathrm{T}} = \begin{bmatrix} 1 & \tau & \cdots & \frac{\tau^{n-1}}{(n-1)!} \end{bmatrix} \tag{17}$$

$$\tilde{\mathrm{T}} = \begin{bmatrix} \frac{\tau^n}{n!} & \frac{\tau^{n+1}}{(n+1)!} & \cdots & \frac{\tau^{n+r}}{(n+r)!} \end{bmatrix} \tag{18}$$

$$\hat{\overline{Y}} = \begin{bmatrix} \hat{y} & \hat{y}^{[1]} & \cdots & \hat{y}^{[n-1]} \end{bmatrix}^T \tag{19}$$

$$\hat{\tilde{Y}} = \begin{bmatrix} \hat{y}^{[n]} & \cdots & \hat{y}^{[n+r]} \end{bmatrix}^T \tag{20}$$

Following the previous procedure, reference output is generated as

$$\hat{y}_r(t+\tau) = \begin{bmatrix} \overline{\mathrm{T}} & \tilde{\mathrm{T}} \end{bmatrix} \begin{bmatrix} \hat{\overline{Y}}_r \\ \hat{\tilde{Y}}_r \end{bmatrix} \tag{21}$$

Now, the objective of the MPC is to minimize (12)

$$\begin{aligned} \Im = \frac{1}{2}\int_0^{T_P} &\begin{bmatrix} (\hat{\overline{Y}} - \hat{\overline{Y}}_r)^T & (\hat{\tilde{Y}} - \hat{\tilde{Y}}_r)^T \end{bmatrix} \begin{bmatrix} \overline{\mathrm{T}}^T \sqrt{Q} \\ \tilde{\mathrm{T}}^T \sqrt{Q} \end{bmatrix} \begin{bmatrix} \sqrt{Q}\overline{\mathrm{T}} & \sqrt{Q}\tilde{\mathrm{T}} \end{bmatrix} \\ &\begin{bmatrix} \hat{\overline{Y}} - \hat{\overline{Y}}_r \\ \hat{\tilde{Y}} - \hat{\tilde{Y}}_r \end{bmatrix} \mathrm{d}\tau + \frac{1}{2}\int_0^{T_P} \hat{\overline{u}}^T \hat{\mathrm{T}} \hat{\overline{u}} \mathrm{d}\tau \end{aligned} \tag{22}$$

For obtaining the optimized control input $\hat{\overline{u}}_c$ to plant, find $\frac{\partial \Im}{\partial \hat{\overline{u}}}$ and equate to zero [18].

$$\hat{\overline{u}}_c = \left(CA^{n-1}B\right)^{-1}\left[-K\left(\hat{\overline{Y}} - \hat{\overline{Y}}_r\right) + \left(y_r^{[n]} - CA^n x - CA^{n-1} D\hat{\varpi}\right)\right] \tag{23}$$

5 Load Frequency Control Using NDO-Based MPC

Representing the linearized model of power system given in Sect. 2 in state space representation as given in (9).

where $x = \begin{bmatrix} \Delta\delta_i & \Delta f_i & \Delta P_{gi} & \Delta X_{gi} \end{bmatrix}^T$.

$$B = \begin{bmatrix} 0 \; 0 \; 0 \; -\frac{1}{T_{Gi}} \end{bmatrix}$$

$$A = \begin{bmatrix} 0 & 2\pi & 0 & 0 \\ 0 & -\frac{1}{T_{Pi}} & \frac{K_{Pi}}{T_{Pi}} & 0 \\ 0 & 0 & -\frac{1}{T_{Ti}} & \frac{1}{T_{Ti}} \\ 0 & -\frac{1}{R_i T_{Gi}} & 0 & -\frac{1}{T_{Gi}} \end{bmatrix} \tag{24}$$

Using the transformation $x \to \Gamma\varsigma$, the modified dynamics are given (25–28)

$$\dot{\varsigma}_1 = \varsigma_2 + d_1\varpi \tag{25}$$

$$\dot{\varsigma}_2 = \varsigma_3 + d_2\varpi \tag{26}$$

$$\dot{\varsigma}_3 = \varsigma_4 + d_3\varpi \tag{27}$$

$$\dot{\varsigma}_4 = f(\varsigma) + bu + d_4\varpi \tag{28}$$

Now, the system represented in (9) is transformed to a new model represented by (27)

$$\dot{\varsigma} = A_c\varsigma + B_c u + D_c\varpi \tag{29}$$

where $\varsigma = \begin{bmatrix} \varsigma_1 & \varsigma_2 & \varsigma_3 & \varsigma_4 \end{bmatrix}^T$.

$$A_c = \Gamma x \Gamma^{-1} \tag{30}$$

$$B_c = \Gamma B \tag{31}$$

$$D_c = \Gamma D \tag{32}$$

Now, calculate $\hat{\overline{Y}}$ and $\hat{\overline{Y}}_r$ from (19) and (21)

$$\hat{\bar{Y}} = \begin{bmatrix} \hat{\varsigma}_1 \\ \dot{\hat{\varsigma}}_1 \\ \dot{\hat{\varsigma}}_2 \\ \dot{\hat{\varsigma}}_3 \end{bmatrix} = \begin{bmatrix} \hat{\varsigma}_1 \\ \varsigma_2 + d_1\hat{\varpi} \\ \varsigma_3 + d_2\hat{\varpi} \\ \varsigma_4 + d_3\hat{\varpi} \end{bmatrix} \tag{33}$$

$$\hat{\bar{Y}}_r = \begin{bmatrix} \hat{\varsigma}_{1r} \\ \dot{\hat{\varsigma}}_{1r} \\ \dot{\hat{\varsigma}}_{2r} \\ \dot{\hat{\varsigma}}_{3r} \end{bmatrix} = \begin{bmatrix} \hat{\varsigma}_{1r} \\ \varsigma_{2r} + d_1\hat{\varpi} \\ \varsigma_{3r} + d_2\hat{\varpi} \\ \varsigma_{4r} + d_3\hat{\varpi} \end{bmatrix} \tag{34}$$

The reference state vector $\varsigma_r = \begin{bmatrix} \varsigma_{1r} & \varsigma_{2r} & \varsigma_{3r} & \varsigma_{4r} \end{bmatrix}^T$ is obtained by equating the right hand side of (27) to zero.

Now, obtain the suitable control law using (24)

$$u = -\frac{1}{CA_c^2B_c}\left(-K\left(\hat{\bar{Y}} - \hat{\bar{Y}}_r\right) + y_r^{[n]} - CA_c^n x_c - CA_c^{n-1}D_c\hat{\varpi}\right) \tag{35}$$

The working procedure of the proposed NDO-based offset-free MPC method for load frequency control is as follows.

1. The net disturbance $\hat{\varpi}$ is estimated by NDO from (10) and (11)
2. Obtain the new state vector
3. MPC minimizes the objective function (9) by using the control (35).

6 Results and Dıscussıons

The proposed method of frequency regulation is tested on single-area system as well as three-area power system with different operating conditions.

The proposed method of frequency regulation is tested on single-area system as well as three-area power system with different operating conditions (Figs. 3 and 4).

The proposed strategy is evaluated using a single-area hybrid power system [20] with wind energy integration. This system is simulated in MATLAB/Simulink with ode4 solver where NDO-based MPC is implemented using embedded function. These are the parameters of a single-area system in Table 1. The design parameters used for NDO and MPC are given in Table 2.

Load tripping or load failure in power systems is a common issue, and this is represented as a sudden load change of 0.01 p.u. at 1 s. The disturbance estimation using NDO is shown in Fig. 3 which exactly tracks the true value within a short time. Figure 5 shows the wind speed profile with an average speed of 12 m/s. Figure 6 shows the load frequency deviations corresponding to the wind speed deviations. Stochastic effect of wind energy system on the load frequency is very less, and this shows the robustness of the proposed approach.

Three-area system:

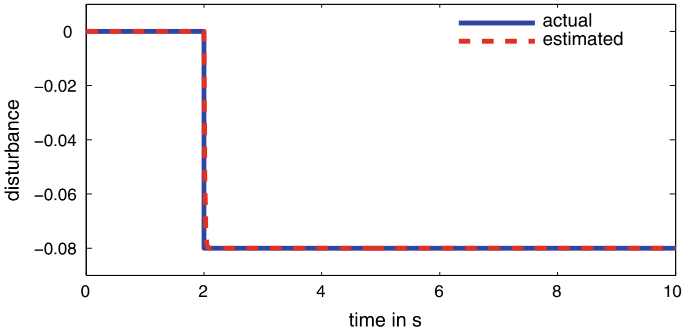

Fig. 3 Disturbance, both actual and estimated

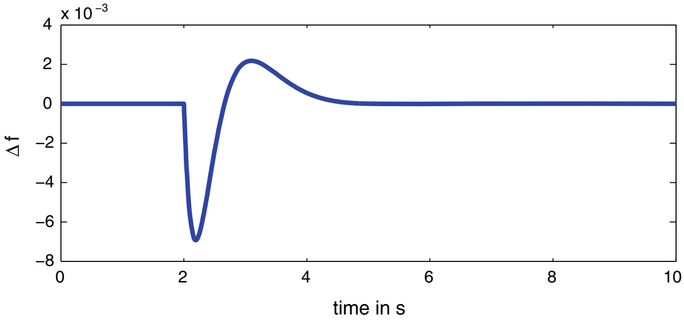

Fig. 4 Conversion in frequency for sudden change in load

Table 1 The parameters of single area power system

Parameter	T_P	K_P	T_T	R	T_G
Value	15	120	0.07	2	0.27

Table 2 Design parameters for the proposed method

Parameter	G	K
Value	$\begin{bmatrix} 0 & 40 & 0 & 0.01 \end{bmatrix}$	$\begin{bmatrix} 70 & 0 & 90 & 4 & 1 \end{bmatrix}$

The parameters of the bench mark three area system are given in Table 3. For further investigating the performance of the proposed controller, the load demand on area-1 is suddenly increased to 0.01p.u. at 2 s, and the load demand on area-2 is raised to 0.01p.u. at 12 s and similarly for the third area at 22 s. Load frequencies for all the three areas are shown in Fig. 7. The adaptability and sturdiness of the controller to parameter uncertainties are verified by considering 20% variation in parameters of T_{Gi}, T_{Ti} and T_{Pi}. The effect of parameter changes on the load frequency is very less, and this is shown in Fig. 8.

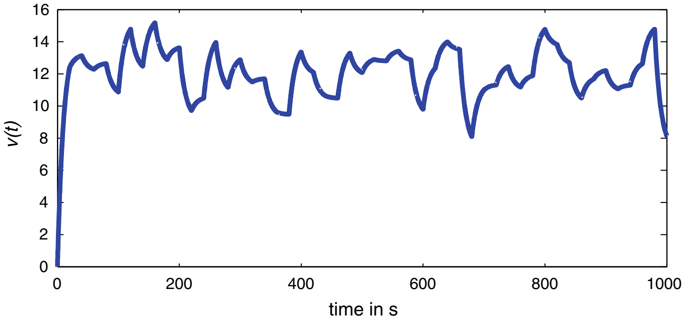

Fig. 5 Wind speed profile

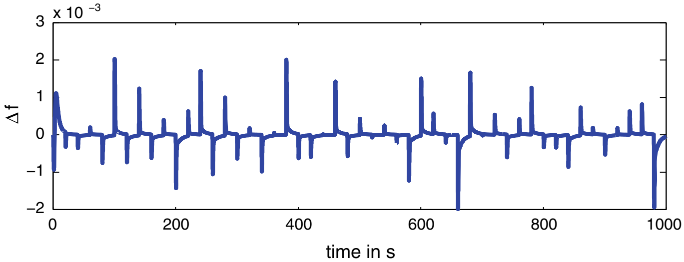

Fig. 6 Change in frequency with change in wind conditions

Table 3 The parameters of three area multi-machine power systems

Area	1	2	3
T_{Pi}	20	25	20
K_{Pi}	120	112.5	115
T_{Ti}	0.3	0.33	0.35
T_{Gi}	0.08	0.072	0.07
Ri	2.4	2.7	2.5
K_{Sij}	0.5	0.5	0.5

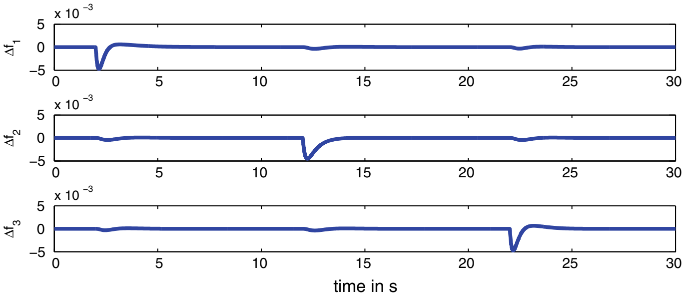

Fig. 7 Load frequencies for three-area system

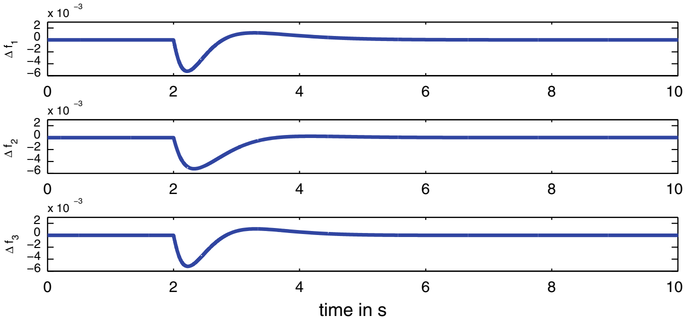

Fig. 8 Load frequencies with parameter uncertainties

7 Conclusion

In this paper, an offset-free MPC is applied for load frequency regulation of interrelated power systems. NDO is employed for the estimating the net disturbance affecting the load frequency of the structure. This estimated disturbance is used in improving the output prediction of the MPC. This proposed method of load frequency regulation is tested on single-area hybrid power system with wind integration and three-area power systems. The simulation results under various conditions show that the proposed method effectively regulates the load frequency under load disturbances and variable wind generation. This work can be extended by controlling a complex practical power system with large-scale wind penetrations.

References

1. Pandey SK, Mohanty SR, Kishor N (2013) A literature survey on load–frequency control for conventional and distribution generation power systems. Renew Sustain Energy Rev 25:318–334
2. Sahu RK, Panda S, Padhan S (2015) A hybrid firefly algorithm and pattern search technique for automatic generation control of multi area power systems. Int J Electr Power Energy Syst 64:9–23
3. Kumar Sahu R, Panda S, Biswal A, Chandra Sekhar GT (2016) Design and analysis of tilt integral derivative controller with filter for load frequency control of multi-area interconnected power systems. ISA Trans 61:251–264
4. Madasu SD, Sai Kumar MLS, Singh AK (2016) A flower pollination algorithm based automatic generation control of interconnected power system. Ain Shams Eng J
5. Sahu RK, Panda S, Padhan S (2014) Optimal gravitational search algorithm for automatic generation control of interconnected power systems. Ain Shams Eng J 5(3):721–733
6. Bevrani H (2014) Robust power system frequency control. Springer International Publishing, Cham
7. Vrdoljak K, Perić N, Petrović I (2010) Sliding mode based load-frequency control in power systems. Electr Power Syst Res 80(5):514–527

8. Cai L, He Z, Hu H (2017) A new load frequency control method of multi-area power system via the viewpoints of port-Hamiltonian system and cascade system. IEEE Trans Power Syst 32(3):1689–1700
9. Chuang N (2016) Robust H∞ load-frequency control in interconnected power systems. IET Control Theory Appl 10(1):67–75
10. Mu C, Tang Y, He H (2017) Improved sliding mode design for load frequency control of power system ıntegrated an adaptive learning strategy. IEEE Trans Ind Electron 0046(c):1
11. Ersdal AM, Imsland L, Uhlen K (2016) Model predictive load-frequency control. IEEE Trans Power Syst 31(1):777–785
12. Zhang Y, Liu X, Qu B (2017) Distributed model predictive load frequency control of multi-area power system with DFIGs. IEEE/CAA J Autom Sin 4(1):125–135
13. Ma M, Zhang C, Liu X, Chen H (2017) Distributed model predictive load frequency control of the multi-area power system after deregulation. IEEE Trans Ind Electron 64(6):5129–5139
14. Liu X, Zhang Y, Lee KY (2017) Coordinated distributed MPC for load frequency control of power system with wind farms. IEEE Trans Ind Electron 64(6):5140–5150
15. Kumar A, Anwar MN, Kumar S (2021) Sliding mode controller design for frequency regulation in an interconnected power system. Prot Control Mod Power Syst 6:6
16. Dev A, Novella Rodríguez DF, Anand S, Sarkar MK (2021) Multi observer-based sliding mode load frequency control with ınput delay estimation. ASME Lett Dyn Syst Control 1(4):041009
17. Camacho EF, Bordons C (2007) Model predictive control. Springer, London
18. Yang J, Zheng WX, Li S, Wu B, Cheng M (2015) Design of a prediction-accuracy-enhanced continuous-time MPC for disturbed systems via a disturbance observer. IEEE Trans Ind Electron 62(9):5807–5816
19. Yang J, Zheng WX (2014) Offset-free nonlinear MPC for mismatched disturbance attenuation with application to a static var compensator. IEEE Trans Circuits Syst II Express Briefs 61(1):49–53
20. Mi Y, Fu Y, Li D, Wang C, Loh PC, Wang P (2016) The sliding mode load frequency control for hybrid power system based on disturbance observer. Int J Electr Power Energy Syst 74:446–452

Chapter 39
Design and Development of a Novel Reverse Polarity Tester for EV Application

K. A. Rahul, T. Rajeev, and P. Sreejaya

Abstract Reverse polarity is a scenario that occurs when LV batteries get connected in the wrong way. The result can be severe damage due to the short circuit caused by the bidirectional switches in the electronic control unit (ECU). This condition is there itself from the beginning of motor vehicles, so was the protection circuits for mitigating this issue. But nowadays, does invest a lot in reverse polarity protection is a question because it is an error with very little probability. In short, reverse polarity is a severe shock to the ECU of the vehicle. The shock handling capacity of MOSFET/IGBT switches used in ECU is depicted as pulsed current rating in the datasheet. The paper presents a novel reverse polarity tester for EV application. The novelty of the reverse polarity tester lies in the fact that the device can be operated with commonly used power supplies and abnormalities like gate ringing and parasitic turn on are eliminated by a suitable design procedure. The system is analysed pretty close to a practical level. Simulations are done in multiple software to confirm the validity

Keywords Reverse polarity · IGBT driver · Gate ringing · Parasitic turn on · Ltspice · Proteus

1 Introduction

The major electronic components in an electric vehicle are inverter, DC-DC converter, battery management system and on-board charger. Inverter gives the AC power to the motor to drive. BMS will monitor the Li-ion battery bank (HV). On-board charger is

K. A. Rahul (✉) · T. Rajeev · P. Sreejaya
Department of Electrical Engineering, College of Engineering Trivandrum, Trivandrum, Kerala, India
e-mail: rahul812922@gmail.com

T. Rajeev
e-mail: rajeev.t@cet.ac.in

P. Sreejaya
e-mail: sreejaya@cet.ac.in

G. Panda et al. (eds.), *Sustainable Energy and Technological Advancements*, Advances in Sustainability Science and Technology,
https://doi.org/10.1007/978-981-16-9033-4_39

the circuitry to charge the HV battery. In EV, different voltage levels are required for infotainment, lead-acid battery (LV) and other accessories. Here, DC-DC converter is used to produce a lower level voltage.

The reverse polarity issue will occur at the low voltage side of the converter. Unlike the HV battery bank, the LV battery requires maintenance. So, there is a chance that the operating personnel may try to re-connect or accidentally touches battery leads in a reverse way. This will certainly damage the electronic control unit (ECU) or even may lead to a blast. During normal working condition, MOSFET offers very low on-state resistance, and the thermal dissipation is taken care of. Consider a scenario when battery at the output port of the converter is connected in opposite to normal. MOSFETs are bidirectional because of their internal body diode. The wrong connection will bias the diode and due to that current can find a short path now. This draws a huge amount of dissipation following larger current and eventually system damage [1]. Reverse polarity conditions may also occur during the operating life of the device, such as when a heavy ground shift between two connected devices takes place. Also, in this case, having polarity protections on the interested pin allows the system to keep working increasing the safety of the system, which is one of the most important figures of merit of automotive systems.

2 Reverse Polarity Tester

There are several reverse polarity protection circuits are being used. Placing a P-N junction/Schottky diode is the simplest way to do it. Placing the diode as shown in Fig. 1a will block the voltage if the battery gets connected incorrectly. Using the right type of diode depends on the current and voltage rating because the diode will produce a considerable drop, and in normal condition, the load will not get the rated voltage. One can go for MOSFET to reduce drop as they are less resistive. Choosing a p- or n-channel MOSFET is strictly according to the requirement. When it comes to driver circuit, p-channel MOSFET is preferred, but when size matters, n-channel is the right one. The n-channel MOSFET of protection circuit is a high-side switch. Drive circuits for the high-side switches are called high-side drivers and are more complicated than low-side drivers because of the required voltage translation to the supply and because it is more difficult to turn off a floating switch. All these techniques can definitely guard the sophisticated automotive circuitry.

Nowadays, mechanical side of the battery has taken more care with design of different sized battery terminals or the use of prominent colour-coding of cables, connectors and terminals. Obviously, this makes the percentage of occurrence of reverse polarity to the least, and now, having the semiconductor protection is a money wastage.

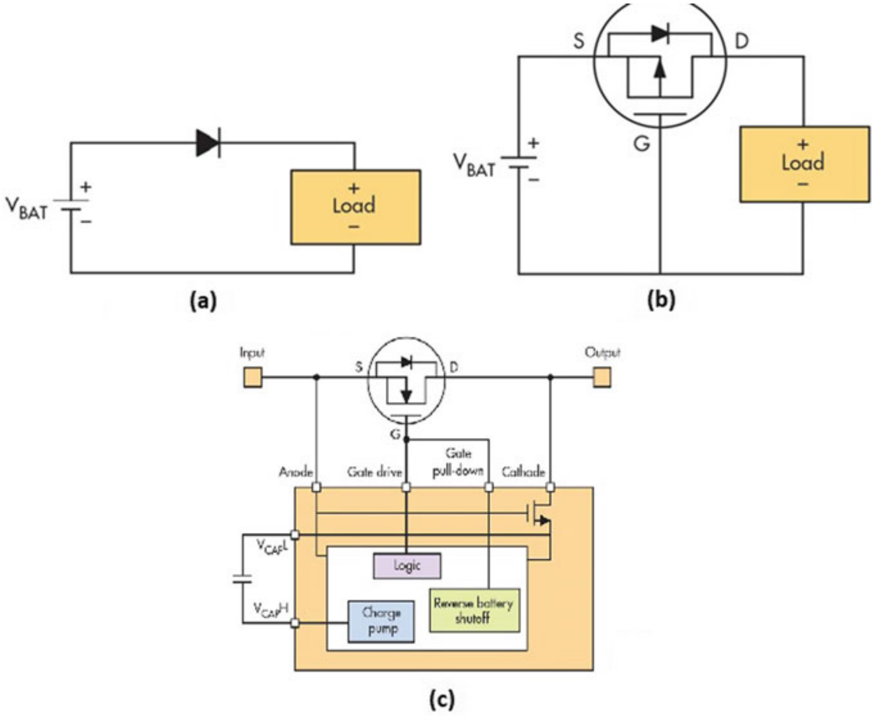

Fig. 1 **a** Diode based protection. **b** P-channel MOSFET based. **c** N-channel MOSFET based

2.1 Necessity of Reverse Polarity Tester

Necessity of RPT can be explained with a scenario. Electric vehicles draw high current in normal state, e.g. $I = 500$ A and on-state resistance offered by devices will be $R_{ds}(\text{on}) = 1.5\ \text{m}\Omega$, then $P_{loss} = 375$ W which is quite large. As in the normal condition, current passes through the protective circuit, it is inevitable to bear with the losses. Also, with an increase in components, price increases. Considering the mechanical side of battery, an unintentional connection is kind of not possible. But if an accidental touch happens that will not last for a sec, because high spark and leads may melt. So, accordingly, a DC-DC converter board is designed and is tested with a high current controlled source which can be termed as reverse polarity tester (RPT).

RPT is a kind of trade-off project considering the assumption that only a few will make the reverse polarity error. With this idea, automotive companies can take statistics of the error made by personnel. This may result in a loss also if the error stat goes high, but that is a possibility pretty close to impossible, like 1 out of 100 cars is an affordable case.

3 Design Procedure

Buck converter is an appropriate choice [2, 3] to implement the idea of RPT. Choosing the right frequency, selecting switch accordingly [4], selecting driver for the switch [5, 6], output inductor and input capacitor calculations [7] are the design procedure.

Device Rating EV manufacturers will have different standards for testing. Here, we are taking a design target of 600 A current for 1 s. Device is operated at 1.25 KHz of frequency and 80 V input voltage.

Operating Frequency There are few reasons which justify the device operation in lower frequency. Considering the fact that RPT is not an internal device of EV, inductor and capacitor size being used is least bothered. Large current at output also demands a lower frequency operation.

Switch Selection MOSFET, IGBT and BJT are the widely used power electronic switches. Considering the application, MOSFET is avoided because of the higher conduction loss among these devices. MOSFET is recommended in high-frequency applications to reduce switching loss. Between BJT and IGBT the choice can be made out for a number of reasons. A high current IGBT is easily available than a BJT. Switching loss of IGBT is better than BJT. All these facts make IGBT the proper choice.

Selection of Power Supply It is clear that RPT needs a power supply with a higher current rating (possibly greater than 100 A). So, considering that fact power supply datasheet should be studied and select the one with an acceptable slew rate. For example, if we need a source current of 100 A in 100 uS, power supply should have a slew rate within that time.

3.1 IGBT Selection

IGBT has three terminals, namely collector, gate and emitter. Operation of IGBT is controlled by the voltage applied across the gate and emitter(V_{ge}). Switch will go into conduction when V_{ge} surpasses a particular value called the threshold voltage. EconoDUAL™3 1200 V shown in Fig. 2 is a 900 A dual TRENCHSTOP IGBT7 module with negative temperature coefficient thermistor (NTC), and PressFIT contact technology is an appropriate choice for the application. The module has a low voltage drop of 1.5 V at saturation, i.e. at $I_c = 900\,\mathrm{A}$. It can operate smoothly at 150 °C and can go up to 175 °C with limited duty. The module has a pulsed current rating of 1800 A which makes it sustainable to sudden shocks. Heat sink is used rather than a coolant flow for heat transfer.

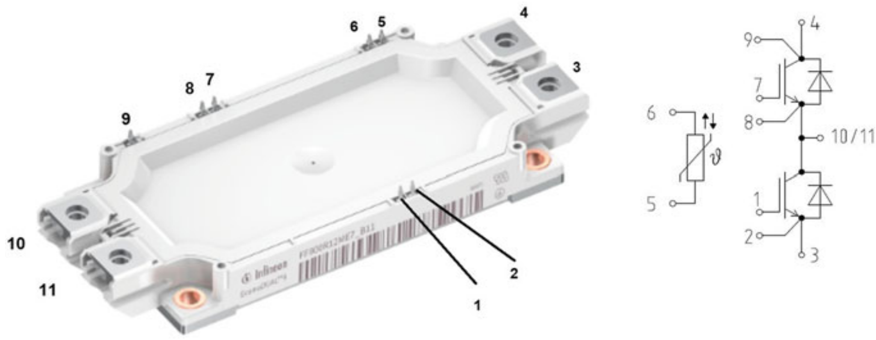

Fig. 2 FF900R12ME7B11 Igbt module

3.2 IGBT Driver Selection

EconoDUAL3 module has dedicated drivers which can be connected to the module through press fit pins. Voltage across gate and emitter needs to be pulse width modulated according to the duty ratio requirement. A suitable microcontroller can be coded to produce the PWM. The output voltage and current level of microcontroller output will not satisfy the rated value for a power IGBT. Because of this PWM generated will be passed to the gate driver, and the output of the driver will be connected to IGBT.

Electrical Features

Power Supply The 2ED100E12-F2 have an integrated DC/DC converter for each leg, which generates the required secondary isolated unsymmetrical supply voltage of +16 V / −8 V. High and low side driver voltages are independently generated by using one unipolar input voltage of 15 V. Additionally, the power supply is protected against gate—emitter short circuit of the IGBTs. In the case of DC/DC converter overload, the output voltage drops. The under voltage lock out function ensures that gate driver operation only takes place within specified IC supply voltages range. The fault is reported to the driver's primary side.

Input PWM PWM signal voltage rating is 0/5V and should be given separately for both IGBT channels. IN+ is used as signal input, whereas IN− is used as enable signal. Therefore, a +5 V signal on the IN+ input pin and a GND signal on the IN− input pin is necessary to turning on the IGBT.

Maximum Switching Frequency The switching frequency of an IGBT is limited either by the maximum output power of the driver voltage supply or by the maximum temperature of the PCB due to the power losses in the external gate resistors. These power losses in the gate resistors depend on the IGBT gate charge, gate voltage magnitude and on the switching frequency of the IGBT. Due to the power losses in the external gate resistors, heat will be generated, which leads to an increase in the PCB temperature in the neighbourhood of these resistors.

Short Circuit Protection and Active Clamping The short circuit protection (desaturation) of the evaluation driver board basically relies on the detection of a voltage level higher than 9 V on the DESAT pin of the 1ED020I12-F driver IC and the implemented active clamp function. When a short circuit occurs, voltage V_{ce} will start to rise, and this voltage is monitored to take necessary actions. Active clamping is a technique that keeps transient overvoltages below the critical limits when the IGBT turns off. The standard approach to active clamping is to use a chain of avalanche diodes connected between the auxiliary collector and the gate of an IGBT module. When the collector–emitter voltage exceeds the diodes breakdown voltage, the diodes current sums up with the current from the driver output.

3.3 *Importance of Gate Resistors*

The on/off status of the gate-controlled power devices, for instance, IGBT or power MOSFET, is defined by the gate voltage. The change of this gate voltage influences the charging and discharging of the power device's gate capacitor, which consists of the gate-collector capacitor C_{GC} and the gate-emitter capacitor C_{GE}.The charging of the gate capacitor by $I_{G_{\text{charging}}}$ will turn the power device on, and the discharging of the gate capacitor by $I_{G_{\text{discharging}}}$ of the gate capacitor will turn it off [8]. The current, charging and discharging the gate, is limited by the gate resistor R_G. This will influence the switching speed of the power device. Besides this, there are also several other influences from the gate resistor:

– Limit peak gate current to protect the driver output stage
– Dissipate power in the gate loop
– Electromagnetic interference
– Prevent gate ringing
– Avoid parasitic turn on by carefully choosing gate resistance.

Gate Charging/Discharging Peak Current The gate driver IC's output stage has the maximum allowed peak current values $I_{\text{OH}_{\text{PEAK}}}$ for turn on and $I_{\text{OL}_{\text{PEAK}}}$ for turn off which are often specified within the driver IC's datasheet. When the output current of the driver IC is higher than this peak current value, the output stage could be damaged. Thus, it is important to limit the output current for safety reasons. A typical driver circuit with charging and discharging path is shown in Fig. 3.

$$I_{G\text{charging peak}} = \frac{V_{CC2} - V_{EE2}}{R_{DS\text{on}} + R_{G\text{on}}} \tag{1}$$

$$I_{G\text{discharging peak}} = \frac{V_{CC2} - V_{EE2}}{R_{DS\text{off}} + R_{G\text{off}}} \tag{2}$$

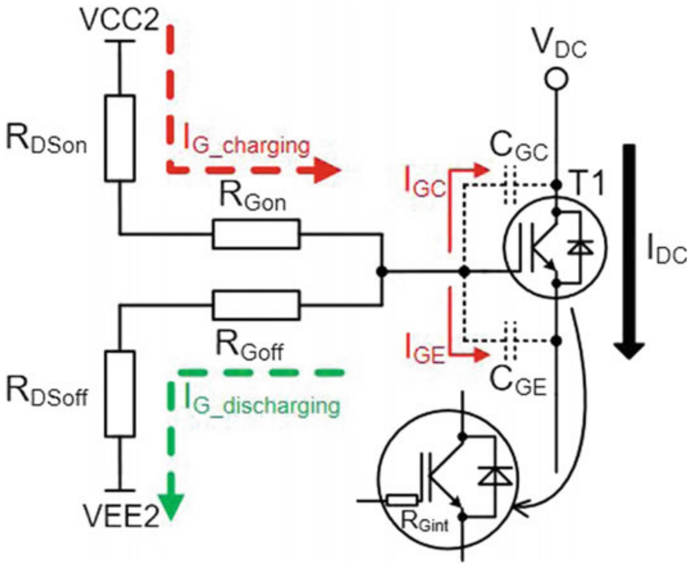

Fig. 3 Gate charging/discharging diagram

This charging/discharging current must be lower than the peak current allowed for the driver IC's output stage to guarantee safe operation.

$$I_{G\text{charging peak}} < I_{\text{OH}_{\text{PEAK}}}$$

$$I_{G\text{discharging peak}} < I_{\text{OL}_{\text{PEAK}}}$$

Switching Speed and Electromagnetic Compatability Generally speaking, with a higher gate resistance value, the switching speed of the power device will decrease. This means that the switching loss will be increased. This, in turn, will finally influence the efficiency. In contrast, when a lower gate resistance is applied, the switching will become faster which can reduce the switching loss. Meanwhile, the noise induced by di/dt and dv/dt will increase with a higher switching speed. Since the electromagnetic compatibility (EMC) regulation must be fulfilled, the gate resistance value needs to be chosen carefully.

Gate Ringing In power electronic applications, gate ringing is an often observed phenomenon due to parasitics along the gate loop. As shown in Fig. 4, OUT is the output of the driver IC, which is used to drive a power device. I_G is the gate current along the gate loop. L_{P} and C_{GE} are the parasitics along the gate loop which form the resonant tank. With excitation, oscillation could appear. Shorten the trace length to physically keep the gate loop as small as possible which can normally reduce the parasitic inductance by 1 nH/mm.

Fig. 4 Gate loop parasitics

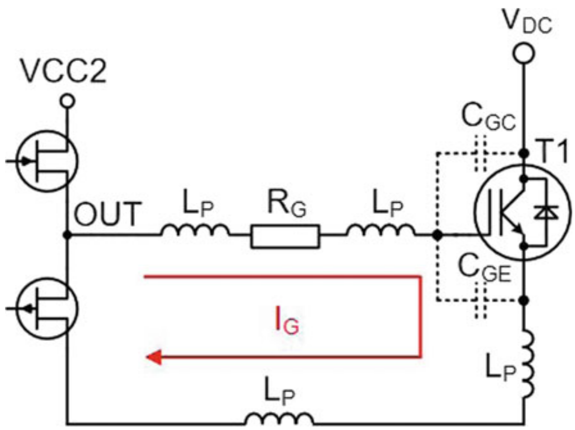

Fig. 5 Parasitic turn on

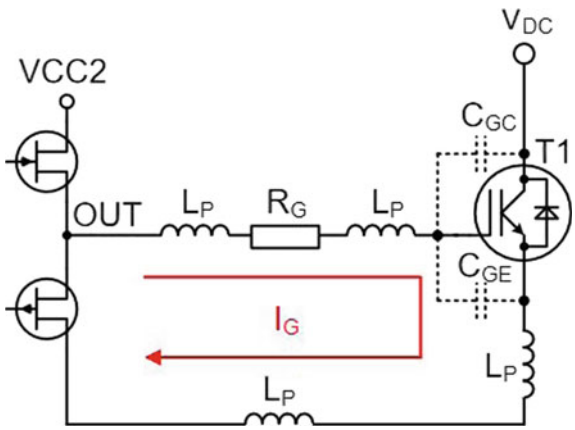

Parasitic Turn on The parasitic turn on is a common phenomenon in many situations. This is a physical effect due to the high $\mathrm{d}v/\mathrm{d}t$ combined with the parasitic Miller capacitance. As shown in Fig. 5, high $d\mathrm{v}_{\mathrm{CE}}/\mathrm{d}t$ across the power device T1 will generate a displacement current I_{DIS} through the Miller capacitor C_{GC}. This is often triggered by turning on the paired device in a half bridge topology. Through the gate resistor R_{G}, this displacement current I_{DIS} will generate a voltage drop across the gate resistor and will lift the gate voltage of the power device.

$R_{DS\mathrm{off}}$ depicts the resistance of the pulling down device of the driver. Here, the pulling down device is on when the power device T1 is off. V_{G} is the voltage that appears at the gate of the power device. When V_{G} is higher than the threshold voltage of the power device T1, the parasitic turn on happens. This will influence the safety of the system as bridge shoot-through could appear.

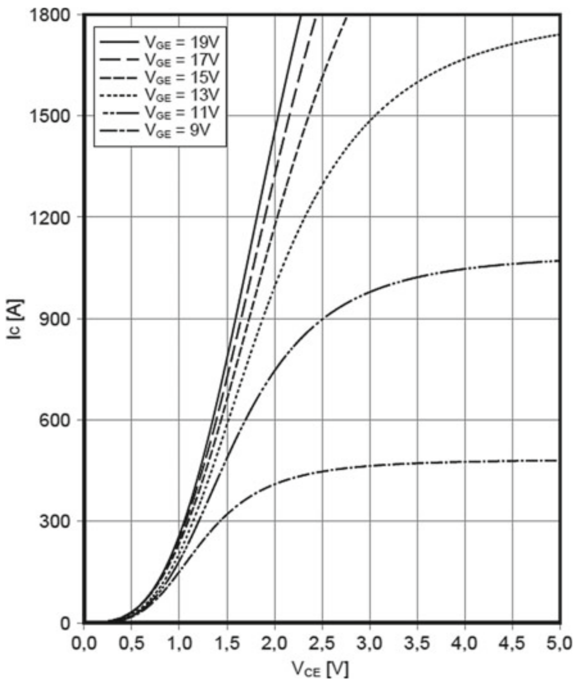

Fig. 6 Output characteristic IGBT

3.4 Gate Voltage Requirement

$V_{\mathrm{ge}} = -15/15\mathrm{V}$ is the typical value specified for explaining every characteristic of IGBT in the datasheet. From $I_c \mathrm{versus} V_{\mathrm{ce}}$ characteristics shown in Fig. 6 under the worst case of 175°, V_{ge} can have voltage down to 11 V to get a current Ic of 600 A. A negative bias is needed when the gate voltage cannot be held safely below the threshold voltage due to noise generated in the circuit [7].

3.5 Input Capacitor Selection

The purpose of RPT is to provide a short circuit level current at output. Now, it is quite impossible to find a source that can give current in the range of 500–1000 A, but the device demands it. In this scenario, we can use capacitor banks to support the input voltage source. Theoretically, a capacitor can supply infinite current, but when it comes to real-life implementation, it does have limitations. Let see how the capacitor can support the system.

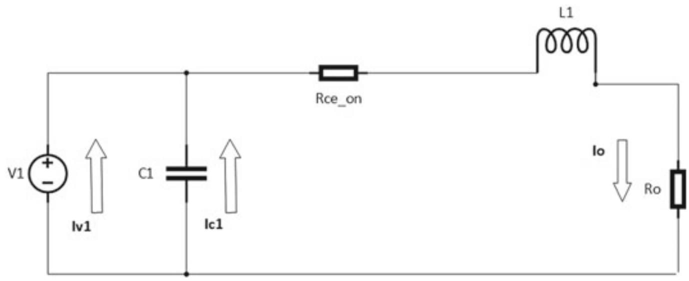

Fig. 7 Discharging in IGBT ontime

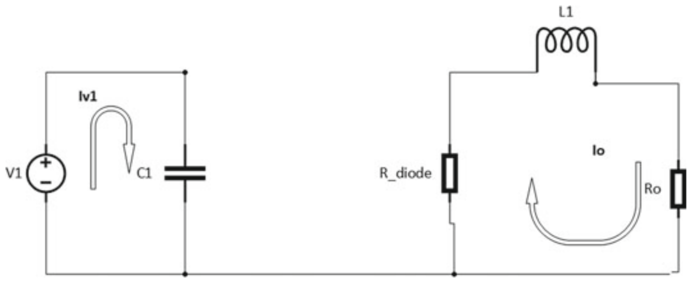

Fig. 8 Discharging in IGBT offtime

Capacitor will be initially charged to the input voltage. When the high-side IGBT is turned on, the capacitor will start to supply current along with the source, shown in Fig. 7

$$I_{v1} + I_{c1} = I_o$$

Let the time period $T = 800\,\mu\text{s}$ and I_{c1} required be 500 A for 150 μs. Then, charge needed to store is

$$Q = Ic * T_{\text{on}} \tag{3}$$

$$Q = 500 * 150\,\mu C = 75\,\text{mC}$$

And the capacitance required when voltage is 80 V

$$C = Q/V \tag{4}$$

$$C = 75\,\text{mC}/80\,\text{V} = 937\,\mu\text{F}$$

The value of capacitance found out is not the exact value to be used. Using atleast two times of the theoretical value will be appropriate. Because by using the calculated value the capacitor is discharged completely which is wrong. Input capacitor will be charged during high-side IGBT off time as shown in Fig. 8. Here, we can calculate how much current from voltage source is required to charge the capacitor to 75 mC. Let off time = 650 μs

$$I_{v1} = Q/T_{\text{off}} \tag{5}$$

$$I_{v1} = 75\,\text{mC}/650\,\mu\text{s} = 115\text{A}$$

3.6 Output Inductor Selection

When a large amount of current passes through an inductor, the following results should be considered

- Heat dissipation
- Saturation
- Electromagnetic interference on other devices.

Using a flatwire coil can efficiently cope with heat loss. Using an air core inductor is a remedy for possible saturation. To avoid EMI, a toroidal shape is the best choice as the magnetic field is confined within. In short, an air-cored toroid is the right choice as output filter.

$$L = \frac{V_{\text{OUT}} \times (V_{\text{IN}} - V_{\text{OUT}})}{\Delta I_L \times f_S \times V_{\text{IN}}} \tag{6}$$

V_{IN}, input voltage = 80 V
V_{OUT}, output voltage = 9 V
f_s, switching frequency of the converter = 1.25 KHz
ΔI_L, estimated inductor ripple current = 30 A
This gives inductance $L = 1$ mH

Considering a suitable cross section for the coil, the radius of the toroid should be calculated

$$L \approx \frac{\mu N^2 A}{2\pi R} \quad \begin{array}{l} A = \text{ cross-sectional area} \\ R = \text{ toroid radius to centerline} \end{array} \tag{7}$$

$L = 1$ mH; assuming $A = 0.672\,\text{cm}^2$, $R = 3.6$ cm gives $N = 52$.

- Calculating length of wire required for 52 turns of radius $r = 2$ cm length $l = N * 2 * \pi * r = 650$ cm.
- Estimating the power loss resulting from these dimension.

$\rho = 1.7 * 10^{-8}\ \Omega$m for copper.
$R = (\rho * l)/A = 1.6\,\text{m}\Omega$.
Power loss = $600 * 600 * 0.0016 = 576$ W.

4 Simulation

4.1 Simulation Results-Ltspice

The circuit shown in Fig. 10 is the synchronous buck converter operating at 1.25 KHz frequency. Here, two different sources of pulse are used for PWM. The input capacitor should be higher than the calculated because the theoretical value is based on the complete discharge of the capacitor which is not practical. If the capacitor is discharged completely, it means voltage of that capacitor is zero which violates KVL as the voltage source is parallel with it. An appropriate capacitor of 1200 μF is selected. The gate resistor value is adjusted primarily based on the ringing in V_{ge}. $R_g = 10\,\Omega$ is a better value where the oscillations in gate voltage are tolerable.

In Fig. 9, At $t = 935.233$ ms, the low-side pulse is 0 V, meaning that the freewheeling switch is off. On the other side, graphs named Vn006 and Vn003 are having non zero values, and the difference between these two is the voltage applied across high-side IGBT. In Fig. 10, the voltage applied across the switch is 6v, and it is verified

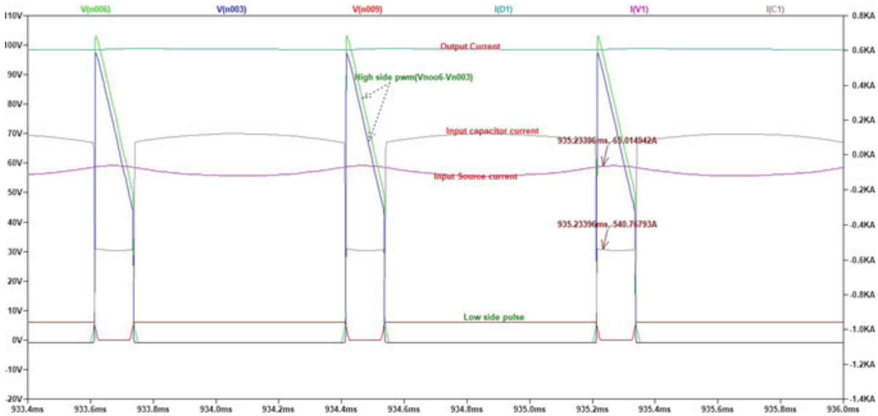

Fig. 9 PWM and current–time graph

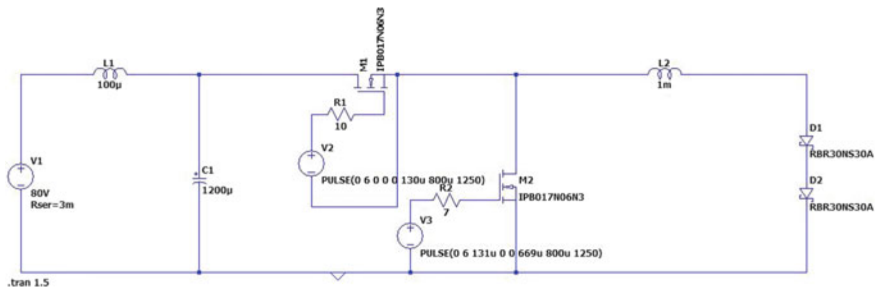

Fig. 10 Ltspice model

graphically. At this instant, the capacitor will be supplying current along with the source, and the PWM-current graph supports this, $I_c = 540.76$ A. The values of currents are labelled. By adding the source and capacitor current, it is evident that the concept is working properly. It is also evident from the graph that no gate ringing or parasitic turn on happens during operation.

4.2 Simulation Results-Proteus

LTspice simulation is more like a high-level thing where information is less. So, for a detailed presentation, Proteus will be appropriate. Here, we are using Arduino as CPU for the project as shown in Fig. 11. Using the library file of Arduino, we can add it to the simulation. This makes it more practical because now it is possible to check the code for PWM also and it has verified successfully. Coming to the driver part, driving a half bridge IGBT set-up is a tricky part where you need different voltage levels for both IGBT referred to the same ground. Here, we are using the bootstrapping technique to drive both IGBT from a single source. It is not feasible to drive IGBT as shown in LTspice with multiple sources. The PWM applied to the driver and output current is shown in Figs. 12 and 13.

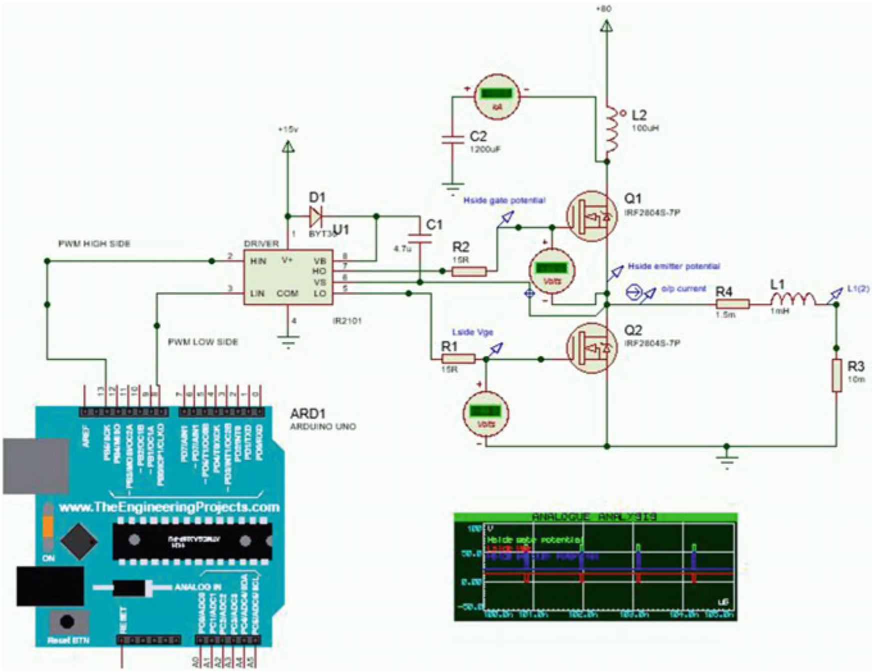

Fig. 11 Proteus model

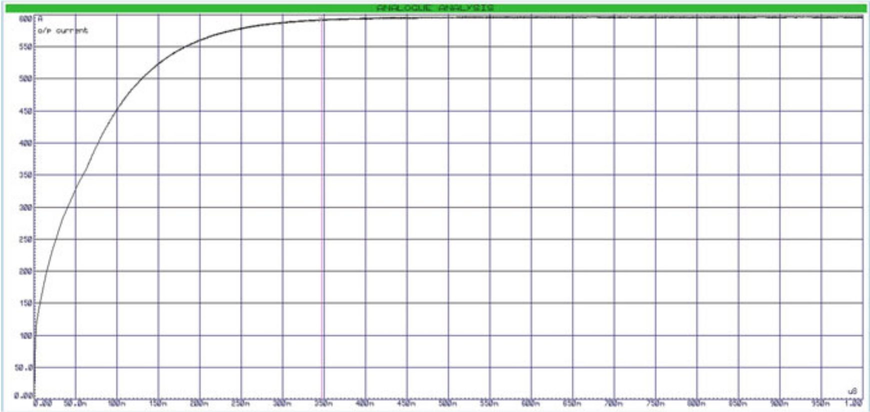

Fig. 12 Output current

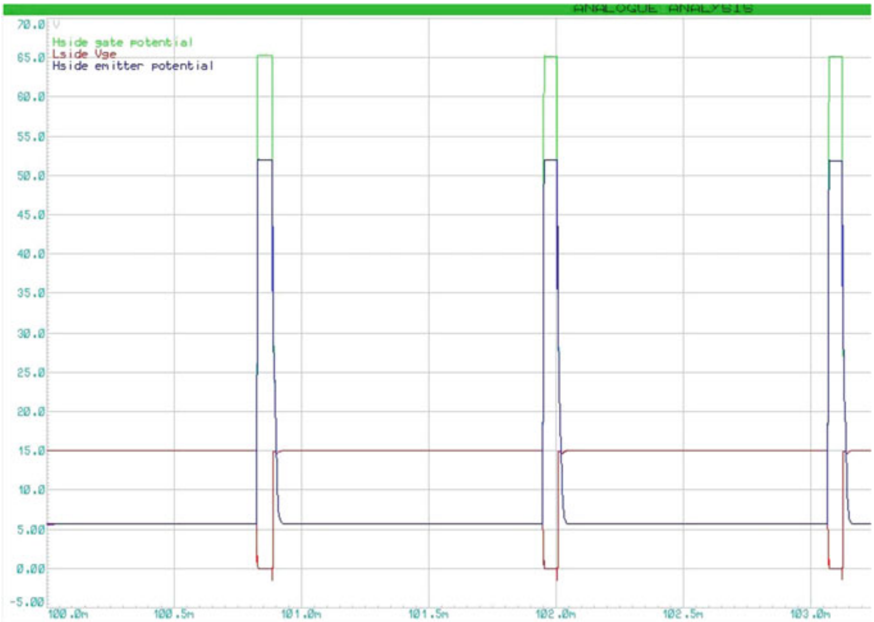

Fig. 13 PWM of both switches

5 Conclusion

The reverse polarity tester is the device designed to create an artificial scenario of a short circuit caused by the reverse connection of the LV battery. Removal of reverse polarity protection and reduction of extra cost was the eventual objective of RPT. The driver part of IGBT has several factors to be considered, which are analysed thoroughly. Input capacitor provides support along with source to provide the required current at the output. The input capacitor is an important part of the system, which generates a large current to support the source, and its design is done properly. The output side inductor needed both electrical and mechanical design consideration as its shape also influenced the operation. The mechanical design of the output inductor had a very good influence on the system based on power loss and EMI. The circuit has been set up and verified with a target output of 600 A for 1 sec. LTspice and Proteus simulation software are used to verify the system. The test results validate the efficacy of the proposed reverse polarity tester.

References

1. Makinde K, Ogbonna VO (2015) Dangers associated with polarity reversal on DC appliances and remedies. Eur Sci J 11(24). ISSN: 1857-7881
2. Deekshitha C, Latha Shenoy K (2017) Design and simulation of synchronous buck converter for LED application. In: 2017 2nd IEEE international conference on recent trends in electronics information communication technology, May 19–20, 2017
3. Texas Instruments (2015) Basic calculation of a buck converter's power stage. Application report
4. Barkhordarian V, Power MOSFET basics. International Rectifier
5. Texas Instruments (2018) Fundaments of MOSFET and IGBT gate driver circuits. Application report
6. Infineon Technologies AG (2011) AN2008-02, Evaluation driver boards for EconoDUAL™3 and EconoPACK™+ modules, v1.3
7. Xie M, How to select input capacitor for buck converter. Analog Appl J
8. Infineon Technologies AG (2015) AN2008-02, Gate resistors for power devices, AN2015

Chapter 40
Design of an EV Charging System with Improved Performance

Sanjiba Kumar Bisoyi, Parveen P. Terang, Luv Pathak, Abhinav Kumar Singh, Sarthak Singh, and Rishabh Khare

Abstract Electric vehicles are a new and upcoming technology in the transportation and power sector. The US Energy Information Administration states that the world has an adequate crude oil supply until about 2050. Basically, electric vehicles are expected to enter the world market such that by 2030, they will make up 10% of the vehicles being used. The most expensive part of an electric vehicle is the battery, and its charging and maintenance need to be taken care of. The major challenges while adopting EVs as an alternative to the fuel vehicles are the charging problems as it varies from one charger to another. Since the advent of electric vehicles, the need for electric chargers and new techniques for a sustainable solution has grown tremendously. The dead batteries are now getting replaced by the charging batteries. In this paper, we have attempted to improve the performance of the electric vehicle chargers by designing and simulating the same on the MATLAB. For this work, three converters, i.e. buck–boost converter, Cuk converter and Sepic converter, have been considered and designed using different methods such as PWM techniques, using PID and by implementing fuzzy logic techniques. The results have been compared, showing an improvement in their performance all of which has been reported in this paper.

Keywords Buck–boost converter · Cuk converter · Electric vehicles (EVs) · Fuzzy logic · Lithium-ion battery · PID controller · PWM technique · Sepic converter

S. K. Bisoyi · P. P. Terang · L. Pathak · A. K. Singh · S. Singh · R. Khare (✉)
Department of Electrical Engineering, JSS Academy of Technical Education, Noida, India

S. K. Bisoyi
e-mail: sanjibabisoyi.eed@jssaten.ac.in

P. P. Terang
e-mail: ppterang.eed@jssaten.ac.in

G. Panda et al. (eds.), *Sustainable Energy and Technological Advancements*, Advances in Sustainability Science and Technology,
https://doi.org/10.1007/978-981-16-9033-4_40

1 Introduction

The climatic changes have brought about many challenges to the suitable development of human civilization. Governments around the world are working hard to implement all possible steps to reduce carbon emissions. One sector causing a significant portion of carbon emissions is the road transport sector [1]. As a result, vehicle emission targets have been put in place in many countries. For this reason, electric vehicles (EVs) are seen as an environmentally friendly option and have gotten extensive attention in recent years [2–5]. Electric drive vehicles are very popular and at the same time attractive due to their low road emissions, ability to strengthen the power system by providing ancillary services and low operating cost compared to fossil fuels all the while being more energy-efficient [6]. Some of the disadvantages of the implementation of EVs are that the grid will be overloaded and with that since the power station is powered by coal and fossil fuel, the long-term implementation of charging the EVs will not be possible. Whenever EVs are charged, a good amount of the emissions is easily moved from the vehicle to the power plant station, due to which electric vehicles are not as eco-friendly as expected [4]. To overcome this issue, it is important that wind and water energy be utilized to charge our electric vehicles.

Nowadays, buck–boost converter is broadly used in many applications and power capability demands. Since the charging systems of EVs use DC-DC converters (generally buck–boost converter) to convert the DC input to required DC value, an improvement in its performance will yield better results [7]. The buck–boost converter is a sort of DC-to-DC converter in which the output voltage magnitude is greater than the input voltage magnitude or much less than the input voltage magnitude, and it also relies on the duty ratio [7–9]. The controller has a better response compared to others. In this paper, a controller has been designed and is controlled with a PID controller and PID with PWM technique [10–12].

Section 2 of the paper discusses the types of EVs, and Sect. 3 discusses the methodology used for design of the EV system. Section 4 gives the results and discussion and conclusion of the work is in Sect. 5. To highlight the efficiency of the proposed model, comparison has been done with the output of different types of converters and reported along with the results. The first converter considered is the Cuk converter. An attempt has been made to design the circuit of the Cuk converter with different types of methodology. The use of the proportional–integral (PI) and fuzzy logic (FL) controllers is frequently used to control the response voltage of the Cuk converter as described in [13]. The basis of assessment of the converter can be done with parameters like steady-state error, settling time and rise time. These have been used to assess the results of all types of controllers and are different with respect to performance parameters. When the results were evaluated in an entirety, it was observed that the PID controller achieved the desired steady-state value with less rise and settling time. Next, the Sepic converter has been analysed in the closed-loop system and its performance was considered with both types of controllers (PID as well as fuzzy logic controller) over the open-loop system because of considerable overshoot value found in the open-loop system. This converter is usually used in renewable energy-based systems, battery-based systems and PV-based systems and has been reported to have better implementation for electric vehicle charging systems [14–18]. In this paper, an attempt has been made to compare the output of the PID and fuzzy controller, and based on the test results, the PID controller is seen to have a better response than the fuzzy controller (PID controller gave only a slight voltage ripple and the recovery time was also less). The results have been compared with [19].

2 Electric Vehicles (EVs)

An electric vehicle is one powered by an electric motor rather than a traditional petrol/diesel engine. This electric motor is powered by rechargeable batteries that can be charged by common household electricity. The main parts in an electric car are a rechargeable battery, controller and electric motor. First, the battery is powered after which the controller converts the current from DC-AC so that it can be used by the motor. The motor converts electrical energy to mechanical energy.

2.1 Types of EVs

As seen in Fig. 1, there are basically three types of EVs. They can be broadly described as follows.

- **Battery Electric Vehicles (BEVs)**

They are electric vehicles which have rechargeable batteries, and they do not have gasoline engines. The total energy to run the vehicle is generated from a battery which is charged by the grid, and the main advantage of BEVs is that they produce zero emission [4, 20, 21].

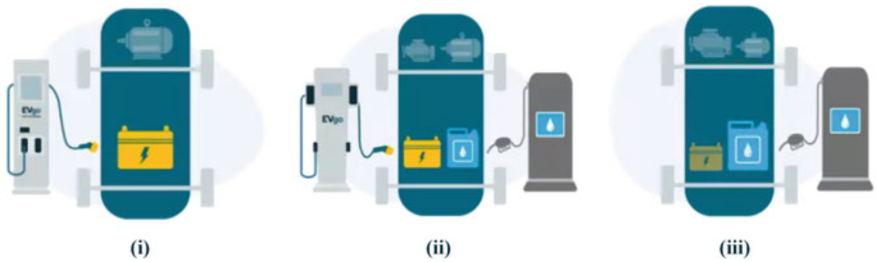

Fig. 1 Types of EVs. (i) Battery electric vehicles (BEVs). (ii) Plug-in hybrid electric vehicles (PHEVs). (iii) Hybrid electric vehicles (HEVs). *Source* https://www.evgo.com/ev-drivers/types-of-evs/

- **Plug-in Hybrid Electric Vehicles (PHEVs)**

In these types of EVs, it consists of both an engine and electric motor which is used to drive the electric vehicle. These EVs can recharge their battery through the method of regenerating braking, and they differ from hybrids as they have larger batteries and can plug into the grid to charge [4].

- **Hybrid Electric Vehicles (HEVs)**

These types of EVs have both electric motors and engines powered by gas to drive the car. To charge the battery, the power is generated through regenerating braking and these cannot be plugged into the grid to recharge the battery [4, 8, 20, 21].

2.2 Charging of EVs

- **Level 1 Charging**

The 120-V current which is found in household outlets is usually used in level 1 charging. Power cords and EVs easily accessible equipment are used to perform this task [20].

The main advantage is that there is no installation cost if there is an outlet nearby, and there will be low impact on electric utility peak demand charge [21]. Whereas the disadvantage is slow charging.

- **Level 2 Charging**

240-V power is used in level 2 charging which helps in faster regeneration of an EV's battery system, and this type of charging not only asks for the installation of an EVSE unit but also demands electrical wiring with this we can easily handle high power [6]. The main advantages are that it has faster charge time, and it is also more energy-efficient than level 1 charging (3% gain in efficiency) [4]. Disadvantages are that it is more expensive than level 1 charging and has a good amount of impact on peak demand.

- **DC fast Charging**

In DC fast charging, the battery is charged by the conversion of AC-to-DC power which can be directly stored. In this charging, the battery can be charged to 80 presents within half an hour. The main advantage is that the charging time is highly reduced [6]. The main disadvantages are that it is highly expensive, and the peak demand charges are increased [4, 4, 8, 20].

2.3 EVs Connectors

There are two connectors in EVs charging cable, one of which is connected to the vehicle socket and the other end is connected to the charging point [8]. Figure 2 shows the vehicle connector, and Table 1 (i) & (ii) highlights the features of slow/fast charging and rapid charging connector types.

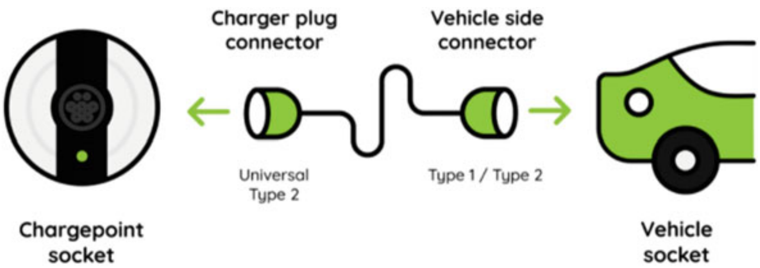

Fig. 2 Vehicle side connector

Table 1 Features of connectors (i) slow/fast charging, (ii) rapid charging

AC connector type	Power ratings (kW)	Approx. range per hour charging (miles)	Features
(i) *Slow/fast charging (AC)*			
Type 1 	3.7 7	12.5 25	5-pins, Standard US connector, No locking mechanism, Single phase only
Type 2 	3.7 7 22 (three ph.)	12.5 25 75	7-pins, most common connector on new cars, Inbuilt locking mechanism, can carry three-phase powers

DC connector type	Power rating	Approx. range per hour charging	Features
(ii) Rapid charging (DC)			
CHAdeMO 	50	75	Original DC connector
Combined  Charging system (CCS)	50 150 350	75 225 525	High power Neat arrangement with 2 × ‘Type 2’ pins

Source https://pod-point.com/guides/driver/ev-connector-types-speed

3 Methodology for Designing of EV Charging System

3.1 Battery System Design

The battery system used in EVs is an essential component and has to be designed carefully. There are different types of batteries which are used such as lead–acid, nickel–metal hydride, zebra and lithium-ion. Here the lithium-ion battery has been used to study the charging and discharging of batteries.

The battery in this work has been implemented using MATLAB as shown in Fig. 3, and the state of charge (SOC) is precisely measured and controlled.

The state of charge (SOC) of a cell denotes the capacity that is currently available as a function of the rated capacity. The value of the SOC varies between 0 and 100%. If the SOC is 100%, then the cell is said to be fully charged, whereas a SOC of 0% indicates that the cell is completely discharged. Here the SOC is not allowed to go beyond 85%, and therefore, the cell is discharged when the SOC reaches 85%. Here the logic is designed in such a way that when the SOC reaches 35% and then the battery should charge and when the SOC reaches 85, then the battery must stop charging and should discharge as shown in Fig. 4.

As shown in Fig. 5, battery is charged till the SOC value is approx. 85 and time taken is also much less as compared to [4]. Soon after SOC hits 85, the battery starts discharging till SOC is approx. 35.

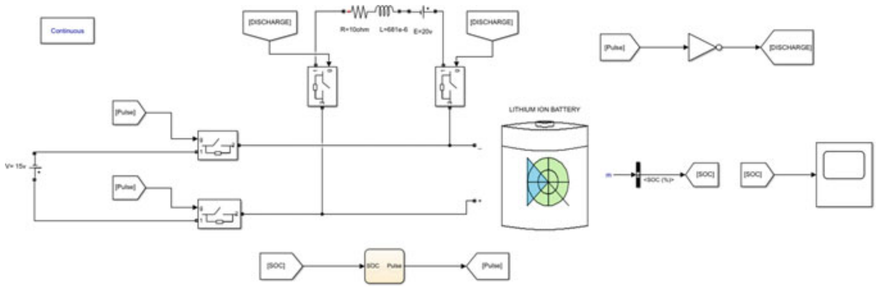

Fig. 3 Battery system in MATLAB

Fig. 4 SOC chart diagram

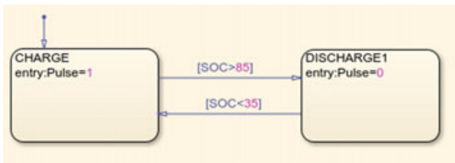

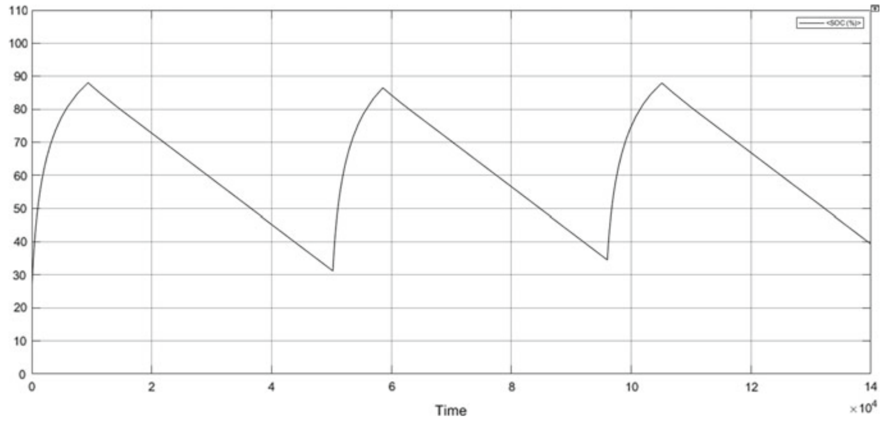

Fig. 5 Simulation result

3.2 *Buck–Boost Converter*

3.2.1 PID Controller

PID tuning is carried out via means of putting the reset time to its maximum value and the rate to zero and increasing the gain until the loop oscillates at a consistent amplitude. The gain of the PID controller is set to 1/2 of that value, and the reset time is adjusted so that it corrects itself for any offset within an appropriate period. For designing the closed-loop PID controller for the converter, state-space modelling was done as seen in Fig. 6, to determine the transfer function of the system after which the PI Controller was used. As seen in the output response shown in Fig. 7, the fluctuation of output voltage or deviation of the output voltage from its settled voltage is negligible. Any error between the reference signal and output signal causes a control signal to be generated by the integral controller. Use of this integral controller reduces the oscillations as well as ripples to a great extent. This voltage with decreased ripple is given to the converter and finally to the load. As seen in the figure below, when the reference voltage was set at 30 V, an output of 29.56 V was obtained with reduced ripple content.

3.2.2 PWM Technique

Pulse-width modulation (PWM) is a technique in which the average power which has been delivered by an electrical signal is lowered, and then it is chopped effectively into discrete parts. The total power supplied to the load is higher when the switch is ON for a longer period as compared to the OFF Period. Pulse-width modulated (PWM) DC-DC converters are circuits based on a controlled switch and a diode cyclically switching and driving the entire converter circuit through many topological

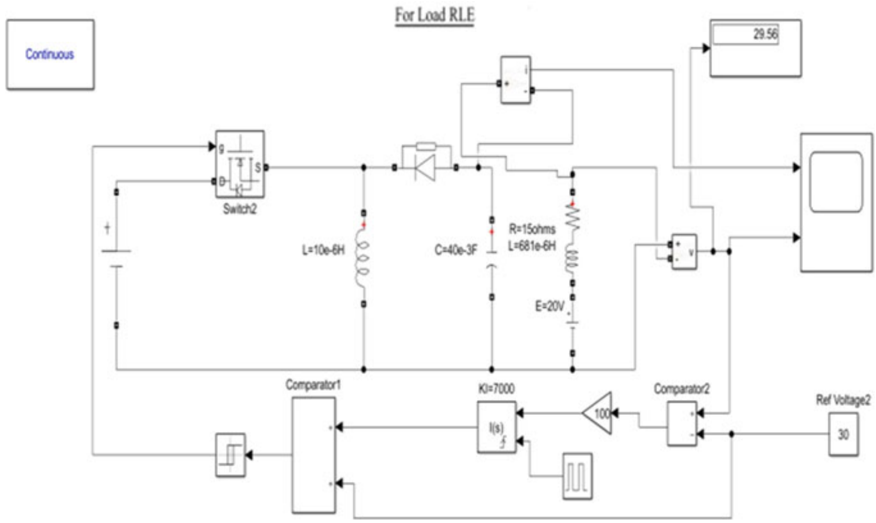

Fig. 6 Buck–boost converter with controller

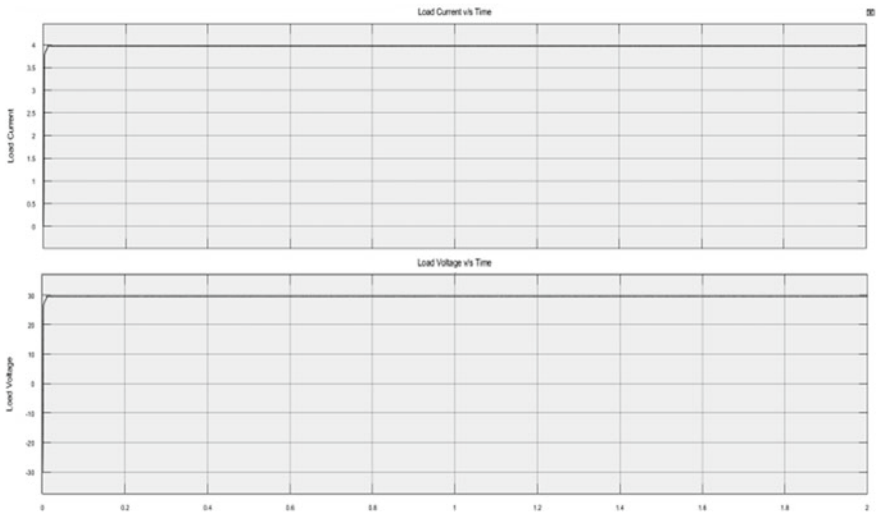

Fig. 7 Output waveform

configurations composed of linear reactive and resistive components, connected to a DC voltage supply. The implementation is shown in Figs. 8 and 9, and it has been observed that while the transient period is very less, the steady-state value is reached with respect to different reference values.

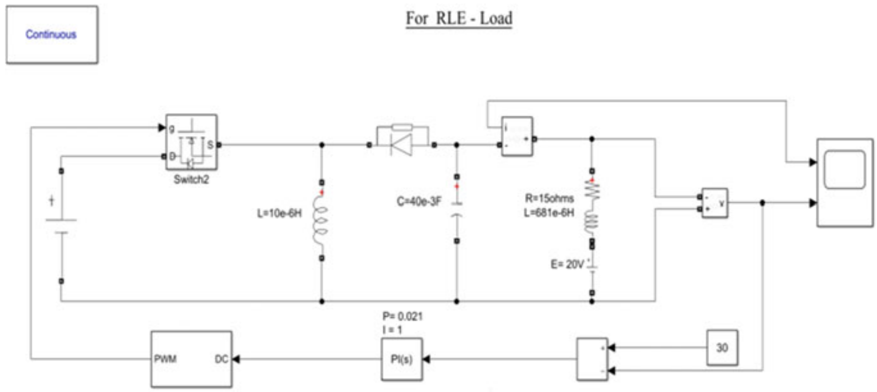

Fig. 8 Buck–boost converter with PWM technique

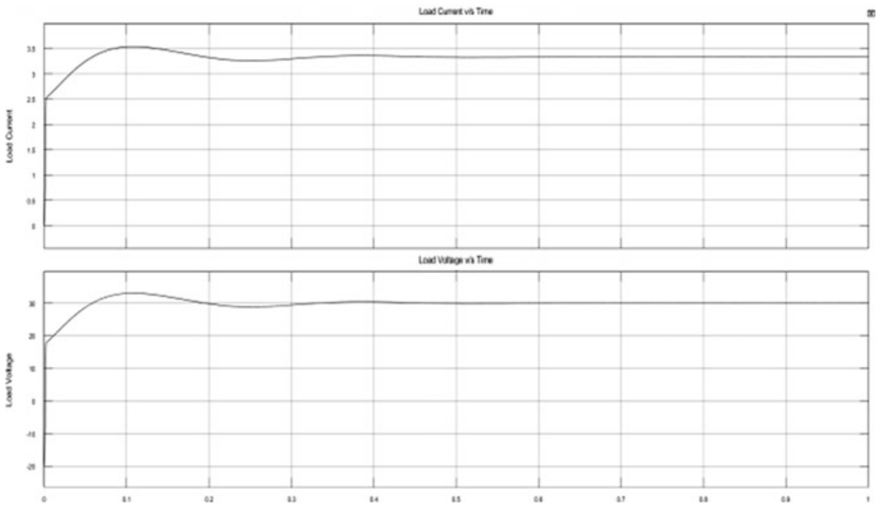

Fig. 9 Output waveform

3.3 Methodology Used with Cuk Converter

3.3.1 PID Controller

The Cuk converter is used in different fields related to hybrid electric renewable energy systems, electric vehicle charging systems, MPPT systems and PV systems. The response of the Cuk converter is good and smooth for practical purposes as reported in [22]. For the PID controller design, a closed-loop system has been considered. The parameters of the PID controller have been set using a hit-and-trial method. Based on the value of the parameters, a response has been obtained for the converter.

For PID tuning, many methods exist [23, 24] but in this work, the traditional method has been used for simplicity. While tuning the PID, it was found that only integral controllers with appropriate value gave satisfactory results for the proposed system. The Simulink model is shown in Fig. 10 while Fig. 11 shows the steady-state value

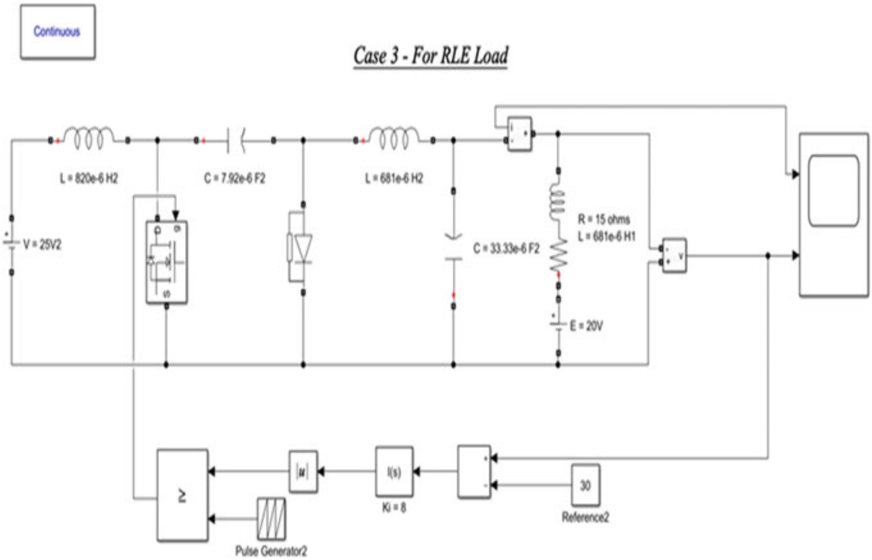

Fig. 10 Cuk converter with integral controller

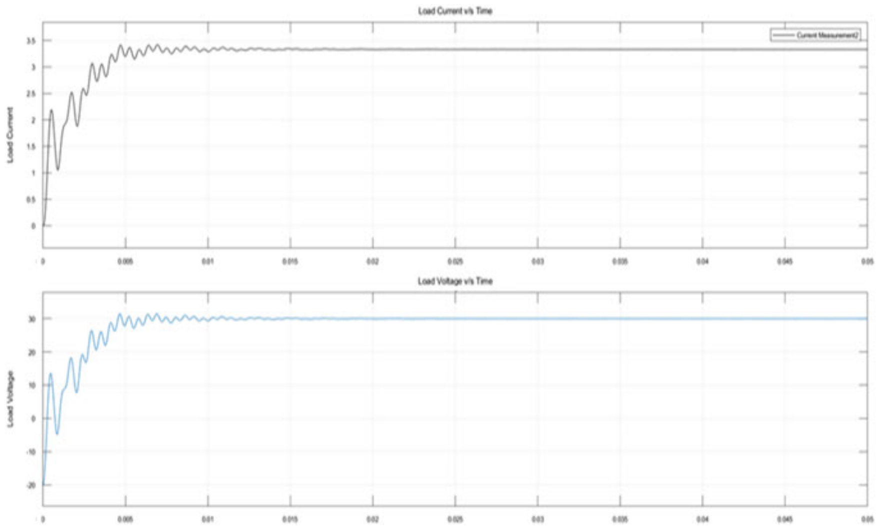

Fig. 11 Output waveform

obtained with respect to different reference values which also shows low ripple in the output.

3.3.2 Fuzzy Controller

In the past decade, fuzzy logic controllers (FLC) have saved time and further simplified the complexity of design. The additional advantage of FLC's is reduced calculations for mathematical operations [7]. With the use of Fuzzy logic-based controllers in almost every domain and sector, they are frequently used in automobile braking systems, washing machines and freezers to produce quality control systems. In classical controllers, a number of mathematical expressions need to be analysed to design the controller [9, 22, 23, 25, 26]. Although this way is simple and easy for linear systems, the same is not for nonlinear systems. While Fuzzy Logic Controllers are designed for any linear or nonlinear system, they are not needed to analyse the mathematical expressions and calculation [23]. When using FLC, the components of the controller are prepared systemically based on verbal and human-based logic expressions rather than a system of mathematical expressions and derivation [24]. The Fuzzy controller has been used in this work, the Simulink model of which is shown in Fig. 12. As shown in Fig. 13 the steady-state value is reached but the value is less than reference value and ripple is also less.

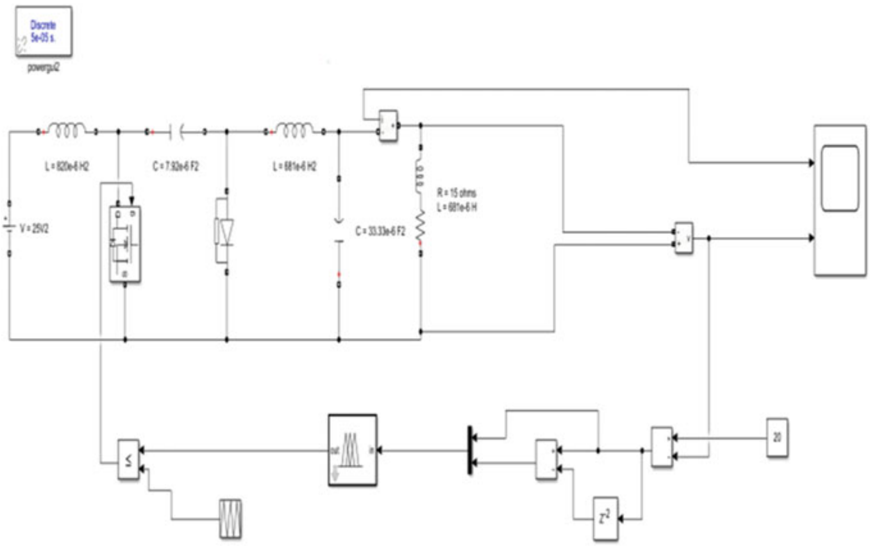

Fig. 12 Cuk converter with fuzzy logic controller

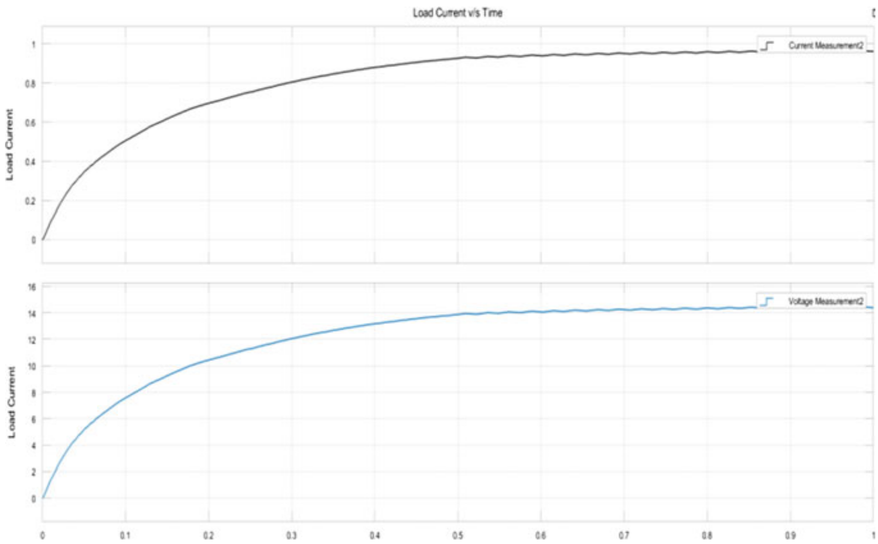

Fig. 13 Output waveform

3.4 Methodology Used with Sepic Converter

3.4.1 PID Controller

The Sepic converter is another converter which finds use in areas related to hybrid electric renewable energy systems, Electric Vehicle charging systems, MPPT systems and PV systems. The response of the Sepic converter is satisfactory with less ripple content [14]. In the PID controller, a closed-loop system has been considered wherein the parameters of the PID controller have been set using a hit-and-trial method. On the basis of the value of the parameters, a satisfactory response of the converter has been obtained. For PID tuning, many methods exist but again, for simplicity, the proposed system uses the traditional method. While tuning the PID, it was found that PI controllers with appropriate value gave satisfactory results for the proposed system which has been designed. The model has been shown in Fig. 14.

It was seen that the result of the Sepic converter with PID controller is better than the response of the system in the base paper [18]. It was observed that there was an improvement in the settling time and the steady state was achieved with minimum ripples. The response of the proposed Sepic converter is shown in Fig. 15, and it can be seen that the steady-state value is attained with respect to different reference values with decrease in the ripple.

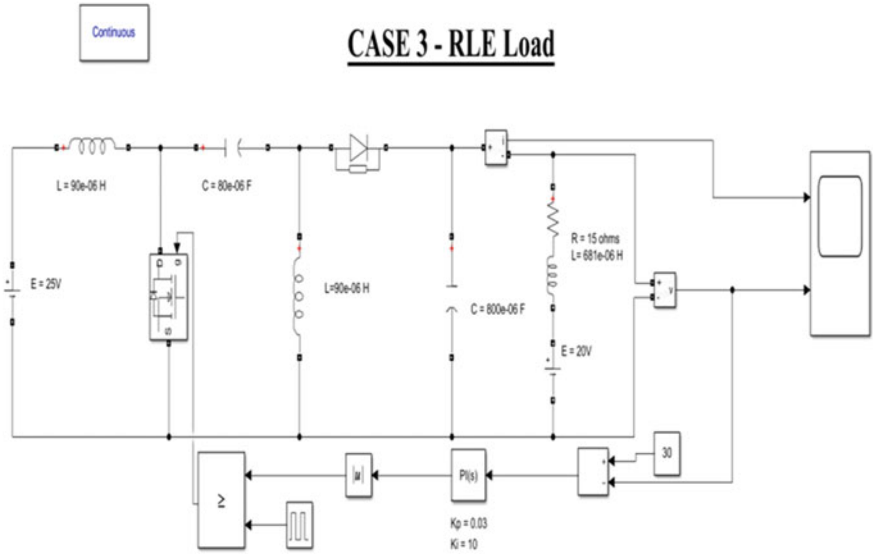

Fig. 14 Sepic converter with proportional–integral controller

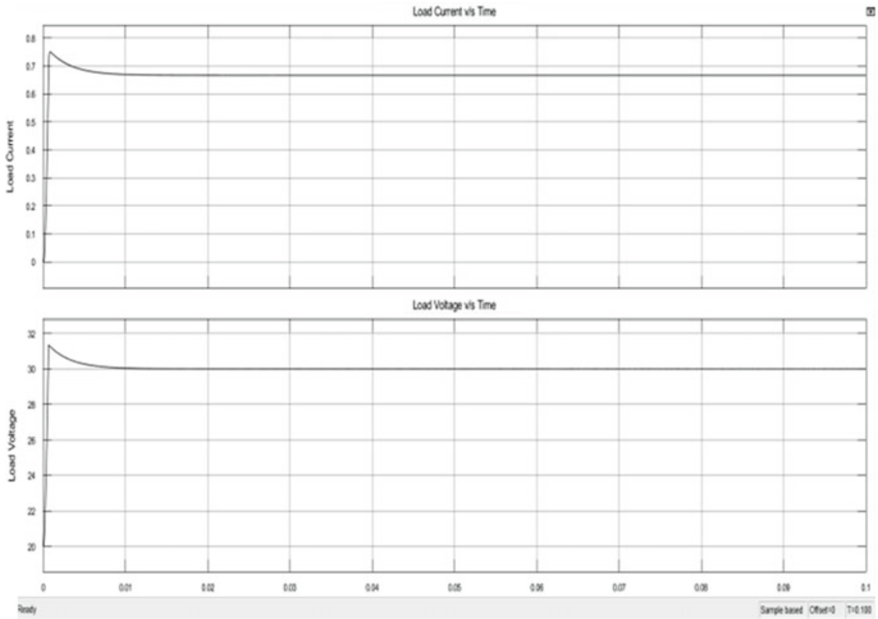

Fig. 15 Output waveform

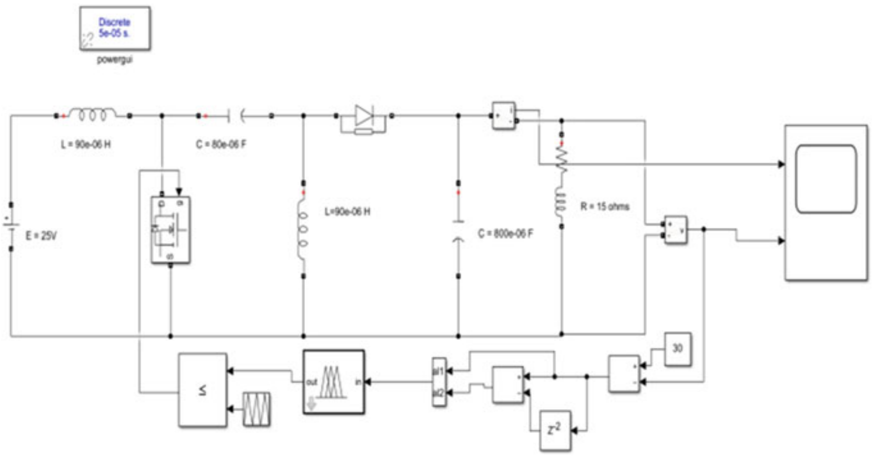

Fig. 16 Sepic converter with fuzzy logic controller

3.4.2 Fuzzy Controller

Fuzzy system is needed for a good closed-loop operation. It is operated in a non-mathematical and nonlinear system with optimal usage of the Sepic converter system [27]. The open-loop system is not able to maintain the constant voltage due to variation of the input applied voltage [28–30]. The components of the controller are prepared systemically based on verbal- and human-based logic expressions rather than a system of mathematical expressions and derivation [10–13, 31, 32]. To maintain the constant voltage some optimization techniques are required. With proper tuning of the fuzzy logic controller and proper rule base design, the steady-state error can be minimized. For this work, the Fuzzy controller has been used and applied on the system. To calculate the error, a delay block has been incorporated in the controller. The model designed is shown in Figs. 16 and 17 show the output waveform obtained for the steady-state value for a reference value. It is observed that there is low ripple in the output. The detailed comparison is reported in the section Results and Discussion.

4 Results and Discussion

From SOC vs time graph, it has been reported in [31] that charging of battery has been allowed till SOC reaches 100%. This is a drawback as lithium-ion battery life decreases, if the battery is charged till SOC becomes 100% and more so if the battery is allowed to be discharged completely. In the proposed system, the design has been done in a manner such that the lithium-ion battery is charged till SOC becomes 85% and the discharging is done till SOC becomes 35%.

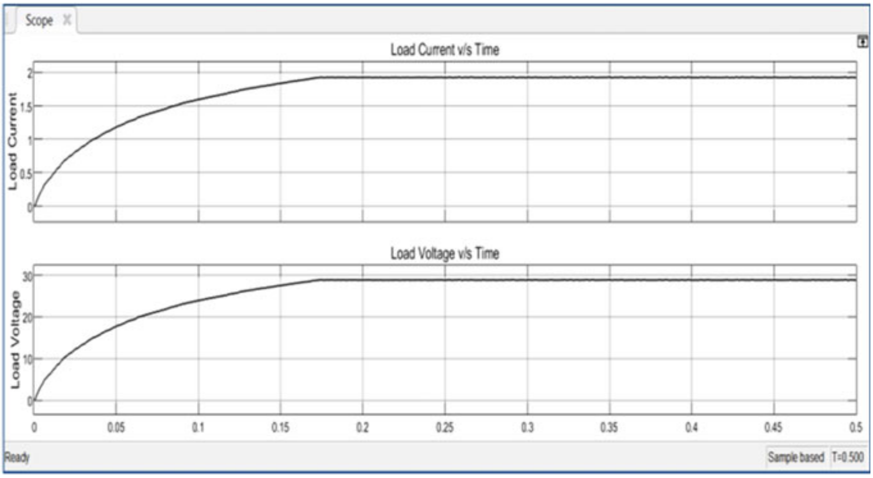

Fig. 17 Output waveform

The proposed system also attempts to improve the outputs of the buck–boost converter, Cuk converter and Sepic converter. The basis of assessing these converters are important performance parameters like steady-state error, settling time and rise time. The parametric comparisons done are shown in Table 10. The performance of the proposed models has been compared with published results of reference papers.

The observations made are compared to the paper [11] and it was observed that the buck–boost converter with PWM Technique has a better response because the settling time is much less and when the buck–boost converter with PID Controller result is compared with the base paper [12], results were similar. For the Cuk converter with PID controller, results obtained from the proposed model were similar to the response of the system in the base paper [33]. The settling time is very less and the steady state achieved has few ripples. When comparing the results of the fuzzy logic controller with base paper [33], the proposed model did not show satisfactory results. For the Sepic converter with PID controller, it was observed that the response of the proposed model is much better than that reported in [16] as the settling time is very less and the steady state is also achieved with minimum ripples. For the fuzzy logic controller, similar results of the proposed model were observed when compared to the base paper [18].

5 Conclusion

In this paper, an attempt has been made to design a battery charging system. The first step was designing the lithium-ion battery after which controlling of its charging and discharging was carried out. An SOP chart was designed in MATLAB which allowed

Table 2 Comparative results with proposed methodology

Converter		Reference paper	Proposed methodology
Buck–boost converter		[13]	
With PID controller	Rise time (ms)	1.397	1.488
	Settling time for 2% tolerance band (ms)	4.798	5.004
With PWM technique		[34]	
	Rise time (ms)	44.78	31.68
	Settling time for 2% tolerance band(ms)	–	–
Cuk converter		[33]	
With PID controller	Rise time (ms)	6.55	1.673
	Settling time for 2% tolerance band (ms)	10	8.459
With fuzzy controller	Rise time (ms)	3.6	11.89
	Settling time for 2% tolerance band (ms)	5	15.78
Sepic converter		[18]	
With PID controller	Rise time (ms)	3.80	0.396
	Settling time for 2% tolerance band (ms)	100	4.940
With fuzzy controller	Rise time (ms)	4.2	12.394
	Settling time for 2% tolerance band (ms)	9	13.67

control of the SOP of the battery to get the desired result. Three different converters, i.e. buck–boost, Cuk and Sepic converters, were compared and implemented using different techniques such as PID controller, PWM technique and Fuzzy logic. After analysis of all the three converters, the results have been compared with similar papers and the results obtained for the Sepic converter have been improved. The output has minimum error, ripple and also reaches appropriate steady-state values when observed with a change in the reference values. The future scope of this work can include optimization of different factors of battery such as nominal voltage and temperature. In addition, use of fuzzy logic technique and implementation in a buck–boost and Cuk converter can also be carried out.

References

1. Mouli GRC, Venugopal P, Bauer P (2017) Future of electric vehicle charging. Int Symp Power Electron 2017:1–7. https://doi.org/10.1109/PEE.2017.8171657
2. Chen T et al (2020) A review on electric vehicle charging infrastructure development in the

UK. J Modern Power Syst Clean Energy 8(2):193–205. https://doi.org/10.35833/MPCE.2018.000374
3. Qian K, Zhou C, Allan M, Yuan Y (2011) Modelling of load demand due to EV battery charging in distribution systems. IEEE Trans Power Syst 26(2):802–810
4. Yilmaz M, Krein PT (2013) Review of battery charger topologies, charging power levels, and infrastructure for plug-in electric and hybrid vehicles. IEEE Trans Power Electron 28(5):2151–2169. https://doi.org/10.1109/TPEL.2012.2212917
5. Lopes JAP, Soares FJ, Almeida PMR (2011) Integration of electric vehicles in the electric power system. Proc IEEE 99(1):168–183. https://doi.org/10.1109/JPROC.2010.2066250
6. Katic V, Subotic I, Bodo N, Levi E, Dumnic B, Milicevic D (2016) Overview of fast on-board integrated battery chargers for electric vehicles based on multiphase machines and power electronics. IET Electr Power Appl 10(3):217–229
7. Gang Z, Yongfang G, Hongbo S (2012) The simulation research of the high-power factor charger in vehicle. Third Int Conf Digit Manuf Autom 2012:939–942. https://doi.org/10.1109/ICDMA.2012.222
8. Hussein B, Abdi N, Massoud A (2020) Design of a single-phase isolated SEPIC-based charger for electric vehicles. IEEE Symp Indus Electron Appl (ISIEA) 2020:1–6. https://doi.org/10.1109/ISIEA49364.2020.9188177
9. Taghizadeh S, Hossain MJ, Lu J (2018) Efficacy of interleaved two-leg buck-boost converter in EV charger design. In: 2018 international symposium on power electronics, electrical drives, automation and motion (SPEEDAM), pp 601–606. https://doi.org/10.1109/SPEEDAM.2018.8445351
10. Corapsiz MF, Erenturk K (2015) Trajectory tracking control and contouring performance of three-dimensional CNC. IEEE Trans Industr Electron 63(4):2212–2220
11. Çorapsız MR (2017) Performance analysis of speed control of PMDC motor using fuzzy logic controller. Eastern Anatol J Sci 3/2:16–29
12. Çorapsız MR (2018) Reduction of commutation torque ripples in brushless direct current motors. Karadeniz Technical University Graduate Institute of Natural and Applied Sciences, Trabzon
13. Gupta Y, Sri P (2014) Analysis and design of CUK converter using PI controller for PV application. Int J Sci Res Technol 2:2321–2613
14. Zhang D (2013) AN-1484 designing a SEPIC converter. Texas Instruments, SNVA168E, May 2006, Revised April 2013
15. Gu W (2007) Designing a SEPIC converter. National Semiconductor Application Note 1484, June 2007
16. Koh H (2012) Modelling and control of single switch bridgeless SEPIC PFC converter. Virginia Polytechnic Institute and State University
17. Taeed F, Salam Z, Ayob SM (2012) FPGA implementation of a single-input fuzzy logic controller for boost converter with the absence of an external analog to digital converter. IEEE Trans Indus Electron 59(2):1208–1217
18. Perry AG, Feng G, Liu Y-F, Sen PC (2007) A design method for PI-like fuzzy logic controllers for DC–DC converter. IEEE Trans Indus Electron 54(5):2688–2696
19. Ardhenta L (2019) An improved PID controller using fuzzy logic for SEPIC DC/DC converter. Department of Electrical Engineering Brawijaya University Malang
20. Stamati T, Bauer P (2013) On-road charging of electric vehicles. IEEE Transp Electrif Conf Expo (ITEC) 2013:1–8. https://doi.org/10.1109/ITEC.2013.6573511
21. Kim D, Choi S, Kim S, Choi B (2011) MATLAB-based digital design of current mode control for multi-module bidirectional battery charging/discharging converters. In: 8th international conference on power electronics—ECCE Asia, pp 2256–2260. https://doi.org/10.1109/ICPE.2011.5944449
22. Zhao B, Abramovitz A, Smedley K (2015) Family of bridgeless buck-boost PFC rectifiers. IEEE Trans Power Electron 30(12):6524–6527. https://doi.org/10.1109/TPEL.2015.2445779
23. Abbas G, Samad MA, Gu J, Asad MU, Farooq U (2016) Set-point tracking of a dc-dc boost converter through optimized PID controllers. In: 2016 IEEE Canadian conference on electrical and computer engineering (CCECE)

24. Tiwari N, Tiwari AN (2018) Performance analysis of unidirectional and bidirectional buck-boost converter using PID controller. In: 2018 2nd international conference on electronics, materials engineering & nano-technology (IEMENTech)
25. Abdulslam A, Mohammad B, Ismail M, Ismail Y (2015) A simple hybrid 3-level buck boost DC-DC converter with efficient PWM regulation scheme. In: 2015 IEEE international conference on electronics, circuits, and systems (ICECS), pp 368–371
26. Colak K, Bojarski M, Asa E, Czarkowski D (2015) A constant resistance analysis and control of cascaded buck and boost converter for wireless EV chargers. IEEE Appl Power Electron Conf Expos (APEC) 2015:3157–3161
27. Morizane T, Shimomori W, Taniguchi K, Kimura N, Ogawa M (2007) PWM technique for non-isolated three-phase soft-switching buck-boost PFC converter. In: 2007 power conversion conference—Nagoya
28. Veerachary M, Khubchandani V (2020) Design and analysis of fifth-order buck-boost converter. In: 2020 IEEE international conference on power electronics, smart grid and renewable energy (PESGRE2020)
29. Yilmaz M, Çorapsiz MF, Çorapsiz MR (2020) Voltage control of Cuk converter with PI and fuzzy logic controller in continuous current mode, 2 Apr 2020
30. Mohan N, Undeland TM, Robbins WP (2003) Power electronics: converters, applications, and design. Wiley
31. Singh MD (2008) Power electronics. Tata Mc Graw-Hill Education
32. Kahveci H (2013) The implementation of an electronic differential system based on fuzzy logic for direct driven electric vehicles. Karadeniz Technical University Graduate Institute of Natural and Applied Sciences, Trabzon
33. Vorpérian V (2006) Analysing the sepic converter. Ridley Engineering Inc. www.switchingpower.com
34. Tsang KM, Chan WL (2012) Fast acting regenerative DC electronic load based on a SEPIC converter. IEEE Trans Power Electron 27(1):269–275

Chapter 41
Cell Balancing and State of Charge Estimation of Lithium-Ion Cells for Electric Vehicle Applications

S. Shilpashree and R. S. Geetha

Abstract Off-late green energy utilization is increasing due to many of its advantages. One of the applications is electric vehicles. Lithium-ion batteries are widely used in electric vehicles because of their advantages over other types of batteries. But the use of lithium-ion batteries will be dangerous if they are not operated properly. One of the factors due to which the battery systems get affected is the cell imbalance. In addition, the estimation of state of charge of any battery is most important in determining the efficiency of the battery. In this paper, shunting resistor passive cell balancing technique is discussed and Coulomb counting method is utilized for state of charge estimation. An algorithm for cell balancing is proposed, and also, corresponding simulation models are developed. The hardware implementation is carried out using Arduino mega 2560 controller.

Keywords Battery management system · Cell balancing · Lithium-ion · State of charge estimation

1 Introduction

Off-late batteries are majorly used as the common energy storage device in electric vehicles. Electricity stored in a battery pack powers electric vehicles. For this, lithium-ion batteries are commonly employed. Increased density, decreased discharge rate, decreased weight, and improved protection are some of the advantages of lithium-ion batteries over other types of batteries [1]. Batteries should work under specified operating conditions to avoid sudden explosion and hence require monitoring. Keeping track of critical operational metrics during the charging and discharging processes is what battery monitoring entails [2]. The key electrical

S. Shilpashree (✉) · R. S. Geetha
B.M.S College of Engineering, Bengaluru, India
e-mail: shilpashrees.epe19@bmsce.ac.in

R. S. Geetha
e-mail: rsgeetha.eee@bmsce.ac.in

G. Panda et al. (eds.), *Sustainable Energy and Technological Advancements*,
Advances in Sustainability Science and Technology,
https://doi.org/10.1007/978-981-16-9033-4_41

parameters such as internal resistance of the battery, ambient temperature, current, and battery voltage should be monitored during battery charge and discharge cycles [3]. In the event of a typical system fault, state of charge (SoC) and state of health (SoH) indicators provide protection by giving alerts or visual warnings. The correct monitoring of the SoC and SoH is required for the smooth operation of heavy mobile devices which is achieved by battery management system (BMS) [4]. For high precision and perfection, an excellent BMS will protect the battery from abnormal conditions and also anticipate the life of the battery [5]. The battery voltage will be affected because of the unequal voltages of the cells during charge and discharge cycle. These variations will decrease battery life and utilization. BMS is utilized to improve the battery life and capacity of the system. Several distinct equalization techniques are discussed in these literatures [6–8]. They are categorized as active and passive cell balancing methods. In passive cell balancing, the additional charge is removed from completely charged cell with the help of passive element or resistor till it matches with low-charged cells in the pack [6]. Whereas in active cell balancing the fully charged cell transfers its energy to the uncharged cells in the pack [6].

The product of average discharge current by the battery and the time required to reach the safe battery cut-off point can be used by BMS to estimate projected run duration under specified discharge conditions [9].

An overview of the various categories and mathematical principles of estimating the SoC and SoH are presented in [10–12]. Programmable dischargers are built for the same purpose using controllers as reported in [13, 14]. In [13], NiMH battery pack is utilized and in [14] a custom BMS is designed and built for high voltage battery packs in formula electric race car. For the estimation of SoC, through various techniques are reported in literature, ideally, Coulomb counting technique will produce reasonably precise SoC [15].

This paper discusses shunting resistor passive cell balancing and SoC estimation by Coulomb counting method using MATLAB/Simulink software. An efficient algorithm is developed for passive cell balancing. In this work, four lithium-ion cells are considered to validate the developed algorithm. Hardware implementation is realized using Arduino mega 2560 controller.

2 Cell Balancing and SoC Estimation

One of the basic balancing techniques is shunting resistor cell balance. This technique extracts excess charge from the highest charged cell by deviating the current of that cell and continue this process till all cells in the battery pack reaches the lowest charge level. Figure 1 depicts the topology for shunting resistor cell balance technique. C1, C2, C3, C4 cells are arranged in series. Every cell is connected to resistor R through MOSFET switch. In this method, S1, S2, S3, S4 are the different SoC values of cells C1, C2, C3, C4, respectively, fed to the controller. Output of the controller Y1, Y2, Y3, Y4 controls the ON/OFF operation of the MOSFET switches. This method is very simple to implement and balancing can be done using simple controllers.

Fig. 1 Shunting resistor cell balancing technique

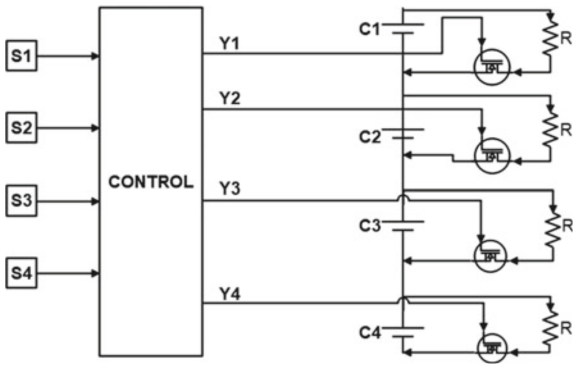

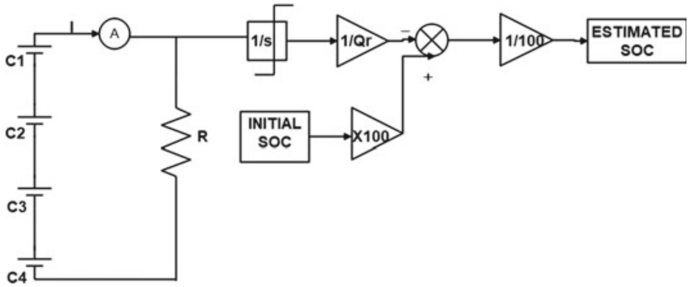

Fig. 2 SoC estimation using Coulomb counting method

The circuit for SoC estimation using Coulomb counting method is shown in Fig. 2. The discharge current I is sensed and integrated over a time period. Output signal from the integrator is divided by the total capacity of the battery pack Qr. Then the result is compared with the initial SoC of the battery with all the cells under the balanced condition. The comparator result is the estimated SoC.

3 Design and Specification

Batteries are applicable to high power applications only if they deliver high voltage, high current, or both. Chemistry of individual cell fixes the voltage range. Hence, for high voltage packs, the cells must be stacked in series and the corresponding equation is:

$$V_{\text{pack}} = n_{\text{s}} V_{\text{cell}} \tag{1}$$

where V_{pack} is pack voltage of battery in volts; n_{s} is the number of series connected cells; V_{cell} is the voltage of the cell in Volts.

Table 1 Lithium-ion cell specification

Parameter	Value	Unit
Nominal capacity	3.7	V
Rated capacity	1.8	A
Cut-off voltage	2.75	V
Fully charged voltage	4.2	V
Nominal discharge current	3	A
Internal resistance	0.03	Ω

Generally, state of charge at time t (SoC_t) is defined as the ratio of its current capacity Q_t to the rated capacity Q. Rated capacity is generally specified in the manufacturer's datasheet. The corresponding equation is:

$$\mathrm{SoC}_t = Q_t/Q \tag{2}$$

where SoC_t is the state of charge of the battery; Q_t is current capacity in Ah; Q is battery's rated capacity in Ah.

Assuming the initial capacity of pack as $Q_{o,}$ i.e., 100% then,

$$\mathrm{SoC}_t = (Q_o - Q_{rl})/Q \tag{3}$$

where Q_o is the initial capacity of the battery in Ah; Q_{rl} is the released capacity of the battery in Ah.

In Coulomb counting method, SoC_t is defined as:

$$\mathrm{SoC}_t = [1 - (1/Q \int i\tau \, d\tau)] * 100\% \tag{4}$$

where $i\tau$ is the discharging current in Amps; Q is the rated capacity of the battery in Ah.

The greatest advantage of this method is that the current can be estimated in real time and hence the SoC. Table 1 shows the different parameter values of a lithium-ion cell which is used both in simulation and hardware setup.

4 Simulation

4.1 Passive Cell Balancing

Figure 3 depicts the Simulink model of shunting resistor passive cell balance technique. Four lithium-ion cells are arranged in series, wherein each cell is connected to a MOSFET switch along with a series resistor. The charge in the cells is monitored

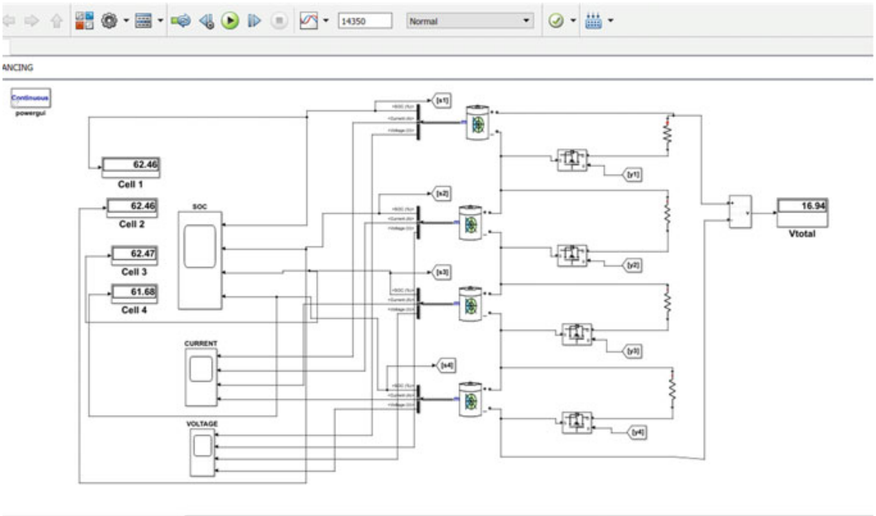

Fig. 3 Simulink model of passive cell balancing

and controlled using developed algorithm. In the model developed, each cell SoC, voltage, and current are displayed to check for balancing condition. The proposed flowchart is shown in Fig. 4.

For the simulation, imbalance in SoC for the four cells is assumed as 75, 80, 70, 85% for cells 1, 2, 3, 4, respectively. The SoC of each cell is the input to the controller, and gate signals to the MOSFET switches are the output from the controller.

4.2 Simulation Model for SoC Estimation by Coulomb Counting Technique

Figure 5 shows the Simulink model of SoC estimation using Coulomb counting method. Initial SoC is assumed to be 62.27% as illustrated in Fig. 5.

4.3 Simulation Results

This section discusses the simulation results obtained in MATLAB. It has been observed that four cells get balanced after discharging for around 4 h. The SoC value is 62.27% on an average after cell balancing. And voltage is 4.235 V/cell. Figures 6 and 7 show the SoC and voltage values of each cell, respectively.

Figure 8 shows the estimated SoC using the Coulomb counting method. It is observed that its value is 59.47% which is less than the desired value of 62.27%.

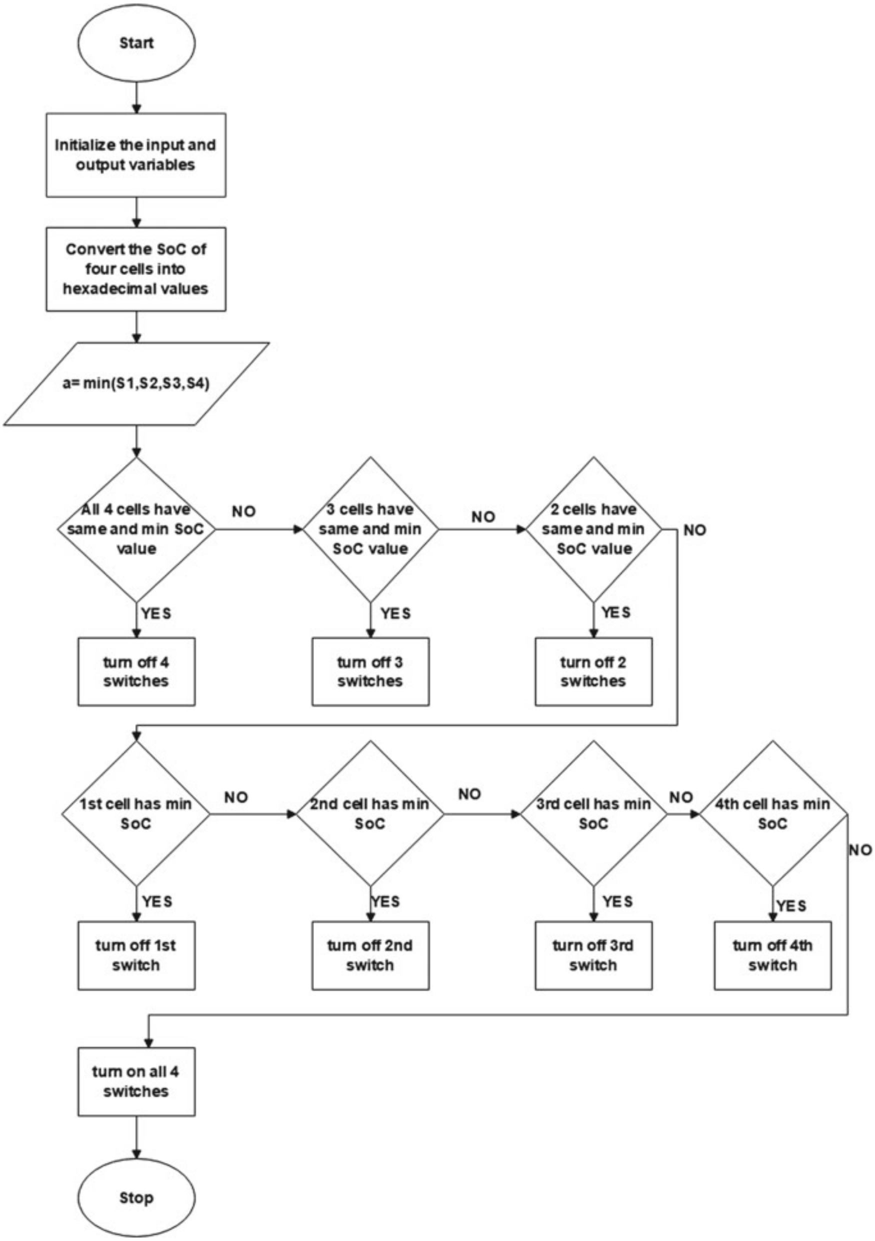

Fig. 4 Shunting resistor passive cell balancing flowchart

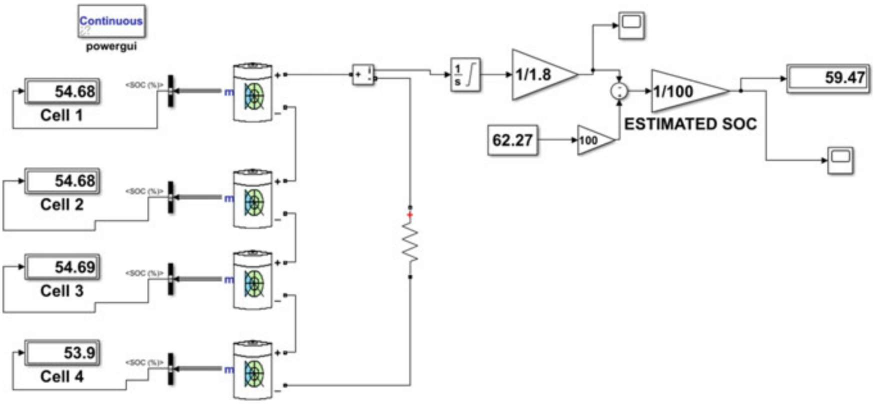

Fig. 5 Estimation of SoC using Coulomb counting method model

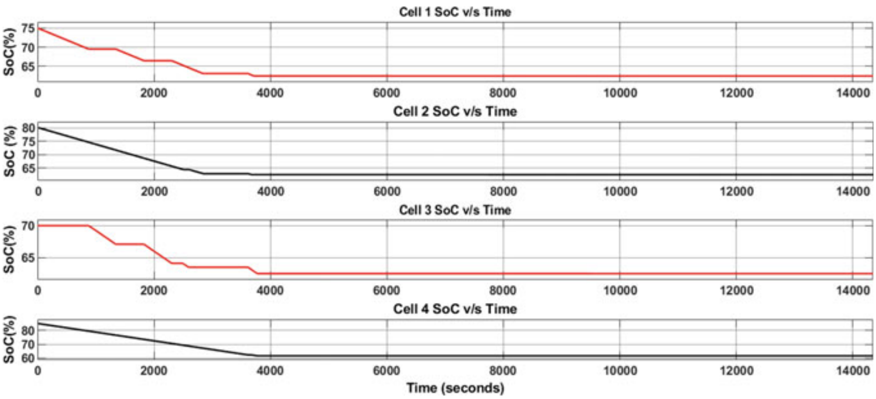

Fig. 6 SoC value of four cells after balancing

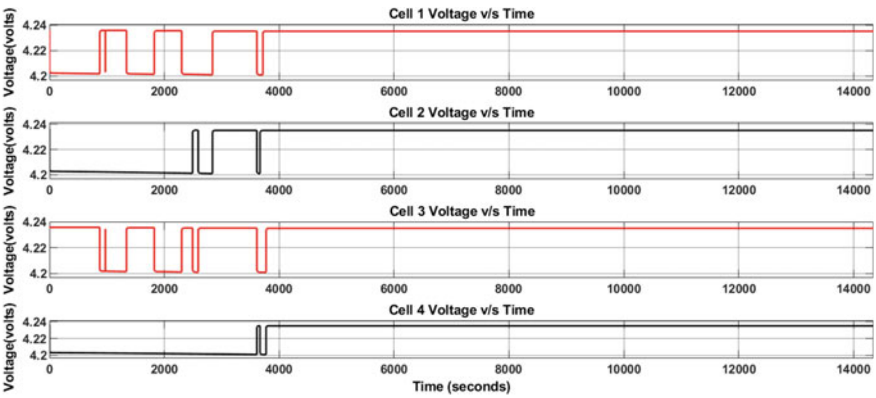

Fig. 7 Voltages of four cells after balancing

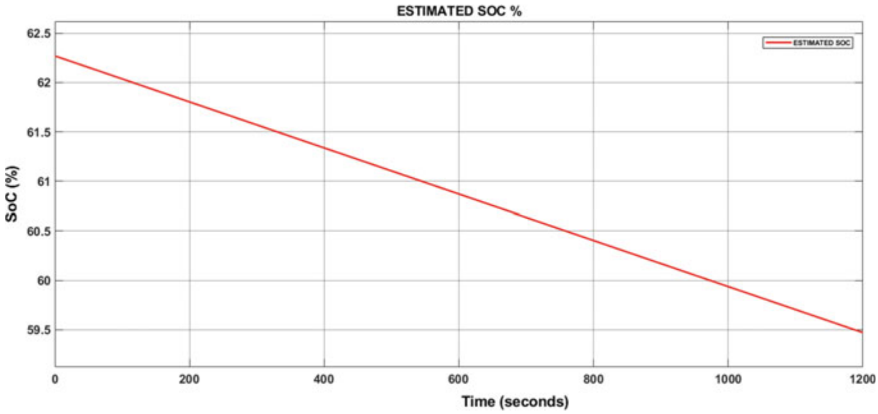

Fig. 8 Estimated SoC

This could be due to the lack of error correction techniques which is to be addressed in the proposed algorithm.

5 Hardware Setup and Results

This section discusses the hardware implementation to show the cell balancing and SoC Estimation. Figure 9 shows the circuit diagram for hardware setup. An Arduino mega 2560 microcontroller is used for the control purpose.

Lithium-ion cells voltage is sensed by the ADC in the controller. The developed algorithm is such that, for voltage greater than 3.9 V and less than 4.2 V, the discharge process will start which is achieved through the 5 V relay module. The relay which is normally open will close and establish connection between the load for discharge and the corresponding battery. For demonstration purpose, the load considered here is a 5 mm, 3 V, 20 mA LED in series with 1kΩ resistor connected to each relay. During discharge process, LED gets turned ON. If the voltage level of all the four cells is less than 3.9 V, then the LEDs will be in the OFF state.

Figure 10 shows the hardware setup. Four cells are used for prototype purpose. The proposed algorithm can be modified for a greater number of cells. Hardware results are displayed on LCD screen. A TP4056 IC is used for charging the cells to the required voltage. A manual charging option is provided using manual switches.

In the initial stage of hardware implementation, it was found that the voltage levels of three out of four cells were almost at the maximum level of 4.2 V, and the voltage of one of the cells was very less and was around 2 V. Figure 11 shows the voltage values of cells after balancing, and this validates the algorithm developed. As four cells are considered, battery pack voltage should be in between 14.8 and 16.8 V. Figure 12 shows that the battery pack voltage is 15.17 V.

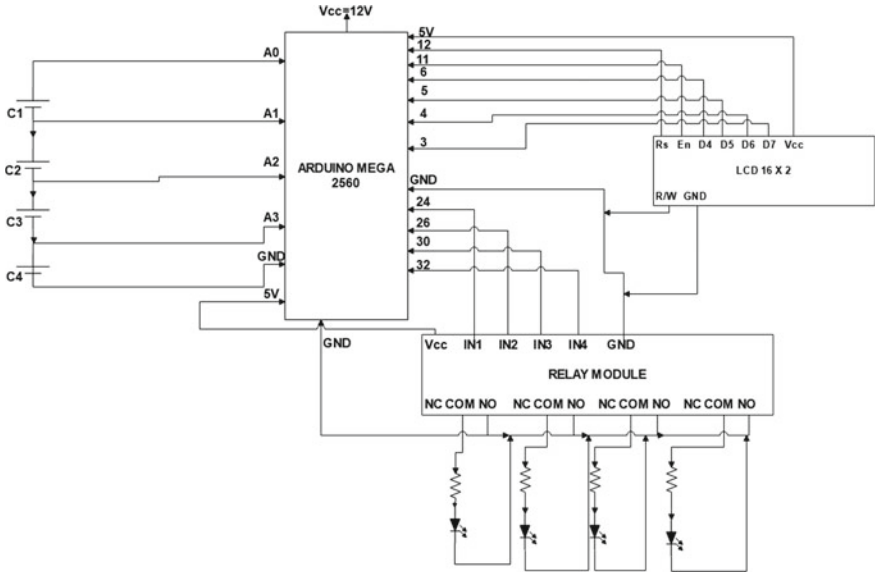

Fig. 9 Circuit diagram for hardware implementation

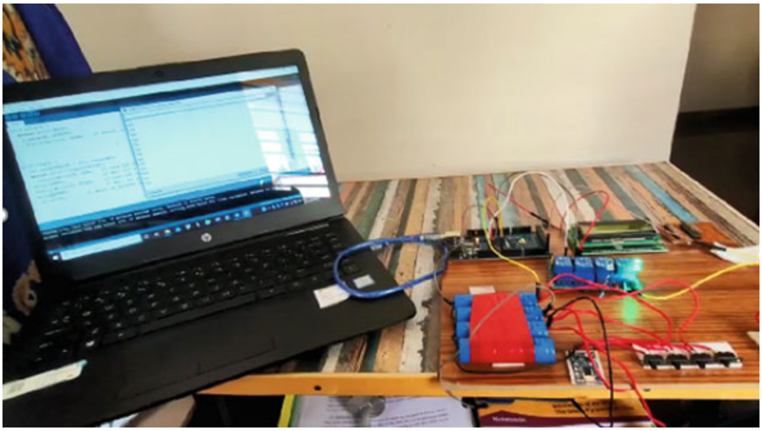

Fig. 10 Hardware setup

Open-circuit voltage method is adopted for SoC estimation in hardware implementation. Figure 13 shows the individual cell SoC values. Figure 14 shows the battery pack SoC which is around 94.79%.

Due to environmental conditions, the cell chemistry changes and hence the voltage of the cell tend to reduce [1]. The proposed algorithm is applied for the cells with the above conditions, and the results are shown in Figs. 15, 16, 17, and 18 for individual cell voltage, battery pack voltage, individual cell SoC, and battery pack

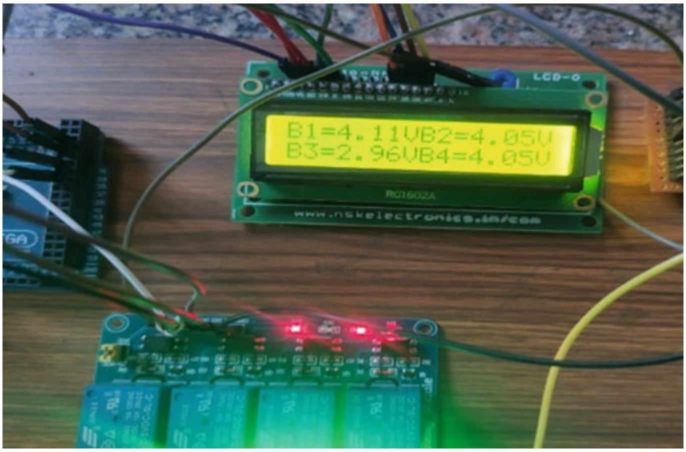

Fig. 11 Individual cell voltages

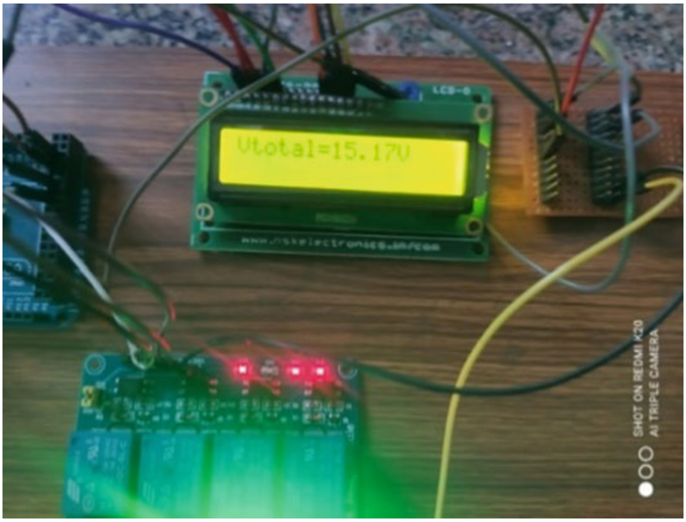

Fig. 12 Battery pack voltage

SoC, respectively. It is observed from Fig. 15 that cell voltages are balanced at 3.8 V. For this condition, the voltage range for discharge of the cell is modified to 3.8–4.2 V. From Fig. 16, it is observed that battery pack voltage is 14.33 V.

From Fig. 17, it is observed that each cell SoC value is above 90%, and from Fig. 18, battery pack SoC is observed to be 89.57%. The flowchart for the Arduino program is shown in Fig. 19.

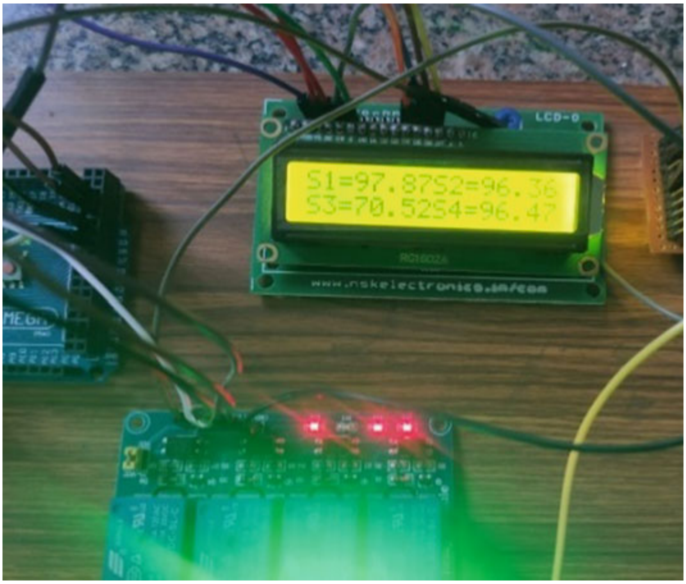

Fig. 13 Individual cell SoC

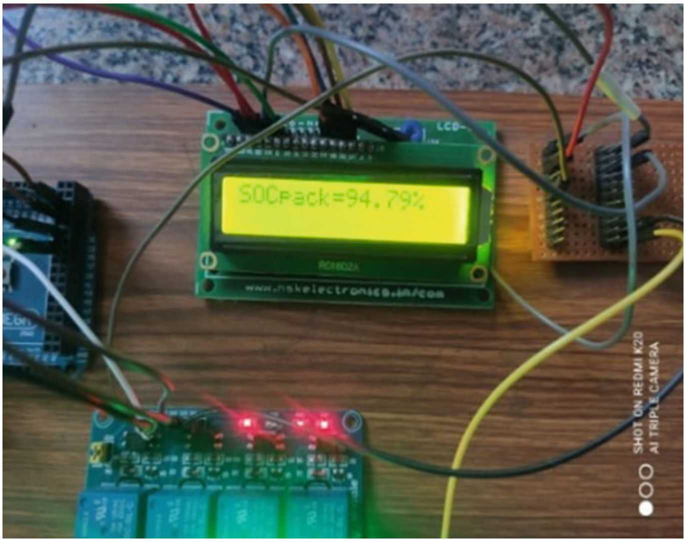

Fig. 14 Battery pack SoC

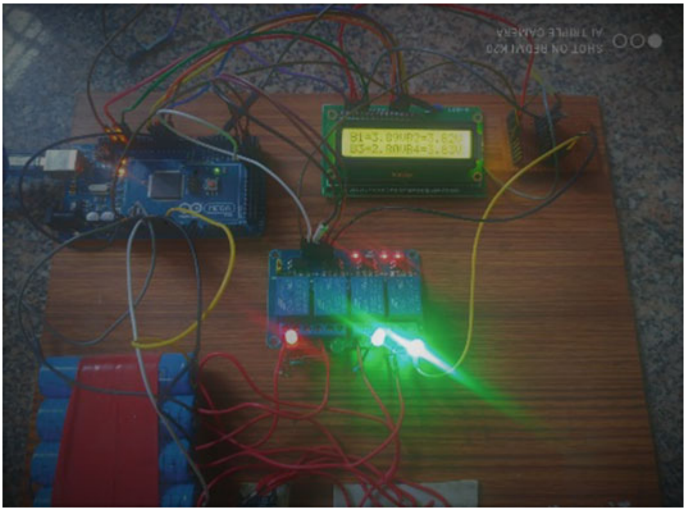

Fig. 15 Individual cell voltages

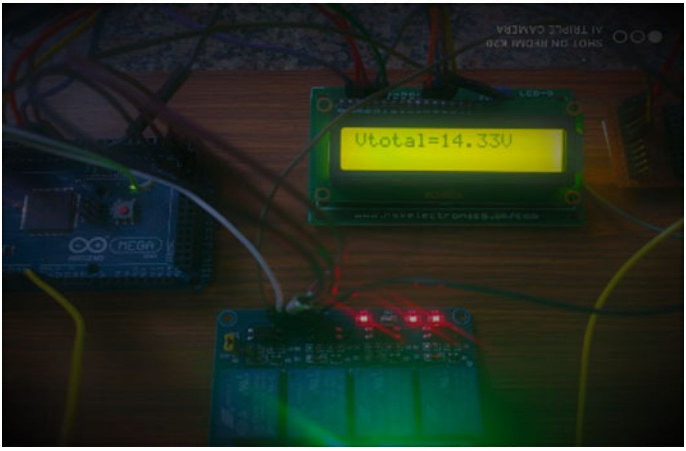

Fig. 16 Battery pack voltage

6 Conclusion

Battery management system plays a vital role in the battery system of electric vehicles. The cell balancing is also an important function of the BMS so as to protect the battery system and to improve the life of the battery. In this paper, an algorithm for shunting resistor passive cell balancing is developed, simulated, and implemented. In addition, SoC of the battery pack using Coulomb counting technique is proposed. The algorithm is validated considering lithium-ion battery having four cells in series. The

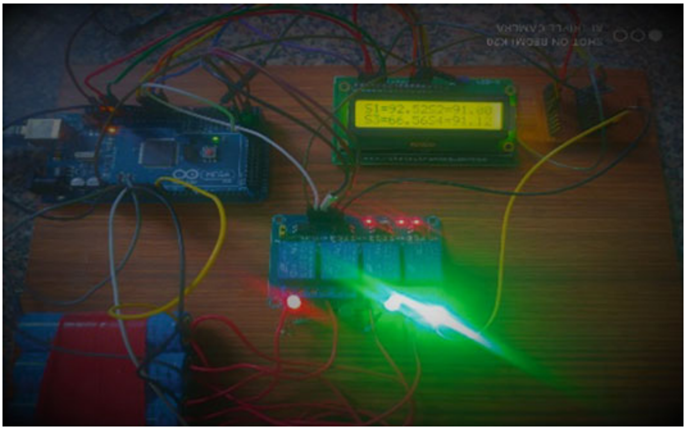

Fig. 17 Individual cell SoC

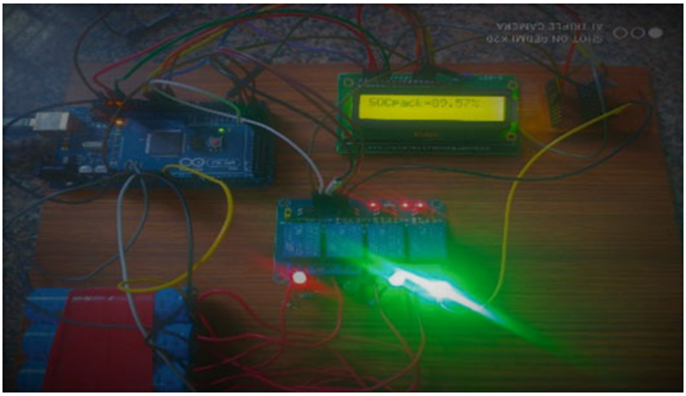

Fig. 18 Battery pack SoC

simulation and hardware results show that the algorithm works effectively. Battery pack voltage in simulation is observed as 16.94 V, whereas in hardware, it is observed as 15.17 V, the difference could be due to the lack of error correction techniques in the algorithm.

Fig. 19 Arduino program flowchart

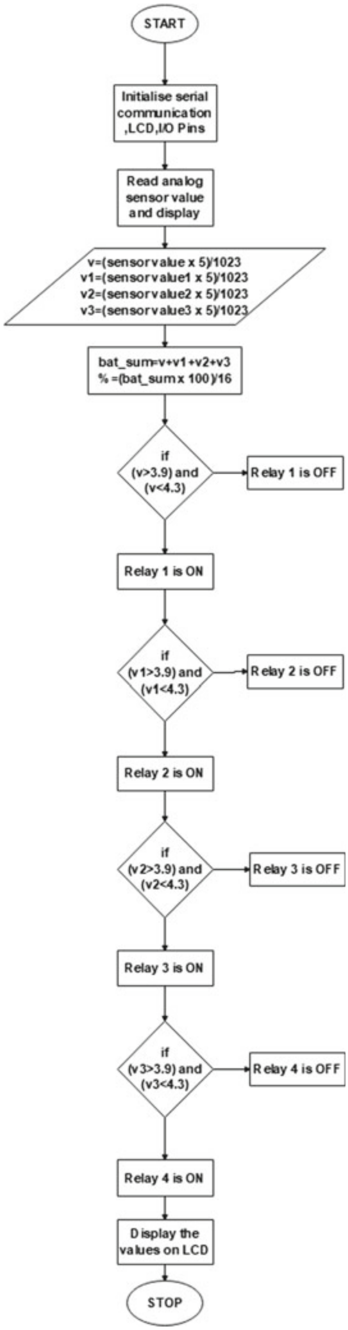

Acknowledgements We truly acknowledge the support extended by the Department of EEE, B.M.S. College of Engineering Bengaluru in carrying out this project.

References

1. Mahammad AH, Hoque MM, Aini H, Yushaizad Y, Ker PJ (2018) State-of-the-art and energy management system of lithium-ion batteries in electric vehicle applications: issues and recommendations. Adv Energy Storage Technol Their Appl 6:19362–19378
2. Bijender K, Neeta K, Chaturvedi P (2015) Advanced battery management system using MATLAB/Simulin. In: 2015 IEEE international telecommunications energy conference (INTELEC)
3. Vinal GW (1924–1955) Storage battery. Wiley, New York, pp 130–336
4. Divakar BP, Cheng KWE, Wu HJ, Xu J, Ma HB, Ting W, Ding K, Choi WF, Huang BF, Leung CH (2009) Battery management system and control strategy for hybrid and electric vehicle. In: 2009 3rd international conference on power electronics systems and applications (PESA)
5. Chen C, Man K, Ting L, Chi-Un TO, Lei K, Tomas J, Seon TT, Guan JK, Wong SU, Prudence WH (2012) Design and realization of a smart battery management system. In: Engineers and computer scientists: 2012 IMECS: proceedings of the international Multiconference, vol 2, pp 1173–1176
6. Jian C, Nigel S, Ali E (2008) Battery balancing methods: a comprehensive review. In: 2008 IEEE vehicle power and propulsion conference, Harbin, China
7. Kong Z-G, Zhu C-B, Lu R-G, Cheng S-K (2017) Comparison and evaluation of charge equalization technique for series connected batteries. In: 2006 37th IEEE power electronics specialists conference, EJU, Korea (South)
8. Moore S, Schneider P (2001) A review of cell equalization methods for lithium ion and lithium polymer battery systems. In: Proceedings of the SAE 2001 world congress
9. Nathan S, Brandon S, Anthony H, Islam MS (2017) Battery management system using Arduino. In: 2017 IEEE technology & engineering management conference (TEMSCON), Santa Clara, CA, USA
10. Prasad V, Divakar BP (2018) Real time estimation of SoC and SoH of batteries. Int J Renew Energy Res 1(8):44–55
11. Dickshon NTH, Mahammad AH, Molla S, Hossain L, Khairul SM, Sahari P, Jern K (2020) State-of-charge estimation of li-ion battery in electric vehicles: a deep neural network approach. IEEE Trans Indus Appl 56(5):5565–5574
12. Chang W-Y (2013) The state of charge estimating methods for battery: a review. ISRN Appl Math 2013:1–7
13. Karsten P, Abbas F, Daniel JA (2015) Low-cost programmable battery dischargers and application in battery model identification. In: 2015 7th computer science and electronic engineering conference (CEEC), Colchester, UK
14. Cherukuri M, Kanthi M (2019) Battery management system design for electric vehicle. In: 2019 IEEE international conference on distributed computing, VLSI, Electrical circuits and robotics (DISCOVER)
15. He L (2019) An improved coulomb counting approach based on numerical iteration for SOC estimation with real-time error correction ability. IEEE Access 7:74274–74282

Chapter 42
Modelling and Analysis of an Electronic Differential-Based Traction Control System for Distributed Drive Electric Vehicle

Pranjal Barman and Sushanta Bordoloi

Abstract Distributed drive electric vehicle (DDEV) power-train provides several potential advantages such as flexibility, controllability, and responsiveness over conventional power-trains. The precise distribution of driving and braking torque of such configuration is crucially vital for improving the overall performance and efficiency of the vehicles. This paper proposes a new electronic differential (ED)-based traction control (TC) strategy for a DDEV. The ED overcomes the drawbacks associated with the conventional mechanical differential (MD) and improves the vehicle's overall efficiency. This work proposes a steering-dependent ED control strategy to stabilize the DDEV at various cornering maneuvers. The primary focus of this work is to reduce the system complexity and improve the overall driving efficiency with the use of look up table. In addition to that, a TC system is introduced, which is associated with the ED system relying on road–tire interaction to regulate the wheel slip during traction and braking conditions. The look-up table is a method that may allow integration of the proposed system in the DDEV controller. Therefore in practice, the proposed model can execute in a real-time platform without the requirement of high processing power and additional hardware units. This work examines a software simulation environment with the necessary constraints for the vehicle geometry. The results affirm the effectiveness of the proposed work.

Keywords Electronic differential (ED) · Traction control (TC) · Distributed drive electric vehicle (DDEV) · Mechanical differential (MD) · Slip ratio

P. Barman (✉)
E&ICT Academy IIT Guwahati, Guwahati, Assam, India

S. Bordoloi
NIT Mizoram, Aizawl, Mizoram, India
e-mail: sushanta.ece@nitmz.ac.in

G. Panda et al. (eds.), *Sustainable Energy and Technological Advancements*,
Advances in Sustainability Science and Technology,
https://doi.org/10.1007/978-981-16-9033-4_42

1 Introduction

Electric vehicles (EV) have been garnering wide attention over traditional internal combustion engine vehicles (ICEV) due to the growing concerns of continuously depleting fossil fuel and ever-increasing carbon emission [1, 2]. Various automotive industries are taking more remarkable initiatives to develop EVs that can reduce global carbon emissions. The modern-day advancement of motor technology accelerates the growth of new design innovations in the existing EV power-trains. The hybridization of EV power-train configurations is emerging research in modern-day vehicular engineering [3, 4]. Distributed drive-train is one kind of power-train hybridization that has been evolving in recent years. In a distributed drive electric vehicle (DDEV) power-train, the motors attach to the wheels independently [5]. Therefore, it offers more flexibility, controllability, responsiveness, safety and provides diverse opportunities to improve the control methodologies [6]. Furthermore, the actuation features like anti-lock braking system (ABS), acceleration slip regulation (ASR), and advanced driver assistance system (ADAS) are effectively incorporated in DDEVs [7].

A single motor is mounted between the driving wheels through gear reduction and the mechanical differential (MD) system in a conventional EV power-train. The purpose of the MD is to change the speed of the inner and outer wheels during cornering. However, MD considerably increases the overall mass of the vehicle along with its battery and in-house peripherals. As a consequence, the energy consumption of the EV increases, and the driving range is restricted. This shortcoming in the MD system is addressed with the proposed distributed drive train with an ED-based TC system. The independently equipped motors provide higher power to weight density, reliability, safety, and better dynamic performances. However, precise torque distribution among each independent wheel is a significant concern for efficiency improvement. Furthermore, this design's significant difficulties are ensuring vehicle stability during cornering and under slippery road conditions. If the wheels are not driven with appropriate running requirements, then EV may experience instability in worse-case situations. The ED-based TC system plays a significant role in tackling these difficulties in a distributed drive EV. The TC system represents a classic and practical approach to control the longitudinal and lateral vehicle dynamics. It maintains the optimal vehicle dynamics by preventing the wheel slip during acceleration and braking conditions. Moreover, a careful ED-based TC approach with a well-defined framework could outreach the shortcomings of DDEVs and make it possible for potential commercial applications.

Despite having significant contributions in ED, there is a lack of cost-effective solutions without trading off the design's simplicity, stability, and robustness. Francisco et al. [8] developed an approach employing a linear synchronization method to derive the wheel reference speed using Ackermann steering geometry. It uses real-time velocity and steering angle feedback to control the speed difference of the inner and outer wheel during a turning maneuver. Similar work in [9] adopted a direct torque control scheme with the same objective. Another approach in [10] employed the speed ratio of the driving wheels as a control variable and improved the transient response of the system. Mutoh et al. in [11], adopted a method by estimating adequate lateral forces for wheel revolution based on multiple feedback variables to enhance the off-road driving performance. Literature is well-versed with control approaches of TC systems. However, real-time estimation of slip ratio is yet a significant concern for researchers. Few strategies deal with the measurement of parameters that influences the friction coefficient [12, 13]. Notwithstanding having better accuracy, those strategies require additional expensive sensors. On the other hand, few strategies rely on the vehicle motion response caused by friction coefficient [14]. Yet, such systems lack an adequate level of accuracy. Considering the viewpoints mentioned earlier, a simplified slip ratio control-based TC strategy is proposed in this work. The proposed strategy relies on the estimation of the tire–road friction coefficient, wherein the reference slip ratio is evaluated with the maximum tire–road friction coefficient. Accordingly, the wheel torque output is regulated with an allowable torque value to reduce wheel slip. Consequently, the effectiveness and adaptability of the proposed ED-based TC method is demonstrated through the simulation, case studies, and analysis.

2 Design Principle

2.1 Electronic Differential

The core focus of the ED is to distribute the necessary torque to the driving wheels to prevent the vehicle from slipping. If the velocity of the vehicle center of gravity (CG) is v, inner and outer wheel velocities must be directly proportional to the distance of the wheels to the turning center as depicted in Fig. 1.

Here, two inputs, steering angle and throttle position, collectively decide the speeds of the inner and outer wheel during a cornering maneuver. In case of a right turn, the ED must maintain a higher speed at the left wheel than the right wheel to prevent the tires from losing traction. In Fig. 1, L_w is the wheelbase, δ is the turning angle, d_w is the track width, R is the radius of the turn, and v_L and v_R represent the angular speeds of the left and the right wheel, respectively. The linear speed of each wheel is represented as a function of the vehicle speed and the radius of the turn as [15, 16]:

$$v_L = \omega_v(R + \frac{d_w}{2}) \ \&\ v_R = \omega_v(R - \frac{d_w}{2}) \tag{1}$$

The relation between the radius of the turn and steering angle and wheelbase is:

$$R = \frac{L_w}{\tan \delta} \tag{2}$$

Fig. 1 Steering geometry involved in the ED system

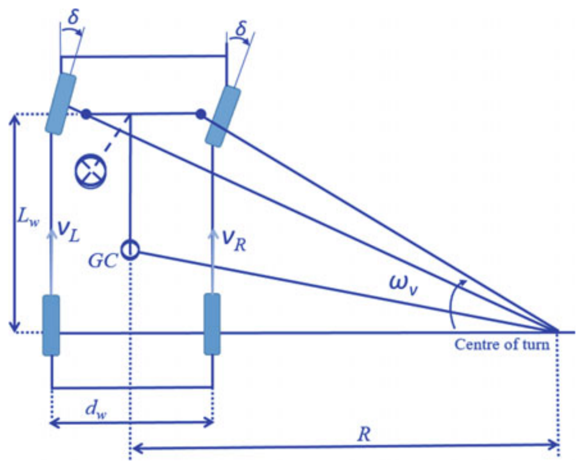

Substituting Eq. 2 in Eq. 1, we get an angular speed of each wheel as:

$$\omega_L = \frac{L_w + \frac{1}{2}d_w \tan\delta}{L_w}\omega_v \text{ and } \omega_R = \frac{L_w - \frac{1}{2}d_w \tan\delta}{L_w}\omega_v \quad (3)$$

The difference between angular speeds of the wheel drives is:

$$\Delta\omega = \omega_L - \omega_R = \frac{d_w \tan\delta}{L_w}\omega_v \quad (4)$$

The sign of the steering angle indicates the direction of the turn, i.e., $\delta > 0$ = Turn Right, $\delta < 0$ = Turn left, $\delta = 0$ = Straight ahead. When the driver gives the steering input, the ED immediately acts by reducing the inner wheel's speed and increasing the outer wheel's speed. The modified driving speed of the wheels are:

$$\omega_L^\star = \omega_v + \frac{\Delta\omega}{2} \text{ and } \omega_R^\star = \omega_v - \frac{\Delta\omega}{2} \quad (5)$$

2.2 Traction Control

The primary objective behind the proposed TC system is to make it simple and effective for DDEV applications. In the real-road environment, the challenges of a TC system are to deal with the slippery surface and random road surface. The slippery surface may be the wet surface or low friction surfaces such as wet tiled surfaces. In this work, we have presented TC system working along with the ED system. The proposed model assumes the vehicle's longitudinal and lateral motion, where the traction analysis is performed over a flat surface. In the simulation analysis, the air drag and rolling resistance are ignored to simplify the model. It is observed that if the traction force applied on the wheel is higher than the friction force that the road can provide, the wheel slip will increase, resulting in vehicle instability. In such a situation, the TC system determines the wheel slip and accordingly controls the wheel torque to reduce the vehicle instability. Therefore, the estimation of tire road friction coefficient is a vital part of the TC system. To estimate the tire road friction coefficient, the evaluation of the longitudinal slip ratio is essential. The longitudinal slip ratio is obtained from dividing wheel velocity by vehicle velocity, as mentioned in Eq. 6.

$$s = \frac{R_g \omega}{v_x} - 1 \tag{6}$$

Here, R_g is the tire geometric and unloaded radius, ω is the tire angular velocity, and v_x is the tire forward velocity. The longitudinal slip ratio is positive for driving and is negative for braking. The friction coefficient reaches a driving peak value μ_{dp} at $s = 0.1$ before dropping to an almost steady-state value μ_{ds}. The friction coefficient may be assumed proportional to s when s is minimal. The tire will spin when $s \geq 0.1$ and the friction coefficient remains almost constant. The same phenomena happen in braking at the negative values as illustrated in Fig. 2a

Some mathematical models have been derived to simulate the longitudinal tire force as a function of longitudinal slip, s. However, most of these models are too complicated to be helpful in vehicle dynamics. One of the accurate and straightforward practical models is proposed by Burckhardt in 1987. This model is expressed as [17]:

$$F_x(s) = C_1(1 - e^{-C_2 s}) - c_3 s \tag{7}$$

Now, if a vehicle turns over a plan surface, then a lateral force F_y will be exerted in its path of motion, making an angle α w.r.t tire plane. The angle is known as

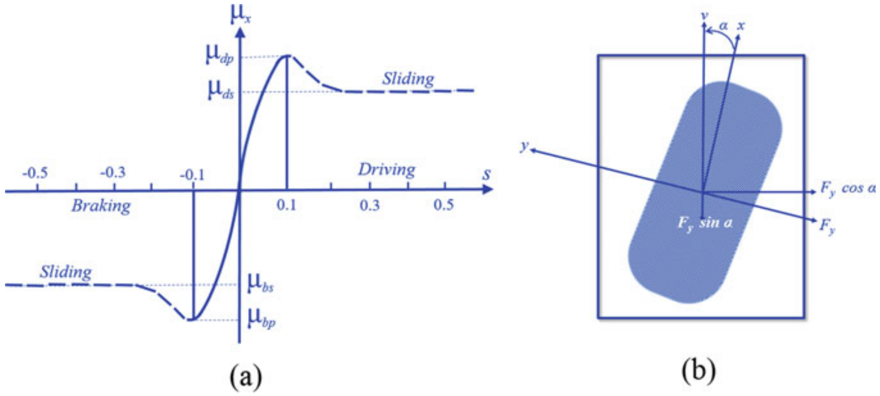

Fig. 2 **a** Longitudinal friction coefficient as a function of slip ratio s,in driving and braking. **b** Sideslip angle as a result of lateral force

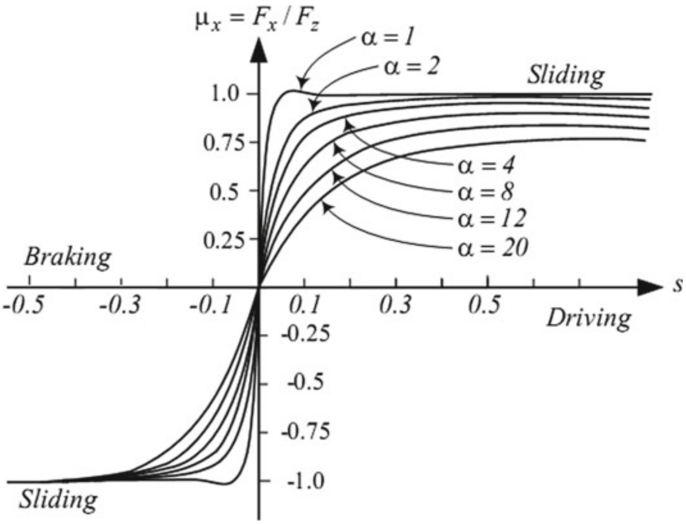

Fig. 3 Longitudinal force ratio F_x/F_z as a function of slip ratio s for different sideslip angle α [17]

sideslip angle as shown in Fig. 2b. From the above definitions, we can conclude that a vehicle tire is a force generator with two major outputs: longitudinal force F_x and lateral force F_y. The input of the force generator is the tire load F_z, sideslip angle α, longitudinal slip s. In this work, we have ignored the camber angle for ease of analysis. When the tire has a combination of tire inputs, the tire forces are called tire combined force. The most important tire combined force is due to longitudinal and sideslips. However, as long as the angles and slips are within the linear range of tire behavior, a superposition can be utilized to estimate the output forces. Driving and braking forces change F_y generated at any α. It is attributed to the longitudinal force that pulls the tire-print in the driving or braking force direction; as a result, the length of lateral displacement of the tire-print changes. Figure 3 illustrates how α affects the longitudinal to normal force ratio F_x/F_z as a function of slip ratio s. In the present work, we have considered this plot to determine the reference slip ratio in the form of a look-up table.

2.3 Control Mechanism

When a vehicle experience a cornering maneuver, the slip of the inner and outer wheels can be defined as:

$$s_i = \frac{R_g \omega_i}{v_{ix}} - 1 \text{ and } s_o = \frac{R_g \omega_o}{v_{ox}} - 1 \tag{8}$$

Here, we have considered that the vehicle is a front-wheel drive, and the driving wheel shared the total driving power equally. When a vehicle makes a turn, the inner wheel speed will decrease, and conversely, the outer wheel speed will increase. In such a situation, the inner wheel slip starts increasing. Therefore, the force applied on the inner wheel has to reduce to a certain value to avoid wheel slip. On the other hand, the outer wheel slip goes to a negative value, which means that the wheel experiences braking. To prevent sliding of the outer wheel, the force necessary to drive the vehicle has to increase for the stable movement of the vehicle. If P is the total driving power and F_i and F_o are a force on the inner and outer wheel, respectively. We can re-write the above expression as:

$$s_i = \frac{2R_g F_i \omega_i}{P} - 1 \text{ and } s_o = \frac{2R_g F_o \omega_o}{P} - 1 \tag{9}$$

Equation 9 is used to determine the requirement-based torque distribution in the ED-based TC system.

3 Torque Allocation Model

The simplified vehicle control diagram is shown in Fig. 4. Two identical motors are independently mounted in each front wheel of the vehicle. The motors are driven by two independent controllers having appropriate specifications. In this work, we have considered DC motor for the analysis. The DC motor acquires its popularity due to several advantages such as simple control, wide speed-torque range, and higher efficiency. It is well-known that induction motor (IM) or brushless DC motors (BLDC) have some superior advantages compared to DC motors. However, the DC motors' low and medium power propulsion applications are still popular because of their technical maturity and cost-effectiveness. Furthermore, the complicated control strategies in IM or BLDC motors make the control system more expensive than the DC motors.

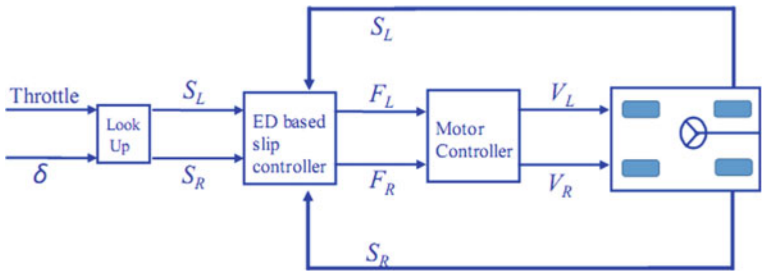

Fig. 4 Vehicle control structure

It is significant for an optimal torque allocation (TA) model to analyze the DDEV driving performances. If the driving torque is distributed among the motors according to the vehicle working conditions, then the vehicle's driving performance is highly improved. In this model, the reference slip values for both the driving wheels are obtained from a look-up table corresponding to the steering angle. It is worth mentioning that we have considered the steering angle and the side slip angles are the same for ease of implications. This approximation can be made in front-wheel drive vehicles as the angle difference between the steering and sideslip is very small. However, in practice, the steering angle is somewhat higher than that of the sideslip angle in rear-wheel drive vehicles. The ED-based TC system supervises the driving force based on reference slip and real-time slip. Accordingly, the controller generates the necessary voltage signal to the electric motor in proportion to the ED-based TC system's force command. The ED-based TC system algorithm is shown in Fig. 5a.

4 Model Simulations

The proposed ED-based TC system is examined in a software simulation environment with the necessary constraints for the vehicle geometry. Here, we have assumed that the driving motors are identical. Furthermore, we consider the cornering maneuvers in a good road adhesion condition where the inner wheel produces an opposite moment to turn the vehicle. In the simulation environment, we have defined one of the most commonly available semicircular testing routes as illustrated in Fig. 5b.

5 Results and Discussions

The merit of the proposed method lies in improving the ED and TC mechanism of the DDEV. Therefore, simulating the vehicle motion parameters is vital for performance analysis. In this simulation, a complete driving trip observes the parameters such as throttle input, steering angle, wheel speed, wheel force, and wheel slips. Therefore, a semicircular driving route is assumed for the simulation analysis. During the simulation, the DDEV accelerates straight ahead from point A to point B. At point B, it experiences a left-turning which continued until point C, as shown in Fig. 5b. From point C, the DDEV moves straightway to reach point D. At point D, it experiences a right turning maneuver that continues until point E. From point E to F, the vehicle again moves straight. At point F, it experiences another right turning having a higher radius of curvature, and it ends at point G. From point G to H, the DDEV moves straight and experience the last right turn that starts from point H. Finally, the vehicle finished a complete driving trip and reached starting point A and halted. Figure 6a shows the velocity of the left and right wheel during the complete trip with and without applying the ED-based TC system. It is observed that the vehicle's movement with an ED-based TC system is stable and smooth compared to the previous result. The variation of the wheel velocity due to the ED system is shown in Fig. 6b.

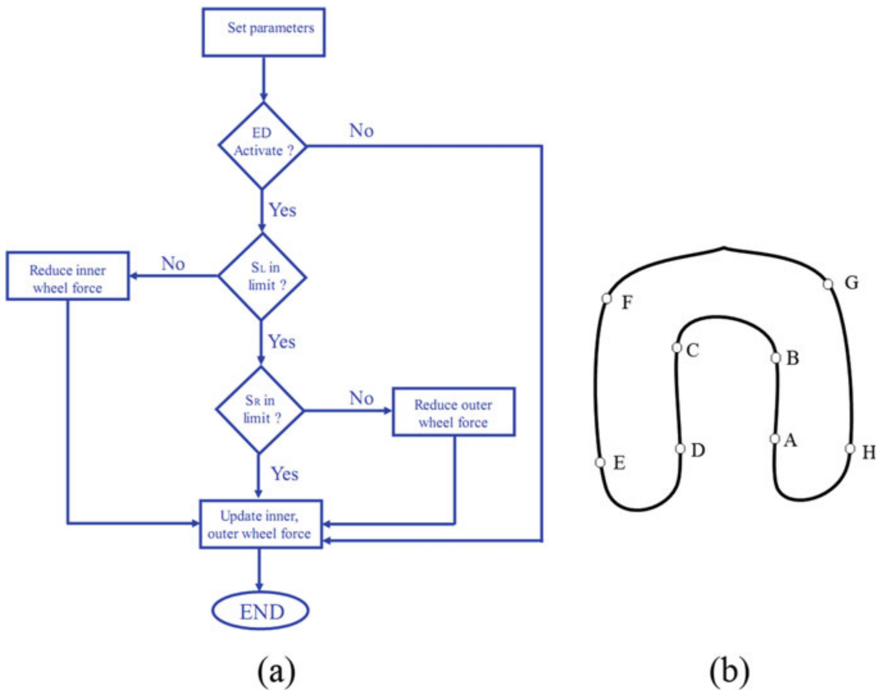

Fig. 5 **a** ED based TC Algorithm. **b** Semicircular testing route assumed for the simulation

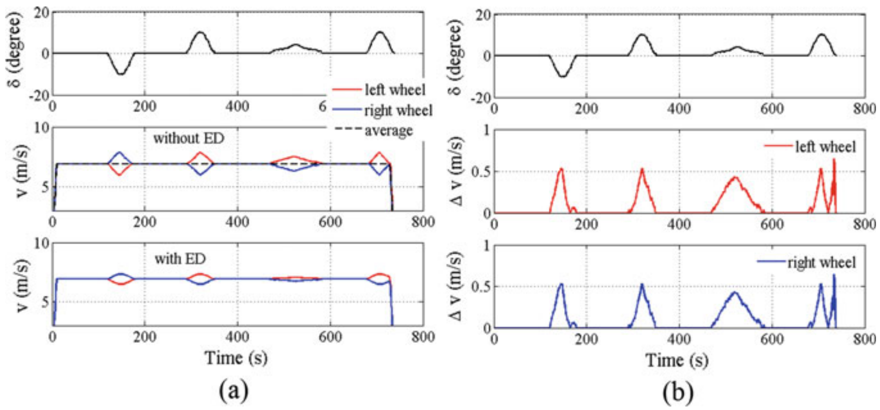

Fig. 6 **a** Driving performance with and without ED. **b** Variation of the wheel velocity during the cornering maneuver

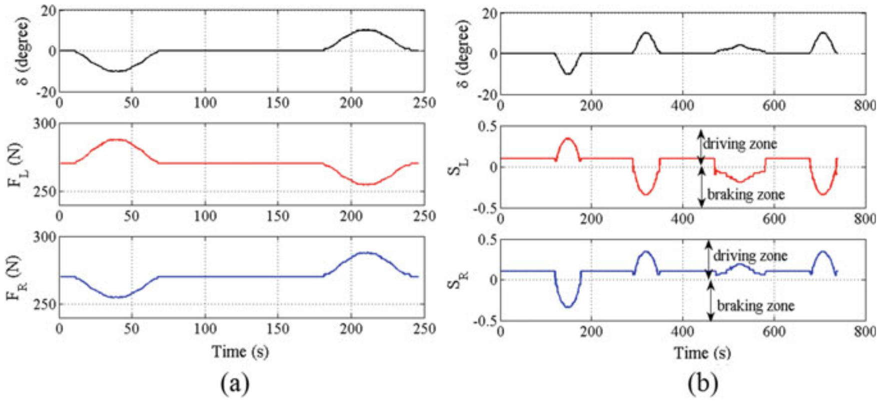

Fig. 7 **a** Driving force on each wheel during the cornering. **b** Reference slip ratio during the driving and braking of the DDEV.

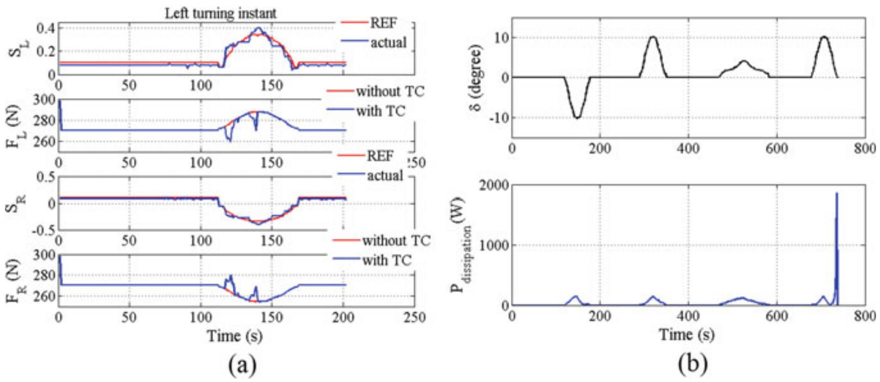

Fig. 8 **a** Slip control by the ED based TC system. **b** Additional power dissipation if we replace the proposed ED with conventional MD

Figure 7a shows the force on each driving wheel during an instance of turning maneuver. It can be observed that the ED distributes an adequate amount of force to each driving wheel to maintain the vehicle's stability. The reference slip ratio for the driving and braking zones of the DDEV is shown in Fig. 7b.

Figure 8a demonstrates the performance of the TC system in the predefined route. Here, the real-time slip ratio of the DDEV is assumed to be random. Therefore, the real-time slip ratio in some instances overcomes the reference slip ratio. As soon as the real-time slip ratio overcomes the set reference, the TC system becomes active and reduces the respective wheels' driving force. Finally, to demonstrate the comparative analysis with the existing method, we have determined the power dissipation using the MD and ED throughout the trip. It is worth mentioning that the MD distributes the driving torque evenly; however, the ED distributes the torque as per the steering demand. Therefore, the power dissipation in ED is less compared to the MD. Moreover, the MD has more friction loss due to the gearing mechanism. Figure 8b shows the additional power dissipation when we replace the proposed ED with the conventional MD. It is evident that the ED significantly saves the overall power compared to the conventional MD. By considering the simulation results and analysis, it can be concluded that there has been a significant power reduction due to incorporating the ED-based TC system into the DDEV.

6 Conclusions

In this work, we have presented a proactive ED-based TC system for a DDEV. The ED system supervises the wheel speed variation during turning maneuvers, and the TC supervises the slip control mechanism during cornering. As an effect of the combined control, the driving performance of the vehicle greatly improves. The proposed method reduces the system complexity and improves the overall driving efficiency. Furthermore, due to the adoption of a look-up table, the proposed work can execute in a real-time platform without requiring high processing power and additional hardware units. It may significantly reduce the cost of the system. The present work is examined in a software simulation environment, and the results indicate that the performance of the proposed ED system is effective and reliable. Even though the study described above does not discuss the types of motor technology, the AC or BLDC motors can significantly improve the proposed DDEV. There could be several possibilities to enhance the proposed work further.

References

1. Ma T, Osama AM (2014) Optimal charging of plug-in electric vehicles for a car-park infrastructure. IEEE Trans Ind Appl 50(4):2323–2330
2. Barman P, Gogoi D, Paul S, Saikia N, Sharma S (2020) Steering independent electronic differential based traction control system for independent wheel drive neighborhood electric vehicle. J Electr Syst 16(4):498–514
3. Chen Y, Wang J (2012) Design and evaluation on electric differentials for overactuated electric ground vehicles with four independent in-wheel motors. IEEE Trans Veh Technol 61(4):1534–1542
4. Barman P, Azzopardi B (2021) Energy efficient torque allocation design emphasis on payload in a light-duty distributed drive electric vehicle. IEEE Access 9:118684–118695
5. Mutoh N, Kazama T, Takita K (2006) Driving characteristics of an electric vehicle system with independently driven front and rear wheels. IEEE Trans Ind Electron 53(3):803–813
6. Ding X, Wang Z, Zhang L (2020) Hybrid control-based acceleration slip regulation for four wheel-independently-actuated electric vehicles. IEEE Trans Transp Electrif
7. Ding X, Wang Z, Zhang L, Wang C (2020) Longitudinal vehicle speed estimation for four-wheel-independently-actuated electric vehicles based on multi-sensor fusion. IEEE Trans Veh Technol 69(11):12797–12806

8. Francisco PPJ, Cervantes I, Emadi A (2009) Stability of an electric differential for traction applications. IEEE Trans Veh Technol 58(7):3224–3233
9. Hartani K, Miloud Y, Miloudi A (2010) Electric vehicle stability with rear electronic differential traction. In: Proceedings of international symposium on environment friendly energies in electrical applicationas, pp 1–5
10. You S, Lee H, Lee D, Mok H, Lee Y, Han S (2011) Speed ratio control for electronic differentials. IET Electron Lett 47(16):933–934
11. Mutoh N, Takayanagi T (2011) Cornering performance of front and rear wheel independent drive type electric vehicles (FRID EVs) under severe road conditions. In: IEEE international conference on intelligent transportation systems , pp 101–106
12. Wang J, Alexander L, Rajamani R (2004) Friction estimation on highway vehicles using longitudinal measurements. J Dyn Syst Measur Control 126(2):265–275
13. Takaji U (2002) Estimation of tire-road friction by tire rotational vibration model. RD Rev Toyota CRDL 37(3):53–58
14. Ivanovic V, Deur J, Kostelac M et al (2006) Experimental identification of dynamic tire friction potential on ice surfaces. Veh Syst Dyn 44(1):93–103
15. Daya JF, Sanjeevikumar P, Blaabjerg F, Wheeler PW, Ojo JO (2015) Implementation of wavelet-based robust differential control for electric vehicle application. IEEE Trans Power Electron 30(12):6510–6513
16. Sharma S, Pegu R, Barman P (2015) Electronic differential for electric vehicle with single wheel reference. In: 2015 1st conference on power, dielectric and energy management at NERIST (ICPDEN), pp 1–5
17. Jazar Reza N (2014) Vehicle dynamics: theory and application, 2nd edn. Springer Science Business Media

Chapter 43
Analysis of Five-Phase Surface PMSM for Application in Electric Vehicles

Sangeeta Sahu, Byamakesh Nayak, and Rudra Narayan Dash

Abstract Polyphase permanent magnet synchronous motors (PMSMs) model outstanding performance in comparison to three-phase permanent magnet synchronous motors, and this is possible because of the recent development in power electronics. Five-phase permanent magnet synchronous motors have significant applications in aerospace and electric vehicles where highly accurate speed and torque control of the motor are a major requirement. This paper presents a detailed analysis of vector controlled five-phase permanent magnet synchronous motors in terms of efficiency, power, speed and torque ripple analysis along with the power factor analysis at different speeds. The average torque, torque ripple, speed, speed ripple and power factor for same are calculated and analyzed. The analysis has been carried out through MATLAB Simulink power graphical user interface.

Keywords Permanent magnet synchronous motor · Phase sequence · Torque ripple · Speed ripple · Hybrid electric vehicle

1 Introduction

The permanent magnet synchronous motors can be of two types: sinusoidally fed PMSM and rectangular-fed brushless DC PM motors [1]. Motors that are currently used in EVs are permanent magnet synchronous motor (PMSM), induction motor (IM) and switched reluctance motor (SRM). PMSM is the most preferred one due to the high torque and high-power density [2]. The stator winding of a PMSM motor is wound such that back emf is sinusoidal which results in a constant torque. It has 32 voltage vectors that have various effects on torque and current is a challenge in selecting the optimal switching state to give best performance. A direct torque control strategy reduces harmonics current and torque ripple [3]. The third-order harmonic component can be used for achieving optimal performance of torque per ampere. The direct torque model predictive control helps in optimizing the torque and reducing the

S. Sahu (✉) · B. Nayak · R. N. Dash
School of Electrical Engineering, KIIT University, Bhubaneswar, India

G. Panda et al. (eds.), *Sustainable Energy and Technological Advancements*,
Advances in Sustainability Science and Technology,
https://doi.org/10.1007/978-981-16-9033-4_43

higher order harmonics, minimizes the losses, thereby increasing the efficiency [4]. More advanced vector control techniques are applicable to sinusoidally fed PMSMs for better controllability over the complete speed range. A five-phase brushless PM motor has concentrated winding so that it produces trapezoidal back emf and overcomes the disadvantages of a PMBLDC motor [5, 6]. The conventional hysteresis current controller has been replaced by synchronous frame current controller. This controller not only possesses the advantage of linear controller but also facilitates the current regulation without a steady state error [7]. Harmonics are undesirable frequencies that are superimposed on the fundamental waveform resulting in a distorted waveform. The theory of the sequence components is usually considered to analyze the unbalanced system. This theory enables one to transform the five unbalanced phases into a set of three balanced phasors. Phase sequence is the order in which the voltage waveforms of a polyphase AC source reach their respective peaks. In a five-phase system According to the sequence component theory/mathematical manipulation, in a balanced system, the negative and zero-sequence components will not be present. However, in practice, a perfectly balanced system does not exist. In a 50 Hz five-phase power system, the phases A, B, C, D and E are 720 apart. The fifth harmonic that is of frequency of 250 Hz and its multiples are exactly in phase with each other.

A double-tuned filtering method which traps two harmonics with one filter has been introduced to mitigate zero-sequence harmonics in power distribution system [8]. It has proved to be a low-cost solution. The zero-sequence harmonic in a three-phase system can be attenuated by 80% using a shunt electromagnetic filter [9]. This is simple cheap and robust equipment. Axial flux PMSM has prevalence over other motors in terms of noise, vibration and efficiency. Torque ripple in these motors can be reduced by 86.71% by applying skew of up to 400 with an angle of 50 to the rotor magnets [10].

2 Phase Sequence in Five-Phase Power Supply

When a five-phase permanent magnet synchronous motor is fed from an inverter, the machine terminal voltage is non-sinusoidal and has half wave symmetry due to which only odd harmonics will be present. A sinusoidal waveform is a combination of fundamental and harmonics, and the waveform can be analyzed using Fourier transform. The harmonics in a three-phase supply can be positive sequence, negative sequence and zero sequence. Whereas, in a five-phase supply, the harmonics can be positive sequence, negative sequence, zero sequence along with two more sequences. The additional sequences can be referred to as double-positive sequence and double-negative sequence. The fundamental phase voltage components can be assumed as $V_{AN} = V_m \sin \omega t$, $V_{BN} = V_m \sin (\omega t - 2\pi/5)$, $V_{CN} = V_m \sin (\omega t - 4\pi/5)$, $V_{DN} = V_m \sin (\omega t - 6\pi/5)$ and $V_{EN} = V_m \sin (\omega t - 8\pi/5)$ having phase sequence of ABCDE. The corresponding 3rd and 7th harmonic voltages are:

$$
\begin{aligned}
V_{AN3} &= V_3 \sin 3\omega t \\
V_{BN3} &= V_3 \sin\left(3\omega t - \frac{6\pi}{5}\right) \\
V_{CN3} &= V_3 \sin\left(3\omega t - \frac{2\pi}{5}\right) \\
V_{DN3} &= V_3 \sin\left(3\omega t - \frac{8\pi}{5}\right) \\
V_{EN3} &= V_3 \sin\left(3\omega t - \frac{4\pi}{5}\right) \\
V_{AN7} &= V_7 \sin 7\omega t \\
V_{BN7} &= V_7 \sin\left(7\omega t - \frac{4\pi}{5}\right) \\
V_{CN3} &= V_7 \sin\left(7\omega t - \frac{8\pi}{5}\right) \\
V_{DN7} &= V_7 \sin\left(7\omega t - \frac{2\pi}{5}\right) \\
V_{EN3} &= V_7 \sin\left(7\omega t - \frac{6\pi}{5}\right)
\end{aligned}
$$

Table 1 shows that that the 11th harmonic has the fundamental phase sequence ABCDE that produces a magnetic field which rotates in the same direction as the fundamental. The 9th harmonic has a negative phase sequence AEDCB that produces a magnetic field which rotates in a direction opposite to the fundamental. Also, the 5th harmonic has zero phase sequence that does not produce any rotating magnetic field.

Table 1 Mathematical table with odd numbered harmonics

Fundamental	A 0°	B 72°	C 144°	D 216°	E 288°	A-B-C-D-E
3rd Harmonic	3 × 0° 0°	3 × 72° 216°	3 × 144° 72°	3 × 216° 288°	3 × 288° 144°	A-D-B-E-C
5th Harmonic	5 × 0° 0°	5 × 72° 360° = 0°	5 × 144° 720° = 0°	5 × 216° 1080° = 0°	5 × 288° 1440° = 0°	No rotation
7th Harmonic	7 × 0° 0°	7 × 72° 144°	7 × 144° 288°	7 × 216° 72°	7 × 288° 216°	A-C-E-B-D
9th Harmonic	9 × 0° 0°	9 × 72° 288°	9 × 144° 216°	9 × 216° 144°	9 × 288° 72°	A-E-D-C-B
11th Harmonic	11 × 0°	11 × 72° 72°	11 × 144° 144°	11 × 216° 216°	11 × 288° 288°	A-B-C-D-E

3 Mathematical Model of Five Phase PMSM

The mathematical model of a five phase PMSM is derived and the equations are developed in the rotating reference frame.

The stator voltage equation is:

$$V_s = R_s I_s + \frac{d\lambda_s}{dx} \tag{1}$$

where $R_{s,}$ I_s and λ_s are the stator resistance, current and flux linkages, respectively.

The air gap flux linkages are:

$$\lambda_s = \lambda_{ss} + \lambda_m \tag{2}$$

Substituting for the flux linking stator windings due to the currents in the stator windings in terms of the stator currents and stator winding inductances,

$$\lambda_s = L_{ss} i_s + \lambda_m \tag{3}$$

L_{ss} is the stator inductance matrix which is a combination of self and mutual inductances of the stator phases. λ_m is the established flux linkage matrix due to the permanent magnets viewed from the stator phase windings.

The stator current i_s is:

$$i_s = [i_{as} i_{bs} i_{cs} i_{ds} i_{es}]^t \tag{4}$$

$$V_{d1} = R_s i_{d1} + L_d \frac{di_{d1}}{dt} - \omega L_q i_{q1} \tag{5}$$

$$V_{q1} = R_s i_{q1} + L_q \frac{di_{q1}}{dt} + \omega L_d i_{d1} + \omega \lambda_m \tag{6}$$

$$V_{d2} = R_s i_{d2} + L_d \frac{di_{d2}}{dt} \tag{7}$$

$$V_{q2} = R_s i_{q2} + L_q \frac{di_{q2}}{dt} \tag{8}$$

For simplification, only the fundamental component of the magnet flux linkage is considered. Hence, the electromagnetic torque equation is given as:

$$T_e = \frac{5}{2} \frac{P}{2} \lambda_m i_{q1} \tag{9}$$

4 Simulation Result

The efficiency, DC link capacitor voltage, power, electromagnetic torque and power factor have been analyzed here. In each case, the speed changes after 3secs and the simulation is set to run for 6secs. Table 2 shows the PMSM model parameters, and Table 3 shows the PMSM model control parameters.

Figure 1 shows the efficiency curve at different speed. The efficiency is constant after around 1/10th of the rated speed. At speed of more than 1/10th of rated speed, the ripple of DC link voltage increases with larger slope, and it increases with lesser slope when speed is less than 1/10th of rated speed. This is illustrated in Fig. 2. From Fig. 3 that shows the torque ripple at different speed, it can be viewed that the oscillation is less at low speeds, hence jerking can be avoided to a large extent. Figure 4 shows the power consumption in a five-phase PMSM at different speed. Figures 5, 6 and 7 show the power factor of PMSM at 900, 600 and 150 rpm, respectively. The power factor can be controlled by controlling the direct axis current which is zero that is id = 0 here.

Table 2 PMSM model parameters

Parameter	Value	Unit
Output power	2	KW
Resistance	0.2468	ohm
Inductance	8.5e−3	Henry
Flux linkage	0.105	Wb
Pole pairs	4	
Inertia	0.089	Kg * m^2
Friction	0.005	Nm * s

Table 3 PMSM model control parameters

Parameter	Value	Unit
A. *Speed controller*		
Speed cut off frequency	250	Hz
Sampling time	80e−6	S
Output torque limit	−35 to 35	Nm
B. *Vector control*		
Current controller hysteresis band	250	A
Sampling time	20e−6	S
Maximum switching frequency	50e3	Hz

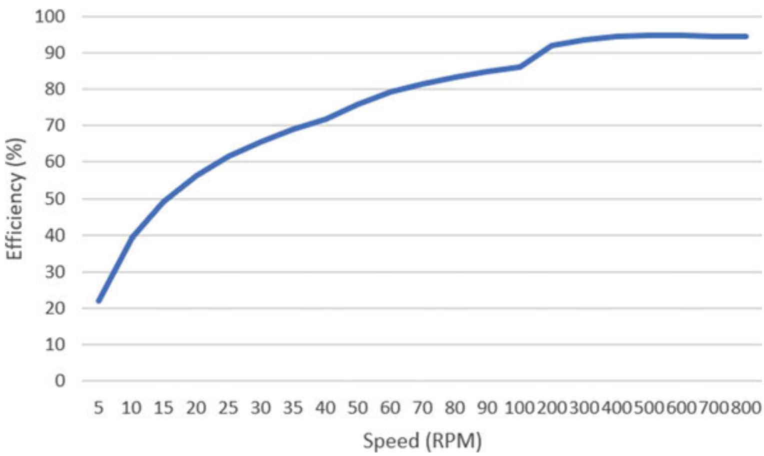

Fig. 1 Efficiency of 5ph PMSM at different speeds

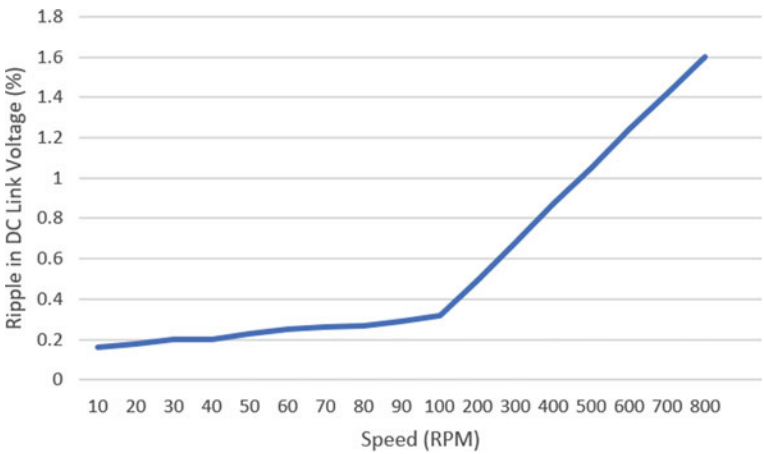

Fig. 2 Ripple in DC link voltage of 5ph PMSM at different speeds

5 Conclusion

Mathematical modeling, simulation and analysis of vector-controlled five-phase permanent magnet synchronous motor provides a clear picture of the its wide application in electric vehicles. PMSM has high efficiency and increased power density. By controlling the direct axis current that is forced to be zero here, the power factor of the motor can be controlled. At very low speed, the power factor of PMSM is leading, whereas it is lagging at high speed and rated speed.

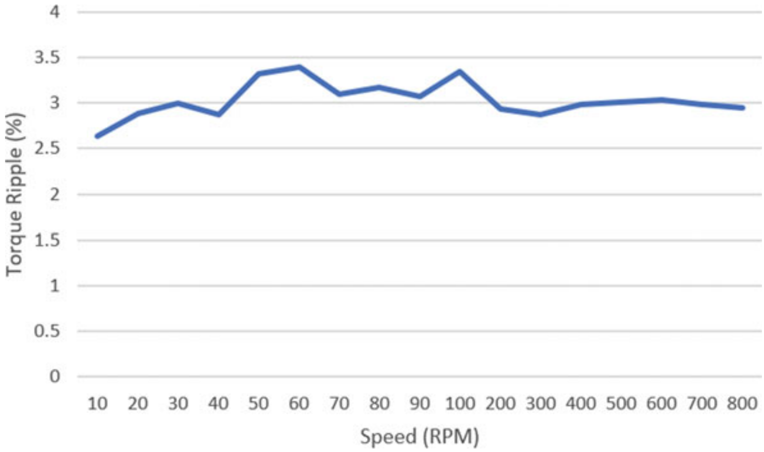

Fig. 3 Torque ripple of 5ph PMSM at different speeds

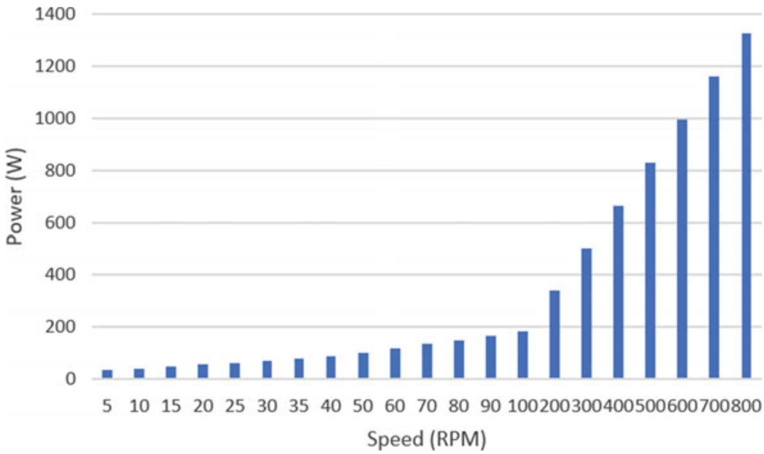

Fig. 4 Input power of 5ph PMSM at different speeds

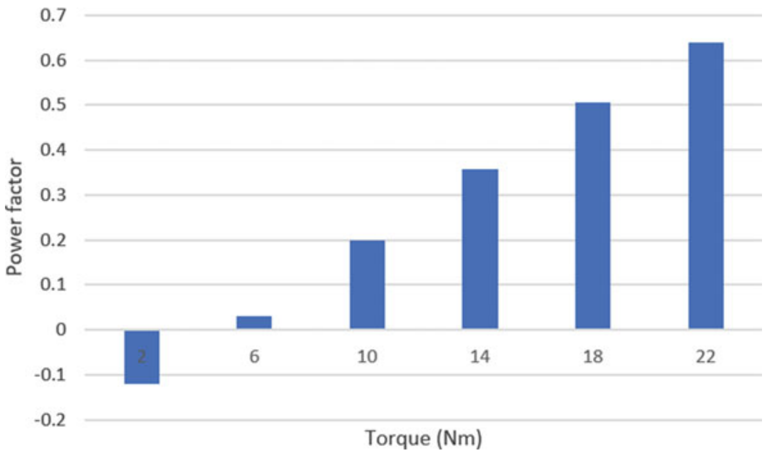

Fig. 5 Power factor of 5ph PMSM at 900 rpm

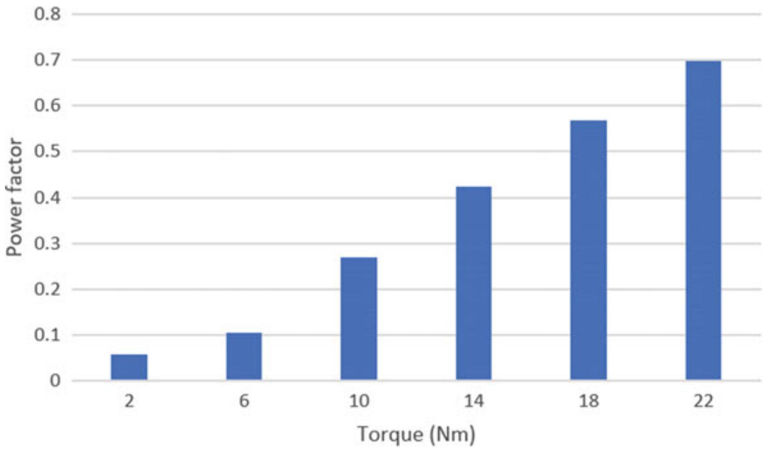

Fig. 6 Power factor of 5ph PMSM at 600 rpm

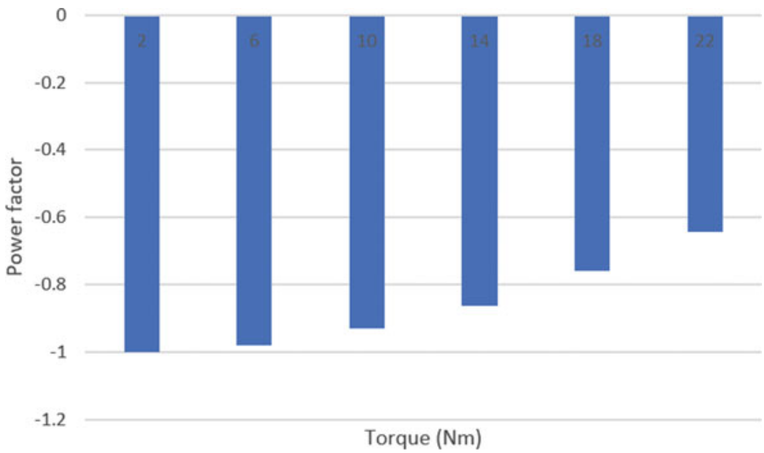

Fig. 7 Power factor of 5ph PMSM at 150 rpm

References

1. Pillay P, Krishnan R (1989) Modeling, simulation, and analysis of permanent-magnet motor drives. II. The brushless DC motor drive. IEEE Trans Indus Appl 25(2):274–279
2. Wang Z, Ching TW, Huang S, Wang H, Xu T (2021) Challenges faced by electric vehicle motors and their solutions. IEEE Access 9:5228–5249
3. Li G, Hu J, Li Y, Zhu J (2019) An improved model predictive direct torque control strategy for reducing harmonic currents and torque ripples of five-phase permanent magnet synchronous motors. IEEE Trans Indus Electron 66(8):5820–5829
4. Cao B, Grainger BM, Wang X, Zou Y, Reed GF, Mao Z (2021) Direct torque model predictive control of a five-phase permanent magnet synchronous motor. IEEE Trans Power Electron 36(2):2346–2360
5. Parsa L, Toliyat HA (2005) Five-phase permanent-magnet motor drives. IEEE Trans Ind Appl 41(1):30–37
6. Parsa L, Toliyat HA (2003) Multi-phase permanent magnet motor drives. In: Industry applications conference, vol 1
7. Ryu H, Kim J, Sul S (2004) Synchronous frame current control of multi-phase synchronous motor part I. In: Modeling and current control based on multiple d-q spaces concept under balanced condition. IEEE industry applications conference, vol 1
8. Bagheri P, Xu W (2014) A technique to mitigate zero-sequence harmonics in power distribution systems. IEEE Trans Power Deliv 29(1)
9. Belchior FN, Ferreira JFV, Oliveira JC, Apolonio R, Vasconcellos AB (2006) Three-phase electromagnetic filter for zero-sequence harmonics. IEEE Trans Magn 42(9):2201–2207
10. Polat M, Yildiz A, Akinci R (2021) Performance analysis and reduction of torque ripple of axial flux permanent magnet synchronous motor manufactured for electric vehicles. IEEE Trans Magnets 57(7)

Chapter 44
A Novel Application of BESO-Based Isolated Micro-grid with Electric Vehicle

Shubham, Sourabh Prakash Roy, R. K. Mehta, A. K. Singh, and O. P. Roy

Abstract This paper presents modelling of isolated micro-grid which includes solar tower, wind as renewable energy sources, flywheel and battery as the energy storages devices and plug-in electric vehicle. The wind turbine is then connected to aqua electrolyser and fuel cell in series configuration. A comparative study of isolated micro-grid thus formed is completed with bald eagle search optimization-based TIDF II and PIDF controller. Moreover, the robustness of the micro-grid is analysed using random load changing pattern. The entire simulation is implemented in the MATLAB software.

Keywords Isolated micro-grid · Solar tower · Wind turbine · Bald eagle search optimizer · TIDF–II & PIDF controller · Random load change

1 Introduction

Due to climate change and many other disadvantages of conventional energy sources (CES), the whole world is shifting towards renewable energy sources (RES). CES are responsible for increased CO_2 generation as evident from the Keeling curve [1]. RES offers many advantages, but due to its novelty and high cost, there is still apprehension in its widespread adoption. But gradually, more and more countries are adopting it and are modernizing their grid for adoption of RES [2].

RES are used verily for establishing micro-grid. They are the localized group of electrical energy sources and load operating synchronously with the grid as well as in islanding mode too. It helps to realize the true potential of RES.

Connecting micro-grid with electric vehicle plays a key role in system stability and is these days becoming prominent in the field of emerging technologies. Some authors like Khalil [3] described the micro-grid with photovoltaic and plug-in electric vehicle considering the time delay. Moreover, system is stabilized using linear matrix

Shubham (✉) · S. P. Roy · R. K. Mehta · A. K. Singh · O. P. Roy
Electrical Engineering Department, NERIST, Nirjuli, Arunachal Pradesh, India

G. Panda et al. (eds.), *Sustainable Energy and Technological Advancements*, Advances in Sustainability Science and Technology,
https://doi.org/10.1007/978-981-16-9033-4_44

inequalities (LMI) function. Mi proposes novel frequency control method for PV-diesel isolated hybrid system. Photovoltaic is modelled in considering maximum power point tracking (MPPT), and system output error is reduced using sliding mode control (SMC) [4].

Mahdi presents to model the micro-grid, and the system stability is performed by fuzzy logic-based PI controller [5]. Khooban in his papers discussed about load frequency control (LFC) of micro-grid as well as vehicle-to-grid (V2G) concept. The performance of the proposed system is studied with help of adaptive PID fuzzy-based control. The system is simulated with help of real-time sun radiation and wind velocity information [6–8]. The contributions of this paper are as follows:

(a) Modelling of solar tower, wind generating unit connected with aqua electrolyser, fuel cell and energy storage devices along with load to form isolated micro-grid.
(b) Inclusion of electric vehicle in the micro-grid, thus incorporation of vehicle-to-grid concept in micro-grid LFC.
(c) Designing of tilt integral derivative filter-double integral (TIDF II) and proportional integral derivative filter (PIDF) controller. Moreover, tuning of TIDF II is utilized using bald eagle search optimisation (BESO) algorithm.
(d) Sensitivity analysis of the isolated micro-grid to check the robust performance of the system.

The basic layout of the paper is as follows. In Sect. 2, the component-wise modelling of hybrid renewable energy system is explained. The proposed study model and controller design are described in Sects. 3 and 4, respectively. Moving on further, Sect. 5 gives a brief overview of the BESO algorithm. The result and discussion, sensitivity analysis are explained in Sects. 6 and 7, respectively. Lastly, the conclusion is expressed in Sect. 8.

2 Component Modelling

The major component of the proposed micro-grid system is solar tower, wind generating unit, aqua electrolyser, fuel cell, diesel generator, flywheel energy storage, battery energy storage and electric vehicle. Let us briefly describe about each component and their modelling in the following subsections.

2.1 Solar Tower

Solar tower (ST) is the centralized receiver which encounters with all the heat and light energy bounced back by the heliostat. Heliostat is an open field with a plenty of mirrors which are so arranged to target the sunlight to the ST. So, ST plant consists up of refocus, receiver, speed governor and turbine to obtain the electrical energy from the sunlight. The transfer function of ST is in the form of Eq. (1), where T_{RE} = 1.33 s, T_{RC} = 4 s, T_G = 0.08 s and T_T = 1 s are the time constant for refocus, receiver, governor and turbine, respectively.

$$\mathrm{Tf}_{\mathrm{ST}} = \left(\frac{1}{1 + sT_{\mathrm{RE}}}\right)\left(\frac{1}{1 + sT_{\mathrm{RC}}}\right)\left(\frac{1}{1 + sT_{\mathrm{G}}}\right)\left(\frac{1}{1 + sT_{\mathrm{T}}}\right) \tag{1}$$

2.2 Wind Generating Unit (WGU)

The mechanical output generated from wind speed is transformed into electrical energy with the help of WGU. Consequently, the wind velocity (W_V) is the deciding factor in the amount of power generated from WGU. W_V can be interpreted as summation of base speed, gusty speed, ramp speed and noisy speed of wind. These are the four main elements of wind speed. The mechanical power output from WGU [9] can be described as $P_{\mathrm{wind}} = 0.5C_pD_aA_r\,(W_V)^3$, where C_p is conversion coefficient of WGU is the function of blade tip to wind speed ratio λ and pitch angle β, D_a is air density as 1.25 kg per m^3, A_r is blade swept area taken to be 1735 m^2, and V_S is wind speed.

The linear transfer function of WGU is interpreted in below in Eq. (2), where T_w is the time constant of wind generator turbine and whose value equal to 1.5 s.

$$\mathrm{Tf}_{\mathrm{WGU}} = \left(\frac{1}{1 + sT_{\mathrm{w}}}\right) \tag{2}$$

2.3 Aqua Electrolyser (AE)

It uses electro-chemical reaction as its working principle. The amount of electrical energy generated depends upon the changing rate of electrons at electrodes. The linearized transfer function of AE is given by Eq. (3), where K_{AE} is AE gain whose value is equal to 0.002, and T_{AE} is time constant of FC which is equal to 0.5 s.

$$\mathrm{Tf}_{\mathrm{AE}} = \left(\frac{K_{\mathrm{AE}}}{1 + sT_{\mathrm{AE}}}\right) \tag{3}$$

2.4 Fuel Cell (FC)

It uses the chemical energy and converts the same into electrical energy. It is attached with AE to make use of generated hydrogen and oxygen molecule to give rise to electricity. The linearized transfer function for the fuel cell is represented in Eq. (4), where K_{FC} is FC gain whose value is equal to 0.001, and T_{FC} is time constant of FC which is equal to 4 s.

$$\mathrm{Tf}_{\mathrm{FC}} = \left(\frac{K_{\mathrm{FC}}}{1 + sT_{\mathrm{FC}}}\right) \tag{4}$$

2.5 Diesel Generator (DG)

It is a diesel-based generating turbine to produce electrical in micro-grid whenever there is scarcity of energy supply by the renewable energy plant associated with the system. In transfer function format, DG is represented as Eq. (5), where K_{DG} is DG gain whose value is equal to 0.04, and T_{DG} is time constant of DG which is equal to 2 s.

$$\mathrm{Tf}_{\mathrm{DG}} = \left(\frac{K_{\mathrm{DG}}}{1 + sT_{\mathrm{DG}}}\right) \tag{5}$$

2.6 Flywheel Energy Storage

FES is the category of energy storage device. It uses rotational speed to produce electricity whenever required within micro-grid for small interval. A new system of FES is considered, which includes flywheel converter, system command measurement and delay measurement of the storage device. The transfer function for FES is depicted by Eq. (6)

$$\mathrm{Tf}_{\mathrm{FESS}} = \left(\frac{1}{1 + sT_{\mathrm{C}}}\right)\left(\frac{1}{1 + sT_{\mathrm{CM}}}\right)\left(\frac{1}{1 + sT_{\mathrm{DM}}}\right) \tag{6}$$

where T_{C}, T_{CM} and T_{DM} are time constant of flywheel converter, command measurement and delay measurement whose values are 0.1, 0.01 and 0.1 s, respectively [10].

2.7 Battery Energy Storage

BES is a category of electrical energy storing device. For this paper, a complicated version of BES is taken which incorporates converter, system command measurement and delay measurement of BES. The transfer function of BES is in the form of Eq. (7)

$$\mathrm{Tf}_{\mathrm{BESS}} = \left(\frac{1}{1 + sT_{\mathrm{C}}}\right)\left(\frac{1}{1 + sT_{\mathrm{CM}}}\right)\left(\frac{1}{1 + sT_{\mathrm{DM}}}\right) \tag{7}$$

where T_{C}, T_{CM} and T_{DM} are time constant of battery converter, command measurement and delay measurement whose values are 0.1, 0.01 and 0.1 s, respectively [10].

2.8 Electric Vehicle

In this paper, we are utilizing aggregated EV model which consists up three transition and three stable conditions. The transition signals are plug-out, plug-in and control-in, and the stable conditions are driving, charging and controllable condition.

An EV enters into driving condition after it is plugged out for the trip (i.e. known as plug-out signal). After the trip, it enters the charging condition to charge its battery (i.e. plug-in signal). It enters into controllable condition from charging condition when the state of charge is charged up to 85% (i.e. control-in signal).

The EVs participating in the LFC repeat this cyclic condition many times in a day. Also, the power sharing between EV and central load dispatch centre is bidirectional with the help of load dispatch centre. The major governing equation for the total stored energy of aggregated EV model is given by

$$\begin{aligned} E_{\mathrm{control}}(t) = {} & 0.85 \times N_{\mathrm{initial}} \times C_{\mathrm{ev}}(t) + 0.85 \\ & \times N_{\mathrm{controlin}}(t) \times C_{\mathrm{ev}}(t) - \int R_{\mathrm{plug\text{-}out}}(t) \\ & \times (E_{\mathrm{control}}(t)/N_{\mathrm{control}}(t))\,\mathrm{d}t - \int P_{\mathrm{LFC}}(t)\mathrm{d}t \end{aligned} \tag{8}$$

where $0.85 \times N_{\mathrm{initial}} \times C_{\mathrm{ev}}(t)$ is the primary EV energy,

$0.85 \times \mathrm{N}_{\mathrm{controlin}}(t) \times \mathrm{C}_{\mathrm{ev}}(t)$ is the Curtailment in Energy When EV Changes Its State from Controllable to Driving Condition,

$\int R_{\mathrm{plug\text{-}out}}(t) \times (E_{\mathrm{control}}(t)/N_{\mathrm{control}}(t))\,\mathrm{d}t$ is the enhancement in energy when EV changes its condition from charging to controllable,

$\int P_{\mathrm{LFC}}(t)\mathrm{d}t$ is energy corresponding to the LFC signal.

Also, $C_{\mathrm{ev}}(t)$ = total inverter capacity of the controllable EVs, $N_{\mathrm{control}}(t)$ = number of the controllable EVs, N_{initial} = initial number of the controllable EVs, $N_{\mathrm{controlin}}(t)$

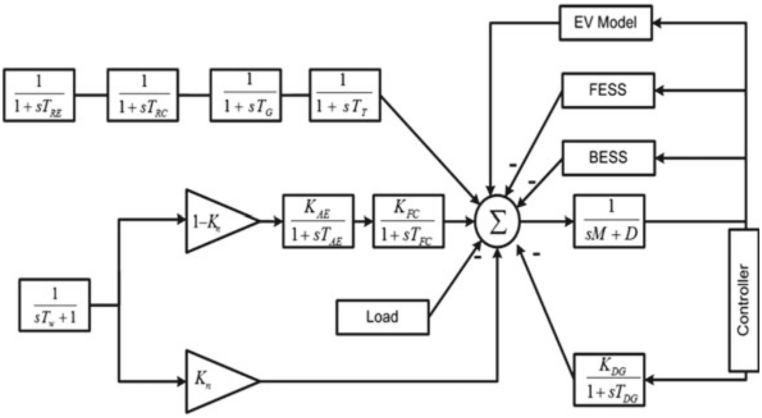

Fig.1 Block diagram for the proposed model

= how often the EVs are controlled in, $N_{\text{plug-out}}(t)$ = how often the EVs are plugged out, $R_{\text{plug-out}}(t)$ = time differentiation of $N_{\text{plug-out}}(t)$ indicating number of the plug-out EVs per unit time [11, 12].

3 Proposed Descriptive Configuration of Micro-grid

As per Fig. 1, it consists up solar tower and wind generator as the power generating units. The power generated from solar tower is fluctuating, and its maximum value is up to 0.5 pu. The power generated from the WGU is 0.06 pu shown in Fig. 5. It acts as the base power for the micro-grid which is always present for the system load. The part of WGU power is feeding the load via AE and FC, whereas remaining part is directly connected to micro-grid load. The DG, FES, BES and EV are connected in the negative feedback path, and they act as the backup supply for the load. The power response of AE, FC, FESS, DG and EV is shown in Figs. 5, 6, 7, respectively.

The power balance equation for the considered isolated system is given by

$$\Delta P_{\text{gen}} = \Delta P_{\text{ST}} + \Delta P_{\text{WGU}} + \Delta P_{\text{DG}} \pm \Delta P_{\text{FESS}} \pm \Delta P_{\text{BESS}} + \Delta P_{\text{EV}} - \Delta P_{\text{load}} \quad (9)$$

4 Controller Design

In this paper, we have used two types of control strategies, namely TIDF II and PIDF for our study purpose. TIDF II also known as tilt integral derivative with filter and double integral is a fractional order controller which improves the system response. Whereas, PIDF is a proportional integral derivative with filter control. The total numbers of variables are six in TIDF II, whereas there are four variables in PIDF [13].

Mathematically, TIDF II can be expressed as $\frac{K_{\mathrm{T}}}{s^{\frac{1}{n}}} + \frac{K_{\mathrm{I}}}{s} + sK_{\mathrm{D}}\frac{N_{\mathrm{c}}}{s+N_{\mathrm{c}}} + \frac{K_{\mathrm{I1}}}{s^2}$, and PIDF can be expressed as $K_{\mathrm{P}} + \frac{K_{\mathrm{I}}}{s} + sK_{\mathrm{D}}\frac{N_{\mathrm{c}}}{s+N_{\mathrm{c}}}$. The pictorial representation of the TIDF II and PIDF is shown in Figs. 2 and 3, and their gain values are shown in Table 1.

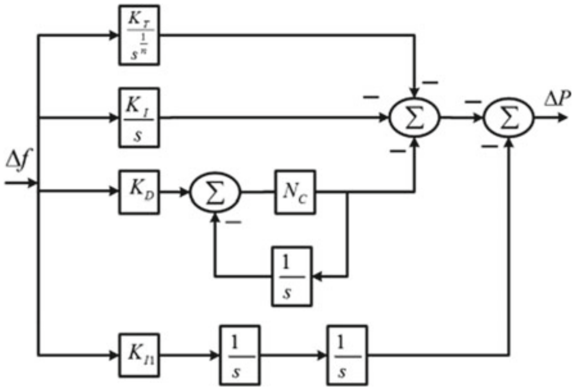

Fig. 2 TIDF II controller representation

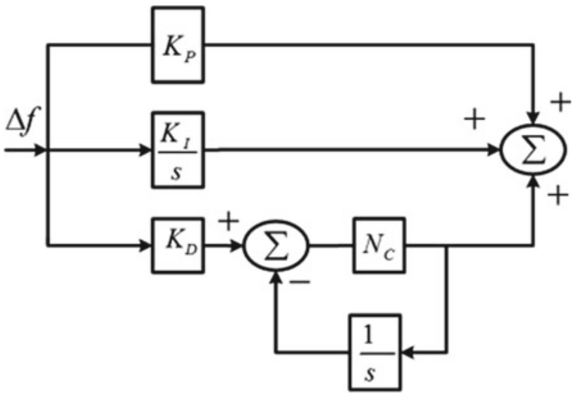

Fig. 3 PIDF controller representation

Table 1 Value of controller parameter

S. no.	Controller		Parameters values			
1	PIDF	K_{P}	K_{I}	K_{D}	N_{c}	
		30.617	16.266	−20.076	1.249	
2	TIDF II	$K_{\mathrm{T,\,n}}$	K_{I}	K_{D}	K_{I1}	N_{c}
		99.728, 0.006	99.998	99.999	0	99.831

5 Algorithm (Bald Eagle Search Optimization)

Alsattar et al. [14] in 2019 proposed the bald eagle search optimization (BESO). It is state-of-the-art metaheuristic algorithm that copies hunting plan of bald eagle. Bald eagle is native of North America and is a variety of raptors. They primarily hunt fishes. Hunting strategy is divided into three parts.

(a) In the first part called 'selecting space', eagle selects the space where preys are located. Mathematically, it can be expressed as

$$A_{\text{new}(i)} = A_{\text{best}} + \alpha * \text{rand}(A_{\text{mean}} - A_i) \tag{10}$$

where α is between 1.5 and 2 and determines the position changes.

(b) 'Searching the space' is the second part. In this, eagle goes inside the selected space for hunting.

$$A_{\text{new}(i)} = A_i + y(i) * (A_i - A_{i+1}) + x(i) * (A_i - A_{\text{mean}}) \tag{11}$$

$$x(i) = \frac{r(i) * \sin(\theta(i))}{\max(|r(i) * \sin(\theta(i))|)},\ y(i) = \frac{r(i) * \cos(\theta(i))}{\max(|r(i) * \cos(\theta(i))|)} \tag{12}$$

$$\theta(i) = a * \pi * \text{rand}, \quad r(i) = \theta(i) + R * \text{rand} \tag{13}$$

where $a \in [5, 10]$ and determines the corner between search points.

$R \in [0.5, 2]$ and determines the search cycles.

(c) 'Swooping' is the third part. Now, eagle selects the prey and determines the best point for hunting the prey.

$$A_{\text{new}(i)} = \text{rand} * A_{\text{best}} + x_1(i) * (A_i - c_1 * A_{\text{mean}}) + y_1(i) * (A_i - c_2 * A_{\text{best}}) \tag{14}$$

$$x1(i) = \frac{r(i) * \sinh(\theta(i))}{\max(|r(i) * \sinh(\theta(i))|)},\quad y1(i) = \frac{r(i) * \cosh(\theta(i))}{\max(|r(i) * \cosh(\theta(i))|)} \tag{15}$$

$$\theta(i) = a * \pi * \text{rand},\ r(i) = \theta(i) \tag{16}$$

where $c_1, c_2 \in [1, 2]$ (Fig. 4).

```
Input: Initialize Point A_i;
       Evaluate the fitness values of initial point f(A_i)
Output: A_best
while N < Max. no. of iterations do
    % Select Space;
    for each point i do
        A_new = A_best + α * rand(A_mean - A_i);
        if f(A_new) is less than f(A_i) then
        |  A_i = A_new
        end
        if f(A_new) is less than f(A_best) then
        |  A_best = A_new
        end
    end
    % Search in Space;
    for each point i do
        A_new = A_i + y(i) * (A_i - A_{i+1}) + x(i) * (A_i - A_mean);
        if f(A_new) is less than f(A_i) then
        |  A_i = A_new
        end
        if f(A_new) is less than f(A_best) then
        |  A_best = A_new
        end
    end
    % Swoop;
    for each point i do
        A_new = rand * A_best + x1(i) * (A_i - c1 * A_mean) + y1(i) * (A_i - c2 *
         A_best);
        if f(A_new) is less than f(A_i) then
        |  A_i = A_new
        end
        if f(A_new) is less than f(A_best) then
        |  A_best = A_new
        end
    end
    Update N = N+1 ;
end
```

Fig. 4 Pseudocode for BESO

6 Result and Discussions

The proposed isolated micro-grid system is depicted in Fig. 1. The designed system is executed in MATLAB software and simulated for 200 s. The limits and values of the BESO tuned controller are indicated in Table 1. The input to the solar tower and wind energy plant is shown in Fig. 5. The power reciprocated from AE, FC, FESS

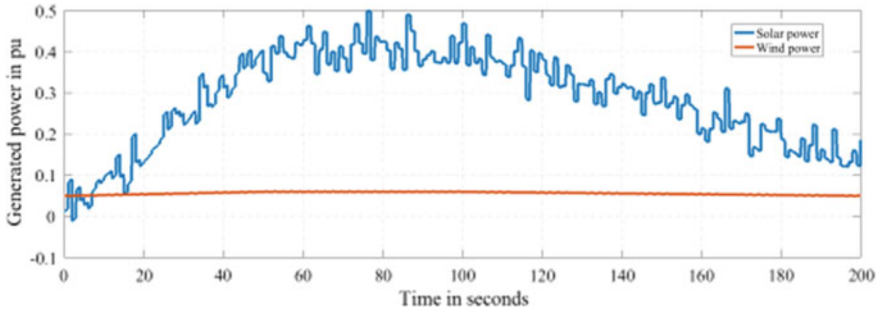

Fig. 5 Power generated from generating unit

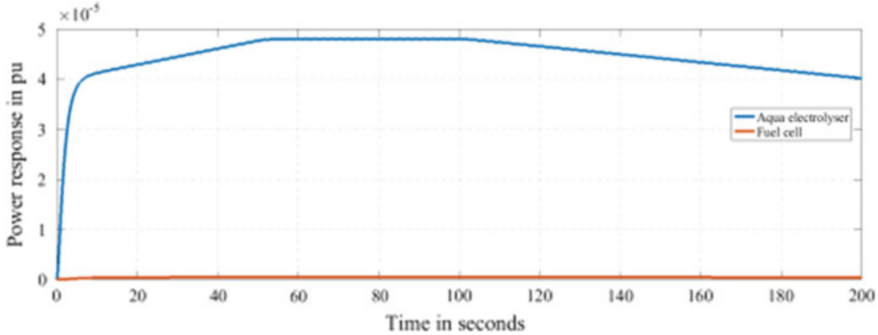

Fig. 6 Power response of AE and FC

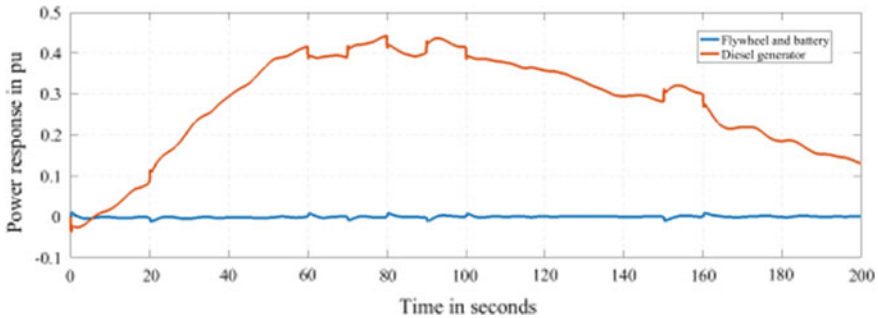

Fig. 7 Power response of flywheel and DG

and DG is represented in Figs. 6 and 7, respectively. The power response of EV is shown in Fig. 8. Lastly, Fig. 9 shows the frequency response indicating undershoot, overshoot, steady state error and settling time for the simulation interval of 200 s. The maximum overshoot for PIDF is 0.05 pu, whereas for BESO-based TIDF II is 0.01 pu. So, there is reduction of 80% in the first frequency overshoot for TIDF II

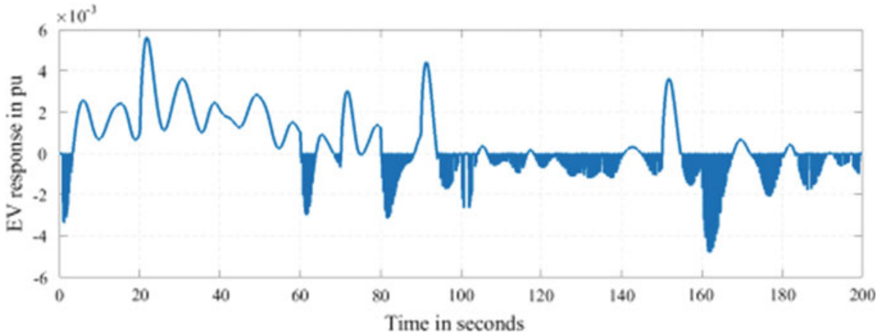

Fig. 8 Power response of EV

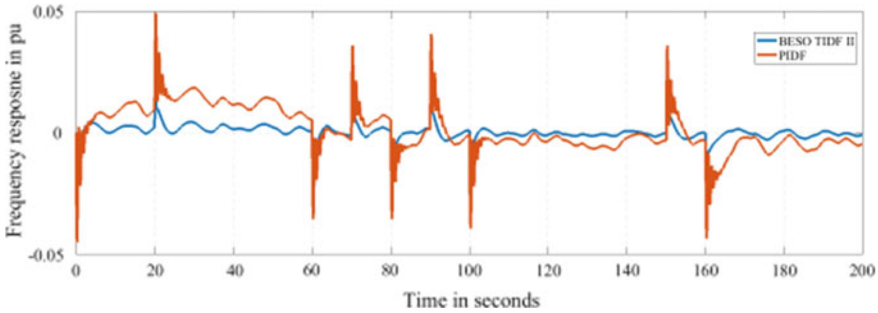

Fig. 9 Frequency response of the microgrid with BESO based TIDF II and PIDF

controller. Also, there is steady state error of $\pm$ 0.01 in case of PIDF and no steady state error for TIDF II. Hence, BESO-based TIDF II gives an improved performance compared to BESO tuned PIDF on the basis of lesser frequency deviation, zero steady state error and insignificant settling time.

7 Sensitivity Analysis

The sensitivity analysis of the proposed isolated micro-grid is considered using the random load pattern as shown in Fig. 10. The random load demand is of 5% which is compared with the step load demand of 7% which is at the interval of 20 s. The system is executed with BESO-based TIDF II controller. After the simulation period is over and from the frequency response indicated in Fig. 11, we monitor that the frequency change is slighter for random load demand in case of TIDF II. So, we can pronounce that TIDF II is having a robust controller nature.

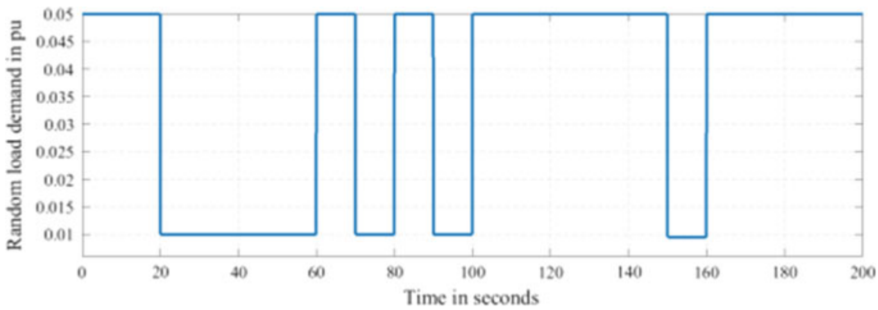

Fig. 10 Random changing load for the micro-grid

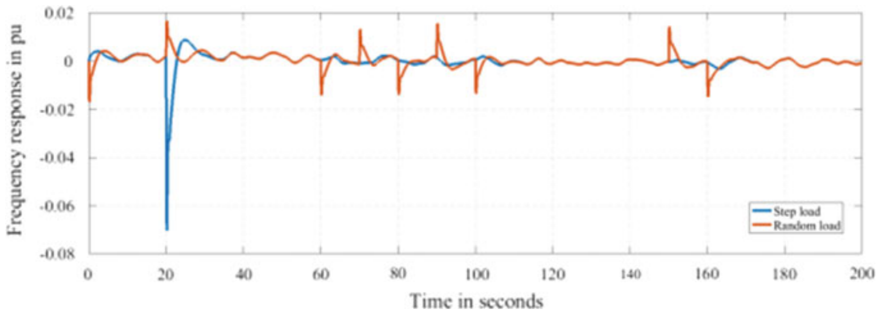

Fig. 11 Frequency response of the microgrid with BESO based TIDF II for step and random load

8 Conclusion

This paper provides maiden application of BESO-based TIDF II controller in isolated micro-grid in the presence of plug-in electric vehicle. The proposed designed TIDF II controller gives improved performance over conventional PIDF controller on basis of lesser frequency variation, zero steady state error. Thus, both transient as well as steady state error of the system are improved greatly with the utilization of TIDF II. The work can be further on extend to multi-area system with cascaded or multi-stage controller.

References

1. Da Rosa AV, Ordóñez JC (2021) Fundamentals of renewable energy processes. Academic Press
2. Probst O, Castellanos S, Palacios R (2020) Transforming the grid towards fully renewable energy. Energy Engineering Series, Institution of Engineering & Technology ISBN: 9781839530210
3. Khalil A, Rajab Z, Alfergani A, Mohamed O (2017) The impact of the time delay on the load frequency control system in microgrid with plug-in-electric vehicles. Sustain Cities Soc 35:365–377

4. Mi Y, Fu Y, Zhao J, Wang P (2013) The novel frequency control method for pv-diesel hybrid system. In: 2013 10th IEEE international conference on control and automation (ICCA), pp 180–183. IEEE
5. Mahdi MM, Ahmad AZ (2017) Load frequency control in microgrid using fuzzy logic table control. In: 2017 11th IEEE international conference on compatibility, power electronics and power engineering (CPE-POWERENG), pp 318–323, IEEE
6. Khooban M-H, Niknam T, Shasadeghi M, Dragicevic T, Blaabjerg F (2018) Load frequency control in microgrids based on a stochastic noninteger controller. IEEE Trans Sustain Energy 9(2):853–861
7. Khooban M-H (2018) Secondary load frequency control of time-delay stand-alone microgrids with electric vehicles. IEEE Trans Industr Electron 65(9):7416–7422
8. Khooban M-H, Dragicevic T, Blaabjerg F, Delimar M (2018) Shipboard microgrids a novel approach to load frequency control. IEEE Trans Sustain Energy 9(2):843–852
9. Lee D-J, Wang L (2008) Small-signal stability analysis of an autonomous hybrid renewable energy power generation/energy storage system part I: time-domain simulations. IEEE Trans Energy Convers 23(1):311–320
10. Babaei M, Abazari A, Muyeen SM (2020) Coordination between demand response programming and learning-based FOPID controller for alleviation of frequency excursion of hybrid microgrid. Energies 13(2):442
11. Khezri R, et al (2018) Coordination of heat pumps, electric vehicles and AGC for efficient LFC in a smart hybrid power system via SCA-based optimized FOPID controllers. Energies 11(2):420
12. Kumari S, Shankar G (2019) Maiden application of cascade tilt-integral–tilt-derivative controller for performance analysis of load frequency control of interconnected multi-source power system. IET Gener Transm Distrib 13(23):5326–5338
13. Shubham SPR, Mehta RK (2020) Reducing frequency deviation of two area system using full state feedback controller design. In: Proceedings of international conference on data science and applications (ICDSA), p 299
14. Alsattar HA, Zaidan AA, Zaidan BB (2020) Novel meta-heuristic bald eagle search optimisation algorithm. Artif Intell Rev 53(3):2237–2264

Chapter 45
Frequency Control of SPV/Wind/Biogas/Biodiesel-Based Microgrid Using Fuzzy-Aided PID Controllers

Arabinda Mahakur and Debidasi Mohanty

Abstract This paper suggests a novel control strategy for load frequency control (LFC) of an isolated microgrid comprising solar photovoltaic (SPV), wind turbine generator (WTG), biogas turbine generator (BGTG), biodiesel engine generator (BDEG) and battery energy storage system (BESS). Two different types of controllers, i.e., proportional integral derivative (PID) and fuzzy-aided PID (FPID) controllers, are used separately for LFC action. A decentralized control system is proposed for the system. Controller parameters are optimized by salp swarm algorithm (SSA) technique. The system is simulated by considering different operating conditions, and for each condition, frequency deviation characteristics are obtained. Superiority of FPID controller over PID controller is validated for all the conditions.

Keywords Microgrid · Load frequency control · Fuzzy-aided PID controller · Salp swarm algorithm

1 Introduction

Modern power system is continuously failing to meet the generation and load demand during load perturbation in several times. One of the main reasons for this issue is the limitation of fossil fuels. Using renewable energy resources (RESs) instead of conventional sources can solve the above issue [1]. RESs have many advantages, but at the same time, it creates some challenges for the power system. The major challenge caused by RESs is the system stability during both connected and disconnected modes. To overcome the above challenge, the concept of microgrid is introduced in modern power system engineering [2, 3].

A. Mahakur (✉) · D. Mohanty
Department of Electrical Engineering, VSSUT, Burla, Sambalpur 768018, India

G. Panda et al. (eds.), *Sustainable Energy and Technological Advancements*,
Advances in Sustainability Science and Technology,
https://doi.org/10.1007/978-981-16-9033-4_45

An isolated microgrid is an independent power system that used to generate power to supply the local loads. As the microgrid is isolated from any central grid so it is free from all the common faults associated with the large central grid. Isolated microgrid is transmission cost effective as it is load centric in nature. Due to its small size, maintenance and operation are quite easy and cost effective. When the remote areas are inaccessible to grid supply, isolated microgrid can power up these areas much easily. But a microgrid can have a lot of issues regarding power system operation and control, while it is operating in isolated mode. Power quality and stability issues arise in isolated microgrid due to the stochastic nature of renewable sources. Energy storage system (ESS) is used to enhance the system dynamics performance and stability [4]. The mismatch between generation and load is suppressed by the use of ESS due to its energy storing capability. Overall, ESS helps in reliable operation of the power system.

One of the major challenges for the isolated power system is to maintain its stability. It arises due to the power imbalance between the generation and load. Frequency deviation is one of the reasons which may affect the stability of the system [5]. Active power discrepancy between the generation and demand results in frequency fluctuation. This problem can be solved by using load frequency controller (LFC) [6]. LFC stabilizes the system by minimizing frequency fluctuations. Usually, PID controller is preferred for LFC due to its ease employment, low cost and least computational time approach. But PID controller fails to control the frequency when the system contains nonlinear elements [7]. Classical controllers are less efficient toward LFC during heavy load perturbations. Recently, fuzzy-aided PID (FPID) controllers are being used in a wide range. FPID is found to be more efficient toward complex or higher order nonlinear system as compared to the conventional PID controller. It is also verified that fuzzy-based controllers are more robust toward dynamical changes in the system than the conventional controller [8]. Designing of FPID controller basically depends upon the designer's knowledge and experience. [9, 10] explains about the performance of fuzzy-aided PI and fuzzy-aided PID controller.

The objective of this paper is to control the frequency of an isolated microgrid using a fuzzy-aided PID (FPID) controller. A popular optimization technique termed as salp swarm algorithm (SSA) has been applied in this paper for tuning of PID and FPID controllers for frequency control of proposed isolated system [11, 12].

2 Microgrid Modeling

A basic model of a microgrid consisting of SPV, WTG, BGTG, BDEG and BESS is illustrated in Fig. 1. This model can be treated as a real-time power system. To control the output of BGTG, BDEG and BESS, three FPID controllers are utilized in this system. Each component of this microgrid is represented by a generalized transfer function using different parameters. Table 1 represents all the parameters and their respective values.

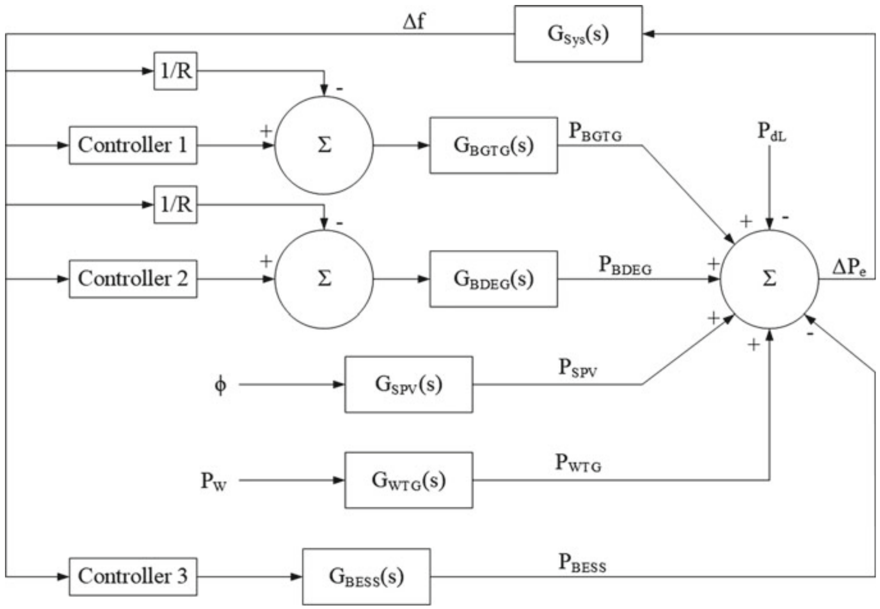

Fig. 1 Microgrid model

Table 1 Different parameters and their values

Parameter	Value
SPV unit	$K_{\mathrm{SPV}} = 1$, $T_{\mathrm{SPV}} = 1.8$ s
WTG unit	$K_{\mathrm{WTG}} = 1$, $T_{\mathrm{WTG}} = 0.3$
BGTG unit	$X_{\mathrm{C}} = 0.6$, $Y_{\mathrm{C}} = 1$, $b_{\mathrm{B}} = 0.05$, $T_{\mathrm{CR}} = 0.01$ s, $T_{\mathrm{BG}} = 0.23$ s, $K_{\mathrm{BT}} = 1$, $T_{\mathrm{BT}} = 0.2$ s
BDEG unit	$K_{\mathrm{VA}} = 1$, $T_{\mathrm{VA}} = 0.05$ s, $K_{\mathrm{BE}} = 1$, $T_{\mathrm{BE}} = 0.5$ s
BESS unit	$K_{\mathrm{BESS}} = 1$, $T_{\mathrm{BESS}} = 0.1$ s
droop constant	$R = 2.4$
damping constant	$D = 0.012$
equivalent inertia constant	$M_{\mathrm{eq}} = 0.2$ s

A. **Solar Photovoltaic**

The SPV unit converts solar energy into electrical energy. It takes solar radiation as its input and gives desired current and voltage as its output. The transfer function of SPV unit is defined as

$$G_{\mathrm{SPV}}(s) = \frac{P_{\mathrm{SPV}}}{\varphi} = \frac{K_{\mathrm{SPV}}}{1 + sT_{\mathrm{SPV}}} \tag{1}$$

where P_{SPV} is the SPV output power in pu, and ϕ is the input solar radiation in pu.

B. Wind Turbine Generator

WTG converts wind energy into electrical energy. A generalized transfer function model of a WTG is represented as

$$G_{\mathrm{WTG}}(s) = \frac{P_{\mathrm{WTG}}}{P_{\mathrm{W}}} = \frac{K_{\mathrm{WTG}}}{1 + sT_{\mathrm{WTG}}} \tag{2}$$

where P_{WTG} is the WTG output power in pu, and P_{W} is the wind turbine mechanical power input in pu.

C. Biogas Turbine Generator

BGTG uses biogas as a fuel input for combustion engine, which develop mechanical power to drive the generator turbine and produce electricity. It is used to supply power during the unusual conditions. The transfer function of BGTG is defined as

$$G_{\mathrm{BGTG}}(s) = \left(\frac{1 + sX_{\mathrm{C}}}{(1 + sY_{\mathrm{C}})(1 + sb_{\mathrm{B}})}\right)\left(\frac{1 + sT_{\mathrm{CR}}}{1 + sT_{\mathrm{BG}}}\right)\frac{K_{\mathrm{WTG}}}{1 + sT_{\mathrm{WTG}}} \tag{3}$$

D. Biodiesel Engine Generator

BDEG is also used to supply power to the system to improve power system stability and maintain system reliability and security. Unit setup is similar to BGTG, but biodiesel is used here instead of biogas for operation of the combustion engine. The transfer function of BDEG is expressed as

$$G_{\mathrm{BDEG}}(s) = \left(\frac{K_{\mathrm{VA}}}{1 + sT_{\mathrm{VA}}}\right)\frac{K_{\mathrm{BE}}}{1 + sT_{\mathrm{BE}}} \tag{4}$$

E. Battery Energy Storage System

BESS stores the surplus energy in the form of DC during light load hour and supplies it to the system during peak load hour by using necessary power conversion system. Prime purpose of using BESS is to maintain continuity of power flow in the system. The transfer function of BESS is defined as

$$G_{\mathrm{BESS}}(s) = \frac{K_{\mathrm{BESS}}}{1 + sT_{\mathrm{BESS}}} \tag{5}$$

F. Power System Model

The equivalent generator dynamics transfer function representation of the overall system is given by

$$G_{\mathrm{sys}}(s) = \frac{\Delta f}{\Delta P_{\mathrm{e}}} = \frac{1}{M_{\mathrm{eq}}s + D} \tag{6}$$

where Δf is the frequency deviation of the system in Hz, and ΔP_e is the net power deviations of the microgrid in pu.

3 Controller Design

PID controller is employed with fuzzy logic to improve the performance of a conventional controller in case of a complex, higher order nonlinear system. Four main components of a fuzzy controller are: (1) the fuzzification interface, (2) the rule base, (3) the decision-making logic and (4) the defuzzification interface. The design of fuzzy control depends on the input/output scaling factors and tuning of controller parameters [8, 10]. The standard design model of a fuzzy-based PID controller is shown in Fig. 2.

The (3 × 3) rule base is reported in Table 2. Where e is the error input, and Δe is the error differential input to the fuzzy controller. NB, Z and PB are the fuzzy linguistic variables, which represent negative big, zero and positive big, respectively. Mamdani fuzzy interface is used for simulation purpose. Triangular membership function as shown in Fig. 3 is used because of its popularity.

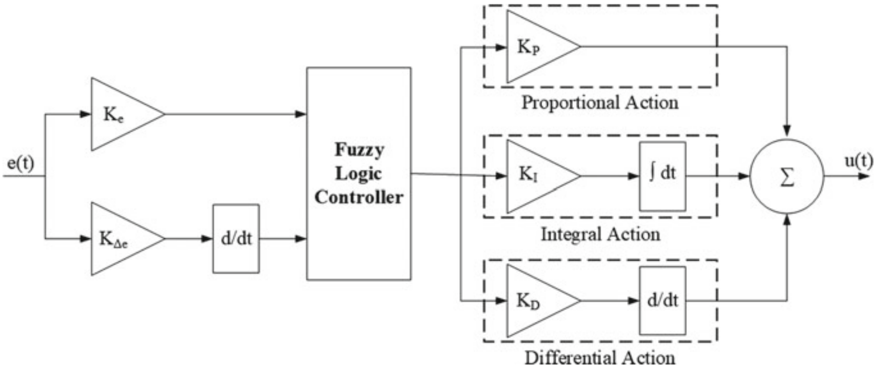

Fig. 2 Structure of PID controller

Table 2 Rule base for FPID

e / Δe	NB	Z	PB
NB	NB	NB	Z
Z	NB	Z	PB
PB	Z	PB	PB

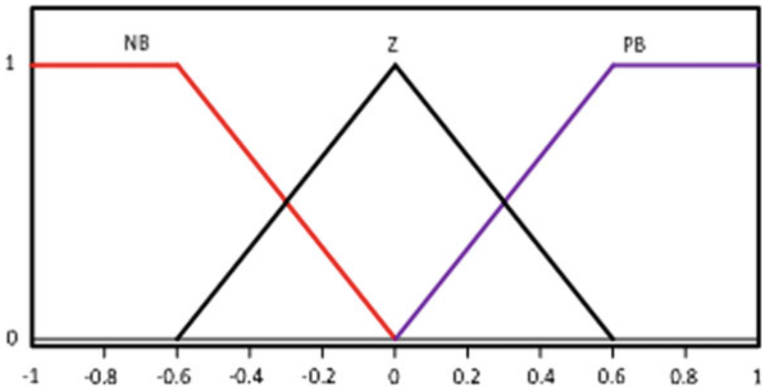

Fig. 3 Membership functions for FPID controller

4 Salp Swarm Algorithm

Salp swarm algorithm (SSA) is a recently proposed popular algorithm used for the optimization purpose. It is basically inspired by the swarming behavior of salps in oceans. It is used widely by the researchers due to its high efficiency in the optimization field.

In case of single-objective optimization problem, only one objective function is taken into consideration. Using SSA, this objective function is used to minimize or maximize accordingly [11, 12]. The algorithm is based on the swarming behavior of the salps. The foraging and navigating moving pattern of the salps helps them to reach the target point. During the motion, salps divides themselves into two groups. The leader always takes the first position and directs other salps. Follower salps follow the leader accordingly. The coordinated action of leader and followers always aims to achieve the target within search boundary [11].

5 Objective Function

Objective function can be any performance index like integral absolute error (IAE), integral square error (ISE), integral time absolute error (ITAE) or integral time square error (ITSE). SSA is used to optimize the controller parameters and to minimize the objective function. Objective function is represented by J. ISE as an objective function and is defined as

$$J = \int_0^{T_{\mathrm{sim}}} |\Delta f|^2 \mathrm{d}t \tag{7}$$

where T_{sim} is the simulation time, and Δf is the frequency deviation of the system. Similarly, IAE, ITAE and ITSE are also defined by their respective error function and are used as the objective function one by one.

6 Result and Analysis

The microgrid shown in Fig. 1 is simulated using MATLAB/Simulink software (version R2016a). SSA, which is used for tuning of controller parameters for optimal operation of system, is executed in a.m file and exhibited in Simulink. For controller parameters K_P, K_I and K_D, the range is set as [0 1], and for K_e and $K_{\Delta e}$, the range is set as [0.001 1]. The system is simulated for different operating conditions for validation purpose. Different operating conditions that were taken into consideration are listed below.

1. Availability of all sources (step variation of renewable sources and load)
2. Non-availability of solar energy
3. Non-availability of solar and wind energy
4. Non-availability of solar, wind and biogas
5. Availability of all sources (random variation of renewable sources and load).

The system is optimized using different performance indices with PID and FPID controllers by considering condition 1. Indices values for respective controllers are reported in Table 3.

Corresponding to performance index, ISE, J_{min} for FPID (0.0441) controller is found to be lower than the J_{min} for PID (0.1009) controller. So, considering ISE as the objective function, the respective optimized parameters of the PID and FPID controller are listed in Table 4. For the rest of the conditions, the controller parameters remain unchanged which reduce the computational burden on the system as well as increase robustness of the system for operating under different conditions at constant controller parameters. The total simulation time is fixed to 120 s for all the conditions.

Table 3 Performance Indices values for respective controllers

Performance index	PID	FPID
IAE	1.1710	0.9959
ISE	**0.1009**	**0.0441**
ITAE	42.0214	37.6147
ITSE	2.4028	1.8949

Table 4 Controller parameters values

	PID	FPID
Controller parameter	$K_{P1} = 0.0461$, $K_{I1} = 0.2104$, $K_{D1} = 0.0343$ $K_{P2} = 0.3441$, $K_{I2} = 0.0007$, $K_{D2} = 0.5822$ $K_{P3} = 0.5507$, $K_{I3} = 0.9083$, $K_{D3} = 0.7808$	$K_{11} = 0.0030$, $K_{12} = 0.2839$, $K_{P1} = 0.0218$, $K_{I1} = 0.0028$, $K_{D1} = 0.0927$ $K_{21} = 0.1901$, $K_{22} = 0.0438$, $K_{P2} = 0.0680$, $K_{I2} = 0.0427$, $K_{D2} = 0.4292$ $K_{31} = 0.9988$, $K_{32} = 0.9260$ $K_{P3} = 1.0000$, $K_{I3} = 1.0000$, $K_{D3} = 0.0085$

6.1 Condition 1

In this condition, step variation of wind and solar radiation are given as input to the microgrid for a multi-step varied load. The steady state PV output power (P_{SPV}) is 0.2 pu, and wind power output (P_{WTG}) is 0.2 pu throughout the simulation period. So, the total generation of SPV and WTG is 0.4 pu, which remain unchanged, and only load demand (P_{dL}) is subjected to different step values for different time interval as shown in Fig. 4.

P_{dL} is within a range of 0–0.4 pu throughout the simulation period. It can be seen that generation by SPV and WTG is enough to meet the demand. But it can also be observed that BGTG and BDEG are still supplying some power to the microgrid. The surplus generated power is getting stored in the BESS which can be utilized during the peak hour. Three separate controllers are used for BESS, BGTG and BDEG to control their output in order to minimize the generation-demand power mismatch. Response of BESS, BGTG and BDEG is shown in Fig. 5. The frequency deviation characteristics for condition 1 is given in Fig. 6. It is observed that fuzzy-aided PID controller reduces the peak overshoot/undershoot minimizing the frequency variation more efficiently as compared to PID controller.

6.2 Condition 2

This is a common power system operating condition where SPV unit fails to generate power due to absence of sun light either in night time or in cloudy weather condition. The system is simulated with SPV = 0. Figure 7 shows superior performance with reduced oscillations in frequency deviation with FPID controller as compared to PID controller. Therefore, FPID controller with more number of controlling parameters makes the system adaptive toward varied operating conditions.

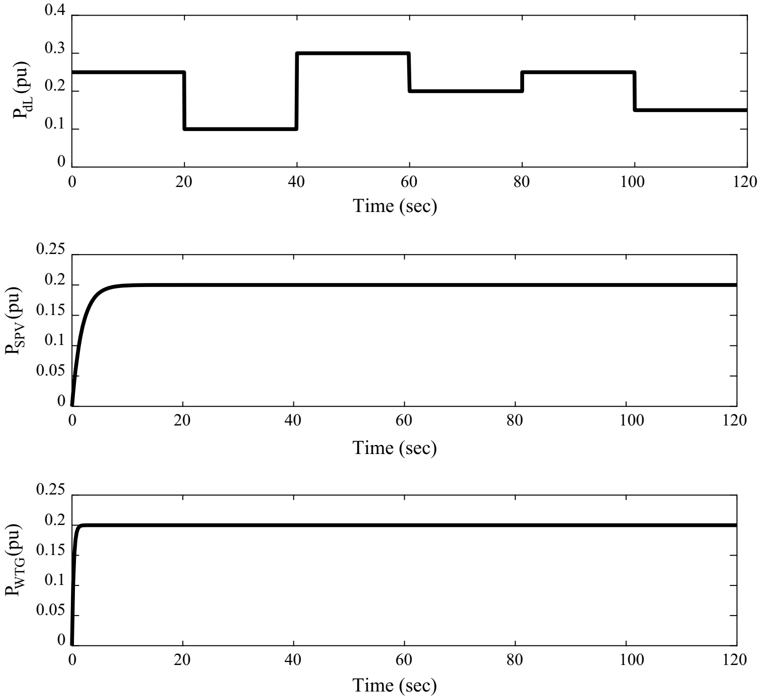

Fig. 4 Demand and RESs (step variation)

6.3 Condition 3

This is a condition when the major power supplier of a microgrid fails to supply. The same system as in the condition 1 with the change SPV = 0 and WTG = 0 is simulated for 120 s. Figure 8 shows the frequency deviation characteristic for the same. FPID controller shows a satisfactory transient performance by lowering the frequency fluctuations for this condition also. The FPID controller outperforms PID controller both in transient as well as in the steady state conditions.

6.4 Condition 4

This condition arises when the BGTG fails to supply any power to the microgrid at a crucial period when SPV and WTG are also not supplying any power. The same system as in the condition 1 with the change SPV = 0, WTG = 0 and BGTG = 0 is simulated for 120 s. The frequency deviation characteristic for this is shown in Fig. 9. FPID controller shows a satisfactory transient performance by lowering the

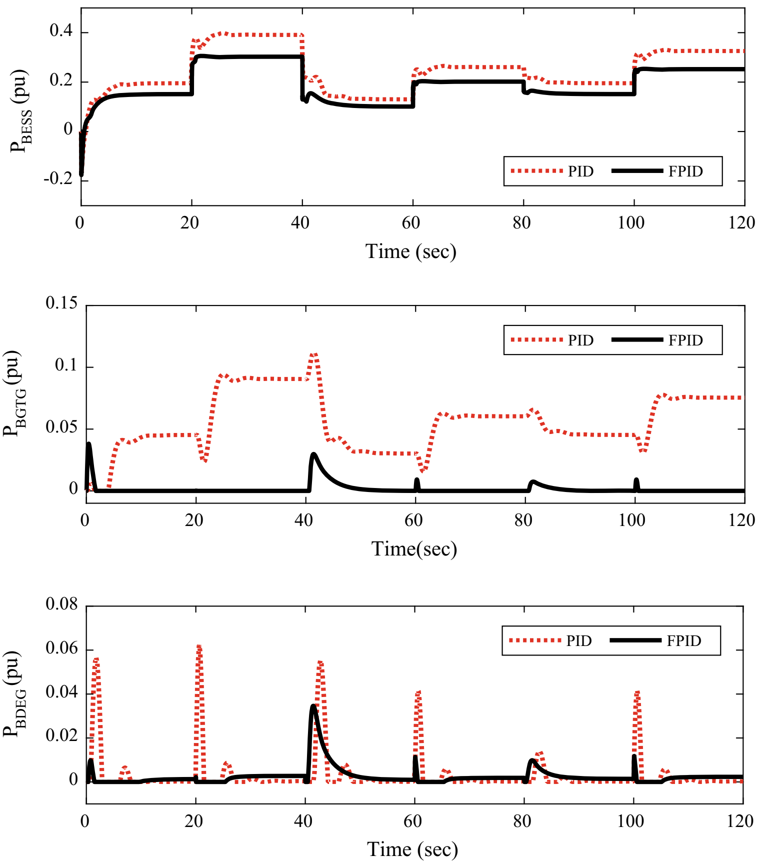

Fig. 5 Response of BESS, BGTG and BDEG

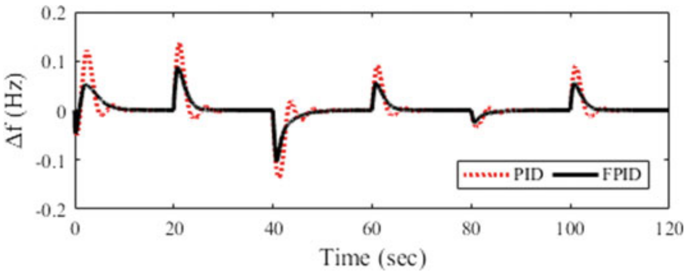

Fig. 6 Frequency deviation characteristics for condition 1

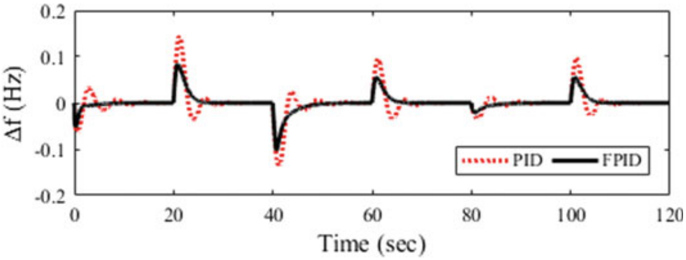

Fig. 7 Frequency deviation characteristics for condition 2

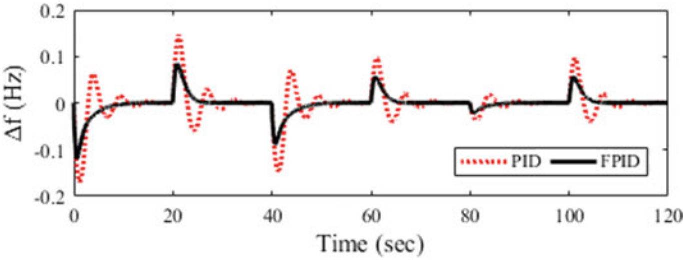

Fig. 8 Frequency deviation characteristics for condition 3

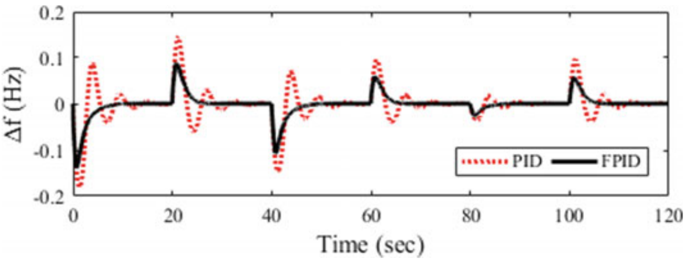

Fig. 9 Frequency deviation characteristic for condition 4

frequency fluctuations for this condition also. The FPID controller outperforms PID controller both in transient as well as steady state conditions in this case also.

6.5 Condition 5

The system is validated with random variation of P_{SPV} within a range of 0–0.2 pu, P_{WTG} within a range of 0.4–0.6 pu along with a randomly varied load (around 1 pu) as shown in Fig. 10.

The frequency deviation characteristic for this condition is shown in Fig. 11. FPID

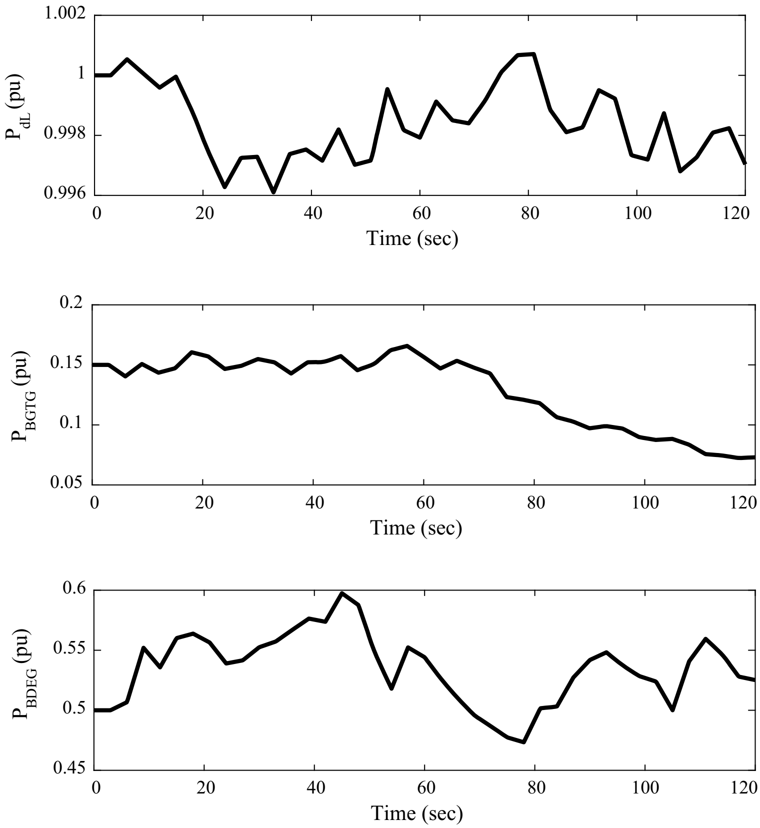

Fig. 10 Demand and RESs (random variation)

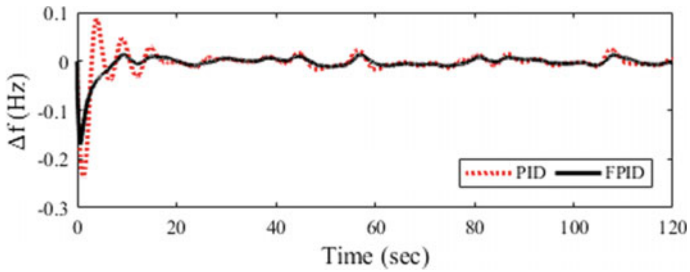

Fig. 11 Frequency deviation characteristics for condition 5

controller shows a satisfactory transient performance by lowering the frequency fluctuations for this condition also. The FPID controller performs better than the PID controller for the whole transient and steady state period.

7 Conclusion

In this paper, an isolated microgrid consisting of SPV, WTG, BGTG, BDEG and BESS is designed. The system is investigated for the different operating conditions using both PID and FPID, and the parameters of PID and FPID are optimized by SSA technique. For all the performance indices, the values are lower with FPID controller as compared to PID controller. The FPID controller performs better in terms of all the parameters, i.e., overshoot, undershoot, settling time and steady state error in load frequency control as compared to the conventional PID controller.

References

1. Barik AK, Das DC (2018) Expeditious frequency control of solar photovoltaic/biogas/biodiesel generator based isolated renewable microgrid using grasshopper optimisation algorithm. IET Renew Power Gener 12(14):1659–1667
2. Bhaskara SN, Chowdhury BH (2012) Microgrids—a review of modelling, control, protection, simulation and future potential. IEEE Power Energy Soc General Meeting 1(7):22–26
3. Sahoo BP, Panda S (2020) Load frequency control of solar photovoltaic/wind/biogas/biodiesel generator based isolated microgrid using Harris hawks optimization. In: IEEE first international conference on power, control and computing technologies (ICPC2T), pp 188–193
4. Abbasi E, Ameli H, Strunz K, Duc NH (2012) Optimized operation, planning, and frequency control of hybrid generation-storage systems in isolated networks. In: 3rd IEEE PES innovative smart grid technologies Europe (ISGT Europe), pp 1–8
5. Elbaz M, Feliachi A (2012) Real time load frequency control for an isolated microgrid system. North Am Power Symp (NAPS) 1(6):9–11
6. Khooban MH, Niknam T, Blaabjerg F, Davari P, Dragicevic T (2016) A robust adaptive load frequency control for micro-grids. ISA Trans 65:220–229
7. Mahto T, Mukherjee V (2016) Evolutionary optimization technique for comparative analysis of different classical controllers for an isolated wind–diesel hybrid power system. Swarm Evol Comput 26:120–136
8. Mohanty D, Panda S (2021) Robust frequency control of hybrid power system with EV and HP. In: 3rd international conference on energy, power and environment: towards clean energy technologies, pp 1–5
9. Bevrani H, Habibi F, Babahajyani P, Watanabe M, Mitani Y (2012) Intelligent frequency control in an AC microgrid: online PSO-based fuzzy tuning approach. IEEE Trans Smart Grid 3(4):1935–1944
10. Ganguly S, Mahto T, Mukherjee V (2017) Integrated frequency and power control of an isolated hybrid power system considering scaling factor based fuzzy classical controller. Swarm Evol Comput 32:184–201
11. Mirjalili S, Gandomi AH, Mirjalili SZ, Saremi S, Faris H, Mirjalili SM (2017) Salp swarm algorithm: a bio- inspired optimizer for engineering design problem. Adv Eng Softw 114:163–191

12. Faris H, Mirjalili HS, Aljarah I, Mafarja M, Heidari AA (2020) Salp swarm algorithm: theory, literature review, and application in extreme learning machines. In: Nature-inspired optimizers. Springer, pp 185–199

Chapter 46
Planning of Power Loss and Fuel Cost Minimization by Deployment of DERs Using Evolutionary Algorithm

Deblina Maity, Sumit Banerjee, and Chandan Kumar Chanda

Abstract In this paper, optimal sizing, type, and placement of distributed energy resources have played very significant role for decrement of power loss and fuel cost in distribution network. Suitable sizing and location of distributed energy resources (DERs) are chosen by loss minimization using teacher–learner relationship algorithm and cost minimization using pollination process algorithm (FPA). With proper allocation of DERs, grid power loss is reduced. Economic load dispatch is optimal power allocation satisfying load demand where cost is minimized. Here micro-grid is combination of three diesel generators (D_g) and two micro-turbines (M_t). The usefulness of the proposed idea has been experienced on a distribution network connected radically (12.66 kV) containing thirty-three nodes.

Keywords Micro-grid · Distributed generator · Flower pollination · Global pollination · Micro-turbine

Nomenclature

Po_{loss}	Total real power loss in the system
Qo_{loss}	Total reactive power loss in the system
Po_{i+1}	Active power at $i + 1$ node
Qo_{i+1}	Reactive power at $i + 1$ node
Re_S	Resistance of the network
Xe_S	Reactance of the network
Vol	Voltage of particular node

D. Maity (✉)
Netaji Subhash Engineering College, Kolkata, India

S. Banerjee
Dr. B. C. Roy Engineering College, Durgapur, India

C. K. Chanda
IIEST, Shibpur, India

G. Panda et al. (eds.), *Sustainable Energy and Technological Advancements*,
Advances in Sustainability Science and Technology,
https://doi.org/10.1007/978-981-16-9033-4_46

$\mathrm{Vol}_{\min}$	Minimum limit of voltage
$\mathrm{Vol}_{\max}$	Maximum limit of voltage
$XX_i^{\min}$	Minimum level of operation region of particular generator
$XX_i^{\max}$	Maximum level of operation region of particular generator
$C_i(XX_i)$	Objective function economic load dispatch problem
XX_i	Electricity energy generated by generators
Mm	Number of existing operated generators
XX_D	System load driven by generators
XX_L	Losses in power plant
pp_i	Running cost of unit *i*.
qq_i	Semi fixed cost of unit *i*.
rr_i	Fixed cost of unit *i*.
dd_i,ee_i	Cost coefficients of particular unit due to valve point loading effect
$\mathrm{PP}_{\mathrm{DER}_{\min}}$	Min active power limit of DERs
$\mathrm{PP}_{\mathrm{DER}_{\max}}$	Max active power limit of DERs
$QQ_{\mathrm{DER}_{\min}}$	Min reactive power range of DERs in distribution network
$QQ_{\mathrm{DER}_{\max}}$	Max reactive power range of DERs in distribution network

1 Introduction

In recent electrical network, demand is increasing day by day. It is very difficult to serve load demand satisfactorily using thermal generators in power station. Thus, the fuel cost, active reactive power loss also will be increased. Being an electrical engineer that should be our prime concern to reduce the losses and fuel cost. To overcome this, several renewable energy resources are to be incorporated with grid due to their less cost and injecting active power properties. There are several renewable energy resources like diesel generators, micro-turbines, fuel cell, and wind farm. When the thermal generators are inadequate to feed the load demand, then the distributed energy resources (DERs) are disconnected with main grid and the group of DERs is responsible of power generation for meeting load demand. The group of DERs is called 'micro-grid'.

For conventional economic load scheduling problem, the objective fuel cost function is represented by simple quadratic algebraic equation with linear nature which can be solved using easy and simple iterative algorithm like lambda iterative algorithm and gradient-oriented method [1]. But in lambda iteration method, incremental fuel cost curve is needed for getting solution. Basically, this curve is linear, but in practical view incremental fuel cost is fully nonlinear due to constraints like valve point loading effect, ramp rate limit, etc. To overcome this problem, such method is suitable which does not enforce any restriction on the nature of the cost curves. Wood and Wollenberg presented [2] that suitable method, i.e., dynamic programming. Holland presented [3] a mathematical model with linear and nonlinear constraints. The model's universality had been proposed and implemented on different era of sciences, i.e., economics, game theory, and soft computing techniques. David E Goldberg proposed [4] genetic algorithm to get the solution in global optimization problems. This algorithm had been executed on several test functions, and obtained results are differentiated with results obtained other several challenging optimization algorithms. Voudouris et. al proposed guided local search (GLS) [5] to solve global and local minimized function. Solis and Wets proposed random search algorithms (RSA) [6] to solve large optimization problems. Random search (RS) is one type of numerical methods that do not need gradient of problem that is to be optimized. Random search is implemented on that functions which are not continuous or differentiable.

Norio et al. [7] investigated the random optimization method for minimization method. This approach can be applied on engineering optimization problem and then may be compared with other evolutionary algorithms. Mondal et al. [8] proposed an artificial intelligence-based method a soft computing based on load matching approach. An optimization algorithm based on Stochastic Hill climbing is implemented for solution of several test functions. The solution of this algorithm had been compared with existing algorithms. Lozano proposed [9] a real-coded memetic algorithm produced by the genetic operators to solve optimization problem. An important aspect of proposed memetic algorithm is that it adaptively assigns different local search probabilities to individuals. Lourenc et al. [10] proposed iterative search method to solve optimization problem for beginners. This approach had been implemented on different benchmark functions.

Mladenovic and Hansen [11] proposed variable neighborhood search (VNS) for solving combinatorial and global optimization problems. Those problems are concerned about systematic change of neighborhood both within constraints to find a local optimum. In [11], some basic schemes of VNS are presented with its extensions. Burke et al. [12] demonstrated that this tabu search method is reusable method, i.e., can provide solutions of acceptable quality with satisfying constraints. The proposed method is competent of getting competitive solutions with other existing evolutionary algorithms for the problems.

Here distflow algorithm is used for calculation of voltages at all nodes and then active and reactive power loss calculated. This theory is presented '***Segment 2***'. Active and reactive power loss is minimized by placing DERs at proper location with proper size using FPA algorithm, described in '***Segment 3***'. With obtained proper size of DERs from FPA, again active and reactive power loss is calculated. ***Segment 4*** presents the obtained result using MATLAB program, and ***Segment 5*** shows the concluding part of this paper.

2 Representation of Fitness Characteristics

The objective of DERs placement in the distribution system is to minimize the active and reactive power loss of the system, subjected to operating constraints. In this paper, firstly distributed energy resources are placed at proper location with optimal sizing at radial distribution network. For this size of DERs, active and reactive power loss is minimized. Secondly, fuel cost should be minimized for proper sizing of DERs in network. The prime concern of incorporations of DERs is to reduce active reactive power loss and fuel cost.

The multi-objective function includes two main components including: total active reactive power losses (TPL) and total fuel cost in distribution grid which is represented in Eq. (1).

$$\text{Min } P_{\text{loss}} + \text{Min } Q_{\text{loss}} + \text{Min Fuel Cos}t \quad (1)$$

2.1 Active and Reactive Power Loss (Size Selection of DERs)

Optimal operation of power system often considers minimization of active reactive power loss as main objective as the mathematical equation below. Active and reactive power loss is calculated by following Eq. (2) by distflow method.

$$\text{Min Po}_{\text{loss}} = \frac{\text{Po}_{i+1}^2 + \text{Qo}_{i+1}^2}{\text{Vol}_q^2} R_S \quad (2)$$

$$\text{Min } Qo_{\text{loss}} = \frac{\text{Po}_{i+1}^2 + \text{Qo}_{i+1}^2}{\text{Vol}_q^2} X_S \quad (3)$$

2.2 Fuel Cost (Economic Load Dispatch Problem)

The economic load dispatch presents minimization of fuel cost satisfying linear and nonlinear constraints. The following objective function shown in Eq. (4) presents minimization of fuel cost.

$$\left\{ \text{Min.}C = \sum_{i=1}^{M} C_i(XX_i) \right. \quad (4)$$

The fuel cost function of ith unit can be defined by

$$C_i(XX_i) = pp_i XX_i^2 + qq_i XX_i + rr_i \quad (5)$$

2.3 Constraints

There are various constraints where objective function has been subjected to. The constraints are the following.

2.3.1 Voltage Constraint

The voltage magnitude at each bus must be maintained within its limits and is expressed as

$$\mathrm{Vol}_{\min} \leq |\mathrm{Vol}_i| \leq \mathrm{Vol}_{\max} \tag{6}$$

2.3.2 Reactive Power Limit

The reactive power and active power of all bus will be within their limits. When DERs are incorporated into grid, then reactive power will be updated.

$$PP_{\mathrm{DER}_{\min}} \leq PP_{\mathrm{DER}} \leq PP_{\mathrm{DER}_{\mathrm{Max}}} \tag{7}$$

$$QQ_{\mathrm{DER}_{\min}} \leq QQ_{\mathrm{DER}} \leq QQ_{\mathrm{DER}_{\mathrm{Max}}} \tag{8}$$

2.3.3 Line Flow Limits

Line flow should be within limits. Congestion of micro-grid is undertaken.

$$\text{Line flow}_{pq} \leq \text{Limits of line flow} \tag{9}$$

2.3.4 System Power Balance

The produced electrical power by generators is to be sum value of demand of load and system losses.

$$\sum_{i=1}^{N} XX_i(t) = XX_D(t) + XX_L(t) \tag{10}$$

2.3.5 Limitations of Generator's Operating Region

The electrical energy produced by generators should be within region of operating limits.

$$XX_i^{\min} \leq XX_i \leq XX_i^{\max} \tag{11}$$

2.3.6 Nonlinear Effect of ELD

In ELD when load is increased, the rate of valve opening and closing is not linear. Nonlinear cost function C is presented in Eq. (12).

$$\begin{aligned} C &= \min\left(\sum_{i=1}^{N} C_i(XX_i)\right) \\ &= \min\left(\sum_{i=1}^{N} pp_i XX_i^2 + qq_i XX_i + rr_i + \left|ee_i * \sin\left\{ff_i * \left(XX_i^{\min} - XX_i\right)\right\}\right|\right) \end{aligned} \tag{12}$$

Power flow problem is to be solved with distflow technique in radial network.

3 Pollination Algorithm for Getting Location and Sizing of DERs

FPA optimization is based on pollination process of flowers. In simple way, population FF_i represents a flower or pollen gamete. There are two steps: one is 'pollination in global way' and another one is 'pollination in local way'.

- Pollination in global way:

  In nature, insects carry pollen and they wing over long distance with carrying pollen. Here Gg represents fittest pollen or fittest solution in optimization problem. The solution is updated using Eq. (13).

$$FF_i^{t+1} = FF_i^t + Ll\left(FF_i^t - Gg\right) \tag{13}$$

  Ll is represented by Eq. (14).

$$L \approx \frac{\lambda\Gamma(\lambda)\sin\left(\pi\lambda/_2\right)}{\pi}\frac{1}{s^{1+\lambda}}, \quad s \geq s_0 \geq 0 \tag{14}$$

- Pollination in local way:

  Pollination is updated using Eq. (15).

$$FF_i^{t+1} = FF_i^t + \varepsilon\left(FF_j^t - FF_k^t\right) \tag{15}$$

where FF_j^t and FF_k^t are pollens from different flowers in same species. ε is uniform distribution in [0, 1].

4 Result and Discussion

The proposed algorithms have been tested on proposed IEEE 33 node system for getting proper location and sizing of DERs for which active, reactive power loss, and fuel cost will be minimized. IEEE system consisting 33 nodes has been taken from [13], and single line diagram of it has been shown in Fig. 1. In this segment, there are three sections.

Step 1: Firstly proper location with proper size of DERs is obtained using power loss methodology.

Step 2: Economic fuel cost analysis is using FPA satisfying constraint of generator limits and meeting load demand.

Step 3: Then active and reactive power loss is calculated by obtained sizing from FPA. So the optimal sizing is obtained where active reactive power loss and fuel cost are minimized.

Case 1: IEEE 33-Bus Distribution Network.

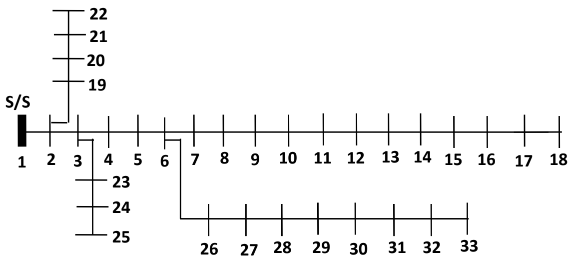

Fig. 1 Single line diagram of 33-nodes radial distribution network

Table 1 Obtained optimal sizing and location of DERs using FPA

Proposed optimal location of DERs	Optimal sizing of DERs (kW)	Type of DERs
8	515	Diesel generator
13	300	Micro-turbine
20	200	Micro-turbine
24	300	Micro-turbine
25	1000	Diesel generator
30	1500	Diesel generator

Table 2 Active power loss of the system without and with placement of DERs in six nodes, six nodes, i.e., micro-grid for 33-node system [min power loss methodology]

	Without DGs	With DERs (Refer to Table 1 for details)
Active power loss (kW)	203	79.8
Reactive Power Loss (KVAR)	135	55.5

4.1 Selection of Location and Sizing of Distributed Energy Resources Using Minimum Loss Methodology

For reducing active power loss and reactive power loss, proper sizing of distributed energy resources (DER) is very necessary at proper location in distribution network. Seven DERs are placed at optimal location with proper size where active and reactive power loss will be minimized. 515 kW sized diesel generator, 300 kW sized micro-turbine, 200 kW sized micro-turbine, 300 kW sized micro-turbine, 1000 kW sized diesel generator, and 1500 kW sized diesel generator are connected at node 8, 13, 20, 24, 25, and 30, respectively. Table 1 shows obtained optimal location of DERs using FPA in distribution network.

Sizing of DERs is required for performing ELD. Economic load dispatch is performed on six DERs. Active and reactive power loss reductions are shown in Table 2 for six DERs placement.

4.2 Economic Fuel Cost Analysis Using FPA

Flower pollination algorithm has been applied on economic load dispatch in the above micro-grid where cost will be minimized. The relevant data for ELD is described in Table 3. Table 4 shows optimal power allocation of six DERs using FPA. Figure 2 shows convergence characteristics of FPA at 3715 kW load micro-grids.

Table 3 DERs data—fuel consumption coefficients and operational limits

DER type	$PG_{i\,\min}$(kW)	$PG_{i\,\max}$(kW)	a_i (\$/h)	b_i (\$/h/MW)	c_i (\$/h/MW^2)
515 kW (Dg)	103	515	5.115	52.36	31.68
300 kW (Mt)	80	300	0.009	8.5	220
200 kW (Mt)	40	200	2.035	60.28	44
300 kW (Mt)	80	300	0.009	8.5	220
1000 kW (Dg)	200	1000	0	84.8	0
1500 kW (Dg)	300	1500	0.3312	15.6	248.4

Table 4 Best power output for six DERs case system using FPA ($P_D = 3715$ kW)

Unit Power Output (KW)	FPA
P_1(kW)	491.3
P_2(kW)	300
P_3(kW)	193.6
P_4(kW)	300
P_5(kW)	1000
P_6(kW)	1430.1
Total generation cost (\$/h)	2,253,000

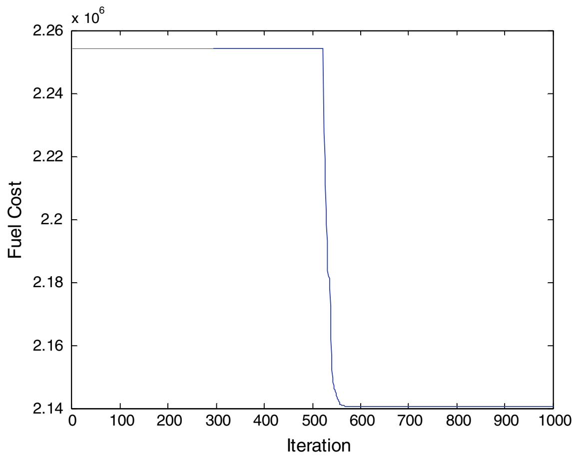

Fig. 2 Convergence characteristic of six DERs case at 3715 kW micro-grid using FPA

4.3 Superiority of FPA with Minimum Loss Methodology

Active and reactive power loss is reduced for modified sizing of DERs obtained from solution of ELD. Reductions of active and reactive power loss are shown in Table 5 from obtained size of DERs using FPA.

Table 5 Active and reactive power loss of the system for obtained size of DERs from minimum fuel cost methodology and FPA

	Without DGs	Size of DERs obtained from minimum active power loss methodology (Refer to Table 1 for details)	Size of DERs obtained from minimum fuel cost methodology FPA (Refer to Table 1 for details)
Active power loss (kW)	203	79.8	77.8
Reactive power loss (KVAR)	135	55.5	54.1
Fuel cost ($/h)		2,337,900	2,253,000

5 Conclusion

The proposed algorithms, i.e., flower pollination algorithm, have been applied successfully to solve load scheduling problem for getting minimum fuel cost and power loss simultaneously. Here linear constraints like meeting load demand, generation of power within limits are considered. This proposed algorithm has capability to achieve suitable best solution with satisfying constraints in less time. Fuel cost obtained from algorithm proves its superiority property by comparing fuel cost compared to power loss methodology algorithm by avoiding premature solution. Due to these supreme qualities, the biological distribution-based method can be applied for unit commitment problem, reactive power dispatch in the near future.

References

1. Saadat H (2002) Power system analysis. Tata McGraw Hill Publishing Company, New Delhi
2. Wood J, Wollenberg BF (1984) Power generation, operation, and control, 2nd edn. Wiley, New York.
3. Holland JH (1992) Adaptation in natural and artificial systems. University of Michigan Press, Ann Arbor
4. Goldberg D (1989) Genetic Algorithms in search, optimization, and machine learning. Addison-Wesley, Reading
5. Voudouris C, Tsang EP, Alsheddy A (2010) Guided local search. In: Handbook of metaheuristics. Springer, Berlin, pp 185–218
6. Solis FJ, Wets RJB (1981) Minimization by random search techniques. Math Oper Res 6(1):19–30
7. Baba N, Shoman T, Sawaragi Y (1977) A modified convergence theorem for a random optimization method. Inf Sci 13(2):159–166
8. Mondal B, Dasgupta K, Dutta P (2012) Load balancing in cloud computing using stochastic hill climbing-a soft computing approach. Procedia Technol 4:783–789
9. Lozano M (2004) Real-coded memetic algorithms with cross overhill-climbing. Evolutionary Computing 12(3):273–302
10. Lourenc HR, Martin O, Stützle T (2001) A beginner's introduction to iterated local search. In: Proceedings of Meta-heuristics International Conference

11. Mladenovic N, Hansen P (1997) Variable neighborhood search. Comput Oper Res 24(11):1097–1100
12. Burke EK, Kendall G, Soubeiga E (2003) A tabu-search hyper-heuristic for time tabling and roistering. J Heurist 9(6):451–470
13. Bhullar S, Ghosh S (2017) A novel search technique to solve load flow of distribution networks. J Eng Res 5:59–75

Chapter 47
Investigation on Stability of DC Microgrid for Large-scale Electric Vehicle Charging Station Deployment

S. Jithin and T. Rajeev

Abstract The recent trends and need for green and sustainable energy tendered automobile industries to switch toward electric vehicles. DC fast charging stations are required for long-distance driving and large vehicles such as buses, trucks. Integration of DC fast charging stations to the existing grid results in congestion and stability problems. These problems can be overcome by deploying small DC microgrid clusters within the microgrid. This paper investigates the effect of massive electric vehicle integration on the operating parameters of DC microgrids, as DC fast charging stations are a necessity. Bidirectional DC/DC buck-boost converters are used for interfacing EVCS into DC microgrid. In addition to the droop controller, the converter control also consists of PI-based voltage and current controllers. Performance and stability analyses are evaluated through mathematical modeling and simulation analysis for the microgrid test model. The DC microgrid provided competent results with large-scale electric vehicle integration. The test results validate that the DC microgrid is a viable solution for integrating electric vehicles considering stability.

Keywords Dc microgrid · Electric vehicle · Charging station

1 Introduction

The tremendous growth of green and sustainable energy has led to the deployment of electric vehicles (EVs) in the transportation sector for reducing the adverse effects of carbon emissions. With the immense impetus of EVs, EV charging stations (EVCS) are the vital requisite. The EV operation can be in two modes: grid to vehicle (G2V) and vehicle to grid (V2G). In G2V mode, EV acts as a load and consumes power

S. Jithin (✉) · T. Rajeev
College of Engineering Trivandrum, APJ Abdul Kalam Technological University, Thiruvananthapuram, Kerala, India
e-mail: jithinsathisan@gmail.com

T. Rajeev
e-mail: rajeev.t@cet.ac.in

G. Panda et al. (eds.), *Sustainable Energy and Technological Advancements*,
Advances in Sustainability Science and Technology,
https://doi.org/10.1007/978-981-16-9033-4_47

from the grid. In V2G mode, the EV acts as a distributed energy resource (DER) [7, 10]. Further, the EV charging stations can provide ancillary grid support such as load leveling, load shifting, generation reserve, and frequency regulation. The large-scale integration of EV charging stations and their effects on the grid have become a hot topic [6]. The deployment of unplanned EVCS will deteriorate the system performance by affecting the voltage and frequency profiles, power quality, and reliability of the distribution network. There are enormous works of literatures, discussing the impact of EV integration in the distribution network [1, 2, 9]. The influence of EV charging load on a residential distribution network is investigated in [8]. The total harmonic distortion (THD)-based analysis shows that the system provided satisfactory results up to EV penetration of 25 %.
DC fast charging stations are required for long-distance driving and also for large fleets such as bus, trucks. These charging stations require higher DC voltage for reducing the charging time. The other benefits of higher DC charging voltage are reduction in weight of the vehicle, reduction in motor size, more space for storage, and improved power retention. The main limitations for the high-voltage DC charging stations are the unavailability of high-voltage DC distribution, the requirement for protective equipment, thicker insulation, and safety measures. Integration of DC fast charging stations to the existing grid requires power converters for each charging station. This creates congestion and stability problems in the utility grid. The adverse effects on the grid due to the higher penetration of EVCS may be mitigated by deploying small DC microgrid clusters within the power grid. A microgrid is defined as a group of DERs, loads, and energy-storage systems (ESS) that operate locally as a single controllable entity [3]. The microgrids operate in grid-connected mode as well as in the islanded mode of operation. In extreme situations, islanding the microgrid, the operational problems due to the higher penetration of EVCS in the existing grid can be alleviated.

2 System Description and Mathematical Modeling

The DC microgrid architecture considered is shown in Fig. 1. The individual state-space models of DC/DC converter, lines, and loads are developed to obtain the DC microgrid model. Droop control method is employed for controlling the source. The droop control technique is more suitable for EVs, as these loads are decentralized. The elimination of communication, simple control, low cost, and plug-play features overcomes the limitations of the droop controller for practical implementation. By changing the droop characteristics, the power-sharing among the sources can be prioritized. Steeper droop characteristic implies more power-sharing. In Fig. 1, the loads connected through DC/DC converter represent the EVCS (at Nodes 646, 670, and 692), and remaining are the normal loads.

Bidirectional DC/DC buck-boost converters are used for interfacing EVCS into DC microgrid. In addition to the droop controller, the converter control also consists of PI-based voltage and current controllers. DC bus voltage is controlled by voltage

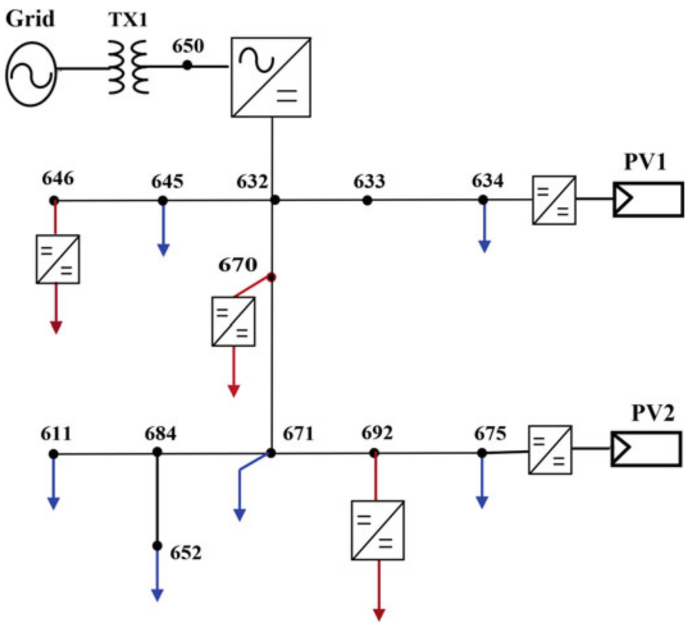

Fig. 1 DC microgrid architecture

controller, and the system stability is achieved through the actions of the inner current controller. The schematic of DC/DC converter control is depicted in Fig. 2. The average model of the buck-boost converter is used for EVCS modeling, and the average model of the boost converter is used for source modeling. As the AC/DC bidirectional converter is fast enough, the analysis is carried by assuming that the system performance is not affected by its dynamics [5]. The state-space model of the DER interfaced DC/DC converter is obtained based on Fig. 2. The detailed procedure of deriving the state-space model has been addressed in [4]. The equations governing the controller are (1)–(4).

$$V_0^* = m_{dc}\left(\frac{\omega_f}{s+\omega_f}v_0 i_0 - P_{dc}\right) \tag{1}$$

$$i_l^* = \left(V_0^* - V_0\right)\left(k_{pv} + \frac{k_{iv}}{s}\right) \tag{2}$$

$$V_{in}^* = \left(i_l^* - i_l\right)\left(k_{pc} + \frac{k_{ic}}{s}\right) \tag{3}$$

$$\dot{V_{dc}} = \frac{1}{C}i_l - \frac{1}{RC}V_{dc} \tag{4}$$

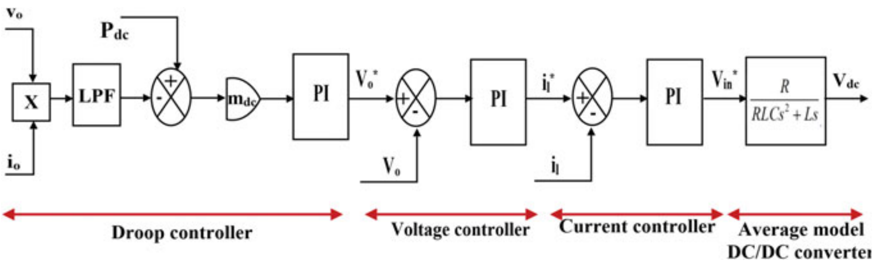

Fig. 2 DC/DC converter controller

where i_l is the inductor current of lth converter, m_{dc} is the droop gain, ω_f is the low pass filter cut-off frequency, and k_{pv}, k_{iv}, k_{pc}, and k_{ic} are the PI gains of voltage and current controller, respectively. The DC bus voltage is V_{dc}, and R, L, C represent the parameters of the DC/DC converter. The final state-space model of the DC/DC converter is represented in (5).

$$\left[\Delta \dot{x}_{conv}\right] = \left[A_{conv}\right]\left[x_{conv}\right] + \left[B_{conv}\right]\left[\Delta V_{dc}\right] \tag{5}$$

where $\left[x_{conv}\right] = \left[\Delta i_l \ \Delta v_0 \ \Delta P_{dc} \ \Delta\psi \ \Delta\gamma\right]^{\mathrm{T}}$ represents the state vector and A_{conv} is the state transition matrix of the DC/DC converter.

The models of lines and loads except EV are considered as a RL network. The equation governing these models is obtained by applying KVL and KCL equations. Assume, a line is connected between ith and jth bus. The corresponding line equations are,

$$\frac{\mathrm{d}i_{\text{line}_{ij}}}{\mathrm{d}t} = \frac{1}{L_{\text{line}_i}}\left(V_{\text{bus}_i} - V_{\text{bus}_j}\right) - \frac{R_{\text{line}_i}}{L_{\text{line}_i}} i_{\text{line}_{ij}} \tag{6}$$

For the load connected to ith bus,

$$\frac{\mathrm{d}i_{\text{load}_i}}{\mathrm{d}t} = \frac{1}{L_{\text{load}_i}}\left(V_{\text{bus}_i}\right) - \frac{R_{\text{load}_i}}{L_{\text{load}_i}} i_{\text{load}_i} \tag{7}$$

The EV load model is assumed to be equivalent to a first-order battery state-space model. This is a reasonable assumption as it does not violate the characteristics of EV as a load for the analysis. The EV battery model is shown in Fig. 3. The equations governing EV load are given in (8)–(11)

$$V_{\text{bus}_i} = V_{\text{bat}} + R_i i_{ib} + V_{cb} \tag{8}$$

$$\dot{V_{cb}} = \frac{V_{cb}}{R_{cb}C_{cb}} + \frac{i_{ib}}{C_{cb}} \tag{9}$$

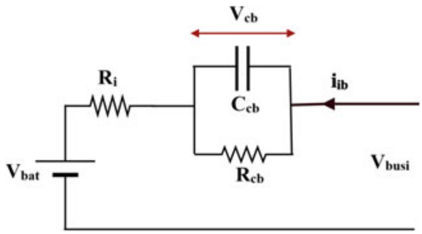

Fig. 3 EV battery model

$$\dot{SoC} = \frac{i_{ib}}{36Q} \tag{10}$$

$$V_{\text{bat}} = f(\text{SoC}) \tag{11}$$

where R_{cb} and C_{cb} are the charging resistance and charging capacitance of the EV battery, respectively, Q is the rated ampere-hour capacity of the battery, and V_{bat} is the rated EV voltage. The complete state-space model of the EV battery is given as,

$$\begin{bmatrix} \dot{\text{SoC}} \\ V_{cb} \end{bmatrix} = \begin{bmatrix} 0 & 0 \\ 1 & \frac{1}{R_{cb}C_{cb}} \end{bmatrix} \begin{bmatrix} \text{SoC} \\ V_{cb} \end{bmatrix} + \begin{bmatrix} \frac{1}{36Q} \\ \frac{1}{C_{cb}} \end{bmatrix} i_{ib} \tag{12}$$

The final state-space model of the DC microgrid by combining the individual state-space models is given in (13).

$$\begin{bmatrix} \dot{\Delta x_{\text{conv}}} \\ \Delta i_{\text{line}} \\ \Delta i_{\text{load}} \end{bmatrix} = [A_{DC}] \begin{bmatrix} \Delta x_{\text{conv}} \\ \Delta i_{\text{line}} \\ \Delta i_{\text{load}} \end{bmatrix} + [B_{DC}][V_{dc}] \tag{13}$$

3 Small Signal Stability Analysis

Small signal stability analysis of DC microgrid is determined using eigenvalue concept. The state transition matrix gives the eigenvalues of the system. For a system to be stable, all eigenvalues must lie on the left half of s-plane. It helps to identify different frequency components in the system. The stability analysis can be further investigated by changing the values of droop gain, proportional gain, and integral gain of the different controllers in the microgrid to determine the stability margins. The eigenvalue plot of the microgrids with normal operating parameters is shown in Fig. 4. The system is stable under normal operating condition as all the eigenvalues are on the left half of s-plane. The small signal analysis shows that the low-frequency components of eigenvalues are more susceptible to the changes in

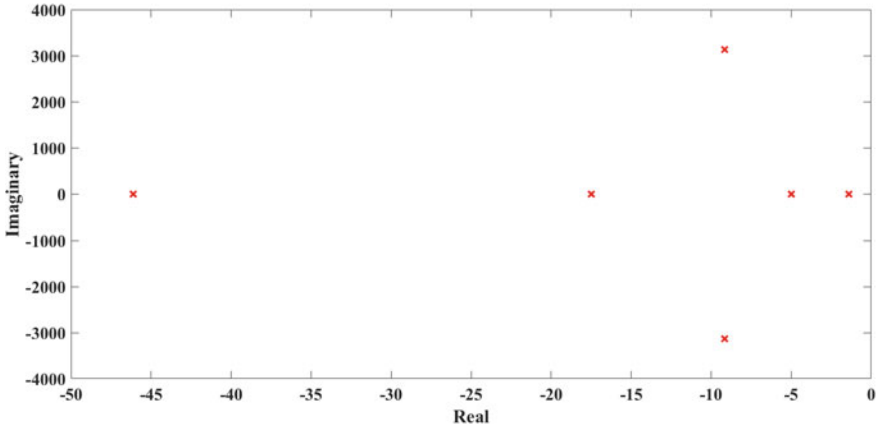

Fig. 4 Eigenvalue plot of DC microgrid

droop gain, whereas middle-frequency components are prone to the changes in the gains of voltage and current controllers.

Power ratings DC fast charging stations are 10, 15, 30, 50 kW or even higher capacity as per Bharat EV specifications. The Mahindra e20 (11–16 kWh Li-ion battery), Hyundai Kona (39.2 kWh Li-ion battery), and Nissan Leaf (40 kWh Li-ion battery) are some of the EVs employing fast DC charger. It is necessary to evaluate the performance and stability of the microgrid with these EV integrations. The effect of the charging station is analyzed by changing the rated ampere-hour capacity of the battery from the developed mathematical model. The changes in the EVCS capacity affect both middle-frequency and high-frequency components of the system. In this paper, only the variation of EVCS penetration on the microgrid is depicted. The variation of eigenvalues with change in ampere-hour capacity is plotted in Fig. 5. From the analysis, it is found that DC microgrid operates satisfactorily up to 70% EV penetration. The mathematical model-based stability analysis demonstrates that DC microgrid is pertinent for large-scale EVCS integration. The effectiveness of integrating EVCS is further investigated from the simulation experiment.

4 Simulation Experiment and Results

DC microgrid with 100 kW rated capacity is simulated using MATLAB/Simulink software to analyze the effects of EVCS. The impact of EV deployment is assessed by switching three EVCS with a rated capacity of 15 kW each, at a time difference of 0.5 s. The worst-case scenario of simultaneous switching is also investigated. The simulation parameters are given in Table 1.

The voltage variation waveforms for switching with a delay and simultaneous switching for 50% loading are shown in Figs. 6 and 7. It is evident that the DC

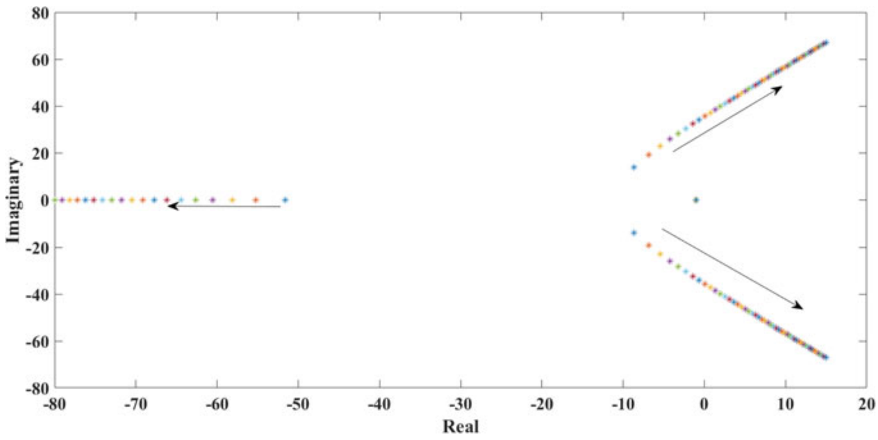

Fig. 5 Eigenvalue variation with EV penetration

Table 1 Simulation parameters

Parameter	Value
Nominal DC voltage	1000 V
Rated microgrid capacity	100 kW
EVCS capacity	15 kW
PV capacity	50 kW
Switching frequency	5 kHz
Cut-off frequency	5 Hz
Voltage controller proportional gain	2.8
Voltage controller integral gain	1
Current controller proportional gain	0.0012
Current controller integral gain	1
Droop coefficient	0.002

bus voltage fluctuations are less. The voltage drops to 0.92 pu when the EVCS are switched simultaneously, which is within the tolerance limit.

When the load due to EVCS exceeds the rated capacity of DC microgrid, power is imported from the AC grid through AC/DC converter. This scenario is also evaluated in this paper, even though it is a rare condition. When microgrid operates with 75% load and three EVCS are switched, load exceeds total microgrid capacity. The power exchange through AC/DC converter under this scenario is plotted in Fig. 8. The DC microgrid alone provides power when two EVCS are in operation. When the third EVCS is switched, power is imported from AC grid.

For ensuring the performance the controller, simulations are conducted under varying load conditions. For analysis, initial load conditions are chosen as 25, 50, and 75% of rated capacity. Then, EVCS switching is evaluated under these scenarios.

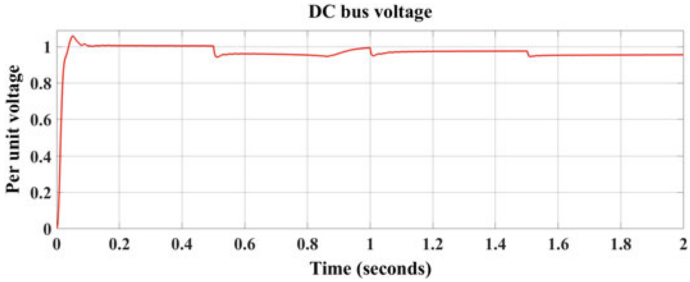

Fig. 6 Voltage variation with delayed switching of EVCS

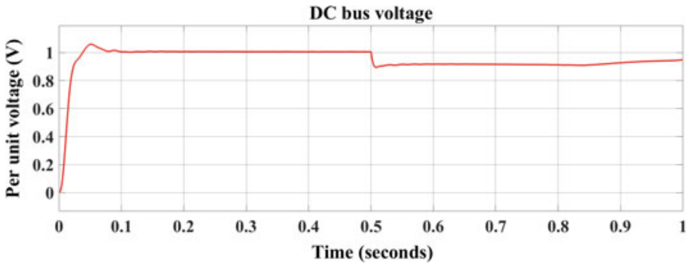

Fig. 7 Voltage variation with simultaneous switching of EVCS

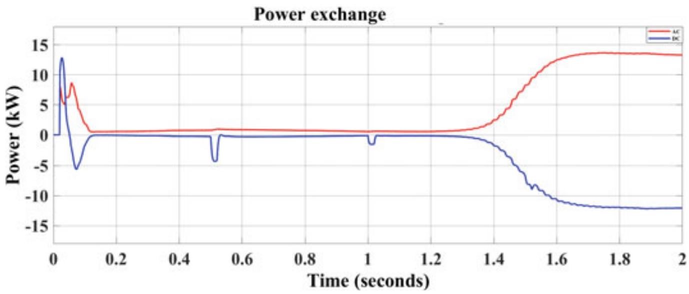

Fig. 8 Power exchange through AC/DC converter

Under 75% initial load setting, the observed voltage variations are 4.5, 7, and 8% with first, second, and third EVCS switching, respectively. Then, 8.4% voltage variation is observed with simultaneous EVCS switching. The performance of the microgrid for different loading conditions is summarized in Table 2. The voltage variations are within the specified limits as per IEEE 1547 standards even with an extreme case of switching. From the results, it is evident that DC microgrid is an effective solution for large-scale EV integration.

Real-time experimental analysis using OPAL-RT is carried out further to verify the effectiveness of the controller. RT-LAB software serves as the interface between the OPAL-RT target platform and the MATLAB/Simulink test model. For execution

Table 2 EVCS switching in DC microgrid

Initial loading (%)	Loading with EVCS (%)	Voltage variation (%)	Simultaneous switching voltage variation (%)
25	40	0.2	0.5
	55	0.3	
	70	0.5	
50	65	3	8
	80	4	
	95	4.8	
75	90	4.5	8.4
	105	7	
	120	8	

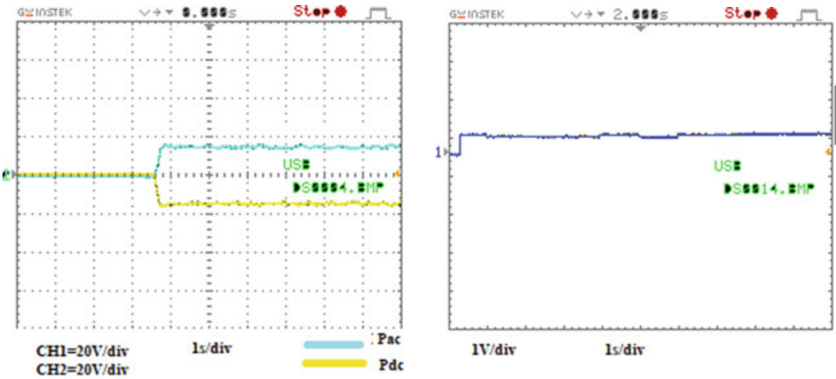

(a) Power exchange through AC/DC converter

(b) Per unit DC bus voltage

Fig. 9 Real-time experimental waveforms

of simulink model in OPAL-RT, the model is divided into two subsystems: master and console. The DC microgrid and controllers are placed in the master. The console consists of displays and changeable control parameters that are accessed during real-time simulation. After model loading and real-time data receiving, real-time waveforms are captured in the digital storage oscilloscope (DSO) through the analog out of OPAL-RT. The real-time waveforms of power exchange through the AC/DC converter and the DC bus voltage are shown in Fig. 9. The real-time analysis also proves the effectiveness of the proposed controller for large-scale EV integration in DC microgrid.

5 Conclusion

The stability analysis and performance evaluation of a DC microgrid with the deployment of EV charging stations are presented in this paper. The performance of the microgrid is evaluated through mathematical modeling and simulation analysis. The mathematical analysis shows that the DC microgrid is stable up to 70% EVCS integration, whereas the distribution grid provided satisfactory results up to 25%. The simulation results and real-time experimental results reveal that DC bus voltage variations are within the specified limits as per IEEE 1547. The simulation experiment results agree with the theoretical stability margin limit. From the results, it is evident that DC microgrid is a viable solution for the deployment of large-scale EVCS.

References

1. Archana AN, Rajeev T (2020) Reliability index based approach for allocating EV charging station in a distribution system. In: 2020 IEEE International Conference on Power Electronics, Smart Grid and Renewable Energy (PESGRE2020). pp. 1–6. https://doi.org/10.1109/PESGRE45664.2020.9070408
2. Cao C, Chen B (2018) Generalized Nash equilibrium problem based electric vehicle charging management in distribution networks. Int J Energy Res 42(15):4584–4596. https://doi.org/10.1002/er.4194
3. Farrokhabadi M, Caizares CA, Simpson-Porco JW, Nasr E, Fan L, Mendoza-Araya PA, Tonkoski R, Tamrakar U, Hatziargyriou N, Lagos D, Wies RW, Paolone M, Liserre M, Meegahapola L, Kabalan M, Hajimiragha AH, Peralta D, Elizondo MA, Schneider KP, Tuffner FK, Reilly J (2020) Microgrid stability definitions, analysis, and examples. IEEE Trans Power Syst 35(1):13–29. https://doi.org/10.1109/TPWRS.2019.2925703
4. Ghanbari N, Bhattacharya S, Mobarrez M (2018) Modeling and stability analysis of a dc microgrid employing distributed control algorithm. In: 2018 9th IEEE International Symposium on Power Electronics for Distributed Generation Systems (PEDG). pp. 1–7. https://doi.org/10.1109/PEDG.2018.8447707
5. Ghanbari N, Shabestari PM, Mehrizi-Sani A, Bhattacharya S (2019) State-space modeling and reachability analysis for a dc microgrid. In: 2019 IEEE Applied Power Electronics Conference and Exposition (APEC), pp. 2882–2886. https://doi.org/10.1109/APEC.2019.8721914
6. Liu H, Hu Z, Song Y, Lin J (2013) Decentralized vehicle-to-grid control for primary frequency regulation considering charging demands. IEEE Trans Power Syst 28(3):3480–3489. https://doi.org/10.1109/TPWRS.2013.2252029
7. Morais H, Sousa T, Vale Z, Faria P (2014) Evaluation of the electric vehicle impact in the power demand curve in a smart grid environment. Energy Convers Manag 82:268–282. https://doi.org/10.1016/j.enconman.2014.03.032
8. Niitsoo J, Taklaja P, Palu I, Kiitam I (2015) Modelling EVs in residential distribution grid with other nonlinear loads. In: 2015 IEEE 15th International Conference on Environment and Electrical Engineering (EEEIC), pp 1543–1548. https://doi.org/10.1109/EEEIC.2015.7165401
9. Rawat T, Niazi KR, Gupta N, Sharma S (2019) Impact assessment of electric vehicle charging/discharging strategies on the operation management of grid accessible and remote microgrids. Int J Energy Res 43(15):9034–9048. https://doi.org/10.1002/er.4882
10. Zhong Y, Xia M, Chiang HD (2017) Electric vehicle charging station microgrid providing unified power quality conditioner support to local power distribution networks. Int Trans Electr Energy Syst 27(3):e2262. https://doi.org/10.1002/etep.2262

Chapter 48
Designing of DC Microgrid with Fast Charging Converter and Control for Solar PV, Fuel Cell and Battery-Integrated Charging Station

Dheeraj Kumar Dhaked, Mayank Singh, and Dinesh Birla

Abstract Sustainable and environment-friendly transportation is need of the hour, and electrical vehicles (EV) are the only option for that. Slow charging time, lesser charging stations and grid instability are major cause for slow growth rate of EV. This charging station aims to reduce the dependency on grid during peak load time, and it will also be helpful where the grid power is not available. This paper has employed a high gain, fast charging DC/DC converter with controller for charging station of EV which contains solar PV, fuel cells (FC) and battery energy storage system (BESS). The converter and its controllers performance are validated with different renewable sources using MATLAB/Simulink tool, and the results for battery charging are presented along with dynamic response. The observed results are satisfactory for validation which gives higher charging current that led to less charging time.

Keywords Microgrid · Electrical vehicle · Fast charging · T-source converter · Battery charging

1 Introduction

Nowadays, EVs are continuously increasing at higher rate for daily transportation purposes. According to the estimates and predictions, more than 125 million EVs will be on road by the year 2030 [1]. Lithium-ion (Li-ion) battery is the core of these innovative vehicles where it stores the energy [2]. Numerous aspects have worked to increase the penetration of renewable sources with EV charging. These aspects are greenhouse gases consequences on environment, continuously reducing PV module prices, rapid technical advancement in EVs [3]. Fuel cell (FC) and solar PV are the outmost capable renewable energy power producing mechanisms. FC has sluggish response and reaction that shall be compensated with super-capacitor bank or battery storage system [4]. Out of various renewable energy sources, FC has been attracting power source for engineers because of its cleanliness, high efficiency and

D. K. Dhaked (✉) · M. Singh · D. Birla
Department of Electrical Engineering, RTU, Kota, India

G. Panda et al. (eds.), *Sustainable Energy and Technological Advancements*, Advances in Sustainability Science and Technology,
https://doi.org/10.1007/978-981-16-9033-4_48

profitable power source to consumers. The output of FC is DC in nature which can also be directly connected to the solar PV output, and it shall work as backup when standalone microgrid loads are considered [5, 6].

A microgrid system can be defined as an autonomous energy grid which shall operate independently or in parallel with conventional grid. Nowadays, the use of renewable energy resources (RER) integrated with microgrid is used across the world. In microgrid system, BESS is used as key component for stabilizing the voltage fluctuation. Mainly Li-on battery is used as storage system, but the lifetime of the Li-on battery is small for stable operation. Thus, to achieve long lifetime operation, a system for charging and discharging a battery is required [7–10]. The major obstruction in moving towards EV is time of recharge, battery size, instability of grid during peak load and inefficient power conversion. The above obstruction can be overcome by use of a system which has less dependency on the grid such as hybrid charging station. Therefore, more research is in practice by researcher and design engineer in the field of RERs connected EV charging system (EVCS) with a battery backup [11, 12]. The modelling of the battery can be classified into three major types. The first type is electrochemical modelling, and it gives high accuracy, but it is difficult to apply. The second type is mathematical modelling, and it can be applied in limited condition. The third and most common type is electrical modelling, and it is mainly used for implementing a battery in a charging system [13, 14].

There are two types of architecture used for charging stations, the first is AC architecture in which AC bus is used, and second is DC architecture in which DC bus is used [15, 16]. The general structure of DC bus architecture is represented in Fig. 1. In this architecture, energy sources are connected at one side of DC bus with the help of DC-DC converter, and another side of loads/charging EV is connected along with DC-DC converter. The converter used in the architecture is bidirectional DC-DC converters. Since last years, academicians and researchers have worked for EV charging methods, architectures and optimizations. Solar PV-based charging method is used for charging stations in [17–19]. Vehicle to grid method was proposed in [20] to sell energy back to grid, and same type of arrangement is described in [21] to inject excess energy to the grid. Paper [22] claims fast functioning outcomes and appropriate application at lower temperature, and reported FC is suitable for backup power with PV source. The architecture of fuel cell can be understood from paper [20]. The operation, control and performance of PV-FC hybrid system are demonstrated in [23]. A comparative study of AC and DC microgrid concept was reported in [24]. It is concluded that DC is more beneficiary because of safe operation, less power electronics (PE) conversion stages, no issues of reactive power control and high energy efficiency. PV-based energy management algorithm-based system is developed in [24]. The design of AC microgrid system also has some issues in synchronization along with frequency handling.

Various converters have already been reported in literature for charging purposes in different architectures, i.e. Z-source converter, multilevel converters [25], single stage bidirectional DC-DC Z-source inverter [26], quasi Z-source bidirectional DC-DC converter [27] and grid tied neutral point clamped [25]. A paper has also reported T-source inverter for solar PV grid tied system [28] that can boost and buck the

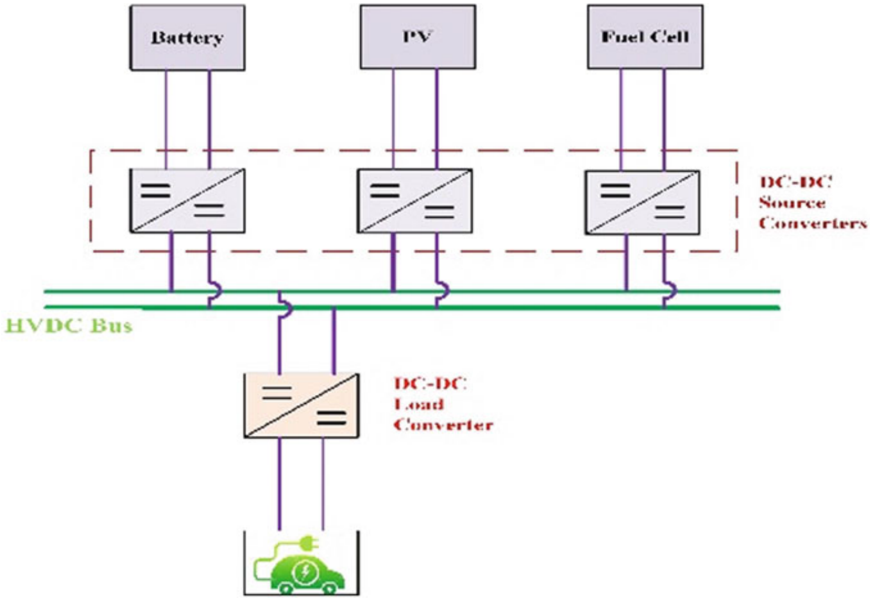

Fig. 1 Microgrid architecture for charging station

voltage according to required level with low output voltage ripple and input voltage along with easy control. A parallel three-level DC-DC converter with an integrated inductor was introduced for EV charging in [29, 30], but it has higher ripples due to high number of switching components, and three-phase hybrid boost converter was employed in [31] for same application that had less switching losses.

Above-mentioned converter had the drawbacks of slow dynamic response, reduced voltage gain because of discontinuous mode of operation, high number of elements that reducing reliability and increasing the switching losses, unable for bidirectional power flow, etc. Hence, the T-source inverter was employed that has less number of switches and conversion stages, fast dynamic response and high gain that motivated authors to work on this topology for EV charging. Various controlling schemes has also employed for control of converters in literature which are as; phase locked loop (PLL) based soft switching technique [32], phase disposition pulse width modulation (PD-PWM) [33], sliding mode control [34], SVPWM PI controller [35, 36] and a cascade two PI controller were used in residential buildings EV charging station [37] that had sluggish dynamic response and resulted in slow charging. Hereafter, getting these above-mentioned controllers, it was concluded that PI controller can filter noise and gives zero steady state error that mainly used in bidirectional control. This paper has also employed modified double PI controller for bidirectional T-source converter (TSC). TSC provides galvanic isolation for converter and loads that enhances voltage stability and power quality, and closed loop control gives lesser current ripples and current THD and gives high voltage gain with double PI controller.

2 Microgrid Arrangement

Fig. 1 shows that battery, solar PV and FC are used as source and TSC is used as DC/DC converter for getting the desired DC voltage level of grid. It has also used T-source bidirectional converter for charging and discharging purposes of EV and buffer battery (Fig. 2).

2.1 T-*Source Converter*

The TSC is a bidirectional DC-DC converter. The circuit of TSC is designed by combination of T-network, LC filter and switch. The T-network is formed by connecting two inductors ($L1$ and $L2$) which are mutually coupled and a capacitor in T-shape [38]. This converter is able to provide chosen DC voltage without any dependency on source voltage changes as in solar PV output changes due to weather conditions. The circuit diagram of the TSC is shown in Fig. 3. Depending on the switching condition, TSC is operated in two modes. The first mode of operation is

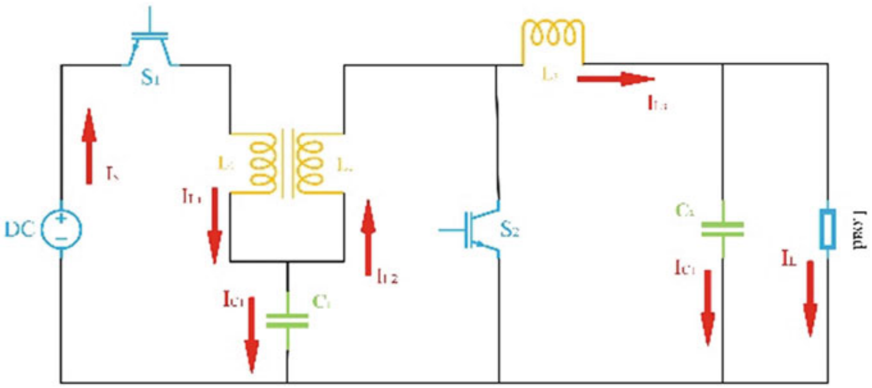

Fig. 2 T-source DC-DC converter circuit diagram

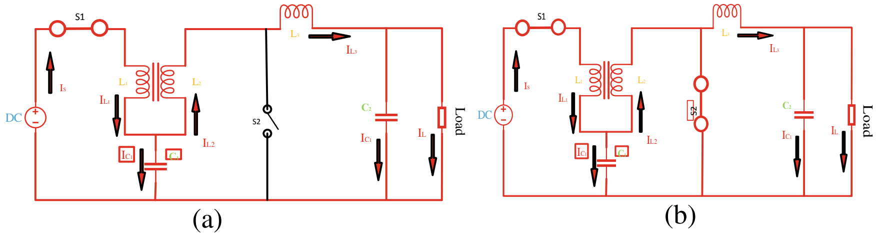

Fig. 3 TSC working modes. **a** NST mode, **b** ST mode

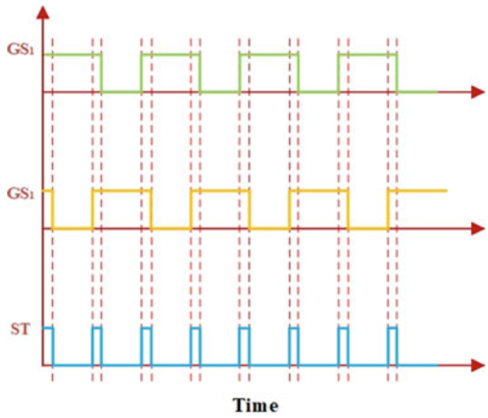

Fig. 4 Switching scheme for TSC

non shoot through (NST), while second is shoot through (ST), and the circuit diagram during these modes is shown in Fig. 4a, b, respectively.

During NST mode of operation, the switch S_1 is on, while switch S_2 is off. In this duration, energy is transferred from source side to load side, and output voltage varies according to switch ($S1$) duty ratio. Further, inductor of output side is energized, and input current charges the input capacitor. In ST mode, switch S_1 and switch S_2 both are in on state. During this duration, charge stored in capacitor C_1 and capacitor C_2 is transferred to inductor L_2 and inductor L_3, respectively.

The switching scheme for TSC is shown in Fig. 5, which is obtained from double PI control scheme. In double PI control scheme, both current and voltage are controlled, and hence, it contains very less ripples in output. Here, GS1 is gate pulse for the switch $S1$, GS2 is gate pulse for the switch $S2$, and ST is the shoot-through pulse signal. The duration for which the shoot-through pulse is low is the NST duration, and duration for which it is high is ST duration. The ST duration is the duration for which both the pulse signal GS1 and GS2 are high.

The voltage across capacitors and inductors (assuming both inductor identical) is given in Eqs. (1) and (2), respectively. The voltage across capacitor and inductors is given as

$$V_C = V_{C1} = V_{C2} \tag{1}$$

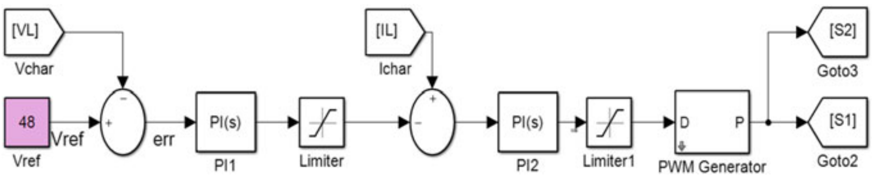

Fig. 5 Double PI control algorithm for T-source DC/DC converter

$$V_L = V_{L1} = V_{L2} \tag{2}$$

During NST mode,

$$V_{L1} = V_S - V_{C1} \tag{3}$$

$$V_d = V_{C1} - V_{L2} = 2V_{C1} - V_S \tag{4}$$

During ST mode, inductor voltage (V_L) and $S2$ voltage (V_d) are as

$$V_d = 0 \tag{5}$$

$$V_{L2} = V_{C1} \tag{6}$$

The switching time over a period is summation of the switching time of NST and ST time and given as shown in Eq. (7).

$$T = T_{nst} + T_{st} \tag{7}$$

By equating inductor voltage to zero over one cycle of period, the capacitor voltage is calculated and given by Eq. (8).

$$V_{C1} = \left(\frac{T_{nst}}{T_{nst} - T_{st}}\right)V_S = \left(\frac{1-D}{1-2D}\right)V_S \tag{8}$$

$$V_\mathrm{om} = \frac{1}{T}\int_0^T V_d(t)\mathrm{d}t = \frac{T_{st}.0 + T_{nst}(2V_{CZ} - V_S)}{T} \tag{9}$$

The relation between duty ratio and output voltage is given by Eq. (10)

$$V_{oD} = \left(\frac{T_{nst}}{T_{nst} - T_{st}}\right)V_S = \left(\frac{1-nD}{1-D(n+1)}\right)V_S \tag{10}$$

where $D = T_S/T$ is the shoot-through duty cycle ratio of converter.

2.2 Solar PV and Fuel Cell

The solar PV array is considered the most essential and prerequisite sustainable resource due to its free and abundant availability in the atmosphere. The solar power in the model mainly depends upon irradiance and ambient temperature. Solar cell radiation is measured by air mass, incident angle and radiation to measure cell power (S) given in Eq. 11 below:

The cell power is calculated by the help of Eq. (11)

$$S = M(G_b R_b (\tau\alpha)_b) + G_d (\tau\alpha)_d \frac{1 + \cos\beta}{2} + G_{pg} (\tau\alpha)_g \frac{1 + \cos\beta}{2} \tag{11}$$

Temperature and irradiance are two major factors on which solar power depends as given in Eq. (12).

$$T_{\text{mod}} = T_{\text{air}} + K_{\text{T}} G \tag{12}$$

Equation (13) gives the efficiency of cell

$$\eta_{\text{cell}} = \frac{I_{\max} * V_{\max}}{P_{\text{in}}} \tag{13}$$

The power output is given in Eq. (14) which is a function of temperature.

$$P = P(S, T_{\text{mod}}) \tag{14}$$

Equation (15) gives the cell output power in kWh.

$$P = \frac{P_{\text{peak}} * S}{1000} \tag{15}$$

FC is an electromechanical conversion device, in which electrical energy is produced from chemical energy with water and heat as by-products using H_2 energy. In existing research, proton exchange membrane fuel cell (PEMFC) is used due to its low-temperature operation suitability and quick response. The output voltage and power of fuel cell are calculated by the help of the Eqs. (16) and (17), respectively.

$$V_{\text{FC}} = E - V_{\text{act}} - V_{\Omega} - V_{\text{con}} \tag{16}$$

$$P_{\text{FC}} = N * V_{\text{FC}} * I_{\text{FC}} \tag{17}$$

The efficiency of fuel cell is given by Eq. (18)

$$\eta_{\text{FC}} = \frac{P_{\text{FC}}}{M_{\text{H}_2} \text{HHV}_{\text{H}_2}} \tag{18}$$

Here, M_{H2} is flow rate of fuel, and P_{FC}, I_{FC} and V_{FC} are FC power output and voltage. Nearly, a FC can yield 0.6–0.75 V, and the power and voltage level can fluctuate from 2 kW to 50 MW and a couple of volts to 10 kV [21], individually relying upon the connections and picked arrangements plan.

3 Simulation Model

The DC microgrid model was designed on MATLAB Simulink tool which has used solar PV, battery and FC as source along with TSC for connecting them to DC link of microgrid. The load or EV for charging was also connected to the DC link with bidirectional TSC. The double PI control scheme was designed for making it closed loop control with voltage and current of battery being charged. The outer voltage control loop regulates the voltage, and the inner loop ensures a ripple free charging current as shown in Fig. 6. Specification for TSC converter is given in Table 1. The battery was charged with each power source at different time, and once all the sources were used for charging the battery. The DC link voltage for microgrid was 48 V, and it is easy to connect each source with DC/DC converter with DC link. Battery used has the energy capacity of 100Ah with 48 V.

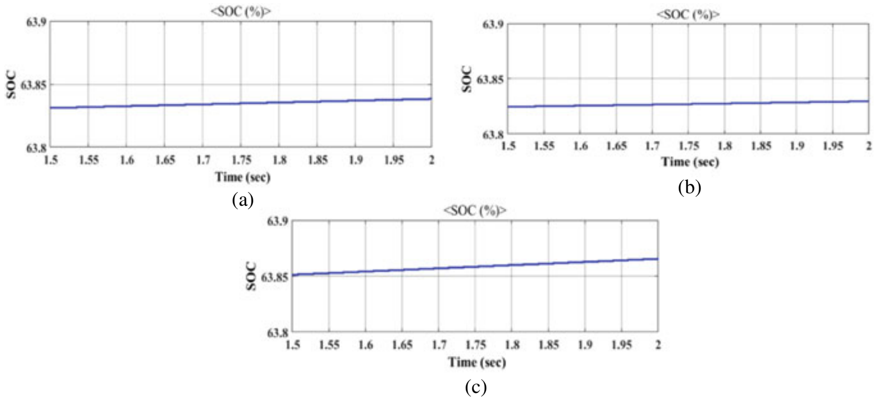

Fig. 6 SOC variation of battery during charge (**a**) with SPV (**b**) with FC (**c**) with DC source

Table 1 Specifications of TSC converter

TSC component	Specification
Switching frequency	2 kHz
Input voltage	200 V
Coupled inductor ratio	1:n
Inductor L_1 and L_2	5 mH
Capacitor C_1	300 µF
Capacitor C_o	220 µF

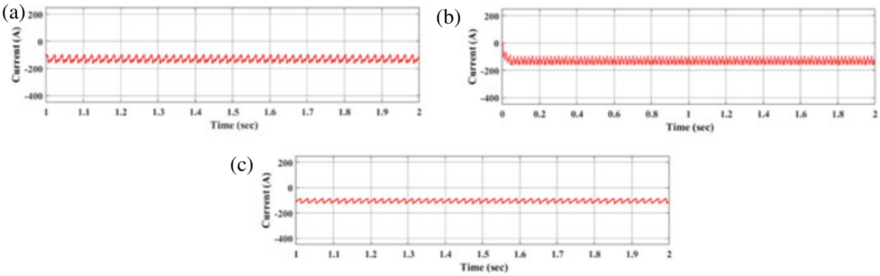

Fig. 7 Current of battery during charge (**a**) with SPV (**b**) with FC (**c**) with DC source

4 Result Analysis

The suggested architecture is designed according to Table 1 with different source of energy. Different sources connected to the battery along with TSC converter are discussed here, and charging performance is analysed in this section. The results obtained for state of charge (SOC) of the battery are represented in Fig. 7 in which Fig. 7a shows the result of battery with SPV source as an input, Fig. 7b shows the result of battery with FC as an input source and Fig. 7c shows the result of battery with DC source as an input. It is observed that battery is charged 0.007% (63.831–63.838%) in duration of 0.5 s (1.5–2.0) when connected with SPV source and is charged 0.005% (63.824–63.829%) in duration of 0.5 s (1.5–2.0) when connected with FC as an input source and charged 0.014% (63.851–63.856%) in duration of 0.5 s (1.5–2.0).

The result obtained for current flowing through battery is represented in Fig. 7 in which Fig. 7a shows the result when SPV is connected as input source and the current flowing is 106.9 A, Fig. 7b shows the result when FC is connected as input source and current flowing is 107.5 A, and Fig. 7c shows the result when DC source is connected as input source and current flowing is 106.7 A.

The result obtained for voltage of battery is represented in Fig. 8 in which Fig. 8a shows the result when SPV is connected as input source and the voltage is 52.47 V, Fig. 8b shows the result when FC is connected as input source and the voltage is 52.28 V, and Fig. 8c shows the result when DC source is connected as an input source and the voltage is 53.19 V.

5 Dynamic Response

The nature of renewable sources and load of the charging structure is variable as the charging vehicles at charging station possess connected/disconnected every time. Hence, it is important to find out the dynamic load checking of this converter. The TSC charging current is around 7–8% higher than conventional buck converter, when

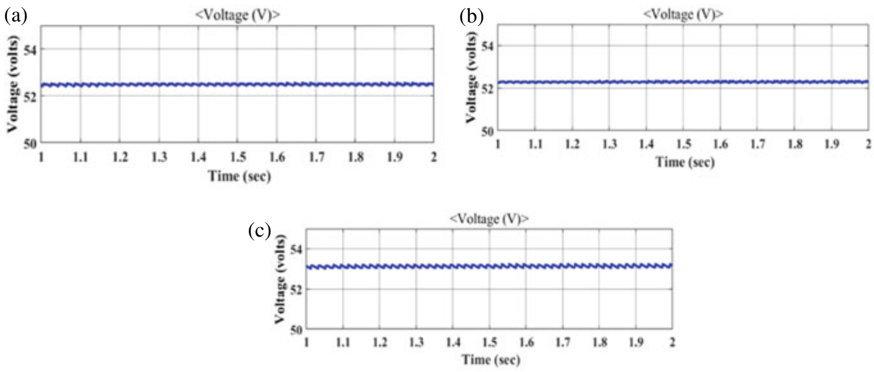

Fig. 8 Voltage of battery during charge (**a**) with SPV (**b**) with FC (**c**) with DC source

checked by comparing as shown in Fig. 9b. Higher gain offered due to impedance network of TSC is the reason behind higher charging current. The charging time reduces with TSC converter integrated charging arrangement as compared to other topologies as given in Table 2.

Figure 9a depicts the TSC charging voltage which is marginally greater than conventional buck converter with less ripples. Switching stress on TSC converter will reduce comparatively by this approach. Charging voltage and current are shown in Fig. 9a, b, and step change response in irradiance from 800 to 600 w/m^2 for buck and TSC is shown in Fig. 9c. The response time for TSC converter is around 50 ms, while buck converter has 250 ms which is five times higher. Figure 9c shows that at

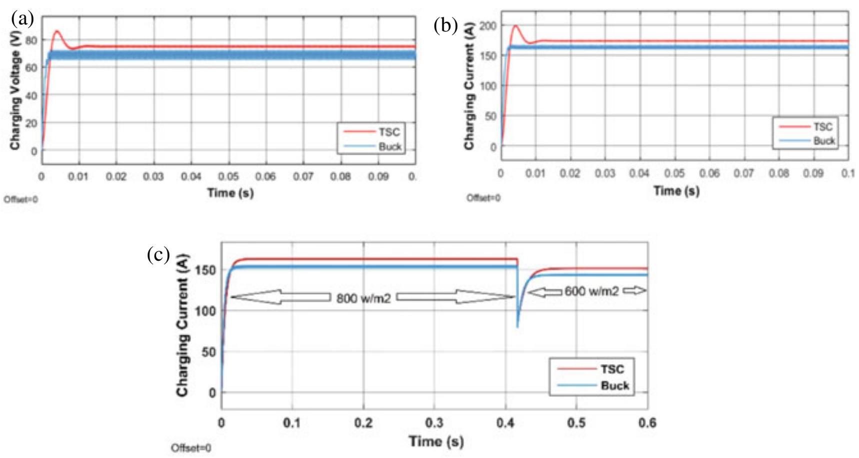

Fig. 9 Dynamic response of TSC. **a** Charging voltage. **b** Charging current. **c** Step change in solar irradiance

Table 2 TSC converter comparison with other DC-DC converter topologies

Parameter	Conventional buck converter	Interleaved boost converter	Z-source DC-DC converter	T-Source DC-DC converter
Gain	Very low	Maximum	High	Very high
Input current THD (%)	8.3	7.2	5.8	3.4
Current ripple (%)	12.5	12.5	<2.5	<2.5
Rise time (%)	1.02	1.08	2.02	1.05
Overshoot	High	Very high	Low	Very low
Charging time	Charging time is high due to low gain property	Charging time is very high	medium	Charging time is low due to high current gain

0.42 s during step change of solar irradiance the response goes for smooth transition for both converters, but it is comparatively less in response of TSC.

6 Conclusion

Fast charging stations are the need of hour for increasing EV on the roads, and TSC converter has been found that it is an ideal converter with double PI controller for charging the EV. This converter provides constant current and voltage for battery charging with low THD, reduced number of switches, less ripple, high gain and fast charging. The designed DC microgrid is also helpful for the charging purposes where the grid availability is not available/possible. DC microgrid with RERs is designed and simulated for EV charging purpose at MATLAB Simulink platform. The charging SOC results with different source of supplies show that the results are satisfactory. The dynamic response is also presented in the study for better understanding, and the fast charging is claimed on the basis of higher charging current, so it will take less time to charge battery than conventional buck converter.

References

1. Di Christopher T (2018) Electric vehicles will grow from 3 million to 125 million by 2030. International Energy Agency forecasts, CNBC
2. Dhaked DK, Gopal Y, Birla D (2019) Battery charging optimization of solar energy based telecom sites in India. Eng Technol Appl Sci Res 9(6):5041-5046
3. Bhagiya RD, Patel RM (2019) PWM based double loop PI control of a bidirectional DC-DC converter in a standalone PV/battery DC power system. In: 2019 IEEE 16th India Council International Conference (INDICON), pp 1–4, Dec 2019

4. Hosseini M, Dincer I, Rosen MA (2013) Hybrid solar–fuel cell combined heat and power systems for residential applications: energy and exergy analyses. J Power Sour 221:372–380
5. Kirubakaran A, Jain S, Nema RK (2009) A review on fuel cell technologies and power electronic interface. Renew Sustain Energy Rev 13(9):2430–2440
6. Samy MM, Barakat S, Ramadan HS (2019) A flower pollination optimization algorithm for an off-grid PV-fuel cell hybrid renewable system. Int J Hydrogen Energy 44(4):2141–2152
7. Deblecker O, Stevanoni C, Vallee F (2016) Cooperative control of multi-functional inverters for renewable energy integration and power quality compensation in micro-grids. In: 2016 International symposium on power electronics, electrical drives, automation and motion (SPEEDAM). IEEE, June 2016, pp 1051–1058
8. Dong J, Gao F, Guan X, Zhai Q, Wu J (2016) Storage-reserve sizing with qualified reliability for connected high renewable penetration micro-grid. IEEE Trans Sustain Energy 7(2):732–743
9. Fernandes NT, Demonti R, de Andrade J, de Melo PF, Bianchin CG, de Almeida AR, Lemos AR (2015) Control strategy for pulsed lead acid battery charger for stand-alone photovoltaics. In: 2015 IEEE 13th Brazilian power electronics conference and 1st southern power electronics conference (COBEP/SPEC). IEEE, pp 1–6, Nov 2015
10. Singh RK, Mishra S (2012) A digital optimal battery charger with the inbuilt fault detection property. In: 2012 IEEE international conference on power electronics, drives and energy systems (PEDES). IEEE, pp 1–6, Dec 2012
11. Gjelaj M, Hashemi S, Traeholt C, Andersen PB (2018) Grid integration of DC fast-charging stations for EVs by using modular li-ion batteries. IET Gener Transmiss Distr 12(20):4368–4376
12. Khan W, Ahmad F, Alam MS (2019) Fast EV charging station integration with grid ensuring optimal and quality power exchange. Eng Sci Technol Int J 22(1):143–152
13. Li X, Xiao M, Malinowski K, Choe S-Y (2011) State-of-charge (SOC) estimation based on reduced order of electrochemical model for a pouch type high power Li-polymer battery. In: Proceedings of the 7th IEEE vehicle power and propulsion conference (VPPC ’11), pp 1–6, Chicago, Ill, USA, Sept 2011
14. Li S, Ke B (2011) Study of battery modeling using mathematical and circuit oriented approaches. In: 2011 IEEE Power and Energy Society General Meeting. IEEE, July, pp 1–8
15. Bai S, Lukic SM (2013) Unified active filter and energy storage system for an MW electric vehicle charging station. IEEE Trans Power Electron 28(12):5793–5803
16. Rivera S, Wu B, Wang J, Athab H, Kouro S (2013) Electric vehicle charging station using a neutral point clamped converter with bipolar DC bus and voltage balancing circuit. In: IECON 2013-39th annual conference of the IEEE Industrial Electronics Society. IEEE, Nov 2013, pp 6219–6226
17. Le T, Phung BN (2021) Load shedding in microgrids with consideration of voltage quality improvement. Eng Technol Appl Sci Res 11(1):6680–6686
18. Guo Y, Xiong J, Xu S, Su W (2015) Two-stage economic operation of microgrid-like electric vehicle parking deck. IEEE Trans Smart Grid 7(3):1703–1712
19. Mouli GC, Bauer P, Zeman M (2016) System design for a solar powered electric vehicle charging station for workplaces. Appl Energy 168:434–443
20. Van Roy J, Leemput N, Geth F, Büscher J, Salenbien R, Driesen J (2014) Electric vehicle charging in an office building microgrid with distributed energy resources. IEEE Trans Sustain Energy 5(4):1389–1396
21. Alam M, Kumar K, Verma S, Dutta V (2020) Renewable sources based DC microgrid using hydrogen energy storage: modelling and experimental analysis. Sustain Energy Technol Asses 42:100840
22. Ghosh PC, Emonts B, Janßen H, Mergel J, Stolten D (2003) Ten years of operational experience with a hydrogen-based renewable energy supply system. Sol Energy 75(6):469–478
23. Lotfi H, Khodaei A (2015) AC versus DC microgrid planning. IEEE Trans Smart Grid 8(1):296–304
24. Mohamed A, Salehi V, Ma T, Mohammed O (2013) Real-time energy management algorithm for plug-in hybrid electric vehicle charging parks involving sustainable energy. IEEE Trans Sustain Energy 5(2):577–586

25. Rivera S, Wu B, Kouro S, Yaramasu V, Wang J (2014) Electric vehicle charging station using a neutral point clamped converter with bipolar DC bus. IEEE Trans Ind Electron 62(4):1999–2009
26. Omran KC, Mosallanejad A (2018) SMES/battery hybrid energy storage system based on bidirectional Z-source inverter for electric vehicles. IET Electr Syst Transp 8(4):215–220
27. Zhang Y, Liu Q, Gao Y, Li J, Sumner M (2018) Hybrid switched-capacitor/switched-quasi-Z-source bidirectional DC–DC converter with a wide voltage gain range for hybrid energy sources EVs. IEEE Trans Ind Electron 66(4):2680–2690
28. Sivaraman P, Prem P (2017) PR controller design and stability analysis of single stage T-source inverter based solar PV system. J Chin Inst Eng 40(3):235–245
29. Tan L, Zhu N, Wu B (2015) An integrated inductor for eliminating circulating current of parallel three-level DC–DC converter-based EV fast charger. IEEE Trans Ind Electron 63(3):1362–1371
30. Prabhakar S, Febin Daya JL (2016) A comparative study on the performance of interleaved converters for EV battery charging. In: 2016 IEEE 6th International conference on power systems (ICPS). IEEE, pp 1-6, Mar 2016
31. Tazay A, Miao Z (2018) Control of a three-phase hybrid converter for a PV charging station. IEEE Trans Energy Convers 33(3):1002–1014
32. Reis FE, Bascopé RP, Tofoli FL (2018) Bidirectional three-phase 3L-SNPC converter for EV charging stations. In: 2018 13th IEEE International conference on industry applications (INDUSCON). IEEE, pp 298–304, Nov 2018
33. Ibanez FM, Echeverria JM, Astigarraga D, Fontan L (2015) Soft-switching forward DC–DC converter using a continuous current mode for electric vehicle applications. IET Power Electron 8(10):1978–1986
34. Serna-Garcés SI, González Montoya D, Ramos-Paja CA (2018) Control of a charger/discharger DC/DC converter with improved disturbance rejection for bus regulation. Energies 11(3):594
35. Lai CM, Cheng YH, Hsieh MH, Lin YC (2017) Development of a bidirectional DC/DC converter with dual-battery energy storage for hybrid electric vehicle system. IEEE Trans Veh Technol 67(2):1036–1052
36. Qu KQ, Niu QQ, Yang C, Zhao JB (2013) Battery charge-discharge control strategy based on the single Z-source three-level SVPWM inverter. In: 2013 IEEE International conference on applied superconductivity and electromagnetic devices. IEEE, pp 30–33
37. De Melo HN, Trovao JPF, Pereirinha PG, Jorge HM, Antunes CH (2017) A controllable bidirectional battery charger for electric vehicles with vehicle-to-grid capability. IEEE Trans Veh Technol 67(1):114–123
38. Prem P, Sivaraman P, Sakthi Suriya Raj JS, Jagabar Sathik M, Almakhles D (2020) Fast charging converter and control algorithm for solar PV battery and electrical grid integrated electric vehicle charging station. Automatika 61(4):614–625

Chapter 49
Location Estimation of Grid Electric Vehicle Aggregator in the Grid System Using Optimization Technique

Pravat Kumar Ray, Pratap Sekhar Puhan, and Premananda Sahoo

Abstract Grid electric vehicles are the future alternatives of diesel and petroleum vehicle. They are connected to the grid through the arrangement of aggregator. Selection of suitable location for aggregator to the grid where vehicle should be connected is one of the important researches in this area. This paper addresses three optimization algorithms such as genetic algorithm (GA), artificial bee colony (ABC) and particle swarm optimization (PSO) to determine the location of the aggregator to the grid where the electric vehicle should be connected so that power loss will be minimum and compare the outcome obtained from all these three methods individually. Estimation of the actual location is analysed by the iterations followed by all the optimization algorithm, and finally, a comparative analysis is presented between these three optimization techniques, and the superiority of the PSO in comparison with the GA and ABC is analysed and proved.

Keywords GEV · V2G · GA · ABC · PSO

1 Introduction

With constantly expanding worries on natural issues and clean energy, the electric vehicle has pulled in increasingly more regard for industries, governments and customers. In the previous years, EV advances optimizing on various EVS segments like batteries, power devices, drive frameworks, on-board renewable energies and electric machines [1–3]. Due to the recent development in the smart grid, an electric vehicle can play a vital role by transferring energy back to the grid known as vehicle to grid at peak hours when the energy demand is more than the energy production.

P. K. Ray · P. Sahoo
Department of Electrical Engineering, National Institute of Technology, Rourkela, India
e-mail: rayp@nitrkl.ac.in

P. S. Puhan (✉)
Department of Electrical and Electronics Engineering, Sreenidhi Institute of Science and Technology, Hyderabad 501301, India
e-mail: pratapsekhar@sreenidhi.edu.in

G. Panda et al. (eds.), *Sustainable Energy and Technological Advancements*,
Advances in Sustainability Science and Technology,
https://doi.org/10.1007/978-981-16-9033-4_49

Moreover, the bidirectional charger has a DC link capacitor which can provide reactive power support to the grid [4–7] So, basically, during charging time, the grid electric vehicle is getting charged by the grid, and during the discharging period, the electric vehicle is providing energy back to the grid. Renewable energy power sources have high effectiveness from source to end-users compare to conventional [7–11], and there is a possibility that when energy production by renewable sources is maximum and demand is minimum, so storing that energy is also essential. At this moment, electric vehicle plays a vital role to keep that additional energy. There is another possibility that when energy production by the renewable source is minimum and demand is maximum at this moment, electric vehicles should act as V2G mode [12] where it can provide energy back to the grid by getting some extra incentive by every electric vehicle user.

Renewable-based solar and wind inputs are not constant throughout the day, and it can affect the active power, reactive power, frequency and voltage of the grid [8, 12]. Furthermore, in suburban areas where small-scale renewable resources are integrated, this compensation becomes more difficult. A single GEV is an excellent candidate for power compensation in the home grid [7, 8]. GEVs are also a viable option for supporting community-grid operations [9, 11, 12]. EV growth results the construction of an increasing number of charging stations in the near future. An increase in the number of EVs causes more strain on power systems, compromising the supply's stability and safety. The impact of EV charging and discharging on power systems has been established in studies [12].

This paper is organized as follows, Sect. 2 of the paper presents location of GEV aggregation, and Sect. 3 presents power quality issues in the grid and discusses the different optimization technique; Sect. 4 and 5 present the result discussion and conclusions, respectively.

2 Location of GEV Aggregation

The energy capacity of a single GEV is small, and controlling a single electric vehicle for grid operation will not affect the grid to a large extent. But if they are clustered together, their energy content will be added up, which can affect the grid power [11]. The fitness function of the aggregator's optimum position by considering minimum power loss is as follows (Fig. 1):

$$\text{Fitt} = \min \sum_{i=0}^{n} \left(\frac{P_i^2 + Q_I^2}{v_i^2} \right) * r_{i+1} \tag{1}$$

According to this fitness function, the actual objective function will be evaluated by minimizing the total power loss of the system. An aggregator $\left(P_{\text{agg}}\right)$ and load (P_L) are connected at bus $i+1$, and a unit circuit to measure power loss between buses i and bus $i+1$ is shown in Fig. 2.

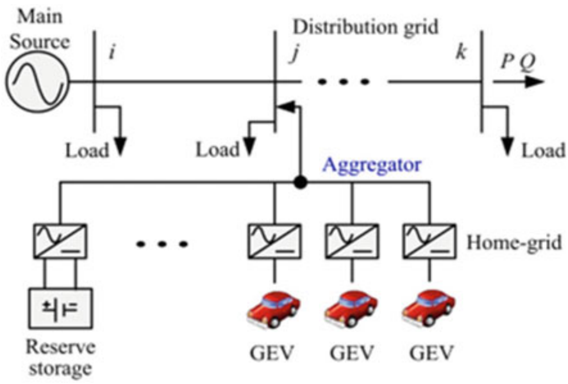

Fig. 1 GEV aggregation for the V2G system

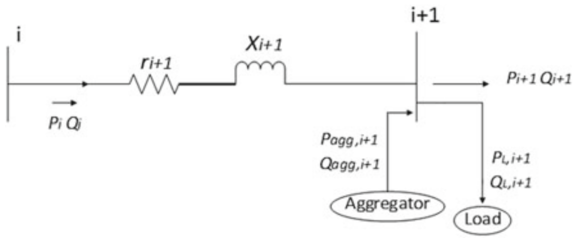

Fig. 2 Unit circuit of power flow between two bus

$$P_{\text{Loss},i,i+1} = P_i - Q_{i+1} = \left(\frac{P_i^2 + Q_i^2}{V_i^2}\right) * r_{i+1} \tag{2}$$

$$P_i - P_{L,i+1} - \left(\frac{P_i^2 + Q_I^2}{V_i^2}\right) * r_{i+1} - P_{i+1} + W_p P_{\text{agg}.i+1} - P_{i+1} = 0 \tag{3}$$

$$Q_i - Q_{L,i+1}, -\left(\frac{p_i^2 + Q_i^2}{v_i^2}\right) * x_{i+1} - Q_{i+1} + W_Q Q_{\text{agg},i+1} - Q_{i+1} = 0 \tag{4}$$

$$V_{i+1}^2 = V_i^2 - 2 * (r_{i+1} * p_i + x_{i+1} * Q_i) + \left(\frac{P_i^2 + Q_i^2}{V_i^2}\right) * \left(P_i^2 + Q_{Ii}^2\right) \tag{5}$$

$$|V_{\min}| \le |V_i| \le V_{\max} \tag{6}$$

$$\begin{aligned}
&\text{SOC}'_{x.\max} \le \text{SOC}_{\max} \\
&\text{SOC}'_{x\min} \ge \text{SOC}_{\min} \\
&0 \le C_{c,x} \le \left(\text{SOC}'_{x,\max} 0 \text{SOC}_x\right) C_x \\
&0 \le C_{d,x} \le \left(\text{SOC}_x - \text{SOC}'_{x,\min}\right) C_x
\end{aligned} \tag{7}$$

The following are summarized considering the parameters and practical considerations in terms of GEV aggregation: where Eq. (2) shows the power loss between bus i and bus $i+1$, Eqs. (3)–(5) at bus i, and (6) and (7) upper limit and lower limit of the bus voltage, the available discharging and charging capacities. The charging and discharging state of GEV is expressed as follows:

$$\begin{aligned} C_{\text{out}} &= \text{TC}_d + \text{TC}_c \\ &= \sum_{x=1}^{k} U_x \varphi_x C_{dx} + \sum_{x=k+1}^{l} \varphi_x \left(\text{SOC}_{x,\max}^{1}\right) C_x - \sum_{x=k+1}^{l} \varphi_x \left(\text{SOC}_{x,\max}^{l} - \text{SOC}_x\right) C_x \\ & k \le l \le m \end{aligned} \tag{8}$$

$$f_{cd} = \frac{c_{\text{out}}}{|\text{Tc}_d| + |\text{TC}_c|} = \frac{\text{TC}_d + \text{TC}_c}{|\text{TC}_d| + |\text{TC}_c|} \tag{9}$$

$$\begin{aligned} & f_{cd} > 0, \text{discharging} \\ & f_{cd} = 0, \text{Isolated} \\ & f_{cd} < 0, \text{charging} \end{aligned} \tag{10}$$

Figure 3 shows the flowchart to be followed to get the actual location of GEV aggregation in the grid system, and $\text{f}_{\text{cd}} f_{cd}$ determines the charging–discharging feature of an aggregation system.

3 Proposed Optimization Technique

In this work, three optimization techniques are used to identify the suitable location of the grid for electric vehicle charging.

Figure 4 shows that the values of input parameters for which the best optimum output can be determined to form the basis of the optimization process.

3.1 Genetic Algorithm

In this work, initialization of the parameter is carried out with upper and lower bounds. Then in each iteration, three steps such as tournament selection, crossing over, mutation to be followed to find out the optimal value of the function and the corresponding parameter value for which the function is providing the optimal value (Fig. 5).

The flowchart of the proposed genetic algorithm implementation is shown in Figs. 6 and 7 which shows that genes from location 8–12 of parent string1 got exchanged with location 8–12 of parent string 2. The crossover site will be selected randomly (Fig. 8).

$$M = \{(2u)^{\frac{1}{C+1}}, \; If\, u \le 0.5 \quad \left(\frac{1}{2(1-u)}\right)^{\frac{1}{C+1}}, \text{ otherwise} \tag{11}$$

where C is the probability distribution means for crossover.

Offspring is generated as

$$O_1 = [(1+M)X_1 + (1-M)X_2], \tag{12}$$

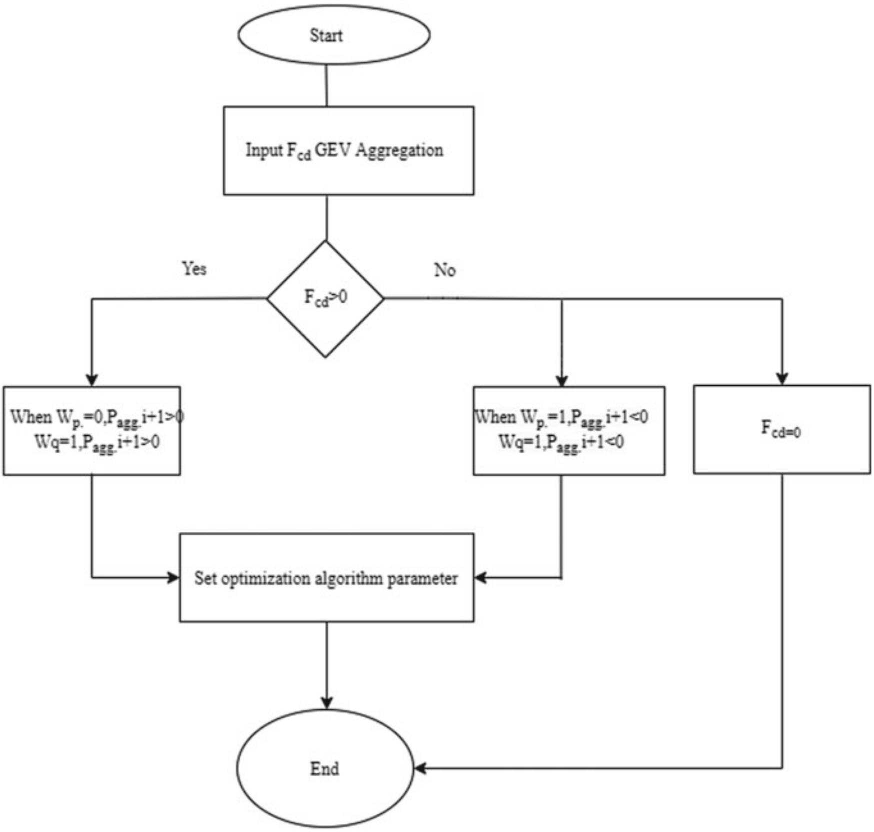

Fig. 3 Flowchart of optimal sizing of GEV aggregation

Fig. 4 Optimization process

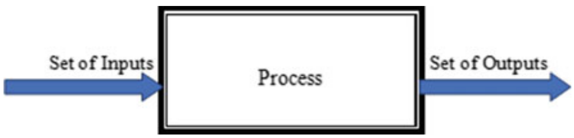

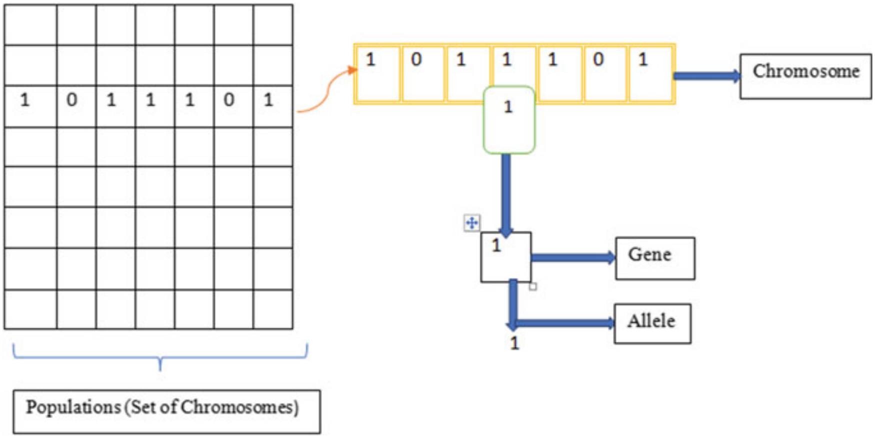

Fig. 5 Basic overview of fundamental of genetic algorithm

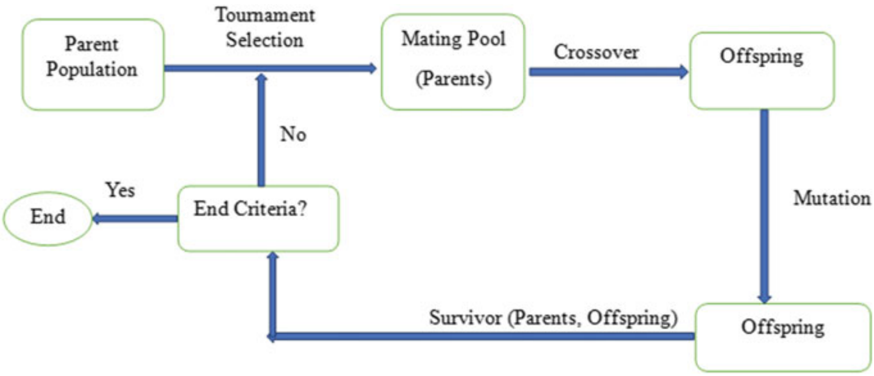

Fig. 6 Different stages of the genetic algorithm

Fig 7 Crossing over process

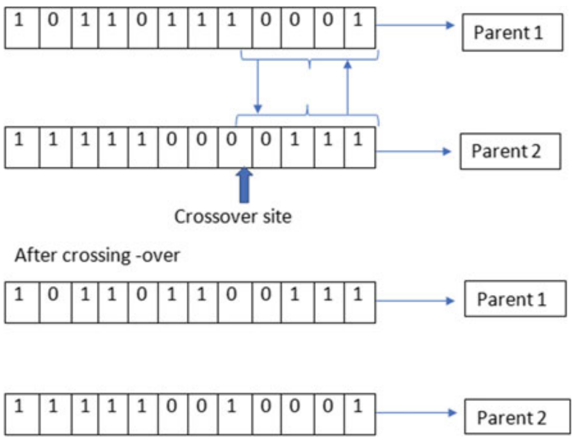

Fig 8 Mutation process

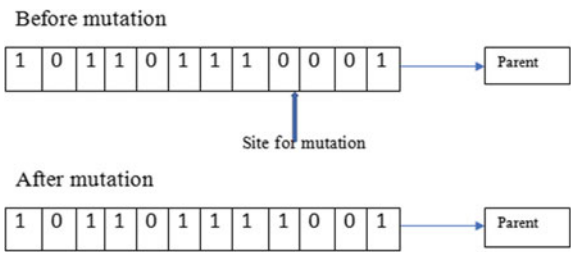

$$O_2 = [(1 - M)X_1 + (1 + M)X_2] \tag{13}$$

where X_1 parent 1 and is X_2 is parent 2, O_1 is offspring 1, and O_2 is offspring 2

$$\begin{aligned} d &= \{(2r)^{\frac{1}{v+1}}, Ifr \leq 0 \\ &(1 - [2(1 - r)])^{\frac{1}{v+11}} \text{otherwise} \end{aligned} \tag{14}$$

where v is the probability distribution means for mutation, offspring is generated as

$$Y = O + (\text{up} - \text{lb})d \tag{15}$$

where Y is offspring generated after mutation, O is the offspring after crossover, ub is upper bound, lb is lower bound.

3.2 *PSO Algorithm*

It is a population-based optimization method influenced by a flock of birds and many fish searching for their food in a unique direction. PSO takes what it learns from the example and applies it to optimization problems [8, 9].

Figure 9 shows the pictorial view of particle swarm optimization where the red dot indicates the particle position at different iteration. The performance of the algorithm and the process of updating the parameter are presented in mathematical equations. The different stages of the algorithm are shown in Fig. 10

Let V = Velocity of each particle, P = Position of each particle.

P_{best} = Personal best of each particle, G_{best} = Global best of all particle.

For velocity update

$$V_{K+1} = Wt * V_K + \text{rand}(0, 1) * C1 * (P_{\text{best}} - X_k) + \text{rand}(0, 1) * C_2 * (G_{\text{best}k} - X_K) \tag{16}$$

For position update

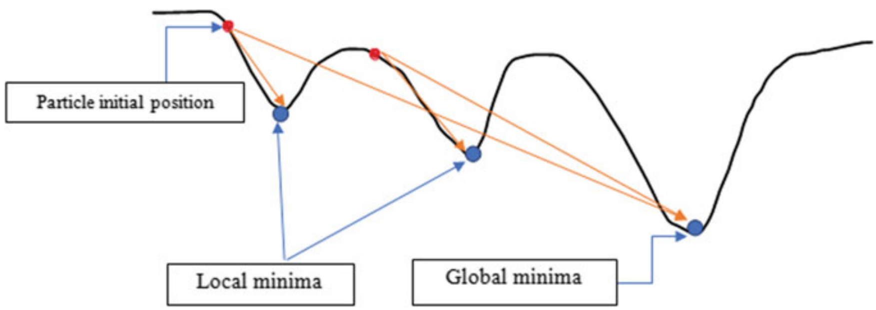

Fig. 9 Particle swarm optimization pictorial view

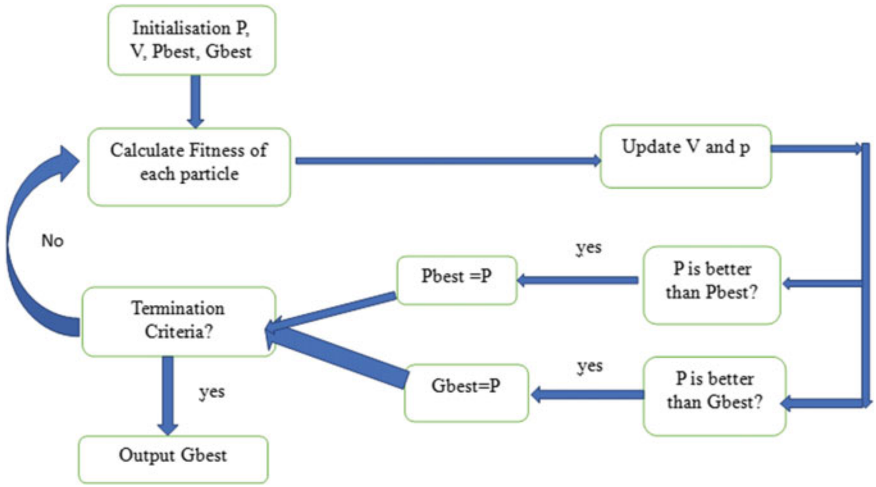

Fig. 10 Different stages of particle swarm optimization sequentially

$$X_{K+1} = X_K + V_{K+1} \tag{17}$$

where Wt is inertia weight and $wE[1- > 0.5]$.

C_1 is the learning rate of P_{best} and $C_1 \in [2.5- > 0.5]$ as the particle has to achieve their personal best first, which is shown as local best in Fig. 9, and C_2 is the learning rate of G_{best} and $C_2 \in [0.5- > 2.5]$ as the particle has to move slowly and steadily towards the optimum global value which is shown as local best in Fig. 10. Value of C_1 is different for different iteration, which is given as:

$$C_1 = 2.5 + (0.5 - 2.5) * \left(\frac{t}{T}\right)$$

$$C_2 = 0.5 + (2.5 - 0.5) * \left(\frac{t}{T}\right)$$

is different for different iteration which can be expressed as, where t = Current iteration, T = Iterations in total.

3.3 Implementation of Artificial Bee Colony Algorithm

This technique is first formulated by Dervis Karaboga in 2005. The colony in the ABC algorithm-based model is made up of three types of bees [3]. Here e employed bee is available for each available source of food. As a result, every possible answer serves as a food source, and the best solution can be found [3] using the mathematical analysis; the corresponding flowchart is shown in Fig. 11

Let, f = Functional value of each particle, fit = Fitness value of each particle

$$p_i = \frac{\text{fit}_i}{\sum_{n=1}^{n} \text{fit}_n} \tag{18}$$

$$\begin{aligned} \text{fit} &= \frac{1}{1+f} \text{if} - -f \geq 0 \\ &= 1 + |f|, if - -f < 0 \end{aligned} \tag{19}$$

$$X_{\text{new}} = X_e + \varphi(X_e - X_P), \varphi \in [-1, 1] \tag{20}$$

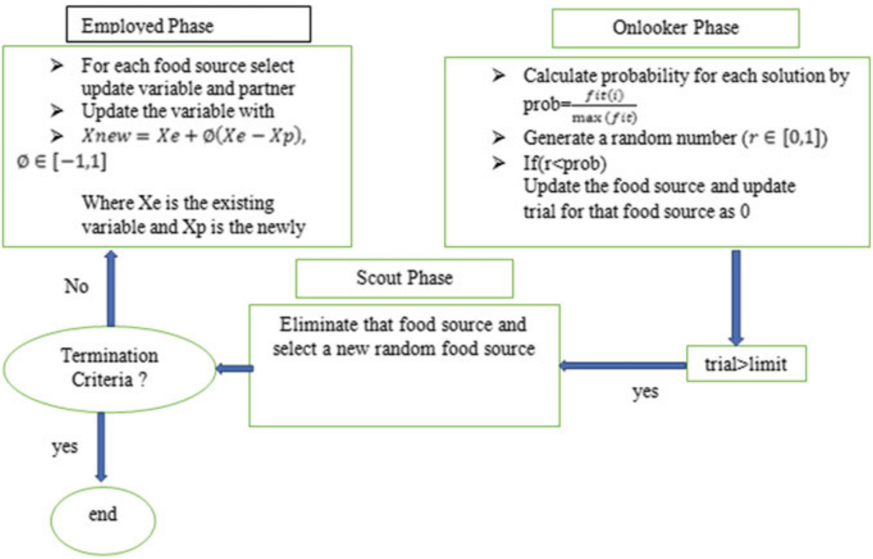

Fig. 11 Flowchart of artificial bee colony

where X_e and X_p denote the newly discovered partner, which correspond to the food source available in the searched region.

4 Results and Analysis

In this section, the results obtained using three optimization techniques have been presented.

Case-1 Genetic Algorithm (GA).

First, genetic algorithm optimization techniques are implemented to optimize the objective function for maintain the different parameters such as active power flow, reactive power flow and voltage at the aggregator location for minimization of power loss.

It is observed from Fig. 12a–c, active power is require only 10 iterations to optimize the objective function whereas reactive power and voltage necessitates 70 iteration, which is not suitable for achieving optimized value with one objective function as the iteration of the parameters are not constant, so it requires more objective function which is not desirable.

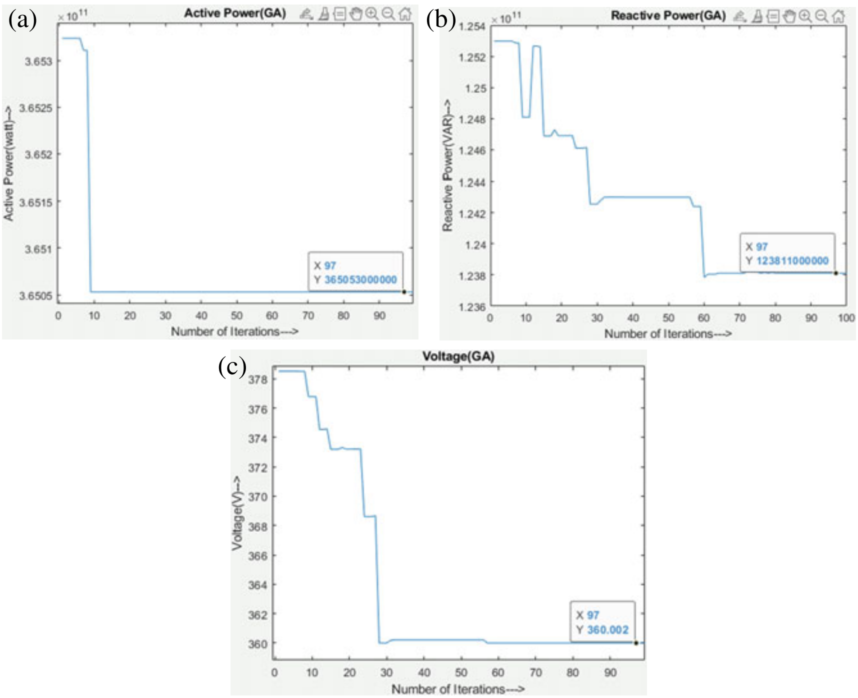

Fig. 12 **a**–**c** Active power curve, reactive power curve, voltage curve using GA

Case-2 Artificial Bee Colony (ABC).

Artificial bee colony (ABC) optimization techniques are implemented to optimize the objective function to achieve minimum power loss at aggregator, but from the below curves from Fig. 13a–c, it is observed that, more iteration above 70 is required for active power and voltage optimization, whereas only 10 itineration is required for reactive power, so this method is not suitable to optimize one objective function.

Case-3 Particle Swarm Optimization Algorithm (PSO).

Particle swarm optimization (PSO) techniques are implemented to optimize the objective function to achieve minimum power loss at aggregator.

From Fig. 14a–c, it is clearly observed that optimization of the objective function is well-achieved as the three parameters active power flow, reactive power flow and voltage is optimized with the same iterations. So it is suitable for choosing the optimal location.

A comparative analysis is presented for clear understanding of the optimization of objective function in Table 1. In case of GA and ABC, for every parameter number of iterations is not constants to achieve optimized objective function but in PSO, for every parameter number of iterations are fixed in between 25 and 30, which

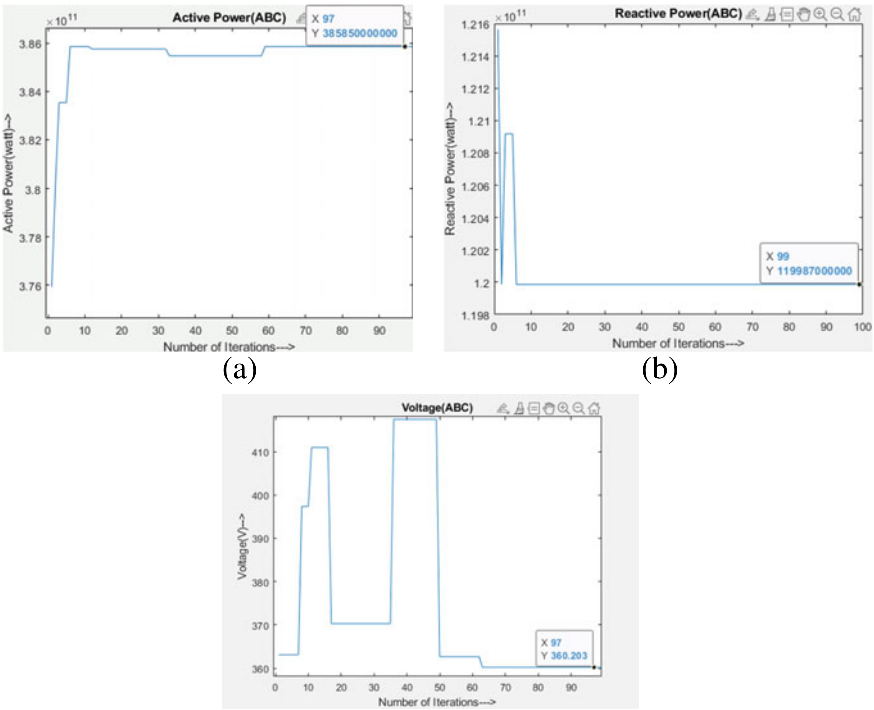

(c)

Fig. 13 **a**–**c** Active, reactive power curve, voltage curve using ABC

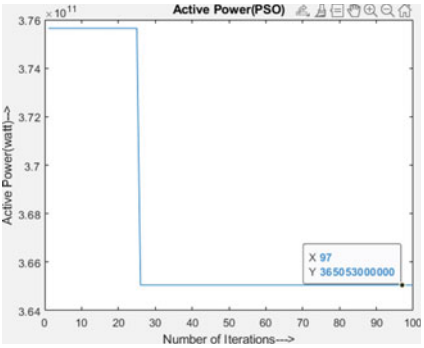

(a)

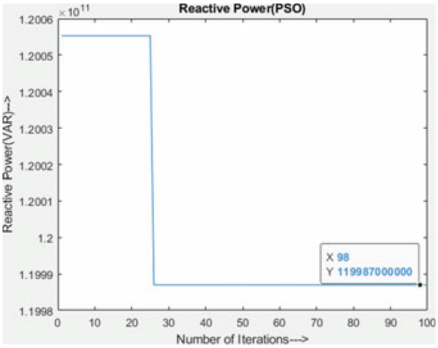

(b)

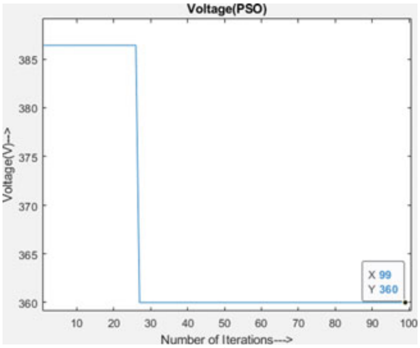

(c)

Fig. 14 **a–c** Active power curve, reactive power curve, voltage curve using PSO

Table 1 Number of iteration for optimization of objective function with different algorithms.

Number of iteration for optimization of objective function	GA	ABC	PSO
Active power flow	10	70	25–30
Reactive power flow	60–70	10	25–30
Voltage	70	70–80	25–30

indicates the best optimization technique to implement for location estimation of the aggregator for grid electric vehicle.

5 Conclusions

The location of the aggregator for grid vehicle aggregation is evaluated using three different optimization algorithms such as GA, PSO and ABC. A comparative analysis is made between the three optimization algorithms to optimize the objective function for which the parameters such as active power flow, reactive power flow and voltage will be optimized with same iteration numbers. It is concluded that PSO gives better results in comparison with GA and ABC for optimization of the objective function, and hence, parameter as the number of iterations for all the parameter is within 25–30 but in case of GA and ABC, number of iteration not fixed and it is also more than 70 which require more objective function to be optimized, so PSO is suitable technique for choosing the best location of the aggregator in GEV. The work can enhance in future with other techniques.

References

1. Liu C, Chau KT, Zhang Z (2012) Novel design of double-stator single-rotor magnetic-geared machines. IEEE Trans Magn 48(11):4180–4183
2. Liu C, Chau KT (2012) Electromagnetic design and analysis of double-rotor flux-modulated permanent-magnet machines. Prog Electromagn Res 131:81–97
3. Kanjiya P, Khadkikar V (2013) Enhancing power quality and stability of future smart grid with intermittent renewable energy sources using electric springs. In: International Conference on Renewable Energy Research and Applications, Madrid, Spain, pp 918–922
4. Deshpande A, Karnataki K, Darshana K, Deshpande P, Shankar G (2015) Smart renewable energy micro-grid for indian scenarios. International Conference on Advanced Computing and Communication, Chennai, pp 22–26
5. Yu J, Wang S, Teng X, Tu M, Ding Q (2019) Frequency regulation market clearing strategy considering renewable energy generation performance risks. In: IEEE Asia Power and Energy Engineering Conference, pp 278–284
6. Juul N, Meibom P (2012) Road transport and power system scenarios for Northern Europe. Appl Energy 92:573–582
7. Ortega-Vazquez MA, Silva V (2013) Electric vehicle aggregator/system operator coordination for charging scheduling and services procurement. IEEE Trans Power Syst 28(2):1806–1815
8. Qian K, Zhou C, Allan M, Yuan Y (2015) Modelling of load demand due to EV battery charging in distribution system. IEEE Trans Power Syst 26(2):802–810
9. Zhang P, Qian K, Zhou C, Stewart BG, Hepburn DM (2012) A methodology for optimization of power systems demand due to electric vehicle charging load .IEEE Trans Power Syst 27(3):1628–1636
10. Burke AF (2007) Batteries and ultracapacitors for electric, hybrid, and fuel cell vechile. In: Proceeding IEEE 95(4):806–820
11. Liu C, Chau KT, Wu D, Gao S (2013) Opportunities and challenges of vehicle-to-home, vehicle-to-vehicle, and vehicle-to-grid techn. Proc IEEE 101(11):2409–2427
12. Kanamaru Y, Amemiya Y (1991) Numerical analysis of magnetic field in superconducting magnetic energy storage. IEEE Trans Magn 27(5)

Chapter 50
Power Management and Control in Microgrid System

Emmanuel Vemuri, Aman Kumar, Ifthakhar Mahmud Tonmoy, Kaibalya Prasad Panda, Satyavarta Kumar Prince, Babu P. Narendra, and Gayadhar Panda

Abstract This work presents grid-connected and islanded microgrid system for power management and power quality improvement by regulating the voltage and frequency using power management and grid-interfacing control schemes. The proposed system relies on an optimization problem. The load energies are optimally managed using proposed control scheme. In the optimization problem, the network constraints, RESs, distributed resources are considered. The microgrid system's voltage and frequency are optimally regulated for different load profiles. Different parameters like line-phase voltages and currents, line frequency, load power factor, power, and net energy metering in the microgrid are measured. Algorithms is used to predict the over-voltage and under-voltage via defined thresholds for voltages and currents with reference to a preset value and thus automates the system and ensures the protection of the connected loads. The simulation analysis is performed using

This research work is supported by the Department of Science and Technology (DST). This is a project sponsored by the Government of India under grant EMR/2017/001880.

E. Vemuri · A. Kumar · I. M. Tonmoy · K. P. Panda · S. K. Prince (✉) · B. P. Narendra · G. Panda
Department of Electrical Engineering, National Institute of Technology Meghalaya, Shillong, Meghalaya793003, India
e-mail: skprince251988@gmail.com

E. Vemuri
e-mail: b17ee033@nitm.ac.in

A. Kumar
e-mail: b17ee035@nitm.ac.in

I. M. Tonmoy
e-mail: b17ee037@nitm.ac.in

K. P. Panda
e-mail: kaibalyapanda@nitm.ac.in

B. P. Narendra
e-mail: narem.perumal@nitm.ac.in

G. Panda
e-mail: gayadhar.panda@nitm.ac.in

G. Panda et al. (eds.), *Sustainable Energy and Technological Advancements*, Advances in Sustainability Science and Technology,
https://doi.org/10.1007/978-981-16-9033-4_50

MATLAB/Simulink platform under several transient conditions which shows the potency of the control scheme during dynamic conditions.

Keywords Power quality · PV system · Microgrid · Power management · Battery energy system

1 Introduction

In today's world, millions of residential, commercial, and industrial customers of electrical energy are dependent on the traditional grids which consist of the existing power generating plants, transmission, and distribution systems [1, 2]. For the traditional grids, the ultimate source of power generation is fossil fuel, coal, and natural gas which adversely affects the environment and also creates intense pressure on the natural resources [3]. For the transition of energy of the conventional power systems, a microgrid is becoming a promising solution in providing renewable and clean electrical energy by integrating with various distributed energy resources (DERs) and energy-storage systems (ESSs) [4].

Growing focus on electricity generation from renewable energy sources, public awareness about pollution, sensitivity of consumers' loads to power quality events on the grid and varying electricity prices have introduced the concept of microgrids into electric distribution systems [5]. In modern distribution systems, microgrids are one of the essential components to be considered in designing the system-level energy management strategies. In case of a microgrid, balancing the energy supply and demand while ensuring the rational priorities of individual energy resources is a challenging task [6]. These necessitate the intervention of optimal decision-making, which is usually performed by an energy management system (EMS) that balances the energy supply and demand by efficiently configuring the available energy resources. The emerging concept of the smart grid (SG) aims toward new ideas, services, and products that encourage consumers to actively participate in the energy management strategies, contributes toward power quality, and promotes high penetration of renewable energy sources integrated with ESSs [7]

The unstable and fluctuating nature of weather-driven sources like solar and wind energy, as well as random user behaviors has introduced significant uncertainties to the microgrid system, which makes the energy management of the microgrid a difficult task. For such a situation, demand side resources (DSRs) have been considered as a new type of distributed resources to provide the required energy storage or reserved power for the system [8]. The diversification and intelligent development of the DSRs are creating new challenges as well as opportunities to the optimal operation of the microgrid system [9]. Given the requirement of making the best use of DSRs, demand side management (DSM) is a viable solution to achieve the potential of DSRs, which has been also considered to be one paradigm for dealing with variable uncertain renewable generations [7]. With the purpose of addressing the uncertainties and coordinating the DSRs in the microgrid, the effective DSM

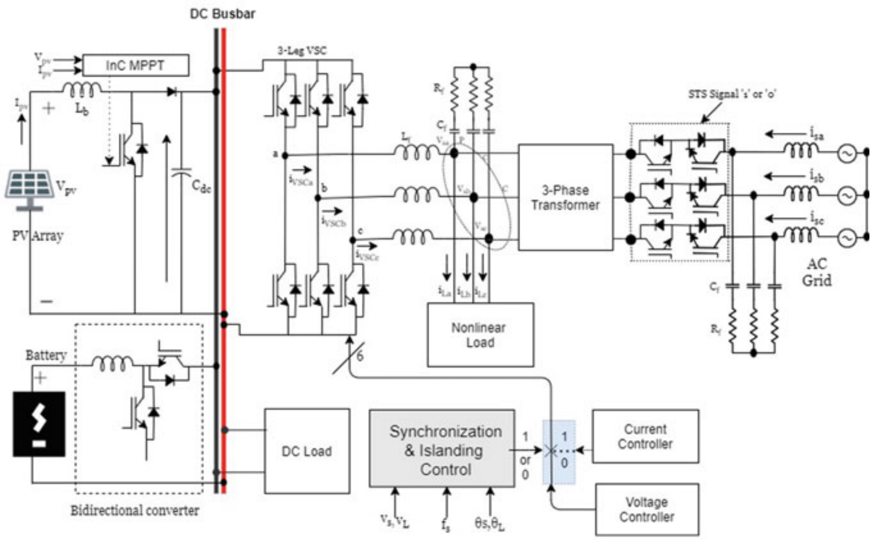

Fig. 1 Schematic of the microgrid system

design has become a subject of significant ongoing research. Several papers have been published on different DSM methods in the microgrid system, from offline control options to online control options [6] (Fig. 1.

To retain the environmental sustainability, stability, security, and reliability of microgrid, Internet of Things (IoT) technologies are employed to facilitate tackling these challenges. IoT is defined as a future network technology in which information, such as people, things, processes, is connected to the Internet to generate, collect, share, and utilize information. Recently, IoT technologies are rapidly grown as they are developed and implemented for enhancing microgrids applications [10], [11]. IoT technologies such as smart metering, decentralization, self-healing, and two-way communication are essential tools for real-time monitoring and controlling all microgrid variables to perform flexible and intelligent energy management system (EMS) [7, 12]. IoT enables microgrid to share information between users, improves microgrid performance, and enhances microgrid components' connectivity. By collecting and analyzing renewable energy resources (RESs) data using IoT, microgrid management systems will be much more comfortable. Also, utilities can perform operational functions such as lowering outage investigation times, improving load balancing, optimizing line voltage, locating the outages, reducing the service costs, and restoring services faster. Moreover, deploying IoT technologies for smart homes, energy-storage systems (ESS), EVs, charging stations, and controllable loads improve microgrid flexibility and reliability. Moreover, they maximize energy efficiency by managing the demand response, collecting information, sharing, and trading energy. To overcome the energy-saving and managing problems, an IoT-based optimal DSM scheme is essentially needed. This scheme should have the ability to keep continuous energy surviving with the future trends and avoiding power peak [7].

2 System Modeling

The equivalent circuit of PV array is assumed as a current source (I_{ph}) parallel to a single diode (D). Also, a parallel resistor (R_{p}) is connected across the diode with series resistor (R_{s}) to indicate the inner resistance for the flow of the leakage current. The output voltage from the solar PV changes according to the climate conditions and temperature and irradiation. Continuous monitoring of solar voltage is required to extract the maximum power from the panel. For this, we implement the incremental conductance algorithm.

$$\left(\frac{\mathrm{d}P}{\mathrm{d}V}\right)\mathrm{MPP} = \frac{\mathrm{d(dVI)}}{\mathrm{d}V}\mathrm{MPP} \tag{1}$$

$$I + V\left(\frac{\mathrm{d}I}{\mathrm{d}V}\right) = 0 \tag{2}$$

$$\frac{\mathrm{d}I}{\mathrm{d}V} = \frac{-I}{V} \tag{3}$$

Equation (3) gives the condition for the maximum power tracking of solar PV. The output of the solar power is low, and boost converter is required to step-up the voltages. By using MPPT algorithm, the duty cycle of the boost converter is controlled and to supply maximum power and to setup the voltages continuously under varying temperature, irradiance conditions.

Inverter connected to the system converters the DC output voltage to AC voltage. Inverters are operated in either grid-connected mode or stand-alone mode. In grid-connected mode, inverter variables should match with grid variables. Voltage sources inverter is controlled by current-control and voltage-control methods. For the current-controlled voltage source inverter, the reactive and active power components of a current injected to the grids are controlled by pulse width modulation (PWM) technique. Current controller is faster than the voltage control, and moreover, voltage controller is sensitive to phase error, and large harmonics currents flow in the system if the grid voltage is distorted.

Power converters play a vital role in grid synchronization of system. The voltage and frequency of the grid and the voltage source inverters should be same for stable operation of the system. Grid is synchronized by extracting phase angles from the grid by phase-locked loop (PLL). The PLL can detect the phase angle of the grid voltage in the presence of noise or higher-order harmonics in the grid (Fig. 2).

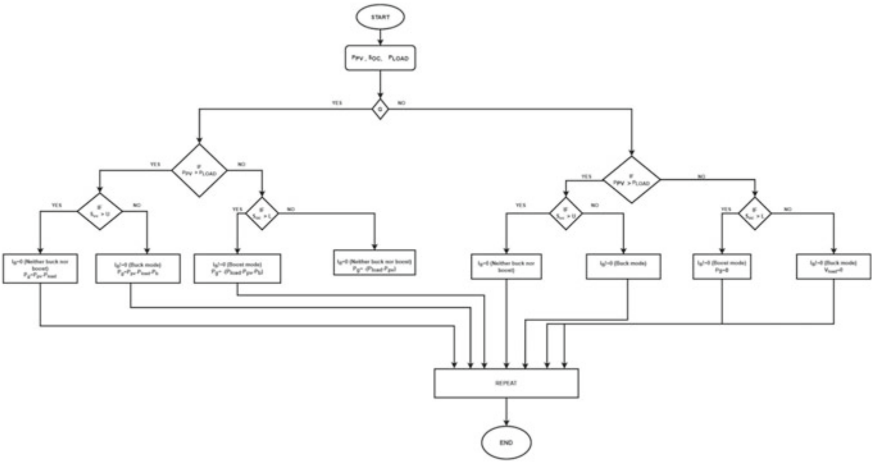

Fig. 2 Power management control flowchart

3 Proposed Control Algorithm

3.1 Power Management Control

Power management in the microgrid system is operated based on the solar power available, power consumed by the load, and power given/drawn from the grid. In case of grid-connected mode during surplus mode of operation where solar power available is much greater than the power required by the loads, the excess power is given to the grid. In case of lacking mode, grid supplies the power to the loads.

$$P_{\text{grid}} = P_{\text{solar}} - P_{\text{load}} \tag{4}$$

In lacking power mode of operation when the grid power is not available, then the loads are shed based on the availability of the solar power. When the battery is connected to the system, the solar power during surplus mode of operation solar PV charges the battery, and remaining power is sent to the grid. During lacking mode of operation, battery delivers power to the loads for continuous supply of power to the loads; in case the battery state of charge is between upper limit and lower limit, the loads are shed.

3.2 Grid-interfacing Inverter Control

Using the parks transformation matrix, three phase currents have been converted into dqo coordinates to reducing the control complexity in the system. Figure 3 shows the

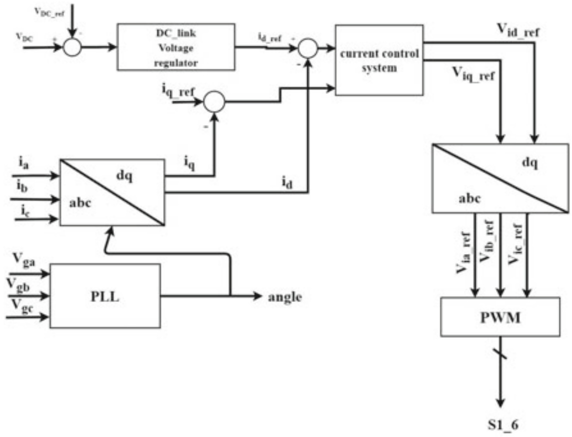

Fig. 3 Grid-interfacing inverter control structure

diagram of the grid-interfacing inverter.

$$\begin{bmatrix} i_{ld} \\ i_{lq} \\ i_{lo} \end{bmatrix} = \sqrt{\frac{2}{3}} \begin{bmatrix} \cos\theta & \cos\left(\theta - \frac{2\phi}{3}\right) & \cos\left(\theta + \frac{2\phi}{3}\right) \\ -\sin\theta & -\sin\left(\theta - \frac{2\phi}{3}\right) & \sin\left(\theta - \frac{2\phi}{3}\right) \\ \frac{1}{\sqrt{2}} & \frac{1}{\sqrt{2}} & \frac{1}{\sqrt{2}} \end{bmatrix} \begin{bmatrix} i_{la} \\ i_{lb} \\ i_{lc} \end{bmatrix} \tag{5}$$

In the above matrix equation, (θ) represents the angular position of the synchronous reference. The reference synchronous current can be divided into two equations which are as follows.

$$i_{ld} = \widetilde{i_{ld}} + \bar{i_{ld}}$$

$$i_{lq} = \widetilde{i_{lq}} + \bar{i_{lq}}$$

The reference synchronous current is having the average and oscillatory terms. The oscillatory terms are having higher-order harmonics.

$$\begin{bmatrix} i_{fd} \\ i_{fq} \end{bmatrix} = \begin{bmatrix} \widetilde{i_{ld}} \\ \widetilde{i_{lq}} \end{bmatrix} \tag{6}$$

By using the inverse parks transformation, the two phases are converted to three phases (Fig. 4).

$$\begin{bmatrix} i_{fa} \\ i_{fb} \\ i_{fc} \end{bmatrix} = \sqrt{\frac{2}{3}} \begin{bmatrix} \cos\theta & -\sin\theta \\ \cos\left(\theta - \frac{2\phi}{3}\right) & -\sin\left(\theta - \frac{2\phi}{3}\right) \\ \cos\left(\theta + \frac{2\phi}{3}\right) & \sin\left(\theta + \frac{2\phi}{3}\right) \end{bmatrix} \begin{bmatrix} i_{fd} \\ i_{fq} \end{bmatrix} \tag{7}$$

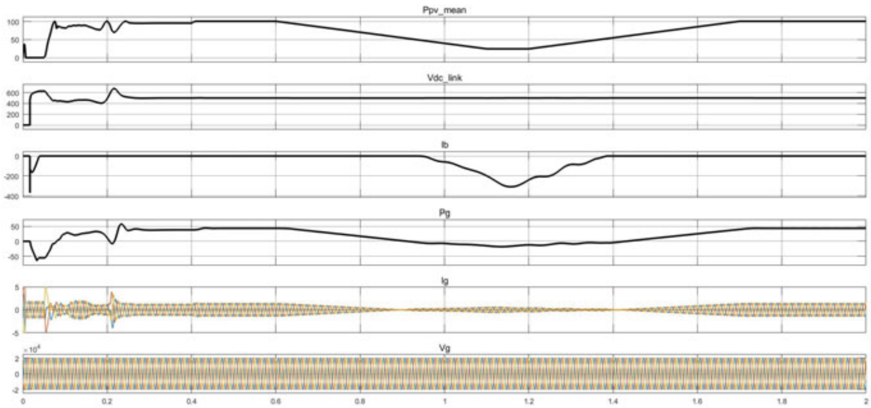

Fig. 4 Operation of microgrid in grid-connected mode under varying solar irradiance and SoC = 95 (upper limit)

4 Results and Discussions

In order to investigate the ability of the PV system and battery source to supply power at any time or whenever it is necessary, we consider some significant operating conditions to highlight our system performance compared to classical grid-connected system having the same peak power. In this view, we simulate the power produced by the PV battery system in normal case and the power availability for grid in three scenarios described below.

4.1 Simulation Results in Grid-connected Mode

Operation of an solar PV with battery connected to the grid has been observed under different cases based on the availability of solar power battery charge and type of load connected.

Case 1:

Varying solar irradiance, SoC = 95 (i.e., SoC>U), and P_{load} = 50 (kW, constant). During the surplus power mode (Ppv > Pload) solar PV supplying the power to the load, since the state of charge of battery is above the upper limit, solar PV supplies excess power to the grid. During the lacking power mode ($P_{pv} < P_{load}$), battery supplies the power required to the load.

Case 2:

Varying solar irradiance, SoC=10 (i.e., SoC<L), and P_{load}=50 (kW, constant). During the surplus power mode (Ppv > Pload) solar PV supplying the power to the

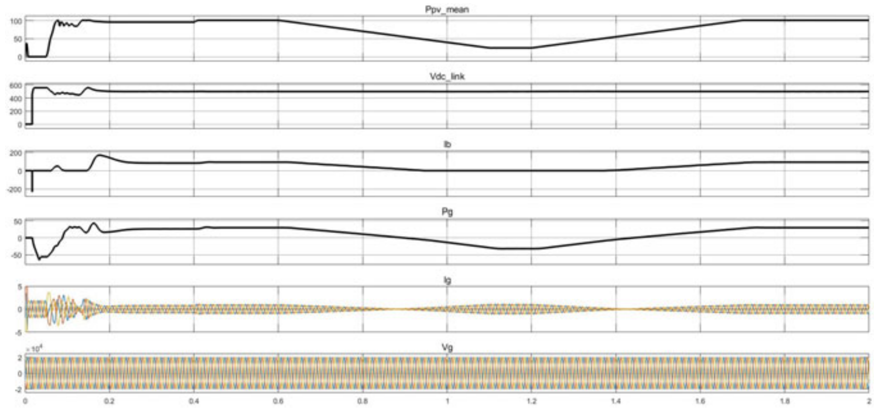

Fig. 5 Operation of microgrid in grid-connected mode with varying solar irradiance and with SoC=10 (lower limit)

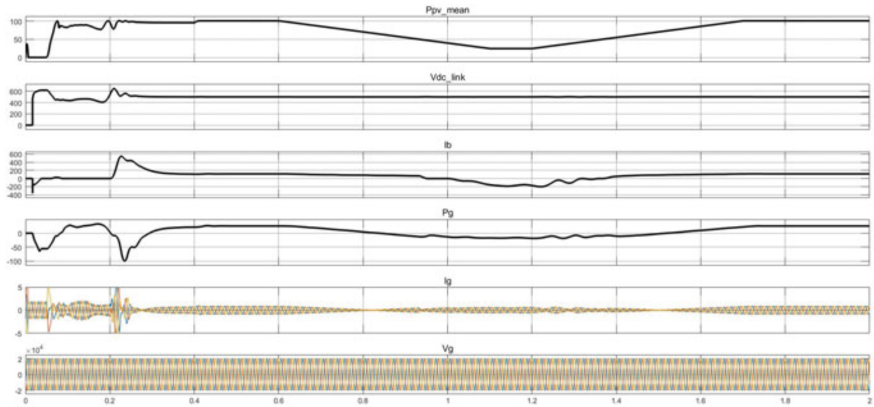

Fig. 6 Operation of microgrid in grid-connected mode with varying solar irradiance and with SoC=40 (in between lower limit and upper limit)

load, since the state of charge of battery below the lower limit, solar PV supplies power to the load as well as it charges the battery. During the lacking power mode ($Ppv < P_{load}$), grid supplies the power to the load as the battery charge is below the lower limit (Figs. 5 and 6).

Case 3:

Varying solar irradiance, SoC = 40 (i.e., L<SoC<U), and P_load=50 (kW, constant). During the surplus power mode ($P_{pv} > P_{load}$) solar PV supplying the power to the load, since the state of charge of battery is in between the lower and the upper limit, solar PV charges the battery. During the lacking power mode ($P_{pv} < P_{load}$), battery supplies the power required to the load (Fig. 7).

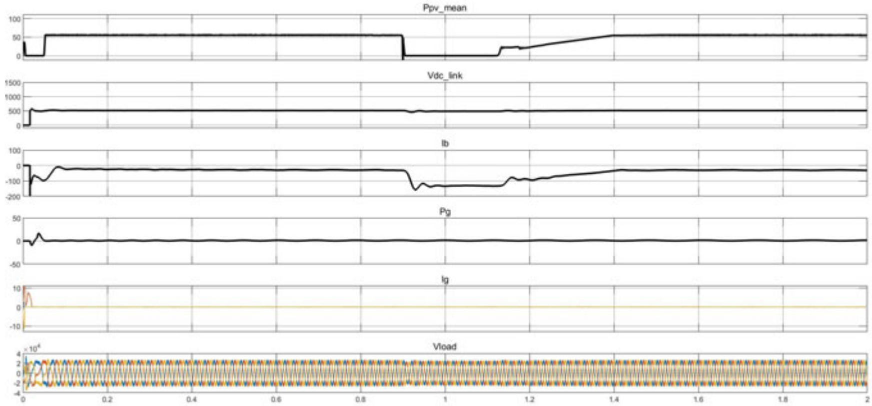

Fig. 7 Operation of microgrid in islanded mode under varying solar irradiance and SoC=95 (upper limit)

4.2 Simulation Results in Islanded Mode

In islanded mode, microgrid is disconnected from the grid and operates on the availability of its own power from solar PV and battery-storage system.

Case 1: Varying solar irradiance, SoC = 90 (i.e., SoC > U), and P_{load}=50 (kW, constant). During the surplus power mode ($P_{pv} > P_{load}$) solar PV supplying the power to the load, since the state of charge of battery is above the upper limit, grid and solar PV array operations change from MPPT to non-MPPT mode. During the lacking power mode ($P_{pv} < P_{\text{load}}$), battery supplies the power required to the load.

Case 2:

Varying solar irradiance, SoC=40 (i.e., L < SoC < U), and P_{load}=50 (kW, constant). During the surplus power mode ($P_{pv} > P_{\text{load}}$) solar PV supplying the power to the load, since the state of charge of battery is in between the lower and the upper limit, solar PV charges the battery. During the lacking power mode ($P_{pv} < P_{\text{load}}$), battery supplies the power required to the load.

Case 3:

Varying solar irradiance, SoC = 10 (i.e., SoC < L), and P_{load}=50 (kW, constant). During the surplus power mode ($P_{pv} > P_{\text{load}}$) solar PV supplying the power to the load, since the state of charge of battery below the lower limit, solar PV supplies power to the load as well as it charges the battery. During the lacking power mode ($P_{pv} < P_{\text{load}}$), loads are shed based on the availability of power from solar PV (Figs. 8 and 9).

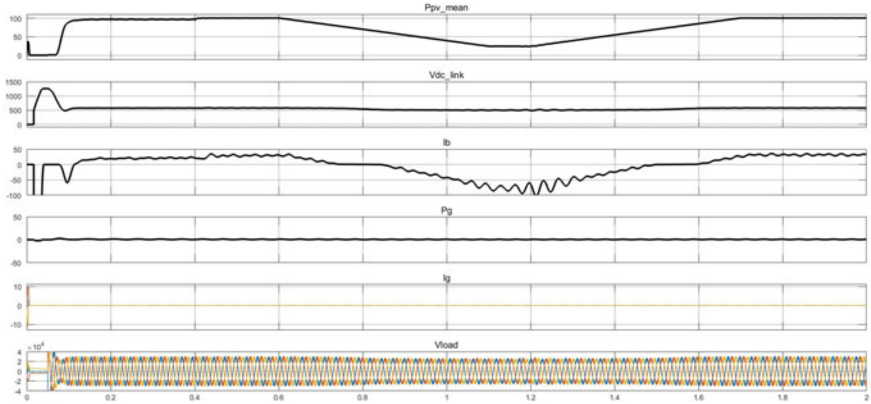

Fig. 8 Operation of microgrid in islanded with varying solar irradiance and with SoC=40 (in between lower limit and upper limit)

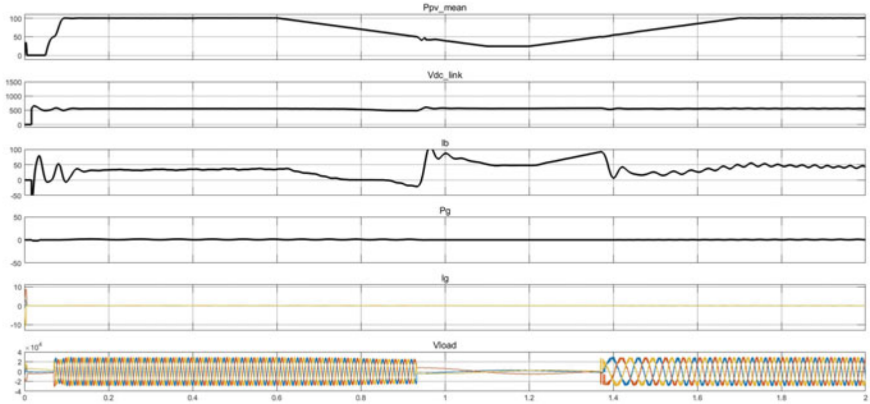

Fig. 9 Operation of microgrid in islanded mode with varying solar irradiance and with SoC=10 (lower limit)

5 Conclusion

In this paper, we have implemented an energy management algorithm in solar PV with grid-tied system. Results that have been obtained from the MATLAB/Simulink platform are well justified and sent the maximum power from the solar PV to the local loads with unity power factor. We have observed that the total real power is increasing with the irradiation and temperature, and the average power factor is almost equal to 1. The total harmonic distortion of voltages and currents of all the phases is below 5%. We can supply the power to grid during the surplus mode which even reduces the burden on the grid. Based on all the results, we conclude that the system is a solution for the increasing energy which makes life easier on this earth.

References

1. Panda KP et al (2020) A novel adaptive fuzzy based controller design using FPGA for grid connected PV systems. In: Advances in smart grid power system: network, control and security. Elsevier, Amsterdam, pp 331–364
2. Prince SK, Panda KP, Patowary M, Panda G (2019) FPA tuned Extended Kalman Filter for power quality enhancement in PV integrated Shunt Active Power Filter. In: 2019 International Conference on Computing, Power and Communication Technologies (GUCON), pp 257–262
3. Prince SK, Panda KP, Kumar VN, Panda G (2018) Power quality enhancement in a distribution network using PSO assisted Kalman filter–based shunt active power filter. In: IEEMA Engineer Infinite Conference (eTechNxT), pp 1–6
4. Kumar Nunna HSVS, Srinivasan D (2016) A multi-agent system for energy measurement in smart microgrids with distributed energy storage and demand response. In: 2016 IEEE International Conference on Power Electronics, Drives and Energy Systems (PEDES), pp 1–5
5. Prince SK, Affijulla S, Panda G (2021) Total harmonic distortion based fault detection in Islanded DC microgrid. In: 2020 3rd International Conference on Energy, Power and Environment: Towards Clean Energy Technologies, pp 1-6
6. Sorte PK, Panda KP, Panda G (2021) Current reference control based MPPT and investigation of power management algorithm for grid-tied solar PV-battery system. In: IEEE Syst J. https://doi.org/10.1109/JSYST.2021.3052959
7. Yang X, Zhang Y, He H (2019) Real-time demand side management for a microgrid considering uncertainties. IEEE Trans Smart Grid 10(3)
8. Rahim S, Javaid N, Nawaz N (2019) A convex optimization based decentralized real-time energy management model with the optimal integration of microgrid in smart grid. J Clean Prod **236**
9. Prince SK, Panda KP, Panda G (2019) Kalman filter variant intelligent control for power quality improvement in photovoltaic active power filter system. Int Trans Electr Energ Syst e12239
10. Sorte PK, Panda KP, Peesapati R, Panda G (2020) An improved control strategy for single-phase single-stage grid-tied PV system with current reference MPPT control. In: 2020 IEEE International conference on computing, power and communication technologies (GUCON), pp 461–466
11. Sedhom BE, El-Saadawi MM (2021) IoT-based optimal demand side management and control scheme for smart microgrid. Int J Electr Power Energy Syst 127
12. Kumar VN, Patowary M, Panda G, Prince SK (2018) Solar plant integration to utility grid with improved power quality by using RNN-Hebbian-LMS current controller. IEEE Innov Smart Grid Technol Asia (ISGT Asia) 2018:546–551

Chapter 51
A Survey of Cyber Security in Smart Microgrid

Zoaya Mohammadi, Smitha Joyce Pinto, Gayadhar Panda, and Surmila Thokchom

Abstract With the large integration of renewable intermittent energy resources, it became challenging to control the microgrid especially in the absence of the electric power systems operating as an infinite bus. A microgrid controller which coordinates and controls the various distributed energy resources (DER) using communication technologies and based on predefined communication protocols is therefore indispensable for smooth and continuous operation. Theory and real-world scenarios have proven that communication networks are never utterly secured and impenetrable. As a result, threat agents could gain unauthorized access, modify, steal, block, or corrupt the information exchanged in microgrid systems causing the mal-operation of the critical control functions they provide. The severity of the impact a cyber-attack could have on the microgrid operation depends on many factors that will be explained throughout this paper.

Keywords Smart microgrid · Cyber-physical network · Vulnerabilities · Communication network · Cyber-attacks

Z. Mohammadi (✉) · S. J. Pinto
Maharaja Institute of Technology, Mysore, Karnataka, India

S. J. Pinto
e-mail: smithapinto_ece@mitmysore.in

G. Panda · S. Thokchom
National Institute of Technology Meghalaya, Shillong, India
e-mail: gayadhar.panda@nitm.ac.in

S. Thokchom
e-mail: surmila.thokchom@nitm.ac.in

G. Panda et al. (eds.), *Sustainable Energy and Technological Advancements*, Advances in Sustainability Science and Technology,
https://doi.org/10.1007/978-981-16-9033-4_51

1 Introduction

Nowadays, electricity utilities are vulnerable to physical and cyber security attacks. The microgrid concept which gives a new light to the problems related to traditional energy supply such as demand flexibility, storage, and renewable generation to produce a more reliable, cost-effective solution, it is under the cyber-attacks causes power outage which impacts the critical loads [1–3]. The impact of the attack increases with the simultaneous increase in the number of system components of the microgrid. Human error or intentional attempts to permeate along the high number of prospect attack vectors within the microgrid are the possible causes for the cyber-attacks. If one system component or the communication path is affected, then other may be compromised [4, 5]. The result of these attacks may compass from disastrous and uncontrollable such as distributed denial of service (DDOS), defacing bill-payer websites, and destruction of automated modules, or 'bricked' meters all the way up to lethal causes. For example, as the result of cyber menace, there could be disruption in the energy supplies which may lead to collapse in the critical services in medical management and military citadel or catastrophic failure of assets such as transformers and loads. The study shows that the threat of cyber terrorism on the utility industry is worsening with 56% of surveyed announcing at a maximum of one shutdown or functioning data mislaying on an annual basis and on a mega scale around 25% are affected [6–8].

The discrete risk inherent in their particular system should be understood by the designers of the microgrid. For example, smart meters used by the end consumers are likely to be anxious about the secrecy violation of household and financial data; at large scale, producers will be concerned about the industrial cyber espionage; at military site, the engineers pay more emphasis on the risk related to the weaponized malware like Stuxnet, Duqu, Flame which causes malfunctioning of the electricity supply. The course of action deployed for cyber security should think about these consumer-related issues [9–12].

To become flexible to a greater extent, microgrid developers and operators need a compendious and integrated proposition to cyber-physical safety. The fundamentals to ensure the security of the critical power configuration are: microgrid strengthening, systematic evaluation of the interconnection security controls, design and formulation of the catastrophe recuperation, reserve for the security procedure. Figure 1 shows the basic block diagram of cyber security in microgrid.

Combination of micro- and mini grids with fine branch and supply system control constitutes a smart grid. The smart grid uses digital communications technology [13, 14]. Advanced technologies like communication and computing, power integration into the smart grid make it more reliable, efficient and provide infrastructure which is integrated with two-way and as shown in Fig. 2. It depicts a typical smart grid with communication links between different parts of the transmission, distribution, generation, and consumption with the vulnerability to cyber-attack and the possibilities of its detection. A significant measure of detected data and control signals stream on the bidirectional communications network in smart grids. In this way, it becomes

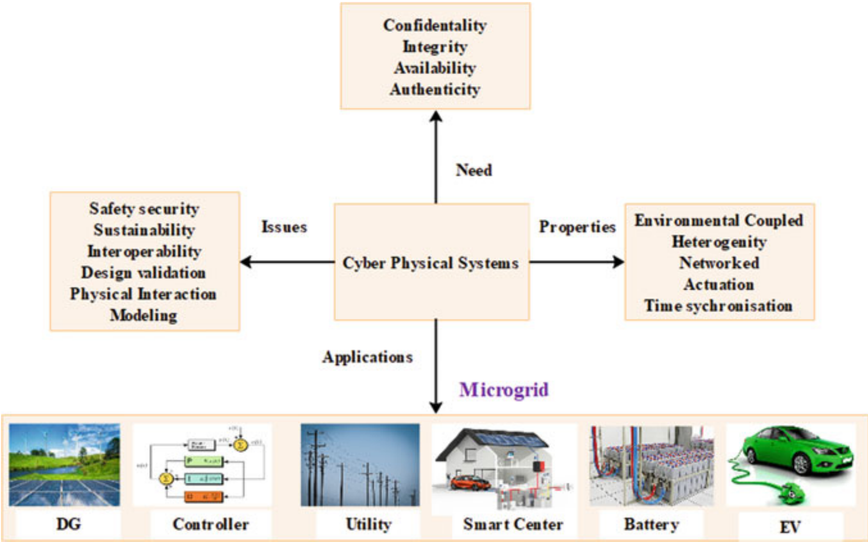

Fig. 1 Basic block diagram of cyber security in microgrid

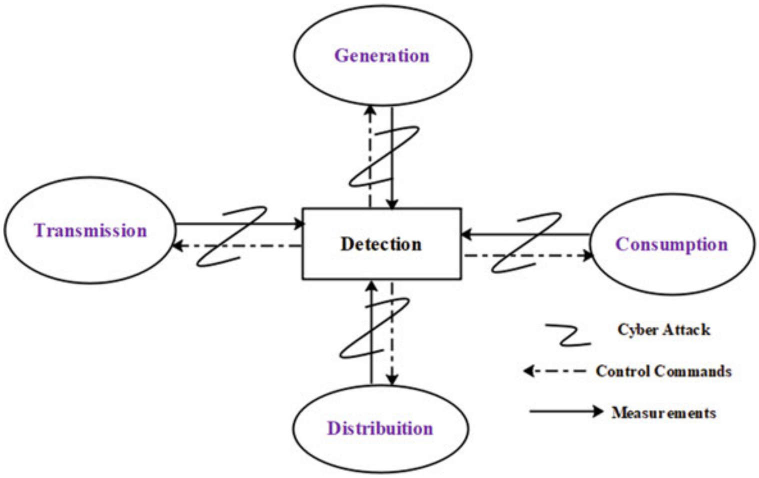

Fig. 2 Cyber-attack in microgrid

imperative to concentrate on an exceptional sort of vindictive user behavior that endeavors to abuse the trustworthiness of the estimation information by embeddings a misleading inclination esteem into the state assessment.

In this paper, Sect. 2 describes microgrid elementary network architecture, Sect. 3 explains threat and vulnerabilities of smart microgrid, Sect. 4 describes cyber-attackers, and Sect. 5 describes cyber detection in Microgrid.

2 Smart Microgrid Elementary Network Architecture

In smart microgrids, power hardware converters which are utilized for interfacing distributed generations and energy stockpiling assume a significant part. In such frameworks, the actual electrical parts are interconnected by the data and communication innovations, and their tasks are safely connected with cyber-physical framework. A archetypal power electronics-intensive smart microgrid with the cyber–physical networks is shown in Fig. 3.

Highly distributed and hierarchical network system is essential for a smart grid. Physical system and network are the two main components of the grid which is explained in the following section.

2.1 *System Component or Physical System*

Renewable resources, smart meters, electric utility functioning center, electric-powered household equipment, distributors, and service providers are the prime system components of the smart grid. The local energy generated from solar and wind which constitutes renewable energy resources supply the household appliances. To supervise power consumption, electric utility center interacts with smart meters and gathers report using GPRS technology. The agreement with users to dispense electricity for individual devices is provided by the service providers. Smart meter is an embedded system that records information related to power consumption, voltage and current levels, power factor and transmits it to utility server and in case of any abnormalities sends an alarm to disconnect the power devices. The communication of electrical household devices and smart meters is through home area network

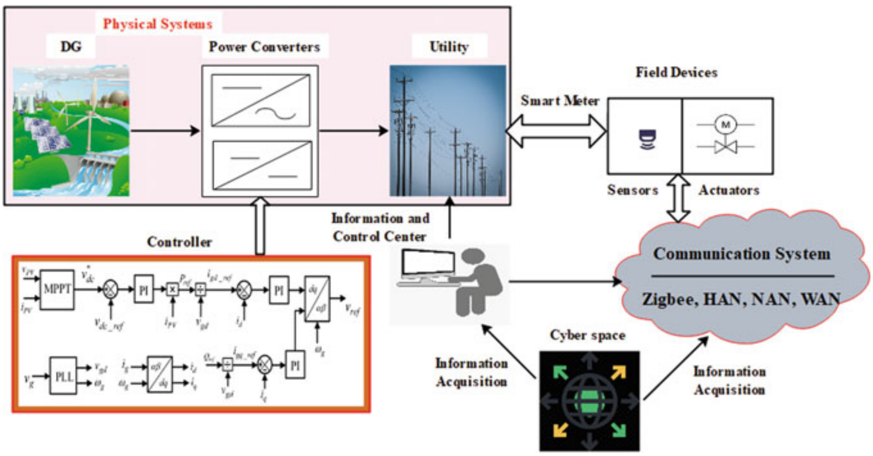

Fig. 3 Cyber-physical network and microgrid

Table 1 Factors affecting on different layers of cyber-physical system in microgrid

Layers	System contents	Factors affected
Physical/power system	Power generation, transmission, distribution, end user	Microgrid
Device layer	Sensors, actuators, and WSN	Status of device, control and measurements
Communication network	LAN: Bluetooth, Wi-Fi, Zigbee WAN: LTE, NB-IOT, Sigfox, LoRa-WAN, Wi Sun, etc.	Network security, Network topology, communication protocols, quality of service,
Management and application	Cloud computing, Fog computing, Edge computing, AI, ML, Big data, etc.	Power flow constraints and availability

(HAN) [15–20]. In general, the cyber–physical system of smart microgrid includes four layers such as physical power system, sensor and actuator, communication and management layers which are described. Table 1 shows the cyber-physical system and factors affecting them.

1. *Physical Power System Layer*

   This layer is comprised of power converters, transformers, circuit breakers, generators, and load.

2. *Sensor and Actuator Layer*

   This layer comprises of sensors and devices for quantifying and to implement control decisions. Information related to system's state, together with frequency, voltage, and current is measured using sensors and measurement devices. The distributed generation controllers, generator controllers, and relays of circuit breakers come under actuators and control devices.

3. *Communication Layer*

   Routers, switches, and the communication medium are present in this layer. This layer is responsible for exchange of information between relevant layers. Depending on the system requirements, wired or wireless communication system can be employed.

4. *Management Layer*

   All microgrid operations are monitored by this layer. It has central control system which receives data from the third layer, i.e., communication, and produces control signals for optimal operation of the smart microgrid [21–23].

2.2 Network Component

Communication can be established through two types of network, i.e., HAN and wide area network (WAN). The household smart devices, equipments across the home, are connected with the smart meter through HAN. The HAN can communicate using

Bluetooth, Zigbee, or wireless or wired Ethernet. The service providers, electric utility, and smart meters are connected with the help of WAN, which is a bigger network. The WAN can communicate using 3G/4G/LTE/GSM, fiber optics, WiMAX [24–27].

Smart microgrid is prone to various threats and vulnerabilities which can be fatal to the system and may cause severe damage to the working of the system, and these have been discussed in Sect. 3.

3 Smart Microgrid Threat and Vulnerabilities

Smart microgrid's reliability and efficiency can be supervised and controlled based on the interaction of the cyber-physical systems. Vulnerabilities are introduced to the system due to the interdependence between cyber-physical components. For their development and faultless operation, challenges and issues should be thoroughly calculated. These vulnerabilities may let the attackers to erupt the network, compromised the integrity and secrecy of the data transmitted, and make the service inaccessible [28].

Vulnerabilities those are serious in smart microgrids which can be protected from are consumer safety, significant number of intelligent devices, physical security, power system's lifespan, implied faith between traditional power devices, poor teamwork, internet protocol usage, etc. [29]. The outdated components act as feeble security spot and may be contradictory to the present power devices. Communication between devices in control systems may cause risk related to data spoofing. The poor teamwork depends on incompetent and disorderly communication causes lot of poor results leading to vulnerability. Internet protocol is naturally at risk to various IP-based attacks such as teardrop, IP spoofing, and others. The management of both electricity supply and network demand is controlled by a substantial number of intelligent devices present in the smart grid. These intelligent devices can be an entry point for attackers into the network. Network monitoring and management are extremely difficult due to the gigantic network. Smart grid network incorporates many elements, and most of them are away from the utility's premises. This causes threat to physical access due to the number of insecure physical sites [30]. These threats and vulnerabilities may be intentionally caused by attackers, and there are various types of attacks which are discussed in Sect. 4.

4 Attackers and Types of Attacks

Attackers could be cybercriminal and script kiddies, white hat hackers, elite hackers, intruders, terrorists, employees, contenders, clients, or customers. Attackers can creep into smart microgrid system using vulnerable access points in the logical border

Table 2 Types of attacks and their effects on smart microgrid

Security threats	Effects
Phishing	Affect a smart grid customer, hacking of personal information
Denial_of_Service (DoS) Attack	Jamming the channel, attacks the physical layer and data link layer of OSI model
Eavesdropping and Traffic analysis Malware Spreading Replay Attack Injection Attack Covert Attack Stealthy Attack Zero Dynamic Attack	Gains sensitive information by monitoring network traffic, smart grid is at risk of data getting stolen Manipulate the functionality of different devices by developing malware and affecting the servers Affect the integrity and authorization Change the online stability check result by declining the real power flow estimation, Undetected errors are introduced into calculations of state variables and values changes in system inputs, thus influencing system output Attacks the state estimation in management of energy systems, affects the power transmission system's operation Affects the communication link which sends the measured AC and DC voltages and AC frequencies, and which transmits set points for controllers Number of yields to be bigger than or equivalent to states, It cannot be utilized for microgrid framework

neighboring a network, known as the electronic security perimeter (ESP). Interferences can be injected through various mediums, such as the software patch cords, and Universal Serial Bus (USB) thumb drive. Cyber breaches on cyber-physical systems (CPSs) can be established under various terms, such as replay attack, injection attack, denial-of-service (DoS) attacks, covert attack, eavesdropping attack, stealthy attack, zero dynamic attack, and dynamic false data injection attacks which are summarized in Table 2. Table 3 summarizes the types of attacks and impacts in microgrid system.

When we look over the cybersecurity of the smart grids, the first step is to analyze the C-I-A triad, which is an illustrious model for cybersecurity development. C-I-A stands for confidentiality, integrity, and availability—these security notions help to guide cybersecurity policies and consider the core underpinning of information security. The mentioned attacks can be grouped according to one or more safety norms they are jeopardizing, as set forth in Fig. 3. Each security control and each security weakness can be seen considering at least one of these critical ideas [31, 32]. Protection of data, resources, and objects from unauthorized access and unofficial viewing comes under confidentiality. Integrity infers that data is protected from unapproved changes to ensure that it is reliable and unerring. Availability suggests that supported and licit customers or clients approach the systems and the data, resources they need.

Detection of attack on the smart microgrid at the earliest is very important. There are various detection methods depending on the attack, and this has been discussed in Sect. 5.

Table 3 Impact of attacks in the microgrid system

Attack Type	Impact
Attack through correspondence channel	Monetary misfortunes of influenced clients Monetary advantages of malignant clients Security threats Unsettling influence of market activity
Attack through gadgets	Increment in energy costs, Load shedding Expand individual additions of pernicious clients Economic impediments of affected clients Disturbance of customary market activity
Attack through antagonistic clients	Load shedding Unsettling influence of ordinary market activity Lessen framework dependability Monetary misfortunes of influenced clients

5 Detection

As we know smart microgrids use information and communication technology (ICT) to impart reliable, efficient transmission and distribution of electricity. Care should be taken related to security issues (Table 4).

Much security-related issues are emerging, among which false data injection attack (FDIA) is one of the most significant ones. FDIA can be used to mangle real

Table 4 Types of attacks and their detection

Attacks	Detection
Phishing	Detection based on black and white list, Detection based on uniform resource locator (URL) features, Detection based on web content, Detection based on machine learning
Denial of service attack	Anomaly detection, probability density function, or distribution free approaches
Replay attack Injection attack Covert attack Stealthy attack	Detection with code signal and bargaining game Detection using several statistical spatiotemporal models, detection using semi-supervised deep learning approach, Anomaly detection of FDI attacks, Detection using signal processing Feature selection-based detection, unsupervised machine learning-based detection Detection using machine learning, Detection using transient analysis

energy demand and supply figures due to which there could be error in the energy distributions which results in added costs or more destructive menace [33–35].

One of the important measures to minimize the impairment caused by the FDIA is the detection at the earliest. Thus, efficient detection methods need to be imparted to have significant impact on the performance of the system. The physical, information, and communication security are the preventive measure against FDIA. Many FDIA detection techniques have been proposed like state estimation processes, e.g., using Kalman filters, sparse optimization, generalized likelihood ratio, Kullback–Leibler distance, Chi-square detector and similarity matching, state forecasting, and machine learning techniques. Few of which are listed below.

5.1 Detection of FDIA by Computing Fourier Singular Values (FSV)

In this approach, FDIA is detected based on singular value decomposition (SVD) and fast Fourier transform (FFT). FFT is used for signal analysis. To detect the cyber-attack, SVD is used to obtain singular values of the components to compare with the threshold. FFT separates the frequency terms from the sequence and makes it easy for analysis. Basic data here refers to reference voltage and frequency data and the estimated data for currents and loads. According to the proposed method, the current and voltage signals are obtained and a comparison is made with the basic signal to get the difference. FFT on the difference to get coefficient's matrix and SVD method to obtain singular value of coefficient's matrix is computed, and finally, FSVs are compared with the threshold to detect the FDI attack. If the obtained FSVs are lesser than threshold, then the system is in normal condition and if the obtained FSVs exceed, the threshold attack is occurred.

5.2 Detection of FDIA Using Blockchain Technology and Hilbert–Huang Transform

FDIA recognition is explained dependent on Hilbert–Huang transform to identify noxious assaults in the sensors and controllers. The offered strategy can recognize different FDIA in voltage and current sensors and regulators or controllers of the converters be characterizing a threshold. Furthermore, a sound and viable data-exchanging design based on blockchain and a community detection system are introduced. As indicated by the past supposition, warrantying information security, the proposed design delivers additional fine-grained data-exchanging services through ordering customers applying mark information.

5.3 Detection of FDIA Using Deep Learning

Detection of FDI attacks can be formulated as a machine learning problem of a binary classification variety. Many methodologies have been proposed which use deep neural networks to solve this binary classification problem. Some of the proposed methods are expectation maximization clustering mechanism to detect if any data in a SCADA system, threshold-based regression model, multivariate Gaussian semi-supervised learning algorithm, measurement-based deviation analysis algorithm, density ratio estimation, sparse principal component analysis approximation-based model, data-centric paradigm to detect FDI attacks, conditional deep belief network, autoencoders, convolution neural network, recurrent neural network, and deep learning-based interval state estimation technique. FDIAs are disastrous, hence for early detection of the faults, efficient detection mechanism needs to be incorporated in order to minimize the destruction.

5.4 Detection of FDIA Using Cooperative Vulnerability Factor

A machine learning problem of a binary classification variety can be formulated by the detection of FDI attacks. The accuracy rate has not compared and considered with other FDIA detection based on the evaluation parameters of miss rate, false alarm rate, hit rate, and correct reject rate. Both voltage and current measurement are investigated separately to preserve system security and energy efficiency in this study. This technique is used by free model-based algorithm.

6 Conclusion

This paper aims to analyze the possibilities of cyber-attacks in smart grid. It gives an insight into the various existing cyber-attacks compromising the microgrid data integrity and availability. Moreover, it has also presented the cyber-attack prevention and detection and the steps that need to be followed to ensure enhanced microgrid resiliency and survivability. The current advancements and new research trends in the field of cybersecurity of smart microgrids for intrusion and anomaly detection, and resilient control strategies is software-defined networking which is a way to deal with network the executives that empower dynamic, asset productive, and programmable organization arrangement to further develop network execution and monitoring, implementation of intrusion detection system (IDS) techniques on electrical devices with a special attention to host-IDS.

References

1. Faquir D, Chouliaras N, Sofia V, Olga K, Maglaras L (2021) Cyber security in smart grids, challenges and solutions. AIMS Electron Electr Eng 5(1):24–37
2. Canaan B, Colicchio B, Abdeslam DO (2020) Microgrid cyber-security: review and challenges toward resilience. Appl Sci 10:5649
3. Nejabatkhah F, Li YW, Liang H, Reza Ahrabi R (2021) Cyber-security of smart microgrids: a survey. Energies 14:27
4. Al-Omar B, Al-Ali AR, Ahmed R (2012) Role of ınformation and communication technologies in the smart grid. J Emerg Trends Comput Inf Sci 3(5):707–716
5. Bidram A, Davoudi A (2012) Hierarchical structure of microgrids control system. IEEE Trans Smart Grid 3(4):1963–1976
6. Dileep G (2020) A survey on smart grid technologies and applications. Renew Energies 146:2589–2625
7. Livingston S, Sanborn S, Slughter A, Zonneveld P (2018) Managing cyber risks in electric power sector. Delloitte insights: US Department of Energy
8. Hemsley KE, Fisher RE (2018) History of ındustrial control system cyber ıncidents. U.S. Department of Energy National Laboratory
9. Kundur D, Feng X, Mashayekh S, Liu S, Zourntos T, Butler-Purry KL (2011) Towards modelling the impact of cyber attacks on a smart grid: Int J Secur Netw
10. Li Z, Shahidehpour M, Aminifar F (2017) Cybersecurity in distributed power systems. Proc IEEE 105(7):1367–1388
11. Bolgouras V, Ntantogian C, Panaousis E, Xenakis C (2020) Distributed key management in microgrids. IEEE Trans Industr Inf 16(3):2125–2133
12. Liu J, Xiao Y, Li S, Liang W, Chen CLP (2010) Cyber security and privacy ıssues in smart grids. IEEE Commun Surv Tut 14:981–997
13. Aloula F, Al-Alia AR, Al-Dalkya R, Al-Mardinia M, El-Hajjb W (2012) Smart grid security: threats, vulnerabilities and solutions. Int J Smart Grid Clean Energy 1
14. Ortiz L, Orizonodo R, Tellez AA, Lopez GJ, Isac I, Gonzalez JW (2019) Hybrid AC/DC microgrid test system simulation: grid-connected mode, Heliyon
15. Nakabi T, Toivanen P (2021) Deep Reinforcement Learning for energy management in a microgrid with flexible demand. Suistain Energy Grids Netw 25
16. Dehghani M, Niknam T, Ghiasi M, Siano P, Haes Alhelou H, Al-Hinai A (2021) Fourier singular values-based false data ınjection attack detection in ac smart-grids. Appl Sci 11:5706
17. Ashrafuzzaman M, Chakhchoukh Y, Jillepalli AA, Tosic PT, de Leon DC, Sheldon FT, Johnson BK (2018) Detecting stealthy false data ınjection attacks in power grids using deep learning. In: Conference Paper
18. Bindra A (2017) Securing the power grid: protecting smart grids and connected power systems from cyberattacks. IEEE Power Electron Mag 4:20–27
19. Rekik M, Chtourou Z, Gransart C (2018) A cyber-physical threat analysis for microgrids. In: 15th International Multi-Conference on Systems, Signals and Devices
20. Zhou Q, Shahidehpour M, Alabdulwahab A, Abusorrah A (2020) A cyber-attack resilient distributed control strategy in Islanded microgrids. IEEE Trans Smart Grid 11(5):3690–3701
21. Venkataramanan V, Hahn A, Srivastava A (2020) CP-SAM: cyber-physical security assessment metric for monitoring microgrid resiliency. IEEE Trans Smart Grid 11(2):1055–1065
22. Cintuglu MH, Mohammed OA, Akkaya K, Uluagac AS (2017) A survey on smart grid cyber-physical system testbeds. IEEE Commun Surv Tutor 19(1):446–464
23. Tan S, Guerrero JM, Xie P, Han R, Vasquez JC (2020) Brief survey on attack detection methods for cyber-physical systems. IEEE Syst J 14(4):5329–5339
24. Li J (2019) Decentralized on-demand energy supply for blockchain in Internet of Things: a microgrids approach. IEEE Trans Comput Soc Syst 6(6):1395–1406
25. Chlela M, Mascarella D, Joós G, Kassouf M (2018) Fallback control for isochronous energy storage systems in autonomous microgrids under denial-of-service cyber-attacks. IEEE Trans Smart Grid 9(5):4702–4711

26. Sahoo S, Mishra S, Peng JC, Dragičević T (2019) A stealth cyber-attack detection strategy for DC microgrids. IEEE Trans Power Electron 34(8):8162–8174
27. Habibi MR, Baghaee HR, Dragičević T, Blaabjerg F (2021) False data injection cyber-attacks mitigation in parallel DC/DC converters based on artificial neural networks. IEEE Trans Circuits Syst II Express Briefs 68(2):717–721
28. Li Y, Qin Y, Zhang P, Herzberg A (2019) SDN-enabled cyber-physical security in networked microgrids: IEEE Trans Sustain Energy 10(3):1613–1622
29. Liu X, Shahidehpour M, Cao Y, Wu L, Wei W, Liu X (2017) Microgrid risk analysis considering the impact of cyber attacks on solar PV and ESS control system. IEEE Trans Smart Grid 8(3):1330–1339
30. Cheng Z, Chow M-Y (2020) Resilient collaborative distributed energy management system framework for cyber-physical DC microgrids. IEEE Trans Smart Grid 11(6):4637–4649
31. Wang Y, Mondal S, Deng C, Satpathi K, Xu Y, Dasgupta S (2021) Cyber-resilient cooperative control of bidirectional interlinking converters in networked AC/DC microgrids. IEEE Trans Industr Electron 68(10):9707–9718
32. Sahoo S, Dragičević T, Blaabjerg F (2020) An Event-Driven Resilient Control Strategy for DC Microgrids. IEEE Trans Power Electron 35(12):13714–13724
33. Sahoo S, Peng JC, Devakumar A, Mishra S, Dragičević T (2020) On detection of false data in cooperative DC microgrids—a discordant element approach. IEEE Trans Ind Electron 67(8):6562–6571
34. Zhang D, Zhang C (2020) A NDO based attack detection observer and ısolation strategy in distributed DC microgrid with FDIA. J Phys: Conference Series, vol. 1754, 3rd International symposium on power electronics and control engineering (ISPECE 2020), Chongqing, China
35. Lu R, Wang J (2020) Distributed control for AC microgrids with false data ınjection attacks and time delays. In: E3S Web of Conferences, vol 194, p 03023

Chapter 52
Data-Driven Event Detection with PMU Data Using a Novel Composite Deep Learning Technique

Pushpak Das, Subhash Kumar, Gayadhar Panda, and D. S. Roy

Abstract Disruptive events frequently occur in power grids and interrupt the normal operation of the system and may eventually cause permanent failure of equipment. Therefore, establishing a data-driven event diagnostic framework to extract useful information such as the cause or location of events is of utmost importance. A novel composite data-driven event detection method is established and analyzed in this paper using a composite deep learning framework based on principal component analysis (PCA), generative adversarial networks (GAN) and long short-term memory (LSTM). The composite model only requires partial expert knowledge in that it combines unlabeled data and partly labeled data in a large margin learning objective to bridge the gap between supervised learning, semi-supervised learning and learning with hidden structures. The developed methodology provides credible information regarding the cause of various events and facilitates post-event decision making to prevent potential cascading failures. The proposed composite model has been trained using PMU data of Indian Power Grid (IPG), and it demonstrates that the developed approach is efficient in classifying and characterizing transient events.

Keywords Event detection · Event classification · Phasor measurement units (PMU) · Principal component analysis (PCA) · Generative adversarial networks (GAN) · Long short-term memory (LSTM) · Deep learning

---

P. Das (✉) · G. Panda · D. S. Roy
National Institute of Technology Meghalaya, Shillong, India
e-mail: pushpakdas@nitm.ac.in

G. Panda
e-mail: gayadhar.panda@nitm.ac.in

D. S. Roy
e-mail: diptendu.sr@nitm.ac.in

S. Kumar
Power System Operation Corporation Ltd. (NERLDC), Shillong, India
e-mail: subhash.tran@posoco.in

G. Panda et al. (eds.), *Sustainable Energy and Technological Advancements*,
Advances in Sustainability Science and Technology,
https://doi.org/10.1007/978-981-16-9033-4_52

1 Introduction

Transient event identification is essential for power system operation and situational awareness. The increased penetration of the high sampling frequency phasor measurement units (PMUs) enables using PMU data to analyze power system events and thus enhances power system visualization, monitoring and control. As utilities have expanded their monitoring systems and sensor networks, the data management, analysis and inference have become the most significant challenges with the shift from a conventional data acquisition system depended on domain experts (supervised) to an automated intelligent analysis system (unsupervised). The grid operators expect visualization techniques using advanced algorithms and intelligent tools to quickly present the received PMU data in the form of actionable intelligence [1]. PMU data are applied to achieve fast decision and high accuracy in system operations, which is consistent to introduce PMUs for power system analysis. In this regard, researchers in the field of situational awareness plan to apply data-driven approaches based on the development of PMU applications. Examples of relevant previous studies are as follows: A CNN application is proposed for the monitoring of power quality with PCA-based preprocessing [2]. The extraction of features for parameter identification using phasor measurement data is proposed in [3]. For dynamic event analysis, general details regarding the real-time monitoring of events are well described in [4]. In addition, correlation analysis is performed for the online monitoring of anomalies and their locations [5]. These studies provide methods for obtaining meaningful information from non-stationary synchrophasor data, as well as guidelines for system operation, and can be improved by implementation conditions in real-world operation. Because PMUs measure the real-time voltage, current and frequency in the form of phasor data, they can identify the faults or events from dynamic signatures in an almost real-time manner [6]. As data acquisition time and accuracy exhibit a trade-off relationship, the main contribution of our study is the complementary sequencing decision process, as well as a fast decision process for successive events conditions. The design process of event identification involves a complementary sequence to provide fast identification and validation, and the proposal content includes a quick judgment accuracy analysis and output category design. The dataset includes no fault, line to ground faults (LG), line to line faults (LL), double line to ground (LLG) and three phase faults (LLL, LLLG). Electrical parameters used for analysis of PMU dataset at IPG are voltage (VRM, VYM, VBM, VPM and VNM), current (IRM, IYM, IBM, IPM, INM and IZ), frequency (Hz & DF/DT), phase angle (IRA, IYA, IBA, VRA, VYA, VBA, IPA, INA, VPA and VNA), MW, MX, PF and PDX 1 and 2 (PDX 1 analysis and PDX 2 analysis).

Figure 1 shows the flowchart of composite model using techniques PCA, GAN and LSTM.

- Principal component analysis—Dimensionality Reduction: The goal is to capture the essential information of a time series while reducing dimensionality.
- Generative adversarial networks (GAN)—Generative modeling is an unsupervised learning task in machine learning that involves automatically discovering

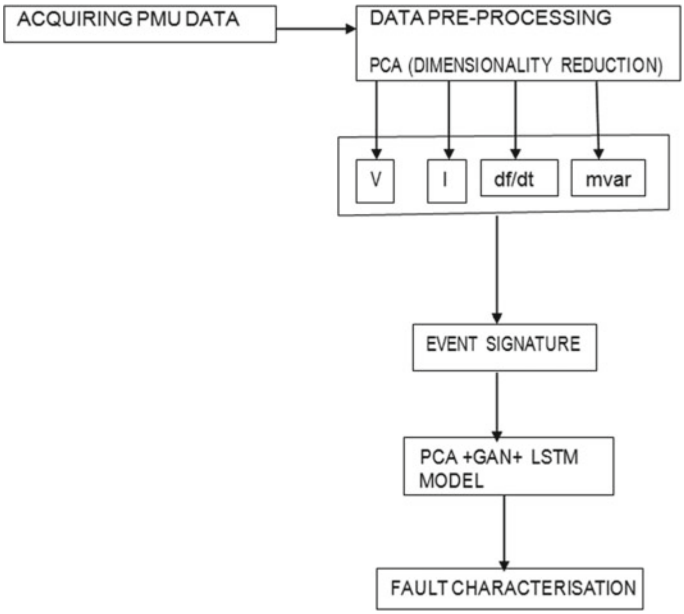

Fig. 1 Flowchart of proposed two-stage fault detection method

and learning the regularities or patterns in input data in such a way that the model can be used to generate or output new examples that plausibly could have been drawn from the original dataset. Here, we want to 'generate' data for the future that will have similar distribution as the one we already have—the historical PMU data.

- LSTM fits time-series data better since it focuses on temporal correlation. PMU data have high sampling rate.

Event characterization is one of the much needed applications, which is directly related to event analysis and feature extraction [6].

The rest of this paper is organized as follows, and in Sect. 2, we introduce the intuition and related works behind this work. Section 3 introduces the formulation of composite deep learning model for event detection. In Sect. 4, the result is established for composite model. The conclusion and future work are given in Sect. 5.

2 Related Work

Researchers have investigated using PMU data to identify power system events such as faults, line tripping and generation loss [7]. Depending on how the data are processed, the developed methods can be grouped into three categories: signal processing methods, heuristic methods and time-series analysis methods. Traditional signal processing techniques such as wavelet analysis, short-time Fourier transform and Hilbert analysis are utilized to analyze the oscillation modes of PMU signals under different transient events [8–10]. However, signal processing methods require an appropriate sampling rate and a proper length for the sample window to guarantee an acceptable event detection performance [7]. As an alternative, a heuristic event identification method is developed in [11, 12], where all PMU data are enclosed into an ellipsoid, so that features such as volume and orientation can be used to identify power system disturbances. Heuristic methods, on the other hand, require significant time for classification, challenging their application for real-time operations [10, 13]. Instead of using all PMU data accumulated in PDC, Brahma et al. [4, 12] develop a time-series analysis method that utilizes data from a single PMU with the largest variation to promptly identify the type of transient events. Using the time-series subsequences called shapelets that maximally represent the PMU data [11], this time-series approach identifies disturbance patterns while enhancing the classification accuracy. Although the aforementioned event classification techniques are promising in terms of accuracy, the challenge of identifying signature, detecting events and characterizing fault in semi-supervised learning manner has not been addressed to the best of our knowledge [14–17]. This particular challenge is addressed in this article.

In this article, a two-phase, data-driven event classification scheme is developed to enable fast online classification of power system transient events (Fig. 2).

Characterization of faults as no fault, line to ground faults (LG), line to line faults (LL), double line to ground (LLG) and three phase faults (LLL, LLLG) is done using the composite model using PCA, GAN and LSTM. It has to be noted that earlier works had focused on challenges imposed in the storage aspects of IPG's PMU data [18], while in [19], SLG faults had been characterized.

3 Proposed Composite Deep Learning Model

Rising deployments of phasor measurement units (PMUs) devices dramatically increased the size of data collected at power grid. This digital information is frequently unstructured, has different time scales and is stored on different servers and databases. The size of the collected datasets is growing rapidly, which complicates data processing and analysis. However, because the collected information contains many insights about the power system's state and its dynamic behavior, extracting this knowledge significantly increases situational awareness, detects system-wide or local anomalies (e.g., under-frequency or voltage events), validates system models and discovers/predicts equipment malfunctions (Fig. 3).

A two-phase data-driven event classification scheme is developed in this work to enable fast online classification of power system transient events.

First we are detecting event using offline process where voltage of three phase R, Y and B is monitored.

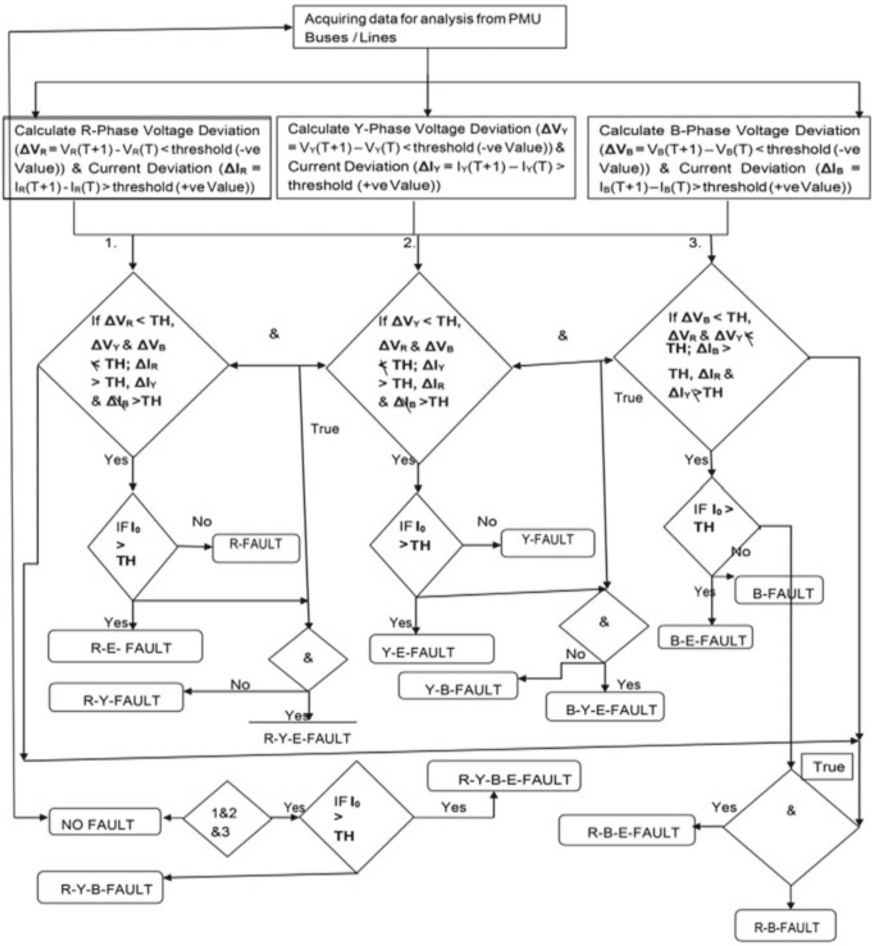

Fig. 2 Flowchart for event detection

In second step, dipping in current, voltage shoot up, fluctuation in rate of change of frequency and reactive power leakage is monitored to classify the fault. PCA is used for dimensionality reduction of sheer volume of PMU data. The fault feature extracted from unbalanced data via deep learning is inaccurate, which can lead to high misclassification rate. To solve this problem, new generator and discriminator of generative adversarial network (GAN) are designed in this paper to generate more discriminant fault samples using a scheme of global optimization. As PMU data have high sampling rate, LSTM fits into data better since it focuses on temporal correlation. PMUs time series are split to training, validation and testing datasets for the 12 units. Training data for the LSTM-based neural network models are created by separating the temporal segments of input and output. The PMUs datasets are preprocessed by normalizing all measurements to be between 0 and 1 with scaling.

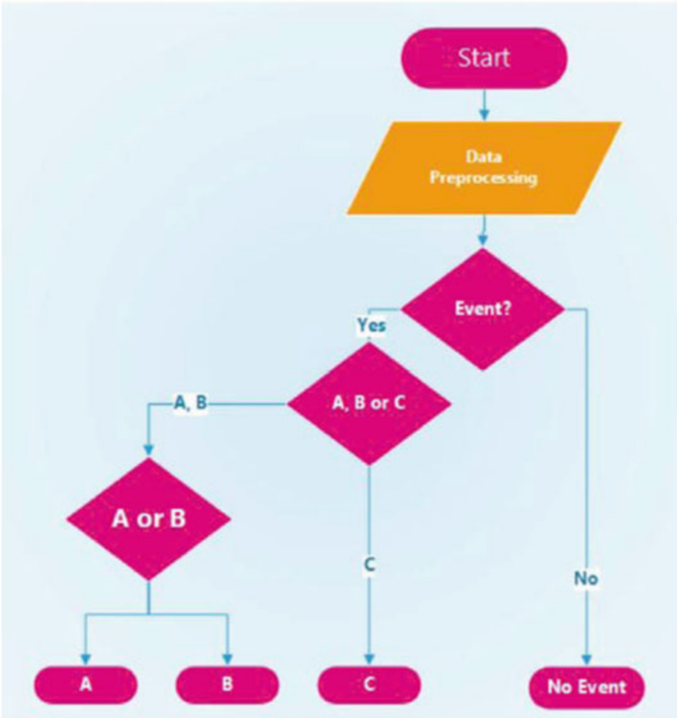

Fig. 3 Event detection and classification steps

During the model fitting process, an LSTM model is trained for 10 epochs over the training dataset. The optimizer with adaptive learning rates is chosen to be Adam (Kingma and Ba 2014), the loss function is defined as mean square error (MSE), and activations functions which reduce gradient issues are set to ReLu (Nair and Hinton 2010). The model configuration contains input and output vector length, the number of units in the neural network, layers of stacked LSTM and dropout rate. Given a model configuration, the model is evaluated to predict multiple steps ahead and compared with testing dataset with the sliding window. The accuracy of the model is calculated by mean absolute error (MAE) at each PMU between predicted values and true observations for each prediction length:

$$\mathrm{MAE} = 1/n \sum_{n=1}^{n} |\mathrm{Prediction} - \mathrm{Observation}|$$

where n is the testing data length.

FAULT MATRIX

S.NO.	V_A (M)	V_B (M)	V_C (M)	O/P
01	1.3	0.5	0.8	R-E- Fault
02	2.1	1.2	0.3	R-Y-E
03	1.8	0.75	1.0	R-B-E
04	0.9	1	1.2	Y-B-E
05	1.3	1	2.1	R-Y-B-E
06	0.8	0.6	0.5	NO FAULT

Fig. 4 Fault matrix for event detection

4 Results and Discussion

Initial step of the fault detection method is to set the threshold values of voltage deviation. As discussed the offline event detection, fault detection is illustrated through table in Fig. 4.

Further faults are classified with all types of faults [i.e., symmetrical faults (SYM), LG faults (RG, YG, BG), LL faults (RY, YB, RB), LLG faults (RYG, RBG, YBG)], and no faults (NF) are classified by the proposed composite model as shown in Figs. 5, 6 and 7.

Fluctuation in oscillation while a fault is encountered is illustrated in Fig. 8.

Accuracy of result:

CNN	LSTM	PCA + GAN + LSTM
97.4%	96.6%	98.2%

Encouraging result is achieved with an accuracy of 98.2% while applying composite model using PCA, GAN and LSTM.

5 Conclusions

In summary, with the help of the proposed composite technique using PCA, GAN and LSTM, a pure data-driven framework is designed for detecting and characterizing

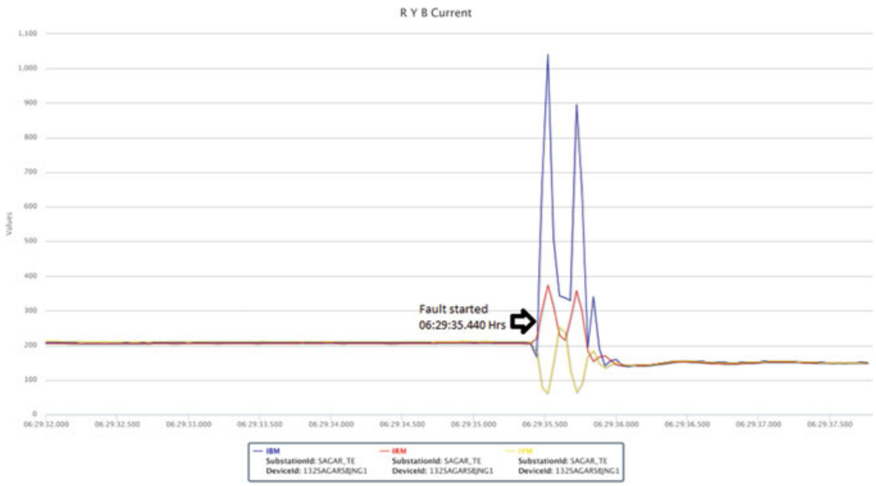

Fig. 5 R-phase fault

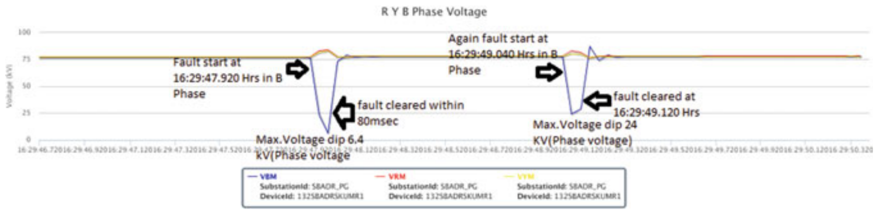

Fig. 6 Recurrent fault in *R*-phase

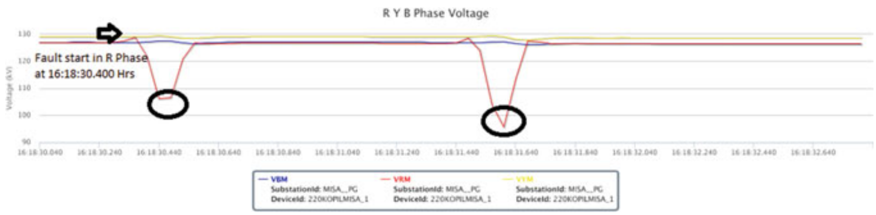

Fig. 7 Fault clearance

faults in the IPG by incorporating all types of accessible labeled, partially labeled and unlabeled data. For future work, we aim to implement a composite model for a large volumes of PMUs data streams. This article introduced a new data-driven approach for classification of transient events in power systems that is based on data received from PMUs. Moreover, useful information recorded by PMUs, such as the rate of frequency change and phase angles, may also be utilized to improve the accuracy and robustness of the developed approach. More recorded events will be used to

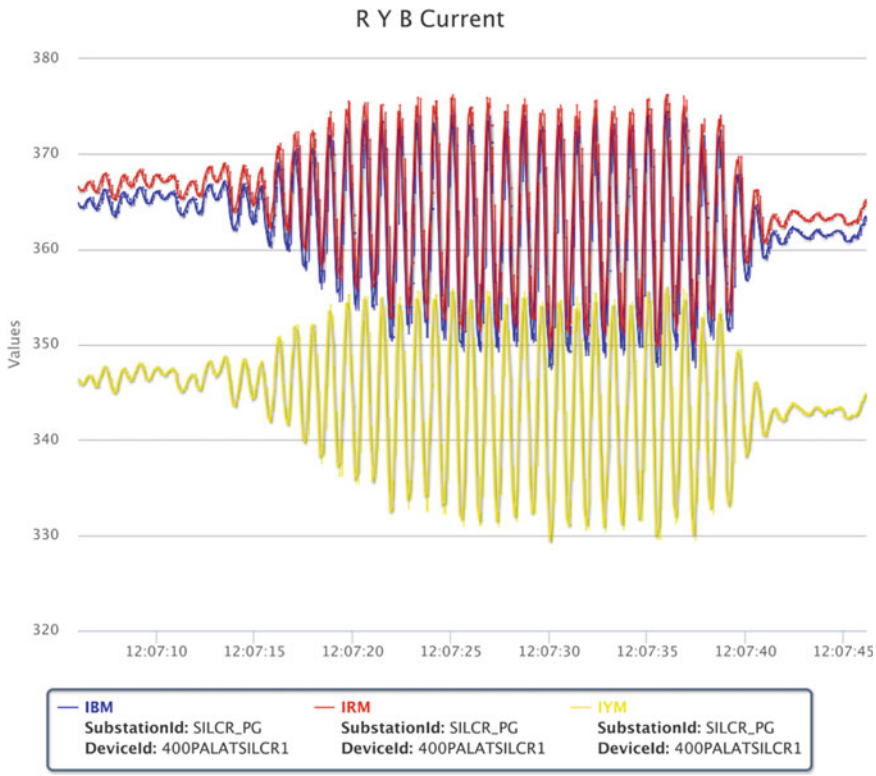

Fig. 8 Fluctuation in oscillation

train our algorithm and perform feature selection. More importantly, the spatial–temporal characters of large-scale events in power systems will be investigated to detect possible cascading effect. Finally, a monitoring system that combines and processes real-time and real-world data of power grids may be implemented in the future.

Acknowledgements The work done in this article was financially supported by the Science Engineering & Research Board (SERB), India, under grant sanction: EMR/2017/001508. The data used was provided by NERLDC POSOCO. The authors gratefully acknowledge the support provided.

References

1. Novosel D, Madani V, Bhargava B, Vu K, Cole J (2008) Dawn of the grid synchronization. IEEE Power Energ Mag 6(1):49–60
2. Shen Y, Abubakar M, Liu H, Hussain F (2019) Power quality disturbance monitoring and classification based on improved PCA and convolution neural network for wind-grid distribution systems. Energies 12:1280

3. Sun J, Xia M, Chen Q (2019) A classification identification method based on phasor measurement for distribution line parameter identification under insufficient measurement conditions. IEEE Access 7:158732–158743. Foster I, Kesselman C (1999) The grid: blueprint for a new computing ınfrastructure. Morgan Kaufmann, San Francisco
4. Brahma S, Kavasseri R, Cao H, Chaudhuri NR, Alexopoulos T, Cui Y (2017) Real-time identification of dynamic events in power systems using PMU data, and potential applications-models, promises, and challenges. IEEE Trans Power Del 32:294–301
5. Shi X, Qiu R, Ling Z, Yang F, Yang H, He X (2020) Spatio-temporal correlation analysis of online monitoring data for anomaly detection and location in distribution networks. IEEE Trans Smart Grid 11:995–1006
6. Yang F, Qiu RC, Ling Z, He X, Yang H (2019) Detection and analysis of multiple events based on high-dimensional factor models in power grid. Energies 12:1360
7. De La Ree J, Centeno V, Thorp JS, Phadke AG (2010) Synchronized phasor measurement applications in power systems. IEEE Trans. on Smart Grid 1(1):20–27
8. Brahma S, Kavasseri R, Cao H, Chaudhuri N, Alexopoulos T, Cui Y (2017) Real-time identification of dynamic events in power systems using PMU data, and potential applications—models, promises, and challenges. IEEE Trans Power Del 32(1):294–301
9. Bruno S, Benedictis M, Scala M (2006) Taking the pulse of power systems: monitoring oscillations by wavelet analysis and wide area measurement system. In: Proceedings of IEEE PES Power Systems Conference and Exposition, pp 436–443
10. Sohn SW, Allen AJ, Kulkarni S, Grady WM, Santoso S (2012) Event detectionmethod for the PMUs synchrophasor data. In: IEEE power electronics and machines in wind applications, July 2012, pp 1–7
11. Messina A, Vittal V, Ruiz-Vega D, Enriquez-Harper G (2006) Interpretation and visualization of wide-area PMU measurements using Hilbert analysis. IEEE Trans Power Syst 21(4):1763–1771
12. Fan L, Kavasseri R, Miao Z, Osborn D, Bilke T (2008) Identification of system wide disturbances using synchronized phasor data and ellipsoid method. In: Proceedings of IEEE Power and Energy Society General Meeting—Conversion and Delivery of Electrical Energy 21st Century, July 2008, pp 1–10
13. Biswal M, Hao Y, Chen P, Brahma S, Cao H, De Leon P (2016) Signal features for classification of power system disturbances using PMU data. In: 19th Power Systems Computation Conference 2016, pp 1–7
14. Ma J, Makarov YV, Miller CH, Nguyen TB (2008) Use multi-dimensional ellipsoid to monitor dynamic behavior of power systems based on PMU measurement. In: Proceedings of IEEE Power and Energy Society General Meeting—Conversion and Delivery of Electrical Energy 21st Century, July 2008, pp 1–8
15. Dahal OP, Brahma SM, Cao H (2014) Comprehensive clustering of disturbance events recorded by phasor measurement units. IEEE Trans Power Del 29(3):1390–1397
16. Negi SS, Kishor N, Uhlen K, Negi R (2017) Event detection and its signal characterization in PMU data stream. IEEE Trans Ind Inf 13(6):3108–3118
17. Ye L, Keogh E (2011) Time series shapelets: A novel technique that allows accurate, interpretable and fast classification. Data Mining Knowl Discov 22(1/2):149–182
18. Singh AP, Hemant Kumar G, Paik SS, Roy DS (2019) Storage and analysis of synchrophasor data for event detection in Indian power system using hadoop ecosystem. In: Proceedings of Data and Communication Networks, pp 291–304. Springer, Singapore
19. Nath B, Roy DS (2019) Characterizing single line to ground (SLG) events with Indian power grid's synchrophasor data. In: Proceedings of ınternational conference on ınnovation in modern science and technology, pp 710–718. Springer, Cham

Chapter 53
Prediction of Solar Power Using Linear Regression

Shubham Thombare, V. N. Pande, R. S. Kulkarni, and S. M. Kakade

Abstract Solar power has been a significant contributor to energy generation and the economy in recent years. The reason for the significant rise in solar energy usage has been its abundance and cost-free nature. Yet, these qualities cannot support the solar to be used at its full potential. The intermittent nature of the solar has been a significant drawback in its progress. With the advancement in artificial intelligence, solar power forecasting can be done by machine learning methods. Therefore, this paper demonstrates the results obtained by a linear regression model using python for predicting solar energy. After the evaluation process, the best performance achieved was RMSE of 44.371 and R^2_value of 0.966 among all the scenarios.

Keywords Solar power · Artificial intelligence · Solar power forecasting · Machine learning · Linear regression · Python

1 Introduction

Solar energy is a clean source of energy leaving behind no harmful residue in the environment. So, by taking into consideration the global demand for energy and the availability of solar energy, there has been massive research in the field of forecasting solar output power. Solar power forecasting can be majorly classified into three categories:

S. Thombare (✉) · V. N. Pande · R. S. Kulkarni · S. M. Kakade
Department of Electrical Engineering, College of Engineering, Pune, India
e-mail: thombaress19.elec@coep.ac.in

V. N. Pande
e-mail: vnp.elec@coep.ac.in

R. S. Kulkarni
e-mail: rsk17.elec@coep.ac.in

S. M. Kakade
e-mail: smk.elec@coep.ac.in

G. Panda et al. (eds.), *Sustainable Energy and Technological Advancements*,
Advances in Sustainability Science and Technology,
https://doi.org/10.1007/978-981-16-9033-4_53

- Meteorological Models: These models consist of numerical weather prediction (NWP) techniques and satellite image processing. The NWP model is an integration of numerical representation of various atmospheric variables into an equation. Building an NWP model requires strong domain knowledge. In the satellite image processing model, the images captured by the digital cameras are used to forecast solar power [1].
- Statistical Models: These models consist of statistical methods like auto-regressive moving average (ARMA), auto-regressive integrated moving average (ARIMA), and exponential smoothing (ES). These are usually used for short-term solar power forecasting, i.e., for within-a-day forecasting.
- Machine Learning Models: These models consist of many algorithms such as linear regression, multiple variable regression, *k*-NN (*k*-nearest neighbors), neural networks (NN), support vector regression (SVR), polynomial regression, decision tree, and random forest. Forecasting is done sometimes using a single model or by grouping several machine learning models.

In [2], linear regression has been used to measure the solar power generation, achieving the mean square error (MSE) of 0.003203 and R^2_value of 0.947459 (94.74%). In [3], the author analyzed the solar prediction from the solar plant in South Korea. The linear regression has shown a root mean square error (RMSE) of 529.37, mean absolute error (MAE) of 334.78, and $R^2\_value = 77.4\%$. In [4], the author has compared different algorithms, and linear regression has a root mean square error (RMSE) of 5.23×10^6. In [5], multiple linear regression has achieved a mean absolute error (MAE) of 0.0707, mean square error (MSE) of 0.0112, and mean absolute percentage error (MAPE) of 0.5433.

In [6], the author has observed a root mean square error (RMSE) of 130 W/m^2. In [7], linear regression has achieved a mean absolute error (MAE) of 2.203 and root mean square error (RMSE) of 2.333. In [8], linear regression has got a R^2_value of 0.5, accordingly lasso and ridge regression has R^2_value of 0.6 each. In [9], linear regression has encountered a significant error of 3.865e + 06. In [10], the linear regression was evaluated with four different evaluation metrics getting a mean absolute error (MAE) of 194.56, R^2_value of 0.8097, root mean square error (RMSE) of 508.675, and mean absolute percentage error (MAPE) of 6.6623.

This paper mainly focuses on predicting the solar power plant output using a ma chine learning algorithm. The machine learning model that has been used in this pa per is linear regression. Even though there has been continuous research for predicting solar power, the error in the prediction can be minimized.

2 System Description

2.1 Solar System Setup

The data analyzed in this project is taken from the photovoltaic system located at the University of Salento in Monteroni di Lecce, Puglia (40° 19′32′′′16 N, 18° 5′52′′′44 E), located in South Italy [11]. This PV module of 960 k Wp is installed on a car parking that has 3000 monocrystalline silicon modules connected in series. The PV system is divided into two groups distinguished by tilt of the module, which is 3° for the PV1 module and 15° for the PV2 module. Further details of the PV modules are given in Table 1.

From the setup mentioned in Table 1, the data variables are collected over nearly more than 500 days. The data collected consist of hourly mean ambient temperature (Ta), hourly mean module temperature (T_{m}), hourly mean solar irradiance measured at two different tilts (I_3 *and* I_{15}), and hourly mean PV power [1].

Data that is collected is measured at a specific time, i.e.,

T_{s} = ambient and module temperature measured every 10 min (°C).

I_{s} = solar irradiance of the plains at 3° and 15° is sampled at 1 min (W/m^2).

P_{s} = photovoltaic output power measured every 1 min (W).

To illustrate the impact of input parameters on the forecasting of solar power, all the input parameters need to be sampled at the same sample steps chosen equal to 1 h, i.e.,

- $T_{\text{a}}(i)$ and $T_{\text{m}}(i)$ are the hourly mean ambient and module temperature measured in 60 min concerning hour *i*.

$$T(i) = \frac{1}{6}\sum_{t=1\,s}^{6} T(t) \tag{1}$$

- $I_3(i)$ and $I_{15}(i)$ are the hourly mean solar irradiance taken from the panel set up at an angle 3°and 15° measured in the span of 60 min concerning hour *i*.

Table 1 Specification of the PV system

Specifications	PV1 module group	PV2 module group
Nominal power(kWp)	353.3	606.7
Number of modules	1104	1896
Net Surface of the modules (m^2)	1733.3	2976.7
Azimuth (°)	– 10	– 10
Tilt (°)	3	15

$$I(i) = \frac{1}{60} \sum_{t=1\,s}^{60} I(t) \tag{2}$$

- $P(i)$ is the hourly mean value of the PV output power measured in the span of 60 min.

$$P(i) = \frac{1}{60} \sum_{t=1\,s}^{60} P(t) \tag{3}$$

Parameters obtained from this setup were:

1. Ambient Temperature (T_a)
2. Module Temperature (T_m)
3. Irradiance at 3° (I_3)
4. Irradiance at 15° (I_{15})
5. Power (P)

2.2 Evaluation Metrics

The performance of the regression model is evaluated based on evaluation metrics. The evaluation metrics that are used in the evaluation are:

1. Root Mean Squared Error (RMSE): It is just the square root of the MSE. It represents the standard deviation of the error. Standard deviation is a measure of how spread our data is,

   If RMSE = low, it signifies that data is less spread or concentrated around the mean or regression line.

   If RMSE = high, then it signifies that data is spread over a large range with respect to the mean or the line of regression.

   RMSE can be represented as

$$\text{RMSE} = \sqrt{\frac{\sum_{i=1}^{n} \left(y_i - \hat{y}_i\right)^2}{n}} \tag{4}$$

2. R^2_value: R-Squared explains how well the independent variables in the regression model explain the variability in the dependent variable. In other words, it is the total variation of the dependent variable that is defined by the variation of the independent variable.

   R-squared can be represented as

$$R^2 = 1 - \frac{SS_{\text{res}}}{SS_{\text{tot}}} \tag{5}$$

where
SS_{res} = sum of squares of residual

$$SS_{\text{res}} = \sum_{i=1}^{m} \left(y_i - \hat{y}_i\right)^2 \tag{6}$$

SS_{tot} = total sum of squares (variance of the data)

$$SS_{\text{tot}} = \sum_{i=1}^{m} (y_i - \overline{y})^2 \tag{7}$$

3. p_value: It is a measure by which two quantities being compared can be declared as same or different. The decision is made based on the significance value (p_value). The two possible outcomes based on the p_value is:

Null Hypothesis: Both quantities are the same.
Alternative Hypothesis: Both quantities are different.
If p_value is greater than 0.05, the null hypothesis is selected (data lies in the confidence interval), or an alternative hypothesis is selected. The p_value of 0.05 is universal, but it can be changed according to the application, like in medical applications the error should be minimum so, there p_value can also be set as 0.01.

3 Linear Regression

3.1 Introduction to Linear Regression

A linear regression model is the most basic regression model. Here, it is expected that the independent and the dependent features will have a linear relationship. The relationship is explained by a line called as a line of regression. This line has the minimum error compared to all the lines drawn over the given plane. There are two types of linear regression models:

3.1.1 Simple Linear Regression

In this type of regression model, there is only one dependent and independent variable. İt can be formulated by a straight-line equation, i.e.,

$$y = mx + c \tag{8}$$

where

y	dependent variable
m	slope of the regression line
x	independent variable
c	*y_intercept*

3.1.2 Multiple Linear Regression

There are two or more independent variables in multiple linear regression. These independent variables combined helps the model to predict the dependent variable. In this case, let if we have two independent variables and one dependent variable, the line of regression thus obtained will be a plane of three dimensions. The multiple linear regression can be represented as:

$$y = c_0 + m_1x_1 + m_2x_2 + \cdots + m_nx_n \tag{9}$$

where

y	dependent variable
c_0	y_intercept
m_1, m_2, m_n	slopes of the corresponding independent variables
x_1, x_2, x_n	independent variables
n	number of independent variables

Multiple linear regression for the problem statement can be formulated as:

$$\begin{aligned}\text{Power} = c_0 + m_1(\text{ambient temperature})\\ + m_2(\text{module temperature}) + m_3(\text{Irradiance})\end{aligned} \tag{10}$$

3.2 *Scenario*

Earth revolves around the sun in an elliptical orbit. Therefore, there are two angle of tilts at which the solar systems are placed. In general, the angle of tilts is in the range ± 5° and ± 10°. For the geographical location mentioned above, 3° and 15° are the angle of tilts. The two modules thus formed are divided into the ratio of 36.8 and 63.2%.

As the solar panels are divided into two modules, and also there are two angle of tilts. Different scenarios are made. Three scenarios have been considered in this paper for the complete analysis of the linear regression model. All the scenarios have ambient temperature and module temperature in common. The main difference between these scenarios is irradiance (Table 2).

Table 2 Different scenarios for evaluation

S. No	Scenario	Dataset
1	Scenario 1	Ambient temperature, module temperature, irradiance at 3° tilt, and power
2	Scenario 2	Ambient temperature, module temperature, irradiance at 15° tilt, and power
3	Scenario 3	Ambient temperature, module temperature, weighted Irradiance between 3° and 15° tilt, and power

1. Scenario 1: Irradiance at 3° tilt
2. Scenario 2: Irradiance at 15° tilt
3. Scenario 3: Weighted Irradiance.

Weighted irradiance can be calculated by:

$$\text{WeightedIrradiance} = \frac{0.368(\text{Irradianceat } 3^\circ \text{ tilt}) + 0.632(\text{Irradiance at } 15\circ \text{ tilt})}{100} \tag{11}$$

where
$0.368 =$ percentage of Module 1
$0.632 =$ percentage of Module 2

4 Results and Discussion

The linear regression is applied to all the scenarios, and results are calculated. The table shows the results obtained after evaluation.

Below are some plots of the predicted and actual power with respect to the number of samples for all the scenarios. This plot shows the predicted and actual value of the power for very few samples. If the whole testing dataset is taken, it would be challenging to observe the change in the predicted values (Fig. 1).

As it is clear from the plot, Scenario 1 is not able to track the edges for the plot since the R^2_value of the irradiance at 3° is least among all the three irradiances (Fig. 2).

Scenario 2 is better than that of Scenario 1 since the R^2_value of the irradiance at 15° is better than Scenario 1 (Fig. 3).

Scenario 3 has shown excellent results as compared to the other two Scenarios since weighted irradiance was best in explaining the variability of the power R^2_value of the irradiance at 3° is least among all the three irradiances.

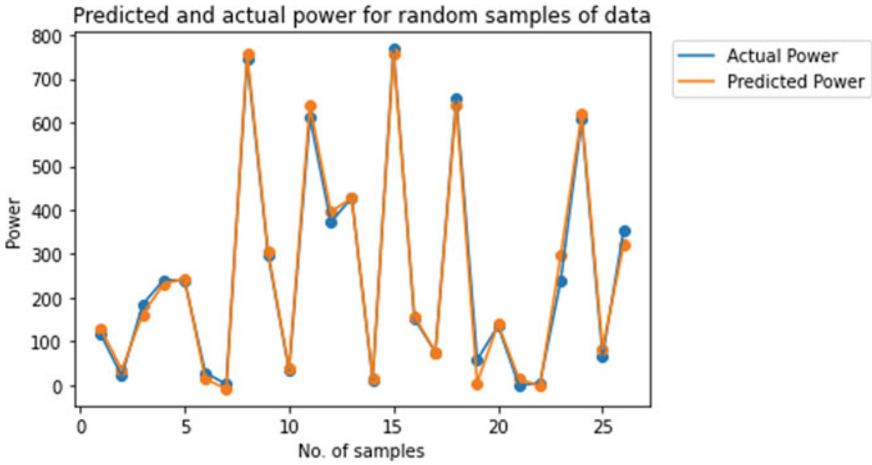

Fig. 1 Scenario 1

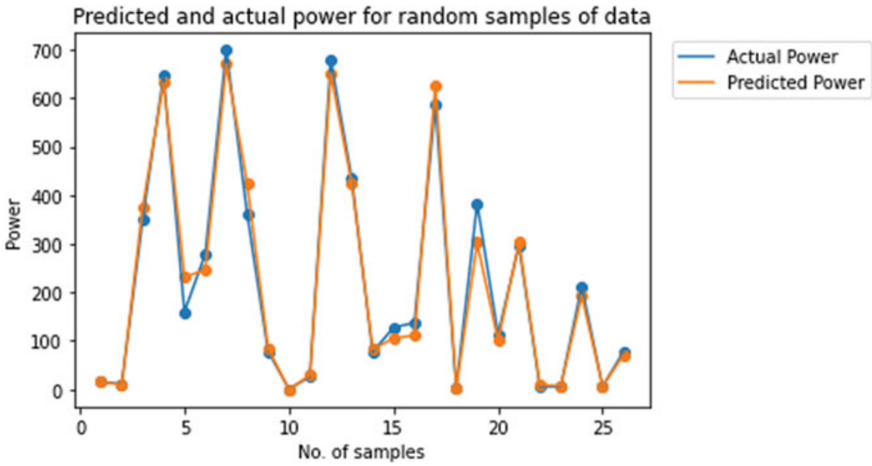

Fig. 2 Scenario 2

4.1 Discussion

From Table 3, an observation can be made that Scenario 3 has the least root mean square error (RMSE), followed by Scenario 1 and then Scenario 2. Irradiance has a significant impact on solar power generation as compared to ambient temperature and module temperature. The reason behind it is irradiance. Table 4 shows the R^2_value of irradiance at 3°, 15°, and weighted irradiance.

It can be seen that weighted irradiance has the highest R^2_value, also R^2_value explains the variability of the dependent variable with respect to independent

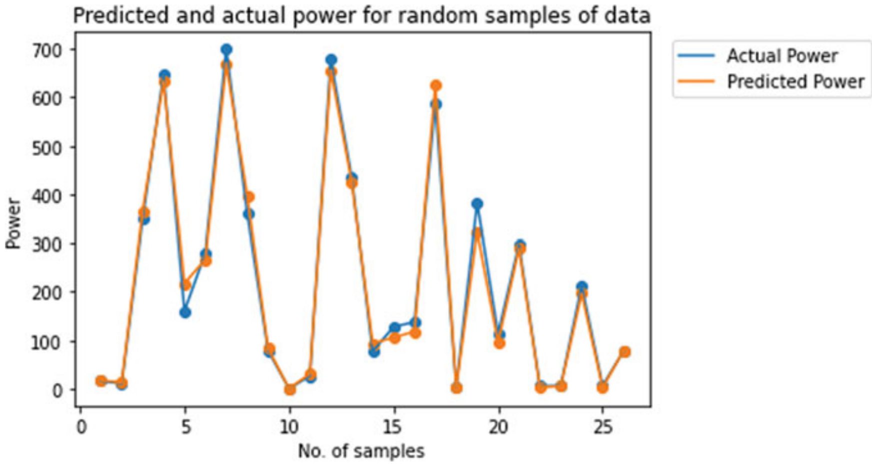

Fig. 3 Scenario 3

Table 3 Result analysis of linear regression using different scenarios

S. No	Scenario	R^2_value	RMSE	p-value
1	Scenario 1	0.958	49.506	0.875
2	Scenario 2	0.958	50.068	0.799
3	Scenario 3	0.966	44.371	0.808

Table 4 R^2 values of Irradiances

S. No	Irradiance	$R^2\_value(\%)$
1	3° tilt	95.60
2	15° tilt	95.78
3	Weighted irradiance	96.35

variables. Therefore, Scenario 3, having weighted irradiance attains the least RMSE compared to Scenario 1 and Scenario 2. After Scenario 3, Scenario 2 has the second-highest R^2_value, therefore, Scenario 2 has less RMSE as compared to Scenario 1.

The p-value of all the scenarios is more significant than 0.05, which means all accept the null hypothesis. Null hypothesis means that the predicted and actual power are in the acceptable range or the confidence interval.

5 Conclusions

Linear regression can be a good alternative for predicting solar power. This paper has shown that irradiance is very vital while predicting solar power. It has a major contribution in predicting power. Weighted irradiance has proven to be the best among all the scenarios considered. Parameters are linear; this was the consideration while doing this project. After experimentation, it has been seen that parameters are nonlinear. Other regression models like polynomial regression, decision tree, random forest, and neural networks can also be applied to better forecast.

References

1. Wang Z (2019) Solar power forecasting. Thesis submitted for the degree of Doctor of Philosophy in the School of Computer Science at The University of Sydney
2. Khan A, Bhatnagar R, Masrani V, Lobo VB (2020) A comparative study on solar power forecasting using ensemble learning. In: 2020 4th international conference on trends in electronics and informatics (ICOEI)(48184), 2020, pp 224–231. https://doi.org/10.1109/ICOEI48184.2020.9142884
3. Carrera B, Kim K (2020) Comparison analysis of machine learning techniques for photovoltaic prediction using weather sensor data. 1 June 2020
4. Prakash A, Singh SK (2014) Towards an efficient regression model for solar energy prediction. In: 2014 innovative applications of computational intelligence on power, energy and controls with their impact on humanity (CIPECH), 2014, pp 18–23. doi: https://doi.org/10.1109/CIPECH.2014.7019040
5. Xu Z, Yang G, Geng H (2019) Power forecasting of photovoltaic generation based on multiple linear regression method with real-time correction term. In: 2019 22nd international conference on electrical machines and systems (ICEMS), 2019, pp 1–4. https://doi.org/10.1109/ICEMS.2019.8922096
6. Sharma N, Sharma P, Irwin D, Shenoy P (2011) Predicting solar generation from weather forecasts using machine learning. In: 2011 IEEE international conference on smart grid communications (SmartGridComm), 2011, pp 528–533. doi: https://doi.org/10.1109/SmartGridComm.2011.6102379
7. Hassan MZ, Ali MEK, Ali ABMS, Kumar J (2017) Forecasting day-ahead solar radiation using machine learning approach. In: 2017 4th Asia-Pacific world congress on computer science and engineering (APWC on CSE), 2017, pp 252–258. https://doi.org/10.1109/APWConCSE.2017.00050
8. Javed A, Kasi BK, Khan FA (2019) Predicting solar irradiance using machine learning techniques. In: 2019 15th international wireless communications and mobile computing conference (IWCMC), 2019, pp 1458–1462. https://doi.org/10.1109/IWCMC.2019.8766480
9. Araf I, Elkhadiri H, Errattahi R, Hannani AE (2019) AMS solar energy prediction: a comparative study of regression models. In: 2019 3rd international conference on intelligent computing in data sciences (ICDS), 2019, pp 1–5. doi: https://doi.org/10.1109/ICDS47004.2019.8942237
10. Kuriakose AM, Kariyalil DP, Augusthy M, Sarath S, Jacob J, Antony NR (2020) Comparison of artificial neural network, linear regression and support vector machine for prediction of solar PV power. In: 2020 IEEE Pune section international conference (PuneCon), 2020, pp 1-6. doi: https://doi.org/10.1109/PuneCon50868.2020.9362442
11. Malvoni M, De Giorgi MG, Congedo PM (2016) Data on photovoltaic power forecasting models for Mediterranean climate. Department of Engineering for Innovation, University of Salento, via per Arnesano I-73100, Italy

Chapter 54
Fuzzy Logic Controller for HVAC System of Passenger Car for Cooling Application

Pratik Ramu Bante, Archana G. Thosar, and S. Srikanth

Abstract Heating, ventilation, and air conditioning (HVAC) system in an automobile provides a pleasant atmosphere for the passenger. The HVAC system should be intelligent and reliable enough to provide a clean and comfortable environment to the passengers. The HVAC system is highly nonlinear because of disturbances and uncertainties like solar heat load, passenger heat load, ambient temperature, cabin space, etc. A brief study of the HVAC system and disturbance parameters is explained. This paper attempts to design a fuzzy logic control (FLC) for the HVAC system of a passenger car. The FLC takes care of disturbances and nonlinearities of the plant. The fuzzy logic controller perfectly maintains the desire cabin temperature at the set point. A conventional PI controller and intelligent fuzzy controller are simulated on the MATLAB/Simulink platform to clarify the robust control method. It is observed that fuzzy logic control outperforms the PI controller.

Keywords Heating ventilation air conditioning (HVAC) · Compressor · Condenser · Evaporator · Thermal expansion valve (TEV) · Vehicle cabin · R134a · Refrigeration cycle · MATLAB · Proportional integral (PI) · Fuzzy logic control (FLC)

P. R. Bante (✉) · A. G. Thosar
College of Engineering Pune, Pune, India
e-mail: bantepr19.elec@coep.ac.in

A. G. Thosar
e-mail: agt.elec@coep.ac.in

S. Srikanth
CREAT Uno Minda Industries Ltd, Pune, India
e-mail: ssrikanth@mindagroup.com

G. Panda et al. (eds.), *Sustainable Energy and Technological Advancements*,
Advances in Sustainability Science and Technology,
https://doi.org/10.1007/978-981-16-9033-4_54

1 Introduction

In modern cars, passengers' comfort is one of the main parameters during the selection of a car. There are many technologies developed to provide comfort to drivers as well as to passengers in the car. Like driving modes, independent suspension, panorama sunroof, power seats, power window, ambient lighting, Bluetooth streaming, ventilated seats, and many more. Out of which heating ventilation air conditioning (HVAC) system in a car plays an important role in drivers as well as passengers' comfort. The instantaneous regulation of temperature, humidity, and air motion is well established by an air conditioning system. In its cycle, automotive air conditioning uses vapor compression refrigeration systems. A compressor, an evaporator, a condenser, and an expansion valve are the main components of an automotive air conditioning system. The compressor is the most important component of any air conditioning system.

During the last few decades, automobile manufacturers and university researchers have focused their attention on the design of mobile air conditioning systems. PID controller for the HVAC system was designed [1]. Comparison of HVAC systems control using simple ON–OFF, intelligent ON–OFF, and optimal controllers are discussed in [2]. Sliding mode control for the air conditioning system is simulated in [3]. The design and the implementation of a PID using internal model control for vapor compression refrigeration system [4]. HVAC energy management and optimization with model predictive control were discussed in [5, 6]. The mathematical model for automotive air conditioning system is referred from [7]. The universal fuzzy logic speed controller is designed in [8] for four switches BLDC motor drive. For membership function designing in the fuzzy controller, [9] is referred. Control of cabin temperature is an important factor for passenger comfort. However, there are so many disturbances present in real-life scenarios that deteriorate the car's cabin temperature. Disturbances such as solar load, passenger heat load, ambient temperature, and many more. Hence, continuous tracking of desired cabin temperature is a challenging task. In this paper, the PI control strategy is used to control the cabin temperature of the car. To overcome the downside of the PI controller, the fuzzy controller is designed to maintain the desired temperature in the vehicle cabin to achieve a comfortable environment for the driver and passengers inside the car. The fuzzy control is a way for replicating and executing the knowledge of a (smart) human about how to govern a system. IF–THEN rules in the form of "if X and Y, then Z" are used by fuzzy controllers to illustrate models or knowledge. Fuzzy rules and membership functions and fuzzification and defuzzification procedures make up a fuzzy inference system. An ordinary crisp input generates a standard crisp output easy to read and understand when fuzzy inference is used.

The brief outline of the paper is as follows. Complete mathematical model for the HVAC is developed in Sect. 2. Section 3 gives brief about FLC. The design of the proposed controllers is represented in Sect. 4. Simulation results are discussed in Sect. 5. Section 6 concludes the paper.

2 Mathematical Modeling

The block diagram of the HVAC system is shown in Fig. 1. The HVAC system of a passenger car consists of the compressor, condenser, thermal expansion valve, evaporator, and passenger's car cabin. It works on principles of heat transfer, thermodynamics, and fluid mechanics. All equations are based on the law of conservation of mass and energy.

2.1 Vehicle Cabin

The energy balance equation of the vehicle cabin is given as,

$$\begin{aligned} M_{\mathrm{r}}.C_{\mathrm{pr}}.\frac{\mathrm{d}Tr}{\mathrm{d}t} &= -C_{\mathrm{pe}}.\rho.f.(T_{\mathrm{me}} - T_{\mathrm{se}}) \\ &+ Q_{\mathrm{s}} + N.Q_{\mathrm{ps}} + U_{\mathrm{o}}.A_{\mathrm{o}}.(T_a - T_r) \\ &+ M_{\mathrm{f}}.C_{\mathrm{pa}}.(T_{\mathrm{a}} - T_{\mathrm{r}}) + K_{\mathrm{spl}}.f \end{aligned} \tag{1}$$

M_{r} = Mass of air inside cabin

C_{pr} = Specific heat at constant pressure

T_{r} = Cabin temperature

C_{pr} = Specific heat at constant pressure in evaporator

ρ = Density of air

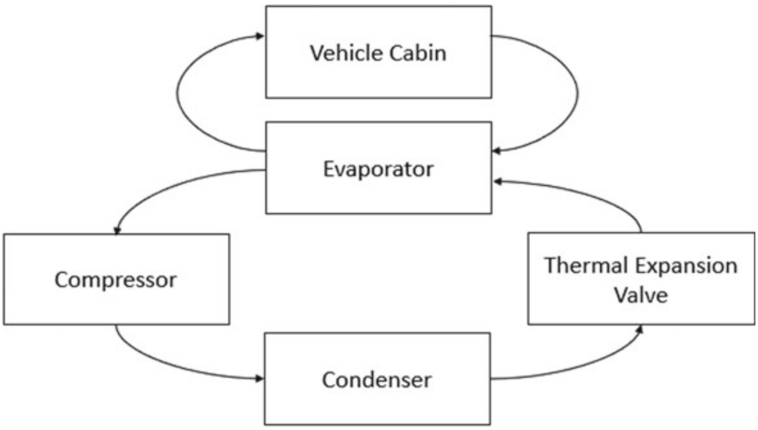

Fig. 1 Block diagram of HVAC system

f = Volumetric flow rate

T_m = Mixing temperature of evaporator

T_s = Wet side temperature of evaporator

Q_s = Heat load due to solar radiation

Q_{ps} = Sensible heat load due to passenger

N = Number of passengers

U_o = Heat transfer coefficient of vehicle wall

A_o = Surface area of cabin

T_a = Temperature of ambient air

M_f = Mass flow rate

C_{pa} = Specific heat at constant pressure

K_{spl} = Heat gain coefficient of blower fan

The heat energy generated by solar radiation from the sun, passenger sensible radiation along with the number of passengers, solar radiation transmitted to the cabin and metal of vehicle, heat transfer with the outside ambiance, and the heat load from blower fan which is to be removed by the cooling capacity of evaporator [7].

2.2 Evaporator

$$C_p.\rho.V_{h1e}.\frac{dT_{de}}{dt} = C_p.\rho.f.(T_{me} - T_{de}) + \alpha_{1e}.A_{1e}.\left(T_{we} - \left(\frac{T_{me} + T_{de}}{2}\right)\right) \tag{2}$$

V_{h1e} = Air side volume of evaporator core

α_{1e} = Heat transfer coefficient between air and evaporator wall in dry cooling region

A_{1e} = Heat transfer area of dry cooling region

T_{we} = Temperature wall of evaporator

$$\begin{aligned} C_p.\rho.V_{h2e}.\frac{dT_{se}}{dt} &= C_p.\rho.f.(T_{de} - T_{se}) + \rho.f.h_{fge}.(W_{me} - W_{ae}) \\ &\quad + \alpha_{2e}.A_{2e}.(T_{we} - \left(T_{de} - \left(\frac{T_{de} - T_{se}}{2}\right)\right) \end{aligned} \tag{3}$$

V_{h2e} = Wet side volume of evaporator core

H_{fge} = Latent heat of vaporization in evaporator

$W =$ Moisture content

$\alpha_{2\mathrm{e}} =$ Heat transfer coefficient between air and evaporator wall in wet cooling region

$A_{2\mathrm{e}} =$ Heat transfer area of wet cooling region

$$\begin{aligned} C_{\mathrm{p}}.\rho.f.\frac{\mathrm{d}T_{we}}{\mathrm{d}t} &= \alpha_{1\mathrm{e}}.A_{1\mathrm{e}}.\left(\left(\frac{T_{\mathrm{me}} + T_{\mathrm{de}}}{2}\right) - T_{\mathrm{we}}\right) \\ &\quad + \alpha_{2\mathrm{e}}.A_{2\mathrm{e}}.\left(\left(\frac{T_{\mathrm{de}} + T_{\mathrm{se}}}{2}\right) - T_{\mathrm{we}}\right) \\ &\quad - M_{\mathrm{ref}}.(h_{\mathrm{r2e}} - h_{\mathrm{r1e}}) \end{aligned} \tag{4}$$

$M_{\mathrm{ref}} =$ Reference mass flow rate of refrigerant

$h_{\mathrm{r2e}} =$ Enthalpy of refrigerant at evaporator outlet

$h_{\mathrm{r1e}} =$ Enthalpy of refrigerant at evaporator inlet

$$C_{\mathrm{pm}}.f.\rho.T_{\mathrm{me}} = M_{\mathrm{f}}.C_{\mathrm{pa}}.T_{\mathrm{a}} + (\rho.f - M_{\mathrm{f}})C_{\mathrm{p}}.T_{\mathrm{r}} + T_{\mathrm{me}}.M_{\mathrm{f}}.C_{\mathrm{pm}} \tag{5}$$

$M_{\mathrm{f}} =$ Mass flow rate of ventilation air

The evaporator model developed in four sections as the dry side of an evaporator, wet side of an evaporator, temperature of the evaporator wall and adiabatic mixing temperature of evaporator represented in Eqs. (2)–(5), respectively.

2.3 *Compressor*

$$M_{\mathrm{ref}} = \omega_{\mathrm{c}}.V_{\mathrm{c}}.\rho_{\mathrm{c}}.\left(1 + C_{\mathrm{c}} - C_{\mathrm{c}}\left(\frac{P_{\mathrm{d}}}{P_{\mathrm{s}}}\right)^{\frac{1}{n}}\right) \tag{6}$$

$n =$ Polytrophic exponent

$\omega_{\mathrm{c}} =$ Compressor speed

$V_{\mathrm{c}} =$ Swept volume

$\rho_{\mathrm{c}} =$ Density of refrigerant at suction side

$C_{\mathrm{c}} =$ Clearance factor

$\frac{P_{\mathrm{d}}}{P_{\mathrm{s}}} =$ Ratio of discharge pressure to suction pressure

$$C_{\mathrm{pr}}.\rho.f.\frac{\mathrm{d}T_{\mathrm{out}}}{\mathrm{dt}} = T_{\mathrm{in}}.M_{\mathrm{ref}}.C_{\mathrm{pr1}} - T_{\mathrm{out}}.M_{\mathrm{ref}}.C_{\mathrm{pr2}} \tag{7}$$

The compressors' energy balance equation and reference mass flow rate represented in Eqs. (7) and (6), respectively.

2.4 Condenser

$$C_{\mathrm{p}}.\rho.V_{\mathrm{h1c}}.\frac{\mathrm{d}T_{\mathrm{d}}}{\mathrm{d}t} = C_{\mathrm{p}}.\rho.f.(T_{\mathrm{mc}} - T_{\mathrm{dc}}) + \alpha_{1\mathrm{c}}.A_{1\mathrm{c}}.\left(T_{\mathrm{wc}} - \left(\frac{T_{\mathrm{mc}} + T_{\mathrm{dc}}}{2}\right)\right) \tag{8}$$

$$C_{\mathrm{p}}.V_{\mathrm{h2c}}\frac{\mathrm{d}T_{\mathrm{sc}}}{\mathrm{d}t} = C_{\mathrm{p}}.\rho.f.(T_{\mathrm{dc}} - T_{\mathrm{sc}}) + \rho.f.h_{\mathrm{fgc}}.(W_{\mathrm{mc}} - W_{\mathrm{ac}}) + \alpha_{2\mathrm{c}}.A_{2\mathrm{c}}.(T_{\mathrm{wc}} - \left(T_{\mathrm{dc}} - \left(\frac{T_{\mathrm{dc}} - T_{\mathrm{sc}}}{2}\right)\right) \tag{9}$$

$$C_{\mathrm{p}}.\rho.f.\frac{\mathrm{d}T_{\mathrm{wc}}}{\mathrm{d}t} = \alpha_{1\mathrm{c}}.A_{1\mathrm{c}}.\left(\left(\frac{T_{\mathrm{mc}} + T_{\mathrm{dc}}}{2}\right) - T_{\mathrm{wc}}\right) + \alpha_{2\mathrm{c}}.A_{2\mathrm{c}}.\left(\left(\frac{T_{\mathrm{dc}} + T_{\mathrm{sc}}}{2}\right) - T_{\mathrm{wc}}\right) - M_{\mathrm{ref}}.(h_{\mathrm{r2c}} - h_{\mathrm{r1c}}) \tag{10}$$

$$C_{\mathrm{pm}}.f.\rho.T_{\mathrm{m}} = M_{\mathrm{f}}.C_{\mathrm{pa}}.T_{\mathrm{a}} + (\rho.f - M_{\mathrm{f}})C_{\mathrm{p}}.T_{\mathrm{r}} \tag{11}$$

The condenser is one type of heat of heat exchanger, similar to that of evaporator. Hence, similar to evaporator, condensers' model is formed with four sections. Dry side, wet side, temperature of the wall and mixing temperature of condenser represented in Eqs. (8)–(11), respectively.

2.5 Thermal Expansion Valve

$$T_{\mathrm{in}}.M_{\mathrm{fv}}.C_{\mathrm{pv}} - T_{\mathrm{out}}.M_{\mathrm{fl}}.C_{\mathrm{pl}} = 0 \tag{12}$$

M_{fv} = Mass flow of vapor

C_{pv} = Specific heat of refrigerant in vapor phase

M_{fl} = Mass flow of liquid

C_{pl} = Specific heat of refrigerant in liquid phase.

The last component in the cooling cycle of refrigeration is the thermal expansion valve. The energy balance equation for the same is represented in Eq. (12). Here, is the condensers' temperature taken in and is fed to the evaporator.

State-Space Representation

State-space representation of HVAC system is given as follows,

$$\dot{x} = Ax + Bu + D \tag{13}$$

In Eq. (13), D represents the disturbances in HVAC system which makes the system nonlinear. To negate the effect of disturbances the fuzzy logic controller is designed.

Where

$$u = M_{\mathrm{ref}}$$

$$A = \begin{bmatrix} A_1 & A_2 \\ A_3 & A_4 \end{bmatrix}$$

$$A_1 = \begin{bmatrix} \frac{-U_0A_0+M_fC_{pa}}{M_rC_{pr}} & 0 & \frac{C_{pe}\rho f}{M_rC_{pr}} & 0 \\ 0 & \frac{2C_p\rho f-\alpha_{1e}A_{1e}}{2C_p\rho V_{h1e}} & 0 & \frac{\alpha_{1e}A_{1e}}{2C_p\rho V_{h1}} \\ 0 & \frac{2C_p\rho f-\alpha_{2e}A_{2e}}{2C_p\rho V_{h2e}} & \frac{-2C_p\rho f-\alpha_{2e}A_{2e}}{2C_p\rho V_{h2e}} & \frac{\alpha_{2e}A_{2e}}{2C_p\rho V_{h2e}} \\ 0 & \frac{\alpha_{1e}A_{1e}+\alpha_{2e}A_{2e}}{2C_p\rho f} & \frac{\alpha_{2e}A_{2e}}{2C_p\rho f} & \frac{-\alpha_{1e}A_{1e}-\alpha_{2e}A_{2e}}{C_p\rho f} \end{bmatrix}$$

$$A_2 = A_3 = 0$$

$$A_4 = \begin{bmatrix} \frac{-M_{\mathrm{ref}}C_{pr2}}{C_{pr}\rho f} & 0 & 0 & 0 \\ 0 & \frac{-2C_p\rho f-\alpha_{1c}A_{1c}}{2C_p\rho V_{h1c}} & 0 & \frac{\alpha_{1c}A_{1c}}{2C_p\rho V_{h1c}} \\ 0 & \frac{2C_p\rho f-\alpha_{2c}A_{2c}}{2C_p\rho V_{h2c}} & \frac{-2C_p\rho f-\alpha_{2c}A_{2c}}{2C_p\rho V_{h2c}} & \frac{\alpha_{2c}A_{2c}}{2C_p\rho V_{h2c}} \\ 0 & \frac{\alpha_{1c}A_{1c}+\alpha_{2c}A_{2c}}{2C_p\rho f} & \frac{\alpha_{2c}A_{2c}}{2C_p\rho f} & \frac{-\alpha_{1c}A_{1c}-\alpha_{2c}A_{2c}}{C_p\rho f} \end{bmatrix}$$

$$\dot{x} = \begin{bmatrix} \dot{T}_r \\ \dot{T}_{de} \\ \dot{T}_{se} \\ \dot{T}_{we} \\ \dot{T}_{out} \\ \dot{T}_{dc} \\ \dot{T}_{sc} \\ \dot{T}_{wc} \end{bmatrix}, x = \begin{bmatrix} T_r \\ T_{de} \\ T_{se} \\ T_{we} \\ T_{out} \\ T_{dc} \\ T_{sc} \\ T_{wc} \end{bmatrix}, B = \begin{bmatrix} 0 \\ 0 \\ 0 \\ -\frac{h_{r1}-h_{r2}}{C_p\rho f} \\ \frac{T_m}{\rho f} \\ 0 \\ 0 \\ -\frac{h_{r1}-h_{r2}}{C_p\rho f} \end{bmatrix}$$

$$D = \begin{bmatrix} \frac{-C_{pe}\rho f T_m + Q_s + N Q_{ps} + U_o A_o T_a + M_f C_{pa} T_a + K_{spl} f}{M_r C_{pr}} \\ \frac{2C_p \rho f T_{me} - \alpha_{1e} A_{1e}}{C_p \rho V_{h1e}} \\ \frac{\rho f h_{fg}(W_m - W_a)}{C_p \rho V_{h2e}} \\ \frac{\alpha_{1e} A_{1e} T_{me}}{C_p \rho f} \\ 0 \\ \frac{2C_p \rho f T_{mc} - \alpha_{1c} A_{1c}}{C_p \rho V_{h1c}} \\ \frac{\rho f h_{fg}(W_m - W_a)}{C_p \rho V_{h2c}} \\ \frac{\alpha_{1c} A_{1c} T_m}{C_p \rho f} \end{bmatrix}$$

3 Fuzzy Logic Control

Fuzzy logic is a mathematical technique to inferring issues that uses intelligent reasoning, probability theory, and multivalued logic to emulate human nature. Fuzzy logic system comprises of four components are as follows.

3.1 Fuzzification

Fuzzification is a technique that converts the system's crisp input into fuzzy set. The crisp numbers are the inputs that the sensors measure, which are subsequently fuzzified and sent to the control systems for further processing.

3.2 Rule Base

The rule base is a technique used for storing the collection of rules. The If–Then conditions provided by experts are used to govern the decision-making systems.

3.3 Inference Engine

Inference engines act as the brain of the fuzzy logic system (FLS). It enables users to determine the degree of match between the current fuzzy input and the rules. Following the matching degree, this system decides which rule should be inserted based on the provided input field. When all of the rules are executed, they are combined to create the control actions.

3.4 Defuzzification

Defuzzification is a technique to transform fuzzy values from the fuzzy inference engine into crisp ones. There are different methods of defuzzification such that centroid, and weighted average.

4 Controller Design

Fuzzy logic is a way of dealing with knowledge that is ambiguous or uncertain. The "max–min" fuzzy inference technique combines approximate knowledge of acceptable control responses for various situations into a set of rules for determining a specific control action. The verbal statement of a circumstance or the control action that follows is converted into a precise computation using membership functions (MF).

Figure 2 shows the overall block diagram of fuzzy-based temperature control for the HVAC system. There are two inputs to the fuzzy controller that are temperature error and change in error that are quantize into three levels each. NE, E, and PE represent negative error, error, and positive error. N, Z, and P represents negative, zero, and positive change in error. Temperature error calculates by the difference of desired temperature and actual cabin temperature. Mamdani-based rule base used in fuzzy controller design which regulates the compressor speed to obtain the desired temperature in the cabin of a car. Figures 3 shows the input and output membership function of fuzzy controller. Linear triangular MF's are chosen because of their good efficiency with computation capability and simplicity. Centroid method is use for defuzzification. Fuzzy rule base shown in Table 1, which has two input and single output.

Proportional Integral Control

Designing of PI is simple due to its ease of construction. The PI controller has long been a popular choice for temperature control. Proportional integral controller designed such that,

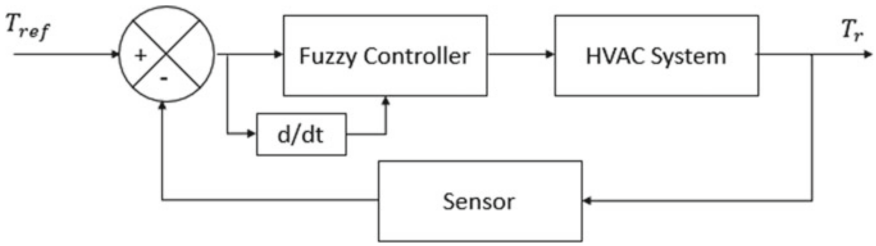

Fig. 2 Block diagram of HVAC system with fuzzy controller

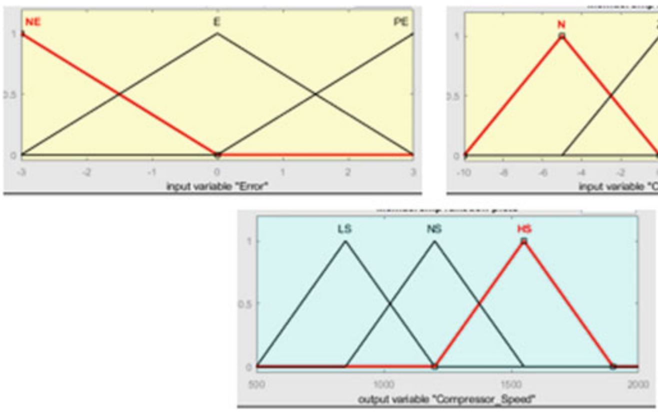

Fig. 3 Output MF's of the fuzzy controller

Table 1 Fuzzy rule

		Change in error		
		N	Z	P
Error	NE	HS	NS	LS
	E	NS	LS	LS
	PE	LS	LS	LS

$$U(t) = K_{\mathrm{P}}.e(t) + K_I \int e(t)\mathrm{d}t \tag{14}$$

where $U(t)$ is control input and $e(t)$ is error. K_{P} and K_{I} are controller's gain.

To simplify these equations into a mathematically appreciable form, some assumptions must be made. These assumptions include the following (Fig. 4):

1. For the temperature range of 18–45 °C, only cooling load is taken into account.
2. Without transportation gap, the plant is modeled as a first-order linear dynamic system.

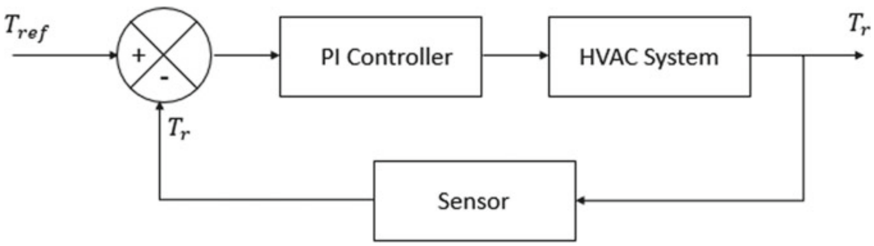

Fig. 4 Block diagram of HVAC system with fuzzy controller

3. There are no pressure drops between the evaporator and the condenser.
4. The cooling coil and the car cabin room have perfect air mixing.
5. On the airside of the cooling coil, only two regions are considered: dry cooling and wet cooling.

5 Simulation/Discussion

Passenger heat load and cabin space these two parameters are considered for sensitivity analysis. As shown in Fig. 5, cabin temperature varies with the number of passengers and changes in cabin space. Hence, to control the car's cabin temperature, fuzzy logic control, and PI control are tested for the HVAC system. The simulation result for PI control is shown in Fig. 6. To designed proportional integral controller gains are considered as 2.36, 1.25 for and respectively. For these values of K_p and K_I the rise time of the system is 0.618 s, settling time is 2.72 s, percent overshoot is 2.86%.

However, the primary disadvantage of the PI controller is that it does not produce good results when control parameters and loading conditions vary quickly. Figure 6 shows the cabin temperature output obtain with PI control strategies. The temperature profile is given as input to the controller to see the controller's performance at different temperature levels. Results explain that the rise time is high with the PI controller, and steady-state error is present. To overcome the drawbacks of the PI controller, fuzzy logic controller is proposed. The simulation results of the fuzzy logic controller are shown in Fig. 6. In which settling time is decreases, rise time also decreases, percent overshoot minimizes, and steady-state error also improves as compare to PI controller results.

The comparison of PI controller and fuzzy logic controller simulation result is shown in Fig. 6.

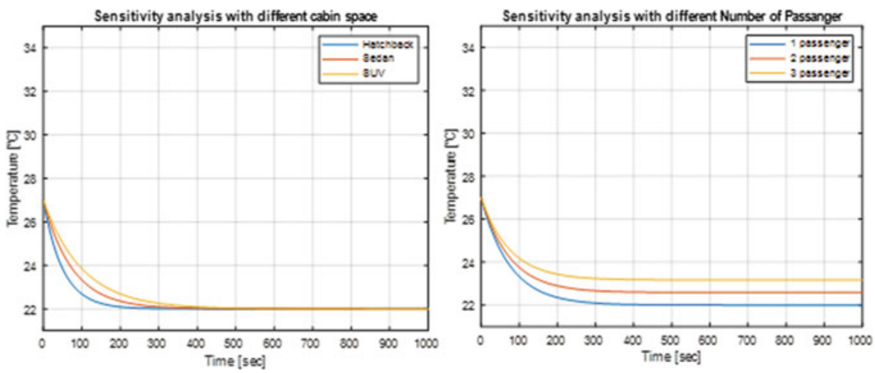

Fig. 5 Sensitivity analysis of passenger heat load and cabin space

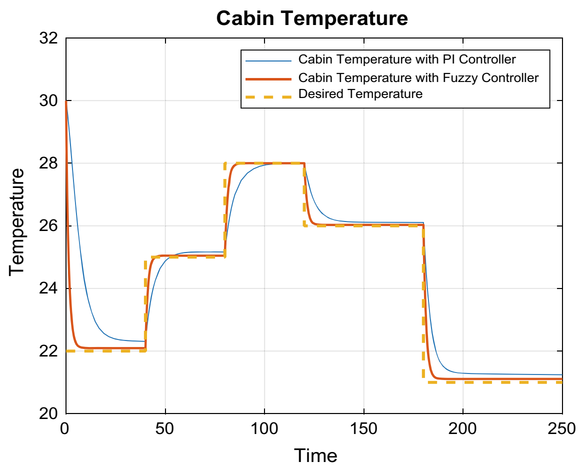

Fig. 6 Comparative simulation results of PI and fuzzy

6 Conclusion

In this paper, mathematical modeling for the HVAC system is developed with the help of mass and energy balance equations. The sensitivity analysis also done to validate the system. To control the HVAC system, two controllers are investigated, PI and fuzzy logic controllers and both are tested by using MATLAB/Simulink platform. It is observed that cabin temperature is accurately tracking the reference temperature.

In comparative study of both the controllers, it is concluded that the rise time and steady-state error of the universal fuzzy controller are better than the standard PI controller. As a consequence of the comparison, the fuzzy controller outperforms the traditional PI controller in terms of dynamic performance. By combining PID and fuzzy controller, a fuzzy PID controller can be designed for even better performance.

References

1. Liu J, Cai W-J, Zhang G-Q (2009) Design and application of handheld auto-tuning PID instrument used in HVAC. https://doi.org/10.1109/ICIEA.2009.5138484
2. Karthik C, Anunay K (2011) Comparison of energy consumption in HVAC systems using simple ON-OFF, intelligent ON-OFF and optimal controllers. https://doi.org/10.1109/PES.2011.6039823
3. Abbas A, Irfan A, Sarfraz A (2020) Design and simulation of variable air volume air conditioning system based on ımproved sliding mode control (ISMC). In: 2020 IEEE 23rd ınternational multitopic conference (INMIC). IEEE, 2020
4. Carrasco L, Manuel M, William I (2020) Design and experimental implementation of a PID-IMC Controller for a VCRS. In: 2020 IEEE 27 ınternational conference on electronics, electrical engineering and computing (INTERCON). IEEE, 2020

5. Godina R et al (2017) Home HVAC energy management and optimization with model predictive control. In: 2017 IEEE ınternational conference on environment and electrical engineering and 2017 IEEE ındustrial and commercial power systems Europe (EEEIC/I&CPS Europe). IEEE
6. Ng BC et al (2013) Dynamic modeling of an automotive air conditioning system and an auto tuned PID controller using extremum seeking algorithm. In: 2013 IEEE symposium on computers and informatics (ISCI). IEEE
7. Subramaniyan AS, Pandian S (2010) A state space approach for the dynamic analysis of automotive air conditioning system. In: International refrigeration and air conditioning conference. Paper 1079
8. Veni KK, Kumar NS, Kumar CS (2019) A comparative study of universal fuzzy logic and PI speed controllers for four switch BLDC motor drive. Int J Power Electr 10(1–2):18–32
9. Ibrahim BSKK et al (2012) Fuzzy-based temperature and humidity control for HV AC of electric vehicle. Procedia Engineering 41:904–910

Chapter 55
Sustainable Farming Using Drone with Seed Dropper

Mohammad Suhel Karkun and Sathish Dharmalingam

Abstract The main source of the Indian economy in common is agriculture. However, due to the extensive work required which causes tiredness and stress, some field workers typically migrate from the agricultural domain to the other industrial fields, which offer them more profitable and stable jobs. This possible reason causes the potential problem of a lack of human labor in agriculture. In this scenario, it becomes necessary to develop a technique for farming with automation and sensing technologies to enhance agricultural productivity and make more use of land in India for agricultural purposes. The aim of this research is to develop a quadcopter drone properly incorporated with a seed sowing mechanism. The construction and maintenance of this drone are much cheaper and less time consuming than the traditional method. The quadcopter can be flown over any specific location and drop seeds all over the region, thereby contributing to the growth of plants.

Keywords UAV systems · Quadcopter drone · Seeds sowing · Agricultural automation

1 Introduction to Unmanned Aerial Vehicle

Drones are also identified as unmanned aerial vehicles (UAV), which can fly without a pilot and passengers. Controlling of UAVs can be achieved either remotely or autonomously following predetermined programs. The UAVs are usually equipped with an accessory used for defense purposes, monitoring, and surveillance. A significant advantage in common is the less time consumption in preparation and commissioning for flight. Firstly, the UAVs were only used by the army and the police for active surveillance and defense purposes. Civilian drones are typically used for

M. S. Karkun (✉)
Aeronautical Engineering, Aditya Silver Oak Institute of Technology, Ahmedabad 382481, India

S. Dharmalingam
Aeronautical Engineering, Silver Oak College of Engineering and Technology, Ahmedabad 382481, India

G. Panda et al. (eds.), *Sustainable Energy and Technological Advancements*, Advances in Sustainability Science and Technology,
https://doi.org/10.1007/978-981-16-9033-4_55

photographing and filming. The United States, Germany, United Kingdom, Israel, and Russia, are the pioneers in the UAV research. In August 1849, the first unmanned flying vehicle was operated by the Austrians. At that time, it was employed as a balloon filled with explosives. This specific technique has been known for almost 150 years as a purpose of bombs. In 1915, the unmanned aerial vehicle named "Kettering Bug" was created by Charles Kettering with Elmer Ambrose Sperry. Orville Wright worked as a consultant on the project. The vehicle was guided by an onboard gyroscope. The control system used an electric system, a pneumatic system, and an aneroid barometer for altitude sensing. The first civilian aircraft drone was produced merely in 1980s by Japan. Public drones are generally driven by an electric motor and are smaller, while military drones are generally driven by an internal combustion engine and comparatively larger in size.

2 Background

The quadcopter can be used for agricultural purposes, especially for spraying water and pesticides on a timely basis [1]. Seed sowing using drones is challenging as it requires special systems and design. There are manually operated seed sowing machines are available, which takes much time, manual work, and less accuracy [2].

There are two UAVs used in the work [3] in which the first, UAV is used for making a map of the agricultural lands by capturing the aerial photos to the imagery analysis with the help of software, and the second, UAV had used as a transportation platform, which has an ability to carry a payload of materials. A canister mechanism had been developed to drop seeds at the desired locations in accordance with UAV's payload carrying capacity. The maximum speed achieved by this UAV is about 5 m/s. There was an autonomous robot, which was developed for sowing seeds. It consists of a cylinder to store the seeds, bevel gear, and pipes were used to drop the seeds. However, this system is a robot and not a UAV [4].

An autonomous drone integrated system had developed, in which the Wi-Fi module is used for communication between the two robots. Arduino Atmega2560 controller with computer module has been used to monitor and control the proper seeding on the land. It has a quadcopter drone and ultrasonic proximity sensor, an under-body sensor to detect the right path for seeds sowing and obstacles. For communication at the ground station, Wi-Fi in the Arduino board was used [5]. Reforestation can be done by drone technology with the help of Mission Planar software and Arduino coding software. The calibration and for a fully-featured ground station applications of the ArduPilot (open-source autopilot), a Mission Planar software has been used. While, Arduino software is used for coding in different Arduino boards [6].

Drone technology combined with machine learning and remote sensing can solve the industrial-scale deforestation problem. In the bio-carbon engineering project, a drone was used to hover over the selected area for surveillance and making reports on the possibility of reforestation. Pre-germinated seeds are plotted into the soil by using a predetermined pattern of the drone. The pressurized canister is used to inject the seeds into the soil with force.

These drone systems have the capacity of planting ten thousand seeds per day and aimed to plant one billion trees in a year [7]. As per researchers, still there is enough space for planting around 1.2 trillion trees that can intake CO_2 emitted by humans. The amphibious UAV has been developed to drop seed balls in the agricultural land without any damage to the seeds and has high stability, and is simple to operate [8]. The vast applications UAV in agricultural farming and animal husbandry like; weed identification and control, animal aerial headcounts and monitoring, soil and pest analysis and control, aerial Geo-fencing, crop health irrigation, and monitoring, mustering, and other farming and livestock-related activities were studied [9].

The patent shows the UAV distribution assembly used for seed sowing. It is an electronic frame and a device distribution attached at the bottom of the drone. This distribution device has excellent coordination between the time, area, and amount of product to drop at the accurate position [10]. UAV attached with wheel mechanism has been developed to drop seeds at the same interval of area and time using controllers. This technology has been developed recently on a vast scale, due to the Fourth Industrial Revolution (IR 4.0) and increases in the demand for food as of population growth [11].

Modernization leads to inadequacy in skilled laborers in the agricultural domain and this affects the development and growth of developing countries. To enhance the productivity, the farmers must properly use upgraded autonomous technology for agricultural activities like seeds sowing, digging, fertilizing, spraying, harvesting, etc. This will minimize the necessary requirement of labor and enhance yield. The objective of this research is to develop a quadcopter with a low-cost seed dropper mechanism to sow seeds on agricultural land for effective production and avoid the wastage of seeds.

3 Components to Build the Quadcopter

3.1 Frame

The frame is the skeleton upon which all the components of the quadcopter and loads will be acted. The size of the frame can be determined by the size of propellers and the size and rating of DC motors. Motors will specify the current ratings of electronic speed controller. It is important to verify that the mountings for the motors and the flight controller board (FCB) match, when designing a quadcopter frame. The frame is made up of glass fiber and aluminum, which is easy to build, relatively inexpensive, and durable. The CAD design of the present quadcopter frame along with the supporting strut is shown in Fig. 1.

Fig. 1 CAD design of quadcopter frame

3.2 Motor

The motors are the essential component of the quadcopter and the main drainer of battery power. The efficient combination of the motor and the propeller is most important for the better performance. Usually, the speed of the motor is measured in terms of Kv (constant velocity). The higher Kv motor spins faster, and the lower Kv motor produces more torque, and this phenomenon is actually without the propeller attached to the motor. The amount of current drawn by the motor from the battery is an important aspect to consider for motor performance apart from the raw thrust and its Kv. The specifications of the motors need to be checked for maximum electrical current load and confirm that the ESC's are rated to withstand those amperages. The motor which is used in this research work is A2212 Kv1000 brushless motor.

3.3 Battery

Most of the batteries used in the quadcopter contain a lithium-based battery. Because it is lightweight and has a high volt carrying capacity and also has a higher charge density as compared to the typical lead-acid and nickel batteries. Generally, lithium batteries are quite expensive, but in most cases, these batteries are more used readily. The present design using a 2200 mAh, 3 cells, and 12 V lithium polymer battery (Li-Po battery) for this research work. The battery has given a flight time of approximately about 4–8 min. Generally, batteries cannot have their own mounting units on the drone, since the screws can damage the battery. Batteries are the heaviest component on a UAV, therefore they are mounted on the dead center of the UAV to offer the same load on all the motors.

3.4 Arduino UNO Micro Controller

The Arduino UNO in common is an ATmega328P Microchip-based open-source microcontroller board. This board is incorporated with 14 digital and 6 analog I/O pins. The Arduino board is operated by a 9-V external battery or by a USB cable, as it can work in the range of voltages between 7 and 20 V.

3.5 Electronic Speed Controller (ESC)

An ESC translates the signals into the phased electrical pulses by interpreting the signals from the flight controller and determines the speed of a brushless motor. ESC has four input terminals, two are used for signals from the flight controller. Signal and signal ground is wired to the flight controller with a positive wire only. Typically, an ESCs have three output terminals, each one of the wires are connected to the brushless motor.

3.6 Propellers

For quadcopter, various types of propellers are available, with every size and material. A lighter propeller is more suitable due to lower torque. Further, the higher pitch blades encounter high air resistance and require more torque, and thereby consuming more current. Thus, the trade-off is required between the amperage and the thrust by the designer. Here, the propeller diameter is 10 inches with the pitch of 4.5 inches were chosen.

3.7 Flight Controller (FC)

The flight controller uses algorithms by the information given by the sensors, to know the spinning of motors as per the command given from the radio transmitter. FC uses the receiver and follows the given command. The video input with the help of a first-person view camera feeds to the video transmitter through the FC with the incorporation of the beta flight on-screen display. Generally, FC needs 5 V to operate, which is given by connecting anyone positive of ESC to FC. Usually, FC can be Arduino, Ardupilot, or any other. In this research work, Ardupilot is used as FC.

3.8 Arduino Pilot

It is a free open-source autopilot firmware that supports multi-copter, ground rovers, planes, and traditional helicopters. This includes an onboard video display, air parameter setting, mission planning, voice synthesis, and data logging. The full mission was scripted with point-and-click desktop utilities. It is feasible to support a large number of 3D waypoints, dual-way in-flight commands, and telemetry with the use of the MAV link protocol. Autonomous landing, take-off, camera, and video controls can be done also. In Ardupilot, input is connected with the receiver, and output is connected with ESC.

3.9 Transmitter

A first-person view (FPV) flying drone transmitter is used to transmit radio signals wirelessly with a particular radio frequency to the receiver. The receiver is usually connected to the drone. All the command given by the pilot has to be transmitted with the help of these electronic transmitters only.

3.9.1 Radio Receiver

A radio receiver is used to receives radio waves and convert the data into a viable form. An electronic filter is used to filter out the expected radio frequency from the incoming signal. An electronic amplifier is used to amplify the signals for processing and desired data is extracted with demodulation. To control the aircraft remotely, a pilot uses a radio transmitter, and that signals are received by the radio receiver, which is generally connected to the flight controller input.

3.9.2 Motor Driver Board

A motor driver is an integrated circuit (IC) chip for controlling the motors. The interface between Arduino and the motor is usually made with the help of the motor driver. L293 series IC's are widely used motor drivers and are used to control two DC motors simultaneously at the same time. L293D contains two H-bridge and 16 pins. H-bridge is suitable to control low current-rated motors. In this research work, L293 motor driver was used for operating 12 V DC motor and 5 V Arduino. The power was supplied to the motor driver by connecting the positive of one ESC to the motor driver. Arduino and motor driver are connected to the receiver, for operating the DC motor from the ground station with the help of the transmitter.

4 Design of Seed Dropper

The sole purpose of the seed dropper is to store and drop out the seeds. This setup is fixed below the quadcopter drone, and the seed is filled in a container before lift-off and can release the seeds aerially wherever required. The seed dropper consists of a seed container, gear with the motor assembly, and base container. The DC motor and motor driver are coded to precisely regulate the flow of seeds. The seeds sowing program would run in the Arduino drives, and the DC motor operates according to the quadcopter's speed. Thus, the seeds are dropped at the desired locations. The seed dropper is designed to exactly fit under the drone and its material is 3D printed to give high durability. The total weight of the seed dropper is 120 g including the DC motor. Arduino and motor driver board were used to controlling the rotational speed as per the input.

4.1 Seed Container

The seed container is used to store the seed temporarily. The seeds will be fed to the base container through the passage (Figs. 2 and 3). The volume of the container depends upon the design and weight carrying capacity of the quadcopter.

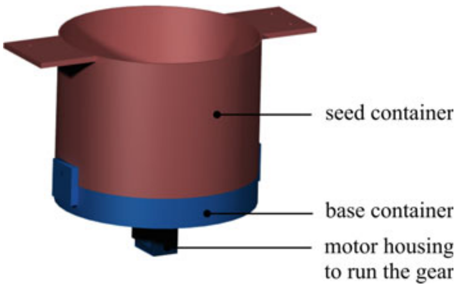

Fig. 2 Assembly of the seeds dropper

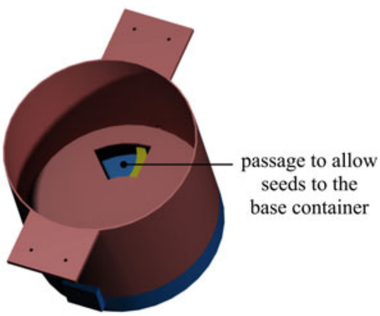

Fig. 3 Passage to allow seed to the base container

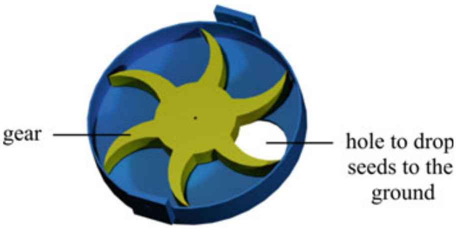

Fig. 4 Base container with gear

4.2 Gear

The gear is used to draw the seeds from the seed container and dropping into the required area with the help of its rotation. RPM of gear is controlled by DC motor attached at the bottom.

4.3 Base Container

The base container is the lower part through that the seeds have been dropped. DC motor is fixed at the bottom of the base container inside the housing to run gear (Fig. 4).

5 Design Calculation

The complete design calculation for the construction of quadcopter with seed dropper is given in Table 1. The design was carried out for 1571 g of the quadcopter, 120 g of seed dropper, and 400 g of payload (seeds).

5.1 Total Weight Estimation

$$\begin{aligned}\text{Total weight} &= \text{Empty weight } + \text{payload weight}\\ &= 1691\,\text{g} + 400\,\text{g} = 2091\,\text{g} \cong 2.1\,\text{kg}\end{aligned}$$

5.2 Thrust Required (F_r)

The thrust force required can be given by

Table 1 Total weight estimation

Components	Estimated weight (g)	Numbers of units	Total weight (g)
Brushless motor	159	4	636
Propellers	10	4	40
ESC	55	4	220
Frame	300	1	300
Li-Po battery	175	1	175
Power distribution board	150	1	150
Receiver	50	1	50
Seed dropper without DC motor (seed container, base container, and gear)	100	1	100
DC motor to drive the gear of seed dropper	20	1	20
Payload (seeds)	400	1	400
Total	919	17	2091

$$F_{\mathrm{r}} = (2 \times \text{Total weight})/n_{\mathrm{p}}$$

where n_{p} is number of propellers and for quadcopter, $n_{\mathrm{p}} = 4$. Thus,

$$\begin{aligned} F_{\mathrm{r}} &= (2 \times 2.1)/4 \\ &= 1.05\,\mathrm{kg} \end{aligned}$$

5.3 Power of Motor (P)

$$P = V \times I \times \eta$$

where V is voltage drawn by the motor, I is current drawn by the motor and η is the efficiency of the motor.

$$P = 12 \times 10 \times 0.80 = 96\,\mathrm{w}$$

5.4 Thrust Generated (F_g)

The thrust generated is given by,

$$
\begin{aligned}
F_{\mathrm{g}} &= \left(2 \times \pi \times r^2 \times \rho \times P^2\right)^{0.3333} \\
&= \left(2 \times 3.14 \times 0.127^2 \times 1.225 \times 96^2\right)^{0.3333} \\
&= 10.45\,\mathrm{N} \\
&= 1.06627\,\mathrm{kg}
\end{aligned}
$$

where 'ρ' is air density (kg/m^3) and 'r' is the radius of propeller (m).

5.5 Torque Required (T_r)

$$T_{\mathrm{r}} = F_{\mathrm{g}} \times r \times \sin\,\theta$$

where 'θ' is angle of the propeller.

$$T_{\mathrm{r}} = 10.45 \times 0.127 \times \sin 20\circ = 0.45419\,\mathrm{N-m}$$

5.6 Torque Generated (T_g)

$$T_{\mathrm{g}} = \frac{I \times V \times \eta}{2 \times \pi \times N/60}$$

where 'N' is rpm of motor and it can be calculated as

$$
\begin{aligned}
N &= 2 \times \pi \times \frac{(1000\,\mathrm{kv})}{60} \\
&= 2 \times \pi \times \frac{(1000 \times 12)}{60} \\
&= 1256.6371\,\mathrm{rad/s}
\end{aligned}
$$

$$
\begin{aligned}
T_{\mathrm{g}} &= \frac{10 \times 12 \times 0.80 \times 60}{1256.6371 \times 2 \times 3.14} \\
&= 0.7295\,\mathrm{N-m}
\end{aligned}
$$

5.7 Rotor Loading

$$\text{Rotor Loading } = F_{\mathrm{g}}/\text{Area of the propeller}$$

$$= 10.45/\left(3.14 \times (0.127)^2\right)$$
$$= 206\,\mathrm{N/m^2}$$

5.8 Endurance (t)

Endurance is the time of flying a quadcopter with the complete consumption of charge from the given battery.

$$t = C/(I \times 60)$$

where 'C' is the battery capacity in Ah.

$$I_{\mathrm{net}} = n_{\mathrm{m}} \times I$$

where n_{m} is number of motors; I_{net} is the net current drawn by motor.

$$\begin{aligned} I_{\mathrm{net}} &= 4 \times 10 \\ &= 40\,\mathrm{A} \end{aligned}$$

$$\begin{aligned} t &= \frac{2.2 \times 3600}{40(\text{for 4 motors})} \times 60 \\ &= 3.3\,\mathrm{min} \end{aligned}$$

6 Result

The assembly of the quadcopter with seed dropper is shown in Fig. 5. The seeds

Fig. 5 Fabricated quadcopter with seeds dropper

Table 2 Time required and quantity of seeds dropped with respect to the speed of gear

Speed of the Gear (deg/s)	Total quantity of Seeds (g)	Rate of seeds Dropped (g/s)	Time required (s)
60	400	2.02	198
70	400	2.424	165
80	400	2.828	142
90	400	3.232	124
100	400	3.636	110
110	400	4.04	99

dropper is fixed at the bottom of the quadcopter. The seed container, gear, and base container were 3D printed with PLA filament. The speed of the gear in the seed dropper is used to vary from 60 to 110 deg/s and seed dropping is estimated in seconds (s) for the pearl millet seeds, as shown in Table 2. As per the design, the maximum of 400 g of seeds can be carried, and the size of the seed varies from 1.82 to 1.86 mm in diameter. At 60 deg/s rotation of gear, 2.02 g/s of seeds can be dropped to complete 400 g of seeds in 198 s, which is the lowest rate as per this design. Similarly, at 110 deg/s rotation of gear, 4.04 g/s of seeds can be dropped to complete 400 g of seeds in 99 s, which is the highest rate.

7 Conclusion

The seed sowing method can minimize the planting cost to a high extent. Drone seed's sowing mechanism can be augmented with lasers or ultrasonic echoing devices to measure the surface distances with more precision. Large quantities of crops can be planted more effectively with the use of fewer materials, and this method is much faster as compared to the traditional methods. Due to the advancement in technology and the easy availability of the key components with other devices such as smartphones, drones have become much more affordable. The Association for Unmanned Vehicle Systems International (AUVSI), informed that the use of drones in the agricultural industry is expected to control 80% of the future commercial UAV market. In agriculture, drones are not just for seeds-dropping purposes, but we can also use drones for spraying insecticides, and for surveillance of the quality of the crops in larger land areas in a short time. The biggest drawback is the range constraint of the quadcopter's operation due to battery issues. Endurance is also one limitation due to power and weight issues. Basically, from the overall research, it is sure that it is going to help society, especially the farmers in their agricultural lands. A Seed dropper can help a farmer get rid of labor shortage problems and reduce costs in a great way. The fabricated quadcopter with a seed dropper is a pilot model and has the capacity to carry seeds weighing 400 g. For real-time applications in agricultural lands, larger quadcopters can be designed along with seed droppers, that can carry 2–3 kg of payloads or even more.

Acknowledgements A part of this research work was carried out as an Internship at Avian Aerospace, Bengaluru, India by the corresponding author.

References

1. Shaik HS, Satish Babu G (2017) Design and analysis of light weight agriculture robot. Glob J Res Eng Mech Mech Eng 17(6). version 1.0
2. Kyada AR, Patel DB (2014) Design and development of manually operated seed planter machine. In: 5th international & 26th all India manufacturing technology, design, and research conference (AIMTDR), IIT Guwahati, Assam, India
3. Andrio A (2019) Development of UAV technology in seed dropping for aerial revegetation practices in Indonesia. In: IOP conference series: earth and environmental science. ISSN: 308 012051
4. Koli M, Kori U, Ahmad A, Abdul R (2017) Seed sowing robot. Int J Comput Sci Trends Technol (IJCST) 5(2)
5. Diwate SK, Nitnaware VN, Argulwar K (2018) Design and development of application specific drone for seed sowing. Int Res J Eng Technol (IRJET) 05(05)
6. Fortes S, Pinheiro E (2017) Seed plant drone for reforestation. Graduate Rev 2:13–26
7. How do you plant 1 billion trees a year? With drones, of course. https://dronelife.com/2015/04/07/how-do-you-plant-1-billion-trees-a-year-with-drones-of-course
8. Kumar MK, Telagam N, Kumar NM, Ismail KM, Rajasekar T (2020) Design and implementation of real-time amphibious unmanned aerial vehicle system for sowing seed balls in the agriculture field. Int J Emerg Technol 11(2):213–218. ISSN: 2249–3255
9. Chika YB, Olasupo A (2020) Sky-farmers: applications of unmanned aerial vehicles (UAV) in agriculture. In: Autonomous vehicles (Chap 6). IntechOpen, Nigeria, pp 107–128
10. Zvara S (2020) Distribution assembly for an aerial vehicle. United States Patent Application Publication, Cleveland
11. Marzuki OF, Teo EY, Rafie ASM (2021) The mechanism of drone seeding technology: a review. Malays Forester 84(02):349–358

Chapter 56
Power System Parameter Estimation Using Signal Processing Techniques

Pratap Sekhar Puhan and Pravat Kumar Ray

Abstract The signal prcessing approach to measure the amplitude and phase of a power system siganl is one of the best approach in the area of signal parameter measurement. In this paper, recursive least square (RLS) and Kalman filtering (KF) approach is implemented to measure the parameters in a signals. The estimation of the parameter is updated recursively at different samples of harmonics signal. Different value of signal to noise ratio are taken for verification of estimation performance. The accuracy level of the two proposed method is analyzed and compared. Finally, it is found that Kalman filtering approach towards measurement of parameters is more accurate than recursive least square and hence it is suitable for online estimation in noisy power system signals.

Keywords Harmonics · PQ · RLS · KF · etc.

1 Introduction

Harmonics level in power system increases gradually due to the tremendous application of power semiconductor devices in the modern power system, generation of harmonics and their mitigation motivates the researchers to work on harmonics to achieve better power quality in power systems, there are several methods used to remove the unwanted harmonics from power system signals such as low pass filter, isolation transformer, active filters [1–3]. The effectiveness of the filters depends on

P. S. Puhan (✉)
Department of Electrical and Electronics Engineering, Sreenidhi Institute of Science and Technology, Hyderabad, India
e-mail: pratapsekhar@sreenidhi.edu.in

P. K. Ray
Department of Electrical Engineering, National Institute of Technology, Rourkela, India
e-mail: rayp@nitrkl.ac.in

G. Panda et al. (eds.), *Sustainable Energy and Technological Advancements*,
Advances in Sustainability Science and Technology,
https://doi.org/10.1007/978-981-16-9033-4_56

the control technique discussed [3, 4], a number of standards and guidelines formulated for the harmonic's measurement and mitigation is discussed [5, 6], measurement, modeling, analysis and mitigation of harmonics components leads to development of different types of filters which will removes the harmonics [7], it is important to measure the harmonics components in an efficient approach, so that the filter can be designed smoothly [14] different types of harmonics measurement of techniques has been investigated [7], one of the most important approach is the fast Fourier transform (FFT) and it is used in many areas for parameter estimation purpose [8], harmonics analyzer associated with FFT, in which 68,000 instruments samples the waveform and then estimate the voltage and current wave form [13], adaptive filtering is one of the techniques [12] which is used for both harmonics and inter harmonics in an efficient manner. Parameter estimation using least square algorithm is used [3] and its effectiveness is verified through experimentation for frequency and harmonics [5], involvement of constant and fix step size in LMS can be overcome by changing the fixed size to variable step size [9], some papers uses the least mean square error as the cost function but due to stalling effect accurate estimation is not achievable [7], but recursive estimation is very much required to get accurate results for the same purpose [6], recursive least square algorithm is implemented in many areas when the system condition such as fault resistance, inception angle, loading, etc. changes [9]. The performance of the least square algorithm is enhanced through variable leaky least square algorithm where leakage factor taken into consideration [8] Kalman filtering algorithm is used by many researchers [4, 7] but optimization of parameter is difficult due to the involvement of Tayler expansion higher order [7], soft computing techniques such as genetic algorithm, bacteria foraging optimization, fuzzy logic, neural network-based algorithm is implemented in many parameter estimation problem [11], computational complexity and rate of convergence are the problems encountered in these technique [9], dynamic tracking of harmonics can be easily access through this technique [10] it provides the possibility of feeding input through feedback scheme [12] it is treated as one of the best method for harmonics estimation [10], performance improvement of the algorithm is carried out through tuning of error covariance matrices "*p*" and "*r*" [1], though several estimation techniques have been developed and utilized in many research purpose with different types of parameter updating techniques which includes incorporating covariance matrix, forgetting factor, leaky factor, etc., but still some analysis is required to verify the effectiveness of the algorithm with different signal to noise ratio. In this work, the effectiveness of two popular harmonics estimation algorithm such as recursive least square and Kalman filtering is verified through different signal to noise ratio and final a comparative analysis is made between the two algorithms.

The paper is organized as Sects. 1 and 2. Section 3, Sects. 4 and 5, in Sect. 1 introduction presented. Section 2 describes the details of the proposed recursive least square algorithm, Sect. 3 proposed Kalman filtering for estimation of amplitude and phase, Sect. 4 presents the result and analysis and finally conclusion presents in Sect. 5

2 Proposed Recursive Least Square Algorithm (RLS)

The recursive least square algorthim used in many parameter estimation purposes [], here a power system signal with noise is taken in to consideration for amplitude and phase estiomation of both fundmental as well as harmonics.

The power system signal with noise consists of fundamental as well as harmonics constitute is presented in below equation

$$y(t) = A_1 \sin(\omega_0 t + \varphi_1) + A_5 \sin(5\omega_0 t + \varphi_5) + A_7 \sin(7\omega_0 t + \varphi_7) + \mu(t) \quad (1)$$

The above signal can be expressed in parametric form for the estimation of amplitude and phase

$$\begin{aligned} y(t) = &\left[\sin\omega_0 t \;\; \cos\omega_0 t \;\; \sin 5\omega_0 t \;\; \cos 5\omega_0 t \;\; \sin 7\omega_0 t \;\; \cos 7\omega_0 t \right] \\ &\left[\alpha_1 \;\; \beta_1 \;\; \alpha_5 \;\; \beta_5 \;\; \alpha_7 \;\; \beta_7 \right] + \mu(t) \end{aligned} \quad (2)$$

In the general form it can be expressed as below

$$y(t) = \varphi(t)\theta + \mu(t) \quad (3)$$

$y(t), \varphi(t), \theta$ are represented as signal with noisy condition, structure of the system matrix and unknown parameter vector, respectively.

The unknown parameter vector is updated as follow

$$\overset{\wedge}{\theta}(t) = \overset{\wedge}{\theta}(t-1) + K(t)\varepsilon(t) \quad (4)$$

The error introduced in the process of measurement is given below

$$\varepsilon(t) = y(t) - \varphi(t)^T \overset{\wedge}{\theta}(t-1) \quad (5)$$

Equation (6) shows the covariance parameter and K which is to be updated

$$K(t) = P(t-1)\varphi(t)[1 + \varphi(t)^T P(t-1)\varphi(t)]^{-1} \quad (6)$$

Matrix inversion lemma used to update the covariance of parameter vector

$$P(t) = [I - K(t)\varphi(t)^T]P(t-1) \quad (7)$$

Initialization of Eqs. (6) and (7) is carried out by choosing some initial values. Since choice of initial covariance matrix is large and it is represented as, where α assumes a large number and I is a square identity matrix, parameter α and β is represented is as follow

$$\alpha_1 = A_1 \cos \varphi_1 \tag{8}$$

$$\beta_1 = A_1 \sin \varphi_1 \tag{9}$$

$$\alpha_5 = A_5 \cos \varphi_5 \tag{10}$$

$$\beta_5 = A_5 \sin \varphi_5 \tag{11}$$

$$\alpha_7 = A_7 \cos \varphi_7 \tag{12}$$

$$\beta_7 = A_7 \sin \varphi_7 \tag{13}$$

α, β relates the amplitude and phase of the signal as follow

$$A_1 = \sqrt{\alpha_1^2 + \beta_1^2} \tag{14}$$

$$A_5 = \sqrt{\alpha_5^2 + \beta_5^2} \tag{15}$$

$$A_7 = \sqrt{\alpha_7^2 + \beta_7^2} \tag{16}$$

$$\varphi_1 = \tan^{-1} \frac{\beta_1}{\alpha_1} \tag{17}$$

$$\varphi_5 = \tan^{-1} \frac{\beta_5}{\alpha_5} \tag{18}$$

$$\varphi_7 = \tan^{-1} \frac{\beta_7}{\alpha_7} \tag{19}$$

After the estimation of α and β, signals having fundamental, 5th harmonics and 7th harmonics can be separated by the following equations

$$y_{\text{o fundamental}} = \left[\sin \omega_0 t \ \ \cos \omega_0 t \right] \left[\alpha_1 \ \ \beta_1 \right]^T \tag{20}$$

$$y_{\text{o 5th}} = \left[\sin 5\omega_0 t \ \ \cos 5\omega_0 t \right] \left[\alpha_5 \ \ \beta_5 \right]^T \tag{21}$$

$$y_{\text{o 7th}} = \left[\sin 7\omega_0 t \ \ \cos 7\omega_0 t \right] \left[\alpha_7 \ \ \beta_7 \right]^T \tag{22}$$

3 Proposed Kalman Filtering (KF) Method

First the observation matrix is formulated and from that the unknown parameter θ estimation can be carried out followed by the below equations

$$k(t) = \hat{p}(t-1)\,\varphi(t)^T\,(\varphi(t)\,\hat{p}(t-1)\,\varphi(t)^T + r)^{-1} \tag{23}$$

In the above equation.

$k, \varphi(t), p, r$ represents the Kalman gain, observation vector, covariance matrix, variance of signal, respectively.

Kalman gain and covariance matrix is related by the equations as follow

$$\hat{p}(t) = \hat{p}(t-1) - k(t)\varphi(t)\,\hat{p}(t-1) \tag{24}$$

Updated and previous state of estimation is related by the equations

$$\hat{\theta}(t+1) = \hat{\theta}(t) + k(y - \varphi(t)\,\hat{\theta}(t)) \tag{25}$$

After updating the parameter, amplitude and phase harmonics are measured as per the steps presented in recursive least square algorithm.

4 Simulation Results and Analysis

First, one synthetic signal having 1 p.u. fundamental amplitude and 30-degree phase along with 5th harmonics components of amplitude 0.2 p.u and phase 150-degree and 7th harmonics components of amplitude 0.14 p.u and phase of 210 degree with random noise 20 dB signals to noise ratio is developed using MATLAB environment, with sampling interval of 1 mill second, estimation of the proposed algorithm is implemented and the obtained amplitude and phase estimation results along with actual signals are presented Figs. 1 and 2. Figure 1 shows the estimation and actual signal amplitude using RLS with 20 dB SNR and Fig. 2 shows estimation of amplitude of fundamental and actual signal using KF algorithm with 20 dB SNR. Actual and estimated value very close to each other but the deviation is 25th, 30th, 55th and 60th sample of signal in case of RLS, in KF deviation occurred only in 12th and 30th sample.

In Fig. 3, it is observed that settlement of amplitude 1p.u of fundamental components is achieved after an initial deviation for few seconds in case of RLS, but in case of KF, it settles down 1 p.u. amplitude immediately for the whole time period.

In Fig. 4, phase estimation of the fundamental component of the signal presented, it is observed that initially oscillation took place for some period after that it come

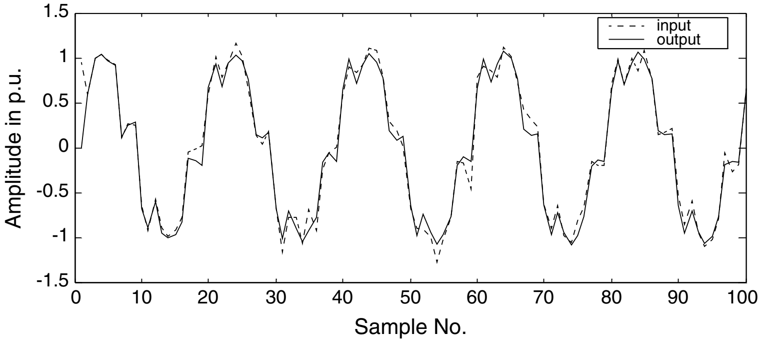

Fig. 1 Actual and estimated-20 dB using RLS

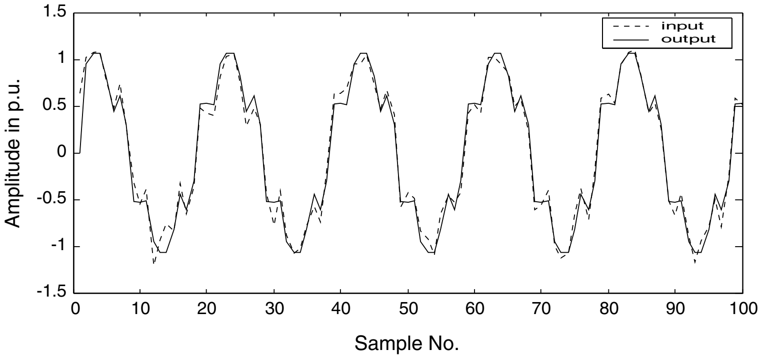

Fig. 2 Actual and estimated-20 dB using KF

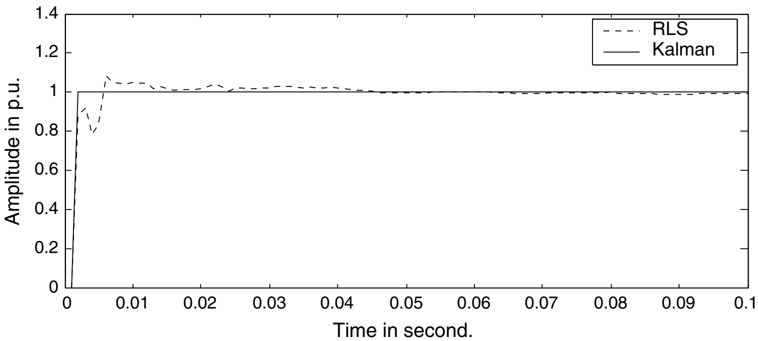

Fig. 3 RLS and KF amplitude estimation comparison of fundamental component

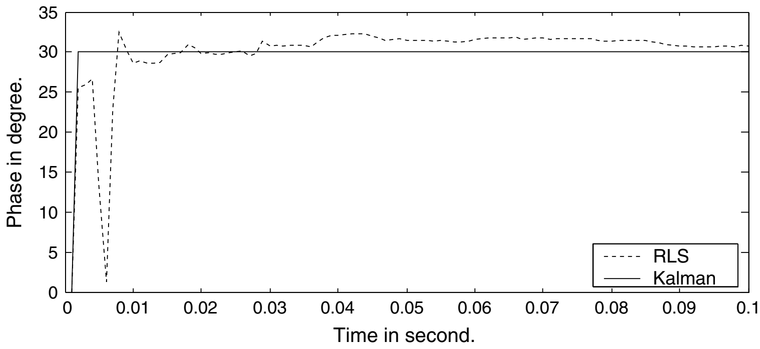

Fig. 4 RLS and KF phase estimation comparison of fundamental component

around 32 p.u in the mid and again it comes down to 31, but in case of KF, it directly settles at 30p.u immediately after implementation.

In Fig. 5, amplitude estimation of the 5th harmonics component of the signal presented, it is observed that initially it goes up to 1p.u for some period after that it settles down after 0.07 s, but in case of KF it settles down to the actual value of amplitude 0,2 p.u immediately after its implementation., in Fig. 6 the phase estimation of RLS and KF presented. In case of RLS the estimated value of phase takes more time to settle down its actual value 150-degree but in case of KF the estimated value settles down to its actual value of 150-degree immediately after its implementation.

Figures 7 and 8 gives the output of fundamental, 5th and 7th harmonics components amplitude with 20 dB signal to noise ratio n in RLS and KF, respectively, from both the figure it is clearly understood that KF perform well in comparison to RLS.

Figures 9 and 10 gives the output of fundamental, 5th and 7th harmonics components amplitude with 10 dB signal to noise ratio n in RLS and KF, respectively, from both the figure it is clearly understood that KF perform well in comparison to RLS.

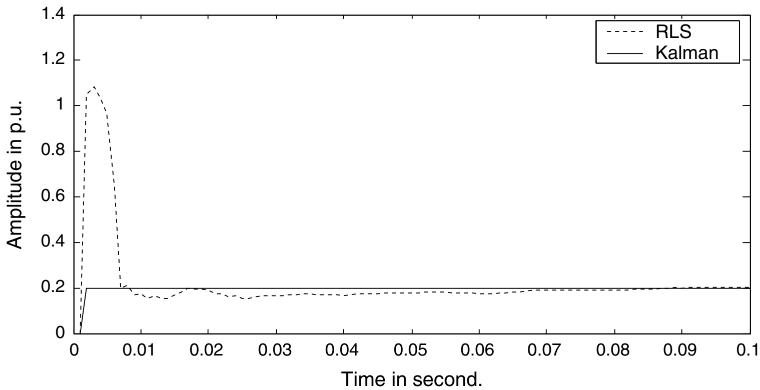

Fig. 5 RLS and KF amplitude estimation comparison of 5th harmonics component

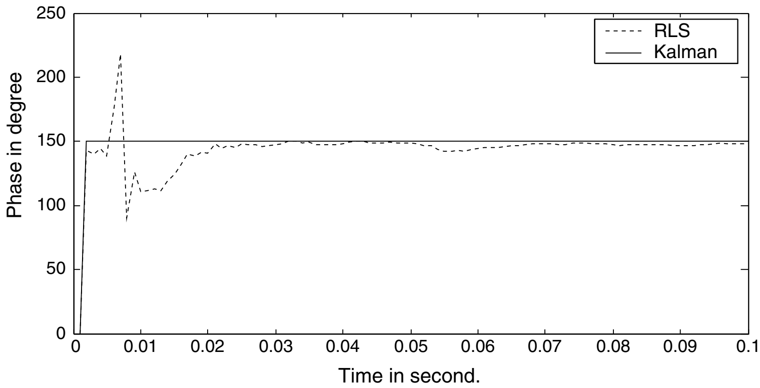

Fig. 6 RLS and KF phase estimation comparison of 5th harmonics component

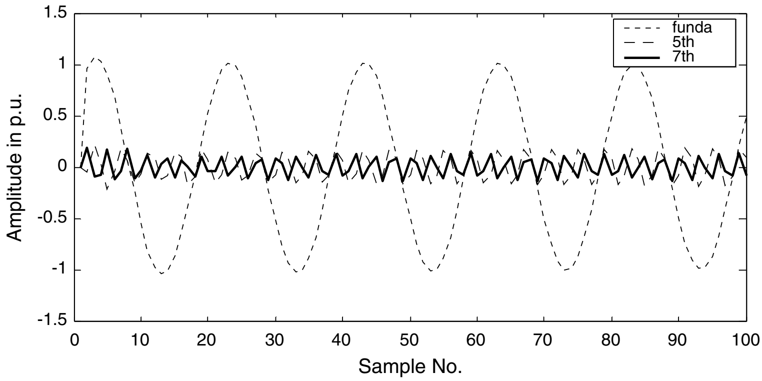

Fig. 7 Fundamental, 5th, 7th amplitude estimation using RLS with 20 dB

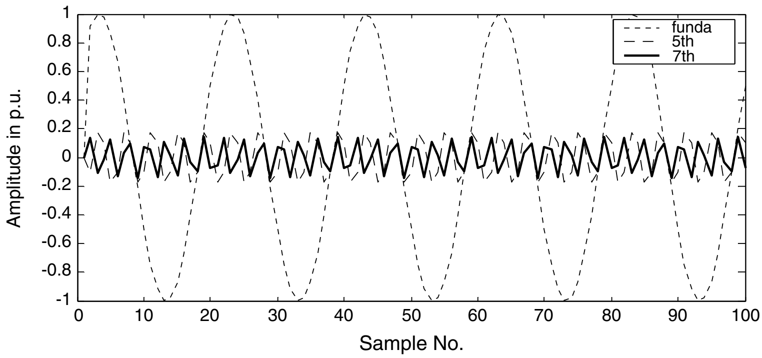

Fig. 8 Fundamental, 5th, 7th amplitude estimation using KF with 20 dB

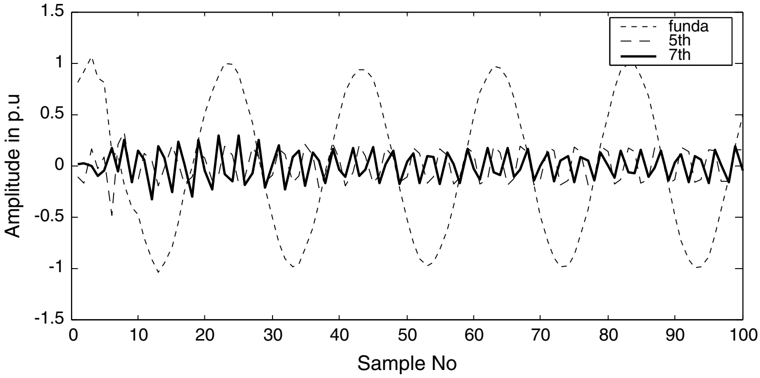

Fig. 9 Fundamental, 5th, 7th amplitude estimation using RLS with 10 dB

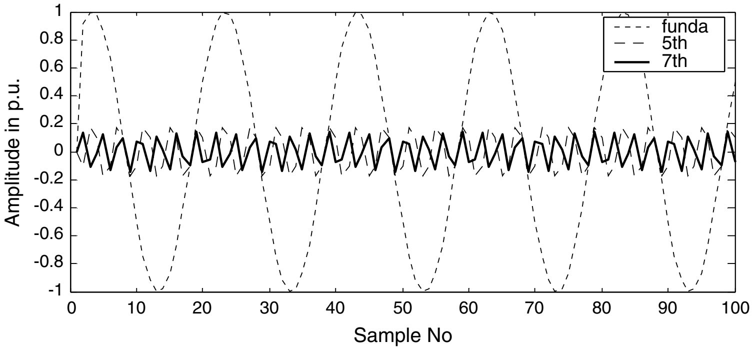

Fig. 10 Fundamental, 5th, 7th amplitude estimation using KF with 10 dB

Figures 11 and 12 presented below shows the mean square error (MSE)comparison in both RLS and KF algorithm with 20 and 10 dB signals to noise ratio. From these figures, it is concluded that the MSE for KF is less in both 20 and 10 dB signal in comparison to RLS.

The fundamental and harmonics components estimated amplitude and phase values in p.u. and degree is presented with their actual value for both RLS and KF for 20 dB signal to noise ratio in Tables 1 and 2, respectively. From the table, it is concluded that KF gives very encouraging results in comparison to RLS.

5 Conclusions

Power system parameter estimation using signal processing techniques is presented in this paper. The developed power system signal considered in this work constituted

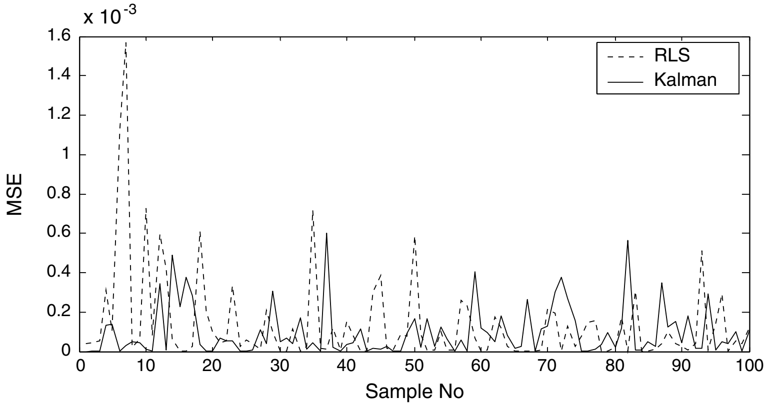

Fig. 11 Mean square error comparison with 20 dB noise

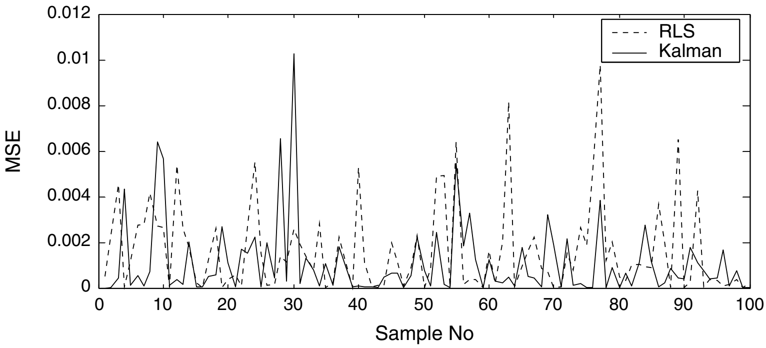

Fig. 12 Mean square error comparison with 10 dB noise

Table 1 Actual and estimated value of magnitude of harmonics components 20 dB

Harmonics component	Actual value of the amplitude in p.u	Estimated value of amplitude in p.u	
		RLS	KF
Fund	1	1.2	1
5th	0.2	0.24	0.2
7th	0.15	0.112	0.144

the fundmental and harmonics, to verify the effectiveness of the proposed algorthim for estimation of amplitude and phase of the signal simulation work carried out. In every and each cases of estimation of amplitude and phase of the fundamental comonent as well as harmonics component KF gives very much accurate results in

Table 2 Actual and estimated value of phase of fundamental and harmonics components

Harmonics Component	Actual value of the amplitude in p.u	Estimated value of amplitude in p.u	
		RLS	KF
Fundamental	30	30–32	30
5th	150	150–210	150
7th	210	205–230	210

comparision to RLS, Hence, it is sugested that KF approach is one of the best method for harmonics estimation as it provides a consistent performance.

References

1. Abi EA, Feilat AI, Amin IE Battayeb M (1994) Power system harmonic estimation a comparative study. Electric Power Syst Res 29:91–97
2. Battayeb M,Oidwai U (1998) Recursive estimation of power system harmonics. Electr Power Syst Res 47:(143–152)
3. Sachdev MS, Girya M (1985) A least error square technique for determining power system frequency. IEEE Trans Power Apparatus Syst 104(2):437–443
4. Kennedy K, Lightbody G. Yacamini R (2003) Power system harmonic analysis using the kalman filter. IEEE Power Eng Soc Gen Meet
5. Kumar A, Das B, Sharma J (2006) Robust dynamic state estimation of power system harmonics. Electr Power Energy Syst 28:65–74
6. Garanayak P, Panda G, Ray P (2015) Harmonics estimation using RLS algorithm and estimation with improved current control technique based SAPF in a distribution network. Int J Electr Power Energy Syst 73:209–217
7. Dash PK, Sharaf A (1998) A Kalman filtering approach for estimation of power system harmonics. In: Proceeding 3rd international conference on harmonics in power systems, Nashville, TN
8. Watson NR, Amillaga J (2003) Review harmonics in large systems. Electr Power Sys Res 66:15–29
9. Lobes T, Kozina T, Kogilini HJ (2001) Power system harmonic estimation using Linear Least Square method & SVD. In: IEE proceedings generations, transmission and distribution 148(6);567–572
10. Puhan PS, Ray PK (2019) Development of Improved Recursive Newton type algorithm to estimate power system harmonics. i-Manager's J Electr Eng 13(2):1–13
11. Lai LL, Tse CT, Chan ATP (1999) Real-time frequency and harmonic evaluation using artificial neural networks. IEEE Trans Power Deliv 14
12. Mandel JM (1987) Lessons in digital estimation theory. Prentice-Halls, NJ
13. Sodestrom T, Stocia P (1989) System identification. Prentice-Hall, NJ
14. Dash PK, Swain DP, Routray A, Liew AC (1996) Harmonic estimation in a power system using adaptive perceptron's. IEE Proc Gener Trans Distrib 143:565–574
15. Ljung L, Söderström T (1983) Theory and practice of recursive identification. MIT Press, Cambridge
16. Dash S, Ray PK (2018) Design and modeling of single-phase PV-UPQC scheme for power quality improvement utilizing a novel notch filter-based control algorithm: an experimental approach. Arab J Sci Eng 43:3083–3102

Chapter 57
Indoor PV-Based Power Management System for Connected Lighting and Shading Control

Anna Merine George, Ciji Pearl Kurian, C. Sravan, and Harsh Garg

Abstract Building automated control schemes and connected systems are part of the innovative building concept. This paper presents a low-cost Raspberry Pi-based connected system suitable for climate-responsive control of window blinds and luminaire and focuses on indoor solar panel-based power management for connected systems. The power management block, along with the control part, makes the automation scheme self-sustained. A prototype of the connected system and the SIMULINK assisted design of the power management system is developed. This paper also investigates the implementation of uploading the data to a suitable cloud server for future monitoring and control using the Internet of things. This work provides two solutions for the power management system, a constant output voltage of 7 and 3.3 V, to suffice the maximum level with a suitable battery capacity for working the control modules.

Keywords Connected system · Raspberry pi · Photovoltaic panel · Power management · Buck-boost converter

1 Introduction

Global energy consumption is expected to rise by three times by the year 2035. With a steep rise in IoT devices, devices are expected to be intelligent enough to make the system more efficient. Extending the battery lifetime and reducing the power consumption using ultra low power sensor nodes and energy harvesting systems are essential to realize IoT devices [1].

Furthermore, daylighting control is essential for balancing the natural sunlight present in a room with artificial light. Studies have shown that daylight exposure

A. M. George (✉)
Department of ECE, Dayananda Sagar University, Kudlu Gate, Bengaluru, India
e-mail: annageorge-ece@dsu.edu.in

C. P. Kurian · C. Sravan · H. Garg
Department of EEE, MIT Manipal, Manipal Academy of Higher Education (MAHE), Karnataka 576104, India

G. Panda et al. (eds.), *Sustainable Energy and Technological Advancements*, Advances in Sustainability Science and Technology,
https://doi.org/10.1007/978-981-16-9033-4_57

has a good advantage on office workers from the view of subjective well-being and sleep quality [2], which leads to an increase in the efficiency of the work with energy savings. However, daylighting can give visual discomfort to a person if it is not controlled efficiently, especially for a window facing the west side. The window blind is the solution to this problem. Kurian et al. [3] have considered fuzzy logic-based window blind and artificial light controllers for the tropical climate in Mangalore, South India, to provide visual and thermal comfort for the user. The paper showed that up to 20–80% of annual energy savings could be achieved compared to the base model. Hence, proper utilization of this concept can reduce the overall energy consumption. This concept can be achieved by using solar panels and controlling the illuminance in the room by adjusting the window blinds and the LED luminaires.

The emergence of wireless-based applications in intelligent building, IoT-based communication systems is discussed for lighting control. The wireless connectivity opens many doors of creativity; the system can be implemented in many ways depending on the sensors, modules, and software used. The low-powered mesh network based on the IEEE 802.15.4 communication protocol is implemented on the digimesh system using XBee S2C modules. A wireless sensory network is required to log the data stored on the Internet so that it is accessible from anywhere. In the system presented, all the data collected from the environment by different sensor nodes is uploaded to ThingSpeak. The coordinator node consists of the Raspberry Pi, which implements the controllers and uploads the data to the ThingSpeak platform. The Arduino IoT helps connect multiple devices and allows the exchange of real-time data. The real-time data can also be monitored from anywhere using the ThingSpeak viewer application.

The concept of daylighting is realized in the testbed [4], where the window blinds and luminaires are adjusted based on the sun position. In addition to that the interior lighting is adjusted based on the amount of daylight entering the room. However, the literature shows many automatic control schemes taking care of inefficient lighting, unnecessary extra light usage, and lights turned on in unoccupied space, leading to energy wastage to a considerable amount. Such an IoT-based automation system needs power for its operation. Here, power management introduces the solar panel to extract energy from the lights and use it for wireless connectivity. As a result, energy harvesting and utilization are essential aspects that can help us reduce power consumption and obtain an efficient operating system.

Susan et al. [5] have discussed the importance of using the daylighting scheme and have experimented with observing how automated lighting occurs concerning the amount of daylight entering the work-plane. Based on the sun position and the time (default), few parameters such as window luminance and glare position are determined using a pyranometer and are used as inputs to estimate the position window blind (alpha value) to be covered. Suppose only 20% of the blind is covered, which means enough daylight can enter the work-plane. Thus, the light automatically dims to neutralize the brightness and comfort. A model is designed in LabVIEW and is interfaced with MyRIO to feed the input and control the motor operating the blind. The energy consumption graph of sensor and actuator nodes is calculated in three modes (idle, transmit, and receive). The PWM signal is generated to maintain the constant illuminance level through the luminaire, and the setpoint used to compare and rectify is decided.

Mathews et al. [6] examined III-V solar cell' performance as a device to harness indoor lighting energy. In an indoor lighting environment, solar cells made of GaAs and GaInP are tested against amorphous-silicon and dye-sensitized cells compared to a traditional 1-sun environment. It has been proved that the former outperforms the latter with almost twice the power densities. Matthew and Frizzell [6] used indoor lighting sources consisting of CFL and LED lighting diffusing optics to ensure uniform distribution over the solar cell. These cases were analysed over a 200–1000 lx range and then compared with each other. Matthew and Frizzell [6] found that the most extensive current produced was 1.61 times the smallest one, and the highest open-circuit voltage is almost double the smallest one.

On the other hand, the power output was 2.4 × greater than DSSC and 2 × more significant than the a-Si cells. Also, Ma et al. [7, 8] analysed different behavioural models and then compared them with a solar panel equivalent circuit model. It was shown the equivalent model had reduced efficiency when operating under low illuminance conditions. The analysis was done by observing the I-V and P–V characteristics of a solar panel.

Along with that different parameter values and power loss on both sides of MOSFET are obtained. Different MPPT methods are specified with their characteristics, allowing the researchers to use efficient methods depending on the conditions. Different power converters were designed using LTspice for energy harvesting applications, and different low power optimizations were discussed in [9]. A new energy harvester based on indoor lighting conditions is developed by modelling the spectrum of daylight and artificial light [10]. Rolf Arne Kjellby et al. [11] highlighted IoT device features and the proof of concept for self-powered IoT devices, which is maintenance-free and completely self-sustainable through energy harvesting. The authors have organized the paper to specify the design and how the nodes communicate in the first section. In the second section, the authors have discussed how energy harvesting modules are designed to power the WSN.

Yau et al. [12] covers the concept of battery charge controlling for a PV-based power management system. The authors have discussed the different MPPT techniques to either control the duty cycle or directly obtain the voltage. It was found that the incremental conductance method would be the best as we have to vary the duty cycle and not keep it constant. This paper also talks about implementing a PI controller for the charging control of the lithium-ion battery. They have explained the four charging control methods: constant voltage (CV), constant current (CC), CC and CV, and pulse charging method. Our objective is to maintain constant voltage, where the voltage is controlled at a set value when the battery is fully charged, avoids overcharging, and minimizes the cost. Furthermore, the author implemented the genetic algorithm (GA) method to calculate the PI controller gain out of other methods like particle swarm optimization (PSO) and the Ziegler Nichols method (ZN). Thus, a feasible integrated system can be designed for the efficient operation of the system.

Dinniyah et al. [13] explain the importance and the role of a buck-boost convertor in a PV-based solar power management system and the use of a PID controller. Due to the irregularity of light intensity on the solar panel, a variation of output voltage produced by the solar panel is observed. So, we are concerned about the input voltage range from the solar panel (light and dark conditions). According to the authors, to analyse the desired design of the convertor, regulation of the output voltage is the main aim. A microcontroller programme that regulates the PWM signals controls the amount of output voltage produced. Our primary goal is to contribute towards the IoT-based building control system making use of daylight. The connected system for the daylight-artificial light scheme monitors the input parameters, control signals, and controlled variables in a room. Here, the central control schemes are window blinds and luminaires based on daylight adaptation. The data gathered is uploaded to an external online server with the help of an IoT-enabled device, a Raspberry Pi (RPi) in this case. In addition, a power management system is designed for the sensors and control system.

This system block diagram shown in Fig. 1 combines power management and IoT integration, where the system is made to be efficient in terms of power consumption and is connected to the Internet, where the data collected by various sensors is sent to online servers to be monitored accordingly. The above block diagram highlights our methodology and basic approach to attain our objective. The following sections mainly discuss (i) the development stages of an IoT-based intelligent lighting and shading control system using RPi (ii) an indoor solar photovoltaic cell-based power management system for the connected system.

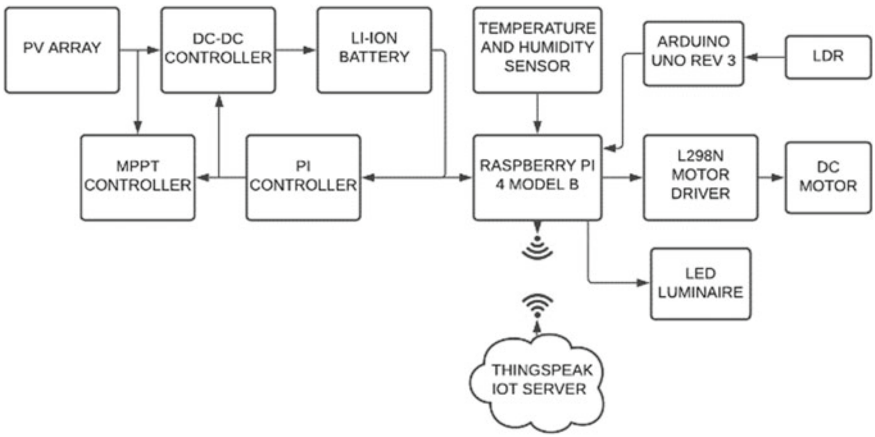

Fig. 1 A block diagram depicting the methodology

2 Experimental and Simulation Approaches

This section deliberates the development of the power management system and wirelessly connected intelligent control system. A PV-based solar power system consists of a PV array, a DC-DC converter, and a battery designed to optimize power consumption. Then, a Simulink model for the power management system is developed according to the specifications. The Perez model implemented in the python algorithm is used to obtain the daylight on window (EDW) on a window facing a particular direction and time of day by giving irradiance as the primary input. The window blinds are positioned based on a fuzzy-based algorithm taking daylight on the window, temperature, and altitude as the inputs. The parameters obtained are then measured against a setpoint/desired value. Depending upon this setpoint value and daylight availability on the work-plane, the LED luminaire output adjusts. The data obtained is monitored via the ThingSpeak IoT server and can be viewed through the PC or mobile phone via the ThingViewer application. The software tools used for the project were Thonny Python IDE, Arduino IDE, MATLAB, and SIMULINK. Finally, this work explains the design and development of indoor PV-based power management for the above set-up.

2.1 Connected Lighting and Shading Control

Various sensor nodes are placed to acquire internal and external temperatures, humidity, internal illuminance, external illuminance, and room occupancy. Two actuator nodes are also present, one for the motorized window blind and another for the LED luminaire. The Arduino-Rpi-based IoT system shown in Fig. 2 primarily has three stages. First, the system is initialized with the room parameters, then determines the output values based on algorithms and then sends them to the actuators. Finally, the values are sent to the IoT server for monitoring and future study. The system uses Raspberry Pi 4 model B as the central processing unit and python as the primary language. Upon initialization, the script calculates the day and estimates daylight on the window (EDW) using the Perez model based on the place latitude and longitude. The solar altitude is calculated using the pysolar library. The Perez sky model is a mathematical model used to describe the relative luminance distribution of the skydome and has become the de-facto standard model for daylighting calculations, as it uses actual data gathered from weather stations all over the world [14]. The value of daylight then obtained is then given to the fuzzy logic algorithm. This system considers an algorithm for visual comfort and energy efficiency, taking daylight and solar altitude inputs. The output is the window blind position (alpha) value, which regulates the LED luminaire output through PWM.

$$E_{Task} = EDW \times D.F \times F_m(x) \tag{1}$$

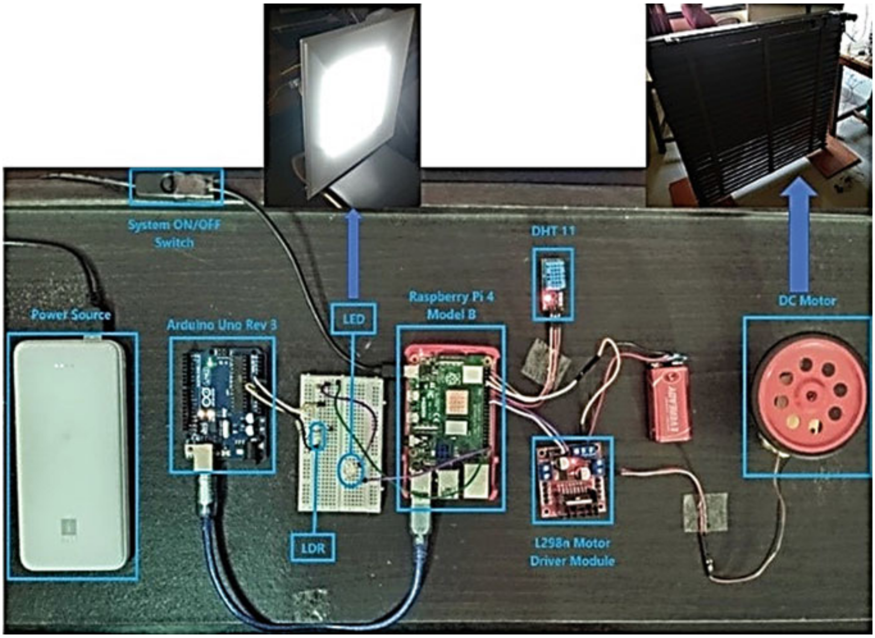

Fig. 2 A picture of the Arduino-Rpi-based IoT system

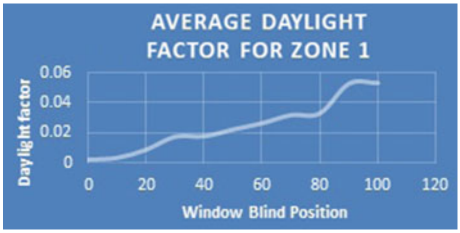

Fig. 3 Daylight factor values for window blind variation (alpha)

This code includes two factors, E_{Task} and Es. Es is the setpoint illuminance, while E_{Task} is calculated as mentioned in [14] where $F_m(x)$ is the function for the control signal based on the available daylight illuminance. Here, if alpha is 100, then it signifies that the window is completely open. Figure 3 shows the estimate of the daylight factor for the corresponding alpha values. If alpha is 0, the window is entirely closed, i.e. fully covered by window blinds.

2.2 Power Management System

The power management system consists of the following components [15]:

Table 1 Values of V(input), duty cycle and V(output) for the power management system designed using webench power designer

Input voltage (V)	Duty cycle	Output voltage (V)
3	0.01	3.27
6	0.55	3.27
9	0.38	3.27

PV array: The inputs to the PV array are variable irradiance and constant temperature.

DC-DC converter: Here are using a buck-boost converter to obtain a specific output voltage from the specified input voltage range.

Battery: It is used to store the surplus energy generated by the PV system. The battery capacity is calculated based on the power consumed by the wireless system modules.

The steps involved in power management would include:

- Measuring the maximum and minimum voltage across the solar panel for different lighting conditions.
- Design and selection of PV panel, buck-boost converter and battery
- Designing controllers for generating PWM signals to the switch and maintain the constant output voltage.
- Calculating the battery capacity based on the wireless module requirement and solar panel capacity.

2.2.1 Designing Buck-Boost Converter

Here two designs considered with two different specifications.

First is a buck-boost converter of input voltage range 3–9 V and output voltage of 3.27 V at 0.02 A current is designed using TI Webench power designer tool and results are shown in Table 1 and Fig. 8.

Second converter is designed to obtain an output voltage of 7 V and the results are tabulated in Table 2. The output voltage is obtained by stepping up or stepping down the input voltage determined by measuring the voltage across the solar panel. The voltage obtained in a complete bright room condition is the maximum voltage, and the voltage obtained in a completely dark room condition is the minimum voltage. Therefore the voltage value across the solar panel increases with the increase in the brightness of the lighting. Considered the readings of light levels under varying dimming conditions as well as different correlated colour temperature (CCT). A series of illuminance (lux) values for different brightness conditions of a tunable light is obtained using a CLA-500 spectrometer. Figure 4 shows the interior irradiance data used as input for the solar panel. To keep the output voltage constant at 7 V, for a varying duty cycle an MPPT controlling technique and PI controller is used in the buck-boost converter. The PI controller gain values are calculated using the

Table 2 Values of V(input), duty cycle and V(output) for the power management system

Input voltage (V)	Duty cycle	Output voltage (V)
0.362	0.950	7.002
1.562	0.777	7.002
2.658	0.620	7.002
3.332	0.510	7.003
4.227	0.396	7.003
5.878	0.160	7.003
6.554	0.064	7.003
7.783	0.899	7.003
8.435	0.830	7.003
9.243	0.757	7.003

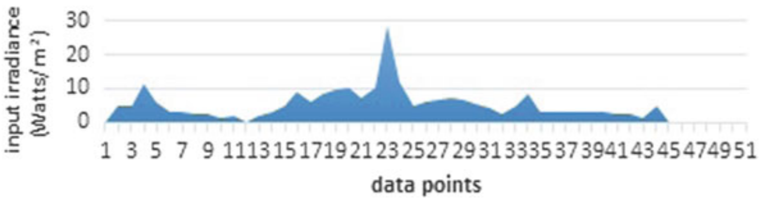

Fig. 4 Interior input irradiance sample data

Ziegler Nichols method. In this method, it is initially required to calculate the open-loop transfer function of the converter. Then, the for the compensated system transfer function Routh Hurwitz stability criteria applied to check the range of the gain values.

3 Result Analysis

The output of the fuzzy system is shown in Fig. 5. The inputs for the system are EDW and solar altitude, with the output being the value of alpha. The value obtained is used to calculate the strength of the PWM signal given to the LED and the position of the window blinds. Fuzzy logic has been implemented using python on the Raspberry Pi module to generate the control signals required. Three fuzzy control blocks are developed for two different cases, yielding different alpha values, when the user is present and when the user is absent.

The data uploaded to ThingSpeak is represented by the graphs shown in Fig. 7. For this purpose, a channel must first be created on the website. Each channel will have its API keys. We have used the “Write API Key” to upload data from the Raspberry Pi 4 to the IoT server. The data uploaded can be downloaded to the system as a.csv file for offline viewing. The data can also be used for MATLAB analysis and visualization. The data can also be viewed on mobile using the ThingViewer

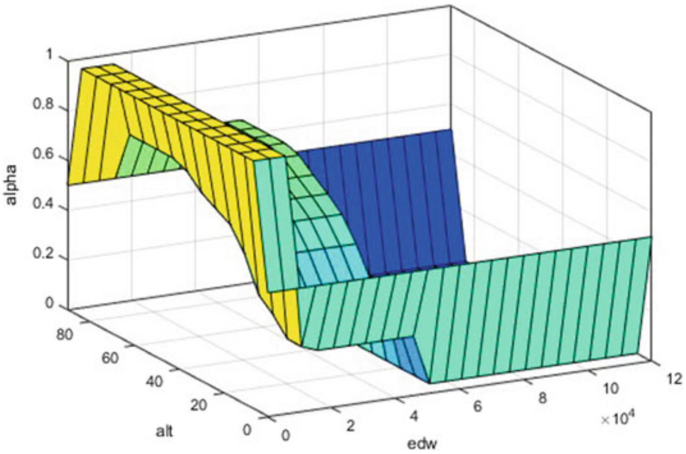

Fig. 5 Surf plot for the output plot of the system

application. The interior light dimming is adjusted based on the amount of daylight entering the room. This depends on the position of the sun. The test room window is considered in the east direction; therefore, the higher irradiance values are recorded during the early part of the day [16]. The value decreases once the sun position goes to the opposite side, which can also be observed from the west direction data. The values for the south direction remain high throughout the day as it receives direct sunlight from that direction. Figure 6 shows the daylight on the window estimated using the Perez model.

The above readings are taken between the ranges of 0–1 s. The MPPT technique controls the duty cycle for the boost mode when the input voltage starts near 0 and gradually increases to 7 V. It switches to the PI controller when the input voltage crosses 7.003 V to operate for the buck mode. The duty cycle values are compared with the repeating sequence to give output in terms of binary values. The controller operates for the compared value is 1 and does not operate for the compared value is 0. As soon as the system starts operating, the output voltage reaches 7.002 V and increases to 7.003 V at around 0.15 s. This value remains constant for the remaining duration of the operation. Thus, from this, we conclude that the operation of the converter and the controllers are as per the requirement. Depending on the

Fig. 6 Daylight on window estimated using Perez model

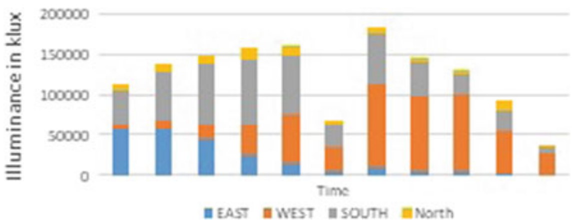

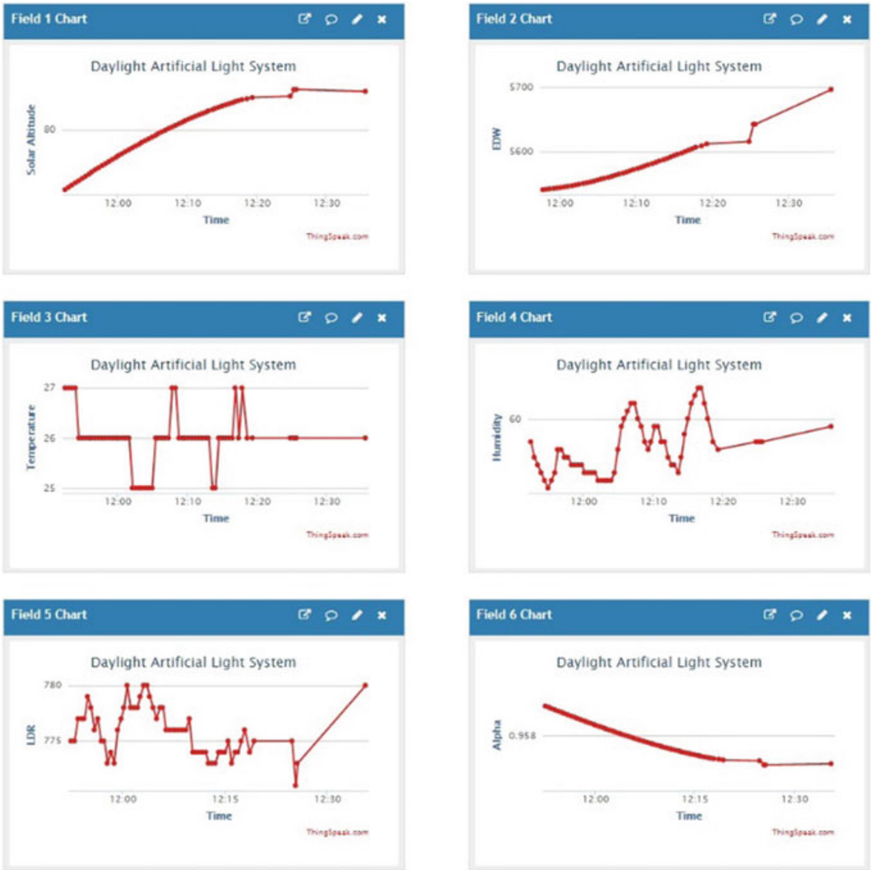

Fig. 7 Real-time data uploaded to ThingSpeak from 11:30 am to 12:30 pm

irradiance and PV array parameter values, the power value varied throughout the system operation. Therefore, the output voltage readings, output current, and power management block power were recorded between the run times of 0 to 1 s, as shown in Table 3.

From the above result, we observe that the power output remains closer to the maximum power value (0.99 W) such that maximum power is extracted for the operation of the wireless system. From the battery capacity calculation mentioned

Table 3 Specification of power management system

Output voltage (V)	Output current (A)	Power (mW)
3.3	0.02	66
7.783	0.1186	923

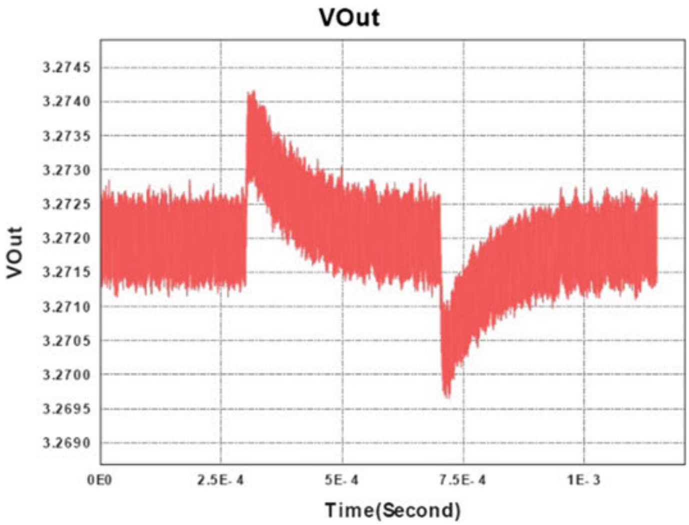

Fig. 8 Output voltage of buck-boost converter designed in webench power designer

earlier, it was found out that the total battery capacity we require is 1.92 Ah for a daily operation of 12 h (Fig. 8).

4 Conclusion and Future Scope

This paper contributes to connected lighting and power management via energy harvesting using indoor photovoltaic panels, a small-scale prototype of a low-cost, low power system for real-time control and monitoring. The paper presents the implementation details of an IoT-based lighting and window blind control module for daylight –artificial light integrated system control providing comfort and energy savings. All the algorithms developed in a test workbench integrated test room is transferred to Raspberry Pi module for ready use in offices. The window blind position controller algorithm is designed to adjust to the characteristics of the Venetian blinds, which are used in most of the offices and homes. The same algorithm can be extended for electrochromic windows as well for any climatic conditions. A dimmable luminaire is used to control the artificial light, to obtain the desired lux value and comfort. An added advantage of this system is the step taken for low power consumption of control, communication, and networking system. The growing demand for computing requires faster and reliable integrated circuits that consume less power. The real-time data of EDW, temperature, window blind position, humidity, and solar altitude are monitored. This data can be further used for AI-based building management systems (BMS). Furthermore, a mobile application specific to the project can be designed. This would allow us to view data remotely and control the system wirelessly from anywhere in the world if an Internet connection is available. The data is stored on the cloud server, ThingSpeak. Here provided 7 and 3.3 V solutions using indoor solar panels. The design of power converter along with appropriate control is required to get the desired voltage. This energy harvesting method can be extended for wearable devices and similar applications. Introduction of indoor photovoltaic cells will solve issues which include battery replacement or sensor performances for a bright future IoT ecosystem. Indoor energy harvesters with specialized solar cells and spectrally tuneable light sources can provide intelligent and self-powered IoT devices.

References

1. George AM, Dr. Kulkarni SY (2020) Characterization of battery life of an IOT based wireless networked office lighting system. IEEE CONECCT 2020, July 2–4, 2020, 978-1-7281-6828-9/20/$31.00 ©2020 IEEE
2. Boubekri M, Cheung IN, Reid KJ, Wang C-H, Zee PC (2014) Impact of windows and daylight exposure on overall health and sleep quality of office: a case-control pilot study. J Clin Sleep Med 10(6):603–611
3. Kurian CP, George VI, Aithal RS, Bhat J (2008) Fuzzy logic based window blind controller maximizing visual comfort, thermal comfort and energy conservation suitable for tropical climate. J Inst Eng (India) Architect Eng D 89:14–22
4. Varghese SG, Kurian CP, George VI, Varghese M, Sanjeev Kumar TM (2019) Climate model-based test workbench for daylight-artificial light integration. Lighting Res Technol 51(5):774–787
5. Varghese SG, Kurian CP, Senior Member, IEEE, George VI, Senior Member, IEEE, Sudheer Kumar TS (2019) Daylight-artificial light integrated scheme based on digital camera and wireless networked sensing-actuation system. IEEE Trans Consum Electron 65(3):284–292
6. Mathews I, King PJ, Stafford F, Frizzell R (2016) Performance of III–V solar cells as indoor light energy harvesters. IEEE J Photovoltaics 6(1):230–235
7 Ma X, Bader S, Oelmann B (2016) Solar panel modelling for low illuminance indoor conditions. In: 2016 IEEE Nordic circuits and system conference (NORCAS), Copenhagen, pp 1–6
8. Othman A, Maga D (2018) Indoor photovoltaic energy harvester with rechargeable battery for wireless sensor node. In: 2018 18th international conference on mechatronics - Mechatronika (ME), Brno, Czech Republic, pp 1–6
9. George AM, Kulkarni SY (2018) Performance of power converters for ultra-low power systems: a review. In: 2018 Second International Conference on Advances in Electronics, Computers and Communications (ICAECC), pp 1–5. IEEE
10. Politi B, Parola S, Gademer A, Pegart D, Piquemil M, Foucaran A, Camara N (2021) Practical PV energy harvesting under real indoor lighting conditions. Sol Energy 224:3–9
11. Kjellby RA, Johnsrud TE, Loetveit SE, Cenkeramaddi LR, Hamid M, Beferull-Lozano B (2018) Self-Powered IoT device for indoor applications. In: 2018 31st International Conference on VLSI Design and 2018 17th International Conference on Embedded Systems (VLSID), Pune, pp 455–456
12. Yau H-T, Liang Q-C, Hsieh C-T. Maximum power point tracking and optimal Li-ion battery charging control for photovoltaic charging system, Department of Electrical Engineering, National Chin-Yi University of Technology, Taichung 411, Taiwan
13. Dinniyah FS, Wahab W, Alif M (2017) Simulation of buck-boost converter for solar panels using PID controller. Energy Procedia 115:102–113
14. Perez R, Ineichen P, Seals R, Michalsky J, Stewart R (1990) Modeling daylight availability and irradiance components from direct and global irradiance. Sol Energy 44(5):271–289

15. Vyas M, Chudasama K, Bhatt M, Gohil B (2016) Real time data monitoring of PV solar cell using LabVIEW. Int J Current Eng Technol 6(6)
16. Kumar S, Kurian CP, Varghese SG, Ensemble learning model-based test workbench for the optimization of building energy performance and occupant comfort, IEEE Access 8, 96075–96087

Chapter 58
Doppler Velocity Estimation Employing mHDFT Phase-Locked Loop

Abhishek Chauhan and Ksh. Milan Singh

Abstract A non-contact Doppler velocity estimation technique is proposed using a modulated-hopping sliding discrete Fourier transform (mHDFT)-based phase-locked loop (PLL). The mHDFT quadrature detector is a modification of single-bin sliding discrete Fourier transform (Sb-SDFT) which is not only computationally efficient but also is inherently stable. The SDFT is a recursive structure that calculates the DFT for only a specific bin. The algorithm is implemented in PLL to enhance the sampling control adaptivity. The proposed mHDFT-PLL estimates velocity from low range of 0.1 m/s suitable for medical applications and high velocity range of 18–22 m/s with very less error. The proposed mHDFT-PLL has a high noise-handling capacity. The effectiveness of the proposed PLL for velocity estimation is verified by simulations in MATLAB environment.

Keywords Single-bin sliding DFT · Modulated DFT · Hopping DFT · mHDFT · Velocity estimation · Phase-locked loop

1 Introduction

Non-contact-type velocity estimation is widely used where limitations of attaching a sensor on the surface are not feasible. Optical methods [1, 2] are used to estimate the velocities with high accuracy but suffer from the problem of opacity and dusty medium. Implementing an optical system is much costlier than acoustical methods. Acoustic methods [3, 4] have been widely used in blood flow measurement [5–7], radar and sonar applications [8–10], industrial applications [11–14], etc. The ultrasonic sensor can transmit a continuous wave-type [15] or pulse wave-type [16] signal to the moving body. For estimating velocity, mostly continuous wave-type sensor is

A. Chauhan (✉) · Ksh. M. Singh
National Institute of Technology Meghalaya, Shillong, India
e-mail: milan.singh@nitm.ac.in

G. Panda et al. (eds.), *Sustainable Energy and Technological Advancements*, Advances in Sustainability Science and Technology,
https://doi.org/10.1007/978-981-16-9033-4_58

employed as the pulse wave encounters echoes in measurement [17]. Pulse mode wave type suffers from issues like crosstalk, signal attenuation, and low resolution [18].

Various techniques have been employed for estimating the velocity of a moving body. Kalman filter [19] is used to reduce effect of noise. Quadrature method [20] is effective for a short distance of around 10 cm after which the noise becomes predominant. Frequency modulation (FM) and demodulation use fast Fourier transform (FFT) to estimate the Doppler parameters but is only limited to estimate when the Doppler modulation index is less than 5. Time-domain correlation approach is another method for velocity estimation with acoustical methods, but the method of correlation usually requires more calculation than the Doppler method. In order to estimate the velocity, owing to Doppler phase changes, the proposed approach explains the theoretical principles of acoustic response of a moving object.

This paper introduces a fast mHDFT technique which is modified from SDFT IIR filter to track the velocity of a moving object. The paper is organized as follows: Sect. 2 discusses the phase shift in the received signal due to interaction of of carrier wave and the moving object. Section 3 discusses the simulations and results for mHDFT-PLL subjected to different velocities along with noise, and conclusions are presented in Sect. 4.

2 System Model

Consider an transmitter emitting a high-frequency sinusoidal wave of center frequency f_c:

$$T(t) = A_c \cos(2\pi f_c t) \tag{1}$$

where A_c and f_c are the amplitude and frequency of the carrier wave, respectively. When this high-frequency ultrasonic wave is directed at a moving body, the received signal undergoes a phase shift owing to the Doppler effect. The phase-modulated ultrasonic signal received at the receiver can be defined as:

$$R(t) = A_r \sin(w_c t + \phi_{vel}(t) + \phi_L + \phi_{par}) \tag{2}$$

where A_r is the amplitude of the received signal and ϕ_{vel}, ϕ_L and ϕ_{par} are the phase shift due to velocity of the body, path length of the wave and parametric effect, respectively. The phase shift due to constant velocity (V_c) is given by:

$$\phi_{vel} = \frac{2(2\pi f_c) V_c \sin(\theta)}{c_0} \tag{3}$$

where θ is the angle formed between the carrier signal and normal of the moving body and c_o is speed of sound at standard ambient temperature and pressure. The phase shift due to the total path length ($2L$) is given as:

$$\phi_L = \frac{2\pi f_c}{c_0}(2L) \tag{4}$$

When an ultrasonic beam travels through a low-pressure medium, it experiences a parametric phase shift. It can be categorized in forward and backward parametric effects. However, the influence of parametric phase shift over Doppler phase shift is dependent on a number of factors including path length, frequency, wavelength, velocity and pressure. If the path length is considered to be less than a meter, the parametric effect can be neglected for low frequencies. Discarding the phase shift due to path length and parametric effect, the phase-modulated signal can be given as:

$$R(t) = A_r \sin(w_c t + \phi_{vel}(t)) \tag{5}$$

The discretized time-domain representation of the received signal (5) can be represented as:

$$R(n) = A_d \sin(w_c n + \phi_{vel}(n)) \tag{6}$$

where A_d is the amplitude value in discrete domain of the received signal. The received signal $R(n)$ is given as input to the proposed mHDFT-PLL technique to extract the velocity.

A phase-locked loop is used to determine the velocity of a moving body. The mHDFT filter is used as a quadrature detector. The quadrature component of the mHDFT filter is subsequently processed by the moving average filter, which removes the carrier frequency from the resonator output. A PI controller is used to further remove the noise. The output is then restricted by a limiter and sent to an NCO, which generates pulses to enable various blocks. The proposed mHDFT-PLL model employed to extract the velocity parameter superimposed with carrier signal is shown in Fig. 1. The different blocks are described in detail from Sects. 2.1 to 2.4.

2.1 mHDFT-Based Quadrature Detector

ARCTAN approach [21], CORDIC vector rotation method [22], baseband delay demodulator [23], polar discriminator are several quadrature detectors. In this article, a quadrature detector is used in conjunction with a recursive DFT filter bank.

The sliding DFT [24] is an efficient recursive structure that calculates the single bin of the DFT. The DFT of M samples is given by:

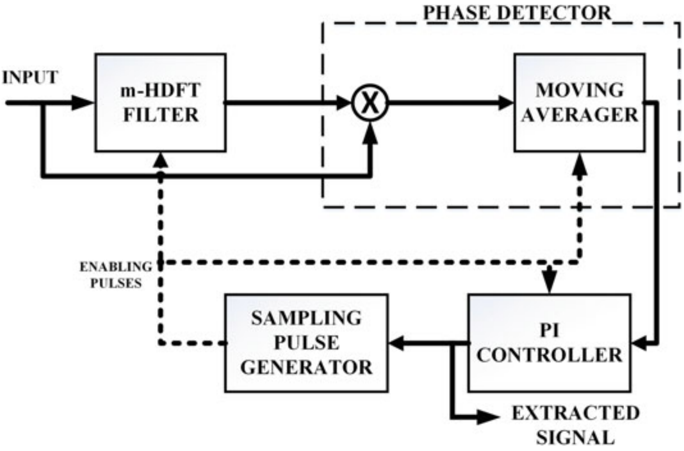

Fig. 1 mHDFT-based PLL

$$X_{\mathrm{n}}(k) = \sum_{n=0}^{M-1} x(n) W_{\mathrm{M}}^{-kn} \tag{7}$$

where W_{M}^{-kn} is the complex root of unity.

The direct implementation of standard DFT technique can be complicated in a variety of real-time applications and requires a significant calculative effort (increases in order of M^2). Furthermore, only a few bins of the M-point DFT are required for real-time applications. In such cases, a Fourier single-bin sliding discrete Fourier transform method (Sb-SDFT) can be utilized which uses a sliding window to compute a single complex DFT spectral bin. Sliding DFT [24] computes the present DFT bin by taking into account the previous DFT bin phase shifted by W_{M}^{k}, adding the incoming sample and discarding the previous sample:

$$X_{\mathrm{n}}(k) = W_{\mathrm{M}}^{k}[X_{n-1}(k) + x(n) - x(n - M)] \tag{8}$$

where k is the frequency bin, $x(n)$ represents sample, and $x(n - M)$ is the discarded sample.

Instead of sliding the window by sample by sample basis, a hopping DFT [25] is proposed in which the rectangular window slides by L samples, where $L = 2^a < M$ and $a > 0$ is termed as the hopping length. While hopping DFT adds some inaccuracy, it significantly decreases calculations as compared to SDFT. The difference equation of SDFT after introducing the hopping length L is modified as:

$$X_{\mathrm{n}}(k) = W_{\mathrm{M}}^{Lk}[X_{n-L}(k) + x(n) - x(n - M)] \tag{9}$$

The twiddle factor introduces error accumulation, and it may cause the filter to go in unstable region. As both SDFT and HDFT techniques suffer from instability due to presence of twiddle factor, a technique exploited modulation property of FFT. Substituting $k = 0$ in (8), we get:

$$X_{\mathrm{n}}(0) = W_{\mathrm{M}}^{0}[X_{n-1}(0) + x(n) - x(n - M)] \tag{10}$$

A modulating sequence of W_{M}^{-km} is multiplied to the output of comb filter, and we get:

$$X_{\mathrm{n}}(0) = [X_{n-1}(0) + W_{\mathrm{M}}^{-km}(x(n) - x(n - M))] \tag{11}$$

From (10), it can be observed that the twiddle factor is now eliminated from the feedback. This would confirm that the poles always reside on the unit circle. Since the modulating sequence is time-dependent, an oscillator is introduced which would replace the modulated sequence to eliminate the phase shift. This leads to an uniform start of each M sample sequence. This method of introducing the modulation sequence in SDFT is known as mDFT [26].

Combining both the concept of modulation and hopping, a mHDFT [27]-based filter is proposed which calculates the single bin by sliding the window by L samples and then introducing a modulating sequence which mitigates the filter instability issue. The transfer function of mHDFT filter is given by:

$$H_{\mathrm{mHDFT}}(z) = \frac{W_{\mathrm{M}}^{(m+L)k}\left[W_{\mathrm{M}}^{-mk}\left(1 - z^{-M}\right)\sum_{t=0}^{L-1} W_{\mathrm{M}}^{(t-L+1)k} z^{-t}\right]}{1 - z^{-L}} \tag{12}$$

The mHDFT structure is shown in Fig. 2 for $M = 16$ and $L = 4$.

Taking the input signal to be complex-valued signal, a computational requirement of various SDFT-based techniques is presented in Table 1. Since the HDFT and

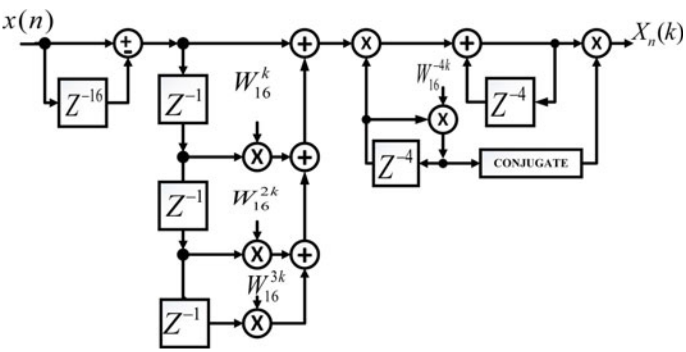

Fig. 2 mHDFT filter structure for $M = 16$ and $L = 4$

Table 1 Computational requirements of various DFT algorithms

Filter	M	Complex multiplications	Complex additions
SDFT	16	64	128
HDFT	16	16	52
mHDFT	16	32	52

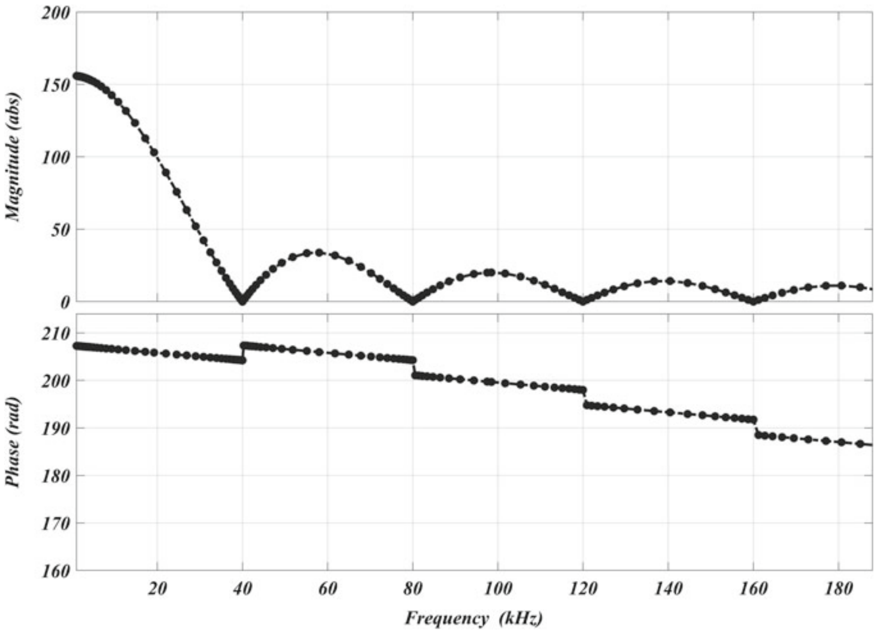

Fig. 3 Frequency response of mHDFT filter

mHDFT filters require hopping, a value of $L = 4$ is considered for reducing the computational requirements. It is observed that the computational requirement is less in HDFT, but considering the mHDFT filter provides stability with increase in around 50% more multiplications requirement. The frequency response of the mHDFT is illustrated in Fig. 3. It acts a low pass filter which allows the carrier frequency to pass through it. It is observed that the cut-off frequency for the proposed filter is 40 kHz which makes it suitable for the proposed PLL.

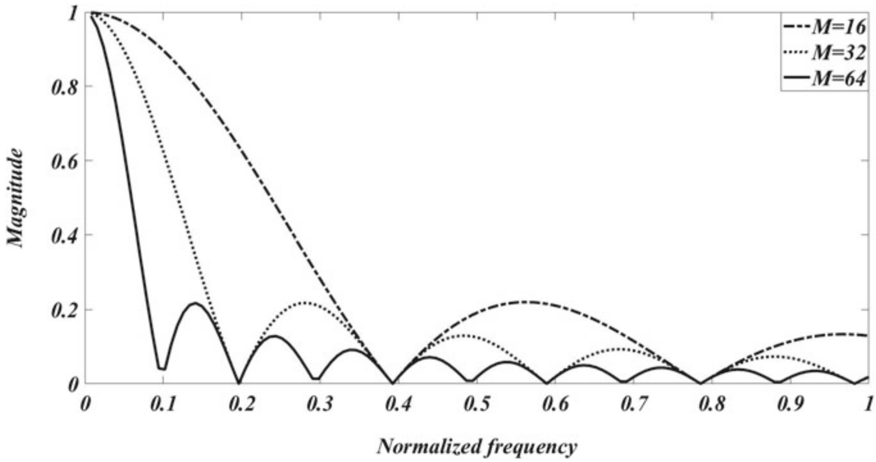

Fig. 4 Frequency response of a moving averager

2.2 Moving Averager

The output of the quadrature detector is fed to the moving average filter. Moving average filter is a low pass filter. Moving average filter filters out the carrier frequency signal from the input allowing only the message signal and its harmonics to pass through (Fig. 4).

Moving average filter can be obtained from the SDFT structure if we consider the bin value, i.e., $k = 0$ and averaging it by $\frac{1}{M}$. The transfer function of the moving average filter from SDFT structure is given by:

$$H_{\mathrm{MA}} = \frac{1}{M}\frac{1 - z^{-M}}{1 - z^{-1}} \tag{13}$$

2.3 PI Controller

The output of the moving average filter comprises of velocity parameter along with noise. While this noise may cause errors in the accurate extraction of parameters, the signal must be smoothed further. A proportional integral (PI) controller is used for noise filtering to smoothen the signal received from moving average filter. The PI controller is designed from the difference equation:

$$Y_{\mathrm{PI}}(n) = [M_{\mathrm{a}}(n) - M_{\mathrm{a}}(n-1)]k_{\mathrm{p}} + K_{\mathrm{i}} + Y_{\mathrm{PI}}(n-1) \tag{14}$$

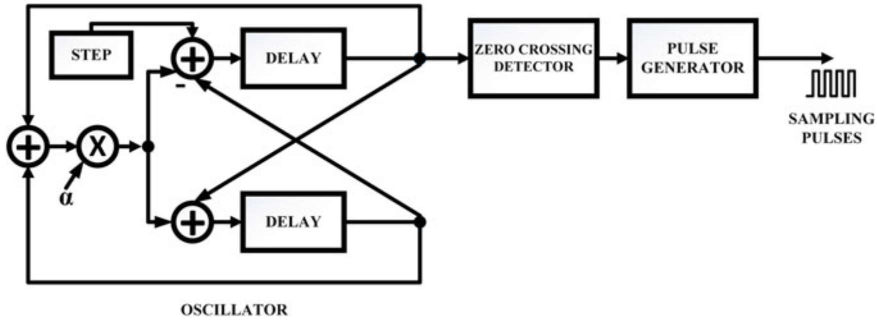

Fig. 5 Block diagram of SPG

The output of this PI controller is the signal of interest. The signal at the output which has constant velocity information V_c is given by:

$$Y = \frac{4\pi f_c V_c M}{c_0 f_{ena}} \tag{15}$$

where $f_{ena} = 4Mf_c$ is the enabling frequency. The constant velocity is determined from (15) and fed to the SPG after limiting Y peak-to-peak amplitude to unity.

2.4 Sampling Pulse Generator

The sampling pulse generator (SPG) provides a suitable sample signal in the proposed system to eliminate the fluctuations occurred in input signal. It is created by combining an oscillator, a comparator and a pulse generator. The sine and cosine signals of the appropriate sampling frequency are generated by the oscillator, which are adjusted using the extracted signal. Further, the zero-crossing detector turns f_s into variable sampling pulses. The SPG provides enabling pulses to all the blocks for a synchronized operation. The carrier frequency variation is reflected by the sampling pulses, which is proportional to value of α. The block diagram of sampling pulse generator is presented in Fig. 5.

3 Simulation and Results

The mHDFT-PLL is designed and simulated in MATLAB/Simulink environment. The frequency of the carrier wave is set to 40 kHz. The length of the window for calculating the DFT is set to $N = 128$. The speed of sound in ambient temperature pressure is taken as 346 m/s. The proportional gain of the PI controller is set at

$k_p = 0.085$, and the discrete integral controller gain is set to $k_i = 0.005$ to track the velocity of the moving body. A DC shift is observed when the input has no velocity term. To mitigate this error, the drift value is initially subtracted from the output of the controller to get the accurate results.

3.1 Velocity Estimation

The performance of mHDFT-PLL for estimating the constant velocities is given in Fig. 6 in terms of percentage error. Simulation for constant velocity measurement is simulated for low velocity and high velocity range. For low velocity range, a step of 0.1 m/s is taken, and the velocity is varied from 0.1 to 0.9 m/s. It is observed that for lower range, the estimation of velocity is very much accurate. Low velocity range estimation could be applicable for medical applications such as tissue motion detection, blood flow measurement. For velocity range 1–22 m/s, a step size of 1 m/s is taken and simulated. It is observed that after 18 m/s velocity value, the error in estimation increases. For 22 m/s, the error in estimating velocity is 0.89%. The proposed PLL technique can be easily implemented in measuring the blood flow measurement and tissue motion detection which are in low velocity range of 0.1 to 1–2 m/s and in traffic speed monitoring systems which may range from low speeds to high speeds around 100 kmph. The proposed PLL can be employed to measure wide range of applications with less error when compared to other PLL methods [28, 29] and fast estimating speed of the moving body.

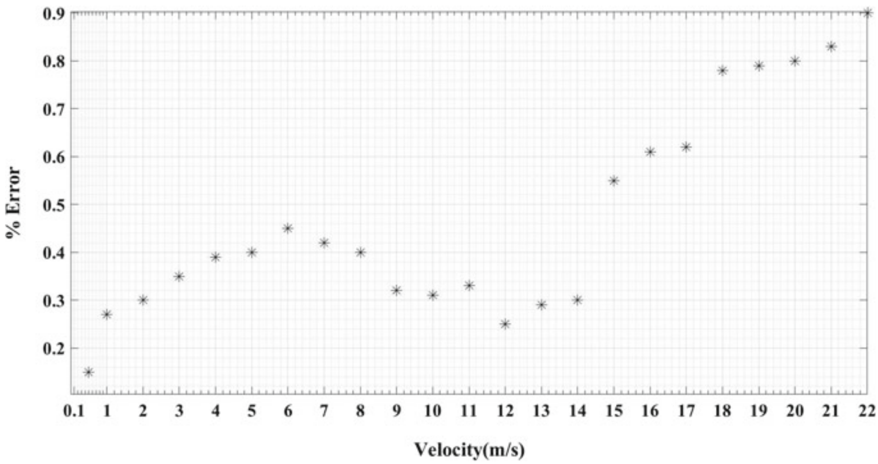

Fig. 6 Percentage error in estimating velocity

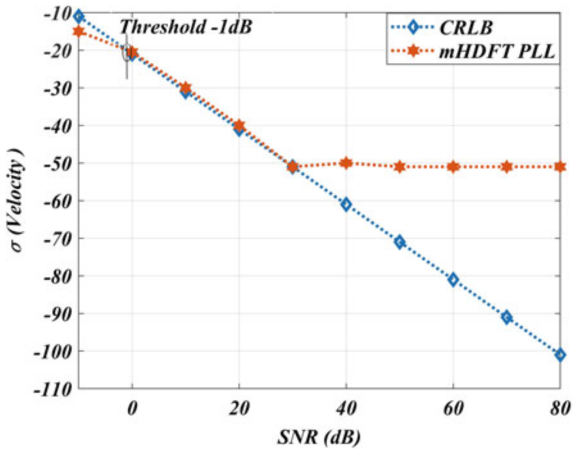

Fig. 7 CRLB plot for mHDFT-PLL for a constant velocity of 15 m/s

3.2 Noise Performance

The Cramer-Rao lower bound (CRLB) is a technique that represents the best value possible from a given available data. The CRLB algorithm assumes an unknown but deterministic parameter and reduces the variance of any unbiased estimation. In real-world applications, immunity to noise in the collected signal is measured by its CRLB, and it is a crucial characteristic of all estimating methods. To determine the performance, simulations were run for by adding noise to the received signal (Fig. 7).

A band-limited white Gaussian noise with varying the variance is added to the input signal. The correlation time of noise is set as $\frac{1}{f_{\text{ena}}}$. The SNR is defined as:

$$\text{SNR (db)} = 10 \log \left(\frac{A^2}{2\sigma^2} \right) \tag{16}$$

where A is power value of the phase-modulated signal and σ^2 is the variance of noise. Under band-limited noise, the CRLB for velocity estimation is given as:

$$\text{CRLB} = \frac{2\sigma^2}{N} \tag{17}$$

The value of N is set to 128, sampling frequency is set to 20.48 MHz, a constant velocity of 15 m/s, and σ is varied to obtain different levels. Figure 6 shows the variance in estimation of velocity. It is observed that at SNR = −1 dB threshold in this case, the CRLB deteriorates which indicates the estimation would no longer be valid for an estimator. The SNR between −1 and 30 dB behaves similar to the ideal CRLB graph. Beyond 30 dB, the mHDFT-PLL deviates from ideal CRLB and approaches asymptotically to a value of −51 dB.

4 Conclusion

A mHDFT-based PLL is employed to track constant velocity of a moving body. Doppler phase shift principle has been utilized in which a carrier signal of high frequency interacts with the information signal, and it causes phase modulation in the signal. The mHDFT resonator not only reduces the computation from traditional SDFT filter but also overcomes the stability issue due to the accumulation of error due to twiddle factor. The proposed mHDFT-PLL can estimate low velocity of 0.1 m/s with an error of 0.12% and can track a constant velocity of 22 m/s with an error of 0.89% at a fixed gain of controller gains at $k_\mathrm{p} = 0.085$ and $k_\mathrm{i} = 0.005$. The proposed system can handle a maximum of -1 dB of noise beyond which the system is not able to track the velocity parameter. Simulation results are used to verify the suggested PLL technique's performance. Finally, the proposed technique can be applied to extract the velocity in non-contact-type velocity estimation which can be applied in medical field as well as motion detection applications with accurate and fast estimation.

Acknowledgements The authors would like to thank SERB-DST, Government of India for financially supporting the research work.

References

1. Yang X, Ren A, Zhu T, Hu F (2016) A novel digital phantom using an optical noncontact measurement system. IEEE Life Sci Lett 2(1):1–4
2. Zhang ZF, Tao XM, Zhang HP, Zhu B (2013) Soft fiber optic sensors for precision measurement of shear stress and pressure. IEEE Sens J 13(5):1478–1482
3. Smith GC (2005) A noncontact method for detecting acoustic emission using a microwave Doppler radar motion detector. IEEE Trans Ultrason Ferroelectr Freq Control 52(9):1613–1617
4. Zeng R, Wang Y (2018) Orthogonal angle domain subspace projection-based receiver algorithm for underwater acoustic communication. IEEE Commun Lett 22(5):1102–1105
5. Willink R (1999) Mean blood velocity measurement with a narrow ultrasound beam and an asymmetric velocity profile. IEEE Trans Biomed Eng 46(3):362–364
6. Pialot B, Gachelin J, Tanter M, Provost J, Couture O (2020) Flow rate and low hematocrit measurements for in vitro blood processing with Doppler ultrasound. IEEE Trans Ultrason Ferroelectr Freq Control 67(7):1293–1302
7. Izadi A, Ghatan Z, Vahdat BV, Farzanch F (2006) Design and simulation of a life detection system based on detection of the heart beat using Doppler frequency. In: IEEE international symposium on signal processing and information technology, Vancouver, BC, pp 685–690
8. Nanzer JA (2016) Micro-motion signatures in radar angular velocity measurements. In: 2016 IEEE radar conference (RadarConf)
9. Atkins PR, Collins T, Foote KG (2007) Transmit-signal design and processing strategies for sonar target phase measurement. IEEE J Sel Top Signal Process 1(1):91–104
10. Jian M, Lu Z, Chen VC (2018) Drone detection and tracking based on phase-interferometric Doppler radar. In: IEEE radar conference (RadarConf18), Oklahoma City, OK, pp 1146–1149
11. Dong X, Chen S, Xing G, Peng Z, Zhang W, Meng G (2018) Doppler frequency estimation by parameterized time-frequency transform and phase compensation technique. IEEE Sens J 18(9):3734–3744

12. Seijo Ó, Val I, López-Fernãndez JA (2020) Portable full channel sounder for industrial wireless applications with mobility by using sub-nanosecond wireless time synchronization. IEEE Access 8:175576–175588
13. Cui L, Jin Z, Huang J, Wang H (2019) Fault severity classification and size estimation for ball bearings based on vibration mechanism. IEEE Access 7:56107–56116
14. Jin G, Sain MK, Spencer BF (2005) Frequency domain system identification for controlled civil engineering structures. IEEE Trans Control Syst Technol 13(6):1055–1062
15. Matar OB, Remenieras JP, Bruneel C, Roncin A, Patat F (1998) Noncontact measurement of vibration using airborne ultrasound. IEEE Trans Ultrason Ferroelectr Freq Control 45(3):626–632
16. Zheng Y, Chen S, Tan W, Kinnick R, Greenleaf JF (2007) Detection of tissue harmonic motion induced by ultrasonic radiation force using pulse-echo ultrasound and Kalman filter. IEEE Trans Ultrason Ferroelectr Freq Control 54(2):290–300
17. Isoda K, Hara T (2011) Doppler velocity measurement method with a second-time-around echoes suppression for synthetic bandwidth radars. In: European radar conference, Oct 2011, pp 134–137
18. Ramachandran S, Nicholson JW, Ghalmi S, Yan MF (2003) Measurement of multipath interference in the coherent crosstalk regime. IEEE Photonics Technol Lett 15(8):1171–1173
19. Yoon J, Peng H (2014) A cost-effective sideslip estimation method using velocity measurements from two GPS receivers. IEEE Trans Veh Technol 63(6):2589–2599
20. Kranjec J, Beguš S, Drnovšek J, Geršak G (2014) Novel methods for noncontact heart rate measurement: a feasibility study. IEEE Trans Instrum Meas 63(4):838–847
21. Eissa HM, Sharaf K, Ragaie H (2002) ARCTAN differentiated digital demodulator for FM/FSK digital receivers. In: The 2002 45th Midwest symposium on circuits and systems, 2002. MWSCAS-2002, Tulsa, OK, p II
22. Volder JE (1959) The CORDIC trigonometric computing technique. IRE Trans Electron Comput EC-8(3):330–334
23. Shima JM (1995) FM demodulation using a digital radio and digital signal processing. University of Florida
24. Jacobsen E, Lyons R (2003) The sliding DFT. IEEE Signal Process Mag 20(2):74–80
25. Park C, Ko S (2014) The hopping discrete Fourier transform [sp tips and tricks]. IEEE Signal Process Mag 31(2):135–139
26. Duda K (2010) Accurate, guaranteed stable, sliding discrete Fourier transform [DSP tips and tricks]. IEEE Signal Process Mag 27(6):124–127
27. Wang Q, Yan X, Qin K (2015) High-precision, permanently stable, modulated hopping discrete Fourier transform. IEEE Signal Process Lett 22(6):748–751
28. Imou K, Ishida M, Okamoto T, Kaizu Y, Sawamura A, Sumida N (2001) Ultrasonic Doppler sensor for measuring vehicle speed in forward and reverse motions including low speed motions. Agric Eng Int CIGR J
29. Yang MH, Xu J, Sun X-W (2008) Velocity error analysis of a k-band dual mode traffic radar. Prog Electromagn Res B 10:105–116

Chapter 59
Efficiency Optimization of Surface and De-centered PMSM with Silicon Steel and Amorphous Iron Materials for E-rickshaw

Anju P. Sivadas and V. P. Mini

Abstract The electric vehicle (EV) industry is developing around the world because of increased air pollution and the rising cost of fuel in traditional vehicles. E-rickshaws are in great demand in nations like India, since three-wheelers are the regular method of transport utilized by citizens. Compared with the induction motor (IM) and switch reluctance motor (SRM), the permanent magnet synchronous motor (PMSM) has the advantages of high power density, high efficiency, and fewer losses. Hence, PMSM is the better choice for E-rickshaw. The efficiency of PMSM is reliant upon the rotor arrangement and materials utilized in the motor. Due to the low cost and simplicity of assembling, silicon steel (SS) is typically utilized in PMSM cores. The intrinsic attributes of SS limit iron loss reduction. The iron loss of amorphous iron (AI) PMSM is less in contrast with SS due to high resistivity, low coercive power, etc. In this paper, efficiency optimization of surface and de-centered PMSM with SS and AI is discussed. The selection of the power rating of PMSM is done based on the E-rickshaw dynamics. The detailed design of PMSM is included. Based on design values, PMSM has virtually evolved from the ANSYS Maxwell stage. The motor parameters are obtained from ANSYS Maxwell, and PMSM is modeled in MATLAB/Simulink.

Keywords E-rickshaw · Efficiency · PMSM · ANSYS Maxwell · MATLAB/Simulink

A. P. Sivadas (✉) · V. P. Mini
Department of Electrical Engineering, College of Engineering Trivandrum,
APJ Abdul Kalam Technological University, Thiruvananthapuram, Kerala, India
e-mail: minivp@cet.ac.in

G. Panda et al. (eds.), *Sustainable Energy and Technological Advancements*,
Advances in Sustainability Science and Technology,
https://doi.org/10.1007/978-981-16-9033-4_59

1 Introduction

Instead of an internal combustion engine, EVs operate on an electric motor. The advantages of EVs are that they reduce emissions, are silent in operation, reduce fuel costs, low maintenance, etc. In a nation like India, the majority of individuals are dependent on three wheelers for their everyday travel. To reduce atmospheric pollution in India, the joint government industry vision dependent on the National Electric Mobility Mission Plan (NEMMP) 2020 designated deals for 6–7 million EVs by 2020 and permitted the sales of EVs without batteries. It is intended to set up quick charging stations at an interval of 50 km on state and public roadways. So, the efficient E-rickshaw has a beneficial outcome for society. The state government has dispatched an E-rickshaw which is driven by BLDC engines, but it has the drawbacks of vibrations, noise, etc. The E-rickshaw with PMSM is in the development stage.

Among the literature reviews carried out, Sreejith et al. [1, 2] discussed three-wheeler load modeling and compared Li-ion and lead acid batteries for EV. A design approach to calculate the engine power rating based on vehicle dynamics is given in [3]. The authors in [4, 5] sized propulsion motors based on the Indian driving cycle (IDC). Mulhall et al. [6] examined the plan and improvement of a solar-powered autorickshaw. AI has physical properties that are well suited for high-efficiency motors and have extremely low core loss and high permeability. A comparison of amorphous metal and silicon steel PMSM is given in [7]. Zhang et al. [8] discussed the loss calculation in high-speed PMSM. The loss performance in an amorphous magnet axial-flux PMSM is analyzed and improved in [9]. The results from a small axial-flux PMSM that utilizes AMSC in tape wound which equipped with toroidally wound stator windings have demonstrated that the combination of iron and stray losses is only 6% of the maximum output power at rated speed.

The block diagram of the E-rickshaw is shown in Fig. 1. The electronic controller gets signals from the brake and accelerator. The battery management system (BMS) controls the charging and discharging of the battery. The transmission unit transmits mechanical power to the driven wheels. The motor is the workhorse of the EV. The efficiency of a motor depends on core materials and can be increased by reducing the core loss. Due to their low cost and simplicity, at the time of manufacture, non-oriented (NO) SS sheets are usually used in PMSM cores. SS is a soft magnetic material that contains a high silicon content of about 3.2% of its mass. M-15, M-19, and M-27 are non-oriented SS grades. AI has physical properties well suited for high-efficiency motors. AI is made as a thin foil-like structure with a thickness of 25 µm. This foil like-structure limits hysteresis and eddy current losses. The four amorphous materials widely used are 2605SA1, 2714A, 2714AF, and Vitroperm 500F. The material composition of AI is iron 85–95%, silicon 5–10%, and boron 1–5%.

In this paper, the efficiency optimization of PMSM by using SS (M1924G) and AI (2605SA1) materials is explained. Under surface-mounted PMSM, surface PMSM (SPMSM) and de-centered PMSM (DPMSM) are considered. The power rating of PMSM is obtained by using E-rickshaw dynamics. The PMSM is constructed by using conventional machine design equations. The SPMSM and DPMSM are

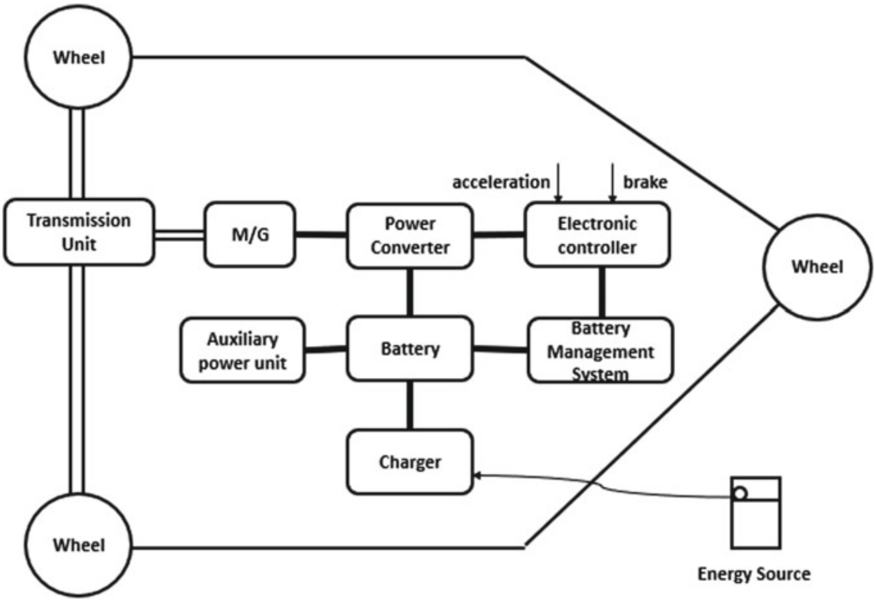

Fig. 1 Block diagram of E-rickshaw

virtually developed in ANSYS Maxwell, and efficiency is compared. By comparing the performances, SPMSM with 2605SA1 material has the highest efficiency and is selected for E-rickshaw. The motor parameters are extracted, and PMSM is mathematically modeled in MATLAB/Simulink.

2 Dynamics of E-rickshaw

Power requested by a vehicle is obtained by determining the various forces acting on a vehicle that oppose its motion. The vehicle has to overcome several forces acting on it while traveling. With tractive force F_t, the vehicle moves forward. It consists of four components: rolling resistance force (F_r), aerodynamic drag force (F_d), climbing force (F_c), and acceleration force (F_a). The forces acting on the E-rickshaw are shown in Fig. 2.

2.1 Rolling Resistance Force

The rolling resistance force is due to the deformation of the wheel and road surface. It depends on pressure and temperature of the tire, vehicle's speed, etc.

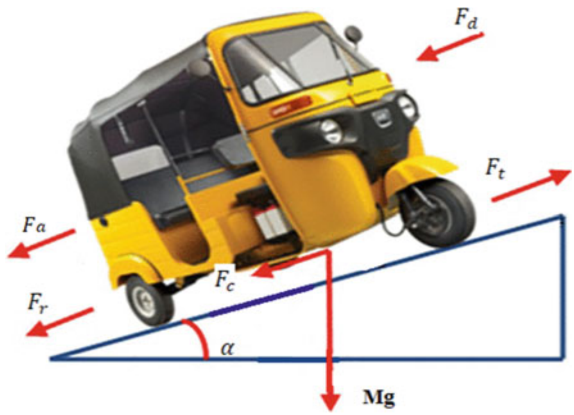

Fig. 2 Forces acting on E-rickshaw

$$F_r = M \cdot g \cdot f_r \tag{1}$$

M, g, and f_r are the mass of vehicle (kg), acceleration due to gravity (m/s^2), and the rolling resistance coefficient.

2.2 Aerodynamic Drag Force

In the air, when a vehicle travels at a particular speed, it encounters a force resisting its motion. This force is aerodynamic drag. It is determined by the shape of the vehicle.

$$F_d = 0.5 \cdot \rho \cdot A_f \cdot C_d \cdot V^2 \tag{2}$$

ρ, A_f, and C_d are the density of air (kg/m^3), vehicle's frontal area (m^2), and drag coefficient.

2.3 Climbing Force

When the vehicle moves up or down a slope, a component of force is produced by its weight that is always directed downward. This force component which opposes the forward motion is the climbing force. The climbing force mainly depends on the road angle. α is the road angle.

$$F_c = M \cdot g \cdot \sin \alpha \tag{3}$$

2.4 Acceleration Force

During the entire journey of a vehicle, it has to vary the speed. This change in speed at the time of acceleration or braking causes acceleration force. It depends on the total mass and the moment of inertia.

$$F_a = \lambda \cdot M \cdot \frac{dV}{dt} \tag{4}$$

The vehicle details and parameters considered for the dynamics calculation of E-rickshaw are given in Tables 1 and 2.

The total force acting on E-rickshaw is calculated by,

$$F_t = F_r + F_d + F_c + F_a \tag{5}$$

Total power required for traction,

$$P_t = F_t \cdot V \cdot 1000/3600 \tag{6}$$

Table 1 Vehicle details

Parameter	Values
Vehicle model	Bajaj RE 4S
No. of seats	4
Kerb weight (kg)	337
Battery	48 V, Li-ion
Gross weight (kg)	550
Vehicle dimension (mm)	2635 × 1300 × 1704
Wheel base (mm)	2000
Ground clearance (mm)	200

Table 2 E-rickshaw dynamics parameters

Parameter	Values
Rolling resistance coefficient, f_r	0.015
Aerodynamic drag coefficient, C_d	0.44
Frontal area, A_f (m^2)	2.09
Maximum speed (km/h)	42
Average speed (km/h)	21.93
Mass (kg)	550
Efficiency of transmission (%)	85
Grading angle (°)	6

Table 3 E-rickshaw dynamics calculated

Parameter	Values
Rolling resistance force (N)	80.93
Aerodynamic drag force (N)	6.23
Climbing force (N)	563.98
Acceleration force (N)	159.5
Total power (W)	2702.68
Motor power (W)	3178.03

Motor power,

$$P_{\mathrm{m}} = P_{\mathrm{t}}/\eta_{\mathrm{tran}} \tag{7}$$

The motor power required for the E-rickshaw is obtained based on the vehicle dynamics. The vehicle model being considered is the Bajaj RE 4S. The values calculated based on equations are given in Table 3. The total power obtained after calculation is 2702.68 W. The motor power calculated is 3178.03 W. The specification of PMSM selected is 3.5 kW, 1500 rpm, 300 V, 4 pole, and 50 Hz.

3 Design of PMSM

The design of SPMSM and DPMSM is explained in this section. Since both come under surface-mounted PMSM, the design equations are the same. The images of the surface and de-centered PMSM are shown in Fig. 3. By using machine designing equations, stator, rotor, and slot dimensions are obtained.

3.1 Main Dimensions of PMSM

The PMSM is designed based on conventional machine design equations. The main dimensions of PMSM are stator inner diameter (D) and axial length (L). The equations are given below.

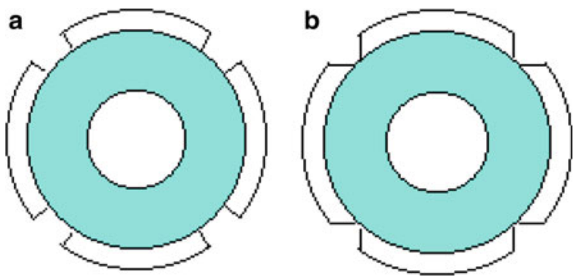

Fig. 3 Surface-mounted PMSM. **a** Surface PMSM, **b** de-centered PMSM

$$\mathrm{KVA}_{\mathrm{output}} = C_0 \cdot D^2 \cdot L \cdot n_{\mathrm{s}} \tag{8}$$

$$C_0 = 11 \cdot B_{\mathrm{avg}} \cdot \mathrm{ac} \cdot K_{\mathrm{w}} \cdot 10^{-3} \tag{9}$$

The input power,

$$P = \frac{(\sqrt{3} \cdot V \cdot I \cdot \cos\phi)}{\eta} \tag{10}$$

$$D^2 \cdot L = \frac{P}{C_0 \cdot n_{\mathrm{s}}} \tag{11}$$

C_0, n_{s}, B_{avg}, ac, and kW are the output coefficient, synchronous speed, specific magnetic loading, specific electric loading, and the winding factor.

3.2 Stator Design

Effective axial length of the machine,

$$L_{\mathrm{i}} = L \cdot k_{\mathrm{st}} \tag{12}$$

Flux/pole,

$$\phi = B_{\mathrm{avg}} \cdot \tau_{\mathrm{p}} \cdot L_{\mathrm{i}} \tag{13}$$

Stator phase voltage,

$$E_{\mathrm{s}} = \frac{V_{\mathrm{L}}}{\sqrt{3}} \tag{14}$$

$$E_{\mathrm{s}} = 4.44 \cdot f \cdot \phi \cdot K_{\mathrm{w}} \cdot T_{\mathrm{s}} \tag{15}$$

No. of phase turns of stator,

$$T_{\mathrm{s}} = \frac{E_{\mathrm{s}}}{4.44 \cdot f \cdot \phi \cdot K_{\mathrm{w}}} \tag{16}$$

Total stator conductors,

$$Z_{\mathrm{s}} = 2 \cdot 3 \cdot T_{\mathrm{s}} \tag{17}$$

No. of conductors in each slot,

$$Z = \frac{6T_{\mathrm{s}}}{S} \tag{18}$$

Stator slot pitch,

$$\tau_{\mathrm{s}} = \frac{\pi D}{S} \tag{19}$$

Maximum tooth width,

$$W_t = \frac{B_g \cdot \pi \cdot D}{B_t \cdot S} \tag{20}$$

Air-gap flux density,

$$B_g = \frac{\pi}{2} \cdot B_{avg} \tag{21}$$

Minimum tooth width,

$$W_{tb} = \tau_s - W_t \tag{22}$$

Slot width,

$$B_{s1} = \tau_s - W_t \tag{23}$$

$$B_{s2} = \tau_s - W_{tb} \tag{24}$$

Stator yoke height,

$$h_s = \frac{B_g \cdot \pi \cdot D}{2 \cdot B_t \cdot P} \tag{25}$$

Area of slot,

$$A_{slot} = \frac{Z \cdot I_s}{k_{fills} \cdot J_s} \tag{26}$$

Slot depth,

$$H_{s2} = \frac{A_{slot}}{(B_{s1} + B_{s2})/2} \tag{27}$$

Stator outer diameter,

$$D_{0s} = D + 2(H_{s0} + H_{s1} + H_{s2} + h_s) \tag{28}$$

Air-gap length,

$$l_g = \frac{0.02\pi D}{P} \tag{29}$$

The k_{st}, V_L, K_{fills}, B_t, d_s, and J_s are stator stacking factor, line voltage, slot fill factor, tooth flux density, shaft diameter, and current density. B_{s0}, H_{s0}, and H_{s1} are the slot opening, slot lip, and wedge value.

3.3 Rotor Design

Rotor outer diameter,

$$D_r = D - 2l_g \tag{30}$$

Rotor inner diameter,

$$D_{\mathrm{ir}} = D_{\mathrm{r}} - d_{\mathrm{s}} \tag{31}$$

3.4 Design Values of PMSM

The SPMSM and DPMSM have same dimensions since both come under surface-mounted PMSM. The permanent magnet used is NdFeB35. The SPMSM and DPMSM model obtained from RMxprt of ANSYS Maxwell is given in Fig. 4.

The motor dimensions for SPMSM and DPMSM obtained from machine design equations are given in Table 4.

4 Efficiency Optimization of PMSM with SS and AI Materials

The materials used for the efficiency optimization of PMSM are SS (M1924G) and AI (2605SA1). The software used for efficiency optimization is ANSYS Maxwell.

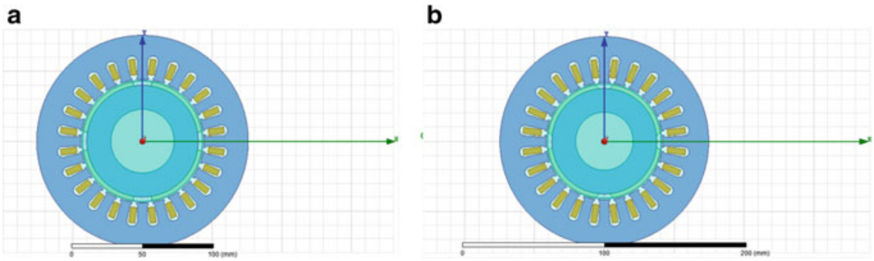

Fig. 4 Surface-mounted PMSM. **a** SPMSM, **b** DPMSM

Table 4 PMSM dimensions obtained

Parameter	SPMSM	DPMSM
Stator outer diameter (mm)	151.92	151.92
Stator inner diameter (mm)	88.63	88.63
Rotor outer diameter (mm)	85.85	85.85
Axial length (mm)	208.83	208.83
Air-gap length (mm)	1.39	1.39
B_{s1} (mm)	5.53	5.53
B_{s2} (mm)	7.73	7.73
H_{s2} (mm)	11.42	11.42

Table 5 Performance comparison of SPMSM and DPMSM

Parameters	SPMSM (M1924G)	DPMSM (M1924G)	SPMSM (2605SA1)	DPMSM (2605SA1)
Rated power (kW)	3.5	3.5	3.5	3.5
Output power (kW)	3.48	3.499	3.5	3.5
Efficiency (%)	94.1	93.81	95.12	94.74
Iron-core loss (W)	38.46	35.16	0.00149	0.00135
Armature copper loss (W)	114.19	129.36	115.343	128.3
Speed (rpm)	1500	1500	1500	1500

Fig. 5 Efficiency comparison of SPMSM and DPMSM with SS and AI

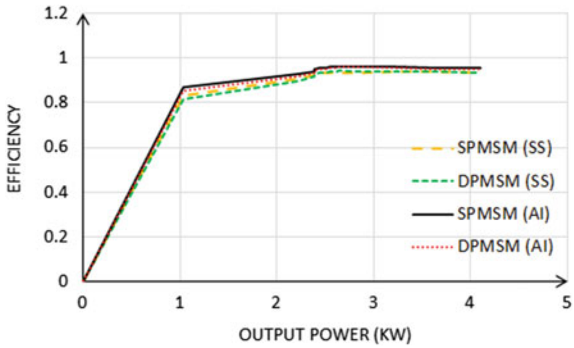

SPMSM and DPMSM are virtually developed with SS and AI materials. The performance comparison of SPMSM and DPMSM with SS and AI materials is given in Table 5.

By comparing the performances, SPMSM and DPMSM with AI have the least iron-core loss and high efficiency than SS materials. Out of these, SPMSM with AI has an efficiency of 95.12%, which is selected for E-rickshaw. The efficiency comparison of PMSM is shown in Fig. 5.

5 Mathematical Modeling of PMSM

PMSM is mathematically modeled in MATLAB/Simulink. It is modeled based on the motor parameters extracted from SPMSM with AI material in ANSYS Maxwell. The motor parameters extracted are given in Table 6.

Table 6 Motor parameters extracted from ANSYS Maxwell

Parameter	Values
Stator resistance, R_s (Ω)	0.334
D–Q axis inductance, L_d, and L_q (mH)	5.17154
Rated speed (rpm)	1500
Rated torque (Nm)	22.2

Parks transformation converting the phase voltages V_{abc} to V_{dq},

$$\begin{bmatrix} V_q \\ V_d \\ V_o \end{bmatrix} = \frac{2}{3}\begin{bmatrix} \cos\theta & \cos(\theta - 120) & \cos(\theta + 120) \\ \sin\theta & \sin(\theta - 120) & \sin(\theta + 120) \\ 1/2 & 1/2 & 1/2 \end{bmatrix}\begin{bmatrix} V_a \\ V_b \\ V_c \end{bmatrix} \tag{32}$$

Stator voltage in *q*-axis,

$$V_q = R_s i_q + p(\lambda_d) + \omega_r \lambda_d \tag{33}$$

Stator voltage in *d*-axis,

$$V_d = R_s i_d + p(\lambda_q) - \omega_r \lambda_q \tag{34}$$

Stator flux linkage in *q*-axis,

$$\lambda_q = L_q i_q \tag{35}$$

Stator flux linkage in *d*-axis,

$$\lambda_d = L_d i_d + \lambda_{af} \tag{36}$$

Electrical speed,

$$\omega_r = \frac{P}{2}\omega_{rm} \tag{37}$$

Electromagnetic torque,

$$T_e = \frac{3}{2} \times \frac{P}{2}\left(\lambda_d i_q - \lambda_q i_d\right) \tag{38}$$

Mechanical torque equation,

$$T_e = T_L + B\omega_{rm} + Jp\omega_{rm} \tag{39}$$

p is the differential operator and λ_{af} is the PM flux. The PMSM model, stator current, electromagnetic torque, and speed are given in Figs. 6, 7, 8, and 9.

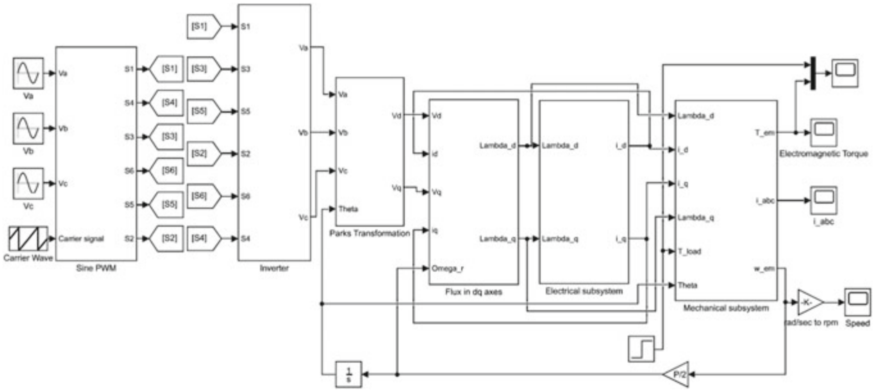

Fig. 6 PMSM model

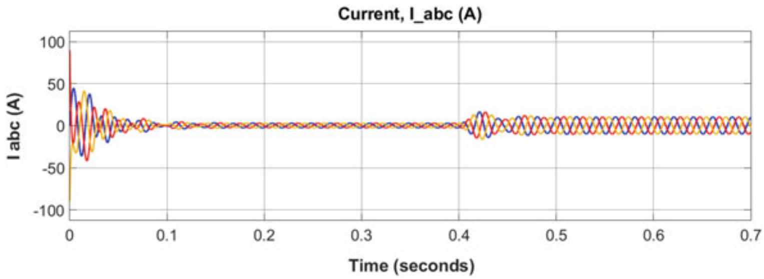

Fig. 7 Stator current

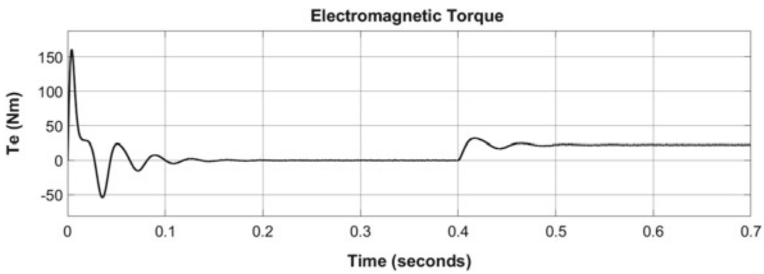

Fig. 8 Electromagnetic torque

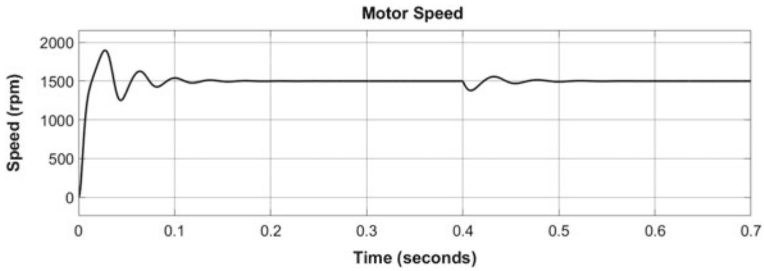

Fig. 9 Motor speed

6 Conclusion

This paper discusses the efficiency optimization of SPMSM and DPMSM with M1924G and 2605SA1 materials for E-rickshaw. Based on the E-rickshaw dynamics, the power rating of PMSM was calculated as **3.5** kW. By using conventional machine design equations, SPMSM and DPMSM are virtually developed in ANSYS Maxwell with SS and AI materials. By comparing the performances, SPMSM with AI has the highest efficiency of about **95.12**% which is selected for E-rickshaw. By using AI instead of SS material, the iron loss is less and the efficiency is greater in SPMSM and DPMSM. This work can be extended to the efficiency optimization of PMSM drive for E-rickshaw.

References

1. Sreejith R, Rajagopal KR (2016) An insight into motor and battery selections for three-wheeler electric vehicle. In: 1st IEEE international conference on power electronics intelligent control and energy systems (ICPEICES), 4–6 July 2016
2. Sreejith R, Rajagopal KR, Singh B (2016) Modelling and analysis of PMBLDC motor based three wheeler EV for closed loop optimum operation. In: IEEE international conference on power electronics, drives and energy systems (PEDES), 14–17 Dec 2016
3. Akhtar MJ, Behera RK, Parida SK (2015) Propulsion system design of electric vehicle. In: 6th international conference on power electronics [::systems::] and applications (PESA), 15–17 Dec 2015
4. Mishra P, Saha S, Ikkurti HP (2013) A methodology for selection of optimum power rating of propulsion motor of three wheeled electric vehicle on Indian drive cycle (IDC). Int J Theoret Appl Res Mech Eng (IJTARME) 2:2319–3182
5. Murali N, Usha Kumari S, Mini VP (2020) Sizing and performance analysis of an electric motor in an E-rickshaw. In: IEEE international conference on power systems technology (POWERCON), 14–16 Sept 2020
6. Mulhall P, Lukic SM, Wirasingha SG, Lee Y-J, Emadi (2010) Solar-assisted electric auto rickshaw three-wheeler. IEEE Trans Veh Technol 59(5):2298–2307
7. Tong W, Dai S, Wu S, Tang R (2019) Performance comparison between an amorphous metal PMSM and a silicon steel PMSM. IEEE Trans Magn 55(6)

8. Zhang C, Chen L, Wang X, Tang R (2020) Loss calculation and thermal analysis for high-speed permanent magnet synchronous machines. IEEE Trans Magn 8:92627–92636
9. Kahourzade S, Ertugrul N, Soong WL (2018) Loss analysis and efficiency improvement of an axial-flux PM amorphous magnetic material machine. IEEE Trans Ind Electron 65(7):5376–5383

Chapter 60
Time Series Forecasting Model for Chaotic Fractional-Order Rössler System

Kishore Bingi, B Rajanarayan Prusty, Kaibalya Prasad Panda, and Gayadhar Panda

Abstract This paper concentrates on developing a forecasting model to reconstruct states in a chaotic fractional-order Rössler system. The proposed model's attractiveness is how relationships between inputs (state variables) and outputs (change in state variables) are modeled for accurate prediction. The prediction model results show the excellent tracking ability for all the changes in state variables with R^2 and MSE values close to one and zero, respectively. Also, the proposed forecasting model's performance shows the best performance on reconstructing the states with minimal MSE errors. This best performance is valid for all three reconstructed state variables of the system.

Keywords Adams–Bashforth method · Chaos · Forecasting · Fractional-order systems · Neural networks

K. Bingi (✉) · B Rajanarayan Prusty
School of Electrical Engineering, Vellore Institute of Technology, Vellore, India
e-mail: bingi.kishore@ieee.org

B Rajanarayan Prusty
e-mail: b.r.prusty@ieee.org

K. P. Panda · G. Panda
Department of Electrical Engineering, National Institute of Technology Meghalaya, Shillong, India
e-mail: kaibalyapanda@nitm.ac.in

G. Panda
e-mail: gayadhar.panda@nitm.ac.in

G. Panda et al. (eds.), *Sustainable Energy and Technological Advancements*, Advances in Sustainability Science and Technology,
https://doi.org/10.1007/978-981-16-9033-4_60

1 Introduction

Due to the power industry's rapid growth and constantly increasing demand, the electrical equipment in power grid structure characteristics makes the system more complex. This complexity behavior is similar to the chaotic system's behavior of nonlinear and sensitivity of initial conditions. Thus, the application of chaos has an excellent approach for the power system's stable operation [1]. Further, the study and application of nonlinear dynamics in chaotic systems using model-free analysis have been a broad research area in various engineering and science fields [2, 3]. The very well-known Rössler's systems chaotic behavior is similar to widespread Lorenz's systems behavior having only one manifold [4]. Rössler's systems' chaotic behavior has been used in various modeling and control applications of physical systems. For instance, in modeling the chemical equilibrium reactions [5], path planning of robots [6], periodic controlling using bispectral wavelet analysis [7], and switching control of coupled systems [8], the Rössler's system's chaotic behavior has been used. The realistic modeling feature with the fractional-order concept provides more freedom to decide the orders [2, 9, 10]. Therefore, in this paper, the fractional version of Rössler's system is adopted.

Over the years, researchers have investigated the fractional-order Rössler's system's chaotic behavior by employing time/frequency domain [2], predictor-corrector [11], and decomposition methods [12]. Further, researchers have also developed numerical solution methods such as Caputo, Grünwald–Letnikov and Riemann-Liouville for solving the governing of the system with assumed step size and initial conditions [2]. These techniques highlight that obtaining the system's chaotic behavior for a desired future time frame is computationally challenging and affected by the step size. Therefore, the research on developing a model-free analysis using the data-driven approach for forecasting the system's states is inevitable. Chaos prediction plays a vital role in many modeling and control engineering applications. This is because the system dynamics should be identified entirely and characterized for designing the effective control action [4]. On this note, the most commonly used neural network models such as multi-layer perceptron [13], recurrent neural network, and deep recurrent neural networks [14] have been used in predicting the chaotic behavior of the system. These applications are limited to Lorenz's chaotic system only. Further, it highlights that the time series prediction in these applications has been achieved using multi-layer networks. The future forecasting of the system states using the prediction model is the research gap that is worth highlighting.

A novel forecasting model for chaotic fractional-order Rössler's system is developed with the help of a single shallow neural network in this paper. The model predicts the values of change in states using the neural network model. With these expected changes in states, the system states are reconstructed using the Adams–Bashforth two-step equations. The initial training data for the prediction model has been obtained by solving the system's governing equations. Further, the performance of the proposed forecasting model is also evaluated for extended testing periods.

The paper is organized as follows: Sect. 2 gives the Rössler system's governing equations and its chaotic behavior. Section 3 presents the proposed prediction and forecasting model's development to reconstruct the state values using neural networks. Section 4 discusses the detailed analysis of various results from proposed models. Section 5 concludes the work.

2 Characteristics of Fractional-Order Rössler System

The Rössler system's governing equations with states x_1, x_2, and x_3 are shown in Fig. 1 (orange box). The fractional version of the system can be obtained using the integer-order model's derivative actions by fractional ordering as shown in Fig. 1 (green box). Further, the Rössler system's numerical solution is also demonstrated in Fig. 1 (red box). The numerical solution model shown in Fig. 1 is obtained using Grünwald–Letnikov (GL) fractional definition. For a function $f(t)$, the GL's definition of order q with step size "h" and simulation time "T" [9] is defined as,

Fig. 1 Fractional-order model of Rössler system and its numerical solution

Integer-Order Model

$$\frac{\mathrm{d}}{\mathrm{d}t}(x_1(t)) = -\big(x_2(t)+x_3(t)\big),$$
$$\frac{\mathrm{d}}{\mathrm{d}t}(x_2(t)) = x_1(t)+ax_2(t),$$
$$\frac{\mathrm{d}}{\mathrm{d}t}(x_3(t)) = b+x_3(t)\big(x_1(t)-c\big).$$

Model Parameters
a, b, and c

Fractional-Order Model

$$\frac{\mathrm{d}^\alpha}{\mathrm{d}t^\alpha}(x_1(t)) = -\big(x_2(t)+x_3(t)\big),$$
$$\frac{\mathrm{d}^\beta}{\mathrm{d}t^\beta}(x_2(t)) = x_1(t)+ax_2(t),$$
$$\frac{\mathrm{d}^\gamma}{\mathrm{d}t^\gamma}(x_3(t)) = b+x_3(t)\big(x_1(t)-c\big).$$

Fractional-Orders
α, β, and γ

Numerical Solution

$$x_1(t_k) = -\big(x_2(t_{k-1})+x_3(t_{k-1})\big)\mathrm{h}^\alpha - \sum_{i=1}^{k} c_i^\alpha x_1(t_{k-i}),$$
$$x_2(t_k) = \big(x_1(t_k)+ax_2(t_{k-1})\big)\mathrm{h}^\beta - \sum_{i=1}^{k} c_i^\beta x_2(t_{k-i}),$$
$$x_3(t_k) = \big(b+x_3(t_{k-1})\big(x_1(t_k)-c\big)\big)\mathrm{h}^\gamma - \sum_{i=1}^{k} c_i^\gamma x_3(t_{k-i}).$$

$$\frac{\mathrm{d}^q}{\mathrm{d}t^q}(f(t)) \approx \frac{1}{h^q}\sum_{i=0}^{\frac{T}{h}} c_i^q f(t-jh), \quad 0 \le q \le 1, \tag{1}$$

where the coefficient values c_i^q are calculated as,

$$c_0^q = 1,\ c_i^q = \left(1 - \frac{q+1}{i}\right) c_{i-1}^q, \quad i = 1, 2, \ldots, \frac{T}{h}. \tag{2}$$

The model parameters used in this study are given as $a = 0.5$, $b = 0.2$, and $c = 10$. Further, the considered simulation parameters are $T = 200$ s and $h = 0.005$ s. This selection of parameters is based on the works reported in [9, 15]. Here, it highlights that the total number of samples in the numerical solution is $\frac{T}{h} = \frac{200}{0.005} =$ 40,000. The Rössler system's attractor with these parameters and different fractional orders and initial conditions is depicted in Fig. 2. The attractor in Fig. 2a for two different fractional orders (0.9, 0.9, 0.9) and (0.9, 0.85, 0.95) with initial condition [0.5 1.5 0.1] shows that the Rössler system's behavior is bounded. Further, it is to be noted that even though the behavior is bounded but is aperiodic. The attractors

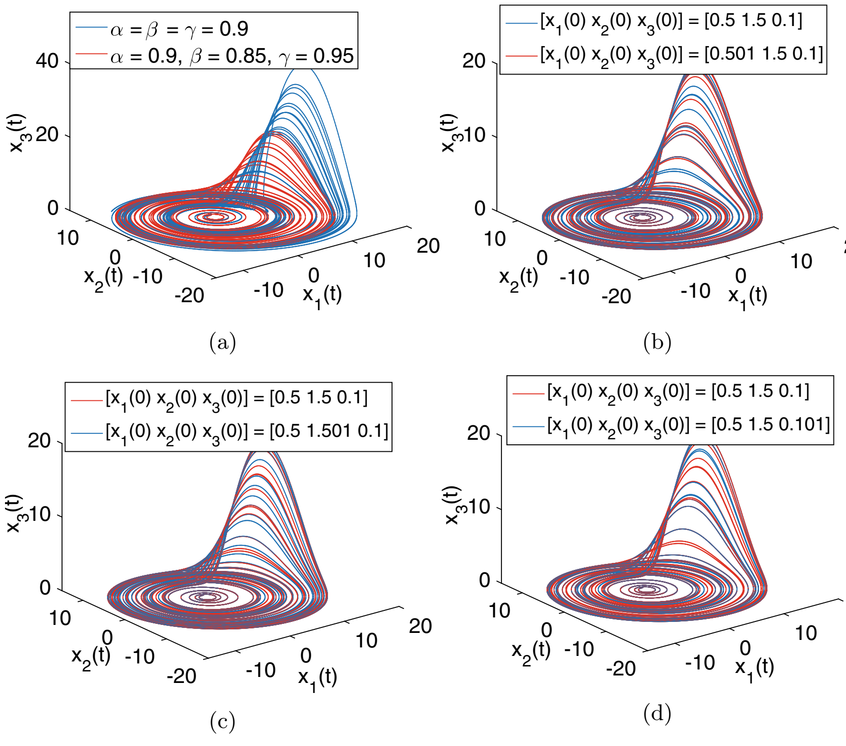

Fig. 2 Chaotic attractors of fractional-order Rössler system with different fractional orders and initial conditions

in Fig. 2b–d for fractional orders (0.9, 0.85, 0.95) highlight the system's sensitive behavior to the change in all the system states' initial conditions. Therefore, from Fig. 2, Rössler's behavior can be categorized as a chaotic system since it is bounded, aperiodic, and sensitive to initial conditions.

3 Development of Proposed Time Series Forecasting Model

3.1 Training Model

The inputs and outputs of the training model are the states and changes in values of the states, respectively. The required training data for the inputs x_1, x_2, and x_3 is obtained from the numerical solution (refer to Fig. 1). Further, the training data for the outputs Δx_1, Δx_2, and Δx_3 is computed from the corresponding states x_1, x_2, and x_3, as discussed underneath.

From the known values of states x_1, x_2, and x_3 and using the predicted change in states Δx_1, Δx_2, and Δx_3, the new state values are computed using the Adams–Bashforth two-step integration method as follows:

$$\begin{aligned}
x_1(t+h) &= x_1(t) + \left[\frac{1}{2}\left(3\Delta x_1(t) - \Delta x_1(t-h)\right)\right],\\
x_2(t+h) &= x_2(t) + \left[\frac{1}{2}\left(3\Delta x_2(t) - \Delta x_2(t-h)\right)\right],\\
x_3(t+h) &= x_3(t) + \left[\frac{1}{2}\left(3\Delta x_3(t) - \Delta x_3(t-h)\right)\right].
\end{aligned} \tag{3}$$

The expression for change in state variable values can be obtained by rearranging (3) as follows:

$$\begin{aligned}
\Delta x_1(t) &= \frac{2}{3}\left[x_1(t+h) - x_1(t) + \frac{1}{2}\Delta x_1(t-h)\right],\\
\Delta x_2(t) &= \frac{2}{3}\left[x_2(t+h) - x_2(t) + \frac{1}{2}\Delta x_2(t-h)\right],\\
\Delta x_3(t) &= \frac{2}{3}\left[x_3(t+h) - x_3(t) + \frac{1}{2}\Delta x_3(t-h)\right].
\end{aligned} \tag{4}$$

The shallow neural network model adopted in this paper with a single hidden layer is shown in Fig. 3. In the network model, the first and the last layers are the inputs (x_1, x_2, and x_3) and outputs (Δx_1, Δx_2, and Δx_3) with three nodes. The hidden layer node number "N_h" is computed from input layer node number "N_i" using the following formula [16]:

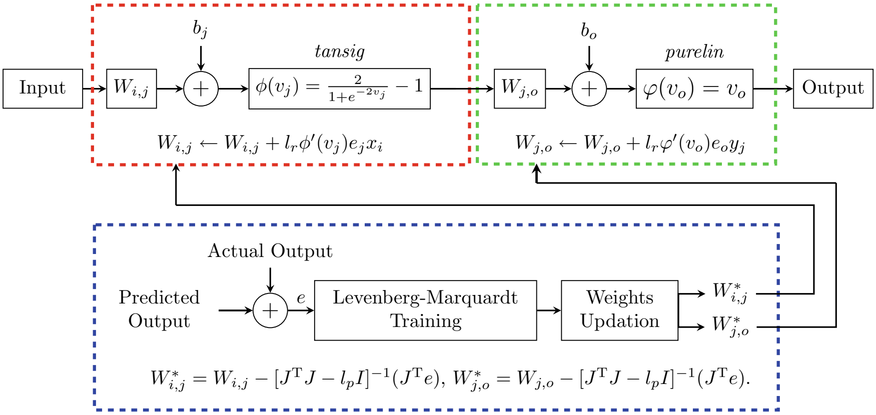

— Notations —

x_i	:	Current value of the input node i, $(i = 1, 2, \ldots, \mathrm{N_i})$
y_j	:	Current value of the hidden node j, $(j = 1, 2, \ldots, \mathrm{N_h})$
$W_{i,j}$	:	Weight between input node i and hidden node j
$W_{j,o}$	:	Weight between hidden node j and output node o
$W^*_{i,j}, W^*_{j,o}$	:	New weights calculated using training algorithm
$W_{j,o}$	:	Weight between hidden node j and output node o
e_j	:	Error at j^{th} hidden node
e_o	:	Error at o^{th} output node
v_j	:	Weighted sum of inputs nodes along with the bias, b_j
v_o	:	Weighted sum of hidden nodes along with the bias, b_o
$\phi(v_j)$	:	*tansig* activation function
$\varphi(v_o)$	:	*purelin* activation function
$\phi'(v_j)$	:	Derivative of *tansig* activation function
$\varphi'(v_o)$	:	Derivative of *purelin* activation function
l_r	:	Learning rate
l_p	:	Learning parameter
J	:	Jacobian matrix
I	:	Identity matrix
e	:	Cumulative error

Fig. 3 Adopted neural network model with a single hidden layer

$$N_{\mathrm{h}} = 4N_{\mathrm{i}}^2 + \frac{3}{N_{\mathrm{i}}^2} - 8. \tag{5}$$

The activation functions used at the hidden and output layers are, respectively, *tansig* and *purelin*. The mathematical formula of *tansig* and delta rule to update weight $W_{i,j}$ is shown in Fig. 3 red dotted box. Similarly, the mathematical formula of the *purelin* and delta rule to update weight $W_{j,o}$ is shown in Fig. 3 green dotted box. The nonlinear and linear combination of functions has been used for achieving an efficient training [17]. Further, the Levenberg–Marquardt's approach [18] has been employed to calculate the new weights $W^*_{i,j}$ and $W^*_{j,o}$ during the training, as shown in Fig. 3. Weight update rules using the algorithm for $W^*_{i,j}$ and $W^*_{j,o}$ are also shown in Fig. 3 (blue dotted box).

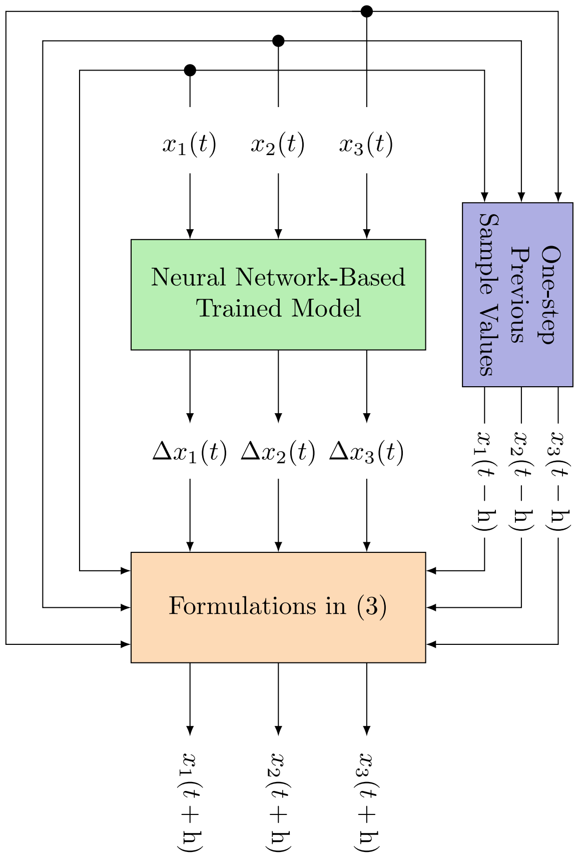

Fig. 4 Proposed modeling steps for the reconstruction of system states

3.2 Proposed Forecasting Model

The proposed forecasting model for the reconstruction of system states values is shown in Fig. 4. As shown in Fig. 4, the state's values can be obtained in two stages. First, at a time instant t, the change in states will be predicted using the trained neural network model given in Sect. 3.1. Then, with the use of these predicted values, the state's value at a time instant $t + h$ will be estimated using the Adams–Bashforth two-step equations shown in Fig. 4. Further, these estimated states will be used as the subsequent inputs for the trained network to estimate the change in states' values. Then, the states' values will be forecasted using the two-step equations. This process will be repeated for the entire out-of-sample testing phase.

3.3 Performance Metrics

In this work, the performance indices R^2 have been used that measure the model's predictive ability in fitting the actual data. Also, the mean square error (MSE) was used to measure the error between the predicted and actual values. The formulas for calculating the values of R^2 and MSE are given as,

$$R^2 = 1 - \frac{\sum_{i=1}^{n} (Y_{\mathrm{A},i} - Y_{\mathrm{P},i})^2}{\sum_{i=1}^{n} (Y_{\mathrm{A},i} - Y_{\mathrm{Avg}})^2}, \tag{6}$$

$$\mathrm{MSE} = \frac{1}{n} \sum_{i=1}^{n} (Y_{\mathrm{A},i} - Y_{\mathrm{P},i})^2. \tag{7}$$

In (6) and (7),

- "n" is number of samples in the dataset under consideration,
- Y_{A} is actual outputs,
- Y_{Avg} is the average values of Y_{A}, and
- Y_{P} is the predicted outputs.

4 Results and Analysis

4.1 Data Preparation

The input and output data for training and testing are depicted in Fig. 5a, b. The data x_1, x_2, and x_3 in Fig. 5a is obtained from the numerical solution of fractional-order model (refer to Fig. 1) with orders $\alpha = 0.9$, $\beta = 0.85$, and $\gamma = 0.95$ (refer to Fig. 2a). The output data Δx_1, Δx_2, and Δx_3 is obtained using (4). The data samples corresponding to the first 180 s are used for training the neural network model. And, the data samples pertaining to the remaining 20 s are used for testing the proposed forecasting model.

4.2 In-Sample Prediction Performance

The hidden layer node number is calculated as 39 using (5). The activation functions used are *tansig* and *purelin* for hidden and output layers. Levenberg–Marquardt's approach has been used for network training. The neural network model's training performance measured in R^2 and MSE values is, respectively, given as 0.9922 and

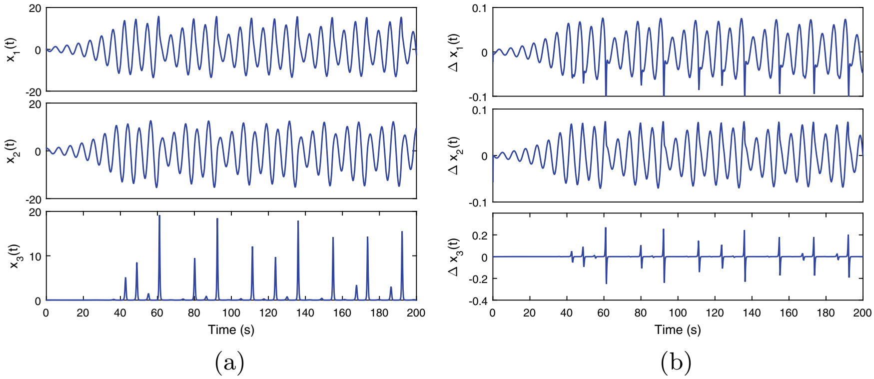

Fig. 5 Input and output data for training and testing of the neural network model

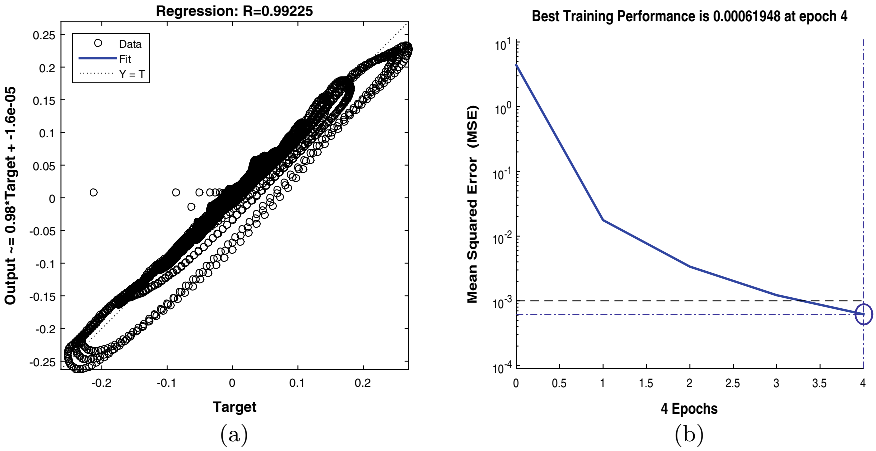

Fig. 6 Regression plot and MSE curve over the number of epochs during training of the neural network model

0.0006 (refer to Fig. 6a, b). Moreover, the prediction response of all the three outputs Δx_1, Δx_2, and Δx_3 is shown in Fig. 7a. The prediction response and the performance measure confirm the best forecasting ability for all three change in state variables.

4.3 *Out-of-Sample Prediction Performance*

In this section, the proposed forecasting model in Fig. 4 is evaluated for out-of-sample predictions during the testing period. The states x_1, x_2, and x_3 are forecasted from 180 to 200 s using the trained network model's predicted change in state values. The proposed forecasting model's performance for all three states is depicted in Fig. 7b.

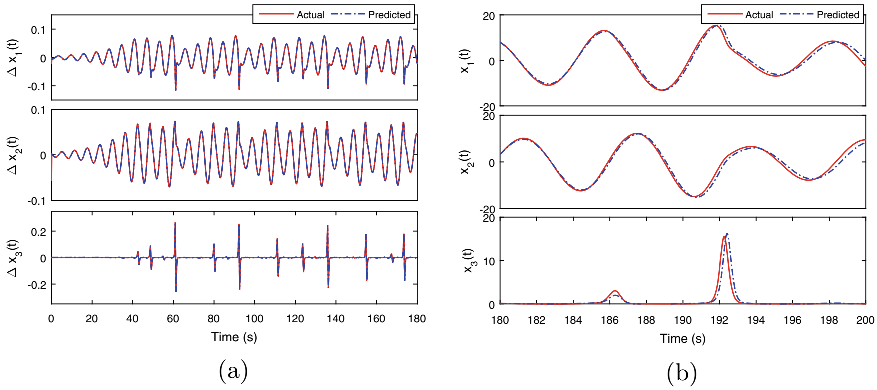

Fig. 7 Performance comparison during the training and testing of neural network model

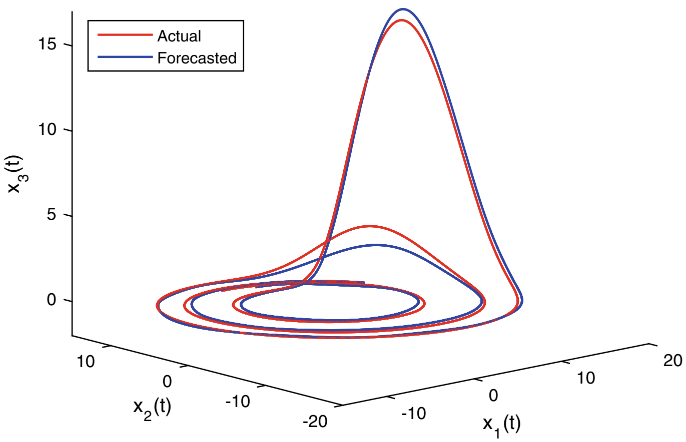

Fig. 8 Chaotic attractor of fractional Rössler system during proposed forecasting model's testing

The performance in Fig. 7b shows that the proposed forecasting model has the best tracking ability in estimating the state's values. Further, the obtained minimum MSE values of three states x_1, x_2, and x_3 are given as 1.1002, 1.2508, and 1.0394, which further confirm the proposed forecasting model's best performance.

The chaotic attractor during the testing period using the proposed forecasting model is shown in Fig. 8. It highlights that the spiral orbit in the $x_1 - x_2$ plane has a better tracking performance. Further, among the two rises and twists in the x_3 plane, the tallest twist has been forecasting much better than the shortest one. This effect can be more clearly seen in the x_3 plane from 190 to 195 s and amplitude range from 10 to 15 (refer to Fig. 8).

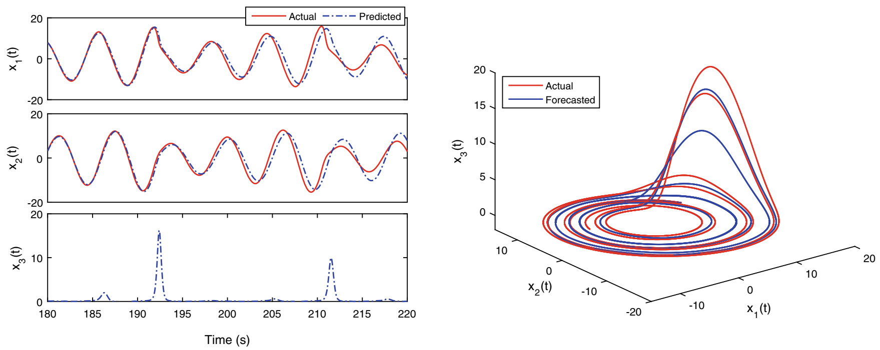

(a) (b)

Fig. 9 Performance comparison and attractor of fractional Rössler system using the proposed forecasting model for a more extended testing periods

Table 1 Numerical assessment of proposed forecasting model for the different horizons of the testing period

Testing period (s)	x_1	x_2	x_3
180–200	1.1002	1.2508	1.0394
180–210	4.8438	4.4022	0.7110
180–220	6.9008	6.0639	4.1039

The proposed forecasting model's performance comparison is further analyzed for an extra 20 s of the testing period (refer to Fig. 9a, b). The numerical assessment in terms of MSE for all three states during this testing period is shown in Table 1. The performance comparison shows that for more extended testing periods, the MSE values increases. Therefore, it is noted that the proposed approach's better performance is limited to a specific testing period only.

5 Conclusion

A novel forecasting strategy for estimating states' future values in a chaotic fractional Rössler system using the corresponding predicted change in state values is developed in this paper. A neural network-based prediction model was developed to estimate the change in state values and trained with the Levenberg–Marquardt approach. The network's training data has been obtained by solving the system's modeling equations. The prediction plots show the best tracking performance with R^2 and MSE values of 0.9922 and 0.0006, respectively. The forecasting model results confirm the best performance for all three system states x_1, x_2, and x_3 with MSE values 1.1002, 1.2508, and 1.0394, respectively. As a future part of the study, it is planned to improve the proposed forecasting model for a more extended testing period. Further, modeling changes would be made for hyperchaotic systems applications.

References

1. Ma H, Min F, Huang G, Dou Y (2019) Chaos and bifurcation behavior in a fundamental power system with electromagnetic disturbance and load disturbance. AIP Adv 9(4):045017
2. Petráš I (2011) Fractional-order nonlinear systems: modeling, analysis and simulation. Springer Science & Business Media
3. Banerjee S, Rondoni L (2015) Applications of chaos and nonlinear dynamics in science and engineering, vol 4. Springer
4. de Jesús Serrano-Pérez J, Fernández-Anaya G, Carrillo-Moreno S, Yu W (2021) New results for prediction of chaotic systems using deep recurrent neural networks. Neural Process Lett 1–18
5. Rajagopal K, Karthikeyan A (2016) Chaos suppression of fractional order Willamowski–Rössler chemical system and its synchronization using sliding mode control. Nonlinear Eng 5(3):177–183
6. Moysis L, Petavratzis E, Marwan M, Volos C, Nistazakis H, Ahmad S (2020) Analysis, synchronization, and robotic application of a modified hyperjerk chaotic system. Complexity 2020
7. Alstrom RB, Moreau S, Marzocca P, Bollt E (2018) Nonlinear characterization of a Rössler system under periodic closed-loop control via time-frequency and bispectral analysis. Mech Syst Signal Process 99:567–585
8. Buscarino A, Frasca M, Branciforte M, Fortuna L, Sprott JC (2017) Synchronization of two Rössler systems with switching coupling. Nonlinear Dyn 88(1):673–683
9. Bingi K, Ibrahim R, Karsiti MN, Hassan SM, Harindran VR (2020) Fractional-order systems and PID controllers. Springer
10. Bingi K, Prusty BR (2021) Chaotic time series prediction model for fractional-order duffing's oscillator. In: 2021 8th international conference on smart computing and communications (ICSCC). IEEE, pp 357–361
11. Wang Y, Sun K, He S, Wang H (2014) Dynamics of fractional-order sinusoidally forced simplified Lorenz system and its synchronization. Eur Phys J Spec Top 223(8):1591–1600
12. Wang H, He S, Sun K (2018) Complex dynamics of the fractional-order Rössler system and its tracking synchronization control. Complexity 2018
13. Zhang L (2017) Artificial neural networks model design of Lorenz chaotic system for EEG pattern recognition and prediction. In: 2017 IEEE life sciences conference (LSC). IEEE, pp 39–42
14. Wang R, Kalnay E, Balachandran B (2019) Neural machine-based forecasting of chaotic dynamics. Nonlinear Dyn 98(4):2903–2917
15. Bingi K, Ibrahim R, Karsiti MN, Hassan SM, Elamvazuthi I, Devan AM (2019) Design and analysis of fractional-order oscillators using scilab. In: 2019 IEEE student conference on research and development (SCOReD). IEEE, pp 311–316
16. Sheela KG, Deepa SN (2013) Review on methods to fix number of hidden neurons in neural networks. Math Probl Eng 2013
17. Abdullah S, Ismail M, Ahmed AN, Abdullah AM (2019) Forecasting particulate matter concentration using linear and non-linear approaches for air quality decision support. Atmosphere 10(11):667
18. Smith JS, Wu B, Wilamowski BM (2018) Neural network training with Levenberg–Marquardt and adaptable weight compression. IEEE Trans Neural Netw Learn Syst 30(2):580–587

Chapter 61
Application of Fractional-Order Signal Filtering Techniques for Dead-Time Process Plants

P. Arun Mozhi Devan, Fawnizu Azmadi Hussin, Rosdiazli Ibrahim, Kishore Bingi, and B Rajanarayan Prusty

Abstract In process control, signal filtering is a required field that needs continuous improvement for effective noise removal from the actual process signal. Processes implemented in noisy and uncertain environments are severely affected by external disturbance and stochastic noise. Properly feeding the necessary process signals like set-point, feedback, and control signals to the appropriate filters will significantly improve the process efficiency and increase the robustness of the control signals from the associated controller. This paper aims to design and implement an effective fractional-order set-point and noise filtering techniques for the processes with longer dead time. Simulation is carried out using the real-time process plants transfer functions to analyze the proposed filter performance. A comparison is made with the existing techniques to prove their effectiveness.

Keywords Dead-time processes · Fractional-order PPI · Noise filter · Process control · Set-point filter

P. Arun Mozhi Devan (✉) · F. A. Hussin · R. Ibrahim
Department of Electrical and Electronics Engineering, Universiti Teknologi PETRONAS, 32610 Seri Iskandar, Malaysia
e-mail: arundevaeie@gmail.com

F. A. Hussin
e-mail: fawnizu@utp.edu.my

R. Ibrahim
e-mail: rosdiazli@utp.edu.my

K. Bingi · B Rajanarayan Prusty
School of Electrical Engineering, Vellore Institute of Technology, Vellore, India
e-mail: bingi.kishore@ieee.org

B Rajanarayan Prusty
e-mail: b.r.prusty@ieee.org

G. Panda et al. (eds.), *Sustainable Energy and Technological Advancements*, Advances in Sustainability Science and Technology,
https://doi.org/10.1007/978-981-16-9033-4_61

1 Introduction

PID controllers family is still used in most process industries, though many advanced control strategies emerged. The reason behind this is due to the PID's easy tuning, industry convenient design and structure, fewer tunable controller parameters, prominently adopted history, etc. [1, 2]. While using them in the noisy and disturbance scenarios, they fail to produce effective control signals due to the aggregation of error in the control loop. In those conditions, the plant response will be more oscillatory and lead to the control valve stiction issues and even may lead to damage to the actuator as well [3]. For amending these problems, many variants like fractional-order PI, set-point weighted PI, fuzzy-PI, predictive PI (PPI), and nonlinear PI have been proposed by different researchers [4, 5].

Further developments for handling the dead-time processes were also carried out by combining the PID controllers family with the dead-time compensators (DTC-PI), model predictive controller-PI, fuzzy adaptive set-point weighted PI, fractional-order PPI (FOPPI), and internal model controller-PI [6, 7]. Even after these developments, a stand-alone controller to remove the noise and disturbance from the control and process signal is impossible because of the standard way of designing and developing the new controllers. Thus, combining external filters with the controllers in the closed-loop process is one of the fast, effective ways to deal with this issue.

In the related development, Hassan et al. successfully designed and implemented a stand-alone filtered PPI controller to handle the stochastic noise and external disturbance in the processes characterized by long dead time [8]. But, they faced sluggish response and destabilization of the closed-loop control system in the higher-order processes. To reduce the output oscillations (offset) and the peak overshoot, the introduction noise filter and set-point filter in the process feedback loop and after set-point signal give satisfactory results in the processes characterized by stochastic noise and external disturbances [9].

Different types of filters are available to remove and reduce the stochastic noise, external disturbance, and peak overshoot, but choosing them for the implementation depends on the end process. Initial research on set-point filtering is carried out by Vijayan and Panda for the two tank-level process [10]. Their initial design used more complex approaches to calculate the filter time constant from the process overshoot. To make the filters more robust and effective against the noise, the researchers introduced the process dynamics parameters like process gain in their design. Such improvement is proposed by Padhan et al. for the dead-time processes where the phase lag causes a more sluggish response [11]. While using the system dynamics in their design, they approximated them during the implementation in the actual process. A set-point filter designed mainly for the fractional control system is proposed by the researchers in [12]. Their successful design structure is limited to fractional-order systems alone, caused them not adaptable for regular processes. However, the researchers themselves agreed on the difficulty of their proposed approach in the industrial-scale implementation. In all the above techniques, calculation of the filter time constant used more assumption parameters which led to the frequent tuning of the filter, and its realization is more complex. Also, the effectiveness of minimizing the peak overshoot and reducing the noise is very minimal while comparing with the actual process.

Application of the fractional-order filters along with the Smith predictor is carried out by the researchers in [7]. Due to the uncertainties in the reference model, obtaining effective control is much reduced in this design. In contradiction with all the above methods, researchers in [1, 13–15] used the combination of conventional first- and second-order low pass filters with the associated controller in their design. Their results indicated the possibility of obtaining the effective noise and overshoot removed original process signal. Thus, it is not essentially higher-order filters needed to achieve good performance with the incorporated controller in the closed-loop processes. Hence, in this paper, the conventional first-order filter structure is utilized with a new method of calculating the filter time constant.

The remaining sections of the paper are organized as follows: A comprehensive discussion of the PI controllers family evolution, their structural design, and the set-point and noise filters strategies are presented in Sect. 2. Simulation results of the real-time processes transfer functions are given in Sect. 3 with detailed numerical and performance comparisons. Simulation outcomes, conclusions, and future directions of the current work are given in Sect. 4.

2 Methodology

In the initial part of the section, the selection of dead-time compensating controllers from the PI controller family is explained, followed by the designing and developing noise and set-point filters.

2.1 Controller Selection

The classical PI control signal $U(s)$ in a closed-loop system from reference $R(s)$ to the output $Y(s)$ can be given as:

$$U(s) = K_{\mathrm{p}}\left(1 + \frac{1}{T_i s}\right)E(s), \quad E(s) = R(s) - Y(s). \tag{1}$$

Introduction of the fractional-order integrator (λ) in the above control signal yields to the control action of the FOPI controller, which provides additional frequency-based controlling options. Thus, the FOPI control signal equation can be achieved as,

$$U(s) = K_{\mathrm{p}}\left(1 + \frac{1}{T_i s^{\lambda}}\right)E(s), \quad 0 < \lambda < 1. \tag{2}$$

Smith predictor design is the widely acclaimed dead-time compensator with industry-accepted and straightforward structure with no additional tuning requirements [16, 17]. To overcome the time delay effects in the processes, hybridizing of dead-time compensators (DTC's) with the conventional controller's structure is essential [18]. Such a combination of the Smith predictor and PI controller yields the PPI controller. The control action of the PPI control signal is given as,

$$U(s) = K_{\mathrm{p}}\left(1 + \frac{1}{T_i s}\right)E(s) - \frac{1}{T_i s}(1 - \mathrm{e}^{-sL_{\mathrm{p}}})U(s). \tag{3}$$

For achieving better frequency-domain controls, robust performance against the dead time, peak overshoot, and external disturbance, designing of FOPPI controller from PPI by the fractional-order integrator is adopted. The FOPPI control signal is given as,

$$U(s) = K_{\mathrm{p}}\left(1 + \frac{1}{T_i s^{\lambda}}\right)E(s) - \frac{1}{T_i s^{\lambda}}(1 - \mathrm{e}^{-sL_{\mathrm{p}}})U(s), \quad 0 < \lambda < 1. \tag{4}$$

The closed-loop block diagram of the dead-time process plant with the FOPPI controller in (4) is shown in Fig. 1. The selection of the FOPPI controller is based on our earlier work reported in [19].

2.2 Filtering

Processes facing the undesired stochastic noises will always produce an oscillatory response, which is due to the higher error present in the processed signal fed to the controller [20]. This, in turn, affects the final control elements of the control

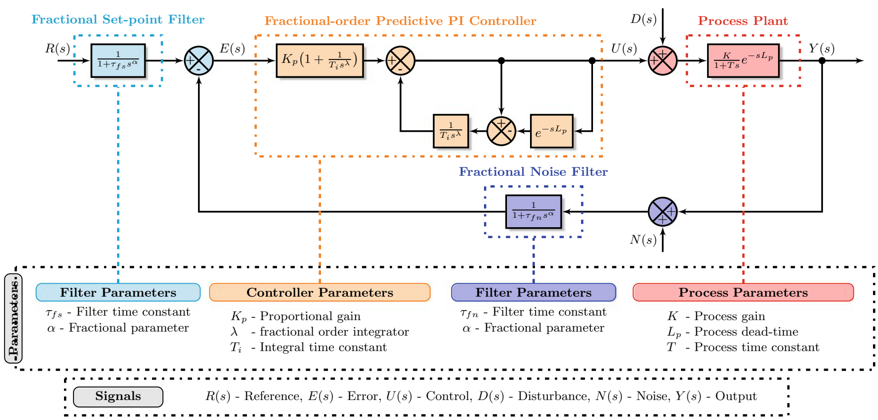

Fig. 1 Closed-loop block diagram of the dead-time process plant with the FOPPI controller and external filters

valve and causes the closed loop to become unstable, which even further escalated to the worst catastrophe due to the process dead time [21]. These issues can be settled down by placing the filters in the appropriate places on the closed-loop process. Thus, placement of set-point and noise filters with time constants τ_{fs} and τ_{fn} in the closed-loop is shown in Fig. 1. The process input signal $R(s)$ is sent to the controller only after passing through the set-point filter F_s, which performs the function of isolating the variations in the load disturbances from the actual input signal $R(s)$. This reduces the peak overshoot oscillations and high-frequency noise changes, which ultimately yields faster settling and rise time.

On the other hand, the noise filter performs the function of nullifying the external disturbance and noise signal from the process feedback signal $Y(s)$ using the roll-off. This roll-off technique is proved to be an effective noise reduction method while operating with the PI and PID controllers [22]. Combining both filters will result in a more significant improvement error signal fed to the controller $G_c(s)$, which produces the noise-free control signal $U(s)$ for effectively controlling the process.

The literature works show that adequate performance of the process can also be achieved with lower-order filters. Therefore, the classical first-order filter is combined with the FOPPI controller for the simulation analysis in this paper. Here, the structure of the filter remains unchanged, but the method of finding the filter time constant (τ_f) is changed by utilizing the system dynamics of the process under consideration. The transfer function of the filter is given as,

$$F(s) = \frac{1}{1 + \tau_f s^{\alpha}}, \tag{5}$$

where τ_f is filter time constant and α is the fractional integrator.

As mentioned earlier, the proposed method for calculating the τ_f includes both process gain (K) and the process model dead time (L_p). Thus, the filter time constant can be calculated as: $\tau_f = \frac{K}{L_p}$. Since the external disturbances and noises arise from the environment where the controller is interfaced with the real-time process, this implementation idea can remove the noise with maximum efficiency since the filter possesses all the system dynamics. For demonstrating the capability of the proposed method, a comparison study is made with the integer-order filter structure used in [19]. During the simulation, constant values were used for both set-point and noise filters and the same fractional integrator value from the FOPPI controller design.

3 Results and Discussion

In this section, a detailed analysis of the real-time processes simulation is discussed with the different filters incorporated over the FOPPI controller.

3.1 Process Model Selection

In this article, the first-order plus dead-time (FOPDT) process model of the process plant as reported in [23] and the real-time second-order plus dead-time (SOPDT) process model reported in [10] are considered for the analysis. The transfer functions of the systems are given as follows:

$$G_{\mathrm{p}1}(s) = \frac{K}{1 + Ts}\mathrm{e}^{-sL_{\mathrm{p}}} = \frac{0.866}{1 + 1.365s}\mathrm{e}^{-s}, \tag{6}$$

$$G_{\mathrm{p}2}(s) = \frac{K}{1 + 2T\zeta + T^2s^2}\mathrm{e}^{-sL_{\mathrm{p}}} = \frac{2}{1 + 15s + 50s^2}\mathrm{e}^{-5s}. \tag{7}$$

During the simulation analysis, a white noise signal with a magnitude of 0.01 is injected in the process feedback loop to mimic the real-time scenario of the industrial processes. The profile of the white noise signal used is shown in Fig. 2. For all the considered process plants, a 30% disturbance is injected at 500 s of the control signal to analyze the disturbance rejection of the FOPPI controller. Since the FOPPI controller is designed empirically based on the FOPDT system, the first-order process controller parameters are obtained directly (refer to [19]). However, for the

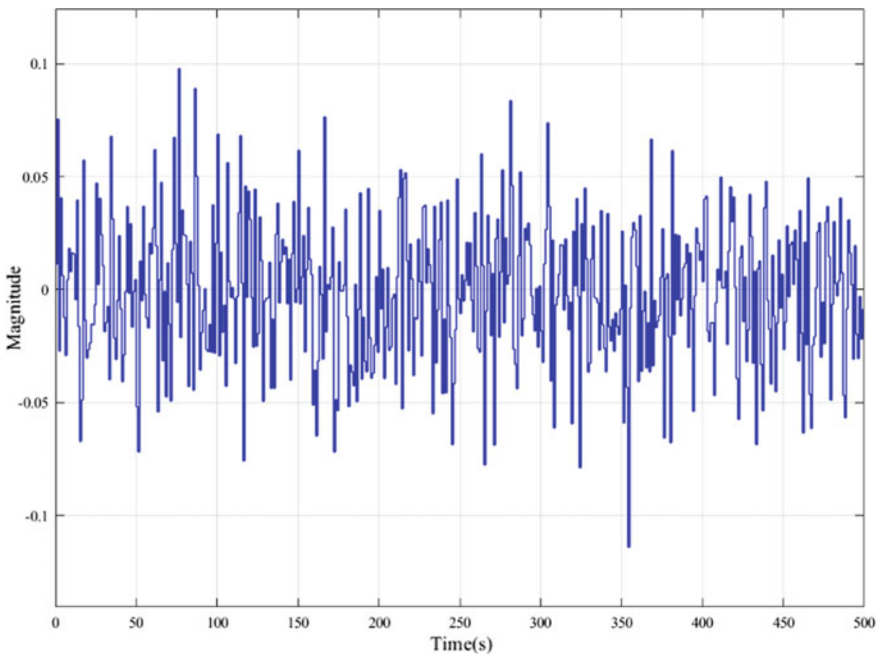

Fig. 2 White noise signal used for the simulation

second-order process, the controller parameters are obtained using the MATLAB-SISO toolbox.

Thus, the optimized controller parameters for the FOPDT model are $K_p = 1.15$ and $K_i = 0.84$. Further, the parameters of SOPDT are $K_p = 0.789$ and $K_i = 0.101$. For both the plants, the fractional integrator is $\lambda = 0.98$. For implementing the fractional integrator, the Oustaloup approximation has been used as reported in [19]. For all fractional filters, the α value is also kept the same as 0.98.

3.2 FOPDT Process Model

In this section, the industrial process model shown in (6) is used for the performance evaluation of the filters and the FOPPI controller. The comparative analysis is carried out in terms of rise time (t_r), settling time (t_s), and peak overshoot (%OS) that are given in Table 1.

The performance analysis of the integer-order and fractional-order set-point filters is shown in Fig. 3, and its detailed numerical analysis is given in Table 1. From the results shown in Table 1, the proposed fractional set-point filter initially lagged in rising time and settling time (t_{s1}) before disturbance with 4.9149 s and 496.0599 s, respectively. But, it produced the most negligible overshoot value of 4.7103% than the integer-order set-point filter (5.0512%) and the actual process (7.5712%). Thus, the proposed filter effectively reduces the initial load disturbance, minimizing the overshoot and making the process settle faster. This performance led to the proposed set-point filter settling faster at 995.2130 s, followed by integer order with 996.3493 s and the actual process 997.3462 s. Furthermore, the dotted sections of A and B are enhanced and shown in the exact figure, which contains the detailed view of process output and control signal.

Table 1 Numerical analysis of FOPDT model with various filters in the presence of external noise

Filter type	Parameter	t_r	t_{s1}	t_{s2}	%OS
	No filter	4.2074	496.0082	997.3462	7.5712
Set-point filter	Integer order	4.4499	494.1031	996.3493	5.0152
	Fractional order	4.9149	496.0599	995.2130	4.7103
Noise filter	Integer order	2.0851	496.6286	996.6322	12.7284
	Fractional order	2.1384	494.9413	994.3601	9.5354
Noise and set-point filter	Integer order	2.6647	496.6168	997.6315	8.0742
	Fractional order	2.5315	494.8479	996.7110	6.0703

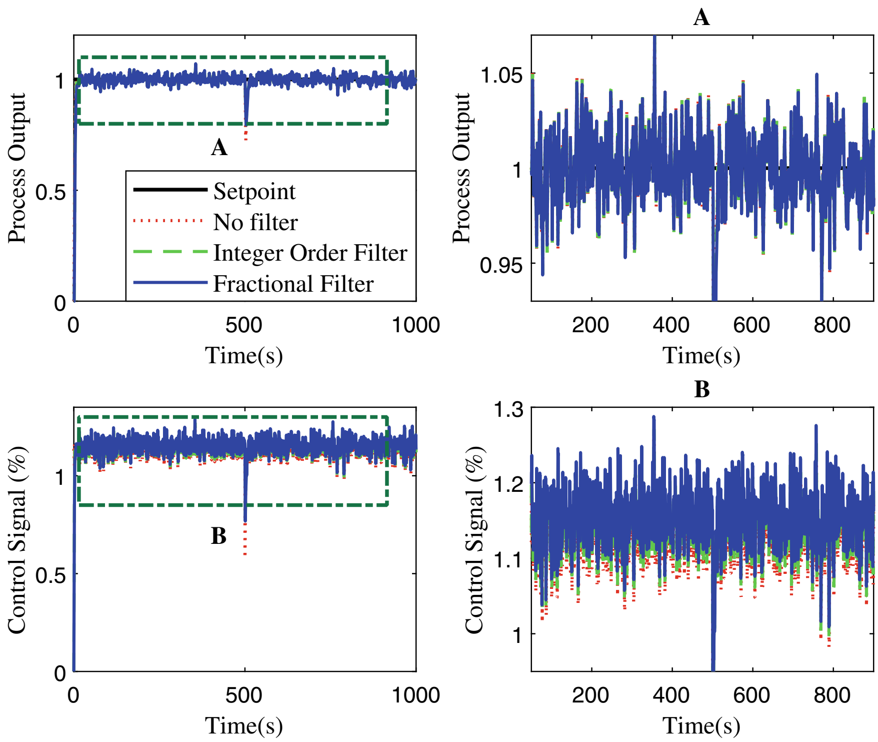

Fig. 3 Performance comparison of FOPDT for disturbance rejection with various set-point filters

The integer-order and fractional-order noise filters performance comparison is shown in Fig. 4 with zoomed-in regions of A and B. Because of the improved noise-free signal from the feedback loop, both the filters produced a faster rise time of 2.1384 s and 2.0851 s for fractional-order and integer-order noise filters, respectively. This situation helped the filters settle faster than the actual process at 997.6322 s for integer order and 994.3601 s for fractional-order noise filter. In contradiction with the set-point filter, the stand-alone noise filter fails to reduce the load variations, which caused the overshoot to increase than the actual process at 12.7284 and 9.5354% for integer order and fractional order.

The combined set-point and noise filter simulation results in the closed-loop are illustrated in Fig. 5. From the numerical analysis shown in Table 1, the proposed fractional filter combination had a faster rise time than its comparators with 2.5315 s followed by an integer-order combination (2.6647 s) and the actual process (4.2074 s). This more rapid rise time helped the proposed fractional filter combination to settle faster than all the filters before and after the disturbance. The integer-order filter combination settled slightly slower than the actual process combination at 997.6315 s due to the lack of additional frequency-based tuning parameters. In terms of overshoot

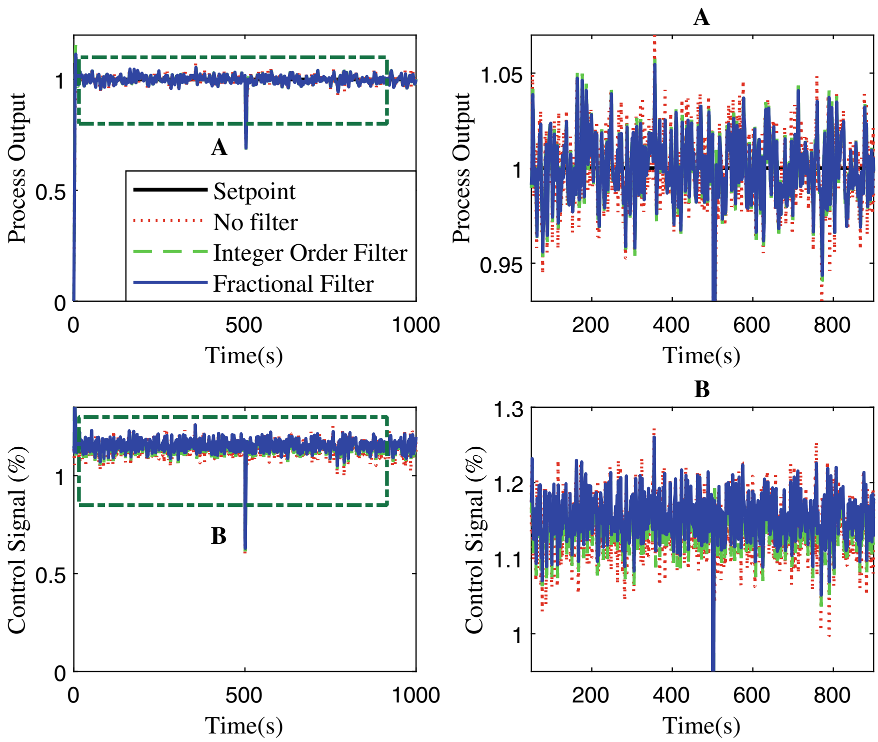

Fig. 4 Performance comparison of FOPDT for disturbance rejection with various noise filters

performance, the proposed filtering combination takes the lead of minimizing them with the value of 6.0703%, followed by an integer-order combination with 8.0742%.

3.3 *SOPDT Process Model*

Similarly, the simulation results of the process plant given in (7) are discussed in this section. The comparative results of second-order system with various set-point filters in the presence of the external noise are shown in Fig. 6, and its corresponding numerical analysis is tabulated in Table 2.

The numerical analysis has shown the same trend that happened in the FOPDT model. There is an initial slowdown in the rise time for the proposed set-point filter with 10.6541 s. But, this does not affect the capability of the proposed fractional filter to settle faster at 364.4879 s followed by integer-order filter (366.2489 s) and actual process (368.3541 s) during the initial period. After the disturbance rejection also, the proposed filter topped with a faster settling time (683.9720 s) and significantly

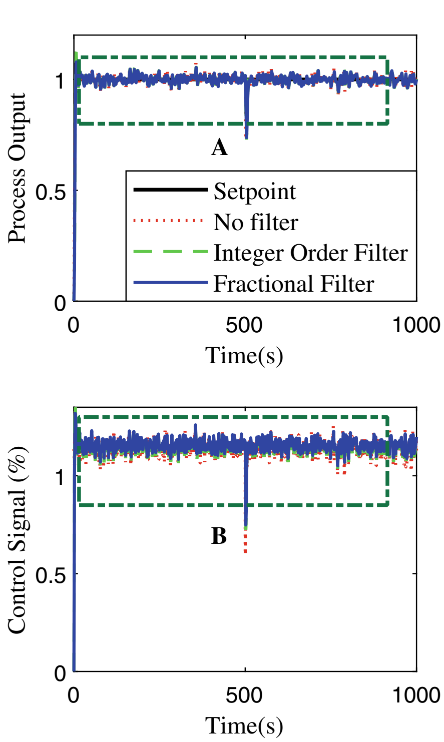

Fig. 5 Performance comparison of FOPDT for disturbance rejection with combined set-point and noise filters

Table 2 Numerical analysis of SOPDT model with various filters in the presence of external noise

Filter type	Parameter	t_r	t_{s1}	t_{s2}	%OS
	No filter	9.8135	368.3541	790.4898	37.5295
Set-point filter	Integer order	9.8452	366.2489	790.3173	35.3543
	Fractional order	10.6541	364.4879	683.9720	31.6825
Noise filter	Integer order	9.6974	366.4210	752.8507	43.4283
	Fractional order	10.4788	364.5488	684.5364	38.0682
Noise and set-point filter	Integer order	9.7239	366.4574	752.9469	37.3058
	Fractional order	10.5136	364.6032	683.5698	35.1010

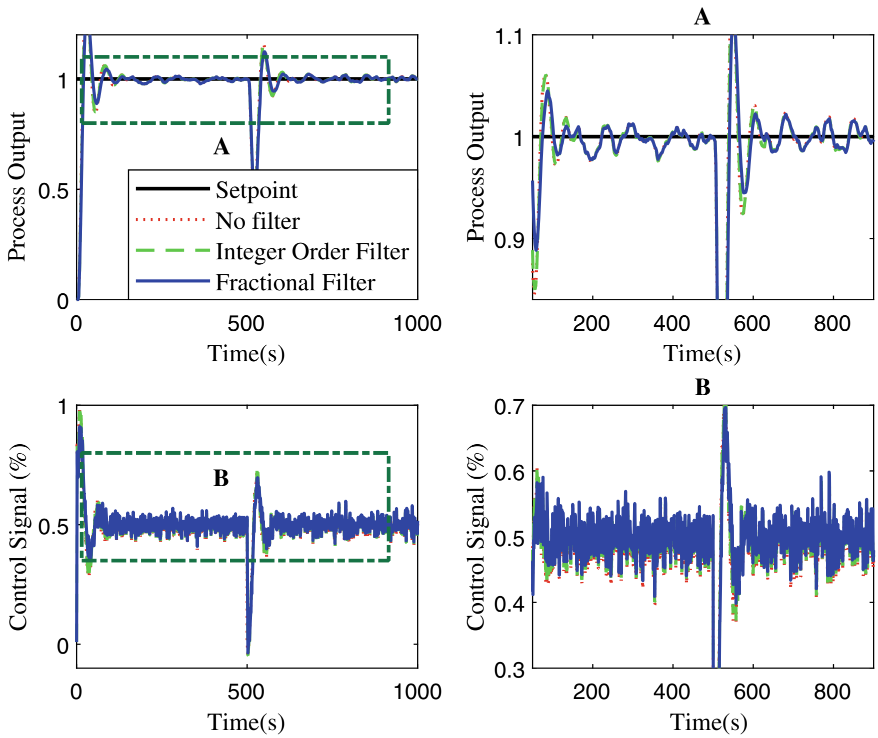

Fig. 6 Performance comparison of SOPDT for disturbance rejection with various set-point filters

less peak overshoot (31.6825%) than others. Different noise filter analysis of the second-order system is given in Fig. 7.

On the contrary with the FOPDT model, both noise filters used in the SOPDT system settled faster than the actual process before and after the disturbance. But, the peak overshoot problem is continued in this system as well. The integer-order noise filter produced the maximum peak overshoot value of 43.4283%, which is 5.8988% and 5.3601% higher than the actual process and fractional-noise filter, respectively. While noticing the performance of the combined filters shown in Fig. 8, the proposed filter settled faster during both instances. The proposed filter is settled at 683.5698 s, which is 106.92 s faster than the actual process and 69.3771 s faster than the integer-order filters. In all the results and discussion figures, it is worth mentioning that the proposed fractional-order filters produced a smooth control signal than all the different combination filters and the actual process.

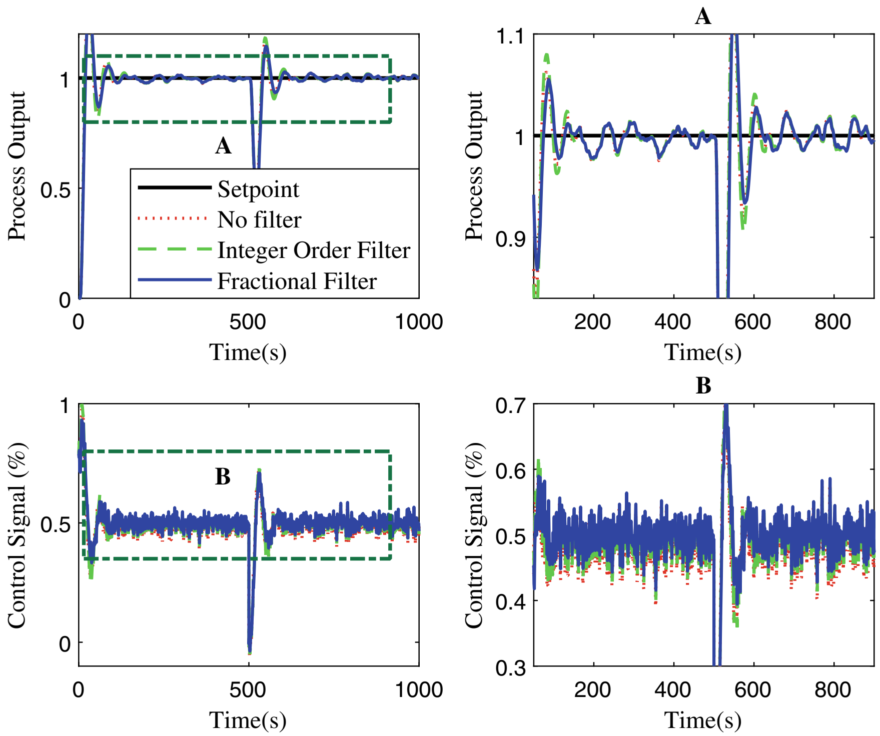

Fig. 7 Performance comparison of SOPDT for disturbance rejection with various noise filters

4 Conclusion

This article proposed a new fractional-order filter design for both the set-point and noise filter under the combination of FOPPI controller for the processes with longer dead time. The performance analysis has shown that the proposed filters are more effective than the conventional integer-order filter without any filters in overshoot minimization and faster settling. This new proposed filter design incorporates the essential system dynamics in its structure, which is advantageous for the new design widely accepted in industrial processes. In the future, the proposed method will be evaluated over the real-time actual process plant along with the optimized parameters using any optimization techniques.

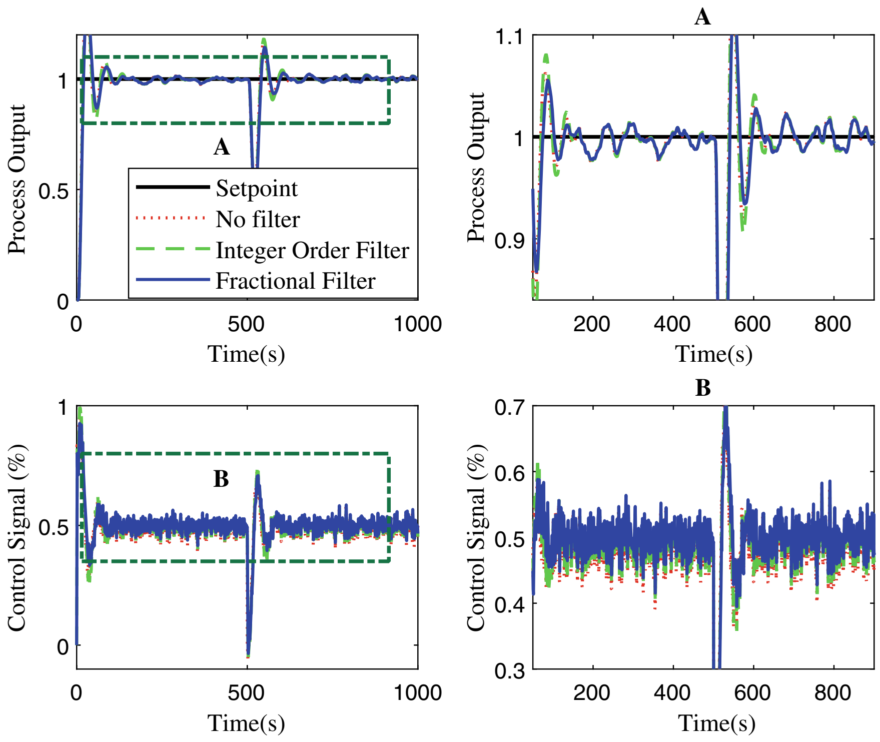

Fig. 8 Performance comparison of SOPDT for disturbance rejection with combined set-point and noise filters

Acknowledgements YUTP 015LC0-045 supported this work, a fundamental research grant from Yayasan Universiti Teknologi PETRONAS.

References

1. Hägglund T (2013) A unified discussion on signal filtering in PID control. Control Eng Pract 21(8):994–1006
2. Devan P, Hussin FA, Ibrahim R, Bingi K, Khanday FA (2021) A survey on the application of wirelesshart for industrial process monitoring and control. Sensors 21(15):4951
3. di Capaci RB, Scali C (2018) Review and comparison of techniques of analysis of valve stiction: from modeling to smart diagnosis. Chem Eng Res Des 130:230–265
4. Anitha T, Gopu G, Nagarajapandian M, Devan PAM (2019) Hybrid fuzzy PID controller for pressure process control application. In: 2019 IEEE student conference on research and development (SCOReD). IEEE, pp 129–133
5. Bingi K, Ibrahim R, Karsiti MN, Hassan SM, Harindran VR (2019) Real-time control of pressure plant using 2DOF fractional-order PID controller. Arab J Sci Eng 44(3):2091–2102

6. Devan PAM, Hussin FA, Ibrahim R, Bingi K, Abdulrab H (2020) Fractional-order predictive PI controller for process plants with deadtime. In: 2020 IEEE 8th R10 humanitarian technology conference (R10-HTC). IEEE, pp 1–6
7. Bettayeb M, Mansouri R, Al-Saggaf U, Mehedi IM (2017) Smith predictor based fractional-order-filter PID controllers design for long time delay systems. Asian J Control 19(2):587–598
8. Hassan SM, Ibrahim R, Saad N, Bingi K, Asirvadam VS (2020) Filtered predictive Pi controller for wirelesshart networked systems. In: Hybrid PID based predictive control strategies for WirelessHART networked control systems. Springer, pp 27–58
9. Medarametla PK (2018) Novel proportional-integral-derivative controller with second order filter for integrating processes. Asia-Pac J Chem Eng 13(3):e2195
10. Vijayan V, Panda RC (2012) Design of a simple setpoint filter for minimizing overshoot for low order processes. ISA Trans 51(2):271–276
11. Padhan DG, Majhi S (2013) Enhanced cascade control for a class of integrating processes with time delay. ISA Trans 52(1):45–55
12. Padula F, Visioli A (2016) Set-point filter design for a two-degree-of-freedom fractional control system. IEEE/CAA J Autom Sin 3(4):451–462
13. Normey-Rico JE, Camacho EF (2008) Dead-time compensators: a survey. Control Eng Pract 16(4):407–428
14. Bingi K, Devan PAM, Prusty BR (2021) Design and analysis of fractional filters with complex orders. In: 2020 3rd international conference on energy, power and environment: towards clean energy technologies. IEEE, pp 1–6
15. Huba M, Bisták P, Huba T, Vrančič D (2017) Comparing filtered PID and Smith predictor control of a thermal plant. In: 2017 19th international conference on electrical drives and power electronics (EDPE). IEEE, pp 324–329
16. Safaei M, Tavakoli S (2018) Smith predictor based fractional-order control design for time-delay integer-order systems. Int J Dyn Control 6(1):179–187
17. Azarmi R, Sedigh AK, Tavakoli-Kakhki M, Fatehi A (2015) Design and implementation of Smith predictor based fractional order PID controller on MIMO flow-level plant. In: 2015 23rd Iranian conference on electrical engineering. IEEE, pp 858–863
18. Pashaei S, Bagheri P (2020) Parallel cascade control of dead time processes via fractional order controllers based on Smith predictor. ISA Trans 98:186–197
19. Devan PAM, Hussin FAB, Ibrahim R, Bingi K, Abdulrab HQ (2020) Fractional-order predictive pi controller for dead-time processes with set-point and noise filtering. IEEE Access 8:183759–183773
20. Ediga CG, Ambati SR (2021) Measurement noise filter design for unstable time delay processes in closed loop control. Int J Dyn Control 1–24
21. Huba M, Bistak P, Vrancic D, Zakova K (2021) Dead-time compensation for the first-order dead-time processes: towards a broader overview. Mathematics 9(13):1519
22. Soltesz K, Grimholt C, Skogestad S (2017) Simultaneous design of proportional-integral-derivative controller and measurement filter by optimisation. IET Control Theory Appl 11(3):341–348
23. Bingi K, Ibrahim R, Karsiti MN, Hassan SM (2018) Fractional order set-point weighted PID controller for pH neutralization process using accelerated PSO algorithm. Arab J Sci Eng 43(6):2687–2701

Chapter 62
A Variant of Rossler Type-IV Chaotic System with a Line of Equilibria and Coexisting Attractors

Rishabh Jaiswal, Himanshu Raj, Priye Ranjan Kumar, and Piyush Pratap Singh

Abstract This paper avows an asymmetric four-dimensional chaotic system with infinite equilibria (a line of equilibria). The proposed chaotic system is modified from Rossler Type-IV system dynamics by adding a fourth equation using negative feedback control and by assuming first state variable as a function of sinusoidal signal to exhibit unique behaviours like chaotic 2-torus, 2-torus quasi-periodic behaviours and coexisting attractors to that of Rossler Type-IV system. Simulation is carried out in MATLAB environment, and simulation results validate numerical analyses and exclaim that objectives are accomplished successfully. The presented study is helpful towards sustainable application and development of physical systems such as power system, smart grid and communication security.

Keywords Asymmetric chaotic system · Bifurcation · Chaos · Coexisting attractors · Line of equilibria · Lyapunov spectrum · Lyapunov dimension · Nonlinear dynamics

1 Introduction

Chaos phenomena have significantly been identified in nature and employed in various natural and physical systems and still open for researchers to explore the chaotic behaviour and its application in different field of science and engineering, Mishra et al. [8], Esteban et al. [3], Rajagopal et al. [17], Mobayen et al. [9]. Owing to this fact, investigation on new chaotic systems has been floated in the field of nonlinear dynamics and complex systems by Kumar and Singh [7], Gupta et al. [5], Das et al. [2]. Various new and modified chaotic systems have been reported in the literature and become the primary motive of this work.

Sprott [31] suggested some standards to be followed in the designing a new chaotic systems like a system should reveal the unsolved problem, unique behaviours and

R. Jaiswal · H. Raj · P. R. Kumar · P. P. Singh (✉)
Electrical Engineering Department, National Institute of Technology Meghalaya, Shillong, Meghalaya 793003, India
e-mail: piyushpratapsingh@gmail.com

G. Panda et al. (eds.), *Sustainable Energy and Technological Advancements*, Advances in Sustainability Science and Technology,
https://doi.org/10.1007/978-981-16-9033-4_62

it should be simpler than the existing systems. Now, researchers are following the guidelines prescribed by Sprott [31], and pethora of new chaotic systems have been reported in the literature. The literature may be classified based on chaotic systems without equilibrium by Singh and Roy [27], with finite equilibria by Singh and Roy [22, 24], Singh et al. [28], Sugandha and Singh [32], Singh [26, 29] and infinite equilibria. It is well accepted that hidden attractors occur in the class of chaotic systems without equilibrium. The well-known and developed chaotic systems like Lorenz, Rossler, Chen, Lu fall under the class of finite equilibria and coexistence of stable, unstable, and stable-unstable attractors arises in the chaotic system with infinite equilibria (line, curve, plane, surface of equilibria, etc.) by Pham et al. [10], Singh and Roy [25]. Chaotic system and its synchronisation is helpful in different applications like secure communication [20, 30], El-Nino Southern Oscillation (ENSO) [19, 33] etc. Chaos behaviour is harmful in sustainable operation of power grid which leads unwanted and serious blackout phenomenon or creates stability problem. In view of this, the chaos control is helpful in the sustainable development of power grid or power systems as reported by Das et al. [2], Gupta et al. [5], Kumar and Singh [7].

Recently, researcher have investigated few chaotic systems with line equilibria and are summarised in Table 1, based on its order of dynamics, number of parameters, total numbers of terms and nonlinear terms used to model the dynamics in addition with quantitative measures like first Lyapunov exponent (LE), Lyapunov dimension and obtained behaviours. It may be observed that some countable 3D, 4D and 5D chaotic systems have been reported where most of chaotic systems are symmetric and very few are asymmetric 4D chaotic systems. An asymmetric chaotic system has good random or chaotic behaviour than symmetric chaotic system as suggested by Qi et al. [16]. Thus, to develop a new or modified 4D chaotic system from existing chaotic system with infinite equilibria with unique properties is still crucial and challenging in the field of nonlinear dynamics.

Motivated with above critical issues, in this paper, a 4D chaotic system is explored form the 3D Rossler Type-IV chaotic system and has infinite equilibria and coexisting behaviours which are not available in original 3D Rossler Type-IV chaotic system. The following points summarise the contribution and novelty of this work.

1. An asymmetric 4D chaotic system has unique chaotic 2-torus and 2-torus quasi-periodic behaviours which are rare in the literature.
2. The 4D chaotic system has only two nonlinear terms, total nine terms and three parameters. It is simpler than other available 4D chaotic systems except [23] (refer Table 1).
3. The asymmetric 4D chaotic system has large value of Lyapunov dimension 3.1178 than the other available 4D chaotic systems (refer Table 1).

Further, the paper is organised as follows. The dynamics of proposed 4D chaotic system is introduced in Sect. 2 followed by analysis of complex dynamic behaviour that is discussed in Sect. 3. Finally, conclusions and future scope are listed in Sect. 4.

Table 1 Summary of reported 3D, 4D and 5D chaotic systems with line of equilibria based on different attributes and behaviours

Chaotic system reported by	No. of parameters	Total no. of terms	Nonlinear terms	First LE	Lyapunov dimension	Behaviours
[12]: 3D	2	6	3	0.0363	2.1303	Chaotic
[12]: 3D	2	6	3	0.1082	2.0969	Chaotic and coexistence
[12]: 3D	3	6	3	0.0584	2.0747	Chaotic and coexistence
[28]: 3D	4	8	2	2.9733		Chaotic
[15]: 3D	1	6	4	0.0727	2.2329	Chaotic
[6]: 3D	2	7	4	0.0421		Chaotic and coexistence
[3]: 3D	1	7	4	0.1120		Chaotic
[14]: 3D	1	6	4	0.1482		Chaotic
[14]: 3D	3	8	3	0.2231		Chaotic and coexistence
[21]: 3D	3	6	4	0.0073	2.869	Chaotic
[13]: 3D	2	6	3	0.1204		Chaotic and coexistence
[27]: 3D	2	6	1	0.0777	2.1148	Chaotic
[34]: 3D	3	6	4	0.2010		Chaotic: 2D lattice
[26]: 3D	3	7	2	2.9733		Wide band chaotic
[11]: 4D	4	11	4	0.1517		Chaotic and coexistence
[23]: 4D	3	8	1	0.110	3.020	Chaotic and coexistence
[14]: 4D	4	8	3	0.2148		Chaotic
[4]: 4D	5	9	7	0.1892		Chaotic
[34]: 4D	3	7	5	0.100		Chaotic: 2D lattice
[24]: 4D	8	13	3	5.5896	2.160	Chaotic and coexistence
[1]: 5D	4	14	3	0.0610		Hyperchaotic
This work: 4D	**3**	**9**	**2**	**0.0736**	**3.1178**	**Chaotic 2-torus 2-torus quasi-periodic and their coexistence**

2 Introduction to 4D Chaotic System

The proposed 4D chaotic system is explored from the prototypes of 3D chaotic systems reported by German biochemist Rossler [18] where the prototype has only two equilibrium points. The proposed 4D chaotic system is modified by using negative feedback control which is added as the fourth equation in the dynamics, and the first variable is the function of sine. The dynamics of modified system is given as:

$$\begin{cases} \dot{x}_1 = -x_2 - x_3 \\ \dot{x}_2 = \sin(x_1) - x_4 \\ \dot{x}_3 = ax_2(1 - x_2) - bx_3 \\ \dot{x}_4 = c(x_2 + x_3) \end{cases} \tag{1}$$

where a, b, c are the positive parameters and x_1, x_2, x_3, x_4 are state variables of the system (1). The system has chaotic behaviour for the value of parameters as $a = 0.55$, $b = 0.55$ and $c = 0.1$. Lyapunov exponents of system (1) are calculated as $L_1 = 0.0736$, $L_2 = 0.0001 \approx 0$, $L_3 = -0.0002 \approx 0$ and $L_4 = -0.6242$. The initial condition is considered as $[x_1(0), x_2(0), x_3(0), x_4(0)] = [0.123, 0.123, 0.123, 0.1]$. The phase plane behaviours and corresponding time series plots of the state variables are shown in Figs. 1 and 2, respectively, and show chaotic nature of 4D system.

The equilibrium points of 4D chaotic system (1) are found using $\dot{x}_1 = 0$, $\dot{x}_2 = 0$, $\dot{x}_3 = 0$ and $\dot{x}_4 = 0$ and calculated as

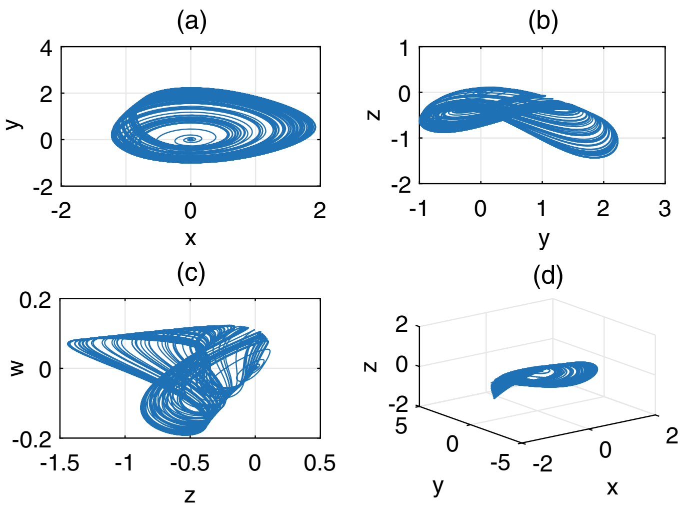

Fig. 1 Phase plane behaviours of asymmetric chaotic system

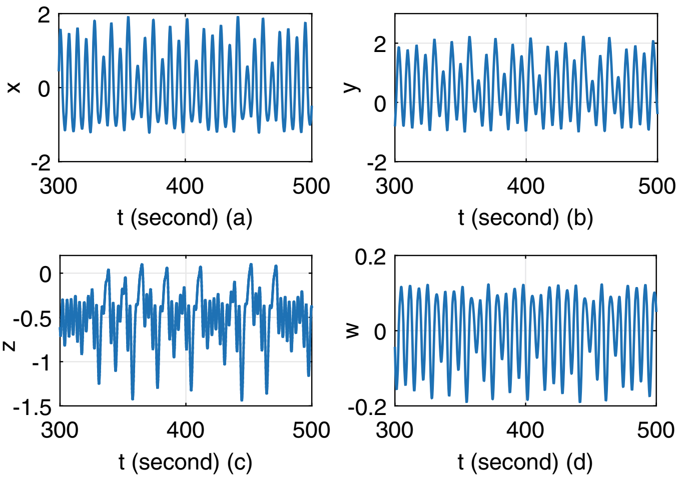

Fig. 2 Asymmetric time series behaviour of 4D chaotic system

$$E = \left[x_1^*, 1 + \frac{b}{a}, -\left(1 + \frac{b}{a}\right), \sin(x_1^*) \right].$$

Thus, the 4D chaotic system has a line of equilibria. In order to calculate eigenvalues and achieve stability nature, the generalised Jacobian matrix of dynamics (1) is obtained as:

$$J_{\mathrm{E}} = \begin{bmatrix} 0 & -1 & -1 & 0 \\ \cos(x_1) & 0 & 0 & -1 \\ 0 & a(1 - 2x_2) & -b & 0 \\ 0 & c & c & 0 \end{bmatrix} \tag{2}$$

The characteristic polynomial is formulated using $|\lambda I - J_{\mathrm{E}}| = 0$ and obtained as:

$$\lambda \left[\lambda^3 + b\lambda^2 + k\lambda - (a + b)k \right] = 0 \tag{3}$$

where $k = c + \cos(x_1^*)$. Equation (3) signifies that there is a zero eigenvalue for all equilibrium points of 4D chaotic system (1).

It is quite tedious to obtain the dynamic behaviours with the knowledge of the location of infinite equilibria because the Jacobian matrix is the function of state variables. The dynamic behaviours of asymmetric 4D chaotic system are analysed with the help of different numerical tools and presented in the next section.

3 Complex Dynamic Behaviours of 4D Chaotic System

Dynamic analysis tools such as Lyapunov spectrum plot, bifurcation diagram, calculation of Lyapunov dimension using Lyapunov exponents (LEs) are utilised to describe different dynamic behaviours in the modified asymmetric 4D chaotic system (1).

3.1 Lyapunov Spectrum and Dimension Analysis

All the three parameters of 4D system (1) are varied one by one keeping other fixed. Lyapunov spectrum with respect to different parameters is shown in Fig. 3. The spectrum of fourth Lyapunov exponents (L_4) is not shown and avoided here. It may be noted that L_4 has negative value between $[-0.3, -0.8]$ for all the range of a, b and c parameters.

Lyapunov spectrum versus a parameter: The parameter a varied from 0.3 to 0.6, and Lyapunov spectrum is obtained. The 4D system shows 2-torus quasi-periodic behaviour for parameter range $0.3 \leq a \leq 0.476$ and chaotic 2-torus behaviour for parameter range $0.476 < a \leq 0.6$ except some quasi-periodic instances, refer Fig. 3.

Lyapunov spectrum versus b parameter: The parameter b ranges between $0.38 \leq b \leq 0.9$. The 4D system shows chaotic 2-torus behaviour for parameter range $0.38 < b \leq 0.58$ and 2-torus quasi-periodic behaviour in the remaining range.

Lyapunov spectrum versus c parameter: Similarly, parameter c is varied from 0 to 0.8 to obtain the Lyapunov spectrum. It is observed that 4D system shows 2-torus quasi-periodic behaviour for $c \in [0, 0.5) \cup [0.62, 0.8]$ and chaotic 2-torus behaviour for parameter range $0.5 \leq c < 0.62$ except some instances where behaviour is quasi-periodic.

Lyapunov dimension D_{KY} with respect to different parameters is shown in Fig. 4. The dimension is $D_{\mathrm{KY}} > 3$ for $0.476 < a \leq 0.6$, $0.38 < b \leq 0.58$ and $0.5 \leq c < 0.62$ where the behaviour is chaotic behaviour; otherwise, dimension is $D_{\mathrm{KY}} < 3$ for quasi-periodic behaviour. Lyapunov dimension of system dynamics (1) is calculated as:

$$D_{\mathrm{KY}} = 3 + \frac{0.0735}{0.6242} = 3.1178 \tag{4}$$

$D_{\mathrm{KY}} = 3.1178$ exclaims the estimate of the volume dimension that remains non-growing or non-decaying.

Fig. 3 Lyapunov spectrum of 4D chaotic system with varying a, b and c parameters

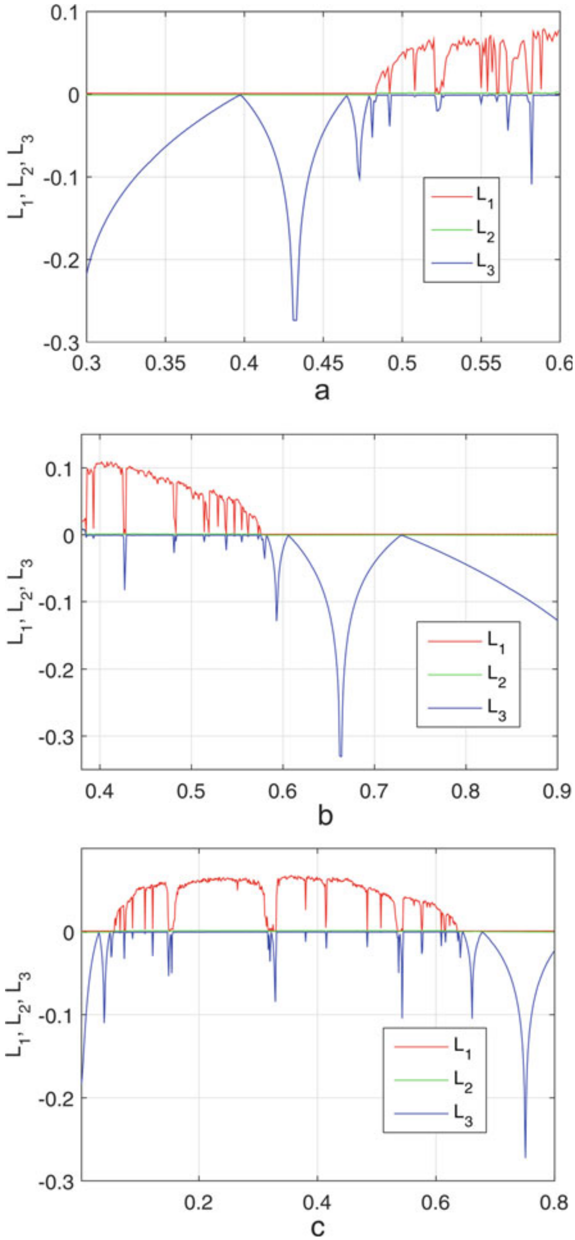

Fig. 4 Lyapunov dimension of 4D chaotic system with varying *a*, *b* and *c* parameters

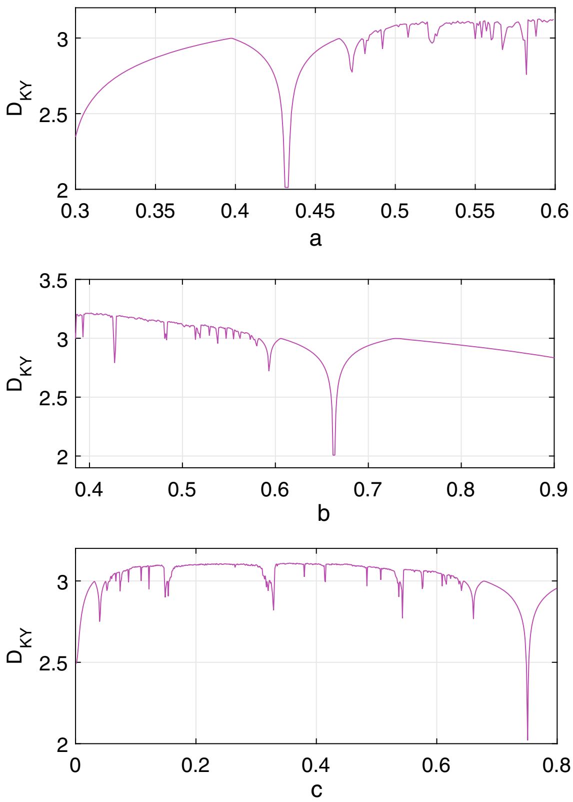

3.2 Bifurcation Diagram Analysis

Bifurcation behaviours are also obtained with respect to parameter a and shown in Fig. 5. Obtained bifurcation behaviours also correspond similar behaviours obtained via Lyapunov spectrum in Fig. 3.

3.3 Analysis of Coexisting Attractors

The coexisting behaviours are also observed and shown in Fig. 6. Two different set of initial conditions are considered to explore the coexisting behaviours of 4D chaotic system. The coexistence of chaotic 2-torus attractors is obtained at one set of initial conditions $[\pm 0.123, 0.123, 0.123, 0.1]$. Other set of initial conditions

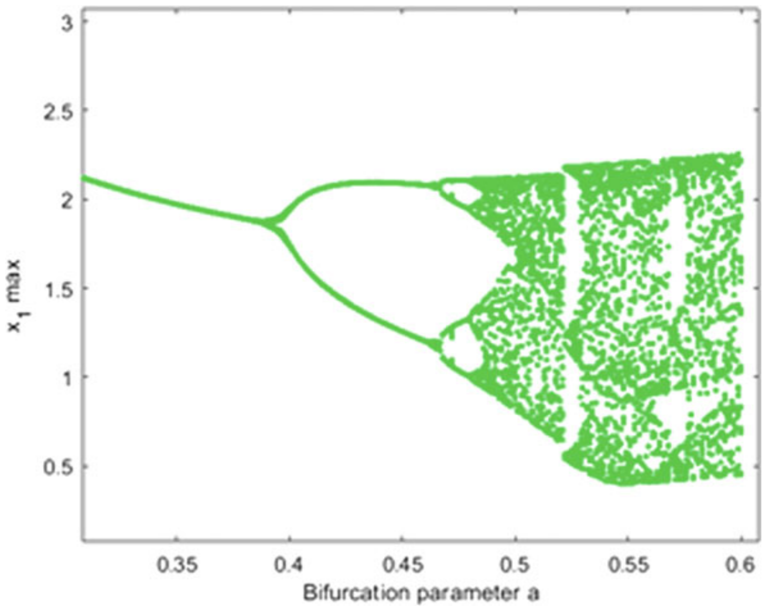

Fig. 5 Bifurcation plot of local maxima of x_1 with parameter a increasing

$[\pm 0.001, 0.001, 0.001, 0.001]$ shows coexistence of 2-torus quasi-periodic and chaotic 2-torus attractors. The chaotic signal with such behaviours may be useful during encryption of message signal in communication.

4 Conclusion and Future Scope

In this paper, a 4D chaotic system is analysed using phase plane, time series, calculation of Lyapunov exponents, Lyapunov dimension, bifurcation diagram. The chaotic attractor of the proposed dynamical system has asymmetric behaviour. The asymmetric chaotic system has a line of equilibria and 2-torus chaotic and 2-torus quasi-periodic behaviours. The Lyapunov dimension of proposed asymmetric chaotic system is 3.1178 which is larger than other available 4D chaotic systems, and the system also has coexisting attractors. Such properties are useful in different applications such as in secure voice and audio communications, image encryption and may be explored in near future.

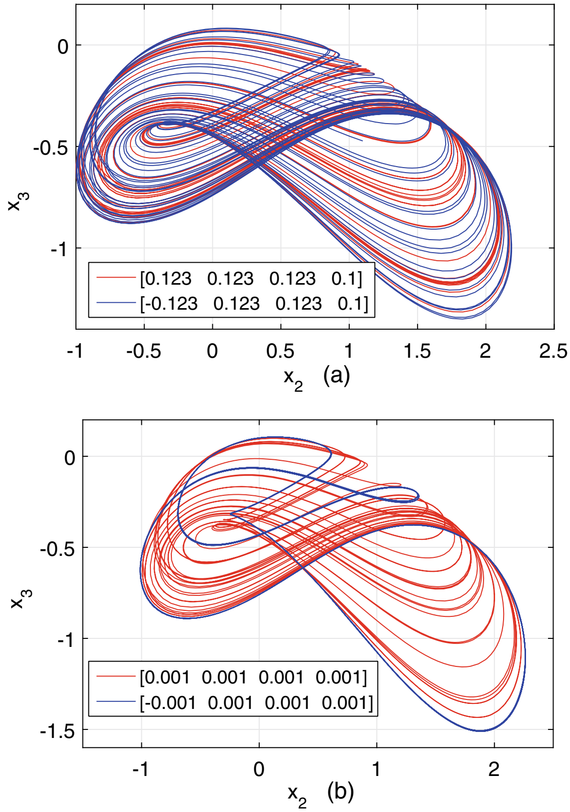

Fig. 6 Coexisting attractors; **a** shows coexistence of two chaotic 2-torus behaviours and **b** shows coexistence of chaotic 2-torus and 2-torus quasi-periodic behaviours

Acknowledgements The research work is supported by TEQIP-III Minor Research Grant Scheme, National Institute of Technology, Meghalaya. Sanctioned Project Ref. No. NITMGH/TEQIP-III/MP/2019-20/269.

References

1. Changbiao X, Xia W, Yinghui H, Yunhui M (2020) 5D hyper-chaotic system with multiple types of equilibrium points. J Shanghai Jiao Tong Univ. https://doi.org/10.1007/s12204-020-2224-x
2. Das P, Gupta PC, Singh PP (2021) Bifurcation, chaos and PID sliding mode control of 3-bus power system. In: 3rd IEEE international conference on energy, power and environment (ICEPE), Meghalaya, 5–7 Mar 2021. IEEE
3. Esteban TC, de la Fraga LG, Pham VT, Volos C, Jafari S, de Jesus Quintas-Valles A (2017) Dynamics, FPGA realization and application of a chaotic system with an infinite number of equilibrium points. Nonlinear Dyn 89:1129–1139
4. Feng W, He Y (2018) Constructing, analyzing and synchronizing a chaotic system with equilibria of rectangle loop. J Softw 13:112–118

5. Gupta PC, Banerjee A, Singh PP (2019) Analysis and control of chaotic oscillation in FOSMIB power system using AISMC technique. In: 5th IEEE students conference on engineering and systems (SCES), Allahabad, 29–31 May 2019. IEEE
6. Kingni ST, Pham VT, Jafari S, Woafo P (2017) A chaotic system with an infinite number of equilibrium points located on a line and on a hyperbola and its fractional-order form. Chaos Solitons Fractals 99:209–218
7. Kumar M, Singh PP (2018) Chaos control of an extended four dimensional fundamental power system using sliding mode control. In: 5th UP section international conference on electrical, electronics and computer engineering (UPCON). IEEE, Gorakhpur, Uttar Pradesh
8. Mishra D, Srinivas J, Mukhopadhyay S (2014) A secure and efficient chaotic map-based authenticated key agreement scheme for telecare medicine information systems. J Med Syst 38:111–120
9. Mobayen S, Volos CK, Kacar S, Cavusoglu U, Vaseghi B (2018) A chaotic system with infinite number of equilibria located on an exponential curve and its chaos-based engineering application. Int J Bifurc Chaos 28:1850112–125
10. Pham VT, Jafari S, Volos C, Giakoumis A, Vaidyanathan S, Kapitaniak T (2016) A chaotic system with equilibria located on the rounded square loop and its circuit implementation. IEEE Trans Circuits Syst II Exp Briefs 63:878–882
11. Pham VT, Jafari S, Kapitaniak T (2016) Constructing a chaotic system with an infinite number of equilibrium points. Int J Bifurc Chaos 26:1650225–31
12. Pham VT, Jafari S, Volos C, Kapitaniak T (2016) A gallery of chaotic systems with an infinite number of equilibrium points. Chaos Solitons Fractals 93:58–63
13. Pham VT, Volos C, Jafari S, Ouannas A, Dao TT (2019) Chaotic behaviors in a system with a line equilibrium. In: 18th European control conference (ECC), Napoli, 25–28 June 2019. IEEE, pp 2603–2607
14. Pham VT, Volos C, Kapitaniak T (2017) Systems with hidden attractors: from theory to realization in circuits, chap 7. In: Fortuna L, Chen G (eds) Applied sciences and technology: nonlinear circuits. Springer, Switzerland, pp 37–50
15. Pham VT, Volos C, Vaidyanathan S, Wang X (2016) A chaotic system with an infinite number of equilibrium points: dynamics, horseshoe, and synchronization. Adv Math Phys P. Article ID 4024836
16. Qi G, Chen G, Zhang Y (2008) On a new asymmetric chaotic system. Chaos Solitons Fractals 37:409–423
17. Rajagopal K, Çiçek S, Khalaf AJM, Pham VT, Jafari S, Karthikeyan A, Duraisamy P (2018) A novel class of chaotic flows with infinite equilibriums and their application in chaos-based communication design using DCSK. Z Naturforsch 37. https://doi.org/10.1515/zna-2018-0068
18. Rossler OE (1979) Continuous chaos: four prototype equations. Ann N Y Acad Sci 316:376–392
19. Samantaray J, Roy BK, Singh PP (2017) A comparative study of PI and PID-based SMC for anti-synchronisation of Vallis system. In: 6th international conference on computer applications in electrical engineering-recent advances (CERA), Roorkee, 5–7 Oct 2017. IEEE
20. Samantaray J, Singh PP, Roy BK (2017) A comparative study of PI and PID-based SMC for anti-synchronisation of Lorenz-Stenflo chaotic system. In: 14th IEEE India council international conference (INDICON), Roorkee, 15–17 Dec 2017. IEEE
21. Sambas A, Vaidyanathan S, Mamat M, Mohamed MA, Sanjaya WM (2018) A new chaotic system with a pear-shaped equilibrium and its circuit simulation. Int J Electr Comput Eng 8:4951–4958
22. Singh JP, Roy BK (2016) Crisis and inverse crisis route to chaos in a new 3-D chaotic system with saddle, saddle foci and stable node foci nature of equilibria. Optik 127:11982–12002
23. Singh JP, Roy BK (2017) The simplest 4-D chaotic system with line of equilibria, chaotic 2-torus and 3-torus behaviour. Nonlinear Dyn 89:1845–1862
24. Singh JP, Roy BK (2018) A more chaotic and easily hardware implementable new 3-D chaotic system in comparison with 50 reported systems. Nonlinear Dyn 91:1121–1148

25. Singh PP, Roy BK (2018) Memristor-based novel complex-valued chaotic system and its projective synchronisation using nonlinear active control technique. Eur Phys J Spec Top 228:2197–2214
26. Singh PP (2021) A novel chaotic system with wide spectrum, its synchronization, circuit design and application to secure communication. Indian J Sci Technol 14:2351–2367
27. Singh PP, Roy BK (2020) A novel chaotic system without equilibria, with parachute and thumb shapes of Poincare map and its projective synchronisation. Eur Phys J Spec Top 229:1265–1278
28. Singh PP, Singh JP, Borah M, Roy BK (2016) On the construction of a new chaotic system. IFAC-PapersOnLine 49:522–525
29. Singh PP (2021) A chaotic system with large Lyapunov exponents: nonlinear observer design and circuit implementation. In: 3rd IEEE international conference on energy, power and environment (ICEPE), Meghalaya, 5–7 Mar 2021. IEEE
30. Singh PP, Roy BK (2018) Secure communication using NAC based synchronisation between nonidentical chaotic systems. In: 2nd international conference on power, energy and environment (ICEPE), Shillong, 1–2 June 2018. IEEE
31. Sprott JC (2011) A proposed standard for the publication of new chaotic systems. Int J Bifurc Chaos 21:2391–2394
32. Sugandha, Singh PP (2020) Complex state variables based novel hyperchaotic system with nine equilibria. In: 17th IEEE India conference (INDICON). IEEE, New Delhi
33. Tiwari E, Kumar V, Singh PP (2018) Anti-synchronisation of Vallis chaotic systems using nonlinear active control technique quantitative features of El-Nino southern oscillation (ENSO) phenomenon. In: 2nd international conference on power, energy and environment (ICEPE), Shillong, 1–2 June 2018. IEEE
34. Wang M, Li J, Zhang X, Iu HHC, Fernando T, Li Z, Zeng Y (2021) A novel non-autonomous chaotic system with infinite 2-D lattice of attractors and bursting oscillations. IEEE Trans Circuits Syst II Express Briefs 68:1023–1027

Chapter 63
New Performance Evaluation Metrics for Outlier Detection and Correction

B Rajanarayan Prusty, Nimish Jain, Kumar Gaurav Ranjan, Kishore Bingi, and Debashisha Jena

Abstract This paper proposes novel metrics for the numeric evaluation of outlier detection and correction. The downsides of the existing comparison approaches are detailed, and substitute metrics, complemented normalized sum of absolute deviations (CNSAD) and overall preprocessing performance (OPP) are proposed. Also, the suitability of two derived metrics in revealing methods' capability in handling extreme outliers is detailed. The merits of CNSAD and OPP are critically analyzed by applying to a set of polluted data with the synthetically embedded trend and volatility effects.

Keywords Clean data · Data preprocessing · Evaluation metrics · Outlier detection and correction · Polluted data · Time series data

1 Introduction

In recent times, there is an overwhelming interest in adopting data analytics in power system research [1, 2]. Time series forecasting using data analytics and machine learning is essential for predicting future values of inputs for power system steady-state analysis [3]. The forecasting accuracy directly depends on the quality of the

B Rajanarayan Prusty (✉) · K. Bingi
School of Electrical Engineering, Vellore Institute of Technology, Vellore, India
e-mail: b.r.prusty@ieee.org

K. Bingi
e-mail: bingi.kishore@ieee.org

N. Jain
School of Information Technology and Engineering, Vellore Institute of Technology, Vellore, India

K. G. Ranjan
Tata Consultancy Services, Bangalore, India

D. Jena
Department of Electrical and Electronics Engineering, National Institute of Technology Karnataka, Surathkal, India

G. Panda et al. (eds.), *Sustainable Energy and Technological Advancements*, Advances in Sustainability Science and Technology,
https://doi.org/10.1007/978-981-16-9033-4_63

data at hand. Therefore, outlier detection and correction, referred to as data preprocessing, are vital in building precise forecasting models for power system planning and operation [4, 5]. The selection of a suitable method requires reliable metric-based performance comparison among methods [6–9]. As detection and correction are two integral stages of data preprocessing, the overall performance depends on each stage's recital. So, the formulation of a metric for unbiased preprocessing result comparison should equally weigh each stage's performances. This paper proposes a new set of metrics for fair numeric comparison amid several methods.

The information about the outliers in a raw time series being unknown prior a preprocessing method's performance can only be evaluated using graphical interpretation [9]. Such an approach is vital in highlighting a method's success or failure. But, a numeric comparison among methods with a set of metrics can only be achieved using each method's obtained corrected dataset z from the polluted dataset y formed by randomly introducing outliers in a clean dataset x [4, 6–8]. In the literature, authors have evaluated the detection performance using F-score (F), calculated using outlier detection indicators: true positive (TP), false positive (FP) and false negative (FN) [4, 6–8]. Although the need for enhanced correction is well recognized [9], metric-based performance evaluation is not suggested in the literature. Besides, two approaches are adopted in the assessment of overall preprocessing performance. The authors in [9, 10], respectively, calculated mean absolute error (MAE) and root mean square error between a method's preprocessed data and clean data. In contrast, [5, 9] evaluated the accuracy based on the forecasting result using the preprocessed data. While better-preprocessed data yield accurate forecasting result, the reverse is not always true as forecasting accuracy depends on several other factors. Moreover, none of the above two approaches signifies the level to which a method is good.

This paper overcomes the above-highlighted lacunae by proposing a new metric named complemented normalized sum of absolute deviations (CNSAD) for the numerical comparison of several methods' correction ability. Secondly, it suggests approaches to examine a method's ability in preprocessing extreme outliers using a new set of derived metrics. Finally, it reveals that the detection performance is under-weighted in the error calculation-based metric, MAE. Since the detection performance evaluation using F-score is directly affected by TP and FP counts, a new evaluation metric, named overall preprocessing performance (OPP), whose formulation weighs detection and correction equally, is proposed by combining F-score and CNSAD for unbiased performance evaluation.

The remainder of the paper is designed as discussed underneath. In Sect. 2, the proposed performance evaluation metrics are elaborated comprehensively. The required numerical analyses and validation for the set objectives are carried out in Sect. 3. The importance of the considered pollution mechanisms and hypotheses are also discussed. Finally, the suitability of the proposed metrics in the context of outlier detection and correction of volatile time series is summarized in Sect. 4.

2 Proposed Performance Evaluation Metrics

Outlier correction is an equally important concern like detection. Accurate outlier correction adds to a method's enhanced overall accuracy. Depending on data characteristics, a method's correction capability may vary while dealing with outliers on the upper and lower extreme sides, respectively, known as upper extreme outliers (UEOs) and lower extreme outliers (LEOs). The total number of data points above and below the time-varying mean line is regarded as "upper side" and "lower side." In this paper, the extreme side refers to the one-third portion toward the time series edge.

In a polluted dataset where outliers' information is known prior, a new metric with a range limit can be designed based on the approaches: (i) averaging absolute relative deviations or (ii) normalizing the sum of absolute deviations. A metric designed based on the first approach, namely average absolute relative deviations (AARD), can be expressed as,

$$\mathrm{AARD} = \frac{1}{\mathrm{TP} + \mathrm{FP}} \sum_{i=1}^{\mathrm{TP+FP}} \frac{|z_{j_i} - x_{j_i}|}{|x_{j_i}|}, \tag{1}$$

where i is the counting variable for detected outliers; j_i is the index of ith outlier; x_{j_i} and z_{j_i} are j_ith values of x and z, respectively.

In (1), there is possibly a high chance that the summand(s) pertaining to extreme outlier(s) may exceed one. This scenario may logically be more likely to happen for LEO(s) than UEO(s). Such cases in AARD calculation would make it unfit for a fair numeric comparison of correction performances. Moreover, the correction is made to the polluted data, whose performance may be affected by the pollution mechanism and pollution level. Therefore, considering all the factors that affect outlier correction is imperative for designing a stable normalized outlier correction metric.

On this note, the second approach seems applicable where the method's correction ability is quantified by the sum of corrected outliers' absolute deviations (SAD) measured from their corresponding clean data values (refer to Fig. 1). The average absolute deviation (AAD) can be calculated from the SAD by adopting the formulations in Fig. 1. The subscripts "U" and "L" in Fig. 1, respectively, refer to upper and lower. The lowest value of SAD is zero, corresponding to the "ideal outlier correction (true outliers are brought back to their original values, leaving the false outliers unchanged)." Its value is maximum, i.e., $\mathrm{SAD}^{\mathrm{M}}$ for the worst-case outlier correction. Hence, the normalized value of SAD, i.e., NSAD can be expressed as,

$$\mathrm{NSAD} = \frac{\mathrm{SAD}}{\mathrm{SAD}^{\mathrm{M}}}. \tag{2}$$

In the correction stage, a typical method corrects an outlier based on an estimation using the polluted data or a statistical parameter, e.g., mean or median of the polluted data. In either of the above cases, the corrected data lie within the range of lower

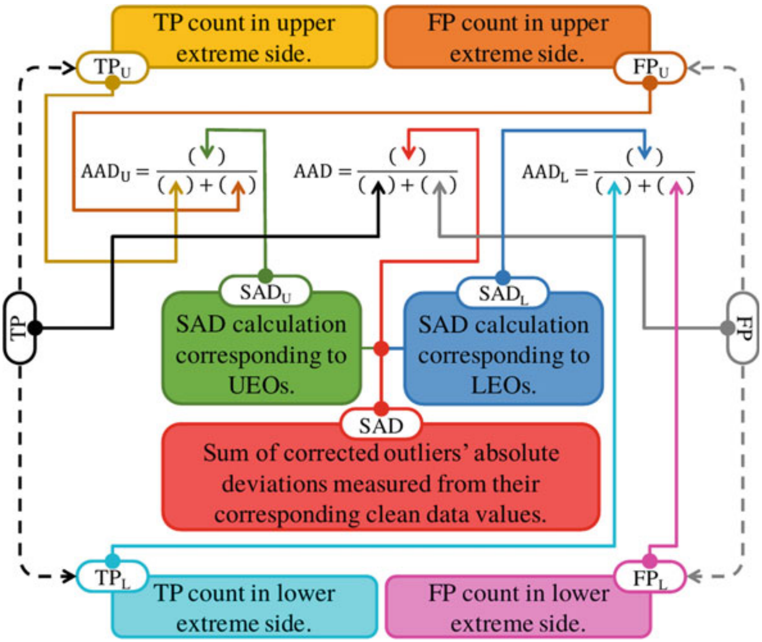

Fig. 1 Calculation of SAD and AAD

limit $y_{\mathrm{L_{Lim}}}$ to the upper limit $y_{\mathrm{U_{Lim}}}$ of the polluted dataset. Therefore, the expression for $\mathrm{SAD}^{\mathrm{M}}$ is proposed as,

$$\mathrm{SAD}^{\mathrm{M}} = \sum_{i=1}^{\mathrm{TP+FP}} \mathrm{Max}\left(|y_{\mathrm{U_{Lim}}} - x_{j_i}|, |y_{\mathrm{L_{Lim}}} - x_{j_i}|\right). \tag{3}$$

A zero value of NSAD denotes the best outlier correction, whereas its unity value corresponds to the worst case of outlier correction. The limiting values of NSAD can be reversed by calculating CNSAD = 1 − NSAD. Here, CNSAD has a similar limiting constraint as F-score, i.e., zero value and unity values indicating worst and best performances, respectively. So, these two scores in unison are the potential candidates to compare the overall performance of multiple preprocessing methods. For contradictory F-score and CNSAD value, a new metric OPP that calculates their harmonic mean is expressed as,

$$\mathrm{OPP} = \frac{2 \times F \times \mathrm{CNSAD}}{F + \mathrm{CNSAD}}. \tag{4}$$

The limiting values of OPP are zero and one, respectively, indicating the worst and best overall performances. The evaluation using metric OPP is unbiased as F-score and CNSAD are unbiased. If F-score is zero (no outliers are detected), the correction does not make any sense; thus, OPP is assigned the zero value and marked as the worst case. While a preprocessing method is expected to perform better detection and correction irrespective of the outliers' positions, there may be a chance of unequal detection and correction performance while handling extreme outliers based on the pollution mechanism used. In that case, F-score and CNSAD cannot evaluate the method's specific performance while dealing with UEOs and LEOs. In contrast, the derived metrics $F_U - F_L$ and $CNSAD_U - CNSAD_L$ are suitable to highlight the inclination of a method's performance toward a particular side. The calculation for (F_U, F_L) and ($CNSAD_U$, $CNSAD_L$), respectively, uses the formulations of F-score and CNSAD, considering the true and false outliers of the respective sides.

3 Numeric Analysis and Validation

The significances of the proposed metrics are validated by considering historical load power data collected from a restaurant in Anchorage, USA [11] as the primary dataset. Three new datasets with the synthetically embedded complex trend and volatility effects are generated using the primary dataset. The plots of the first 250 samples of all four datasets are shown in Fig. 2. The time-varying mean line and boundary lines to highlight extreme one-third portions are also shown. The paper's objective is twofold. Firstly, the importance of metrics, $F_U - F_L$ and $CNSAD_U - CNSAD_L$, is examined. Further, the level to which inclination of methods' performance to a particular side is affected by trend, and volatility effect using the metrics is investigated. Secondly, the unbiased evaluation of overall preprocessing performance by OPP compared to MAE is presented.

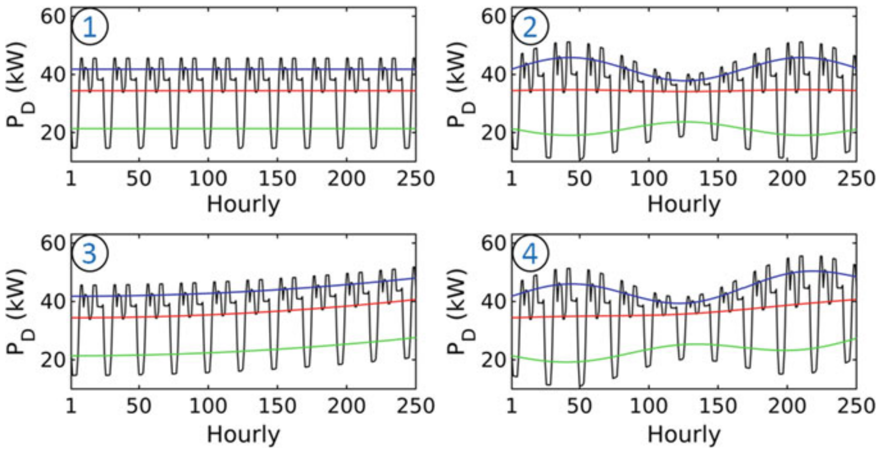

Fig. 2 Clean datasets used for result analyses

An ideal method's equilibrium performance refers to its consistent dealing with extreme outliers. Statistical methods, such as the portrait dataset-based (PDB) method [7] and the improved sliding window prediction (ISWP) method [9], have quite a possible chance to deal with extreme outliers inconsistently as they compute confidence interval/outlier region for outlier detection, hence are considered in this paper. On this note, two pollution introducing mechanisms, M_1 and M_2, which can bring appreciable deviation, would help revealing methods' performance in this context. Pollution level is set to 10% of total samples (50 outliers), with the number of outliers on the extreme sides proportional to the data samples contained in those sides. The indices of randomly introduced outliers are kept the same for all cases and mechanisms. The pollution mechanisms are as discussed underneath.

- M_1: A sample value is randomly altered by 50% of the clean data value.
- M_2: A sample value is randomly altered by a fixed value.

The hypotheses for the first objective are: (i) a method's detection performance for M_1 is better while dealing with upper extreme outliers, (ii) a methods correction performance for M_1 is better while dealing with lower extreme true outliers, and (iii) both shift toward the equilibrium performance for M_2.

For M_1, there is a high chance that a method detects an extreme outlier whose deviation from the corresponding clean data value is significant than an outlier with a low magnitude deviation. Further, the upper extreme true outliers' corresponding corrected data point's deviation from the clean data value is also likely to be higher, whereas for M_2, extreme outliers have a nearly similar deviation in terms of magnitude, therefore have almost equal chances of being detected by a method. Also, a method is likely to perform almost identical correction while dealing with extreme true outliers because of similar deviation. Let two clean data points (say 50 units and 20 units present in upper and lower extreme sides, respectively) be changed by the same 25% by M_1. The UEO with 62.5 units is more likely to be detected than the LEO of 15 units because the net deviation is significant in the former case. And, the latter case is more likely to lie outside the outlier region. Assuming that both extreme outliers are detected, a method is more likely to bring back the LEO of 15 units significantly closer to its original value of 20 units than UEO of 62.5 units to a value substantially nearer to 50 units as the deviation of 12.5 is high. Let those clean data points be changed to 60 units and 10 units, respectively. Now, a method is likely to detect both the outliers and perform similar correction if both are detected.

Table 1 compares the proposed metrics' values for both mechanisms using PDB and ISWP for evaluating detection, correction and overall preprocessing. In Case 1, due to the absence of trend and volatility effects, the accuracy of computing the outlier region is high. Therefore, it becomes relatively easy for both methods to detect outliers irrespective of the mechanism. However, the observations are as per the hypothesis for Case 2 through Case 4. The observations considering two randomly chosen data points of the Case 2 dataset using the ISWP method are detailed. Two extreme clean data points, upper of 39.4 kW and lower of 17.1 kW, when polluted using M_1, the UEO of 59.1 kW is detected, whereas the LEO of 8.5 kW is not because the net deviation of 8.5 kW is minor in the latter case compared to the deviation of

Table 1 Preprocessing performance comparison using proposed metrics

Method			PDB				ISWP			
Case No.			1	2	3	4	1	2	3	4
Objective-1	M_1	$F_U - F_L$	−0.065	0.252	0.221	0.223	0.059	0.252	0.088	0.228
		$C_U - C_L$	−0.005	−0.060	0.021	0.038	−0.077	−0.056	−0.064	−0.035
		Avg.	$F_U - F_L = 0.158$ $C_U - C_L = -0.002$				$F_U - F_L = 0.157$ $C_U - C_L = -0.058$			
	M_2	$F_U - F_L$	−0.065	−0.101	−0.031	−0.083	0.059	0.081	0.059	0.059
		$C_U - C_L$	−0.004	−0.025	0.033	0.032	−0.021	−0.023	−0.025	−0.017
		Avg.	$F_U - F_L = -0.070$ $C_U - C_L = 0.009$				$F_U - F_L = 0.064$ $C_U - C_L = -0.022$			
Objective-2	M_1	F	0.444	0.816	0.484	0.465	0.630	0.563	0.649	0.630
		C	0.996	0.908	0.787	0.773	0.915	0.923	0.934	0.930
		OPP	0.615	0.859	0.599	0.581	0.746	0.700	0.766	0.751
		MAE	0.051	0.567	2.879	2.911	1.045	1.067	1.230	1.199
	M_2	F	0.444	0.935	0.497	0.416	0.630	0.622	0.630	0.630
		C	0.997	0.925	0.809	0.797	0.926	0.942	0.938	0.941
		OPP	0.615	0.930	0.616	0.547	0.750	0.749	0.754	0.755
		MAE	0.051	0.463	2.927	3.084	1.250	1.231	1.247	1.234

19.7 kW in the former. However, both outliers are detected when polluted using M_2. Similar observations are also noted for most of the other data points of the same case and other cases for both methods. It is worth highlighting that, with the help of the metric $F_U - F_L$, it becomes possible to reveal that both methods have significant average $F_U - F_L$ for M_1, and the value moves toward the equilibrium performance for M_2.

The mechanism-wise outlier correction performances are also compared in Table 1 ("C" stands for CNSAD). Although it is well-known that the correction is affected by detection, it is still inferred from the analysis that the correction performance is nearly as per the hypothesis. There is a shift in the inclination of correction performance toward the equilibrium in M_2 in all the cases but Case 3 and Case 4 using PDB as the performance is majorly affected due to the trend effect in the data. Further, to highlight that with the assistance of $\mathrm{CNSAD_U} - \mathrm{CNSAD_L}$, it becomes possible to envisage the impact of outliers' position on the correction performance. The metrics $F_U - F_L$ and $\mathrm{CNSAD_U} - \mathrm{CNSAD_L}$ are always helpful as they depict a method's sensitivity to a specific data characteristics, pollution mechanism used and level of pollution introduced. Further, their consideration as one of the criteria helps propose an accurate preprocessing method with above metric values nearly zero. Further, using the synthetic datasets that have embedded trend and volatility effects, the above two metrics can reveal how sensitive a method's inclination to a particular side concerning the above effects. In reality, outliers may be of any magnitude, hence, irrespective of the mechanism used method's performance should be stable.

Finally, the suitability of metric OPP over MAE is justified in light of the critical observations as elucidated underneath. For Case 1, although the ISWP method performs better detection than the PDB method but nearly a similar correction, the MAE score is less for the PDB method, indicating its superior preprocessing. Further, the difference between the F-score of both the methods is much higher in Case 2 than in Case 3 and Case 4, and still the difference between MAE of both the methods in Case 2 is much lower than Case 3 and Case 4 because the difference between CNSAD of both the methods is higher in Case 3 and Case 4 than in Case 2. Based on the above peculiar observations, it is inferred that MAE result is biased as it undermines the detection performance of a method and gives higher weight to the correction. However, MAE-based comparison is unbiased when methods with different correction performances have ideal detection ($F = 1$). On the other hand, OPP accounts equally for detection and correction performances and, therefore, provides an unbiased result in all cases. Also, OPP gives a meaningful comparison between the methods for a given case, e.g., in Case 1, ISWP performs 13.1% better than PDB.

4 Conclusion

Two novel metrics, named CNSAD and OPP, are proposed to evaluate outlier correction and overall data preprocessing performances. Further, two derived metrics' capability to reveal methods' success or failure in handling extreme outliers of different magnitude deviations is suggested. The validity of the above metrics is elucidated through detailed result analysis considering various polluted datasets and pollution mechanisms. The proposed metrics provide a fair comparison among outlier detection and correction methods for selecting the best method. Further, the proposed metrics' role would be vital while proposing a new outlier detection and correction method.

References

1. Prusty BR, Jena D (2019) A spatiotemporal probabilistic model-based temperature-augmented probabilistic load flow considering PV generations. Int Trans Electr Energy Syst 29(5):e2819
2. Jose S, Itagi RL (2021) Data analytics in solar photovoltaics power forecasting for smart grid applications. In: 2021 international conference on intelligent technologies (CONIT), pp 1–5
3. Prusty BR, Jena D (2017) A critical review on probabilistic load flow studies in uncertainty constrained power systems with photovoltaic generation and a new approach. Renew Sustain Energy Rev 69:1286–1302
4. Ranjan KG, Prusty BR, Jena D (2021) Review of preprocessing methods for univariate volatile time-series in power system applications. Electr Power Syst Res 191:106885
5. Akouemo HN, Povinelli RJ (2017) Data improving in time series using ARX and ANN models. IEEE Trans Power Syst 32(5):3352–3359
6. Chen J, Li W, Lau A, Cao J, Wang K (2010) Automated load curve data cleansing in power systems. IEEE Trans Smart Grid 1(2):213–221
7. Tang G, Wu K, Lei J, Bi Z, Tang J (2014) From landscape to portrait: a new approach for outlier detection in load curve data. IEEE Trans Smart Grid 5(4):1764–1773
8. Lin Y, Wang J (2019) Probabilistic deep autoencoder for power system measurement outlier detection and reconstruction. IEEE Trans Smart Grid 11(2):1796–1798
9. Ranjan KG, Tripathy DS, Prusty BR, Jena D (2021) An improved sliding window prediction-based outlier detection and correction for volatile time-series. Int J Numer Model Electron Netw Devices Fields 34(1):e2816
10. Ma L, Gu X, Wang B (2017) Correction of outliers in temperature time series based on sliding window prediction in meteorological sensor network. Information 8(2):60
11. Hourly load consumption (2021) https://openei.org/datasets/files/961/pub

Chapter 64
Time Series Decomposition Techniques for Renewable Generation Applications

Satyabrata Das, B Rajanarayan Prusty, Kishore Bingi, Kaibalya Prasad Panda, and Gayadhar Panda

Abstract Time series decomposition is extensively used recently for nonlinear nonstationary time series modeling and forecasting. A relevant set of monocomponents obtained using an adaptive decomposition method is a potential candidate for predictions using point and probabilistic forecasting frameworks. Time series decomposition has been widely applied to time series of input variables of various power system analyses. This paper comprehensively reviews the decomposition-based data cleaning approaches, selection of a forecasting model for renewable generations, and challenges in model development. This critical review is expected to help a novice reader in the area of time series decomposition significantly.

Keywords End effect · Forecasting · Mode mixing · Renewable generations · Time series decomposition

Nomenclature

AI	Artificial intelligence
ALIFD	Adaptive local iterative filtering decomposition
ANN	Artificial neural network
BEMD	Basic empirical mode decomposition

S. Das · B Rajanarayan Prusty (✉) · K. Bingi
School of Electrical Engineering, Vellore Institute of Technology, Vellore, India
e-mail: b.r.prusty@ieee.org

K. Bingi
e-mail: bingi.kishore@ieee.org

K. P. Panda · G. Panda
Department of Electrical Engineering, National Institute of Technology Meghalaya, Shillong, India
e-mail: kaibalyapanda@nitm.ac.in

G. Panda
e-mail: gayadhar.panda@nitm.ac.in

G. Panda et al. (eds.), *Sustainable Energy and Technological Advancements*,
Advances in Sustainability Science and Technology,
https://doi.org/10.1007/978-981-16-9033-4_64

CEEMD	Complete ensemble empirical mode decomposition
CEEMDAN	Complete ensemble empirical mode decomposition with adaptive noise
DMD	Dynamic mode decomposition
EEMD	Ensemble empirical mode decomposition
EMD	Empirical mode decomposition
ESMD	Extreme-point symmetric mode decomposition
ESSD	Empirical signal separation decomposition
EVD	Eigen value-based decomposition
EWMD	Extreme-point weighted mode decomposition
EWT	Empirical wavelet transform
FEEMD	Fast ensemble empirical mode decomposition
ICD	Intrinsic characteristics-scale decomposition
IMF	Intrinsic mode function
ITD	Intrinsic timescale decomposition
LCD	Local characteristic-scale decomposition
LMD	Local mean decomposition
LSSVM	Least-squares support vector machine
NMD	Nonlinear mode decomposition
RVM	Relevance vector machine
SSSA	Sliding singular spectrum analysis
SVM	Support vector machine
SVR	Support vector regression
VMD	Variational mode decomposition

1 Introduction

A move toward data-driven power system research necessitates adequate knowledge of data analytics and machine learning. The development of prediction models is preeminent in the majority of power system research [1–3]. Load power prediction has gained tremendous research attention in power systems for several decades and is continuing. In recent years, renewable generations have become significant energy sources. Integration of renewable generations to the power systems is encouraged both at the transmission and distribution levels. Renewable generations are variable and highly unpredictable [3]. In renewable energy-rich power systems, several uncertain inputs make the system analysis challenging. Depending on the characteristics of the input time series, the prediction model development steps are also different. Besides, the generation of high-quality synthetic information from real-world low-level data is imperative. Data preprocessing prepares the raw data suitable for further processing. Several preprocessing approaches have been applied to time series data in the literature depending on the type of application. In the field of time series forecasting, data preprocessing is accomplished in one or more steps. The first step preprocessing, basically refers to (i) updating the missing values and (ii) accomplishing the detection of outliers and their apt correction [4]. The second step preprocessing is used to (i) characterize the predictable components [3], (ii) adoption of time series decomposition [5], etc., for ensuring an effective forecasting model development. In some instances, the combination of more than one of the above tasks is performed before developing a forecasting model. This paper mainly focuses on the critical review of the application of adaptive decomposition methods to power system input variables.

Extensive research on adaptive decomposition for nonlinear and non-stationary time series has been made over the years and is continuing. In 1998, the first adaptive decomposition method BEMD was proposed [5]. Since then, several adaptive decomposition methods and their improved versions were presented by researchers for time series originating from different nonlinear and non-stationary processes. Various adaptive decomposition methods can broadly be classified into four categories such as sifting-based methods, Eigen value-based methods, spectrum segmentation-based methods, and surrogate model-based methods. The members of sifting-based adaptive decomposition include EMD, LMD, ITD, ALIFD, LCD, EWMD, and ICD. The adaptive decomposition methods DMD, EVD, and SSSA, are the eigenvalue-based methods, whereas EWT and VMD are included under the spectrum segmentation category. The NMD method is the only surrogate model-based adaptive decomposition method that exists in the literature.

Several research interests are devoted toward comparing well-established methods of a category or methods under various types, improvisation of techniques, application of these methods to different engineering fields, etc. [6]. The pertinent issues like frequency resolution, sampling frequency, mode mixing were critically analyzed. Detailed analysis of various adaptive decomposition methods applied to time series of renewable generation is never discussed in detail in the literature. This paper focuses on the aspects such as decomposition-based data correction approaches, challenges, and application of adaptive decomposition for the forecasting of highly volatile power system variables such as renewable generations.

2 Decomposition-Based Data Correction

2.1 *Denoising*

Time series data used in power system applications are prone to various uncertainties affecting the data acquisition process. These time series usually have randomness, fluctuation, and nonlinearity, which often lead to difficulties in the forecast. Filtering the noisy components of time series by data processing techniques often leads to a time series that can improve prediction accuracy. So, noise elimination is an essential step in a renewable energy forecast system. Removal of noise from the time series is often termed data preprocessing. It can be accomplished in various ways. Decomposing a time series into its constituent components helps extract salient features using adaptive decomposition methods, thus improving accuracy. Denoising of input time series enhances the performance of forecasting models by strengthening the adequate information and simultaneously removing the noise information that interferes with the forecasting model. It does not hamper natural dynamics present in the original time series. Denoising helps in reducing the instability and randomness characteristics of the time series.

Unlike Fourier series expansion, BEMD can decompose a time series into a finite number of IMFs. The obtained IMFs' instantaneous frequencies with clear physical meanings describe the original time series oscillation. First obtained IMF with higher frequency will most likely have noise information, whereas the last IMF having lower frequency represents trend term. The middle-order IMFs reflect the periodicity of the original time series and are hence known as periodic components. Sometimes first two IMFs are also considered as noise. Removal of the high-frequency IMFs from the original time series yields smooth data used for forecasting. Decomposition methods like BEMD [7], EEMD [8], CEEMDAN [9], and EWT [10] have shown their effectiveness in noise removal for renewable energy applications by removing high-frequency IMFs. The CEEMDAN method exhibits better noise removal performance than BEMD, EEMD, and CEEMD in terms of reduced mean absolute percentage error [9], thus helps in improving prediction accuracy. In recent years, few advanced adaptive decomposition methods are applied to renewable energy time series for denoising, such as VMD, EWT, ITD, LMD, ESMD, and SSSA. Commonly associated errors with the BEMD due to mode mixing, end effect are avoided by VMD, thus yielding improved noise robustness and IMF separation helping in better forecast [11].

2.2 Missing Value Updation

Instruments used to acquire data often fail due to various reasons resulting in gaps or missing values in time series. These gaps prevent the BEMD algorithm from properly sifting through the data. When the sifting process encounters a data gap, the splines cannot interpolate, halting the sifting process. A new set of piecewise spline functions begins on the next stage of continuous data to resume sifting. It is assumed that the data remains constant to overcome this difficulty for small data gaps in the time series. This approach may be helpful for small data gaps; however, it is unsuitable for more significant gaps in a time series with fluctuating data. If missing data are not corrected with their true value, then obtained IMFs will be erroneous, and the magnitude of error increases as the number of missed data lengths is more. The mirror extension technique updates the missing values to reduce the error between true IMF (time series without missing value) and extracted IMFs from the time series (after missing value updated) [12]. The mirror extension method is effective in reducing error for high-frequency IMFs as compared to low frequencies. Gaps in the time series data produce errors in the decomposed components or IMFs. These errors affect differently to low- and high-frequency IMFs. Gap duration in the time series data accounts for errors in low-frequency IMFs. In contrast, high-frequency IMFs have errors around the vicinity of the gaps, and it is maximum at the endpoints. Hence conventional endpoint suppression algorithms can tackle the errors in high-frequency IMFs [13].

2.3 Outlier Detection and Their Apt Correction

The presence of outliers in a time series disturbs the true identification of the local extremas. Hence, sifting-based adaptive decomposition methods cannot determine the true mean envelope of the time series contaminated with outliers using these extrema values. Optimal smoothing parameter technique-based statistical EMD [14], and its improved version, i.e., quantile smoothing-based BEMD [15] both overcome this problem. In these methods, the lower and upper envelopes are determined from the time series corrupted with outliers by performing quantile smoothing splines followed by a regular BEMD process. The performance of this method depends on the suitable selection of quantile level and smoothing parameters in the algorithm. To measure the performance of evaluation of this method, mean square error between true and extracted IMFs are computed, which reveals the effectiveness of the method. Different signals such as chirp and Heavisine corrupted with Gaussian noise, t-distribution, and contaminated Gaussian mixture are applied to test the efficacy of these methods. The t-distribution and Gaussian mixture scenario represent the outliers' presence in time series. The sifting process of BEMD is modified by using t-distribution to reduce the effect of outliers on the forecasting model. Both upper and lower envelopes are computed from the extremas by using the t-distribution function. The resulting IMFs are fed to a backpropagation ANN-based forecasting model, which yields better forecasting accuracy than BEMD [16].

3 Adaptive Decomposition for Renewable Generation Forecasting

3.1 Challenges of Decomposition for Forecasting Application

(i) **Extraction of Stationary Component for Better Prediction**: PV output power and wind speed time series data are inherently non-stationary. The forecasting models for these time series preferably require stationary inputs for better performance which can be obtained using suitable preprocessing techniques such as adaptive mode decomposition. Use of adaptive mode decomposition in preprocessing enables extracting stationary components from time series data. This is accomplished by using the various original decomposition methods and their variants, such as FEEMD, CEEMDAN, EWT, LMD, and VMD. These decomposition methods help to decompose the time series deeper to extract the stationary components useful in multistep prediction.

(ii) **Developing Accurate and Stable Forecasting Model**: The accuracy and stability of a forecasting model depend on the extracted components derived from time series data. These extracted components should be devoid of mode mixing phenomena. They should not be derived from an over or under decomposed method to have better accuracy and stability. Bias–variance framework and Diebold–Mariano test exhibit CEEMDAN and VMD-based decomposition methods have better performance in this aspect.

(iii) **Reduction of Computational Complexity in Forecast Model Development**: Orthogonal components extracted from the raw time series using various adaptive decomposition methods help reduce computational complexity, primarily when used with the SVR forecasting model. This orthogonal nature of components helps reduce the complexity of the inner product in the regression function of SVR, thus avoiding the possibility of overfitting, hence improving the prediction performance.

(iv) **Better Denoising Ability**: EWT decomposition method has inherited the excellent features of wavelet-based decomposition algorithm and EMD-based adaptive decomposition method. Wavelet-based algorithms are popular in denoising, whereas EMD-based methods are suitable for extracting stationary components. Thus EWT-based algorithm exhibits better denoising and extraction of stationary components from the time series, which helps in improving the prediction performance.

(v) **Multiscale Feature Extraction**: To improve the forecasting performance of the model, often input features at different scales are needed. These can be obtained by employing two different adaptive decomposition methods in succession. EEMD followed by the VMD method helps in extracting features at multiple scales thus exhibits improved performance.

3.2 Selection of Optimal IMF Set and Compatible Forecasting Model

(i) **Reduction of IMFs**: Adaptive decomposition methods produce several IMFs from raw time series. The obtained number of IMFs decides the required number of forecasting models. An optimum number is always desirable because it reduces the overall computational burden on the forecasting framework. To reduce the number of IMFs obtained from adaptive decomposition methods, they are clubbed into different groups based on their degree of randomness. For this purpose, sample entropy [11] and Lempel–Ziv complexity [17] are used. This helps recombine the IMFs based on the similarity of randomness, thus yielding a lesser number that is subsequently used for prediction purposes.

(ii) **Forecasting Model Selection**: The forecasting models are used in connection with renewable energy time series can be broadly categorized into two types such as AI-based methods and statistical methods. AI-based forecasting methods such as ANN, SVM, LSSVM, and RVM are primarily responsible for forecasting the nonlinear and non-stationary components of the time series. In contrast, statistical autoregressive models predict the linear components. IMFs obtained from the adaptive decomposition process are applied to different forecasting models developed using the above-mentioned methods. Generally, the prediction accuracy of the forecasting model, which is based on both AI and statistical methods, is better in comparison with models based on either AI or statistical methods. Decomposition methods like CEEMDAN and VMD have shown improved performance when used with SVM-based forecasting models. Commonly most of the forecasting models carry out point forecasting. But because of uncertainties associated with time series, probabilistic or interval forecasting is preferable. Most of the EMD-based decompositions are used for deterministic forecasting, whereas EWT, VMD, and LMD-based decomposition methods are used for probabilistic forecasting. EWT-Gaussian process regression [18], and VMD-probabilistic extreme learning machine [19] are prevalent in the literature for probabilistic forecasting.

3.3 Review of Application of Decomposition Methods to Different Time Resolution Data

Most of the forecasting models based on adaptive decomposition methods are used for short-term prediction [20]. Different methods use different time resolution data in preprocessing. It is difficult to draw any conclusion between sampling time and the decomposition method employed. There is no standardized format of sampling time that is being used by different preprocessing methods. It depends on the sampling rate used in the field devices. EMD is a popular decomposition method applied in renewable energy time series. This can be applied to both PV and wind data. This method requires a higher sampling frequency for better performance. At a low sampling rate, the mode decomposition error becomes prominent. Moreover, this EMD method has issues like mode mixing [21], end effect [22], and overshoots and undershoots. LMD method also exhibits mode mixing [23]. ITD method is devoid of mode mixing, end effect but is not suitable for high sampling frequency time series [24]. Similarly EWT, VMD methods are not ideal if the time series is highly non-stationary. If the non-stationarity is low or the time series is almost periodic, then these methods produce comparatively better results.

3.4 Scopes for Improving Forecasting Accuracy

In the literature, there are many adaptive decomposition methods available most of which are applied for analyzing machinery fault diagnosis, structural health monitoring, healthcare monitoring, and seismic applications, to mention a few. Only a selective adaptive decomposition methods are applied in the renewable energy domain: EMD [5], LMD [25], ITD [24], ESMD [26], EWT [27], VMD [28], and SSSA [29]. There are ample scopes for other decomposition methods like LCD [30], ESSD [31], ICD [32], and NMD [33] that are yet to be applied in forecasting renewable energy time series in the preprocessing step. Among all the adaptive decomposition methods, NMD seems to be more suitable because it can be applied to any time series, removing noise greatly compared to other decomposition methods. At the same time, it yields an optimum number of IMFs compared to other adaptive decomposition methods. Hence, the application of NMD as a preprocessing technique for renewable energy time series will improve the prediction performance.

4 Conclusion

This paper accomplished a critical review on applying time series decomposition methods to renewable generation time series in power system applications. Time series decomposition-based data corrections approaches are summarized. Hybridizing strategies for developing better predictions are also enlightened. Challenges of decomposition and selection of optimal IMF set for a compatible forecasting model development are discussed. Finally, the application of adaptive decomposition methods to time series data of different resolution and scopes for improving forecasting accuracy are enlightened.

References

1. Tripathy DS, Prusty BR, Jena D (2020) Short-term PV generation forecasting using quantile regression averaging. In: 2020 IEEE international conference on power systems technology (POWERCON). IEEE, pp 1–6
2. Ranjan KG, Prusty BR, Jena D (2019) Comparison of two data cleaning methods as applied to volatile time-series. In: 2019 international conference on power electronics applications and technology in present energy scenario (PETPES). IEEE, pp 1–6
3. Prusty BR, Jena D (2018) Preprocessing of multi-time instant PV generation data. IEEE Trans Power Syst 33(3):3189–3191
4. Ranjan KG, Prusty BR, Jena D (2021) Review of preprocessing methods for univariate volatile time-series in power system applications. Electr Power Syst Res 191:106685
5. Huang NE, Shen Z, Long SR, Wu MC, Shih HH, Zheng Q, Yen NC, Tung CC, Liu HH (1998) The empirical mode decomposition and the Hilbert spectrum for nonlinear and non-stationary time series analysis. Proc R Soc Lond Ser A Math Phys Eng Sci 454(1971):903–995

6. Feng Z, Zhang D, Zuo MJ (2017) Adaptive mode decomposition methods and their applications in signal analysis for machinery fault diagnosis: a review with examples. IEEE Access 5:24301–24331
7. Guo Z, Zhao W, Lu H, Wang J (2012) Multi-step forecasting for wind speed using a modified EMD-based artificial neural network model. Renew Energy 37(1):241–249
8. He Q, Wang J, Lu H (2018) A hybrid system for short-term wind speed forecasting. Appl Energy 226:756–771
9. Wang J, Yang W, Du P, Li Y (2018) Research and application of a hybrid forecasting framework based on multi-objective optimization for electrical power system. Energy 148:59–78
10. Wang J, Li Y (2019) An innovative hybrid approach for multi-step ahead wind speed prediction. Appl Soft Comput 78:296–309
11. Tian C, Hao Y, Hu J (2018) A novel wind speed forecasting system based on hybrid data preprocessing and multi-objective optimization. Appl Energy 231:301–319
12. Zeng K, He MX (2004) A simple boundary process technique for empirical mode decomposition. In: IGARSS 2004. 2004 IEEE international geoscience and remote sensing symposium, vol 6. IEEE, pp 4258–4261
13. Barnhart BL, Nandage HKW, Eichinger W (2011) Assessing discontinuous data using ensemble empirical mode decomposition. Adv Adapt Data Anal 3(04):483–491
14. Kim D, Kim KO, Oh HS (2012) Extending the scope of empirical mode decomposition by smoothing. EURASIP J Adv Signal Process 2012(1):1–17
15. Park M, Kim D, Oh HS (2014) Quantile-based empirical mode decomposition: an efficient way to decompose noisy signals. IEEE Trans Instrum Meas 64(7):1802–1813
16. Lahmiri S, Boukadoum M (2014) Adjusted empirical mode decomposition with improved performance for signal modeling and prediction. In: 2014 IEEE 5th Latin American symposium on circuits and systems. IEEE, pp 1–4
17. Zhang C, Ding M, Wang W, Bi R, Miao L, Yu H, Liu L (2019) An improved ELM model based on CEEMD-LZC and manifold learning for short-term wind power prediction. IEEE Access 7:121472–121481
18. Hu J, Wang J, Xiao L (2017) A hybrid approach based on the Gaussian process with T-observation model for short-term wind speed forecasts. Renew Energy 114:670–685
19. Qi M, Gao H, Wang L, Xiang Y, Lv L, Liu J (2020) Wind power interval forecasting based on adaptive decomposition and probabilistic regularised extreme learning machine. IET Renew Power Gener 14(16):3181–3191
20. Liu H, Tian HQ, Li YF (2015) Comparison of new hybrid FEEMD-MLP, FEEMD-ANFIS, wavelet packet-MLP and wavelet packet-ANFIS for wind speed predictions. Energy Convers Manag 89:1–11
21. Chu PC, Fan C, Huang N (2012) Compact empirical mode decomposition: an algorithm to reduce mode mixing, end effect, and detrend uncertainty. Adv Adapt Data Anal 4(03):1250017
22. Wu F, Qu L (2008) An improved method for restraining the end effect in empirical mode decomposition and its applications to the fault diagnosis of large rotating machinery. J Sound Vib 314(3–5):586–602
23. Wang L, Liu Z, Miao Q, Zhang X (2018) Complete ensemble local mean decomposition with adaptive noise and its application to fault diagnosis for rolling bearings. Mech Syst Signal Process 106:24–39
24. Frei MG, Osorio I (2007) Intrinsic time-scale decomposition: time-frequency-energy analysis and real-time filtering of non-stationary signals. Proc R Soc A Math Phys Eng Sci 463(2078):321–342
25. Smith JS (2005) The local mean decomposition and its application to EEG perception data. J R Soc Interface 2(5):443–454
26. Wang JL, Li ZJ (2013) Extreme-point symmetric mode decomposition method for data analysis. Adv Adapt Data Anal 5(03):1350015
27. Gilles J (2013) Empirical wavelet transform. IEEE Trans Signal Process 61(16):3999–4010
28. Dragomiretskiy K, Zosso D (2013) Variational mode decomposition. IEEE Trans Signal Process 62(3):531–544

29. Harmouche J, Fourer D, Auger F, Borgnat P, Flandrin P (2017) The sliding singular spectrum analysis: a data-driven nonstationary signal decomposition tool. IEEE Trans Signal Process 66(1):251–263
30. Zheng J, Cheng J, Yang Y (2013) A rolling bearing fault diagnosis approach based on LCD and fuzzy entropy. Mech Mach Theory 70:441–453
31. Li L, Cai H, Jiang Q, Ji H (2019) An empirical signal separation algorithm for multicomponent signals based on linear time-frequency analysis. Mech Syst Signal Process 121:791–809
32. Li Y, Xu M, Wei Y, Huang W (2015) Rotating machine fault diagnosis based on intrinsic characteristic-scale decomposition. Mech Mach Theory 94:9–27
33. Iatsenko D, McClintock PV, Stefanovska A (2015) Nonlinear mode decomposition: a noise-robust, adaptive decomposition method. Phys Rev E 92(3):032916

Author Index

A
Affijulla, Shaik, 247
Alam, Perwez, 81
Anuradhika, Krosuru, 435
Arun Mozhi Devan, P., 811
Ayyarao, Tummala S. L. V., 513

B
Banerjee, Sumit, 15, 625
Bante, Pratik Ramu, 719
Barisal, Ajit Kumar, 353
Barman, P., 575
Behera, Sasmita, 353
Behera, Soudamini, 353
Bhanuchandar, Aratipamula, 95, 135
Bhuyan, Gourab, 369
Bingi, Kishore, 799, 811, 837, 847
Birla, Dinesh, 647
Bisoyi, Sanjiba Kumar, 181, 233, 541
Bordoloi, Sushantha, 575
Buduma, Parusharamulu, 81, 381

C
Chanda, Chandan Kumar, 15, 625
Chauhan, Abhishek, 773
Chippalkatti, Vinod, 121

D
Das, Arun K., 147
Dash, Puja, 435
Dash, Rudra Narayan, 587
Dash, Santanu Kumar, 195
Das, Madan Kumar, 81, 381
Das, Pushpak, 699
Das, Satyabrata, 847
Deepika, Padiyar Dharani, 221
Dhaked, Dheeraj Kumar, 647
Dharmalingam, Sathish, 733
Dinesh, L., 513
Dishashree, T. N., 121

G
Ganthia, Bibhu Prasad, 423, 497
Garg, Harsh, 759
Geetha, R. S., 559
George, Anna Merine, 759
Ghoshal, Snehashis, 15
Ghosh, Arnab, 67
Gopal, Yatindra, 105
Gurugubelli, Vikash, 67

H
Hari Krishna, B., 259
Hussin, Fawnizu Azmadi, 811

I
Ibrahim, Rosdiazli, 811

J
Jain, Nimish, 837
Jaiswal, Rishabh, 825
Jena, Ashutosh, 483
Jena, Chitralekha, 465

G. Panda et al. (eds.), *Sustainable Energy and Technological Advancements*,
Advances in Sustainability Science and Technology,
https://doi.org/10.1007/978-981-16-9033-4

Jena, Debashisha, 837
Jena, Smrutisikha, 497
Jha, Vandana, 43
Jithin, S., 637

K
Kabat, Subash Ranjan, 423
Kakade, S. M., 709
Kandali, Aditya Bihar, 279
Karkun, Mohammad Suhel, 733
Khare, Rishabh, 541
Krishna, Aviral, 233
Krishna, Swathi., 29
Kubendran, G., 121
Kulkarni, R. S., 709
Kumar, Aman, 675
Kumar, Ashish, 395
Kumari, Pallavi, 181
Kumar, Priye Ranjan, 825
Kumar, Subhash, 699
Kurian, Ciji Pearl, 759

L
Lahon, Pranobjyoti, 279

M
Mahakur, Arabinda, 611
Maity, Deblina, 625
Majhi, Somanath, 53
Mallajoshula, Ravikanth, 411
Manjari, Kamakshi, 53
Manoj, Vasupalli, 307, 513
Meher, L., 147
Mehta, R. K., 267, 597
Mini, V. P., 785
Mishra, Sthitprajna, 497
Mishra, Sukumar, 81, 381
Mohammadi, Zoaya, 687
Mohan, Akhila., 163
Mohanty, Debidasi, 611
Murthy, Bhagwan K., 95, 135

N
Naidu, I. E. S., 411
Naik, Namrata, 353
Nair, Divya S., 1
Nandkeolyar, Shobhit, 339, 449
Narendra Babu, P., 181, 675
Nayak, Byamakesh, 587

P
Pahadasingh, Sunita, 465
Panda, Anup Kumar, 67
Panda, Gayadhar, 181, 195, 209, 247, 279, 293, 321, 381, 675, 687, 699, 799, 847
Panda, Kaibalya Prasad, 105, 181, 675, 799, 847
Panda, Sidhartha, 293
Pande, V. N., 709
Panigrahi, Chinmoy Kumar, 423, 465
Pathak, Luv, 541
Patowary, Moushumi, 279
Pinto, Smitha Joyce, 687
Pothauri, Manidra, 195
Pradeep, G. V., 105
Pradhan, D., 147
Prince, Satyavarta Kumar, 247, 675
Priyadarshini, Subhashree, 465
Puhan, Pratap Sekhar, 147, 195, 221, 395, 661, 747

R
Rahul, K. A., 525
Rajanarayan Prusty, B, 799, 811, 837, 847
Rai, Aysuh Raman, 233
Rajeev, T., 1, 525, 637
Rajesh, D., 259
Raj, Himanshu, 825
Rakesh, B., 259
Ramakrishna, Nuvvula S. S., 307, 513
Ramarao, G., 259
Ranjan, Chitra, 233
Ranjan, Kumar Gaurav, 837
Ravikumar, A., 259
Ravikumar, N. V. A., 307
Ray, Pravat Kumar, 147, 195, 339, 395, 449, 661, 747
Rout, Bidyadhar, 293, 483
Roy, D. S., 699
Roy, O. P., 267, 597
Roy, Sourabh Prakash, 267, 597

S
Saha, Nutan, 293, 483
Sahoo, Ashwin Kumar, 43
Sahoo, Dillip Ku., 293
Sahoo, Premananda, 661
Sahoo, Satyabrata, 321
Sahoo, Subham Kumar, 293
Sahu, Sangeeta, 587
Samal, Sidhartha Kumar, 497

Samina, T., 163
Sen, Priyanka, 43
Shadangi, Pushpanjali, 209
Sharma, Ashwani Kumar, 381
Shereef, R. M., 29
Shilpashree, S., 559
Shubham, 267, 597
Singh, Abhinav Kumar, 267, 541, 597
Singh, Anushka, 233
Singh, Bhoopendra Kumar, 121
Singh, Ksh. Milan, 773
Singh, Mayank, 647
Singh, Piyush Pratap, 825
Singh, Sarthak, 541
Sivadas, Anju P., 785
Sravan, C., 759
Sreejaya, P., 525
Srikanth, S., 719
Swain, Sushree Diptimayee, 209

T
Talukdar, Bani Kanta, 369
Terang, Parveen Poon, 233, 541
Thokchom, Surmila, 687
Thombare, Shubham, 709
Thosar, Archana G., 719
Tonmoy, Ifthakhar Mahmud, 675

U
Usha, A., 121

V
Valiveti, Nikhil Sai Rama, 339
Vemuri, Emmanuel, 675
Vijay Kumar, Y. N., 105